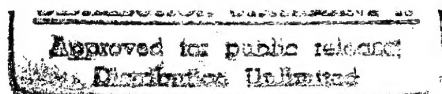AGARD-CP-600 Vol. 3

AGARD

ADVISORY GROUP FOR AEROSPACE RESEARCH & DEVELOPMENT

7 RUE ANCELLE, 92200 NEUILLY-SUR-SEINE, FRANCE

AGARD CONFERENCE PROCEEDINGS 600

Future Aerospace Technology in the Service of the Alliance
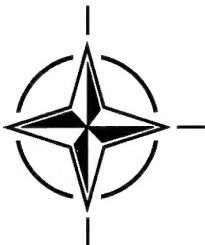(les Technologies aéronautiques et spatiales du futur au service de l'Alliance atlantique)

Volume 3:
   Sustained Hypersonic Flight
   (le Vol en croisière hypersonique)

Unclassified papers presented at the AGARD Symposium held at the Ecole Polytechnique, Palaiseau, France, 14-17 April 1997.

19980128 087

NORTH ATLANTIC TREATY ORGANIZATION

DTIC QUALITY INSPECTED 3

Published December 1997

Distribution and Availability on Back Cover

AGARD

ADVISORY GROUP FOR AEROSPACE RESEARCH & DEVELOPMENT

7 RUE ANCELLE, 92200 NEUILLY-SUR-SEINE, FRANCE

AGARD CONFERENCE PROCEEDINGS 600

Future Aerospace Technology in the Service of the Alliance

(les Technologies aéronautiques et spatiales du futur au service de l'Alliance atlantique)

Volume 3:
   Sustained Hypersonic Flight
   (le Vol en croisière hypersonique)

The other volumes contain:

Volume 1:
   Affordable Combat Aircraft
   (le Coût de possession des avions de combat)
   and
   Plenary Sessions:
      Future Directions in Aerospace Systems
      (Futures orientations pour les systèmes aéronautiques et spatiaux)
      Future NATO trends and Mission Scenarios
      (Tendances et scénarios futurs des missions de l'OTAN)
      Human Machine Interaction in the Future
      (Interactions homme-machine du futur)

Volume 2:
   Mission Systems Technologies
   (les Technologies des systèmes de conduite de mission)

Unclassified papers presented at the AGARD Symposium held at the Ecole Polytechnique, Palaiseau, France, 14-17 April 1997.

North Atlantic Treaty Organization
Organisation du Traité de l'Atlantique Nord

DTIC QUALITY INSPECTED 3

The Mission of AGARD

According to its Charter, the mission of AGARD is to bring together the leading personalities of the NATO nations in the fields of science and technology relating to aerospace for the following purposes:

— Recommending effective ways for the member nations to use their research and development capabilities for the common benefit of the NATO community;

— Providing scientific and technical advice and assistance to the Military Committee in the field of aerospace research and development (with particular regard to its military application);

— Continuously stimulating advances in the aerospace sciences relevant to strengthening the common defence posture;

— Improving the co-operation among member nations in aerospace research and development;

— Exchange of scientific and technical information;

— Providing assistance to member nations for the purpose of increasing their scientific and technical potential;

— Rendering scientific and technical assistance, as requested, to other NATO bodies and to member nations in connection with research and development problems in the aerospace field.

The highest authority within AGARD is the National Delegates Board consisting of officially appointed senior representatives from each member nation. The mission of AGARD is carried out through the Panels which are composed of experts appointed by the National Delegates, the Consultant and Exchange Programme and the Aerospace Applications Studies Programme. The results of AGARD work are reported to the member nations and the NATO Authorities through the AGARD series of publications of which this is one.

Participation in AGARD activities is by invitation only and is normally limited to citizens of the NATO nations.

Sustained Hypersonic Flight

(AGARD CP-600 Vol. 3)

Executive Summary

Sustained Hypersonic Flight capability is envisioned for several future military and civilian applications, such as long range immediate reaction reconnaissance, high speed interception of air targets, long range precision strike against hardened or time critical targets, and access to space. The inherent reduction in time-to-target and low vulnerability will permit new operational tactics.

The symposium outlined mission needs and operational scenarios for hypersonic vehicles. Addressed were: Technological issues and challenges in external hypersonic aerodynamics and design, propulsion and engine/airframe integration, military ramjet applications, overall system design including structures and materials development needs, and test facilities.

Ground based test facilities cannot provide full simulation at Mach numbers above 5. Therefore, the use of Computational Fluid Dynamics design tools is essential. For routine use of the computational tools in analysis, design and optimization, it is necessary to reduce the time for the entire computational process by two orders of magnitude. Hypersonic boundary layer transition remains a critical design issue because of the important impact on engine drag and on heating, which can affect the choice of materials and thermal protection systems. In addition, reliable prediction of scramjet net thrust is an absolute must in resolving hypersonic air breathing vehicle design issues. Due to current facility and computational shortfalls, the development of future hypersonic flight systems requires research flight tests in the technology areas of boundary layer transition and air-breathing propulsion engine performance.

For sustained hypersonic flight beyond Mach 6, the supersonic combustion ramjet (scramjet) engine is the only choice for the near future. Only this air-breathing concept offers a significant promise of large reductions in required propellant fractions, increased payload fractions, and reduced size vehicles, together with a foreseeable technological feasibility. Airframe/engine integration, combustor design and thermal management are the predominant engineering tasks. Fuels - hydrogen or hydrocarbon - must be matched to the operational needs of military or civil use. Experience in existing ramjet propelled missiles capable of speeds up to Mach 4 can support the development effort.

The potential mission and cost benefits of sustained hypersonic flight to both military and civil applications are tremendous. From the budget point of view, the possibility of sharing development costs between military and civil programs offers a specific advantage.

Vol hypersonique soutenu
(AGARD CP-600 Vol. 3)

Synthèse

Le vol hypersonique soutenu est envisagé pour différentes applications civiles et militaires futures, et notamment la reconnaissance lointaine de réaction immédiate, l'interception à grande vitesse de cibles aériennes, la frappe de précision à grande distance contre des cibles durcies et contre des cibles à temps de démasquage réduit, ainsi que l'accès à l'espace. La réduction du temps nécessaire pour arriver sur l'objectif, ainsi que la faible vulnérabilité, permettront d'adopter de nouvelles tactiques opérationnelles.

Le symposium a souligné les exigences des missions et les divers scénarios opérationnels relatifs aux véhicules hypersoniques. Les sujets suivants ont été évoqués : les problèmes technologiques et les défis en matière de conception aérodynamique hypersonique externe, la propulsion et l'intégration moteur/cellule, les applications aux statoréacteurs militaires, la conception globale des systèmes y compris les exigences en matière de structures et matériaux, et les installations d'essais.

Les installations d'essais au sol ne peuvent pas assurer la simulation intégrale aux nombres de Mach supérieurs à 5. La mise en œuvre d'outils pour la conception à l'aide de l'aérodynamique numérique est, par conséquent, indispensable. Cependant, le temps de cycle du calcul doit être réduit de deux ordres de grandeur si l'on veut utiliser ces outils pour des opérations courantes d'analyse, de conception et d'optimisation. La transition de la couche limite hypersonique reste l'un des points critiques de la conception CFD en raison de son impact sensible sur la traînée moteur et l'échauffement, qui peut, à son tour, influencer le choix des matériaux et des systèmes de protection thermique. En outre, il est absolument indispensable de pouvoir prédire de façon régulière et fiable la poussée nette des statoréacteurs si l'on veut résoudre les problèmes qui se posent pour la conception des véhicules aérobies hypersoniques. Vu les insuffisances actuelles au niveau des installations et des moyens de calcul, le développement des futurs systèmes de vol hypersonique dépendra de la possibilité de réaliser des essais en vol dans certains domaines technologiques, à savoir la transition de la couche limite et les performances des propulseurs aérobies.

Dans un avenir proche, le statoréacteur représente le seul choix pour le vol hypersonique soutenu au delà de Mach 6. Seul ce concept aérobie offre, à la fois, des réductions potentielles suffisamment importantes pour réduire la part du carburant et augmenter la charge utile et des véhicules de dimensions réduites, compte tenu de la faisabilité technologique prévisible. Les défis techniques majeurs sont l'intégration cellule/moteur, la conception des chambres de combustion et la gestion thermique. Les carburants - l'hydrogène ou les hydrocarbures - doivent correspondre aux besoins opérationnels civils et militaires. Ces efforts de développement pourront tirer un large profit de l'expérience acquise sur les missiles à statoréacteur qui atteignent des vitesses allant jusqu'à Mach 4.

Les avantages opérationnels et économiques offerts par le vol hypersonique soutenu dans le cadre des applications civiles et militaires sont énormes. Du point de vue budgétaire, la possibilité de répartir les coûts de développement entre les programmes civils et militaires est particulièrement intéressante.

Contents

* Published in Classified Supplement

---

* Published in Classified Supplement

Preface

In the Spring of 1997, AGARD (NATO's Advisory Group for Aerospace Research and Development), which was celebrating its 45 years of dedication to the improvement of military and civilian aerospace research and development in the NATO nations, held a major conference on "Future Aerospace Technology in the Service of the Alliance" at the Ecole Polytechnique at Palaiseau near Paris, France. The conference comprised three main parallel symposia, three forward-looking plenary sessions, and a presentation of the results of a two-year visionary study entitled "Aerospace 2020"*. Each symposium was organised by two AGARD Panels, with contributions from the Aerospace Medical Panel.

The papers presented at the conference are contained in this and three other volumes, one of them classified.

This volume contains the papers from the symposium on **"Sustained Hypersonic Flight"**, which was organised by the 'Fluid Dynamics' and 'Propulsion and Energetics' Panels (FDP and PEP). It had overview papers on:

- Mission Needs and Operational Scenarios for Hypersonic Vehicles
- Vehicle Configurations and Aerothermodynamic Challenges

and sessions on:

- Propulsion for Hypersonic Flight
- External Hypersonic Aerodynamics and Design Challenges
- Military Ramjet Applications
- Test Facilities for Ramjets
- Configurational Design and Flight Validation
- Engine/Airframe Integration
- System Challenges

Volume 1 contains the papers from the three plenary sessions:

"Future Directions in Aerospace Systems"
"Future NATO Trends and Mission Scenarios"
"Human Machine Interaction in the Future";

and the papers on "Affordable Combat Aircraft"

Volume 2 contains the papers on "Mission Systems Technologies".

*The results of Aerospace 2020 are contained in an Advisory Report, AR-360, "Aerospace 2020". Vol. I is the Summary, Vol. II contains the full text of the report, and Vol. III contains supporting papers. It is planned to issue translations into French of volumes I and II later.

Recent Publications of
the Fluid Dynamics Panel

AGARDOGRAPHS (AG)

Turbulent Boundary Layers in Subsonic and Supersonic Flow
AGARD AG-335, July 1996

Computational Aerodynamics Based on the Euler Equations
AGARD AG-325, September 1994

Scale Effects on Aircraft and Weapon Aerodynamics
AGARD AG-323 (E), July 1994

Design and Testing of High-Performance Parachutes
AGARD AG-319, November 1991

Experimental Techniques in the Field of Low Density Aerodynamics
AGARD AG-318 (E), April 1991

Techniques Expérimentales Liées à l'Aérodynamique à Basse Densité
AGARD AG-318 (FR), April 1990

A Survey of Measurements and Measuring Techniques in Rapidly Distorted Compressible Turbulent Boundary Layers
AGARD AG-315, May 1989

Reynolds Number Effects in Transonic Flows
AGARD AG-303, December 1988

REPORTS (R)

Aerothermodynamics of Planetary Entry Capsule
AGARD R-808, Special Course Notes, May 1997

Turbulence in Compressible Flow
AGARD R-819, Special Course Notes, May 1997

Advances in Cryogenic Wind Tunnel Technology
AGARD R-812, Special Course Notes, January 1997

Aerothermodynamics and Propulsion Integration for Hypersonic Vehicles
AGARD R-813, Special Course Notes, October 1996

Parallel Computing in CFD
AGARD R-807, Special Course Notes, October 1995

Optimum Design Methods for Aerodynamics
AGARD R-803, Special Course Notes, November 1994

Missile Aerodynamics
AGARD R-804, Special Course Notes, May 1994

Progress in Transition Modelling
AGARD R-793, Special Course Notes, April 1994

Shock-Wave/Boundary-Layer Interactions in Supersonic and Hypersonic Flows
AGARD R-792, Special Course Notes, August 1993

Unstructured Grid Methods for Advection Dominated Flows
AGARD R-787, Special Course Notes, May 1992

Skin Friction Drag Reduction
AGARD R-786, Special Course Notes, March 1992

Engineering Methods in Aerodynamic Analysis and Design of Aircraft
AGARD R-783, Special Course Notes, January 1992

ADVISORY REPORTS (AR)

Sonic nozzles for Mass Flows Measurements and thrust Calibration
AGARD AR-321, Report of WG-19, June 1997

Cooperative Programme on Dynamic Wind Tunnel Experiments for Manoeuvering Aircraft
AGARD AR-305, Report of WG-16, October 1996

Hypersonic Experimental and Computational Capability, Improvement and Validation
AGARD AR-319, Vol. I, Report of WG-18, May 1996

Aerodynamics of 3-D Aircraft Afterbodies
AGARD AR-318, Report of WG-17, September 1995

A Selection of Experimental Test Cases for the Validation of CFD Codes
AGARD AR-303, Vols. I and II, Report of WG-14, August 1994

Quality Assessment for Wind Tunnel Testing
AGARD AR-304, Report of WG-15, July 1994

Air Intakes of High Speed Vehicles
AGARD AR-270, Report of WG-13, September 1991

Appraisal of the Suitability of Turbulence Models in Flow Calculations
AGARD AR-291, Technical Status Review, July 1991

Rotary-Balance Testing for Aircraft Dynamics
AGARD AR-265, Report of WG11, December 1990

Calculation of 3D Separated Turbulent Flows in Boundary Layer Limit
AGARD AR-255, Report of WG10, May 1990

Adaptive Wind Tunnel Walls: Technology and Applications
AGARD AR-269, Report of WG12, April 1990

CONFERENCE PROCEEDINGS (CP)

The Aerodynamics of Wind Tunnels and their Components
AGARD CP-585, June 1997

The Characterization & Modification of Wakes from Lifting Vehicles in Fluids
AGARD CP-584, November 1996

Progress and Challenges in CFD Methods and Algorithms
AGARD CP-578, April 1996

Aerodynamics of Store Integration and Separation
AGARD CP-570, February 1996

Aerodynamics and Aeroacoustics of Rotorcraft
AGARD CP-552, August 1995

Application of Direct and Large Eddy Simulation to Transition and Turbulence
AGARD CP-551, December 1994

Wall Interference, Support Interference, and Flow Field Measurements
AGARD CP-535, July 1994

Computational and Experimental Assessment of Jets in Cross Flow
AGARD CP-534, November 1993

High-Lift System Aerodynamics
AGARD CP-515, September 1993

Theoretical and Experimental Methods in Hypersonic Flows
AGARD CP-514, April 1993

Aerodynamic Engine/Airframe Integration for High Performance Aircraft and Missiles
AGARD CP-498, September 1992

Effects of Adverse Weather on Aerodynamics
AGARD CP-496, December 1991

Manoeuvering Aerodynamics
AGARD CP-497, November 1991

Vortex Flow Aerodynamics
AGARD CP-494, July 1991

Missile Aerodynamics
AGARD CP-493, October 1990

Aerodynamics of Combat Aircraft Controls and of Ground Effects
AGARD CP-465, April 1990

Computational Methods for Aerodynamic Design (Inverse) and Optimization
AGARD CP-463, March 1990

Applications of Mesh Generation to Complex 3-D Configurations
AGARD CP-464, March 1990

Fluid Dynamics of Three-Dimensional Turbulent Shear Flows and Transition
AGARD CP-438, April 1989

Validation of Computational Fluid Dynamics
AGARD CP-437, December 1988

Aerodynamic Data Accuracy and Quality: Requirements and Capabilities in Wind Tunnel Testing
AGARD CP-429, July 1988

Aerodynamics of Hypersonic Lifting Vehicles
AGARD CP-428, November 1987

Recent Publications of
the Propulsion and Energetics Panel

CONFERENCE PROCEEDINGS (CP)

Advanced Instrumentation for Aero Engine Components
AGARD CP 399, November 1986

Engine Response to Distorted Inflow Conditions
AGARD CP 400, March 1987

Transonic and Supersonic Phenomena in Turbomachines
AGARD CP 401, March 1987

Advanced Technology for Aero Engine Components
AGARD CP 421, September 1987

Combustion and Fuels in Gas Turbine Engines
AGARD CP 422, June 1988

Engine Condition Monitoring — Technology and Experience
AGARD CP 448, October 1988

Application of Advanced Material for Turbomachinery and Rocket Propulsion
AGARD CP 449, March 1989

Combustion Instabilities in Liquid-Fuelled Propulsion Systems
AGARD CP 450, April 1989

Aircraft Fire Safety
AGARD CP 467, October 1989

Unsteady Aerodynamic Phenomena in Turbomachines
AGARD CP 468, February 1990

Secondary Flows in Turbomachines
AGARD CP 469, February 1990

Hypersonic Combined Cycle Propulsion
AGARD CP 479, December 1990

Low Temperature Environment Operations of Turboengines (Design and User's Problems)
AGARD CP 480, May 1991

CFD Techniques for Propulsion Applications
AGARD CP 510, February 1992

Insensitive Munitions
AGARD CP 511, July 1992

Combat Aircraft Noise
AGARD CP 512, April 1992

Airbreathing Propulsion for Missiles and Projectiles
AGARD CP 526, September 1992

Heat Transfer and Cooling in Gas Turbines
AGARD CP 527, February 1993

Fuels and Combustion Technology for Advanced Aircraft Engines
AGARD CP 536, September 1993

Technology Requirements for Small Gas Turbines
AGARD CP 537, March 1994

Erosion, Corrosion and Foreign Object Damage Effects in Gas Turbines
AGARD CP 558, February 1995

Environmental Aspects of Rocket and Gun Propulsion
AGARD CP 559, February 1995

Loss Mechanisms and Unsteady Flows in Turbomachines
AGARD CP 571, January 1996

Advanced Aero-Engine Concepts and Controls
AGARD CP 572, June 1996

Service Life of Solid Propellant Systems
AGARD CP 586, May 1997

Aircraft Fire Safety
AGARD CP 587, September 1997

ADVISORY REPORTS (AR)

Producibility and Cost Studies of Aviation Kerosines *(Results of Working Group 16)*
AGARD AR 227, June 1985

Performance of Rocket Motors with Metallized Propellants *(Results of Working Group 17)*
AGARD AR 230, September 1986

Recommended Practices for Measurement of Gas Path Pressures and Temperatures for Performance Assessment of Aircraft Turbine Engines and Components *(Results of Working Group 19)*
AGARD AR 245, June 1990

The Uniform Engine Test Programme *(Results of Working Group 15)*
AGARD AR 248, February 1990

Test Cases for Computation of Internal Flows in Aero Engine Components *(Results of Working Group 18)*
AGARD AR 275, July 1990

Test Cases for Engine Life Assessment Technology *(Results of Working Group 20)*
AGARD AR 308, September 1992

Terminology and Assessment Methods of Solid Propellant Rocket Exhaust Signatures *(Results of Working Group 21)*
AGARD AR 287, February 1993

Guide to the Measurement of the Transient Performance of Aircraft Turbine Engines and Components *(Results of Working Group 23)*
AGARD AR 320, March 1994

Experimental and Analytical Methods for the Determination of Connected — Pipe Ramjet and Ducted Rocket Internal Performance *(Results of Working Group 22)*
AGARD AR 323, July 1994

Recommended Practices for the Assessment of the Effects of Atmospheric Water Ingestion on the Performance and Operability of Gas Turbine Engines *(Results of Working Group 24)*
AGARD AR 332, September 1995

LECTURE SERIES (LS)

Design Methods Used in Solid Rocket Motors
AGARD LS 150, April 1987
AGARD LS 150 (Revised), April 1988

Blading Design for Axial Turbomachines
AGARD LS 167, June 1989

Comparative Engine Performance Measurements
AGARD LS 169, May 1990

Combustion of Solid Propellants
AGARD LS 180, July 1991

Steady and Transient Performance Prediction of Gas Turbine Engines
AGARD LS 183, May 1992

Rocket Motor Plume Technology
AGARD LS 188, June 1993

Research and Development of Ram/Scramjets and Turboramjets in Russia
AGARD LS 194, December 1993

Turbomachinery Design Using CFD
AGARD LS 195, May 1994

Mathematical Models of Gas Turbine Engines and their Components
AGARD LS 198, December 1994

AGARDOGRAPHS (AG)

Measurement Uncertainty within the Uniform Engine Test Programme
AGARD AG 307, May 1989

Hazard Studies for Solid Propellant Rocket Motors
AGARD AG 316, September 1990

Advanced Methods for Cascade Testing
AGARD AG 328, August 1993

REPORTS (R)

Rotorcraft Drivetrain Life Safety and Reliability
AGARD R 775, June 1990

Impact Study on the use of JET A Fuel in Military Aircraft during Operations in Europe
AGARD R 801, January 1997

The Single Fuel Concept and Operation Desert Shield/Storm
AGARD R 810, January 1997 *(NATO Unclassified)*

Propulsion and Energy Issues for the 21st Century
AGARD R 824, March 1997

Programme Committee

Prof. C. Çiray, Chairman
Aeronautical Eng. Department
Middle East Technical University
Inonu Bulvari PK: 06531 ANKARA

Fluid Dynamics Panel

Mr C. Dujarric
Future Launchers Office
ESA Headquarters
8-10, rue Mario Nikis
75015 Paris, France

Mr H. Hollanders
Head of Aerodynamics Dept
Aerospatiale, Space & Defense
Route de Verneuil, BP 2
78133 Les Mureaux Cedex, France

Prof. R. Kind
Dept of Mechanical and
Aerospace Engineering
Carleton University
Ottawa, Ontario K1S 5B6, Canada

Mr R. Lacau
Aerospatiale Missiles (E/ECN)
Centre des Gatines
91370 Verrieres le Buisson Cedex, France

Mr J. Muylaert
ESTEC
Aerothermodynamic Section
Postbus 299
2200 AG Noordwijk, Netherlands

Dr A. Panaras
Consulting Engineer
P.O. Box 64053
Athens 157 10, Greece

Prof. D. Poll
Head of the College of Aeronautics
Cranfield University, Cranfield
Bedford MK43 OAL, United Kingdom

Dr Helen Reed
Arizona State University
Mechanical & Aerospace Engineering
Box 876106
Tempe, AZ 85287-6106, United States

Prof. M. Rodriguez
Head Fluid Dynamics Section
SENER-Parque Technologico de Madrid
c/Severo Ochoa, N° 4 - Edificio 2
28760 Tres Cantos - Madrid, Spain

Prof. F. Sabetta
Universsita di Roma "La Sapienza"
Dipartimentao di Meccanica e Aeronautica
Via Eudossiana 18
00184 Roma, Italy

Dipl. Ing. P. Sacher
Daimler Benz Aerospace
LMLE3
Postfach 801160
D-80663 Munchen, Germany

Prof. J. van Ingen
Dept of Aerospace Engineering
Delft University of Technology
Kluyverweg 1
2629 HS Delft, Netherlands

Panel Executive

Mr J.K. Molloy
AGARD/FDP
7 rue Ancelle
92200 Neuilly-sur-Seine
France

tel: +33 (1) 55 61 22 70/72
fax: +33 (1) 55 61 22 98/99

Propulsion and Energetics Panel

Chairman: Prof. R.S. Fletcher
Deputy Vice Chancellor
Cranfield Institute of Technology
Cranfield, Bedford MK43 OAL
United Kingdom

Deputy Chairman: Mr. Don Rudnitski
Head, Engine Laboratory
Institute for Aerospace Research
National Research Council of Canada
Ottawa, Ontario K1A 0R6

Mr. P. Kuentzmann (Chairman)
Directeur Scientifique de l'Energetique
ONERA, BP 72
92322 Chatillon, France

Mr. Gonzalo Moreno Labata
Subdirector de Cooperacion
Cientifica y Technologia - INTA
Carretera de Ajalvir km.4
28850 Torrejon de Ardoz
Spain

Mr. Ivan Sollien
Norwegian Defence Research Establishment
P.O. Box 25
N-2007 Kjeller, Norway

Mr. L. Meyer
Deputy Director, Propulsion Directorate
OL-AC PL/RK
5 Pollux Drive
Edwards AFB, CA 93524 7084
United States

ICA P. Lusseyran
DGA - Direction des Missiles et de l'Espace
00460 Armees
France

Prof. L. De Luca
Politecnico di Milano
Dipartimento di Energetica
Piazza Leonardo da Vinci 32
20133 Milano
Italy

Mr. H.-L. Besser
Bayern-Chemie GmbH
Postfach 1131
84544 Aschau a. Inn
Germany

Dr. C. Russo
Director of Aeronautics
NASA Lewis Research Center
MS 3-8
21000 Brookpark Road
Cleveland, Ohio 44135
United States

Mr. A. Whitehouse
Manager, Design Section
Royal Ordnance plc
Rocket Motors Division
Summerfield, Kidderminister
Worcestershire DV11 7RZ
United Kingdom

Host Nation Coordinator
Dr. G. Meauze

Panel Executive

Dr P. Tonn
AGARD/PEP
7 rue Ancelle
92200 Neuilly-sur-Seine
France

tel: +33 (1) 55 61 22 85/87
fax: +33 (1) 55 61 22 98/99

Quelques réflexions sur les missions militaires
et les scenarios opérationnels relatifs aux véhicules hypersoniques
-----
par Ph. CAZIN
ONERA
BP 72
92322 CHATILLON CEDEX
FRANCE

SOMMAIRE

On examine l'intérêt du vol propulsé dans l'atmosphère, à vitesse hypersonique, pour certaines applications militaires telles que:

1) les missiles d'attaque au sol ou en surface à grande distance, pour lesquels la grande vitesse améliore les capacités de pénétrtion des défenses,

2) les drones de reconnaissance et de surveillance,

3) les missiles air-air très rapides, capables d'intercepter, soit des missiles balistiques en phase accélérée, soit des cibles aériennes de haute valeur à grande distance,

4) les systèmes de défense sol ou surface/air à longue portée,

5) l'accès plus rapide et plus souple à l'espace, en particulier en temps de crise.

Deux aspects du problème sont étudiés:
- la supériorité que la possession de tels véhicules hypersoniques apportera à l'OTAN, en évaluant leurs avantages et inconvénients par rapport aux systèmes qui utilisent d'autres filières technologiques,
- les menaces que pourraient faire peser sur l'OTAN des adversaires possesseurs de tels véhicules.

INTRODUCTION

Lors du symposium d'avril 1997 consacré aux technologies aérospatiales futures, l'AGARD a choisi d'examiner les perspectives militaires offertes à l'OTAN, à l'horizon 2020, par le vol sustenté à vitesse hypersonique.

C'est un thème qui est étudié depuis le milieu de ce siècle dans de nombreux pays, mais qui n'a pas encore produit de matériels militaires opérationnels.

A l'horizon 2020, les perspectives peuvent changer par suite, d'une part de la meilleure connaissance des phénomènes liés au vol hypersonique dans l'atmosphère (navette spatiale américaine), d'autre part de la progression des technologies permettant aux missiles de voler en croisière jusqu'à Mach 4 ou 5 (propulsion par statoréacteur).

Ces acquis techniques permettent ainsi d'envisager des véhicules capables d'un vol sustenté à vitesse hypersonique (c'est-à-dire au-delà de Mach 5), et bénéficiant d'une efficacité militaire accrue en terme de réduction du temps de vol ou d'amélioration de la capacité de pénétration des défenses. Cet avantage de la haute vitesse sera primordial lorsque les systèmes de détection auront fait des progrès tels que les qualités de furtivité de l'attaquant ne seront plus un atout déterminant.

Si aujourd'hui on se contente de voler dans l'atmosphère à vitesse subsonique ou supersonique, en s'échappant de l'atmosphère pour atteindre l'hypersonique, c'est bien en raison des immenses difficultés technologiques rencontrées.

Mais ces possibilités font rêver ! C'est pourquoi on va s'efforcer ici de passer du rêve d'aujourd'hui à la réalité de demain ... avec le risque d'erreur inhérent à toute réflexion prospective, en examinant quelques applications militaires de ces technologies hypersoniques qui paraissent prometteuses.

Parmi celles-ci :

1) L'attaque au sol ou en surface à grande distance
2) Les drones de reconnaissance et de surveillance
3) L'interception aéroportée à grande distance
4) La défense sol ou surface-air à longue portée
5) L'accès rapide et souple à l'espace.

1 - ATTAQUE AU SOL OU EN SURFACE A GRANDE DISTANCE

L'utilisation d'un missile capable d'une vitesse de croisière élevée (Mach 8) en altitude présente plusieurs avantages :

1.1 - **Le temps de vol** pour atteindre la cible peut être :

- bien sûr, plus court que celui d'un missile de croisière subsonique,
- mais aussi, plus court que celui d'un missile balistique, pour des portées inférieures à 1000 km (Fig.1).

Ce *temps de vol réduit* est particulièrement favorable :

- pour l'attaque des cibles mobiles (navires),
- pour limiter l'erreur de navigation.

En effet la réduction du temps de vol permet de limiter l'erreur de navigation inertielle essentiellement due aux dérives gyrométriques, et proportionnelle à $(T_{vol})^3$.

La figure 2 illustre le fait que, si l'on accepte une erreur de navigation de 1000 m avec un missile volant à Mach 3, la portée devra rester inférieure à 1000 km, alors qu'avec un missile Mach 8, on peut envisager une portée atteignant 2200 km. Ceci suppose une très bonne initialisation de la centrale et l'emploi de gyromètres de la classe 0,1 °/h de haute performance et donc de technologie relativement coûteuse.

En résumé, l'augmentation de la vitesse de croisière permet, à précision donnée, d'augmenter la portée accessible d'une arme sans utiliser de dispositifs actifs de recalage, facteurs d'indiscrétion.

Mais si une précision décamétrique, voire métrique, est requise l'utilisation du GPS et d'un guidage terminal de précision, par exemple au moyen d'un autodirecteur radar ou infrarouge, est impérativement nécessaire.

Un compromis devra alors être trouvé entre la précision du recalage de la navigation en croisière, la portée d'accrochage de l'autodirecteur et la capacité de manoeuvre du missile.

Exemple :
La portée d'accrochage nécessaire doit être telle que la durée d'autoguidage soit au moins égale à 10 fois la constante de temps du missile piloté, à savoir environ 3 secondes.

La portée d'accrochage est égale à 3 V_M . Si V_M = 1200 m/s, on aura P = 3600 m

En supposant que le missile ait une capacité de manoeuvre de 15 g, sa capacité maximale de rattrapage d'une erreur (navigation ou mouvement cible) sera :
$$X = 1/2 \, Gt^2 = 675 \text{ m}$$

Ainsi, à performance d'autodirecteur donnée, on peut être amené, soit pour améliorer la capacité de rattrapage, soit pour limiter les effets thermiques sur le radome ou l'irdome, à limiter la vitesse du missile en phase finale à basse altitude.

1.2 - **Les capacités de pénétration d'une défense** adverse peuvent être excellentes dans les différentes phases du vol. Ainsi :

- un missile hypersonique pourra pénétrer les défenses de barrage en passant au-dessus du plafond des sol-air les plus avancés. Ainsi la figure 3 montre l'altitude de croisière envisageable pour le missile attaquant en fonction du Mach de vol, ainsi que le plafond utile de deux types de missiles sol-air, soit Mach 5/6, soit Mach 8 (improved SAM).

- En ce qui concerne la manoeuvrabilité terminale, la vitesse du missile attaquant

permet une supériorité en facteur de charge sur le missile défenseur. Ainsi la figure 4 montre la manoeuvrabilité maximale du missile de croisière selon sa vitesse, en comparaison de celle du missile intercepteur, sachant que ce dernier doit avoir plus de 2 fois la manoeuvrabilité de l'assaillant pour que l'interception soit possible avec une forte probabilité.

D'une façon générale, un missile capable d'un vol de croisière hypersonique peut mettre en difficulté la défense ; en effet :

- il passera au-dessous des zones d'action des ABM exo-atmosphériques,
- il passera au-dessus du plafond des intercepteurs endo-atmosphériques,
- sa grande vitesse entraînera une diminution des délais de réaction de la défense, et donc risquera de condamner les politiques TCT (Tir/Contrôle/Tir). L'imprévisibilité de sa trajectoire aura le même effet (en comparaison avec le cas d'un missile balistique). Enfin, par rapport à un missile balistique, un missile hypersonique sera détecté plus tard par les radars au sol, car plus bas sur l'horizon[*].
- à basse altitude, il peut rendre inopérant tous les systèmes de défense contre les missiles de croisière subsoniques (canons, SATCP, SACP).

Bien sûr, un compromis devra être trouvé en phase finale d'attaque entre les exigences de pénétration, qui favorisent les hautes vitesses, et les exigences de précision finale ou les problèmes technologiques (échauffement) qui incitent à limiter la vitesse.

1.3 - Une arrivée à grande vitesse sur l'objectif favorise *les effets terminaux*, grâce à l'énergie cinétique élevée. Cet avantage peut être marquant contre des navires, des radars de haute valeur fortement défendus, ou des postes de commandement enterrés.

1.4 - Néanmoins, un tel système offre *quelques inconvénients* :
- en version aéroportée, ses dimensions et donc sa masse, seront supérieures à celles d'un missile subsonique. Pour qu'il soit utilisable sur la plupart des avions de l'OTAN, sa masse maximale ne devra pas excéder 1,5 tonne environ.

[*] Nota : L'horizon radioélectrique est
$X(km) = 4,2 [H(m)]^{0,5}$

- l'utilisation d'aides à la pénétration (électromagnétique ou infrarouge) est difficile sur un missile hypersonique.

2 - DRONES DE RECONNAISSANCE ET DE SURVEILLANCE

L'utilisation militaire des *drones HALE* (Haute Altitude Longue Endurance) est plus particulièrement orientée vers l'acquisition de renseignements en profondeur, derrière les frontières d'un pays hostile ou les lignes de front en cas de conflit : par exemple l'écoute radar, l'analyse des réseaux de communications ou la détection du départ d'un missile balistique.

En revanche, la recherche d'images à haute résolution n'est pas le domaine privilégié des drones HALE, car elle requiert des capacités de pénétration en territoire hostile qu'ils ne possèdent pas : ils ne peuvent que "regarder de loin".

Comment faire pour obtenir très rapidement, et par tous les temps, des images de haute résolution sur une zone profonde (500 à 1000 km) réputée interdite de survol ?

- **Le satellite** ne peut pas offrir de réponse rapide, sauf si l'OTAN décidait, de s'équiper d'une constellation de satellites d'observation capables d'assurer une couverture quasi-permanente du globe. De plus, compte tenu des contraintes propres au satellite (trajectoires, encombrement des antennes), l'obtention d'une résolution inférieure au mètre, est difficile à obtenir au moyen d'un radar SAR. Enfin, la trajectoire du satellite étant parfaitement connue à l'avance, ceci favorise chez l'adversaire les opérations de camouflage.

- **Les drones ou avions furtifs** volant à basse altitude offrent la possibilité de s'approcher de l'objectif d'assez près, mais néanmoins ils présentent quelques limitations d'emploi pour une telle mission (longue durée du vol, portée limitée à basse altitude, vulnérabilité si l'adversaire a une bonne défense anti-aérienne, prises de vues rasantes ...).

C'est pourquoi, dans la lignée de l'avion de reconnaissance SR 71, d'autres concepts, tels celui des *drones hypersoniques*, méritent d'être étudiés. Pour offrir un réel intérêt

militaire par rapport aux autres systèmes d'observation, les **drones HAHV** (Haute Altitude Haute Vitesse) devraient avoir les caractéristiques suivantes :

- capacité à recueillir très rapidement des informations de haute valeur, par tous les temps (par exemple pour évaluer les dommages causés par une première frappe),
- forte immunité vis-à-vis des défenses anti-aériennes adverses,
- coût réduit, par rapport à celui des satellites et des avions ; ceci devant être obtenu par une utilisation de technologies proches de celles des missiles tactiques.

Avec un rayon d'action atteignant 1000 à 1500 km, le drone hypersonique de reconnaissance devrait être capable de reconnaître tout objectif hostile en moins d'une douzaine de minutes après le lancement. Il offrirait ainsi un temps de réaction très court vis-à-vis de cibles de haute valeur, à apparition fugitive.

Volant à très haute altitude (30 000 à 35 000 mètres), il serait bien adapté à l'emport d'un radar SAR lui donnant une capacité d'observation à haute résolution, par tous les temps, avec une bonne couverture au sol. L'adjonction de senseurs optiques fonctionnant lors de certaines brèves phases du vol pourrait être envisagée.

Une autre mission bien adaptée à un tel véhicule serait l'écoute électromagnétique, en particulier celle des systèmes de défense adverse situés au-delà de l'horizon.

Si le drone transmet des données en continu, en particulier des images, ceci conduira à des débits d'information très importants qu'il faudra protéger contre le brouillage. La transmission vers les zones amies se fera, soit par l'intermédiaire d'un satellite-relais, soit en direction d'une station aéroportée, soit en fin de vol vers une station au sol dans la zone amie.

Après avoir ralenti jusqu'à une vitesse subsonique, le drone sera récupéré en vol, par exemple au moyen d'un hélicoptère, lors de sa descente à basse vitesse sous parachute.

Pour que la flexibilité opérationnelle du drone hypersonique puisse être exploitée au maximum, il pourrait avantageusement être aéroporté sous avion de combat, en utilisant les interfaces standard, en particulier les lance-missiles. Sa masse au lancement devrait par conséquent être sensiblement inférieure à 2 tonnes (Fig.5).

Sa propulsion en vol hypersonique serait assurée, soit par un statoréacteur (croisière entre Mach 4 et 5), soit par un stato mixte (croisière entre Mach 6 et 8). Bien entendu le combustible devra être stockable (par exemple hydrocarbure endothermique).

3 - INTERCEPTION AEROPORTEE A GRANDE DISTANCE

L'utilisation de missiles aéroportés hypersoniques, utilisant une propulsion aérobie (stato/superstato) jusqu'à Mach 6 ou 8, pourrait être d'un grand intérêt pour des interceptions à grande distance, en particulier pour les deux missions suivantes :

3.1 - **Interception d'un missile balistique tactique en phase accélérée** : c'est en principe le cas idéal, puisque l'autoguidage de l'intercepteur est facilité par la forte signature infrarouge du jet propulsif et parce que les débris du missile balistique retomberont dans le pays hostile.

Mais c'est aussi le cas le plus difficile puisque la fenêtre de tir ne dure que quelques dizaines de secondes, ce qui limite la portée utile de l'intercepteur à moins de 150 km. Celui-ci devra avoir la vitesse de croisière la plus élevée possible, avec de sévères contraintes de tenue thermique des structures et des équipements (en particulier de l'autodirecteur).

Or lorsque l'on compare les performances d'un missile propulsé par moteur fusée doté d'une forte capacité d'accélération, à celles d'un missile hypersonique à propulsion aérobie, on met en évidence les limitations de ce dernier en portée et en altitude (Fig.6).

Par ailleurs, à l'horizon envisagé, d'autres systèmes seront capables de remplir une telle mission d'interception : par exemple les lasers aéroportés, de forte puissance, qui bénéficient d'un temps de réponse très bref et d'une portée utile de plusieurs centaines de kilomètres à haute altitude (avec une efficacité réduite à basse altitude).

Ce type de missile hypersonique à propulsion aérobie ne semble donc pas adapté à cette mission d'interception.

3.2 - Interception à grande distance de cibles aériennes de haute valeur (avions pilotés ou drones équipés de radars de surveillance, ou de systèmes d'écoute et de brouillage).

Un missile capable d'attaquer une telle cible, à une distance de plusieurs centaines de kilomètres en volant à Mach 6/8 à une altitude telle qu'il passe au-dessus des lobes du radar de surveillance, offre un réel intérêt. Sa grande vitesse simplifie son guidage inertiel et offre peu de temps à l'adversaire pour mettre en oeuvre des contre-mesures.
Notons que la possession par un adversaire d'une telle arme capable d'intercepter des AWACS ou JSTARS à grande distance, serait d'un grand danger pour les pays de l'OTAN.

4 - DEFENSE SOL OU SURFACE/AIR A LONGUE PORTEE

Une autre application, assez proche de la précédente, concerne la défense sol-air ou surface-air capable d'intercepter à une distance comprise entre 100 et 500 km une cible aérienne menaçante, par exemple un avion volant à haute altitude et équipé d'armement air-sol tel que des missiles de croisière subsoniques... qui proliféreront à l'horizon 2020. Dans ce cas, une grande vitesse de l'intercepteur (croisière hypersonique à Mach 6/8) réduit le temps de réponse du système et favorise une interception de la cible hostile avant que celle-ci n'ait eu l'occasion de tirer ses armements.

Pour ce type de mission, la contrainte de limitation de la masse du missile, contrainte très sévère pour les armements aéroportés, peut être relâchée (par exemple, utilisation d'un moteur d'accélération très puissant).

5 - ACCES RAPIDE ET SOUPLE A L'ESPACE

A l'horizon 2020, il est évident qu'une Alliance militaire, telle l'OTAN, utilisera de plus en plus de moyens spatiaux pour remplir sa mission : ce besoin conduira à des lancements de satellites de télécommunication, de navigation, d'observation, ou éventuellement de satellites équipés d'armes laser. Ces satellites seront distribués, aussi bien sur l'orbite géostationnaire (pour les télécommunications ou l'alerte) que sur des orbites basses (observation, écoute, télécommunication).

5.1 - Pour des *missions qui ne sont pas urgentes*, l'utilisation d'un lanceur commercial sera de plus en plus recherchée afin de réduire le coût du lancement. C'est d'ailleurs ce qui se passe actuellement en Europe avec l'utilisation d'ARIANE pour le lancement de satellites militaires.

Pour les lanceurs spatiaux futurs, on ne sait pas si ce besoin d'une réduction des coûts conduira à des lanceurs à propulsion fusée ou à propulsion partiellement aérobie. A l'horizon 2020, il est hautement probable que la propulsion fusée restera prédominante.

Pour ces missions non-urgentes, la nécessité pour l'OTAN de développer un lanceur militaire spécifique est d'autant moins évidente qu'apparaîtront au tournant de ce siècle, une famille de nouveaux lanceurs classiques qui devraient réduire sensiblement le coût du lancement d'un satellite.

5.2 - Pour une *mission urgente*, telle que le lancement de satellites tactiques miniaturisés (observation, écoute) en temps de crise, plusieurs solutions techniques peuvent être envisagées :

a) utilisation de lanceurs classiques consommables, multi-étages, à propulsion fusée à propergol solide. Ceux-ci peuvent être dérivés de missiles balistiques et être lancés, soit à partir d'une base terrestre, soit à partir d'un navire ou d'un avion gros porteur. Ce dernier concept correspond au système américain PEGASUS, dont on pourrait augmenter la masse satellisable en remplaçant le moteur fusée du premier étage par un moteur combiné fusée-statoréacteur-superstatoréacteur.

b) utilisation d'un nouveau véhicule hypersonique récupérable et réutilisable, dont la mise en oeuvre s'apparenterait à celle d'un avion militaire. On sait qu'un tel véhicule, de préférence mono-étage, aura probablement une masse au décollage de quelques centaines de tonnes et utilisera un système propulsif complexe combinant propulsion fusée

et propulsion aérobie, celle-ci devant impérativement fonctionner au moins jusqu'à Mach 10.

Il faut alors rapprocher les contraintes militaires inhérentes à l'urgence de la mission (c'est-à-dire un lancement dans un délai de quelques heures, et au maximum de 24 heures) et les incertitudes techniques d'un tel projet:

- peut-on utiliser les aérodromes de l'OTAN (longueur des pistes, type de carburant à mettre en oeuvre, ateliers de maintenance)?

- peut-on utiliser, comme pour un avion, un décollage et un atterrissage horizontaux ? Si oui, n'est-il pas nécessaire de disposer pour le décollage d'un chariot auxiliaire ?

- l'utilisation d'ergols cryogéniques (LH_2 et LO_2) est probablement indispensable pour atteindre la satellisation : est-ce compatible avec l'urgence de la mission ?

En résumé, on peut dire que, à ce jour :
- la faisabilité technique de tels véhicules hypersoniques n'est pas prouvée,
- l'incertitude sur les performances garanties (par exemple : masse satellisée/masse au décollage) reste grande, et ceci est malheureusement inhérent à l'utilisation de la propulsion aérobie aux très hautes vitesses,
- les conditions de maintenance et de réutilisation sont mal connues.

Par ailleurs, la nécessité, pour impératif militaire, de se lancer d'ici 2020 dans le développement d'un tel système n'apparaît pas, puisque d'autres solutions, certainement moins coûteuses, permettent ou permettront de remplir cette mission :

- pour une mission non urgente, utilisation de lanceurs commerciaux,
- pour une mission urgente, utilisation de lanceurs classiques dérivés de missiles balistiques, ou utilisation d'autres systèmes, tels les drones hypersoniques.

Enfin la menace que pourrait faire peser sur l'OTAN un adversaire équipé de tels véhicules spatiaux hypersoniques paraît extrêmement lointaine.

6 - CONCLUSION

Cette première analyse montre que les technologies qui permettent le vol propulsé dans l'atmosphère à vitesse hypersonique pourraient avoir un grand intérêt militaire à l'horizon 2020.

6.1 - Les missions susceptibles de faire appel à ce type de technologies sont principalement:

- *l'attaque au sol ou en surface* à grande distance,
- *l'interception aéroportée*, à grande distance, de cibles aériennes de haute valeur.

La possession de tels armements pourrait donner à l'OTAN une incontestable supériorité.

Ces missiles auraient une masse de 1000 à 1500 kg, et pourraient se monter sous la plupart des avions de l'OTAN. Leurs performances seraient approximativement :
- croisière hypersonique à 6 < Mach < 8
- altitude de croisière : jusqu'à 35000 mètres
- portée maximale : 500 à 1000 km

La propulsion serait assurée par un moteur combiné fusée à propergol solide/statoréacteur/superstatoréacteur. Pour le moteur aérobie le combustible doit impérativement être stockable et si possible posséder une capacité de refroidissement.

Les problèmes techniques à résoudre concernent :
- le système propulsif
- les structures et les matériaux (légèreté et tenue à l'échauffement)
- le guidage (précision et tenue aux contraintes thermiques)

6.2 - D'autres missions sont concernées par ces techniques. Il s'agit :

a) *des drones Haute Altitude Haute Vitesse*, qui utiliseraient des technologies proches des précédentes

Pour ces deux cas une analyse technico-opérationnelle plus poussée devrait permettre d'en préciser l'intérêt par rapport à l'utilisation d'autres systèmes militaires.

6.3 - Les missiles hypersoniques à propulsion aérobie sont mal adaptés à l'**interception des missiles balistiques** en phase propulsée, en raison de leur faible capacité d'accélération.

6.4 - Il semble que l'implication de l'OTAN dans le **développement de lanceurs spatiaux -non classiques-** ne présente pas d'intérêt militaire évident, eu égard aux contraintes financières actuelles et futures auxquelles doivent faire face les pays de l'Alliance.

6.5 - Le concept américain **d'avion hypersonique** capable de voler à plus de Mach 10 et d'atteindre n'importe quel point du globe à partir du continent américain puis d'y revenir semble dépasser largement les besoins et les possibilités des autres pays de l'OTAN.

6.6 - D'autres emplois de véhicules à vitesse de croisière hypersonique peuvent êtres intéressants pour des **missions à courte portée** : il s'agit d'armes capables de détruire des cibles durcies ou enterrées, et des obus propulsés anti-chars.

6.7 - L'organisation qui succédera à l'AGARD devrait s'intéresser aux **recherches et aux technologies relatives aux armements hypersoniques** précisés en 6.1 et 6.2, en conduisant les recherches de façon progressive vers les nombres de Mach les plus élevés, sans brûler les étapes intermédiaires. Ces efforts devraient conserver un certain caractère de confidentialité compte-tenu des menaces que pourraient faire peser, à l'horizon 2020, sur la supériorité, en particulier aérienne, de l'OTAN, des adversaires possesseurs de tels armements.
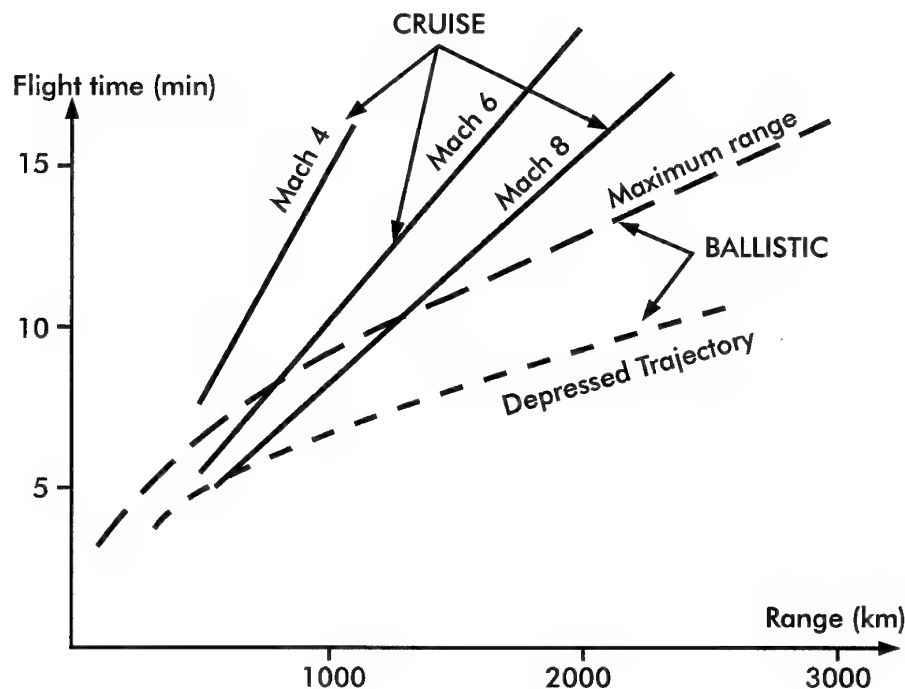
Fig.1 - Temps de vol d'un missile balistique et d'un missile de croisière hypersonique.
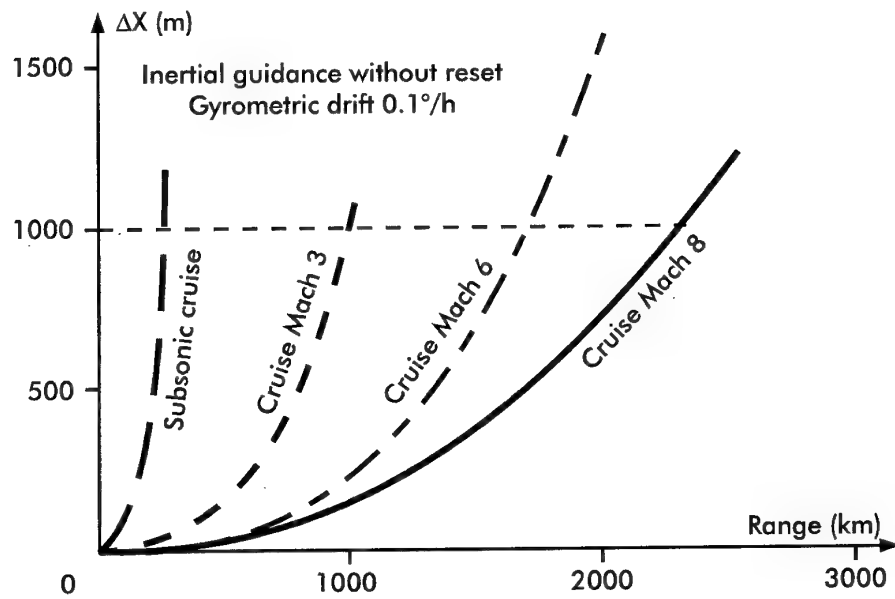
Fig.2 -Erreur de navigation inertielle en fonction de la portée.
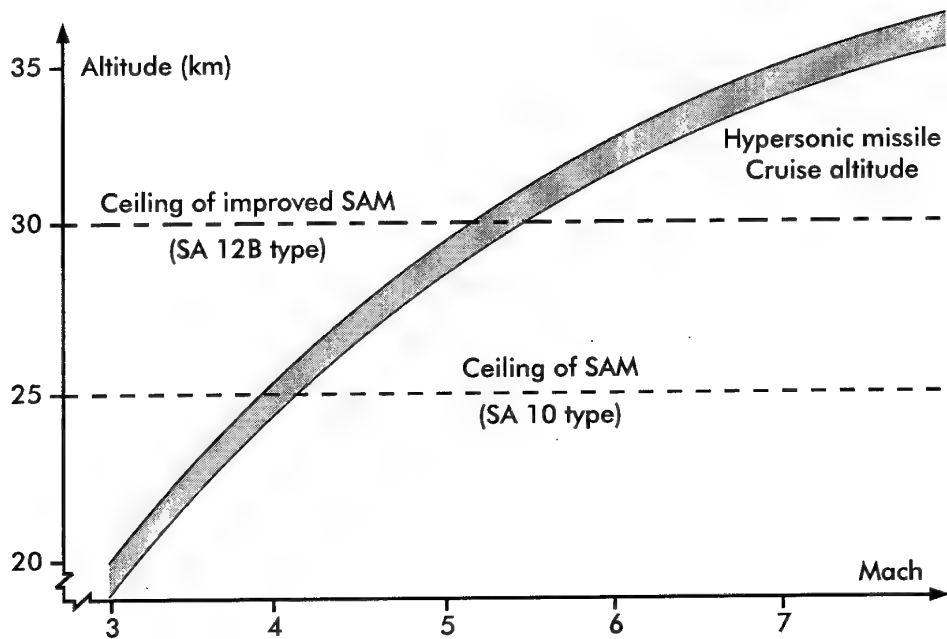
Fig.3 - Altitude de croisière d'un missile hypersonique.
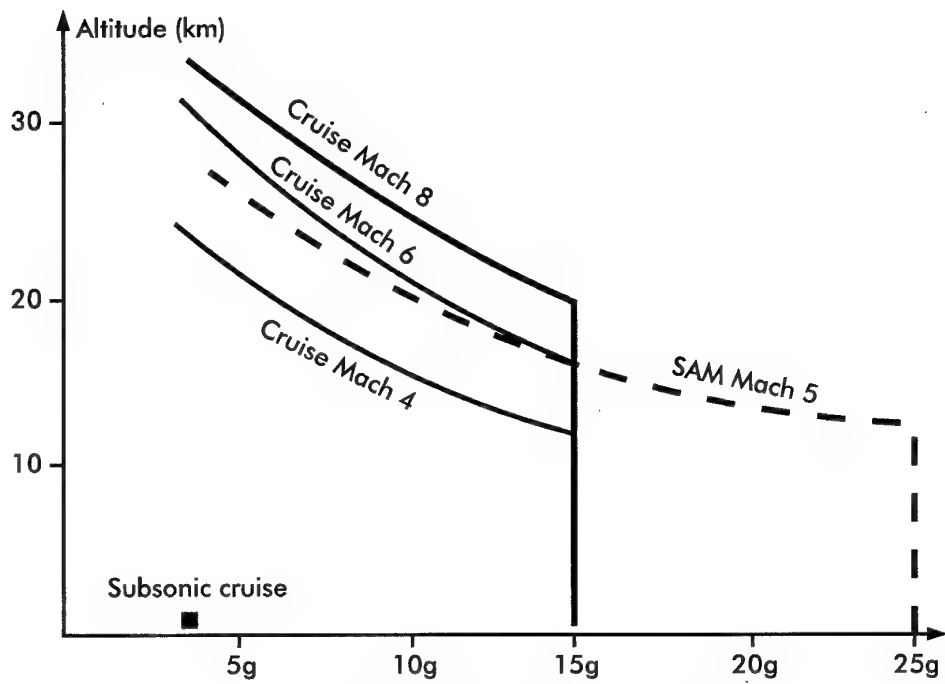
Fig.4 - Manœuvrabilité dans le piqué sur l'objectif.
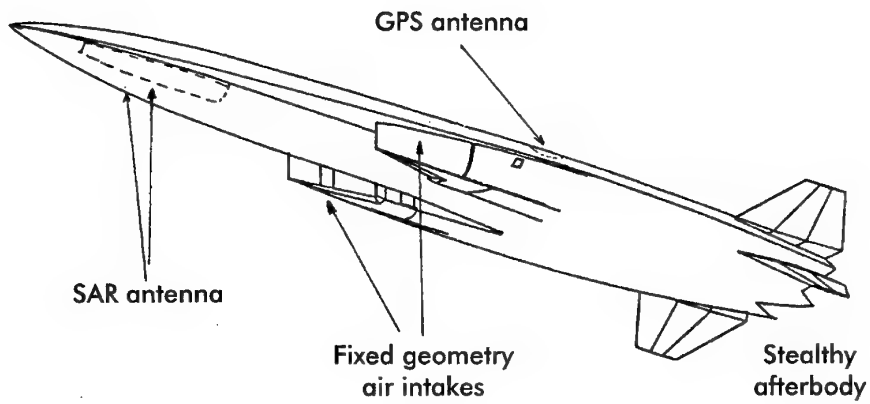
Fig. 5 - Drone HAHV.
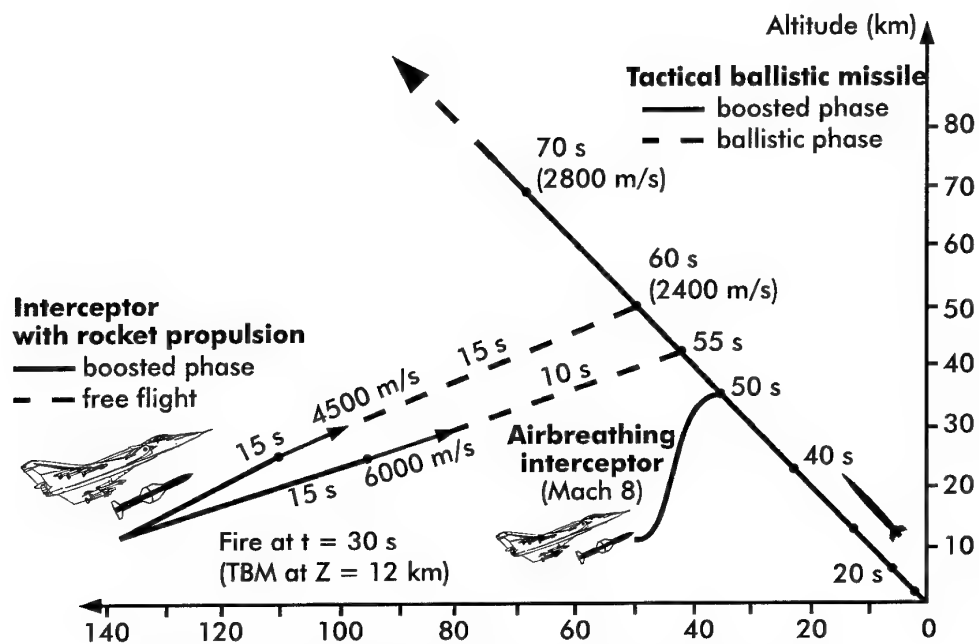
Fig. 6 - Interception de missile balistique en phase accélérée.

CONFIGURATIONS DE VEHICULES ET DEFIS DE LA CONCEPTION AEROTHERMODYNAMIQUE

(VEHICLE CONFIGURATIONS AND

AEROTHERMODYNAMIC CHALLENGES)

P.C. PERRIER
Dassault Aviation
78, Quai Marcel Dassault
92552 St. Cloud Cedex 300
France

E.H. HIRSCHEL
Daimler-Benz Aerospace A.G.
DASA LMLE3
Postfach 80 11 60
81663 München, Germany

Summary

Sustained hypersonic flight appears as a challenge for 3 classes of concepts quite different in their use : one is relative to constant cruise, the second to transient (but slowly varying) high altitude flight, the latter to low altitude penetration. For each of the concepts, a review will be presented of the more promising configurations and the associated aerothermodynamic challenges. In conclusion a proposal for a common technology program is given with demonstration filling the envelope of specifications and dealing with the critical points they generate.

Slowly varying high altitude flights may be part of the mission of satellite launchers in the acceleration phase or in reentry cross range cruise with or without rebouncing effects. During these flights, convective ratio to radiative heat transfer is a driving parameter of vehicle configuration, associated with the search for better lift over drag ratio. Low altitude penetrators are specified by the high pressure generated and heavy flutter requirements. On the contrary, the search for configurations with relatively low drag and fuel consumption per mile, for a minimum structural weight, leads to configurations of pure cruisers to be at the pinpoint of aerodynamic efficiency only compromised by carry-and-release constraints.

Compatibility with future European launch technology, as reviewed in the Festip program, is evaluated and general challenges, sufficiently open to variation with respect to future needs, are summarized.

0.1 INTRODUCTION

Never has been so important, for the efficiency of aerospace vehicles, the aerothermodynamic configuration as for sustained hypersonic vehicles. It is clear that sustained hypersonic flight might afford fast and cheap long range capabilities ; it requires sufficient level of aerodynamic quality, otherwise design will be poor and its feasibility difficult to support.

That can be more precisely expressed by consideration of the Breguet formula for constant propulsion efficiency :

$$R = Isp \times V \times \frac{L}{D} \log \frac{M_1}{M_2}$$

R being the range of sustained flight, Isp the specific impulse (related to a given combustion), V the sustained velocity, L/D the lift-over-drag ratio, M_1 and M_2 the mass of the vehicle with or without fuel or ergols. The critical aerodynamic characteristic may then be evaluated first by the level of product V x L/D as compared to more classical cruise conditions : than in figures as large as 2, for L/D, and ten times more velocity than in subsonic cruise conditions gives by the parameter V x L/D, better cruise efficiency than the subsonic commercial aircraft in present long range operation.

However a good performance assumes good balance between aerodynamics for ascent and descent terminal trajectories and other constraints coming from general design (volume and center of gravity acceptable locations) or from aerothermics and from stress analysis particularly for the high pressure in air ducts. So we cannot avoid to address the accelerated and decelerated part of the trajectory with a specific attention devoted for that class of vehicle that have almost no cruise as the satellite launcher or vehicles going to or coming back from orbital position. Alternatively it is also possible to use specific designs aimed to go from the ground to the starting point of the sustained hypersonic flight, like solid propellant boosters, or a flighter-bomber used as launcher.

To be addressed particularly are the vehicles ending their flight by a dive towards target ; their kinetic energy, with or without addition of explosive mass, may be used as a passive mean for penetrating defences. In the final part of their trajectory constraints on internal pressure of airbreathing engines are critical.

We have to evaluate if cruise vehicles aerodynamics (with their specific optimization in Isp. V. L/D, plus specific constraints related to ascent and descent phases of their trajectory), may appear as the alternate path to the derivation of rational configurations of hypersonic vehicles compared to blunt aerothermally constrained

shapes without propulsion. Are they particularly interesting for exploration of advanced concepts, and evaluation of inclusion of such concepts in compromised vehicles ? A survey of different applications of the concepts will help to do such evaluation.

1. CRUISE VEHICLE DERIVATION

1.1 Aerothermics constraint from the leading edge

The search for L/D maximisation is obviously the search for extreme slenderness and low angle of attack optimization of vehicles. Such overall tendency is correct as far as simplified Newtonian approach is considered because the local contribution to general maximisation of $1/tg\alpha \times ds$ L/D is a weighting of $1/tg\ \alpha ds$, α being local angle of attack of the local surface ds. However it is quite evident that we cannot avoid blunt leading edge for acceptable heat fluxes, because stagnation of incoming flow is requiring at least one point without sweep for symetry accounting ; local extreme heat flux may be predicted acurately by the Fay-Ridell formula, with a direct proportionality to the local gradient of velocity, source of shearing and so of thermal fluxes, itself related to the local mean curvature at stagnation point. Curvature C may be expressed as the square root of the product of principal curvatures of the surface of the vehicle at the stagnation point : $\sqrt{C_1 C_2}$.

If the flux constraint is maximised, the optimal shape is a sphere and, by symetry, its L/D is zero. Having large thermal constraints mean that we may put low angle of attack surfaces in the continuity with spherical noise, and two families of vehicle with largely increased L/D may be derived : one with axis of symmetry kept and geometrically not to far of sphere-cone topology, the other using a flatness higher with ellipsoïd-cone topology. One interesting effect of L/D optimization with Newtonian law and sphere or ellipsoïd constraint at stagnation point, is to produce curved shapes where the transition to small angles is as abrupt as the ellipsoïdal shape is constrained, except if volume constraint smooth transition from ellipsoïdal shape. Consideration of real flows appear then as the main driver to real optimization and it leads to continuous curvature with a newtonian perturbation of the shape of the bow-shock. This lead to the <u>bow-shock shielding concept</u> where the avoidance of any peak local overheating, built with shock-shock interactions, led to generic shapes of X-24 and Hermes vehicles. Such derivation is summarized in Figure 1.1.

On Figure 1.2 the specific constraint of bow-shock shielding is examplified by the critical point design of Hermes with angle of attrack and sideslip, effect of real gases and of local deflection of fin control surfaces.

The final L/D of such configuration is also given in figure 2 for checking that the L/D level of more than 1 may be attained with angle of attack of 30 to 40 degree, when the $1/tg\alpha$ value is 1.7.

It then appears that the thermal constraints are the major driver in the shape derivation due to non-Newtonian interaction of bow-shock and the downstream part of the shape. As flat as will be the ellipsoïdal leading edge as large will be the L/D. So we can derive a family of high L/D by optimization of flatness of elliptic nose with the constraint of surface and volume. It is clear that volume constraints for a given length will be the major limiter in the trend toward flat vehicles but we have now to consider also the problem of stability.

Longitudinal stability cannot be achieved with full volume utilisation because the center of volume of the expanding body is aft the center of surface (assuming any X^α distribution of local span or thickness, implies a $(\frac{2+\alpha}{3+\alpha} - \frac{1+\alpha}{2+\alpha})$ necessary shift of rearward location of the center of gravity). Relying on non-linear behaviour of pressure derivatives, it is possible however to select a forward stable longitudinal center of pressure with higher lift on the front fuselage ; so it lets the hypersonic stability compatible with subsonic requirements, but it reduces again the fill-up of the rear volume. On lateral stability the same trend asks to increase rear lateral surfaces and their outward canting.

1.2 The Dassault Launac* generic shape
* (launac, lônaz, losnes is an old french word that depicts a damp meadows site : it marks optimal location for a village in a valley)

Taking in account the above conclusions it is now obvious that we can identify the optimal hypersonic lower surface of a generic hypersonic shape as a sole devoted to hypersonic constraints fulfilment plus a volume that needs to be in the wake of the forebody. Two ways are now open for such derivation, one related to an « almost flat plate concept » and the other to the « V shaped concept ». for such derivation we may consider again the problem of the leading edge, not near the stagnation point in the plane of symmetry, but on the lateral sides with increasing sweep angle φ. If we fit to the maximum heat flux constraint identical to the nose problem, it is no more necessary to keep low curvature, as on the latest shapes of X-24 and Hermes concepts, but we can reduce the curvature with the cos² φ, and so the sole concept will appear in the shape derivation given in Fig. 1.3.

If we consider now a circular cylinder at effective angle of attack as will appear the lateral high curvature border with the combination of angle of attack α, ellipsoïd bow shock shielding, we can examine the generation of the oblique shock surface past a circular cylinder at incidence. Fig. 1.4 gives the shape of shock wave induced by a circular cylinder in the hypersonic M=8 Poitiers CEAT wind tunnel. One can check that the local swept bidimensionality appear only after 8 diameters, so that the transition from the leading edge to the lateral border allows a significative snow-plough effect, that leads to the proposal of a U or rounded V basis for critical thermal parts of the design to be fitted to the low flux low curvature sole surface baselines.

V is reinforced in the Figure 1.3 drawing of the Dassault « Launac » sole concept.

One interesting feature of the V is that we may consider what topology of the bow shock geometry is induced by different ratios of radius of the leading edge to the vertical spacing of leading edge and bottom surfaces. Such topology is presented in the Figure 1.5 below ; it shows that it is possible to build a concave sole (it cannot be too concave because the self reradiating effect will increase the heat fluxes as for the sole of an oven for pottery) and so to derive an optimal wave rider with constraints on heat fluxes at leading edges. Major parts of the lower surface drag may then be cancelled, whatever the fact that it contributes typically only to one third of the drag breakdown but to ninety percent of the lift.

1.3 The interaction of propulsion in Launac concept

One major requirement for propulsion efficiency is to include air intakes and exits in the design in such a way that negative interactions will be always minimised if positive cannot be obtained.

One positive effect is the directional stability improvement by rearward location of the air intake because the deflection of upstream flow to a vehicle-fixed duct is a major contributor to lateral stability coefficients. If a very short duct and combustion chamber may be designed, such rear position is possible and very attractive. On the other side the compression by the bowshock cannot be neglected in the entropy losses related to the air intake drag (Ref. 1).

Two ways are open for selection of vehicles configurations with air breathing propulsion more demanding that smaller rocket engines : rocket propulsion has just to include in the base the large expansion ratio of high altitude nozzle design (however such rocket propulsion, including air augmented rocket, have very low specific impulse demanding large volume constraints for the high mass of ergols if cryogenic). One way to baseline is to build a convex compression ramp and the other a concave one. In the first case the design configuration is examplified by the NASP configuration ;

the second is typified in axisymmetric or highly convex shapes, not so attractive due to difficulties for low speed control constraints in longitudiual and lateral stability and under carriage location.

One major problem it related to the nozzle exit integration, knowing that the performance weight of the efficiency of the nozzle is much larger than the performance weight of the air intake efficiency for the global performance. The higly convex design is not compatible with other than convex exit, and so with plug nozzle that are of limited efficiency without very narrow (and so difficult to control) throat and exit areas. The highly concave shape are similarly complex to control but on a much smaller peripheral length ; the intermediate, almost square, exit is very simple to control with simple hinge and almost flate plate deflection flaps ; but square shapes are not so able to whitstand high pressure levels induced by high Mach number. Airbreathing propulsion efficiency requires a ratio of the mean pressure in the ducts and combustion chamber to wing surface loading much higher than in low speed design; except for futuristic attractive external combustion.

1.4 Off-design constraints related to out of cruise conditions

Two different pathes of configuration compromise, with out-of-cruise conditions, are generated by the compatibility with launching and recovery constraints.

For recovery constraints major problems are induced by the landing phases. If the recovery is by chutes, the constraints are not so large and include mainly mechanical constraints and geometrical volume reservation for the related packs and ropes. However the runway landing is to be favored more and more, due to difficulties and high costs of recuperation on large areas. Launac type designs are compatible with empty landing on runways if some additive aerodynamic devices (winglets, fins, canards, ...) are properly designed and integrated ; more difficult is the landing of highly convex bodies - like axisymmetric bodies.

For the acceleration to cruise conditions major difficulties are generated for inclusion of boosters outside in parallel or in integrated design. The first one requires the same separation studies than external store in aircraft separation development aircraft strategy. The second one needs a long body volume reservation for propellants, unfortunatelly around the center of gravity position, increasing the overall maximum cross area of the vehicle. Such selection of configuration is in direct relation with the slenderness of the design. Easier to implement are the internal liquid rocket or the external first stage or air-breather booster allowing use of

balanced tanks in or outside (external tank as for the shuttle Orbiter of Rockwell) the main fuselage.

2. DECELERATING/ACCELERATING VEHICLES

In this chapter some major design issues of hypersonic vehicles are highlighted by looking at configurations employed or studied for space-transportation purposes. The discussion is restricted to winged vehicles flying in the earth atmosphere. The related aerothermodynamic design and verification problems are not commented on in detail.

2.1 The "Classical" Re-entry Vehicle

The "classical" re-entry vehicle, like the US Space Shuttle, is ascending in a typical rocket mode, i.e. it climbs fast out of the atmosphere, without the heat loads connected to aeroassisted flight. For the descend, however, such a vehicle is essentially an aeroassisted (winged) braking device, which reduces the total energy of (low) orbital flight to zero on the ground after landing. In order to create enough drag, such a vehicle is blunt and flies at large angle of attack, Fig. 2.1. The blunt configuration and the large angle of attack flight are on the other hand necessary to reduce the ensuing heat loads to such a degree, that the vehicle is in principle fully reusable. The reduction of the heat loads is due to the large bluntness of the nose region and the leading edges together with the large angle of attack ($\alpha = 30°$ to $40°$), which leads to boundary layers of such large thickness, that (passive) surface-radiation cooling becomes very effective, and sufficiently reduces the heat loads to a level, at which no additional active cooling is necessary, Ref. 4.

At the leading edges of wings it is on the one hand the leading-edge radius and on the other hand the sweep, which, when increased, reduces the heat loads. Usually a large sweep is preferred in order to reduce drag at lower angles of attack, when down and/or cross range is flown. Low-speed flight demands larger aspect ratios, which can be obtained by a double-delta wing plan form (US Space Shuttle, BURAN), or by winglets (HERMES, and, e.g., some FESTIP configurations, Sub-Chapter 4.4).

Surface radiation cooling can reduce effectively the heat loads on the structure, i.e. the radiation-adiabatic temperature. Of course conduction processes will always convey some heat into the structure, hence a heat insulation becomes necessary. The insulation system should be the lightest and cheapest system possible with the smallest technological risk, as easy and inexpensive as possible to manufacture and to support in operation. The optimal solution for pure re-entry vehicles sofar is a

materials & structure concept with a cold primary (load bearing) structure with a heat-protection system (tiles, shingles), which has a thickness according to the penetration depth of the heat front during the re-entry flight. The opposite solution would be a hot primary structure with an internal insulation system, and, of course, mixtures of both. A cold primary structure has the additional benefit, that it is not prone to aerothermoelastic effects, which does not rule out ordinary aeroelastic effects especially on wings, fins and control surfaces.

2.2 The airbreathing lower stage of a two-stage-to-orbit vehicle

Some years ago especially in Europe some two-stage-to-orbit concepts were studied, with an airbreathing lower stage and a staging Mach numbers predominantly in the 5 to 7 range (SÄNGER, STAR-H, RADIANCE). Although the airbreathing lower stages of such concepts at the considered Mach numbers are also hypersonic vehicles, the configurational issues are significantly different from those of "classical" re-entry vehicles, Fig. 2.2. First, and most important of all, the mission of the configuration is not a braking mission. It is an acceleration mission, which asks for a low drag, and sufficiently large lift to drag ratio layout. Very important is the role of the lower side of the forebody, which, while flying at angle of attack, entails a pre-compression of the inlet-onset flow, and hence a reduction of the inlet capturing area. This in turn reduces the vehicle length, because the bow shock must not interfere with the propulsion-system package, and especially its foremost part, the inlet (inlet shielding), Ref. 5.

A special problem is the nozzle/afterbody of airbreathing hypersonic vehicles. Since the flight Mach number and altitude span of such vehicles is very large, the nozzle throat must be controlled, which leads to a rectangular cross-section, and to an asymmetric outer nozzle (single expansion ramp nozzle (SERN)). The outer nozzle then must be considered as a constituent part of the afterbody, which becomes larger with larger flight speed. Nozzle/afterbody efficiency (thrust) and the thrust-vector angle couple strongly into the pitching moment and the lift of the vehicle. Plug nozzles in principle could overcome the thrust-vector angle problem, if they would be employed with a bell nozzle. However, vehicle integration needs make a combination with an asymmetric outer nozzle (Plug SERN) necessary, which poses other problems.

This short discussion shows, that the lower side of an airbreathing hypersonic vehicle actually is a coupled lift/propulsion system, Ref. 5, which unfortunately, depending on the degree of forebody pre-compression, is strongly influenced by the aero(thermo)elastic behaviour of the forebody. This in turn will depend on the structural concept. A cold primary structure could have a better stiffness/weight relation than a hot one. However, the thermal protection system for a cold structure ought to have a sufficiently smooth surface in order to avoid roughness and waviness induced viscous drag increments of the (below approximately 50 km altitude on a large portion of the surface) turbulent boundary-layer (see also Sub-Chapter 4.1).

Wave drag considerations enforce a small nose radius, small leading-edge radii, and large edges sweep. At noses and leading edges hence heat loads have to be traded against wave drag: small radii lead to thin boundary layers and hence to reduced surface-radiation cooling effectivity. If the radii become too small, active cooling becomes necessary, with the related penalties of weight and systems complexity. At the inlet and in the propulsion system of course radiation cooling is reduced, or not possible at all, respectively. The entailed cooling needs enforce a carefully designed overall heat management of the vehicle.

The strong coupling of aerodynamics, propulsion, aerothermoelasticity and surface radiation cooling poses very large design problems ("positive thrust minus drag"). Low speed performance demands (usually also double-delta plan-form approaches), and especially off-design (engine-out) flight pose additional problems, the latter because of the coupling of the thrust vector into the pitching moment of the vehicle.

2.3 Rocket-propelled single-stage-to-orbit vehicle solutions

Provided the structural mass and the thrust problem, respectively, can be solved, both ascend and descend flight will lead to shapes similar to those of the "classical" re-entry vehicles. Advanced rocket motor concepts like the linear plug nozzle bring in the, otherwise not so important, problem of aerodynamic airframe/propulsion integration. New vehicle shapes, like that of the Venture Star, will further reduce heat loads due to the very large radii, but apart from structure-topology problems, can lead to lateral stability problems, and a general Reynolds number sensitivity, which can pose extra design problems.

In the frame of FESTIP a concept with extreme large down-range is studied (once-around concept, Ref. 6). For such a system the demand to have low drag, and a sufficiently large lift to drag ratio on the down range segment of the trajectory contradicts the bluntness and large angle of attack demands on the re-entry segment down to 50 to 70 km altitude. Skip trajectories might be

a way to reduce heat loads, wave-rider vehicle elements might improve the aerodynamic performance. Active cooling will be a problem during descend flight because no fuel-flow per se is given.

Delta-clipper like concepts have other problems, which must be overcome: heat loads, if a nose-first descend is considered (small nose radius: large heat loads combined with long flight times for deceleration), very low roll-damping, asymmetric side forces at large angle of attack (vortex shedding), and small lift to drag ratio (down and cross range restrictions).

2.4 The airbreathing single-stage-to-orbit vehicle

Airbreathing single-stage-to-orbit concepts demand low drag configurations with a very large coupling of the lift and the propulsion system (see the preceding Chapter 1 and Sub-Chapter 2.2), together with very large heat loads, which will make active cooling of larger portions of the airframe necessary. Such a vehicle might fly with airbreathing propulsion modes (RAM, SCRAM) up to 60 km altitude ($M = 12$ to 16), then rocket propulsion must take over, Fig. 2.3. This is due to the fact that on the one hand the inlet capture area (mass flow) will become too large (also the wing area, because with declining thrust, flight would have to become increasingly aeroassisted), and on the other hand the specific impulse falls below that of rocket propulsion (see introduction). Even with air (oxygen) collection and combined SCRAM/rocket propulsion systems the limits will not go up much. The early employment of rocket propulsion, however, will be beneficial, since it reduces the flight time with large heat loads, because of the rapid climbing out of the atmosphere.

Remains the descend. It is not conceivable at this time, how the inlet (and the propulsion-system package) can be shielded from the heat loads during re-entry without a massive weight penalty. Even if this would be possible, trim of the vehicle appears not to be achievable. Upside-down solutions would entail further large weight penalties, because of the need of a full-fledged thermal-protection system also on the upper side of the vehicle. Certainly a very large technological effort would be necessary in order to achieve such type of vehicle.

2.5 Specific heat-loads constraints and compromises

As was mentioned above, surface-radiation cooling is the major cooling means of (outer) surfaces of a hypersonic vehicle, Ref. 4. Heat loads on "classical " re-entry vehicles can be considered decoupled from the aerodynamic performance, because these vehicles are not drag critical (on the contrary), except for possible vehicles with very large down-range demands. Airbreathing vehicles in general will be drag critical, and hence heat loads and the outer shape and its drag (wave drag and viscous drag) are intimately coupled via the coupling of surface-radiation cooling with the boundary-layer properties (boundary-layer thickness, transition laminar-turbulent, laminar and turbulent state, influence of surface temperature on wall-shear stress (increasing temperature reduces wall-shear stress), catalytic surface recombination and surface near mass-diffusion mechanism with non-equilibrium thermo-chemical effects). In general a trade-off must be made at the nose and leading edges with regard to wave drag and heat loads. Active cooling will entail weight and system-complexity penalties. With increasing speed also cooling needs of the propulsion system rise and the overall heat budged (cryogenic fuel as heat sink vs. cooling needs) may become the limiting factor.

Extra coolants (water) might help to solve local problems (heat sink, transpiration cooling). Heat transport, e.g. by heat pipes, from hot zones to cooler ones, where the heat can be radiated away, is also a possible solution for local problems. Slender vehicle shapes (Chapter 1), which fly upper and lower surfaces both at similar low angle of attack, do not have the large differences (heat loads differentials) of the radiation-adiabatic temperatures between windward side and leeside, found, for instance, on a re-entry vehicle (several hundreds up to one thousand Kelvin). Therefore the possibility to get rid of excess heat by cross-fuselage transport is limited.

Heat loads differentials on a forebody, e.g. SÄNGER forebody at $M = 6.8$: ≈ 200 K, can give rise to deformation problems with hot primary structures. An elegant way-out would be the tailoring of the radiation emissivity coefficient ε, in such a way that with $\varepsilon_{upper\ side} < \varepsilon_{lower\ side}$, equal (but then larger) temperatures on the upper side result. This would have the additional benefit of reducing the viscous drag of the turbulent boundary layer on the upper side (the drag of the laminar boundary layer is only weakly affected). Anyway a tailoring of the emissivity coefficient everywhere on the vehicle, just in order not to exceed locally the materials limit, would help to reduce the overall viscous drag to a not negligible degree.

3. LOW LEVEL PENETRATORS

3.1 The high dynamic pressure static constraint

When the dynamic pressure increases, two types of problems are emerging, one static and related to high pressure in some parts of the vehicle and associated high heat fluxes management, the other dynamic and related to flutter constraints.

Major pressure and heat fluxes are present at leading edges of wing and air intake and in the combustion chamber. For the leading edge of the wing there is no particular requirement except to rely on the smallest radius as possible associated with radiative cooling (see sub-chapter 2.5) : pressure is decreasing with sweep angle, so extreme high heat fluxes at leading edge are localised. It will be very beneficial to use liquid cooling or maintaining larger surface than the stagnation area at high temperature and using the upper surface like a crest or tuft emerging upwards. Such device is to be avoided for the lips of the air intake but it is possible to retain a V shape for the inlet lip avoiding portions without sweep and their peak heating.

For the combustion chamber it is clear that the only circular cross section baseline, self stabilized in tension by pressure, is the possible, geometrical candidate and has to include the begining of the nozzle. Similarly the internal compression air duct, before the open concave configuration, has to avoid the complexity by axisymetric design. The skin of the combustion chamber has also to be an external radiating piece of hardware, if possible open to lower and upper side radiation.

3.2 The high pressure dynamic constraints

The flutter problem is of major importance for hypersonic penetrators and appears not in the very high pressure of the combustion chamber, where the thickness of the skin is large, but in the aerodynamic fairings, where flutter of panels are of major concern for the designers. It is clear that flat, or slightly convex or concave surfaces, may have too small rigidity to avoid panel flutter. More contoured design is better from that point of view, however it generally implies inflexions areas that need specific reinforcement as far as the movable parts.

Low transient phenomena, coming from necessary insulation of fuel and equipments bay areas, are also generating transient thermal stresses and are feeding instabilities of panels. A very powerful aeroelastic multidisciplinary tool is mandatory for the feasibility of a hypersonic penetrator.

4. RESEARCH TO SUPPORT ADVANCED CONFIGURATIONS

In this chapter research and development problems are sketched, which are seen to be necessary to support the design and development of cruise vehicles and also of low-level penetrators. A short reference to FESTIP work is given in Sub-Chapter 4.4. Table 4.1 contains a summary of the technology issues.

4.1 Critical Issues of Surface-Radiation Cooling/Thermal Protection

Surface-radiation cooling depends (locally) inversely on the boundary-layer thickness ($T_{ra}^4 \sim 1/\delta$). The efficiency of surface radiation cooling in general reduces, if the Reynolds number rises, i.e. vehicles flying with hypersonic speed at low altitudes are not amenable to full-fledged radiation cooling.

Surface-radiation cooling in any case depends strongly on the state - laminar or turbulent - of the boundary layer, which holds also for heat fluxes at surfaces with fixed temperature (target temperature of actively cooled surface portions). It is influenced by attachment lines (hot-spot situation: "vortex scrubbing"), and separation lines (cold-spot situation). Because a ground-facility simulation of the flight situation is not possible, the determination of the radiation-adiabatic surface temperature as conservative estimation in the design phase, has to be done with computational tools. This also holds for the sizing of the thermal protection system, or that of a hot primary structure, when part of the heat enters the structure, regardless of the effectivity of radiation cooling.

Six research and development topics can be identified:

1. With or without radiation cooling, effective and reliable aerothermodynamic computational tools, and especially the flow-physics (transition laminar-turbulent, turbulence) and thermochemical modelling (surface catalytic effects, (turbulent) mass diffusion) are of utmost importance. Indeed the biggest problem is the determination of the transition zone, followed by the modelling of turbulent heat conduction and mass diffusion processes. Of equal importance, because of the ensuing large heat (and mechanical) loads, is the

determination of location and strength of strong-interaction phenomena.

2. Effective and reliable computation tools, which permit the coupling of aerothermodynamics and structures, in order to determine - on the whole trajectory - the penetration depth of the heat front in thermal protection systems, the heat loading of hot primary structures, the thermal deformation and stresses, et cetera.

3. Criteria for the permissible surface roughness, waviness, gaps, steps et cetera, because these can give rise to peak heating by loosing radiative cooling and/or by premature transition ; surface irregularities are also generating large mean viscous drag and heat-loads increments. On the other hand manufacturing tolerances should be as large as possible in order to keep down manufacturing costs.

4. Aeroelastic and aerothermics multidisciplinary working tools with their experimental validation.

5. Integrated, heat-loads oriented vehicle design and optimization strategies, which take into account in a holistic manner all aspects and interrelations of vehicle aerodynamics and surface-radiation cooling, Ref. 4.

6. Active flow control of unsteadiness of propulsion (unstart of air intake, combustion instabilities, ...) for reduction of design stresses and increase of safety.

4.2 Critical Issues of Inlet and Nozzle/Afterbody Development

The major problem is the design for the large Mach number and altitude span, in view of the strong viscous and interaction effects, and especially at the nozzle/afterbody, also thermochemical effects. Both the inlet and the nozzle/afterbody flow path must be minutely supported and controlled by light-weight structures with movable parts, which demands exact and reliable predictions of mechanical and heat loads and flow/structure couplings.

The most important research and development topics are:

1. Computer-aided design and optimization strategies and tools for the mean flow paths of both the inlet and the nozzle/afterbody.

2. Effective and reliable aerothermodynamic computation tools with adequate flow-physics and thermo-chemical models. The time has come, with present codes and super computer performances, to take into account the possible unsteadiness of the flow and its control. The source of unsteadiness is mainly related in hypersonics to incoming and self generated turbulence and to the fluctuations induced by shock-waves and separated areas ; advanced multiscale unsteady codes, with convenient simplification in smooth flowfields and mesh refinement in critical areas, open the way to the control of flow with combustion and its extended range of safe and efficient flight.

3. Effective and reliable computation tools, which permit the coupling of aerothermodynamics and the structure, with special attention to the length of correlations in unsteady excitation by noise and turbulence of the structural panels.

4. Ground-simulation facilities and techniques, as well as in-flight techniques for the experimental investigation and verification of aerothermodynamics and (hot) structures. This is economically possible only with sub-scale models, appropriate and reliable transfer models, (Ref. 5) so the development of the full-scale hardware must be provided for validation of such advanced design.

4.3 Critical Issues of Aerothermodynamic Airframe/Propulsion Integration

Aerothermodynamic airframe/propulsion integration, i.e. the shaping of the (controlled, elastic) vehicle, is the most demanding design problem, since the vehicle actually is a highly integrated lift and propulsion system, as was discussed above. Most important is the development of effective and reliable integration and optimization strategies and tools, and the verification by means of suitable experimental (ground-facility) strategies and experimental flight vehicles. A prerequisite is the advancement of the critical issues discussed in the preceding Sub-Chapters 4.1 and 4.2. and a specific effort devoted to the validation of integration problems because they generally include complex interfaces between different industrial partners (Ref. 3).

4.4 Compatibilities with European Launch-System Technology Development (FESTIP)

The Future European Space Transportation Investigation Programme (FESTIP), Ref. 6, is an effort to provide the enabling technologies for the development of an

advanced, cost-effective, reusable European space transportation system, which should become operational in the time frame 2015 to 2020. Presently system-concept studies are performed with harmonized mission scenarios, system requirements, design standards, technology assumptions, analysis tools and assessment criteria in order to identify potential system concepts, for which then the needed technologies will be developed. The system-concept studies cover a wide range of rocket-propelled and airbreathing single- and two-stage-to-orbit systems, which will be narrowed to one or two most promising system concepts within the next few years. Present technology work in several technology areas is aimed at the development of general and long-term technologies. This work is focused gradually in time according to the narrowing of the range of potential system concepts. System-concept study and technology work directly related to the present topic is that with regard to system concept FSS-12 (airbreathing SÄNGER-like two-stage-to-orbit concept). Elements of technology work (on structures, materials, aerothermodynamic and thermal management) with regard to other system concepts are of direct relevance (FESTIP) and natural programs for the present topic, too.

National research programs, outside FESTIP, particularly the French one, are oriented towards military and space applications and need. They have a lot in common on basic research, but a larger basis covering all the items ; all efforts enhance the global European knowledge for the various applications emerging in hypersonics.

4.5   Critical issues for the preliminary phases of hypersonic programs

Major issue remain the correct prediction of the viabililty of future programs. It first relies on the accurate prediction of anticipated performances (mainly related to thrust minus drag and specific consumption) and of the technologically critical points. They need to be precisely identified soon and put in as sound and securely scheduled development program as possible. Studies assume at this stage the building of sensitivity derivatives and of alternate pathes or alternate solutions with degraded performances in order to secure the feasibility : it is no more acceptable to engage a major program without a step by step reassessment of the research and development work from the view of the technical and managerial problems encountered in ended parts of the work.

In the aerodynamic configuration assessment such principles mean that the preliminary work has to go deeper in the demonstration by computation of the target performances and of critical detailed parts and by

validation of the involved tools in comparison with reduced size model tests.

In the preliminary conceptual phasis, the proof of concept has to rely on wind tunnel tests of a complex model with combustion (if needed as critical), and thermal fluixes ; wind tunnel test has to be rebuilt with the same tools used for flight prediction, including the comparative building of sensitivity derivaties and uncertainties (Ref. 2). In the industrial feasibility phases, same type of demonstration-validation has to be rebuilt, but using a reduced scale flight model, covering the same or higher criticity where needed on the same concept and flow topology if possible. No large scale demonstration of elementary critical part has to be put away from such step by step simulation - experimentation continous self substantation procedure.

Conceptually in aerothermodynamic such validation procedure has to go from elementary research workshops, for elementary codes and a given scale of phenomena, to multiphysics, multidisciplinary and optimisation industrial workshops supported by specific models able to validate integration capabilities and interfaces correctness. Such models, in wind tunnel and then in flight. Have a specific validation of integration models aimed to reduce future globally catastrophic misunderstanding or incorrect fittings between major industrial partners.

5.   CONCLUDING REMARKS

Generation of advanced configurations of hypersonic vehicles may be put at a level of quality that was not possible earlier, thanks to the development of multiphysics-multiscale simulation tools and the identification of major constraints in technology by past program experience.

We have shown that a new rationale for vehicle aerothermodynamics configurations allows the selection of more generics test vehicles. They are useful for assessing future possible performances, if sufficient optimization is carried out. Reduced scale flight models in a progressive (compatible) modular configuration relying on a generic basic sole concept, able to be extended to include later propulsion, seems from now attractive : such real flight demonstration concept is mandatory for the validation of design tools and the technology of future programs.

6.   REFERENCES

1.   Perrier P., Rostand P., "Hypersonic Airbreathing Aircraft Integration through CFD : Global Simulations for global thinking"

      30th AIAA/ASME/SAE/ASEE Joint Propulsion - Conference, AIAA paper 3090, June 27-29, 1994

2.   Perrier P., Stoufflet B., Rostand P., Baev V., A. Latypov, Shumsky V., Yaruslavtsev M., "Integration of an hypersonic airbreathing vehicle : assessment of overall aerodynamic performances and uncertainties",

      AIAA Paper, 6100, 6th Aerospace Conf., 3.7 April 1995

3.   Perrier P. "Problèmes mathématiques posés par l'estimation des incertitudes des simulations numériques", Mélanges offerts à R. Dautray - Masson 1993.

4.   Hirschel, E.H., "Heat Loads in Hypersonic Vehicle Design", Paper C-16 of this conference.

5.   Hirschel, E.H., "Aerothermodynamics and Propulsion Integration: Synthesis of the AGARD-FDP-VKI Special Course, April 15-19, 1996", Paper C-34 of this conference.

6.   Kuczera, H., Sacher, P.W., Dujarric, Ch., "FESTIP System Study-An Overview", AIAA-Paper, 1996.
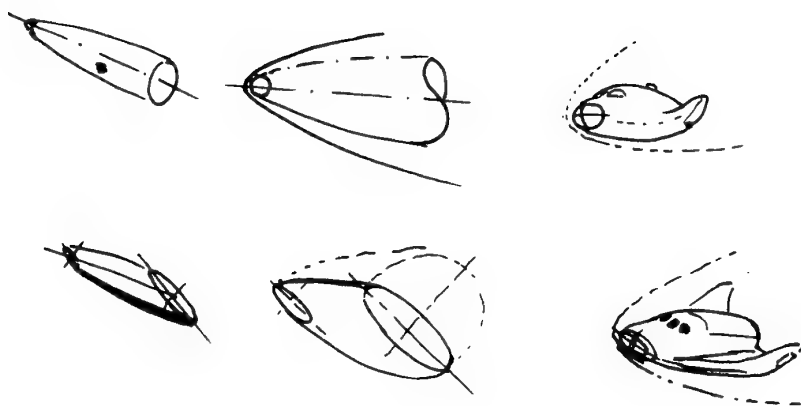
Fig. 1.1   *Axisymetric and elliptic bodies*
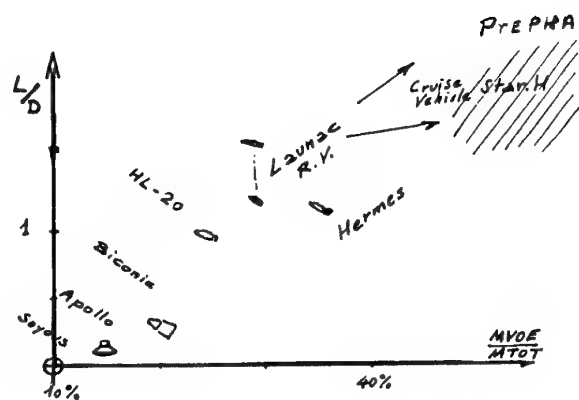
Fig. 1.2   *L/D for bow-shock shielding bodies*
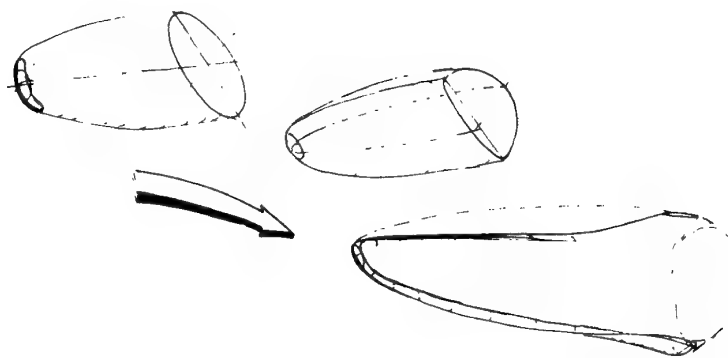
Fig. 1 3   *Launac hypersonic lower surface as a sole*

Fig. 1.4   Schlieren picture of bow shock wave past a circular cylinder at incidence at M = 8

Fig. 1.5   Wave-rider concave sole optimisation
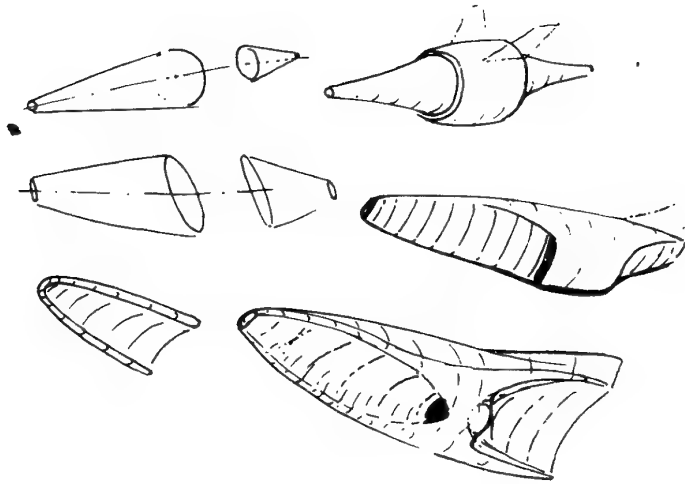
Fig. 1.6   Concave and convex airbreathing propulsion pack integration

Fig. 1.7   Concave and convex flow ducts and its control
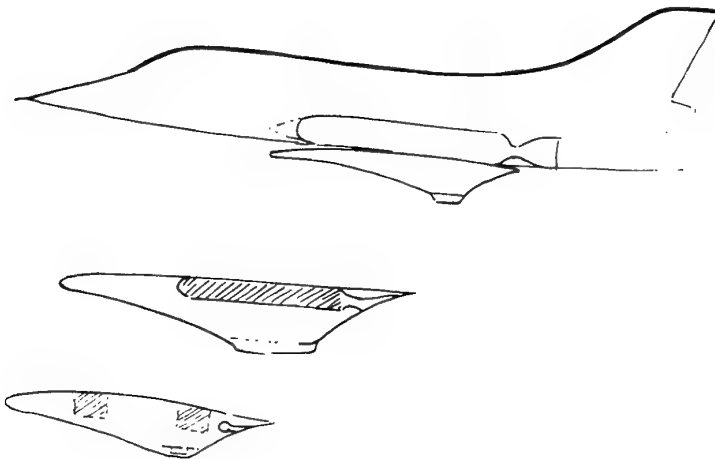
Fig. 1.8   External and internal booster/launcher constraints

blunt configuration

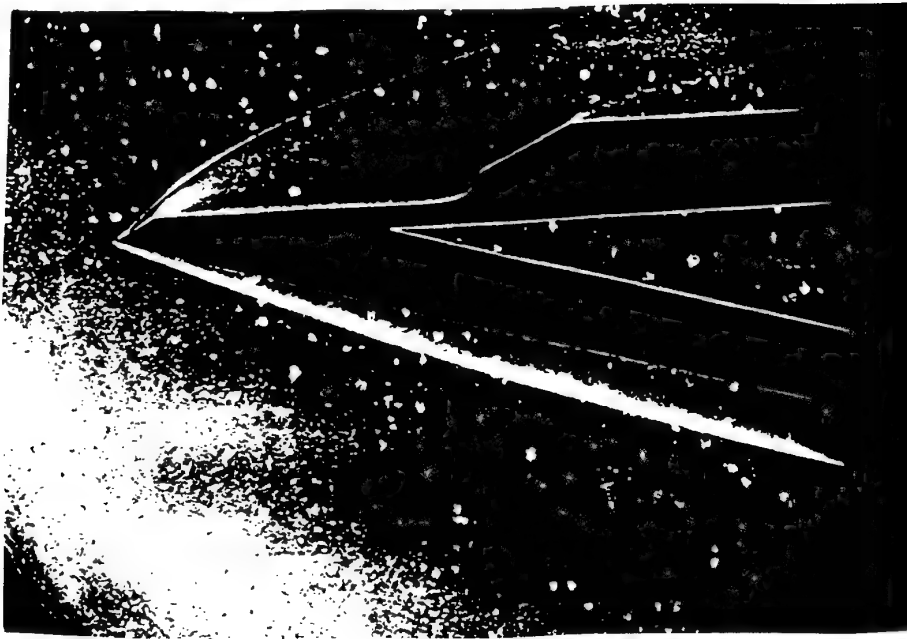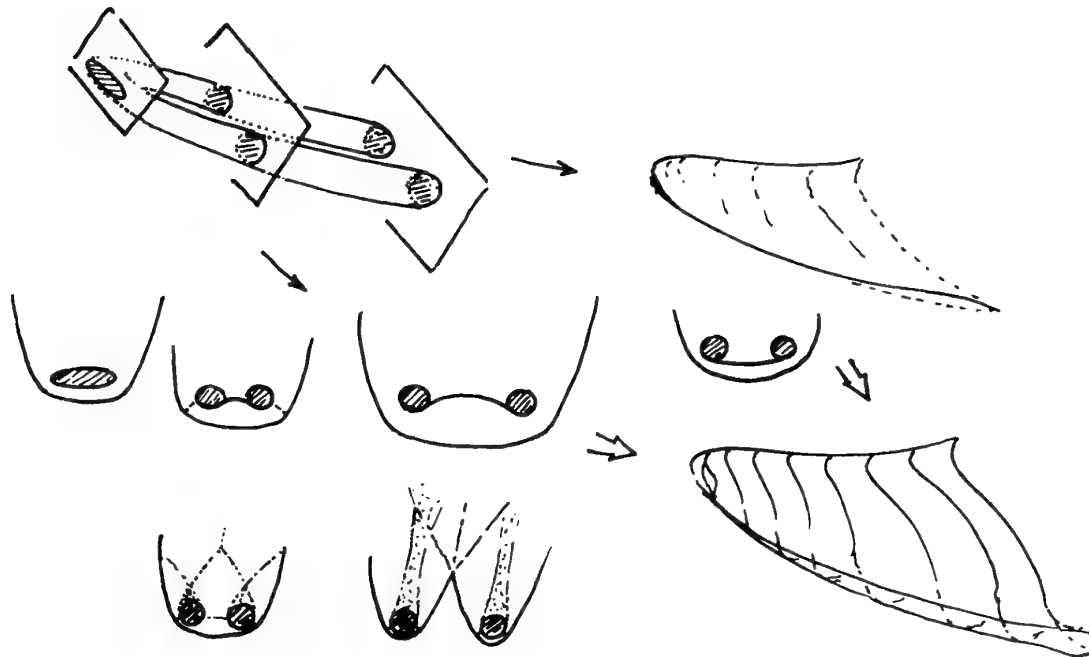radiation-cooled surface

winglets (inside bow shock) for lateral control and aspect-ratio enhancement

large angle of attack

cold primary structure with heat protection system

body flap for trim

outer flow path:
- pressure-effects dominated
- strong thermo-chemical effects
- surface-radiation cooling
- low-density effects
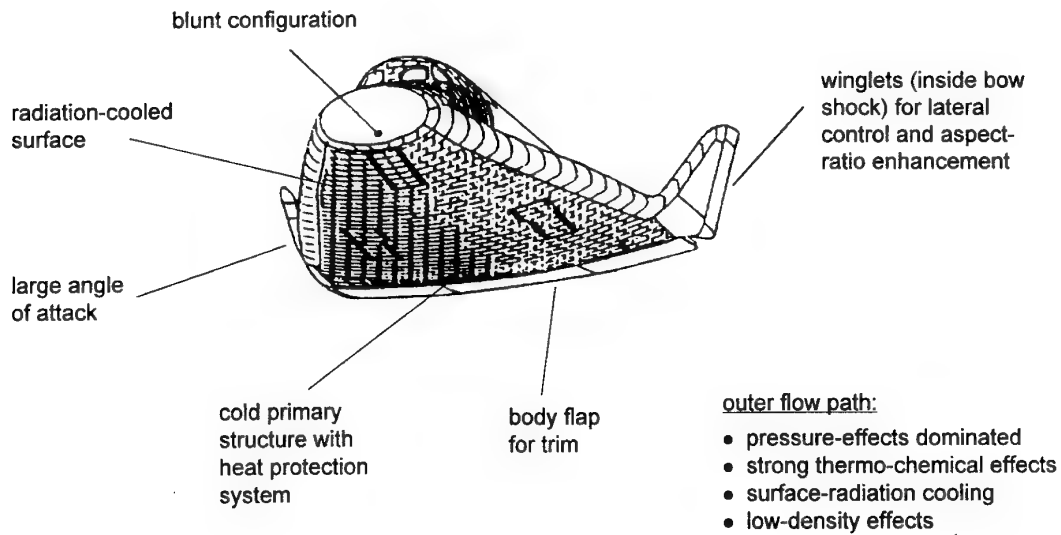
Fig. 2.1   *"Classical" reentry vehicle and some configurational aspects (schematically)*

slender configuration

hot primary structure

small nose radius

radiation-cooled surface

single expansion ramp nozzle

pre-compression

elastic forebody

integrated lift/propulsion system

actively cooled propulsion (turbo/RAM) package inside bow shock

outer flow path:
- viscous-effects dominated
- transition laminar-turbulent
- surface-radiation cooling
- weak thermo-chemical effects

Fig. 2.2   *An airbreathing lower stage of a two-stage-to-orbit vehicle and some configurational aspects (schematically)*

slender configuration

hot primary structure

small nose
radius (actively
cooled)

radiation-cooled
surface, partly
actively cooled

elastic
forebody

pre-compression

highly integrated
lift/propulsion
system

single expansion
ramp nozzle

rocket engines

actively cooled propulsion (RAM/
SCRAM) package inside bow shock

outer flow path:

- viscous-effects dominated
- transition laminar-turbulent
- surface-radiation and active cooling
- strong thermo-chemical effects
- low-density effects

Fig. 2.3   Schematic of an airbreathing single-stage-to-orbit-vehicle and some configurational aspects

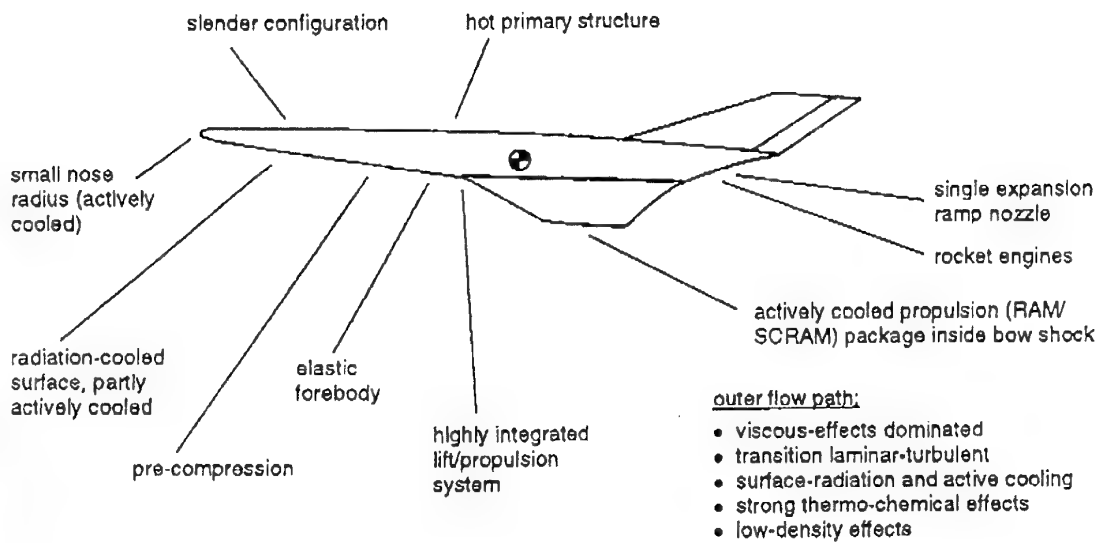
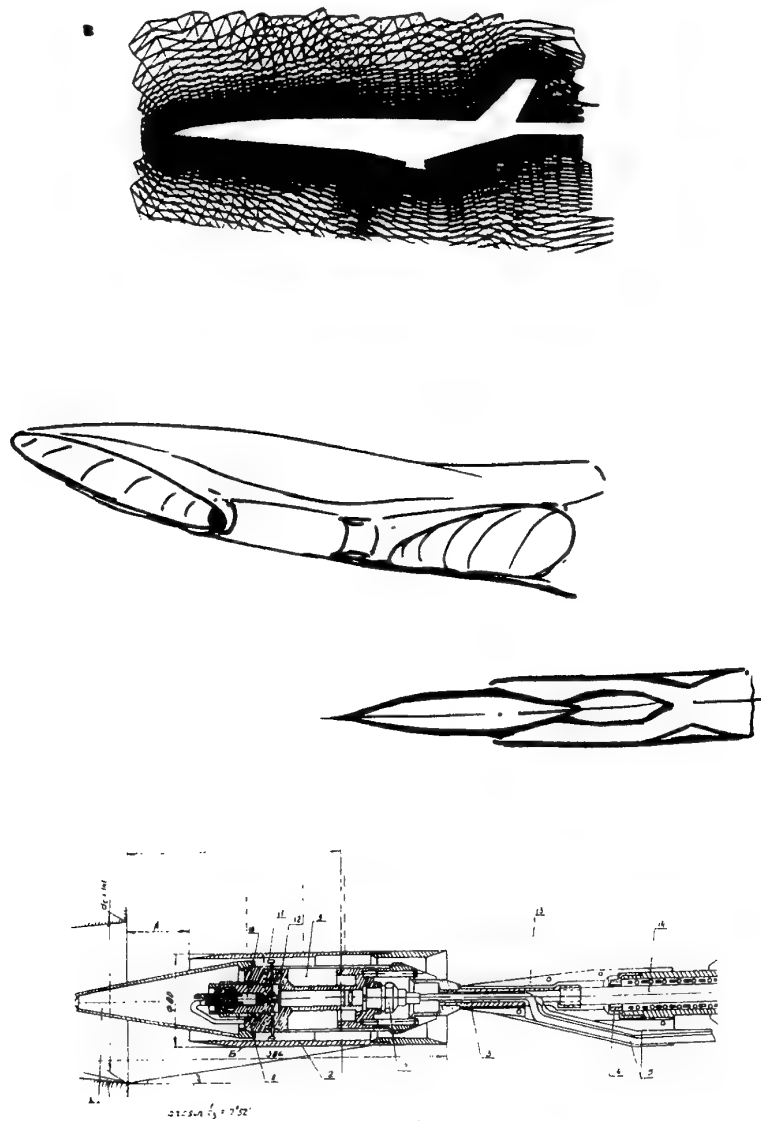Fig. 3.1   Shock-margin for propulsion pack as validated by Launac Schlieren picture at M = 8

Fig. 3.2   Concave Launac derivative and axisymetric penetrators

Table 4.1   Summary of technology issues (X: major topic)

Technology Issue / Vehicle	Surface-radiation cooling/ thermal protection	Inlet and nozzle/ afterbody	Airframe/ propulsion integration	Design and optimization strategies and tools	Flow physics and thermo-chemical modelling	Ground-facility simulation	Experi-mental vehicle(s) necessary
Cruise vehicle	X	X	X	X	X	restricted (sub-scale)	yes
Low-level penetrator	surface-radiation cooling is not effective	with air-breathing propulsion	with air-breathing propulsion	X	X	restricted (sub-scale)	yes
FESTIP system-study concepts	X	X	X	X	X	restricted (sub-scale)	yes

Hypersonic Air-Breathing Missile Propulsion

Paul J. Waltrup
The Johns Hopkins University
Applied Physics Laboratory
Johns Hopkins Road
Laurel, Maryland 20723 USA

ABSTRACT

A comparison of the performance of storable, liquid hydrocarbon fueled, scramjet-powered axisymmetric missile configurations using several types of fuel piloting/fuel pre-preparation methods are presented along with an initial methodology to permit these comparisons to be made. The merits of each engine type are discussed, and a first attempt at defining an upper flight Mach number bound on these types of engines ispresented.

NOMENCLATURE

A	area
C_D	drag coefficient
C_f	wall skin friction coefficient
C_{T_g}	gross engine thrust coefficient
C_{TN}	net vehicle force coefficient
ER_e	effective fuel-air equivalence ratio
M	Mach number
q	dynamic pressure
p	pressure
α	angle of attack
η_{KE}	inlet kinetic energy efficiency
η_c	fuel combustion efficiency

Subscripts

c	combustor
des	design
i	inlet geometric
max	maximum
ref	reference
w	wall
0	free-stream
1–5	engine stations (see Figs. 1 and 2)

INTRODUCTION

High-speed air-breathing technology, using storable fuels, has evolved over the last several decades to a point where it is appropriate to proceed with a demonstration of these technologies in a system configuration aimed at Mach 8.0 capability. However, before discussing the technology challenges and potential of the Mach 8 vehicle, it is appropriate to review the historical evolution of this high-speed, air-launched capability from its origins.

The conventional ramjet engine was used primarily for missile propulsion in the post World War II period. Many countries developed ramjet-powered surface-to-air missiles, such as Bloodhound (UK), Bomarc and Talos (USA), and the Russian SA-4 (Ganaf). In France, the Vega and a ramjet-powered target vehicle, the CT41, were also developed. Many other ramjet-powered projects were undertaken to develop improved surface-to-air missiles, such as the Typhon (USA), and also to expand the flight envelope of such systems. In the latter class were the UK National Gas Turbine Establishment (NGTE) test vehicle series and the French Stateltex project. Ultimately, very large subsonic-burning engines were developed for the intercontinental range missiles Navajo (USA) and Buran (USSR).

These early ramjet systems were essentially axial flow systems, using single- or multi-cone inlets with modest turning angles: following supersonic compression, the flow was subsonically diffused and axially introduced into a combustor that typically used gutter stabilizers and/or can-type burners. An extensive international database for inlet and combustor design was generated during the late 1940s and the 1950s. Furthermore, extensive research and development flight testing took place, adding to the database for engine development; for example, in the USA, the Lockheed X-7 vehicle alone resulted in over 100 test flights. Of course, rocket boosters were essential for these early ramjet systems, and externally mounted solid-fuel boosters of both parallel and tandem configurations were used.

Following the initial period of extensive ramjet development and the maturing of the associated technology base, flight performance of this class of engine was widely demonstrated in the Mach 4.0–5.0 region. There was considerable interest in the performance of hydrocarbon-fueled ramjet engines at still higher Mach numbers, and this interest was captured in many of the discussions recorded in the Fourth AGARD Colloquium held in Milan in 1960.[1] However, there was some divergence of views on the practicability of extending the performance of such ramjet engines to speeds of Mach 5.0–10.0. Mallinson, of NGTE, noted[2] the rapid fall-off in predicted engine performance

between Mach 4.0 and Mach 7.0, but other authors maintained that much higher speeds might be achieved. At NGTE, significant exploratory work was undertaken in the mid-1960s on a ramjet type of combustor, using a tube-matrix injector, at Mach 6.0 conditions. This work was led by A. B. P. Beeton and demonstrated the engineering feasibility of such combustors. During the same period, an interesting study of real gas effects on a Mach 7.0 kerosene-fueled engine was performed by Hawkins and Fox,[3] with particular emphasis on the nozzle recombination problem. In the USA, there were also continuing studies of hypersonic engine component design and performance. Much work was performed on high-speed inlet design. Also, regenerative cooling of the combustor was developed; much of this work was to find application to a hydrogen-fueled combustor designed for Mach 8.0 conditions. The key problem of exhaust-nozzle performance continued to attract much effort.

However, in retrospect, not enough work was performed to establish the realistic performance capabilities of conventional ramjet engines at the higher flight Mach numbers; preferred engineering design approaches also were not firmly established, and candidate engines did not proceed into flight test. Moreover, beginning in the late 1950s, research interest in high-speed propulsion was increasingly turning to the study of supersonic combustion ramjet (scramjet) engines. Two early foundational papers on this topic were published, one by Weber and Mackay in 1958[4] and the other by Dugger in 1960.[5] The latter paper was largely concerned with the relative flight performances of the subsonic and supersonic combustion engines. Although this discussion of performance was fairly straightforward from a cycle-analysis point of view, the then existing lack of knowledge concerning actual scramjet component behavior (flow phenomena and performance characterization) on the one hand and the lack of accurate hypersonic ramjet performance data on the other clouded quantitative comparisons of the ramjet and scramjet candidate engines in the Mach 6.0–8.0 regime. In any event, as a result of the rapidly emerging interest in space launch vehicles, scramjet engine research was soon focused on the potential performance of hydrogen-fueled engines at very high Mach numbers and on their applications to the single stage-to-orbit aerospace plane concept.[6] Interest in the conventional hydrocarbon-fueled engine rapidly faded, and a major thrust to develop scramjet engines was launched; the major achievements of this effort, funded by the U.S. Air Force (USAF), including the development of the dual-mode ramjet engine, are well documented in Ref. 7. Much of this emerging work was led by Dr. Antonio Ferri.[8]

Initially in the aerospace plane program, it was assumed that the vehicle would be accelerated to about Mach 8.0 by a combined-cycle turbo-accelerator; the vehicle would then accelerate from Mach 8.0 to near-orbital speeds on scramjet power. Later studies looked at the possibilities of operating the scramjet engine duct at lower flight speeds, in the subsonic combustion mode.[9] This gave rise to the concept of a dual-mode combustor in which the ramjet duct could operate over a wide speed range, initially in a subsonic combustion mode and later transitioning to supersonic combustion. A Marquardt dual-mode scramjet was successfully demonstrated,[10] with smooth transition between modes, in 1967, using hydrogen fuel. Later, when the attention of the USAF turned to scramjet-propelled missiles, the supersonic combustion of hydrocarbon fuel was demonstrated using a relatively longer combustor and an energetic piloting system.[10] Many more details of dual-combustion operation can be found in Refs. 11–13.

Unfortunately, these early focused scramjet development efforts did not proceed into a successful flight test, and USAF-funded scramjet work was to lay fallow until the initiation of the National Aerospace Plane program in 1985. Fortunately, some limited work on the development of scramjet engines for missiles was to proceed. Under NASA and U.S. Navy sponsorship,[13] detailed work on scramjet engine technology continued and, in particular, work on a liquid-fueled Supersonic Combustion Ramjet Missile (SCRAM) was sponsored at the Applied Physics Laboratory (APL) of The Johns Hopkins University starting in 1961 and continuing until 1977. This engine program provided significant fundamental scramjet missile technology, and this effort is well documented by Billig.[14] Unfortunately, this engine development was based on pyrophoric and toxic fuel blends, which were not ultimately acceptable to the operational community. However, liquid-fueled scramjet work continued through the 1980s at APL, focused on a dual-combustor ramjet concept using storable heavy hydrocarbon fuels.[15]

Meanwhile, the potential of the integral rocket ramjet (IRR) concept as a viable missile propulsion system attracted much attention, particularly with the advent of the Soviet SA-6 missile. The IRR concept of integrating the rocket booster inside the ramjet engine combustor led to a compact air-launched missile configuration. Although most of these IRR systems operated at modest Mach numbers, the USAF air-launched ASALM missile was tested to flight speeds approaching hypersonic Mach numbers. Unlike the French ASMP missile and the FSU kH17 missile, the ASALM was not to see operational service;

however, the fully successful flight tests of the ASALM conclusively showed the potential of a high-speed, air-launched IRR missile that could be carried internally in a bomber aircraft and could possess long stand-off strike capability. In summary, the marriage of the high-speed capability of the ramjet and a compact air-launched missile has been successfully demonstrated.

One should also note in passing the significant French exploratory work on the surface-to-air missile SCOR-PION.[16] This missile used a subsonic combustion ramjet operating up to Mach 6 after a tandem boost to Mach 3. Although this work did not proceed to flight demonstration, the analysis and experimental work demonstrated an important advance in high-speed ramjet technology.

Turning now to the subject of future developments in scramjet technology, it appears that a need is emerging for a high-speed, fast-response, air-launched missile. This military need is discussed at length in Ref. 17, and the candidate system for study is a hypersonic air-breathing, hydrocarbon-fueled, scramjet-propelled weapon achieving mission speeds as high as Mach 8.0. The technology for such a system concept is already being addressed in the USA by the USAF-funded "HyTech" program.[18]

It is tacitly assumed that hydrocarbon-fueled scramjets will be used for a variety of other missions, and it is appropriate to investigate the ultimate flight performances and engineering constraints of various engine configurations.

Obviously the existing hydrocarbon scramjet technology base is currently very limited, largely empirical, with testing largely restricted to a few engine geometries and with limited approaches to pilot and combustor design. Future technology efforts will be planned to derive a structured approach to the synthesis of a preferred engine configuration.

Although the scramjet engine is simple in concept, the creation of an optimally performing engine operating over a wide range of Mach numbers is a significant engineering challenge. This is particularly true for a dual-mode engine using hydrocarbon fuel and operating over the speed range of Mach 4.0–8.0. Also, compared to the conventional ramjet engine, the scramjet development is much more complex. In the ramjet engine, the overall engine could largely be developed by integrating the basic engine components: inlet, fuel injector/flame holder/combustor, and nozzle. The component interactions, although not insignificant, could be addressed in a relatively straightforward manner. In the scramjet engine, operating with mixed flow or predominantly supersonic flow,

the gas dynamic interactions are severe. Typical internal flow phenomena include, but are not limited to, shock propagation along the duct; shock-boundary layer interactions leading to unsteady mixed-flow areas; boundary layer separations and reattachments; fuel-injection/core flow interactions, spatially evolving mixing and combusting flows; thermal choking, both global and local; and severe boundary condition interactions involving pseudo-shocks, shock impingement on the wall, and wall physical-chemical effects such as quenching.

These phenomena present severe challenges to engine development for hydrogen-fueled systems; it is possible that successful, effective engine operation may only be achieved with a sophisticated active-control system.

A further problem is that despite some 40 years of research, a standard scramjet design configuration has yet to emerge that would provide a focus for ongoing scramjet research. The same can be said for a standardized design methodology for the integrated engine and its individual components. The closest approach to commonality has been the axisymmetric dual-mode engine configuration typified by the NASA Hypersonic research engine,[7] the U.S. Navy SCRAM[14] engines, the French ESOPE engine,[15] and the Russian dual-mode scramjet engine flight tested on the Kholod vehicle. Two additional distinct configurations are the two-dimensional NASA airframe integrated engine,[7] which has also been studied at CIAM and TsAGI, and the U.S. Navy dual combustor ramjet[16] engine developed at APL. As a consequence of the lack of a standard configuration, engine development to date has been diverse and lacking focus on common approaches to a specific preferred design incorporating standardized subprocesses such as combustor configuration, fuel injection, and flame holding. In the exploration of new engine concepts operating over different speed ranges and employing hydrogen and storable fuels, such diverse approaches are to be anticipated. However, development will be speeded if more effort is placed on configurations that lend themselves to engineering approaches that will enable control of flowpath phenomena, e.g., a multistep burner where a standard "step" component is used sequentially to spatially anchor heat release along the combustor.

The current USAF HyTech program is evaluating various design approaches to the Mach 4.0–8.0 hydrocarbon-fueled dual-mode scramjet engine. These engines initially included designs by United Technologies/Pratt & Whitney, Aerojet, Rocketdyne, and Kaiser-Marquardt but were subsequently reduced to the United Technologies and Aerojet configurations. It is to be hoped that a configuration will emerge from these and/or other current research

and development studies that can be confidently developed using standardized and sophisticated computational fluid dynamics analyses and state-of the-art experimental tools.

The purpose of this paper is to present, discuss, and compare the performance of a number of various engine concepts in terms of how they are able to meet and overcome fundamental performance issues associated with efficient scramjet operation; these issues are presented and discussed in the next section. Subsequent sections of the paper will address the relative performance of a limited number of these emerging engine concepts. Finally, an initial attempt to define an upper bound on flight Mach number for hydrocarbon-fueled scramjet engines is presented and discussed.

SCRAMJET DEVELOPMENT/PERFORMANCE ISSUES

One fundamental and several primary issues are associated with the development and efficient operation of a supersonic combustion ramjet (scramjet) engine that inhibit its use in its simplest form (Fig. 1). The fundamental issue is the pure scramjet's inability to operate on storable liquid hydrocarbon fuels alone for flight speeds at or below Mach 8. The primary issues include distribution, mixing, and ignition of the injected fuel with the air stream, and the thermal balance required between the cooling available from the engine fuel flow (for thrust generation) and the actual cooling needed for structural survival. There are other issues, such as inlet and nozzle efficiency, inlet/combustor isolator requirements, engine/combustor wall friction losses, etc., that are not insignificant but are also not fundamental to the "yes" or "no" operation of a scramjet engine, and no further discussion of them is proposed. However, one item of key interest for engine applications is the determination of a practical upper bound on flight speed with hydrocarbon fuels.

The requirement to add either a very energetic and/or reactive fuel or oxidizer source to a liquid heavy hydrocarbon fuel or to pre-prepare the fuel for efficient combustion in the supersonic combustor has been well documented experimentally over the past 30 years.[10,13-16,19,20]
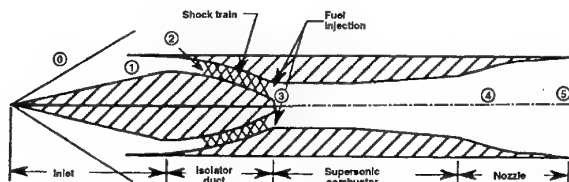

Fig. 1 Engine schematic of supersonic combustion ramjet.

One only need read Ref. 9, written in 1963, to appreciate how long this has been an issue and how long many of the resolution methods have been recognized.

Solutions to the fuel ignition and efficient combustion issue tested to date include the addition of very reactive, pyrophoric (and generally toxic) fuels (such as boranes) to the liquid hydrocarbon fuel, the injection of a very reactive oxidizer (such as chlorine trifluoride) or fuel near the point of hydrocarbon fuel injection, or the use of pilots in which a portion (or all) of the liquid heavy hydrocarbon fuel is pre-prepared for efficient combustion in the supersonic combustor. Of the solutions successfully tested, only the fuel pre-preparation solution is logistically acceptable in today's operational environment.

However, this solution includes a number of fuel pre-preparation options that are quite dissimilar; many of the concepts that have appeared in the literature have been or are being investigated. These include the dual combustor ramjet (DCR) engine[16] (Fig. 2), a wall piloted scramjet concept[21,22] (Fig. 3), a split inlet piloted scramjet[23] (Fig. 4) concept, a catalytic pilot scramjet concept[20] (Fig. 5), and strut-ducted-rocket/scramjet concepts[13] (Fig. 6). Each may also be used in combination with an endothermic liquid hydrocarbon fuel,[21,24,25] such as JP-7, to provide some or all of the requisite structural cooling. However, it must be kept in mind that an initial, non-flow-path heat source is needed to initiate the endothermic process should it be needed at the takeover flight condition of the ramjet or scramjet engine. There has also been international interest in the enhancement of kerosene-type fuel combustion in scramjets, mostly in Russia (see, e.g., Ref. 26), but this topic is not included in these discussions for, among other reasons, a lack of flight configuration detail.

To compare the relative merits of each engine type or concept is not an easy task. However, a set of criteria (figures of merit) such as those described next is used herein in an attempt to do just that. These criteria include the following:

1. The fuel type that can be used in the engine, whether it be liquid, gaseous, or both, including endothermic fuels in either of their phase states, and whether an energetic fuel or oxidizer pilot source is required to sustain combustion. Note that endothermic fuels (or other active cooling heat sinks) are generally required for flight speeds above Mach 6–6.5, depending on the specific engine or vehicle design and flight dynamics.

2. If a cold start ignition source is required, what it might be, and the ability of the ignition source chosen to relight the engine should its flame be extinguished.
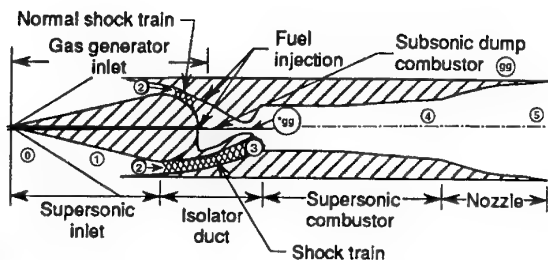
Normal shock train
Gas generator inlet
Fuel injection
Subsonic dump combustor ⓖⓖ
②
③
gg
④
⑤
⓪
①
Supersonic inlet
Isolator duct
Supersonic combustor
Nozzle
Shock train

Fig. 2 Engine schematic of dual combustor ramjet.

3. The stability of the fuel pilot/pre-preparation system and its sensitivity to such things as inlet stability, dynamic pressure variations (Reynolds number), wall effects (viscosity and heat transfer), geometry, required fuel distribution, and pressure matching.
4. Weight and volume penalties associated with the proposed engine cycle (including multiple fuel supply/control systems).
5. The engine's performance compared to that of a pure scramjet.

With these criteria, let us now turn our attention to a description and discussion of the candidate engine cycles.

CANDIDATE HYDROCARBON-FUELED, HYPERSONIC ENGINE CYCLES

Pure Scramjet

The pure scramjet has been around since the late 1950s, at least in concept.[13] In its simplest form, as shown in Fig. 1, it comprises an air inlet to diffuse the hypersonic air stream to a supersonic speed, an isolator duct to prevent combustion-induced disturbances from interacting with the performance of the air inlet, a fuel injection station, a simple flame holder (such as a wall step increase in area), a constant or moderately diverging area combustor, and an exit nozzle. As previously discussed, this engine can only operate with very reactive fuels (such as alkylated boranes) or fuel mixtures[14]; even gaseous hydrogen fuel will not ignite and efficiently burn at the lower (Mach 3–5) flight speeds. Storable liquid hydrocarbon fuels alone will not burn with any acceptable efficiency, even at Mach 8. Consequently, modifications to this concept are necessary if storable, logistically suitable hydrocarbon fuels are to be used.

Dual Combustor Ramjet

The DCR (Fig. 2) was originated by J. L. Keirsey at APL in the late 1970s to permit the efficient combustion of storable liquid heavy hydrocarbon fuels in a hypersonic air-breathing engine. In the DCR concept,[16] a small fraction of the air captured by the inlet (12.5–25%) is diffused to a small embedded subsonic dump combustor, where all of the liquid fuel is nonuniformly injected at or near the dump plane. This nonuniform fuel injection pattern permits a stoichiometric flame to be maintained in the center of the dump plane via a spark plug, the heat

(a)
(b)
Section
a
b
c
d
e
f
a
b
c
d
e
f
Sections
(c)
Views looking downstream
Air-breathing pilot injectors (combustor entrance)
Fuel injectors
(d)
Flow
Primary Injectors
Pilot Injectors
Exit

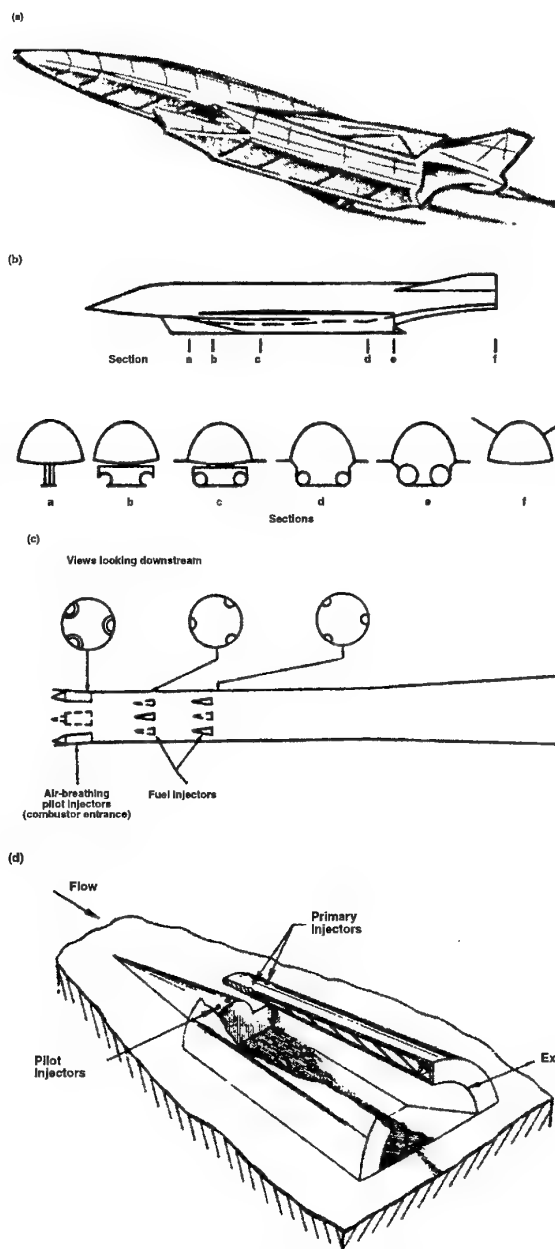

Fig. 3 Wall-mounted pilot scramjet concept.[22] (a) Hydrocarbon-fueled scramjet missile; (b) scramjet vehicle; (c) combustor concept; (d) air-breathing pilot/injector.
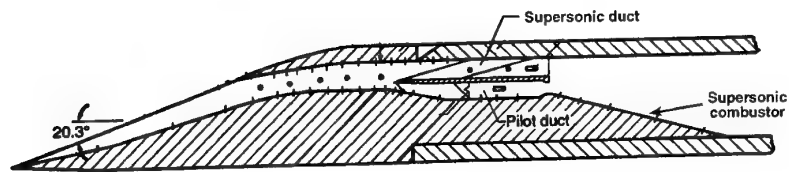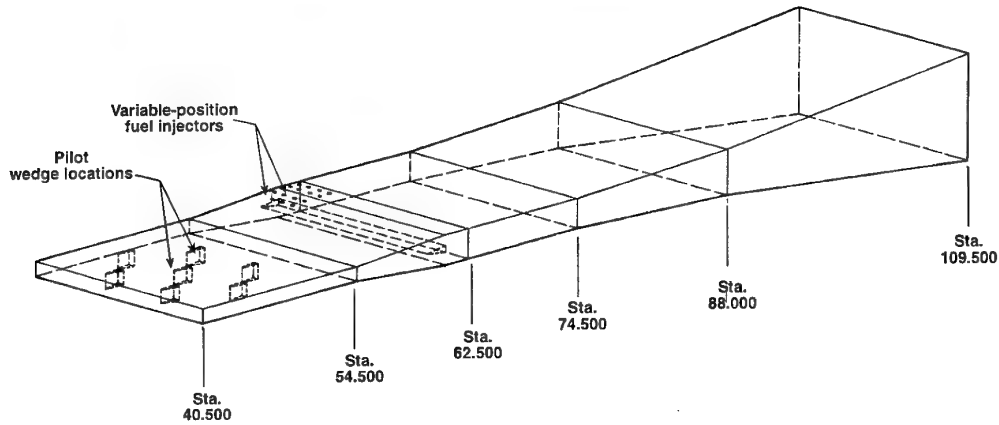
Fig. 4 Split inlet piloted scramjet concept.[24]

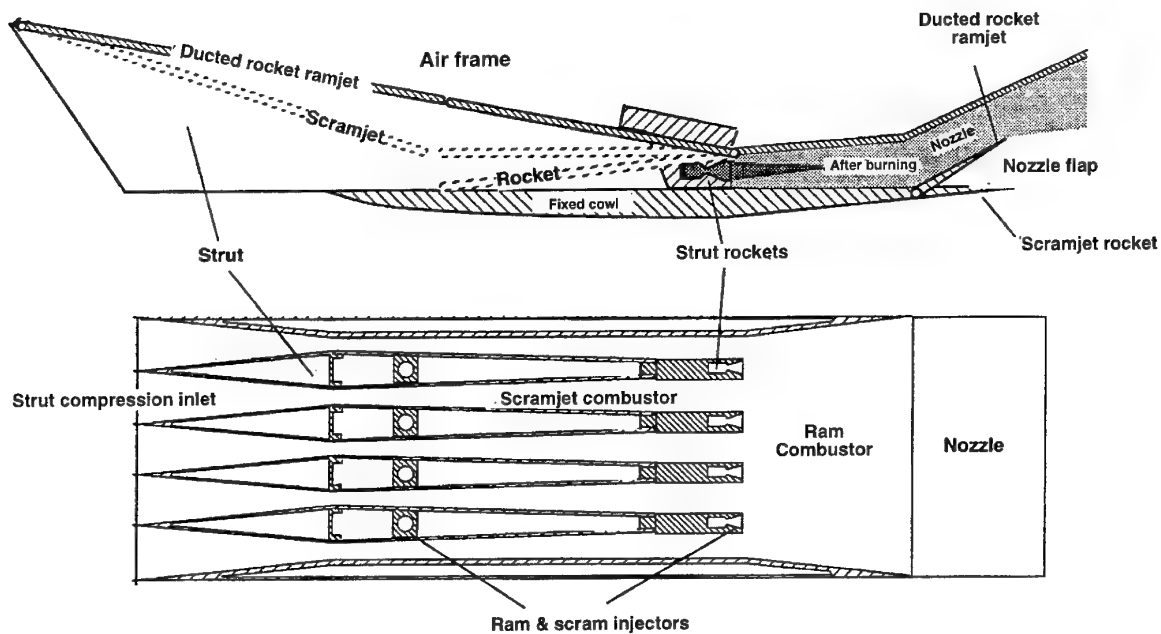**Fig. 5** Catalytic piloted scramjet combustor concept.[10]

Fig. 6 Strut-ducted-rocket/scramjet engine concept.[28]

from which is used to vaporize and crack the remaining liquid fuel. This hot, molecularly light, mostly gaseous effluent is then axially (or nearly axially) injected into the supersonic combustor, where it mixes and reacts with the main supersonic inlet airflow as shown in Fig. 2.

With respect to the above five criteria, the DCR can operate with either a cold, liquid heavy hydrocarbon or a hot, light gaseous fuel. Endothermic (e.g., JP-7) fuels are permitted whether structural survivability requires their use or not. Remember, however, that the volumetric energy density of typical endothermic hydrocarbon fuels is only 70–80% of that of other liquid heavy hydrocarbon fuels (such as JP-10). The DCR uses a simple spark plug located in the gas generator's dome region that operates continuously. The DCR, therefore, does not require a cold start energy source and is capable of re-establishing combustion should a flameout occur.

The gas generator and its interaction with the main supersonic combustor have been experimentally demonstrated to be stable in the Mach 3–4 speed regime, a regime where one would expect any combustion or aerodynamic instabilities to be most pronounced. These tests were conducted with both cold (room temperature) JP-5 and RJ-5. Moreover, this full-scale, axisymmetric version of the DCR combustion system has demonstrated combustion efficiencies in excess of 90% at these flight speeds with dynamic pressures as low as 35 kN/m^2 (750 lbf/ft).

At low flight Mach numbers, however, the DCR can be sensitive to the pressure matching requirements of the gas generator exit and supersonic combustor entrance flows. In this flight regime, the gas generator inlet may unstart, but since the gas generator inlet(s) are separated from the supersonic combustor inlets, there are no additional adverse interactions.

Some weight and volume issues are also associated with using the DCR (as there are with all of the engines described below). The DCR requires a separate gas generator air inlet system and a rather large (compared to the other concepts described below) fuel pre-preparation system (gas generator). It does not, however, require more than one fuel supply and control system.

The performance of the DCR is compared in detail to both a scramjet and ramjet in Ref. 15. The results show that the DCR's performance is comparable to a subsonic combustion ramjet at Mach 3 but is better at Mach 6. This is to be expected since the DCR operates more like a scramjet at the higher flight speeds. Reference 15 also shows that the DCR performs much better than the scramjet at Mach 4 but has poorer performance at Mach

8, again due to the fact that the DCR operates much like a ramjet at the lower flight speeds. Their comparative performances are discussed in detail in the next section.

Wall Piloted Scramjet
An alternate piloting scheme involves the use of a wall-mounted subsonic combustion pilot within the combustor. In one implementation of this approach, small half-axisymmetric, fixed-geometry, conical inlet, subsonic combustion ramjets are attached to the engine's wall(s) at the entrance of the supersonic combustor[21,22]; the number of ramjets varies with the particular engine size and combustor design. These ramjets are designed to provide a pilot flame for the main supersonic flow. Each ingests less than 5% of the supersonic flow entering the combustor, including the wall boundary layer, and operates at or near stoichiometric with a gaseous hydrocarbon fuel. The projected frontal area of each pilot is on the order of 15-20% of the air stream tube to be piloted.

The remainder of this engine concept is identical to that of a pure scramjet except for a rather short inlet/combustor isolator duct that may be required to provide adequate flow into the pilots. The main fuel injection locations are either around the periphery of the pilot's exit plane or from discrete normal hole wall injectors staged downstream and outboard of the pilot flame.

Tests of the wall-mounted pilot indicate that this engine concept operates most efficiently using a heated gaseous fuel, such as would be present when an endothermic liquid hydrocarbon fuel is used to actively cool the engine and select portions of the airframe. Tests with the pilot alone show that it cannot operate on liquid or heated/flash vaporized JP-5 and that its best operation is achieved when either a pyrophoric fuel is added to the ethylene (SiH_4-silane), the ethylene is heated (such as would be present in an endothermic process), or a bluff body in-stream flame holder is located in the ramjet combustor. The preferred option is to use the heated products of an endothermic fuel cracking and heating process. The tests also show that the pilot will need a separate ignition source for speeds below approximately Mach 4.5.

Operation of the pilot in conjunction with the main fuel injectors shows that the integrated pilot/supersonic combustor performs best when using heated ethylene fuel. Unheated ethylene injected through the primary fuel injectors also works well for flight Mach numbers above approximately Mach 5.4. Unheated liquid hydrocarbon fuels, such as JP-5 or JP-7, on the other hand, exhibit very little heat release at any of the simulated flight conditions tested. However, if either is heated and flash vaporized

during injection into the main supersonic combustor flow, increased performance is realized, but only at low equivalence ratios. At the higher equivalence ratios, performance is still poor. This poor performance of the liquid heavy hydrocarbon fuels is to be expected since they require on the order of 36 MJ/kg (15,000 BTU/lbm) of fuel[15] to achieve 80% or greater combustion efficiencies, whether this energy comes from the air static enthalpy or an energetic pilot.

In summary, engine concepts using small wall-mounted pilots may require the use of a light gaseous fuel in the pilot(s) and a light (heated or unheated) gaseous fuel in the main supersonic combustor if it is to operate efficiently. The heated, gaseous products of a liquid endothermic hydrocarbon fuel reactor process used to cool the engine structure would be an ideal fuel. Cold or heated liquid heavy hydrocarbon fuels do not work very well, especially at the lower flight speeds. Furthermore, an independent ignition source for the gaseous pilot fuel is needed below Mach 4.5, and this concept will need to carry a separate energy source to provide heat to start the endothermic liquid hydrocarbon reaction process at the end-of-boost flight condition. It has yet to be determined if a third energy source would be needed to relight the engine in the event of a flameout; the hysteresis and residual gaseous fuel products in the endothermic reactor may be sufficient for this purpose.

Another issue to be considered is how effective these wall pilots are in achieving the requisite combustor performance as the cross-stream dimension of the supersonic combustor increases. Two major issues in scramjets is how to get the fuel out into the center of the combustor and then how to get it to burn efficiently. Pilots located on both walls of a two-dimensional combustor and around the periphery of an axisymmetric design can only penetrate so far (approximately 100 mm), especially with downstream wall fuel injection where the cross-stream dimension of the combustor has increased. This issue needs to be carefully addressed in any missile design, especially two-dimensional designs where pilots located on the cowl side would be difficult to integrate, cool, and supply with a controlled fuel flow rate.

As with any piloted scramjet engine concept, this approach also has weight and volume penalties for the pilot(s), pilot fuel supply and control system, multiple staged main combustor fuel injectors and controls, and cold start energy source for the endothermic reactor.

Split Inlet Piloted Scramjets

A third alternate for piloting involves splitting the inlet flow at the throat and directing a portion of the flow into a subsonic combustion pilot. An example of this approach is described in Ref. 23. In this approach, a two-dimensional, fixed-geometry, subsonic combustion ramjet pilot is used to sustain combustion in the main supersonic combustor. The pilot is embedded in the throat of the supersonic inlet diffuser (Fig. 4) and sized to capture approximately 25–30% of the ingested air. The exit of the pilot is the entrance of the supersonic combustor. The pilot is operated either stoichiometrically or slightly fuel rich using an in-stream v-gutter flame holder and a hydrocarbon fuel. The remainder of the hydrocarbon fuel is injected at or downstream of the entrance of the supersonic combustor from wall orifices.

The literature available on the split flow inlet concept includes only an initial set of experimental data on the inlet performance at a free-stream Mach number of 4.[23] These data indicate that the inlet's performance is sensitive to the amount of backpressure induced to simulate combustion, even in this low inlet area contraction design (A_2/A_i = 3.4). No data with combustion are available.

With respect to the criteria for assessing the merits of each engine concept given at the beginning of this section, the split inlet piloted concept is intended to operate on either liquid or gaseous hydrocarbon fuels. However, like the wall-mounted pilot concept, it is expected that this concept will require light gaseous hydrocarbon species injected in both the pilot and main supersonic combustor if efficient combustion is to occur. The pilot is quite small, i.e., the residence time is quite short, and it only pre-prepares a quarter to a third of the liquid heavy hydrocarbon fuel. Consequently, it most likely will require light, gaseous, and perhaps heated fuel species in both the pilot and main supersonic combustor to operate efficiently.

This concept would be another good candidate for liquid hydrocarbon endothermic fuel use, especially since the engine side of the pilot structure as well as the flame holder will require active cooling at all flight speeds. It would also require a cold start energy source for an endothermic process to be initiated at end-of-boost flight speeds, and the ignition source for the pilot is not discussed. In addition, since this two-dimensional concept will scale with size in the normal direction, fuel and pilot flow distribution and mixing do not appear to be a problem for missile-size engines.

In addition to the combustion issues, there are issues associated with the operability and stability of the inlet/pilot system. As alluded to in the initial discussion on the experimental data, the initial tests were conducted on a very low area contraction ratio inlet, one that would not be very efficient for flight up to Mach 8. Furthermore, the

data indicate a stability problem, especially with the pilot flow. At very low values of backpressure, indicative of low heat release levels in the supersonic combustor, the pilot unstarted, creating large wall boundary layer separated zones upstream of its inlet. This type of operation has serious implications for the performance and operability of the pilot alone and its ability to effectively pilot and maintain high-efficiency combustion in the supersonic combustor. In addition, these effects would only be exacerbated with heat addition in the pilot, especially at the low fight speeds.

Again, since this is a piloted scramjet engine concept, there are weight and volume penalties associated with it compared to the pure scramjet engine. These include the weight and cooling requirements of the pilot, a separate pilot fuel supply and control, and a cold start energy source. Because of a lack of design information, no performance estimates for this concept or comparisons with other concepts are attempted in the next section.

Catalytic Pilot Scramjet

A fourth approach to the piloting problem attempts to minimize the size of the pilot through the use of a catalyst within the pilot. An example of this approach is a modern version of a 1960s MA194 "Alligator Inlet" scramjet design[10] (Fig. 5). The original design used a series of small flame holder wedges located along the upper and lower walls of this two-dimensional engine concept. These were preceded by two sets of small wall orifice fuel injectors. The first set was used to inject chlorine trifluoride into the airstream, followed by the injection of a liquid heavy hydrocarbon fuel. While this piloting system worked, ClF_3 is not an environmentally friendly nor logistically suitable pilot. This piloting concept, however, is the closest to that of a pure scramjet of the piloting concepts discussed in this paper.

Because ClF_3 is an unacceptable pilot oxidizer, the original ClF_3 pilots and flame holder are replaced with split wedge fuel pilots with catalytic internal screens. One could consider these pilots to be smaller, two-dimensional versions of the wall-mounted pilot concept with the addition of catalytic surfaces and "hypermixing" interdigitated wedges on the external and internal flow exit nozzle surfaces (Fig. 5).

While early results on configurations with catalytic pilots are encouraging, a number of issues (or figures of merit) still require attention. These include the ability of this concept to use liquid heavy hydrocarbon fuels, its cold start and relight energy requirements, the stability of the pilots with variations in Mach number, Reynolds number, and

wall boundary layer thickness, the stability of the pilot with variations in the combustor shock system, the active cooling requirements and durability of the pilot and other structures, and the weight and volume penalties associated with the above.

The performance of this engine would be expected to most closely match that of a pure scramjet of the four alternate piloted concepts discussed thus far. However, because of the combustor drag losses associated with the pilot(s), its performance would still be less than that of the pure scramjet. Further discussions of its performance potential are left for the next section.

Strut-Ducted-Rocket Scramjet (SDRSJ) Concepts

There is no particular engine concept in the literature that has been proposed using this piloting scheme for Mach 4–8 flight but, like the previous piloting concepts, it is considered as a candidate concept in these discussions. Recent applications of this concept by Aerojet have been for space transportation, generally as a first-stage, combined cycle engine accelerator from take-off to Mach 8–10.[28,29] In the SDRSJ concept, one or more in-stream struts are placed partially or completely across the inlet throat/isolator duct region of a scramjet engine (see Fig. 6)[28] to provide one or more of the following:

- Static thrust from either a high-pressure ejectant or rocket motor located in the downstream base region
- Reduced combustor/inlet isolator length
- Increased inlet area contraction
- Enhanced in-stream fuel distribution
- Base flame holding region
- Fuel piloting source

The penalties one pays for these "enabling" features are increased internal leading edge, wave and friction drag, increased structural cooling capacity, weight and complexity, and increased fuel system supply and control weight, volume, and complexity. Multiple fuel and oxidizer systems may also be required.

Since the purpose of this paper is to discuss hypersonic missile propulsion, the static thrust feature will not be addressed nor will the attendant ejector performance and mixed cycle static-to-supersonic speed engine performance. Rather, the discussions will focus on the operation and performance of the engine in the Mach 3–8 speed regime, i.e., during dual-mode scramjet operation.

During dual-mode scramjet operation, the strut(s) provide an excellent platform on which to place small fuel/oxidizer pilots, whether they be in the form of wall orifice injectors or small, hot, fuel-rich axial rocket motors. They

are also ideal for enhanced fuel distribution in the main supersonic combustor when the maximum cross-stream dimension exceeds that permitted for center stream penetration from normal wall orifice injectors (generally 75–100 mm for liquid fuels).[30] It is clear, however, that a liquid hydrocarbon pilot will not operate in this configuration for all of the same reasons listed for the previous three pilot concepts. The pilot would have to use a gaseous reactant that was heated and close to an ignition source to be effective, especially at the low flight Mach numbers. In addition, use of an endothermic liquid hydrocarbon fuel (for active cooling) would most likely be required for flight speeds above Mach 6–6.5, at least for the aft end(s) of the strut(s) and the supersonic combustor.

As mentioned previously, a fuel-rich rocket pilot could also be used, provided the requisite fuel and oxidizer system are logistically suitable and used in the low-speed ejector system. Carrying an oxidizer system just for scramjet operation would be detrimental to the overall engine fuel specific impulse, and hypergolic fuels are not logistically suitable. However, the use of a very energetic pilot would permit the use of conventional liquid heavy hydrocarbon fuels rather than require the use of their endothermic cousins.

Addressing the figures of merit previously discussed, the SDRSJ piloting concept will require either an ignition and cold start energy source for end-of-boost ignition, low Mach number operation, and restart potential, or a fuel-rich rocket pilot using a logistically suitable fuel and oxidizer. The hydrocarbon fuel injected in the main supersonic combustor should be a gas, preferably heated, but this would depend on the energy level of the pilot. An endothermic liquid hydrocarbon fuel would meet these requirements, as would, perhaps, a heated conventional liquid hydrocarbon fuel when flash vaporized. Other systems advantages and penalties for this concept have been discussed above.

The performance of this engine cycle compared to that of a pure scramjet will depend on the type and extent of piloting from the strut(s). The configuration that would perform comparably to the pure scramjet would be one where the strut pilot comprised a series of small hot gaseous fuel injectors with independent, active ignition sources. The only performance decrement compared to a pure scramjet's performance would be due to the increased isolator duct wall friction drag and weight attributable to the strut(s). When the pilot used is a rocket motor, this difference in performance would increase. While the thrust of the SDRSJ will increase with increasing flow rate and size of the rocket pilot, its efficiency will decrease, eventually approaching that of a pure rocket.

HYDROCARBON-FUELED HYPERSONIC ENGINE PERFORMANCE COMPARISONS

Comparisons of engine and vehicle performance for the ramjet, pure scramjet, dual combustor ramjet, and internally piloted designs are discussed and presented next.

The performance of the pure scramjet is based on the analytical techniques described in Ref. 31 and updated with the advances described in Ref. 32, and that for the DCR is based on the techniques described in Ref. 15. The performance of the other piloted scramjet concepts is based on an internal drag decrement assessed against the supersonic combustor in the form of an increase in the combustor wall skin friction coefficient.

The magnitude of this additional drag decrement depends primarily on the projected frontal area of the pilot. A second-order effect will be the internal pilot performance penalty associated with its being a subsonic, rather than supersonic, combustion process. However, since at the lower flight Mach numbers ($M_0 < 5$–6) and higher levels of heat addition (during vehicle acceleration) the dual-mode scramjet engine is generally operating in its subsonic combustion mode (see Ref. 31 for further details), the differences in performance between the subsonic pilot and dual-mode supersonic combustion combustor are expected to be very small. At the higher flight speeds (above Mach 6), these differences in performance are expected to be somewhat larger but still not of the same order as the pilot external drag.

In any event, only the external surface drag increment of the fuel pilot is included in this study. This drag increment is estimated by computing the cowl leading edge and wave drag generated by generic pilots as a function of combustor inlet conditions, pilot size, pilot projected frontal area, and pilot shape (external pilot cowl angle). Skin friction on the external wetted surface areas of the pilot are assumed to be equivalent to what would be present on this surface in the supersonic combustor, the net first-order effect being no change in the overall supersonic combustor skin friction drag. In all cases, two-dimensional (rather than conical) shocks were assumed. The resulting two-dimensional drag coefficients, therefore, represent a probable upper bound on pilot external drag.

These internal engine drag increments were calculated for the internally piloted scramjet concepts for flight at Mach 4 with the angle of attack, $\alpha = 0°$ and $ER_e = 1$, which is representative of an accelerating vehicle after boost, and at Mach 8 with $\alpha = \pm 5°$ and $ER_e = 0.5$ or 1.0, which is representative of cruise or acceleration at the cruise altitude, as a function of the inlet design Mach number, M_{des}.

These conditions are also consistent with engine and vehicle performance previously presented.[15,31] While combustor inlet conditions at each M_0 will vary somewhat with M_{des}, a fixed value at each M_0 regardless of M_{des} was assumed in this study for simplicity. For example, at Mach 4, the combustor inlet Mach number, M_2, was taken to be 1.8 for all values of M_{des}, even though M_2 varied between 1.7 and 2.1 for $4 \leq M_{des} \leq 8$. Note that the computed pilot drag coefficients, when transformed into an increment in the combustor wall skin friction coefficient, must be on the same area basis as the skin friction coefficient, i.e., on a wall wetted area rather than combustor inlet area basis.

The internal engine drag increment associated with the catalytic piloting concept was computed assuming that five pilots are used with the pilot leading edge diameter assumed to be 0.25 cm and the wedge angle 5°. The inlet capture area of a single pilot is 1.33 cm² and its maximum projected (axial) area is 4.1 cm². The combustor inlet area was varied between 245 and 375 cm². The resulting increment in wall skin friction coefficient is 0.00015 at Mach 4 and 0.00011 at Mach 8 for five pilots. These compare with a combustion-induced wall skin friction coefficient that varies between 0.00408 and 0.00470 when $ER_e = 0.5$ and 1.0, respectively; the internal drag loss will be 2% to 3% above the combustor wall friction loss at both flight speeds.

The internal drag increase due to the wall-mounted pilots, however, is larger because the pilots are assumed to be physically larger and to have a different shape. The projected area of the pilot is 20% of the area to be piloted. Again a 0.25-cm diameter for the cowl lip and an external cowl angle of 15° were assumed. The increment in combustor wall skin friction coefficient will be 0.00192 and 0.00091 at Mach 4 and 8, respectively. These represent 47% and 19% increases in the internal combustor drag loss for $ER_e = 0.5$ and 1.0, respectively. These drag coefficients were added to the supersonic combustor skin friction coefficients in the cycle analysis (RJPA) of Refs. 31 and 32 to account for pilot drag losses in the engine performance calculations.

These engine performance numbers, generated for Mach 4 and 8 flight in the stratosphere, were then combined with the scramjet external drags and engine comparisons in Refs. 15 and 31. Here, the reference missile configuration is a 50-cm-diameter axisymmetric, nose inlet configuration with a length-to-nozzle exit diameter of 8 (length = 400 cm) that is boosted by a tandem rocket to the sustainer take-over Mach number of 4 at an altitude of 15.24 km. Other inlet types could have been chosen but would not have altered the conclusions presented

herein, only the absolute values of performance. For consistency, the combustor exit-to-inlet area ratio for the scramjet and piloted concepts is taken to be the same as in Ref. 31, i.e., $A_4/A_2 = 4$. The nozzle stream thrust efficiency in all cases is 0.98, the nozzle exit-to-inlet area ratio is unity ($A_5/A_i = 1$), and the nozzle chemistry is assumed to be two-thirds of the way between equilibrium and frozen. Each engine is assumed to operate with other component efficiencies and performances as described in Refs. 15 and 31. The fuel in all cases is RJ-5, a dense, storable liquid heavy hydrocarbon, and the combustion efficiency is taken to be 100%. The air flow split between the supersonic combustor and subsonic gas generator for the DCR is 7:1.

Externally, each configuration is identical except for the DCR's split inlet configuration. Internally, the only difference in the configurations assessed is the sustainer air-breathing engine type, i.e., the pure scramjet, a piloted scramjet, or the DCR. Vehicle drags are as presented in Ref. 31, and the performances of the scramjet and DCR are taken from Refs. 31 and 15, respectively. The reference area is taken to be a 50-cm-diameter circle.

The resulting performance comparisons are presented as a function of M_{des} in Fig. 8 for $\alpha = 0°$ and a flight Mach number of 4, and in Fig. 9 for $\alpha = \pm5°$ and a flight Mach number of 8. In Fig. 7, comparisons of the pure scramjet[31] with the DCR[15] and the internally piloted scramjet powered vehicle concepts at Mach 4 show that the DCR powered vehicle exhibits the best thrust performance and that the lower the inlet design Mach number the higher the thrust performance of all of the engine concepts. This latter effect is to be expected since the inlet air capture increases at a fixed M_0 with decreasing M_{des}.

Compared to the pure scramjet, the DCR powered vehicle exhibits 10–15% better thrust performance, primarily because both the DCR gas generator and supersonic inlets are operating near their critical pressure recovery while the scramjet inlet is not. Furthermore, the performance of the catalytically piloted engine/vehicle combination is, as one might expect, nearly identical to that of the pure scramjet. This performance is less than 1% less than that of the scramjet. The thrust performance of the wall-mounted pilot engine concept, on the other hand, is on the order of 2–3% lower than that of the scramjet.

However, at Mach 8 with $\alpha = \pm5°$, there is an optimum M_{des} and the DCR and scramjet performance are reversed, as shown in Fig. 8. Here, the scramjet exhibits the optimum thrust performance at both $ER_e = 0.5$ and 1.0 with M_{des} near 6. The stoichiometric performance of the
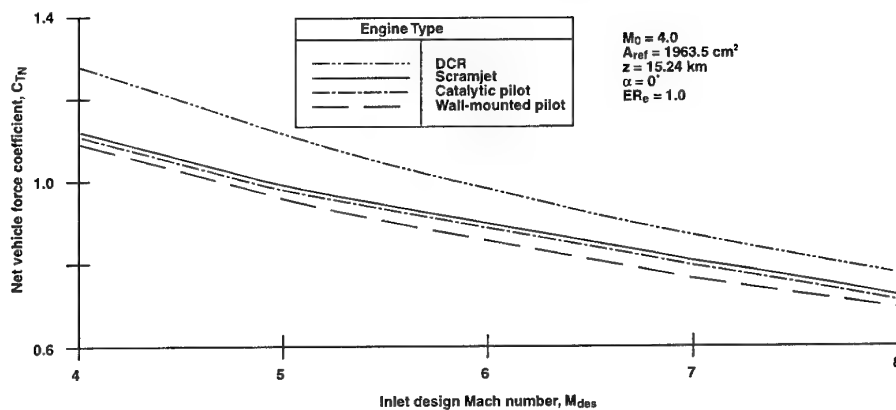
Fig. 7 Effect of engine type and design Mach number on vehicle performance at Mach 4, $\alpha = 0°$, and $ER_e = 1.0$.
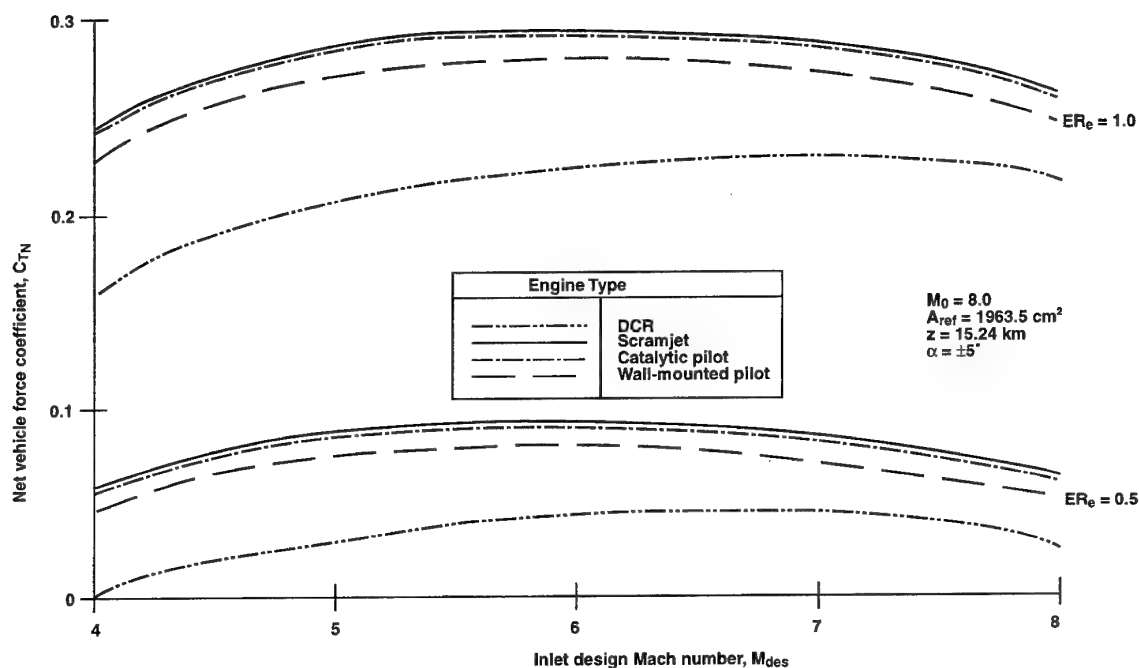

Fig. 8 Effect of engine type and design Mach number on vehicle performance at Mach 8, $\alpha = 5°$, and $ER_e = 0.5$ or 1.0.

DCR is 19% lower than that of the scramjet when $M_{des} = 7$, the optimum for the DCR, and 23% lower when $M_{des} = 6$, the optimum for the scramjet. When $ER_e = 0.5$, these differences increase to 47% and 54%, respectively.

The performance of the catalytically piloted concept with $M_{des} = 6$, conversely, is less than 1% below that of the scramjet powered vehicle at either equivalence ratio. For the wall-piloted engine concept, the decrease in performance increases to 4% when $ER_e = 1$ and 15% when ER_e

$= 0.5$. These differences are larger at all other values of M_{des}, but all are still well above the performance of the DCR powered concept.

UPPER BOUNDS ON FLIGHT MACH NUMBER

In addition to assessing the merits of each of the candidate engine configurations, performance sensitivity studies were performed to provide some guidance on an upper flight Mach number bound for liquid hydrocarbon fueled scramjet-powered missiles based on the physics,
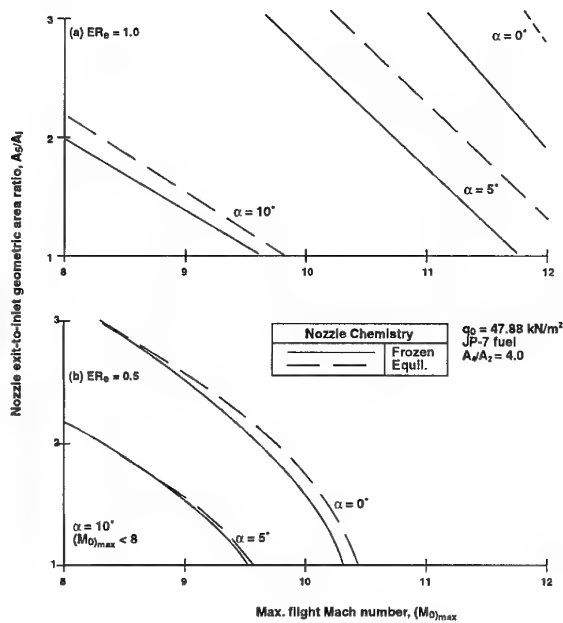
Fig. 9 Maximum flight Mach number for axisymmetric scramjet powered vehicle versus A_5/A_i for $\alpha = 0°$, $5°$, and $10°$.

chemistry, and requisite energy balance. To keep the initial computational matrix to a manageable level, only the axisymmetric nose inlet scramjet engine/missile configuration was considered[15,31]; all other candidate engine configurations would have lower thrust performance, primarily because of their lower air capture. It was also assumed that the inlet design Mach number was the same as the flight Mach number and that the vehicle flew at a constant dynamic pressure, q_0, equal to 47.88 kN/m² (1000 lbf/ft²).

Furthermore, an alternative to the semi-empirical inlet area contraction limit $[(A_0/A_2)_{max} = 8.5]$ given in Refs. 15 and 31 was used since the original is based on fixed-geometry inlets designed and tested at flight Mach numbers of 8 or less. The bounds on inlet area contraction chosen are based on work with variable-geometry inlets and, therefore, are more representative of the upper limits on inlet area contraction for all flight speeds, including those above Mach 8. The corresponding inlet kinetic energy efficiencies were also obtained from Ref. 33.

JP-7 endothermic liquid hydrocarbon fuel was chosen rather than RJ-5 as used in Refs. 15 and 31 and the previous section since such a fuel will likely be required for structural cooling at flight Mach numbers above 6 to 6.5.

For simplicity, it was assumed that any engine structural cooling required was accomplished with the engine fuel flow, the net effect on the energy balance being zero. Here, it is assumed that the energy transferred to the fuel during structural cooling exactly equals the energy added to the fuel prior to its injection in the combustor. While this would not be the exact case in an actual engine or flight vehicle, it is representative of what happens in an engine, i.e., any energy extracted from the engine's structure via fuel cooling to maintain its integrity will end up being injected into the combustor (or the exit nozzle if the cooling fuel flow rate is higher than that required by the engine). The best circumstance is when all of the heated fuel is injected into the combustor, resulting in a nearly adiabatic energy extraction and addition process. Any influence on engine performance other than this is beyond the scope of the current study.

The remainder of the reference engine and vehicle geometry is as described in Ref. 31, i.e., as in Table 1 herein.

Sensitivity studies were then performed wherein gross engine thrust coefficient (C_{Tg}) was computed as a function of these inputs using the following parametric variations:

Inlet η_{KE}	$= \pm 0.01$ from the nominal
Inlet A_i/A_2	$=$ nominal to -35% of the nominal
Combustor A_4/A_2	$= 1$ to 4
Fuel	$=$ JP-7, RJ-5, and ethylene
Nozzle A_5/A_i	$= 1$ to 3
Angle of attack, α	$= 0°$, $5°$, $10°$

The resulting engine performance was plotted as a function of M_0 and total vehicle drag coefficient (C_D), with the flight Mach number at which the two curves cross defined as the maximum flight Mach number, $(M_0)_{max}$. These curves are presented in Appendix A at the end of the paper for reference. Note that fuel temperature (or enthalpy) is not among the variables investigated since, as discussed above, the energy used to heat the fuel would have come from energy extracted from the engine's structure to maintain its integrity, and the net effect on engine performance (other than enhancing the ability of the fuel to ignite and burn) is essentially nil.

The results are given in Figs. 9–13 wherein the Mach number at which the net thrust coefficient of the engine and vehicle equal to the vehicle's external drag is plotted against the sensitivity parameter. Here, the vehicle external drags are those presented in Ref. 31 or an extension thereof from Mach 8 to 12. Included in each plot are the

Table 1. Reference engine and vehicle geometry.

Missile maximum diameter	50 cm				
Reference area, A_{ref}	1963.5 cm^2				
Missile length	400 cm				
Engine					
Inlet[18]	$A_0 = A_i$ when $\alpha = 0°$				
M_0	8	9	10	11	12
$(A_i/A_2)_{max}$	12.278	13.922	15.500	17.002	18.428
η_{KE}	0.9662	0.9673	0.9700	0.9722	0.9740
Cowl angle	6°				
Isolator L/D	10				
Combustor area ratio	4				
Combustor wall area	$40\,A_2$				
Combustion efficiency, η_c	100%				
Effective equiv. ratio, ER_e	0.5, 1.0				
Inlet and combustor chemistry	Equilibrium				
Nozzle efficiency	0.98				
Nozzle chemistry	Equilibrium or frozen				

engine performance curves at $ER_e = 0.5$ and 1.0 for both equilibrium and frozen flow in the exit nozzle.

In Fig. 9, the influence of A_6/A_i on $(M_0)_{max}$ is presented for all three angles of attack. Note that in all cases, the value of $(M_0)_{max}$ for frozen nozzle flow is less than or equal to that for equilibrium nozzle flow. Since the nozzle chemistry at these flight speeds will be assumed to be frozen, subsequent discussions will be focused on the frozen chemistry results. The results show that for $ER_e = 1.0$, the maximum flight Mach number experiences a substantive drop (about 2 Mach numbers) as A_5/A_i increases from 1 to 3 for $\alpha = \pm 5°$ with a similar trend at the other two values of α. Here, $(M_0)_{max}$ decreases from 11.75 to 9.65 for $\alpha = \pm 5°$. When $\alpha = 0°$, $(M_0)_{max}$ is 11 or greater. However, when $\alpha = 10°$, $(M_0)_{max}$ is 9.6 or less, falling below Mach 8 for $A_5/A_i > 2$.

A similar trend is noted for $ER_e = 0.5$ as well, although the absolute values of $(M_0)_{max}$ are substantially lower. For $\alpha = 0°$, $(M_0)_{max}$ drops from 10.3 to 8.3 as A_5/A_i increases from 1 to 3, and at $\alpha = \pm 5°$, it drops from a maximum value of 9.5 when $A_5/A_i = 1$ to below 8 when A_5/A_i exceeds 2.15. For $\alpha = \pm 10°$, $(M_0)_{max}$ is always less than 8.

What does all of this mean? First, when $ER_e = 1.0$, the vehicle will have no additional axial acceleration capabilities, so the values of $(M_0)_{max}$ are just that: absolute maximums. If acceleration capabilities are desired or required (as they almost always are) at these flight speeds, a reduced ER_e is necessary. In this study, the lower bound on this reduced ER_e is assumed to be 0.5. Furthermore, for

the altitudes of interest in these studies (>30 km), the vehicle will require an angle of attack of 5° or greater to cruise, so the $\alpha = 0°$ results are not applicable unless a ballistic trajectory is commanded, a highly unlikely scenario since this is an air-breathing engine. As a consequence, the
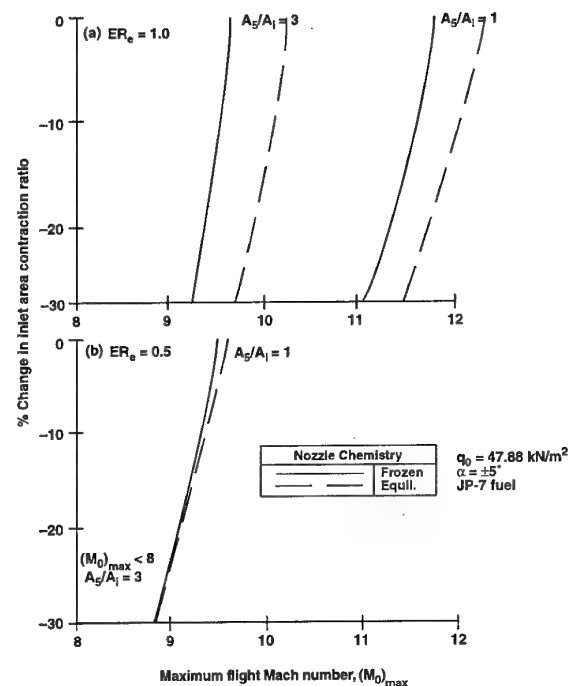

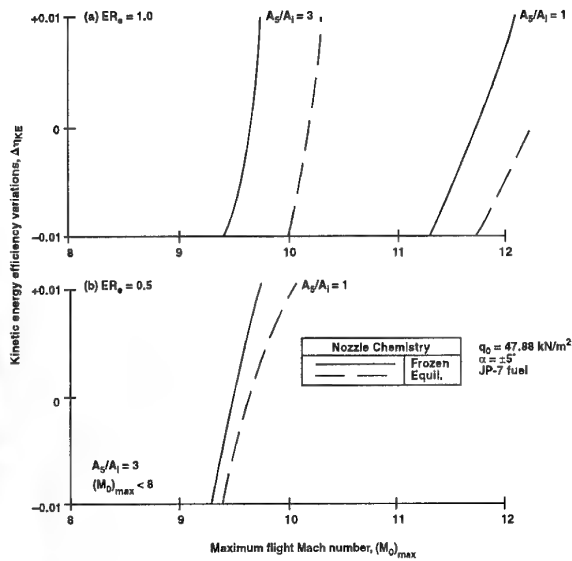**Fig. 10** Maximum flight Mach number as a function of inlet area contraction.

Fig. 11 Maximum flight Mach number as a function of inlet kinetic energy efficiency for $\alpha = 5°$.

Fig. 12 Maximum flight Mach number as a function of combustor area ratio.

maximum Mach number curves applicable to this vehicle when cruising at a dynamic pressure of 47.88 kN/m² are those bounded by $ER_e = 0.5$ and 1.0 and $\alpha = \pm 5°$.

While these arguments compress the bounds on $(M_0)_{max}$, there is still a substantial spread. For example, for $A_5/A_i = 1$, the maximum flight Mach number will vary between 9.5 and 11.75, the choice depending on the acceleration capability desired. Note that engine thrust and fuel specific impulse (I_{sp}) exhibit opposing trends with the value of A_5/A_i. The lower the value of A_5/A_i, the higher the absolute value of thrust (for a fixed nozzle exit area) because of an increase in the amount of air captured by the engine. The opposite is true, however, for I_{sp}. As a result, an engine with a "high" I_{sp} may well have a low thrust and vice versa. These trends are apparent in the curves of Fig. 9 wherein the maximum Mach number decreases with increasing A_5/A_i because of decreasing engine thrust. Ultimately, the actual value of $(M_0)_{max}$ will depend on the specific vehicle design and mission range and acceleration requirements. Because of this dichotomy, subsequent sensitivity curves are present for $\alpha = \pm 5°$ and two values of A_5/A_i, 1 and 3.

Figure 10 presents the sensitivity of $(M_0)_{max}$ to decreases in the inlet area contraction ratio given above (increase in the inlet throat area, A_2). The results indicate that $(M_0)_{max}$ is not very sensitive to increases in the inlet throat area, irrespective of the value of A_5/A_i, at least in the 0% to 30% range investigated herein. For $ER_e = 1$, $(M_0)_{ma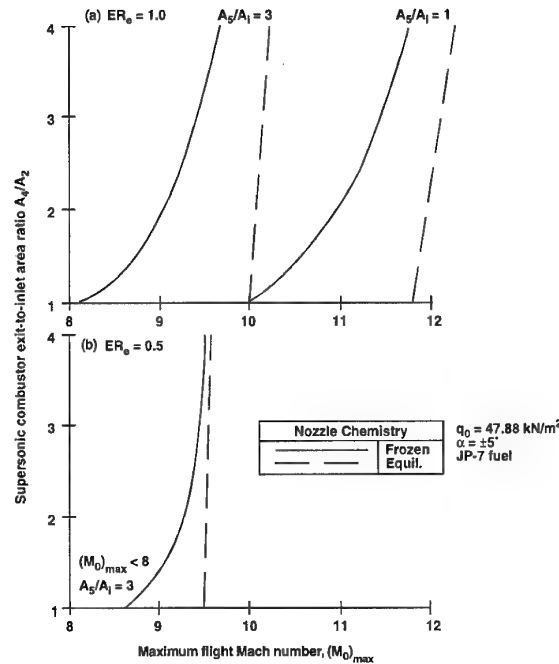x}$ decreases from 11.75 to 11.05 with a 30% increase in the inlet throat area (A_2) with $A_5/A_i = 1.0$. When $A_5/A_i = 3.0$, $(M_0)_{max}$ decreases from 9.65 to 9.25. For $ER_e = 0.5$ and $A_5/A_i = 1.0$, $(M_0)_{max}$ decreases from 9.5 to 8.8. For $A_5/A_i = 3.0$, $(M_0)_{max}$ is always less than 8.

Figure 11 presents the corresponding curves for a ± 0.01 variation in inlet kinetic energy efficiency, η_{KE}. These results show that $(M_0)_{max}$ is not sensitive to large changes in inlet pressure recovery, at least at the flight speeds of interest. When ER_e and $A_5/A_i = 1.0$, a ± 0.01 change in η_{KE} changes $(M_0)_{max}$ only by +0.35 and −0.45, respectively, ranging in value from 12.1 to 11.3. When $A_5/A_i = 3.0$, the range is from 9.75 to 9.4, respectively, and when $ER_e = 0.5$ and $A_5/A_i = 1.0$, the range is from 9.75 to 9.3, respectively. $(M_0)_{max}$ is always less than 8 when $ER_e = 0.5$ and $A_5/A_i = 3.0$.

Figure 12 presents the sensitivity of $(M_0)_{max}$ to the combustor area ratio, A_4/A_2. The sensitivity of $(M_0)_{max}$ to changes in combustor area ratio is large and on the same order of magnitude as its sensitivity to A_5/A_i. For the cases studied with $ER_e = 1.0$, $(M_0)_{max}$ varies from 11.75 when $A_4/A_2 = 4$ to 10 for a constant area combustor for $A_5/A_i = 1$. The respective values when $A_5/A_i = 3$ are 9.65 and 8.1. When $ER_e = 0.5$, $(M_0)_{max}$ varies between 9.5 and 8.6 when $A_5/A_i = 1$ (about 50% of the variation at $ER_e = 1$) and is always less than 8 when $A_5/A_i = 3$.
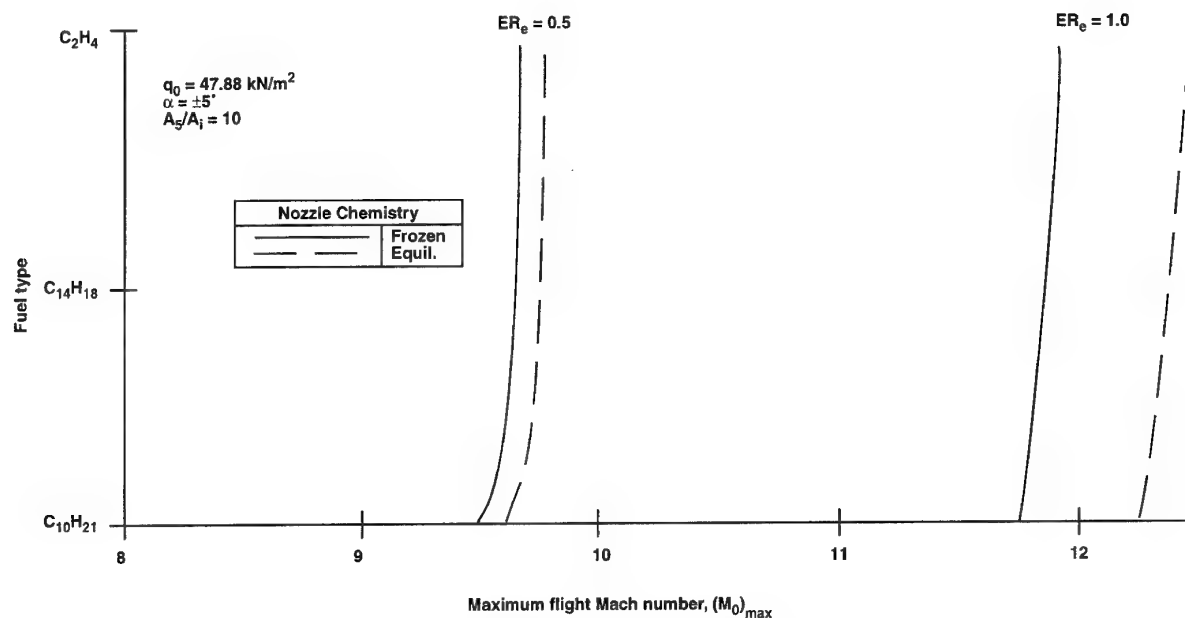
Fig. 13 Maximum flight Mach number as a function of fuel type for $\alpha = 5°$.

Why this sensitivity to combustor and nozzle exit area ratio? Because of the influence of the type of kinetics in the exit nozzle. The larger the area expansion in the exit nozzle, the stronger the influence of frozen chemistry on engine performance. For example, for a fixed exit nozzle area, a low value of combustor area ratio will result in a larger nozzle exit-to-combustor exit area expansion than for a larger combustor exit area (or combustor area ratio). This, in turn, results in more of the total nozzle exit-to-combustor inlet area expansion taking place in the nozzle when the chemistry is nearly frozen, as compared to the expansion taking place in the combustor, where the chemistry is assumed to be in equilibrium.

As a result, care must be taken in the amount of area expansion permitted (or assumed) in the combustor when performing engine cycle performance calculations such as those in this (or any previous) study. Since the total area expansion between the combustor entrance and nozzle exit can be assigned to either the combustor or exit nozzle, and equilibrium chemistry is assumed in the combustor and frozen chemistry in the exit nozzle, quite different engine and vehicle performance estimates can be computed for the same engine configuration depending on where this area expansion (and, therefore, type of chemistry) is assumed to take place. For example, the limits shown in Figs. 10–14 would move to the left as less area expansion is taken in the combustor (less energy is available for thrust; it is tied up in dissociated chemical

species) and to the right as the combustor area ratio approaches the total area expansion available.

Consequently, care must be exercised as to where the total combustor-plus-exit nozzle area expansion is taken. Remember that the assumption of equilibrium chemistry in the combustor is based on a low to moderate area expansion in the combustor. Otherwise, the actual combustor exit chemistry will move away from equilibrium and toward frozen flow. As a result, an upper bound on A_4/A_2 of 4 was taken for this study.

The last set of sensitivity curves is for the type of hydrocarbon fuel used in the engine. As shown in Fig. 13, $(M_0)_{max}$ is quite insensitive to the type of fuel used, irrespective of ER_e, for $A_5/A_i = 1.0$. Here, RJ-5 is a dense (sp. gr. = 1.08) storable hydrocarbon, JP-7 is a lighter (sp. gr. < 0.8) storable endothermic hydrocarbon, and ethylene (C_2H_4) is a light gaseous hydrocarbon and one of the endothermic decomposition products of JP-7. Since these same trends (with lower absolute values) are valid for other values of A_5/A_i, they are not included for brevity.

Finally, if one were to limit the value of ER_e to 0.5, it is possible to set a more precise (and also reasonable) bound on $(M_0)_{max}$. If this hypothesis is accepted, the maximum flight Mach number of a hydrocarbon-fueled, scramjet-powered vehicle flying a $q_0 = 47.88$ kN/m^2 trajectory would be between Mach 9 and 10.

To summarize this section, a reasonable upper bound on flight Mach number would appear to be around Mach 10, but the precise value is a strong function of the vehicle design and mission acceleration and cruise range requirements. The upper bound is most sensitive to variations in the nozzle exit-to-diffuser-inlet and combustor area ratios and much less sensitive to inlet area contraction and inlet efficiency. It is very insensitive to the type of hydrocarbon fuel used, but range and other systems considerations may be quite sensitive to the fuel type.

CONCLUDING REMARKS
A number of piloting and fuel pre-preparation approaches to ensure efficient combustion of storable liquid hydrocarbon fuels in scramjet engines have been presented. A methodology for comparing the relative performance of piloted and unpiloted scramjet engines has been promulgated based on first-order physics and chemistry within these engines. Comparisons of the Mach 4–8 integrated performance of each of the engine types in an axisymmetric missile configuration show the pure scramjet to perform best at Mach 8 and the DCR to perform best at Mach 4. Alternately, the DCR exhibits the lowest performance at Mach 8. Integrated missile performance using the other piloted engine types falls below the performance of the scramjet at both flight speeds, with the choice of engine type dependent on other factors discussed in the paper.

An initial attempt at defining an upper flight Mach number bound on hydrocarbon-fueled scramjets has also been presented. The results indicate that this upper bound lies between Mach 9 and 10 for the configurations of interest in this paper.

ACKNOWLEDGMENTS

REFERENCES

1. *Proceedings of the Fourth AGARD Colloquium*, Milan, Italy, 1960; also *Combustion and Propulsion—High Mach Number Air Breathing Engines*, Pergamon Press, NY, 1960.

2. Mallinson, D. H., *Combustion and Propulsion—High Mach Number Air Breathing Engines*, Pergamon Press, NY, pp. 80–83.

3. Hawkins, R., and Fox, M. D., "An Investigation of Real Gas Effects Relevant to the Performance of a Kerosene Fueled Hypersonic Ramjet," *Supersonic Flow, Chemical Processes and Radiative Transfer* (X. Olfe and X. Zakkay, eds.), MacMillan Co., NY, 1964, pp. 113–135.

4. Weber, R. J., and McKay, J. S., "An Analysis of Ramjet Engines Using Supersonic Combustion," NACA TN-4386, 1958.

5. Dugger, G. L., "Comparison of Hypersonic Ramjet Engines with Subsonic and Supersonic Combustion," *Proceedings of the Fourth AGARD Colloquium*, Milan, Italy, 1960; also *Combustion and Propulsion—High Mach Number Air Breathing Engines*, Pergamon Press, NY, 1960.

6. Curran, E. T., and Stull, F. D., "The Potential Performance of the Supersonic Combustion Ramjet Engine," ASD-TDR-63-336, Aeronautical Systems Division, USAF, Wright Patterson AFB, Ohio, May 1963.

7. Waltrup, P. J., Stull, F. D., and Anderson, G. Y., "Supersonic Combustion Ramjet (Scramjet) Engine Development in the United States," *Proceedings of the Third International Symposium on Airbreathing Engines*, DGLR A77-17266-05-07, 1976, pp. 835–861.

8. "Antonio Ferri: Selected Papers on Advanced Design of Air Vehicles," AGARDograph No. 226, Aug 1977.

9. Curran, E. T., and Stull, F. D., "The Utilization of Supersonic Combustion Ramjet Systems at Low Mach Numbers," AF Aero Propulsion Laboratory Report No. RTD-TDR-63-4097, Jan 1964.

10. Jensen, J., and Braendlein, R., "Review of the Marquardt Dual Mode Mach 8 Scramjet Development," AIAA-96-3037, Jan 1996.

11. Andrews, E. H., and Mackley, E. A., "Review of NASA's Hypersonic Research Engine Project," AIAA-93-2323, Jan 1993.

12. Contensou, P., Marguet, R., and Huet, C., "Etude Theoretique et Experimental d'un Statoreacteur a Combustion Mixte," ICAS Paper No 72-24, 1972.

13. Waltrup, P. J., "Hypersonic Airbreathing Propulsion: Evolution and Opportunities," AGARD CP-426, Paper No. 12, April 1987.

14. Billig, F. S., "SCRAM: A Supersonic Combustion Ramjet Missile," AIAA-93-2329, June 1993.

15. Waltrup, P. J., "The Dual Combustor Ramjet: A Versatile Propulsion System for Hypersonic Tactical Missile Applications," AGARD-CP-526, Paper No. 8, Sept 1992.

16. Marguet, R, Berton, P., and Hirsinger, F., "L'etude du Statoreacteur Supersonique et Hypersonique en France de 1950 e 1974 (Application aux Moteurs Combines Aerobies)," AGARD-CP-479, Dec 1990.

17. Henderson, R. E., "Hypersonic Air Breathing Engine," AGARD Report, *Propulsion and Energy Issues for the 21st Century*, AGARD R824, Chap. 1, 1996.

18. Mercier, R. A., and Ronald, T. M. F., "US Air Force Hypersonic Technology Program (HyTech)," presented at the AIAA 7th International Spaceplanes and Hypersonics Systems and Technology Conference, Norfolk, VA, Nov 1996.

19. Billig, F. S., Pirkle J. C., and Dugger, G. L., "Scramjet Fuels Evaluation," AFAPL-TR-72-21, July 1972.

20. Braendlein, B., Jensen, J., and Mays, J., "Advancements in Scramjet Flameholding and Fuel Injection," *Proceedings of the 1996 JANNAF Propulsion Meeting*, Albuquerque, NM, Dec 1996.

21. Kay, I. W., Peschke, W. T., and Guile, R. N., "Hydrocarbon-Fueled Scramjet Combustor Investigation," AIAA-90-2337, June 1990; also *Journal of Propulsion and Power*, 8(2), 507–512, March-April 1992.

22. Kay. I. W., "Hydrocarbon-Fueled Ramjet/Scramjet Technology Program: Phase II Extension Final Report," NASA CR-189659, July 1992.

23. Andrews, E. H., Trexler, C. A., and Emami, S., "Tests of a Fixed-Geometry Inlet-Combustor Configuration for a Hydrocarbon-Fueled Dual-Mode Scramjet." AIAA-94-2817, June 1994.

24. Jackson, K., Corporan, E., Buckley, P., and Leingang, J., "Test Results of an Endothermic Fuel Reactor," AIAA-95-6028, April 1995.

25. Ianovski, L., and Sapgir, G., "Heat and Mass Transfer to Hydrocarbon Fuels at Thermal Decomposition in Channels of Engines," AIAA 96-2683, July 1996.

26. Vinogradov, V. A., Kobigsky, S. A., and Petrov, M. D., "Experimental Investigation of Kerosene Fuel Combustion in Supersonic Flow," *Journal of Propulsion and Power*, 11(1), 130–138, Jan–Feb 1995.

27. Sullins, G. A., and McLafferty, G. H., "Performance of Rectangular Isolators and Diffusers," *Proceedings of the 1995 JANNAF Propulsion Meeting*, Tampa, FL, Dec 1995.

28. Siebenhaar, A., and Bulman, M. J., "The Strutjet Engine: The Overlooked Option for Space Launch," AIAA-95-3124, July 1995.

29. Bulman, M. J., and Siebenhaar, A., "The Strutjet Engine: Exploding the Myths Surrounding High Speed Airbreathing Propulsion," AIAA-95-2475, July 1995.

30. Waltrup, P. J., "Liquid-Fueled Supersonic Combustion Ramjets: A Research Perspective," *Journal of Propulsion and Power*, 3(6), 515–524, Nov-Dec 1987.

31. Waltrup, P. J., Billig, F. S., and Stockbridge, R. D., "Engine Sizing and Integration Techniques for Hypersonic Airbreathing Missile Applications," AGARD-CP-307, Paper No. 8, March 1982.

32. Billig, F. S., Corda, S., and Pandolfini, P. P., "Design Techniques for Dual Mode Ram-Scramjet Combustors," AGARD-CP-479, June 1990.

33. Billig, F. S., Waltrup, P. J., et al., "Proposed Supplement to the Proposed Propulsion System Management Support Plan," JHU/APL-NASP 6-1, July 1986.

**APPENDIX A: Scramjet Performance Curves for Determination of
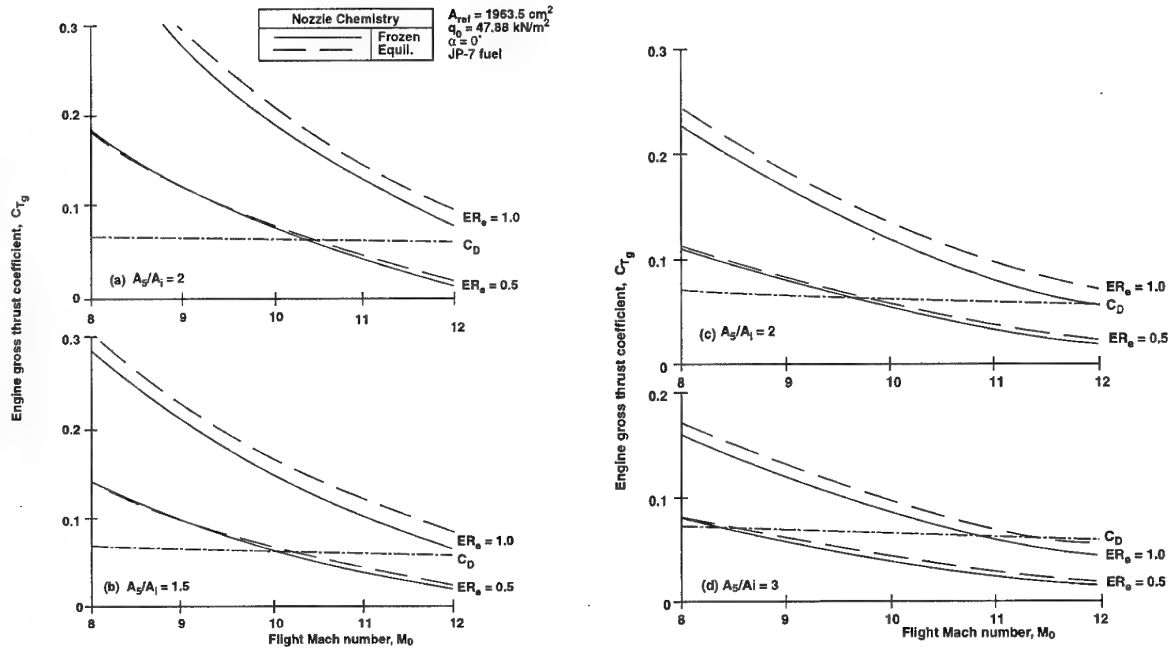Maximum Flight Mach Number**

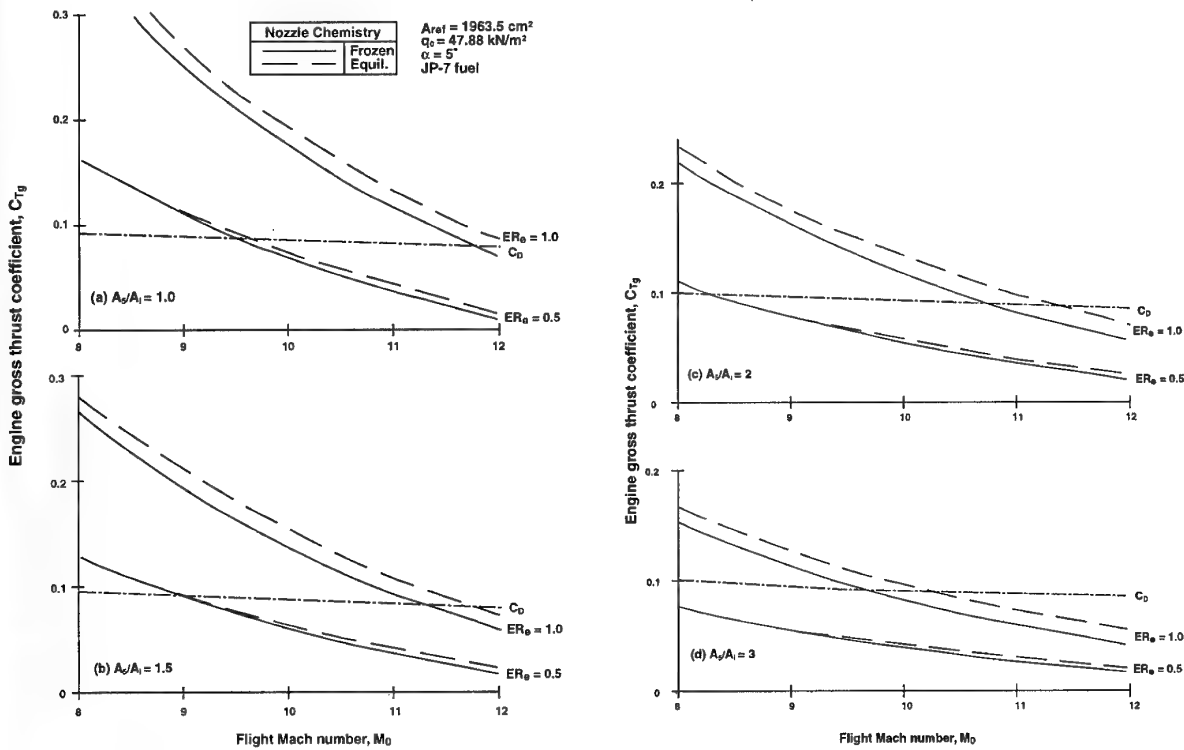**Fig. A-1** Engine gross thrust as a function of flight Mach number for $\alpha = 0°$.

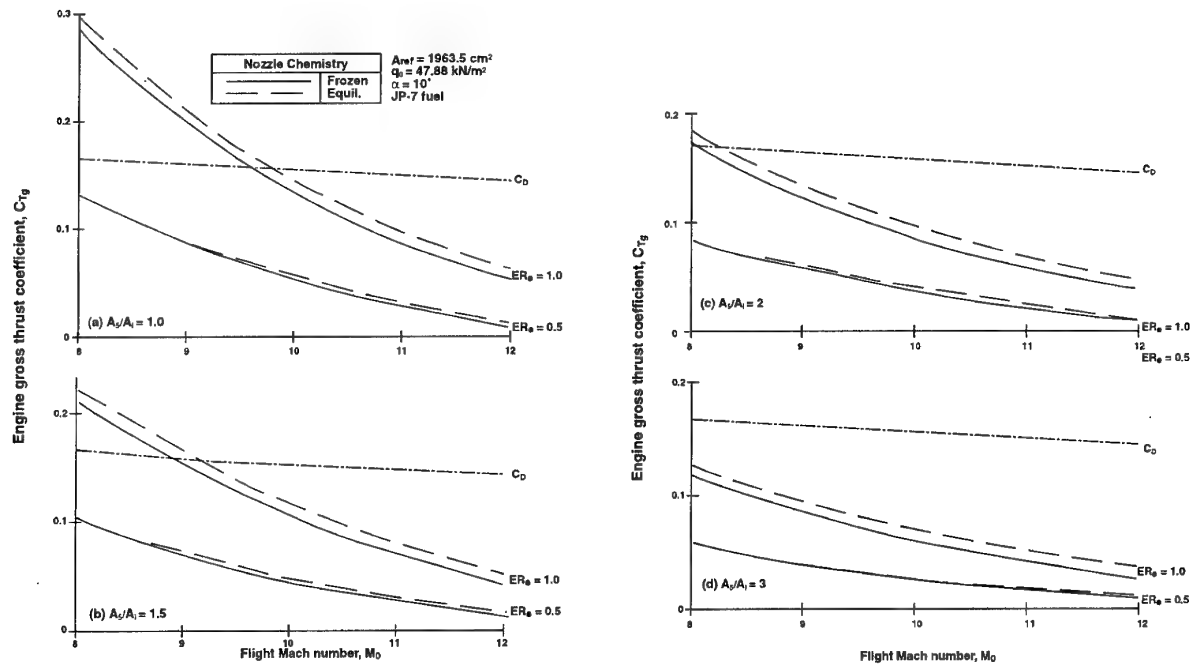**Fig. A-2** Engine gross thrust as a function of flight Mach number for $\alpha = 5°$.

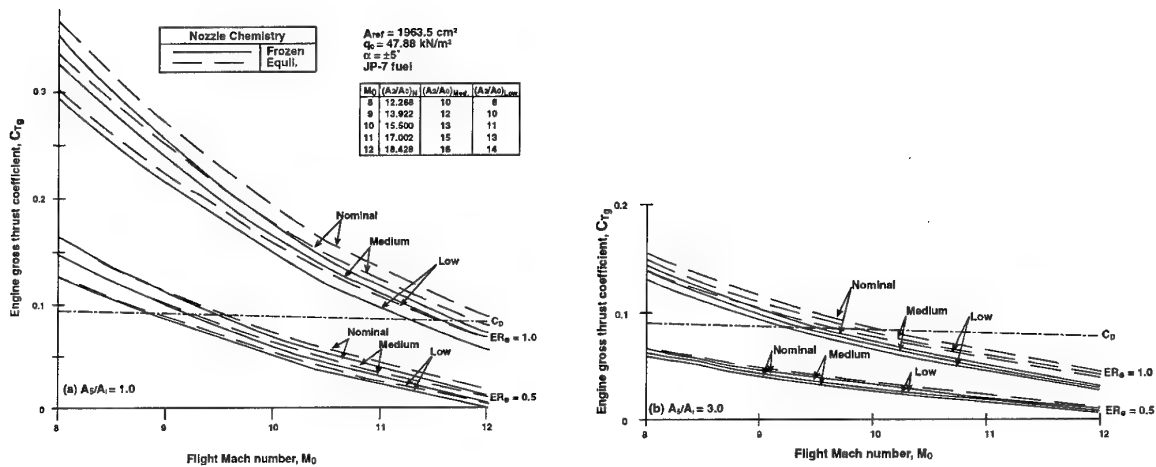**Fig. A-3** Engine gross thrust as a function of flight Mach number for $\alpha = 10°$.

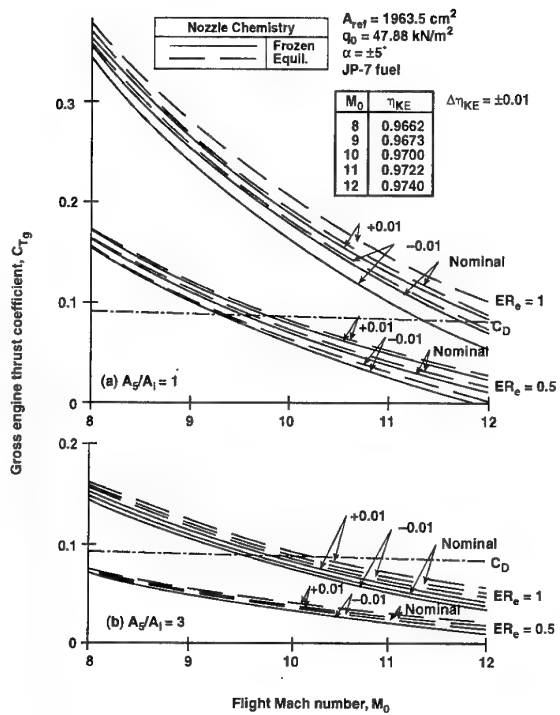**Fig. A-4** Effect of inlet area contraction on engine gross thrust at $\alpha = 5°$.

Fig. A-5 Effect of inlet kinetic energy efficiency on engine gross thrust at $\alpha = 5°$.
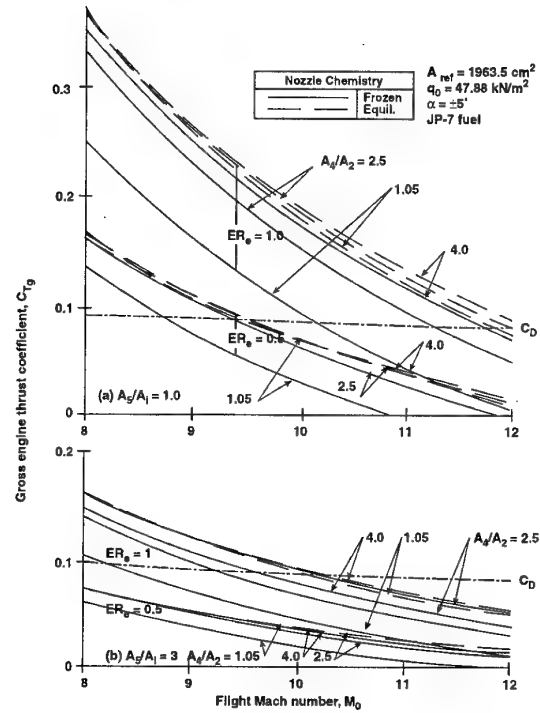
Fig. A-6 Effect of combustor area ratio on engine gross thrust at $\alpha = 5°$.
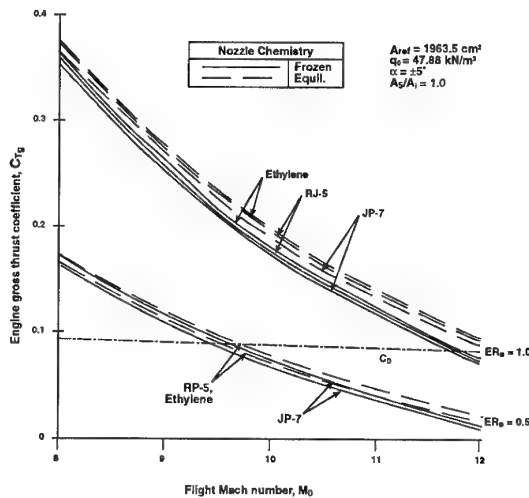
Fig. A-7 Effect of fuel type on engine gross thrust at $\alpha = 5°$.

Scramjet and dual mode ramjets.

Marc BOUCHEZ
Aerospatiale Missiles
8 rue Le Brix
18000 Bourges
France

François FALEMPIN
ONERA
29, avenue de la Division Leclerc
92322 Châtillon Cedex
France

1. RESUME

Extended Abstract in English

Airbreathing sustained hypersonic flight could have operational advantages for military applications. By an other way, airbreathing propulsion could have a potential interest for the future reusable launcher, in connection with rocket engines. High speed ramjets (scramjet and dual mode ramjet) are a key technology for these two kinds of military or space future applications.

Airbreathing launcher using scramjet have been recently studied in France within the scope of PREPHA program. The chosen concept, which seems to be the most powerfull and robust, is a dual mode ramjet, associated with rocket engines completely separated. More generally, the use of scramjets for launchers is typically associated with hydrogen as a fuel, a maximum airbreathing Mach number of 12, and reusability. Less energetic fuels could also be used in dual fuel ramjets to take benefit of their higher density.

Hypersonic military applications ares typically associated with liquid hydrocarbons, a maximum Mach number of 8 and in general non reusability. Advanced studies of such missiles have been conducted in France by AEROSPATIALE Missiles and ONERA. Reusability (for aircraft of for recognition missiles) could also be specified, and some studies (in particular in the USA) are dealing with Mach 10 military aircraft.

The typical performance of scramjets and dual mode ramjets suitable to these two kinds of applications will be presented in the paper as a typical enveloppe.

The considered engines use subsonic combustion (with movable or thermal nozzle throat) and/or supersonic combustion, and could possibly be associated with other cycles such as rocket, detonation, cooled air, ...

The integration with the vehicle and the key points of the engine development (and its associated components design and tests) will be presented in the paper with the state of the art in France.

Forebody and air intake are the first key components, as detailed in paper C36 of the present symposium, for example.

Combustion chamber can be fixed or integrate jetisonable parts (missiles) or movable walls. Problems and state of the art of injection and combustion will be detailed in paper C7. The French experimental scramjet called « chamois » is an example of realistic scramjet combustor for tests up to Mach 6.5. Three dimensionnal Navier-Stokes computations of supersonic combustion of air and hydrogen in such a 3D scramjet have been performed and compared with experimental measurements.

The difference in the range of variation of the fuel mass flow along the trajectory is one of the noticeable differences between dual mode ramjet for military or space vehicles.

To take benefit of the previous elements, the expansion has to be carefully taken into account. Different concepts (axisymetrical, 2D, 3D, single expansion ramp nozzle, ...) could be integrated with the vehicle and the engine. The small size of the air-launched missiles and the high speeds of operation for the launchers could in particular led to different methodology for the design of the nozzles.

The confluence, trim and kinetics effects are to be taken into account for all the applications.

A very important point is the structural point of view, which has to be taken into account in the preliminary design of the scramjets.

Heat fluxes and mechanical loads have to be estimated and simulated during ground tests.

The behaviour of protected or cooled structures of the engine has to be designed and analysed and tested. The analysis is often difficult because of the combination of thermal and mechanical structures, of the possible use of non isotropic composite materials and because of the fact that generally hypersonic engines are not axisymetrical.

The fuel could be used in an integrated way to cool the structures. In case of military applications, the endothermic effect is a key point to be investigated.

Some elements on the structural challenge will be given in the present paper and also in other papers of the symposium.

In the methodology of design and upgrade of hypersonic ramjets, a close connection between numerical studies and experimental work is required.

Experimental facilities are of course the key point for the development of these engines.

For example, ground tests facilities available in France present a high complementarity between the laboratory level (highly instrumented), the small scale facilities (several kg/s of hot air) and the available big size test benches (20 to 100 kg/s of hot air). The effect of vitiation, the measurement technics (sometimes optical technics can be adapted and used even in industrial facilities), the possible new concepts have to be studied. Free jet testing ang flight test have to be prepared.

Some propulsion systems have also to be studied and qualified, such as the fuel feeding components and the overall thermal management.

The effect of the integration between the engine and the vehicle is a well-known key point, even if the sensitivity of the propulsion performance could depend on the application. The iterative way to optimize the hypersonic integrated system is really a challenge for the hypersonic airbreathing flight.

Whatever the application (military or space launcher), the interest and the communality between ramjets, scramjets and dual mode ramjets is noticeable. In France, the tools are well in place at AEROSPATIALE and ONERA. To prepare future use of hypersonic scramjets or dual mode ramjets, this know-how has to be emphased in particular in case of military application.

2. INTRODUCTION

Le statoréacteur se confirme de plus en plus comme le système propulsif le plus prometteur pour le vol de longue durée dans l'atmosphère à des vitesses supérieures à Mach 3. Différentes applications, civiles (lanceurs spatiaux réutilisables) ou militaires (missiles, ...) sont envisagées. Les performances théoriques sont attrayantes, mais de nombreux défis technologiques doivent être relevés (performances des différents composants du moteur, tenue thermique et mécanique, moyens d'essais). Il faut, pour maîtriser la propulsion à base de statoréacteur de tels véhicules hypersoniques, disposer du savoir-faire et des moyens numériques et expérimentaux de mise au point de chacun de ses composants, mais aussi mettre en oeuvre une méthodologie « système » qui demande à être approfondie et validée. En France, AEROSPATIALE-Missiles et ONERA, qui maîtrisent la technologie pour statoréacteurs des missiles supersoniques opérationnels, travaillent depuis plusieurs années à étendre ce savoir-faire aux très hautes vitesses, que ce soit pour les applications militaires (avec le soutien de la DGA) ou pour les applications spatiales (PREPHA, en coopération avec DASSAULT-AVIATION, SNECMA, SEP).

3. MISSIONS ET VEHICULES-SUPPORTS

3.1. Lanceurs réutilisables aérobies

Depuis plusieurs années, diverses études ont été menées de lanceurs spatiaux récupérables utilisant une propulsion aérobie, qui doit théoriquement limiter le gain d'indice constructif à réaliser pour assurer la faisabilité du système [1, 2]. Dans le cas d'un lanceur monoétage, la masse supplémentaire liée à l'emport d'un moteur aérobie autre que le moteur fusée nécessite pour être rentabilisée d'utiliser l'oxygène de l'air sur une plage la plus large possible, d'où l'emploi du statoréacteur au delà de Mach 7, si possible jusqu'à Mach 12 ou davantage.

En France, dans le cadre du programme PREPHA différents concepts ont été étudiés. Le concept propulsif qui a été retenu finalement est l'association d'un statoréacteur mixte (à combustion subsonique puis supersonique) intégré sous le

fuselage et fonctionnant dans la gamme Mach 1,5 à 12 avec de l'hydrogène et de moteurs fusée installés dans le culot du véhicule. A la différence du concept américain « RBCC », le statoréacteur mixte à éjecteur n'est pas apparu meilleur (ni en terme de charge utile ni en terme de robustesse) lors de l'analyse menée dans le cadre du PREPHA [3, 4,5,6].
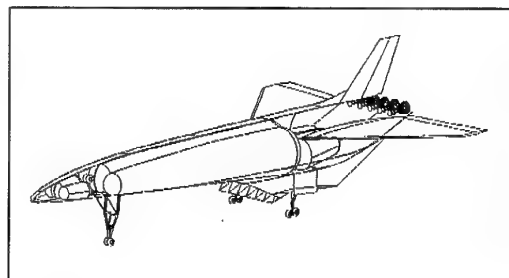

figure 1 :
vue du véhicule générique du programme PREPHA
generic vehicle of French PREPHA program

On peut envisager également d'utiliser des ergols plus denses mais moins énergétiques que l'hydrogène sur une partie de la trajectoire, le gain en volume permet de diminuer la traînée du véhicule sur toute la mission (notamment quand le bilan propulsif aérobie devient délicat, à partir de Mach 10). Il faut dans ce cas utiliser un statoréacteur mixte bi-combustible [6, 10].

3.2. Applications militaires

Les applications militaires impliquent l'emploi d'hydrocarbures stockables liquides (kérosène, ...) avec un Mach maximal de 8. Un certain nombre d'avant-projets a été réalisé en France par AEROSPATIALE-Missiles et par ONERA, en ce qui concerne l'application missile.
Parmi les différentes missions envisagées lors de ces avant-projets, on peur citer la reconnaissance (dans ce cas la portée était de l'ordre de 3000 km et la masse au départ de l'ordre de 3 tonnes), l'attaque au sol et l'interception à longue distance (masse au largage de l'ordre de 1 à 2 tonnes).
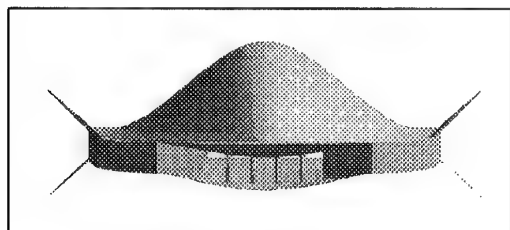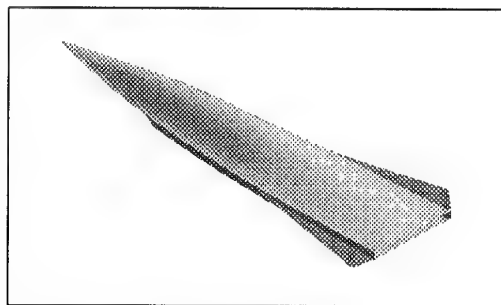

figure 2

figures 2 et 3 : concept de missile hypersonique
étudié à AEROSPATIALE-Missiles
hypersonic missile concept studied at
AEROSPATIALE-Missiles

Certaines missions (reconnaissance) ou certains concepts d'avions militaires peuvent introduire une contrainte de réutilisation même pour des applications militaires. Ainsi le concept d'avion militaire américain « Global Reach » [4] est réutilisable, utilise un superstatoréacteur à l'hydrogène et vole à Mach 10.

4. UTILISATION DES STATOREACTEURS

4.1. Performances attendues

La poussée d'un statoréacteur peut en première approximation être considérée comme proportionnelle à la pression dynamique de vol notée Pdyn. Si on le normalise par la section de captation de la prise d'air A1, l'évolution du coefficient de poussée d'un statoréacteur avec le Mach de vol est typiquement comprise dans la gamme de la figure 4. L'ordre de grandeur varie peu entre le kérosène et l'hydrogène, mais bien sûr l'incidence de vol, la richesse équivalente et l'intégration influent sur les performances du statoréacteur.

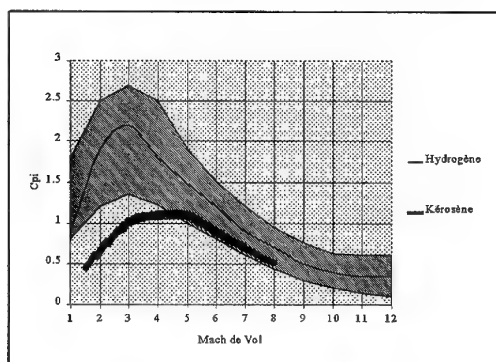$$C_\pi = \frac{Pouss\acute{e}\,e}{A_1 * Pdyn}$$

figure 4 : évolution typique du coefficient de poussée maximum de statoréacteurs en fonction du Mach de vol.

Typical evolution of Thrust coefficient of ramjets depending on flight Mach number

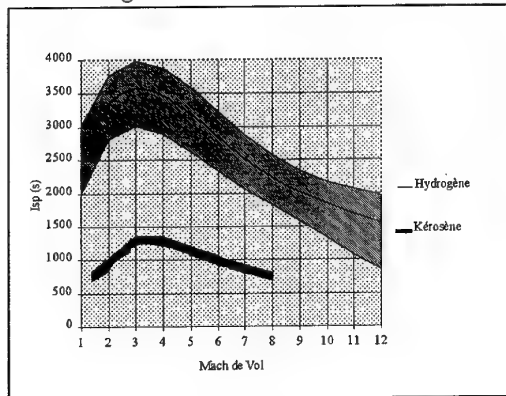L'impulsion spécifique dépend quant à elle notablement du combustible utilisé, comme le montre la figure 5.

figure 5 :
évolution typique de l'impulsion spécifique de statoréacteurs en fonction du Mach de vol.
Typical evolution of fuel specific impulse of ramjets depending on flight Mach number

Ces ordres de grandeur sont des grandeurs réalistes, typiques de statoréacteurs devant fonctionner sur un large domaine : ils peuvent paraître faibles et ne correspondent pas au maximum que l'on peut obtenir du cycle thermodynamique des statoréacteurs (à combustion subsonique ou à combustion supersonique).

4.2. Différents types, association de cycles propulsifs.

Le statoréacteur mixte associe dans le même moteur la combustion subsonique et la combustion supersonique. La combustion subsonique peut se faire en utilisant un col de tuyère à géométrie variable [2, 6] ou un col thermique [7]. Si la carène de prise d'air est souvent mobile, la géométrie du statoréacteur mixte peut-être fixe ou mobile, le choix résulte d'un niveau technologique, de la mission à réaliser, d'un compromis performances/masse du moteur, ...
Le statoréacteur peut être associé de façon plus ou moins combinée à d'autres cycles comme la fusée (éjecteurs à oxygène ou à air refroidi ou liquéfié étudiés en France par AEROSPATIALE et ONERA en collaboration avec SEP [2, 4, 7, 20, ...]).
AEROSPATIALE envisage également d'associer au statoréacteur un cycle basé sur la détonation, qu'elle

soit pulsée (« PDWE ») jusqu'à Mach 2 [5] ou stable et oblique à partir de Mach 10 (« ODWE ») [5, 6].

5. DEFIS LIES AUX DIFFERENTS COMPOSANTS

5.1. Avant-corps et prises d'air
Les avant-corps font l'objet d'une optimisation liée à l'aérodynamique interne (champ aérodynamique à l'entrée de la prise d'air), mais aussi externe (traînée, portance, équilibrage) en prenant en compte les contraintes liées notamment à l'aménagement du véhicule, à la tenue thermique (nez émoussé).
Dans le cas des missiles, des problèmes spécifiques peuvent apparaître (senseurs, furtivité, ...) ou être accentués (transition de la couche limite, importance relative de la couche d'entropie) par rapport aux lanceurs 10 fois plus longs.
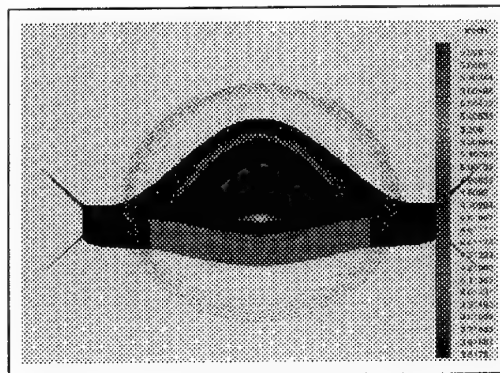

figure 6 : calcul du champ aérodynamique sous un missile hypersonique
CFD analysis of hypersonic airbreathing missile

Les prises d'air font l'objet d'études à AEROSPATIALE-Missiles et ONERA et donnent lieu à différents concepts : 2D, 3D, à géométrie fixe ou mobile. La difficulté principale dans la conception de prise d'air d'un statomixte est de définir une géométrie alliant un débit d'air important à bas Mach et un taux de contraction suffisant à haut Mach (performances du superstatoréacteur). La méthodologie [2, 3, 5, 8, 9] associe prise en compte des contraintes autres qu'aérodynamiques, approche empirique, calculs Navier-Stokes et études expérimentales. On trouvera dans la présentation C36 [9] de plus amples détails.

5.2. Chambre de combustion

Suivant la mission, la chambre de combustion du statoréacteur hypersonique peut être fixe ou à géométrie mobile (avec des éléments éjectables dans le cas d'une application missile par exemple). La

chambre de combustion d'un statoréacteur mixte nécessite théoriquement pour être optimum des formes très différentes le long de la trajectoire. En phase d'accélération continue, on désire augmente par exemple typiquement :

− la présence d'un col de tuyère de plus en plus fermé lorsque le nombre de Mach en combustion sonique,

− une section très divergente en débit de combustion supersonique (risque de blocage thermique si l'apport de chaleur est trop rapide par rapport à la divergence),

− une section très peu divergente en combustion supersonique à haut Mach (performances maximales).

Il faut noter que si une chambre de combustion à géométrie mobile permet ainsi de meilleures performances qu'une chambre fixe, sa réalisation est cependant plus difficile et délicate. Les défis concernant l'injection, le mélange et la combustion et l'état de l'art associé sont davantage détaillés dans la présentation C7 [10].

Le superstatoréacteur CHAMOIS est un exemple de réalisation de chambre de combustion de superstatoréacteur essayée à une échelle réaliste jusqu'à Mach 6,5.
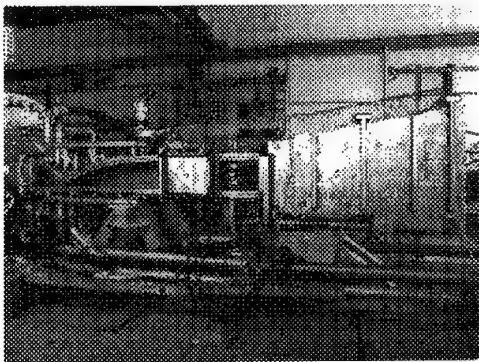

figure 7 :
Superstatoréacteur CHAMOIS à Bourges-Subdray
CHAMOIS scramjet tested at Bourges-Subdray

La chambre mono-mât des cellules ATD permet d'étudier la combustion supersonique à échelle plus réduite, mais jusqu'à Mach 7,5.

Divers calculs Navier-Stokes 2D et 3D réactifs turbulents ont été réalisés sur ces configurations réalistes et des cas-tests plus simples dans le cas de combustion supersonique air - hydrogène. La comparaison avec les résultats expérimentaux a été effectuée dans un certain nombre de cas [5, 10, 11]. Les modèles physiques et les temps de calcul demandent encore à être améliorés , et les outils numériques ne sont pas encore utilisables au niveau

opérationnel dans le cas des superstatoréacteurs fonctionnant avec du kérosène [10].

Parmi les différences entre les statoréacteurs pour applications spatiales (accélération continue) et militaires (accélération, croisière, manoeuvres), il convient de noter la différence sur l'évolution du débit de combustible lors du vol, rapporté par exemple au débit à Mach 2.
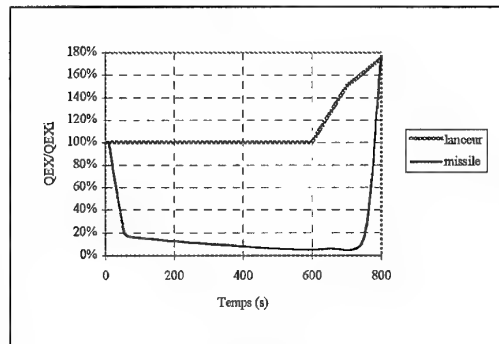

figure 8 :
évolution du débit réduit en fonction du temps
typical evolution of normalized fuel mass flow for
airbreathing vehicles

5.3. Tuyère

Pour transformer efficacement l'énergie apportée par la combustion, il faut prêter une attention toute particulière à la détente des gaz brûlés afin d'optimiser le torseur propulsif résultant. La tuyère peut être axisymétrique, bi ou tri-dimensionnelle, interne ou externe. Dans le cas de lanceurs spatiaux, elle est généralement prolongée par l'arrière-corps du véhicule, avec un volet (mobile ou fixe) prolongeant la partie basse du moteur. Sur les petits véhicules comme les missiles, la détente peut souvent être moins optimale que pour un lanceur spatial.

Comme les autres composants, la tuyère doit être optimisée non pas en un seul point mais sur toute la gamme d'utilisation du moteur et même du véhicule. Une attention toute particulière doit être portée à l'influence de la cinétique chimique (recombinaisons, ...) et à l'équilibrage (suivant le point de vol et le fonctionnement moteur, la même tuyère peut créer un moment piqueur ou cabreur). La figure 9 montre à titre d'exemple l'évolution de la poussée entre une détente figée et une détente à l'équilibre, et un calcul prenant en compte la cinétique chimique qui peut être considéré comme représentatif de la réalité. on remarque que malheureusement quand le Mach de vol augmente l'écoulement est plutôt du type figé, et que les

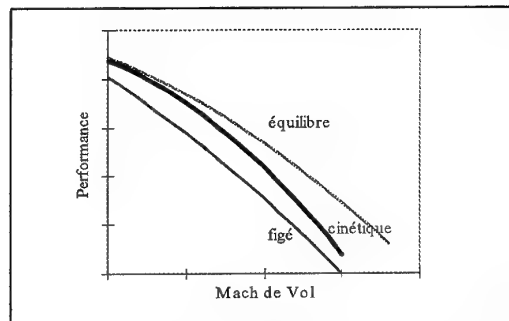performances sont encore diminuées par rapport au maximum que l'on peut espérer théoriquement.

figure 9 :
évolution avec le Mach des performances du moteur en fonction de la cinétique chimique dans la tuyère
effect of kinetics on nozzle performance

Du point de vue structural, la partie externe est refroidie en partie par rayonnement vers l'extérieur, mais la partie interne doit être généralement traitée comme la chambre de combustion. Pour les applications militaires, une contrainte supplémentaire peut être donnée par la signature du jet propulsif.

5.4. Tenue thermique et mécanique

Compte tenu des importantes vitesses de vol (température d'arrêt de l'air de 1650 K à Mach 6 et 5000 K à Mach 12) et de l'apport de chaleur dû à la combustion, le moteur subit des contraintes thermiques très importantes. Pour les parties internes du moteur, aucun refroidissement passif n'est possible vers l'atmosphère à - 60°C, contrairement aux éléments du véhicule. Les flux thermiques en jeu varient typiquement entre 1 et 100 MW/m^2.

Les efforts induits sont également importants (pression interne jusqu'à 8 bars). Pour les missiles hypersoniques, on considère généralement un accélérateur externe pour éviter d'avoir à supporter pendant quelques secondes la pression de fonctionnement d'un accélérateur à propergol solide intégré à une chambre de combustion de forme bidimensionnelle (les statoréacteurs des véhicules hypersoniques sont en général de forme bidimensionnelle essentiellement pour des raisons d'intégration sous le fuselage) donc beaucoup moins propice à la tenue mécanique qu'une chambre classique asymétrique.

Ces efforts thermiques et mécaniques sont à prendre en compte dès la conception du moteur [5] : par exemple les rayons des bords d'attaque utilisés pour la conception de l'aérodynamique interne et de la combustion ne peuvent raisonnablement être pris inférieurs à 1,5 mm.

Différents outils de calcul de structures refroidies activement ou passivement sont utilisés dès la phase d'avant projet. Par exemple, le Département Propulsion d'AEROSPATIALE-Missiles utilise différents logiciels décrivant la conduction (1D ou 2D), le refroidissement pariétal, les refroidissements par impact ou par circulation... Leur utilisation se fait généralement de façon couplée avec les logiciels d'aérothermochimie permettant d'estimer le fonctionnement (et donc les flux thermiques générés dans le moteur) et les performances du statoréacteur (itérations sur les températures de paroi et l'échauffement du combustible, prise en compte de la diminution du frottement en cas de refroidissement pariétal, ...).

Une attention particulière est apportée aux méthodes d'évaluation des flux thermiques, délicate du point de vue expérimental (fluxmètres, méthodes inverses, pyromètres optiques à balayage, ...) comme de celui de la simulation numérique [5, 11, 16].

Pour tous ces aspects, une validation expérimentale systématique est recherchée, éventuellement sur des composants à échelle réduite, en privilégiant la simulation simultanée des contraintes mécaniques et thermiques. Les surflux liés aux interactions des chocs incidents avec la couche limite et avec les chocs détachés aux bords d'attaque [14] doivent être caractérisés puis traités en général par une méthode de refroidissement locale [15].

L'emploi de matériaux avancés disponibles et adaptés aux contraintes spécifiques du vol hypersonique aérobie peut se révéler, lorsqu'il est démontré, un atout notable afin d'augmenter les performances. Ainsi le mât d'injection en carbone/carbone réalisé par AEROSPATIALE dans le cadre de l'opération de R&D interne baptisée SAINT-ELME permet un gain substantiel en masse (au moins divisée par deux par rapport à une solution métallique refroidie) et en traînée, puisque les calculs thermomécaniques par éléments finis détaillés effectués montrent que le bord d'attaque refroidi est capable de résister aux flux thermiques d'un Mach de vol de 12 avec un rayon inférieur à 2 mm [13, 15].
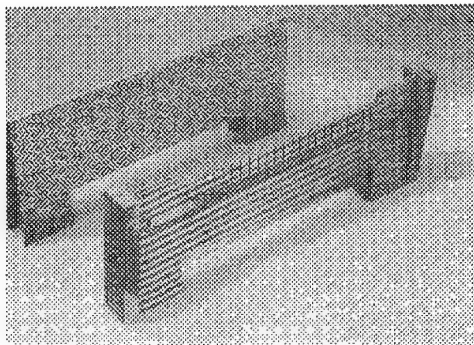
figure 10 :
le mât d'injection SAINT-ELME de
AEROSPATIALE
The SAINT-ELME injection strut developped and
tested at AEROSPATIALE

Le fluide refroidisseur est typiquement le combustible qui refroidit le moteur avant d'être injecté. Une analyse système doit être conduite afin de déterminer compte tenu de la mission et des contraintes thermomécaniques le trajet optimal en double peau. Par exemple le fluide disponible à une forte pression (30 à 150 bars) et faible température (50 à 300 K) est divisé en trois circuits :

– le premier refroidit la tuyère puis la chambre de combustion avant d'être injecté par les mâts,
– le second refroidit la carène et la partie interne de la prise d'air avant d'être injecté par les mâts,
– le troisième refroidit le bord d'attaque des mâts d'injection avant d'être injecté.

Le choix du combustible doit prendre en compte les contraintes de refroidissement en terme de nature du fluide (capacité de refroidissement), de débit à utiliser (le débit peut en certains points de la trajectoire être imposé par le refroidissement et non pas la combustion) et de compatibilité avec les matériaux. La figure 11 fournit une évolution typique de la puissance spécifique à absorber pour refroidir un statoréacteur métallique en vol hypersonique, et les capacités calorifiques de 3 combustibles (kérosène, hydrogène et endothermique). Pour les applications missiles, la mise en oeuvre des combustibles endothermiques est clairement une technologie clé et un axe de recherche à privilégier.
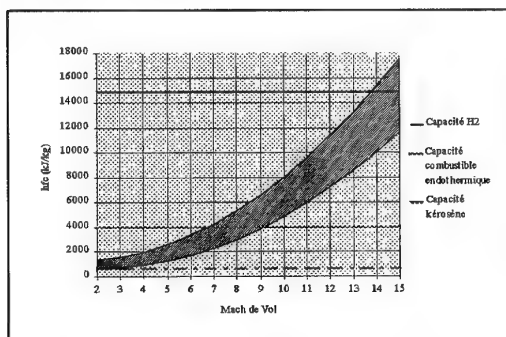

figure 11 : besoins et capacités en refroidissement
du statoréacteur hypersonique
needs and heat sink capabilities of ramjets

5.5. Moyens d'essais

Dans la méthodologie de mise au point de statoréacteurs hypersoniques, une synergie entre analyse numérique (du logiciel d'avant-projet aux approches 3D Navier-Stokes) et études expérimentales est plus que jamais nécessaire, compte tenu des limitations de chacune des deux approches.

Les moyens d'essais sont ainsi un point clé pour le développement de statoréacteurs hypersoniques [3, 5, 16, 17, 18, 19].

On remarque que les moyens d'essais disponibles en France par exemple permettent une grande complémentarité « complexité des phénomènes - taille - niveau d'investigation » entre le niveau du laboratoire (hautement instrumenté, pour l'étude d'un phénomène isolé), les installations d'essais de taille réduite (quelques kg/s d'air chaud) et les installations industrielles (20 à 100 kg/s) et le module propulsif en vol.
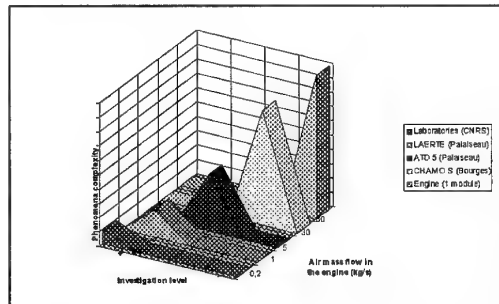

figure 12 : complémentarité des moyens d'essais
hypersoniques aérobies français
complementarity of French hypersonic airbreathing
test benches.

Davantage que pour la mise au point des moteurs plus basse vitesse, l'utilisation de méthodes optiques non intrusives est indispensable, mais nécessite un important travail afin de choisir et d'adapter aux besoins et aux contraintes industrielles des méthodes de mesure mises en oeuvre par des organismes de recherche dans des installations souvent spécifiquement étudiées pour y faire des mesures très fines[16]. Un exemple de cette nouvelle approche est donné par la cartographie de la température statique et de la concentration en vapeur d'eau en sortie du superstatoréacteur CHAMOIS (dans les moyens industriels de AEROSPATIALE à Bourges-Subdray) par spectroscopie passive mise en oeuvre par un laboratoire spécialisé [18].

Les effets de la viciation de l'air à l'entrée du moteur doivent être quantifiés. En effet, la température de l'air doit être préalablement augmentée jusqu'à la température d'arrêt du point de vol de façon artificielle à son passage dans la tuyère

d'alimentation du moteur avec un système de brûleur (H_2/O_2 ou hydrocarbure/O_2) ou à travers un échangeur préalablement chauffé. La composition de l'air sortant du brûleur et entrant dans le moteur peut ainsi contenir de la vapeur d'eau, par exemple, qui aura un effet physique (modification de la chaleur massique...) et un effet chimique (modification du délai d'allumage par exemple).

Outre les moyens d'essais existants, un certain nombre de réflexions et de premières réalisations sont conduites pour les moyens d'essais futurs :
– nouveaux moyens sols, tels que le Tunnel de Compression Adiabatique [5, 17], dont la faisabilité a été démontrée par une étude théorique et expérimentale (air non vicié à fort débit délivré pendant plusieurs secondes à 2400 K), mais qu'il reste à construire,
– essais en vol [3, 5, 19].

5.6. Systèmes liés à la propulsion

Les spécificités de la propulsion aérobie dans le cas des lanceurs, et de l'ambiance thermique dans le cas des missiles conduisent à mener des études particulières pour tous les systèmes liés à la propulsion (réservoirs, alimentation, ...).
Les calories doivent être évacuées ou stockées pour assurer la réussite de la mission , mais peuvent aussi être utilisées afin d'augmenter le rendement du système propulsif voire du véhicule (amélioration de l'aérodynamique externe par refroidissement de la couche limite, initiation de piles thermiques par l'échauffement, ...).

6. LES ASPECTS SYSTEME :

Les lois de guidage pilotage, déjà critiques du fait de la vitesse des véhicules considérés, doivent en outre prendre en compte la sensibilité du système propulsif et sa régularité aux évolutions d'altitude.
Par ailleurs, compte tenu de la limitation des possibilités d'essais complets et représentatifs au sol, le système de pilotage/guidage devra sans doute intégrer une proportion plus ou moins importante d'identification du comportement aérodynamique et d'autoadaptation.
Etant donné les limitations très fortes des moyens d'essais au sol, et malgré la disponibilité espérée de moyens d'évaluation numérique puissants et validés, la connaissance du comportement aéropropulsif du système complet véhicule/ensemble propulsif avant-vol sera réduit. De ce fait, les systèmes de pilotage et de guidage devront être dotés de moyens importants d'identification du système de vol et d'une large capacité d'autoadaptation. Par ailleurs,

ces systèmes, dont la mise au point est toujours délicate pour des véhicules évoluant à vitesse élevée, devront prendre en compte l'extrême sensibilité du système propulsif et de sa régulation aux variations d'altitude.

Plus généralement, la conception d'un véhicule très grande vitesse à propulsion aérobie requiert un niveau très poussée d'intégration et la réalisation d'un grand nombre de compromis interdépendants. Au-delà de la mise au point de moyens numériques et expérimentaux très puissants, le développement d'une méthode de conception itérative, intégrant au plus près toutes les disciplines scientifiques et les spécificités technologiques, restera, même au niveau de l'avant-projet, l'élément clé pour le développement de futures applications du statomixte et du superstatoréacteur [20].

7. CONCLUSION

Quelle que soit l'application (militaire ou lanceur spatial), l'intérêt et la communalité des technologies des statoréacteurs à combustion subsonique, des superstatoréacteurs et des statoréacteurs mixtes est claire. En France, on peut considérer que les outils sont bien en place à ONERA et AEROSPATIALE. Les résultats obtenus sont encourageants. Pour préparer les statoréacteurs nécessaires pour propulser les véhicules hypersoniques du XXIème siècle, en particulier pour des applications militaires, ce savoir-faire et ces investissements doivent être développés, en tirant parti des équipes et des installations existantes.

References :

[1]- A. Wagner, R. Thevenot,
Future Launch Vehicles at AEROSPATIALE : A Survey,
AIAA-93-5051

[2]- A. Wagner et al.,
Integration of a Combined Engine Propulsion System into a SSTO launcher, 1995,
AIAA-95-6044

[3] F. Falempin
Overview of French Research Center ONERA activities on hypersonic airbreathing propulsion
XII ISABE, Melbourne, 1995
published in Australian Mechanical Engineering Transactions
Vol. ME20 N°4, 1955

[4] J. L. Hunt, E. A. Eiswirth
NASA's Dual-Fuel Airbreathing Hypersonic Vehicle
Study
AIAA 96-4591

[5] Alain Chevalier, Marc Bouchez, Dominique
Bouchaud, Isabelle Auneau, Nicole Montmayeur
An industrial point of view on scramjet combustor
design.
IUTAM symposium, Poitiers, october 1995

[6] A. Chevalier, V.M. Levin, D. Davidenko, M.
Bouchez
French-Russian Partnership on hypersonic Wide
Range Ramjets
AIAA-96-4554-CP

[7] C. Rothmund, D. Scherrer, M. Bouchez
Propulsion System for Airbrathing Launcher in the
French Prepha Program
AIAA-96-4498, Norfolk, November 18-22, 1996

[8] I. Auneau, P. Garnero, P. Duveau,
Design and Optimization Methods for Scramjet
Inlets, 1995,
AIAA-95-6017

[9] I. Auneau, P. Duveau
Entrée d'air et interaction entrée d'air/chambre de
combustion
(Intake/Combustor Interaction)
AGARD Symposium April 1997
« Hypersonic Sustained Flight »

[10] D. Scherrer, M. Bouchez
Conception de la chambre de combustion et des
systèmes d'injection
(Combustor Design and Injector Devices)
AGARD Symposium April 1997
« Hypersonic Sustained Flight »

[11] M. Bouchez et al.
Scramjet combustor design in France,
AIAA 95-6094.

[12] A. Dufour
Some single expansion ramp nozzles studies
AIAA-93-5061, Munich, 1995

[13] P.Peres, J. Lansalot, M. Bouchez, E. Saunier
Advanced Carbon-carbon Injection Strut for Actual
Scramjet
AIAA 96-4567

[14] F. Bertrand et al.
Experimental Investigation of shock Wave
Interference Heating on a Blunt Body
AIAA 96-2045

[15] J. Valaza, V. Protat, C. Ferrier, J.C. Nugeyre
Chambre de combustion, Protection thermique,
Refroidissement par air pour statoréacteur
(Combustion Chamber, thermal Insulation, Active
Cooling by Air for Ramjet)
AGARD Symposium April 1997
« Hypersonic Sustained Flight »

[16] A. Chevalier, F. Falempin,
Review of New French Facilities for PREPHA
Program. 1995,
AIAA 95-6128

[17] A. Chevalier, D. Piton,
An original concept of hypersonic facilities : the
Adiabatic Compression Wind Tunnel (A.C.W.T.),
ESA/ESTEC, 11/94

[18] D. Bouchaud, D. Fournet, P. Hervé
Temperature and concentration Measurements in a
hydrogen-Air Scramjet
AIAA 96-4583.

[19] F. Falempin, B. Forrat, J. Baldeck, E. Hermant,
1992,
Flight test vehicles, a mandatory step in scramjet
development,
AIAA-92-5052

[20] F. Falempin, G. Laruelle, Ph. Ramette, M.
Lepelletier, J. Hauvette
Les défis technologiques du superstatoréacteur
(The SCRAMJET technical challenges)
AAAF, Paris, 1996

Paper C-4

Question 1:   L.M.B.C. Campos

You mentioned the interest of an endothermic fuel for cooling, as an alternative to hydrogen; the problem is to avoid the volume occupied by hydrogen, or are there other issues? Which are the candidates for endothermic fuels?

Author's reply:

Endothermic fuels could be used for military applications (essentially for missiles and drones) in the case of "limited" flight Mach number (up to Mach 8). For these applications, they have the following advantages:

-    better volume impulse for compatibility with volume constraints (specially for airborne applications);

-    operational constraints (long time storage, immediate disposability, safety...).

Preferred candidates would probably be hydrocarbon fuels with cracking temperature strongly reduced by using a catalyst covering the regenerative cooling system.

Critical Physical Phenomena in Scramjet Propulsion

G. Kurth
Bayern Chemie GmbH
Postfach 1131
84544 Aschau am Inn
Federal Republic of Germany

SUMMARY

This paper gives a short overview about the critical physical phenomena occuring in scramjet propulsion systems.
After the description of these phenomena, an enginee-ring approach will be given to analyze and predesign scramjet combustion processes and complete scramjet propulsion systems respectively.

NOMENCLATURE

a	combustion chamber width
A	combustion chamber area
b	combustion chamber height
c	dimensionless heat transfer rate
c_T	$(\partial h/\partial p)\vert_T$
h	static enthalpy
H	total enthalpy
p	static pressure
Pr_t	turbulent Prandtl number
u	velocity
δ	boundary layer thickness
ε_m	turbulent eddy viscosity
Φ	arbitrary source term
μ	molecular viscosity
π	dimensionless pressure
ρ	density

indices

1	entrance
2	exit
BL	boundary layer
core	core flow
H_M	enthalpy related mass addition contribution
H_Q	enthalpy related heat flux contribution
M	mass related
P_R	impulse related friction contribution
P_M	impulse related mass addition contribution
P_W	impulse related drag contribution

1   INTRODUCTION

Scramjet propulsion covers a broad range of physical phenomena not to be encountered in "conventional" low speed propulsion [1,2]. Especially the nonlinear high speed viscosity dominated effects result in phe-nomena not to be encountered within "low speed" pro-pulsion. Especially the shock wave - boundary/mixing layer interactions which are strongly coupled in high speed aerothermodynamics govern the character of the flow field of the scramjet engine. Further, nonequilibri-um effects also have an impact on the fluiddynamic structure of the engine flow field and, with it, on its performance characteristics. Although these phenome-na must not be neglected when determining the engine performance characteristics they can be regarded as "uncritical" according to the engine operability since they alter only the thermodynamic behaviour of the flow field [3-6] while the strong viscous interaction phenomena are able to change the whole character of the flow field, f.e. a pressure rise within the combus-tion chamber can cause engine thermal choking/block-age through boundary layer detachment or inlet un-start caused by local separated flow regions [7].
Therefore, in this presentation major emphasis will be laid on these phenomena prior to the nonequilibrium effects which become dominant with accelerated ex-pansion flows only.

2   THE SCRAMJET PROCESS

The scramjet cycle consists of three different subcycles which are closely linked (figure 1):
- the aerodynamic compression of the incoming flow by the intake,
- the mixing and combustion processes within the combustion chamber generally requiring some kind of isolator to decouple the combustion chamber pressure rise from the intake flow , and
- the acceleration of the combustion products within a nozzle which does not exhibit a decisive nozzle throat.
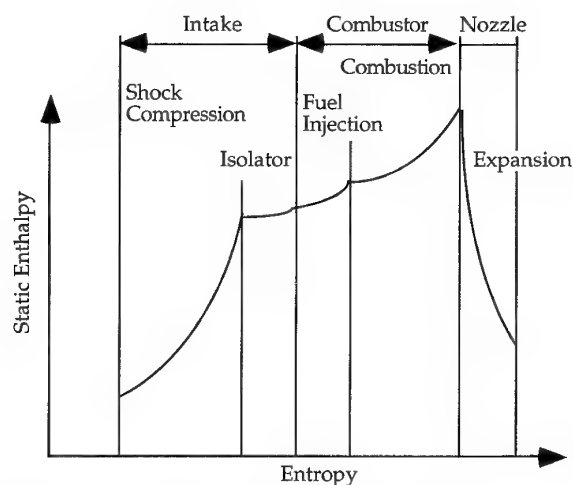

Fig. 1:   Sketch of scramjet thermodynamic cycle

Within the total scramjet process physical phenomena can be associated as well with defined locations of the propulsion system as with the propulsion system in general. While the problem of strong shock wave - boundary layer interaction or strong viscous interac-tions respectively is present at every location of the propulsion system, other phenomena such as super-sonic mixing and combustion can be restricted to the combustion chamber duct flow in total. Further, the nonequilibrium effects occurring in hypersonic flow grow in their influence in the downstream direction. While they might be of marginal interest concerning the intake flow field, their importance grows within the combustion chamber where the mixing and reac-tion processes have to take place within a geometrical-ly limited area. During the expansion process of the combustion products nonequilibrium effects become dominant since recombination effects determine the performance characteristics strongly.

Therefore, the presentation of the critical phenomena will be given in relation to their location within the engine cycle.

3 PHYSICAL PROBLEMS RELATED TO SCRAMJET OPERATION

The nonlinear viscous effects that take place in hypersonic flow are strongly related to the turbulence level of the flow.

Turbulent flows reveal higher heat transfer rates into the structure than laminar ones. This leads to significantly higher thermal structural loads which have to be compensated by active cooling mechanisms. Also, the upstream influence of a pressure rise caused by oblique shocks, f.e., depends on the boundary layer thickness which itself depends on the turbulence level of the flow field again.

Further, boundary layer separation leads to very high heat loads in the reattachment region of the separated boundary layer.

Within super/hypersonic duct flows boundary layer separation due to complicated shock wave - boundary layer interactions leads to upstream influences causing a shock train or pseudo shock system which might block the complete flow section leading to a complete collapse of the internal flow field.

Within the combustion chamber the mixing processes are also determined by viscous effects, especially the shear layer development after fuel injection. Here, a strong coupling between chemistry, turbulence, and gasdynamic structure of the surrounding flowfield can be observed.

Therefore, the phenomena arising from strong viscous interactions are dominating the whole scramjet process to a high extend and should be understood completely. Up to now, a detailed understanding of the strong viscous interaction phenomena could not be gained.

The figure 2 shows the different strong viscous interactions taking place in scramjet propulsion.

3.1 Intake Ramp Flow Field

The intake precompresses the incoming flow field by the forebody nose and structural shape. In general, the intake can be regarded as composed of flat plates with different slopes. At these corners shock waves are generated which compress the flow by oblique shock waves which focus in the vicinity of the intake lip in the ideal case. At these compression corners boundary layer detachment can take place, supposed the static pressure rise is sufficiently large.

The upstream influence and the size of these separated flow regions depend strongly on the turbulence level of the incoming flow since the boundary layer thickness is directly related to it [8]. The separation bubble and the upstream pressure rise deviate the position of the oblique shock wave causing either additional spillage or shock impingement on structural components. Both effects are not favourable, since mass deficiencies or elevated heat transfer rates into the structure caused by impinging shocks have a negative impact on the overall scramjet performance.

Therefore, it appears to be desirable to have an idea about the transitional Reynolds number.

On the other hand, computational and analytical efforts to simulate transition and with it skin friction and heat transfer appear to deliver satisfactory results only partially. Since stability theory is not able to predict transition for arbitrary shapes [9], skin friction and heat transfer prediction is validated for generic shapes only [10]. Further, the prediction of the separated flow regime considering upstream influence, detachment and reattachment appears to deliver reliable data only if semi-empiric information is incorporated into the modelling [11-13].

3.1.1 Boundary Layer Transition

Transition takes place only on the ramps of the inlet, mainly on the first ramp.

Due to the very high speeds and long distances from the leading edge, boundary layer growth is dominated completely by transition since the thickness of the boundary layer is related to the transition point from

oblique shock reflection

supersonic mixing

multiple shock interaction

hypersonic boundary layer transition

detached blunt body curved shock waves

hypersonic compression ramp flow

glancing shock waves

combustion chamber viscous flow interactions
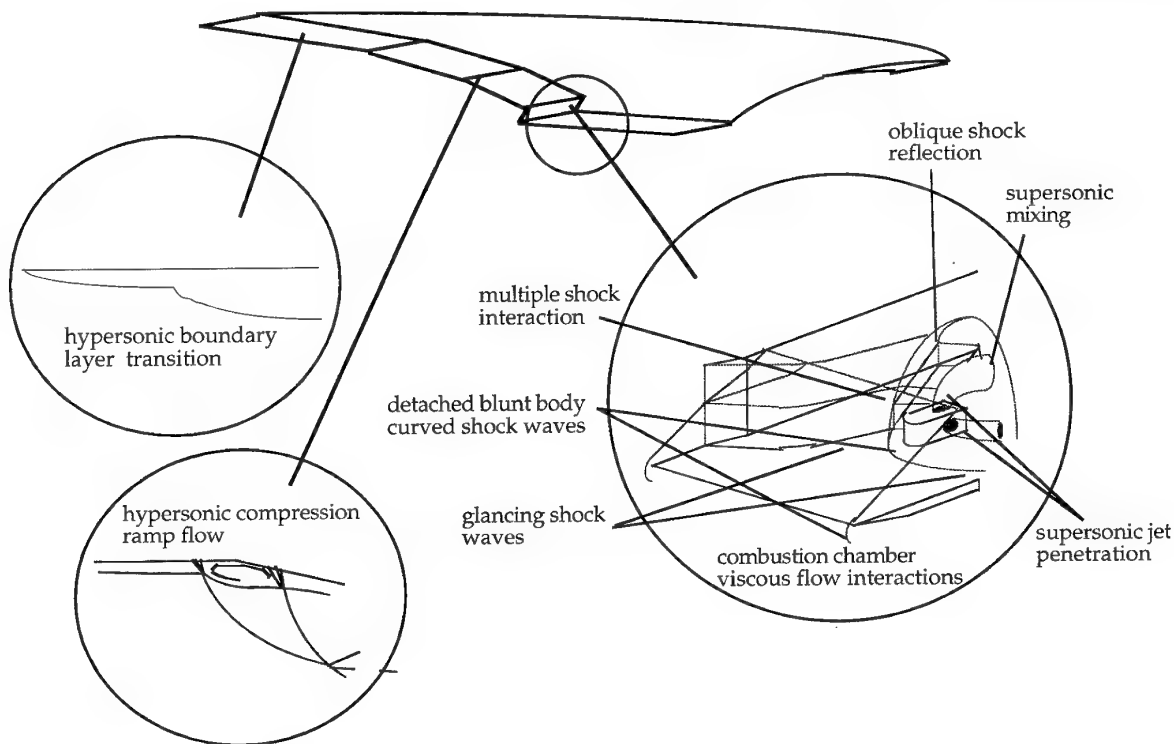
supersonic jet penetration

Fig. 2: Schematic representation of viscous interaction taking place during scramjet operation

laminar to turbulent flow and the length of the transition region [14].

This onset of transition depends on the free stream Mach number in the first instance. As experimental results show the transition Reynolds number grows with free stream Mach number (Fig. 3). The results gained from free flight experiments develop higher transition Reynolds numbers than wind tunnel experiments, even if the experiments are performed in quiet wind tunnels. The turbulence level of the incoming flow plays therefore a dominant role too in boundary layer transition.
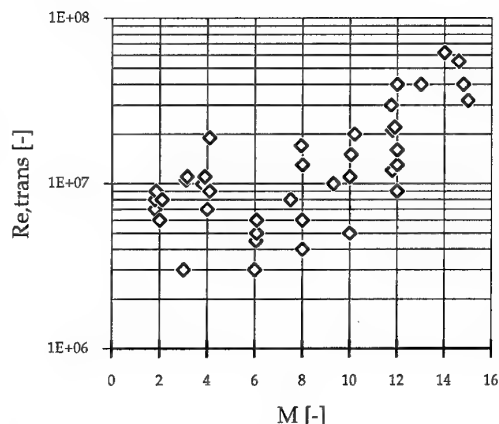
Fig. 3: Transition Reynolds numbers as a function of free stream Mach number (Data taken from [14])

Besides the free stream Mach number, other effects affect the transition significantly. The most important are commented below.

3.1.1.1 Wall Temperature

As has been gained by a lot of experimental and theoretical investigations, the wall temperature plays a dominant role in boundary layer transition. Namely, the cooling of the wall significantly below the adiabatic wall temperature increases the stability of the boundary layer and, therefore, results in a delayed transition to turbulence which reduces the boundary layer thickness.
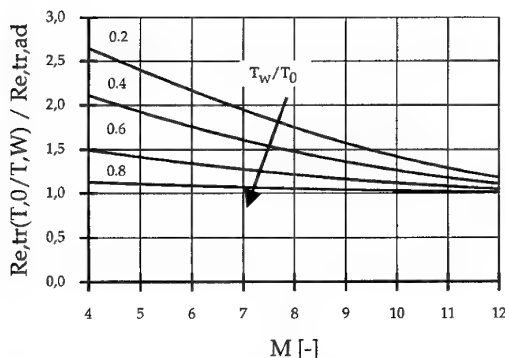
Fig. 4: Extrapolated "stretch" factor of the transition Reynolds number for cooled walls (Data taken from [14])

3.1.1.2 Pressure Gradient

Positive pressure gradients in boundary layers are able to cause boundary layer separation, but also decrease the stability of the boundary layer such that transition to turbulence takes place earlier. Otherwise negative pressure gradients are favourable every time, due to their stabilization effects. Unfortunately, the biggest

pressure gradients occurring in the intake flow field are generated by the oblique shock waves emanating from the wedges, so that transition to turbulence and boundary layer separation might take place at the wedge location.

3.1.1.3 Nose Bluntness

The nose bluntness effects in hypersonic flow are quite irritating. While sharp leading edges show lower transition Reynolds numbers than small radius leading edges [15], this effect is reversed with growing leading edge radius [16]. Although not fully understood, an explanation might be that the entropy layer generated by a small radius blunt leading edge stabilizes the initial high frequency disturbances while with growing radius low frequency instabilities between the boundary layer and the detached nose shock appear to accelerate transition [17]

3.1.1.4 Three-dimensional Effetcs

With growing Mach number, real geometries develop secondary flow patterns that strongly interact with the main flow. These crossflows also generate instabilities which are superposed to the almost two dimensional main profile. In the existence of negative pressure gradients as exist in the vicinity of leading edges of side walls, for example, the flow gets locally accelerated, developing crossflow patterns which lead to inflection of the flow profile causing instabilities causing quicker transition. Experimental [18] and computational [19,20] investigations on hypersonic three dimensional boundary layers have been performed, but it appears that the three dimensional effects are not being understood in detail.

3.1.1.5 Structural Vibration and Roughness

Structural vibration and roughness can cause a quicker transition to turbulence, since the nonlinearities encountered in hypersonic flow amplify the disturbances originated by them in a manner such that no natural transition occurs but a bypass transition takes place. In this case, the amplitudes of the disturbances become so large that the linear mechanisms were completely ignored and, as a result, the problem becomes fully nonlinear.

3.1.2. Shock Wave- Boundary Layer Interactions in Compression Ramp Flow

Compression ramp flow field is dominated by the oblique shocks generated by the intake ramps. If the pressure rise is strong enough boundary layer detachment occurs incorporating recirculating subsonic flow regimes and local stagnation point flows caused by reattachment [11, 21, 22].

Within this separated flow field elevated heat transfer rates are observed at the reattachment region causing significant local structural loads.

Further, the upstream pressure rise depends on the turbulence level/boundary layer thickness of the incoming flow. Besides the boundary layer thickness the upstream interaction length depends on the Mach number of the incoming flow and the deflection angle of the wedge.

With constant free stream Mach number the interaction length grows proportional to the deflection angle while on the other hand a higher free stream Mach number at constant deflection angle reduces the interaction length due to the fact that the influence of relative subsonic boundary layer compared to the overall boundary layer thickness vanishes.

These tendencies can be simulated qualitatively by most numerical schemes incorporating different turbulent models. Nevertheless their quantitative analysis exhibits methodical and modelization dependent deviations from experimental data [11, 23] which cannot be explained satisfactorily. On the other hand, even very simplified analytical models show the same phenomenological and numerical congruence concerning pressure distribution along the ramp while the length of the upstream interaction region can be correlated by

empirical data of limited validity [24-27].

The following figures show a comparison between measured [for details see: 13] and calculated dimensionless pressure and heat transfer rate distribution along a 15° flat plate compression ramp at Mach 14 free stream conditions. Calculations have been performed using a fourth order accurate TVD method for two-dimensional turbulent flow incorporating Cebeci-Smith turbulence modelling (in house development by the author) for fully turbulent flow and an artificial turbulence onset at the reattachment point. The comparison shows that the fully turbulent flow heat transfer prediction are arbitrarily inaccurate while the forced turbulence onset at the reattachment location shows a comparatively good agreement between computation and experiment. Nevertheless, these results could only be obtained incorporating an a priori knowledge of the transition point into the code. Further, the numerical results gained by the BC-TVD-code match quite well with the Dornier code used to compute the flow field in [13].
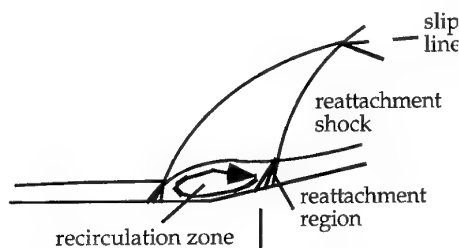
Fig. 5: Schematic representation of compression ramp flow field with separation
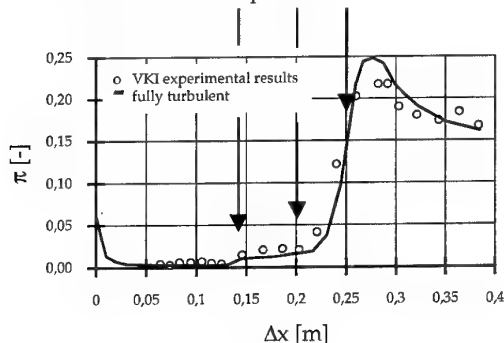
Fig. 6: Comparison of experimental and numerical data for Mach 14 compression ramp (15°) flow (dimensionless pressure distribution)
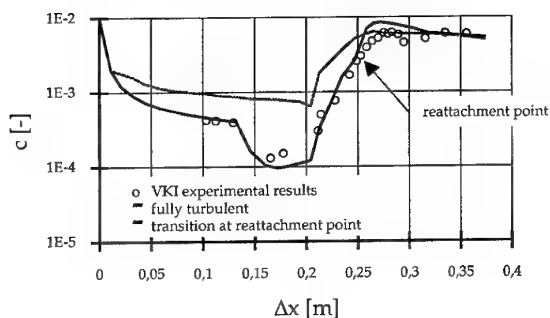
Fig. 7: Comparison of experimental and numerical data for Mach 14 compression ramp (15°) flow (dimensionless heat transfer rate distribution)

The pressure distribution on the other hand, is nearly independent of the turbulence modelling and exhibits

the inability of predicting the pressure rise in the reattachment region correctly.

3.2 Hypersonic Isolator and Combustion Chamber Flow

The part of the scramjet engine housed in the airframe of the vehicle consists of an engine module inlet followed by an isolator which decouples the inlet flow field from the adjacent combustion camber.

Since the module inlet is bounded by side walls, shocks originating from these side walls cross the incoming flow field, interact with the shock from the intake lip and, as glancing shock waves, with the boundary layer in the vicinity of the walls. Due to the pressure rise within the combustion chamber caused by either fuel injection, combustion, and shock interaction phenomena an isolator has to be employed between the module inlet and the combustion chamber in order to reduce the upstream influence of the pressure rise within the combustion chamber, especially during moderate flight Mach number operation [28,29]. With increasing flight Mach number, the ability of the pressure rise to cause an unstart decreases because the combustion enthalpy become small compared to the total enthalpy of the captured air flow. At flight Mach numbers above Mach 8, an unstart is quite unlikely. Nevertheless even in the "non-unstart regime", strong interactive phenomena can cause severe damage to the structure since heat loads increase significantly with flight Mach number. On the other hand, the stronger the interactions the higher the thermodynamic losses and with them the loss of engine performance. Since at high flight Mach numbers the performance decreases relatively to the total enthalpy and momentum of the captured air, even losses which at the first sight appear to be neglectible can result in diminished thrust.

In order to reduce the influence of the pressure rise, it appears to be reasonable to reduce boundary layer thickness and, with it, the potential of high entropy production through local flow separation and separation induced oblique shock systems.

3.2.1 Interactions between Supersonic Flow and Cavities with Bleed

The most common way of boundary layer diversion is the introduction of a bleed cavity within the upper side wall of the combustion chamber since the boundary layer thickness is maximum there. The flow field developing from this configuration is depicted in figure 8 schematically.
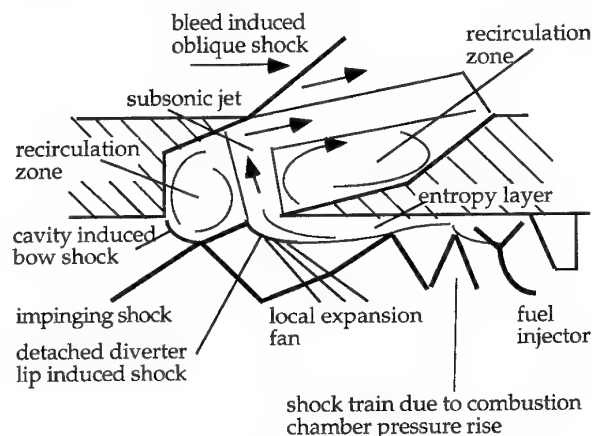

Fig. 8: Schematic representation of the flow field resulting from boundary layer diversion by a cavity with bleed

Here it can be seen that the incoming main flow accelerates the flow within the cavity. Due to the final radius of the diverter lip a detached bow shock develops which results in a steep pressure rise in the vicinity of the lip. While on the combustion chamber wall side an

entropy layer develops, a subsonic jet intrudes the cavity interacting with the flow in the bleed channel and the cavity. The pressure rise within the cavity forces a bow shock to emanate from the starting corner of the diverter cavity.

The entropy layer which exhibits a comparatively thick subsonic flow region in the vicinity of the upper wall interacts with the pressure rise of the combustion chamber in a manner such that in case of the concurrence of the entropy layer with separated boundary layers a backflow through the entropy can occur which causes higher mass deficits. On the other hand, such a backflow can definitively reduce the risk of inlet unstart since a stabilization of the flow field takes place.

At this place it has to be mentioned that boundary layer bleed of course is limited to moderate hypersonic flight Mach numbers (i.e. total temperature) to avoid excessive internal kinetic heating.

Experiments performed at DLR-Cologne and BC indicate that especially within the moderate Mach number regime the functionality of the internal inlet can be improved. To simulate the pressure rise through combustion, a throttle was used to obtain a sufficient pressure rise by a normal shock at the end of the isolator.
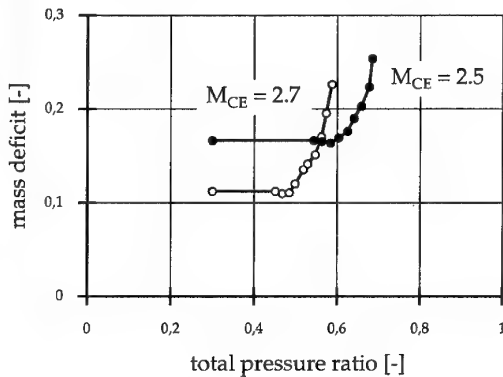
Fig. 9: Mass diversion through cavity as a function of isolator total pressure ratio for different combustor entrance Mach numbers M_{CE}

3.2.2 Glancing Shock - Boundary Layer Interactions

Glancing shock waves are generated either by obstacles within the main duct flow field (fuel injectors, f.e.) or by the side walls of the combustion chamber. A special character of glancing or swept shock waves is that although being generated as oblique shock waves they develop qualities of pseudo normal shock waves in the vicinity of the wall. The resulting flow field consists of complicated separation and secondary flow zones which are not fully understood up to now [30, 31]. Especially the unsteady interactions between the subsonic part of the boundary layer and the secondary flow pattern, which seem to exist for special flow conditions only, exhibit immense problems as well in basic physical understanding as in analytic or numeric modelling [32].

As has been observed the general far side flow field structure is in principle independent of the near wall interaction in the vicinity of the apex. As has been pointed out by [31] even a gap between wedge and wall has no significant influence the shock location and downstream flow field, although the upstream interaction line moves downstream with growing gap height. With increasing free stream Mach number the flow field pattern downstream of the main shock changes from the smooth recompression sketched in figure 10 to a steep pressure rise in the reattachment region due to the impinging jet characteristic of the reattaching flow which causes a local normal shock(figure 11).
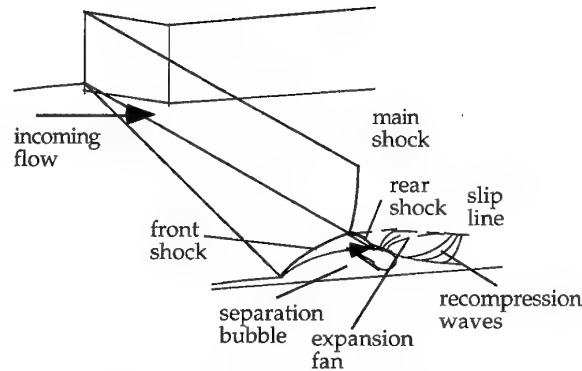

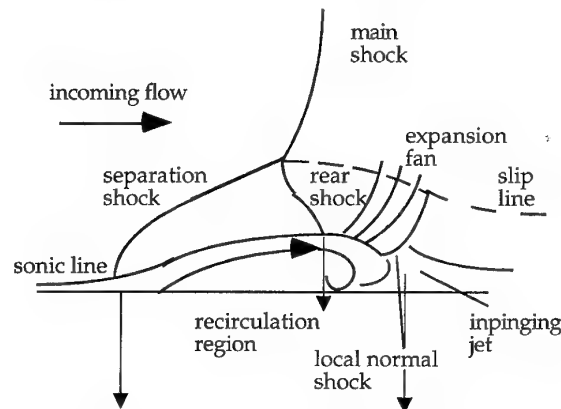Fig. 10: Sketch of general glancing shock wave flow field

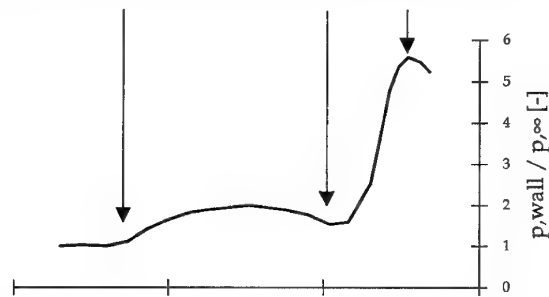Fig. 11: Sketch of flow pattern of a swept high Mach number shock wave (after [33]).

Fig. 12: Dimensionless wall pressure distribution for swept shock wave (after [33])

3.2.3 Shock- Boundary Layer Interactions due to Blunt Body Obstacles and Fuel Injection

Within the combustion chamber major disturbances are caused by fuel injection or fuel injectors, respectively. While the fuel injectors work as blunt body obstacles within the supersonic flow which generate strong detached bow shock waves the injected flow itself acts as a geometric blunt body area contraction as well as a gasdynamic contraction due to mass momentum and enthalpy addition. In general the blunt body detached shock wave pattern looks like the one depicted in figure 13. Here, highest pressure and heat loads are encountered in the subsonic flow region. Further, the detached normal shock in front of the injector element causes separation and, with it, a counterrotating recirculation zone at the injector wall. Both vortices form a reattachment line which generates a divergent streamline pattern (figure 13). Heat transfer rates are extremely high at this location, too [34].

Fuel injection on the other hand generates similar flow

patterns with even more complicated recirculation regions embedding the fuel jet (figure 14).

The primary bow shock is due the obstruction of the incoming main flow by the injected fuel. Boundary layer separation takes place right before the emergent jet due to the shock induced pressure rise causing an oblique separation shock which intersects with the bow shock.

Here, maximum interest is focussed on the mixing capabilities of the fuel injection system, i.e. the interaction of the separation, bow shock and fuel with the incoming flow. On the one hand, mixing is enhanced when the bow shock lifts from the wall allowing a partially subsonic mixing between injected fuel and the incoming boundary layer [35].

This phenomenon is observed mainly with very thick boundary layers where large eddies influence the flow pattern significantly and with separated boundary layers. With this phenomenon occurring fuel can travel upstream and react with the incoming subsonic part of the boundary layer. This worsens the hot spot heat loads encountered in transverse fuel injection even more. Therefore, despite of the mixing enhancement through shock elevation fuel injection should take place in regions of comparatively narrow boundary layers, to avoid on the one hand hot spots in the vicinity of the wall and the undesirable pressure rise in front of the fuel injection due to precombustion phenomena.
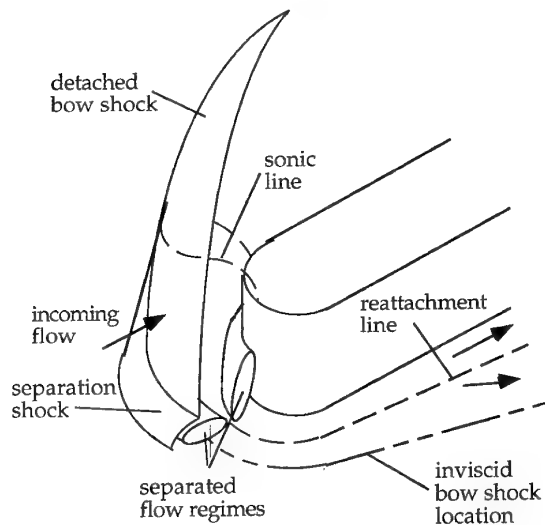

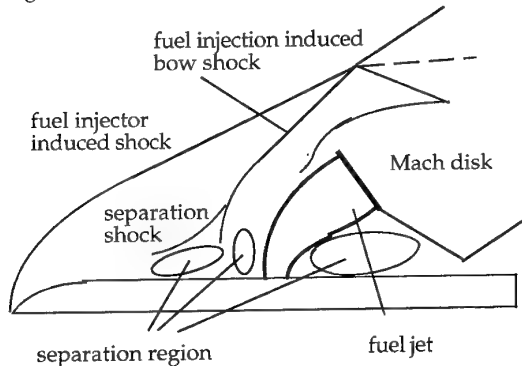Fig. 13: Sketch of flow field at the fuel injector nose

Fig. 14: Sketch of the flow field for perpendicular fuel injection into a supersonic main flow

Further, it should be mentioned that, despite of the undesired hot spot effects, the penetration height is only marginally affected by the size of the separation re-

gion. This is due to the fact, that for constant dynamic pressure and mass flow rate of the injected fuel the height of the Mach disk does not vary very much for separated or attached boundary layer flow respectively. The location of the Mach disk can be interpreted as the penetration depth of the fuel jet due to the fact that the momentum losses across the Mach disk limit the penetration of gaseous jets into supersonic flow. In fact, the high momentum of the incoming supersonic main flow is the limiting factor for jet penetration since the fuel jet will be turned downstream very rapidly.

3.2.4   Shock Impingement

The shocks generated by the obstacles, walls, and fuel injection hit the combustion chamber walls and are reflected there. This reflection produces local pressure peaks and, even more important, heat loads.

Under certain circumstances, the reflected impinging shock may cause boundary layer separation, resulting in local hot spots due to reattaching separated flows.

The criterion for boundary layer separation is the strength of the impinging shock, represented through the deflection angle of the flow.

For moderate deflection angles of about 5° and moderate Mach numbers in order of 2, the boundary layer stays attached to the wall exhibiting a marginal growth of the subsonic part of the boundary layer due to the slightly upstream influence of the pressure rise generated by the impinging shock (figure 15).

The pressure rise observed is nearly identical to the one obtained by inviscid calculations. Therefore, the influence of the shock impingement appears to be neglectible small.

On the other hand, with increasing deflection angle, boundary layer separation occurs, changing the character of the flow field. Here, a dead-air recirculation region develops with a pressure plateau exhibiting nearly the level of a wedge flow. The imaginary wedge angle is nearly proportional to the deflection angle of the incoming flow up to 5°, approximately, jumping to a constant level of about 10° for higher deflection angle levels [36].

The figures 15 to 18 show the flow field characteristics in correlation with the wall pressure profiles.
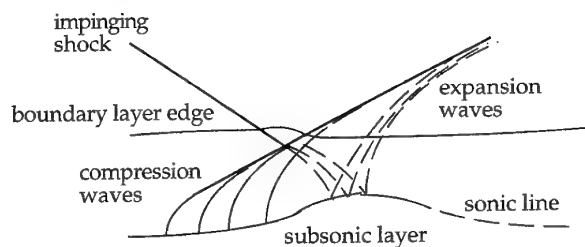

Fig. 15: Sketch of the impinging shock reflection without boundary layer separation
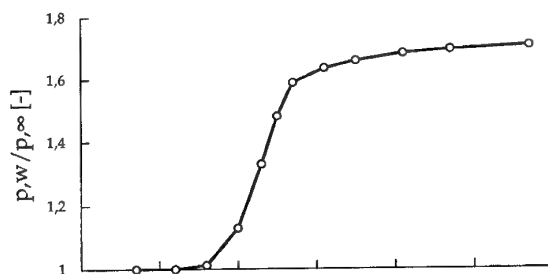

Fig. 16: Dimensionless pressure distribution for impinging shock reflection without boundary layer separation (data taken from [37])
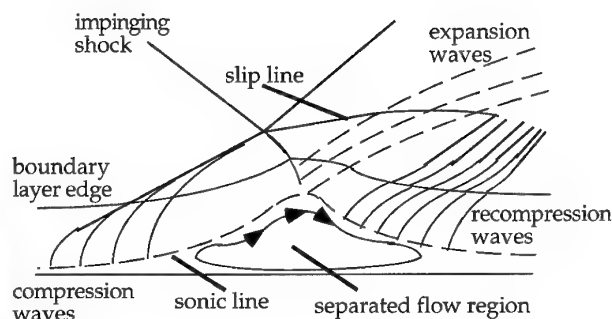
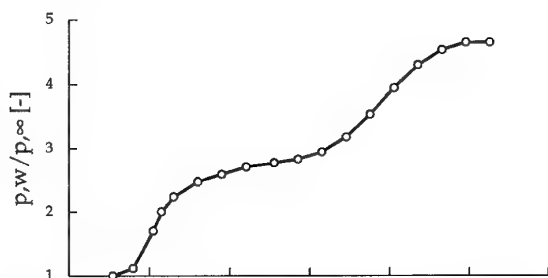Fig. 17; Sketch of the impinging shock reflection with boundary layer separation

Fig. 18: Dimensionless pressure distribution for impinging shock reflection with boundary layer separation (data taken from [37])

3.2.1.6 Hypersonic Mixing and Combustion Processes

The injected fuel has to be mixed with the incoming air to be burned completely. Therefore, it is mandatory for the fuel jet to penetrate as deeply as possible into the air stream. The deepest penetration will be gained for perpendicular injection, causing high additive losses by injection induced shocks and separated flow regions. On the other hand, the induced shocks and separated flow regions generate higher turbulence levels of both injected fuel and incoming air stream resulting in enhanced mixing by breaking the fuel jet macroscopic into smaller eddies. Therefore, the required mixing length decreases sensibly.

As an alternative, parallel fuel injection can be utilized resulting in less losses through shock generation but an increased mixing length since the mixing process will be dominated by the shear layer solely. In this case, mixing takes place as the shear layer decays into smaller eddy-like macroscopic structures. Contrary to the perpendicular injection the development of a decisive mixing zone depends strongly on the convective Mach number between the fuel and the airflow. For example, convective Mach numbers between 0.4 and 0.8 seem to be optimum for an parallel H_2 - air mixing.

Further mixing will be enhanced by shocks crossing the developing shear layer since they first rise the microscopic turbulence level of flow field, second force a macroscopic decay of the shear layer due to local pressure gradients, and third decelerate the flow enlarging the time scales for mixing.

Combustion can only take place if mixing is completed, at least locally. Reaction efficiency is defined as the ratio of the actual amount of fuel burned within the combustion chamber and the amount of fuel that can be burned theoretically. Therefore, combustion efficiency is closely coupled with the mixing properties of the combustion chamber under investigation.

If the reaction rates are considerably higher than the mixing rates, so that the reactions proceeds very fast, the complete combustion process can be regarded as mixing dominated. Since the fuel is injected into the combustion chamber the resulting combustion process is mostly mixing dominated, resulting in so called diffusion flames.

Within the low Mach number operational regime, the pressure rise due to combustion can result in the generation of a terminal shock train system which could lead to unstart, since the aerodynamic contraction resulting from the pressure rise induced boundary layer separation forces the terminal shock train and the separated flow regime to move upstream. Methods to delay unstart are:

• staged fuel injection to distribute the heat addition along a spacially broader region,
• a prolongation of the isolator duct by placing the fuel injector far downstream of the module inlet exit, and
• an increasing of the combustion chamber divergence at the location of the fuel injection to compensate geometric and aerothermodynamic blockage.

3.3 Hypersonic Expansion Flow

Since the scramjet engine does not exhibit a decisive nozzle throat which decouples combustion chamber and nozzle flow regimes for conventional propulsion systems, all disturbances generated in the combustion chamber influence the expansion flow without damping by sonic transition.

Besides the high heat loads resulting from the high stagnation temperatures of the combustion products, the shock impingement phenomena due to exhaust gas flow and outer flow field interactions and the nonequilibrium recombination effects, expansion corner effects on the transition from combustion chamber to nozzle occur which cause boundary layer detachment.

Interaction with impinging shocks further results in enhanced total pressure losses which decrease the overall cycle efficiency significantly.

4 A SIMPLIFIED ENGINEERING MODEL FOR SCRAMJET DESIGN AND ANALYSIS

On the basis of the main effects dominating the scramjet process, a highly simplified engineering model has been developed. This model incorporates

- the calculation of the intake flow field by a two dimensional zeroth order coupling of the steady, non similar, turbulent boundary layer equations for high temperature equilibrium gases with a Riemann problem based method of waves capable of computing wave-wave and wave-wall interactions respectively of any kind,
- the calculation of isolator and combustion chamber flowfield utilizing a highly coupled boundary layer - one dimensional core flow solver which takes into account the pressure rise due to shock trains, fuel injectors and combustion as well as their interactions by semi-empirical correlations. Further, the supersonic mixing process is included by an empirical diffusion flame correlation adopted to numerous experiments performed at the MAI.
- the calculation of the high speed nozzle flow using the same coupling as applied to the intake calculations. To take into account the nonequilibrium phenomena occurring in the accelerated flow (freezing of chemical recombination) a modified Bray criterium [38] is applied which checks the individual recombination rates according to the characteristic time scales.

4.1 Modelling Approach

The physical gas model applied to the whole set of computations is that of an equilibrium high temperature gas with variable thermal, caloric, and transport properties. The gas model is based on the computation of partition functions for the single constituents of a gas mixture and the solution of the law of mass action for the whole gas mixture to obtain the correct composition. The transport properties of the single parts are obtained by the well known formulas obtained by ki-

netic theory, while the gross values of the gas mixture are obtained by applying Wilke's law.

The set of boundary layer equations solved is generated by applying a generalized Falkner-Skan-transformation on the well known steady, two-dimensional, turbulent boundary layer equation with pressure gradient in downstream direction. The turbulence model employed is the Cebeci-Smith model. This results in a set of five ordinary differential/algebraic equations. This set can be solved by any ordinary boundary value problem solver (DASSL f.e.).
The external two-dimensional flow field is described by the steady Euler equations. This set of partial differential equations can be solved analytically when treated as an initial value problem (Riemann problem).
A coupling between the boundary layer and the external flow field can be achieved as far as the pressure rise by the intake ramps does not induce boundary layer separation.
Within the isolator duct a semi-empirical approach is used [39] which delivers typical performance characteristics of a constant area isolator duct with shock trains. Alternatively, a diverging isolator duct can be taken into account which does not exhibit a shock train of the strength observed in a constant area isolator.
The combustion chamber process is simulated in a manner such that the pressure rises due to fuel injector-flow interactions are taken into account through a semi-empirical approach proposed by Billig [40] and Schetz [41].
Here, the injected fuel stream is mimicked by an equivalent half body and an detached curved shock wave, following the correlation of Billig. The influence of the injector is included by an detached shock wave which delivers a pressure rise in the part of the combustion chamber not reached by the injected fuel. This approach was introduced by Baranovsky [42].
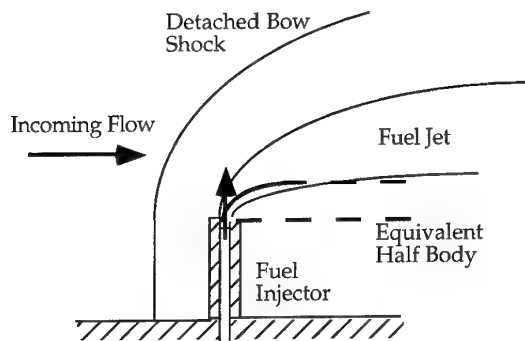

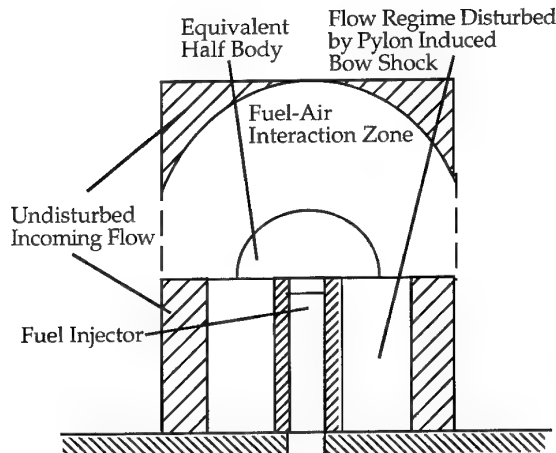Fig. 19: Sketch of fuel inejction system modelling

Fig. 20: Sketch of flowfield simulation in the vicinity of fuel injectors

To cope with the chemical energy conversion through mixing and combustion processes, a distribution function is introduced which couples the pressure rise in the combustion chamber with the equilibrium values obtained for an imperfect burned gas mixture through a semi-empirical correlation. The resulting combustion chamber efficiency depends on the geometry, the number of fuel injectors, and the equivalence ratio can be described as an "if it is mixed it is burned" approach.

$$\eta = 1 - \exp(-\alpha\xi)$$

Here, η can be interpreted as the combustion chamber efficiency which depends on

$$\xi = \nu \zeta \omega$$

$$\nu = \sqrt{\pi \, N_{fuel\ injectors}/4}$$

$$\zeta = \sqrt{\frac{x^3/A_{injection}}{\int_0^x A(x)/A_{injection}\,dx}}$$

$$\omega = \left(\frac{\Omega^b}{2.5}\right)^a \sqrt{\frac{\Omega}{2.5}}$$

$$a = \begin{cases} 0 \\ 1 \end{cases} \text{für } \Omega \begin{cases} \geq 2.5 \\ < 2.5 \end{cases}$$

$$b = \begin{cases} 1 \\ -1 \end{cases} \text{für } \Omega \begin{cases} > 1 \\ \leq 1 \end{cases}$$

$$\Omega = \frac{(\dot{M}_{air}/\dot{M}_{fuel})}{(\dot{M}_{air}/\dot{M}_{fuel})_{stoichiometric}} = 1\ /\ ER$$
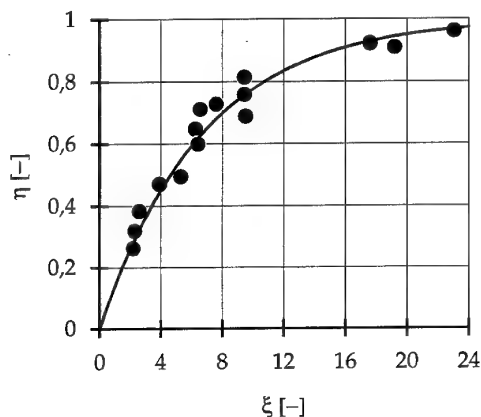

Fig. 21: Combustion chamber efficiency according to Baranovsky [42]

The simplified combustion chamber simulation is a semi-two-dimensional one, which couples an one-dimensional core flow with two-dimensional boundary layers while simultaneously taking into account the gross gasdynamic structure of the flow and the strong viscous effects occurring during turbulent supersonic mixing.

The balance equations solved for combustion chamber analysis are formulated in conserved quantities as mass-, momentum and enthalpy currents instead of the usual primitive variable approach in pressure, velocity and temperature, f.e. The advantages of this formulation lie in the inherent conservative structure of the set of equations neglecting approximate approaches to equilibrium gas flows via variable γ for example.

The equations are:

Mass balance:

$$[\rho u]_{2,\text{Core}}\left[A_2 - 2(a + b - 2\delta)\int_0^\delta \left[1 - \frac{(\rho u)_{BL}}{(\rho u)_{\text{Core}}}\right] dy\right]$$

$$= \dot{m} + \Phi_M$$

Momentum balance:

$$p_2(A_2 + A_1)/2 + (\rho u^2)_{2,\text{Core}} *$$

$$\left[A_2 - 2(a + b - 2\delta)\int_0^\delta\left[1 - \frac{(\rho u^2)_{BL}}{(\rho u^2)_{\text{Core}}}\right]dy\right]$$

$$= \dot{P}_1 + \Phi_{PR} + \Phi_{PM} + \Phi_{PW} + p_1(A_2 - A_1)/2$$

Enthalpy balance:

$$(\rho uH)_{2,\text{Core}}\left[A_2 - 2(a + b - 2\delta)\int_0^\delta\left[1 - \frac{(\rho uH)_{BL}}{(\rho uH)_{\text{Core}}}\right]dy\right]$$

$$= \dot{H}_1 + \Phi_{HM} + \Phi_{HQ}$$

The boundary layer equations solved are the ones for turbulent nonsimilar equilibrium flow with strong density changes due to chemical reactions. The turbulence model employed is the algebraic Cebeci-Smith model.

Mass conservation:

$$\frac{\partial \rho u}{\partial x} + \frac{\partial \overline{\rho v}}{\partial y} = 0$$

x-momentum balance:

$$\frac{\partial \rho uu}{\partial x} + \frac{\partial \overline{\rho v}u}{\partial y} - \frac{\partial}{\partial y}\left[(\mu + \rho\,\varepsilon_m)\frac{\partial u}{\partial y}\right] = \rho_{\text{Core}}\, u_{\text{Core}}\frac{d\,u_{\text{Core}}}{dx}$$

y-momentum conservation:

$$\frac{\partial p}{\partial y} = 0$$

Total enthalpy balance for chemical equilibrium flow:

$$\frac{\partial \rho uH}{\partial x} + \frac{\partial \overline{\rho v}H}{\partial y} -$$

$$\frac{\partial}{\partial y}\left[\left\{\mu\left(1 - \frac{1}{Pr}\right) + \rho\,\varepsilon_m\left(1 - \frac{1}{Pr_t}\right)\right\}u\frac{\partial u}{\partial y} + \left(\frac{\mu}{Pr} + \frac{\rho\,\varepsilon_m}{Pr_t}\right)\frac{\partial H}{\partial y}\right]$$

$$= \frac{\partial}{\partial x}\left[\left(\frac{\mu}{Pr} + \frac{\rho\,\varepsilon_m}{Pr_t}\right)c_T\,\rho_{\text{Core}}\,u_{\text{Core}}\frac{d\,u_{\text{Core}}}{dx}\right]$$

The nozzle flow field is calculated by a coupling of the turbulent boundary layer equations with the Euler equations for steady two-dimensional high temperature equilibrium flow. Here, the nonequilibrium effects are taken into accout by applying the Bray freezing criterion [38] locally. If the local recombination rate is far less than the local production rate, the flow is regarded as frozen, i.e. no chemical reactions take place, while the molecular energetic contributions (rotation, vibration) are treated as equilibrium ones.

4.2   Results

The results to be presented are an analysis of the combustion chamber flow within a dual mode scramjet and a predesign of a complete scramjet propulsion system . The experimental results were obtained within the German Hypersonic Research Program as a joint effort between the russian research institute TsAGI and several german research agencies and companies (DLR,DASA,TU Stuttgart, TH Aachen). Experiments took place at TsAGI with support from german re-

searchers concerning combustion chamber design and modern measurement methods.

The predesign of the complete scramjet propulsion system is closely related to the results obtained during the ESA WLC study [43].

4.2.1   Combustion Chamber Analysis

The figures 23 to 26 show the pressure distribution along the combustion chamber walls of a dual mode scramjet combustion chamber for both cold and hot flow. As can be seen quite clearly, the supersonic flow entering the combustion chamber remains supersonic throughout the whole regime when no combustion takes place. Even the fuel injection system does not cause any notable pressure rise at the walls.
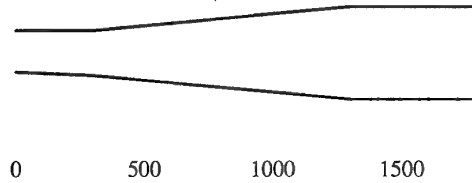

Fig. 22: Geometry of the combustion chamber under investigation (divergence angle at the injection point 1°)
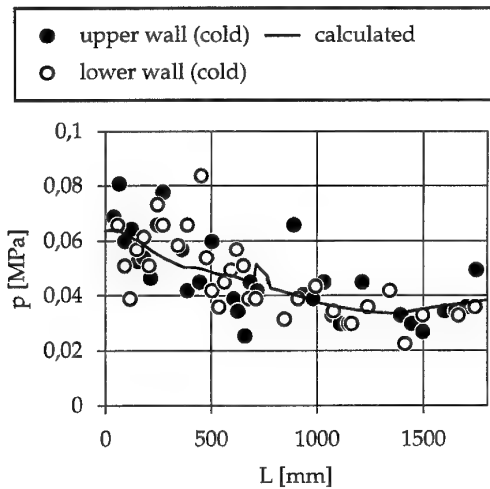

Fig. 23: Comparison between measured and calculated wall pressure distribution for cold combustion chamber flow
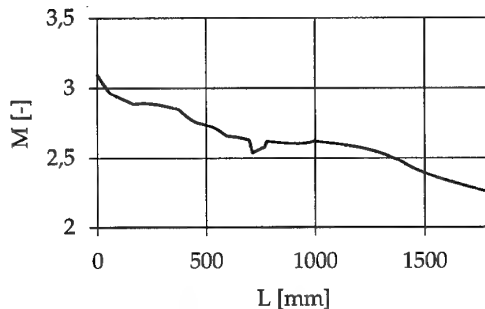

Fig. 26: Calcualted combustion chamber core flow Mach number distribution without combustion

On the other hand, the hot flow produces a pressure rise after the fuel injection strong enough to slow down the flow to subsonic regime clearly upstream of the fuel injection. This is due to the complicated detached shock - boundary layer - mass addition coupling effects gen-

erated by the fuel injection. The figure demonstrates clearly that this very strong induced shock train decelerates the flow in a manner such that a subsonic flow regime is encountered and a enhanced mixing process takes place. Therefore, in this case the combustion process apppears to be similar to premixed combustion.
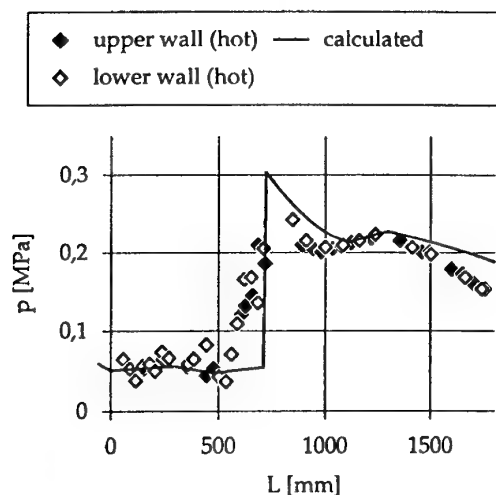
◆ upper wall (hot)	—— calculated
◇ lower wall (hot)	

Fig. 25: Comparison between measured and calculated wall pressure distribution for hot combustion chamber flow
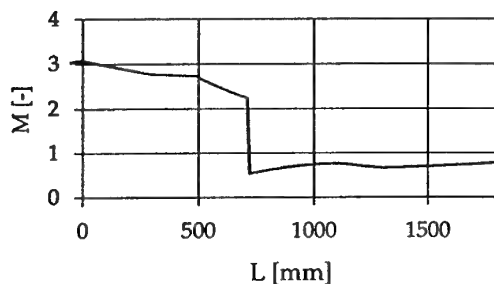
Fig. 26: Calcualted combustion chamber core flow Mach number distribution with combustion

4.2.2 Scramjet Propulsion System Predesign

The predesign data presented here relate to a vehicle designed within the ESA-WLC study [Berry] with an preliminary issue of the design tools utilized now. The application of the advanced design tool shows that the generated performance data for this SSTO vehicle could be improved by a slight modification of the geometry. For details see [43].
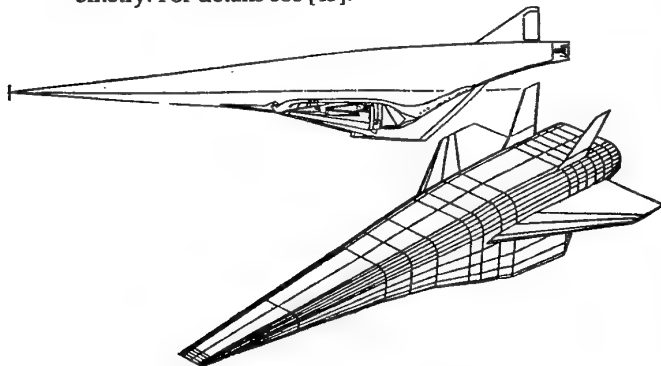
Fig. 27: Sketch of the generic SSTO vehicle under investigation [43]
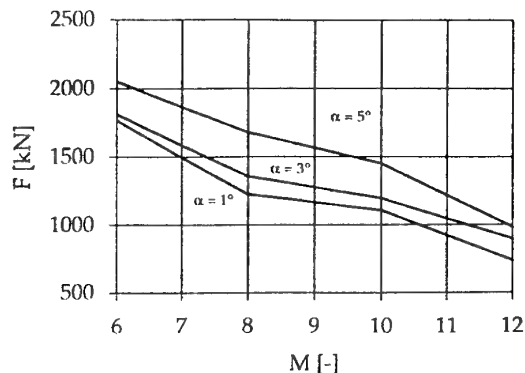
Fig. 28: Installed thrust of the vehicle according to figure 27 as a function of flight Mach number with incidence as parameter

5 CONCLUSION

Scramjet propulsion systems house most of the nonlinear high temperature effects to be encountered in fluid dynamics. While experimental investigations are limited to a narrow Mach number range computational simulations of the effects to be observed appear to exhibit unsatisfactory results as well in single phenomenon simulation as in whole combustion chamber flow. While some physical effects as nonequilibrium relaxation phenomena might have an important impact on the performance of the vehicle, but are as a consequence of hypersonic propulsion inevitable, other effects also resulting from the high speed are substantially more prohibiitve to proper scramjet operation. These effects are the strong viscous-shock wave interaction phenomena which have the capacity of being a show stopper to all scramjet activities.

As has been said in this - at best - short and incomplete survey, all these interactions work in the same direction, which means that on the one hand they decelerate the flow within the combustion chamber sensibly prolonging the residence time of the fluid and weaken the influence of nonequilibrium relaxation effects. On the other hand these interactions have the unpleasant quality of developing strong upstream influences which narrow the effective aerodynamic cross section through flow separation which might cause a complete collapse of the supersonic flow in the combustion chamber or the whole engine, respectively.

The understanding of these highly nonlinear phenomena is far from being complete since neither theoretical nor numerical nor experimental methods can supply us with satisfying explanations or sound data. While theoretical approaches and numerical simulations lack from a complete understanding of the phenomenon of turbulence or the behaviour of genuine nonlinear systems, the experimental facilities available up to now can deliver only data for minimized geometries or very short measure times referring to more or less generic problems and not to the interacting phenomena occurring in the scramjet engine.

Therefore, besides the basic research and investigation efforts, flight experiments with engine modules as big and complex as possible are mandatory to gain a deeper understanding of the phenomena taking place within a scramjet engine.

6 REFERENCES

[1] Hunt, J.L.: Hypersonic Airbreathing Vehicle Design (Focus on Aero-Space Plane). in: Bertin, J.J et al. (eds): Hypersonics, Volume I. Birkhäuser, Boston 1989

[2] Roudakov, A.: Some Problems in Scramjet Propulsion for Aerospace Planes. Part I - Scramjet: Aims and Features. AGARD-LS-194, paper 3

[3] Brun, R.: Non-Equilibrium Effects in High Speed Flows: Modelling and Experimentation. in: Bertin, J.J

et al. (eds): Hypersonics, Volume I. Birkhäuser, Boston 1989

[4] Clarke, J.F.: Physico-Chemical Gas Dynamics and its Relation to Hypersonic Flow. in: Bertin, J.J et al. (eds): Hypersonics, Volume I. Birkhäuser, Boston 1989

[5] Marsilio, R. and Pandolfi, M.: Nonequilibrium 3D Flow of Air through Inlets. AGARD-CP-510, paper 42

[6] Scott, C.D.: Effects on Thermochemistry, Nonequilibrium, and Surface Catalysis on the Design of Hypersonic Vehicles. in: Bertin, J.J et al. (eds): Hypersonics, Volume I. Birkhäuser, Boston 1989

[7] Tretyakov, P.K.: The Study of Supersonic Combustion for a Scramjet. in: Désidéri, J.A. et al. (eds): Experimentation, Modelling, and Computation in Flow, Turbulence, and Combustion. John Wiley and Sons, Chicester 1994.

[8] Délery, J.M.: Basic Experiments on High Mach Number Two-dimensional and Three-dimensional Separated Flows. in: Désidéri, J.A. et al. (eds): Experimentation, Modelling, and Computation in Flow, Turbulence, and Combustion. John Wiley and Sons, Chicester 1994.

[9] Herbert, T. and Esfahanian, V.: Stability of Hypersonic Flow over a Blunt Body. AGARD-CP-514, paper 28

[10] Galassi, L. and Scaggs, N.E.: Experimental and Computational Comparisons of Mach 6 High Reynolds Number Heat Transfer and Skin Friction. AGARD-CP-514, paper 21

[11] Dolling, D.S.: Problems in the Validation of CFD Codes through Comparison with Experiment. AGARD-CP-514, paper 19

[12] Dolling, D.S. and Narlo II, J.C.: Driving Mechanisms of Unsteady Separation Shock Motion in Hypersonic Interactive Flow. AGARD-CP-428, paper 7

[13] Simeonides, G. et al. Experimental, Analytical, and Computational Methods Applied to Hypersonic Compression Ramp Flows. AGARD-CP-514, paper 22

[14] Arnal, D.: Laminar-Turbulent Transition. in: Murthy, T.K.S. (ed.): Computational Methods in Hypersonic Aerodynamics. Kluwer Academic Publishers, Dordrecht 1991

[15] Potter, J.L. and Whitfield, J.D.: Effects of Slight Nose Bluntness and Roughness on Boundary Layer Transition in Supersonic Flows. Journal of Fluid Mechanics, Volume 12, Part 4 (1964)

[16] Stetson, K.F. et al.: Laminar Boundary Layer Stability Experiments on a Cone at Mach 8 - Part 2: Blunt Cone. AIAA-84-0006 (1984)

[17] Malik, M.R. et al.: Effect of Nose Bluntness on Boundary Layer Stability and Transition. AIAA-90-0112 (1990)

[18] Stetson, K.F. et al.: Laminar Boundary Layer Stability Experiments on a Cone at Mach 8 - Part 3: Sharp Cone at Angle of Attack. AIAA-85-0492 (1985)

[19] Balakumar, P. and Reed, H.L.: Three-dimensional Stability of Boundary Layers. Physics of Fluids A. Volume 3 (1991)

[20] Reed, H.L et al.: Stability of Hypersonic Boundary Layer Flows with Chemistry. AGARD-CP-514, paper 29

[21] Mallison, S. et al.: High-Enthalpy, Hypersonic Compression Corner Flow. AIAA-Journal, Volume 34, Number 6 (1996)

[22] Mallison, S. et al.: Upstream Influence and Peak Heating in Hypervelocity Shock Wave/Boundary-Layer Interaction. Journal of Propulsion and Power, Volume 12, Number 5 (1996)

[23] Zheltovodov, A.A.: Investigation of Supersonic Turbulent Separated Flows. in: Désidéri, J.A. et al. (eds): Experimentation, Modelling, and Computation in Flow, Turbulence, and Combustion. John Wiley and Sons, Chicester 1994.

[24] Roshko, A. and Thomke, G.: Supersonic Turbulent Boundary-Layer Interaction with a Compression Corner at Very High Reynolds Number. Proceedings of the Symposium on Viscous Interaction in Supersonic-Hypersonic Flow. University of Dayton Press, Dayton 1969.

[25] Settles, G.S. et al.: Incipient Separation of a Supersonic Turbulent Boundary-Layer at Moderate toHigh Reynolds Numbers. AIAA-75-0007 (1975)

[26] Settles, G.S. et al.: A Detailed Study of Attached and Separated Compression Corner Flow Fields in High Reynolds Number Supersonic Flow. AIAA-78-1167 (1978)

[27] Settles, G.S. et al.: Upstream Influence Scaling of 2d and 3d Shock/Turbulent Boundary Layer Interactions at Compression Corners. AIAA-81-0334 (1981)

[28] Waltrup, P.J.: The Dual Combustor Ramjet: A Versatile Propulsion System for Hypersonic Tactical Missile Applications. AGARD-CP-526, paper 7

[29] Waltrup, P. and Billig, F.: Prediction of Precombustion Wall Pressures in Scramjet Engines. AIAA-72-1181 (1972)

[30] Fomison, N.R. and Stollery, J.L.: The Effects of Sweep and Bluntness on an Glancing Shock Wave Turbulent Boundary Layer Interaction. AGARD-CP-428. paper 8

[31] Bogdonoff, S.M.: A Study of the Structure of Highly Swept Shock Wave Turbulent Boundary Layer Interactions. AGARD-CP-438, paper 21

[32] de Roquefort, T.A. and Daghsstani, K.: Experimental Study of Unsteadiness in Sharp Fin-Induced Turbulent Boundary Layer/Shock Wave Interaction. in: Désidéri, J.A. et al. (eds): Experimentation, Modelling, and Computation in Flow, Turbulence, and Combustion. John Wiley and Sons, Chicester 1994.

[33] Garg, S. and Settles, G.: Unsteady Pressure Loads Generated by Swept-Shock-Wave/Boundary-Layer Interaction. AIAA Journal, Vol. 34, No. 6 (1996)

[34] Hummel, D.: Experimental Investigations on Blunt Bodies and Corner Configurations in Hypersonic Flow. AGARD-CP-428, paper 6

[35] Gruber, M.R. et al.: Bock Shock/Jet Interaction in Compressible Transversi Injection Flow Fields. AIAA-Journal Volume 14, Number 10 (1996)

[36] Green, J.E.: Reflection of an Oblique Shock-Wave by a Turbulent Boundary Layer. Journal of Fluid Mechanics, Volume 40, Part I, (1970)

[37] Délery, J.M. and Marvin, J.G.: Shock Wave - Boundary Layer Interactions. AGARD-AG-280.

[38] Bray, K.N.C.: Atomic Recombination in a Hypersonic Wind-Tunnel Nozzle. Journal of Fluid Mechanics, Volume 6, Part 1 (1959)

[39] Waltrup, P.J. and Billig, F.: Prediction of Precombustion Wall Pressure Distributions in Scramjet Engines. AIAA-72-1181 (1972)

[40] Billig, F.: Shock Wave Shapes around Spherical- and Cylindical-Nosed Bodies. Journal of Spacecraft and Rockets, Volume 4, Number 6 (1967)

[41] Schetz, J.: Interaction Shock Shapes for Transverse Imjection in Supersonic Flows. Journal of Spacecraft, Volume 2, Number 2 (1970)

[42] Baranovslky, S. et al.: A Program of the Scramjet Design and Optimization. AIAA-91-5073 (1991)

[43] Berry, W. et al.: Studies on a Scramjet-propelled, Horizontal Launch and Landing, Single-Stage-to-Orbit Launcher. AIAA-93-5053 (1993)

Question 1: N. Malmuth

We strong agree about the need to study the effects of bluntness on transition in connection with scramjet inlet flows. We have been working on this problem for some time. Not only does it involve strong interaction but upstream interaction as well. This issue was also indicated by the previous speaker.

Author's reply:

Yes, I agree

EVALUATION OF AN EJECTOR RAMJET BASED PROPULSION SYSTEM FOR AIR-BREATHING HYPERSONIC FLIGHT

Scott R. Thomas, H. Douglas Perkins, and Charles J. Trefny
National Aeronautics and Space Administration
Lewis Research Center, M.S. 86-6
21000 Brookpark Road
Cleveland, Ohio 44135, USA

1. ABSTRACT

A Rocket Based Combined Cycle (RBCC) engine system is designed to combine the high thrust to weight ratio of a rocket along with the high specific impulse of a ramjet in a single, integrated propulsion system. This integrated, combined cycle propulsion system is designed to provide higher vehicle performance than that achievable with a separate rocket and ramjet. The RBCC engine system studied in the current program is the Aerojet strutjet engine concept, which is being developed jointly by a government-industry team as part of the Air Force HyTech program pre-PRDA activity. The strutjet is an ejector-ramjet engine in which small rocket chambers are embedded into the trailing edges of the inlet compression struts. The engine operates as an ejector-ramjet from take-off to slightly above Mach 3. Above Mach 3 the engine operates as a ramjet and transitions to a scramjet at high Mach numbers. For space launch applications the rockets would be re-ignited at a Mach number or altitude beyond which air-breathing propulsion alone becomes impractical. The focus of the present study is to develop and demonstrate a strutjet flowpath using hydrocarbon fuel at up to Mach 7 conditions.

Freejet tests of a candidate flowpath for this RBCC engine were conducted at the NASA Lewis Research Center's Hypersonic Tunnel Facility between July and September 1996. This paper describes the engine flowpath and installation, outlines the primary objectives of the program, and describes the overall results of this activity. Through this program 15 full duration tests, including 13 fueled tests were made. The first major achievement was the further demonstration of the HTF capability. The facility operated at conditions up to 1950 K and 7.34 MPa, simulating approximately Mach 6.6 flight. The initial tests were unfueled and focused on verifying both facility and engine starting. During these runs additional aerodynamic appliances were incorporated onto the facility diffuser to enhance starting. Both facility and engine starting were achieved. Further, the static pressure distributions compared well with the results previously obtained in a 40% subscale flowpath study conducted in the LeRC 1X1 supersonic wind tunnel (SWT), as well as the results of CFD analysis. Fueled performance results were obtained for the engine at both simulated Mach 6 (1670 K) and Mach 6.6 (1950 K) conditions. For all these tests the primary fuel was liquid JP-10 with gaseous silane (a mixture of 20% SiH_4 and 80% H_2 by volume) as an ignitor/pilot. These tests verified performance of this engine flowpath in a freejet mode. High combustor pressures were reached and significant changes in axial force were achieved due to combustion. Future test plans include redistributing the fuel to improve mixing, and consequently performance, at higher equivalence ratios.

2. INTRODUCTION

A Rocket Based Combined Cycle (RBCC) engine system is designed to combine the high thrust to weight ratio (T/W) of a rocket with the high specific impulse of a ramjet in a single, integrated propulsion system. This integrated, combined cycle propulsion system is designed to provide higher vehicle performance than that achievable with a separate rocket and ramjet. The potential performance advantages of RBCC engine systems for various applications such as space access or global transportation vehicles are outlined in Refs. 1 to 3. The potential benefit of air-breathing engine cycles over a rocket only system is shown in Fig. 1 (as presented in Ref. 1). Air-breathing engines, such as turbojet and ramjet engines, have much higher specific impulse. These systems add weight and system complexity, and it is necessary to incorporate a rocket system at high Mach numbers where air-breathing propulsion is no longer practical. As shown in Fig. 2, (presented in Ref. 2) combined cycle propulsion systems may require a significantly lower vehicle propellant mass fraction compared to an all rocket system. This will ultimately yield a much increased payload capacity for comparably sized vehicles.

The RBCC engine system studied in the current program incorporates the Aerojet strutjet engine concept, which is being developed jointly by a government-industry team. The features of the basic engine concept are presented in Refs. 1, 3, and 4, and shown in Fig. 3. The strutjet is an ejector-ramjet engine in which small rocket chambers are embedded into the trailing edges of the inlet compression struts. This engine is a compromise between the high Isp, low T/W all air-breathing options and the low Isp, high T/W of an all-rocket system. An advantage of the strut-ducted concept is that it transitions from an air augmented rocket to ramjet and finally to pure rocket with a minimum of variable geometry. The engine operates as an ejector-ramjet from take-off to slightly above Mach 3. Above Mach 3 the engine operates as a ramjet and transitions to a scramjet at high Mach numbers. For space launch applications the rockets would be re-ignited at a Mach number or altitude beyond which air-breathing propulsion alone becomes impractical. The focus of the present study is to develop and demonstrate a candidate strutjet flowpath. The primary application of consideration is a hydrocarbon fueled missile engine designed for up to Mach 8 cruise conditions. This report presents the freejet engine test results obtained at the HTF (Hypersonic Tunnel Facility) at Mach numbers up to 6.6. Details of this facility are

presented in Refs. 5 to 7. The HTF is a blowdown, nonvitiated, free-jet facility capable of testing large-scale propulsion systems at Mach numbers up to 7. Models typically up to 3 meters in length and 0.6 meters in diameter can be tested. Illustrations of the major HTF components are presented in Fig. 4. The energy source of the facility is the graphite core magnetic induction nitrogen heater which can supply nitrogen up to 59 kg/sec at conditions of 2800 K and 8.3 MPa. Ambient oxygen and nitrogen (if required) are mixed with this hot nitrogen downstream of the heater to produce a test flow with true temperature, composition, and altitude · simulation. The HTF facility is one of the few operational freejet hypersonic propulsion test facilities in the United States. The HTF facility is unique because it combines the capabilities of large scale (107 cm nozzle diameter) and up to Mach 7 enthalpy clean air.

Prior to the present program, two other test activities were completed to provide information to maximize the efficiency and minimize the risk of this HTF testing. The first study, presented in Ref. 8, was the testing of a 40% scale model of the inlet used in the current RBCC engine. This study was conducted to explore the operability and performance of this inlet with three different inlet compression strut geometries. This established that the best performance and operability was achieved with the untapered strut design which was subsequently used in the RBCC model for the present study. A CFD analysis, presented in Ref. 9, complemented the test results and provided more detailed information on the RBCC inlet flow. The second experimental study was a direct connect combustor test discussed in Refs. 1, 3, and 4. In this activity the combustor configuration used in the freejet model was demonstrated. This program established a fueling scheme for this geometry and operating conditions (Mach numbers and simulated altitudes) which resulted in both successful ignition and piloting as well as high combustion efficiency. These two studies verified adequate inlet and combustor performance at the component level. The goal of the present study, therefore, was to demonstrate that this engine design would operate effectively as an integrated propulsion system.

3. APPARATUS AND PROCEDURES

3.1 RBCC Engine Geometry
The engine model is a fixed geometry, heat sink design shown in Fig. 5. The leading edges of the inlet are water cooled; the remainder of the engine is uncooled and constructed largely from 5.1 cm thick OFE copper plates. The inlet incorporates two identical struts which segment the inlet into three channels. This engine is a modular design which may utilize more channels in some applications. The center passage represents a full channel. The sidewalls are flat representing symmetry planes and the two side passages are approximately half the width of the center channel. The struts reach a maximum thickness at the cowl lip (inlet entrance). The net internal geometric cross-sectional area is constant from the cowl lip station to the base of the struts but the cross sectional geometry varies. Convergence between the cowl and the top wall is compensated for by a reduction in strut thickness. Since there is no internal contraction downstream of the cowl

leading edge, the inlet is able to self start at Mach numbers below approximately 4 (approaching the inlet). The last 27.3 cm of the struts are constant height and width such that the cross sections of all channels are rectangular and constant geometry.

The struts are assembled in sections and include the inlet compression and two fuel injection stations. The first section is entirely for the inlet compression process. The next two sections make up a constant geometry area of the model and incorporate fueling stations as shown in Fig. 6. The forward station includes normal fuel injection from both sides of each strut approximately 25 cm upstream of the base. The forward fueling scheme was normal injection of silane (a mixture of 20% SiH_4 and 80% H_2 by volume) coupled with normal injection of ambient liquid JP-10 1 cm downstream (and in line with) the silane injectors. The aft strut section is the region where the strut rockets are incorporated. In the present study the rockets were not used, therefore, a set of "dummy blocks" with the same dimensions were used which included the same fueling scheme as the rockets. Liquid JP-10 is injected into the base of the struts through trapezoidal shaped "shower heads" as shown.

Downstream of the base of the struts is the continuation of the combustor and the nozzle. The bottom plate (cowl) and side wall surfaces remain flat throughout the engine. In this combustor/nozzle region the top wall is made up of manually adjustable sections; including two 30.5 cm long sections and one 49.9 cm long section. These are adjustable using a set of jack screws located above the model. Throughout this test program the engine configuration remained constant and these three top wall sections were positioned with the geometry shown in Fig. 5.

3.2 Installation of Engine into HTF
The engine was installed into the Hypersonic Tunnel Facility as shown in the isometric drawing of Fig. 7(a) and the photograph of Fig. 7(b). The engine assembly was suspended from the overhead thrust stand using two I-beams. To protect the instrumentation and equipment immediately above the engine from the test flow this region is protected by shrouding with copper plate. A flat plate designed to simulate a representative vehicle forebody was mounted upstream of the inlet as shown; it is 71 cm long, 63 cm wide at the leading edge and tapers back to the engine inlet width of 23 cm. The plate is mounted at an 8° angle relative to the facility test flow direction, which matches the top wall angle of the inlet. During the present study the plate was positioned such that the bottom surface of this plate is flush with the top wall surface of the engine such that the engine ingests the boundary layer. It can also be mounted offset (2.5 cm) to the inlet top wall to divert the boundary layer although this was not done during the test program.

The HTF has three existing axisymmetric contoured nozzles with nominal exit Mach numbers of 5, 6, and 7, each with a 107 cm exit diameter. During the current study the Mach 5 nozzle was used for a few tests and the Mach 6 nozzle was used for the majority of the tests. Based on the nozzle calibrations as reported in Ref. 7, both of these facility nozzles have exit flow distributions with uniform

cores of approximately 76 cm diameter. In this installation, the leading edge of the cowl is 15.7 cm below the nozzle centerline, and the leading edge of the precompression plate is 15 cm above the nozzle centerline. The capture area of the plate and the engine inlet fit within this region of uniform flow. The precompression plate is mounted to a support structure which is not part of the thrust measurement system (non-metric), therefore, the loads measured by the thrust stand include only those of the engine. There is a gap of approximately 0.6 cm between the trailing edge of the precompression plate and the engine inlet top wall leading edge. This gap is sufficient to prevent interaction between these surfaces due to thermal growth or deflection of the thrust stand mounts; an interlocking, noncontacting seal was installed across this gap to prevent excessive flow spillage.

The engine instrumentation consists primarily of 82 static pressure taps located along the top and side walls of the engine and along the top surface of the precompression plate. Additional static pressure taps were included in the engine shrouding to determine approximate thrust loads for those surfaces. Other measurements included the engine thrust and 5 combustor wall temperatures. The HTF is equipped with 3 data systems serving 3 different applications. Overall facility data recording and display is accomplished using an ESCORT D system which scans a maximum of 527 channels at a rate of 1 Hz on all channels. A 64 channel high speed MassComp system was set up to sample the following research data at a rate of 20 times/sec: engine thrust, model wall temperatures, fuel system properties and flow rates, and facility stagnation conditions. There is also a 192 channel Electrically Scanned Pressure (ESP) unit which was used to sample engine static pressures at a rate of approximately 17 samples/sec.

3.3 Test Objectives and Sequence

The first test objective was to further demonstrate reliable operation of the HTF at conditions up to simulation of Mach 7 flight. These initial tests were unfueled and focused on verifying that both the facility and engine flow path started at all conditions. The unfueled data was also compared to the results of the 40% subscale flowpath study. Fueled engine performance tests were then conducted to demonstrate the free-jet performance of this engine flowpath in a ramjet/scramjet mode at both simulated Mach 6 and Mach 6.6 conditions. For all these tests the primary fuel was ambient temperature liquid JP-10 with gaseous silane as an ignitor. Although this engine flow path is designed to incorporate the strutjet system and operate as a Rocket Based Combined Cycle (RBCC) engine, the rocket system was not demonstrated in the current program. The fueled engine tests were, in part, an extension of the direct-connect combustor test activity discussed in Refs. 1, 3, and 4. This data base would, therefore, provide a comparison between the resultant performance and operability of the freejet engine relative to the direct-connect experiment. Achieving equivalent performance in the freejet configuration requires effectively managing the inlet flow, which is inherently less stable and has significant flow distortion at the exit (entering the combustor). It is also essential to establish

the proper fuel distribution in order to achieve ignition and flameholding, as well as efficient fuel/air mixing.

The HTF operation requires that the graphite heater be brought up to the required operating temperature and the supporting systems be energized prior to facility operation. The test total temperature is limited by the maximum temperatures to which the graphite blocks can be heated without exceeding any temperature limits within the heater. During the present study a facility total temperature of 1950 K was reached; this was limited by some high temperature readings observed in the heater insulation and support pedestal (not limitations in the blocks). Reaching full Mach 7 enthalpy (approximately 2200 K) with the HTF will require some facility modifications. During the operating sequence, the facility is ramped up to the required test condition, then a dwell time of approximately 3 sec is allowed for the pressure and temperature to settle before the engine operation is initiated. At that point a specified schedule of silane and liquid JP-10 fuel are injected into the model; the total fuel on run time for the engine was typically 15 to 20 sec. These total run times were limited by thermal constraints of the model and facility. In general, the silane/H_2 mixture was introduced about 1 sec prior to the JP-10 fuel to establish a pilot flame. Tests were conducted to establish the maximum forward station fuel flow. Subsequent tests were conducted where the forward fuel flows were set at near (75 to 80%) maximum to generate the greatest possible pilot flame. Fuel was then increased in 2.5 to 5 sec increments (based on test objectives) through the aft fuel station. The primary goal in these tests was to achieve maximum performance at both the Mach 6 and Mach 6.6 conditions by optimization of the fuel schedule.

4. RESULTS AND DISCUSSION

Through this activity 15 full duration tests were made; 10 were at Mach 6 conditions and 5 were at Mach 6.6 conditions; 13 of the runs were fueled. The facility conditions and test configuration for this test series is outlined in Table I. Fueled performance results were obtained at both simulated Mach 6 (1670 K) and Mach 6.6 (1950 K).

4.1 Inlet Operability and Performance

The initial tests were unfueled and focused on verifying that both the facility and engine flow path started at all conditions. An unfueled test was conducted for each Mach number and unfueled static pressure profiles were obtained at the first increment of each test prior to fuel incrementing. The subscale inlet flowpath study of Ref. 8 was conducted prior to the HTF test program. In this experiment the model shown in Fig. 8, which is a 40% scale of the inlet used in the current RBCC engine, was tested at the correct Mach numbers and Reynolds numbers to validate inlet operability and performance. The CFD analysis of Ref. 9 also complemented this study. Figures 9 and 10 compare the unfueled static pressure distributions achieved within the HTF RBCC flow path using both the Mach 5 and the Mach 6 facility nozzles with the equivalent results from the 40% scale 1X1 SWT tests. Corrected for scale, these profiles show that for facility exit Mach numbers of both 5 and 6 the subscale test results provided an accurate assessment of the full scale inlet performance. These

earlier studies along with supporting CFD analysis provided detailed information regarding inlet air mass capture and flow distortion.

4.2 Fueled Engine Performance

As previously described, the engine has three fueling stations and the focus of these engine tests was to achieve and quantify performance with different fuel schedules. The combustor configuration used in this study was previously demonstrated in the direct-connect experiment of Refs. 3 and 4. This established a fueling scheme for this geometry and operating conditions which resulted in both successful ignition and piloting as well as high combustion efficiency. The behavior of the inlet with backpressure in the combustor area was also characterized during the subscale 1X1 SWT flow path study. The results for this subscale study at Mach 6 are presented in Fig. 11; backpressure was achieved using the mechanical mass flow plug at the exit (Fig. 8(a)). These results indicate that significant combustor backpressure and, therefore, high engine performance is possible without inlet unstart.

A total of 13 fueled engine tests were conducted during the present program. The fueled engine test results are presented in Ref. 10. Figure 12 shows a representative pressure distribution along the length of the engine for a fueled case overlaid with a plot of a subscale inlet result. As shown, the subscale testing accurately modeled the pressure profile in the inlet/isolator region. Generally, at higher simulated Mach number, decreased combustor/inlet interaction and lower pressure ratio were observed, and higher forward fuel equivalence ratio was achieved without engine unstart. Future test plans with this engine include enhancing engine performance through the optimization of fuel distribution.

5. SUMMARY

This test program served to demonstrate the freejet ramjet operability and performance of a candidate engine flowpath for application as a Rocket Based Combined Cycle (RBCC) propulsion system at simulated Mach 6 and Mach 6.6 conditions. This engine is the strutjet concept which is designed to operate as an ejector-ramjet engine in which small rocket chambers are embedded into the struts. This activity was accomplished between July and September 1996, and 15 full duration tests were conducted. Ignition and piloting of the liquid hydrocarbon (JP-10) fuel was achieved using a gaseous pyrophoric mixture (20% SiH_4 and 80% H_2) as an ignitor. The results of this study also compared well with the results of previous studies including a 40% subscale (aerodynamic) flowpath test conducted in the LeRC 1X1 SWT, CFD analysis, and direct-connect tests of this combustor geometry.

6. CONCLUSIONS AND RECOMMENDATIONS

This test program provided a strong technical foundation by successfully demonstrating freejet performance of the engine flowpath studied. This engine system is a first generation design and several improvements could significantly enhance the performance. Optimization of the inlet is possible in order to improve the stability and reduce the distortion of the flow entering the combustor. Since subscale inlet test results were shown to accurately characterize the full scale inlet behavior, a parametric

inlet development program, including subscale testing and CFD analysis, would provide an improved inlet configuration. Optimization of the fuel distribution including both the axial stations (i.e. scheduling) and the vertical distribution of this fuel to match the air flow distribution would enhance performance. The RBCC model is relatively parametric and can be easily modified to change the inlet, struts, or combustor geometry. Additional fuel stations (manifolds) could be added within the struts or on the model side walls. Achieving good performance using liquid hydrocarbon fuels was a challenging technical objective. Obtaining comparative results with other fuels (for example, gaseous hydrocarbon or hydrogen) and/or other ignitor and piloting techniques would also be a valuable objective. The focus of these tests could be directly relevant to the current application (Mach 4 to 8 hydrocarbon fueled air-breathing missile) or could be more generic in nature providing data relative to the performance potential of candidate RBCC systems for broader applications such as space access or global transportation vehicles.

7. REFERENCES

1. Bulman, M., and Siebenhaar, A., "The Strutjet Engine: Exploding the Myths Surrounding High Speed Airbreathing Propulsion," AIAA-95-2475, July 1995.
2. Escher, W.J.D., Hyde, E.H., and Anderson, D.M., "A User's Primer for Comparative Assessments of All-Rocket and Rocket-Based Combined-Cycle Propulsion Systems for Advanced Earth-to-Orbit Space Transport Applications," AIAA-95-2474, July 1995.
3. Siebenhaar, A., and Bulman, M., "The Strutjet Engine—The Overlooked Option for Space Launch," AIAA-95-3124, July 1995.
4. Engers, R., Cresci, D., and Simonsen, R., "Test Facility Requirements for Combined Cycle Engines at Supersonic Flight Conditions," AIAA-94-2486, June 1994.
5. Thomas, S.R., Woike, M.R., and Pack, W.D., "Mach 6 Integrated Systems Tests of the NASA Lewis Research Center Hypersonic Tunnel Facility," NASA TM-107083, December 1995.
6. Thomas, S.R., Trefny, C.J., and Pack, W.D., "Operating Capability and Current Status of the Reactivated NASA Lewis Research Center Hypersonic Tunnel Facility," AIAA-95-6146, NASA TM-106808, April 1995.
7. Cullom, R.R., and Lezberg, E.A., "Calibration of Lewis Hypersonic Tunnel Facility at Mach 5, 6, and 7," NASA TN D-7100, 1972.
8. Fernandez, R., Trefny, C.J., Thomas, S.R., and Bulman, M., "Parametric Data from a Wind Tunnel Test on a Rocket Based Combined Cycle Engine Inlet," NASA TM-107181, July 1996.
9. DeBonis, J.R., and Yungster, S., "Rocket Based Combined Cycle Engine Technology Development Inlet CFD Validation and Application," AIAA-96-3145, NASA TM-107274, July 1996.
10. Thomas, S.R., Perkins, H.D., Trefny, C.J., and Bulman, M. "Mach 5 to 7 Performance Evaluation of a Rocket Based Combined Cycle Propulsion System at NASA LeRC HTF," NASA TM-107376, December 1996.

TABLE I.—FACILITY CONDITIONS SUMMARY

Run number	Data number	SiH$_4$/H$_2$ flow, Y/N	FOR. JP-10 flow, Y/N	AFT JP-10 flow, Y/N	Facility nozzle, Mach number	Average heater temperature, K	Nozzle mass flow, kg/s	Nozzle inlet total temperature, K	Nozzle inlet total pressure, MPa	Steady state test time, sec	Facility nozzle exit static pressure, MPa
1	8	N	N	N	5	2060	73	1360	2.52	9	0.0050
2	10	Y	Y	N	5	2250	86	1540	3.55	16	0.0049
3	14	Y	Y	N	6	2300	84	1640	7.34	20	0.0044
4	15	Y	Y	N	6	2270	84	1645	7.34	20	0.0044
5	17	Y	Y	Y	6	2270	86	1595	7.34	15	0.0043
6	18	Y	Y	Y	6	2290	84	1645	7.34	20	0.0044
7	25	Y	Y	N	6	2290	84	1645	7.34	17	0.0040
8	32	Y	Y	Y	6	2370	84	1680	7.34	18	0.0041
9	33	Y	Y	Y	6	2380	86	1585	7.34	18	0.0043
10	34	Y	Y	Y	6	2400	86	1615	7.34	23	0.0039
11	36	N	N	N	6	2610	75	1925	7.41	3	0.0038
12	38	Y	Y	N	6	2610	77	1945	7.34	15	0.0039
13	39	Y	Y	Y	6	2590	77	1915	7.34	15	0.0039
14	40	Y	Y	Y	6	2570	77	1930	7.34	17	0.0040
15	41	Y	Y	Y	6	2610	77	1945	7.34	15	0.0040
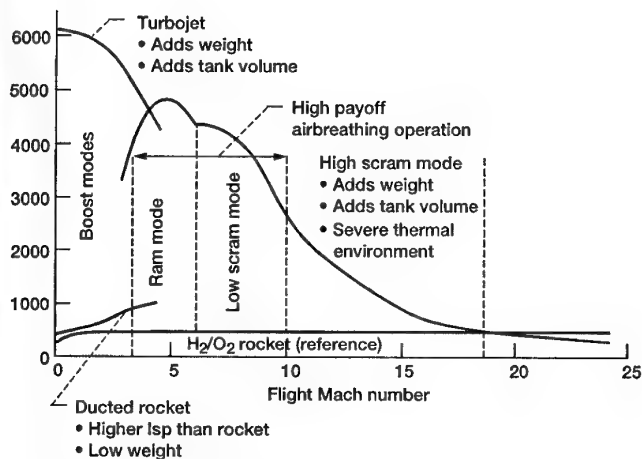
Figure 1.—Performance benefit of air-breathing engine cycles.
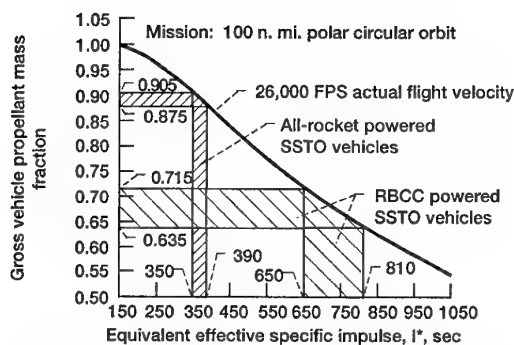
Figure 2.—Comparison of required propellant mass fraction between all-rocket and RBCC powered SSTO vehicles. (LH$_2$, LO$_2$ rocket propellants)
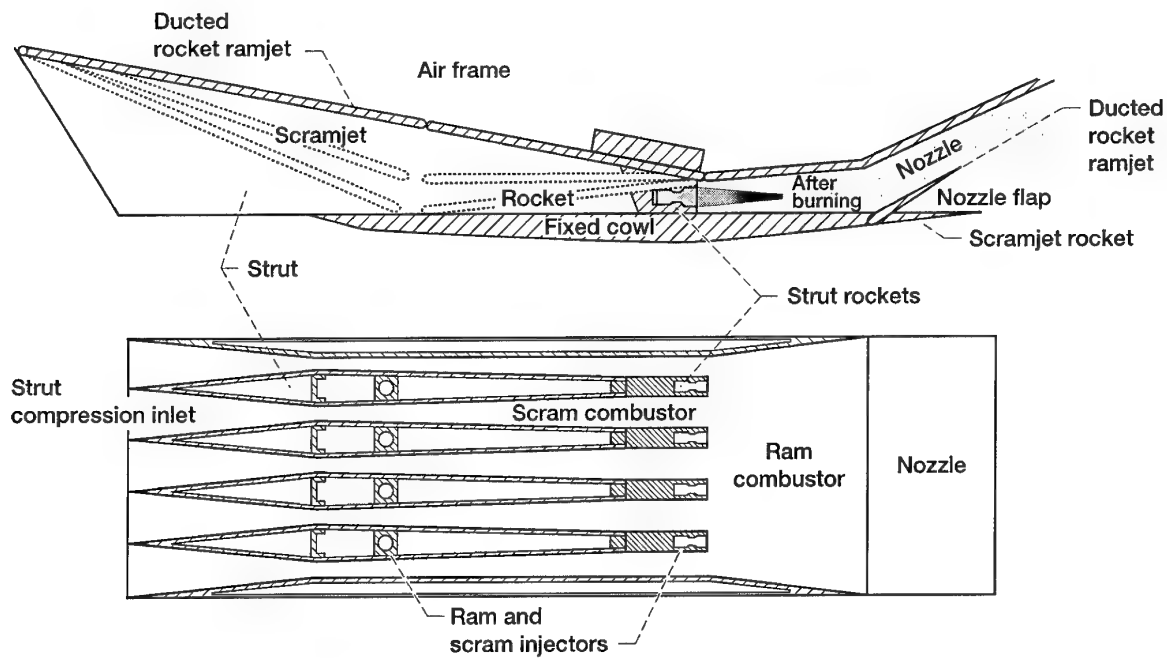
Figure 3.—Features of the strutjet engine which integrates a rocket into a ramjet propulsion system.
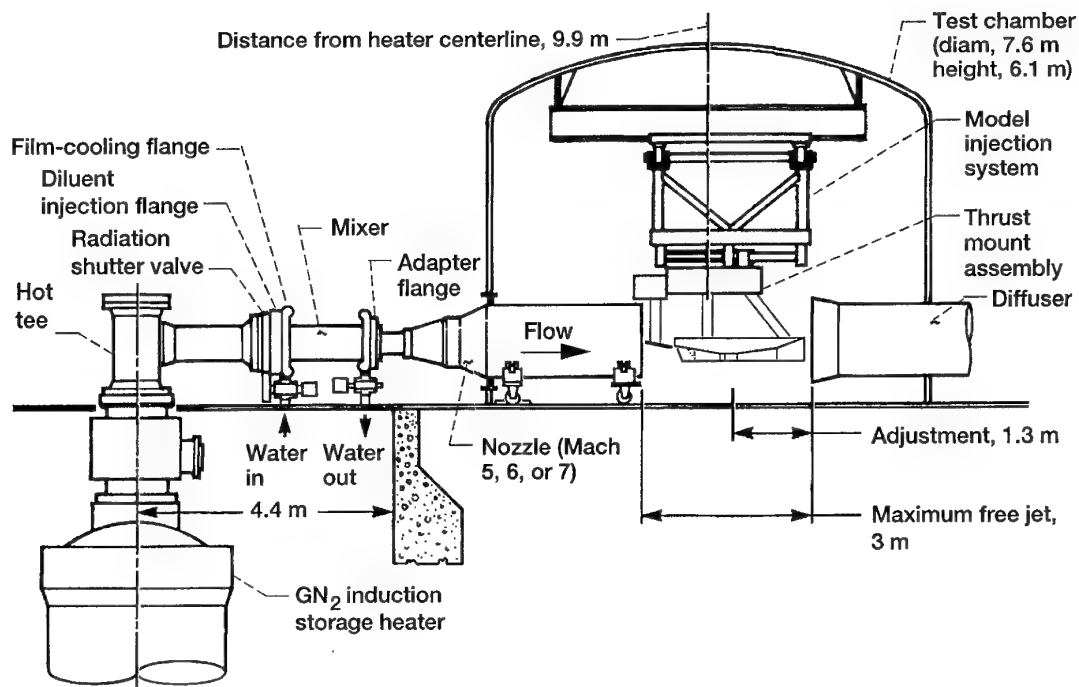
Figure 4.—Hypersonic tunnel facility (HTF) hot train and test chamber.
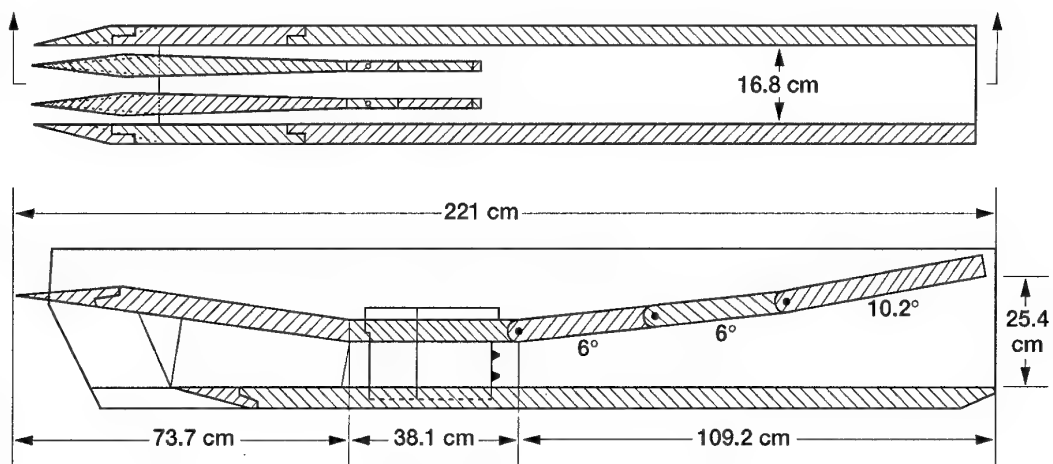
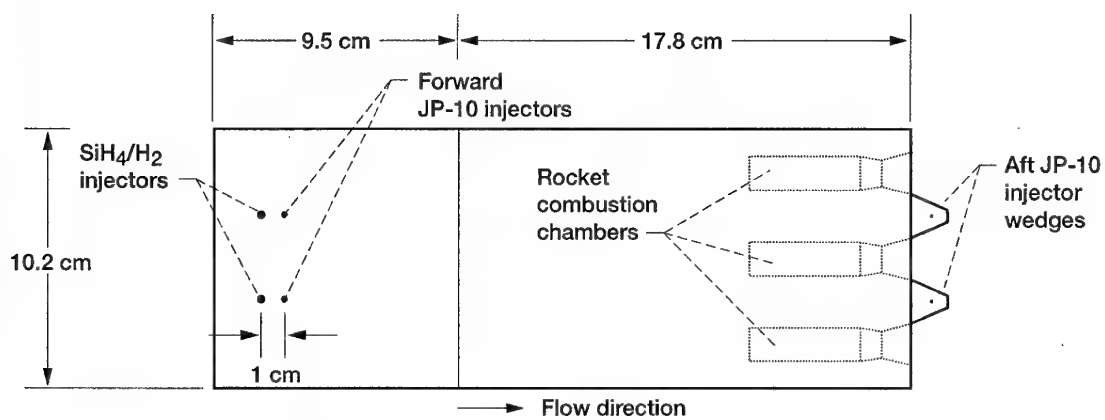Figure 5.—RBCC engine geometry.

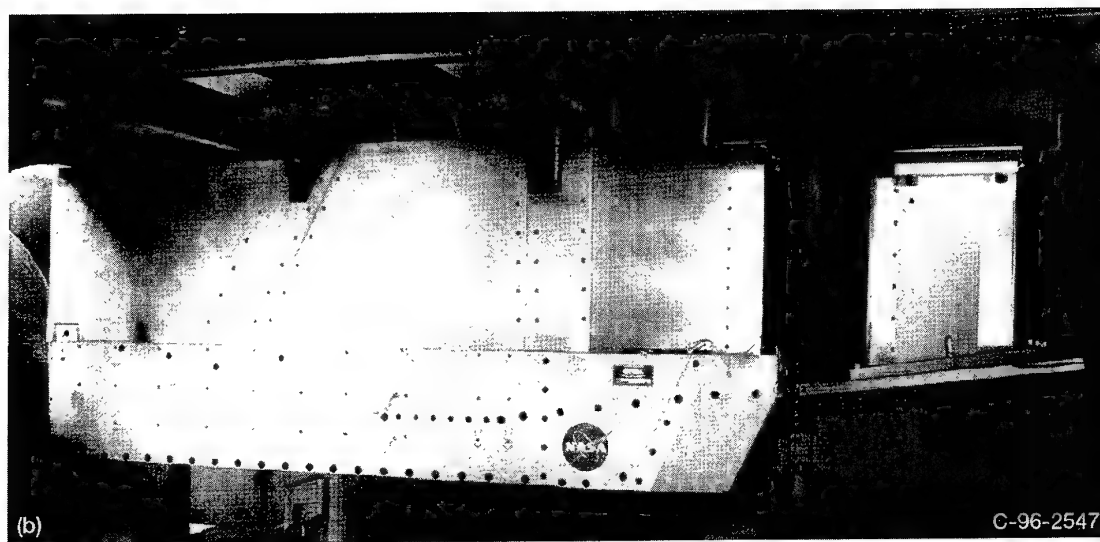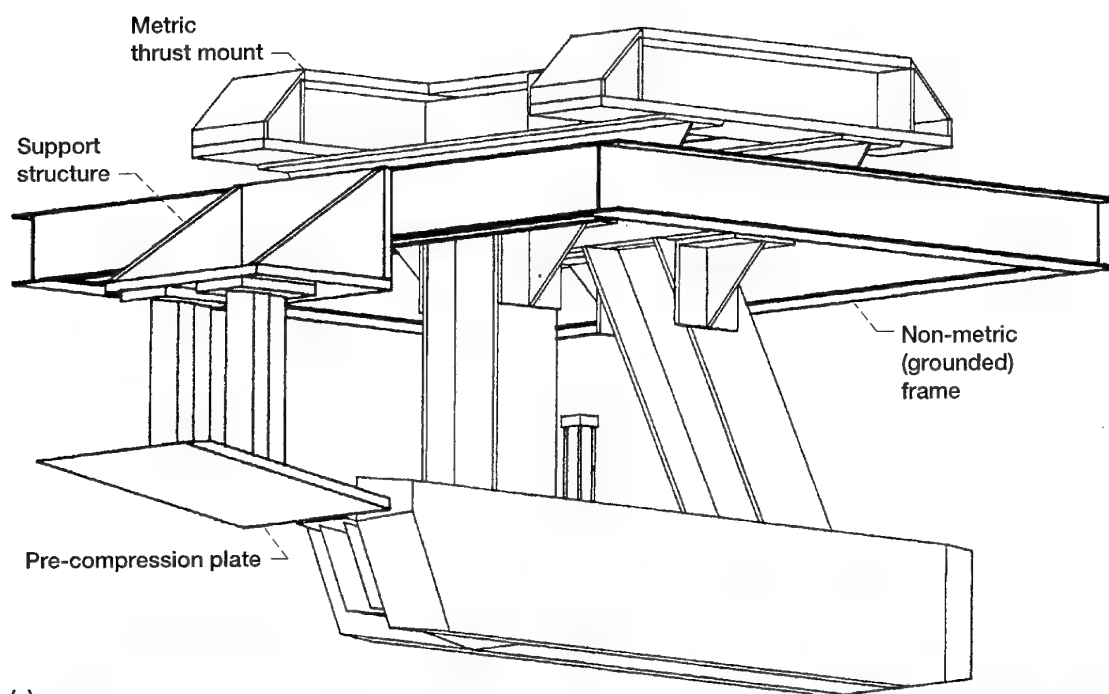Figure 6.—Side view of forward and aft fuel injection blocks with rockets.

Figure 7.—Installation of RBCC engine and pre-compression plate into HTF. (a) Isometric view of model mounting. (b) Photograph of model.
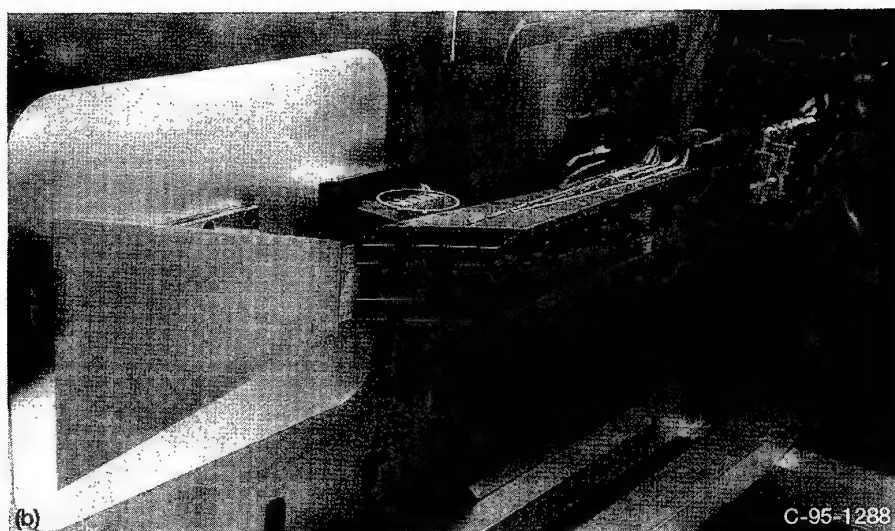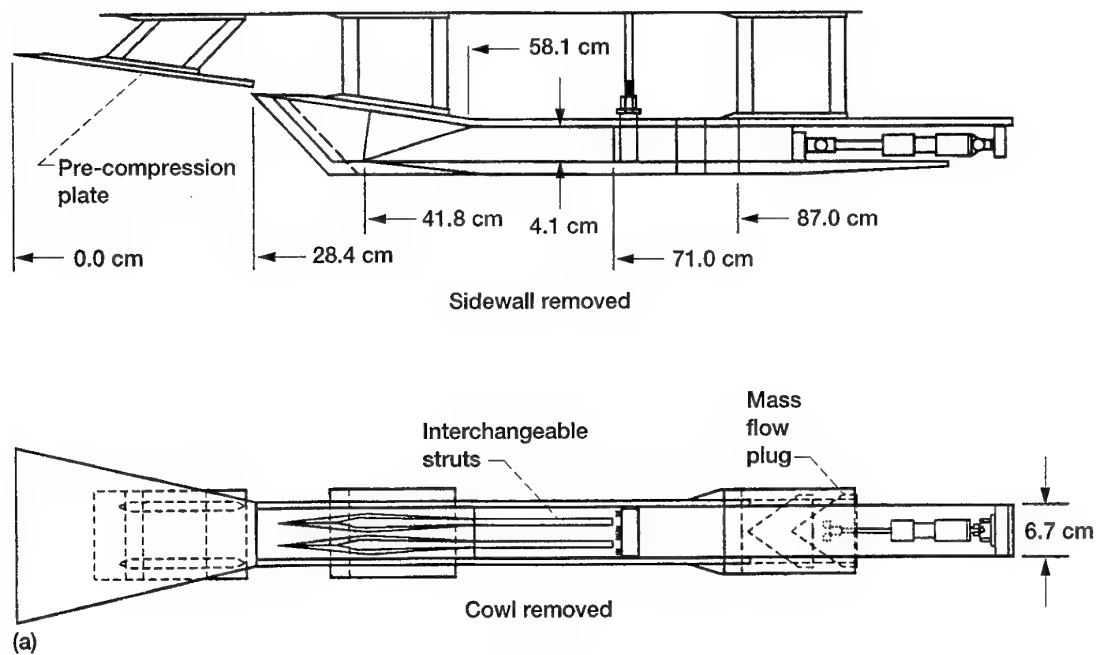
Figure 8.—Sub-scale RBCC inlet model. (a) Schematic of model flow path. (b) Photograph of model mounted on tunnel sidewall in 1x1 SWT.
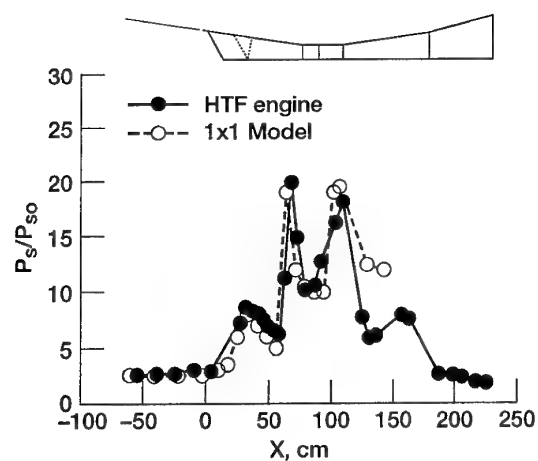
Figure 9.—Unfueled pressure distributions of HTF full scale engine and 1x1 sub-scale inlet model at Mach 5.
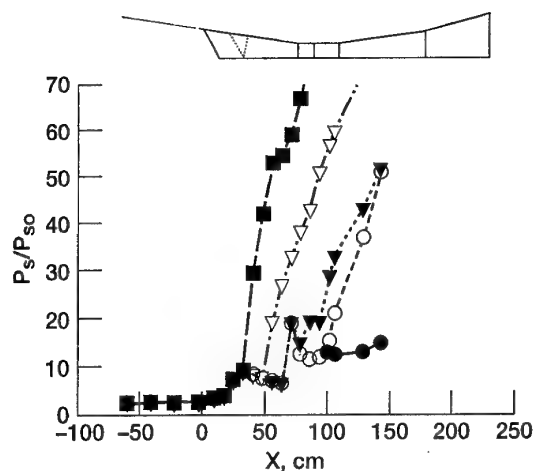
Figure 11.—Static pressure distributions for the sub-scale inlet model with increasing back-pressure at Mach 6.
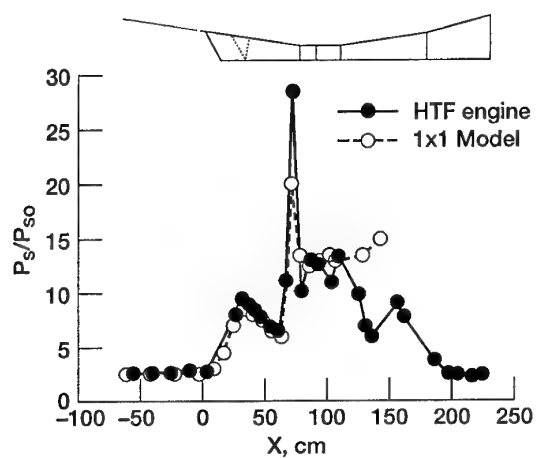
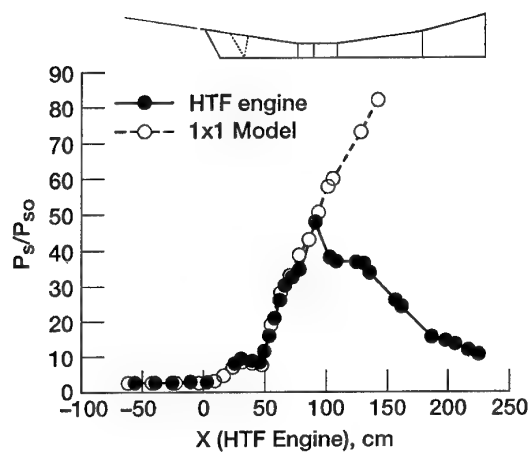Figure 10.—Unfueled pressure distributions of HTF full scale engine and 1x1 sub-scale inlet model at Mach 6.

Figure 12.—Pressure distribution of fueled HTF full scale engine and mechanically backpressured 1x1 sub-scale inlet model.

Question 1)

1. Reference No. of the paper: C-6

2. Discussor's Name: Robert H. Korkegi

3. Authors name: Scott R. Thomas

Question: In response to shock wave turbulent boundary layer interaction, the glancing shock causes much earlier separation than the two dimensional case. That is to say in an inlet, the shocks generated by compression surfaces cause much earlier separation on the side walls than on the compression surface and, therefore, offset the flow in a combustion chamber. This effect is exacerbated as Mach number increases.

Author response: This question was really more of a statement made to point out a behavior observed with high Mach number inlets. The discussor wanted to know if we had considered the behavior of glancing shocks in the interpretation of the engine test results. We have established the inlet performance both analytically and experimentally through the research activities described and referenced in the paper. These studies served to characterize the inlet with various degrees of back pressure and provided a detailed understanding of the overall inlet performance, including the resulting shock systems through the inlet.

Question 2)

1. Reference No. of the paper: C-6

2. Discussor's Name: Dr. David Van Wie

3. Author's name: Scott R. Thomas

Question: In the preliminary tests conducted thus far, has the engine produced thrust?

Author response: I cannot discuss the specifics of the thrust data in this forum since this information is restricted; but the answer is no and we did not expect to produce a positive net thrust during the ramjet testing of this engine. The reason for this is that the freejet test configuration is not aerodynamically streamlined like an engine installed onto a vehicle. In a freejet test the engine is mounted onto a strut and hangs out in the flow stream, compared to an installed engine which is integral with undersurface of the vehicle. This strut as well as all the tubing that is connected to the model (used for cooling supply or fuel supply, pressure/temperature measurements) must be heavily shrouded for thermal protection and results in a high zero fuel drag. The change in thrust (i.e. the reduction in drag) between the fuel on and fuel off was the thrust measurement used in the evaluation of engine performance.

Conception de la chambre de combustion
et des systèmes d'injection

D. Scherrer (ONERA), M. Bouchez (AEROSPATIALE)
B.P. 72, 92322 Châtillon Cedex, France

Résumé: La conception de la chambre de combustion et du système d'injection d'un statoréacteur hypersonique sont présentés au travers de trois aspects:

- conception d'une chambre de combustion de stato mixte alimentée à l'hydrogène et analyse de ses modes de fonctionnement entre Mach 5 et 7,5
- concepts de mâts d'injection pour un superstatoréacteur alimenté à l'hydrogène
- problèmes spécifiques posés par l'utilisation d'hydrocarbures stockables

INTRODUCTION

Le superstatoréacteur ou statoréacteur à combustion supersonique est le seul moteur aérobie apte à assurer la propulsion des véhicules hypersoniques au-delà de Mach 7 environ. Les difficultés associées à la conception d'une chambre de superstatoréacteur et de son système d'injection sont bien connues et sont liées principalement à l'optimisation du mélange et à la minimisation des pertes de pression d'arrêt. Dans le cadre du programme PREPHA, les activités liées à ces aspects ont conduit à l'expérimentation à Mach 6 dans les installations de l'AEROSPATIALE au Subdray d'un superstatoréacteur de grandes dimensions [1, 2].

Pour la plupart des applications, ces difficultés sont accrues par le fait qu'il y a intérêt à utiliser le statoréacteur le plus tôt possible en combustion subsonique (on parle alors de stato mixte): pendant ce mode de fonctionnement, les problèmes sont plutôt liés à la stabilisation de la flamme et à la prévention du désamorçage et les contraintes de conception qui en résultent sont difficilement compatibles avec l'optimisation du mode superstatoréacteur. Ces aspects, qui concernent surtout la géométrie du foyer, sont abordés dans la première partie de ce papier.

La deuxième partie est consacrée plus spécifiquement aux aspects liés à l'injection d'hydrogène dans une chambre de superstatoréacteur. Un travail important a été réalisé dans le cadre du programme français PREPHA, tant pour ce qui concerne la conception de mâts d'injection que pour l'étude des phénomènes de mélange et de combustion de jets élémentaires.

La troisième partie est consacrée à une analyse des difficultés spécifiques liées à l'utilisation d'hydrocarbures (kérosène, combustible endothermique,...) dans un statoréacteur mixte. Indispensables pour les applications militaires pour des raisons opérationnelles, les hydrocarbures ont un intérêt potentiel pour les lanceurs à bas Mach de par leur densité beaucoup plus élevée que celle de l'hydrogène.

CONCEPTION D'UNE CHAMBRE DE STATO MIXTE

On présente dans cette partie une étude préliminaire d'influence des principaux paramètres de dimensionnement sur le mode de fonctionnement et les performances d'un statoréacteur mixte entre Mach 5 et 7,5 . Cette étude, basée sur des calculs tridimensionnels, est relative à une chambre expérimentale de petites dimensions (100X100 mm^2), munie d'un mât d'injection disposé verticalement dans le plan de symétrie de la veine. Cette chambre a pour vocation l'étude et la caractérisation des régimes de combustion dans un statoréacteur mixte. Elle doit faire prochainement l'objet d'essais dans les installations de l'ONERA à Palaiseau entre Mach 4 et 7,5.

La chambre, schématisée sur la figure 1, comprend une case à injection de section constante suivie d'un foyer à double divergence. Le mât, représenté sur la figure 2, prévoit deux niveaux d'injection, aux parois (jets à 45°) et au culot du mât. Un isolateur, constitué de quatre tronçons identiques, peut être implanté en partie ou en totalité en amont de la case à injection. Un générateur d'hétérogénéité, constitué d'une cale en forme d'accent circonflexe peut être placé sur la paroi inférieure en entrée de l'isolateur.

Après une rapide description du code de calcul utilisé pour cette étude, on présente plus particulièrement les aspects suivants:

- analyse des régimes de combustion à Mach 7,5 , 6 et 5
- influence de la divergence du foyer sur le régime de combustion supersonique à Mach 6
- effet d'un générateur d'hétérogénéité (cas Mach 6)

Conditions générales des calculs

Code de calcul

Les calculs ont été effectués avec le code MSD, développé à l'ONERA [3]. Ce code résout les équations de Navier-Stokes pour un fluide compressible multi-espèces réactif. La version utilisée dispose en particulier de la fonctionnalité multidomaine adaptatif qui permet d'ajouter ou retirer des domaines en cours de calcul lors d'une reprise.

Le modèle de combustion utilisé est le modèle purement cinétique de Rogers&Chinitz à deux équations [4]. Ce modèle fait l'hypothèse que le mélange turbulent à l'échelle de la maille est beaucoup plus rapide que la chimie. Dans ce cas la combustion est localement contrôlée seulement par la cinétique chimique, représentée ici par un schéma global à deux réactions réversibles :

$$H_2 + O_2 \longleftrightarrow 2 \, OH$$
$$2 \, OH + H_2 \longleftrightarrow 2 \, H_2O$$
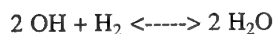
Le modèle de turbulence est le modèle k-l, sans effets de compressibilité.

Conditions d'alimentation

Les calculs ont été effectués pour les conditions simulant Mach 5 , 6 et 7,5 .

Un profil de couche limite est imposé en entrée de l'isolateur pour toutes les variables afin de se rapprocher des conditions expérimentales (les valeurs indiquées dans le tableau correspondent à l'écoulement sain). L'épaisseur de couche limite δ est de 14 mm pour les conditions Mach 5 et 6, et 28 mm pour les conditions Mach 7,5.

Les conditions de calcul relatives à l'alimentation en air et hydrogène sont rassemblées dans le tableau ci-dessous. Cinq grandeurs aérodynamiques sont imposées: la pression d'arrêt P_i, la température d'arrêt T_i, le nombre de Mach, l'échelle de turbulence l et le taux de turbulence τ. La composition de l'air est exprimée en fractions massiques Y.

	Mach 5	Mach 6	Mach 7,5
Air			
M	2,5	3	4
P_i (bar)	12	27	32
T_i (K)	1250	1650	2400
k	1%	1%	1%
l (mm)	1	1	1
δ (mm)	14	14	28
Y_{N2}	0,640	0,589	0,524
Y_{O2}	0,250	0,251	0,261
Y_{H2O}	0,110	0,160	0,215
H₂			
M	2,5	2,5	2,5
T_i (K)	280	280	280
ϕ	1	1	1
	0,80	1	
	0,60		

Maillage

Du fait de l'existence d'un plan de symétrie, seule la moitié de la chambre est maillée et calculée.

Pour les calculs sans générateur d'hétérogénéité, le maillage est composé de deux domaines se raccordant exactement. Le premier domaine s'étend de la sortie de la tuyère d'alimentation au plan de culot du mât: il comprend l'isolateur et la case d'injection du mât. Le second domaine décrit le foyer et s'étend du plan du culot à la sortie du foyer. Le maillage comprend dans ce cas 186992 mailles au total.

La prise en compte du générateur d'hétérogénéité conduit à insérer un domaine supplémentaire pour décrire le premier tronçon de l'isolateur muni de cet élément. Le maillage initial de l'isolateur est dans le même temps concentré sur les trois derniers tronçons et raccordé exactement au domaine supplémentaire, ce qui autorise une description satisfaisante de la réflexion des ondes de choc et de détente dans l'isolateur.

Analyse des régimes de combustion à Mach 7,5 , 6 et 5

On présente dans ce paragraphe une description et une analyse des régimes de combustion obtenus sans générateur d'hétérogénéité pour des conditions simulant Mach 7,5 , 6 et 5. Pour les conditions Mach 6 et 5, la répartition du débit injecté est de 20% aux parois du mât et 80% au culot; pour les conditions Mach 7,5 , elle est respectivement de 40 et 60%.

Conditions Mach 6

Pour les conditions Mach 6 richesse 1, on obtient un régime de combustion supersonique en moyenne dans tout le foyer, sans remontées de décollements dans l'isolateur.

La figure 3 présente les champs de température statique et d'espèces H_2O, H_2 et OH dans un plan horizontal d'injection pariétale. On remarque que l'allumage des jets pariétaux n'est pas instantané: il intervient peu avant le culot. L'écoulement est très stratifié, ce qui est la caractéristique des écoulements à haute vitesse. Cependant, les vues en perspective de la température (figure 4) montrent que le mélange est relativement bon dans la direction verticale. C'est dans la direction horizontale qu'il se fait très mal, une grande partie du flux d'air n'étant pas concernée par la combustion.

L'évolution longitudinale du nombre de Mach moyen (figure 5) montre que l'écoulement reste supersonique en moyenne dans tout le foyer, atteignant Mach 1,3 en fin de foyer. Les plans de coupe transversale représentés sur la figure 6 montrent toutefois que la zone de combustion proprement dite est subsonique dans la première partie du foyer. On qualifiera toutefois ce régime de combustion supersonique dans la mesure où l'écoulement est supersonique en moyenne dans la totalité du foyer. Le champ de pression (figure 7) est caractéristique de ce type de régime. On note en particulier l'absence de chocs de précombustion: le gradient de pression dans la zone de l'injection est insuffisant pour provoquer des remontées de décollements.

L'évolution longitudinale des débits massiques d'eau et d'OH (figure 8) confirme l'allumage des jets pariétaux avant le culot. On note également que la pente de la courbe du débit d'eau reste forte en fin de foyer, ce qui indique que la combustion est loin d'être terminée et qu'une augmentation de longueur du foyer serait certainement bénéfique sur le plan du rendement de combustion.

Cette dernière observation est confirmée par le calcul du rendement de combustion (calculé sur l'hydrogène) que l'on trouve égal à 54,4% en fin de foyer, ce qui est faible. Le rendement de pression d'arrêt est lui aussi assez faible, égal à 17,7% en fin de foyer.

Conditions Mach 7,5

Pour les conditions Mach 7,5 , la première constatation est que, contrairement aux conditions Mach 6, les jets pariétaux ne s'allument pas avant le culot, comme le montre la figure 9 qui représente les fractions massiques de OH et H_2O dans un plan d'injection pariétale. Si la production de OH débute dès l'injection pariétale, on n'observe pas de production de H_2O ni d'élévation de température. Le tracé des courbes de débit massique de OH et H_2O (figure 10) confirme que la production d'OH commence dès l'injection pariétale alors que la production d'eau ne commence que très en aval du culot, au niveau de la rupture de pente du foyer: c'est le choc oblique généré à ce niveau qui déclenche alors l'allumage. On note d'ailleurs que celui-ci est assez violent, car intervenant dans un écoulement déjà bien prémélangé.

L'obtention d'un délai d'allumage plus élevé à Mach 7,5 qu'à Mach 6 peut sembler a priori surprenant, mais s'explique principalement par le fait que la tuyère d'alimentation Mach 4 produit une température statique assez basse. En outre, la pression d'arrêt étant limitée par les capacités du banc, elle n'est pas représentative des conditions réelles de vol à Mach 7,5: de ce fait, la pression statique obtenue est elle-même trop faible.

La visualisation du nombre de Mach dans le foyer (figure 11) permet de mettre en évidence des décollements de couche limite dans les coins de la chambre dans la première partie du foyer. Ces décollements sont dus au fort gradient de pression généré par l'allumage, assez violent comme le montre la figure 12. En dehors des couches limites, on note que l'écoulement est partout supersonique: on a donc clairement un régime de combustion supersonique, ce que confirme la courbe d'évolution du Mach moyen (figure 13). On voit aussi clairement sur cette courbe la chute brutale du Mach moyen due aux zones décollées et à l'allumage.

Le rendement de combustion calculé en fin de foyer est égal à 69,0% . Cette valeur assez élevée peut s'expliquer par la forte turbulence générée par les décollements de couche limite. Il semble aussi que la pénétration et le mélange des jets d'hydrogène, en particulier les jets pariétaux, soient plus forts en non réactif qu'en réactif, sans doute à cause d'une pression d'air plus faible. De ce point de vue, le "retard à l'allumage" serait favorable au rendement de combustion.

En revanche, le rendement de pression d'arrêt est très faible, égal à 6,2% . On peut noter à ce propos que l'épaisseur de couche limite générée par la tuyère Mach 4 est très importante (deux fois plus que la tuyère Mach 3 utilisée pour les conditions Mach 6) et il en résulte une perte de pression d'arrêt de plus de 40% rien que dans l'isolateur, comme le montre la courbe d'évolution de la pression d'arrêt moyenne (voir figure 14). On remarque sur cette même courbe que la pression d'arrêt moyenne subit une chute brutale au moment de l'allumage: il s'agit ici de la perte de Rayleigh associée à la combustion dans un écoulement à vitesse élevée (dans le cas Mach 6, elle est moins visible car plus continue).

Conditions Mach 5

Pour les conditions Mach 5, quatre valeurs de la richesse ont été explorées: successivement 1, 0,8 et 0,6 . Les résultats de ces calculs sont présentés dans les paragraphes suivants.

Calcul à richesse 1

Le calcul est dans un premier temps réalisé à richesse 1 avec une répartition paroi-culot de 20% et 80% respectivement. On observe dans ce cas la formation de décollements dans les coins de la chambre au niveau du mât. Ces décollements sont initialement dus aux forts gradients de pression générés par la combustion. Par l'obstruction qu'ils constituent et les pertes de pression d'arrêt qu'ils induisent, ces décollements provoquent le blocage de l'écoulement avec amorçage d'un col sonique au niveau du culot du

mât, précédé d'un système de chocs de désamorçage. Le débit passant par ce col étant inférieur au débit entrant, on assiste alors au désamorçage de l'ensemble de la veine: la pression monte progressivement en amont du col, repoussant le système de chocs qui remonte dans l'isolateur, entrainant avec lui des décollements de plus en plus importants. Ce processus est visible sur la figure 15 qui représente le nombre de Mach dans l'isolateur et la case à injection dans un plan de coupe horizontal proche de la paroi inférieure à différents instants successifs. Aucun état stationnaire n'est atteint dans ce cas, le calcul étant finalement interrompu lorsque le choc de désamorçage atteint l'entrée de l'isolateur: on a alors en effet incompatibilité avec la condition d'entrée supersonique du calcul, seul un maillage incluant la tuyère d'alimentation pouvant permettre de poursuivre le calcul.

Calcul à richesse 0,8

Suite au désamorçage constaté à richesse 1, un second calcul est effectué à richesse 0,8, avec la même répartition débit-culot. Là encore on observe un désamorçage de l'écoulement. La figure 16 représente pour cette richesse le nombre de Mach dans l'isolateur et la case à injection peu avant que le choc de désamorçage n'atteigne la section d'entrée de l'isolateur. On observe bien que le dernier plan de coupe, situé au niveau du culot du mât, est sonique. Dans l'isolateur, le choc de désamorçage est très étalé et s'accompagne d'un décollement très important sur la paroi supérieure.

Calcul à richesse 0,6

Un troisième calcul est réalisé à richesse 0,6 (dont toujours 20 % injectée à la paroi et 80% au culot). Ce calcul a cette fois convergé sans désamorçage. On observe cependant des décollements dans les coins de la chambre au niveau du mât (figure 17) mais ces décollements sont stables et insuffisants pour bloquer l'écoulement qui reste supersonique en moyenne dans l'isolateur et la case à injection. Le tracé de l'évolution du nombre de Mach moyen le long de la veine (figure 18) montre que l'écoulement est supersonique en moyenne sur toute la longueur du

foyer, on est donc ici en régime de combustion supersonique semblable à celui constaté dans le cas Mach 6. L'écoulement est toutefois en limite de blocage peu après la deuxième divergence du foyer, le choc oblique causé par le changement de pente de la paroi supérieure faisant passer subsonique une grande partie de la zone réactive. L'écoulement ne redevient partout supersonique qu'en fin de foyer.

La figure 19 présente les champs de température statique et d'espèces H_2O et OH pour un plan d'injection pariétal. On constate que les jets pariétaux s'allument rapidement. Comme pour les conditions Mach 6, l'écoulement est très stratifié. L'effet sur la combustion du choc généré par le changement de pente de la paroi supérieure du foyer est très net. Il est aussi visible sur la figure 20 qui représente l'évolution longitudinale du débit d'eau: là où la production d'eau diminue habituellement assez vite, on assiste ici à un léger regain à la traversée du choc.

Le rendement de combustion calculé sur l'hydrogène est égal à 73,7% et le rendement de pression d'arrêt est égal à 29,9%. Ces valeurs élevées s'expliquent principalement par le fait que la richesse injectée est assez faible. La perte de pression d'arrêt dans l'isolateur seul s'élève à 22,8% (figure 21).

Influence de la divergence du foyer (conditions Mach 6 richesse 1)

Une divergence de foyer moins élevée est envisagée dans un second temps. Pour les conditions Mach 6, richesse 1, on obtient avec cette nouvelle géométrie un régime de combustion non plus supersonique mais transsonique avec amorçage d'un col thermique en fin de foyer. sans remontées de décollements dans l'isolateur (figure 22). L'écoulement est successivement supersonique, subsonique et supersonique en moyenne. On voit sur la figure 23 que la partie subsonique de l'écoulement est beaucoup plus étendue transversalement et longitudinalement que pour la géométrie à divergence forte. La combustion proprement dite a même lieu quasi-intégralement dans un écoulement localement subsonique. La présence de

cette zone subsonique dans presque tout le foyer fait que l'adaptation de l'écoulement au col thermique ne se fait pas par un choc droit comme dans un statoréacteur conventionnel mais par un processus quasi-continu.

La figure 24 révèle un niveau de pression statique dans le foyer beaucoup plus fort qu'avec la géométrie plus divergente, ce qui est logique, l'écoulement étant plus lent. Cependant, on n'observe pas non plus de remontées de chocs de précombustion.

Le délai d'allumage est le même pour les deux géométries, ce qui est logique dans la mesure où l'allumage a lieu avant la divergence. Ceci est visible sur la figure 25 représentant la température statique dans la première partie du foyer pour les deux géométries. Dans la direction de la largeur de la veine, la part de l'écoulement non concernée par la combustion est moins importante avec la géométrie la moins divergente: l'écoulement est moins stratifié car moins rapide. Pour la même raison, le rendement de combustion calculé sur H_2 est nettement plus élevé avec la divergence faible qu'avec la divergence forte (65,3% contre 54,4%). Le rendement de pression d'arrêt est de 20,0% en fin de foyer, meilleur aussi qu'avec la géométrie plus divergente (17,7%).

Dans les conditions Mach 6, le régime de combustion transsonique auquel conduit la géométrie de foyer à faible divergence semble donc le plus performant. Cependant, cette conclusion serait probablement sinon inversée, du moins atténuée avec un système d'injection plus favorable à l'obtention d'un rendement de combustion élevé: dans ce cas, il est même possible que le fonctionnement à richesse 1 conduise à un désamorçage de la veine avec la géométrie à faible divergence.

Influence du générateur d'hétérogénéité (conditions Mach 6)

Le générateur d'hétérogénéité est constitué d'une cale en forme d'accent circonflexe d'angle égal à 8° et de hauteur maximale égale à 15 mm, située au centre du premier tronçon d'isolateur sur la paroi

inférieure. Il génère successivement un choc, une détente et un deuxième choc, qui subissent ensuite plusieurs réflexions et interactions successives dans l'isolateur, conduisant à un écoulement fortement hétérogène en entrée de foyer. L'avantage de cette configuration est qu'elle permet en particulier d'avoir une section identique en amont et en aval du générateur d'hétérogénéité: celui-ci peut donc être mis en place ou retiré sans autre modification de géométrie.

L'effet du générateur d'hétérogénéité est très visible sur la figure 26 qui représente le champ de pression statique. On voit en particulier les ondes de choc et de détente générées et leurs réflexions successives sur les parois de l'isolateur.

La figure 27 présente les champs de température statique et d'espèces H_2O, H_2 et OH dans un plan d'injection pariétale. Le mélange et la combustion sont très semblables à ceux obtenus sans le générateur d'hétérogénéité pour la même divergence de veine.

L'évolution longitudinale du Mach moyen (figure 28) montre que la combustion reste supersonique. Cependant, le nombre de Mach moyen est plus faible avec le générateur d'hétérogénéité: la raison en est certainement une perte de pression d'arrêt plus élevée dans l'isolateur qui se traduit par une compression et un ralentissement de l'écoulement. Il en résulte d'ailleurs un rendement de combustion un peu plus élevé (56,7% contre 54,4% en écoulement homogène), dû aussi à un niveau de turbulence plus grand. Une autre conséquence est un niveau de température statique maximal plus élevé en écoulement hétérogène (2650 K contre 2466 K en homogène). En revanche, le générateur d'hétérogénéité est sans influence dans ce cas sur le délai d'allumage.

Le rendement de pression d'arrêt calculé est de 16,8% en fin de foyer, donc assez proche de celui (17,7%) obtenu en écoulement homogène. Ce résultat, assez surprenant a priori, s'explique au vu de la figure 29 qui représente l'évolution de la pression d'arrêt avec et sans générateur d'hétérogénéité. La présence du

générateur d'hétérogénéité génère comme prévu une perte plus importante dans l'isolateur (effet des chocs), mais cette tendance s'inverse dans le foyer où les pertes de Rayleigh sont réduites du fait d'une vitesse d'écoulement plus faible en entrée de foyer.

mettent en évidence la forte influence de la géométrie du mât sur les conditions d'allumage, mais aussi sur le régime de combustion: ils confirment en particulier que l'étagement de l'injection est une voie intéressante pour éviter l'apparition de décollements néfastes.

INJECTION D'HYDROGENE DANS UN SUPERSTATOREACTEUR

Dans le cadre du programme PREPHA, de nombreux travaux théoriques et expérimentaux relatifs à la pénétration et à l'allumage de jets d'hydrogène dans un flux d'air supersonique ont été effectués et sont décrits dans les références 5 à 7. Ils ont mis en évidence en particulier l'influence prépondérante de l'angle d'injection. Divers dispositifs destinés à favoriser l'allumage d'un jet oblique ont aussi été évalués: injection dans une cavité, injection de petits jets perpendiculaires en amont du jet oblique principal.

Sur un plan plus appliqué, différents concepts de mâts d'injection ont été définis et évalués par des calculs tridimensionnels. Deux d'entre eux, représentés sur la figure 30, ont fait l'objet d'expérimentation dans les conditions Mach 6 à l'ONERA Palaiseau. Le concept A est caractérisé par la présence de deux niveaux d'injection: le premier, aux parois du mât, par des jets obliques, et le second, au culot du mât, par des jets parallèles. Le concept B, ne comprend qu'un niveau d'injection au culot du mât; il est caractérisé par l'alternance de rampes de compression et de détente sur les parois, générant dans le flux d'air des tourbillons longitudinaux destinés à favoriser le mélange. Les mesures de pression statique relevées dans la veine pour différentes richesses sont représentées sur la figure 31. On observe que le concept A conduit à un régime de combustion supersonique stable à toutes les richesses; un délai d'allumage relativement important est observé pour les richesses les plus faibles. Le concept B se caractérise par un défaut d'allumage à richesse faible, et par la remontée de décollements importants à richesse élevée, conduisant au désamorçage partiel de l'écoulement. Ces résultats, décrits et commentés plus en détail dans la référence 6,

UTILISATION D'HYDROCARBURES DANS UN STATOREACTEUR MIXTE

Il est envisagé d'utiliser non seulement l'hydrogène mais aussi des hydrocarbures stockables (kérosène, combustibles endothermiques,...) dans les statoréacteurs hypersoniques. En effet, bien que l'hydrogène présente des avantages importants en terme de pouvoir calorifique et de capacité de refroidissement, il est pénalisé par une masse volumique dix fois plus faible que le kérosène et par le fait qu'il n'est pas stockable facilement sous forme liquide. Les hydrocarbures présentent un intérêt:

- pour les lanceurs spatiaux s'ils sont utilisés pendant la première partie de la trajectoire, typiquement jusqu'à Mach 6, tant que le pouvoir calorifique et les capacités de refroidissement ne sont pas critiques: le gain dû à la meilleure impulsion spécifique volumique avec un hydrocarbure stockable (impulsion spécifique divisée par deux par rapport à l'hydrogène mais masse volumique dix fois supérieure) permettrait théoriquement de diminuer la masse sèche et surtout le volume et donc la trainée du véhicule, ce qui aura des répercutions favorables sur toute la trajectoire, en particulier à très haut Mach quand le bilan poussée-trainée tend à s'annuler,
- pour les applications militaires où l'hydrogène ne parait pas adapté, notamment pour des raisons de stockage.

L'utilisation de carburants stockables dans un statoréacteur hypersonique nécessite cependant des études complémentaires, parmi lesquelles on peut citer:

1. Recherches de base sur l'injection et la combustion.

Dans les années 60, des essais de combustion supersonique de kérosène ont été réalisés

par Mestre [8] à l'ONERA. A la même époque, l'ENSMA a travaillé sur la stabilisation d'une flamme air-kérosène dans un écoulement supersonique par création d'une zone subsonique localisée derrière un disque de Mach. De nombreux travaux russes ont aussi été effectués dans les années 60 et 70 (MAI, CIAM,...). Un effort important a aussi été consenti à cette époque aux Etats-Unis; actuellement, l'accent est mis sur l'utilisation de combustibles endothermiques permettant le refroidissement de la chambre par décomposition au contact d'un revêtement catalytique approprié.

2. Essais de différents combustibles dans un même moteur.

Le principe de ce type d'essais est de mettre en évidence les différences de performances, voire de régimes de combustion, lorsque dans un moteur conçu et optimisé pour un certain combustible on injecte un autre combustible. En 1990, AEROSPATIALE Missiles a ainsi réalisé des essais de combustion subsonique d'hydrogène dans un statoréacteur conçu pour le kérosène le long d'une trajectoire de lanceur spatial aérobie type STS2000 entre Mach 3 et 4,7 (figure 32). Un rendement de combustion très proche de 1 a été obtenu. L'auto-allumage a été constaté à partir de Mach 4 environ.

AEROSPATIALE Missiles a aussi effectué des premières estimations par des calculs monodimensionnels de la différence de fonctionnement d'une chambre de superstato de type CHAMOIS alimentée soit en hydrogène soit en kérosène, et dont on ne modifierait que le système d'injection. L'apport de chaleur plus faible avec le kérosène induit un Mach plus élevé et une pression et une température plus faible qu'avec l'hydrogène pour une même géométrie de foyer (figure 33).

3. Conception d'un système d'injection adapté aux hydrocarbures.

Des travaux sur ce thème sont notamment prévus dans le cadre du programme HyTech aux Etats-Unis.

4. Conception et expérimentation d'une chambre de combustion adaptée aux hydrocarbures.

Des essais de ce type ont eu lieu en Russie dans les années 70. Aux Etats-Unis, deux superstatos différents sont en cours d'essais dans le cadre du programme HyTech.

5. Conception et expérimentation d'un système d'injection bi-combustible.

Un système d'injection bicombustible, capable d'alimenter un stato mixte soit en hydrogène, soit en kérosène, pour une application spatiale, nécessite des circuits et une conception particulière, compte tenu notamment des différences de comportement entre un liquide de masse volumique de 800 kg/m^3 et un gaz de masse volumique de 2 à 3 kg/m^3. Dans le cadre d'une coopération entre AEROSPATIALE Missiles et le M.A.I. [9], un tel système d'injection est actuellement à l'étude.

6. Conception et expérimentation d'un statoréacteur hypersonique bi-combustible.

Outre le système d'injection spécifique, un fonctionnement bi-ergol d'un statoréacteur mixte nécessite une optimisation particulière. Si la géométrie est fixe, il sera plus difficile d'optimiser les performances, compte tenu des différences mises en évidence notamment lors des simulations monodimensionnelles citées plus haut. Une géométrie mobile de la chambre de combustion peut grandement permettre cette optimisation pendant les campagnes d'essais de mise au point au sol, et éventuellement en vol. C'est ce qui est envisagé dans l'étude commune AEROSPATIALE/M.A.I. évoquée précédemment.

7. Conception et expérimentation d'un superstatoréacteur à combustible endothermique.

L'utilisation des combustibles endothermiques est à la fois plus prometteuse et plus complexe que l'utilisation de kérosène ou d'hydrogène

ou des deux dans le même moteur. En effet le combustible endothermique a des performances intermédiaires entre le kérosène et l'hydrogène en termes de capacité de refroidissement, de pouvoir calorifique et de masse volumique dans les conditions de stockage. Outre les questions liées à la définition des structures refroidies (catalyse, limitation des suies,...), le couplage entre allumage, combustion, échanges thermiques et injection est particulièrement fort et nécessite une bonne connaissance des phénomènes en jeu et la mise au point et la validation d'une méthodologie intégrée spécifique. Des études sur ces thèmes débutent à l'ONERA.

8. Adaptation et validation des outils numériques.

La combustion supersonique d'hydrocarbures est un défi de taille pour les codes de calcul: on y rencontre simultanément et de façon couplée des aspects diphasiques, de la cinétique chimique, de la turbulence, des forts effets de compressibilité, des discontinuités,... La plupart de ces ingrédients sont présents ou en cours de développement dans les logiciels modernes, en particulier le code MSD développé à l'ONERA. AEROSPATIALE Missiles a ainsi effectué un calcul d'injection de kérosène dans la marche d'un mât d'injection de superstatoréacteur: les figures 34 (fraction massique de kérosène) et 35 (trajectoire des gouttes de kérosène) montrent que, dans ce cas particulier, la différence de pression entre intrados et extrados est la cause d'un entrainement du kérosène vers le bas.

Un effort important doit cependant encore être consenti pour adapter et valider les modèles physiques par rapport aux conditions extrêmes rencontrées dans un statoréacteur hypersonique.

CONCLUSION

Au cours des cinq dernières années, un travail important a été effectué dans le cadre du programme PREPHA sur le thème du superstatoréacteur, avec le soutien de la DGA, du CNES et du MENESR. Ce travail est illustré en particulier par l'expérimentation dans les conditions Mach 6 d'un superstatoréacteur de grandes dimensions.

Il s'est prolongé récemment par l'étude préliminaire des différents régimes de fonctionnement d'un statoréacteur mixte. Cette étude, basée à ce stade exclusivement sur des calculs tridimensionnels, a permis de quantifier l'importance de paramètres tels que le taux de divergence de la chambre, l'hétérogénéité de l'écoulement ou le rôle de l'isolateur. La campagne d'essais prévue en 1997 devra cependant confirmer les enseignements apportés par les calculs.

L'utilisation du kérosène ou de combustibles endothermiques dans un statoréacteur hypersonique a un intérêt potentiel évident, en particulier pour les applications militaires. L'effort sur ce thème a été important en Russie dans le passé, il s'intensifie actuellement aux Etats-Unis, et il serait souhaitable qu'il augmente notablement en France.

Références

[1] *Scramjet Combustor Design in France*
M. Bouchez, N. Montmayeur, C. Leboucher
AIAA 95-6094, Chattanooga, 1995

[2] *Scramjet Combustor Design in French PREPHA Program - Status in 1996*
M. Bouchez, J.V. Hachemin, C. Leboucher, D. Scherrer, D. Saucereau
AIAA 96-4582-CP

[3] *Scramjet Flowfields Investigation by Numerical Simulation*
P. Novelli, D. Scherrer, D. Gaffié
12th ISABE, Melbourne, 1995

[4] *Using a global hydrogen-air combustion model in turbulent reacting flow calculation*
R.C. Rogers, W. Chinitz
AIAA Journal, vol. 21, n° 4, 1983

5 *Scramjet Injectors Calculation and Design*
D. Scherrer, N. Montmayeur, O. Ferrandon, D. Tonon
AIAA 93-5171, Munich, December 1993

6 *Injection Studies in the French Hypersonic Technology Program*
D. Scherrer, O. Dessornes, O. Ferrandon, N. Montmayeur
AIAA 95-6096, Chattanooga, 1995

7 *Injection and Combustion Challenges in Scramjets*
D. Scherrer, O. Dessornes, C. Jourdren, C. Leboucher, M. Bouchez, E. Saunier, D. Saucereau
AAAF Paris, 1996

8 *Etude expérimentale de la combustion de kérosène dans un écoulement supersonique*
A. Mestre
NT ONERA n° 2/7583EY (1963), n° 3/7583EY (1964), n° 11/7583EY (1965)

9 *French-Russian Partnership on Hypersonic Wide Range Ramjet*
A. Chevalier, V.M. Levin, D. Davidenko, M. Bouchez
AIAA-96-4554-CP
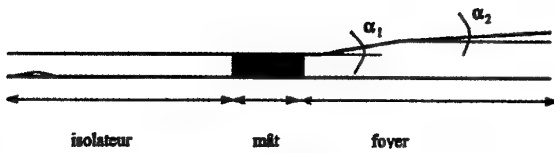
Figure 1 : Géométrie de la veine

isolateur   mât   foyer
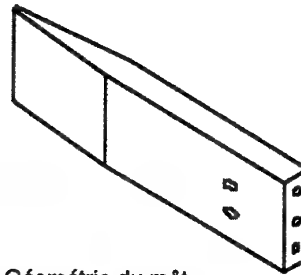
Figure 2 : Géométrie du mât

Température

Fraction massique H2O

Fraction massique H2

Fraction massique OH
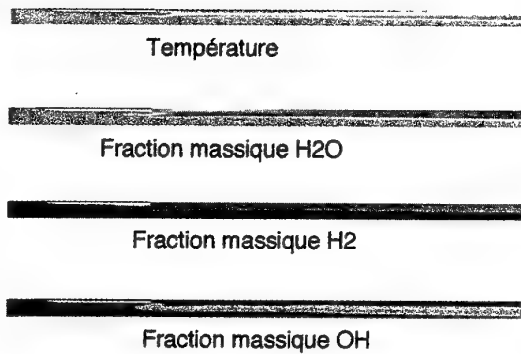
Figure 3 : Conditions Mach 6, richesse 1
Température et fractions massiques
dans un plan d'injection pariétale
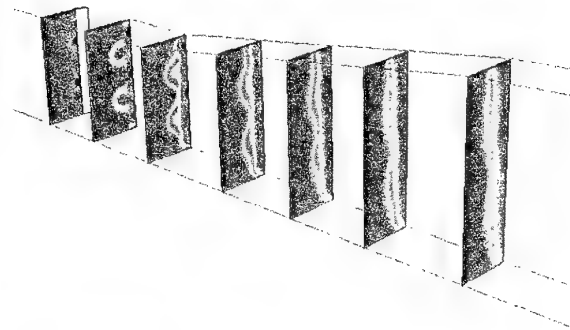
Figure 4 : Conditions Mach 6, richesse 1
Température dans la première partie
du foyer (plans de coupe)
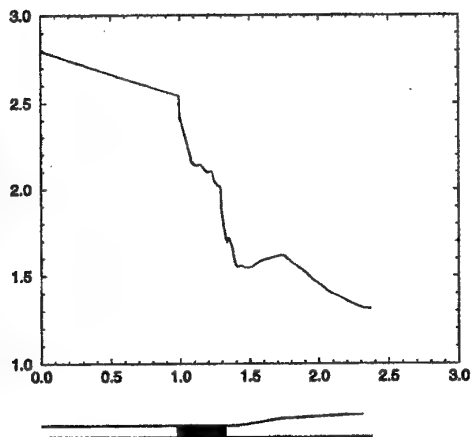
Figure 5 : Conditions Mach 6, richesse 1
Evolution longitudinale du
Mach moyen dans le foyer

3.000e+00
2.710e+00
2.420e+00
2.130e+00
1.840e+00
1.550e+00
1.260e+00
9.699e-01
6.799e-01
3.900e-01
1.000e-01
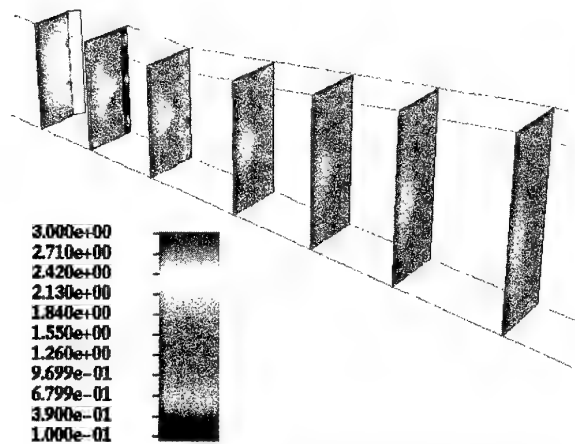
Figure 6 : Conditions Mach 6, richesse 1
Mach dans la première partie
du foyer (plans de coupe)
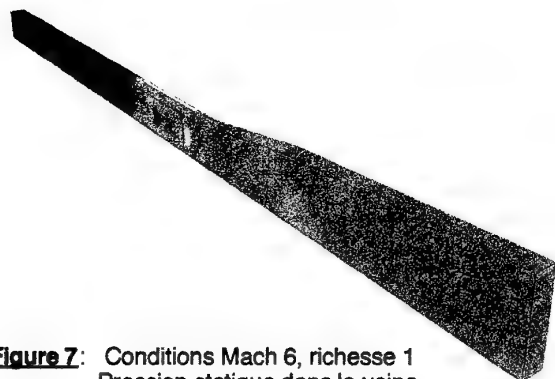
Figure 7: Conditions Mach 6, richesse 1
Pression statique dans la veine
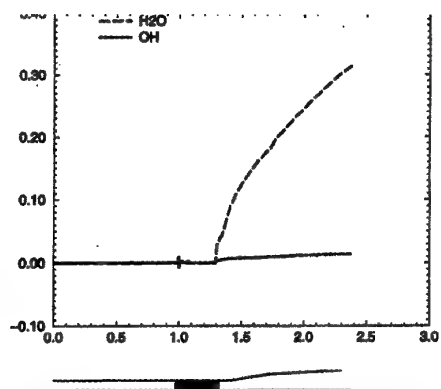
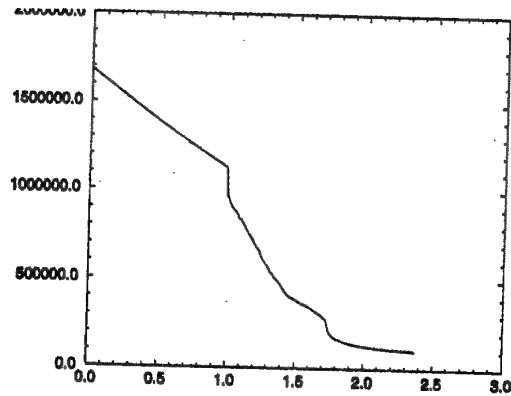**Figure 8**: Conditions Mach 6, richesse 1
Evolution longitudinale des
débits massiques de H2O et OH

OH

H2O
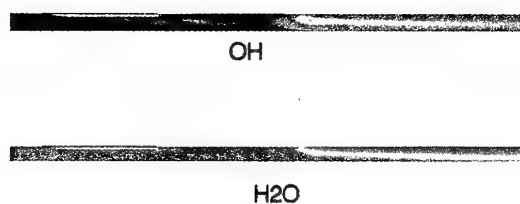
Figure 9: Conditions Mach 7,5 , richesse 1
Fractions massiques de H2O et OH
dans le foyer (plan d'injection pariétale)
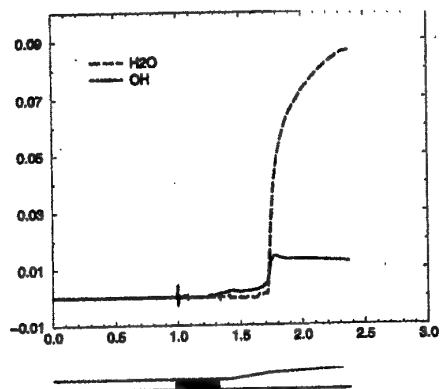
Figure 10: Conditions Mach 7,5 , richesse 1
Evolution longitudinale des débits
massiques de H2O et OH

4.000e+00
3.610e+00
3.220e+00
2.830e+00
2.440e+00
2.050e+00
1.660e+00
1.270e+00
8.800e-01
4.900e-01
1.000e-01
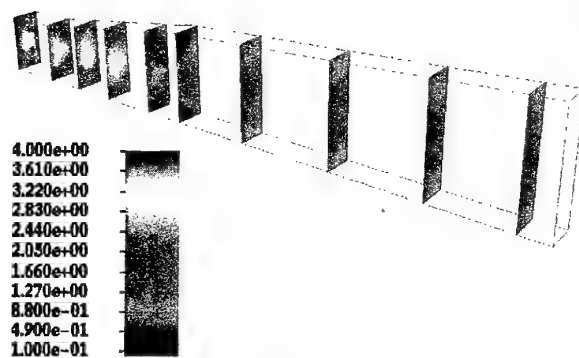
Figure 11: Conditions Mach 7,5 , richesse 1
Mach dans le foyer

Figure 12: Conditions Mach 7,5 , richesse 1
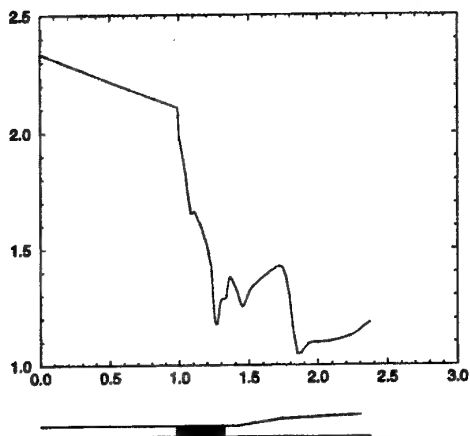Pression statique dans la veine
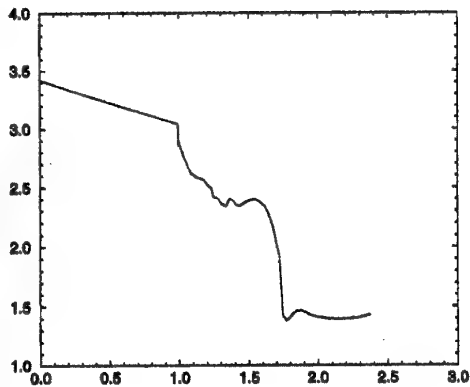
Figure 13: Conditions Mach 7,5, richesse 1
Evolution longitudinale du
nombre de Mach moyen

Figure 14: Conditions Mach 7,5, richesse 1
Evolution longitudinale de la
pression d'arrêt moyenne

Itération n

Itération n+1000

Itération n+2000

Itération n+3000

Itération n+4000

Itération n+5000

Itération n+6000
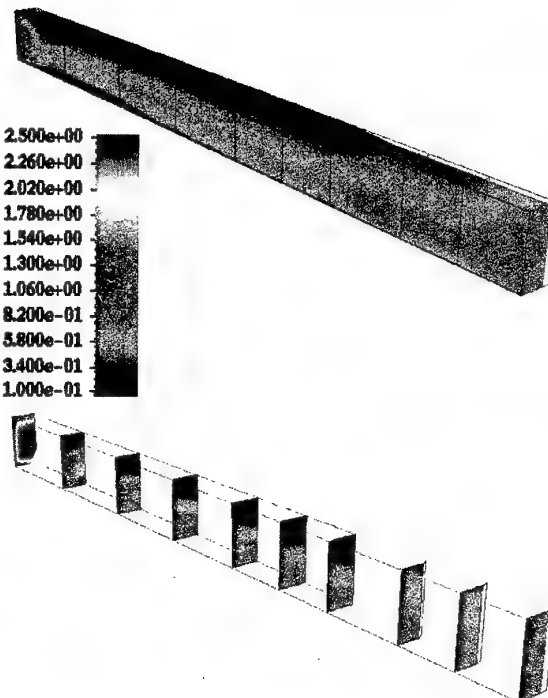
Figure 15: Conditions Mach 5, richesse 1
Nombre de Mach dans la veine
à différents instants successifs

Figure 16: Conditions Mach 5, richesse 0,8
Nombre de Mach dans l'isolateur
peu avant le désamorçage complet

a) Plans de coupe dans l'isolateur
et la case à injection

b) Enveloppe de l'ensemble
de la maquette
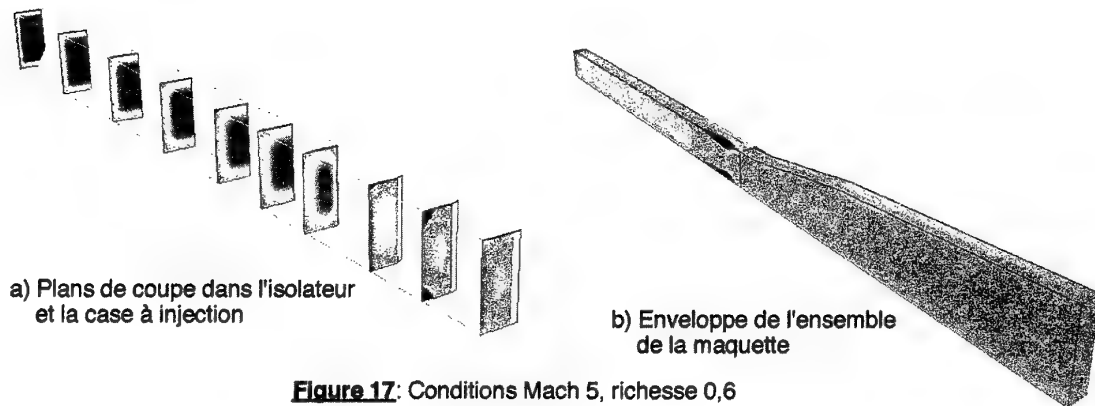
Figure 17: Conditions Mach 5, richesse 0,6
Nombre de Mach

Figure 18: Conditions Mach 5, richesse 0,6
Evolution longitudinale
du Mach moyen

Température statique

Fraction massique H2O

Fraction massique OH

Figure 19 : Conditions Mach 5, richesse 0,6
Température statique et fractions
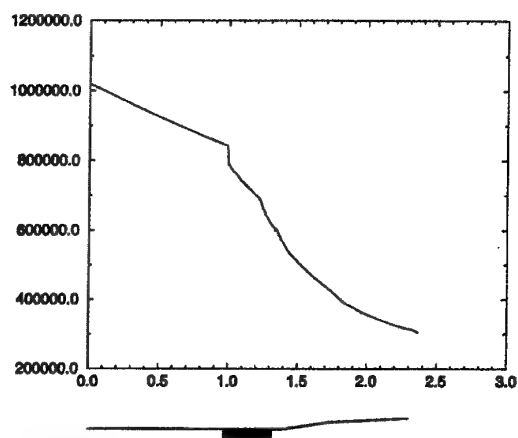massiques H2O et OH
dans un plan d'injection pariétale
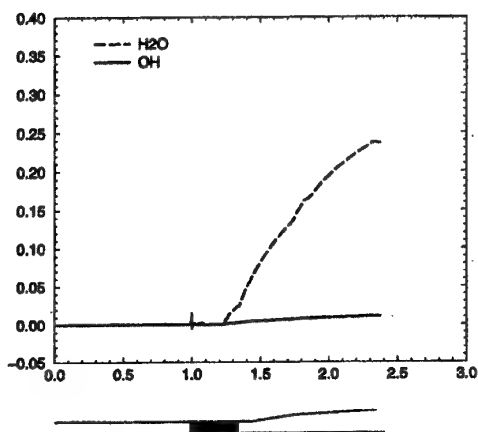
Figure 20: Conditions Mach 5, richesse 0,6
Evolution longitudinale des
débits massiques de H2O et OH

Figure 21: Conditions Mach 5, richesse 0,6
Evolution longitudinale de la
pression d'arrêt moyenne
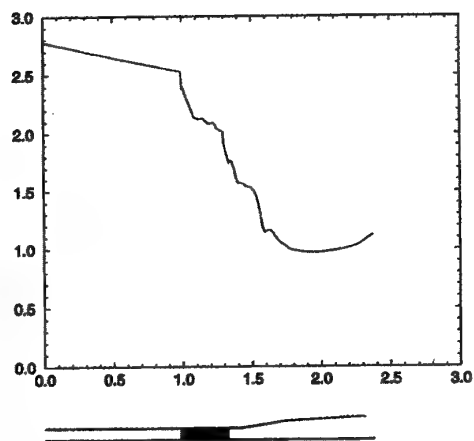
Figure 22: Conditions Mach 6, richesse 1,
géométrie de foyer à divergence faible
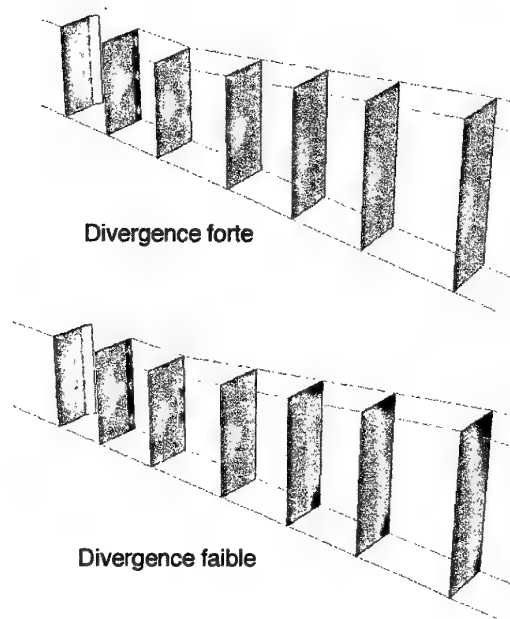Evolution longitudinale du Mach moyen

Divergence forte

Divergence faible

Figure 23: Conditions Mach 6, richesse 1
Nombre de Mach dans la première
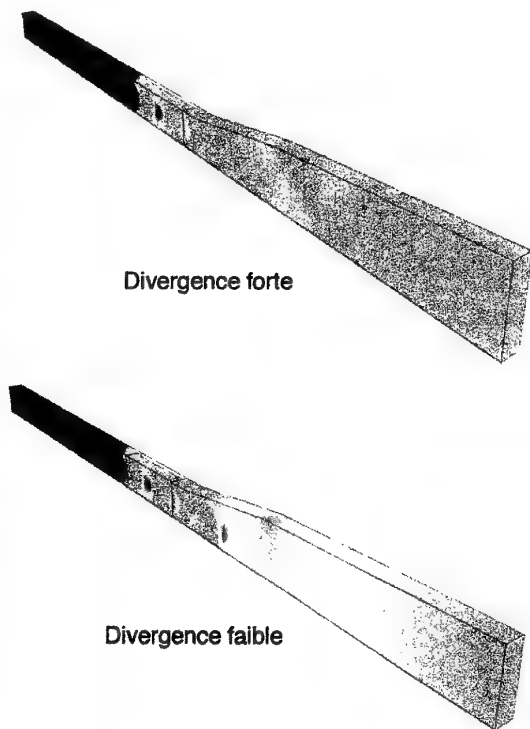partie du foyer pour les deux géométries

Divergence forte

Divergence faible

Figure 24: Conditions Mach 6, richesse 1
Pression statique dans la veine
pour les deux géométries
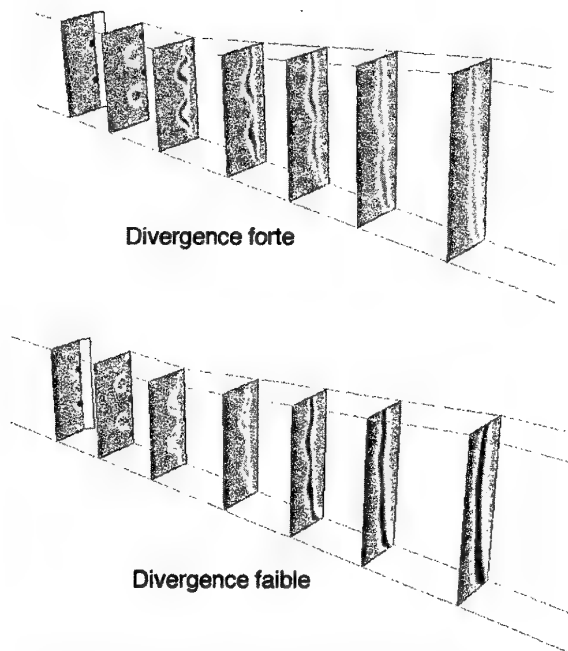

Divergence forte

Divergence faible

Figure 25: Conditions Mach 6, richesse 1
Température statique dans la veine
pour les deux géométries

Figure 26: Conditions Mach 6 , richesse 1
Effet du générateur d'hétérogénéité
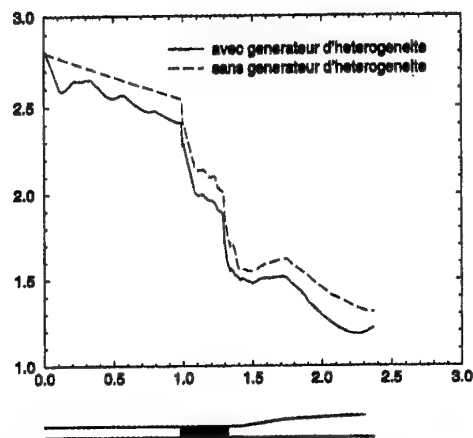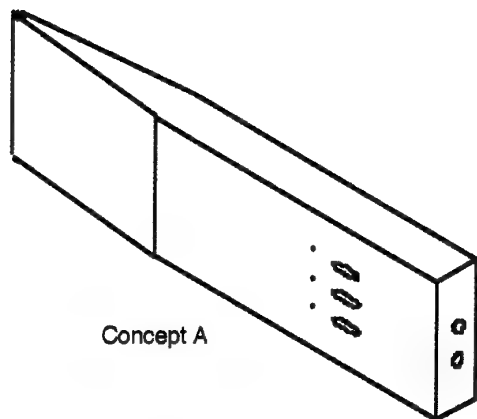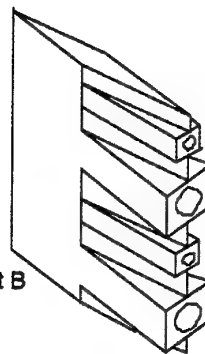Pression statique dans la veine

Température

Fraction massique H2O

Fraction massique H2

Fraction massique OH

Figure 27: Conditions Mach 6 , richesse 1
Effet du générateur d'hétérogénéité
Température et fractions massiques
H2O, H2 et OH dans le foyer

Figure 28: Conditions Mach 6 , richesse 1
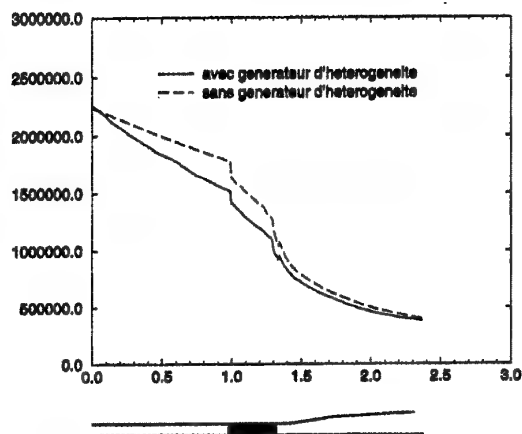Effet du générateur d'hétérogénéité
Evolution longitudinale du Mach moyen

Figure 29: Conditions Mach 6 , richesse 1
Effet du générateur d'hétérogénéité
Evolution longitudinale de la
pression d'arrêt moyenne

Concept A

Concept B

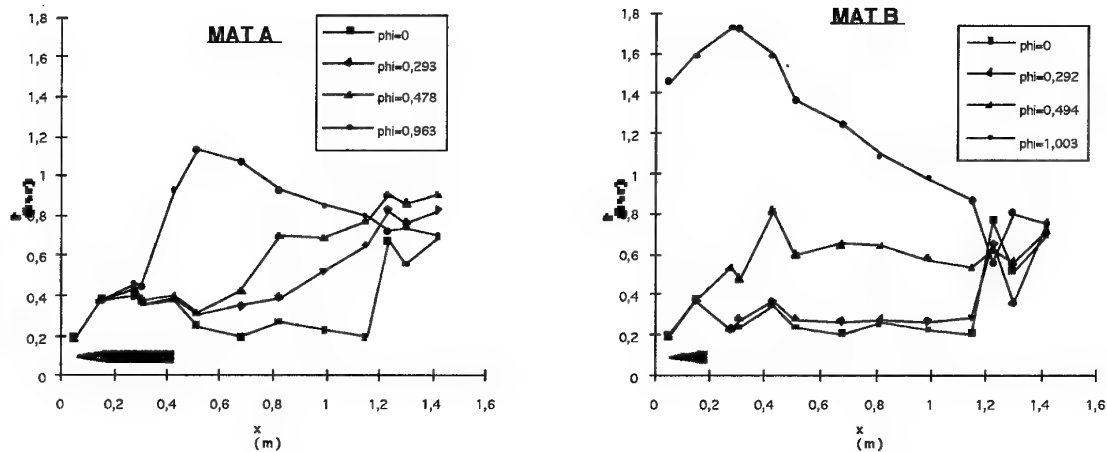**Figure 30**: Concepts de mât d'injection

Figure 31: Essai des concepts A et B dans les conditions Mach 6
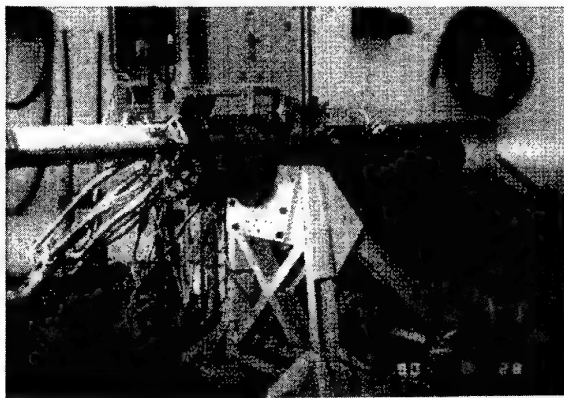Evolution longitudinale de la pression statique dans la veine

Figure 32: Combustion d'hydrogène dans un stato conçu pour le kérosène
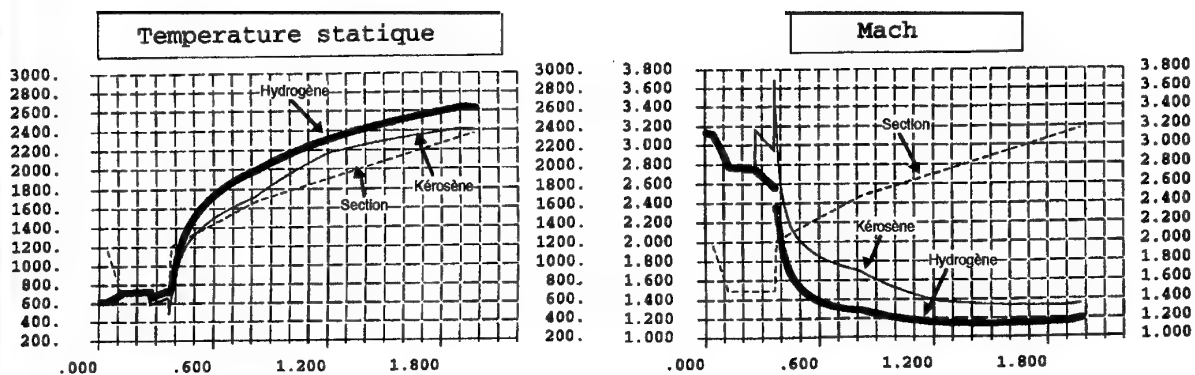

Figure 33: Calcul monodimensionnel d'un superstato alimenté
en hydrogène ou kérosène
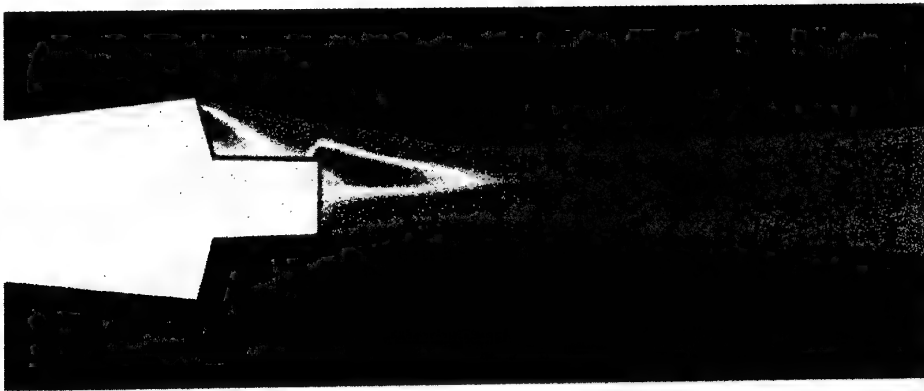
Figure 34: Calcul d'injection de kérosène dans un superstato
Fraction massique de kérosène
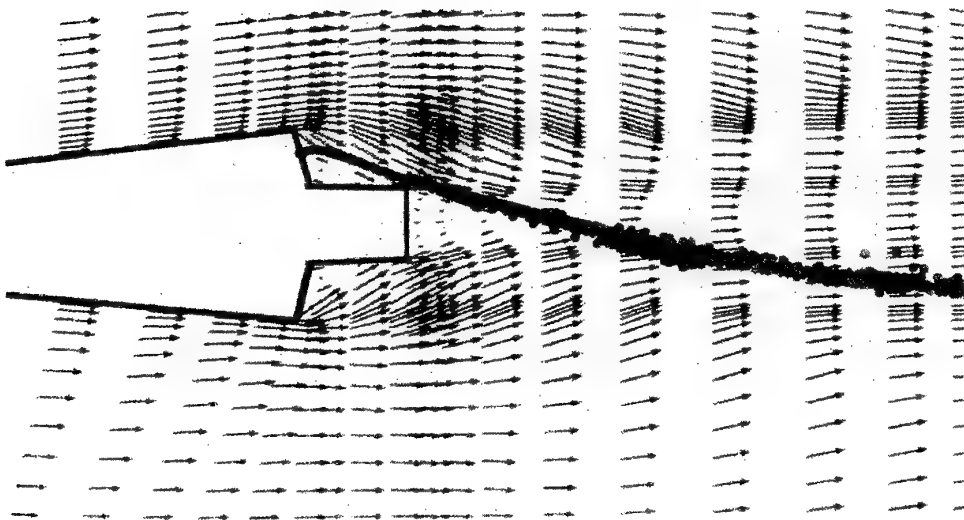
Figure 35: Calcul d'injection de kérosène dans un superstato
Trajectoire des gouttes de kérosène

C-7

Question 1: Zanchetta

How do you couple the air-fuel (kerosene) interaction in your numerical simulation?

Author's reply:

Kerosene droplets trajectories are computed by a lagrangian solver. The coupling with the eulerian gaseous solver is made at each time step through an exchange of mass, momentum and energy computed from drag and evaporation laws. For this computation, the velocity of the gas is deduced from the mean velocity, the turbulent kinetic energy and a gaussian assumption for the fluctuations.

Rocket Ramjet Boosters For Sustained High Speed Flight

Drew DeGeorge Phillips Laboratory, Edwards AFB, CA 93524 7084
Pat Hewitt, Atlantic Research Corporation (ARC), Gainesville, VA 20155
Adam Siebenhaar, GenCorp Aerojet, P.O. Box 13 222,
Sacramento, California 95813, USA

SUMMARY
Sustained high speed flight requires the highest levels of propulsive and aerodynamic performance. One of the highest performance classes of propulsion system envisioned is the air-augmented rocket. The potential for significant Isp increases to be gained using an air-augmented rocket (with either liquid, solid or hybrid propellant boost propulsion systems) has long been recognized. Using intake air as the primary oxidizer with rocket fuel significantly reduces on-board propellant mass, vehicle mass and volume for the same total impulse delivered compared to conventional chemical rockets. The list of technical challenges for viability and use include;

1. Booster configuration including integrated (boost propellant inside air-augmented combustion chamber, with or without a typical rocket nozzle), parallel or tandem boosters, and propellant combination drives booster complexity, need for ejecta, boost system ballistic requirements, air-augmented rocket performance and vehicle aerodynamics.

2. Complexity of starting flow through the inlets and initiating efficient air-augmented ignition.

3. Aerodynamics involved in starting and unstarting inlets in supersonic flow while performing high angle of attack maneuvers can negatively impact missile performance.

The previously discussed configuration differences combined with multiple applicable propellant systems and associated system implications represent a large range of systems with varying technical limitations. This paper will provide a summary of the applicable integrated, tandem and parallel booster development efforts. Liquid and solid propellant boost propulsion systems will be included. The integral rocket ramjet (IRR) booster and a rocket based combined cycle (RBCC) approach will be discussed in more detail including test results. Technical maturity, results, conclusions, recommended technology projects and goals for ramjet boosters supporting sustained high speed flight will be discussed. Analysis quantifying the payoff of achieving the goals for a representative mission(s) will also be discussed.

1. INTRODUCTION: THE PROMISE OF RAMJET PROPULSION

Whereas in the classical rocket vehicle the energy source and the reaction mass are carried on board, a vehicle propelled by an airbreathing engine carries only the energy source, the fuel, and the atmosphere provides the bulk of the reaction mass and with it the oxidizer. Since the air consists approximately 40 percent of nitrogen the reaction mass available to the airbreather is five times as great as in the rocket. It can be shown that for the case of a hydrocarbon fuel which burns at a mixture ratio of 15:1, this increased reaction mass provides more than twice the thrust and almost six times the specific impulse (Isp) relative to a LOX/RP rocket engine operating at a mixture ratio of 2.6:1. These increases in thrust and performance are required for sustained high speed flight for practical missiles. Excellent performance, however, doesn't come for free. The price to be paid is a larger size engine with an associated potential for greater inert mass due to the added functions of capturing and compressing ambient air and in some cases more complex propellant management systems.

In a turbojet, these tasks are performed by a multi-stage compressor, making it a highly efficient thrust producer but limiting its maximum speed to a flight Mach number range of 3. Higher speeds are achievable with a ramjet and its even higher speed brother the scramjet. Existing essentially of an open duct, these jets are the simplest engine devised to date. They are significantly lower in weight than the turbojet. In ram/scramjets, air capture and compression oc-

curs as the result of the vehicle's forward motion. Since at static and low speed conditions both ram pressure and air capture are zero or negligible, ramjet engines are incapable of providing thrust at takeoff. They must be boosted to approximately Mach 2 by another propulsion system before they become self sustaining.

Rocket boosters for ramjets have been pursued for many decades. The reason for such continued development interest in ramjet boosters is the leverage between booster and ramjet performance. The Isp of a ramjet is on the order of six times the Isp of a typical rocket. Figure 1 shows an example of typical air-launched missile performance improvements attainable with increased ramjet booster total impulse.

2. HISTORICAL SUMMARY OF RAMJET DEVELOPMENT EFFORTS

Table 1 shows a summary many of the recent ramjet efforts. A more inclusive historical review is included in Ref 1. It is worthwhile to review some of these previous applications of ramjet propulsion to missiles in more detail and to discuss why they are not operational today.

Bomarc - This ground launched experimental surface-to-air missile (SAM) was actually a small ramjet powered unmanned aircraft. It was over 46 feet long with a 14 feet wingspan weighing 15,000 pounds. Its maximum speed was Mach 3 flying at an approximate ceiling of 70,000 feet with a range of 200-300 miles. Long range bombers were its main target. It was self boosted with a liquid or solid propellant rocket and sustained with two ramjets. Its high cost together with improvements in solid propellant SAMs, and the successful advancement of Inter-Continental Ballistic Missiles made it obsolete.

Talos - This two stage Navy missile had a launch weight of 3000 lbm, was 20 feet long, and 30 inches in diameter. It had a Mach 3 class speed and a range in excess of 65 miles. Launched from ships at sea permitted the dropping of the booster stage. Its intended target were bombers and fighters attacking the fleet. Its main limitations were in the terminal intercept phase. At the extreme range of this missile, the beam riding guidance system was not accurate enough for maneuvering targets. In addition, the axisymmetric inlet would unstart if the missile was experiencing high angles of attack followed by loss of control. This missile became obsolete when the Navy developed the Combat Air Patrol (CAP) tactic, where fighters with short range air-to-air missiles orbit the task force at all times.

ASMP - This air launched French ground attack missile is still in service. It employs the integrated rocket ramjet propulsion concept. This missile is 14 feet long, weighs 1,900 pounds, has a speed of approximately Mach 4, and, at 190 miles, a range beyond the Exocet.

Kh 31 - This air launched Russian long range air-to-ground missile is also still in service and also employs the integrated rocket ramjet propulsion concept. It is 15 feet long, weighs 1,430 pounds, and has a range of 100 miles at Mach 4.5.

2.2 Shortcomings of Currently Operational Conventional Propulsion Missiles

With the exception of the few operational ramjets, tactical missiles fall into two classes with regard to propulsion.

2.2.1 Rockets
   a) Rocket propulsion is highly developed and relatively inexpensive
   b) Rockets are typically limited to ranges less than 100 miles
   c) Extending the range increases the missile weight exponentially

2.2.2 Cruise Missiles
   a) Powered by small turbojets, these subsonic missiles have ranges in the hundreds of miles and precision guidance systems
   b) Their main drawback is their subsonic speed leading to excessive time-to-target and intercept vulnerability
   c) Their high costs, $1,000,000 plus per missile, is an issue.

2.3 Shortcomings of Previous Ramjet Powered Missiles

Significant improvements have been made since the late 1950s and early 1960s but the application of ramjet missiles is still limited by shortcomings relative to rocket powered missiles or subsonic cruise missiles
   a) Excessive time-to-target for short range targets (low initial average velocity)
   b) Inadequate maneuverability due to angle-of-attack limits

Vehicles must overcome the limitations of the previous generations of ramjets and to provide viable systems in the future.

3. RAMJET MISSILE BOOSTERS

Booster type and configuration selected has a direct impact on ramjet missile configuration. Three basic options can be defined for providing this ramjet booster function. They are defined as the boosted ramjet, integral rocket ramjet (IRR) and the self boosted ramjet. Recognizing the positive and negative aspects of these three basic types of boosters is necessary for near term system design and to define the technical challenges to be overcome for future improvements. A brief discussion of these follows.

As part of these discussions, two state-of-the-art booster designs will be discussed: 1) A high performance integral rocket ramjet nozzleless booster suited for volume-limited air-launched missile applications and 2) The strutjet self-boosted ramjet/scramjet engine which is currently better suited for larger diameter missiles and launch vehicles. Hybrid propulsion (liquid or solid) has promise for increased performance over a solid propellant booster, but has yet to be demonstrated and will be discussed in future presentations.

3.1 BOOSTED RAMJET

This option uses a separate booster stage(s), typically a solid rocket motor, to accelerate the ramjet stage to the required Mach number resulting in a multi-stage system (tandem or parallel) with some very distinct advantages and disadvantages:

a)   Using solid propellant improves logistics and mitigates liquid safety issues
b)   Performance may be improved by minimizing the amount of mass and inertia being carried through the mission
c)   The high drag of the non-functioning ramjet engine requires a large booster stage
d)   Two stage missiles are usually longer and heavier than single stage missiles
e)   Dropping the first stage may be unacceptable when flying over friendly territory.

The selection of a boosted ramjet configuration is highly driven by mission requirements, missile envelope and policy regarding missile ejecta.

Separating a tandem booster allows you to minimize the amount of mass carried on the missile, but adds functional and aerodynamic complexity. In addition, for parallel boosters, the additional negative aspect of increased missile frontal area and surface area drastically increase drag requiring a larger booster(s). Although not optimized for ramburner geometry the integral rocket ramjet has improved packaging and less complexity.

3.2 Integral Rocket Ramjet Solid Propellant IRR Booster Development

The Phillips Laboratory and ARC have been working towards providing tactical booster designs for ramjet missiles for the past fifteen years. The work has concentrated on providing a design which is compatible with air-launched missile requirements (no debris), conforms to the ramjet combustor geometry and meets performance and service life requirements. This section describes work performed to develop a reduced-smoke nozzleless booster design for the VFDR engine currently in Advanced Development by the U.S. Air Force. In the process, ballistic and structural models and analysis techniques were developed specifically for the nozzleless motor configuration which significantly advanced current design capabilities.

3.2.1 BACKGROUND

The straightforward objective of the IRR booster development was to design and demonstrate a high-performance, reliable booster which can meet all air-launched missile environmental requirements. Attendant to the main objective is the desire to develop analysis techniques uniquely suited to nozzleless boosters, adequately treating the non-standard interior flow-field and grain load conditions. A third objective was to treat producibility as a high priority since high-volume production rates would be required for a potential production system. This means minimizing the amount of processing steps and labor involved in manufacturing and loading the booster grain, as well as reducing the sensitivities of the motor design to variations in the manufacturing process.

An immediate application has been presented for this motor technology in the VFDR, currently in Advanced Development by the USAF. This ramjet engine has been under development for many years as an improved propulsion system

TABLE 2. RECENT IRR BOOSTER DEVELOPMENT HISTORY

Program	Description
Booster for the Tactical Ramjet program.	Heavywall motors were used to investigate full-scale performance. A high-burning-rate Catocene-catalyzed propellant was developed and successfully stabilized; however, problems with bore cracks at -65°F were experienced.
Ducted Rocket Booster Program	A flightweight FEP barrier system was developed, and a pyrogen igniter was utilized to reduce ignition shock and motor failure at ignition. The grain capability was limited to -45°F, short of the -65°F requirements
Ducted Rocket Propulsion Technology Validation Program	The design was qualified for flight testing in a Pre-Flight Rating Test (PFRT) series conducted with a low temperature limit of -45°F. Additional motor geometry was also defined such as port covers, cases, ramjet nozzle, insulation and the closure.
Alternate Booster Concepts Program	This program included a dual-concentric grain design which reduces ignition pressure extremes and improves grain structural load conditions, the development of a high-rate, 47 percent total solids HTPB/AP reduced-smoke propellant formulation with superior physical properties, demonstration of the -65°F requirement.
Variable Flow Ducted Rocket Program	Replacement of the FEP barrier system to simplify manufacturing further and increase propellant loading, replacement of the Catocene burning rate catalyst with Butacene, increase motor performance to exceed delivered total impulse requirement.

for an advanced air launched missile. The VFDR missile inboard profile is shown in Figure 2. The ARC program sought to develop and demonstrate a producible motor design which meets all engine requirements specified for the VFDR ramjet engine. A summary of the development history is shown above in Table 2.

4.2.2 Nozzleless IRR Booster Design Requirements

Challenging mechanical and performance design requirements have combined to create a restrictive design window. As the name implies, the booster motor is now part of the missile structure, with the accompanying system level-requirements imposed. A summary of design requirements considered is provided below.

4.2.3 Mechanical Requirements:

Internal Launch Hook Reinforcement: The location of the VFDR aft hook is dictated by launcher interfaces and is located in the thin-wall region of the combustor case. Because of this, structural reinforcement is required on the case inside diameter, creating an asymmetric internal surface.

Port Covers: Port covers are used to seal the inlet opening during booster operation. The design of these covers can influence the booster grain configuration locally since the cover provides support to the grain during boost.

Thermal Protection System: A char-retention system is required to retain charred internal case insulation during ramjet operation. Typical solutions are a steel wire grid embedded in the insulation, stamped ribbons or a collapsible steel cage.

Booster Igniter: A significant amount of testing has been performed to establish a viable head-end pyrogen igniter. The igniter was designed to minimize ignition delay and to keep the pressurization rate low enough to prevent bore cracking on ignition at -65°F.

Ramjet Nozzle: The ramjet nozzle geometry is determined by airbreathing operation (primarily the throat area) and booster grain design (entrance region and exit cone). The ramjet entrance region has been optimized for erosion resistance. The length of the nozzle is determined by the recess in the case to accommodate the missile fin actuation system. The optimum nozzle exit angle is closely coupled to the booster grain exit angle to produce the optimum expansion contour as the propellant grain burns back.

Propellant: The booster propellant was required to be a Hazards Classification 1.3, reduced-smoke formulation.

4.2.4 Performance Requirements

Maximum Expected Operating Pressure (MEOP): For the VFDR design, the critical case load condition is stiffness at maximum free-flight temperatures. By designing the booster to limit initial pressurization rate, the maximum pressure was kept low enough to avoid becoming a design driver.

Thrust: The booster thrust output is limited primarily by the missile axial acceleration limit. A sufficient initial thrust is also required to minimize rail launch tip-off loads and to clear the aircraft during certain maneuvers.

Action Time: In order to minimize the aerodynamic losses associated with a longer, lower-thrust boost profile, a short booster action time is desirable. High propellant burn rate is critical.

Tailoff: In order to transition efficiently from rocket to ramjet operation, the time at which thrust is less than drag must be minimized. Part of this time is attributable to booster tailoff, when internal pressures are too low to produce sufficient thrust, yet too high to allow opening of port covers and gas generator ignition.

Total Impulse: The integral of the thrust vs. time curve as specified by a system prime typically.

Temperature: The environmental conditioning requirements for the booster are: satisfactory operation after a hot soak at 63°C (145°F) for 45 days, after cold soak at -54°C (-65°F) for a period of five days, firing with the maximum thermal gradient across the propellant grain. Captive-carry temperature profiles were also imposed. The motor was also required to perform satisfactorily at a soak temperature of -65°F after being subjected to three polar-day temperature cycles.

4.2.5 Motor Engineering Design

The booster propellant ballistic properties and grain design were chosen to maximize motor average pressure while observing the performance limitations described above. The design goal is to remain as close as possible to the maximum thrust limit through manipulating propellant burning rate, pressure exponent and grain geometry. The principal load conditions imposed on the propellant and bondline occur during:

1) thermal cycling between 145°F and -65°F and 2) during hot pressurization. The latter results from the large pressure drop at the nozzle end of the motor. During a hot firing, this pressure drop is at a maximum and the propellant shear strength is at a minimum. Therefore, a propellant stiffness suitable for use in the nozzleless booster must have sufficient shear strength to prevent shearing out the aft end of the grain, yet be soft enough such that resulting bondline stresses do not fail the outer-diameter propellant-to-insulation bond during thermal cycling. The ramjet nozzle is installed in pieces prior to case insulation and barrier coating, creating a transition from insulation to silica phenolic. A design was developed in which the insulation is gradually tapered into the nozzle region, resulting in a substantial processing improvement, as well as a reduction in local stresses.

In order to maximize booster performance within the design constraints of the system and insure adequate safety margins, concurrent ballistic trade studies were conducted. The design of the booster grain configuration was determined by conducting a parametric trade study on several ballistic parameters including:

    a) Inner Bore and Main Grain Propellant Burning Rates
    b) Inner Bore and Main Grain Pressure Exponents
    c) Propellant Total Solids Loading
    d) Grain Bore Diameter
    e) Exit Cone Angle
    f) Exit Cone Length
    g) Forward Grain Termination
    h) Inner Grain Thickness

Many different propellants were considered. To date, the high burn rate Butacene propellant as reported in Ref 2 is one of the most attractive. Compared to the nominal thrust time profile in Figure 4, the Butacene case in Figure 5 provides a longer sustained high burn rate and thrust. In the future the Integrated High Payoff Rocket Propulsion Technology Program (IHPRPT) is developing new propellants delivering 15percent higher delivered impulse.

The Nozzleless Booster Internal Ballistics code developed for the USAF by ARC was used to optimize the performance of the motor analytically. Other empirical information was used to supplement the analysis such as exit cone effects,

propellant erosive burning, and combustion instability.

4.2.5 Motor Processing
A barrier system is required between the DC93-104 silicone-based ramjet insulation and the propellant. The first system developed was composed of an adhesive (DC93-076) and a chemically-etched Teflon FEP film. Additional work was performed on an alternative migration barrier to replace the FEP film. These efforts succeeded in developing a paint-on barrier coat which simplified to manufacturing process, and resulted in a thinner layer leaving more volume for propellant.

3.2.6 Demonstration Motors
Demonstration testing in heavywall and flight-weight hardware has been conducted, including environmental conditioning and motor firings at hot and cold temperature extremes. The results of over 100 full scale tests have validated the design and manufacturing processes, and demonstrated motor operability from -65°F to 145°F.

The primary shortcoming of the nozzleless booster to date has been the low- temperature (-65°F) storage and operation. This problem has been solved and demonstrated by temperature cycling one motor six times and firing at -65°F, and temperature cycling another motor 12 times and firing at 70°F. The design requirement is three cycles.

3.3 Self Boosted Ramjet
In this option the boost rocket is retained after burnout. If the boost rocket is independent of the ramjet, the problem of dropping the spent stage is solved by carrying it along for the rest of the mission. When the boost rocket is integrated into the ramjet engine the combined engine (Rocket Based Combined Cycle, RBCC) is called a ducted rocket or ejector ramjet. This approach has the advantage of lower drag and the potential for higher thrust during boost than any of the other options since the ramjet is always functioning with increasing effectiveness.

4.3.1 Benefits Of RBCC Powered Missiles
RBCC propulsion for use in high speed aircraft and space launch applications has been explored for over 30 years. Figure 6 shows all combined cycle and RBCC engine options. The simplest configuration is the rocket/ramjet sometimes

referred to as the "Ejector/Ramjet" which in higher speed applications includes the scramjet mode. The rocket in the RBCC is not merely the booster for the ramjet, it is an integral part of the engine and operable at any time in the mission. Its thrust level and mission velocity increment contribution is selected for mission performance optimization. This gives the missile designer more freedom than before when defining missile acceleration, velocity and range. One example of an operational benefit of an RBCC powered missile is the ability to refire the rockets to provide increased speed or maintain energy during high g-maneuvers.

The "Strutjet" is the Aerojet version of this type of engine. In recent publications (Ref 3,4,5) the application of hydrogen fueled Strutjet engines for space launch is described. Since 1992, in cooperation with Martin Marietta, the Strutjet's application for tactical missiles using storable propellants was explored. Although the propellants and design specifics differ, these Strutjet engines share a common design philosophy.

Aerojet's Strutjet engine represents a significant departure from other airbreathing engine concepts, because improved off-design inlet performance and lighter engine weight. The Strutjet inlet is based on the well characterized sidewall compression inlet first introduced by NASA Langley Research Center. In the Aerojet engine the struts are integrated in the inlet such that each flow passage between two struts behaves like the original Langley inlet with sidewall compression. The term "strut compression" is also often used in this context, meaning sidewall compression between the struts. The most significant benefit derived from this inlet is geometric contraction and isolation in a shorter length than conventional inlets. This leads to an engine that is easier to integrate into the vehicle, is lighter weight, has less drag, and absorbs less heat.

Aerojet's Strutjet engine is classified as a self boosting ramjet engine. One discriminator relative to other self boosted ramjets is the retention of the rocket function after the boost phase is complete. The ability to re-fire the rockets give the missile significantly greater mission flexibility as shown in Figure 7. All propulsion elements are contained within a single engine using common propellant feeds, cooling systems, and controls.

The rockets provide the bulk of the thrust for takeoff and acceleration to ramjet takeover speed. A conceptual Strutjet is shown in Figure 8. The rockets are contained in compact struts placed within the ramjet duct as shown in Figure 9. This degree of functional integration is possible with the platelet[4,5] construction technique. The air drawn into the engine by the ejector effect at subsonic speeds and rammed in at higher speeds provides significant thrust augmentation during boost. The inlet uses struts as the last stage of compression (Figure 10). Strut compression is characterized by "soft start", low spill drag, and good capture and recovery efficiencies. The "soft start" results from the increased openness of the inlet on the cowl side which allows for a gradual decrease in spillage with increasing Mach number. The inlet is designed with minimal internal contraction to permit inlet starting at Mach numbers as low as 2.5. This in turn provides smooth increases in captured air mass and pressure recovery.

As the air mass flow increases with increasing speed, supplemental fuel is injected through ramjet injectors to maximize engine performance (Figure 11). Ramjet contribution occurs gradually starting at Mach 1 with full takeover at Mach 2 to 4 depending on mission requirements. The rockets can be left on longer to reduce time of flight to short range targets or shut down early to save propellant for an exoatmospheric dash.

Shutting down the rockets provides the full benefit of the ramjet mode of operation with an specific impulse approaching 1500 seconds. The transition to ramjet operation is smooth and reliable. Unlike typical boosted ramjets the Strutjet is operating from launch and the fuel injection system is functioning prior to the cutoff of the rockets. The transition to ramjet operation is accomplished by shutting the rockets off and ramping the ramjet fuel flow to match the loss in fuel no longer provided by the rocket plume.

In summary, the benefits of the Strutjet are:
a) Highly Integrated Design And Reduced Engine Weight Facilitate Integration Into The Vehicle
b) High Boost Phase And Very High Cruise Specific Impulses Providing Up To Four Times The Range Of Rocket
c) Increased Mission Flexibility

- Up To A Ten Fold Reduction In Time Of Flight Of A Cruise Missile
- No Dropped Stage Or Engine Components
- High Maneuverability Due To Rocket Restart Capability

4.3.2 Strutjet Engine Test Data

During the period from 1992 through 1995 Aerojet carried out a test program which systematically explored the Strutjet propulsion system over Mach number and flight altitude ranges of 0 to 4 and 0 to 100,000 feet, respectively. In over 200 hot fire tests the concept of a Strutjet powered long range missile has been proven. The following achievements are noteworthy:

a) The strut inlet provides adequate air capture, pressure recovery, and unstart margin
b) The integration of compact high chamber pressure rockets using gelled hypergolic propellants into a strut is structurally and thermally feasible
c) An engine flowpath geometry suitable for all modes of operation has been established and its thrust and specific impulse evaluated
d) Static sea level thrust augmentation of 13percent is achieved due to the interaction of air ingested with the fuel rich rocket plume
e) The ducted rocket thrust increases with increased flight Mach number. At Mach 2.45 and an altitude of 20,000 feet the thrust increase is over 100percent
f) At Mach 3.9 and 40,000 feet the ramjet thrust exceed the rocket sea level thrust
g) Dual mode operation with a thermally choked nozzle has been demonstrated
h) Hypergolic pilots have been found to be essential for achieving high efficient combustion at high altitudes and with short combustion chamber
i) 90 percent combustion efficiency has been demonstrated in a combustor only 30 inches long
j) Efficient operation has been demonstrated with a rapidly expanding engine geometry

More information regarding these achievements is provided in the following.

4.3.3 Inlet Test

A typical Strutjet inlet configuration which was sponsored and evaluated by NASA Lewis Research Center is shown in Figure 12. Tests verified excellent compression performance. Capture efficiency is 95 percent, and pressure recovery including the isolator shock train is over 30 percent. A pressure rise of over 100:1 is generated without unstarting. At greater than Mach 4 the unstart margin can still approach 100 percent. High insensitivity to boundary layer ingestion has also been observed.

4.3.4 Rocket Tests

For this test series each strut contained three water-cooled rockets. These rockets are designed for a useful cycle life of 100 firings. After the 40 hot firings performed to date no significant deterioration of the chamber has been observed. The injector pattern consist of 36 pairs of fuel and oxidizer elements arranged in concentric. The outermost ring with 24 elements provides fuel film cooling to the chamber. The characteristic parameters of this injector-chamber design are summarized in Table 3.

Table 3. Strut Rocket Design Parameters

Parameter	Unit	Nominal Design	Operation
Mixture ratio	-	1.6	1.4
Chamber Pressure	(psia)	2,500	1,600-2,000
Thrust	lbf	1,000	600-700
Expansion Ratio	5:1 and 11:1		5:1 and 11:1

The baseline rocket performance is established to evaluate subsequent performance improvements due to the ejector effect of the ducted rocket.

4.3.5 Strutjet Test Rig

The rig representing the Strutjet engine is designed as a sandwich with hinged side wall sections allowing the duct geometry to be adjusted at 12 inches intervals. The duct section housing the strutrockets has a fixed geometry of 4.0 inches x 6.6 inches. The isolator section in front of the strut duct can be connected to either a bell mouth for static tests or to a hydrogen vitiated air heater. Two struts are positioned in the strut duct dividing the flowpath in the inlet into three channels.

4.3.6 Sea Level Static Ducted Rocket Tests

For these tests the isolator section in front of the strut duct is connected to a calibrated bell mouth. The duct geometry is varied to find the configuration giving the maximum thrust. The primary variables explored are the initial divergence in the mixing/diffusion section of the engine and the throat area for the ram burner. Sensitivities

of rocket chamber pressure, mixture ratio, and rocket nozzle expansion ratio are also established. Figure 13 is a photo taken looking through the bell mouth showing the intense afterburning of the rocket plumes.

Thrust enhancement is a strong function of the ram burner throat area and a somewhat weaker function of the ramburner duct geometry. More thrust than the reference rocket only test (13 percent) are obtained in test 213 with a throat area of about 32 square inches and a duct geometry of 3^0-3^0. Data analysis indicates the oxygen content of the induced air is completely consumed in approximately 4 inches from the rocket bases.

Operation at a chamber pressure of 2,000 pounds per square inch generated more thrust than operation at 1,600 pounds per square inch, but airflow and thrust augmentation were reduced by 19percent and 3percent, respectively. The area ratio of 11:1 generated 12 percent higher induced airflow and 6percent more thrust than the lower area ratio of 5:1. Also, more airflow and higher thrust result from more stoichiometric mixture ratios due to reduced thermal occlusion resulting from the afterburning scheme.

4.3.7 Direct Connect Ducted Rocket Tests
For these tests the isolator section in front of the strut duct is connected to a hydrogen vitiated air heater with a Mach 2 nozzle. The duct geometry which provided the maximum take off thrust augmentation in the static test is maintained for all subsequent direct connect tests. Measuring the total duct pressure and assuming a particular inlet performance simulated flight altitude and flight Mach number can be determined. This techniques allows the evaluation of the engine as it flies along a simulated trajectory.

4.3.8 Direct Connect Ducted Rocket/Ramjet Test
The objective of this series is the performance optimization of the test engine operation in the ducted rocket and the ramjet modes over the Mach range suitable for SAM applications.

Figure 14 plots the net thrust in these Ducted Rocket and Ramjet tests. The ducted rocket tests are conducted with a fuel rich rocket mixture ratio. The excess fuel is sufficient to support 10 pounds per second of air flow. The simulated trajectory provides 10 pounds per second of air at approximately Mach 1.5. Tests

above Mach 1.5 are thus "lean" on an overall engine stoichiometric basis. Auxiliary fuel injection can be used to increase the thrust the engine can produce. The peak thrust is seen to occur at a simulated flight altitude of 23,000 feet and a Mach of 2.45 with 31 pounds per second of air being supplied to the engine. The peak thrust is over twice the rocket only value representing an augmentation of over 100 percent.

Ramjet tests were conducted at Mach numbers of 2 and higher without rocket operation to optimize the ramjet injector performance. The primary ramjet test variables of interest are the fuel and pilot injection parameters such as injector location and staging, piloted injection and flow rate, and mixture ratio. In support of the employed strategy which tries to minimize heatloads and hot spots, the main emphasis is placed on achieving a short combustor length.

4.3.9 Direct Connect Ram/Scramjet Test
Three scramjet test entries have been conducted. In the first tests the scramjet geometry was explored and high combustion efficiency with a fixed geometry over the Mach number range of 2-4 has been demonstrated. Mach 2 and 4 tests were conducted using JP-10 fuel.

With a slightly modified duct geometry of $0°$- $2°$, indicating a constant area for the first 12 inches down stream of the struts followed by a $2°$ double sided expansion. Autoignition was not achieved, but when the pilots were used for ignition and flame sustaining, stable combustion at 95 percent efficiency was observed. This in essence duplicated the performance previously achieved with the ethene with only a slight change in the duct geometry.

4.3.10 Hypergolic Pilot Test
The Strutjet design provides for a contact pilot at each injection point of the hydrocarbon ramjet fuel. This pilot derives its energy from the combustion of small amounts of the gelled rocket propellants which are injected and burned upstream of the hydrocarbon injection. Due to the hypergolic nature of the rocket propellants the pilots act initially as igniters and subsequently as flame sustainers allowing flight at high Mach numbers and high altitudes. The demonstration of this feature is verified by the data presented in Figure 15. At a simulated flight condition of Mach 4 and 40,000 feet of altitude JP-10 is ig-

nited by the pilot resulting immediately in a thrust increase of about 2,000 pounds. Combustion and thrust production are sustained as long as the pilot stays on. When turned off, the combustion ceases and thrust collapses.

4.3.11 Combustion Tests

The successful integration of a scramjet into a flight vehicle in general and into a missile in particular depends to a large degree on how long the engine has to be in order to provide high thrust and high specific impulse. These parameters are directly related to fuel-air equivalence ratio and combustion efficiency. The tested Strutjet configuration advanced the state-of-art in scramjet propulsion significantly. Combustion efficiencies between 90 and 100 percent are achieved with cold JP-10 over the Mach range of 2 to 4 and the equivalence ratio range from 30 to 100 percent. Furthermore, the presence of the contact pilot is essential under high Mach flight conditions. Paramount to all these positive results is the fact that 90 percent combustion efficiency can be achieved with a combustor only 30 inches long. This has far reaching consequences. Short combustor means: shorter lighter weight engine, reduced friction losses, reduced thermal loads, reduced cooling requirements.

5. SUMMARY AND CONCLUSIONS

Many ramjet propulsion types and configurations have been pursued. The three primary classes of configurations discussed in this paper are the boosted ramjet, the IRR booster and the self boosted Strutjet approach. Each approach has positive and negative attributes. Mission driven requirements and implementation dates will ultimately dictate which approach is appropriate to pursue for a given missile development effort. Greater detail was provided for two of the approaches being pursued and evaluated most recently in the United States. These are the IRR (solid) and the self boosted Strutjet.

The VFDR IRR booster work has successfully developed and demonstrated a nozzleless booster design meeting all tactical air-launched environmental and performance requirements. This was achieved through the development of a dual-concentric grain design, improved propellant properties and a sound engineering design effort. The motor testing demonstrated that a wide margin exists over the required environmental exposure, ensuring reliable operation in the field.

Ballistic and structural design methodologies have been established that provide a framework for the design of nozzleless motors, and an improved understanding of the fundamentals of the operation of such motors. Technology advances are needed in the areas of:
a) Innovative inlet design to minimize drag during non-ramjet operation
b) High burn rate, high energy propellant
c) High angle-of-attack inlet aerodynamics and configurations
d) Innovative non-ejecting nozzle designs

In three years of testing, a new high level of performance for tactical RBCC engines has been achieved. Although the development of this engine is far from complete, significant advances have been made:
a) The strut compression inlet has demonstrated its ease of starting, 95 percent capture efficiency, and good pressure recovery.
b) A simple storable propellant engine geometry capable of efficiently operating from takeoff to Mach 4 has been established.
c) Ducted Rocket thrust augmentation has been shown rising from 13 percent at sea-level to over 100 percent at Mach 2.45 and 20,000 feet.
d) The employed injection and piloting system has yielded efficiencies as high as 90 percent in as little as 30 inches.
e) High efficiency has been demonstrated in a rapidly expanding combustor at dynamic pressures below 1,000 pounds/square foot.
f) Preliminary missile and engine designs indicate significant mission payoff for the family of Strutjet engines.

Technology advances needed for the RBCC and Strutjet specifically include:
a) Lightweight componentry
b) High angle-of-attack inlet aerodynamics and configurations
c) Integrated flight vehicle testing

In conclusion, ramjet booster designs have significant impact on missile cost, performance and physical envelope. Continued booster technology development will continue to make hypersonic missile systems increasingly more practical in the future.

Active Cooling of Fully Variable
Hypersonic SERN Nozzles

R. Lederer

MTU Motoren- und Turbinen-Union München GmbH
Dachauer Strasse 665
80995 Munich, Germany

Abstract

Within the last few years MTU has made a great development effort towards high-speed nozzle design, manufacturing, hot-gas testing and test analysis as part of the German Hypersonics Technology Programme.

Within the framework of this programme two actively cooled nozzles were designed, fabricated and tested in 1993 and 1995, respectively. Whereas the first nozzle was cooled with cryogenic hydrogen, gaseous hydrogen was used for the latter.

In this paper the associated nozzle design, fabrication and test effort will be described and highlighted. Focus will be placed on the experience gained by testing the actively cooled, fully variable nozzle structures.

1 Introduction

At the beginning of the German Hypersonics Technology Programme (GHTP) in 1988 a comprehensive validation and verification philosophy and hardware matrix was elaborated, Fig. 1. According to these plans four different classes of subscale nozzles were identified. Each group covers a major technological area (aerodynamics, cooling etc.) and further additional aspects. Furthermore, each test campaign has been prepared carefully by definition of the investigation goal, the expected physical results and the applied measurement means. The tests were time-scheduled with increasing complexity.

	Subscale Nozzles (Cold Flow)	Subscale Nozzles (Hot Gas Flow)	Technology Demonstration Nozzle	Integration Model
Aerodynamics	▨	☐	☐	☐
High Temperature, Thermodynamics		▨	☐	
Cooling System		☐	▨	
Structures, Materials		☐	▨	
Integration				▨

☐ Additional Aspects   ▨ Focus

Fig. 1   Nozzle Test and Evaluation Matrix

Whereas the focus of phase 1a (1988 - 1990) was on basic technological work (e.g. cold flow nozzle tests), within phase 1b (1990 - 1993) representative component hardware was designed and tested, e.g. the cryogenic cooled demonstrator nozzle TDN1, see /2-5/. Phase 1c lasted from 1993 until 1996. The goal was to extend the hypersonic nozzle demonstration further on with

○ Throat adjustment during hot gas firing
   (i.e. variable actively cooled structures)
○ Altitude simulation

Tests were successfully carried out in late 1995 /1/. In addition, free jet testing of a complete ram-jet engine (intake, combustor and nozzle) was planned at the AEDC APTU facility, but cancelled due to programmatic reasons and funding constraints.

2 Aerodynamics & Design

As a prerequisite fundamental knowledge of the relevant nozzle working conditions - normally derived from performance calculations - is mandatory. These are listed below (Fig. 2).

Flight Ma (-)	Throat Area (m²)	Tt_7 (K)	pt_7 (bar)
3.6	0.110	2546	1.97
3.9	0.093	2541	2.68
4.5	0.065	2658	2.86
5.5	0.048	2793	4.41
6.9	0.031	3010	7.16

Fig. 2   Typical Hypersonic Nozzle Working Conditions

Starting point for the nozzle design is the definition of the aerodynamic contours. This normally is accomplished by 2D-MOC (method of characteristics) codes corrected by Euler and/or Navier-Stokes codes. Additionally, installation effects (mainly base drag during transonic) have to be included. Depending on the flight path and the intake recovery characteristics a variation of the nozzle throat area and the expansion ratio is required for optimum performance. A typical resulting nozzle flap schedule is shown in Fig. 3. Note that with increasing flight Mach number the nozzle throat area decreases whereas the flap 2 angle (expansion ratio) increases.
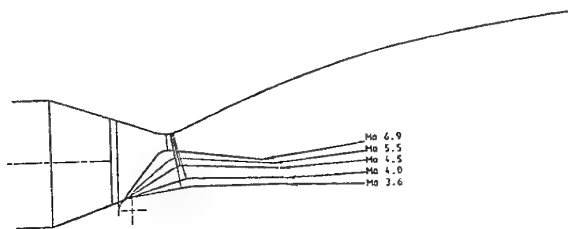
C9-2

Fig. 3   Aerodynamic Contours

These contours have to be transformed (after thermomechanical analysis) into an actual design. Due to the 2D-design special emphasis has to be placed on the hot gas sealing concept. The nozzles discussed here feature ceramic (SiC) strips. The width of both nozzles is 0.33 m (TDN1) and 0.5 m (TDN2) respectively. Fig. 4 shows the general arrangement of the TDN2 nozzle.
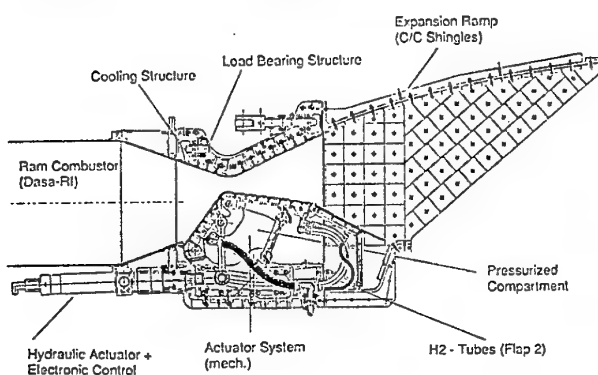

Fig. 4   General Arrangement (TDN2 Nozzle)

3 Cooling & Heat Management

The complete nozzle structure including the expansion ramp is heavily loaded by the elevated temperatures and pressures. Therefore, an efficient and advanced cooling system has to be elaborated. With hydrogen on board an excellent coolant with a favourable heat sink capability (which exceeds ten times the value of air) is available.

The cooling system design objectives are

O lowest possible coolant consumption
O lowest possible weight
O safety

The thermomechanical design point is the maximum flight Mach number, where maximum heat transfer is reached locally.

The expected temperature distribution along the nozzle favour two separate thermomechanical concepts:

• Actively cooled structure for the subsonic and the initial supersonic part of the nozzle flow

• Uncooled structure for the expansion ramp. The preferred high-temperature resistant material is fibre-reinforced ceramics. Both nozzles feature an uncooled C/C expansion ramp with oxidation barrier coating.

The heat transfer coefficients (hot gas side and coolant side) are shown in Fig. 5. On the hot side a maximum is reached shortly before the nozzle throat with values in excess of 1400 W/m^2/K, whereas downstream the heat transfer decreases strongly due to the pressure drop. Upstream heat transfer is also somewhat lower. It is important that radiation is taken into account. Heat transfer on the coolant side is even higher due to the favourable properties of hydrogen. Hydrogen outlet temperatures were restricted to 900 K.
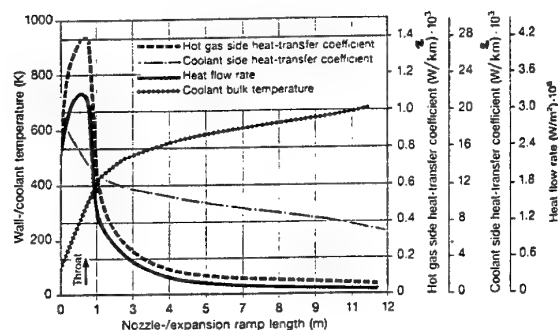

Fig. 5   Heat Transfer along the Nozzle

To reduce coolant consumption a thermal barrier coating based on zirconia oxide was introduced.

On the basis of the above statements a cooling path consisting of parallel and serial elements was elaborated and the cross-section of the tubes was determined. Fig. 6 shows the analytical model of the cooling system.
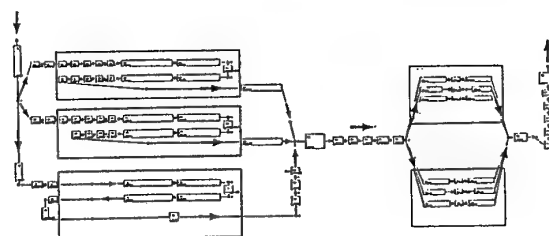

Fig. 6   Analytical Model of the Cooling System

Theoretically optimum shapes have to be reflected by feasible fabrication techniques. As an example two variants of possible fabrication techniques were given in Fig. 7. The tubes of variant (a) were fixed by vacuum plasma spraying, whereas variant (b) shows machined channels joined with a cover plate by electron beam welding. Other techniques like brazing were also investigated /5/. Finally, variant (b) was chosen.
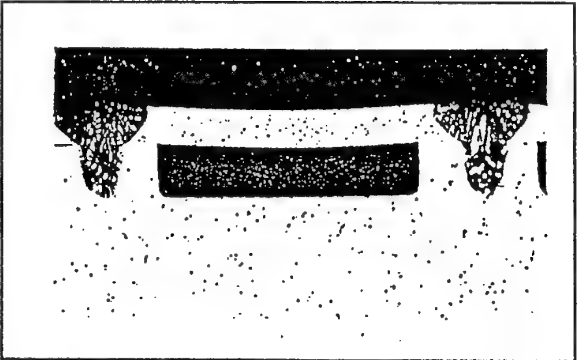
(a)
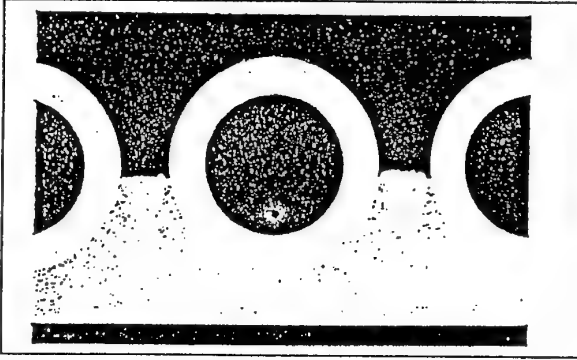
(b)

Fig. 7   Cooling Structure Fabrication Techniques

With the results of the cooling path calculations (temperature rise, pressure drop, cooling side heat transfer) 3D temperature calculations of the cooling structure itself were performed and used as input for the stress analysis. As a typical example the temperature distribution inside the upper wall (design point) is plotted in Fig. 8. As expected, the maximum wall temperature is located at the nozzle throat. Note, the use of the thermal barrier coating allows very high wall temperatures which exceed 1450 K. The gradient between gas side and the cooling channels is very high.
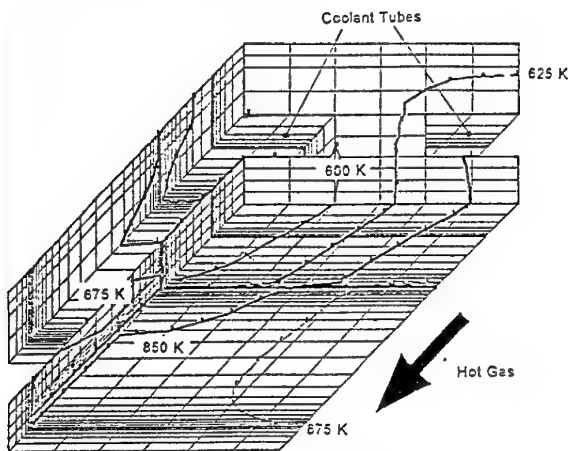
Fig. 8   Temperature Profile (Cooling Structure)

As stated in chapter 1 it was one major goal of the test campaigns to compare calculated values for the cooling system with measured data.

Fig. 9 shows a comparison of coolant temperatures and pressures at various locations. Whereas a ΔT of 379 K was predicted for the overall system, the measured value was 385 K, i.e. in very good agreement. The measured outlet pressure of 12.3 bar (predicted value 12.5 bar) indicated that the overall loss assumptions were well modelled.

A very low coolant consumption was achieved which validates the high-efficiency approach adopted for the design.

Temperature (K)

Location	Nozzle Entry	Sidewall Entry	Nozzle Exit
Calculation	50 K	347 K	429 K
Measurement	41 K	387 K	426 K

Pressure (bar)

Location	Nozzle Entry	Sidewall Entry	Nozzle Exit
Calculation	19.3	14.6	12.5
Measurement	19.3	15.3	12.3

Fig. 9   Comparison of Measured and Predicted Data

The influence of nozzle flap variation on the thermal system is illustrated in Fig. 10. During the plotted test run the nozzle flap changes from the Ma=4.5 to the Ma=6.9 position. It is obvious, that by decreasing the throat area and increasing the nozzle pressure flap 1 is unloaded whereas flap 2 is additionally loaded. The overall heating decreases slightly.
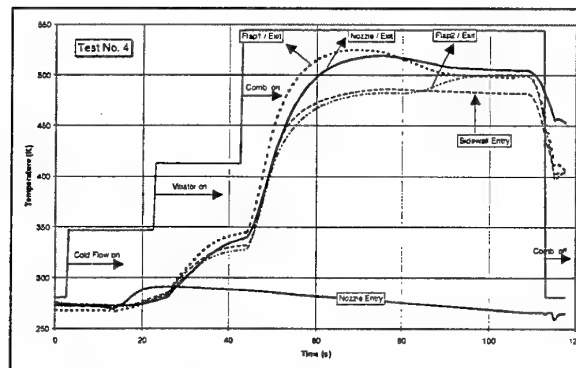

Fig. 10 Cooling Fluid Temperatures over Time

For the uncooled expansion ramp two measurement methods, namely

O Pt/Rh-Pt thermocouples, and

○ infrared screening

were applied for wall temperature measurements with the latter allowing measurement of the complete visible area in one shot.

The ramp typically reaches steady-state conditions in about 60 seconds. A comparison with respect to the start-up and shutdown periods is given in Fig. 11. It should be noted that the infrared camera measures the real spot temperature whereas the thermocouples cover a greater area which results in a much slower response. This approach illustrates how results can be cross-checked by using different methods of measurement. Note, that the wall temperature exceeds 1500 K.
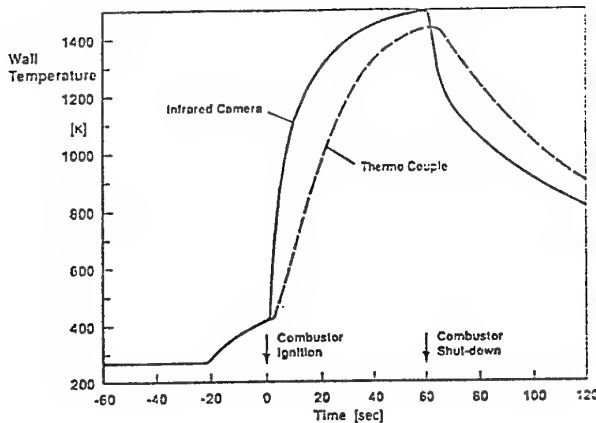
Fig. 11 Wall Temperature (Expansion Ramp)

The combined coolant flow rate of all hydrogen consumers (nozzle, combustor and others) should not exceed the flow rate necessary for cumbustion to avoid penalties of the take-off weight and the vehicle performance. In deed the calculations show that for the ascent phase no additional hydrogen for cooling purposes is needed, Fig. 12. However, in the phase of the nearly unpowered decent the hydrogen flow rate necessary for cooling exceeds the hydrogen demand for combustion.
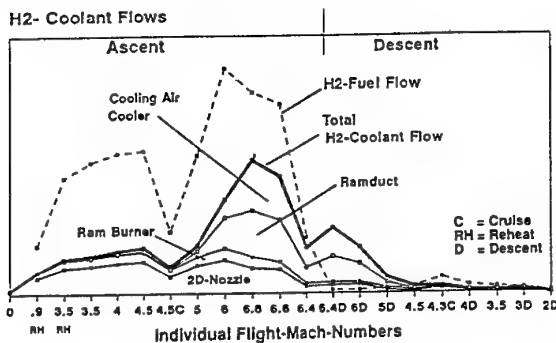

Fig. 12 Hydrogen Cooling Requirement
(Overall Propulsion System)

4 Materials & Structures

Apart from the thermomechanical design the fabrication process is a major challenge. Preferred materials for the cooling structure are high-temperature resistant and ductile alloys such as C263. The cooling channels itself were milled and EB-welded. The next step consisted in bending the two flaps and the upper contour. Critical aspects with regard to the feasibility were the cold-forming characteristics of the base material and welded joints. Finally, on the hot gas side a ZrO_2 coating was applied by low-pressure plasma spraying (LPPS). A nozzle flap - ready for final assembly - is shown in Fig. 13.
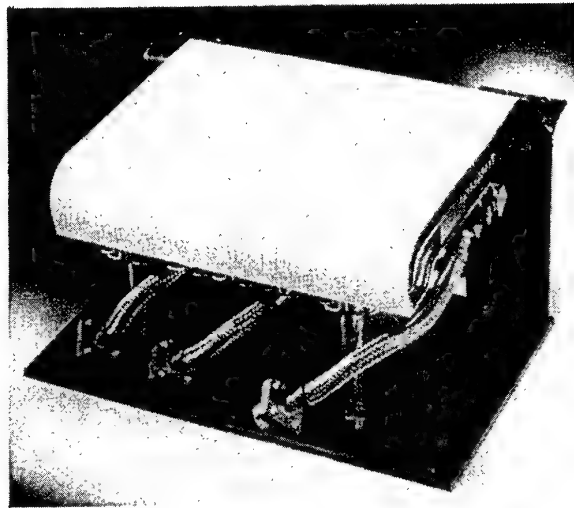

Fig. 13 Actively Cooled Flap (Hardware)

Furthermore, the complete hydrogen feeding system has to be designed carefully. As the coolant collectors are rigidly connected with the casing structure, a thermo-elastic link must be provided which is capable of compensating the relative movements between both structures resulting from the thermal expansion. This is accomplished by the use of inlet and outlet pipes (expansion sleeves) fixed by brazing (nickel-base braze).

Additionally, a great deal of effort was put on the flap feeding system design with the flaps moving during operation. Flexible feeding tubes were chosen inside and rigid tubes outside the nozzle.

Because of the presence of hydrogen sophisticated quality assurance methods were applied to avoid any leakage in the complex system. These include

○ pressure test with air (1.5 x nominal value)

○ pressure test with helium

O thermo-shocks of the complete cooling structure (i.e. heating and rapid cooling with liquid nitrogen)

O test of the EB-welding by optical means (thermography)

O measurement of the coolant flow rate

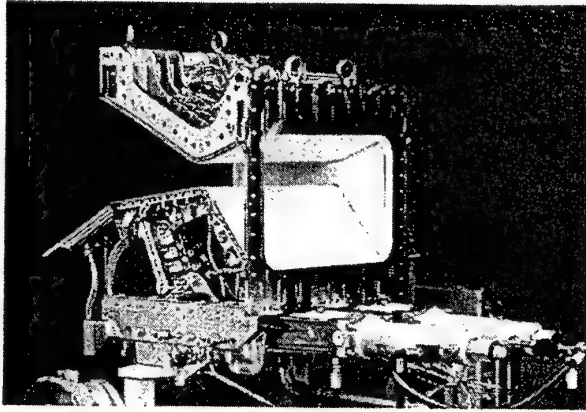Fig. 14 shows the TDN2 nozzle after final assembly (without expansion ramp)

Fig. 14 TDN2 Nozzle 'ready to test'

5 Test & Verification

After installation at the test stand and pre-testing of all subsystems the hot gas tests mark the major milestone after all efforts.

The test set-up for the TDN2 tests (at the DASA ramjet facility at Ottobrunn near Munich) is shown in Fig. 15 and 16. In this case a diffuser was added for high altitude simulation. The complete length was more than 12 meter.
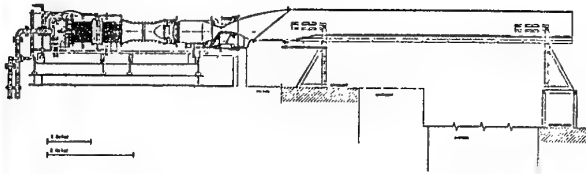

Fig. 15 Nozzle Test Set-up (incl. Diffuser)

A complex start-up and shut-down procedure was developed, applying a variety of 'red lines' for safety reasons. A typical test sequence with the main parameters total temperature, preheating level and total pressure versus time is shown in Fig. 17. The main flow (cold) starts at t=-50 seconds, preheating starts at t=-20 s, the cryogenic coolant flow starts at t=-2 s, combustor ignition occurs at t=0 s and the shutdown process typically starts at t=60 s, giving a total of 1 min of hot gas firing.
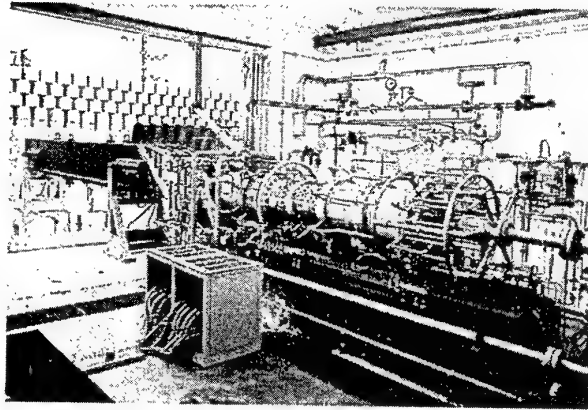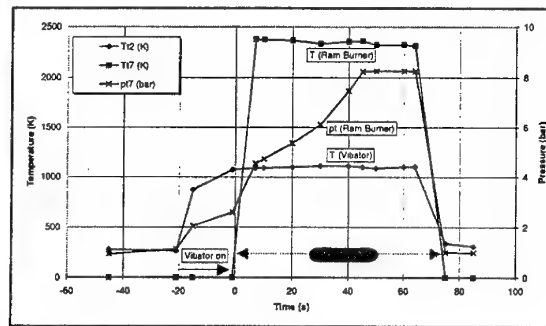

Fig. 16 Test Hardware at the Ottobrunn Facility

Fig. 17 Typical Test Sequence

The following highlights have been achieved in the test campaigns conducted:

O Simulated Ma points tested: up to Mach 6.9
O Throat variation during hot gas firing
O Hot gas temperatures up to 2600 K
O Nozzle pressure ratios in excess of 100

6 Concluding Remarks

Based on the above discussion, the following conclusions can be drawn:

❏ A successful nozzle development requires an interdisciplinary approach, especially between aerodynamics, heat management and structural aspects.

❏ Furthermore, it is necessary to combine hardware testing with analytical predictions and appropriate measurement techniques to maximise knowledge gained from testing

❏ Important milestones within the nozzle development were achieved with the successful testing of the two TDN nozzles in 1993 and late 1995.

❏ The next logical step would be free-jet testing of a complete variable geometry ramjet engine (as previously planned but cancelled later)

References

/1/ R. Lederer
Testing the Actively Cooled Fully Variable
Hypersonic Demonstrator Nozzle
AIAA-96-4550-CP, Norfolk/Va., USA, 1996

/2/ Heitmeir, Lederer et al.
Turboramjets and Installation
in: Developments in High Speed Vehicle Propulsion Systems, Progress in Astronautics and
Aeronautics, Vol.165, 1996

/3/ R. Lederer, W. Krüger
Testing the Hypersonic Technology Demonstration Nozzle - Results from the Test Campaign
1993/94
AIAA 95-6084, Chattanooga, TN, USA, 1995

/4/ R. Lederer, W. Krüger
Nozzle Development as a Key Element for
Hypersonics
AIAA 93-5058, Munich/Germany, 1993

/5/ K. Pirker, U. Knott
Technology Demonstration Nozzle for Mach 7
Turboramjets
94-GT-392, The Hague/Netherlands, 1994

/6/ P. Krammer et al.
German Hypersonic Technology Programme
Status: Air-breathing Propulsion
AIAA 93-5094, Munich/Germany, 1993

/7/ R. Lederer, F. Heitmeir
Hyperschalltechnologie-Programm
Status: Luftatmender Antrieb
DGLR Annual Meeting 1993, Göttingen/Germany

/8/ R. Lederer, R.R. Schwab, N. Voss
Hypersonic Propulsion Activities for SÄNGER
AIAA 91-5040, Orlando/USA, 1991

/9/ Ebenhoch et al.
Beiträge zur Entwicklung von Düsen für Hyperschallanwendungen in Zusammenarbeit
MTU/TU Dresden
DGLR Anual Meeting 1993, Göttingen/Germany

/10/ H. Hungenberg, K. Stursberg, H. Weyer
Thrust Nozzle Test Facility at DLR Cologne
AIAA 91-5024, Orlando/USA, 1991

/11/ C. Strobel et al.
Light-Weight Structures for Hypersonic Propulsion Systems, AIAA 93-5037, Munich/Germany,
1993

/12/ R. Lederer, J. Hertel
Exhaust System Technology
Space Course, TU München, Oct. 1993

EXTERNAL HYPERSONIC AERODYNAMICS:
STATE-OF-THE-ART AND FUTURE PERSPECTIVE

John F. Wendt
von Kármán Institute for Fluid Dynamics
Chaussee de Waterloo, 72
1640 Rhode-Saint-Genèse, Belgium

1. SUMMARY

An overview is provided on the activities, conclusions and recommendations of AGARD Working Group 18. Four issues were defined and addressed; shock wave boundary layer interactions, transition, real-gas effects, and rarefied-flow effects. Three status reports were prepared on calibration procedures for high-enthalpy facilities, extrapolation of wind tunnel results to flight, and real-gas facilities.

While considerable progress has been made in our understanding of external hypersonic flows through experiments in new facilities, advances in CFD, and impoved modelling of complex phenomena, more efforts must be devoted to this area if the risks of failure or overdesign are to be reduced to accceptable levels. Specifically, resources should be allocated to:
- resolve facility, computational, and modelling deficiencies
- accelerate the multiple facility/multiple computation strategy with standard models employed by Working Group 18.

2. INTRODUCTION

AGARD Working Group 18, "Hypersonic Experimental and Computational Capability, Improvement and Validation", was formed in 1992. Its objectives were two-fold:

1. to enumerate key issues in external hypersonics and to define and carry out experiments and corresponding computations relevant to each issue so as to identify present strengths and weaknesses. The issues selected were:
   - shock wave boundary layer interactions
   - transition
   - real-gas effects
   - rarefied-flow effects
2. to carry out analyses leading to status reports on:
   - calibration procedures for high-enthalpy facilities
   - extrapolation of wind tunnel tests to flight
   - real-gas facilities

Recommendations for future directions of research were formulated.

The results of these studies, carried out over a four-year period by approximately 36 persons (plus their local colleagues) at 21 establishments in seven countries on both sides of the Atlantic, will be published as an AGARD Advisory Report. (An initial version covering the final two years of activity, and carrying the same title as this paper, was published as AGARD Advisory Report 319, Volume I).

The purpose of this paper is therefore to summarise the activities, conclusions and recommendations of AGARD Working Group 18.

3. KEY ISSUES

3.1 Shock wave boundary layer interactions
The objective was to assess the capability for numerical simulation of two-dimensional and three-dimensional shock wave laminar and turbulent boundary layer interactions. Shock wave boundary layer interactions occur on many regions of a high-speed vehicle: flaps, elevons, canopy, protuberances, inlets, etc., When these interaction are strong, they give rise to locally high heating; uncertainty in predicting the location of reattachment will force the designer to adopt excessively heavy thermal protection systems. In addition, flap efficiency depends on the detailed pressure distribution; uncertainty will force an overdesign of the flap system. Thus, the risk associated with inadequate prediction of surface pressure and/or heat transfer is excessive vehicle weight. Obviously, if prediction methods do not identify the existence of a strong interaction, the vehicle performance may be severely compromised due to unexpectedly high ratios of heating.

Emphasis was placed on supersonic and hypersonic non-reacting cases; the ability of codes to predict quantities of interest to designers of high-speed vehicles, namely mean and fluctuating pressure, skin friction and heat transfer, as well as flowfield structure was assessed.

Three configurations shown in Fig. 1 were considered: the single fin, the double fin and the hollow cylinder flare. Thirteen test cases, for which high quality data with uncertainty estimations were available, were examined by an international group of researchers using the Reynolds-averaged Navier-Stokes (RANS) equations with turbulence models ranging from zero equation to full Reynolds stress equation formulations.
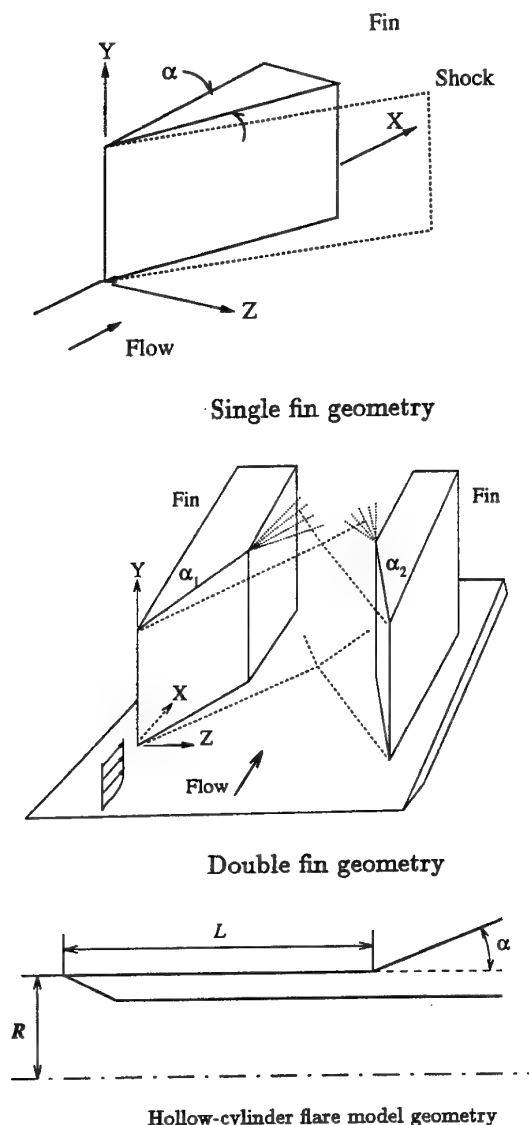
Single fin geometry

Double fin geometry

Hollow-cylinder flare model geometry

Figure 1: Geometries analyzed fin shock wave boundary layer interactions

An evaluation of comparisons between predictions and experiments concluded that laminar interactions can be predicted correctly , but only if very fine and carefully generated grids are employed. Turbulent interactions, if weak, were generally well predicted, especially for three-dimensional interactions. In the case of strong interactions, pressure distributions, mean Pitot pressure and flow-angle profiles were reasonably well-predicted for three-dimensional interactions. Primary separation lines were also generally well-predicted, but secondary separation was found to be very sensitive to the turbulence model employed and generally inaccurate. Furthermore, heat transfer and skin friction were poorly predicted in the case of strong interaction; differences of up to 100 per cent between computations and experiments were observed (see Fig. 2). Finally, no RANS computation was able to predict flowfield unsteadiness, neither for pressure nor heat transfer.
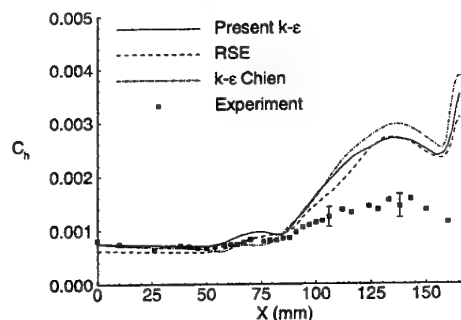

Figure 2: C_h on throat middle line for $7° \times 11°$ double fin

The principal recommendations for the future directions of research are:

- develop Large Eddy Simulation (LES) solvers for the prediction of fluctuating pressures and heat transfer. This activity may also aid in the development of better turbulence models for RANS.
- grid adaptivity strategies based on reliable error estimates must be improved to allow accurate and affordable computations.
- more accurate experimental data for flowfield Reynolds stresses and turbulent heat flux, as well as wall pressure and heat transfer fluctuations, are needed for validation purposes; present uncertainties are too large.

3.2 Transition

Hypersonic boundary layer transition remains a critical design issue because of the important impact on heating and therefore on the choice of a thermal protection system. As an example the U.S. STS experienced transition at a Reynolds number which varied by a factor of 5 depending on the flight Mach number. Furthermore, it has been stated that the uncertainty in transition location for some classes of vehicles can lead to an uncertainty of 20% in total vehicle weight.

It was also stated that a 1 mm uncertainty in thermal tile alignment can lead to a 5 km uncertainty in the altitude at which transition on a reentry vehicle will occur.

Also, a 10% error on T_{max} at reattachment on a flap, due to transition at an upstream location, will lead to a 5° error on the allowable flap deflection. It is clear that the risks due to an uncertainty in transition location and the resulting peaks in heat transfer and skin friction are significant and at present can only be compensated by heavier thermal protection systems.

Thus, the objective was to assess the state-of-the-art of transition prediction. Therefore, the objective was to assess

the state-of-the-art of transition prediction in hypersonic flows and to recommend new areas of research. A cooperative effort between selected centers in the NATO countries resulted in a review of recent research.

On the subject of streamwise instabilities, it was concluded that the e^N method has been further improved, that non-equilibrium chemistry can be included in transition models, that linear and non-linear parabolized stability equations (PSE) have been formulated and solved for selected cases, and a better understanding of bluntness effects has developed.

On the subject of crossflow instabilities, Fig. 3 shows the sensitivity of transition at small angle-of-attack on a cone. A transition correlation with a modified crossflow Reynolds number predicts experimental results on yawed cones. It has been shown that roughness near the attachment line has a strong effect in low disturbance environments and that weak surface curvature has a strongly stabilizing effect.

Deutsche Forschungsanstalt für Luft- und Raumfahrt e.V.
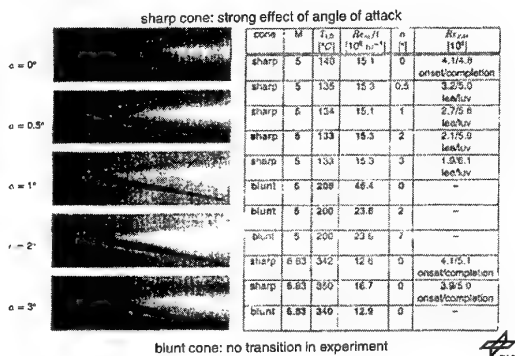
Synthesis of Results

Figure 3: Cross flow instabilities leading to transition on sharp and blunt cones

On the subject of Görtler instabilities, a non-linear parabolized Navier-Stokes equation has been developed. It seems that wavy surfaces have little net Görtler effect. Finally, it has become clear that Görtler instabilities are the most important control issue for the design of quiet supersonic nozzles.

Attachment line phenomena have been examined experimentally in different establishments and analytic efforts have extended incompressible results.

Finally, on the subject of receptivity, which is crucial for understanding wind tunnel experiments and designing quiet tunnels, some progress has been made with Direct Numerical Simulation at Mach 15.

The commonality of views from members representing all countries participating in WG-18 was that while an understanding of transition has improved, much work remains. Paradoxically, this subject, judged the most crucial aerodynamic issue in hypersonic flight, receives a low priority in many of the NATO countries.

The principal recommendations for future research are:
- accelerate development efforts towards quiet tunnels
- develop and implement LES and DNS methods for studies of receptivity and non-linear behaviour
- carry out well-documented experiments on 3D boundary layer to produce a data base for transition code validation
- the mechanism for roughness/protuberance-induced transition needs to be elucidated.

3.3 Real-gas effects

Real-gas effects have been shown conclusively to be largely responsible for the seriously inadequate prediction of body flap performance on the U.S. space shuttle. While this particular geometry seems to be well understood now, it is clear that real gas effects may play an important role in different hypersonic applications. The risks involved due to an inadequate knowledge of real-gas effects are that the integrity and performance of the vehicle may be severely compromised due to the additional weight of thermal protection systems.

The objective of this element in the activity of WG-18 was to identify the status of our simulation capability in the hypervelocity environment. In addition to a review of the current resources, both CFD and experimental facilities, a set of experiments was designed and carried out in different high enthalpy facilities on two basic models: a blunt-body, base flow configuration, similar to an aeroshell or AOTV shape (Fig. 4); and a blunted cone (the ELECTRE model). A variety of measurement techniques was employed and common test points allowed comparisons between facilities to be more useful.
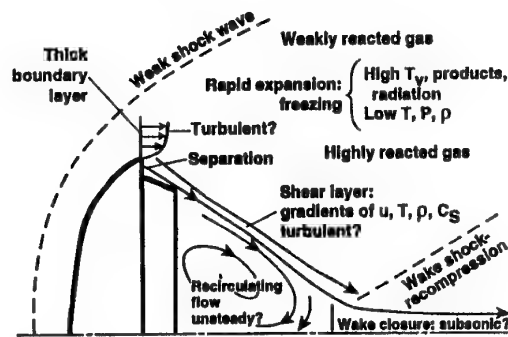

Figure 4: Schematic of hypervelocity bluff body near-wake flowfield

C10-4

The recommendations for future research are:

- accelerate the development of diagnostics for high-enthalpy real-gas flows with emphasis on non-intrusive optical techniques capable of assessing the thermodynamic state of the gas and of providing quantitative data and qualitative imaging to describe and understand the flow and to develop and verify CFD models and tools. Continue development of classical measurement methods and the hot-model testing technique
- a synergistic use and further development of real-gas ground test and real-gas CFD is imperative. The CFD must be used in the definition of ground test experiments and in the interpretation of test results. Conversely, the ground test data must be used to verify the CFD models and simulation results. CFD simulations must include the flow environment produced in the ground test facility.
- the approach illustrated with the blunt cone activity, in which a common model is tested in a variety of real-gas facilities, with common instrumentation, is strongly recommended.
- continue development of CFD tools with emphasis on reacting flow model enhancement and verification for non-equilibrium conditions, particularly for expanding flows, and emphasis on improvement in numerical issues involving discretisation errors and boundary conditions. Issues with turbulence modelling and transition in high-enthalpy compressible flows are complex and demand a sustained and focused program.
- to finalise the development of simulation capability, verification with flight data will be required. This point must be considered in developing ground test campaigns and CFD methods.

3.4 Rarefied-flow effects

Rarefied flows are encountered principally at low Reynolds number and high Mach number; their understanding is critical in cases such as jet-structure interaction with resultant forces and moments on the vehicle and the wake flows of blunt bodies entering planetary atmospheres. The design risks due to insufficient prediction capabilities in the rarefied regime, although not as severe in some sense as the three issues discussed above, are nevertheless substantial: unexpected moments due to plume-vehicle interaction, inadequate protection of instruments in the base region of an aeroshell, misinterpretation of measurements performed in the aeroshell wake during planetary entry, etc.

Experiments were conducted in five different hypersonic facilities, two of which were high-enthalpy, for a variety of rarefaction parameter values; comparisons of the experimental results with several continuum Navier-Stokes computations and non-continuum Direct Simulation Monte Carlo (DSMC-computations were made. Two configurations were examined; the corner-flow/ jet interaction and the blunt-body wake flow configuration (Fig. 4).
An extensive experimental and computational data base was

generated. (See, for example, one result for the blunt-body, base flow configuration in Fig. 5 which compares experimental and numerical density profiles.) The capabilities and limitations of DSMC and Navier-Stokes codes were demonstrated for cases in which continuum and rarefaction effects are present simultaneously. Finally, the synergy of computational and experimental studies resulted in a more extensive assessment for the sensitivity of the results to modelling and computational issues.
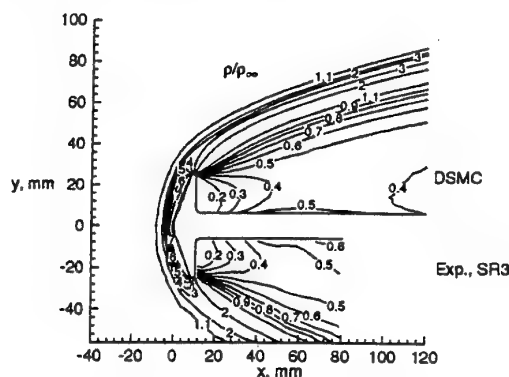

Figure 5: Comparison of measured and calculated density on aeroshell configuration

The pricipal recommendations from these studies were:

- experiments in new facilities can now incorporate rarefied chemistry but new and improved non-intrusive diagnostic methods are required for flow-field characterisation, species concentration and molecular state determination
- an improved understanding of molecular interactions is necessary
- combine Navier-Stokes and DSMC to form a hybrid code
- extend particle simulation methods deeper into the continuum regime to resolve problems with rapidly expanding flows
- reduce computational time by adaptive-mesh and dynamic domain-decomposition methods.

4. STATUS REPORTS

4.1 Calibration procedure for high enthalpy facilities

The objective was to review the status of calibration procedures for high enthalpy facilities and to provide recommendations for future actions. The importance of calibration has been made very clear because of the standard model testing in various facilities during the course of the Working Group.

These facilities must reproduce the effects of dissociation, vibrational excitation, and in the high altitude region, ionization. An example of the ability of certain types of facilities to reproduce the conditions of dissociation of nitrogen is shown in Fig. 6 where X_D is the length scale for nitrogen dissociation, L is the length scale of a typical lifting reentry vehicle and the abscissa is the freestream kinetic energy normalized by the dissociation energy of nitrogen.
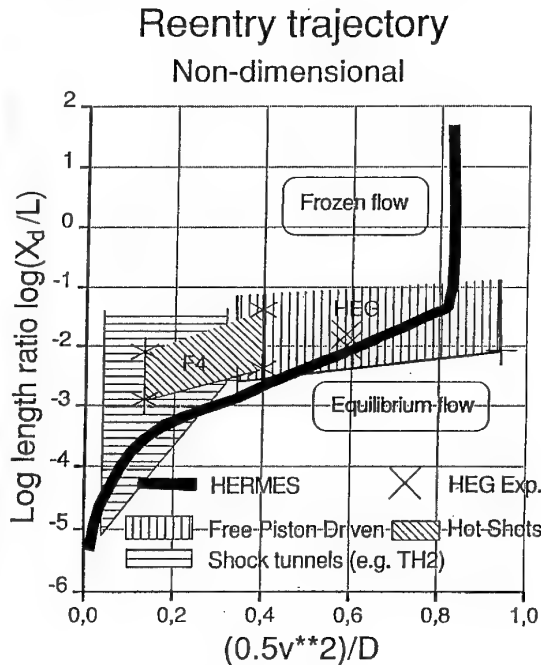
Reentry trajectory
Non-dimensional

Figure 6: Non-dimensional reentry trajectory

Calibration is performed by measuring parameters at various positions within the facility and then making comparisons with currently available modelling. Of principal importance is the characterization of the freestream condition and uniformity which provides the input to the model. At present, the aerothermodynamic state of the gas at the nozzle exit cannot be fully measured. Therefore, the test conditions are determined by combining available experimental data with CFD simulations of the facility behaviour. Clearly the CFD simulation can only be as accurate as is the knowledge of the characterization of the hot gas produced in the reservoir which implies a good knowledge of the mechanism (mechanical expression, electrical discharge, etc.) by which the hot gas is produced. A systematic approach to the information monitoring procedure in a shock-tube-driver, high-enthalpy facility is given.

The conclusions are:
- the calibration of facilities, with uncertainties, is of critical importance and deserves the highest priority if the vehicle designer is to have confidence in the results;

- standard model testing has brought an increased awareness of the need to carefully calibrate each facility;
- non-intrusive, spectroscopic information is the key, but important uncertainties remain when facilities are operated at peak conditions;
- the use of conical nozzles to allow for a broader range of operating conditions and an overlap of conditions between facilities should be considered. Matching Navier-Stokes codes with DSMC codes for nozzle flow conditions has provided a better understanding of both the codes and the facilities.

The principal recommendations are:

- define new standard model tests to stimulate competition, improve test techniques and further validate CFD to reduce uncertainties;
- define standard test techniques, e.g. laser diode absorption, to assure compatibility of results.

The adoption of these recommendations will lead, by definition, to a network of users; this will be invaluable not only for the discussion of successes, but also failures and the reasons behind these failures.

4.2 Extrapolation to flight

The objective was to examine the status of the methodology of extrapolating wind tunnel data to flight conditions; the plan adopted was to carry out classical wind tunnel experiments in a semi-continuous low-hypersonic-Mach-number facility, the ONERA S4 Mach 10 tunnel; to perform similar experiments in the NASA CF4 facility which has a low value of gamma; to perform experiments in the real-gas ONERA F4 facility; and finally to use CFD methods for a reconstruction of the wind tunnel results. The CFD codes, which were examined in a dedicated Halis Workshop concerning grid refinement and chemistry, contained different assumptions: perfect gas, equilibrium chemistry and non-equilibrium chemistry and the boundary conditions were given by the "real" tunnel conditions as determined by a mix of experiments and computations. The specific problem examined was the famous "pitch-up" anomaly noted on the first U.S. Orbiter flight and which has been widely studied by many authors.

The conclusions were:

- the overall agreement between flight, computations in flight conditions, and measurements in the heavy-gas CF4 tunnel was good,
- a comparison of results in the "cold" Mach 10 S4 tunnel and the "hot" F4 tunnel clearly exhibited the pitch-up anomaly as shown in Fig. 7 and indicated that the best agreement between experiment and computation was obtained with the equilibrium gas assumption.
- in addition, pressure measurements performed on the aft portion of a Halis configuration in the DLR HEG "hot" facility confirmed that the pitch-up is mainly attributed to a reduction of pressure due to a local decrease in gamma.
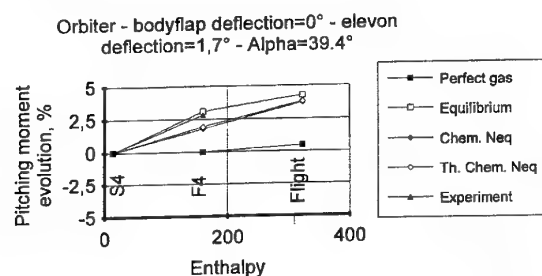
Orbiter - bodyflap deflection=0° - elevon
deflection=1,7° - Alpha=39.4°

*Figure 7: Real-gas effect on pitching moment of Orbiter,
from CFD and experiment*

Recommendations, in light of the success of this "pitch-up" study, were to accelerate the process of interaction between experts within the NATO countries on other critical issues that can only be resolved by a multiple-code/ multiple facility approach, such as:

- RCS interactions
- base flow/plume interactions
- surface catalysis
- transition and turbulence

4.3 Real-gas facilities

The objective of this status report was to provide an overview of current aerothermodynamic facilities and to discuss the role of CFD in ground testing. With this basis, an assessment of the current status of instrumentation for real-gas facilities and of the newest facilities was made. The report concluded with a statement of future needs and specific recommendations.

The facility overview summarizes the performance and status of a large number of high-Mach facilities including ballistic ranges; arc jets for TPS studies were excluded.

The role of CFD in aerothermodynamics has become very broad. CFD is essential for even a reasonably accurate extrapolation of wind tunnel results to flight conditions and thus has become indispensable in the vehicle design process . It has also become of considerable value in the design and use of facilities: for nozzle design validation, for sensitivity studies to aid decisions on the relative importance of a given wind tunnel flow parameter on vehicle design features, and for estimating the allowable uncertainty in a given measurement technique. Finally CFD has proven very useful in the study of new facility concepts, e.g., the prediction of the time-dependent operation of a short-duration facility. The pacing item in the continued use of CFD for these purposes is code validation by means of "building block" experiments; this process is essential to build confidence in the use of CFD.

An assessment was made of the instrumentation used in high-enthalpy facilities. Unlike conventional perfect-gas facilities, those operating at high temperatures require the measurement of all free-stream properties including chemical species. In addition, the determination of certain quantities of interest,

e.g. heat transfer, requires reliable information on transport properties. Because of the high temperatures and, usually, short duration of the flows, emphasis has been placed on non-intrusive optical techniques for the determination of flowfield properties. Many laboratories are engaged in the development of optical laser-based systems for these purposes; some are based on particulate interactions, some on molecular species interactions. The permutations and combinations seem endless. At the present time, the field is a state of flux and, fortunately, the learning curve is steep. However, what has marked the last five years is the challenge of transfering a laboratory technique into a successful measurement tool for large impulse facilities often characterized by pollutants and vibrations.

An assessment was also made of the major new facilities that have become operational in the last five years or so: LENS and T5 in the United States, and HEG and F4 in Europe. Since they all represent the state-of-the-art in high enthalpy wind tunnel design, it is natural that many problems, often entirely unexpected, have been encountered; in most cases, they have been resolved. Even if the predicted peak conditions have not always been realized in practice due to losses, pollutants, component damage, etc., the performance level and reliability reached are impressive. The success of these facilities, of measurements made in them, and in the understanding of observed phenomena (e.g. the interaction of chemistry, turbulence and shock waves) has been due to the combined efforts of computational fluid dynamicists, experimentalists (both engineers and physicists) and computational chemists. Studies carried out with these facilities have involved both "building-block" experiments for code validation and configuration studies.

Recommendations are:

- while the new real-gas facilities are already producing a better understanding of key problem areas in hypervelocity flows, greater support to fully determine flow conditions and uncertainties in these facilities is essential
- AGARD-FDP/PEP-sponsored Symposia, workshops, exchanges of people and standard models should focus on real-gas hypersonics, stressing experiences with the new generation of real-gas facilities
- studies on future hypersonic facility needs have been conducted in the U.S.; a similar study should be undertaken in Europe
- in the near and mid-term, research on new facility types and new instrumentation techniques must be conducted so that rational decisions can be made in the longer term if and when new large-scale hypersonic facilities are proposed
- exchanges of experiences with Russian facilities are essential to provide a background for later decisions concerning the possibility of new large-scale facilities in the West
- complementarity and cooperation have been essential elements and must continue to be encouraged and supported. A multi-national project would provide a

focus for an international team of aerothermodynamicists and their facilities/codes.

5. CONCLUSIONS

Working Group 18, "Hypersonic Experimental and Computational Capability, Improvement and Validation", was composed of a circle of senior managers and researchers from the United States and Western Europe; its four-year study, summarized herein, has led to a sharing of experiences and the development of trust through well-defined cooperative projects.

Conducting experiments on standard test models in a wide range of hypersonic facilities provided a unique opportunity for facility and code validation. An important contribution was made by the Working Group to the success of the initial calibration and "shake-out" of four new real-gas facilities on both sides of the Atlantic.

The studies performed by the various teams have resulted in a better identification of the risks involved in hypersonic vehicle design and have led to a wide range of recommendations to reduce these risks. In broad terms, Working Group 18 urges that resources be allocated within the NATO nations to:

- resolve facility, computational, and modelling deficiencies with targeted research efforts.
- accelerate the multiple facility/multiple computation strategy with standard models

Only in this way will we be ready to meet the inevitable challenges that will arise. In conclusion, the need for sustained hypersonic flight has been expressed by a number of NATO member states. Working Group 18 and other AGARD activities have demonstrated that many member states possess not only the intellectual and physical resources necessary to accomplish this goal, but have shown their ability and readiness to collaborate efficiently at the R & D level. Let us capitalise on these facts and move ahead by supporting the above recommendations and by defining specific NATO-wide projects which will serve as drivers for increased collaboration in the future.

ACKNOWLEDGEMENTS

Survey of Aerothermodynamics Facilities Useful for the Design of Hypersonic Vehicles Using Air-Breathing Propulsion

James O. Arnold
Chief, Space Technology Division
MS: 229-3

and

George S. Deiwert
Retired

NASA Ames Research Center
Moffett Field, California 94035-1000
USA

Summary

This paper surveys the use of aerothermodynamic facilities which have been useful in the study of external flows and propulsion aspects of hypersonic, air-breathing vehicles. While the paper is not a survey of all facilities, it covers the utility of shock tunnels and conventional hypersonic blow-down facilities which have been used for hypersonic air-breather studies.

The problems confronting researchers in the field of aerothermodynamics are outlined. Results from the T5 GALCIT tunnel for the shock-on lip problem are outlined. Experiments on combustors and short expansion nozzles using the semi-free jet method have been conducted in large shock tunnels. An example which employed the NASA Ames 16-Inch shock tunnel is outlined, and the philosophy of the test technique is described.

Conventional blow-down hypersonic wind tunnels are quite useful in hypersonic air-breathing studies. Results from an expansion ramp experiment, simulating the nozzle on a hypersonic air-breather from the NASA Ames 3.5 Foot Hypersonic wind tunnel are summarized. Similar work on expansion nozzles conducted in the NASA Langley hypersonic wind tunnel complex is cited. Free-jet air-frame propulsion integration and configuration stability experiments conducted at Langley in the hypersonic wind tunnel complex on a small generic model are also summarized.

List of Symbols

C_N = normal - force coefficient

C_A = axial - force coefficient

C_m = pitching - moment coefficient

C_l = rolling - moment coefficient

C_n = yawing - moment coefficient

C_Y = side - force coefficient

M = Mach number

p = pressure

Re = Reynolds number per meter

T = temperature

x = streamwise coordinate

z = vertical coordinate

α = angle of attack

Subscripts

jet = internal nozzle exit condition

t = stagnation condition

∞ = freestream condition

Introduction

The dream of producing an air-breathing, hydrogen fueled hypervelocity aircraft has inspired the aerospace community for decades. Despite the simplicity and beauty of the concept such a craft has not yet been realized, even in an experimental form. Many formidable problems must be overcome to make this dream a reality.

This paper surveys U.S. aerothermodynamic facilities and techniques which have been used to make good progress in solving these problems.

A simplified concept of an air-breathing hypersonic vehicle is presented herein and the nose-to-tail aerothermodynamics' issues and special aerodynamic problems that arise with such craft are discussed. The utility of aerothermodynamic facilities and companion Computational Fluid Dynamics (CFD) analysis is then illustrated by reviewing results from recent United States publications wherein these problems have been addressed. Papers selected for the discussion have been chosen such

that the review will serve to survey typical[*] U. S. aero/aerothermodynamic real gas and conventional wind tunnel facilities that are useful in the study of hypersonic, hydrogen or hydrocarbon fueled hypervelocity vehicles. The issue of transitional/turbulent flows for hypersonic air-breathing aircraft is beyond the scope of this paper even though this is identified as a critical focused research area.

Overview of Vehicle Flow Path

Clearly, air frame-propulsion integration is a critical issue for the hypersonic air-breather. In fact, it is difficult to even conceptually separate the airframe and propulsion systems for such a vehicle.

Figure 1, adopted from Deiwert, Cavolowsky and Loomis (1994), depicts the cross-sectional view of a conceptual hypersonic, air-breathing aircraft operating at a cruise condition. Such a craft has a slender side view and sharp leading edges on its nose and cowl lip at the entrance to its propulsion module. Since the flow in the combustor is supersonic, the propulsion system is known as a scramjet (short for supersonic combustion ram jet). The forebody is generally long and serves as a compression surface for the air entering the scramjet inlet. The nose of the vehicle creates a body shock wave which at optimum cruise, just touches the cowl lip of the scramjet inlet. In this way, the air captured in the body shock is compressed, shock-heated, and fed into the scramjet combustor. Therein, energy is released and the products of combustion exit the chamber onto the aft of the aircraft. This portion of the craft serves as an expansion half nozzle, and its design is critical to the installed performance of the scramjet. Supersonic combustion begins at free stream Mach number of six and continues to be important up to Mach 25, the maximum Mach number contemplated for such craft.

Because of the combination of both chemical and aerodynamic time scales and the highly integrated propulsion flow path, ground test and analysis ideally should include long flow duration, and large to full scale testing at actual flight condition. Facilities with such a test capability do not currently exist, and it is unlikely that one will be available in the foreseeable future. Consequently, sub-scale, often, very short duration, component testing must be conducted and complimented by modern, real-gas CFD analysis, and where possible, flight experiments.

Nose Tip and Forebody

The nose and forebody flow can be reliably analyzed with modern, real-gas CFD codes which have been validated in shock tunnels and conventional wind tunnels. CFD issues requiring attention are converged grids to ensure reliable prediction of heat transfer and body shock capturing, and the choice of appropriate transition/turbulence models. Iterative calculations are conducted in nose-to-tail solutions, and the outcome of such efforts yield body

configurations ensuring body shock-on-cowl lip impingement and inlet flow profiles which can yield optimum scramjet performance. These calculations also provide aeroheating environments required for the design of thermal protection systems (TPS). Sharp vehicle leading edge nose and cowl lip profiles present formidable TPS challenges. The TPS problems are treated with their own set of analysis and facilities (usually arcjets) which provide flows lasting from 10's of minutes to an hour. It is important to note that valid simulation of scramjet inflow conditions for ground test experiments require reliable modeling of facility flow characteristics.

Body-Shock on Cowl Lip

From the perspective of engine performance at cruise conditions, the hypersonic air-breather ideally has the forebody bow shock impinging on the cowl lip ensuring that all of the air processed by the forebody flow passes into the scramjet inlet. This design objective brings with it the problem of a shock-shock interaction on a relatively sharp surface where time-dependent, real-gas effects are important. A thorough understanding and predictive capability here is crucially important to define the requirement for a reusable thermal protection system on the cowl lip.

Important progress developing an understanding of the shock-on-cowl lip problem has been made at the California Institute of Technology using the real-gas free-piston-driven shock tunnel, T5. T5 is a member of the family of facilities of this type existing in Australia, Germany (HEG), and the United States. T5 has a compression tube 30 m in length and 30 cm in diameter, while its driven tube is 12 m in length with a 9 cm diameter. The nozzle has a throat diameter of 3.1 cm and exit diameter of 31 cm. T5 can give flow durations of several milliseconds. A complete description of the tunnel is given by Horung (1992).

Sanderson (California Institute of Technology Ph.D. thesis, 1995) describes prior research on the shock-on-body problem. This includes prior categorization into six flow types I - VI, results of experiments with nitrogen test gases in T5 at low (3.88) MJ/kg and high (19.1 MJ/kg) nozzle reservoir conditions, effects of unsteady flows, and models of the flows accounting for real-gas effects.

The T5 experiments were conducted in a nominal 2-dimensional flow that results from the impingement of an oblique shock onto a 40 mm diameter cylinder with an aspect ratio of 4.5. The oblique shock was created by a shock generator placed near the exit of the T5 nozzle. Observations were made with a holographic interferometer and fast-response thermocouples placed at 24 circumferential locations on the model forebody.

A typical real-gas experimental result from the T5 testing discussed by Candler, et al., (1995) is shown in figure 2. This flow condition is of type IV where a supersonic jet penetrates into the region of low subsonic flow about the body. Table 1 lists the T5 tunnel conditions for this case.

---

[*] Many of the U.S. real-gas facilities discussed in the document AGARD AR-319, 1996 have made notable contributions to this field but cannot be discussed here. Examples are the LaRC HYPULSE facility (Erdos, et al,., 1994 and the Large Enthalpy National Shock Tunnel (LENS) described by Holden, et. al., 1995.

Table 1. T5 Test Conditions		
Nozzle reservoir conditions	Pressure (MPa)	28.3 ±1.9
	Temperature (K)	8960
	Enthalpy (MJ/kg)	19.1
Test section conditions	Velocity (m/s)	5350
	Density (kg/m^3)	0.0157
	Pressure (kPa)	11.4
	N (kg/mole)	3.65×10^0
	M_∞	5.3
	Reynolds number per mm	1350

The hologram in figure 2 clearly shows the nature of the flow. Also shown in figure 2 is a plot of Stanton number normalized by the Fay & Ridell St prediction for the body without the impinging shock versus the body location. While the enhancement caused by the impinging shock is very significant, it is not as large as would be predicted on the basis of an ideal gas analysis.

The Cal Tech study has quantitatively demonstrated the importance of including real-gas effects for the shock-on-lip problem. It is clear that the use of the real-gas capability of the T5 tunnel was a key element in the recent progress. Clearly, additional work on the shock-on-shock problem with air as a test gas is desirable.

Scramjet Inlet and Combustor Flows

Large shock tunnels such as the NASA Ames 16-Inch or CUBRC LENS and the Calspan 96" shock tunnel facilities which were originally designed for the study of aerothermodynamics have provided valuable information on scramjet inlet and combustor flows. Because of the authors' experience, this summary is based on the paper by Deiwert et al., (1994). Similar work has been conducted in the LENS facility, (Holden 1995) and in the 96" shock tunnel which can operate at similar, but higher pressure levels. This fact is important because it allows closer simulation of flight conditions.

There are four basic techniques for configuring scramjet combustor tests illustrated in figure 1. These include (1) the free-jet configuration whereby the free stream and flow over the entire vehicle forebody is reproduced, (2) the semi-free jet configuration whereby the compressed forebody flow just ahead of the cowl inlet is produced, (3) the semi-direct-connect configuration, and (4) the direct-connect configuration in which a one-dimensional flow is produced at the combustor entrance. In the free-jet configuration, the entire forebody and combustor flow path is replicated. Current ground test capability does not yet exist to test in this configuration at or near full scale. In the semi-free jet configuration, the flow behind the leading edge body shock is replicated by the flow from the ground test facility nozzle. Not simulated in this test configuration are leading edge bluntness effects, boundary layer transition and thickness, and the shock-on-cowl interaction. Included, however, is the influence of the cowl and cowl shock, and a thin body-side boundary layer. A segment of a one-sided nozzle may be included at the end of the combustor. Hence, it is possible to account for two-dimensional inflow

effects, including the important influence of the cowl shock on combustor and nozzle performance. A facility sized to accommodate test articles of large scale is required.

In the semi-direct-connect configuration, the cowl is eliminated and an over expanded flow from the test facility nozzle is turned through an oblique shock to produce one-dimensional flow conditions at the combustor entrance. A segment of the one-sided nozzle may be included at the combustor exit. This technique uses the excess facility total pressure by over expanding the flow to a large test section and recompressing to desired combustor entrance conditions. High pressure is, of course, desirable, but the LENS facility can only offer this at substantially reduced scale. The high pressure capability is off-set by having to test in the semi-direct connect mode and small test article scale.

The direct connect configuration also neglects the cowl; it provides one-dimensional flow conditions at the combustor entrance directly from the facility nozzle. Here the facility must be large enough to provide the mass flow rate for the combustor and need only have enough total pressure to provide the proper combustor inlet properties.

Given the limitations for testing full flight scale articles at flight test conditions the next best alternative is to establish a ground test capability for full scale integrated components. The preferred configuration is the semi-free jet concept as was done in the 16-Inch NASA Ames tests by Deiwert, et al, (1994).

"Full scale" is defined here to mean full scale fuel injectors in a full throat height, full length combustor. This is required to provide good simulation of both mixing and combustion time scales simultaneously. This implies a combustor entrance height on the order of 15 cm and a width at least twice that to minimize undesirable three-dimensional effects. For such a "full scale" test article, the corresponding lengths of the cowl, combustor, and nozzle components are each of the order of 1 m.

To assure proper inlet profile and mass capture comparable to the full flight vehicle, the test article should capture a two-dimensional flow from the uniform core flow of the facility nozzle. One way to assure this is to design the inlet body surface to minimize spillage and cross flow effects. This can be accomplished by flaring the surface outward laterally, in a trapezoidal shape, such that Mach waves generated at the corners of the leading edge are not captured in the combustor inlet. The cowl could be configured in a similar manner or configured with parallel sides using side strakes to control spillage. In this case the cowl should be substantially wider than the combustor entrance so that the vortical corner flow generated by the side strakes can be spilled to the outside of the test article and only two-dimensional core flow is captured. A schematic of such a model is shown in figure 3 as installed in a shock tunnel test section in semi-free jet configuration. The 16-Inch shock tunnel with its contoured nozzle designed by method of characteristics analysis provides a uniform core flow of 0.6 m at the nozzle exit diameter of about 1 m.

To produce the required combustor inflow conditions for a given flight condition, the critical facility parameters are reservoir pressure and nozzle area ratio. These two parameters provide the first order control of static pressure, temperature and Mach number at the combustor entrance. A

third parameter, namely cowl turning angle, may be used to provide fine tuning adjustment if it is not fixed by model design constraints. For a cowl turning angle of 12 degrees, the reservoir pressures to produce Mach 12 and 16 combustor inflow conditions are 6600 psi and 48,000 psi, and the nozzle expansion ratios are 130 and 940 respectively for a flight dynamic pressure of 1000 psf. Keeping in mind the requirement for a 1 m nozzle exit diameter, the limiting facility parameter for the lower Mach number regime, therefore becomes the nozzle area ratio. For a reflected shock tunnel an area ratio of 100 calls for a facility with a 4 inch diameter throat which implies a 12 inch diameter reservoir to maintain a minimum 9:1 area ratio between the reservoir and throat; larger area ratios are preferable. The 9:1 reservoir/throat area rates is necessary to produce a nearly planer reflected shock and uniform reservoir test gas conditions. At the higher Mach number regime, the limiting facility parameter is reservoir pressure. Reservoir pressures of 10 ksi will permit good simulation up to M =13, 20 ksi up to M = 14, and 30 ksi up to M = 15.

In addition to facility reservoir pressure and nozzle area ratio, a third critical test simulation requirement is test gas slug length or steady test time. To perform direct thrust and drag measurements, discrete pressure and heat flux, and instream measurements, the steady test gas slug length should be at least three test article body lengths. For a model 3 m long this requires a slug length of 9 m to assure proper flow establishment with a steady flow. For the velocities at Mach 12 and 16 test conditions the total steady flow test time should be at least 2.6 ms and 1.8 ms respectively. Some segments in the combustor flow path may require test times substantially longer than these to assure proper flow establishment and to permit data acquisition.

Before installing the integrated combustor test article, calibration runs and pre-test CFD analyses should be performed. The calibration runs should include pitot measurements across the entire nozzle exit plane. Real-gas CFD computations can also be made for conditions corresponding to the facility operating conditions and results compared with calibration data.

For a fixed test article configuration the combustor inflow conditions can be estimated. Using the above computed shock tunnel nozzle exit conditions, including effects of viscosity and finite rate chemistry, flow through the model inlet to the combustor entrance plane can be computed for the test Mach numbers. Three-dimensional Navier-Stokes computations can also be performed to assess the influence of three-dimensional viscous effects, to confirm the spillage of the vortical corner flow generated by the cowl side strakes and confirm the two-dimensional inflow, and to determine the combustor inlet mass capture, which is critical in determining combustor performance. The inlet flow computations can be verified, in part, by comparison with inlet wall static pressure and heat flux measurements.

The integrated combustor model should be fully instrumented with surface pressure and heat flux gages. Additional surface instrumentation should also be installed on the fuel injectors, on the facility walls, and external surfaces of the model and supports to monitor the flow in the facility. Accelerometers can be installed to determine vibrational loads and frequencies of various model and facility components. Acceleration data could be used to eliminate vibrationally induced noise in the data from

surface instruments. Further available surface instrumentation can include skin friction gages installed on the body and cowl inlet and combustor surfaces, and a metric thrust balance installed in the one-sided nozzle. The skin friction gages are particularly useful in assessing combustor drag, and the nozzle metric balance provides a direct measurement of incremental thrust. A schematic illustrating a typical layout of surface instruments used in the NASA Ames 16-Inch test is shown in figure 4.

In-stream measurements can include removable pitot probes mounted on the body and cowl leading edges and pitot rakes installed in the combustor exit plane. The removable in-stream probes will cause downstream flow disturbance, and surface mounted instruments are severely limited in providing information on in-stream thermodynamic and chemistry phenomena. Hence, extensive use should be made of nonintrusive diagnostics, notably laser diagnostic methods, to provide accurate and detailed in-stream information.

Nonintrusive laser diagnostics can include rapid scanning multiple line-of-sight laser absorption spectroscopy. Specific applications include measurements of O_2 at the combustor inlet and OH at the combustor exit plane and along the nozzle. The O_2 diagnostic also provides a capability for cross beams for the determination of velocity via the Doppler shift technique. Additionally, multiple line-of-sight laser absorption for H_2O can be installed in the combustor exit plane and down the nozzle. O_2 measurements allow assessment of inlet mass capture OH measurements allow assessment of combustion progress. H_2O measurements assess combustion efficiency. All of these data are essential in evaluating combustion performance.

To determine combustor performance with a comprehensive data acquisition system it is important to have a high spatial density of instruments in the facility and test article and to make highly accurate measurements of the proper flow parameters. Precise measurements of parameters such as static and pitot pressure and mass flux at the facility nozzle exit are critical to proper reduction and analysis of scramjet combustor performance data. Without the full suite of instruments and data described above, assessment of inlet mass capture, engine fuel equivalence ratio, and ultimately combustion efficiency and combustor performance cannot be reliably made.

It is also important to accurately measure the proper flow parameters in the scramjet to determine combustor efficiency and performance. Given the existing technology and methodology to accurately measure pressure in the combustor as well as the CFD capability to simulate 3-D scramjet internal flow pressure, a natural analytical process to evaluate combustor performance could be accomplished via comparison of measured and computed pressure. Test results and computations should include cases with and without fuel injection and with and without combustion. For Mach numbers at or below 10, the pressure rise due to combustion is large enough that direct evaluation of performance, based on pressure rise only, is viable. For the flight Mach number range above 10 , the pressure rise due to combustion is small compared to tare and mixing values. Shock structures in the combustor region also complicate this analysis technique. Shocks initiated by fuel injectors impinge on the combustor surface at locations which vary relative to the positions during tare shots for cases of mass addition (as with fuel

addition during injection) and for energy addition (as with heat release during combustion). Measurement of overall pressure rise due to mixing or due to combustion is difficult to estimate. Integrating pressure along the combustor eliminates some of the ambiguity and clearly demonstrates a measurable pressure rise. Resolution, however, is lost and comparison with CFD becomes less accurate. It is better to make a direct measure of combustor performance or efficiency. Performance or thrust can be directly measured with the metric balance. Combustion efficiency can best be determined by measuring the mole fraction of water at the combustor exit. Comparison of exit pressure with exit water mole fraction as a direct measure of combustion efficiency for a nominal 5 percent measurement error is shown in figure 5. A 5 percent error in the measurement of pressure leads to about a 35 percent uncertainty in the assignment of combustion efficiency, whereas a 5 percent error in the measurement of water vapor mole fraction leads to about a 5 percent uncertainty in assignment of combustion efficiency.

In summary, a capability for performing large-to-full scale integrated scramjet tests can be provided with a large reflected shock tunnel. Tests over the flight Mach number range of 12 to 16 have been performed in the Ames 16-Inch shock tunnel. It is possible to measure to a high degree of certainty the combustion efficiency and incremental thrust and to assess the relative performance of different design concepts. Instrumentation developed and demonstrated specifically for high Mach number pulse facility testing coupled with advanced CFD analysis, can provide a data base to greatly increase our understanding of scramjet technology and performance for flight Mach numbers greater than 10.

Nozzle Flows

The hypersonic nozzle flow study discussed here was performed by Ruffin, Venkatapathy, Keener, and Spaid (1992) and utilized the NASA Ames 3.5 foot Hypersonic Wind Tunnel. This facility is a conventional, closed-circuit, blow down, ideal gas tunnel which has contoured nozzles giving free stream Mach numbers of nominally 5, 7 and 10. The tunnel derives its name from the diameter of its exit nozzle, 3.5 ft., and is currently in a standby mode.

The approach taken by the authors was to use CFD to design a wind tunnel model whose flow field would embody many important aspects of the actual hypersonic aircraft nozzle flow, conduct an experiment with this model, and use the results to validate the CFD. Once verified by the experimental results, the CFD code could then be used to design the aircraft with lower overall risk.

Figure 6 depicts the model so designed; it is known as the Single (or one-sided) Expansion Ramp Nozzle, SERN. The sharp upper surface was fitted with a boundary layer trip 4 inches downstream of the model leading edge to ensure turbulent flow in the forebody boundary layer and in the plume shear layer. High pressure air was supplied to the plenum and expanded throughout the model's nozzle to simulate hypersonic aircraft afterbody/nozzle flows.

The test conditions for the experiment and the CFD calculations are given in table 2. The CFD analysis was conducted using a laminar boundary layer model. While plans were in place to incorporate 2-equation turbulence models in the CFD, this was not accomplished owing to the termination of the supporting NASP program.

Table 2. Test conditions for computed solutions*	
Condition	
M_∞	7.4
α, deg	-1.1
T_∞, K	71.5
p_∞, Pa	673
Re/m	1.5×10^8 m [1]
P_{fjet}/P_∞	337
T_{fjet}/P_∞	3.9
P_{jet}/P_∞	≈ 10.7
M_{jet}	≈ 2.87

* Both the free stream and nozzle jet gases are air.

Figures 7 and 8, based on CFD results, illustrate the important features of the flow field. This flow has many of the features present in the hypersonic aircraft depicted in figure 1. (Note that the SERN model is upside-down in comparison to figure 1).

Figure 9 illustrates the comparison of computed (3-D) and measured surface static pressures along the model's center line. As can be seen, the comparison is excellent, but this is not sufficient to claim that all important parameters of the flow, e.g. heat transfer, are predictable.

Figure 10 compares experimental and computational shadowgraphs of the expansion. The computed shadowgraph is based on a 2-D CFD solution with a grid consisting of 300 by 300 points. The forebody shock is clearly seen in the experimental shadowgraph in the upper left-hand corner. Also clearly shown is the outer plume shock, the thick, turbulent shear layer, and the barrel shock. There is a separation of the flow near the trailing edge of the upper cowl surface. While the laminar flow CFD did not reproduce the model's turbulent boundary layer feeding into the shear layer, the CFD does a very nice job of predicting the location and geometry of the overall features of the flow in the symmetry plane.

Despite the fact that this activity was not brought to consummation, this work is a good example of how conventional wind tunnel testing and companion CFD can be used to analyze complex nozzle flows and, ultimately, in the design of nozzles for actual hypersonic air breathers.

Similar studies to these discussed above by Ruffin, et al. (1992) have been reported by Huebner and Tatum (1991). Their work compared schlieren photographs from the afterbody of a cruise missile with 2-D CFD results. They also reported on the powered afterbody effects of fitting a fairing to divert the flow through the engine as compared with operating a flow through inlet on a generic hypersonic vehicle. They reported that a two-dimensional analysis showed little, if any difference in fairing over the inlet. This result is significant for design of wind tunnel afterbody experiments.

AIRFRAME PROPULSION INTEGRATION

The final task confronting aerodynamicists interested in hypersonic, air-breathing craft is that of putting all of the constituent components into one aerodynamically controllable vehicle. This process is referred to as airframe propulsion integration. Phillips and Cruz (1993) have approached this task by using the NASA Langley wind tunnel complex described by Miller (1990). The approach taken by these authors was to conduct free-jet experiments, as shown in figure 1, on a 17.6 inch long model of an air-breathing Test Technique Demonstrator TTD. They compared the test results of aerodynamics to those calculated from a preliminary Analysis System Design Code called APAS (Cruz, et al, 1989). In this work, APAS modeled the vehicle as a combination of tangent-cone and tangent-wedge with Prandtl-meyer expansion methods to approximate pressure distributions over the model.

A sketch of the model adopted from the authors' paper is shown in figure 11. The model was fabricated from stainless steel with dimensions controlled to $\pm$ 0.003 inches of the model design specifications. The model consisted of the fuselage, wings, twin inboard-mounted vertical tails and a body flap. The forebody has a compression surface leading to a variety of engine modules. These modules included the following : (1) an unrestricted flow-through engine module, (2) and flow-thru model with a center strut, and (3) a blocked engine module formed by deflecting the compression ramp trailing edge downward to close off the inlet cowl. This is a concept to protect the inlet from re-entry heating. The wings and control surfaces were movable to study their effect on the vehicle aerodynamics. The model's center of gravity was at a fraction 0.599 of the body length referenced from the model nose.

The authors tested the configuration in the Langley 20-inch Mach 6 Tunnel, the Langley 31-inch Mach 10 Tunnel, and the Langley 22-inch Mach 20 Helium Tunnel. The range of angle of attack was from - 4° to 20° for fixed sideslip angle of 0° and -2°. No sideslip data were obtained at the Mach 20 condition. Reynolds numbers based on fuselage length were 2.5 and 3.6 million at Mach 6, 1.5 and 3.0 million at Mach 10, and 3.7 and 9.7 million at Mach 20. Aerodynamic forces were measured with a blade sting mounted, six component stain gage balance arrangement. Estimates of the experimental uncertainties are as follows:

ΔC_N	± 0.005
ΔC_A	± 0.001
ΔC_m	± 0.0004
ΔC_l	± 0.0002
ΔC_n	± 0.0001
ΔC_Y	± 0.001

Figure 12 shows a comparison between the APAS and experimental results for Mach 20 with the model in a baseline configuration consisting of the fuselage and the wing at an incidence angle of -1.5°, and the vertical fins and the body flap at 0°. No engine module or yaw fin are included in the baseline configuration.

According to the authors, the predicted aerodynamic coefficients using APAS assuming a laminar boundary layer were in good agreement with all experimental data at low angles of attack and with normal-force coefficients over the complete angle of attack range. APAS underpredicted the pitching moment and axial-force coefficients at moderate-to-high angles of attack.

The effect of adding the engine module with the centerline strut is depicted in figure 13. As can be seen, the effect is to produce small positive increments in lift C_N and drag C_A along with small negative pitching moment changes. The authors attributed this to local flow changes in the flow-thru engine cowl which reduces the boundary layer thickness on the afterbody/nozzle.

Figure 14 shows the effects of removing the twin vertical tails from the configuration at Mach 10. The data show the baseline configuration to be directionally unstable and to exhibit positive effective dihedral at positive angles of attack. It was noted that the vertical tails contribute to stabilization, but their benefit falls far short of making the model directionally stable.

The above examples illustrate the results obtained by the authors and demonstrate the utility of conventional hypersonic wind tunnels in airframe propulsion integration and the study of complete configuration hypervelocity, air-breathing vehicles using the free-jet approach.

Acknowledgment

References

AGARD-AR-319, 1996, Vol. 1, Hypersonic Experimental and Computational Capability, Improvement and Validation. Ed. William S. Saric, Jean Muylaert, and Christian Dujarric.

Candler, G.V., Dimotakis, P.E., Hornung, H.G., Leonard, A., Meiron, D.I., McKoy, B.V., Pullin, D.I. and Sturtevant, B., 1995, Interaction of Chemistry, Turbulence and Shock Waves in Hypervelocity Flow, GALCIT Report FM 95-2.

Cruz, C.I. and Wilhite, A.W., 1989, Prediction of High Speed Aerodynamic Characteristics Using the Aerodynamic Preliminary Analysis System (APAS), AIAA Paper 89-2123.

Deiwert, G. S., Cavolowsky, J.A., and Loomis, M.P., 1994, Large Scale Sramjet Testing in the Ames 16-Inch Shock Tunnel, AIAA Paper 94-2519.

Erdos, J. I., Calleja, J. F., and Tamagno, J., 1994, Increase in the Hypervelocity Test Envelope of the HYPULSE Shock-Expansion Tube, AIAA Paper No. 94-2524.

Holden, M. S., Kolly, J., and Chadwick, K., 1995, Hypervelocity Studies in the LENS Facility, AIAA Paper No. 95-0291.

Hornung, H., 1992, Performance Data on the New GALCIT Free Piston Shock Tunnel, AIAA Paper 92-3943.

Huebner, L.D. and Tatum, K.E., 1991, Airbreathing Configurations with Scramjet Flow Simulation, AIAA Paper 91-1709.

Miller, C.H., 1990, Langley Hypersonic Aerodynamic/Aerothermodynamic Testing Capabilities-Present and Future, AIAA Paper 90-1376.

Phillips, W.P. and Cruz, C.I., 1993, Hypersonic Aerodynamic Characteristics for Langley Test Technique Demonstrator, AIAA Paper 93-3443.

Ruffin, S.M., Venkatapathy, E., Keener, E.R., and Spaid, F.W., 1992, Hypersonic Single Expansion Ramp Nozzle Simulations, Journal of Spacecraft and Rockets, Vol 29, No. 6, pp. 749-755.

Sanderson, S., 1995, Shock Wave Interactions in Hypervelocity Flow, Ph.D. Thesis, Graduate Aeronautics Laboratories, California Institute of Technology.

Saric, W.S., Muyleart, J., and Dujarric, C., Editor, 1996, Hypersonic Experimental and Computational Capability, Improvement and Validation, AGARD-AR-319.
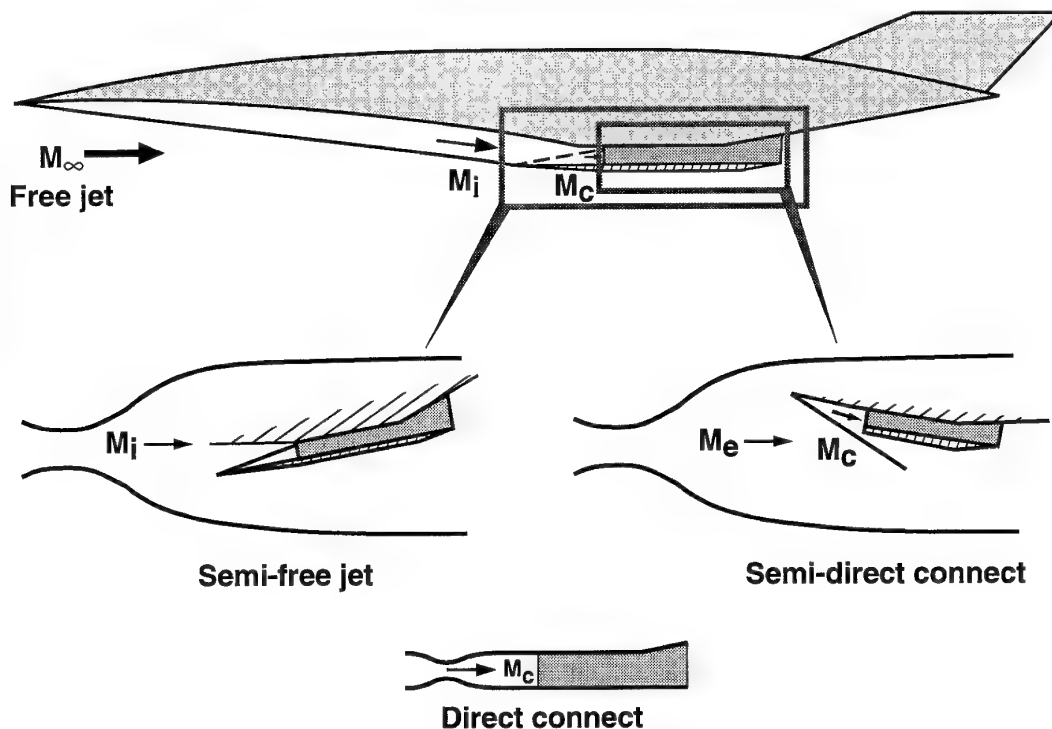
Figure 1. Integrated scramjet ground test simulation configuration.
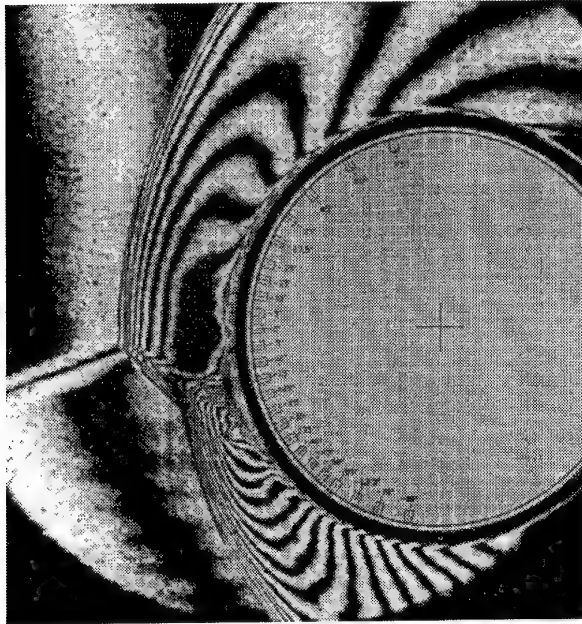
Shot T5-830
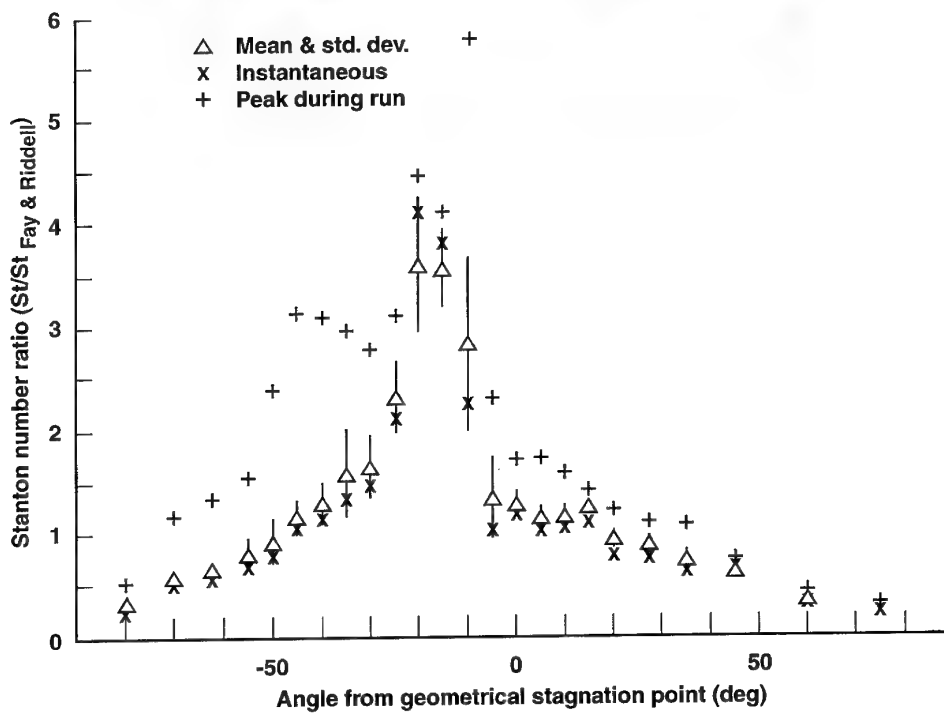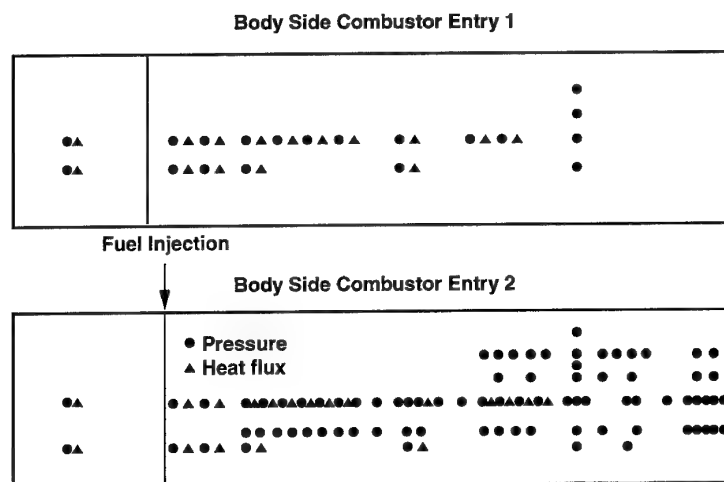
Figure 2. Shot T5-830; condition C.
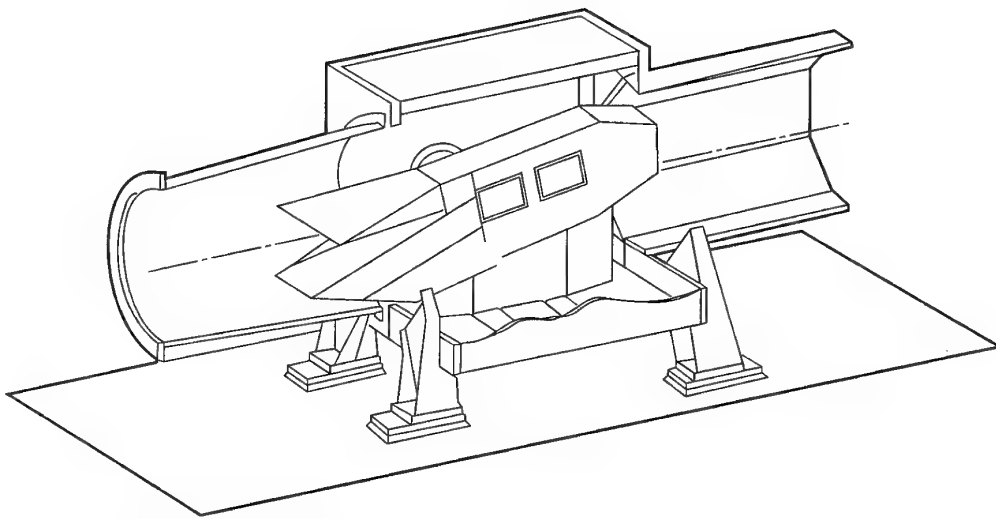
Figure 3. Semi-free jet installation of integrated combustor model installed in the Ames 16-Inch Combustion-Driven Shock Tunnel.
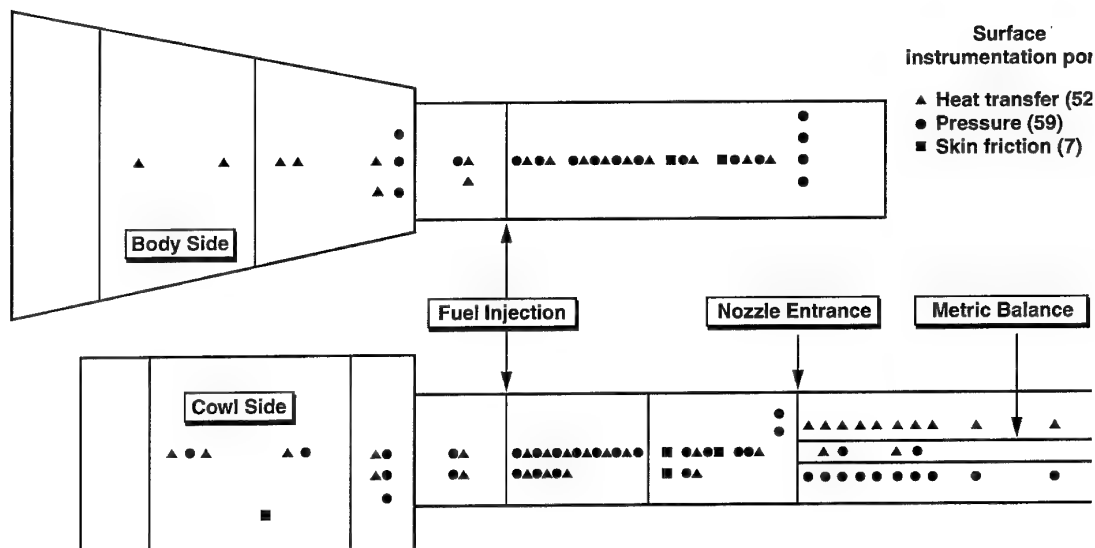
(a)

(b)

Figure 4. Surface instrumentation distribution on integrated scramjet test article.
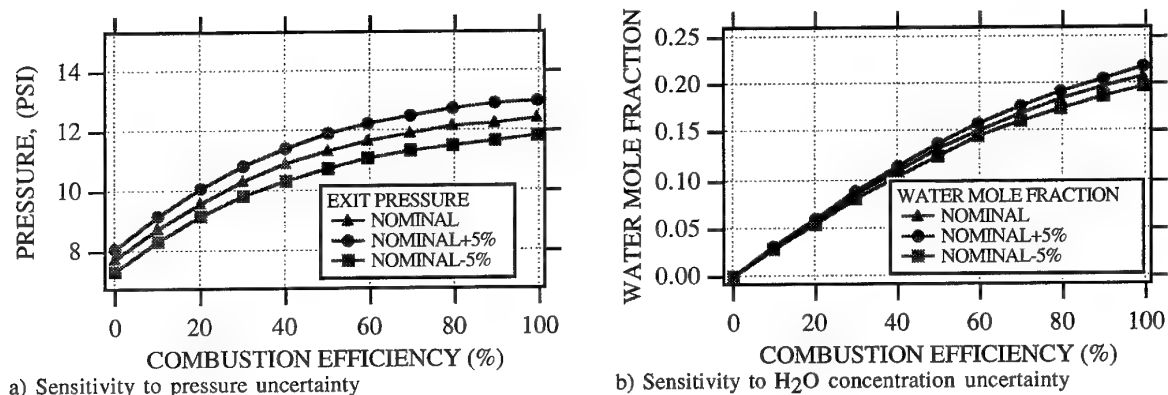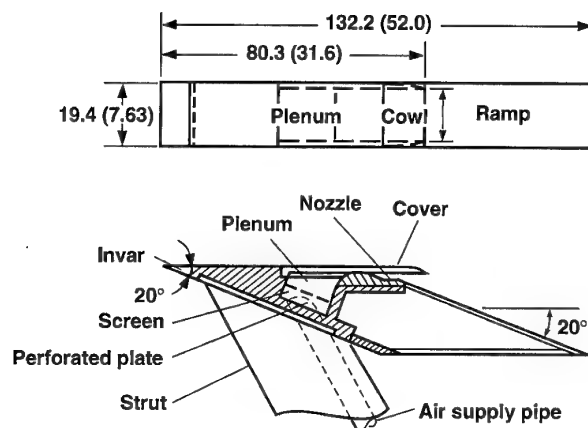

a) Sensitivity to pressure uncertainty

b) Sensitivity to H_2O concentration uncertainty

Figure 5. Combustion efficiency sensitivity.

Figure 6. Schematic of the baseline SERN model, (all dimensions are in cm (in.)).
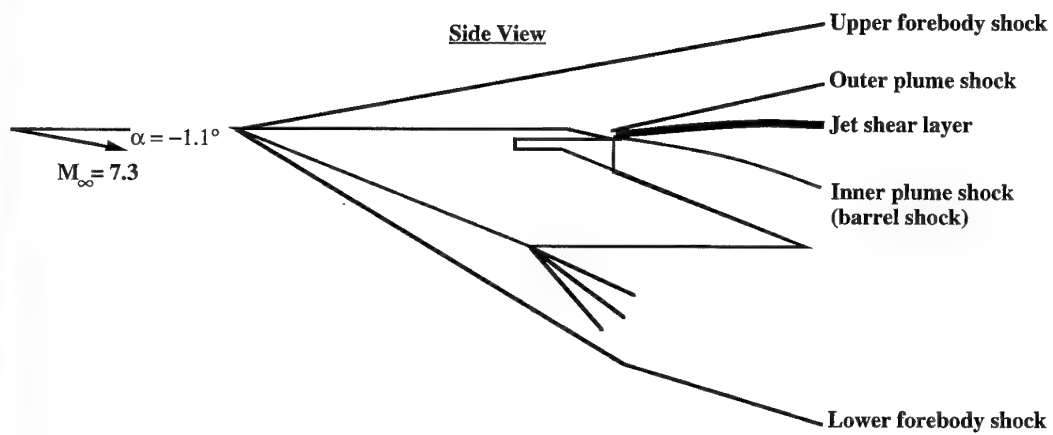
Figure 7. Symmetry plane schematic of the SERN flowfield.
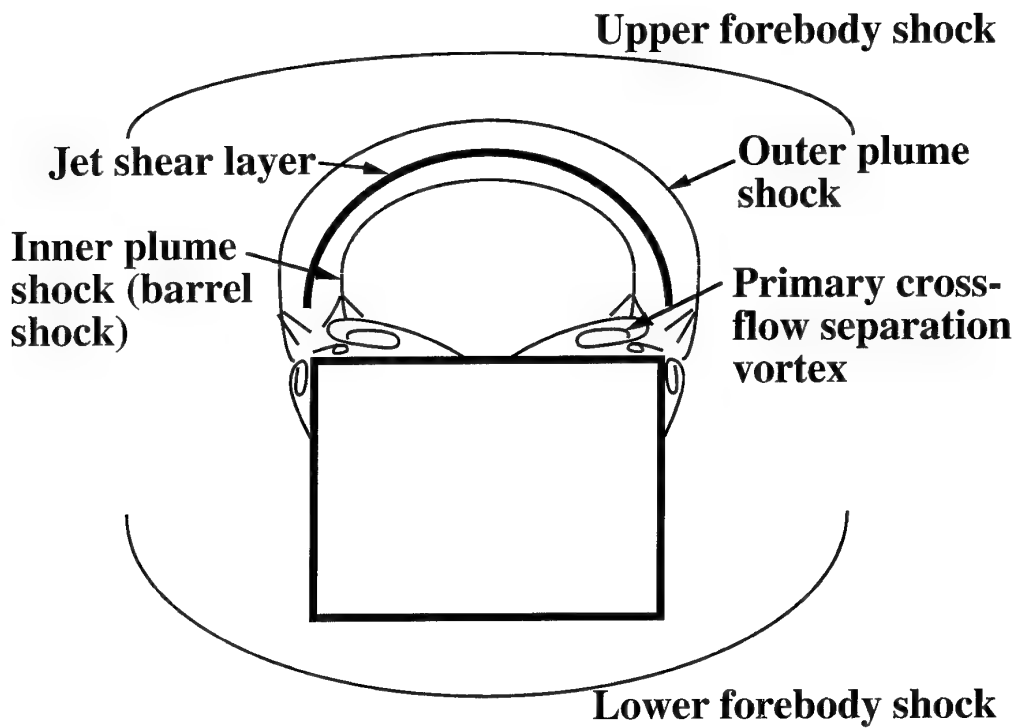
Figure 8. Cross-sectional schematic of the plume flowfield for the baseline model.
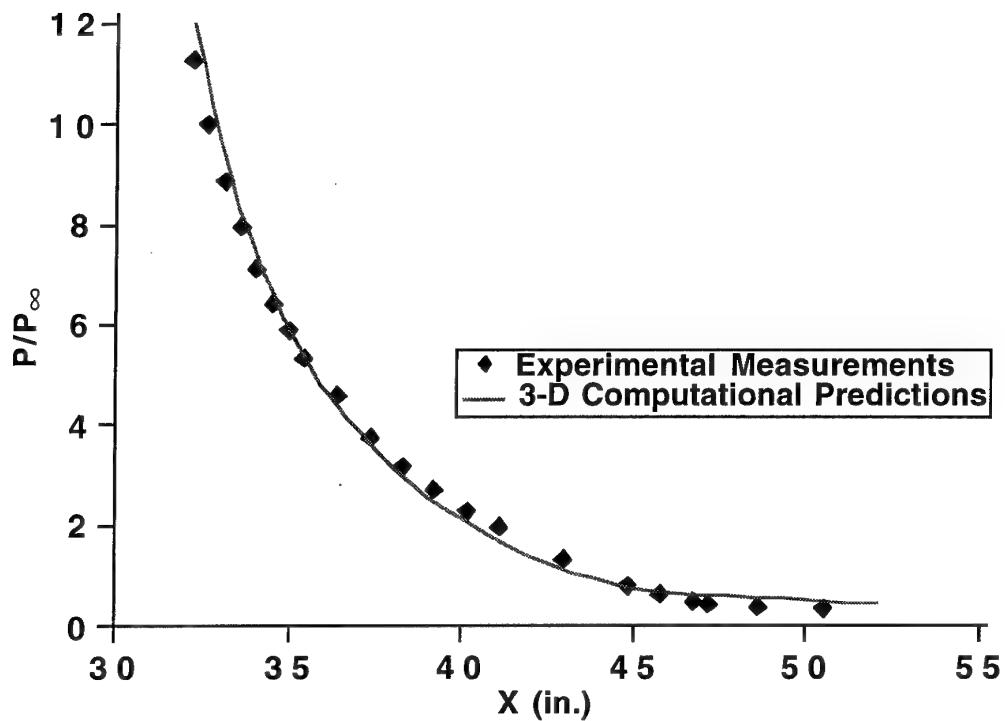
Figure 9. Comparison of computed and experiment surface static pressure along the baseline model centerline.
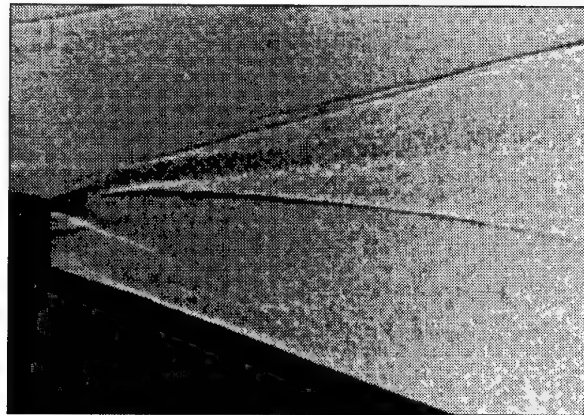
(a)
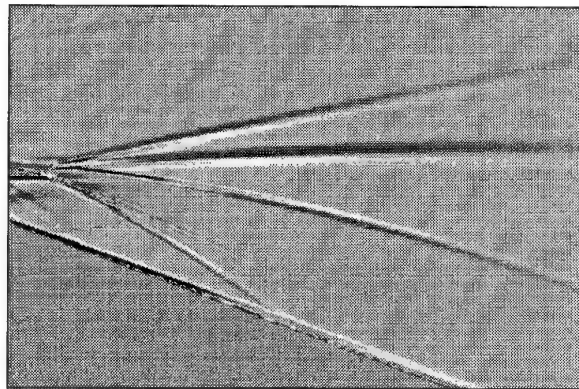
(b)

Figure 10. Experimental and computational shadowgraphs in the symmetry plane of the baseline model. Simulated shadowgraph is based on two-dimensional fine grid results: a) experimental; and b) computational.

$L = 17.60"$
$S_{ref} = 42.666"^2$
$X_{CG/L} = 0.599$
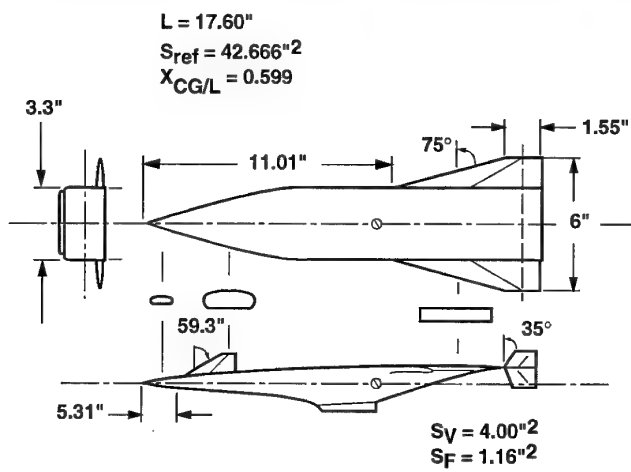
Figure 11. Schematic of the wind-tunnel model.
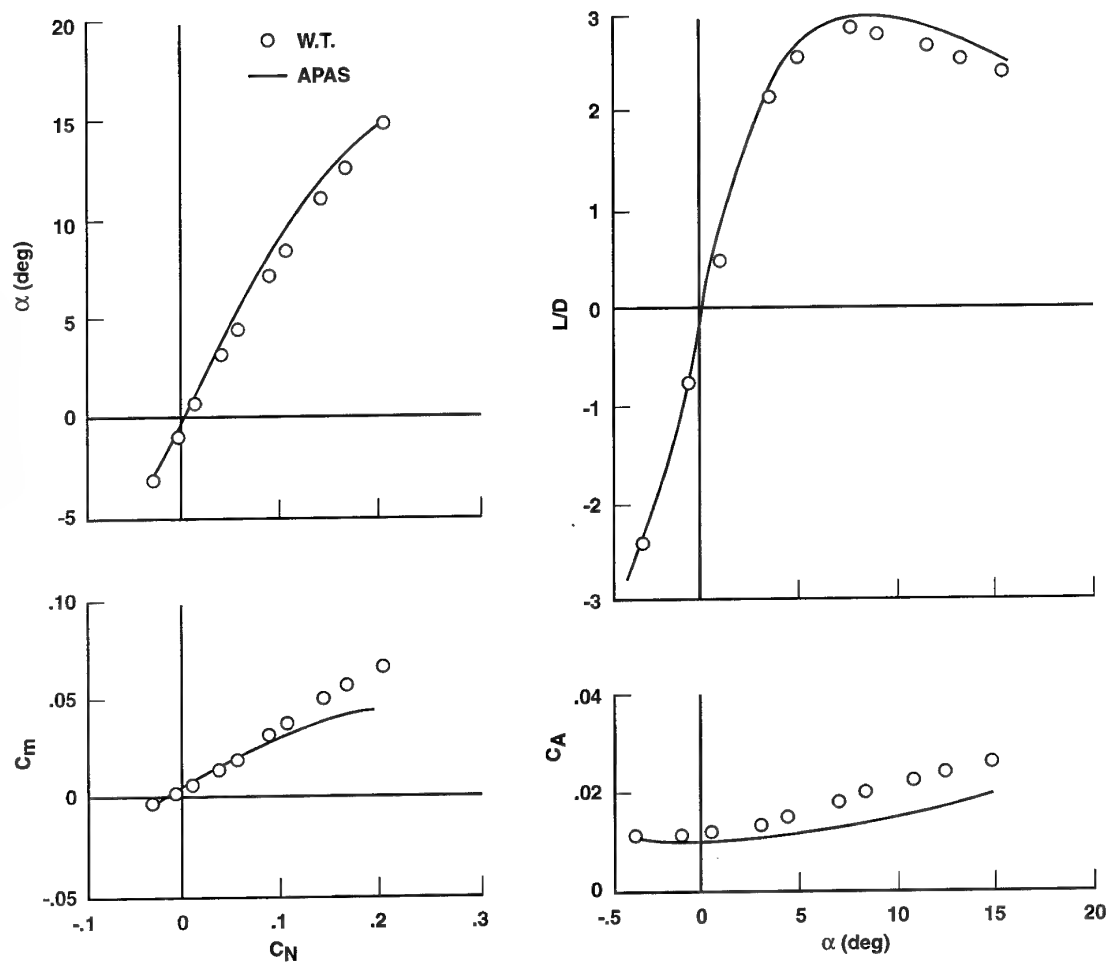
Figure 12. Comparison of predicted longitudinal aerodynamic characteristics with experimental values for configuration BWVB/F.

$M = 6.0; \quad R = 3.6 \times 10^6$
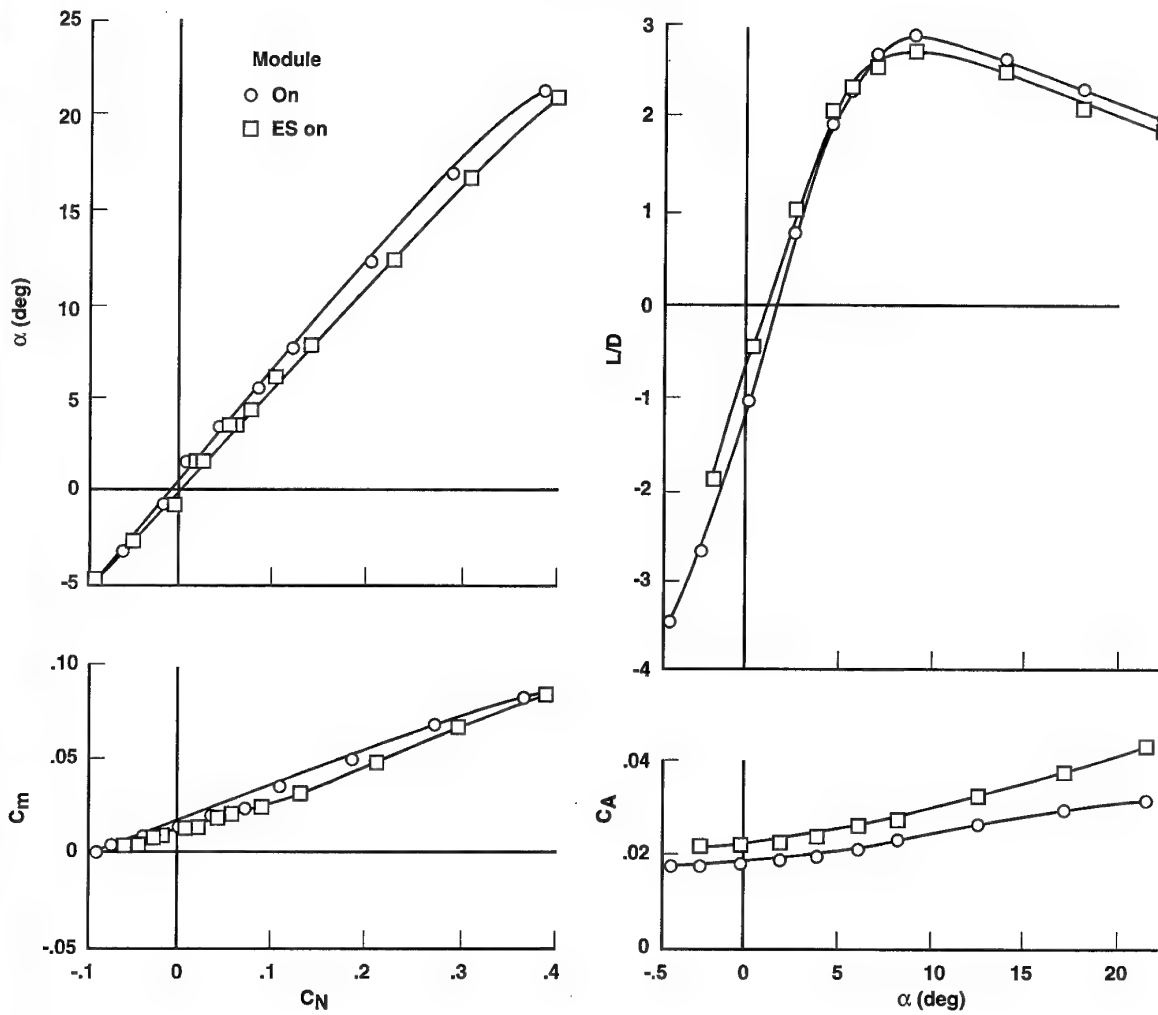
Figure 13. Flow-thru module with centerline strut (ES).
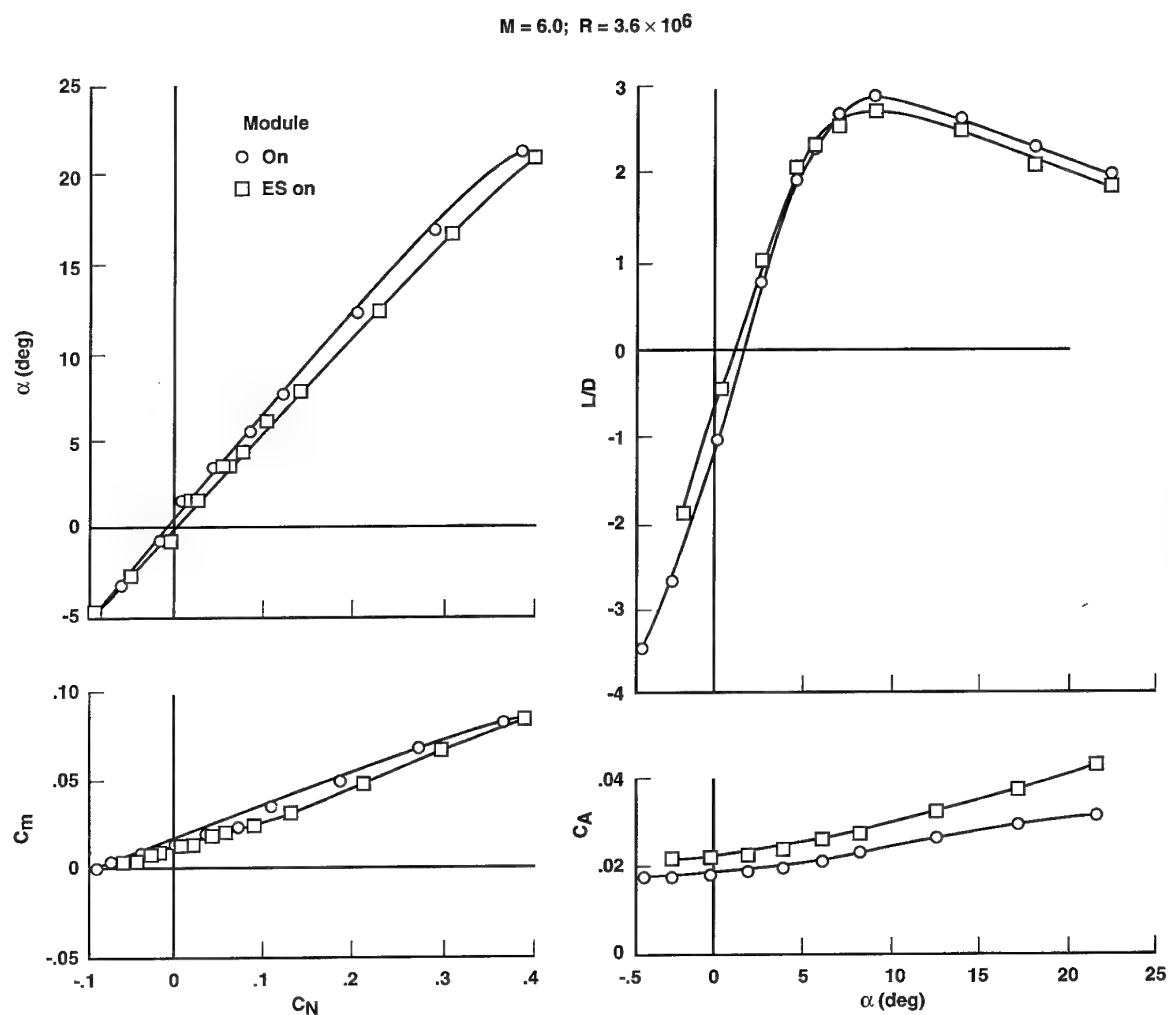
$M = 6.0; \ R = 3.6 \times 10^6$

Figure 14. Lateral-directional effects of adding the twin vertical tails to configuration BW-B/F.

AEROTHERMAL CHARACTERISTICS OF
SHOCK/SHOCK INTERACTION REGIONS IN HYPERSONIC FLOWS[*]

Michael S. Holden

Research Fellow

Calspan-University at Buffalo Research Center (CUBRC)

4455 Genesee Street, P.O. Box 400

Buffalo, New York 14225

SUMMARY

A review is presented of the aerothermal characteristics of regions of shock/shock interaction in hypersonic flow. Here, we discuss four aspects of the problem: (1) the requirements for accurate measurements in these flows; (2) the characteristics of shock/shock interaction regions in rarefied and laminar flows; (3) the aerothermal loads generated in transitional regions of shock/shock interaction; and (4) real-gas effects in regions of shock/shock interaction. The characteristics of shock/shock interaction regions and the influence of Mach number and Reynolds number on the heating loads developed in them are discussed. Correlations are presented together with the results of semi-empirical prediction methods to describe the aerothermal loads spanning the non-continuum to high Reynolds number flow regime. Some preliminary results are presented to demonstrate that the real-gas effects act to diffuse and lower the aerothermal loads relative to the ideal gas environment.

1. INTRODUCTION

The heating levels in shock/shock interaction regions are severe and, because such flows are invariably transitional, they are extremely difficult to predict accurately. The large heating loads developed in these regions result principally from the large pressure rises generated by an efficient recompression process coupled with the development of transitional shear layers and boundary layers. Traditionally, shock/shock interaction phenomena have been modelled in terms of a stagnating flow, such as in Type IV interaction, or a reattaching shear layer, such as in Type III interaction. However, when examining these flows experimentally, it is difficult to distinguish between the heating loads generated by a Type IV interaction and those generated by Type III interaction because of the strong viscous effects in completely laminar

interactions and the transitional nature of the shear layer which can introduce noise into the stagnation region and influence turbulence levels in the reattaching shear layer, as discussed in Section 6.

The heating rates generated in two and three-dimensional interaction regions by shock-shock interaction can pose serious problems for the designer of thermal protection systems and scramjet engines. Heating levels up to two orders of magnitude larger than the stagnation point value can be generated at hypersonic speeds by shock-shock interaction over the leading edge of fins, inlets and injectors inside scramjet engines. These regions of sharply peaked heating levels are accompanied by high pressures, and unlike the stagnation point their position cannot be defined with ease, and can be unsteady.

The severe heating loads developed in a shock/shock interaction region were first studied in detail following the X-15 scramjet program where shock/shock heating resulted in a structural failure in the pylon supporting the scramjet engine (Ref. 1). A series of studies were conducted in the late 1960s where the main focus was the interaction between a shockwave and vertical fin. The studies by Edney (Ref. 2) of shock interactions on spherical configurations, coupled with his analysis of various interaction geometries that can be developed over cylinders and struts, provided the basic groundwork for the semi-empirical prediction of these flows. These studies were followed by the studies by Keyes and Hains (Ref. 3) who in addition to making further measurements, developed a computer code to predict the major aerothermal features of shock/shock interaction regions based principally on the semi-empirical models suggested by Edney. In retrospect, the measurements employed to support the semi-empirical formula used in this code suffered from the lack of spatial and temporal resolution, and had

significant lateral heat conduction effects. Therefore, predictions were based on measurements where the magnitude of the peak heating and severity of the gradients in the shock/shock interaction region were significantly lower than the imposed aerothermal heating load. With the advent of the NASP program, the peak heating level developed in regions of shock/shock interactions on a cowl lip and the leading edges of the cowl injector become major issues. The study by Holden, et al. (Ref. 4) indicated that to fully resolve these interactions on a cylindrical leading edge requires gages to be spaced with less than 1° separation, on an insulating surface with instrumentation that has a frequency response of greater than 2 kHz as discussed in Section 3.

2. SEMI-EMPIRICAL AND NUMERICAL PREDICTION METHODS

Comparisons between the peak heat transfer and pressure measurements made by Holden et al. (Ref. 4) on cylindrical leading edges made in these studies with the empirical prediction techniques devised by Edney (Ref. 2) and Keyes and Hains (Ref. 3) indicated that these prediction techniques are capable of bounding the levels of heating generated by laminar and turbulent Type III and IV interaction (see Figure 1). Also in laminar ideal gas flows, both DSMC and Navier Stokes codes (with careful gridding) can be employed to describe the aerothermal loads generated in these flows as discussed in Section 7. However, for transition interaction, the theoretical and experimental studies also suggest that it is necessary to understand and describe the role of the turbulence and radiated noise generated in the shear layer, and the influence of viscous effects on jet structure, on the boundary layer developed in the stagnation region of a Type IV interaction to accurately predict these flows. No matter the level of sophistication of the numerical scheme, and the resolution of the gridding, to produce an accurate prediction requires the modeling of the shear layer transition process and the development of low Reynolds number turbulence in the strong pressure gradients associated with shear layer attachment. Clearly, the task of predicting the aerothermal loads in regions of transitional shock/shock interaction is extremely difficult if not intractable. To examine the accuracy of the basic numerical techniques employed to describe these flows, detailed and accurate sets of measurements in flows which remain fully laminar throughout the interaction region are required. Within the past several years, both Navier-Stokes and Direct-Simulation Monte Carlo (DSMC) solvers have been employed to calculate a variety of low-density and laminar flows including those associated with regions of shock/shock and shock/boundary layer interaction.

To obtain an accurate prediction for these types of flows, it is necessary to perform a careful and detailed gridding of the flowfield in the shear-layer flows and in the recompression region as the shear layer reattaches to the surface. A principal requirement for an experimental study to be employed for code validation in addition to remaining fully laminar is that the flows in the region of peak heating be highly resolved both spatially and temporally.
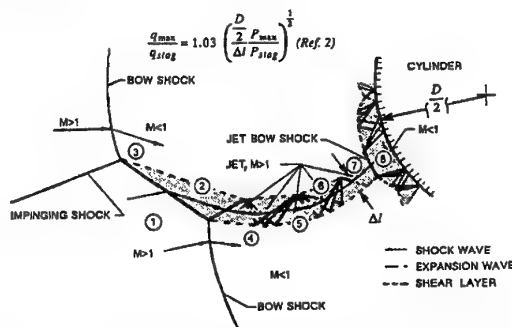

$$\frac{q_{max}}{q_{stag}} = 1.03 \left(\frac{\frac{D}{2} P_{max}}{\Delta l \, P_{stag}}\right)^{\frac{1}{3}} \; (Ref.\ 2)$$

Figure 1a   Schematic Diagram of a Type IV Interference Pattern Impinging on a Cylinder

$$\frac{q_{max}}{\varrho_{ws}U_s(H_{aw}-H_w)} \;\; LAMINAR \to 0.19 \left[\frac{\varrho_{ws}U_s\delta_{SL}}{\mu_{ws}\sin a}\right]^{-0.5} \; where \; \delta_{SL} = 5 \left(\frac{\ell_{SL}\mu_2}{\varrho_2U_1}\right)^{0.5}$$

$$TRANSITIONAL \to 0.021 \left[\frac{\varrho_{ws}U_s\delta_{SL}}{\mu_{ws}\sin a}\right]^{-0.2} \; where \; \delta_{SL} = 0.123 \, \ell_{SL}$$
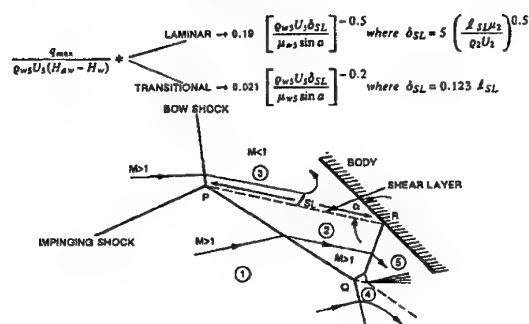
Figure 1b   Schematic Diagram of Type III Interference

3. REQUIREMENTS FOR ACCURATE AEROTHERMAL MEASUREMENT

The accurate measurements of the distribution of properties in regions of shock/shock interaction is one of the most difficult tasks in the experimental evaluation of hypersonic flows. The severe heat transfer gradients generated in Type III and Type IV shock/shock interactions can result in large lateral heat transfer gradients, which, in turn, can reduce the measured peak heating value and increase the width of the measured peak heating region. Measurement errors introduced by lateral heat conduction in regions of shock/shock interaction were first noted by Heirs and Loubsky (Ref. 5) and explored further by Holden (Ref. 6). While it is possible to correct for lateral conduction effects if the flow remains steady, in most shock/shock interaction regions, there is an intrinsic unsteadiness which can cause significant

spatial variations in the peak heating region. Unresolved unsteady effects will also introduce a reduction in peak heating and a broadening of the peak heating region. Because of the random nature of the unsteadiness, correcting for these effects are practically impossible. Thus, deconvolving and correcting for the combined effects of lateral heat conduction and flow unsteadiness represents an impossible task in regions of shock/shock interaction.

It has been found that the peak heating region induced by shock/shock interaction extends over a region subtended by an angle of between 3 and 10 degrees (Ref. 4). To specify the distribution of properties in this region, at least 10 individual data points are required; therefore, each gage must subtend angles on the order of 0.5 degree, or a spacing of 0.01 inch between centers on a 1-inch-nose-radius leading edge. It would not be possible, except on really large models, (nose radii greater than 6 inches), to employ discrete, commercially available heat transfer instrumentation, and achieve the required gage size and spatial resolution. An example of specialized instrumentation required to provide the necessary gage spacing is shown in Figure 2. Even for the short duration associated with shock tunnel flows, employing stainless steel models instrumented with miniature chromel/constantan thermocouples would result in significant errors in the heat transfer measurements caused by transverse heat conduction, as discussed in Reference 5.
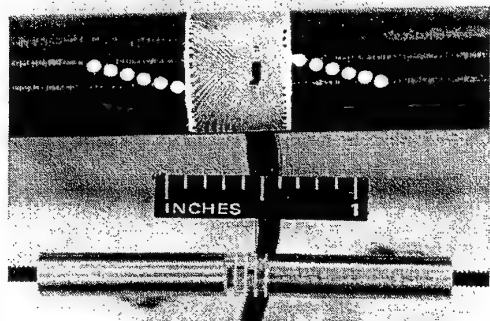

Figure 2   Heat Transfer Instrumentation Layout on .138 and .375-Inch Radius Cylinders

The high-frequency requirements for the heat transfer and pressure instrumentation to accurately measure the distributions in regions of shock/shock interaction are controlled by the basic frequencies introduced by the unsteady movements of the interaction region. A primary source of this high frequency movement is fluctuation of the incident shock induced by acoustic radiation from the transitional or turbulent boundary layer on the shock generator. Other sources of movement are associated with the transitional and turbulent shear layers

generated in the interaction region. A typical turbulent scale size on the shock generator is of the order of 0.01 ft for freestream velocities of 8,000 ft/sec; therefore, frequencies from 100 kHz to 1 MHz can be anticipated. Calculations of the turbulent scale size in the shear layers generated in Types III and IV interaction regions lead to calculations of even higher frequencies. The fluctuating nature of the gross unsteadiness observed for certain classes of Type IV interactions suggests that much lower frequencies, in the 10 kHz range, must be resolved. Thus, to accurately measure the peak heating rate and the highly spiked distributions occurring in the interaction regions, it is mandatory that the instrumentation be capable of following frequencies at least into the 30 kHz range.

It has been suggested by Neumann (Ref. 7) that for code validation purposes, models and instrumentation with intrinsically high-thermal conductivity should be employed to minimize the variation in surface temperature around the model. However, as discussed in Ref. 6, this approach would introduce significant indeterminate errors in the heat transfer measurements. A better approach, as discussed earlier in References 4 and 6, is to accurately measure the heating distribution employing high-frequency instrumentation on non-conducting surfaces; then for the small number of cases where the surface temperature rise is important to tabulate the distribution of surface temperature together with the heat transfer rate. In this way, the surface-temperature distribution can be input as a boundary condition in the numerical prediction techniques to produce predictions in a manner similar to those that would have to be employed for the flight case.

4.   DEFINING SHEAR LAYER CONDITIONS FOR INTERACTION REGIONS

Defining the conditions under which regions of shock/shock interaction remain fully laminar is not a simple task. From the experimental viewpoint, the intrinsic problem is that, even for fully laminar interaction regions, some degree of unsteadiness is present in the experimental data and it is not possible to easily separate instabilities associated with transition from the basic flow instability. The principal approaches which have been employed to define the occurrence of transitional interaction regions induced by shock/shock interaction are based on exploring the variation of peak heating with Reynolds number, examining the unsteady characteristics of the heating in the reattachment region, and attempting to detect unsteadiness in the shear layers on the basis of observation from schlieren or shadowgraph photography. In most

studies, the boundaries between transitional and fully laminar interaction have been drawn on plots of shear layer Reynolds number versus Mach number. It has been found that for shear layer Reynolds number below 5×10^3, the shear layer remain laminar, while for shear-layer Reynolds numbers above 5×10^5, a fully turbulent interaction region should be expected. The exact Reynolds number at which shear-layer transition will occur, will of course, also depend upon the disturbances that are radiated from upstream surfaces of the vehicle and those present in the freestream. Correlations of transition measurements for shock interactions are presented in Section 6.

5. SHOCK/SHOCK-INTERACTION HEATING MEASUREMENTS IN LOW DENSITY AND LAMINAR FLOWS

Recently, a series of measurements were made (Ref. 6) on small models in low Reynolds number flow to ensure that sets of measurements for fully laminar flows were obtained for aerothermal load prediction and code validation. In these studies, variation in the magnitude and distribution of heat transfer and pressure in laminar regions of shock/shock interaction with interaction geometry were made for a range of Reynolds numbers based on cylinder diameter from 800 to 8,000, which span the continuum to non-continuum flow regimes. Both the unit Reynolds number and the cylinder diameter were varied to hold the Reynolds number (based on the model diameter) constant. Measurements of the variation of the distribution of heat transfer rate with the position of the shock impingement point for a range of test conditions and model size (taken from Ref. 6) are shown for increasing Reynolds numbers based on model diameter in Figures 3 through 9. Figure 3 shows the variation of the heat transfer distribution with shock impingement point for the lowest absolute Reynolds number obtained with the 3/4-inch cylinder. Note that the maximum values of the peak heating in the interaction region are no greater than 5 times the Fay-Riddell value. Also note that, in contrast with measurements at significantly higher Reynolds numbers, the locus of the peak heating levels peaks at close to 20 degrees below the axis. As shown in Figure 4, a similar trend is observed on the 1/4-inch cylinder at a higher unit Reynolds number. Again, the peak heating level of the distribution with the greatest heating is increased. Increasing cylinder size to increase Reynolds number causes the peak heating to again increase as shown in Figure 5, and the distribution of the highest heating level to move downward is close to 20 degrees below the axis. As the interactions move lower around the cylinder, the peak heating levels decrease and the distribution of heating broadens. Increasing the unit Reynolds number on the 3/4-inch cylinder causes the

peak heating level to increase and the distribution with the highest heating rate to occur at 25 degrees below the axis as shown in Figure 6. Again, we observe a lowering of the peak heating value and a broadening of the distribution as the interaction is moved lower around the nosetip.
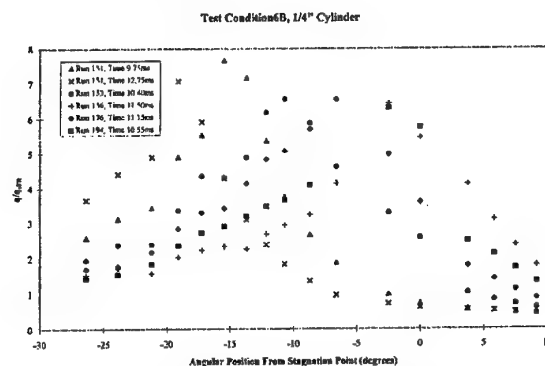

Figure 3   Variation of the Distribution of Heat Transfer in the Shock Interaction Region with Interaction Position in Low-Reynolds Number Flow Over the .375-Inch Radius Cylinder
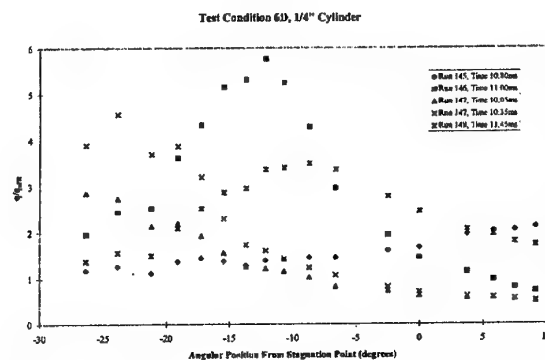

Figure 4   Variation of the Distribution of Heat Transfer in the Shock Interaction Region with Interaction Position in Low-Reynolds Number Flow Over the .138-Inch Radius Cylinder
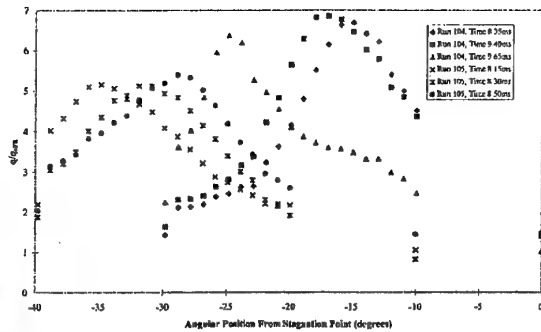
Test Condition 6AA, 3/4" Cylinder

Figure 5   Variation of the Distribution of Heat Transfer in the Shock Interaction Region with Interaction Position in Laminar Flow Over the .375-Inch Radius Cylinder
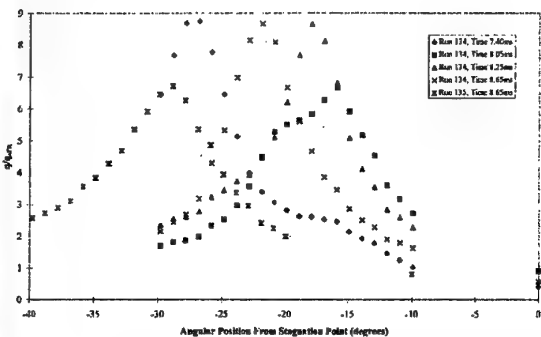
Test Condition 5A, 3/4" Cylinder

Figure 6   Variation of the Distribution of Heat Transfer in the Shock Interaction Region with Interaction Position in Laminar Flow Over the .375-Inch Radius Cylinder

Changing the unit Reynolds number and the cylinder diameter to keep the absolute Reynolds number the same, the measurements on the 0.27D cylinder, shown in Figure 7, indicate that the heating levels do not significantly vary with interaction position for shock interactions between 5 and 20 degrees below the axis. Although these measurements were made at a large freestream Reynolds number, the variation of the distribution with shock impingement position is similar to the measurements on the 0.27D cylinder with the lower Reynolds numbers. Increasing the cylinder diameter to 3 inches, but reducing the freestream Reynolds number to hold the absolute Reynolds number constant, results in the series of distributions shown in Figure 8a, and the associated pressure distributions as shown in Figure 8b. Here, we observe that the peak heating for all the interaction positions is increased and that the variation of peak heating with interaction position does not change significantly from 15 to 40 degrees. Increasing the unit Reynolds

number on the 3-inch cylinder results in a further increase in the maximum peak heating level and distributions, as shown in Figure 9a, where the maximum peak heating occurs at approximately 25 degrees with the peak heating falling off above and below this peak heating region. The associated pressure distributions are shown in Figure 9b. At this condition, and possibly for the measurements at the lower Reynolds number on the 3-inch cylinder, we may have transition occurring in the reattaching boundary layer in the cylinders. All of these sets of measurements have been incorporated into the CUBDAT database (Ref. 8) where it is possible to obtain numerical values of the individual data points as well as material on model configuration and freestream conditions. Figures 10 and 11 show typical plots of pressure and heat transfer information that can be obtained from the CUBDAT database from the 3-inch cylinder data.
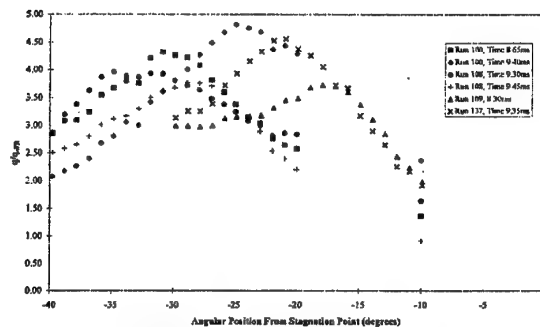
Test Condition 10C, 3/4" Cylinder

Figure 7   Variation of the Distribution of Heat Transfer in the Shock Interaction Region with Interaction Position in Laminar Flow Over the .138-Inch Radius Cylinder
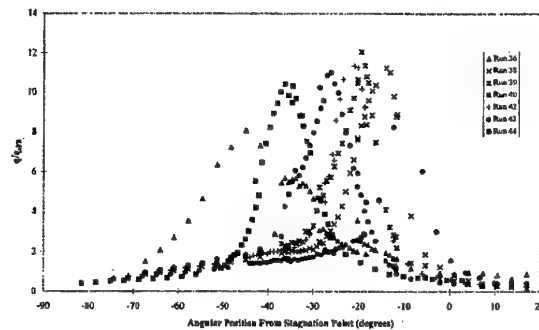
Test Condition 10C, 3" Cylinder

Figure 8a   Variation of the Distribution of Heat Transfer in the Shock Interaction Region with Interaction Position Over the 1.5-Inch Radius Cylinder
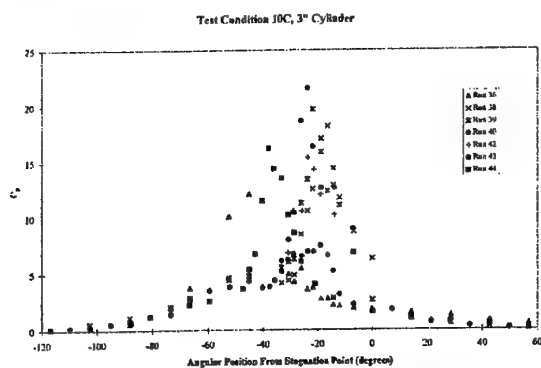
Test Condition 10C, 3" Cylinder

Figure 8b   Variation of the Distribution of Pressure in the Shock Interaction Region with Interaction Position in Laminar Flow Over the 1.5-Inch Radius Cylinder
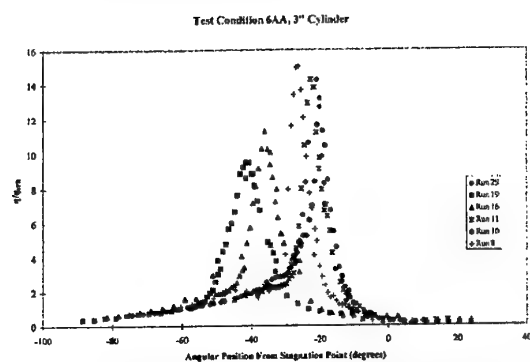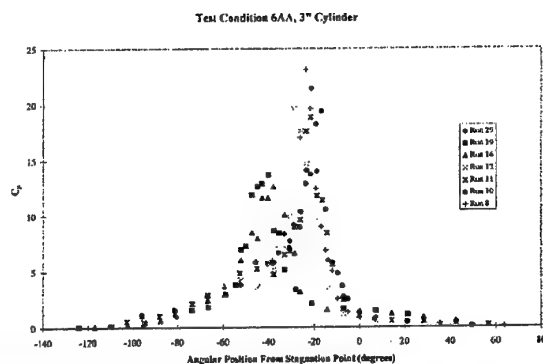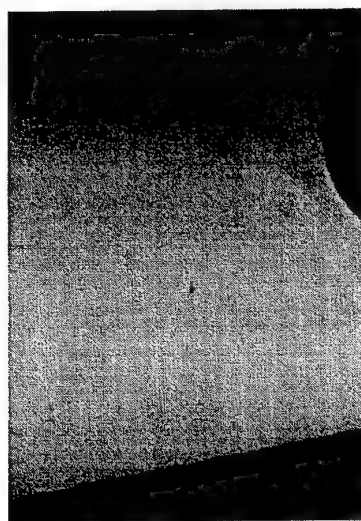

Test Condition 6AA, 3" Cylinder

Figure 9a   Variation of the Distribution of Heat Transfer in the Shock Interaction Region with Interaction Position Over the 1.5-Inch Radius Cylinder

Test Condition 6AA, 3" Cylinder

Run 19

Run 10

Figure 9b   Variation of the Distribution of Pressure in the Shock Interaction Region with Interaction Position in Laminar Flow Over the 1.5-Inch Radius Cylinder
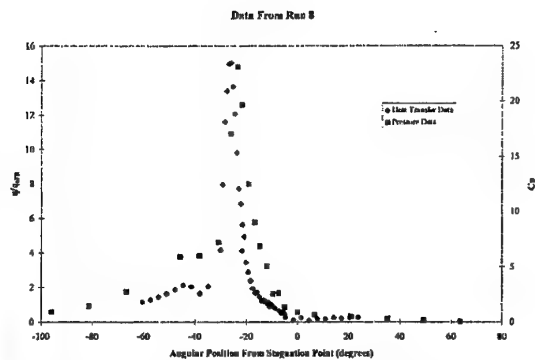
Data From Run 8

Figure 10   Distribution of Heat Transfer and Pressure in Type III Region of Shock/Shock Interaction Over 1.5-Inch Radius Cylinder which is Typically Obtained from the CUBDAT Database (Run 8)
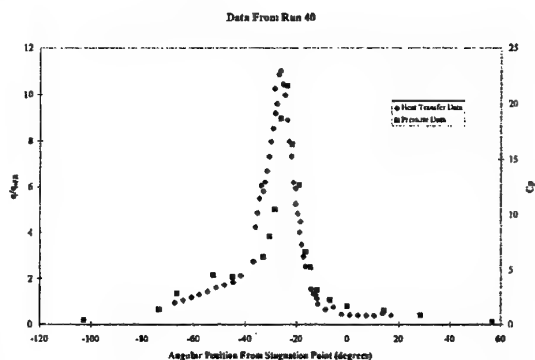

Data From Run 40

Figure 11   Distribution of Heat Transfer and Pressure in Type IV Region of Shock/Shock Interaction Over 1.5-Inch Radius Cylinder which is Typically Obtained from the CUBDAT Database (Run 40)

Correlating these heat transfer measurements, together with those from Reference 2 in terms of the rarefaction parameter to emphasize the importance of viscous effects in the shock layer, we see as shown in Figure 12, that the peak heating enhancement levels for flows where the viscous interaction parameter is less than 0.2, drop below 10 reaching values of close to 0.5 for viscous dominated shock layers. Alternatively, plotting the peak heating level from this data in terms of the shear layer Reynolds number (as shown in Figure 13), results in approximately a linear increase from values of the shear layer Reynolds number from 600 to just less than 1,000, at which point significant increases can be observed in the peak heating level suggesting possible effects of transition. Again, determining and defining when transition influences heating in regions of shock/shock interaction is a difficult but key task in the prediction of heating in shock/shock interaction regions.
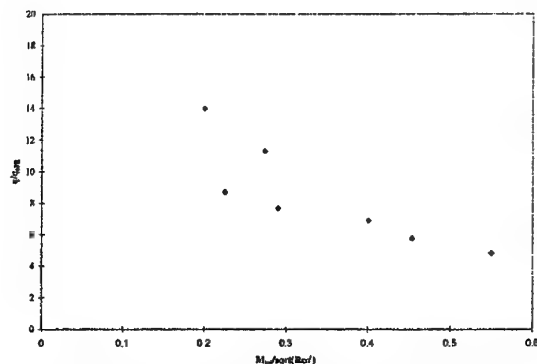

Figure 12   Variation of Heating Enhancement Ratio Versus Rarefaction Parameter
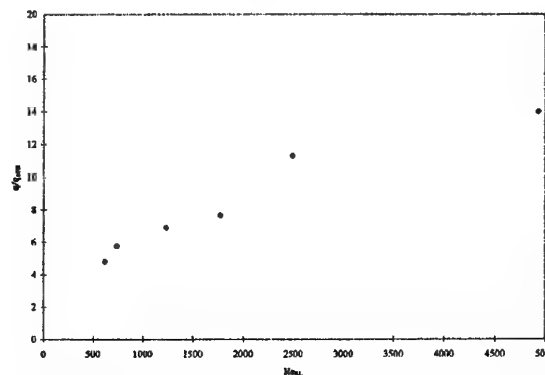

Figure 13   Variation of Heating Enhancement Ratio Versus Shear Layer Reynolds Number

6.   AEROTHERMAL LOADS IN TRANSITIONAL AND TURBULENT FLOWS

Because the shear layer generated in Types III and IV interaction regions easily becomes transitional, the majority of the aerothermal loads generated in regions of shock/shock interaction will be controlled by transitional and turbulent transport mechanisms. Described in terms of the jet or shear layer attachment models of Edney (Figure 1a), the noise radiated from the transitional shear layer can and does enhance the stagnation heating rate at the base of the jet. For Type III interaction, the large eddies generated in the shear layer will significantly increase the energy transport in and downstream of the attachment region. The complexity of such phenomena presents a significant and possibly insurmountable task for turbulence modellers attempting to predict the heating loads within the framework of the time-averaged Navier-Stokes equations. Therefore, here, we attempt to provide measurements and correlations to provide semi-empirical prediction techniques to calculate the

magnitude of the peak heating. Since detailed numerical techniques can provide relatively accurate values for the pressure generated in shock/shock interaction regions the most useful correlation is based on the peak pressure and the undisturbed stagnation region heating generated in these flows. Measurements, by Holden et al. (Ref. 9), in transitional flows over a range of Reynolds numbers at Mach numbers from 6 to 18 provide an extensive database that can be used to estimate the aerothermal loads in shock-shock interaction regions in the presence of radiated noise and transitional reattachment.

Determining the conditions where the shear layer becomes turbulent represents the first task in estimating the aerothermal loads in these flows. For separated flows in compression corners and in base regions, it has been observed that transition Reynolds numbers, based on shear layer length, are typically an order of magnitude less than those for attached flows or 5E4 for low Mach number flows. Correlations of shear layer transition in terms of the local properties and length and the Mach number have often been used for separated flows and the data obtained from the most recent shock-shock interaction studies are shown in Figure 14. The most recent data based on examining the variation of heating rate with Reynolds number suggest that for shear layer Reynolds numbers greater than 2E4 the flows should be considered transitional.
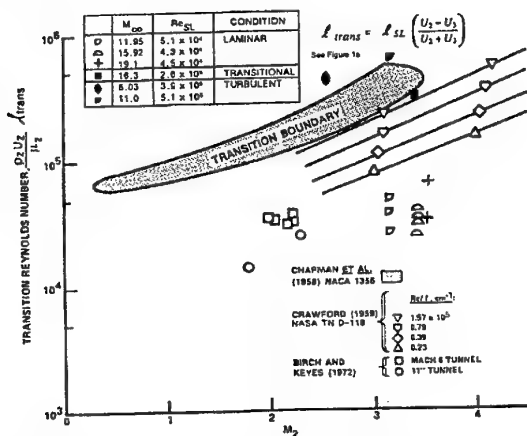
A characteristic of transitional interaction regions is that there is very little variation in the peak heating level with the position for interactions between 18 and 38 as shown in Figure 18. This, we believe, results in increasingly turbulent characteristics of the shear layer as its length is increased and may be responsible for this trend. As expected, there is an increase in the peak pressure in shock/shock interaction regions with increasing Mach number (see Figure 19); however, this is possibly a result of transitional effects because we did not observe as strong a trend in the heat transfer measurements (see Figure 20). Plotting the peak heating for Types III and IV interactions occurring at angles between 20° and 35° (where we do not observe a significant variation of peak heating with angle) with peak pressure (see Figure 21), we observe a relative good correlation that is roughly linear on the log/log plot which suggests the power law relationship:

$$q_{peak}/q_{tr}=(p_{peak}/p_n)^{0.85}$$

which is similar to the relationship obtained for turbulent reattachment heating in separated flows. Simple calculations of the pressures and heat transfer rates for Types III and IV interaction regions can also be made with reasonable accuracy with the Keyes and Hains code; however, for shear layer heating, the more recent measurements suggest a coefficient of 0.025 rather than 0.021 employed in the code (see Figure 1b).

Figure 14 Correlation of Shear Layer Transition Measurement

Figure 15 Heat Transfer and Pressure Distribution in Transitional Shock/Shock Interaction Region at Mach 8 with 10° Shock Generator

Typical distributions of heating and pressure in transitional regions of shock/shock interaction for Mach numbers of 8, 11 and 16 are shown in Figures 15, 16, and 17, respectively. These figures illustrate very similar characteristics for both heating and pressure distributions over this Mach number range.
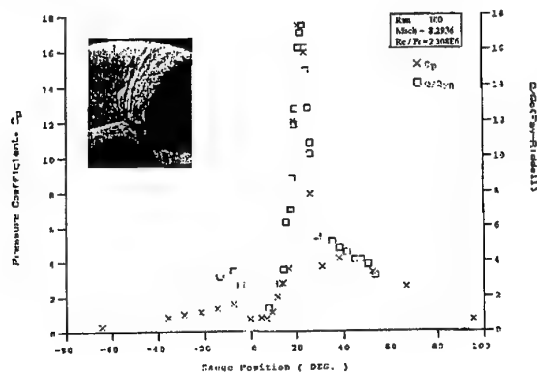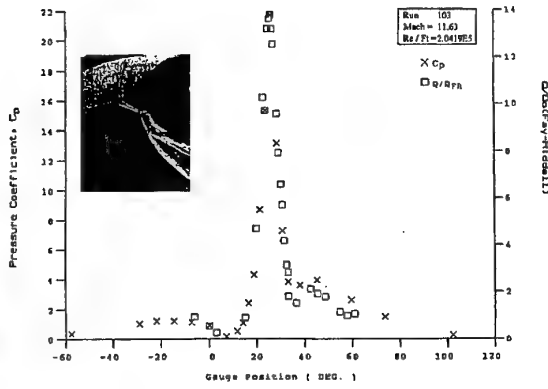
Figure 16   Heat Transfer and Pressure Distribution in Transitional Shock/Shock Interaction Region at Mach 10 with 10° Shock Generator
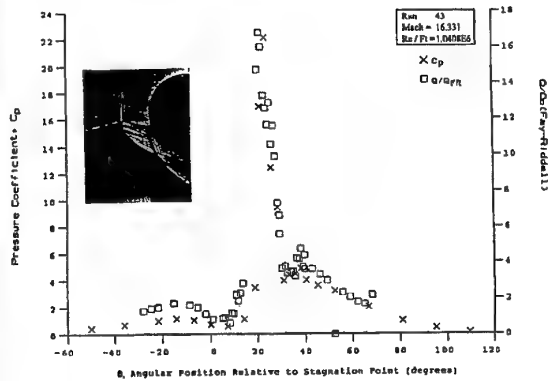
Figure 17   Heat Transfer and Pressure Distribution in Transitional Shock/Shock Interaction Region at Mach 17 (Reference 4)

Figure 18a   Variation of Peak Heating with Interaction Position for Mach 6.4 (Reference 4)

Figure 18b   Variation of Peak Heating with Interaction Position for Mach 6.4 and 8.0 (Reference 4)

Figure 19   Variation of Real Pressure with Mach Number (Reference 4)

Figure 20   Variation of Peak Heating with Mach Number (Reference 4)

Figure 21   Variation of Peak Heating with Peak Pressure

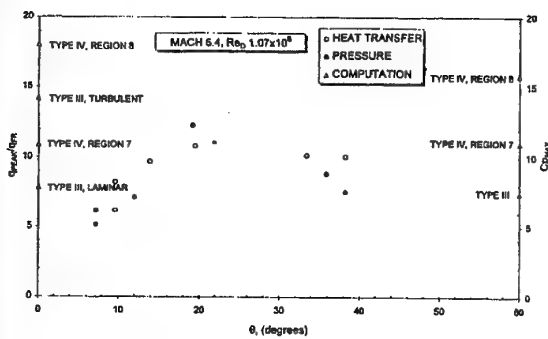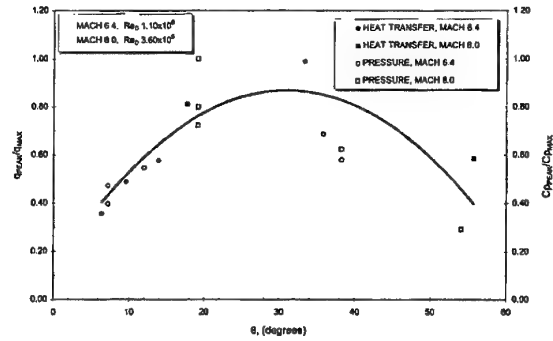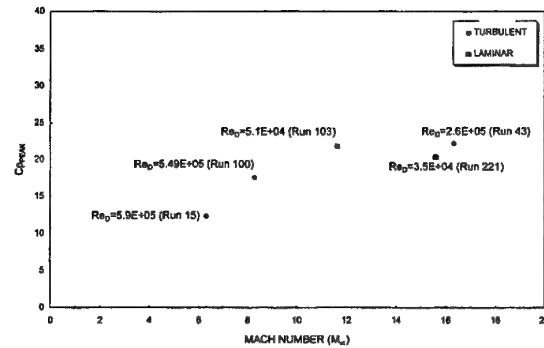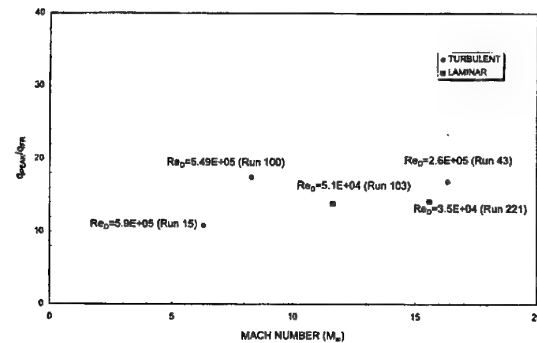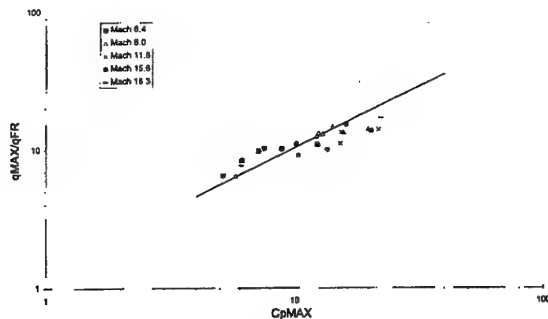## 7.   REAL GAS EFFECTS IN REGIONS OF SHOCK/SHOCK INTERACTION

Because the peak pressure and heat transfer for a Type IV interaction region are so strongly related to the structure of the compression and expansion wave trains, which may be formed in the Edney jet model (see Figure 1a) and, which in turn are strongly linked to the Type V interaction region, Edney speculated that real gas effects would cause a significant increase in the pressure recovery and the heat transfer rate in the stagnation region at the base of the jet. However, each of the three experimental studies conducted to investigate such real gas effects, have demonstrated the opposite trend, a decrease in the heat transfer rate resulting from dissociation and real gas chemistry. Studies by Kortz et al. (Ref. 10) in the HEG and Sanderson et al. (Ref. 11) in the T5 piston-driven shock tunnels have both indicated that in high energy flow, the flow pattern (see Figures 22 and 23) and the heat transfer and pressure distribution are strongly influenced by nitrogen dissociation for the Type IV interaction region. As for the Type IV interaction, the peak heating and pressure in the Type III interaction were lower by real gas effects as discussed in References 10 and 11. More recently, measurements of real gas effects on the aerothermal loads in shock -shock interaction regions were made in air and nitrogen at 10 MJ/kg which is approximately equivalent to 5km/sec. At this enthalpy level, pure nitrogen behaves like an ideal gas while oxygen in air is fully dissociated and the NO shuffle reactions are of key importance. Highly resolved spatially- and temporally-resolved measurements on nonconducting surfaces were made to examine the differences in the heating for Type IV interaction for nitrogen and airflows. The shock/shock model used in this study is shown in Figure 24.
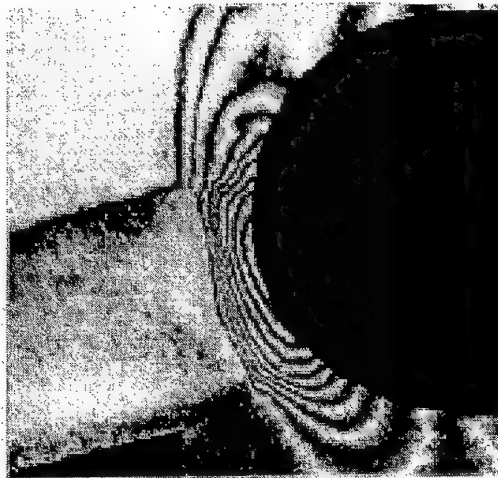

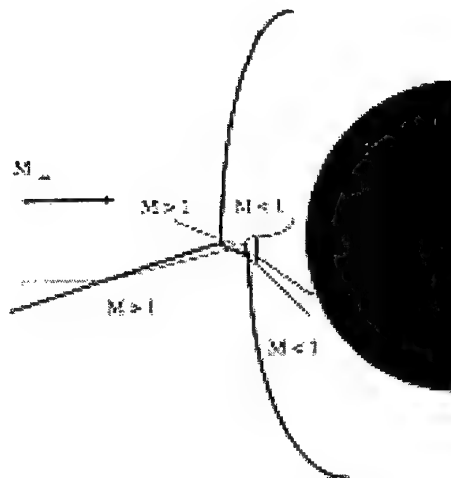**Figure 22**   Interferogram for Type IV Shock/Shock Interaction (Reference 10)

Figure 23   Diagram Illustrating Type IV Interaction for High Enthalpy Real Gas Flow (Reference 10)

Figure 24   Shock/Shock Interaction Model Installed in the LENS Facility

Typical measurements of the distribution of heating in a Type IV interaction region for flow velocities of 14,000 ft/sec with air and nitrogen freestreams are shown in Figure 25. These measurements indicate that the real-gas effects associated with the air flow reduced rather than increased the levels in shock/shock interaction regions. For the air case, observe that the region of peak heating is broadened and the peak heating level is reduced. These measurements are being compared with calculations based on the Navier-Stokes code and will be discussed in a later paper.
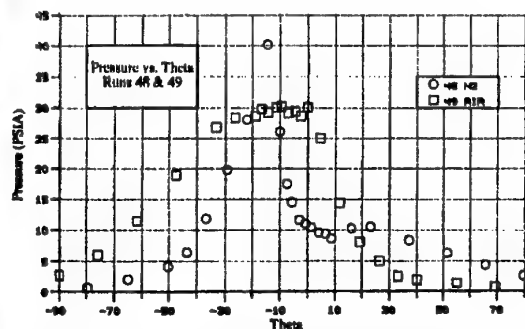

Figure 25 Heat Transfer Measurements in Shock/Shock Interaction for Nitrogen and Air Flows (Reference 9)

Several numerical studies (References 12-15) have been conducted using both DSMC and Navier-Stokes codes to investigate real gas effects on the structure and heating in regions of shock/shock interaction. Studies by Carlson and Wilmoth (Ref. 15) using a Monte-Carlo simulation (see Figure 26) examined the effect of flowfield chemistry in a low-density flow. In addition to examining the critical effect of grid selection on the peak heating levels, they also demonstrated that real-gas effects can significantly change the structure of the flowfield and influence the structure of the interaction region Figure 26. A similar study in continuum flows by Furumoto and Zhong (Ref. 13) also demonstrate the sensitivity of the flowfield to real-gas effects and, for the cases they studied, demonstrated that non-equilibrium real-gas effects increase the magnitude of the peak heating enhancement relative to perfect gas flows over isothermal, non-catalytic walls (see Figure 27). Thus, both the experiment results and theory indicate that real-gas effects reduce the level of peak pressure by enlarging the interaction region in contrast to the analysis by Edney, would suggests the opposite result. Again, these conclusions can only be made for flows that remain completely laminar. It remains almost impossible to calculate with any accuracy flows with boundary layer transition.
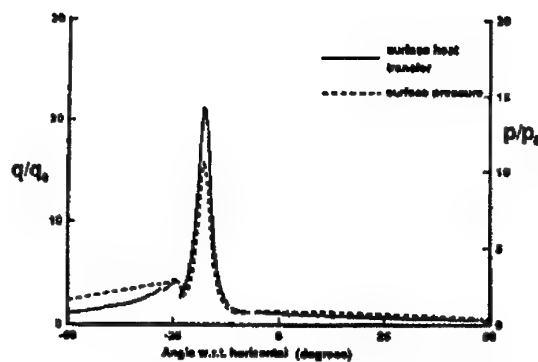
a. Surface Properties for Near Perfect Gas Case.

$q_0 = 24Mw / m^2, P_0 = 1.9 \times 10^5 Pa$
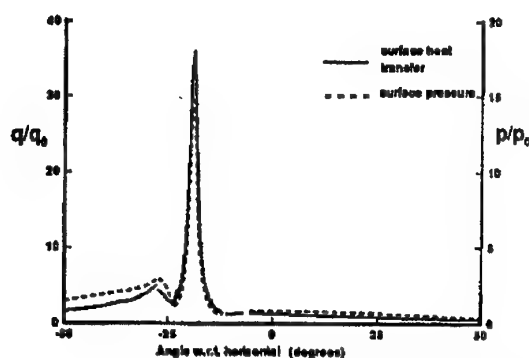
b. Surface Properties for Finite-Rate Chemistry Case.

$q_0 = 15Mw / m^2, P_0 = 2.0 \times 10^5 Pa$

Figure 27 DSMC Computations of Real Gas Effects on Aerothermal Loads Generated in Shock/Shock Interaction Regions by Carlson and Wilmoth (Reference 15)

a. Perfect Gas Model Heat Transfer
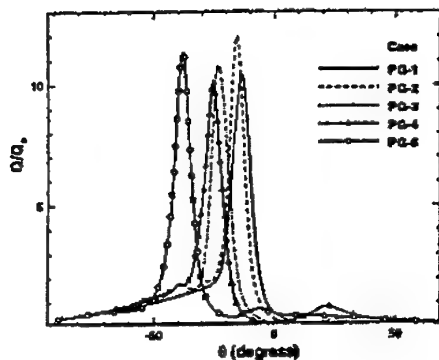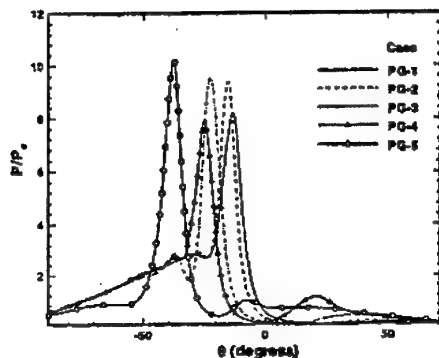

b. Perfect Gas Model Pressure Profiles
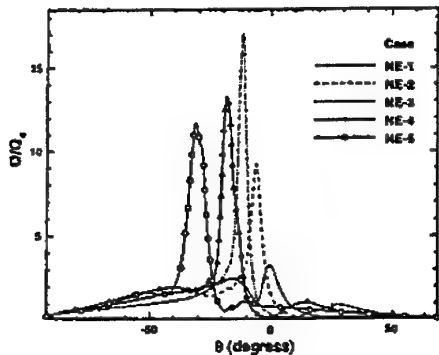
c. Nonequilibrium Model Surface Heat Transfer

Figure 28 Navier Stokes Computations of Real Gas Effects on Aerothermal Loads Generated in Shock/Shock Interaction Regions by Furumoto and Zhong (Reference 13)
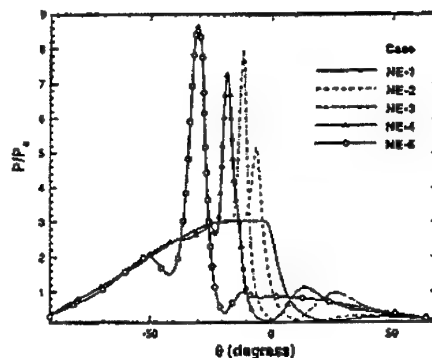
d. Nonequilibrium Model Surface Pressure Profiles

Figure 28 Navier Stokes Computations of Real Gas
(cont.) Effects on Aerothermal Loads Generated in Shock/Shock Interaction Regions by Furumoto and Zhong (Reference 13)

8. CONCLUSIONS

Measurements and correlations are presented to estimate the aerothermal loads in regions of shock/shock interaction for non-continuum to fully turbulent flow regimes. While it is possible to compute (employing careful gridding of these flows) the aerothermal loads developed in laminar regions of shock/shock interaction accurately, computing the heating rates generated in these regions when shear layer transition occurs is difficult if not impossible. For these latter cases, computing the pressure flowfield with Navier-Stokes solutions and estimating the heating loads employing semi-empirical correlations may be the most realistic approach. Accurately predicting real-gas effects in shock/shock interaction regions for flows which remain laminar, while tractable, remains to be validated. Combining modeling turbulence and non-equilibrium flows to describe shock/shock interaction regions where the shear layer is transitional, represents a significant task, the validity of which must rely on carefully conducted experiments in high-pressure, high-enthalpy flows.

9. REFERENCES

1. Watts, J.D., "Flight Experience with Shock Impingement and Interference Heating on the X-15-2 Research Airplane," NASA TM X-1669, 1968.

2. Edney, B., "Anomalous Heat Transfer and Pressure Distributions on Blunt Bodies at Hypersonic Speeds in the Presence of an Impinging Shock," FFA Report 115, Aeronautical Research Institute of Sweden, 1968.

3. Keyes, J.W. and Hains, F.D., "Analytical and Experimental Studies of Shock Interference Heating in Hypersonic Flow," NASA Report TN D-7139, May 1973.

4. Holden, M.S., Moselle, J.R., Lee, J., Weiting, A.R., and Glass, C., "Studies of Aerothermal Loads Generated in Regions of Shock/Shock Interaction in Hypersonic Flow," NAS1-17721, April 1991 (Revised 1996).

5. Heirs, R.S. and Loubsky, W. J., "Effects of Shock-Wave Impingement on the Heat Transfer on a Cylindrical Leading Edge," NASA TN D-8859, February 1967.

6. Holden, M.S. and Kolly, J., "Measurements of Heating in Regions of Shock/Shock Interaction in Hypersonic Flow," AIAA95-0640, paper presented at the 33rd Aerospace Sciences Meeting in Reno, NV, January 9-12, 1995.

7. Neumann, R.D., "CFD Code Validation-An Instrumentation Perspective," AIAA 94-2541, Paper presented at the 18th AIAA Aerospace Ground Testing Conference, Colorado Springs, CO, June 20-23, 1994.

8. Holden, M.S. and Moselle, J.R., "A Database of Aerothermal Measurements in Hypersonic Flow for CFD Validation," AIAA-92-4023, Paper presented at the AIAA 17th Aerospace Ground Testing Conference, Nashville, TN, 6-8 July 1992. (A copy of this database is available by contacting the authors.)

9. Holden, M.S. and Walker, B.J., "A Review of Recent Development, Testing and Code Validation Studies in the LENS Facility," AIAA Paper No. 96-4598.

10. Kortz, S., McIntyre, T.J. and Eitelberg, G., "Experimental Investigation of Shock-on-Shock Interactions in the High-Enthalpy Shock Tunnel Gottingen (HEG)," Shock Waves at Marseilles I, Hypersonics, Shock Tube and Shock Tunnel Flow, Proceeding Marseilles, France, 1993.

11. Sanderson, S.R. and Sturtevant, B., "Shock Wave Interactions in Hypervelocity Flow," Shock Waves at Marseilles I, Hypersonics, Shock Tube and Shock Tunnel Flow, Proceeding Marseilles, France, 1993.

12. Sanderson, S.R. and Sturtevant, B., "Shock-Interference Heating in Hypervelocity Flow," Proceedings of the 20th International Symposium on Shock Waves, Volume I, World Scientific, Pasadena, CA, July 1995.

13. Furumoto, G.H. and Zhong, X., "Numerical Simulation of Viscous Unsteady Type IV Shock-Interaction with Thermochemical Nonequilibrium," AIAA 97-0982, Paper presented at 35th Aerospace Sciences Meeting and Exhibit, Reno, NV, January 1997.

14. Comeaux, K.A., Chapman, D.R. and MacCormack, R.W., "Viscous Hypersonic Shock-Shock Interaction On a Blunt Body at High Altitude," AIAA 93-2722, Paper presented at AIAA 28th Thermophysics Conference, Orlando, FL, July 1993.

15. Carlson, A.B. and Wilmoth, R.G., "Monte Carlo Simulation of a Near-Continuum Shock-Shock Interaction Problem," Paper presented at AIAA 27th Thermophysics Conference, Nashville, TN, July 1992.

ADVANCES IN COMPUTATIONAL CAPABILITIES FOR HYPERSONIC FLOWS

Ajay Kumar
Peter A. Gnoffo
James N. Moss
J. Philip Drummond
Aero- and Gas-Dynamics Division
NASA Langley Research Center
Hampton, VA 23681
U.S.A

1. SUMMARY

The paper reviews the growth and advances in computational capabilities for hypersonic applications over the period from the mid-1980's to the present day. The current status of the code development issues such as surface and field grid generation, algorithms, physical and chemical modeling, and validation is provided. A brief description of some of the major codes being used at NASA Langley Research Center for hypersonic continuum and rarefied flows is provided, along with their capabilities and deficiencies. A number of application examples are presented, and future areas of research to enhance accuracy, reliability, efficiency, and robustness of computational codes are discussed.

2. INTRODUCTION

Over the years, worldwide research and technology development in hypersonics seems to follow a cyclic pattern with activities peaking around specific missions and technology programs such as Apollo, Space Shuttle, and more recently, NASP and HERMES. The current hypersonic activities are predominantly focused around the development of low cost reusable launch vehicles and associated propulsion systems. This new generation of vehicles is primarily driven by economic considerations, although it does have military implications. The cyclic pattern of technology development in hypersonics has had severe impact on the scientific community in its ability to maintain necessary skills and test facilities during the period when there are no approved hypersonic projects. It has been even more difficult to recreate them when new projects do appear. However, since the early 1970's, a new engineering tool, known as Computational Fluid Dynamics (CFD), started to emerge for aerospace applications, and its growth through the mid 1980's was not tied to any specific technology program or mission. Significant growth in CFD capabilities took place during this period, ranging from the solution of inviscid incompressible flow fields to the solution of Navier-Stokes equations for high Reynolds number and Mach number [1,2,3]. Even with this rapid growth in CFD, it did not yet become a routine analysis and design tool for aerospace applications. However, in the mid 1980's, CFD was accepted as an attractive analysis and design tool mostly due to demands of the programs such as the National Aero-Space Plane (NASP) Program and aerobraking research program, and not necessarily because it had become a mature design tool. These programs had no other design tools immediately available to them. Due to lack of available ground facilities for testing at high Mach numbers (the ones that were available did not simulate the flight enthalpies at these high Mach numbers) and due to the complex and integrated nature of the flow field, traditional wind-tunnel based design techniques were not adequate. CFD was offered as a promising alternative for analysis, design, and even optimization of hypersonic vehicles and propulsion systems. However, up to around this time, most of the available CFD capabilities were either two-dimensional Navier-Stokes codes with limited physical/chemical modeling or were simplified codes (viscous-shock layer, parabolized Navier-Stokes) with limited applicability. Fully three-dimensional Navier-Stokes codes were just beginning to appear, and they were generally applicable only for perfect gas flows. In addition, none of the codes had been properly validated.

However, in the period between 1985 and 1990, there was a significant increase in the application of CFD for modeling hypersonic flows. Industry slowly accepted it as a viable alternative, and significant resources were invested in the development of CFD codes by both industry and government labs. Several fully three-dimensional Navier-Stokes codes, along with their space marching versions, were developed with detailed chemistry modeling, both for high-speed combustion and aerothermodynamic applications. Most of these codes used algorithms developed in the seventies and early eighties, namely, implicit or explicit central differences methods (including multistage methods) and upwind methods. Simple phenomenological turbulence models were employed, none of which was truly applicable to either nonreacting or reacting hypersonic flows. The Direct Simulation Monte Carlo (DSMC) based methods for computing low density, high altitude flows also experienced a much expanded role in aerospace applications including complex three-dimensional simulations.

From 1991 to the present day, only modest progress has been made on either the algorithms or the physical/chemical modeling used in hypersonic CFD codes. With the exception of modeling in DSMC methods, most codes continue to use the same algorithms and models with minor refinements, and little data is available to validate these refinements. However, significant progress has been made on surface and flow field discretization using structured and unstructured grid methods, and significant gains in efficiency are being achieved through the increasing use of parallel computers and "smart" ways of applying available CFD codes to a given problem.

The paper reviews the growth and advances in CFD for hypersonic applications over the period from 1985 to the present time. Since the flow on a hypersonic vehicle may include domains that vary all the way from subsonic, high pressure and temperature stagnation regions behind strong bow shock waves to high speed, low density (high Knudsen number) regions, the discussion of computational capabilities has been divided into the following two main areas:

Hypersonic continuum flow capabilities: Most of the discussion in this area is focused on the solution of Reynolds-

Averaged Navier-Stokes (RANS) equations with appropriate modeling of various physical and chemical phenomena present in the flow field. The applications include aerothermodynamic analysis of the external flow over hypersonic vehicles and planetary entry probes and internal flow analysis of the hypersonic airbreathing propulsion flow path.

Rarefied and free-molecular flow capabilities: The capabilities are required for computing hypersonic flow over a wide spectrum of conditions ranging from low density flow at high altitude to relatively high density flow with small characteristic dimensions. Under these conditions, the continuum modeling of the flow becomes deficient, and it is necessary to recognize the molecular structure of the gas. A number of codes have been developed to analyze such flows using the DSMC method and are being used extensively to analyze flow over hypersonic vehicles, planetary entry probes, etc.

In the following sections, basic issues in the development and application of each of the preceding computational capabilities are discussed. A brief summary of some of the currently available popular CFD codes is provided in each of the preceding areas along with their capabilities and deficiencies, computational speed, and example applications. Future areas of research to enhance accuracy, robustness, and reliability of the computational codes are also discussed.

3. HYPERSONIC CONTINUUM FLOW CAPABILITIES

The growth of RANS-based computational capabilities in the United States for external and internal, continuum hypersonic flow during the period of 1985 to 1990 was driven primarily by generic studies of aeromaneuvering and aeroassisted orbital transfer vehicles, Space Transportation System (STS) support, defense interceptors design, and the NASP program. In Europe, programs such as HERMES, Sanger, and HOTOL provided similar impetus. These computational capabilities were further developed to maturity during the period 1991 to the present, and their applications during this period include closeouts or continuations of several of the preceding programs as well as some new programs such as X-33 (a technology demonstrator for a fully Reusable Launch Vehicle (RLV)), X-34 (a Mach 8 test vehicle), X-38 (an assured crew return concept from the International Space Station), Hyper-X (a subscale vehicle to flight demonstrate integrated scramjet engine performance at Mach 5, 7, and 10), and a number of planetary entry missions (Mars Pathfinder, Mars Penetrator, Stardust, etc.).

In general, hypersonic flows, with the presence of strong shocks and complex interactions and the need to model complex physical and chemical phenomena, present significantly larger challenges in the development of computational capabilities than the subsonic or supersonic flow. However, even within hypersonic vehicles, design of a hypersonic airbreathing aircraft places a different set of demands on computational tools than does a rocket-powered vehicle. These demands stem largely from the following dominating requirements for the hypersonic airbreathing aircraft:

- Close integration of the airframe and propulsion system driven by very small performance margins, which is the difference of two large numbers, thrust and drag, of almost equal magnitude. The actual value of this performance margin is at least an order of magnitude smaller than either the thrust

or drag, thus necessitating highly accurate prediction of vehicle aerodynamics and engine performance. Also, the close integration of airframe and propulsion system produces highly interacting, complex three-dimensional viscous external and internal flow, thus further complicating the prediction of such flows.

- Integrated vehicle aerodynamics and engine performance optimization over a Mach number range.
- Vehicle reusability with minimum refurbishment between flights.

It is obvious from the preceding requirements that a nose-to-tail computational capability for a highly integrated hypersonic airbreathing aircraft has to deal with flow fields of substantially greater complexity, both geometrically and physical/chemical modeling wise, than that for a rocket-powered vehicle (although physical and chemical modeling requirements for high energy entries (>8 km/sec.) of aerocapturing and aeromaneuvering vehicles may involve an even higher degree of complexity). The use of CFD as a tool in the analysis and design of such vehicles requires development of advanced codes which can deal with preceding requirements of complexity of the flow field and geometry, and are accurate, efficient, and robust. In order to meet these requirements, the basic issues that need to be addressed in the development of a CFD code are:

- Physical and Chemical Modeling
- Surface Modeling and Grid Generation
- Computational Algorithms
- Code Validation

Once a code is developed and validated, proper strategy must be applied for its efficient application in the analysis, design, and optimization processes. In what follows now, a brief discussion is given on each of these issues for the RANS level of modeling.

3.1 Physical and Chemical Modeling

In order to address all the modeling issues present in the flow field of a hypersonic vehicle, discussion is focused on a vehicle propelled by an airbreathing engine. For this discussion, the vehicle is divided into four components, namely, forebody, inlet/isolator, combustor, and nozzle/afterbody. Most modeling issues for a rocket-propelled vehicle or a planetary entry probe are discussed in the forebody part of this section.

3.1.1 Forebody

The Mach number on the forebody of a hypersonic vehicle varies from low subsonic to hypersonic and the pressure and temperature also vary over a wide range. The flow features present in the forebody flow field include the bow shock, embedded shocks due to the presence of compression ramps and other surfaces, laminar-transitional-turbulent boundary layer, and shock-boundary layer interaction and associated flow separation. It is essential to accurately predict the shape of the bow shock, all embedded shocks, and the entire shock layer profile on the forebody, including the viscous layer, so that forebody wall properties such as pressure, skin friction, and heat transfer, as well as the mass and momentum flux entering the engine inlet, can be calculated. The forebody wall properties are required for accurate prediction of forebody aero and heating loads, whereas the entire engine performance depends upon the

accuracy of mass and momentum flux predictions at the face of the inlet. The reusability of the vehicle implies a nonablative surface, thus simplifying the wall boundary conditions which need not to account for surface ablation and associated shape change. However, sophisticated wall boundary conditions, which include surface catalysis and possible thermal deformation of the forebody surface, may also become important at higher Mach numbers.

It is desirable to maintain a laminar boundary layer on the forebody as far back as possible before it transitions to fully turbulent to reduce drag and heating loads. This requires accurate prediction methods for transition onset that can be used in designing the forebody shape. Most currently available transition onset prediction methods use empirical e^N method, which is based on the compressible linear stability theory [4,5]. These methods require a transition onset database from quiet wind tunnels and flight tests to correlate the value of N. Since there is very limited flight test data available and since most wind tunnel data is taken in noisy environments and at non-representative flight conditions, the transition onset prediction methods are not reliable, yet they are being used in the preliminary design of hypersonic vehicles. Once the transition onset takes place in the compressible boundary layer, there is usually a transition region before the boundary layer becomes fully turbulent. At hypersonic Mach numbers, this transition region is normally quite long and, therefore, has significant impact on the total drag and heating loads on the forebody. This region may also contain areas of heating rates higher than those encountered in the fully turbulent region. Modeling of the extent of transition for hypersonic boundary layers is in the poorest state, as compared to all other type of modeling. Most computational codes today either model this transition region in some adhoc manner or use models that were developed for incompressible flow. The turbulent boundary layer is modeled mostly by either an algebraic or a two-equation eddy viscosity model. Some type of empirical compressibility correction is applied to these models; however, little or no consideration is given to the presence of real gas effects, shock-boundary layer interactions, surface catalyticity effects, etc. In general, accurate modeling of transitioning and turbulent boundary layers needs the most attention if we have to increase the accuracy and reliability of the computational predictions.

In the preceding discussion, the presence of real gas effects on the forebody has been mentioned, which normally become important as the flight Mach number increases in the range of 10 and above. These effects, in their simplest form, are sometimes approximated by an effective gamma that yields the correct density ratio across the shock. This approach may provide useful results for aerodynamic analysis if the perfect gas option is the only one available in the code; however, it is not satisfactory for evaluation of aeroheating. High temperature effects are more appropriately handled with chemical equilibrium (CE) or chemical nonequilibrium (CNE) models. In the CE models, the functional dependence of pressure on density and energy for a generalized gas mixture, in which the elemental mass fractions are known constants or are solved from elemental continuity equations, can be determined by the method of free energy minimization or equilibrium constants. In the CNE models, the species concentrations are determined by solving species continuity. Mixture pressure is defined as a summation of the partial pressures of each constituent. The partial pressure of free electrons is computed using the electron temperature if different from the heavy particle temperature.

Within CNE models, the chemical source terms may be expressed as functions of thermal equilibrium (TE) or thermal nonequilibrium (TNE) chemical kinetic models [6,7,8]. The TNE models may be divided into four subclasses. The simplest one is the two-temperature model in which it is assumed that the translational and rotational energy content of all heavy particles is defined by temperature T. The vibrational energy content of all molecules is defined by temperature T_v. The electronic and free electron translational energy modes are usually assumed to be in equilibrium with the vibrational modes at temperature T_v. The next logical TNE subclass is the three-temperature model. It is identical to the two-temperature model except that the electronic and free-electron translational energy partition is defined by a third temperature T_e. This model has been considered primarily for high-speed earth entries characteristics of return from geosynchronous earth orbit or above. The third subclass of TNE is the multi-temperature model which is again similar to the two-temperature model except that each molecular species retains its own vibrational temperature $T_{v,s}$. Such models are most often used in the code validation process using ground-based experimental data in which separate vibrational temperature measurements have been made.

All of the above subclasses of TNE models invoke an assumption of equilibrium partitioning of energy within two or more groupings of internal modes. This assumption can be relaxed further by discretizing each species into multiple sub-species (excited states) as a function of vibrational and/or electronic quantum number(s) [9]. In this fourth subclass of TNE models, a unique translational temperature is still appropriate within the context of a continuum flow simulation; however, the role played by modal temperature in defining energy distribution within the mode is replaced by a discrete accounting of various excited states. Each state requires its own continuity equation, with appropriate models for transport and source terms.

To solve the governing equations for the diffusion of mass, momentum, and energy in a gas mixture, thermodynamic and transport properties are required. The specific heat for each species may be defined, for example, by a fourth-order polynomial in temperature [10]. Transport properties of a gas mixture are defined as functions of constituent species transport properties and respective mole fractions in the mixture [11]. Individual species transport properties are defined either by Sutherland's law or as functions of collision cross sections [12]. Direct curve fits are also available for air viscosity and conductivity under thermochemical equilibrium [13]. The Chapman and Cowling law is used to determine the binary diffusion coefficients which describe the diffusion of each species into the remaining species [14]. Knowing the diffusion coefficients, the diffusion velocity of each species is determined by solving the multicomponent diffusion equation [15]. However, in most engineering calculations, it is assumed that each species present in the flow has the same diffusivity, and pressure and thermal diffusivity may be ignored. Under this assumption, the diffusion of each species into the remaining species varies only with its concentration gradient and can be described by Fick's law.

3.1.2 Inlet/Isolator

For hypersonic airbreathing vehicles, the inlet/isolator of a scramjet supplies the combustor with air at a specified pressure, velocity, and flow uniformity. The flow physics in this region include three-dimensional compressible turbulent boundary layers, transitioning boundary layer on some inlet surfaces, oblique shocks, shock-boundary layer interactions and associated flow separation, localized high leading edge thermal loads due to shock-shock interactions, unsteady flow due to possible inlet unstart and module to module interactions, and internal-external flow interactions due to the spillage as a result of the requirement that the inlet need to operate over a Mach number range. In addition, modeling of flow in this region may be further complicated by the presence of wings. Even though in most preliminary inlet design cycles, inviscid Euler codes iterated with boundary layer code may be used, the physics of the inlet flow field requires the use of full Navier-Stokes codes with compressible turbulence models. In most current codes for inlet flow field analysis, turbulence is modeled by either algebraic or two-equation turbulence models with empirical compressibility corrections and wall functions. The flow is assumed to be fully turbulent on all surfaces of the inlet. Very limited computational studies have been conducted of inlet unstart and module to module interactions [3] due to the unsteady nature of the flow, inability of the codes to model strong shock-boundary layer interactions and large regions of separated flow, and large computational resources required to conduct such calculations. As for the forebody, the most limiting area for accurate modeling of inlet flow fields is the development of advanced transition and turbulence models. Promising work is currently underway to develop new algebraic Reynolds stress turbulence models which have the computational efficiency of a two-equation turbulence model but include more physics.

3.1.3 Combustor

The flow field in the combustor of a scramjet engine is probably the most complex amongst all the components of the hypersonic vehicle. It is characterized by much of the flow physics of the inlet/isolator region, but it is further complicated by a wide range of flow velocities inhomogeneously distributed throughout the combustor, small and large scale vortical flows for fuel-air mixing, finite rate chemical reactions for ignition and combustion resulting in high temperatures and heat fluxes, anisotropic and nonequilibrium transfer of turbulence energy, and turbulence/chemical kinetics interactions. Computations of combustor flow fields require the use of RANS based codes; however, a parabolized Navier-Stokes code may be used in some analyses. Turbulence is again modeled using algebraic or two-equation models with empirical compressibility corrections and wall functions. Few codes account for turbulence chemistry interactions through an assumed probability density function approach. Chemical reaction is modeled with reduced reaction set finite rate models. For the hydrogen-air reactions occurring in a hydrogen-fueled scramjet, a typical reaction mechanism includes nine chemical species and eighteen chemical reactions, although other less or more elaborate mechanisms may be used depending upon the case [16]. In a hydrocarbon-fueled scramjet, combustion mechanisms are much more complex and require carefully reduced mechanisms to allow practical computations.

In the analysis of a combustor, apart from predicting the overall flow field, there are a number of locations where highly detailed analysis of very localized processes is required such as in the neighborhood of fuel injectors and flame holders. Accurate and detailed prediction of such localized flow regions is required if computational tools are to be used in the design of an efficient combustor.

3.1.4 Nozzle/Afterbody

The flow field in the nozzle/afterbody of a hypersonic vehicle retains some of the physics of the inlet and combustor, but also includes additional requirements of modeling highly expanding nonuniform flow that may relaminarize and then retransition back to turbulent flow, significant divergence and skin friction losses, energy-bound chemical radicals that will not relax in the nozzle, and excited vibrational states and their relaxation. Nozzle/afterbody flow field calculations are usually made with either an Euler code iterated with a boundary layer code or a parabolized Navier-Stokes code. Calculations may also be continued with the same Navier-Stokes code that has been used in the analysis of combustor flow field. Finite-rate reaction chemistry is still required in the nozzle to assess the degree of reaction that continues to take place and to determine the extent of recombination reactions that add to the available thrust. The reduced kinetics models currently being applied to nozzle/afterbody flow appear to be reasonably accurate, although some further work to improve the description of recombination may be warranted. At present, there is little or no modeling of the relaminarization and retransition of the boundary layer that might occur in the region of large expansion. Overall, nozzle/afterbody flow field computations are much less demanding than either the inlet/isolator or combustor flow field.

3.2 Surface Modeling and Grid Generation

With the acceptance of RANS technology in analysis and design of complex configurations, the requirements for rapid solutions dictated that all elements of the solution process be refined and streamlined. Surface modeling and grid generation appear to be the most significant contributors to the total time required to generate a solution. Reference [17] summarizes the advances and remaining challenges in this area. A surface modeling data-exchange standard has been developed to provide a link to computer-aided-design surface modeling packages, and the surface model definition is now routinely incorporated into grid generation packages to maintain surface fidelity as the grid is enriched or adapted. An extensive array of block-structured methods, unstructured grid methods, and hybrid schemes are now available, although no single method has emerged as the preferred approach. The block structured methods, including patched and overset grids, are the most efficient methods for high Reynolds number simulations, but are the most labor intensive in terms of grid generation; automated methods are being developed but are still in their infancy. However, to speed up the grid generation process, libraries of efficient topologies for classes of configurations are being developed which can be used to automatically generate a new three-dimensional grid for changes to an existing model in a very short time.

The unstructured grid methods have emerged as the methods of choice for nonlinear inviscid simulations because of their relative speed and lack of the need of user interaction in the grid generation process [18]. The viscous unstructured grid methods are also becoming available for complex three-dimensional configurations [19]. However, for high Reynolds

number viscous flow, a hybrid approach may be more useful. In this hybrid approach, a structured layer of points is developed near the surface and these near-field layers are then connected to the outer field through an isotropic distribution of unstructured grid. Reference [20] describes this advancing-layer, advancing-front hybrid grid generation method and uses it successfully for a three-dimensional viscous calculation.

3.3 Computational Algorithms

Some of the most important algorithmic advances for the computation of hypersonic flows have been in the development of upwind and non-oscillatory schemes for improved shock capturing. Central difference schemes with upwind-biased or non-oscillatory dissipation operators are included in this class of algorithms. Upwind schemes evolved more to satisfy an intuitive valuation that consistency between physics and numerics is important. High-resolution, non-oscillatory schemes more directly confront issues of accuracy in the region of high gradients such as in the vicinity of shocks and shear layers. Prior to these advances, flows with strong shocks (pressure ratio in the range of 100 or more) could not be computed accurately with shock-capturing methods based on central differencing; either the requisite dissipation excessively smeared the shock or Gibb's phenomena caused large enough oscillations to generate negative temperatures in the neighborhood of shocks. Shock-fitting methods have advanced to a much lessor extent as compared to more flexible, easily coded shock-capturing methods.

In general, the RANS equations are solved to steady state by properly posed, time dependent problem and marching the solution to large time with steady state boundary conditions. In hypersonic flows, this approach has its principal advantage in being able to maintain fully conservative differencing, thus providing accurate shock capturing. The algorithms that are in use for time-stepping can be classified as either explicit or implicit schemes. Although explicit schemes are relatively easy to code, they are prohibitively expensive for the highly stretched grids associated with high Reynolds number viscous simulations because the explicit time step scales as the square of the mesh size for pure diffusion model problems. However, one of the most popular and widely used algorithms through the early to mid eighties was the explicit MacCormack algorithm [21]. An implicit algorithm, such as the Beam and Warming [22] algorithm, allows to advance the solution with much larger time step as compared to an explicit algorithm and also has the flexibility in the selection of the actual time step. This aspect becomes particularly important as the predominantly reduced frequencies become small.

The Runge-Kutta time-stepping method, originally applied to Euler equations by Jameson, Schmidt, and Turkel [23] in 1981, is another extensively used method for steady and unsteady viscous flow computations. Although the basic algorithm is explicit, residual smoothing is used to extend its stability limit. The three-dimensional RANS technology has become even more acceptable by the aerospace industry with the advancements in multigrid algorithms [24] which have significantly accelerated the convergence to steady state over a single-grid algorithm. This technology is still not fully developed, especially for hypersonic flows due to difficulties in the treatment of chemical source terms and strong shocks, but the prospects exist for considerable further enhancements to the convergence rate [25,26]. Local preconditioning [27] is another algorithmic

enhancement that is currently under development to address problems associated with convergence and truncation errors in very low velocity flows, such as in the stagnation region of a blunt body in hypersonic flow or in the regions with significant viscous effects. Here again, much work remains to establish optimum performance of local preconditioning.

Most central-difference algorithms require explicit addition of dissipation terms, such as the second- and fourth-difference operators of Jameson et al. [23], which provide a third-order dissipation in smooth regions of the flow and a first-order dissipation in discontinuous regions of the flow. A pressure gradient-based switch is used to turn off the fourth-difference dissipation in discontinuous regions to avoid small scale oscillations. A modified pressure switch was developed by Turkel et al. [25] and Vatsa et al. [26] for hypersonic flows to avoid negative density or pressure near strong shocks. An alternate way to add dissipation is through the use of flux-difference or flux-vector splitting, upwind-difference methods which have more physical, inherent dissipation and do not require it to be added explicitly [28].

As discussed earlier, hypersonic flows require modeling of real gas, equilibrium or nonequilibrium chemical phenomena which involve chemical energy source terms and additional species equations. In cases where the chemical time scale is much longer than the fluid dynamic time scale, the species equations can be solved in a weakly coupled fashion as a subset of the Navier-Stokes equations. Even though this approach is computationally efficient, in most cases the chemical time scale is of the same order or smaller than the fluid dynamic time scale. In these situations, the species equations are solved in a fully coupled fashion with the remaining equations. The species equations have a chemical source term that describes the production and loss of each chemical species in the reaction process. This source term normally causes the overall system of governing equations to be numerically stiff, when the chemical time scale is relatively smaller than the fluid dynamic time scale, and is typically solved implicitly with either explicit or implicit time-stepping methods. With implicit discretization of the source term, the resulting system is rescaled by a matrix containing the source Jacobian that allows the equation system to be advanced in time at nearly the fluid dynamic time scale [29,30].

3.4 Code Validation

Before a computational code can be used in the development of aerospace vehicles, it is necessary to determine its accuracy in predicting the flow field through a validation process. This validation process is required to ensure that the physical modeling used in the code approximates the actual flow physics and that the algorithm employed in the code to solve the governing equations is not adding significant numerical error. In order to validate a code and establish its range of applicability, it is necessary to compare numerical results from the code with some well-posed experiments. Since computational codes are being applied to highly complex and interacting flow field analysis, it is no longer adequate to compare against global experimental data such as surface or other integral quantities. As an example, it was mentioned in the earlier section that it was not sufficient to just calculate the surface pressure and heating on the forebody, but was also necessary to accurately predict the whole shock layer profile entering the inlet/isolator region because the accuracy of

performance prediction of the inlet/isolator region depends upon the inflow profile.

In general, the validation process for a newly developed code first requires some internal checks for consistency to ensure that the code preserves mass, momentum, and energy and also preserves the freestream on an arbitrary grid in the absence of a body. The newly developed code can also be checked against some other established codes. However, the major step in validation of a code consists of comparison against detailed experimental data. Normally, two types of experiments are necessary to determine the accuracy of the code. The first type of experiments, called the building block experiments, are necessary to validate physical and chemical modeling. These experiments should provide measurements which not only show the deficiencies in the modeling but also help identify the aspects of models which need improvements. The second type of experiments, called the benchmark experiments, are used to determine prediction capability of the code and to establish limits and range of applicability.

As an aerospace vehicle goes through its flight envelope, the physical and chemical processes that need to be modeled change, the characteristics of the algorithm change, and the grid requirements for resolving the flow change. It is, therefore, necessary to validate the code over small ranges of the flight envelope, and its use should be limited to the appropriate range of validation to avoid large uncertainty in predictions. It must be realized that due to a lack of high-enthalpy facilities that can simulate the flight conditions, a very limited amount of experimental databases are available for hypersonic flow. This is even more true for the combustor flow field where extensive velocity, pressure, temperature, and species concentration measurements are required along with the correlation of these quantities with each other if validation of advanced turbulence and turbulence-chemistry interaction models is required. Another factor that is pushing the accuracy requirements on the measurements and, thus, tighter limits on validation, is the necessity of predicting aerodynamics and engine performance very accurately due to overall small performance margins for a hypersonic airbreathing vehicle, as discussed earlier.

Even though over the last decade or so there appears to be a general consensus on the lack of hypersonic experimental database for code validation, very limited resources have been allocated to remedy the situation. The cost of obtaining code validation quality data on a flight experiment/technology demonstrator also remains a serious obstacle. There is always a challenge to show that the cost and risk of validation data acquisition on a flight project is justified by the risk reduction in future applications.

3.5 Major Continuum Flow Codes
This section describes some of the RANS-based codes that are representative of capabilities for hypersonic flow analysis. It is not an all-inclusive list; rather, it is restricted to those codes that are currently being employed by various groups at the NASA Langley Research Center for external and internal hypersonic flow analysis.

3.5.1 LAURA (The Langley Aerothermodynamic Upwind Relaxation Algorithm)
The LAURA code was primarily developed for external aerothermodynamic analysis of flow over hypersonic vehicles

and planetary entry bodies. It can solve Euler, thin-layer Navier-Stokes, or Navier-Stokes equations. Inviscid flux definition in LAURA employs Roe's averaging [31] and Yee's Symmetric Total Variation Diminishing (STVD) [32] for second-order accuracy away from discontinuities. Harten's entropy fix (eigenvalue limiter) [33] is applied across cell faces. Special variations of the limiter are employed across viscous dominated boundary and shear layers. These treatments overcome problems often encountered with the baseline Roe's method regarding the "carbuncle" phenomenon or the baseline Harten's method in which numerical dissipation (proportional to an unnaturally large eigenvalue) competes with physical dissipation. Central differences are used to define viscous flux. Point-implicit relaxation of the steady form of the conservation laws at each control volume in a computational plane is implemented, sweeping from plane to plane in a block and from block to block across the entire domain of interest.

The basic features of LAURA.4.1 [34] include options for five thermochemical kinetic models for 11 species air, two equilibrium air models [35,36], two-temperature thermal model, two algebraic turbulence models, six models for wall catalysis, a radiative equilibrium wall, discretization on up to six, simply connected, structured blocks, and mesh sequencing. Solution Jacobians may be stored out-of-core for significant reduction in memory requirement. New features offered in LAURA.4.4 (user manual not yet updated) include options for Martian atmospheric chemistry, 1000 structured blocks with integer stride connectivity (175 block solution tested), and post-processing files generated to support integral-boundary-layer analyses of variations in surface catalysis and emissivity of the thermal protection system. A PVM/MPI version of the code is being tested which currently supports all of the options in LAURA.4.1 and most of the options in LAURA.4.4.

The LAURA code exploits macrotasking (parallel execution of a code on a shared memory machine) on Cray computers at the subroutine level. The use of macrotasking, along with provisions for asynchronous relaxation, enables exceptionally high average concurrency of tasks for LAURA. An asynchronous relaxation also enables physically motivated load balancing in which CPU cycles are concentrated in regions known to converge slowly such as separated flow regions, near wake regions, etc. An additional feature of LAURA is its built-in grid adaptation routine that simultaneously aligns the outer boundary of the computational domain with the captured bow shock and enforces near wall grid resolution required for aeroheating analysis. This feature greatly simplifies the grid generation process for mutliple cases over a wide range of Mach numbers, Reynolds numbers, and angles of attack on a single configuration.

LAURA has been validated with flight data from the shuttle orbiter [37,38] and with ground-based data from the Aeroassist Flight Experiment [39] and the hypersonic compression corner [40].

3.5.2 GASP (The General Aerodynamic Simulation Program)
The development of the GASP code started around 1987 under the NASP Program, and was motivated by the need for a 'nose-to-tail' analysis capability for an airbreathing hypersonic aircraft. It supports a rich variety of options for steady and unsteady solution of Euler, parabolized Navier-Stokes, thin-layer Navier-Stokes, and Navier-Stokes equations. These

options include mesh sequencing, preconditioning, approximate factorization, Line Gauss Seidel, Generalized Minimal Residual (GMRES) [41], mesh sequencing and multigrid. Inviscid flux definition in GASP employs several options, including Roe's and Van Leer's upwind biased formulations and central differencing with artificial viscosity. Central differences are used to define viscous flux.

Both algebraic and two-equation turbulence models with wall function options are supported. Generalized zonal-boundary interpolation is supported across zonal intersections defined by a single logical boundary. Parallel processing is supported on shared memory computer architectures. A comprehensive set of thermochemical kinetic models is offered for air chemistry, hydrogen-air combustion, and hydrocarbons in a database containing 455 reactions and 34 species. Thermal nonequilibrium may be modeled using a separate vibrational temperature for each molecule or a lumped vibrational temperature common to all molecules. The comprehensive GASP V3 Users Manual [42] and the Graphical User Interface (GUI) for problem setup and data manipulation make GASP more user friendly.

Due to the comprehensive set of physical and chemical modeling options available in the GASP code, it is being used in the analysis of the complete hypersonic vehicle flow field. It has been validated for a number of external and internal flow fields such as discussed in References [43,44,45].

3.5.3 LARCK (Langley Algorithm for Research in Chemical Kinetics)

Several RANS-based codes have been developed and used at NASA Langley for modeling the internal flow field in scramjet inlets, combustors, and nozzles. These include some earlier codes such as NASCRIN/SCRAMIN [46,47] for inlets and SPARK series of codes [48,49,50] for combustors which were developed in the early to mid-eighties. However, at present, there are two more recently developed codes which are being used extensively. One of them is the previously discussed GASP code and the other code is the LARCK code. Development of the LARCK combustor code began in 1992 to incorporate some of the algorithmic advances and geometric generalizations that had appeared in the literature during the late 1980's and early 1990's. Its development was driven by the need to consider more complex internal engine geometries with algorithms that were very efficient for solving high-speed reacting flows. LARCK is a multiblock, multigrid code that uses a cell-centered, second-order finite-volume integration scheme. Each region in the code is constructed of a number of blocks. Blocks within a region can be connected either elliptically or hyperbolically, whereas regions are connected parabolically. Convection terms in the governing partial differential equations are discretized in a second-order manner using either central differencing with scalar matrix artificial dissipation, or with an upwind MUSCL scheme with Roe's approximate Riemann solver. Diffusion terms are discretized in a second-order manner with either a full gradient evaluation using Green's theorem or an approximate gradient evaluation using finite differences.

Once the spatial terms have been discretized, LARCK has several options for advancing the governing equations in space and time. For elliptic flows, either steady or unsteady solution procedures can be used. The equations are solved using either a

Runge-Kutta scheme with or without residual smoothing, a diagnolized approximate factorization scheme, or a FMG/FAS multigrid aceleration scheme using either of the above two approaches. The governing equations can also be marched in space using the pseudo time interative method of Newsome et al. [51]. To specify boundary conditions for the governing equations, LARCK utilizes a generalized system of boundary conditions that can be imposed on any block face or subset of block faces. Currently, fourteen different boundary condition classes can be specified or additional boundary conditions can be input by the user.

The thermodynamics model in LARCK provides a generalized model for an arbitrary mixture of thermally perfect gases based on curve fits for specific heat and Gibbs energy. The code has an Arrhenius based finite-rate chemistry model with a generalized scheme that allows for the specification of any chosen reaction model.

A number of turbulence models have been incorporated into the LARCK code. The turbulence kinetic energy class of models include the Spallart-Allmaras model [52], the Wilcox high and low Reynolds number k-ω models (which can be used to solve the governing equations to the wall), or Wilcox's compressible pressure gradient corrected wall matching procedure. In addition, Menter's baseline and SST models [53,54] have been incorporated, again to solve to the wall or with Wilcox's compressible pressure gradient corrected wall matching procedure [55]. The k-ε low Reynolds number model of Abid et al. [56] has also been included. In addition to the turbulent kinetic energy models, several algebraic Reynolds stress models have been incorporated into LARCK. These models include the algebraic Reynolds stress models of Abid et al. [57] (both the k-ε and the k-ω variants) and Givi et al. [58]. Coupling between the turbulence and chemistry fields has also been included. Gaussian or beta assumed probability density functions have been used to account for temperature variance effects on the forward and backward kinetic rate coefficients in the chemistry model [59]. Turbulence effects on the species production rates have also been accounted for by modeling the sum of the species variances using a multivariate assumed probability density function [60].

The LARCK code has been used to model individual scramjet component flow as well as the entire flow field from inlet to nozzle in a scramjet engine. It has been validated against a number of 2-D and 3-D unit problems such as the flat plate flow [61], high Mach number compression ramp flow, and Mach 3 corner flow.

3.5.4 FELISA_HYP

The FELISA_HYP [18] code employs an unstructured grid algorithm specifically constructed for robust, hypersonic flow simulation. It is a finite-volume based formulation that employs an efficient edge data structure. Second-order accuracy is maintained in smooth regions using linear reconstruction following MUSCL concepts [62,63]. The Local Extremum Diminishing criteria [64] is used as a limiter near flow discontinuities. A simple, forward Euler explicit time stepping is used to relax the equations. The code is currently limited to inviscid flows. Options for equilibrium air chemistry are available.

In spite of its current limitation to inviscid flows, FELISA_HYP has proven particularly valuable in the CFD design environment because of the relatively quick grid generation capability. In the X-33 Design Phase I, the FELISA grid tools could be applied by an experienced user to generate unstructured surface and volume grids in days, as compared to a multiple-block structured grid for LAURA, which took several weeks. The actual FELISA_HYP solver is somewhat slower than the inviscid version of LAURA; however, the FELISA_HYP solver would finish several inviscid solutions on a new configuration before LAURA could even get started with a usable grid.

The FELISA_HYP inviscid flow solutions can be combined with engineering codes to extract heating data.

Even though only four codes have been discussed here, there are a number of other codes that are being used at Langley for high Mach number flows such as CFL3D [65], TLNS3D[24], PAB3D [66], OVERFLOW [67], etc. However, most of these applications have been to subsonic, transonic, and supersonic flows with only limited use to moderately high Mach number flows. This is due to the fact that these codes have no, or only limited, capability of modeling chemical processes and real gas effects present at high Mach numbers.

3.6 Applications

RANS-based computational codes are being used these days at all levels in the design and development process of advanced aerospace vehicles, but with the current state of physical and chemical modeling, their applications are reliable and quantitative only for certain flow situations. The codes can fairly well predict attached laminar and turbulent flows, including skin friction and heat transfer, over forebodies, planetary entry probes, etc. However, their predictions are, at best, qualitative for highly interacting flows at high Reynolds numbers (the type of flows encountered in high-speed inlets, combustors, corner regions, etc.). These codes play an important role in the preliminary design studies to screen out poor designs and to conduct sensitivity studies of various design parameters and their impact on incremental performance.

A number of application strategies can be used to enhance the efficiency of computational codes in an overall analysis and design process. Mesh sequencing and solution sequencing are two procedural approaches to speed up the convergence. Mesh sequencing refers to obtaining a solution on a sequence of finer grids, where each successive solution is initialized using the previous coarse grid solution. Solution sequencing refers to initializing a simulation at one trajectory point using a converged solution from a neighboring trajectory point. Solution sequencing can be used in conjunction with mesh sequencing to generate a matrix of solutions across a trajectory for a single configuration.

Another procedural strategy consists of block space marching. This strategy is useful when embedded subsonic or separated flow regions may arise in domains which are otherwise amenable to parabolized Navier-Stokes (PNS) methodology. A user probably can devise many other strategies for efficient use of computational codes to various applications.

Several application examples are now presented using some of the codes discussed earlier in the paper.

3.6.1 COMET
Aerodynamics and surface heating for the Commercial Experiment Transporter (COMET) at several points along its trajectory on return from low earth orbit were calculated with LAURA and a DSMC method [68]. The COMET module (later renamed METEOR), shown in Fig. 1, had no active control system, and relied entirely on aerodynamic forces for stability and proper orientation during its maximum heating pulse. The aerodynamic data base was used within a six degree-of-freedom trajectory code to define a splashdown footprint. The DSMC method was used to define the flow field in a transitional, rarefied regime (above 90 km); LAURA was used to define the flow field in the transitional to continuum regime (below 90 km). Wake flow had to be included prior to the peak heating point because of the large initial angle of attack. Continuum and rarefied aerodynamic predictions for lift, drag, and moment were in good agreement at 90 km. Thermochemical nonequilibrium models including 7 species for air were used down to Mach 15. Both viscous and inviscid solutions were used below Mach 15. Wake flow was included at Mach 1.5 to account for important base flow effects on aerodynamics. A matrix of 46 solutions was completed between February 14 and March 23, 1995. This matrix included 10 reacting, viscous flow solutions with wake; 13 reacting, viscous flow solutions without wake, 6 perfect gas, viscous flow solutions with wake, and 17 perfect gas, inviscid flow solutions without wake. Angles of attack varied from 0 to 90 degrees. A solution adaptive grid was employed to swing the extended grid in the wake around the body behind the base at 0 degrees to off the side at 90 degrees. Maximum job size was 71.2 MW on the C-90 and required 8.8 hours on a 72x36x64 cell domain. Actual time on the computer for this case was only 0.98 hours because of extensive use of asynchronous macrotasking relaxation. The large average concurrent CPU usage enabled fast turnaround for this large matrix of cases.

Computed results were obtained prior to initiation of the wind tunnel test program and were in excellent agreement with wind tunnel data at Mach 6, as can be seen in Fig. 2. Flight data is not available because the mission was aborted on ascent.

3.6.2 X-33 and Reusable Launch Vehicle (RLV)
Numerical simulations of hypersonic flow over preliminary configurations for a RLV and X-33, a technology demonstrator for the RLV, in support of Phase I Lockheed Martin Design are described. The simulations were executed using both chemical equilibrium and nonequilibrium gas models. Simulations were generated over six representative trajectory points for descent of the B1001 RLV configuration in order to establish traceability of aerothermodynamic design issues. Simulations were generated over five representative trajectory points for descent of the B1001A X-33 configuration. Trajectory points for simulation were chosen near peak heating and peak dynamic pressure; other points were selected on the basis of convenient anchors for Mach number and angle of attack variation. Representative surface heating, temperature and pressure distributions were provided to the design team, some examples of which are presented here. Procedures for incorporating CFD solutions into engineering code (like MINIVER [69]) format for subsequent use by the thermal design team are also discussed.

Figures 3 and 4 show the B1001 RLV configuration (reference length 1419.25 inches) and the B1001A X-33 configuration (reference length 752.2 inches), respectively, which were used

in simulations. Both configurations assume a moment center at 66 percent of the reference length behind the nose. The vehicle geometries are identical to scale from the nose to upstream of the wing (hypervator) root. B1001A is tapered more toward the base to reduce base drag as compared to its predecessor. It has body flaps on wind and lee sides that terminate at the cowl trailing edge but extend across most of the base lateral dimension. B1001 has no control surface preceding the central base region surrounding the aerospike engines. Instead, there is an expansion surface in the central region with outboard body flaps that extend past the cowl trailing edge. Parts of the body flap that extend past the trailing edge of the B1001 were not modeled in Phase I studies because body shape had already evolved to the B1001A based on wind tunnel test results.

Surface grids for B1001 RLV configuration were constructed in four sections as shown in Fig. 5. Solutions were generated in each section sequentially in a block marching mode. The first section extended from the nose to the first terminal plane approximately 10 inches upstream of the wing (hypervator) root. The grid density in the first section was 52x64 cells. The second section was constructed with 9 blocks in the circumferential direction and a total grid density of 18x116 cells. The third section was constructed with 12 blocks in the circumferential direction and a total grid density of 18x186 cells, and the final section was constructed with 23 blocks in the circumferential direction and a total grid density of 6x293 cells.

In the case of B1001A X-33 configuration, surface grids were constructed in two sections as shown in Fig. 6. Solutions were generated again in each section sequentially in a block marching mode. However, in some cases, solutions were then regenerated in a fully coupled mode. The grid density in the first section was 64x64 cells, and the grid in the second section was constructed with 12 blocks in the circumferential direction with a total grid density of 100x247 cells.

The computational aerothermodynamic analyses were focused on defining global temperature distributions around the RLV and X-33. Thermal analysis of the tanks required time dependent data in a readily accessible format as commonly provided by the MINIVER code. The required temporal resolution on the flight trajectory was much finer than the matrix of points selected for analysis by the LAURA code alone. The MINIVER code is capable of making reasonably accurate estimates of centerline heating distributions on vehicles like RLV and X-33. However, three-dimensional flow effects occurring off-centerline generally are not well approximated by it without some externally derived corrections. The necessary corrections were provided by LAURA at off centerline locations at the times defined in the CFD matrix.

Implementation of this procedure in Phase I for both RLV and X-33 analyses occurred as follows. Heating and temperature distributions over the vehicle were generated by LAURA and compared with the windward centerline results from MINIVER. These comparisons established MINIVER as a reasonably accurate tool for the geometries and trajectories considered in the study. Off-centerline values were keyed to centerline values of laminar heating rate in a relatively dense matrix of computational planes through plots of $q_{Lam}/q_{Lam,CL}$ as a function of spanwise location in the plane. This data was input to MINIVER in a tabular form.

Transition to turbulence was assumed to occur for values of Re/M_e between 250 and 300. Turbulent heating levels were computed downstream of this plane and values of q_{turb}/q_{Lam} were defined using earlier laminar solutions. These turbulent to laminar factors were also input into MINIVER in a tabular form. Heating at any point on the body was then predicted by MINIVER by computing the windside centerline value at the same axial location, multiplying by an appropriately interpolated value for q/q_{CL} for the spatial location on the body and temporal location along the trajectory, and applying an additional correction factor for turbulent flow if the transition criteria is exceeded.

Prediction of transition by LAURA and MINIVER along the windward centerline was in significant disagreement (LAURA predicted the threshold transition criteria to occur earlier in the trajectory than MINIVER). However, because these transition criteria have historically been derived from engineering code analysis like MINIVER, Phase I studies proceeded using MINIVER criteria. Establishment of a proper criteria is a subject of ongoing research.

Temperature maps of the vehicle, as predicted by LAURA for the 1200 s trajectory point of the RLV entry with undeflected flap, are presented in Fig. 7. These solutions were generated sequentially across four sections of the vehicle. It is seen that the highest temperatures occur near the wing root but are only slightly higher than the stagnation point temperature on the nose. A comparison of LAURA predictions of temperature and heating rates with the engineering code MINIVER along the windside centerline are shown in Fig. 8. In general, there is a reasonably good agreement.

Reference [70] provides additional simulations for these configurations with a flap deflection of 50 deg. and discusses the sensitivity of results to physical (turbulent viscosity) and numerical (grid-related) dissipation.

3.6.3 Sidewall Compression Scramjet Inlet
The LARCK code was used to simulate the flow at Mach 4 through a forward swept, sidewall compression scramjet inlet shown in Fig. 9 [71,72]. Sidewall compression, open bottom inlets with forward swept leading edges have greater mass capture and reduced cowl shock strengths as compared to inlet sidewalls with no sweep or aft sweep due to reduced mass transport. The results of the LARCK simulation are shown in Figures 10–12. Figure 10 shows static pressure contours along the vehicle body surface, the cowl surface, and a central plane located midway between these surfaces. Pressure contours along the streamwise symmetry plane are also shown. All contour values are keyed to the static to freestream pressure scale in the figure. Shock and expansion structure is clearly visible along each solution plane. Along the streamwise plane, the coalescence of sidewall shocks can be seen downstream of the inlet inflow plane. The reflections of this shock structure with downstream movement can also be seen along the central horizontal plane. Identical shock structure can also be seen in the Mach contours given in Figure 11. A fairly uniform inlet outflow Mach number of 2.7 is predicted. A comparison between the predicted and measured bodyside centerline wall pressure data is given in Figure 12. The agreement between the computation and the data is excellent along the entire inlet length.

3.6.4 *Mixing in Scramjet Combustor*

The LARCK code was also used to study fuel-air mixing performance of the injection scheme in a scramjet combustor. The design consists of 6 interdigitated struts (3 along the top wall and 3 along the bottom wall). The mean flow Mach number at the entrance of the combustor is about 4.5. Helium is injected at the base of each strut through 3 injection ports. The Roe flux difference scheme with the van Leer limiter was used to evaluate the inviscid fluxes. The turbulence model employed was the Menter SST model [53] with a compressible, pressure gradient corrected wall matching procedure developed by Wilcox [55]. A total of approximately 8 million grid points was used to discretize the computational domain. The facility nozzle was computed separately to provide the combustor inflow conditions. The inside of the injectors were included in the computational domain, thus obviating the need of ad hoc approximations for the fuel injectant profiles. Figures 13 and 14 illustrate the resulting helium distribution and Mach number field, respectively. The helium injectors were highly underexpanded which accelerated the fuel from Mach 2.71 at the injection plane to approximately Mach 8. The high pressure flow between adjacent struts forces the flow over the strut tips, creating a counter rotating vortex pair. This vortex pair is responsible for the fuel plume roll up of the injectant closest to the top of each strut. These calculations required approximately 150 Cray C90 hours to complete.

4. RAREFIED AND FREE MOLECULAR FLOW CAPABILITY

Rarefaction effects in hypersonic flows occur over a wide spectrum of conditions ranging from low density (high altitudes) situations to relatively high density flows where the characteristic dimension is small. Examples are the aerothermodynamics of space vehicles at high altitude, the heating along leading edges at lower altitudes, and very localized aerothermal loads occurring at even lower altitudes such as that resulting from a shock on cowl lip interaction. Entry vehicles encompass the complete flow spectrum in terms of rarefaction, that is, from free molecular to continuum flows. During the higher altitude portion of entry where the flow is free molecular, gas-surface interactions are the dominant process influencing vehicle aerodynamics. For the transitional flow regime, bounded by the free molecular and continuum regimes, both gas-surface and intermolecular collisions are important in establishing vehicle aerothermodynamics.

For the transitional flow regime, the molecular mean-free path in the gas is significant when compared with either a characteristic distance over which flow properties change or when compared with the size of the object creating the flow disturbance. The flow that envelopes a vehicle will be in a nonequilibrium state, that is, one in which nonequilibrium exists among the various energy modes (translational and internal), the chemistry, and radiation for the more energetic flows. Furthermore, expansion of the forebody flow into the wake of a planetary probe or aerobrake extends to lower altitudes the conditions for which rarefaction effects are important and establishes the near wake closure and the level of heating experienced on a probe's afterbody or payload. This is particularly true of aeroassisted space transfer vehicles (ASTV's) where determination of wake closure is a critical issue because the low lift-to-drag ratio aeroshell designs impose constraints on payload configuration/spacecraft design. The issue is that the payload should fit into the wake in such a manner as to avoid the shear layer impingement and thereby minimize heating.

Transitional flows present unique difficulties for numerical simulations since the model equations used to describe continuum flows (Navier-Stokes) become deficient as the flow becomes more rarefied. A condition for the validity of the continuum approach is that the Knudsen number (ratio of the mean free path to a characteristic dimension) be small compared with unity. For low density flows, the particulate or molecular structure of the gas must be recognized. The basic mathematical model of such flows is the Boltzmann equation which presents overwhelming difficulties to computational methods for realistic flows. Consequently, the mathematical models that are readily applicable to both continuum and free molecular (collisionless) flows experience serious limitations when applied to transitional flows. Fortunately, direct simulation methods have evolved over the past 35 years that readily lend themselves to the description of rarefied flows. These developments have generally been concerned with the DSMC method. The DSMC method of Bird [73] along with many variants is the most used method today for simulating rarefied flows in an engineering context. The DSMC method takes advantage of the discrete structure of the gas and provides a direct physical simulation as opposed to a numerical solution of a set of model equations. This is accomplished by developing phenomenological models of the relevant physical events. Phenomenological models have been developed and implemented in the DSMC procedure to account for translational, thermal, chemical, and radiative nonequilibrium effects.

The basic DSMC algorithms have been more or less unchanged since 1985, while major improvements in geometry and grid generation have led to codes that can be more readily applied to complex configurations, as demonstrated by the flow simulations for the Shuttle Orbiter in 1990. Since 1990, efforts have continued to extend the functionality of DSMC for complex 3-D simulations. A substantial factor in the increased application of DSMC has been the rapid increase in computer capabilities that have resulted in major improvement over the past ten years for calculations on the fastest reasonably available computers.

With vector processing of DSMC codes being restricted to about a factor of five speedup over unvectorized codes, workstations have become the preferred platform for DSMC simulations. Advantages of the workstations are that they are generally more accessible and allow interactive control. However, really large DSMC simulations benefit from using parallel computing, and recent research [74] has shown that it is possible to perform simulations with over 100 million particles on a 400 node IBM SP2 computer while achieving a parallel efficiency of 90 percent.

With regard to physical models that are important in hypersonic calculations, the major advances during 1985–90 were in the modeling of slightly ionized flows and thermal radiation motivated by the technology issues associated with orbital transfer vehicles and the work initiated on the development of an Aeroassist Flight Experiment (AFE) vehicle. During the 1990–95 time period, the quantum vibrational model was introduced, which has not only improved the

vibrational modeling, but has allowed the integration of the chemical reaction and vibration modeling.

Many validation examples are currently available that provide results comparing DSMC solutions with experimental data. Results of these comparisons have, in general, been very favorable. Two examples of validation studies are reviewed herein that include Shuttle Orbiter aerodynamics at high altitude and the blunt body/wake studies conducted under the aegis of AGARD Fluid Dynamic Panel Working Group 18. Examples of current applications are presented describing the aerodynamics for both a generic single-stage-to-orbit vehicle and planetary capsules.

4.1 Algorithm

The DSMC method is a technique for the computer modeling of simulated molecules (atoms, molecules, ions, and electrons). The velocity components, position coordinates, and other relevant state information of these molecules are stored in the computer and are modified with time as the molecules are concurrently followed through representative collisions and boundary interactions in simulated physical space. This direct simulation of the physical processes contrasts with the general philosophy of CFD which is to obtain solutions of mathematical equations that model the processes. The computational task associated with the direct physical simulation becomes feasible when the gas density is sufficiently low. It also becomes necessary under these conditions because the Navier-Stokes equations do not provide a valid model for rarefied gases, and conventional CFD methods are unable to cope with the large number of independent variables that are involved in applications of the Boltzmann equation to realistic multi-dimensional problems. The time parameter in the simulation may be identified with real time, and the flow is always calculated as an unsteady flow. A steady flow is obtained as the large time state of an unsteady flow. There is no iterative procedure for convergence to the final solution, and, most importantly, there are no numerical instabilities. There is a requirement to collect a sufficient number of samples to reduce the statistical scatter to an acceptable level.

The two basic steps in a DSMC computation are the movement of the molecules and the pairing and selection of nearby molecules for collisions. The uncoupling of the molecular motion and collisions over small time steps and the division of the flowfield into small cells are the key computational assumptions associated with the DSMC method. The time step should be much less than the mean collision time, and a typical cell dimension should be less than the local mean free path. The sampled density is used in the procedures for establishing the collision rate, and it is desirable to have the number of simulated molecules of the order of ten to twenty per cell. There is a statistical consequence of the replacement of the extremely large number of real molecules by a very small number of simulated molecules. The statistical scatter generally decreases as the square root of the sample size, and, in order to attain a sufficiently small standard deviation, the simulations employ either time averaging for steady flows or ensemble averaging for unsteady flows.

The DSMC algorithm consists of the following basic steps: 1) move all molecules through a computational grid spanning physical space according to the product of the velocity of each molecule and a small time step and compute interactions with boundaries as required; 2) determine the cell location of each molecule; 3) on a statistical basis, compute collisions between molecules occupying the same cell; and 4) sample information on the molecules residing in each cell. Even though the large number of molecules in a real gas is replaced by a much smaller number of model molecules in a simulation, thousands to millions of model molecules are still needed, which can lead to substantial computer requirements.

DSMC codes have traditionally focused on algorithms that allow the greatest flexibility in modeling the physics rather than on algorithms that offer the most efficient computations. However, architectural differences between traditional vector supercomputers and workstations lead to different requirements for algorithmic implementation. Research [74] has shown that significant improvements are possible by using data structures optimized for specific platform architecture.

Much of the current development efforts are focused on extending the functionality of DSMC for complex 3-D simulations. These capabilities must be incorporated into software capable of running on massively parallel systems as well as engineering workstations to achieve useful "engineering" tools for the more demanding current applications and to provide the opportunity to explore problem areas that are currently being approached with the continuum-based methods. While it is unlikely that DSMC will replace the continuum-based methods, the particle-based methods may give new insight into these problems from a molecular point of view.

4.2 Physical and Chemical Modeling

4.2.1 Collision Cross-Section

The collision of two molecules can be simulated using models ranging from simple hard sphere interactions to more sophisticated models that include the potential fields and the internal quantum states. The engineering approach used in most DSMC calculations is based on the Variable Hard Sphere (VHS) model proposed by Bird [73]. This model is based on observations that it is the change in collision cross section with the relative energy of the colliding molecules, rather than the variation in the scattering law, that is most responsible for the observed effects of the molecular model on rarefied flows. The VHS model has a well-defined cross-section and follows the classical hard sphere scattering law, but the cross-section is an inverse power law function of the relative collision energy between the colliding molecules. The model parameters for the VHS model are deduced from the species viscosity data. Koura and Matsumoto [75] extended this model by introducing the variable soft sphere (VSS) model which has an additional parameter that accounts for anisotropic scattering. This parameter is fitted by comparing the diffusion coefficient of the model gas with that of the real gas. Another recent model that accounts for the attractive part of the potential is the generalized hard sphere (GHS) model of Hash and Hassan [76]. It bears the same relationship to the Leonard-Jones class of interaction potentials as the VHS or VSS models bear to the inverse power law interaction.

4.2.2 Energy Exchange

A detailed description of molecular interactions includes internal energy exchange, chemical reactions, and for sufficiently energetic flows, thermal radiation. Such phenomena

can only be fully described using quantum mechanics. Since such an approach would be much more computationally expensive, the models implemented to deal with the inelastic aspects of real molecules are generally phenomenological in nature. The phenomenological approach is to create the simplest possible mathematical model of a process that reproduces the physically significant aspects of the real process.

The most important of these models is the Larsen-Borgnakke [77] model for the calculation of the internal energy exchange during binary collisions of polyatomic species. The essential feature of this model is that a fraction of the collisions are regarded as completely inelastic, and for these, new values of the translational and internal energies are sampled from the distributions of these quantities that are appropriate to an equilibrium gas. The remainder of the molecular collisions are regarded as elastic. The fraction of inelastic collisions can be chosen to match the real gas relaxation rate. While the model is physically unrealistic at the microscopic level, it is one of the few that satisfies the principle of detailed balancing and gives satisfactory results in numerous applications.

The recent introduction of quantum vibration models by Haas et al. [78] and Bergmann and Boyd [79] has led to a generalized Larsen-Borgnakke scheme [73] where the treatment of the vibrational states is in the form of quantum states. The introduction of the quantum vibrational model has not only improved vibration modeling but has allowed the integration of chemical reaction and vibration modeling.

4.2.3 Chemical Reactions
The procedures used to implement chemical reactions since the 1970's are essentially extensions of the elementary collision theory of chemical physics. The binary reaction rate is obtained as the product of the collision rate for collisions with energy in excess of the activation energy and the probability of reaction (or steric factor).

The chemical data for gas phase reactions are almost always quoted in terms of macroscopic rate coefficients $K(T)$. A form of the collision theory that is consistent with the interaction model is used to convert these temperature dependent rate coefficients of continuum theory into collisional energy dependent steric factors. The reactive cross section is the product of the steric factor and the elastic cross section. If a comprehensive data base of reactive cross sections was available, it could be incorporated directly into the simulation, but this is not the case. In addition, the use of the rate coefficients guarantees consistency with the continuum theories that become valid at the higher densities.

Modification to the Bird model to include the effects of vibrational energy promoting a reaction have been proposed by Haas and Boyd [80]. In Bird's [73] latest model, the dissociation is closely linked with the vibrational levels of the diatomic molecules. That is, dissociation can be regarded as vibration to the level at which the bond between the atoms break. Given the vibrational relaxation rate, the Larsen-Borgnakke theory can be used with kinetic theory to derive analytical expressions for the reaction rate equations. The approach has been extended to treat recombination reactions and also exchange reactions in air. Experiments for reacting

systems other than air must be conducted to determine if this approach is generally valid.

4.2.4 Thermal Radiation
The major advances during 1985–90 were in the modeling of slightly ionized flow and thermal radiation. These advances were motivated by the technology requirements to support the orbit transfer vehicle studies and the development of an Aeroassist Flight Experiment (AFE) vehicle. These flowfields are characterized by velocities of the order of 10 km/s with atmospheric encounter at high altitudes. The partial ionization of such flows is accompanied by electronic excitation and thermal radiation. Radiation from bound-bound transitions between electronic states can be significant in 10 km/s flows. The procedures used for calculating the population of electronic states are analogous to the Larsen-Borgnakke model that has proved successful for the rotational and vibrational degrees of freedom. Unlike the procedures for the rotational and vibrational modes in which each molecule is assigned a single energy or state, each molecule is assigned a distribution over all the available electronic states. This overcomes the computational problems associated with radiation from sparsely populated states. Details of the modeling developed for air species which account for molecular band and atomic transitions is described in [81].

4.3 Major Codes
The DSMC codes utilized at NASA Langley are those that have either been developed by Bird, or have a close heritage with the algorithm and modeling implemented in Bird's codes. The primary code used for 2-D/axisymmetric simulations is the G2 code of Bird [82] . The G2 program provides a flexible system for the specification of the flow geometry using a body fitted grid. This code can be applied to a wide variety of flows ranging from the flow past aerodynamic bodies and rocket plume flows to internal flows in high vacuum equipment. The time-averaged flow properties may be sampled if the flow is such that it becomes steady at large times. Alternatively, an ensemble average may be made over multiple runs of an unsteady flow.

For general three-dimensional simulation, three different codes are utilized: G3, F3, and DAC. A key feature distinguishing these codes is the surface and volume grid treatment. Of the 3-D codes, G3 is the one most closely aligned with the organization and features of G2. G3 utilizes a body-fitted grid where the surface and volume grid may be either structured or unstructured. The latter capability has been recently expanded and demonstrated by Wilmoth et al. in [83].

The F3 code developed by Bird [84] and further evolved by Rault [85] utilizes a two-level Cartesian grid to define the surface and unstructured computational cells. An advantage of the Cartesian based cells is the reduction in the time associated with molecule movement and assignment of molecules to grid cells. The unstructured cells are achieved through clustering of Cartesian elements. For low-Knudsen-number flows, a modification to the basic grid scheme has been implemented [85] where a local body-fitted mesh is used to resolve gradients normal to the wall. A recent addition to the Cartesian grid DSMC codes is an algorithm named DAC (DSMC Analysis Code) that has been developed by LeBeau [83]. DAC uses a variable-resolution Cartesian grid currently consisting of two levels of cells. The resolution of the first level of cells is

constant and is typically set based on the minimum desired flowfield sampling resolution for a given problem. To further refine the flowfield grid in areas of increased density or high gradients, each level-1 cell can have an additional level of embedded Cartesian refinement. This second level of refinement is independent for each level-1 cell. The ability to refine the flowfield grid locally allows DAC to meet the spatial resolution requirement without excessive global refinement. As with the unstructured G3 code, the surface geometry for DAC is specified as a collection of planar triangular elements which form an unstructured triangular grid. The surface grid is defined independently of the volume grid. The reduced volumes of Cartesian cells that are clipped by the surface are computed and, to minimize the computational effort required to determine molecule-surface interactions, the surface triangles are mapped to the Cartesian cells.

4.4 Validation
When careful attention is given to satisfying numerical requirements and implementing physical models appropriate to the problem, the DSMC method yields results that agree well with experiments. Examples of computations performed at the NASA Langley Research Center where comparisons have been made with experimental measurements include: surface aerothermal loads produced by shock/shock interactions resulting from an oblique shock interacting with the bow shock of a cylindrical model [86,87], shock-boundary-layer interactions induced by ramps [88] and flares [89] as they influence the extent of separation and surface quantities, the effects of rarefaction on blunt body flows and their associated wake flows [90], the aerodynamics and heating of a delta wing as a function of rarefaction, [91] high altitude Space Shuttle aerodynamics [85,92], and the aerothermodynamics [93] of a spherically blunted 50° half angle capsule flown as the Japanese orbital re-entry flight experiment (OREX). Additional details concerning the blunt body wake studies and Orbiter aerodynamics follows.

4.4.1 Blunt Body/Wake Flows
The AGARD Fluid Dynamics Panel WG 18 began in late 1991 to focus on several problem areas associated with hypersonic flows. One of the problems selected for investigation was blunt body flows and their associated wake closure which is important for entry probes and aerobrakes. A number of fundamental issues exists concerning such flows: how does the wake structure change as a function of rarefaction, what role does thermochemical nonequilibrium play in the near wake structure, and to what limits are continuum models realistic as rarefaction in the wake is progressively increased. Experiments have been conducted in five hypersonic facilities using the same model configuration: a 70° spherically blunted cone with nose radius equal to one-half the model base radius, a shoulder or corner radius equal to 5 percent of the base radius, and for the sting supported models the sting radius was one-fourth the model base radius. Figures 15 through 19 present comparisons of measured and computed results using the G2 code of Bird, demonstrating the ability of the DSMC method to simulate complex flows that span a range of conditions (nonreacting to reacting flows) in the transitional to continuum regime. Figure 15 demonstrates that good agreement is achieved between the measured [94] and calculated [90] heating rate values along the sting where the model is at zero incidence in a nonreacting Mach 20 nitrogen flow at three levels of rarefaction where the overall freestream Knudsen number, Kn_∞, is the freestream mean

free path divided by the base diameter. The model base diameter is 5 cm (Rn = 1.25 cm). The measurements [94] were conducted in the SR3 facility of the CNRS, Meudon, France.

Nonintrusive electron beam fluorescence measurements of the flowfield density were also made for the two more rarefied test conditions in the CNRS experiments. Figure 16 presents a comparison of the DSMC calculation with measured values for the Kn_∞ = 0.0045 condition. The overall quantitative features of the two data sets are similar with the exception of the expansion of the flow about the outer corner of the model and the sudden up-turn of the 0.5 density contour adjacent to the sting. The calculated density contours in the near wake show a concentrated expansion from the rewarded facing portion of the outer corner. This behavior is consistent with other DSMC calculations that have been made for this test condition as summarized in [95], both at 0° and 10° incidence. The measurements show a more diffuse expansion extending down the base of the model. Part of this discrepancy may be due, in part, to a measurement resolution issue, since the gradients in density are substantial near the surface and occur in a rather small volume. As suggested in [95], the up-turn of the measured density contours along the sting are most likely due to an increase in the cross sectional area of the sting starting 80.4 mm downstream of the forebody stagnation point of the model. The change in the sting configuration was not included in the numerical simulations.

Within the near wake, a stable vortex is calculated for each of the three flow conditions where the calculated size of the wake vortex as measured from the base plane to the wake stagnation point (the point in the wake where the separated flow reattaches and the velocity is zero) increases with decreasing Kn_∞. The calculated behavior of the size of the wake vortex as influenced by rarefaction was later confirmed by the experiments performed in the vacuum wind tunnel V2G of the DLR, Göttingen. Experiments were made at three levels of rarefaction (bounded by the CNRS tests) in Mach 16 nitrogen flow with 5 cm base diameter models that had no afterbody sting. That is, the model was supported by three tungsten wires of 0.1 mm diameter. Patterson probe measurements [96,97] were made in the near wake to extract information concerning the molecular fluxes as a function of location and view direction. Figure 17 presents calculated and measured results for Kn_∞ = 0.002 indicating good agreement for the wake centerline number flux, nu, ratioed to the freestream flux, $(nV)_\infty$. The agreement is good in terms of both the extent of separation and the magnitude of the molecular fluxes.

Experiments were also made at much higher enthalpy flows where rarefaction effects were potentially present utilizing the Calspan LENS and Göttingen HEG shock tunnels. The LENS tests used sting supported models with a base diameter of 15.24 cm. One test was conducted at a Kn_∞ = 0.0023 by operating the facility at low pressure conditions. The test by Holden et al. [98] was made in Mach 15.6 nitrogen at an enthalpy of about 5 MJ/kg. For the DSMC simulation, the freestream quantities were: $V_\infty = 3245.8\,m/s$, $n_\infty = 2.807 \times 10^{21}\,m^{-3}$, and $T_\infty = 103.7\,K$. For this test condition, the nitrogen gas that envelopes the test model is in thermal nonequilibrium, yet there is negligible dissociation. Measurements were made for surface heating and pressure with a concentration of instrumentation along the

sting to capture the free shear layer reattachment. As shown in Fig. 18 for the heat transfer distribution, the agreement between calculation and measurements is fairly good, both in the separated region and toward the end of the recompression process, indicating that the size of the base flow region is well predicted. With only two heat transfer measurements along the forebody, it is not possible to establish the experimental trend for heat transfer distribution.

Tests were conducted at higher enthalpy levels (10 to 23 MJ/kg) at the DLR, Göttingen, using both large (d_b = 15.24 cm) and small (d_b = 0.5cm) models tested in HEG. The mini cone tests were at conditions where significant dissociation and potential rarefaction effects would be present. Measurements by Legge [99] consisted of only forebody heat transfer rates at the stagnation point and at an s/R_n location of 0.6. The tests were in air at Mach numbers of approximately 10. Two of the test cases have been simulated with the DSMC method using a 5-species reacting air gas model. For the lower enthalpy condition ($V_\infty = 4539\,m/s$, $T_\infty = 489.9\,K$, $\rho_\infty = 4.085 \times 10^{-3}\,kg/m^3$, and $Kn_\infty = 0.003$), the maximum mole fraction of atomic nitrogen along the forebody was of the order of 0.01 while the value for the higher enthalpy ($V_\infty = 6075\,m/s$, $T_\infty = 856.4\,K$, $\rho_\infty = 1.564 \times 10^{-3}\,kg/m^3$, and $Kn_\infty = 0.009$) test condition was of the order of 0.2. The calculated heating rate distributions for both cases are presented in Fig. 19 where the surface is assumed to be non-catalytic at a cold wall temperature of 300 K. Also shown are the measured values obtained using the thin wall technique. Good agreement is obtained for both test conditions in terms of distributions and absolute values. The estimated error of the heat transfer measurements of the mini cone tests was ±25 percent with the scatter shown [99] to be within ±20 percent.

These examples where one DSMC code has been applied to several experimental test conditions involving compressive forebody flows followed by rapid expansion into the near wake of a blunted cone provide enhanced confidence in the DSMC method to accurately simulate the complexities of such flows.

4.4.2 Shuttle Orbiter Aerodynamics
Several computational studies have been made comparing the results of 3-D DSMC computations with the aerodynamic data extracted from sensitive accelerometer measurements on the Orbiter during re-entry. The measurements [92] were made on orbit down to an altitude of 60 km using the Orbital Acceleration Research Experiment (OARE) which contained nano-g accelerometers along with a calibration station. Bird [84] first demonstrated good agreement with measured results at altitudes greater than 120 km using his F3 code which was later extensively evolved by Rault [85] and applied to altitudes as low as 100 km. More recent calculations (Blanchard et al. [88]) have been made by LeBeau using the DAC code and Wilmoth using an evolved version of Bird's G3 code (see [83] for a description of both codes). As shown in Fig. 20, the results from these three different 3-D codes are in excellent agreement with the flight measured normal-to-axial force ratios. Common to these calculations is the use of the variable hard sphere (VHS) intermolecular collision model and the gas-surface interaction model which was assumed to be diffuse with full thermal accommodation.

4.5 Applications
For reentry and planetary missions, analysis tools will be needed in both the continuum and the rarefied hypersonic regimes for predicting aerodynamics and heating. These analysis tools will be increasingly relied upon to provide data that historically have been obtained from ground-based and flight tests in order to reduce the overall development costs. Two current areas where analysis tools are actively supporting technology and flight missions are the Reusable Launch Vehicle (RLV) Technology Program and NASA's new decade-long program of robotic exploration of Mars.

In the rarefied regime, DSMC codes will be required for predicting vehicle aerodynamics and for predicting reaction control system (RCS) plume interactions. With the increasing computational demand that these activities will place on DSMC, the codes should be increasingly flexible and easy to use. This is particularly true for complex configurations and applications where it is necessary to couple DSMC with continuum CFD analyses such as that for RCS plume interactions.

4.5.1 DSMC Solutions for Generic SSTO Concept
The study of Wilmoth et al. [83] addressed the accuracy, efficiency and ease of use of different grid and geometry methodologies when applied to the DSMC computations about a generic single-stage-to-orbit (SSTO) concept for which continuum flowfield solutions at lower altitude flight conditions have been presented. The two DSMC codes used in this study were the G3 and DAC codes discussed earlier. As implemented in this study, G3 used an unstructured tetrahedral grid and DAC used a 2-level Cartesian grid, variable resolution approach. Common to both codes was the body geometry definition with emphasis on achieving geometric flexibility to deal with complex geometries. This was accomplished by specifying the surface as a collection of planar triangular elements which form an unstructured triangular grid.

DSMC simulations were performed for an altitude of 120 km with the following freestream conditions: V_∞ = 7818 m/s, n_∞ = $5.107 \times 10^{17}\,m^{-3}$, and T_∞ = 360 K. For the results presented in Fig. 21, the vehicle was at 32° angle of incidence with an assumed wall temperature of 1000 K. Based on the freestream conditions and body length of 56.57 m, the overall Knudsen number was about 0.08. A Knudsen number based on mean aerodynamic cord length would be closer to unity, indicative of a more rarefied flow.

Comparisons of surface contours of heat transfer with the two codes are shown in Fig. 21 for both upper and lower surfaces. The results match extremely well both qualitatively and quantitatively. A comparison of aerodynamic results obtained with Newtonian calculations is shown in Fig. 22 for the lift-to-drag (L/D) ratio. The DSMC result with collisions enabled is higher than the free molecular value, which is indicative of transitional effects. Yet the flow is significantly rarefied as the DSMC result is much lower than the Newtonian limit.

The calculated center-of-pressure is ahead of the center of gravity for this flight condition, resulting in a positive (nose-up) pitching moment at all angles of attack for both the free molecular and DSMC results. This is in contrast to the nose-down pitching moment predicted for the Space Shuttle Orbiter

with similar control deflections and under similar flight conditions [85]. However, the magnitude of the pitching moment predicted by DSMC is very small, and only a small force would be required to trim the vehicle at the attitudes shown.

The general conclusion from the study of Wilmoth et al. [83] was that even though the Cartesian schemes appear to offer the most advantages, it seems that no single grid methodology is universally superior for all problems. In fact, it is likely that a hybrid scheme in which a Cartesian grid is used for the bulk of the problem together with a local body-fitted grid near the body may offer significant advantages for near continuum solutions about RLV type vehicles.

4.5.2 Capsule Transitional Aerodynamics

Transitional aerodynamics becomes more critical for missions where passive aerodynamic control is relied upon for orientation and stabilization. For such missions, DSMC calculations can be used to more accurately define the transitional aerodynamics and validate the bridging relations used in trajectory analyses. Examples of recent applications of detailed computational tools for defining entry transitional aerodynamics is given in [68] for a commercial experiment transporter (COMET) reentry capsule, [100,101] for Mars Microprobes, [102,103] for the Stardust reentry capsule, and [101] for the Mars Pathfinder.

A unique aspect of the two Mars Microprobe entries is that the vehicles will encounter Mars' outer atmosphere in a random state, potentially backward and tumbling after deployment from their host Mars '98 lander. The passive reorientation requirement in the upper atmosphere is a requirement that has not been addressed by previous planetary programs. Results of DSMC calculations using the DAC code are presented in Fig. 23 for the moment coefficient about the center of gravity. These results demonstrate that the spherically blunted 45° half angle cone forebody (overall diameter of 0.35 m) followed by a hemispherical backshield centered at the center of gravity is statically unstable in the rear facing configuration for high Knudsen number conditions. Trajectory calculations show nominal reorientation occurs in the rarefied regime and the potential range of angle of attack is reduced prior to encountering continuum flow conditions.

DSMC calculations have shown that both the Mars Pathfinder (70.19° spherically blunted forebody followed by a 46.63° conical afterbody with an overall diameter of 2.65m) and the Stardust comet sample return capsule (60° spherically blunted forebody followed by a 30° conical afterbody with an overall diameter of 0.812m) experience static instabilities over the more rarefied portion of their transitional flow encounter when oriented at small angles of attack (Fig. 24 presents the calculated static pitching moment coefficient for Pathfinder). The trim angles for these vehicles at free molecular conditions are near 70° and 180°. For Pathfinder, trajectory simulations indicate that the gyroscopic effect of the vehicle spin is adequate for preventing unacceptable increase in vehicle attitude during the transitional portion of entry. For Stardust, however, the transitional static instability identified has required additional spin stabilization to prevent unacceptable excursions in angle of attack as the vehicle traverses the rarefied portion of Earth reentry and approaches peak heating conditions.

5. FUTURE AREAS OF RESEARCH

Advanced computational tools are playing a significantly increasing role in the analysis and design of hypersonic transportation and planetary entry systems in both continuum as well as rarefied flow regimes. Their rapid use in hypersonics has been driven primarily by necessity since there are not adequate ground-based facilities to simulate flight conditions. As discussed in the paper, a number of 3-D viscous codes are now available that include modeling for complex physical and chemical phenomena present in hypersonic flows. The solution algorithms in these codes are also becoming increasingly reliable and robust. However, the improvements in both solution algorithms and phenomenological modeling have been incremental, at best, over the last decade. It is necessary to reduce the time for the entire computational process by at least two to three orders of magnitude for routine use of these computational tools in analysis, design, and optimization.

Surface modeling and field grid generation on complex configurations continues to take the most time in the computational process. Currently, it takes anywhere from a few days to several weeks to generate a reasonable viscous grid for a real configuration. Although this is an area where significant progress has been made, further developments are required to reduce the discretization time to not more than a few hours with the use of automation and by creating grid libraries on a variety of shapes, appendages, configurations, etc. that can be called up, assembled, and suitably modified. The approaches in grid generation should be flexible and should allow quick definition and alterations of configurations. Although gridding strategies in the near future will continue to use both structured and unstructured approaches, it appears that the unstructured grid approach is superior for complex configurations and takes much less time than the structured grid approach. It also allows optimum use of grid cells and their adaptation to high gradient regions. Once algorithms compatible with unstructured grids are well-developed, structured grid capability will probably no longer be required.

Convergence acceleration of the computational algorithms by an order of magnitude is another aspect of the solution process that can reduce the total time. Most algorithms being used today in the codes were developed in the seventies and early eighties and since then, only marginal progress has been made in improving their convergence. Further developments in multigrid algorithms and local preconditioning have the potential to provide this order of magnitude of improvements in convergence. There is also a need to build some intelligence in these algorithms so that they can sense the convergence problems or instabilities and automatically modify or adjust the algorithm to avoid catastrophic failure. Another feature that can accelerate the overall convergence is the ability of the algorithm to conduct local iterations in regions of slow convergence.

A significant savings in total computer time can be achieved by efficient use of parallel computers, which are fast becoming the computational platforms of choice. Of course, this requires development of algorithms that are compatible with the requirements of parallelization and that the code developer be knowledgeable of the architectural features of parallel computers to take full advantage of their capabilities. The preceding type of efficiency gains are essential in general, but for nonequilibrium, chemically reacting flows, they are almost mandatory if the computational tools for such flows are to be

used on a routine basis in the analysis and design of hypersonic systems. Currently, a well resolved analysis of a complete scramjet engine flowpath can take anywhere from one to several hundred hours on a Cray C-90 class machine, making such analysis extremely expensive for routine use.

Advances in physical and chemical modeling for hypersonic flows are necessary to increase the reliability and robustness of the codes and to reduce uncertainty in the predictions. Most of the codes currently use simple models which were not intended to be used in hypersonic flows. New models for turbulence, onset and transition from laminar to turbulent flow, turbulence-chemical kinetics interactions, energy exchange mechanisms, and radiation are required. There is also evidence that local speed of sound, drag, and heating rates may be significantly affected by externally produced, weakly ionized flow in ways that are not fully understood or predicted by the current physical models. Some of these models, when incorporated in the governing equations, introduce new complexities which may require modifications in the solution algorithms. Inherent in the development of these models is the need of very detailed and well designed experimental databases, both mean and fluctuating, at appropriate flow conditions. These databases are essential not only to develop new or improved models, but also are required to understand the deficiencies of a model.

Code validation, especially for hypersonic turbulent, interacting, and chemically reacting flows, remains a major concern. Both local and global (at subsystem or component and overall system level) validation of the codes is required. Global evaluation of uncertainties is necessary to predict overall performance numbers because the combination of uncorrelated local and component or subsystem level uncertainties may sum up to very large global uncertainties. The complexity comes from the fact that the validation databse is obtained in ground facilities having different environment (flow quality, contaminants, enthalpy, dynamic pressures, etc.) than that encountered in flight. Of course, geometric scaling and its impact on combustion chemistry, in particular, also remains an issue in code validation. Unless progress is made in developing improved models and codes are adquately validated, the codes will continue to remain tools only for preliminary design and incremental performance prediction in sensitivity studies.

The paper has focused primarily on the steady flow simulations. Unsteady flows produce their own challenges. Both efficient, time-accurate algorithms and techniques for storage, analysis, and display of large volumes of data generated in unsteady flow simulations are required. In addition, the paper discusses computational codes for aerodynamic analysis and design only. However, for multidisciplinary research, CFD codes need to be integrated with other disciplinary computational tools. For example, to study the aerothermostructural behavior of a vehicle, an aerodynamic code needs to interface and interact with material properties and structural analysis codes.

Many of the issues facing the continuum CFD with respect to surface and field grid generation are also relevant to the rarefied flow codes. Much of the current efforts in rarefied flow code development are focused on enhancing the functionality of DSMC for complex 3-D simulations, incorporating added "intelligence" to reduce user intervention, and implementing them on massively parallel computers. Physical models are also

being enhanced. The quantum vibrational model that has evolved recently could be used to improve the modeling of thermal radiation due to vibrational transitions. A future area of research involves integration of electronic excitation and ionization in the same way that vibrational excitation and dissociation has been integrated. This would similarly improve the modeling of radiation due to electronic transitions.

It is now several years since the DSMC approach was shown [87] to be an effective tool for studying the Edney Type IV wave interaction that was important to the aerospace plane project at that time. Computers have become significantly faster since then and it is possible that DSMC could now be applied to study even some aspects of hypersonic propulsion. For example, the combustion process and the degree of recombination in the nozzle are among some of the critical issues and, whatever the density, DSMC could now be applied to one-dimensional models of these elements of the propulsion system.

REFERENCES
[1] White, M.E.; Drummond, J.P.; and Kumar, A: Evolution and Status of CFD Techniques for Scramjet Applications. J. of Propulsion and Power, Vol. 3, No. 5, 1987, pp. 423-439.
[2] Dwoyer, D.L.; and Kumar, A.: Computational Analysis of Hypersonic Airbreathing Aircraft Flow Fields. AIAA Paper No. 87-0279, 1987.
[3] Kumar, A: CFD for Hypersonic Airbreathing Aircraft. Proceedings of 11th International Conference on Numerical Methods in Fluid Dynamics, Lecture Notes in Physics, Vol. 323, Edited by Dwoyer, Hussaini, and Voigt, 1988, pp. 40-56.
[4] Malik, M.R.: Numerical Methods for Hypersonic Boundary Layer Stability. HTC Report No. 88-6, High Technology Corporation, Hampton, VA, June 1988.
[5] Malik, M.R.; and Anderson, E.C.: Real Gas Effects on Hypersonic Boundary- Layer Stability. Physics of Fluids A, Vol. 3, No. 5, 1991, pp. 803-821.
[6] Park, C.: Review of Chemical-Kinetic Problems of Future NASA Missions, I: Earth Entries. J. of Thermophysics and Heat Transfer, Vol. 7, No. 3, 1993, pp. 385-398.
[7] Park, C.; Howe, J.T.; Jaffe, R.L.; and Candler, G.V.: Review of Chemical-Kinetic Problems of Future NASA Missions, II: Mars Entries. J. of Thermophysics and Heat Transfer, Vol. 8, No. 1, 1994, pp. 9-23.
[8] Bose, D.; and Candler, G.V.: Simulation of Hypersonic Flows Using a Detailed Nitric Oxide Formation Model. AIAA Paper No. 96-1801, 1996.
[9] Candler, G.V.; Olejniczak, J.; and Harrold, B.: Detailed Simulation of Nitrogen Dissociation in Stagnation Regions. AIAA Paper No. 96-2025, 1996.
[10] McBride, B.J.; Heimel, S.; Ehlers, J.G.; and Gordon, S.: Thermodynamic Properties to 6000 K for 210 Substances Involving the First 18 Elements. NASA SP-3001, 1963.

[11] Wilke, C.R.: A Viscosity Equation for Gas Mixtures. J. of Chemistry and Physics, Vol. 18, No. 4, 1950, pp. 517-519.

[12] Gupta, R.N.; Yos, J.M.; Thompson, R.A.; and Lee, K.-P.: A Review of Reaction Rates and Thermodynamic and Transport Properties for an 11-Species Air Model for Chemical and Thermal Nonequilibrium Calculations to 30,000 K. NASA RP-1232, 1990.

[13] Gupta, R.N.; Lee, K.-P.; Thompson, R.A.; and Yos, J.M.: Calculations and Curve Fits of Thermodynamic and Transport Properties for Equilibrium Air to 30,000 K. NASA RP-1260, 1991.

[14] White, F.M.: Viscous Fluid Flow. McGraw-Hill, Inc., 1974.

[15] Drummond, J.P.: High-Speed Flight Propulsion Systems. Progress in Astronautics and Aeronautics, Vol. 137, Edited by S.N.B. Murthy and E.T. Curran, 1991.

[16] Jachimowski, C.J.: An Analytical Study of Hydrogen-Air Reaction Mechanism with Application to Scramjet Combustion. NASA TP-2791, 1988.

[17] Surface modeling, grid generation, and related issues in CFD. NASA CP 3291, 1995.

[18] Bibb, K.L.; Peraire, J.; and Riley, C.J.: Hypersonic Flow Computations on Unstructured Meshes. AIAA Paper No. 97-0625,1997.

[19] Prizadeh, S.: Viscous Unstructured Three-Dimensional Grids by the Advancing-Layers Method. AIAA Paper No. 94-0417, 1994.

[20] Frink, N.T.: Recent Progress Towards a Three-Dimensional Unstructured Navier-Stokes Solver. AIAA Paper No. 94-0061, 1994.

[21] MacCormack, R.W.: The Effect of Viscosity in Hypervelocity Impact Cratering. AIAA Paper No. 69-354, 1969.

[22] Beam, R.; and Warming, R.F.: An Implicit Factored Scheme for the Compressible Navier-Stokes Equations. AIAA J., Vol. 16, 1978. pp. 393-402.

[23] Jameson, A.; Schmidt, W.; and Turkel, E.: Numerical Solutions of the Euler Equations by Finite Volume Methods Using Runge-Kutta Time-Stepping Schemes. AIAA Paper No. 81-1259, 1981.

[24] Vatsa, V.N.; and Wedan, B.W.: Development of a Flexible and Efficient Multigrid Code for 3-D Navier-Stokes Equations and its Application to a Grid-Refinement Study. Computers and Fluids, Vol. 18, No. 4, 1990, pp. 391-403.

[25] Turkel, E.; Swanson, R.C.; Vatsa, V.N.; and White, J.W.: Multigrid for Hypersonic Viscous Two- and Three-Dimensional Flows. AIAA Paper No. 91-1572, 1991.

[26] Vatsa, V.N.; Turkel, E.; and Abolhassani, J.S.: Extension of Multigrid Methodology to Supersonic/Hypersonic 3-D Viscous Flows. International J. for Numerical Methods in Fluids, Vol. 17, 1993, pp. 825-837.

[27] Turkel, Eli: A Review of Preconditioning Methods for Fluid Dynamics. Applied Numerical Mathematics, Vol. 12, September 1993, pp. 257-284.

[28] van Leer, B.; Thomas, J.L.; Roe, P.; and Newsome, R.A.: Comparison of Numerical Flux Formulas for the Euler and Navier-Stokes Equations. AIAA Paper No. 87-1104,1987.

[29] Bussing, T.R.A.; and Murman, E.M.: A Finite-Volume Method for Calculation of Compressible Chemically Reacting Flows. AIAA Paper No. 85-0311, 1985.

[30] Widhoph, G.F.; and Victoria, K.J.: On the Solution of the Unsteady Navier-Stokes Equations Including Multicomponent Finite Rate Chemistry. Computers and Fluids, Vol. 1, 1993, pp. 159-184.

[31] Roe, P.L.: Characteristic-Based Schemes for the Euler Equations. Annual Review in Fluid Mechanics, Vol. 19, 1986, pp. 337-365.

[32] Yee, H.C.: Construction of Explicit and Implicit Symmetric TVD Schemes and Their Applications. J. of Computational Physics, Vol. 68, 1987, pp. 151-179.

[33] Harten, A.: High Resolution Schemes for Hyperbolic Conservation Laws. Journal of Computational Physics, Vol. 49, No. 2, 1983, pp. 357-393.

[34] Cheatwood, F.M.; and Gnoffo, P.A.: User's Manual for the Langley Aerothermodynamic Upwind Relaxation Algorithm (LAURA). NASA TM 4674, 1996.

[35] Srinivasan, S.; Tannehill, J. C.; and Weilmuenster, K. J.: Simplified Curve Fits for the Thermodynamic Properties of Equilibrium Air. NASA RP 1181, 1987.

[36] Liu, Y.; and Vinokur, M.: An Analysis of Numerical Formulations of Conservation Laws. NASA CR-177489, 1988.

[37] Weilmuenster, K.J.; Gnoffo, P.A.; and Greene, F.A.: Navier-Stokes Simulations of Orbiter Aerodynamic Characteristics Including Pitch Trim and Bodyflap. J. of Spacecraft and Rockets, Vol. 37, No. 3, 1994, pp. 355-366.

[38] Gnoffo, P.A.; Weilmuenster, K.J.; and Alter, S.J.: Multiblock Analysis for Shuttle Orbiter Re-entry Heating from Mach 24 to Mach 12. J. of Spacecraft and Rockets, Vol. 31, No. 3, 1994, pp. 367-377.

[39] Gnoffo, P.A.: Code Calibration Program in Support of the Aeroassist Flight Experiment. J. of Spacecraft and Rockets, Vol. 27, No. 2, 1990, pp. 131-142.

[40] Rudy, D.H.; Thomas, J.L.; Kumar, A.; Gnoffo, P.A.; and Chakravarthy, S.R.: Computation of Laminar Hypersonic Compression Corner Flows. AIAA Journal, Vol. 29, No. 7, 1991, pp. 1108-1113.

[41] Saad, Y.; and Schultz, M.: GMRES: A Generalized Minimum Residual Algorithm for Solving Nonsymmetric Linear Systems. SIAM J. of Scientific and Statistical Computing, Vol. 7,No. 3, 1986, pp. 856-869.

[42] AeroSoft, I.: GASP Version 3 User's Manual. 1872 Pratt Drive, Suite 1275, Blacksburg, VA 24060: AeroSoft Inc., May 1996.

[43] Huebner, L.D.; and Tatum, K.E.: CFD Code Calibration and Inlet-Fairing Effects on a 3D Hypersonic Powered-Simulation Model. AIAA Paper No. 93-3041, 1993.

[44] Huebner, L.D.; and Tatum, K.E.: Computational and Experimental Aftbody FLow Fields for Hypersonic, Airbreathing Configurations with Scramjet Exhaust Flow Simulation. AIAA Paper No. 91-1709, 1991.

[45] Srinivasan,S.; Bittner, R.D.; and Bobskill, G.J.: Summary of GASP Code Application and Evaluation Effort for Scramjet Combustor Flowfields. AIAA Paper No. 93-1973, 1993.

[46] Kumar, A: Numerical Analysis of the Scramjet Inlet Flow Field by Using Two-Dimensional Navier-Stokes Equations. NASA TP-1940, 1981.

[47] Kumar, A: Numerical Simulation of Scramjet Inlet Flow Fields. NASA TP-2517, 1986.

[48] Drummond, J.P.; Rogers, R.C.; and Hussaini, M.Y.: A Detailed Numerical Model of a Supersonic Reacting Mixing Layer. AIAA Paper No. 86-1427, 1986.

[49] Carpenter, M.H.; and Kamath, H.: Three-Dimensional Extensions to the SPARK Combustion Code. NASP CP-5029, Paper 15, Oct. 1988, pp.107-134.

[50] Carpenter, M.H.: A Generalized Chemistry Version of SPARK. NASA CR-4186, 1988.

[51] Newsome, R.W.; Walters, R.W.; and Thomas, J.L.: An Efficient Iteration Strategy for Upwind/Relaxation Solutions to the Thin-Layer Navier-Stokes Equations. AIAA Paper 87-1113, 1987.

[52] Spalart, P.R.; and Allmaras, S.R.: A One-Equation Turbulence Model for Aerodynamic Flows. AIAA Paper 92-0439, 1992.

[53] Menter, F.R.: Zonal Two Equation k-ω Models for Aerodynamic Flows. AIAA Paper No. 93-2906, 1993.

[54] Mentor, F.R.: Improved Two-Equation k-omega Turbulence Models for Aerodynamic Flows. NASA TM 103975, 1992.

[55] Wilcox, D.W.: Wall Matching , a Rational Alternative to Wall Functions. AIAA Paper No. 89-0611, 1989.

[56] Abid, R.: Evaluation of Two-Equation Turbulence Models for Predicting Trasitional Flows. International Journal of Engineering Science, Vol. 31, No. 6, 1993, pp. 831-840.

[57] Abid, R.; Morrison, J.H.; Gatski, T.B.; and Speziale, C.G.: Prediction of Complex Aerodynamic Flows with Explicit Algebraic Stress Models. AIAA Paper 96-0565, 1996.

[58] Adumitroaie, V.; Colucci, P.J.; Taulbee, D.B.; and Givi, P.: LES, DNS, and RANS for the Analysis of High-Speed Turbulent Reacting Flows. Annual Report, NASA Grant NAG 1-1122, 1994.

[59] Girimaji, S.S.: Assumed Beta-pdf Model for Turbulent Mixing: Validation and Extension to Multiple Scalar Mixing. Combustion Science and Technology, Vol. 78, 1991, pp. 177-196.

[60] Gaffney, R.L.; White, J.A.; Girimaji, S.S.; and Drummond, J.P.: Modeling Temperature and Species Fluctuations in Turbulent, Reacting Flow. Computing Systems in Engineering, Vol. 5, No.2, 1994, pp. 117-133.

[61] Srinivasan, S.: Numerical Simulation of Turbulent Flow Past a Flat Plate. HNAG Report 95-2-057, NASA Langley Research Center, 1995.

[62] van Leer, B.: Towards the Ultimate Conservation Scheme: A Second-Order Sequel to Gudonov's Method. J. of Computational Physics, Vol. 32, 1979, pp. 101-136.

[63] Arminjon, P.; and Dervieux, A.: Construction of TVD-like Artificial Viscosities on Two-Dimensional Arbitrary FEM Grids. INRIA Report 1111, 1989.

[64] Jameson, A.; Reuther, J.; and Martinelli, L.: Computational Algorithms for Aerodynamic Analysis and Design TLSP: Annual Report, 1 Oct. 1993 - 30 Sept. 1994. AFOSR 95-0082 TR, Princeton University, 1995.

[65] Thomas, J.L.; and Walters, R.W.: Upwind Relaxation Algorithms for the Navier-Stokes Equations. AIAA Paper No. 85-1501 CP, 1985.

[66] Abdol-Hamid; Khaled, S.; Lakshmann, B.; and Carlson, John B.: Application of Navier-Stokes Code PAB3D with k-ε Tubulence Model to Attached and Separated Flows. NASA TP 3480, 1995.

[67] Jespersen, D.C.; Pulliam, T.H.; and Buning, P.G.: Recent Enhancements to OVERFLOW. AIAA Paper No. 97-0644, 1997.

[68] Wood, W.A.; Gnoffo, P.A.; and Rault, D.F.G.: Aerodynamic Analysis of Commercial Experiment Re-Entry Capsule. Journal of Spacecraft and Rockets, Vol. 33, No. 5, 1996, pp. 643-646.

[69] Engle, C.D.; and Praharaj, S.C.: MINIVER Upgrade for the AVID System, Vol. I: LANMIN Users Manual. NASA CR 172212, August 1983.

[70] Gnoffo, P.A.; Weilmuenster, K.J.; Hamilton, H.H.; Olynick, D.R.; and Venkatapathy, E.: Comptational Aerothermodynamic Design Issues for Hypersonic Vehicles. AIAA Paper No. 97-2473, 1997.

[71] Rodi, P. E.: An Experimental Study of the Effects of Bodyside Compression on Forward Swept Sidewall Compression Inlets Ingesting a Turbulent Boundary Layer. AIAA Paper No. 93-3125, 1993.

[72] Rodi, P.E.; and Trexler, C.A.: The Effects of Bodyside Compression on Forward and Aft Swept Sidewall Compression Inlets at Mach 4. AIAA Paper No. 94-2708, 1994.

[73] Bird, G.A.: *Molecular Gas Dynamics and the Direct Simulation of Gas Flows*. Clarendon Press, Oxford, 1994.

[74] Dietrich, S.; and Boyd, I.D.: Scalar and Parallel Optimized Implementation of the Direct Simulation Monte Carlo Method. J. of Computational Physics, Vol. 126, 1996, pp. 328–342.

[75] Koura, K.; and Matsumoto, H.: Variable Soft Sphere Molecular Model for Inverse-Power-Law or Lennard-Jones Potential. Phys. of Fluids A, Vol. 3, 1991, pp. 2459–2465.

[76] Hash, D.B.; and Hassan, H.A.: Monte Carlo simulation Using Attractive-Repulsive Potentials. Rarefied Gas Dynamics: Theory and Simulations, edited by B. D. Shizgal and D. P. Weaver, Progress in Astronautics and Aeronautics, Vol. 159, 1994, pp. 284–293.

[77] Borgnakke, C.; and Larsen, P.S.: Statistical Collision Model for Monte Carlo Simulation of Polyatomic Gas Mixtures. J. of Computational Physics, Vol. 18, 1975, pp. 405–420.

[78] Haas, B.L.; McDonald, J.D.; and Dagum, L.: Models of Thermal Relaxation Mechanics for Particle Simulation Methods. J. of Computational Physics, Vol. 107, 1993, pp. 348–358.

[79] Bergemann, F.; and Boyd, I.D.: New Discrete Vibrational Energy Model for the Direct Simulation Monte Carlo Method. Rarefied Gas Dynamics: Experimental Techniques and Physical Systems, edited by B.D. Shizgal and D.P. Weaver, Progress in Astronautics and Aeronautics, Vol. 158, 1994, pp. 174–183.

[80] Haas, B.L.; and Boyd, I.D.: Models for Direct Monte Carlo Simulation of Coupled Vibration-Dissociation. Physics of Fluids A, Vol. 5, No. 2, Feb. 1993, pp. 478–489.

[81] Bird, G.A., "Nonequilibrium Radiation During Re-Entry at 10 km/s," AIAA Paper 87-1543, June 1987.

[82] Bird, G.A., "The G2/A3 Program System Users Manual," G.A.B. Consulting Pty Ltd, Killara N.S.W., Australia, March 1992.

[83] Wilmoth, R.G.; LeBeau, G.J.; and Carlson, A.B.: DSMC Grid Methodologies for Computing Low-Density, Hypersonic Flows About Reusable Launch Vehicles. AIAA Paper No. 96-1812, 1996.

[84] Bird, G.A.: Application of the Direct Simulation Monte Carlo Method to the Full Shuttle Geometry. AIAA Paper No. 90-1692, 1990.

[85] Rault, D.F.G.: Aerodynamics of the Shuttle Orbiter at High Altitudes. J. of Spacecraft and Rockets, Vol. 31, No. 6, 1994, pp. 944–952.

[86] Holden, M.; and Kolly, J.: Measurements of Heating in Regions of Shock/Shock Interaction in Hypersonic Flow. AIAA Paper No. 95-0640, 1995.

[87] Carlson, A.B.; and Wilmoth, R.G.: Monte Carlo Simulation of a Near-Continuum Shock-Shock Interaction Problem. J. of Spacecraft and Rockets, Vol. 31, No. 1, 1994, pp. 25–30.

[88] Moss, J.N.; Price, J.M.; and Chun, Ch.-H.: Hypersonic Rarefied Flow About a Compression Corner—DSMC Simulation and Experiment. AIAA Paper No. 91-1313, 1991.

[89] Moss, J.N.; and Dogra, V.K.: DSMC Simulation of Viscous Interactions for a Hollow Cylinder-Flare Configuration. AIAA Paper No. 94-2015, 1994.

[90] Moss, J.N.; and Price, J.M.: Review of Blunt Body Wake Flows at Hypersonic Low Density Conditions. AIAA Paper No. 96-1803, 1996.

[91] Celenligil, M.C.; and Moss, J.N.: Hypersonic Rarefied Flow about a Delta Wing—Direct Simulation and Comparison with Experiment. AIAA Journal, Vol. 30, No. 8, 1992, pp. 2017–2023.

[92] Blanchard, R.C.; Wilmoth, R.G.; and LeBeau, G.L.: Orbiter Aerodynamic Acceleration Flight Measurements in the Rarefied-Flow Transition Regime. AIAA Paper No. 96-2467, 1996.

[93] Moss, J.N.; Gupta, R.N.; and Price, J.M.: DSMC Simulations of OREX Entry Conditions. Presented at 20th International Symposium on Rarefied Gas Dynamics, Beijing, China, August 1996.

[94] Allegre, J.; and Bisch, D.: Blunted Cone at Rarefied Hypersonic Conditions—Experimental Density Flowfields, Heating Rates, and Aerodynamic Forces. CNRS Report RC 95-2, September 1995.

[95] Coron, F.; and Harvey, J.K.: Synopsis for Test Case 6—Rarefied 70° Spherically Blunted Cone. Presented at 4th European High-Velocity Database Workshop, ESTEC, Noordwijk, The Netherlands, Nov. 1994.

[96] Legge, H.: Patterson Probe Measurements in the Wake of a 70 Deg. Half Angle Cone in Hypersonic Rarefied Flow. DLR Report-IB 223-94 A 15, December 1994.

[97] Danckert, A.; and Legge, H.: Experimental and Computational Wake Structure Study for a Wide-Angle Cone. J. of Spacecraft and Rockets, Vol. 33, No. 4, 1996, pp. 476–482.

[98] Holden, M.; Kolly, J.; and Chadwick, K.: Calibration, Validation, and Evaluation Studies in the LENS Facility. AIAA Paper No. 95-0291, 1995.

[99] Legge, H.: Experiments on a 70 Degree Blunted Cone in Rarefied Hypersonic Wind Tunnel Flow. AIAA Paper No. 95-2140, 1995.

[100] Mitcheltree, R.A.; Moss, J.N.; Cheatwood, F.M.; Green, F. A.; and Braun, R. D.: Aerodynamics of the Mars Microprobe Entry Vehicles," AIAA Paper No. 97-3658, 1997.

[101] Moss, J.N.; Wilmoth, R.G.; and Price, J.M.: DSMC Simulations of Blunt Body Flows for Mars Entries. AIAA Paper No. 97-2508, 1997.

[102] Mitcheltree, R.A.; Wilmoth, R.G.; Cheatwood, F.M.; Rault, D.F.G.; Brauckmann, G.J.; and Green, F.A.: Aerodynamics of the Stardust Sample Return Capsule. AIAA Paper No. 97-2304, 1997.

[103] Wilmoth, R.G.; Mitcheltree, R.A.; and Moss, J.N.: Low-Density Aerodynamics of the Stardust Reentry Capsule. AIAA Paper No. 97-2510, 1997.
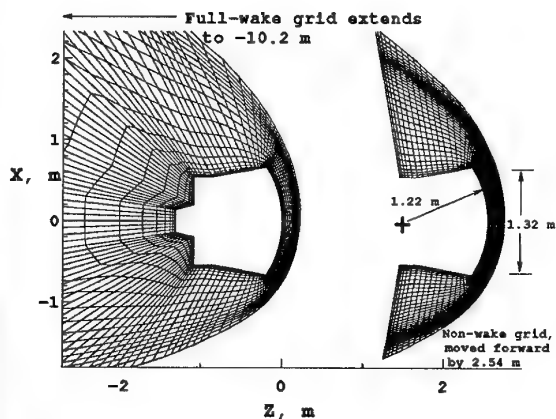
Figure 1. Full flow field and non-wake grid in symmetry plane of COMET (every other body-normal point shown)
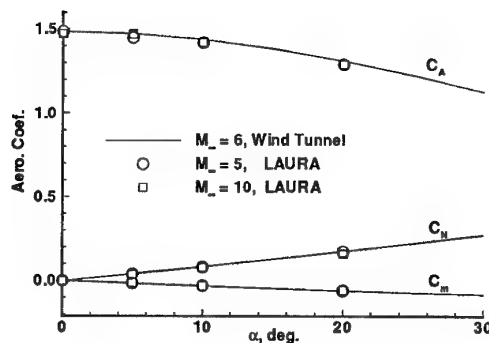
Figure 2. Comparison of experimental results on 7% scale COMET model in Mach 6 Tunnel with computed results
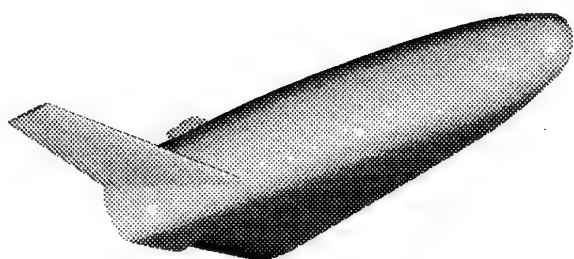
Figure 3. B1001 configuration (RLV)
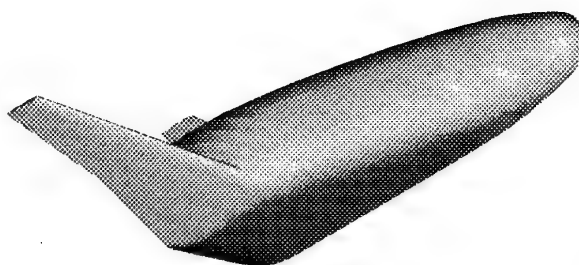
Figure 4. B1001A configuration (X33)
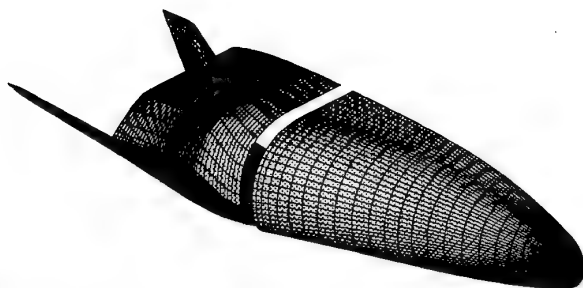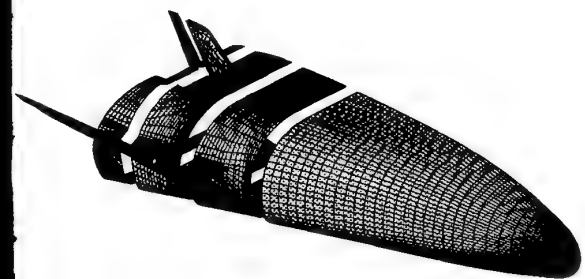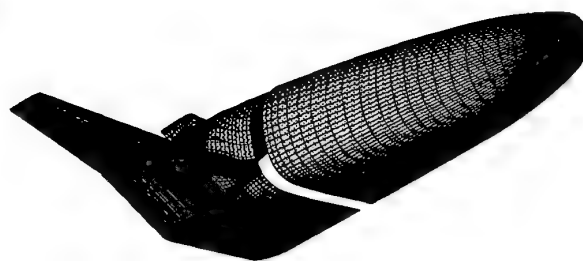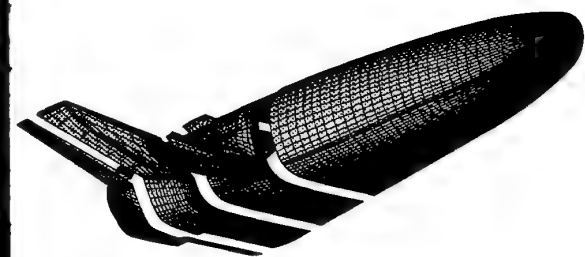
Figure 5. B1001 surface grid (RLV)
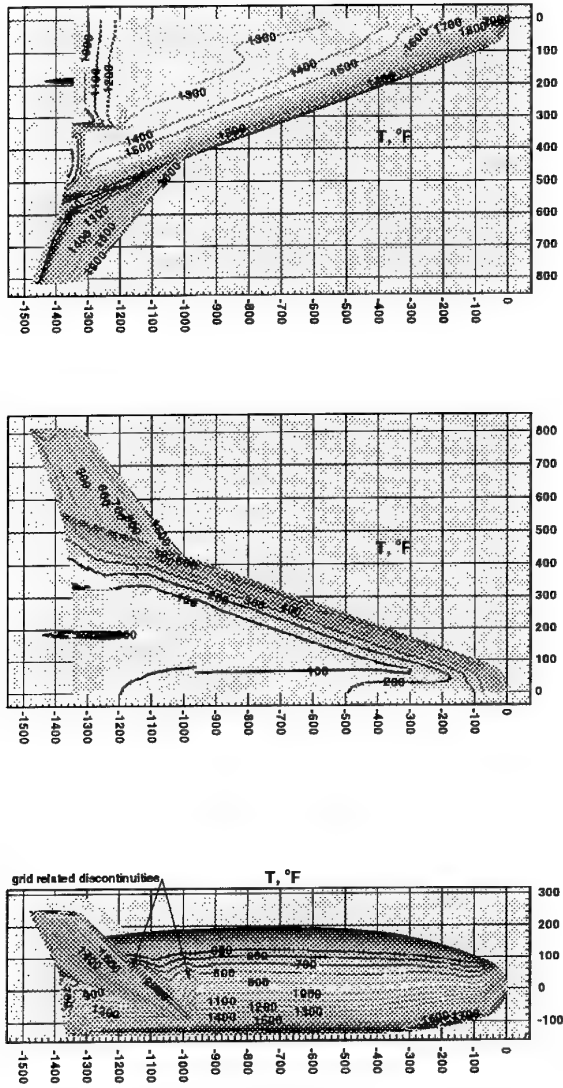
Figure 6. B1001A surface grid (X33)

Figure 7. Temperature contours on RLV for fully catalytic wall, laminar flow, at 1200 s
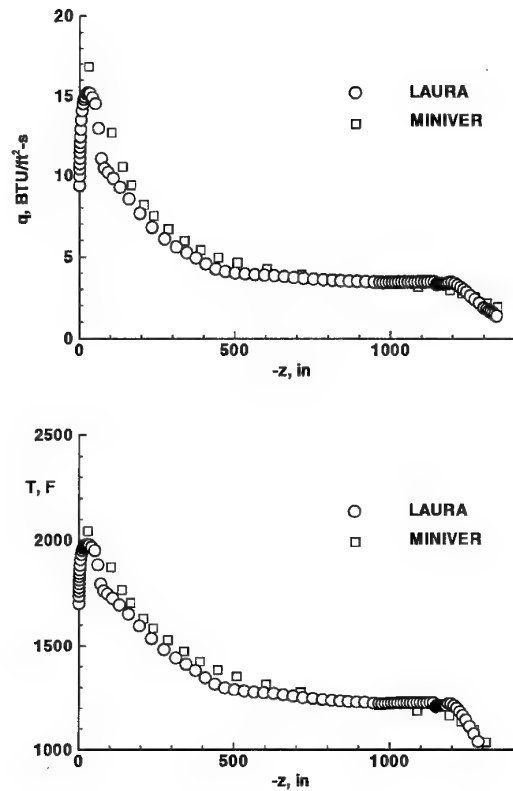

Figure 8. Windside centerline comparisons of LAURA and MINIVER results at the 1200 s trajectory point for the RLV
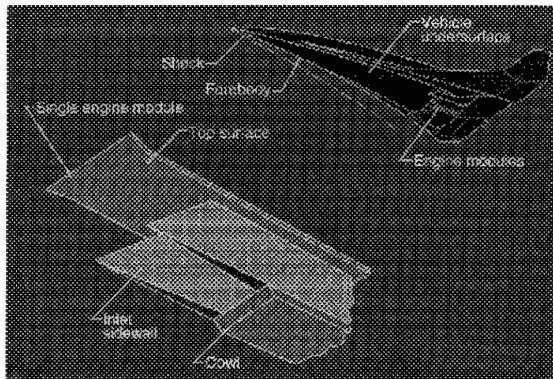
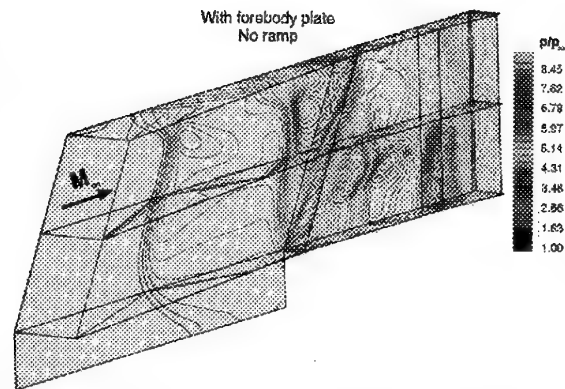Figure 9. Forward-swept, sidewall compression inlet concept
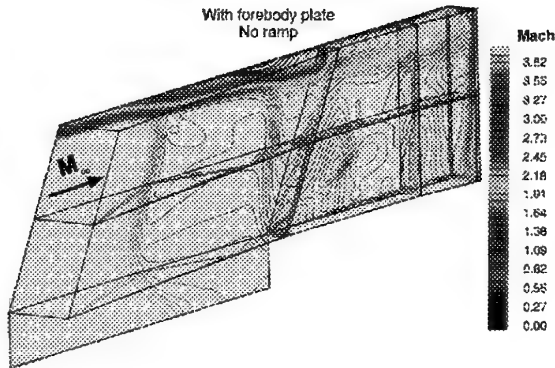

Figure 10. Pressure contours through the inlet at Mach 4

Figure 11. Mach number contours through the inlet at Mach 4
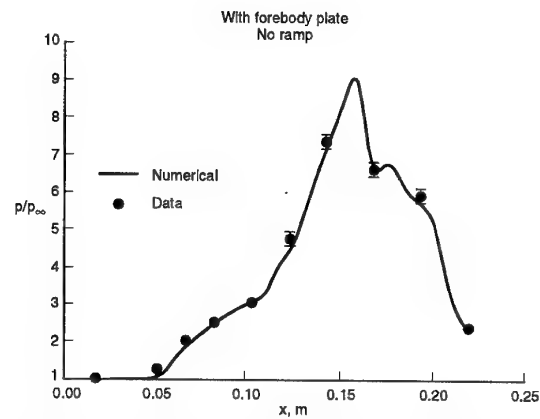
Figure 12. Pressure comparison with experimental data on the bodyside centerline
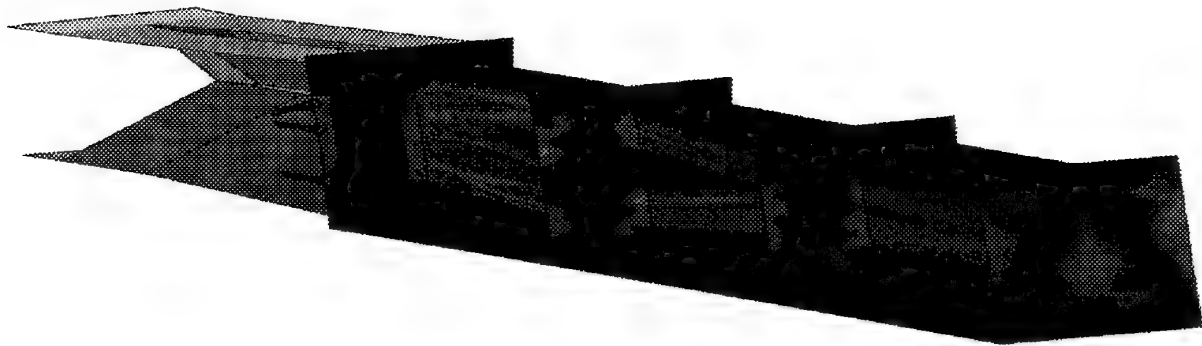
Figure 13. Concentration contours for helium in the combustor
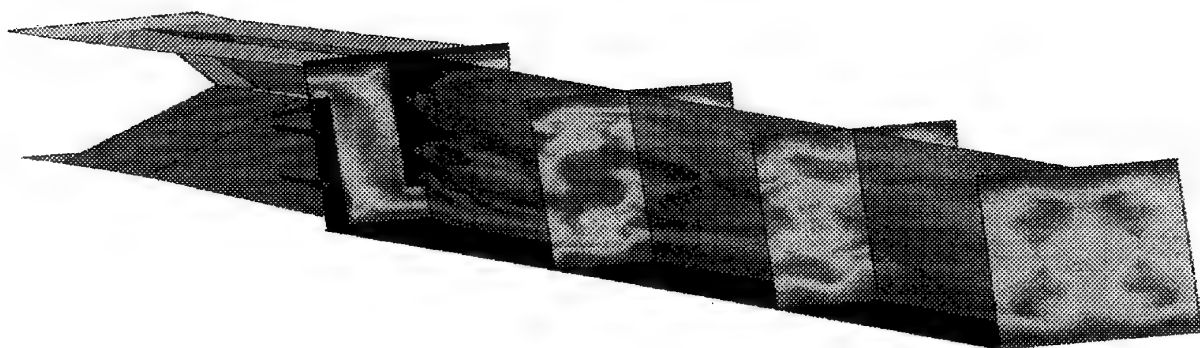
Figure 14. Mach number contours through the scramjet combustor
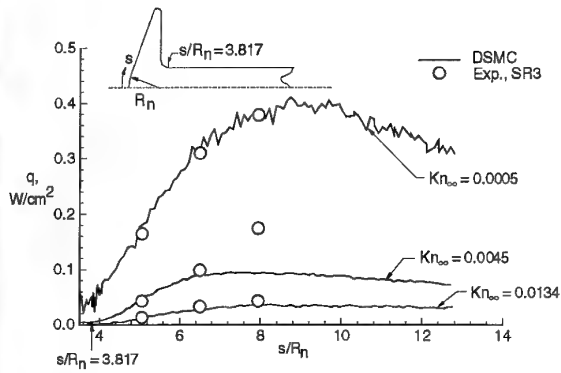
Figure 15. Measured and calculated heating rates along sting of a 70° spherically blunted cone in Mach 20 nitrogen (d_b = 5 cm).
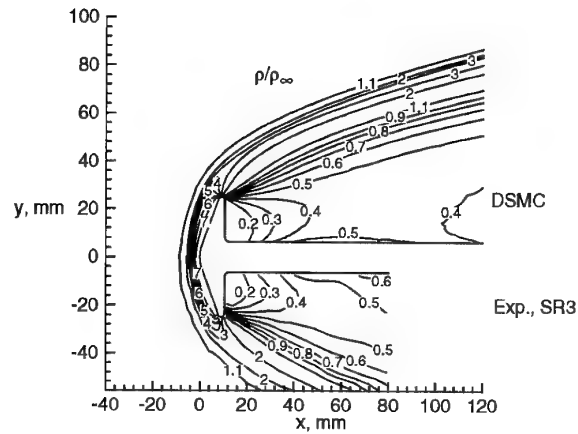
Figure 16. Measured and calculated density contours for SR3 test in Mach 20 nitrogen (Kn_∞ = 0.0045, d_b = 5 cm).
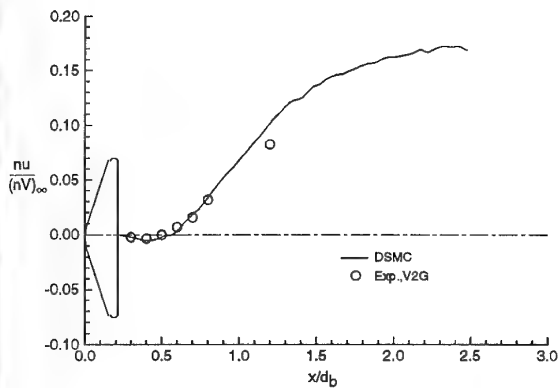
Figure 17. Measured and calculated number flux along centerline of near wake for V2G test in Mach 16.5 nitrogen (Kn_∞ = 0.0021, d_b = 5 cm).
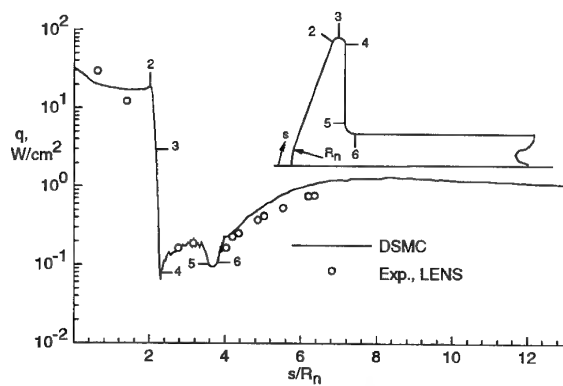
Figure 18. Measured and calculated heating rate distributions for LENS test in Mach 15.6 nitrogen (Kn_∞ = 0.0023, d_b = 15.24 cm).
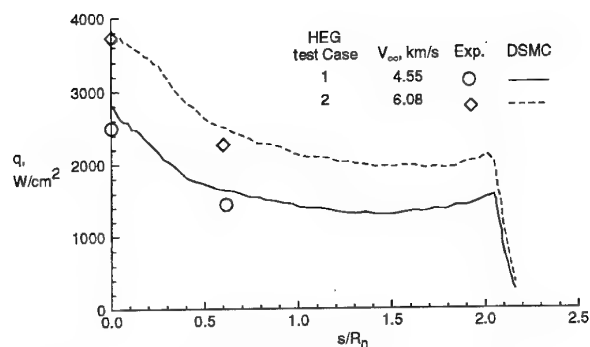
Figure 19. Measured and calculated heating rate distributions for HEG test in air (Case 1: M_∞ = 10.1 and Kn_∞ = 0.0034, Case 2: Mach 9.5 and Kn_∞ = 0.0088) (d_b = 0.5 cm).
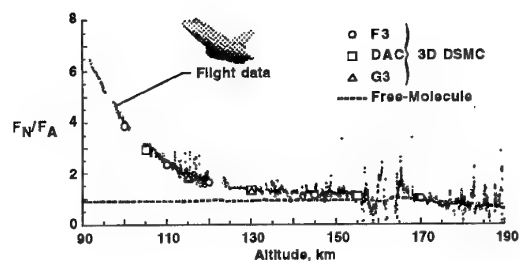
Figure 20. DSMC comparisons with Shuttle flight data.
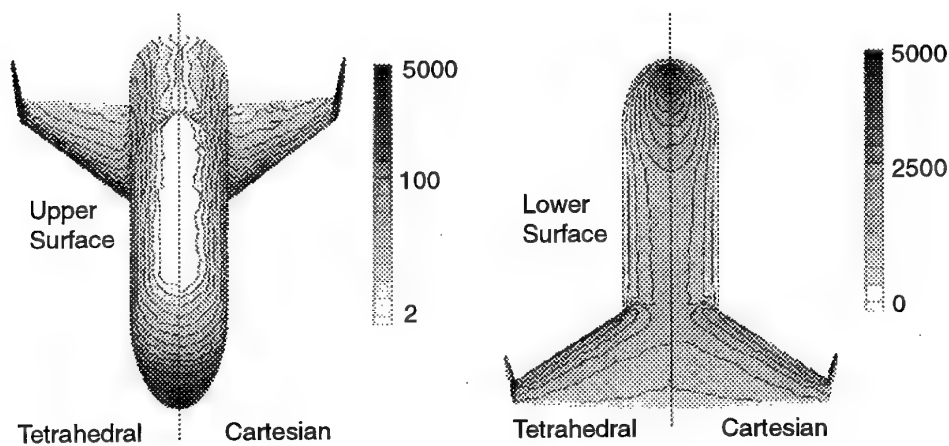
Figure 21. Heat transfer contours (W/m^2) on upper and lower surfaces of generic single-stage-to-orbit model (V_∞ = 7.8 km/s at 120 km altitude).
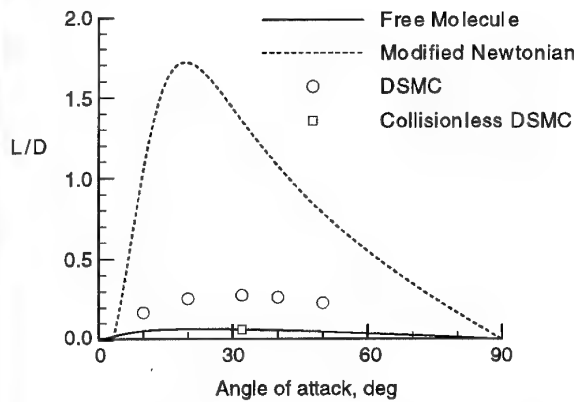
Figure 22. Lift-to-drag results for generic SSTO vehicle computed with tetrahedral code.
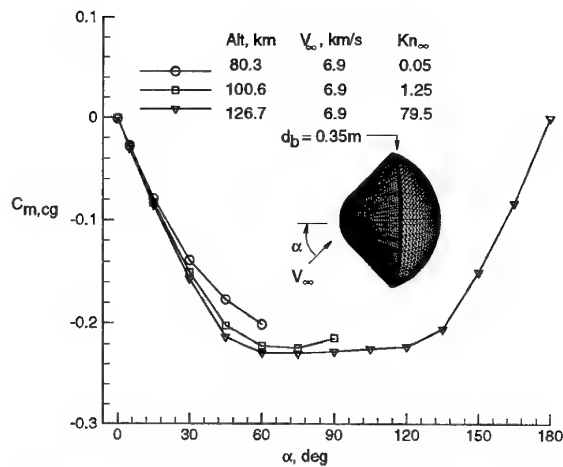
Figure 23. Computed pitching moment about C.G. for Mars Microprobe ($d_b = 0.35$ m).
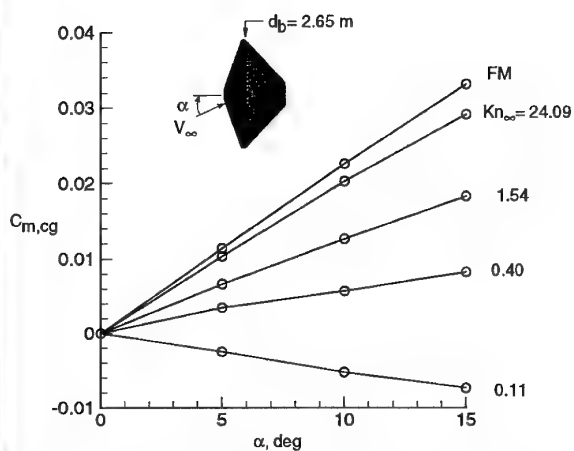
Figure 24. Computed pitching moment about C.G. for Mars Pathfinder ($d_b = 2.65$ m).

COMPUTATIONAL SIMULATION OF HYPERSONIC EXTERNAL FLOW
– Status of CFD in Europe –

W. Kordulla
Deutsche Forschungsanstalt für Luft- und Raumfahrt e.V.
Institut für Strömungsmechanik
Bunsenstraße 10, D-37073 Göttingen

Ph. Morice
Office National d'Etudes et de Recherches Aérospatiales
Direction de l'Aérodynamique
BP 72, F-92322 Châtillon Cedex

SUMMARY

This paper attempts to review the status of computational simulation of hypersonic flow achieved in Europe (except for the work performed in the countries of the former Soviet Union) within the past five to ten years. It is shown that national and concerted European efforts fostered the development of CFD in intimate combination with experimental work, in particular for validation purposes. It is believed that the state achieved, although not yet perfect, will be of tremendous help for the design process of an operational vehicle.

1   INTRODUCTION

More than twenty-five years ago, the design of space transportation systems was mainly based on extensive wind-tunnel work, extrapolations there from and a few free-flight experiments, but hardly on computational work. Today, the development of new space transportation vehicles is believed to be possible in less time and to result in better and more reliable performance if, in addition to experimental tools, computational tools are employed in a complementing fashion. This has become possible owing to the rapid mutual development of both, Computational Fluid Dynamics (CFD) and computer hardware since the early eighties. The development of computational hypersonics in Europe has experienced a dramatic impetus in the second half of the eighties after the beginning of the HERMES development programme initiated by CNES and then supported by ESA (European Space Agency) for the design of a reusable lifting reentry space vehicle. In fact, thanks to the innovative approach to accompany the programme by a Research and Development programme under the responsibility of Dassault Aviation, computational hypersonics was strongly promoted in universities and research institutions across Europe. National technology programmes such as those for vehicles with sustained hypersonic flight with air-breathing propulsion, SÄNGER in Germany and later PREPHA in France, were amplifying the efforts substantially. In Germany, in the late eighties, the Deutsche Forschungsgemeinschaft (DFG), a government agency to support research at universities, started to finance hypersonics research (Hyperschall-Sonderforschungsbereiche, SFBs) at initially four, later reduced to three universities. This research is still continuing until 1998, and perhaps, until

around 2001. This further fueled the enthusiasm for hypersonics in the community. Note, that most of the computational tools developed for hypersonics, could as well be used for the design of supersonic commercial transport vehicles. After having stopped the HERMES development programme by the end of 1993, ESA launched the Manned Space Transportation Programme MSTP until the end of 1995. This technology programme permitted further improvement of numerical and experimental tools, including wind tunnels, which had been created and/or were improved during the HERMES phase. The ultimate purpose was the validation and finalization of the tools needed to carry out the design of an operational vehicle. More recently, ESA launched new studies and technology programmes, e.g. FESTIP (Future European Space Transportation Initiative Programme, without the participation of France) and CTV (Phase B, under the responsibility of an industrial group given by Aérospatiale, MAN Technologie and ALENIA SPAZIO) (Crew Transport Vehicle for the international space station ALPHA). In these programmes, the European research teams, in concert with the industry, use the available tools and continue to increase their knowledge and abilities to further develop and employ, in particular, computational tools in hypersonics. Unfortunately, a European demonstrator for a transport vehicle has not yet flown to demonstrate the quality of design procedures and, especially, of computational tools.

CFD is the combination of numerical mathematics, fluid-mechanical know how, physical modeling and computer science, hence a truly interdisciplinary, intimate combination of research areas. CFD is a comparatively young, but nevertheless well-established discipline producing tools which are increasingly accepted as helpful to better understand phenomena occuring both in experiments and in nature, or to optimize the performance of flow-dominated technical devices. Ten years ago, when, again, the hypersonics wave hit Europe, the state of the art in CFD was largely for two-dimensional and/or inviscid flows and focussed on, in general, classical perfect-gas flows such as transonics or supersonics. Owing to the above mentioned programmes, the development towards the simulation of viscous flows in three dimensions including thermo-chemical reactions was highly accelerated. One reason is the fact that ground-based facilities cannot model completely free-flight conditions. Free-flight hypersonic experiments on the other hand, in

particular of reentry type, are very expensive to perform. Therefore, computational tools can be used to undertake e.g. sensitivity studies. When validated or certified by appropriate ground-based experiments, CFD simulation methods with suitable thermo-chemical models then serve as a tool extrapolating to free flight. While the focus of the activities was on continuum flows, the understanding and simulation of rarefied flows were considered as well. In addition to computational simulations, emphasis was put on strong links between computations and experiments for a mutually better understanding and prediction of complex hypersonic flows.

The present paper attempts to survey the progress achieved in Europe with respect to the development of computational tools for the simulation of hypersonic external flows. Note, that the contributions from Eastern

Figure 1:
Spatial amplification rates for blunt cones (adiabatic walls). M=8. Top: classical analysis according to different authors, nose radius R=381mm, S/R≈175. Bottom: entropy instabilities R=42.672mm, S/R≈66.25, wave angles in degree [83].

countries are not considered. Also, the choice of examples is somewhat arbitrary and by no means complete, but representative. First, some essential ingredients of computational methods are discussed, before selected numerical approaches and achievements are presented for continuum and rarefied flows with emphasis on continuum flows. Although reentry-type applications are dominant it is believed that the application to vehicles for sustained flight – shown elsewhere in the conference – is included. A summary of the assessments and a perspective end the paper.

For accurate and realistic flow simulations three ingredients are essential. The pacing item is the modeling of the physics of the considered flow: the prediction cannot be better than the physical model implemented into the solver. The basic ingredient is, of course, the algorithm of the numerical approach itself. Then, since there are usually certain parameters of the physical model or of the algorithm or owing to the quality of the used computational grid, which influence the results, an appropriate validation of the solver is required.

2   PHYSICAL MODELING

Here, we focus our attention on transition and turbulence, high-temperature effects, gas-surface interaction and, to a less extent, on ionization phenomena.

Reentry vehicles quite often experience highest heat loads while still being in laminar-flow regimes. Nevertheless, the knowledge of transition from laminar to turbulent boundary-layer flow is important to know, in particular with respect to the heat load on control surfaces. For air-breathing vehicles the transition from laminar to turbulent flow on the forebody in front of the inlet of the engines decides upon success or failure of the design of the vehicle. In short, knowledge on transition is not only essential for optimising aerodynamic efficiency in transonics, as is known, but also for optimising aerothermodynamic efficiency, especially if radiation adiabatic walls are considered [71 to 73]. Usually, semi-empirical criteria, based on the e^N approach, and assumptions for N are employed, in order to derive estimations for transition, see an overview in [6]. Figure 1 compares the instability analysis of various researchers with experimental data for a slightly blunted cone and shows the first available data for entropy-layer instabilities. However, worldwide work is underway to get rid of empiricism by moving from an analysis of local and linear disturbance equations to one for nonlocal and nonlinear spatially parabolic disturbance equations. The current state of the art is that this can be achieved for the assumption of symmetry-plane or locally infinite-swept-wing flows, see e.g. [84,86,123]. The extension to fully three-dimensional flows requires new concepts with respect to modeling the process of disturbance interactions with the base flow. Up to now, boundary-layer flows past complex configurations can only be investigated based on local analysis. In any case, it is important for the analysis to rely on highly accurate laminar base boundary layers [86]. If Navier-Stokes solvers are used this implies an extremely high computational effort. An alternative is to use a comparatively coarse Navier-Stokes
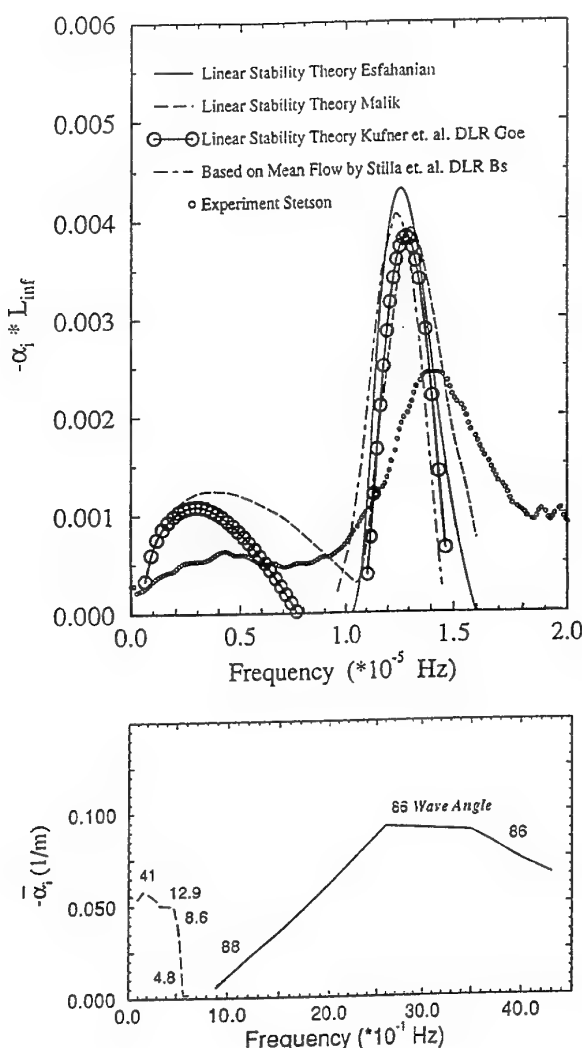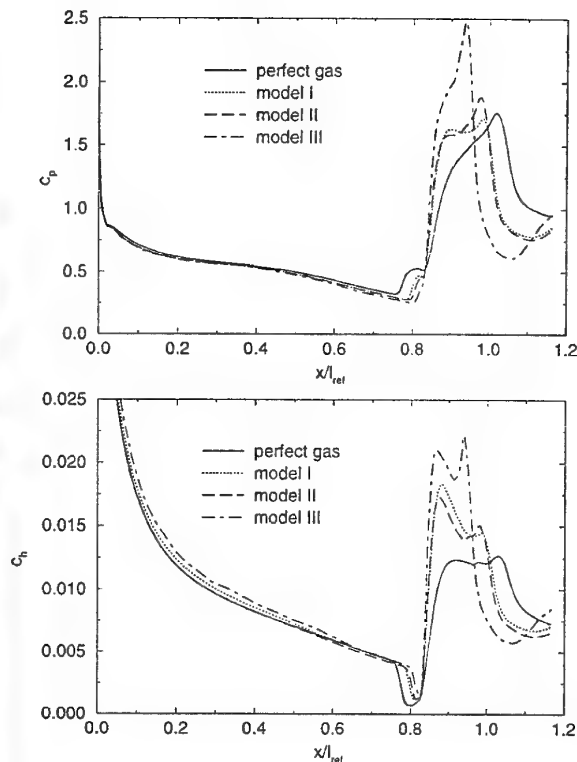
Figure 2:
Surface pressure (top) and heat-flux (bottom) distributions on a hyperboloid flare, M=25, Pr=0.73, Re=14680, H=75km for perfect gas. Additional gas models: I: chemical and thermal nonequilibrium; II: chemical nonequilibrium; III: equilibrium [83].

grid and to produce appropriate initial and boundary conditions for more efficient boundary-layer computations. Finally, a coupled Euler/boundary-layer solution could be employed [84,126]. Europe has achieved therean excellent standing with the cooperation between DLR and FFA/KTH as a major axis for advanced instability analysis in hypersonic boundary layers which contributed to FESTIP activities. Recently ESA launched also a Technical Research Programme (TRP) on hypersonic laminar-turbulent transition; a large amount of experimental and numerical results has been obtained in the framework of this European cooperation involving ONERA, DLR, CFD Norway and Manchester University under the responsibility of Aérospatiale.

The importance of knowledge of transition and, consequently, the modeling of turbulence as well, is evidenced e.g. in ref. 124 which considers the transitional flow past a corner with separating and reattaching boundary layer. A systematic variation of the „point" of transition has led to a good comparison of predicted and experimentally observed pressures and heat-transfer data. In spite of the fact maybe that turbulence may increase heat transfer dramatically, not very much work has been dedicated to the investigation and development of turbulence models in hypersonics. In practice, either eddy viscosity models or two-equation models are employed, sometimes in modified form [e.g. 37,56,88,100,126], seldom higher-order approximations are used [67].

Some work has been done to directly model turbulent boundary layers by means of Large-Eddy Simulations [25].

High-temperature effects are important for ascent-type vehicles with air-breathing propulsion only near stagnation points, in the immediate neighbourhood of the entrance of the engines and in the nozzle flow of the combustion products. However, all the way during reentry, vehicles experience high-temperature effects in the flow field between bow shock and surface [e.g. 112]. The consideration of such effects in flow predictions is not only important for the localization of hot spots on the surface but also to determine its influence on the efficiency of control surfaces. Note that Weilmuenster and Gnoffo have shown in a recent paper that the unexpectedly large flap angle, necessary to trim the Space
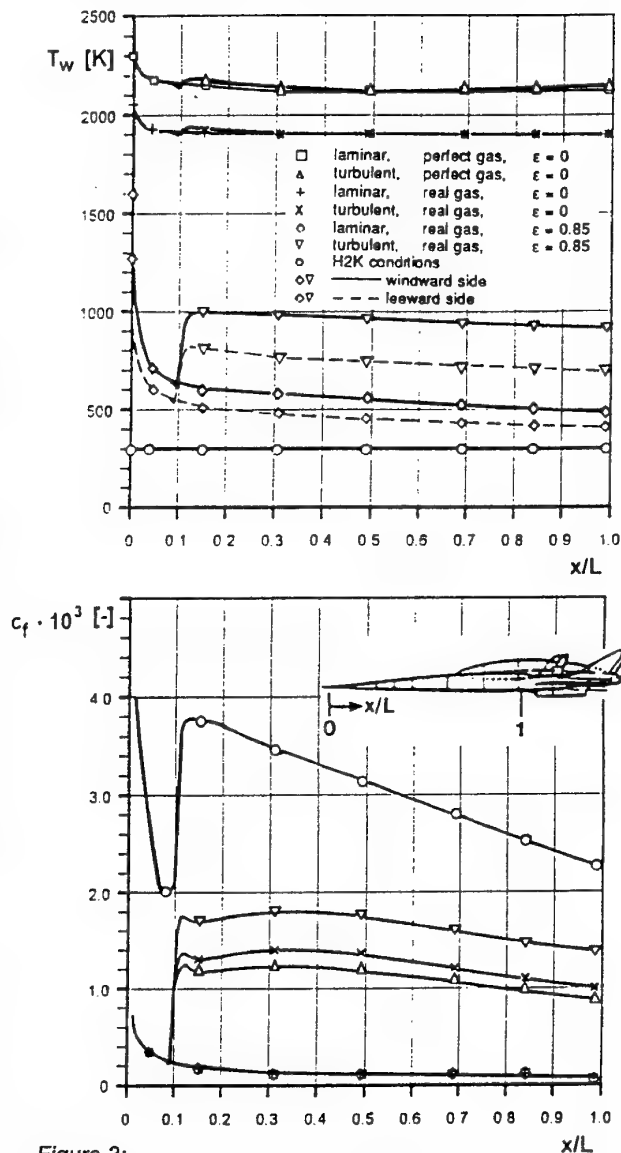

Figure 3:
Influence of the state of the boundary layer (transition, high-temperature effects, radiation cooling) on wall temperature (top) and skin friction (bottom) along the symmetry line of Sänger, M=6.8, Re=1.22·10^8, α=6° [72].

Shuttle during its first flight, was mainly due to the inaccurate consideration of high-temperature effects. Usually, the limiting assumptions of ideal-gas or equilibrium flow are made to estimate the influence of dissociating or recombining air. Figure 2 suggests that nonequilibrium effects must be taken into consideration for a more precise design of reentry vehicles. For a hyperboloid-flare configuration, approximating the windward symmetry plane surface of a reentry vehicle at large angle of attack, the chosen model of thermo-chemical nonequilibrium results in considerable differences in heat and pressure loads on the flap leading to different trade-offs between permissible loads and wanted efficiency. Note that there is still room to define the appropriate thermo-chemical model needed for reentry conditions in spite of considerable efforts, also in Europe [e.g. 32,39,55,78,81,112,114,140]. Furthermore, the constants involved in the modeling, generally, have been determined decades ago for temperature ranges which are actually inadequate for the current use and require extrapolations.
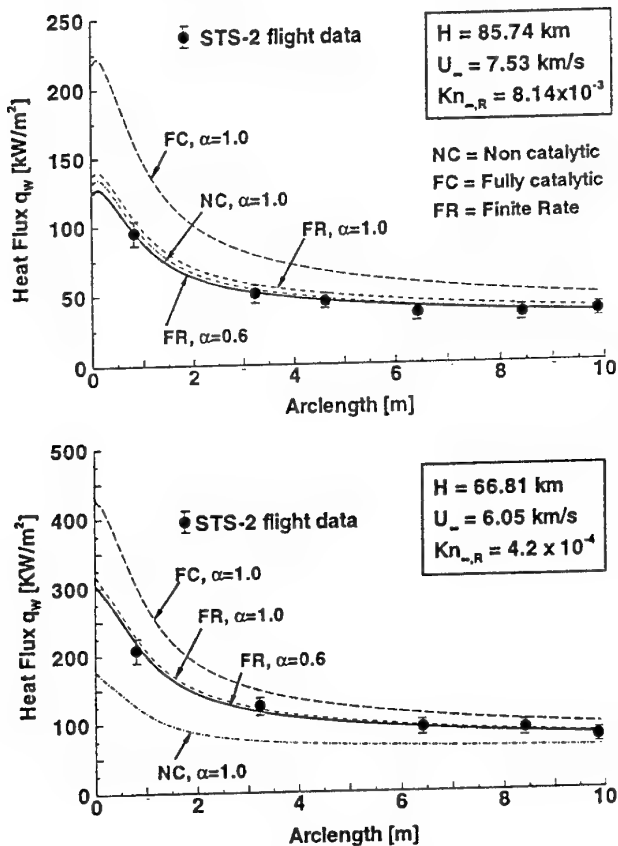

Figure 4:
Heat-flux distributions for a Shuttle-shape equivalent hyperboloid and STS-2 free-stream conditions at 2 different altitudes [32].

The interaction between flow and surface is, usually, considered only with respect to radiation, i.e. away from the surface according to Boltzmann's law assuming the air itself not to radiate [72,122]. Figure 3 gives an impression of the influence of radiation cooling ($\varepsilon \neq 0$) for sustained hypersonic flight. Note, that radiation-

adiabatic walls can only be considered by means of CFD. For carrying out corresponding experiments hot measurement techniques must be developed. For the simulation of nonequilibrium flows the effect of the surface on the chemical action in the nearby flow must be considered, as well. In general, it is assumed that the surface is non-catalytic or else fully catalytic. The real situation yields a surface with finite catalycity which cannot yet be modelled easily in continuum [7,58] or rarefied [11,32] regimes because of missing parameters. Figure 4 shows the influence of finite catalycity for the STS-2 flight for 2 points on the trajectory.

Ionization, i.e. the existence of air plasma, plays a role for the early phase of reentry with velocities larger than roughly 8 km/s. The duration of corresponding 'black outs' is particularly required to determine possible intervals of interruptions of communications between vehicle and observing ground station. In the European literature this topic is seldom treated, although it is also of interest to understand and describe the flow in arc-jet driven facilities [115]. In [39], the emphasis is laid on the study of different approximate models for the diffusion phenomena in weakly ionized mixtures and better results on the ionized species density numbers are obtained with Blottner's approximation correlated to the electrical field. The study conducted in [27], for a weakly ionized gas with two different translational temperatures, one for the heavy species and one for the electron gas, is linked to the treatment of non-conservative products appearing in the momentum equation of electrons.

3   CFD FOR CONTINUUM FLOWS

Since the assumption of continuum flow is usual practice for subsonic and transonic aerodynamics most of the numerical techniques developed for these regimes are candidates for hypersonic external flow simulation. However, the value and usefulness of the different simplified mathematical models are not preserved when transferred from classical aerodynamics to hypersonics. Inviscid flow modeling means using Euler equations since the potential flow approximation is no more valid behind strong curved bow shocks. Euler equations have to be completed by the inclusion of real-gas effects which are not leading to a large modification of the set of equations in the case of thermo-chemical equilibrium but which add many equations for nonequilibrium flows and, therefore, this can hardly be called a simplified modeling with respect of the complete set of viscous reactive flow equations. As indicated above, viscous effects can be accounted for by Euler/boundary-layer coupling but it then appears mandatory to use either the Van Dyke higher-order boundary-layer theory or the defect formulation to cope with entropy-layer effects [16,31,139].

Grid generation is part of the pre-processing for numerical simulations and is an important step to ensure the quality and efficiency for CFD methods. This remains true for hypersonics even though the complexity of vehicle shapes in applications is seldom as severe as for subsonic and transonic configurations with e.g. complicated high-lift devices. Therefore, the currently

developed grid-generation tools for classical aerodynamics are directly applicable. The speciality of hypersonic flows is due to the presence of the strong bow shock limiting the required computational domain to the immediate vicinity of the hypersonic vehicle for high Mach number. Shock-fitting has been used in the past mainly for tracking the bow shock for 2D or axisymmetric flows but its use on 3D configurations seems not to be very suitable for complex geometries. Moreover, the presence of internal shocks is asking for shock-capturing methods which, of course, can handle bow shocks as well. However, due to the strength of the flow gradients, special attention has to be paid to grid refinements in order to capture details of shock/shock or shock/boundary-layer interaction phenomena. We will come back to this subject below.
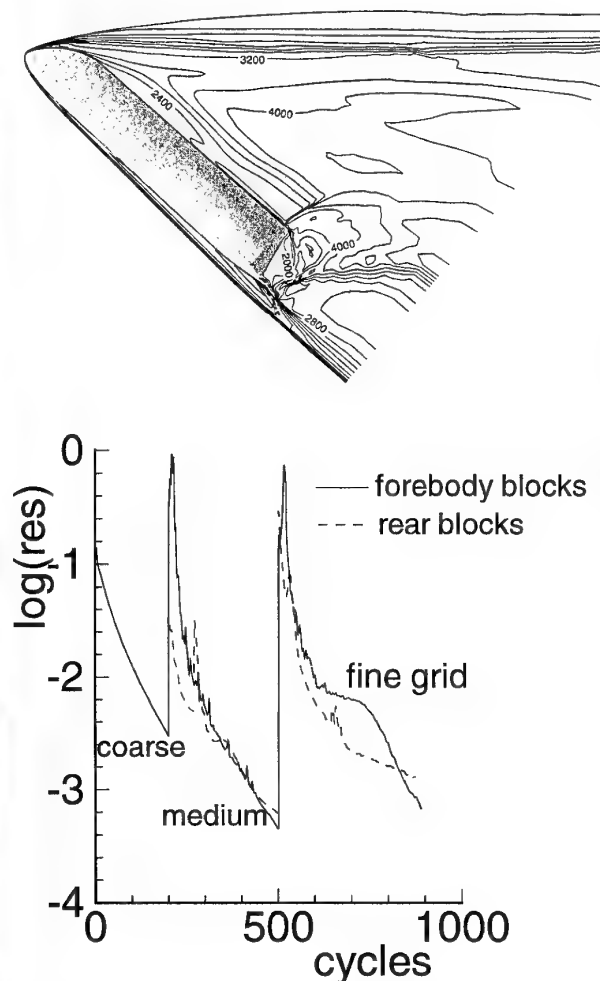
Figure 5:
Typical convergence behaviour of DLR's basically explicit time-stepping code CEVCATS for HALIS free-flight flow simulation (M=24, H=72km, α=40°, chemical nonequilibrium) [19].

To be capable of handling the strong discontinuities and reactions present in hypersonic flows, the discretization methods developed for classical aerodynamics have to be adapted. This addresses the aspects of code robustness and, at the same time, accuracy which must be maintained. For shock-capturing methods used for the majority of computations carried out in Europe, upwinding is the rule for evaluating the fluxes either in finite-volume or in finite-element methods since centered approaches are not robust enough near discontinuities. Cell-centered upwind finite-volume methods based on one-dimensional Riemann problems in the direction normal to cell faces are used in the majority of present CFD codes for hypersonic applications. Because first-order accurate upwind approximations are too diffusive higher-order schemes are needed. However, there is a large variety of flux formulae from the classical Flux-Difference Splitting or FDS (Roe, Osher) and Flux-Vector Splitting or FVS (Steger-Warming, van Leer) to more recently studied ones either for improving robustness and accuracy or in view of their extension to reactive flows. To the first category belongs the family of Hybrid Upwind Splitting methods (HUS) devised by Coquel and Liou [28] to combine the accuracy of FDS and the robustness of FVS methods. The interest of these schemes is clear when aplied to standard problems such as the hypersonic flow past an hyperboloid flare where robustness is needed at the nose because of the strong bow shock, and accuracy is mandatory in the region with recirculating flows. Various FVS schemes can be used in an hybrid pair with the Osher FDS scheme. If the use of van Leer's scheme for this hybridizing has been first proposed by the authors of HUS schemes, kinetic FVS schemes are often chosen for their efficiency like in [94] where the equilibrium flux method from Pullin has been extended to a hybrid scheme. The compromise between accuracy and robustness is also studied in [104] where HCUSP, AUSM und AUSM+ schemes are tested and compared. Also worth to mention are the mixed finite-volume/finite-element method [110] and the multi-dimensional upwind-matrix distribution scheme on a compact stencil combined with Galerkin finite-element approximation for the viscous terms [131]. The extension to thermochemical nonequilibrium flows was the subject of recent studies for Roe's Riemann solver [45], kinetic schemes [134], and HUS schemes [26].
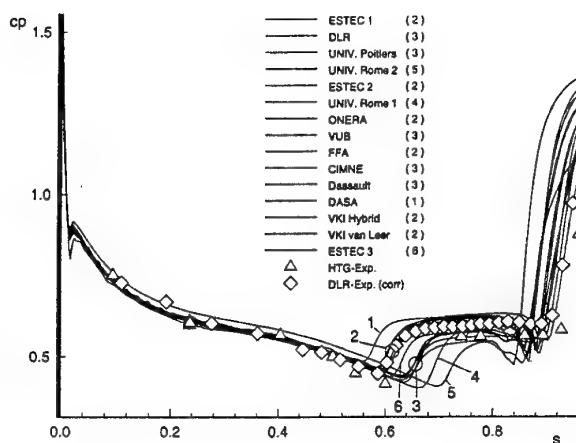

Figure 6:
Surface pressure on the hyperboloid-flare configuration for the flow in RWG with M = 6.83, Re/m = 7 10^6/m given by workshop participants [117].

Both structured and unstructured grid methods are represented in Europe for CFD in hypersonics. As said above, the relative simplicity of hypersonic vehicle shapes provides a natural choice for flow domain discretization with structured grids, see e.g. [65]. The main three-dimensional codes used for hypersonic flow calculations are of this type and rely on upwind finite volume discretization [19,36,38,46,57,63,64,89,99, 104,121,138]. For methods based on unstructured grids, e.g. [20,62,92,110,131], there are still large variations in the chosen numerical techniques and very few three-dimensional results. If most of them are based on the Galerkin finite-element approximation for the treatment of second-order derivative terms, several variants of finite-volume methods are used to ensure accuracy and robustness in the treatment of convective terms [92,110,131]. The case of the finite-element Galerkin least-square approach with entropy variables as developed by the team of Dassault Aviation [20,92,97] can be set apart both for its non-conventional formulation and for its application to three-dimensional complex geometry such as for the flow past the HERMES canopy. In this case, local grid refinement has been made for a better description of heat fluxes and separated regions [97]. Automatic grid adaptation to flow features is highly advocated for shock capturing, sometimes with structured grids by means of node displacement and

more frequently with unstructured methods by adding and removing nodes [20,24,62,110,134], but the demonstration is generally made only in two dimensions.

As concerns the efficiency of numerical algorithms, convergence acceleration techniques are necessary for hypersonic CFD. Two reasons are present which limit the practical time step used for time marching towards a steady-state solution of the system of equations. The first one is the classical CFL limitation on the time step due to the grid refinement in viscous layers and eventually in strong shocks. The second one is the stiffness brought about by the presence of thermo-chemical source terms with time scales much smaller than those of the flow field. The first reason is shared with classical aerodynamics while the second one is more familiar from the numerical simulation of combustion. The natural remedy is found in implicit algorithms. Therefore, a fully implicit approach is often used in stiff cases with solution of the linearized systems through a preconditioned GMRES method, e.g. [26,62], or Gauss-Seidel symmetric line relaxation, e.g. [141]. Semi-implicit algorithms, with some implicit procedure applied only to the reactive terms [4,19,110], are sufficient for coarse or moderately fine grids. For fine grids, a good efficiency can be achieved by combining the implicit treatment of thermo-chemical source terms and the multigrid approach. Many efforts were devoted, in particular at DLR, to improve the multigrid method in order to adapt it to hypersonic flow features [19,103,104,105,142], including the concept of semi-coarsening [103]. Figure 5 shows a typical convergence behaviour of the DLR code CEVCATS for 3D nonequilibrium flow simulations.

Other studies to get an efficient solution of CFD problems concern the parallelization of algorithms. The classical methods based on the multiblock or domain-decomposition approach remain suitable for hypersonic CFD with only some care to be exercised for the choice of the interface orientation. Demonstrations of a relatively efficient parallelization have been made for PNS [63], classical multiblock [19,89] or unstructured [106,107, 131] codes. The implicit treatment of thermo-chemical source terms leading essentially to point-implicit operators is not an obstacle for the use of parallel machines. However, in spite of the efforts done for such parallel code adaptation and the gradual availability of massively parallel computers with distributed memory (INTEL Paragon, IBM SP2, CRAY T3D and T3E), the use of machines with a moderate number of powerful processors, such as NEC-SX4 or CRAY J90, is generally preferred for practical applications. This is currently the case e.g. at DLR in Göttingen where a nonequilibrium flow steady-state solution past a complex configuration is achieved in about 15 hours on one processor of a NEC-SX4 or roughly 5 hours on four processors for a grid of more than two million points [19,104].

In the course of the ESA programmes the concept of using 2D or axisymmetric so-called standard models evolved. This concept employed nominally simple shapes in order to approximate components and, therefore, typical flow features of space vehicles. The flows past these shapes served as validation test cases for CFD (see e.g. [2,3,40,41,116]) and to qualify the flows in the
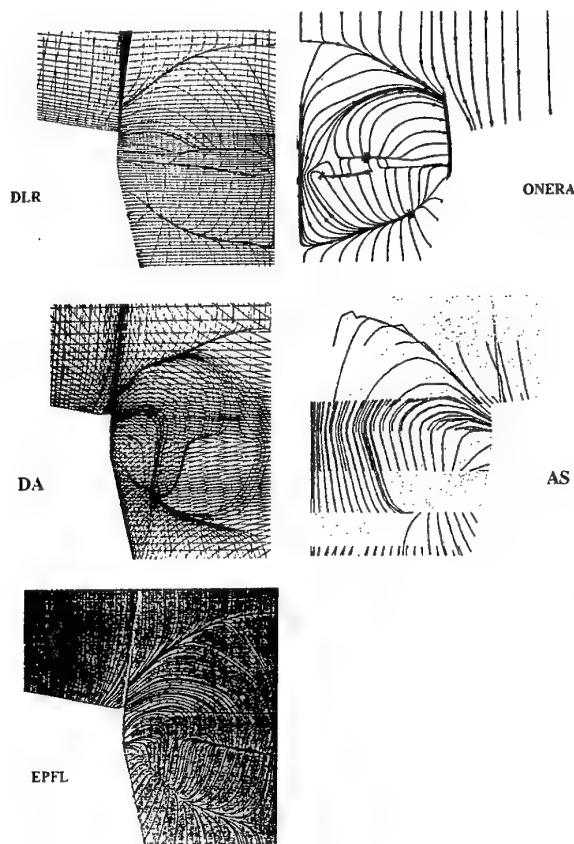

Figure 7:
Comparison of skin-friction lines on the lower surface of HALIS near the body flap for S4 conditions, body flap angle 15°, as a result of an ESTEC workshop [135].

test sections of different wind tunnels. The wedge-cylinder combination is e.g. representative for shock-shock interactions at inlets of air-breathing hypersonic vehicles or near wing leading edges for reentry flows, see e.g. [18,116]. The blunt-body shapes of Electre (with free-flight data from earlier French research programmes) and hyperboloid-flare configuration reproduce blunt-body flow features and flow-separation features. They were investigated in cold as well as in hot hypersonic facilities (see e.g. [116]). Figure 6 presents the comparison of various predicted pressure results for the hyperboloid flare in RWG for the ESTEC workshop in March 1996 [117], showing still some scatter of results, in particular in the area of separation of the assumed laminar flow.
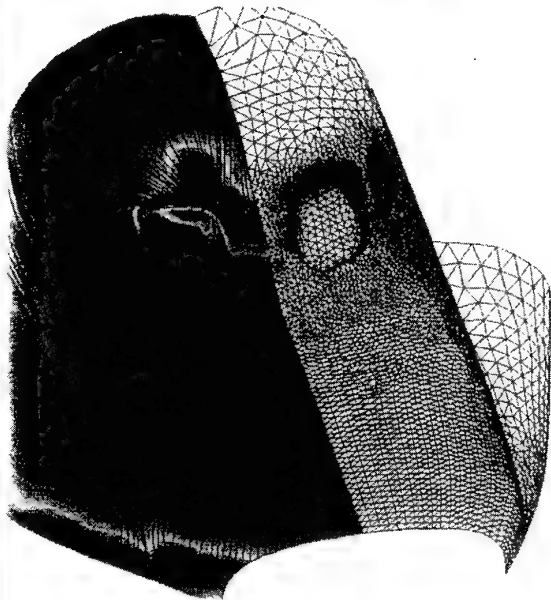
Europe, in addition to the work for the ARIANE [99] development, considerable efforts have been spent on reusable transportation systems with air-breathing propulsion – associated with the names and abbreviations SÄNGER, PREPHA and ELAC, see e.g. [53,64,73,113, 122]. This concerned not only fundamental CFD work with respect to e.g. transition, vortical phenomena, cooling due to radiation and intake phenomena associated with air-breathing engines but also the integration of propulsion in complete designs (see e.g. [71] to [73]). Another result is the consideration of alternative designs based on modern wave-rider concepts in mission analysis considerations, see e.g. [46 to 48,128].

Most of the European CFD work, however, seems to have been directed towards the mastering of reentry-type problems. This is due to the corresponding European programmes and gets significance more recently with a NASA-ESA cooperation begun with respect to reusable winged transportation sytems to and from the planned international space station (CTV-CRV).

A few examples of applications of CFD are shown next. First, from the 1996 ESTEC workshop [116] results of the prediction of the flow past HALIS are shown. HALIS duplicates exactly the lower surface of the US Orbiter. Figure 7 compares for this test case skin-friction line predictions for the laminar flow at S4MA conditions (M=9.8, α=40°, Re_L=1.67·10^6, flap angle 15°). The corresponding global quantities C_L, C_D and C_M don't differ by more than 1.6, 3.4 and 8.5 percent which is, in part, caused by large differences in grid size [135]. Figure 8 displays the surface grid of the unstructured mesh and predictied results near the canopy for a HERMES computation done to investigate the peaks of the heat load near the windows [97]. Figure 9 shows the skin-friction line pattern and the heat-transfer distribution on the lower surface of a X-CRV shape at reentry conditions with deflected body flap (25°). This DLR result was part of ESA's '90-days' study in 1996 for this configuration. The study and additional unfunded work showed that the European CFD tools are perfectly suitable to rebuild
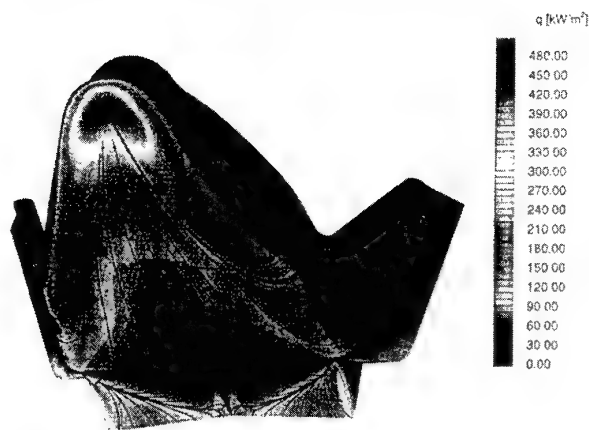

Figure 8:
Unstructured surface grid, heat-flux distributions and skin-friction lines (bottom) for the canopy region of HERMES (top) [97].

More challenging in terms of computer resources, grid-generation capabilities and physical modeling is the simulation of the flow past complex configurations. In

Figure 9:
Skin-friction lines and heat-flux distributions on the lower surface of an X-CRV shape (M=25, α=40°, H=75km, nonequilibrium), obtained with CEVCATS.

experimental results also in the transonic flow regime. Note, that the CFD capabilities have also been demonstrated in ESA's ARD capsule programme. Strong CFD capabilities have as well been developed in technology programmes like SÄNGER and PREPHA with respect to the prediction of e.g. inlet and nozzle flows [e.g. 9].

It is clear that the projects HERMES, SÄNGER, FESTIP, CTV, ... require the formation of integrated teams in order to arrive at verified system designs. The corresponding necessary combination of the various disciplines is practically achieved in a way which is seldom laid open to the public because of the proprietary character of the knowledge involved. However, strategies are published, see e.g. [73,102]. CFD people have a vision that the optimization process of the considered vehicle design occurs entirely on the computer, of course profiting from an experimental data base. In aircraft industry, see e.g. the development of the Boeing 777 plane, this process has started.

4   CFD FOR LOW-DENSITY FLOWS

Rarefied flows, in the transitional regime at altitudes above roughly 80 km, where the mean free path is of the order of characteristic lengths of the flying geometry, cannot be described with solutions of the Navier-Stokes equations but require solutions of Boltzmann's equation or of approximations thereto. In Europe, essentially two approaches prevail. One is based on Bird's Direct Simulation Monte Carlo (DSMC) approach given e.g. by Aérospatiale's method or DLR's code DIMOS or variations thereof [10,29,30,33,42,54]. The other method is the finite pointset method (FPM) developed at the University of Kaiserslautern [80,98,125,129,130].

The use of DSMC, which treats the interaction of particles and their displacement in a decoupled manner, requires large computational resources in three dimensions. The denser the gas the higher the total number of particles needed to represent the flow correctly in a statistical way, and hence the more computer time is needed for a given computer. Based on knowledgeable assumptions Aérospatiale has been able to carry out some 3D simulations of the flow past HERMES, thus producing some meaningful results, even including the effect of plume-external flow interaction. Most of the computations, in particular near continuum, were, however, carried out in two dimensions or based on axisymmetry in spite of the fact that enhancements of the computational speed were achieved [42] by reducing the effort to determine the paths of the particles. This also allowed to estimate the correctness of the use of Navier-Stokes equations with no-slip conditions by comparing e.g. heat-transfer or skin-friction distributions, using otherwise the same high-temperature modeling. For the heat transfer on the surface of a hyperboloid flare it can be shown for a Knudsen number of about 10^{-3} that the DSMC result converges towards that of the Navier-Stokes solver for a sufficiently refined grid only [83]. Besides the familiar use of velocity slip and temperature jump boundary conditions with Navier-Stokes equations to simulate intermediate Knudsen number flows it is worth to mention a proposal for the replacement of Navier-Stokes equations by the quasidynamic equations [49] which differ from the Navier-Stokes system by the structure of the dissipative terms in the right-hand side of the momentum and energy equations and by the presence of a divergence term in the right-hand side of the continuity equations. Results closer to DSMC reference results are obtained for moderate values of Knudsen number.

While some efforts have been undertaken to introduce massive parallelism into the DSMC codes, this is not yet widely used in Europe.

The FPM derives its name from the finite pointset given by the collection of all chosen particles. The idea is then to construct suitable so-called low-discrepancy sequences of finite pointsets which in the limit approximate the solution of the time-space discretized Boltzmann equations. This approach has been refined and rendered highly efficient by the group of Neunzert. More recently, the code in question ParBoSS has also been parallelized to enable the use of massively parallel super computers. In [5] a nearly linear speed-up is reported for axisymmetric computations on computers such as CRAY T3D or IBM SP-2.

The European codes can handle high-temperature effects where the thermal and chemical effects are described by molecular models which are developed, as proposed by Choquet, to satisfy detailed balance and entropy theorem and to reproduce at the macroscopic scale experimental relaxation times [21,22,23], see also e.g. [10,32,42]. As well they can handle gas-surface interaction where e.g. – following ideas of Warnatz – the wall-catalytic effects are described by rate equations for the change of particles due to elementary surface reactions [11]. Hence, perhaps with the exception of modeling ionization, the available codes are well prepared to simulate the behaviour of reentry vehicles in the transitional regime. For preliminary estimates it is also possible to use quick local-bridging methods for forces and heat transfer [13]. The ultimate goal is, of course, an appropriate coupling of rarefied- and continuum-flow simulation in one approach.

5   VALIDATION PROBLEM

It was mentioned earlier that even those computational flow solvers which are mathematically correct and accurate require a process which is called code validation because of the need to employ an appropriate grid and the right physical models, in order to properly simulate realistic flows. CFD code validation has become a buzz word which has been and is being associated with various philosophies linking code validation to notions such as calibration, verification, certification or confidence. Here, code validation is meant as a concept allowing for sufficient confidence in CFD to use it in design procedures. Such a concept includes ground-based experiments as well as flight experiments and should yield a quantification of the capabilities of the code with respect to the simulation of a particular type of flow. Because hypersonic data, in particular reentry free-flight data, are hard to obtain, it is common to as-

sume that codes do predict free-flight flow fields and aerothermodynamics using appropriate physical models once the code has been validated by means of dedicated ground-based experiments. For reentry-type flows this is thought to be the right way to extrapolate to flight [73,102].

There are many sources for uncertainties of CFD results, ranging from purely numerical ones to those owing to the chosen physical models. The purely numerical uncertainties can be taken care of to a large extent. One approach would use code-to-code comparisons, preferably in the frame work of a workshop with dedicated test cases. Quite a few workshops of this kind have been sponsored or even organised by ESA and/or ESTEC since the beginning of this decade, initially as part of the HERMES development programme and then in the MSTP [2,3,40,116,119]. Another means to determine the degree of uncertainty is to carry out grid-dependence studies. While this still seems to be rather difficult in three dimensions, being rigorously feasible only locally in blocks (see e.g. [91]), in two dimensions it has to be done, in principle. Figure 10 from [61] nicely indicates the importance of such refinement studies: in an attempt to rebuild the flow field in a contoured hypersonic nozzle of a Ludwieg tube, the grid for the axisymmetric flow simulation was continuously refined yielding finally a good agreement of predicted and experimentally observed pressure profiles in the non-reacting flow field. Such a mutual verification is, of course, also necessary for a reacting flow field. A third possibility to
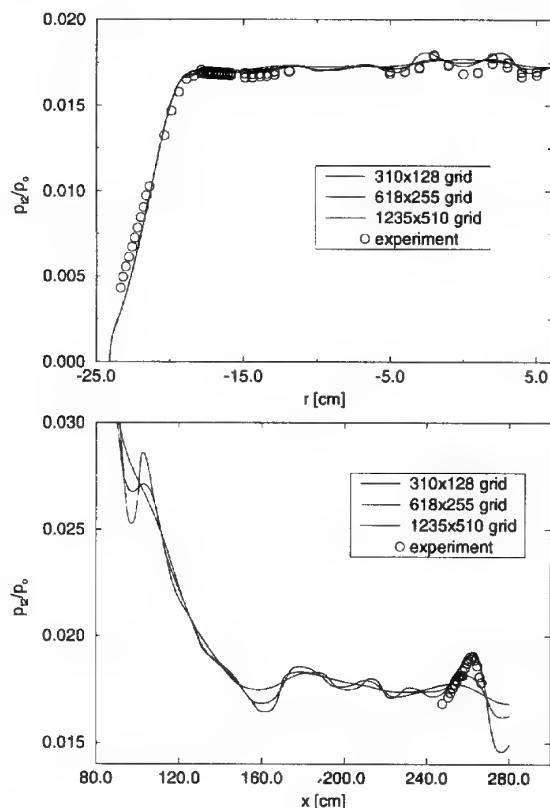
reduce the purely numerically caused uncertainty is to carry out sensitivity studies with respect to the amount of numerical diffusion by changing the corresponding parameters if possible, see above. This is a rather delicate matter because sometimes one has to look for a good compromise between sufficiently large robustness and sufficiently accurate results.

When the above parameters are under control the credibility of the predictions with respect to the choice of the appropriate physical models must be determined. This is achieved by comparison with a dedicated experiment, usually in ground-based facilities. This topic is the objective of the above-mentioned workshops or other events, such as the AGARD WG 18. For classical cold hypersonic flows this concerns only the modeling of transition and turbulence. For laminar 3D flow, figure 11 shows that experimentally observed data can be rebuilt even in regions with separated flow. This is non-trivial for transitional or turbulent flow situations. For the more reentry-related hot hypersonic flows, e.g. in the arc-heated facility F4 in Le Fauga or in the piston-driven high-enthalpy tunnel HEG in Göttingen, it is possible to
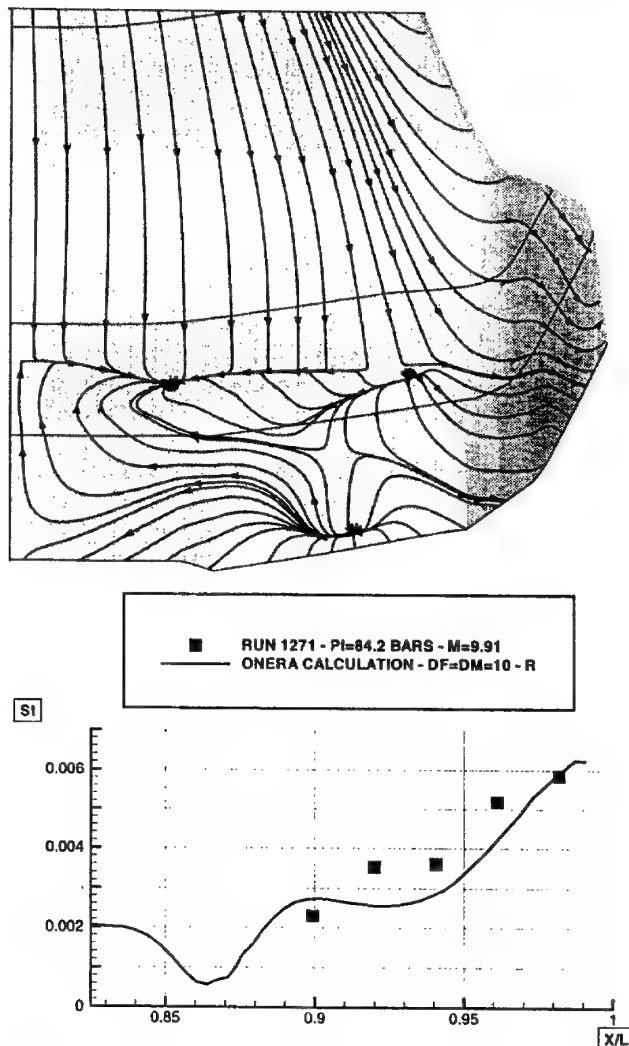

Figure 10:
Computational rebuilding of the measured Pitot-pressure profiles in the test section of the contoured Ludwieg-tube (RWG) nozzle at M=6.8, Re/m=9·10⁶/m: radial (top) and axial (bottom) distributions [61].

Figure 11:
Flow structure (top) at Re=2.1·10⁶ and heat flux (bottom, Y/L=0.12) for HERMES with deflected flap and elevon (δ=10°) at S4MA wind-tunnel conditions (M=10, α=30°) [99].

investigate in addition the appropriate thermo-chemical models. Here, ESA's Hypersonic Ground Testing Pro-gramme showed that code validation is not a one-way street but allows both experimentalist and computational engineer to profit mutually from each other. Computa-tional experimentation showed e.g. that the experimen-tally observed pressure on the wall and at the exit of a nozzle in F4 (figure 12) can be predicted if it is assumed that the flow is in equilibrium and the boundary layer goes turbulent in a linear fashion between nozzle throat and exit [133]. The check of the ability of the considered code to cope with phenomena, such as shock/shock or shock/boundary-layer interactions and high-temperature effects like reduced shock stand-off distances, requires flow field measurements with sufficient accuracy and, in any case, the definition of error bars. Here, the measu-rement of concentrations and temperatures in addition to velocities is of large importance. It is often not ob-vious beforehand if an accuracy of, say, 10 percent, which is considered excellent for the experiments of a high-enthalpy tunnel, is sufficient for the decision about the choice of the correct physical model. Therefore, sensitivity studies with the various models must be carried out before a dedicated experiment is performed with a given measurement device. Figure 13 points at the importance of knowing the appropriate state of the flow.

The real thing is the validation based on free-flight ex-perimental data. However, Europe has not yet produced reentry data, and the code developer has to take re-course to published Space Shuttle or HYFLEX II data. The more CFD develops the more demanding it be-comes with respect to the request for flow-field data, not only for „simple" surface data. While the development of measurement techniques for use in wind tunnels goes in this direction with new optical devices, this is not obvious for free-flight experiments.

It is well-known that hypersonic ground-based facilities can offer only partial simulation and therefore partial validation. This is also true for high-enthalpy facilities. If one takes the HEG, this facility is able to simulate the same fluid, the right air speed and the similarity parame-ter for binary dissociation, but e.g. not at the same time the similarity parameter for recombination. The free-stream condition in the test section will never be compa-rable to that one in free flight because the air is highly dissociated and frozen due to the expansion in the nozzle. Nevertheless, assuming that CFD is able to predict and simulate the flow in ground-based facilities, it is further assumed that the considered code can as well simulate free-flight behaviour. The extrapolation to flight therefore occurs more and more via computational simulations.

For code validation and design purposes data bases are of large value. This is why ESA/ESTEC, during the Hypersonic Ground Testing programme, financed the creation of a data base at EPFL in Lausanne. This data base collected experimental as well as computational data produced in the frame of ESA's programmes and, in particular, for some of the above-mentioned works-hops [136]. Note also the existence of a data base at INRIA, Sophia Antipolis [41].The existence of AGARD

working groups is of large help because the effort can be split among the participants in some sense, and the number of code-to-code or code-to-ground-based-experiment comparisons can be increased resulting in more reliable bench-marking data for all parties invol-ved.
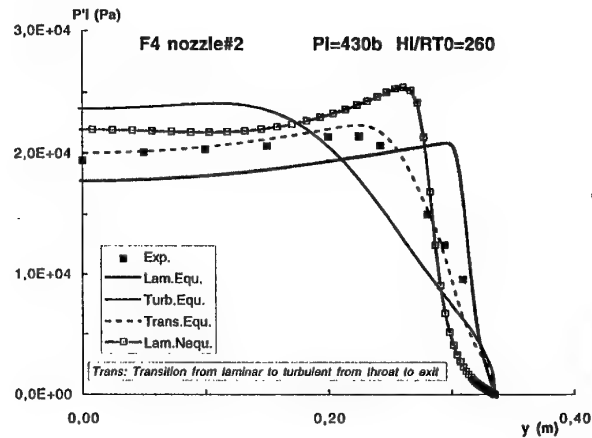

Figure 12:
Computational rebuilding of the measured pitot-pressure profile in the test section of the F4 nozzle [133].
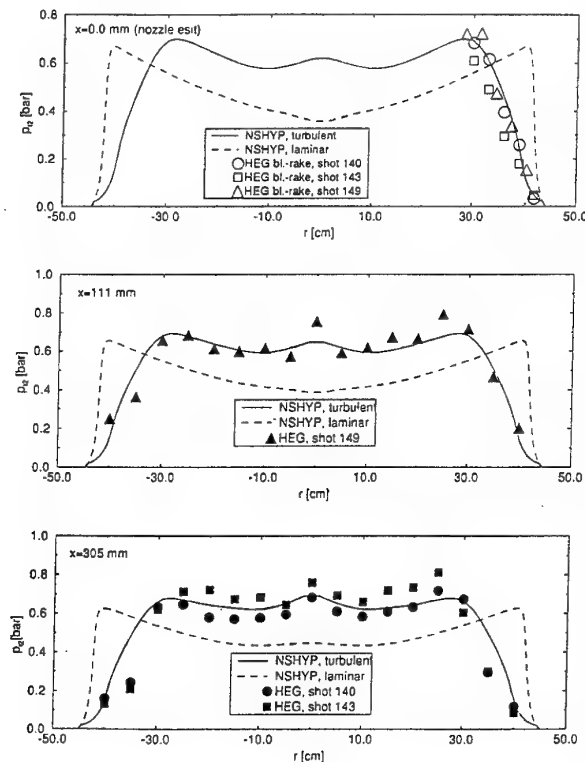

Figure 13:
Comparison of experimentally observed and predicted Pitot-pressure profiles in the HEG test section (p_0=908 bar, h_0=13.19 MJ/kg) [60].

6   CONCLUDING REMARKS AND PERSPECTIVE

The paper shows that – owing to ESA-supported and national programmes (note, however, that e.g. the German SÄNGER technology programme enjoyed also the participation of some European industries and research institutes) – CFD in hypersonics experienced tremendous improvement within the last five to ten years. The result is a quite competitive standing with full three-dimensional capabilities in all hypersonic flow regimes. The tools are waiting to be used for the design of operational vehicles, in fact to be used to extrapolate results from wind-tunnel to flight conditions.

This could only be achieved by working not only on numerical algorithms (including grid generation) but also on the modeling of physics as necessary input. Important was and is, as well, the intimate link between CFD and dedicated experimental work to arrive at a mutual validation. The concept, initially established by Dassault Aviation, to have workshops from time to time helped to estimate the advancements made. At the moment, European hypersonic CFD is lacking own dedicated free-flight results to really judge the usefulness of the developed tools. Therefore the European CFD community is very much in favour of, at least, a demonstrator project.

There are, nevertheless, still gaps to fill and improvements to be made. Starting with purely numerical features, one needs increased speed of 3D computations in order to make the more routine use of e.g. Navier-Stokes solutions attractive for industry. This requires both improvements in algorithms and better use of continuously improving computer architectures. Even more important, the gaps in knowledge of physical modeling have to be covered to increase the independence of the results from the knowledge of the engineer using a particular tool. This refers to the modeling of transition and turbulence and of reactions in air (combustion has not been considered here) but also to the improvement of wind-tunnel technology and measurement techniques, such as hot experimental techniques and non-intrusive measurements of reacting flows.

A topic not covered here which is absolutely necessary for the use of CFD in three dimensions is the availability of appropriate efficient tools for pre- and post-processing of the geometries and data.

In spite of missing elements in the system 'CFD', it is obvious that CFD in hypersonics has matured sufficiently to be successfully combined with other disciplines in order to arrive at better multi-disciplinary optimization results.

7   ACKNOWLEDGEMENT

The authors appreciate the help of those who have responded to their request for information which is, to a large extent, included in the list of references exceeding those being cited in the text.

8   REFERENCES

The references given represent some arbitrarily chosen overview over activities in Europe. They are far from being complete and are mostly those provided by the parties addressed.

1. AGARD Conference Proceedings 514, „Theoretical and Experimental Methods in Hypersonic Flows", Torino, Italy, May 4-8, 1992.

2. Abgrall, R., Désidéri, J.A., Mallet, M., Périaux, J., Perrier, P., Stoufflet, B., „Synthesis of the Workshop on hypersonic flows for reentry problems"; held in Antibes, France, in January 1990 and April 1991. AGARD-CP-514, Paper No. 18, 1992.

3. Abgrall, R., Désidéri, Glowinski, R., Mallet, M., Périaux, J., „Hypersonic flows for reentry problems". Vol. III, Springer-Verlag, 1992.

4. Alavilli, P., Hirsch, Ch., „Computation of the thermochemical nonequilibrium flow about the hyperboloid flare in the F4 tunnel". MSTP Workshop 1996 – Reentry Aerothermodynamics and Ground-to-Flight Extrapolation, Noordwijk, The Netherlands, 1996.

5. Antonov, S., Pfreundt, F.-J., Struckmeier, J., „Adaptive Load Balance Techniques in Parallel Rarefied Gas Simulations". Universität Kaiserslautern, Berichte der Arbeitsgruppe Technomathematik, Bericht 167, Juli 1996.

6. Arnal, D., „Boundary layer transition: predictions based on linear theory". AGARD Report 793, April 1994.

7. Barbato, M., Muylaert, J., Reggiani, S., Bruno, C., „Numerical simulation of wall catalyticity similarity problem for hypersonic flows". 3rd ECCOMAS CFD Conference, Paris, pp. 243-247, 1996.

8. Battrich, B. (Ed.), „Aerothermodynamics for Space Vehicles", ESA SP-318, 1991.

9. Behrens, T., Bissinger, N., „Study on Forebody Precompression Effects and Inlet Entry Conditions for Hypersonic Vehicles". AIAA Paper 96-4531, 1996.

10. Bergemann, F., Boyd, I.D., „New Discrete Vibrational Energy Model for the Direct Simulation Monte Carlo Method". In Shizgal, B.D., Weaver, D.P. (Eds.) Rarefied Gas Dynamics, Progress of Astronautics and Aeronautics, AIAA Vol. 158, pp. 125, 1994.

11. Bergemann, F., Brenner, G., „Investigation of Wall Effects in Near-Continuum Hypersonic Flow Using the Direct Simulation Monte Carlo Method". AIAA Paper 94-2020, 1994.

12. Bertin, J.J. Périaux, J., Ballmann, J. (Eds.), „Advances in Hypersonics". Vol. I to III, Birkhäuser, 1992.

13. Boettcher, R.-D. „HERMES 1.0 Bridging Calculations Using Euler Continuum Data". DLR-IB 222-93 A 26, also ESA H-NT-O-2064-DLR, 1993.

14. Bogstad, M.C., Leyland, P., „Flow over the Hyperboloid Flare - RWG (Cold) Conditions".MSTP-Workshop, ESTEC, Noordwijk, The Netherlands, March 1996.

15. Bousquet, J.M., Demargne, A., Faubert, A., Oswald, J. „Hyperboloid flare (cold) test case computation with the FLU3M code". Fourth European High Velocity Database Workshop, Noordwijk, The Netherlands, November 1994.

16. Brazier, J.Ph., Seror, S., „Extension of the defect boundary layer theory to nonequilibrium flows". EURO-MECH 342, Göttingen, September 1995.

17. Broglia, R., Manna, M., Degrez, G., Deconinck, H., „Axisymmetric Navier-Stokes computation of the two hyperboloid flares in reentry configuration". 4th European High Velocity Database Workshop ESA-ESTEC, Noordwijk, November 1994.

18. Brück, S., „Investigation of Shock-Shock Interactions in Hypersonic Reentry Flows". Proceedings of the 20th Int. Symposium on Shock Waves, Pasadena, USA, July 23-28, 1995.

19. Brück, S., Radespiel, R., Longo, J.M.A., „Comparison of Nonequilibrium Flow Past a Simplified Space Shuttle Configuration". AIAA Paper 97-0275, 1997.

20. Chalot, F., Mallet, M., Ravachol, M., „A comprehensive finite element Navier-Stokes solver for low and high-speed aircraft design". AIAA Paper 94-0814, 1994.

21. Choquet, I., „Thermal nonequilibrium modeling using the direct simulation Monte Carlo method: Application to rotational energy". Physics of Fluids, Vol. 6, No. 12, December 1994.

22. Choquet, I., „Vibrational nonequilibrium modeling using direct simulation, Part 1: Continuous internal energy". Journal of Thermophysics and Heat Transfer, Vol. 9, No. 3, July - September 1995.

23. Choquet, I., „Chemistry modeling in rarefied gas flows". 20th International Symposium on Rarefied Gas Dynamics, Beijing, August 1996.

24. Ciccoli, M.C., Désidéri, J.A., „Numerical computation of steady homenthalpic nonequilibrium flows". Computers and Fluids, Vol. 24, No. 6, pp. 719-737, 1995.

25. Comte, P., David, E., „Large-eddy simulation of Görtler vortices in a curved compression ramp", in Experimentation, Modelling and Computation in Flow, Turbulence and Combustion, Désidéri, J.A., Chetverushkin, B.N., Kuztnetsov, Y.A., Périaux, J., Stoufflet, B., Eds. John Wiley & Sons, pp. 45-61, 1995.

26. Coquel, F., Joly, V., Marmignon, C., „Méthodes de décentrement hybrides pour la simulation d'écoulements en déséquilibre thermique et chimique". AGARD-CP-578, Paper No. 34, September 1995.

27. Coquel, F., Marmignon, C., „A Roe-type linearization for the Euler equations for weakly ionized multi-component and multi-temperature gas". AIAA Paper 95-1675, 1995.

28. Coquel, F., Liou, M.S., „Hybrid Upwind Splitting (HUS) by a field decomposition". NASA TM 106843, ICOMP-95-2, 1995.

29. Coron, F., Harvey, J.K., Lengrand, J.C., „Rarefied gas flow simulation: a review". Proceedings of the 2nd European Symposium on Aerothermodynamics Vehicles, ESTEC, Noordwijk, The Netherlands, ESA SP-367, November 1994.

30. Coron, F., Pallegoix, J.F., „Direct simulation Monte Carlo method". Symposium on High Velocity Flows, Gujan-Mestras, France, May 1996.

31. Cousteix, J., Arnal, D., Aupoix, B., Brazier, J.Ph., Lafon, A., „Shock layers and boundary layers in hypersonic flows". Progress in Aerospace Sciences, Vol. 30, pp. 95-212, 1994.

32. Daiß, A., Frühauf, H.-H., Messerschmid, E.W., „Modeling of Catalytic Reactions on Silica Surfaces with Consideration of Slip Effects". AIAA Paper 96-1903, 1996.

33. Danckert, A., „Entwicklung und Anpassung von Streukernmodellen der Molekül-Oberflächen–wechselwirkung und ihrer Anwendung in der numerischen Simulation verdünnter Hyperschallströmungen". Dissertation, DLR-FB 96-29, 1996.

34. Dieudonné, W., Charbonnier, J.M., Deconinck, H., „ESA/MSTP Workshop 96: Test case III.B.: Hyperboloid flare standard model at RWG reference calibration point". ESA MSTP Workshop 96, Noordwijk, March 1996.

35. Dieudonné, W., Boerrigter, H.L., Charbonnier, J.M., „Shock wave boundary layer interaction on a blunt cone flare in hypersonic". 4th World Conference on Experimental Heat Transfer, Fluid Mechanics and Thermodynamics, Brussels, June 1997.

36. Delattre, N., Coron, F., Jacquelard, C., Hollanders, H., Lemaire, D., Moules, G., „Numerical prediction of hypersonic reactive flows with the finite volume solver FLU3NEQEV". AIAA Paper 97-0343, 1997.

37. Délery, J.M., Panaras, G., „Shock-Wave/Boundary-Layer Interactions in High-Mach-Number Flows". Paper 2, in AGARD AR 319, Vol. 1, 1996.

38. Demargne, A., Oswald, J., „Halis test case computation with the FLU3M code". 4th European High Velocity Database Workshop, Noordwijk, The Netherlands, November 1994.

39. Desmeuxes, C., Duffa, G., Dubroca, B., *„Different levels of modelization for diffusion phenomena in neutral and ionized flows"*. AIAA Paper 94-2412, 1994 (also Journal of Thermophysics and Heat Transfer, Vol. 11, No. 1, 1997).

40. Désidéri, J.A., Glowinsky, R., Périaux, J., *„Hypersonic flows for reentry problems"*. Vol. I and II, Springer-Verlag 1991.

41. Désidéri, J.A., Périaux, J., *„Validation of high-speed flow simulation by means of network data base"*. 2nd ECCOMAS Conference, Paris, pp. 300-306, September 1996.

42. Dietrich, S., *„Erweiterung des Monte-Carlo-Simulationsverfahrens zur Behandlung von kontinuumsnahen Hyperschallströmungen mit chemischen Reaktionen"*. Dissertation, DLR-FB 93-01, 1993.

43. Domröse, U., Krause, E., Meinke, M., *„Numerical simulation of laminar hypersonic shock-boundary layer interaction"*. ZFW, Vol. 20, No. 2, pp. 89-94, 1996.

44. Drouin, N., Coron, F., Hollanders, H., Lemaire, D., Moules, G., *„Calculations of nonequilibrium real gas flows with the finite-volume Euler/Navier-Stokes solver FLU3NEQEV"*. AIAA Paper 94-0761, 1994.

45. Dubroca, B., *„An extension of Roe's Riemann solver applied to reactive viscous flows for the computation of laminar hypersonic wake"*. Numerical Methods in Laminar and Turbulent Flows, Vol. 8, part 2, Ed. Taylor, C., Pineridge Press, Swansea, pp. 1168-1179, 1993.

46. Eggers, Th., Radespiel, R., Waibel, M., Hummel, D. *„Flow Phenomena of a Hypersonic Waverider and Validation of Design Methods"*. AIAA Paper 93-5045, 1993.

47. Eggers, Th., Strohmeyer, D., Nickel, H., Radespiel, R., *„Aerodynamic Off-Design Behavior of Integrated Waveriders from Take-off up to Hypersonic Flight"*. In: Proc. ESA/ESTEC 2nd Symposium on Aerothermodynamics for Space Vehicles and 4th European High-Velocity Database Workshop, Noordwijk, 21.-25.11. 1994.

48. Eggers, Th., Sobieczky, H., Center, K. *„Design of Advanced Waveriders with High Aerodynamic Efficiency"*. AIAA Paper 93-5141, 1993.

49. Elizarova, T.G., Graur, I.A., Lengrand, J.C., Chpoun, A., *„Rarefied gas flow simulation based on quasi-gasdynamic equations"*. AIAA Journal, Vol. 33, No. 12, pp. 2316-2324, 1995.

50. Esch, Th., Bauer, A., Rick, H. *„Simulation and nozzle/afterbody integration of hypersonic propulsion systems"*. ZFW, Vol. 19, No. 1, pp. 19-28, 1995.

51. Fey, M., *„Decomposition of the multidimensional Euler equations into advection equations"*. ETH Zürich, SAM Research Report 95-14, 1995.

52. Fox, U., Rick, W., Koschel, W. *„Computation of hypersonic high-temperature nozzle flow"*. ZFW, Vol. 17, No. 2, 139-148, 1993.

53. Friedrichs, R., (Ed.), *„2nd Space Course on Low Earth Orbit Transportation"*. Proceedings Vol. I and II, Technical University München, October 1993.

54. Gallis, M.A., Harvey, J.K., *„Validation DSMC Computations for the flowfield around a 70° blunted cone"*. Proceedings of the 19th International Symposium on Rarefied Gas Dynamics, Oxford, August 1994.

55. Gazaix, M., *„Hypersonic inviscid and viscous flow computations with a new optimized thermodynamic equilibrium"*. AIAA Paper 93-0893, 1993.

56. Gerhold, Th., Krogmann, P., *„Investigation of the Hypersonic Turbulent Flow Past a Blunt-Fin/Wedge Configuration"*. AIAA Paper 93-5026, 1993.

57. Gerlinger, U., Frühauf, H.-H., Bönisch, R. *„Implicit Upwind Navier-Stokes Solver for Reentry Nonequilibrium Flows"*. AIAA Paper 97-2547, 1997.

58. Godart, C., Salvetti, M.V., Désidéri, J.A., *„Numerical comparison of wall catalysis models for hypersonic reactive air flows"*. Proceedings of the 3rd Workshop on Modeling of chemical Reactions Systems, Heidelberg, Germany, July 1996.

59. Grotowsky, I.M.G., Ballmann, J. *„A numerical algorithm for calculating flows in hypersonic inlets"*. ZFW, Vol. 20, No. 2, pp. 95-104, 1996.

60. Hannemann, K., *„Computational Rebuilding of the Flow in the HEG Contoured Nozzle and the Flow Past the Standard Model Electre"*. DLR-IB 223-95 A45, also ESA HT-TR-E-1-202-DLRG, 1995.

61. Hannemann, K., *„Numerical Flow Field Analysis of the RWG Mach 6.8 Contoured Nozzle"*. ESA HT-TR-E-1-203-DLRG, 1995.

62. Hannemann, V., *„Numerische Simulation von Stoß-Stoß-Wechselwirkungen in Hochenthalpieströmungen unter Berücksichtigung von chemischen und thermischen Nichtgleichgewichtseffekten"*. Doctoral Thesis, Uni Göttingen, DLR-FB 97-07, 1997.

63. Hachemin, J.V., Vérant, J.L., *„3D parallel multi-block thermo-chemical nonequilibrium simulation with a PNS solver"*. 2nd European Symposium on Aerothermodynamics for Space Vehicles. ESTEC, Noordwijk, The Netherlands, November 1994.

64. Hänel, D., Henze, A., Krause, E. *„Supersonic and hypersonic flow computations for the research configuration ELAC I and comparison to experimental data"*. ZFW, Vol. 17, No. 2, pp. 90-98, 1993.

65. Häuser, J., Xia, Y., Muylaert, J., Spel, M. *„Aerodynamic Simulation for the Halis Configuration using Object-Oriented Grid Generation"*. Deutscher Luft-

und Raumfahrtkongreß 1996, Dresden 24-27. September 1996. DGLR Jahrbuch 1996 II, DGLR-JT96-106.

66. Häuser, J., Xia, Y., Spel, M., Paap, H.-G., Eiseman, P.R., Cheng, Z.M. „Grid Generation for Microaerodynamics Simulations of the Cassini-Huygens Space Probe". Proceedings of the 5th International Conference, Mississippi State University April 1 - April 5, 1996.

67. Haidinger, F.A., Friedrich, R. „Numerical simulation of strong shock/turbulent boundary layer interactions using a Reynolds stress model". ZFW, Vol. 19, No. 1, pp. 10-18, 1995.

68. Hempel, D., „Local Mesh Adaption in Two Space Dimensions". Impact of Computing in Science and Engineering, Vol. 5, pp. 309-317, 1993.

69. Henze, A., Houtman, E.M., Jacobs, M. Vetlutsky, V.N. „Comparison between experimental and numerical heat flux data for supersonic flow around ELAC 1". ZFW, Vol. 20, No. 2, pp. 61-70, 1996.

70. Herrmann, U., Radespiel, R., Longo, J.M.A., „Critical Flow Phenomena on the Winglet of Winged Reentry Vehicles". AIAA Paper 94-0629, 1994. See also: ZFW, Vol. 19, No. 5, pp. 309-319, 1995.

71. Hirschel, E.H., „Introduction to the AGARD-FDP-VKI Special Course Aerothermodynamics and Propulsion Integration for Hypersonic Vehicles". AGARD Report 813, pp. 1-1 – 1-3, 1996.

72. Hirschel, E.H., „Aerothermodynamics of Radiation-Cooled Surfaces". AGARD Report 813, pp.3-1 – 3-16, 1996.

73. Hirschel, E.H., „The Technology Development and Verification Concept of the German Hypersonics Technology Programme". AGARD Report 813, pp. 12-1 – 12-15, October 1996.

74. Hollanders, H., „Numerical challenge for the future in high velocity flows". Symposium on High Velocity Flows, Gujan-Mestras, France, May 1996.

75. Hollanders, H., Coron, F., Baillon, M., Durand, G., „Aerocapsule: Prediction tools for the re-entry capsule aerothermodynamics". AIAA Paper 97-0407, 1997.

76. Horvath, T.J., McGinley, C.B., Hannemann, K., „Blunt Body Near Wake Flow Field at Mach 6". AIAA Paper 96-1935, 1996.

77. Hunt, J.J. (Ed.), „Second European Symposium on 'Aerothermodynamics for Space Vehicles', 1994". ESA SP-367, 1995.

78. Joly, V., Coquel, F., Marmignon, C., Aretz, W., Metz, S., Wilhelm, H., „Numerical modeling of heat transfer and relaxation in nonequilibrium air at hypersonic speeds". La Recherche Aérospatiale, No. 3, pp. 219-234, 1994.

79. Kastell, D., Hannemann, K., Eitelberg, G., Horvath, T.J., „Recompression of Nonequilibrium Flow in the Wake of a blunted cone". Proceedings of the 20th Int. Symp. on Shock Waves, Pasadena, USA, July 23-28, 1995.

80. Klar, A., „Domain decomposition for kinetic problems with nonequilibrium states".European Journal of Mechanics, B/Fluids, Vol. 15, pp. 203-216, No. 2, 1996.

81. Knab, O., „Konsistente Mehrtemperatur-Modellierung von thermochemischen Relaxationsprozessen in Hyperschallströmungen". Fortschritt-Berichte VDI, Reihe 7, Strömungstechnik Nr. 300, 1966.

82. Kordulla, W., Radespiel, R., Krogmann, P., Maurer, F., „Aerothermodynamics Activities in Hypersonics at DLR". AIAA Paper 92-5031, 1992.

83. Kordulla, W., Radespiel, R., „Computational High-Speed Compressible Flows – Recent Developments at DLR". Proceedings, US-Europe Conference on High-Speed Flow Fields, November 1995, Houston, to be published by John Wiley & Sons Ltd. (also: DLR-IB 223-97 A 04).

84. Kufner, E., Dallmann, U., Stilla, J., „Instability of Hypersonic Flow Past Blunt Cones". AIAA Paper 93-2983, 1993.

85. Kuczera, H., Sacher, P.W., Dujarric, Ch., „FESTIP System Study – An Overview". AIAA 7th Int. Space Planes and Hypersonic Systems and Technologies Conference, Norfolk, November 1996.

86. Kufner, E., „Numerische Untersuchungen der Strömungsinstabilitäten an spitzen und stumpfen Kegeln bei hypersonischen Machzahlen". Dissertation, DLR-FB 95-11, 1995.

87. Larsson, R., „Sänger Hypersonics Technology Programme. Phase 1b, 1c, Applied Aerodynamics WP2143: CFD static stability analysis on the Hypersonic Flight Test Vehicle HYTEX 2-91" Report Saab Aircraft, August 1996.

88. Leclere, F., Aupoix, B., „Hypersonic turbulent nonequilibrium reactive flow calculations". 19th ICAS Conference, Anaheim, CA, September 1994.

89. Leyland, P., Vos, J.B., „NSMB: A Modular Navier Stokes Multiblock Code for CFD". AIAA Paper 95-0568, 1995.

90. Leyland, P., „Shock-Wave/Boundary Layer Interactions at Hypersonic Speed by an Implicit Navier-Stokes Solver". Computational Fluid Dynamics, Vol. 6, pp. 71-87, 1996.

91. Longo, J.M.A., Radespiel, R., „Flap Efficiency and Heating of a Winged Reentry Vehicle". Journal of Spacecraft and Rockets, Vol. 33, No. 2, pp. 178-184, 1996.

92. Mallet, M., Périaux, J., Stoufflet, B., *„Hypersonic flow simulations on unstructured meshes"*. ECCOMAS conference, Paris, September 1992.

93. Marini, M., Schettino, A., *„Contributions to hyperboloid flare test-cases I.c and III.b"*. MSTP Workshop 1996 – Reentry Aerothermodynamics and Ground-to-Flight Extrapolation, Noordwijk, The Netherlands, 1996.

94. Moschetta, J.M., Pullin, D.I., *„Computation of hypersonic Viscous Flows: Are robustness and accuracy compatible?"* AIAA Paper 96-2087, 1996.

95. Müller, C.A., Ballmann, J. *„Flow computation for the hypersonic configuration ELAC I at low speeds and large incidence"*. ZFW, Vol. 17, pp. 108-115, 1993.

96. Muylaert, J., Walpot, L., Hironde, N., Tumino, G., Simeonides G., Koppenwallner, G., Davis, J., *„Computational analysis of experiments in T5 and HHK for the study of flap-induced separation on an axisymmetric configuration"*. In: Shock Waves, Proceedings of the 20th ISSW, Sturtevant B, Shepherd JE, Hornung, H.G. (eds.), World Scientific, Vol. 1, pp. 203-208, 1996.

97. Naim, A., Mallet, M., Rostand, P., Hasholder, J.M., *„Local aerothermal problems during Hermes reentry"*. AGARD CP-514, Paper No. 42, 1992.

98. Neunzert, H., Struckmeier, J., *„The Finite Pointset Method for Hypersonic Flows in the Rarefied Gas Regime"*, in [10], Vol. 3, pp. 342-370, 1992.

99. Oswald, J., Bousquet, J.M. *„Space-planes and launchers aerodynamic study with Euler and Navier-Stokes computations"*. 20th ICAS Congress, Sorrento, Italy, September 1996.

100. Paciorri, R., Deconinck, H., Degrez, G., *„Implementation and validation of the Spalart-Allmaras turbulence model for application in hypersonic flows"*. Technical Note VKI, January 1996.

101. Panni, F., Pandolfi, M., *„Numerical prediction of waves in nonequilibrium flows"*. 3rd ECCOMAS CFD Conference, Paris, pp. 50-56, September 1996.

102. Perrier, P., Rapuc, M., Rostand, P., Sagnier, P., Vérant, J.L., Eitelberg, G., Bogstad, M.C., Muylaert, J., *„Ground to flight extrapolation of reentry aircraft aerodynamics; an experimental and computational approach"*. AIAA Paper 96-2434, 1996.

103. Radespiel, R., Swanson, R.C. *„Multigrid Schemes for Viscous Hypersonic Flows"*. In: Proc. 6th Copper Mountain Conference on Multigrid Methods, Copper Mountain, Colorado, 04. - 09.04.1993.

104. Radespiel, R., Longo, J.M.A., Brück, S., Schwamborn, D. *„Efficient Numerical Simulation of Complex 3D Flows with Large Contrast"*. AGARD-CP-578, Paper No. 33, 1995.

105. Radespiel, R., Swanson, R.C. *„Progress with Multigrid Schemes for Hypersonic Flow Problems"*. Journal of Computational Physics, Vol. 116, pp. 103-122, 1995.

106. Richter, R., Leyland, P. *„Dynamic Mesh Adaptation for Unsteady Flows within a True Parallel Environment"*. École Polytechnique Fédérale de Lausanne, T-96-17, presented at PARALLEL CFD' 96, Capri, May 1996.

107. Richter, R., Leyland, P. *„Completely Parallel Flow Solvers on Unstructured Meshes for Complex 3D Compressible flows on the CRAY-T3D"*. Proceedings Third ECCOMAS CFD Conference, Paris, September 1996, John Wiley CFD '96, pp. 1038-1044, 1996.

108. Rochholz, H., Huber, Th., Matyas, F. *„Unsteady airloads during the separation of an idealized two-stage hypersonic verhicle"*. ZFW, Vol. 19, No. 1, pp. 2-9, 1995.

109. Sagnier, Ph., Vérant, J.L., *„Validation of high enthalpy wind tunnel simulations"*, 3rd ECCOMAS CFD Conference, Paris, September 1996.

110. Salvetti, M.V., Désidéri, J.A., *„Implicit finite element method for the computation of viscous nonequilibrium hypersonic viscous flows"*. 3rd ECCOMAS CFD Conference, Paris, pp. 250-256, September 1996.

111. Saric, W.S., Muylaert, J., Dujarric, C. (Eds.), *„Hypersonic Experimental and Computational Capability, Improvement and Validation"*. AGARD AR 319, Vol. I, 1996.

112. Sarma, G.S.R., *„Relevance of Aerothermochemistry for Hypersonic Technology"*, in 'Molecular Physics and Hypersonic Flows', M. Capetelli (Ed.), Kluwer, pp. 1-20, 1996.

113. Sancho, M., Colin, Y., Johnson, C., *„Programme Overview, The French Hypersonic Research Programme PREPHA"*. AIAA 7th Int. Space Planes and Hypersonic Systems and Technologies Conference, Norfolk, November 1996.

114. Schall, E., Burtschell, Y., Druguet, M.C., Zeitoun, D., *„A complete description of the thermo-chemical coupling in hypersonic viscous flows"*. 3rd ECCOMAS CFD Conference, Paris, pp. 236-242, September 1996.

115. Schönemann, A.T., Auweter-Kurtz, M., Habiger, H.A., Sleziona, P.C., Stöckle, T., *„Analysis of the Argon Additive Influence on a Nitrogen Arcjet Flow"*. Journal of Thermophysics and Heat Transfer, Vol. 8, pp.466-472, 1994.

116. Schwane, R., *„Description of the Test cases: MSTP Workshop 1996, Reentry Aerothermodynamics and Ground-to-Flight Extrapolation"*. Report ESTEC YPA/1889/RS, 1996.

117. Schwane, R., *„Validation of High Mach Number Shock Wave/Boundary Layer Interaction"*, in Proceedings ECCOMAS 96, Computational Methods in Applied Sciences, John Wiley, pp. 324-331, 1996.

118.Schwane, R., „A Parallel Implicit Navier-Stokes Solver for Viscous Hypersonic Flows". In: Proceedings of 6th international symposium on Computational Fluid Dynamics, Lake Tahoe 1995, Vol. 3, pp. 1081-1086, 1995.

119.Schwane, R., Muylaert, J., „Description of the test cases: Fourth European High Velocity Database Workshop". ESTEC Report YPA/1495/RS, 1994.

120.Seror, S., Schall, E., Zeitoun, D., „Extension of the defect boundary layer theory to thermodynamical none-quilibrium hypersonic flows around a blunt body". 3rd ECCOMAS CFD Conference, Paris, September 1996.

121.Sillén, M. „German Hypersonics Technology Pro-gramme. Phase 1c, Computational Aerodynamics Work Package 2132: Flow computations around Hytex R-A$_3$ in side-slip". Saab Military Aircraft, December 1995.

122.Sillén, M. „German Hypersonics Technology Pro-gramme. Comparison beetween wind tunnel and free flight flow computations about the Hytex R-A$_3$ vehicle". Report Saab Aircraft, September 1996.

123.Simen, M., Dallmann, U., „On the Instability of Hy-personic Flow Past a Pointed Cone – Comparison of Theoretical and Experimental Results at Mach 8". Proceedings, AGARD 70th FDP Meeting and Symposi-um on Theoretical and Experimental Methods in Hyper-sonics Flows, Torino, Italy, 4-8 May, Paper 31-1 to -13., 1992.

124.Simeonides, G., Haase, W., „Experimental and computational investigations of hypersonic flow about compression ramps". Journal of Fluid Mechanics, Vol. 283, pp. 17-42, 1995.

125.Steiner, K. „Weighted Particle Methods Solving Kinetic Equations for Dilute Ionized Gases". NNFM, Vol. 52, pp. 322-339, Vieweg Verlag, 1996.

126.Stilla, J. „Engineering Transition Prediction of a Hypersonic Axisymmetric Boundary Layer". Journal of Aircraft Vol. 31, No. 6, pp. 1358-1364, 1994.

127.Streit, Th. „Euler and Navier-Stokes Solutions for Supersonic Flow Around a Complex Missile". Journal of Spacecraft and Rockets, Vol. 31, No. 4, pp. 600-608, 1994.

128.Strohmeyer, D., Eggers, Th., Heinze, W., Barden-hagen, A. „Planform Effects on the Aerodynamics of Waveriders for TSTO Missions". AIAA Paper 96-4544, 1996.

129.Struckmeier, J., Pfreundt, F.J. „On the efficiency of simulation methods for the Boltzmann equation on paral-lel computers".Parallel Computing, No. 19, pp. 103-119, 1993.

130.Struckmeier, J. „Fast generation of low-discrepancy sequences".Journal of Computational and Applied Ma-thematics, No. 61, pp. 29-41, 1995.

131.Van de Weide, E. Issman, E., Deconinck, H., De-grez, G., „A parallel implicit multidimensional upwind cell vertex Navier-Stokes solver for hypersonic applicati-ons". Aerothermics and Propulsion Integration for Hy-personic Vehicles, AGARD-VKI Special Course, April 1996.

132.Vérant, J.L., Radespiel, R., Hugues, E. „Development of Three-Dimensional Real Gas Navier-Stokes Codes Application to HERMES Space Shuttle". AIAA Paper 93-0675, 1993.

133.Vérant, J.L., Sagnier, Ph., „Assessment of total conditions and flow thermo-chemical nature in the ONERA F4 high enthalpy wind tunnel". AIAA Paper 96-2239, New Orleans, 1996.

134.Villedieu, P., Mazet, P.A., „Schémas cinétiques pour les équations d'Euler hors équilibre chimique". La Recherche Aérospatiale, No. 2, pp. 85-102, 1995.

135.Vos, J.B., Pallegoix, J.-F. „Synthesis of the Halis S4 Test Case".MSTP-Workshop, ESTEC, March 1996.

136.Vos, J., „Proposal for the Development of a Hyper-sonic Aerothermodynamic European Data Base (HAEDB)". Contract ESA 11169/94/F/WE, see also http://haedbwww.epfl.ch:8080/doc/proposal.

137.Walpot, L., Muylaert, J., Bakker, P., Simeonides, G., „High enthalpy nozzle flow sensitivity study and effects on heat transfer". In: Shock Waves, Proceedings of the 20th ISSW, Sturtevant B, Shepherd JE, Hornung, H.G. (eds.), World Scientific, Vol. 2, pp. 1587-1592, 1996.

138.Weiland, C., Menne, S., Schröder, W., Hartmann, G., Behr, R., „The Role of Numerical Aerothermodyna-mics for the Development of New Space Transportation Systems". Proceedings ECCOMAS CFD '94, John Wi-ley, pp. 190-199, 1994.

139.Wütrich, S., Perrel, F., Sawley, M.L., Lafon, A., „Hypersonic flow in chemical nonequilibrium: A compa-rison of thin-layer Navier-Stokes and coupled Eu-ler/Boundary layer computations". Computers and Fluids, Vol. 23, No. 2, pp. 415-432, 1994.

140.Zeitoun, D., Schall, E., Burtschell, Y., Druguet, M.C., „Vibration – dissociation coupling in nonequilibri-um viscous flows". AIAA Journal, Vol. 33, No. 1, pp. 79-85, 1995.

141.Zeitoun, D., Boccaccio, E., Druguet, M.C., Imbert, M., „Reactive and viscous flow in hypersonic nozzles". AIAA Journal, Vol. 32, No. 2, pp. 333-340, 1994.

142.Zhu, Z., Alavilli, P., Lacor, C., Hirsch, C., „Efficiency and robustness of multigrid methods for hypersonic flows". AIAA Paper 97-0342, 1997.

Drag Prediction and Transition in Hypersonic Flow

Helen L. Reed[a]
Arizona State University
Tempe, Arizona 85287-6106 USA

Roger Kimmel[b]
U.S. Air Force / Wright Laboratory
WPAFB OH 45433-7913 USA

Steven Schneider[c]
Purdue University
West Lafayette, IN 47906-3371 USA

Daniel Arnal[d]
CERT/ONERA
Toulouse, France

1. SUMMARY

This paper discusses progress on issues such as instability studies, nose-bluntness and angle-of-attack effects, and leading-edge-contamination problems from theoretical, computational, and experimental points of view. Also included is a review of wind-tunnel and flight data, including high-Re flight transition data, the levels of noise in flight and in wind tunnels, and how noise levels can affect parametric trends. A review of work done on drag accounting and the role of viscous drag for hypersonic vehicles is also provided.

2. EFFECT OF BOUNDARY-LAYER TRANSITION ON THE DRAG OF A GENERIC HYPERSONIC VEHICLE

The importance of transition and its effect on skin friction in subsonic vehicle drag has been investigated for many years and is well known. Although of more serious issue is the cooling-requirement difference, the focus of this paper is on drag. The prominence of transition in hypersonic vehicle drag is more uncertain, because of the small amount of hypersonic flight experience we have. A useful starting point is to see how much drag on a hypersonic vehicle is due to skin friction under plausible flight conditions. There is no simple answer, of course, since the contribution of skin friction to overall vehicle drag depends heavily on factors such as the configuration, Mach number, altitude, and so on. Nevertheless, it is useful to consider a generic hypersonic configuration to obtain an order of magnitude estimate. The hypersonic transport described by Small et al. (1970) was chosen as a baseline to assess the relative effects of skin friction. For this study, the vehicle was sized at 61 m in length, which is typical for vehicles designed for sustained hypersonic flight. The longer the vehicle, the greater the wetted area and the greater the contribution of skin friction. The analysis conditions were Mach 8, 10, 12, and 14. The altitude was varied at each Mach number to keep the freestream dynamic pressure constant at 71.8 kPa, which is a typical airbreathing trajectory. These conditions produced Reynolds numbers based on freestream conditions and model length from 131×10^6 (Mach 14) to 247×10^6 (Mach 8). The configuration was analyzed using the Supersonic, Hypersonic, Arbitrary Body Program (SHABP; Burns et al.

1995). SHABP calculates skin friction using correlations based on the length Reynolds number along each body panel. The boundary layer was treated as either all laminar or all turbulent to provide upper and lower bounds on skin friction. Calculations were carried out for zero angle of attack. The inlet was treated as flow-through, and no drag was calculated for the internal surfaces. The results here are representative of large vehicles with significant wetted area.
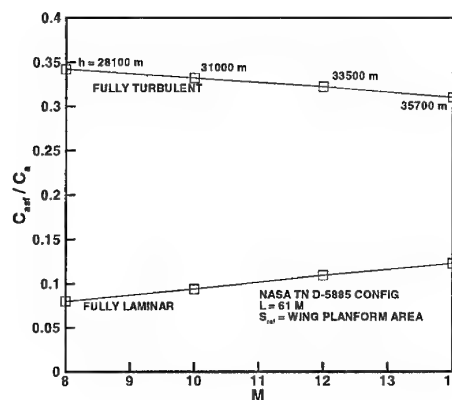
Figure 1. Fraction of axial-force coefficient due to skin friction for a generic hypersonic configuration.

Figure 1 shows that the percentage drag due to skin friction varies little over the Mach number range examined under fully laminar or fully turbulent conditions. For fully turbulent flow, skin friction contributes over 30% of the overall vehicle drag. For fully laminar flow, the skin friction contribution is about 10%. It is quite likely that transition occurs at some point on the vehicle, even at the highest Mach number. Transition on the compression surface is especially likely due to the adverse pressure gradient there. A similar vehicle analyzed by Finley (1990) showed 65% to 100% of the vehicle area turbulent at Mach 15, depending on whether a correlating factor of $Re_\theta/M = 300$ or 100 (respectively) was used. [Note: This criterion

is not recommended by the present authors.] Clearly, transition location can be a significant source of uncertainty in vehicle drag predictions. Also, the efficacy of transition control depends largely on where transition is predicted. Realistic estimates of transition location indicate the importance of transition control.

3. THEORETICAL AND COMPUTATIONAL RESULTS

Due to limited space, we primarily describe recent efforts in modeling hypersonic-flow physics and outlining the various challenges to the transition community. The reviews by Arnal (1994) and Reed et al. (1996) on linear stability theory, Herbert (1997) on Parabolized Stability Equations (PSE), Kleiser & Zang (1991) and Reed (1994) on direct numerical simulations (DNS), and Haynes et al (1996) on validation issues serve as complementary companions. Moreover, the reader is referred to the numerous recent meetings, courses, and workshops devoted to the topic of stability and transition. Various recent AGARD Special Courses provide important sources of information on the aerodynamic applications of transition; in particular, the report of AGARD/FDP Working Group 18 is recommended reading.

3.1 Linear Stability Theory

The paper by Mack (1984) is the most complete description of compressible stability available anywhere. The linear stability analysis of high-speed boundary layers uncovers three major differences between it and the subsonic analysis: the presence of a generalized inflection-point, multiple acoustic modes (Mack Modes), and the dominance of 3-D viscous disturbances.

The lowest-frequency Mack mode, the so-called second mode, is found to be the dominant instability for Mach number greater than about 4; it is more unstable than either the 3-D first mode or any of the other higher modes. With regard to the second mode, there is a strong tuning with the boundary-layer thickness, so that the frequency of the most amplified disturbance may be predicted from this flow parameter. In particular, the fluctuation wavelength is approximately twice the boundary-layer thickness. This implies that if the boundary-layer thickness is changed, for example by cooling, a corresponding, predictable change in frequency should be observed. Mack observed that whereas the first mode is stabilized by cooling in air, the second mode is actually destabilized. The Mack modes can be destabilized without the presence of a generalized inflection point.

3.2 Effects of Chemistry and Bow Shock

Linear stability solutions for hypersonic flows are complicated for some of the following reasons. 1) At hypersonic speeds, the gas often cannot be modeled as perfect because the molecular species begin to dissociate due to aerodynamic heating. In fact, sometimes there are not enough intermolecular collisions to support local chemical equilibrium and a nonequilibrium-chemistry model must be used. 2) The bow shock is close to the edge of the boundary layer and must be included in studies of transition.

Malik (1987, 1989, 1990) investigated the stability of an equilibrium-air boundary layer on an adiabatic flat plate. Malik et al. (1990) used the e^N method for the reentry-F

experiments; the basic state was calculated by equilibrium-gas Navier-Stokes and PNS. Gasperas (1990) studied stability for an imperfect gas. Stuckert & Reed (1994) analyzed the stability of a shock layer in chemical nonequilibrium and compared results with the flow assuming 1) local chemical equilibrium and 2) a perfect gas.

Stuckert & Reed's coordinate system for both the basic-state and stability analysis fit the body and bow shock as coordinate lines. This makes it easier to apply the linearized shock-jump conditions as the disturbance boundary conditions (e.g. Stuckert 1991). At the surface of the cone, for the nonequilibrium calculations, the species mass fluxes were set to zero (noncatalytic wall), whereas for the equilibrium calculations the disturbances were assumed to be in chemical equilibrium. It is clear that the equilibrium and nonequilibrium solutions can differ significantly depending on the rates of the reactions relative to the time scales of convection and diffusion. For example, some of the equilibrium modes were determined to be supersonic modes, each of which was a superposition of incoming and outgoing amplified solutions in the inviscid region of the shock layer. (No similar solutions were found for the nonequilibrium shock layer.) The magnitudes of these modes oscillated with y in the inviscid region of the shock layer. This behavior is possible only because the shock layer has a finite thickness. They are also unlike Mack's higher modes (except for the second) in that the disturbance-pressure phase for all of these supersonic modes changed most across the inviscid region of the shock layer. (The disturbance-pressure phase change for Mack's higher modes occurs across the viscous region of the flow, i.e. the boundary layer.) In fact, the disturbance-pressure phase change for all of these supersonic modes through the boundary layer is comparable to that of Mack's second mode.

Another effect of the chemical reactions is to increase the size of the region of relative supersonic flow primarily by reducing the temperature in the boundary layer through endothermic reactions, increasing the density, and hence decreasing the speed of sound. This reduces the frequency of the higher modes; in particular, the most unstable one, the second mode. The higher modes in the reacting-gas cases are also more unstable relative to the corresponding perfect-gas modes. The first modes are, however, more stable.

Finally, the finite thickness of the shock layer has a significant effect on the first-mode solutions of all of the families. The effect on higher-mode, higher-frequency solutions does not seem to be as large as long as they are subsonic. This is perhaps what one would intuitively expect because the shock is likely "stiff" and hence difficult to perturb with smaller-wavelength, larger-wavenumber, higher-frequency disturbances. However, the nonparallel effects are known to be large for first-mode solutions, and so a complete quantitative description of the effects of the finite shock-layer thickness awaits either a PSE solution or a DNS analysis.

The inclusion of the bow shock is especially critical to studies of leading-edge receptivity as demonstrated by Zhong (1997). His DNS results over a blunt wedge show that the instability waves developed behind the bow shock

consist of both first and second modes. His results also indicate that external disturbances, especially entropy and vorticity disturbances, enter the boundary layer to generate instability waves mainly in the leading-edge region.

3.3 Linear Stability Studies Performed within ESA TRP

Quite recently, ESA (European Space Agency) launched a TRP (Technological Research Programme) involving several European research centers (DLR, ONERA, Flow Science, CFD Norway) under the responsibility of AEROSPATIALE. The general objective was to analyze laminar-turbulent transition problems for hypersonic flow over slender lifting configurations. Two generic shapes have been studied, both experimentally and numerically: a highly swept delta wing (experiments performed in the gun tunnel at Imperial College) and a conical shape (experiments performed in the Mach 7 wind tunnel at ONERA CERT). This paragraph summarizes the numerical results obtained for the latter shape, with emphasis on the nose-bluntness and angle-of-attack effects (Tran et al. 1995, Arnal et al. 1996)

3.3.1 *Nose-bluntness effects*

The conditions used for the experiments and then for the computations are: freestream Mach number $M_\infty = 7$, unit Reynolds number = 25×10^6/m, length of the model = 0.2m, wall temperature = 310K. Three values of the cone nose radius R_n were considered: $R_n = 0$ (sharp cone), 0.2mm, and 0.5mm. The experimental results indicated that the onset of transition (detected by infrared thermography) moved downstream with increasing R_n, a trend which has been already reported by many investigators, see Stetson et al. (1984) for instance.
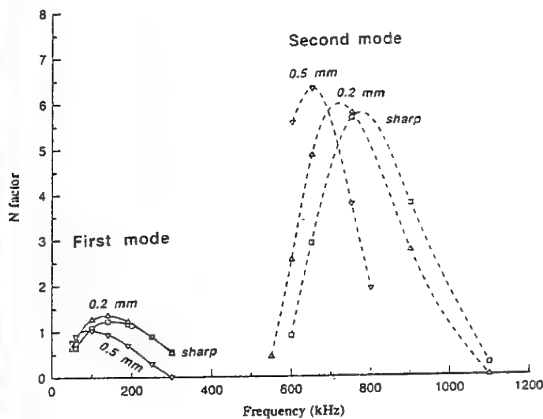
Figure 2. N factor at transition for blunt cones.

The mean flow field was computed by CFD Norway by solving the Navier-Stokes equations (Arnal et al. 1996). Then linear, local stability computations were performed by using the CASTET code developed at ONERA. The integrated growth rates at transition are plotted in Figure 2 as a function of the disturbance frequency. As expected, the frequency range for first- and second-mode disturbances are clearly separated. First-mode waves are around 150 kHz, while second-mode waves are around 700 kHz. However, one can observe a shift to lower frequencies when R_n increases, both for first- and second-mode disturbances.

We now assume that transition occurs when the N factor for first or second mode waves reaches a fixed value. This value is taken from the sharp cone results (N = 1.27 for first mode, N = 5.85 for second mode). The theoretical and measured transition locations are plotted in Figure 3 as a function of R_n, by considering separately first- and second-mode disturbances. The agreement is quite good for $R_n = 0.2$mm. For $R_n = 0.5$mm, the transition abscissa is overestimated when first-mode waves are considered, whilst it is underestimated when second-mode waves are considered. As the differences with the experimental data are nearly the same, it is very difficult to decide which mode is responsible for transition in these experiments.
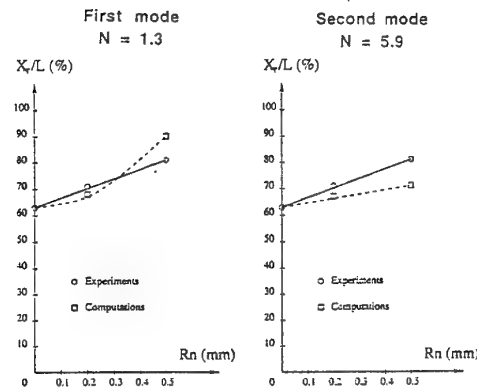
Figure 3. Blunt cones: measured and computed transition locations.

3.3.2 *Angle-of-attack effect*

Experiments have also been performed for a sharp cone at 2° angle of attack. As observed in other experiments (Stetson et al. 1985, King 1991, for instance), transition occurred earlier on the leeward ray than on the windward ray; transition location was $X_T/L = 0.40$ and 0.76 for the leeward and windward rays, respectively ($X_T/L = 0.61$ for the sharp cone without incidence).
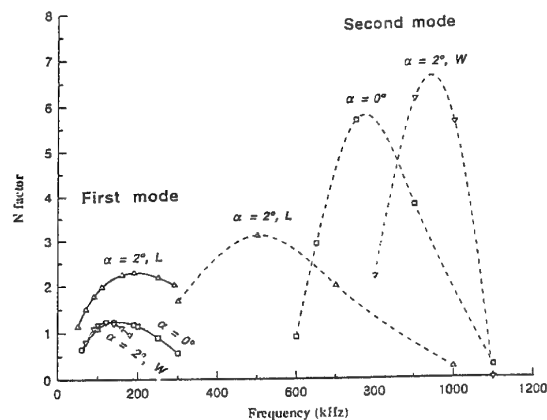

Figure 4. N factor at transition for sharp cone at angle of attack.

Figure 4 shows the integrated growth rates of first- and second-mode disturbances at the measured transition location on the leeward ray (denoted as L in the figure) and on the windward ray (denoted as W). Results at zero angle of attack are given for comparison. The most striking feature is that N increases from windward to leeward ray for first-mode disturbances, whereas it decreases for second-mode disturbances. It can also be observed that a wide gap exists on the windward ray between first- and second-mode frequencies; the mean value of the latter reaches very large values, up to 1000 kHz. On the leeward ray, first- and second-mode frequency ranges overlap. The shift in the second-mode frequency range can be easily explained by the fact that the disturbance frequency scales with the inverse boundary-layer thickness. As the boundary layer is much thinner on the windward ray, the disturbance frequency is higher.

The sharp cone at zero angle of attack was again chosen as reference case for the application of the e^N method. The results are summarized in Figure 5. If it is assumed that transition is induced by second-mode disturbances, the theoretical transition line exhibits a wrong slope (by comparison with the experiments). On the other side, a qualitative agreement is achieved when considering first-mode waves. This could indicate that high-frequency, second-mode instability does not play any role in these experiments, because the free stream environment does not contain disturbances in this frequency range (see discussion of this problem in Stetson et al. 1986).

First mode : N = 1.3
Second mode : N = 5.9
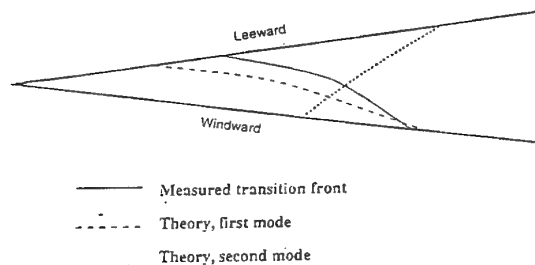
Figure 5. Sharp cone at angle of attack: measured and computed transition locations (on the windward and leeward rays).

3.4 Numerical Simulations of Nonlinear Stages

In contrast to incompressible flows, there is no guidance from experiments regarding the nonlinear stages of transition in high-speed flows. Detailed measurements are difficult due to the severe, high-temperature environments and tunnel design must feature quiet flow; this complicates the validation issue for CFD. Moreover, the complexity of the equations, which must include chemical reactions, and the need for both accuracy and resolution demand that the most powerful supercomputers available be used, and used efficiently, in order to perform direct numerical simulations. Initial CFD efforts have indicated that the amount of resources required can far exceed an incompressible calculation; gradients of disturbance quantities are generally steeper and compressibility is known to reduce disturbance amplitudes, thus "delaying" the normal appearance of breakdown in a given computational box.

To illustrate the progress in DNS for the nonlinear stages of high-speed flows, although done for a low supersonic Mach number, Thumm et al. (1990) and Bestek et al. (1992a,b) studied spatially growing 3-D waves in a growing 2-D flat-plate boundary layer; the disturbances were introduced via periodic wall blowing/suction. They pointed out that a secondary instability calculation based on a finite 2-D amplitude may not be relevant for supersonic flow and they investigated other possible routes to turbulence at low supersonic Mach numbers. To this end they simulated a Mach-1.6 base flow subjected to a pair of 3-D waves of amplitude O(1%) and discovered a new breakdown mechanism, termed "oblique-wave breakdown". The disturbances quickly became nonlinear and through direct nonlinear interactions, a strong longitudinal vortex system was observed. The resulting structures, which differed from the Λ-shaped vortices usually reported for fundamental or subharmonic breakdown, were described as "honeycomb-like".

Spatial simulations are still too expensive to use for routine design [$O(10^3)$ cpu hours on a CRAY] and at present we cannot provide a completely resolved solution all the way through transition to turbulence even on a flat plate. Ongoing efforts in spatial computations have been vigorous and have recently realized successes in the improvement of numerical methods to reduce required computer resources and in the prediction of more complicated physical processes and the explanation of different mechanisms at work in the experiments. The downstream boundary condition also seems to be more under control now.

Transition is highly initial-condition and operating-condition dependent. Considerable uncertainty exists in the modeling, prediction, and control of transition in high-speed flows due to the dearth of reliable experiments. Validation requires comparison with careful archival experiments, but few such experiments have been performed. The encouraging news is that the CFD formulations validated to date (in subsonic flow) demonstrate that if the environment and operating conditions can be modeled and input correctly, the computations agree quantitatively with the experiments. What is especially significant and exciting is that the PSE, which have significantly less resource overhead associated with them compared with DNS, have been shown to accurately model a variety of relevant flows. Therefore, an important and exciting role for the simulation is now in the development and calibration of simpler models for hypersonic flows. The abundance of information provided is invaluable and complements any experimental effort. The other major challenge to the CFD community is to provide leadership in the determination of critical, relevant validation experiments in hypersonic flow.

3.5 Transition Prediction - Correlation Parameters

With the current interest in high-speed flight, there is also a keen desire to determine correlating parameters, based purely on basic-state profiles, that can be easily incorporated into existing basic-state codes and will predict transition location (or trends) for crossflow-dominated problems. To evaluate parameters quantifying stability characteristics, Reed & Haynes (1994) examined the linear stability of the supersonic flow over a rotating cone at zero incidence. When compressibility and cooling effects are included, a correlating parameter is found at transition. This result has been verified with the yawed-cone data of King (1991), Stetson (1982), and Holden et al. (1994). The new parameter is calculated solely from the basic-state profiles and, as such, it can aid in *preliminary (only)* transition prediction and design, including the evaluation of parameter trends, for 3-D boundary layers. Once a preliminary shape is selected, further linear stability theory or PSE calculations are strongly urged.

4. EXPERIMENTAL RESULTS IN STABILITY AND TRANSITION

4.1 Background

Stability theory forms a foundation for the prediction of transition and the interpretation of experimental results (Mack 1984, Reshotko 1968). Wright Laboratory, under the auspices of the Air Force Office of Scientific Research, has for a number of years conducted an experimental program to experimentally examine stability and transition in hypersonic boundary layers. Recent computations have demonstrated the importance of linear wave superposition and nonlinear wave interactions in instability wave growth and the breakdown process (Pruett & Zang 1992, Pruett & Chang 1995, Herbert et al. 1993, Chang & Malik 1993). Very few experiments on hypersonic boundary layer stability (Kendall 1975, Demetriades 1975, Stetson & Kimmel 1992, Lachowicz et al. 1996) exist. These measurements have been single-point, hot wire measurements on axisymmetric bodies. Multiple point measurements of parameters describing the spatial structure of instability waves, such as wavelength, convection velocity, and wave angle, are required to better understand the stability and transition process.

To address deficits in our knowledge of the spatial structure of hypersonic boundary layer stability, the Wright Laboratory program has recently been extended to examine the three-dimensional structure of instability waves and transition on fully three-dimensional bodies.

4.2 Test Procedures

Tests were conducted in the Arnold Engineering Development Center von Karman Facility (AEDC VKF) Tunnel B. The Tunnel B freestream mean and fluctuating flow has been extensively monitored and calibrated (Donaldson & Coulter 1995). Tunnel B is not a "quiet" facility in the sense that extraordinary measures are taken to keep the tunnel sidewall boundary layers laminar, but it appears that early instability growth is linear. Transition mechanisms measured for circular cones in Tunnel B are well-described by linear theory and are not bypass (Stetson & Kimmel 1992), although measured transition Reynolds numbers are lower than free flight. Comparison of stability measurements with Parabolized Stability Equation (PSE) computations (Chang & Malik 1993) for a sharp-nosed, 7° half-angle circular cone indicate that the second-mode disturbance growth in Tunnel B was linear to Reynolds numbers of 2.6×10^6.

Cones with elliptical and circular cross sections were examined. The circular cone had a 7° half-angle with a sharp nose of spherical radius 4×10^{-5} m. The elliptical cone had a 2:1 eccentricity with a 7° half angle in the minor axis. It also had a nose radius of 4×10^{-5} m in the major axis. Both models were 1.016 m long. Tests were conducted at a freestream Mach number of 7.93. The stagnation temperature was 728 K, and the cone wall conditions for probing were adiabatic. The circular-cone instrumentation consisted primarily of hot-film probe measurements in the boundary layer. Hot-film probe flowfield measurements and surface heat transfer measurements were taken on the elliptic cone. Tests were carried out at freestream (upstream of the model bow shock) unit Reynolds numbers of $Re_u = 1.64 \times 10^6$ to 6.56×10^6 per meter by varying tunnel stagnation pressure.

4.3 Space-Time Correlation Measurements on the Circular Cone

Measurements on the circular cone were carried out at $x/L = 0.881$, producing local x-Reynolds numbers of 2.3×10^6 to 9.1×10^6 based on the local boundary layer edge unit Reynolds number and x-distance. One hot-film probe was mounted on-board the model at a fixed location $x/L = 0.881$. A rake containing up to four additional hot film probes was mounted on the tunnel overhead drive. Measurements in the circumferential (or z) direction were carried out by positioning the probes at the maximum energy location in the boundary layer, holding the rake fixed, and rolling the model to drive the on-board probe away from the rake. The maximum energy location is defined here as the y-location in the boundary layer at which the broadband rms signal from the hot film probe is a maximum. Streamwise correlations were obtained by holding the on-board probe fixed with a circumferential separation of 6.35 mm from the nearest rake probe, and moving the rake up to 25.4 mm downstream of the on-board probe. The on-board probe was fixed at the maximum energy location, and the downstream probe was relocated at the maximum energy point at each downstream station. Correlations in the vertical dimension were obtained by replacing the probe rake with two probes separated vertically by 1.47 mm and traversing them vertically through the boundary layer. Correlations with separation in each of the three spatial dimensions (ξ_x, ξ_y, ξ_z) were thus obtained. Kimmel & Poggie (1997a) and Poggie & Kimmel (1997) give additional information on this experiment.

Contours of constant broadband space-time correlation for circumferential probe separation in Figure 6 emphasize the wave packet nature of the second mode waves. The extent of the wave packet is limited in space and time. This wave packet behavior is similar to Tollmien-Schlichting wave packets excited by weak freestream turbulence in low speed flow (Kendall 1990). The cross correlation of Figure 6 was reconstructed from the ensemble averaged cross spectrum, so any wave obliquity would be washed out by the averaging process. Histograms of instantaneous wave angle (Poggie & Kimmel 1997), however, indicate that the

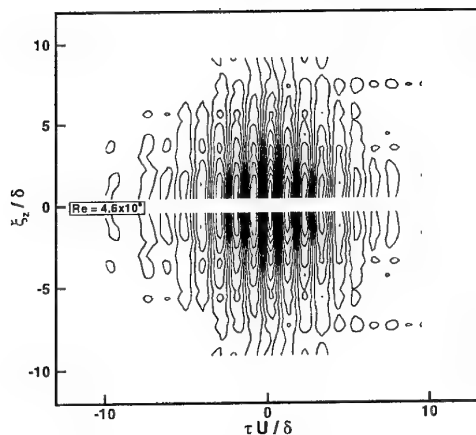second-mode waves are, for the most part, two-dimensional.

Figure 6. Circumferential correlations on the axisymmetric cone for $Re_x = 2.3 \times 10^6$ (Kimmel & Poggie 1997a)

Cross-correlation contours developed from vertically spaced probes, shown in Figure 7 illustrate the breakdown process of the second mode wave packets. Additional effort is required to reconstruct the cross correlations since these measurements were obtained by holding both probes fixed relative to each other and traversing them through the boundary layer, rather than holding one probe fixed and traversing the other relative to it. In order to present these data in a form analogous to that used for the variable probe separation experiments, the correlations are shown as a function of the time delay integrated across the boundary layer. Since the zero reference of the time delay is arbitrary, the contours have been shifted to place the maximum positive correlation near the boundary layer edge at zero time delay.
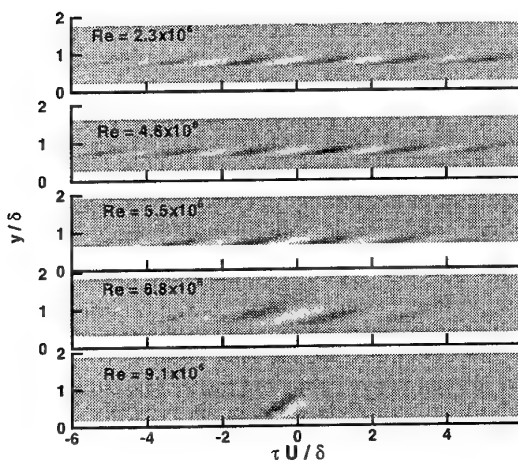
Figure 7. Vertical correlations on the axisymmetric cone (Kimmel & Poggie 1997a).

The second-mode waves at the lowest Reynolds number are periodic, with a streamwise wavelength of approximately two boundary-layer thicknesses. The correlation persists several second-mode wavelengths away from the zero reference. The waves tend to have a flattened or elongated structure. These features agree qualitatively with shadowgraphs of "rope" waves (Kimmel & Poggie 1997a) for the same configuration. The rope waves, which appear prior to boundary layer breakdown, appear to be a nonlinear remnant of the second mode. As the Reynolds number increases and the boundary layer begins to transition, this coherence length decreases and the disturbances begin to stand more erect (i.e., their phase shift in the y-direction decreases). At the highest Reynolds number, the angle between the correlation contours and the wall have increased further, reminiscent of typical "turbulent structures" seen in boundary layers (Spina et al. 1991, Owen & Horstman 1972). Also, the dominant disturbances have shifted to a shorter wavelength, reflecting the spread of energy from the second mode to higher wavenumbers.

Space-time correlations in laminar and transitional boundary layers give a picture of the spatial structure of second-mode waves and their breakdown. Most notably, the second-mode waves are coherent over only a limited streamwise and circumferential extent. This behavior is no doubt due to the stochastic nature and limited spatial coherence of the disturbance sources. The turbulent "burst rings" observed by Fischer (1972) on a cone in helium flow at Mach 18 would be an unlikely breakdown scenario for the current investigation.

4.4 Transition Measurements on the Elliptic Cone

Parabolized Navier-Stokes (PNS) calculations were used to design the elliptic cone model. Kimmel et al. (1996) describe PNS calculations of the boundary layer basic state for elliptic cones at freestream Mach 8. A salient feature of this calculation is a crossflow directed from the high-pressure leading edge (major axis) to the lower pressure centerline (minor axis), which produces a "ballooning" of the centerline boundary layer due the influx of lower momentum fluid from the sides of the model. This produces unstable, inflected velocity profiles near centerline. Lyttle & Reed (1995) also find this feature for elliptic cones at Mach 4 in a separate study.

Kimmel et al. (1996) also reported linear stability calculations for the adiabatic-wall elliptic cone. Cones with eccentricities of e = 1.5, 2.0 and 4.0 were all unstable to standing crossflow vortices. Detailed stability computations for the e = 1.5 and 2.0 configurations also showed unstable traveling waves over a broad frequency band. Disturbances of 40 to 60 kHz were the first non-zero frequencies to obtain N-factors of five. An N of five had been shown to correlate transition on axisymmetric cones in the AEDC Tunnel B windtunnel (Mack 1986, Stetson & Kimmel 1992). Traveling waves showed two distinct regions of high amplification, one near the centerline, associated with the unstable velocity profiles, the other near the "shoulder" of the model, associated with high crossflow. The model leading edge was more stable, with low amplification rates. These computational results are consistent with the limited experimental data base for elliptic cones. Experiments by Burke (1965), replotted in

Kimmel et al. (1996), on a sharp-nosed elliptic cone of eccentricity e = 1.43 at freestream Mach 10, are consistent with these findings, indicating that transition began first on the model centerline at a Reynolds number $Re_x = 1.7 \times 10^6$.

Experimental heat transfer contours are shown in Figure 8. These contours were constructed with data obtained at each of the unit Reynolds numbers tested, assuming similarity in Re_x. The locations of the transducers in Re_x, θ coordinates used to construct the contours are superimposed. Discontinuities in heat transfer at $Re_x = 10^6$ and 4.8×10^6 are artifacts due to interpolation between circumferentially arrayed transducers and transducers located along rays of the model. The measured heat transfer was divided by the calculated laminar heat transfer to obtain a ratio, h, which was near unity for laminar flow, and greater than unity for turbulent flow. Since the computations underpredicted heat transfer somewhat, a threshold value of h = 1.5 was chosen to indicate transition. Transducer locations with h < 1.5 are colored white, and those with h > 1.5 are colored black. A third-order, least-squares polynomial was fitted through the transition front obtained in this fashion and is shown on the graph. This transition front coincides with the first departure of heat transfer values away from their local minima. A unit Reynolds number effect was observed in the data, i.e., the transition Reynolds number varies with freestream unit Reynolds number. The maximum variation was 20% at θ = 45°.
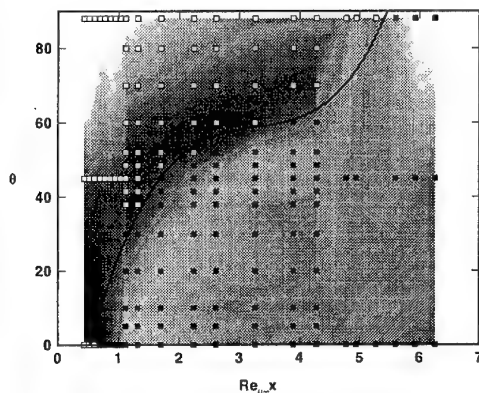
Figure 8. Contours of elliptic-cone heat transfer. Symbols indicate transducer locations. Open - laminar, closed - turbulent (Kimmel & Poggie 1997b).

The earliest transition occurred on model centerline due to the highly inflected, unstable boundary-layer profiles there. The most downstream transition occurred on the leading edge. Traveling waves were evident on both leading edge and centerline in Schlieren photographs (Kimmel & Poggie 1997b). Hot-film probe measurements also indicated traveling waves. Signatures of stationary crossflow vortices in surface oil flow or heat transfer were weak to nonexistent. This may be due to the attenuation of crossflow vortex eigenfunction magnitudes near the wall, unsteadiness of crossflow vortices, or simply their

weakness or nonexistence. Roughness placed near the model leading edge had little effect on heat transfer at lateral measurement stations, but circumferentially spaced roughness caused increased, circumferentially periodic heating downstream (Kimmel & Poggie 1997b). These results indicate that disturbances from surface roughness propagated along streamlines external to the boundary layer, rather than along surface streamlines. Since stability computations indicated that crossflow vortices were aligned with the edge streamlines (Kimmel & Poggie 1997b), the surface roughness effects may be related to crossflow vortices.

These results are similar to those obtained by Cattafesta et al. (1995) on a delta wing at Mach 3.5. Stationary waves on this configuration were weakly manifested except in the presence of roughness, and traveling waves appeared dominant, based on comparison of transition results with linear stability theory calculations. Further analysis of hot-film probe data obtained on the elliptic cone should shed more light on the influence of traveling waves and their exact nature.

Two ramifications for transition prediction arise from this experiment. First, the dominance of traveling waves in crossflow highlights the accuracy with which they must be calculated for transition prediction. Also, their relative influence compared to stationary waves must be accurately predicted. Second, leeside flow or influx due to crossflow at symmetry planes must also be accurately predicted, both in mean flow and stability analysis. Although heating rates here are generally lower than windward or leading-edge locations, these flows are highly unstable, and transition here can spread laterally. This lateral contamination must also be calculated for three-dimensional transition fronts.

5. LEADING-EDGE CONTAMINATION AND BOUNDARY-LAYER TRIPPING ON ATTACHMENT LINE OF A SWEPT LEADING EDGE

5.1 Empirical Criteria
In the case of swept (delta) wings, the so-called attachment line is a particular streamline which divides the flow into one branch following the upper surface and another branch following the lower surface. Let us observe that the windward ray of a cone at incidence can also be considered as an attachment line. Along this line, transition can be the result of the amplification of *"natural" waves* excited by the available disturbance environment; this phenomenon can be modelled by the linear stability theory, either in its classical form or in a particular form applicable to low-speed flows only (Görtler-Hämmerlin disturbances). This problem will not be discussed in this paragraph. Other possibilities for the appearance of turbulent flow along the attachment line are *leading-edge contamination*, which is likely to occur when a swept wing is attached to a solid surface, and *boundary-layer tripping* by large roughness elements. For these problems, one of the relevant parameters is the leading-edge Reynolds number $\overline{R}$ defined as:

$$\overline{R} = W_e \eta / \nu_e \quad \text{with } \eta = (\nu_e/k)^{1/2} \quad \text{and } k = (dU_e/dX)_{X=0}$$

where U_e and W_e are the freestream velocity components normal and parallel to the leading edge, X is the curvilinear distance normal to the attachment line (X = 0), and ν_e is the kinematic viscosity at the boundary-layer outer edge. For low-speed flows, it has been shown from experimental data that leading-edge contamination and boundary-layer tripping by large roughness elements occur as soon as $\overline{R}$ exceeds a critical value close to 250 (Pfenninger 1965, Poll 1978). For compressible flows, $\overline{R}$ is replaced by $\overline{R}^*$ which has the same definition as $\overline{R}$ except that ν_e is replaced by ν^*. The latter quantity is the kinematic viscosity computed at a reference temperature T^*, which may be estimated from the following empirical relationship (Poll 1985):

$$T^* = T_e \, [1 + 0.1 \, (T_w / T_e - 1) + 0.6 \, (T_{aw} / T_e - 1)]$$

T_w and T_{aw} denote the wall temperature and the adiabatic wall temperature, respectively. As demonstrated by Poll (1985), the critical value of $\overline{R}^*$ for leading-edge contamination and boundary-layer tripping by large protuberances remain close to 250 for high-speed flows. The objective of the experiments described below was to check the validity of this criterion for swept cylinders placed in supersonic wind tunnels.

5.2 Experimental Set-up

Two cylinders (diameter D = 4 cm and 6 cm) equipped with a hemispheric nose were tested at various sweep angles φ in the R1 ($M_\infty = 3$) and in the R3 ($M_\infty = 10$) wind tunnels located at the ONERA Chalais Meudon Centre. The models were made of steel and equipped with a row of thermocouples and a row of static pressure taps distributed in the spanwise direction. Rotating the cylinder around its axis made it possible to obtain the wall heat flux and the pressure fields on a large region around the attachment line. Details on the experimental setup in the R3 wind tunnel are provided in Arnal et al. (1991).
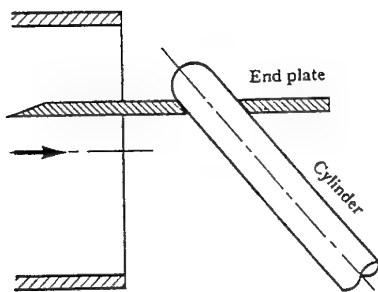
Figure 9. Swept cylinder with end plates: experimental arrangement.

5.3 Leading-Edge Contamination by End Plates

For these experiments, end plates of length L = 0.2m were fixed to the model at the junction between its spherical and its cylindrical parts (Figure 9). These end plates were placed at zero angle of attack with respect to the incoming flow direction. The experiments were conducted in the R1

wind tunnel at Mach 3, with a stagnation temperature around 350K and stagnation pressures between 0.8 and 3 bar. The cylinder of diameter D = 4 cm was used at angles of sweep of 20° and 30°.

As an example of results, Figure 10 shows the variation of the wall heat flux coefficient C_H as a function of $\overline{R}^*$. The theoretical laminar and turbulent values are also plotted for comparison. The measured values increase from the laminar level to the turbulent one for $\overline{R}^*$ around 250, in agreement with the criterion proposed by Poll.
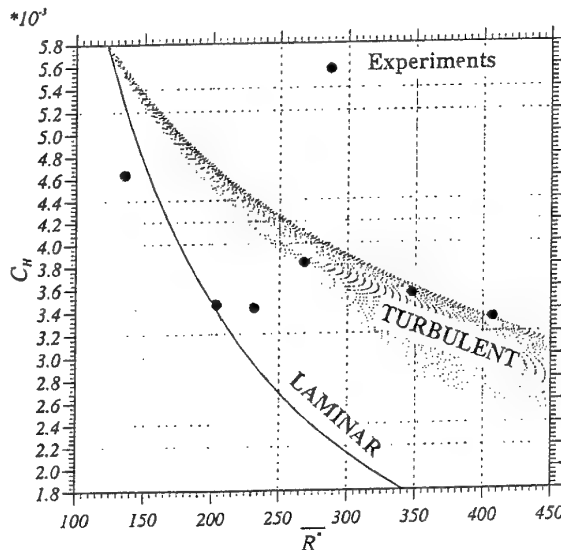
Figure 10. Determination of leading-edge contamination limit.

5.4 Roughness Elements on the Attachment Line

The roughness elements are small steel cylinders (height = diameter = k) which are fixed normal to the model wall. Experiments were conducted both in the R1 and in the R3 wind tunnels with roughness elements located on the attachment line at Z = 1.5 D, Z = 0 corresponding to the junction between the nose and the cylindrical part of the model.

The results obtained in the R3 wind tunnel ($M_\infty = 10$, sweep angles between 20° and 70°, stagnation temperature = 1050K, stagnation pressure = 120 bar) are summarized in Figure 11 in the ($\overline{R}^*$, k/η^*) plane. η^* is the value of η at the reference temperature T^*. The full circles correspond to experiments in which a turbulence starts to develop downstream of the roughness element; the open symbols correspond to cases where the tripping device has no visible effect on the wall heat flux, except in the vicinity of the protuberance. For large ratios of k/η^*, it appears that the tripping becomes effective as soon as $\overline{R}^*$ exceeds a critical value close to 250, which is also the critical value for leading-edge contamination. Similar results have been obtained in the R1 wind tunnel at a much lower Mach number and for completely different wall conditions ($T_w/T_{aw} \cong 0.3$ and 0.9 in the R3 and in the R1 wind tunnels,

respectively). This seems to indicate that, within the experimental uncertainty, the simple criterion $\overline{R}^* = 250$ can be applied to predict the occurrence of transition induced by large disturbances (end plates or roughness elements) for a rather wide range of experimental conditions.
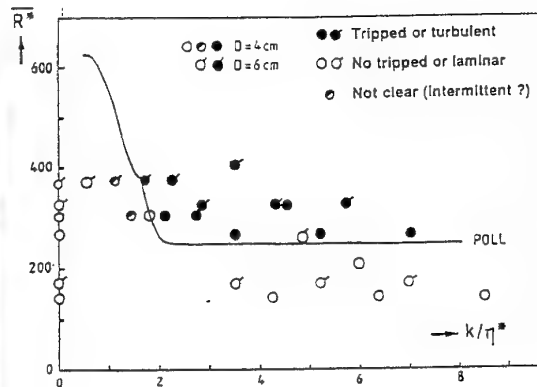

Figure 11. Roughness effects on the attachment line of a swept cylinder.

5.5 Roughness Elements off the Attachment Line

Additional experiments were performed in both wind tunnels by placing the roughness elements at non-zero values of θ_k (θ_k denotes the azimuthal angle of the roughness location, $\theta_k = 0°$ corresponding to the attachment line). The results obtained in the R3 wind tunnel have been already reported (Arnal et al. 1991). The new results obtained at a much lower Mach number in the R1 wind tunnel exhibit the same trend: for given values of $\overline{R}^*$ and k, the efficiency of the roughness element rapidly decreases as soon as the protuberance is slightly displaced off the attachment line. This implies that boundary-layer tripping at non-zero values of θ_k (values of θ_k equal to 5°, 10°, and 15° have been investigated) requires us to increase $\overline{R}^*$ up to values which are larger than 250. In other words, for a constant value of $\overline{R}^*$, the minimum roughness height which is necessary to trigger transition increases with θ_k. As previously stated by Morrisette (1976) and Poll (1985), the attachment line is the location where a laminar boundary layer is the most sensitive to roughness elements. A complete analysis of this phenomenon as observed in the R3 wind tunnel can be found in Arnal et al. (1991).

6. EXPERIMENTAL DATA FOR HYPERSONIC LAMINAR-TURBULENT TRANSITION: EFFECTS OF FACILITY NOISE

6.1 Introduction

It is well known that the high levels of noise present in conventional hypersonic ground-test facilities cause transition to occur earlier than in flight (Beckwith & Miller 1990). Flight measurements of incoming noise are reviewed and compared to measurements in ground-test facilities, of both conventional and quiet design. The low noise present in flight is apparently the reason for the very

large transition Reynolds numbers sometimes measured in flight, when roughness, crossflow, and other factors are controlled. Design will usually involve consideration of the trend in transition when a parameter is varied. The effects of facility noise on these trends is reviewed. In some cases, the trend of conventional-tunnel data is opposite to the trend in quiet-tunnel data. Thus, transition measurements in conventional ground-test facilities are not reliable predictors of flight performance, except perhaps in special cases.

6.2 Noise Levels in Flight and Ground Testing

The sources of disturbances in flight and in ground testing were recently reviewed by Bushnell (1990). These include temperature spottiness, particulates, vorticity fluctuations, and acoustic disturbances. Acoustic disturbances are particularly difficult to remove from ground-test facilities, since high levels of acoustic disturbances are radiated from the turbulent boundary layers normally present on the test-section walls (Laufer 1961). The magnitude of this noise increases with the square of the Mach number, so the effect is much worse in hypersonic facilities as compared to supersonic ones. Pate (1969) showed that transition measurements in conventional tunnels could be correlated by tunnel-wall boundary-layer noise parameters, independent of Mach number. Pate (1978) reviews the data in detail, and concludes that *"if a true Mach number effect exists, it is doubtful it can be determined from data obtained in conventional supersonic/hypersonic wind tunnels because of the adverse effect of radiated noise."* What are the noise levels in flight and in ground-test facilities?

6.2.1 *Measurements of free-air noise in flight*

There are few measurements of noise levels in flight that are carried out at sufficiently high frequencies to be useful for transition studies. The available literature was recently reviewed by Bushnell (1990), who cites 61 references. The primary source is the work of Fisher and Dougherty (1982a,b), who performed measurements with a 5° half-angle cone and a pitot tube, in wind tunnels and in flight. B&K microphones were used for static-pressure measurements at the cone surface, and a Kulite pressure transducer was used for the impact-pressure measurements. The bandwidth for both instruments was roughly 0-25kHz. Both cone and pitot tube were placed ahead of the F-15 aircraft. As might be expected, the rms pressure fluctuations on the pitot tube decrease by a factor of 6 as the Mach number increases from 0.4 to 1.6. This is presumably caused by the inability of aircraft noise to propagate forward in a supersonic flow. At the highest Mach number flown, Mach 2, Table 1 in Fisher (1982b), shows that P′ / $\overline{P}$ was 0.020% for flight 346 and 0.0057% for flight 340. Here, P′ is the rms pitot pressure fluctuation, and $\overline{P}$ is the mean pitot pressure; both flights were at about 38kft. altitude. Fisher (private communication, August 1996) believes that both of these values were obtained with good signal/noise ratio, and that the difference reflects real variations in small-scale turbulence at altitude. The corresponding values of P′/q are 0.058% and 0.016%, where q is the dynamic head. Considerable care was required to achieve these measurements; for example, Fisher commented that it was necessary to require that the pilot not use the radio during periods of data acquisition. Static pressure measurements were obtained on the cone surface

for these same two flights; the values for the forward microphone are $\tilde{P}/q$ = 0.059% and 0.033%, respectively. Fisher and Dougherty compare these flight results for noise and transition on the cone to values measured in various supersonic wind tunnels around the world. They show that the flight noise level is at least 3 times smaller than in the best wind tunnels, even at Mach 2.

Haigh (1972) performed the only hypersonic noise measurements that are known to us. Details are sparse since much of the work is classified. A 10kHz-200kHz microphone was placed flush with the surface of a cone that re-entered the atmosphere at a speed of 7 km/s. Haigh reports that $\tilde{P}/q$ was 0.003 to 0.0055% at transition onset, and 0.055% to 0.09% for "fully turbulent" conditions.

6.2.2 *Measurements of freestream noise in wind tunnels*
Donaldson & Coulter (1995) report measurements of freestream fluctuations carried out at Mach numbers ranging from 4 to 8, in AEDC tunnels A and B. These measurements are less conservative than Fisher's flight data, for the wind-off noise was directly subtracted from the measurements during flow. A direct subtraction assumes complete correlation of the two "random" signals -- a more conservative approach would be to difference the squares of the signals and take the square root (Beckwith et al. 1983). The mass-flow fluctuations at Mach 8 in Tunnel B are about 1-2% of the mean; the total temperature fluctuations are about 0.1% of the mean. The levels measured at Mach 6 are similar. Although the scaling between pitot-pressure fluctuations, mass-flow fluctuations, and static-pressure fluctuations remains unresolved, available data indicates these quantities normalized by their mean values are generally within a factor of 2 (Stainback & Wagner 1972). The high level of mass-flow fluctuations reflects the high levels of acoustic noise radiated from the nozzle walls. These noise levels are 10 to 100 times larger than those measured in flight by Fisher.

6.2.3 *Measurements in quiet wind tunnels*
Quiet wind tunnels have been constructed to reach much lower levels of freestream noise (Beckwith et al. 1990). In these tunnels the fluctuation levels normalized by their averages are reduced to less than 0.1%. However, the clearest indication of quiet flow is the absence of noise radiated from the turbulent spots that form on the wind-tunnel walls when the flow is not quite quiet (Wilkinson et al. 1994, Schneider & Haven 1995). Hypersonic tunnels are considered quiet when such turbulent spots pass by only a small percentage of the time, and the rms fluctuation levels are less than 0.1%. Although the fluctuation level in these tunnels is an order of magnitude smaller than that measured in conventional tunnels, it still appears to be larger than that measured by Fisher in flight. Figure 12 shows that transition Reynolds numbers measured in the Mach 3.5 quiet tunnel are for the first time in the range of flight data (Chen et al. 1989). The "bleed valve closed" data is noisy data obtained with flow through the throat-region suction slot turned off. Also, x_s is the streamwise location of the tip of the cone; a larger percentage of the cone flow is inside the quiet-flow region, when x_s is reduced.
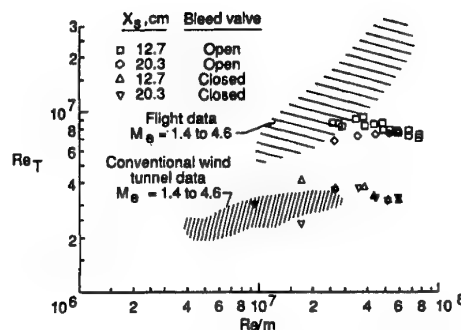
Figure 12. Comparison of transition onset Reynolds numbers for sharp cones at zero angle of attack. From Chen et al. (1989).

6.2.4 *Measurements of freestream noise in shock tunnels*
It is sometimes said that the noise levels in shock tunnels may be lower than in conventional hypersonic wind tunnels (e.g., Holden & Chadwick 1995). This argument is usually made by comparing transition measurements carried out in conventional wind tunnels and flight, and by assuming a particular scaling. Unfortunately, direct measurements of the fluctuation levels in shock tunnels are sparse. Ross (1971) measured heat-transfer fluctuations to a thin-film gauge positioned on a small wedge, at Mach 14, with a bandwidth reported at 800Hz to 1 Mhz. The rms heat transfer divided by the mean ranged from 1.5% to 3%. These measurements are in the same range as those in conventional wind tunnels. This might be expected, since turbulent boundary layers should still form on the nozzle walls, and in addition there are likely to be substantial fluctuations in entropy or stagnation temperature. Bergstrom (1979) reports hot-wire measurements in a Mach-7 gun tunnel, with static-pressure fluctuations of 1-3%. Bergstrom's hot-wire mode diagrams indicated that the primary source of disturbances was the turbulent boundary layer on the nozzle walls (Bergstrom & Raghunathan 1977). No hot-wire or fast pitot-probe measurements of the fluctuations in a shock tunnel are known to us.

6.2.5 *Summary of noise-level data*
For predictions of hypersonic boundary-layer transition in flight one would like to have measurements of the noise levels at appropriate altitudes. Detailed measurements of the spectra of the entropy, vorticity, and acoustic fluctuations are desirable, along with measurements of the particle content and so on. A consistent set of measurements is also needed for ground-test facilities, using a consistent method for determining instrument bandwidth and signal/noise ratio.

Some preliminary conclusions can nevertheless be drawn. Although there is little flight data above Mach 2, the fluctuation level in the atmosphere should not be affected by the (supersonic) speed of the aircraft carrying the measurement device. The key limitation to the Fisher data is rather the limited and poorly understood bandwidth, and the relatively low altitudes. The Fisher data do clearly show that the fluctuation levels present in the atmosphere at short spatial frequencies are very small, and they correspond to pressure-fluctuation levels that are 10 to 100

times smaller than in conventional wind tunnels. Even the "quiet" wind tunnels appear to suffer from fluctuation levels that are larger than in flight.

It is often argued (e.g., Stetson 1990) that most of the freestream noise is not important for instability and transition studies; the only part of significance is said to be that which is at frequencies similar to those of the dominant instabilities on the model. A conventional hypersonic wind tunnel is thus sometimes said to be effectively quiet, since the noise at the high frequencies of the second-mode instability may be small. However, there is at present no direct evidence to substantiate this interesting conjecture. True, the noise measurements in Tunnel B reach a signal-noise ratio of 1 at about 70-200 kHz (Donaldson & Coulter 1995); however, AEDC has not yet reported a quantitative upper bound for the noise in this high-frequency 2nd-mode band, nor has it been shown that this noise does not affect the measurements. In fact, second-mode transition in Tunnel B occurs at an N-factor of about 5 (Kimmel et al. 1996). Although it is possible that this relatively low N-factor is due to the inherent properties of the second-mode transition, or to the relatively large wave amplitude at which it is possible to detect the waves in the ambient noise, it seems more likely that it is caused by the large noise level.

The work of Stetson et al. and also of Kosinov et al. (e.g. Kosinov et al. 1990) is based on the idea that the local growth of the instability waves is affected only by the portion of the noise in the frequency band of the unstable waves; broadband noise outside this frequency band is assumed to have no effect. The problem is clearly very difficult, and measurements based on this assumption clearly are more useful than measurements of transition-onset only. However, the assumption neglects all nonlinear and three-dimensional interactions, whereas 3D interactions in particular have been shown to be significant in low-speed flow (e.g. Watmuff 1997). It would be interesting to see the assumption tested by repeating some of the existing measurements in a different facility with a substantially different noise level, although in this case it might be difficult to rule out the effects of "unit Reynolds number". As Stetson has noted, it is possible that unit Reynolds number effects may be traced to differences in the local boundary-layer profiles which might make the integrated growth of the instability waves scale with something other than the overall length Reynolds number of the model (e.g., temperature effects or transverse curvature). It would seem that quiet-tunnel measurements will be needed to determine the effect of tunnel noise on instability measurements in conventional tunnels.

6.3 Measurements of Transition at High Reynolds Numbers

6.3.1 *Re-Entry F*
This flight test was of a 4-m long beryllium cone with a half-angle of 5° and an initial nose radius of 0.25 cm. Surface heat-transfer and pressure data were obtained during reentry at altitudes ranging from 30.5 to 18.3 km. The heat-transfer data allowed determining both the beginning and the end of transition -- the ratio of the end to the beginning varies from 1.6 to 5.4 with decreasing altitude. The freestream Mach number was about 20, and the ratio of wall temperature to total temperature was about 0.1. The angle-of-attack was controlled within a degree of zero, and the total enthalpy ranged from 18.3 to 16.9 MJ/kg. Length Reynolds numbers at transition, based on edge conditions, ranged from 40 to 60 million at the higher altitudes. Limited e^N computations indicate that transition was dominated by second-mode disturbances (Malik 1989). This excellent and expensive dataset is well-documented in several NASA reports, although distribution of many is limited to U.S. nationals. Wright & Zoby (1977) is the most readily available, although the computations reported there should be rechecked with a modern method. Note in particular that Table I in Wright & Zoby (1977) mislabels the dimensions of the boundary-layer thicknesses as inches, when they are almost certainly actually presented as feet (Zoby, private communication, 1996). This flow has since been recomputed with various modern methods (Thompson et al. 1989), but detailed study of the scaling in these modern solutions has not yet been performed.

6.3.2 *Sternberg V-2 flight test*
This was a cold-wall flight test of a 10° half-angle cone at an angle of attack less than 1 degree, and about Mach 3. The nose radius was small, the cone was more than 2.4 m long, and the wall was cold. The length Reynolds number at transition was more than 40 million (Sternberg 1952).

6.3.3 *Flight tests of re-entry vehicles*
Although much of this literature is classified, some of it is openly available. Haigh et al. (1972) summarizes various flight tests most of which are classified. Haigh's figure 48 shows that some zero angle-of-attack flight data exhibited local length Reynolds numbers at transition that were about 20 million or more. Unfortunately, the open literature apparently contains few details about the Mach numbers, surface roughness, geometry, or wall temperature condition. Figure 27a in reference (Williamson 1992) shows that local arc-length transition Reynolds numbers above 10 million have been measured numerous times. Part (b) of this same figure shows flight data plotted in Re_θ vs. M_e coordinates. Although the typical correlation of $Re_\theta = 150 M_e$ fits the data fairly well, scatter as large as a factor of 4 is sometimes observed.

6.3.4 *Rumsey & Lee flight test*
This cold-wall 1956 flight test of a 7.5° half-angle cone with a 0.25-mm nose diameter exhibited local length transition Reynolds numbers as high as 30 million, at a local Mach number of 2.91 (Rumsey & Lee 1961). The ratio of wall to static temperature was 1.2. Mujeeb Malik (private communication) did some N-factor computations for this flow in 1982-83, and recalls finding very low N-factors at transition (such as 2-3); the results were never published. The roughness was reported at 6-10 microinches rms, according to profilometer measurements.

6.3.5 *Ground tests in NASA Langley Mach 3.5 Quiet Tunnel*
The only comparable high-speed ground test results were obtained in the Mach 3.5 Quiet Tunnel at NASA Langley (Chen et al. 1989). These results were obtained under conditions that were only partially quiet -- only the forward portion of the model was in the quiet-flow region. Transition onset on a flat plate with a nose bluntness of

0.02 mm occurred at length Reynolds numbers as high as 17.9 million (Chen et al. 1988). Transition onset for a 5° half-angle cone occurred as late as 9.1 million; this cone was at zero angle of attack and had a sharp tip. Both these models were studied at adiabatic wall temperatures. A small bluntness would be expected to delay transition further; however, quiet flow can only be maintained in this facility to a length Reynolds number of about 10 million. Thus, the quiet-flow length Reynolds number in this facility is still insufficient to allow duplicating the Rumsey & Lee flight test.

6.3.6 *Other hypersonic ground tests*

Softley et al. (1969) report transition at length Reynolds numbers of 10 million or more, on sharp cones at an edge Mach number of 12 in a shock tunnel, in a residual favorable pressure gradient. Maddalon & Henderson (1968) reported values as high as about 50 million for measurements at an edge Mach number of 16 in the NASA Langley helium tunnel. These length Reynolds numbers are again based on edge conditions. Although it is sometimes argued that these (and other) high transition Reynolds numbers are an indication of relatively low levels of facility noise, the shock-tunnel noise measurements discussed above suggest that a receptivity or instability mechanism must instead be sought. This is directly shown by Fischer & Wagner (1972), who measure high freestream noise levels above a sharp cone in the helium tunnel at NASA Langley, while at the same time measuring transition length Reynolds numbers in the 30-40 million range. The use of local length Reynolds number as an appropriate scaling for hypersonic transition is of course open to question. Adam & Hornung (1997), for example, report measurements at high-enthalphy conditions and Mach 5, on a sharp cone, in T5. Their transition length Reynolds numbers, scaled on edge conditions, were 2-4 million, an order of magnitude below the flight data; but both the T5 measurements and the Re-entry F measurements show transition at length Reynolds numbers of about 1 million when based on the reference temperature. In view of the differing Mach number, the difference in wall temperature, and the high noise levels in T5, this agreement is probably fortuitous. The comparison points out clearly how flight and ground tests carried out under different conditions can appear to agree or disagree depending on the scaling chosen.

6.3.7 *Summary of high-Reynolds number transition data*

It is clearly possible to delay transition in flight to very high Reynolds numbers, when roughness, crossflow, ablation, and other effects are controlled appropriately. It is also possible to achieve high transition Reynolds numbers in ground tests (especially in the helium tunnel). Noise levels are clearly a significant factor in ground tests, so transition Reynolds numbers reported without measurements of freestream noise levels are of limited value. The 50-year search for a single correlating parameter that will reconcile the various flight and ground-test measurements appears futile, in view of the many factors influencing transition.

6.4 The Effect of Tunnel Noise on Parametric Trends in Transition Location

6.4.1 *Ratio of transition Reynolds numbers for cones and flat plates*

Although an e^N estimation suggests that transition should occur on flat plates at length Reynolds numbers higher than those on round cones, measurements in conventional wind tunnels consistently showed the opposite behavior (Chen et al. 1989). Figure 13 shows a correlation from conventional-tunnel data, along with measurements in the Langley quiet tunnel. When the bleed valve is closed, the Langley tunnel becomes noisy, yet even in this case the results are substantially different from those measured in conventional tunnels. Figure 14 shows the comparison to e^N theory, along with a few measurements from conventional tunnels. These quiet-tunnel results did much to validate the e^N approach.
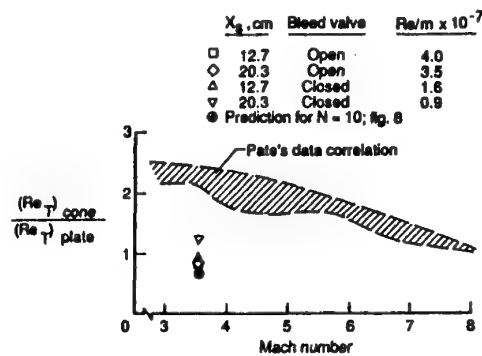
Figure 13. Ratios of cone-to-flat-plate transition Reynolds numbers from Pate, compared to quiet-tunnel data and linear stability theory predictions. From Chen et al. (1989).
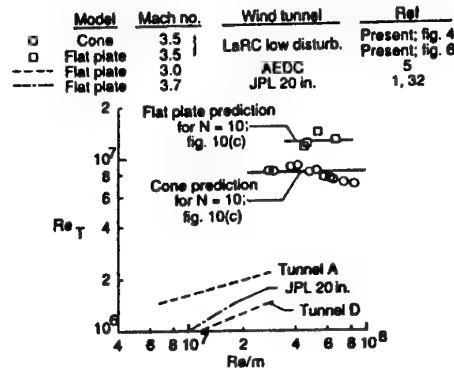
Figure 14. Comparison of transition-onset Reynolds numbers on cone and flat plate. From Chen et al. (1989).

Note that a designer relying on the conventional-tunnel data in Figure 13 would seek to create a conical forebody, in order to delay transition; only with quiet tunnel data does the designer now see that the flat-plate geometry is to be preferred. The cause of the anomaly in the conventional-tunnel data is addressed by Stetson & Kimmel (1992).

6.4.2 *Bluntness effects are influenced by noise levels*
Figure 15, taken from Beckwith et al. (1990), shows transition Reynolds numbers measured on flat plates in various wind tunnels with various bluntnesses. The highest-noise data, from the conventional tunnels at AEDC, shows not only the lowest transition Reynolds number, but the strongest effect of bluntness. Noise affects not only the levels of the curves but the slope. The quantitative significance of the effect remains unclear; for example, Stetson has commented that the slopes are fairly similar except for the Tunnel D data. See Pate (1978) for a detailed discussion of the AEDC data.
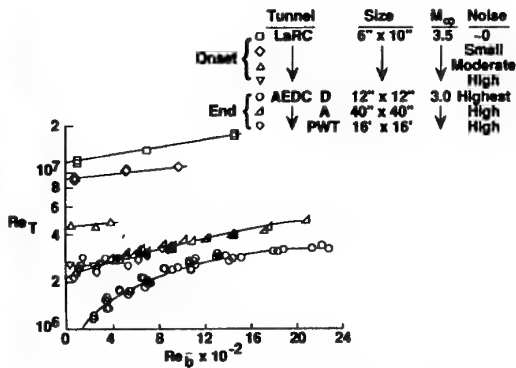
Figure 15. Effects of noise levels and leading-edge bluntness on flat plate transition. From Beckwith et al. (1990).

6.4.3 *Effect of noise on roughness and waviness effects*
The limited data of Morrisette et al. (1986) showed little effect of surface waviness for transition on round cones at zero angle of attack. In their measurements in the Mach 3.5 quiet tunnel at Langley, transition moved forward about 20% when a surface waviness with height/length ratio of 0.01 was introduced. Morrisette et al. also showed that the trends appeared similar with high and low levels of tunnel noise.
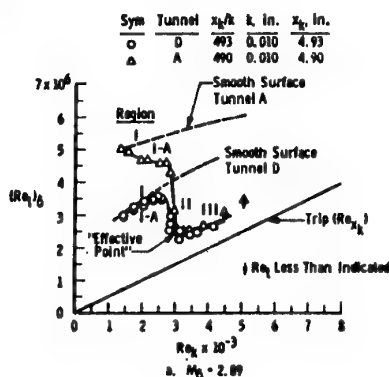
Figure 16. Variation of transition Reynolds number with trip Reynolds number for $M_c = 2.89$, Tunnels D and A. From Pate (1971).

Figure 10a from Pate (1971), reproduced here as Figure 16, shows the effect of tunnel noise on roughness effects, for a round cone at zero angle of attack with hemispherical

roughness elements. Although tunnels A and D are both conventional, the noise level in tunnel A should be smaller since it is larger. The figure shows that for smooth models transition indeed occurs later in tunnel A. However, it also shows that the parametric effect of roughness also enters differently. As the roughness Reynolds number Re_k is increased, there is a gradual forward movement of transition in tunnel A, while transition moves aft in tunnel D (region I-A). At an Re_k of about 2500, transition moves suddenly forward in tunnel D, with the same sudden movement occuring in tunnel A at a slightly higher Reynolds number. The 10% forward movement of transition that occurs in tunnel A for Re_k between 1000 and 2500 is *opposite* to the 20% rearward movement that occurs in tunnel D. What variation would occur under the much lower noise conditions expected in flight?

For roughnesses large enough to cause transition directly at the roughness element ("effective" roughnesses), it appears that noise has little effect. However, in case of design for flight what is needed is a specification of the roughness which will not move transition forward too far; this roughness will not be an "effective" roughness, and the level of noise in a ground-test facility can have a major influence on the determination of these kinds of roughness effects. *It is the ambient noise levels interacting with the roughness which cause transition - both are in general important.* This has been clearly shown in various low-speed receptivity experiments (e.g., Wlezien 1994). Figure 17 shows low-speed data collected by Dryden (1959), in which the effect of freestream noise on roughness effects is clearly demonstrated. Dryden states that this data "disprove" his earlier and often-quoted hypothesis that transition Reynolds number depends on roughness Reynolds number alone (Dryden 1953).
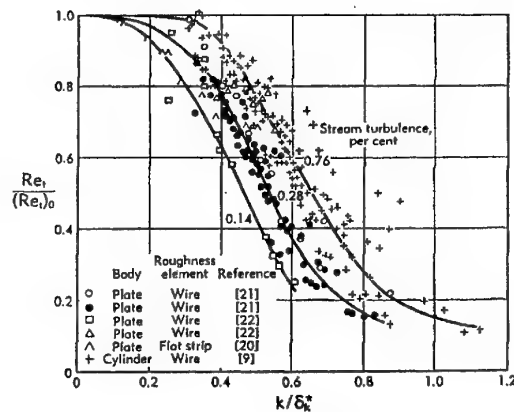
Figure 17: Ratio of transition Reynolds number for a plate with single roughness element to that for a smooth plate in air streams of different turbulence. From Dryden (1959), his reference numbers, his fig. A,5h.

Preliminary measurements of roughness effects were also carried out by Morrisette & Creel (1987), in the NASA Langley Mach 3.5 quiet tunnel. These showed that noise changed the critical roughness height of hemispherical elements by only 10%, so the sparse available data are not clearcut.

6.4.4 *Effect of noise on transition extent*

A last example, taken from Chen (1993), shows the effect of noise on measurements of transition extent (the length of the region of intermittent flow between the onset of transition and its end). Figure 18 shows measurements for a round cone at zero angle of attack; the aft end of the cone is outside the quiet flow region. At the highest unit Reynolds number, at noisy conditions with the bleed valve closed, transition onset occurs at about half the distance to the end of transition. This is typical of measurements in conventional wind tunnels (Kimmel 1993). Under low noise conditions, with the bleed valve open, at the same unit Reynolds number, transition onset occurs at about 70% of the distance to the end of transition. This trend, of transition onset occuring closer to the point where transition is complete as noise decreases, appears to agree with the flight measurements of Fisher (1982a), who shows transition onset occurring at about 85% of the length to transition end.
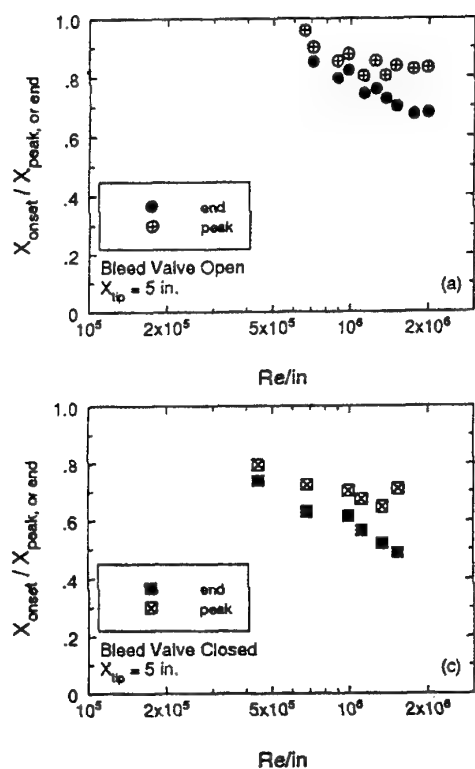
Figure 18. Ratios of transition locations measured on a sharp cone. From Chen (1993).

6.5 Summary of Noise Effects

Since laminar-turbulent transition is affected by a substantial number of parameters, reliable estimates of transition must be based on an understanding of the relevant mechanisms. Since variation in noise levels can have dramatic effects on transition, experimental measurements should be carried out at noise levels comparable to those in flight. Most quiet-tunnel experiments to date have only measured transition locations, however. Just as in the low-speed case, detailed measurements of the mechanisms of transition under controlled conditions will be required, if reliable prediction methods are to be developed.

8. REFERENCES

Adam, P.H. and H.G. Hornung, "Enthalpy effects on hypervelocity boundary layer transition: experiments and free flight data", AIAA Paper 97-0764, 1997.

Arnal, D., "Predictions based on linear theory", AGARD Rep. No. 793 (Special course on progress in transition modelling), Von Kármán Inst., Rhode-St.-Genese, Belg., 1994.

Arnal, D., E. Kufner, I. Oye, and Ph. Tran, "PROGRAMME TRP TRANSITION: computational results for transition prediction", Study Note 7, 1996.

Arnal, D., F. Vignau, and F. Laburthe, "Recent supersonic transition studies with emphasis on the swept cylinder case", Conf. on Boundary Layer Transition and Control, Cambridge, April 1991.

Beckwith, I.E., T.R. Creel, F.-J. Chen, and J.M. Kendall, "Freestream noise and transition measurements on a cone in a Mach 3.5 pilot low-disturbance tunnel", NASA TP-2180, 1983.

Beckwith, I.E. and C.G Miller III, "Aerothermodynamics and transition in high-speed wind tunnels at NASA Langley", Annual Reviews of Fluid Mechanics, v. 22, pp. 419-439, 1990.

Beckwith, I., F. Chen, S. Wilkinson, M. Malik, and D. Tuttle, "Design and operational features of low-disturbance wind tunnels at NASA Langley for Mach numbers from 3.5 to 18", AIAA Paper 90-1391, 1990.

Bergstrom, E.R. and S. Raghunathan, "Nonstationarity in gun tunnel flows", AIAA Journal v. 15 n. 9, pp. 1362-1364, September 1977.

Bergstrom, E.R., "A correlation of Mach-7 boundary layer transition data from the Loughborough gun tunnel", Report TT-7904, Loughborough Univ. of Technology, October 1979. Available from NASA STI as citation 80N28332.

Bestek, H., A. Thumm, and H.F. Fasel, "Numerical investigation of later stages of transition in transonic boundary layers", First European Forum on Laminar Flow Technology, 16-18 March, Hamburg, Germany, 1992a.

Bestek, H., A. Thumm, and H.F. Fasel, "Direct numerical simulation of the three-dimensional breakdown to turbulence in compressible boundary layers", 13th International Conference on Numerical Methods in Fluid Dynamics, 6-10 July, Rome, Italy, 1992b.

Burke, G. L., "Heat transfer and pressure distributions about sharp and blunt elliptic cones at angles of attack and high Mach numbers", Air Force Flight

Dynamics Laboratory Technical Report AFFDL-TR-64-172, May 1965.

Burns, K. A., K.J. Deters, C.P. Haley, and T.A. Khilken, "Viscous effects on complex configurations", Air Force Wright Laboratory Technical Report WL - TR-3059, August 1995.

Bushnell, D.M., "Notes on the initial disturbance fields for the transition problem", in Instability and Transition, vol. I, ed. by M.Y. Hussaini and R.G. Voigt, Springer-Verlag, pp. 217-232, 1990.

Cattafesta, L. N., V. Iyer, J.A. Masaad, R.A. King, and J.R. Dagenhart, "Three-dimensional boundary-layer transition on a swept wing at Mach 3.5", AIAA Journal, v. 33, n. 11, pp. 2032-2037, November 1995.

Chang, C.-L. and M.R. Malik, "Non-parallel stability of compressible boundary layers", AIAA Paper 93-2912, 1993.

Chen, F.-J., M.R. Malik, and I.E. Beckwith, "Comparison of boundary layer transition on a cone and flat plate at Mach 3.5", AIAA Paper 88-0411, 1988.

Chen, F.-J., M.R. Malik, and I. E. Beckwith, "Boundary-layer transition on a cone and flat plate at Mach 3.5", AIAA Journal v. 27 n. 6, pp. 687-693, June 1989.

Chen, F.-J., "Boundary-layer transition extent measurements on a cone and flat plate at Mach 3.5", AIAA Paper 93-0342, 1993.

Demetriades, A., "Hydrodynamic stability and transition to turbulence in a hypersonic boundary layer over a sharp cone", Air Force Office of Scientific Research AFOSR TR-75-1435, July 1975.

Donaldson, J. and S. Coulter, "A review of freestream flow fluctuation and steady-state flow quality measurements in the AEDC/VKF supersonic tunnel A and hypersonic tunnel B", AIAA Paper 95-6137, 1995.

Dryden, H. L., "Review of published data on the effect of roughness on transition from laminar to turbulent flow", J. Aero. Sci., vol. 20, pp. 477-482, July 1953.

Dryden, H. L., "Transition from laminar to turbulent flow", pp. 3-74 in "Turbulent flows and heat transfer", vol. V in the series on High Speed Aerodynamics and Heat Transfer, Princeton Univ. Press, 1959, edited by C.C. Lin.

Finley, D., "Hypersonic aerodynamics considerations and challenges", AIAA Paper 90-5222, 1990.

Fischer, M. C., "Turbulent bursts and rings on a cone in helium at Me=7.6", AIAA Journal, v. 10, n. 10, pp. 1387-1389, October 1972.

Fischer, M.C. and R.D. Wagner, "Transition and hot-wire measurements in hypersonic helium flow", AIAA Journal v. 10, n. 10, pp. 1326-1332, October 1972.

Fisher, D.F. and N.S. Dougherty, Jr., "Flight and wind-tunnel correlation of boundary-layer transition on the AEDC transition cone", paper 5 in AGARD CP-339, Ground/Flight Test Techniques and Correlation, A symposium held at Cesme, Turkey, October 1982. Also NASA TM 84902, November 1982a.

Fisher, D.F. and N.S. Dougherty, Jr., "In-flight transition measurement on a 10-deg. cone at Mach numbers from 0.5 to 2.0", NASA TP-1971, 1982b.

Gasperas, G., "Stability of the laminar boundary layer for an imperfect gas", in Laminar-Turbulent Transition, ed. D. Arnal, R. Michel, pp. 291-302. Berlin: Springer-Verlag, 1990.

Haigh, W.W., B.M. Lake, and D.R.S. Ko, "Analysis of flight data on boundary layer transition at high angles of attack", NASA CR-1913, April 1972.

Haynes, T.S., H.L. Reed, and W.S. Saric, "CFD validation and verification questions in transition modelling", AIAA Paper 96-2051, 1996.

Herbert, Th., "Parabolized stability equations", Annual Review of Fluid Mechanics, v. 29, p. 245-284, 1997.

Herbert, Th., G.K. Stuckert, and N. Lin, "Method for transition prediction in high-speed boundary layers", Air Force Wright Laboratory WL-TR-93-3097, 1993.

Holden, M.S., D.R. Bower, and K.M. Chadwick, "Measurements of boundary layer transition on cones at angle of attack for Mach numbers from 11 to 13", Calspan-University of Buffalo Research Center Report to University of Dayton Research Institute, May 1994.

Holden, M. and K. Chadwick, "Studies of laminar, transitional, and turbulent hypersonic flows over curved compression surfaces", AIAA Paper 95-0093, 1995.

Kendall, J. M., "Wind tunnel experiments relating to supersonic and hypersonic boundary-layer transition", AIAA Journal, Vol. 13, No. 3, 1975, pp. 290-299; also AIAA Paper 74-133, 1974.

Kendall, J. M., "Boundary layer receptivity to freestream turbulence", AIAA Paper 90-1504, 1990.

Kimmel, R.L., "Experimental transition zone lengths in pressure gradient in hypersonic flow", in Transitional and Turbulent Compressible Flows, ASME FED v. 151, pp. 117-127, 1993.

Kimmel, R. L. and J. Poggie, "Disturbance evolution / breakdown to turbulence in a hypersonic boundary layer: ensemble averaged structure", AIAA Paper 97-0555, 1997a.

Kimmel, R. L. and J. Poggie, "Transition on an elliptic cone at Mach 8", ASME Third Symposium on Transitional and Turbulent Compressible Flows, 1997b.

Kimmel, R.L., S.N. Schwoerke, and M.A. Klein, "Three-dimensional hypersonic laminar boundary layer computations for transonic experiment design", AIAA Paper 96-2080, 1996.

King, R.A., "Mach 3.5 boundary layer transition on a cone at angle of attack", AIAA Paper 91-1804, 1991:

King, R.A., "Mach 3.5 boundary layer transition on a cone at angle of attack", AIAA Paper 91-1804, 1991.

Kleiser, L. and T.A. Zang, "Numerical simulation of transition in wall-bounded shear flows", Annual Review of Fluid Mechanics, v. 23, pp. 495-537, 1991.

Kosinov, A.D., A.A. Maslov, and S.G. Shevelkov, "Experiments on the stability of supersonic laminar boundary layers", Journal of Fluid Mech., v. 219, pp. 621-633, 1990.

Lachowicz, J.T., N. Chokani, and J.P. Wilkinson, "Hypersonic boundary layer stability over a flared cone in a quiet tunnel", AIAA Paper 96-0782, 1996.

Laufer, J., "Aerodynamic noise in supersonic wind tunnels", J. Aero. Sci., v. 28, pp. 685-692, Sept. 1961.

Lyttle, I.J. and H.L. Reed, "Use of transition correlations for three-dimensional boundary layers within hypersonic flows", Second Symposium on Transitional and Turbulent Compressible Flows, 1995 Joint ASME/JSME Fluids Engineering Conference, August 1995.

Mack, L.M., "Boundary-layer linear stability theory", Special Course on Stability and Transition of Laminar Flows, edited by R. Michel, AGARD Report No. 709, pp. 3-1 to 3-81, 1984.

Mack, L.M., "Boundary-layer stability analysis for sharp cones at zero angle-of-attack", Air Force Wright Aeronautical Laboratory Technical Report AFWAL-TR-86-3022, Aug. 1986.

Maddalon, D.V. and A. Henderson Jr., "Boundary-layer transition on sharp cones at hypersonic Mach numbers", AIAA Journal v. 6, n. 3, pp. 424-431, March 1968.

Malik, M.R., "Prediction and control of transition in hypersonic boundary layers", AIAA Paper 87-1414, 1987.

Malik, M.R., "Transition in hypersonic boundary layers", in Numerical and Physical Aspects of Aerodynamic Flows IV, ed. T. Cebeci. New York: Springer, 1989.

Malik, M.R., "Stability theory for chemically reacting flows", in Laminar-Turbulent Transition, ed. D. Arnal, R. Michel, pp. 251-60. Berlin: Springer-Verlag, 1990.

Malik, M.R., T. Zang, and D.M. Bushnell, "Boundary layer transition in hypersonic flows", AIAA Paper 90-5232, 1990.

Morrisette, E.L., "Roughness induced transition criteria for space shuttle-type vehicles", Journal of Aircraft, v. 13, n. 2, 1976.

Morrisette, E.L., T.R. Creel, and F.-J. Chen, "Effects of cone surface waviness on transition in quiet and noisy supersonic freestreams", AIAA Paper 86-1086, 1986.

Morrisette, E.L. and T. R. Creel, "The effects of wall surface defects on boundary-layer transition in quiet and noisy supersonic flow", in Research in Natural Laminar Flow and Laminar Flow Control, NASA CP-2487, part 3, pp. 965-980, 1987.

Murrow, H.N., W.E. McCain, and R. Rhyne, "Power spectral measurements of clear-air turbulence to long wavelengths for altitudes up to 14,000 meters", NASA TP-1979, 1982.

Owen, F.K. and C.C. Horstman, "Hypersonic transitional boundary layers", AIAA Journal, v. 10, n. 6, pp. 769-775, 1972.

Pate, S.R. and C.J. Schueler, "Radiated aerodynamic noise effects on boundary-layer transition in supersonic and hypersonic wind tunnels", AIAA Journal, v. 7, n. 3, pp. 450-457, March 1969.

Pate, S.R., "Supersonic boundary-layer transition: effects of roughness and freestream disturbances", AIAA Journal v. 9, n. 5, pp. 797-803, May 1971.

Pate, S.R., "Dominance of radiated aerodynamic noise on boundary-layer transition in supersonic/ hypersonic wind tunnels", AEDC-TR-77-107. DTIC citation AD-A052621, March 1978.

Pfenninger, W., "Flow phenomena at the leading edge of swept wings", AGARDograph 97, Part 4, 1965.

Poggie, J. and R.L. Kimmel, "Disturbance evolution / breakdown to turbulence in a hypersonic boundary layer: instantaneous structure", AIAA Paper 97-0556, 1997.

Poll, D.I.A., "Some aspects of the flow near a swept attachment line with particular reference to boundary layer transition", Technical Report 7805/K, Cranfield, College of Aeronautics, 1978.

Poll, D.I.A., "Boundary layer transition on the windward face of space shuttle during reentry", AIAA Paper 85-0899, 1985.

Pruett, C.D. and C.-L. Chang, "Spatial direct numerical simulation of high-speed, boundary-layer flows part II: transition on a cone in Mach 8 flow", Theoretical and Computational Fluid Dynamics, v. 7, n. 5, pp. 397-424, 1995.

Pruett, C.D. and T.A. Zang, "Direct numerical simulation of laminar breakdown in high-speed, axisymmetric boundary layers", Theoretical and Computational Fluid Dynamics, v. 3, n. 6, pp. 345-367, 1992.

Reed, H.L., "Direct numerical simulation of transition: the spatial approach", AGARD Rep. No. 793 (Special course on progress in transition modelling), Von Kármán Inst., Rhode-St.-Genese, Belg., 1994.

Reed, H.L. and T.S. Haynes, "Transition correlations in 3-D boundary layers", AIAA Journal, v. 32, pp. 923-29, 1994.

Reed, H.L., W.S. Saric, and D. Arnal, "Linear stability theory applied to boundary layers", Annual Review of Fluid Mechanics, v. 21, pp. 235-284, 1996.

Reshotko, E., "Stability theory as a guide to the evaluation of transition data", AIAA Journal, v. 7, n. 6, pp. 1086-1091, 1969; also AIAA Paper 68-669, 1968.

Ross, D.H., J.W. Ellinwood, and R.L. Varwig, "Hypersonic shock tunnel transition studies", paper 8 in the Proceedings of the Boundary Layer Transition Workshop Held 3-5 November 1971, ed. by W.D. McCauley, Aerospace Corp. Report TOR-0172(S2816-16)-5, accession number AD909223 in the Defense Technical Information Center of the USA, also NASA Recon citation 91N71710, 1971.

Rumsey, C.B. and D.B. Lee, "Measurements of aerodynamic heat transfer and boundary-layer transition on a 15-degree cone in free flight at supersonic Mach numbers up to 5.2", NASA TN-D-888, August 1961. Supersedes NACA RM L56F26.

Schneider, S.P. and C.E. Haven, "Quiet-flow Ludwieg tube for high-speed transition research", AIAA Journal, v. 33, n. 4, pp. 688-693, April 1995.

Small, W.J., F.S. Kirkham, and D.E. Fetterman, "Aerodynamic characteristics of a hypersonic transport configuration at Mach 6.86", NASA Technical Note NASA TN D-5885, June 1970.

Softley, E.J., B. C. Graber, and R. E. Zempel, "Experimental observation of transition of the hypersonic boundary layer", AIAA Journal, v. 7, n. 2, pp. 257-263, February 1969.

Spina, E.F., J.F. Donovan, and A.J. Smits, "On the structure of high-Reynolds-number supersonic

turbulent boundary layers", Journal of Fluid Mechanics, v. 222, pp. 293-327, 1991.

Stainback, P.C. and R.D. Wagner, "A comparison of disturbance levels measured in hypersonic tunnels using a hot-wire anemometer and a pitot pressure probe", AIAA Paper 72-1003, 1972.

Sternberg, J., "A free-flight investigation of the possibility of high Reynolds number supersonic laminar boundary layers", J. Aero. Sci., v. 19, n. 11, pp. 721-733, November 1952.

Stetson, K.F., "Mach 6 experiments of transition on a cone at angle of attack", J. Spacecraft Rockets, v. 19, n. 5, pp. 397-403, 1982.

Stetson, K.F., "Hypersonic transition testing in wind tunnels", in "Instability and Transition", Proceedings of a Workshop held in Hampton, VA, May 1989, volume I, edited by M.Y. Hussaini and R.G. Voigt, Springer-Verlag, New York, pp. 91-100, 1990.

Stetson, K.F. and R.L. Kimmel, "On hypersonic boundary-layer stability", AIAA Paper 92-0737, 1992.

Stetson, K.F., E.R. Thompson, J.C. Donaldson, and L.G. Siler, "Laminar boundary layer stability experiments on a cone at Mach 8 - Part 2: blunt cone", AIAA Paper 84-0006, 1984.

Stetson, K.F., E.R. Thompson, J.C. Donaldson, and L.G. Siler, "Laminar boundary layer stability experiments on a cone at Mach 8 - Part 3: sharp cone at angle of attack", AIAA Paper 85-0492, 1985.

Stetson, K.F., E.R. Thompson, J.C. Donaldson, and L.G. Siler, "Laminar boundary layer stability experiments on a cone at Mach 8 - Part 4: on unit Reynolds number and environmental effects", AIAA Paper 86-1087, 1986.

Stuckert, G.K., "Linear stability theory of hypersonic, chemically reacting viscous flows", Ph.D. Dissert. Dept. Mech. Aerosp. Eng., Ariz. State Univ., Tempe, USA, 1991.

Stuckert, G.K. and H.L. Reed, "Linear disturbances in hypersonic, chemically reacting shock layers", AIAA J., v. 32, n. 7, pp. 1384-93, 1994.

Thompson, R.A., E.V. Zoby, K.E. Wurster, and P.A. Gnoffo, "Aerothermodynamic study of slender conical vehicles", J. of Thermophysics and Heat Transfer", v. 3, n. 4, pp. 361-367, October 1989.

Thumm, A., W. Wolz, and H.F. Fasel, "Numerical simulation of spatially growing three-dimensional disturbance waves in compressible boundary layers", in Laminar-Turbulent Transition, (Arnal, D. and Michel, R., eds.), Springer-Verlag, Berlin, 1990.

Tran, Ph., A. Seraudie, V. Wendt, and D.I.A. Poll, "PROGRAMME TRP TRANSITION: experimental results for transition prediction", Study Note 6, 1995.

Watmuff, J.H., "Interactions between Klebanoff modes and TS waves in a Blasius boundary layer", AIAA Paper 97-0558, 1997.

Wilkinson, S.P., S.G. Anders, F.-J. Chen, and J.A. White, "Status of NASA Langley quiet-flow facility developments", AIAA Paper 94-2498, 1994.

Williamson, W.E., "Hypersonic flight testing", AIAA Paper 92-3989, 1992.

Wlezien, R.W., "Measurement of acoustic receptivity", AIAA Paper 94-2221, 1994.

Wright, R. L. and E.V. Zoby, "Flight boundary layer transition measurements on a slender cone at Mach 20", AIAA Paper 77-719, 1977.

Zhong, X., "Direct numerical simulation of hypersonic boundary-layer transition over blunt leading edges, Part II: Receptivity to sound", AIAA Paper 97-0756, 1997.

Heat Loads in Hypersonic Vehicle Design

E.H. Hirschel
Daimler-Benz Aerospace AG
81663 München
Germany

SUMMARY

Heat load of hypersonic vehicles flying in the earth atmosphere at speeds below 8 km/s are considered. The general aspects are discussed, definitions are given. Surface-radiation-cooling as the basic cooling mode is investigated, related peculiarities are explained. It is shown that heat loads are not only of interest for the materials and structure layout, but that strong couplings in both directions exist with the aerodynamic shape and the aerodynamic performance. The heat-loads oriented design as a perspective is discussed. Finally an overview over the status and the development needs of the prediction and verification capabilities is given.

1. INTRODUCITON

Heat loads are a major issue in hypersonic vehicle design, Ref. 1. They concern all outer (airframe flow path) and inner (propulsion flow path) surfaces, are major selection and dimension drivers for the materials & structures concept, and influence strongly the aerodynamic performance and the aerodynamic airframe/propulsion integration especially of airbreathing vehicles.

The implications for cold primary (load bearing) structures with a heat protection system (TPS), which is typical for "classical" winged (rocket propelled) (ascent/) re-entry-vehicle airframes, are quite different from those for hot primary structures without TPS (but with internal insulation). The latter are candidates for airbreathing launch or sustained flight vehicles. In reality, however, these two basic structure concepts will always be mixed to a certain degree.

In this paper the qualitative and the quantitative aspects of heat loads on vehicles flying in the earth atmosphere at speeds below 8 km/s are discussed. Qualitative aspects are important for the designer in order to understand the problems and implications of heat loads for the vehicle. The quantitative aspects, of course, are important for the actual prediction of heat loads and the sizing of the vehicle in the most general sense. Details like for instance the classical correlations et cetera, see e.g. Ref. 2, are not considered and reviewed in this paper.

The paper is structured in the following way. Chapter 2 is devoted to general considerations and definitions. Surface-radiation cooling as basic cooling mode is discussed in Chapter 3. Heat loads and vehicle design is the topic of Chapter 4 Finally in Chapter 5 an overview over the status and the development needs of the prediction and verification capabilities is given.

2. HEAT LOADS: GENERAL CONSIDERATIONS

"Heat loads" is a term, which describes the thermal state of the vehicle surface. It has two major aspects. The first is the wall temperature, the other the heat flux into (or out of) the wall. These two aspects must always be considered together, because to speak only about one of them does not give the full picture. A wall temperature can exist with at the same time zero or very large heat flux, a heat flux into (or out of) the wall can exist at any wall temperature level.

The (maximum) wall temperature at a given surface portion on the trajectory of the vehicle is determining the material limit (strength, integrity, erosion). The heat flux into the wall determines the heat penetration depth (as function of the trajectory), which sizes the thickness (and internal structure) of the heat protection system of a cold primary structure. If a hot primary structure without TPS is considered, the heat flux into the wall leads to heat induced stresses and deformations (both to be handled by an appropriate topology of the structure), and determines the internal insulation (penetration depth). In reality very particular design problems can be present, for instance if a load bearing (integral) cryo tank solution is pursued.

Depending on the speed of the vehicle, heat loads can be very large, with very large surface temperatures as the result. In view of the fact that no material exist, which can stand temperatures of more than approximately 2000 K, a heat loads alleviation becomes necessary already at speeds of 1 to 2 km/s (M > 3 to 5), depending on the materials & structures concept. This concept should always be the lightest and cheapest concept with the smallest technological risks, easy and inexpensive to manufacture and to support in operation (operation and life cycle costs).

The basic heat-loads alleviation mode is surface-radiation cooling. At flight below approximately 8 km/s in the earth atmosphere it is also the only radiative transport mode of energy, i.e. emission and absorption of radiative energy in the flow around the vehicle can be neglected. Of course, depending on the vehicle shape, which depends on the mission type (aeroassisted re-entry only/aero-assisted ascent (and re-entry)/sustained hypersonic flight) additional active cooling might be needed. If a full reusability is demanded, this will be accomplished by heat pipes, regenerative cooling et cetera. The target temperature in this case will be determined (again) by the respective material limit. Surface-radiation cooling indeed is one of the most effective cooling means and is employed as long as high-speed vehicles exist. This is illustrated with Fig. 1 for the HERMES vehicle, Ref. 3. The computations were made with a coupled Euler/second-order boundary-layer

code, Ref. 4. The maximum temperature reduction of about 4000 K occurs at approximately 70 km altitude.

The different aspects of heat loads are put together in Fig. 2. For the detailed discussion see Ref. 5. Here it is only noted that in vehicle design in general the following aspects of heat loads are considered:

o vehicle definition

- outer surfaces: radiation-adiabatic temperature T_n as conservative temperature estimation,
- inner surfaces: recovery temperature T_r as conservative temperature estimation,

o vehicle development

- actual T_w ($< T_n$, T_r),
- actual heat flux q_w.

Accordingly the materials & structure concept is selected and sized, and if necessary active cooling means are devised.

In closing this chapter a topic is mentioned, which has not found much attention sofar: the low speed flight after prolonged high speed flight with a surface temperature larger than the actual recovery temperature. This can be of importance for vehicles with hot primary structures, and for the low speed aerodynamic properties of high-speed vehicles in general.

3. SURFACE RADIATION COOLING AS BASIC COOLING MODE

Surface-radiation cooling in the past was more a concern of structural airframe design, because winged re-entry vehicles are in general not drag critical. The recent technology work for airbreathing launch vehicles has shown, that strong implications exist for the whole vehicle design., Refs. 5, 6. A simple local one-dimensional consideration, Ref. 5, reveals basic insight into the aerothermodynamics of radiation-cooled surfaces. The radiation-adiabatic case is given by (see Fig. 2)

$$q_w = 0 = q_{gw} + q_r. \qquad (1)$$

From this, see Ref. 5, the proportionality relation

$$T_{ra}^4 \sim \frac{k}{\sigma \varepsilon} \frac{T_r}{\Delta} \left(1 - \frac{T_{ra}}{T_r}\right), \qquad (2)$$

can be derived, with k the heat conductivity, σ the Stefan-Boltzmann constant, ε the surface radiation emissivity, and Δ a characteristic boundary-layer length.

Assuming a planar surface, Δ being the temperature boundary-layer thickness δ_T, and neglecting the influence of the wall temperature on the boundary-layer thickness, relation (2) can be rewritten to

$$T_{ra}^4 \sim \frac{k}{\sigma \varepsilon} Pr^n \frac{Re_L^{1-n}}{(x/L)^n} \frac{1}{L} T_r \left(1 - \frac{T_{ra}}{T_r}\right); \qquad (3)$$

with Pr the Prandtl number, $Re_L = \rho_\infty u_\infty L / \mu_\infty$ the flight Reynolds number, L the characteristic body length, x the downstream axis coordinate ($0 \le x/L \le 1$), and n = 0.5 for laminar flow, n = 0.2 for turbulent flow. Generalized relations, also for vehicle noses and leading edges, can be found in Refs. 5 and 7.

A term by term consideration of relations (3) and (4) reveals that the radiation-adiabatic temperature is inversely proportional to the emissivity, the characteristic boundary-layer thickness, the characteristic body length, direct proportional to the Reynolds number (equivalent to the $1/\Delta$ proportionality), to the recovery temperature, and reduces from the tip to the tail with $(x/L)^{-n}$.

For the vehicle design this means (see also the general relations and discussions in Ref. 5):

- On planar surfaces T_n^4 is inversely proportional to the boundary-layer thickness,

- different boundary-layer thicknesses on windward and leeward side lead to heat-loads differentials,

- at a nose with the boundary-layer thickness $\delta \sim \sqrt{R}$, T_{ra}^4 is inversely proportional to the square root of the nose radius R, of course like the heat-flux relation of Fay and Ridell, Ref. 8,

- at leading edges the boundary-layer thickness is $\delta \sim \sqrt{R} / \sqrt{\cos \varphi}$ (φ : sweep angle), and hence $T_{ra}^4 \sim \sqrt{\cos \varphi} / \sqrt{R}$,

- at attachment lines, where the flow diverges, the boundary-layer thickness is reduced, which leads to hot-spot situations (Space Shuttle experience: „vortex scrubbing"), at separation lines, where the flow diverges, „cold" spot situations ensue,

- where surfaces face each other, non-convex effects reduce the cooling efficiency.

Relation (3) can be used in design work for a scaling of the radiation-adiabatic temperature from e.g. a smaller vehicle to a larger one, if the flow topology is the same in both cases. The scaling laws are simple and effective, Ref. 5.

In the following a few illustrations are given. Fig. 3, Refs. 9 and 10, shows results from a solution of the Navier-Stokes equations for laminar flow past a delta wing with leeside separation at $M_\infty = 7.15$. All the features discussed above are present. Note especially the skin-friction line topology at the windward side, where between the two primary attachment lines the flow is nearly two-dimensional. On the leeside the secondary attachment line tapers off down-stream. The tertiary attachment line (schematic see Fig. 9) of course also is a hot-spot line. The presence of a fuselage, however, would change the leeside flow topology. For a better understanding what

happens, the topological structure of the flow is sketched in Fig. 4.

The cross-section distribution of the radiation-adiabatic temperature is given in two cuts of the delta wing in Fig. 5. On the leeside the temperature is about 300 K lower than on the windward side, with strongly marked hot spots at the attachment lines (up to 300 K), and cold spots at the separation lines. Fig. 5 shows also the results, which were found with a simple scaling law. Scaled was the solution from the body length $L = 4.6$ m (case 1) to the body length $L = 13$ m (case 2) with the same Mach number, unit Reynolds number and of course also angle of attack, which is the pre-requisite to have similar flow topologies. Case 2 was recomputed in order to permit the accuracy check. The accuracy indeed is very acceptable. Deviations are present only where large three-dimensional effects exist, nevertheless, the hot and cold spot situations are sufficiently well scaled. In addition the $1/L$ scaling effect is well discernible.

An example for the non-convex effect at a wing root finally is given in Fig. 6. The concept of the fictitious emissivity coefficient, Ref. 11, was applied in Ref. 12 at the lower wing root of the HYTEX R-A_3 vehicle, which was investigated in the German Hypersonics Technology Programme. There means of heat loads alleviation by introducing a fillet were studied. The introduction of non-convex effects in the computation for the non-fillet case resulted in a temperature rise of 50 K to 100 K. The wing surface in the root region was less strongly affected compared to the propulsion unit surface there. This is due to the fact, that the boundary layer is thicker on the latter. Note that the classical viscous corner-flow effects were not prescribed with the employed approximative methods. The introduction of the fillet, which anyway would reduce the viscous corner-flow effects, resulted as expected, in a reduction of the radiation-adiabatic temperature by about 50 K towards the end of the wing root. Unexpectedly the temperature rose a the leading edge by up to 30 K. A closer examination showed, that this was due to the compression of the flow, which was induced by the fillet. The resulting local rise of the unit Reynolds number then decreased the boundary-layer thickness, and the temperature rose, which can be understood in light of the results of the local analysis sketched in this chapter.

Although the non-convex effects were not large in this case, the results of the investigation show clearly the influence of non-convex effects on the radiation-adiabatic temperature. Remembering that the viscous drag is affected too, non-convex effects must, like local strong-interaction effects, be monitored and quantified if necessary, in the design of hypersonic vehicles.

4. HEAT LOADS AND VEHICLE DESIGN

The heat loads, especially on sustained flight vehicles, cannot be decoupled from the overall vehicle design.

As was shown in the preceding chapters, the thermal state of the surface influences and is influenced by
- the vehicle shape (radii, edges sweep, surface portion inclination, non-convex portions),
- vehicle surface properties (emissivity, catalycity, roughness, waviness (the latter two with regard to transitional and turbulent flow)),

- active cooling needs.

This all has implications for
- the wave drag,
- the viscous drag,
- static and dynamic structural aerothermoelastics (especially for hot primary structures),
- airframe/propulsion integration,
- manufacturing (surface properties),
- system aspects (active cooling).

Heat loads on the other hand are coupled to flow-physics and thermochemical phenomena, which occur in the flow past a vehicle, and which depend on the speed, altitude and shape of the vehicle.

The thermal state of the vehicle surface thus influences and is influenced by (Ref. 13)

- the boundary-layer thickness,
- the boundary-layer state: laminar or turbulent → transition laminar-turbulent,
- attachment and separation lines,
- catalytic surface recombination,
- strong interaction phenomena,
- hypersonic viscous interaction phenomena,
- low density effects.

The prediction of location and strength of some of these phenomena, especially the transition zone, attachment lines, strong interaction locations, poses big problems. Prediction uncertainties can lead to large weight and performance penalties.

As an example a Navier-Stokes solution for the SÄNGER forebody, Ref. 14, is given in Fig. 7. It shows that radiation cooling enhances very strongly the influence of the boundary-layer state on the wall temperature and the skin friction. Without radiation cooling the wall temperature (recovery temperature) is some thirty to forty degrees larger for turbulent flow than for laminar flow, Fig. 7a. The transition location was chosen arbitrarily to lie at $x/L = 0.1$. With radiation cooling the difference is about ten times larger and hence the location of transition laminar-turbulent becomes much more important. Note that real-gas effects at that Mach number also play a role, at least in the case of no radiation cooling. Note further that ist is not known how reliable present-day turbulence models are in such cases. The figure shows well that the radiation-adiabatic temperature decreases with x/L for the laminar as well as for the turbulent case in contrast to the recovery temperature.

Fig. 7b shows the influence of surface radiation cooling on the skin friction, which is low for the laminar case, but is large for the turbulent case. In this case, a skin-friction estimation based on the recovery temperature would give values about 30 per cent too low. This shows also that for drag minimization the surface should be as hot as possible.

In Fig. 7a also the computed radiation-adiabatic temperatures for the leeward side are indicated. The temperature for the turbulent case is approximately 270 K, and that for the laminar case approximately 90 K lower than on the windward side.

For a typical cold hypersonic wind-tunnel situation, that in the H2K at the DLR Köln-Porz, a computation has been performed for the present case, Ref. 15. With the tunnel data at $M_\infty = 6.8$: $Re = 3 \cdot 10^6$, $T_\infty = 61$ K and $T_w = 300$ K (Fig. 7a) the turbulent skin-friction shown in Fig. 7b is two times larger than that for the radiation-cooled flight case, with a much steeper slope, which partly is due to the smaller Reynolds number.

The large influence of the state of the boundary layer - laminar or turbulent - on the wall temperature and on the skin friction for the radiation-cooled wall, compared to that in the case of the adiabatic wall poses very large problems in vehicle design. The transition location is very important in view of the thermal loads, especially if a hot primary structure is foreseen. On the other hand the prediction and verification of the viscous drag is affected strongly, if the vehicle, typically for airbreathers, is drag critical. Fig. 7 demonstrates that with presentday wind-tunnel techniques the skin friction cannot be found with the needed degree of reliability and accuracy.

As a consequence it appears to be necessary in future to integrate stronger the heat load aspects with the general aerodynamic and structural vehicle design, Refs. 5, 16. Fig. 8, which is discussed in detail in Ref. 5, gives this perspective schematically. Needed is an appropriate shaping of the vehicle definition and development processes. Such an integrated approach permits the rational identification of necessary research and technology developments, too.

5. STATUS AND DEVELOPMENT NEEDS OF PREDICTION AND VERIFICATION CAPABILITIES

As was discussed in the preceding chapters, the prediction and verification of heat loads, apart from the perspective of the „integrated, heat-loads oriented vehicle design", has its major problems in the proper simulation of several transport phenomena, either with computation methods or with ground-simulation facilities.

Starting from the general relations (definitions see Fig. 2)

$$q_{gw} + q_r = q_w \Leftrightarrow T_w , \qquad (4)$$

the problem can be detailed as follows

o flow (convective and diffusive heat transport, thermo-chemical phenomena, heat capacity, surface properties, flow topology)

⇑
coupling (a)
⇓

$$- \left(k_{lam} \left(+ k_{turb} \right) \right) \frac{\partial T}{\partial y} +$$

(diffusive heat transport)

$$+ \sum_i \left(j_{iy,lam} \left(+ j_{iy,turb} \right) \right) h_i -$$

(heat transport by mass diffusion →
catalytic surface recombination)

$$- \mu_{lam} \, u \frac{\partial u}{\partial y} + \sigma \varepsilon T^4 = q_w \qquad (5)$$

(heat transport
due to slip flow)   (radiative
heat transport q)

⇑
coupling (b)
⇓

o materials & structures (heat conduction, heat capacity, surface properties, structure topology),

with j_{iy} and h_i the diffusive mass transport of species i in y-direction, and the enthalpy of species i, respectively (y > 0: turb).

In the (conservative) design the coupling (b) is neglected:

$$q_w = 0 \quad \left/ \begin{array}{l} q_r = 0 \Rightarrow T_w = T_r , \\ q_r > 0 \Rightarrow T_w = T_{ra} , \end{array} \right. \qquad (6)$$

and either the recovery temperature T_r or the radiation-adiabatic temperature T_{ra} is asked for.

For the development, in some cases already for the design, the coupling (b) must be modelled

$$q_w \neq 0 \Rightarrow T_w \Leftrightarrow f(q_{gw}, q_r, q_w) . \qquad (7)$$

If active cooling is to be considered

$$T_w = T_{target} \Rightarrow q_w = q_{gw} + q_r . \qquad (8)$$

The general status of heat loads prediction capabilities in this respect is

o Computational simulation suffers from serious deficits in flow-physics and thermo-chemical models (transition laminar-turbulent, turbulent heat and mass transfer, catalytic surface recombination).

o Cold-surface experimental simulation usually is made with an uncontrolled thermal state of the surface and simulates at best selected aspects of heat loads.

o In general only simplified structure couplings are used in design work (coupling (b)).

o A full ground-facility simulation respective verification is not possible, especially if surface-radiation cooling is involved. In Ref. 17, therefore a Transfer-Model approach is proposed, which combines in a structured way computational, ground-facility and in-flight simulation. Fig. 9 gives a schematic overview over the status and the development needs of the tools of the integrated, heat-loads oriented vehicle design.

6. CONCLUSION

Heat loads are the major issue in high-speed vehicle design. Heat loads prediction capabilities need to be improved → materials & structure concept, aerodynamic and propulsion performance. Surface radiation cooling is the basic means to reduce heat loads on high-speed vehicles. Strong couplings exist with the aerodynamic performance of vehicles, the structure & materials design, and flow-physics and thermochemical phenomena. Qualitative knowledge is available to interpret (computation) results and flight data, and to give the designer insight into related disciplinary and interdisciplinary vehicle design problems. Flow-physics and thermo-chemical models in prediction tools are inadequate, a "hot experimental technique" is needed. Heat loads and the related surface-temperature effects pose very important and challenging research and development problems.

7. REFERENCES

1. . Hirschel, E.H., "Heat Loads as Key Problem of Hypersonic Flight", Zeitschrift für Flugwissenschaften und Weltraumforschung (ZfW), Vol. 16, No. 6, 1992, pp 349-350.

2. Bertin, J.J., "Hypersonic Aerothermodynamics", AIAA Education Series, Washington, 1994.

3. Monnoyer, F., "Personal communication", 1992.

4. Monnoyer, F., Mundt, Ch., Pfitzner, M., "Calculation of the Hypersonic Viscous Flow Past Reentry Vehicles with an Euler/Boundary-Layer Coupling Method", AIAA-Paper 90-0417, 1990.

5. Hirschel, E.H., "Aerothermodynamics of Radiation-Cooled Surfaces", AGARD-R-813, pp. 3-1 to 3-16.

6. Perrier, P., Courty, C.J., "Configuration Aerothermodynamics of RAM and SCRAM Propelled Vehicles", AGARD-R-813, 1996, pp. 7-1 to 7-36.

7. Simeonides, G., "Simple Formulations for Convective Heat Transfer Prediction Over General Aerodynamic Configurations and Scaling of Radiation-Equilibrium Wall Temperature", ESA EWP-1860, 1995.

8. Fay, J.A., Riddell, F.R., "Theory of Stagnation Point Heat Transfer in Dissociated Air", J. of Aeronautical Science, Vol. 25, No. 2, 1958, pp 73-85.

9. Riedelbauch, S., "Aerothermodynamische Eigenschaften von Hyperschallströmungen über strahlungsadiabate Oberflächen", Doctoral Thesis, Technical University München, 1991.

10. Riedelbauch, S., Hirschel, E.H., "Aerothermodynamic Properties of Hypersonic Flow Over Radiation-Adiabatic Surfaces", Journal of Aircraft, Vol. 30, No. 6, 1993, pp 840-846.

11. Höld, R.K., Fornasier, L., "Investigation of Thermal Loads of Hypersonic Vehicles with Emphasis on Surface Radiation Effects", ICAS-Paper 94-4.4.1, 1994.

12. Åslund, H., "Configurational Heat Loads Calculations on the Hypersonic Flight Test Vehicle HYTEX R-A₃", SAAB TM L-0-1 B 789, 1994.

13. Hirschel, E.H., "Review of Surface Temperature Effects on Vehicle Aerothermodynamics in High-Speed Flow", Dasa-LMLE3-S-STY-209-A, 1996.

14. Schmatz, M.A., Höld, R.K., Monnoyer, F., Mundt, Ch., Rieger, H., Wanie, K.M., "Numerical Methods for Aerodynamic Design II", Space Course Aachen, 1991, Paper No. 62, also MBB/FE211/ S/PUB/442, 1991.

15. Radespiel, R., personal communication, 1994.

16. Hirschel, E.H., Heindl, H.A., "Aerothermodynamics Analysis Tools and Strategy for the Design of Reusable Launch Vehicles", Dasa/LME12/S/STY/188/B, 1996.

17. Hirschel, E.H., "Similitude Analysis, Simulation Parameters and Development / Implementation of Ground Test Techniques for Surface Temperature Effects in High Speed Flow", Dasa-LMLE3-S-STY-210-A, 1996.

8. FIGURES
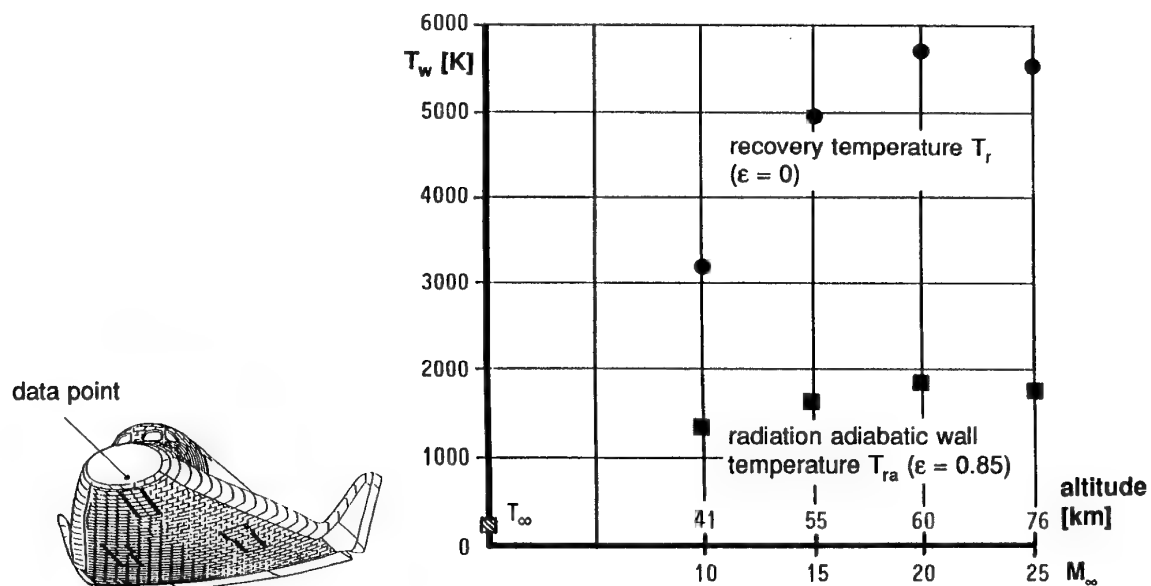
Fig. 1 *Effect of surface-radiation cooling at a given point on the lower symmetry line of HERMES (x = 1 m, α = 40°) laminar flow, equilibrium real-gas model, at different trajectory points (altitude, Mach number), Ref. 3*
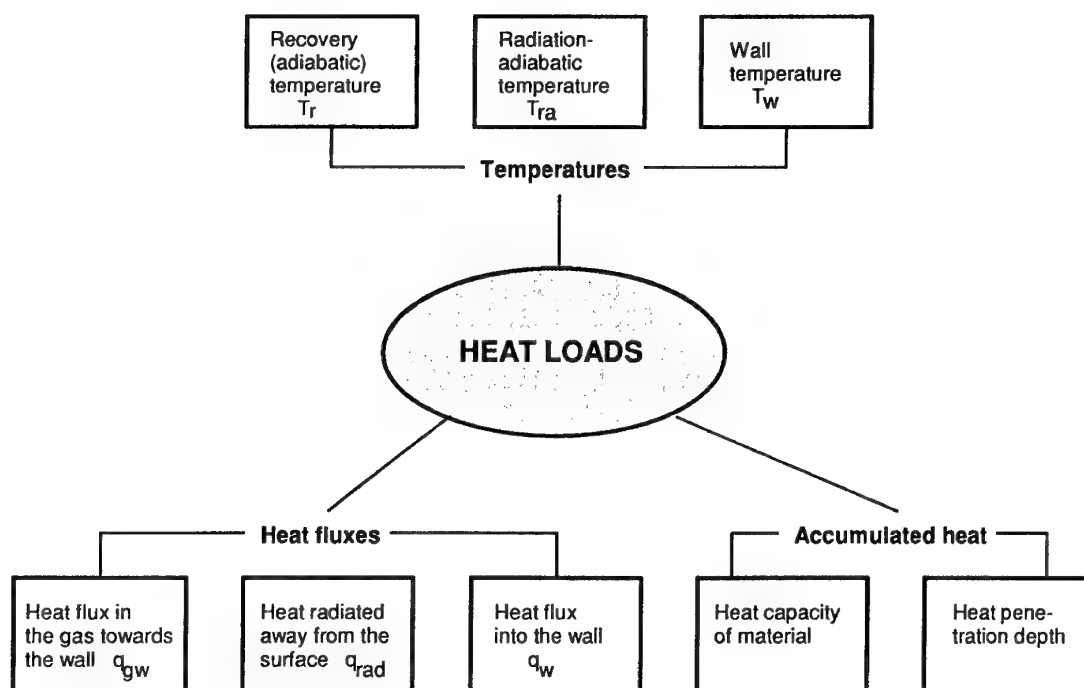
Fig. 2 *Definition of heat loads*
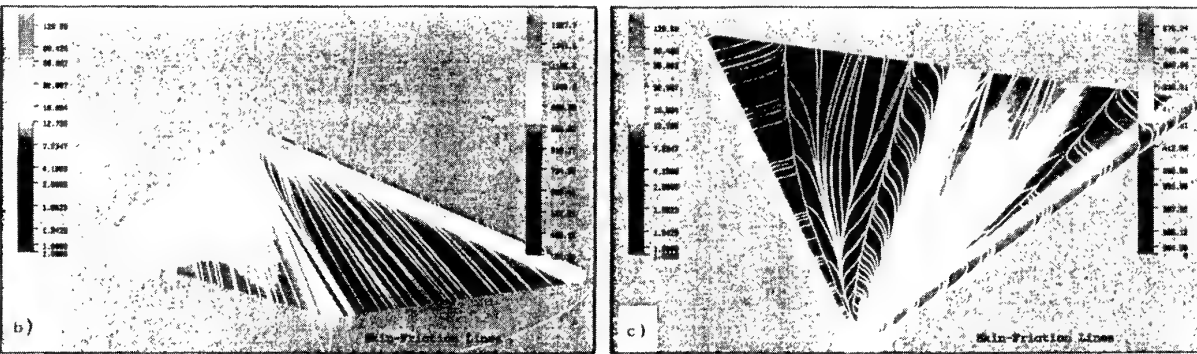
Fig. 3   Hot spot phenomena at attachment lines of a delta wing with surface radiation cooling, a) windward side, b) leeward side, Refs. 9 and 10, $M_\infty = 7.15$, $Re = 5 \cdot 10^5$, $L = 13$ m, $\alpha = 15°$, $\varepsilon = 0.85$ (right-hand sides: wall temperatures (cold areas are dark), left-hand sides: radiation heat fluxes)
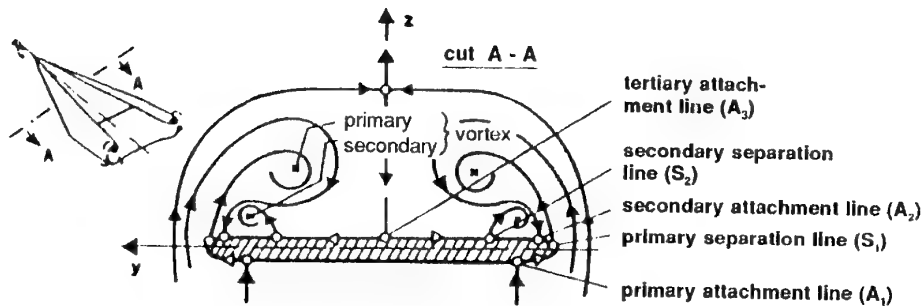
Fig. 4   Topological structure (schematically) of delta wing flow (A: attachment line, S: separation line): attachment flow transports original enthalpy towards surface at A_1, A_2, A_3, Ref. 5
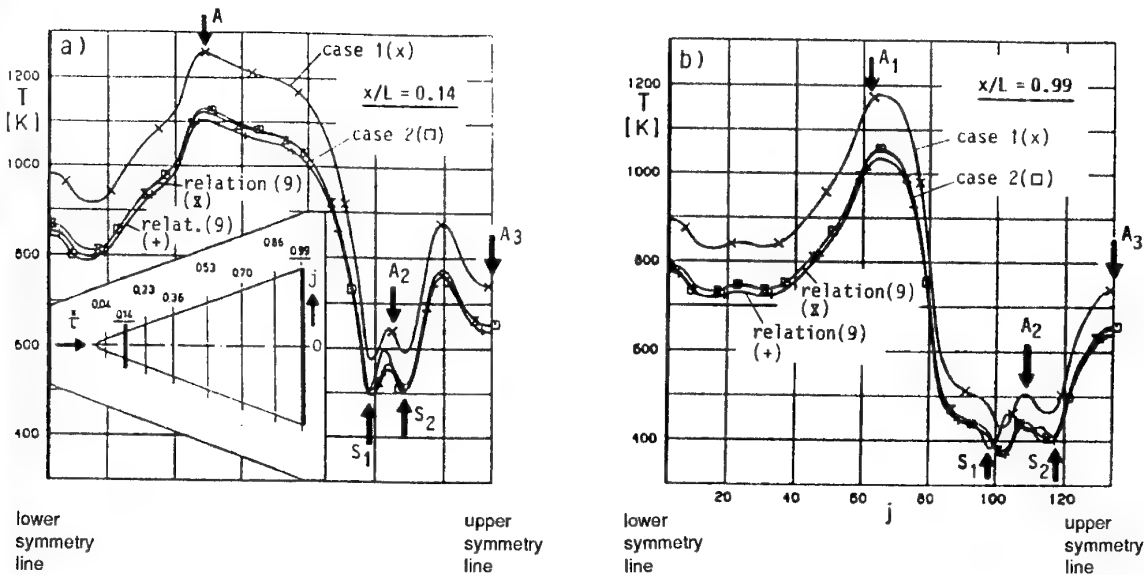
Fig. 5   Comparison of numerical (x, o) and scaled (+: exact relation; X: relation with $k_1 = k_2$) radi-ation-adiabatic wall temperatures, Refs. 9,10, for the delta wing of Fig. 3; indicated are the lo-cations of attachment and separation lines (schematic see Fig. 4), cross-section at 14 per cent and 99 per cent body length

T_W
(Kelvin)

HYTEX R-A₁: No Fillet

M=6.8   H=30 km   ε=0.85
α=5°   β=5°   ε_net=f(x,y,z)

HYTEX R-A₁: Baseline

M=6.8   H=30 km   ε=0.85
α=5°   β=5°   ε_net=f(x,y,z)
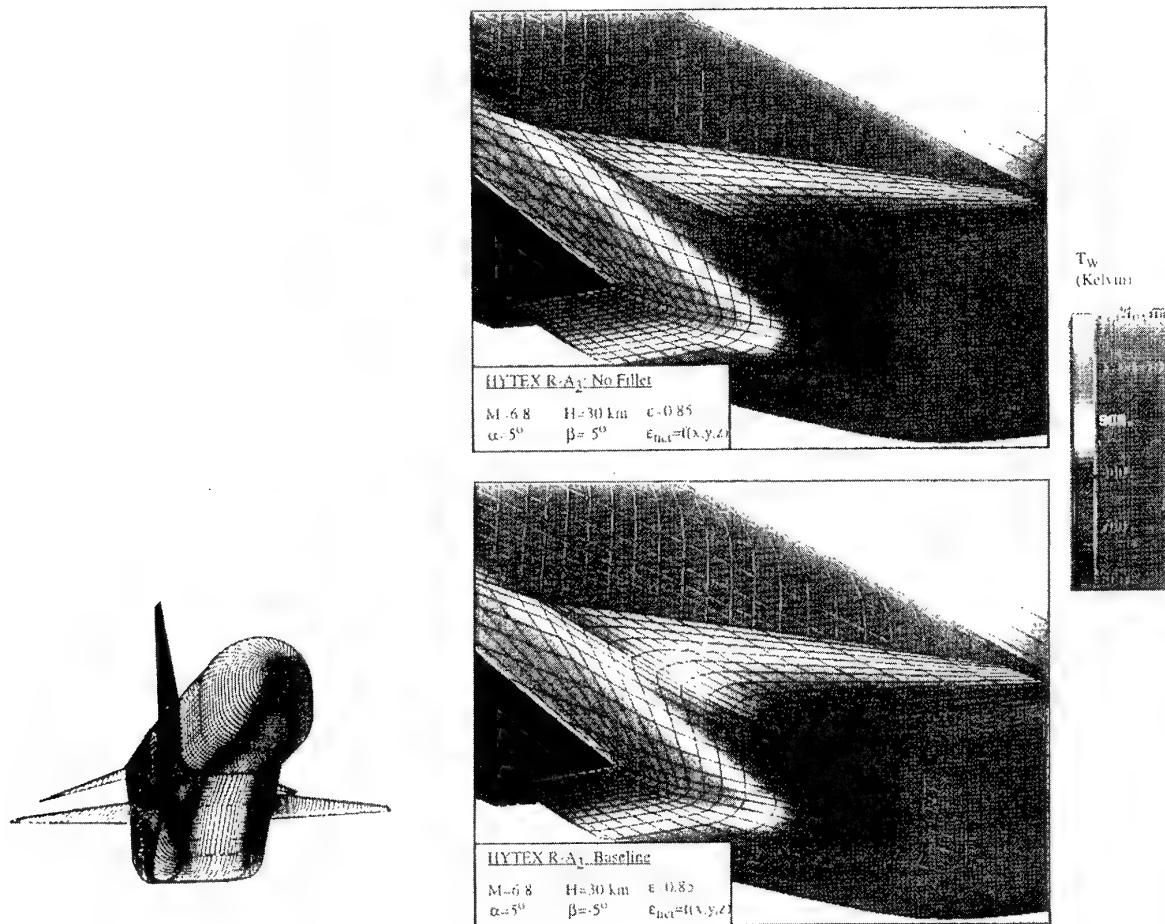
Fig. 6   Heat loads alleviation at the wing root of a HYTEX vehicle, Ref. 12, $M_\infty = 6.8$, A = 30 km, α = 5°, β = 5°, $\varepsilon_{nom} = 0.85$, approximative method, turbulent flow; radiation-adiabatic temperature: a) without fillet, b) with fillet
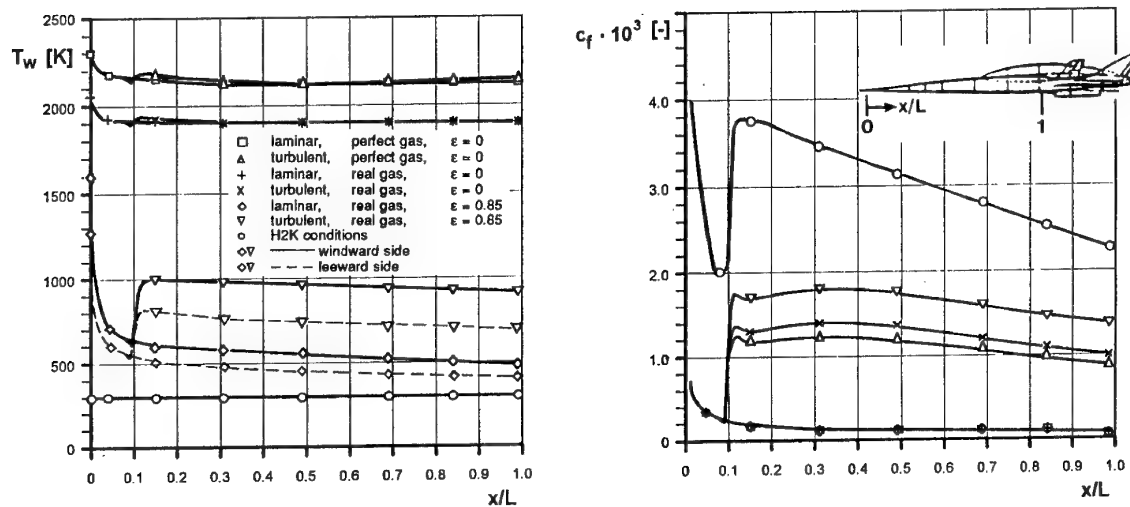
Fig. 7   Influence of the state of the boundary layer (laminar/turbulent, real-gas effects, and radiation cooling on a) wall temperature, b) skin friction. Lower symmetry line of SÄNGER forebody, $M_\infty = 6.8$, Re = 1.22×10^8, L = 55 m, α = 6°, Ref. 14
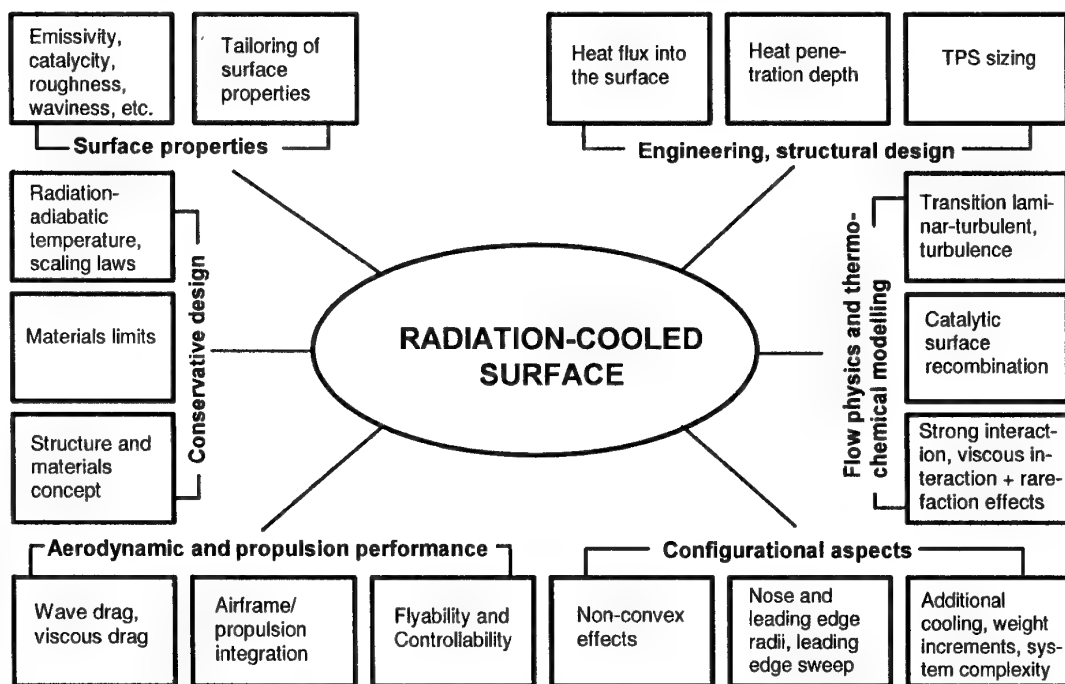
Fig. 8   *Elements of the integrated, heat loads-oriented vehicle design and their interrelations with the radiation-cooled surface, Ref. 5*
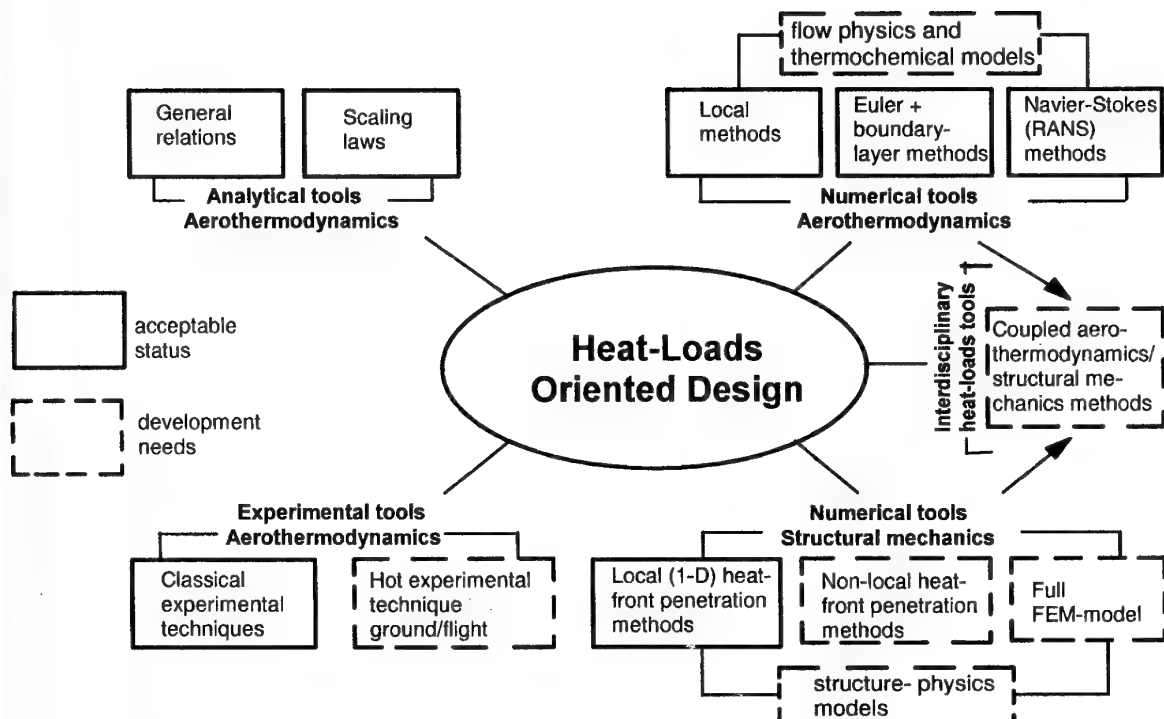
Fig. 9   *Tools of the integrated heat-loads oriented design: simplified overview over status and development needs, Ref. 5*

THERMAL LOADS AND PROTECTION SYSTEMS FOR
TRANSITIONAL AND SHOCK INTERACTION REGIONS IN HYPERSONIC VEHICLE DESIGN[*]

Michael S. Holden

Research Fellow

Calspan-University at Buffalo Research Center (CUBRC)

4455 Genesee Street, P.O. Box 400

Buffalo, New York 14225

SUMMARY

In this paper, we discuss some of the more difficult to predict phenomena that control the sizing of thermal protection systems for sustained hypersonic flight, and the methods which are available to provide estimates of the requirements for backface, film-cooling and transpiration cooling techniques. The prediction of boundary layer transition on leading edges, in regions of pressure gradient, shock interaction and crossflow induced by vehicle incidence, represents key tasks in vehicle design. We review prediction methods that can be used to estimate the thermal loads when transition occurs. Film and transpiration cooling are two techniques that can be employed to flexibly handle the large and spatially-variable heating loads that can occur in shock interaction regions in and around airbreathing propulsion systems for hypersonic vehicles. Correlation of measurements made to assess the performance of these systems are presented to provide estimates of their effectiveness in constant pressure and shock interaction regions.

1. INTRODUCTION

The design of thermal protection systems to handle the aerothermal loads generated in sustained hypersonic flights generally involve systems that employ backface cooling, film-cooling or transpiration-cooling. The complexity of the skin structure for backface and transpiration-cooling systems are greater than those for film-cooling system hardware. However, backface and transpiration-cooled systems are more flexible in handling regions of spiked heating, such as those generated in shock interaction and flow transition. Because the position and magnitude of the heating loads developed in regions of shock/boundary layer interaction, separated shear layers, and transitional boundary layers are very difficult to predict, it is important to have a thermal protection system capable of handling a large range of heating rates and peak heating locations. The design of thermal protection systems is further complicated because such flows are generally unsteady and the location of the peak heating loads are sensitive to vehicle attitude and freestream conditions. With the availability of advanced Computational Fluid Dynamic (CFD) codes based on Navier-Stokes and Monte Carlo solvers, it is possible to predict with good accuracy the flowfield characteristics and thermal loads for flow configurations without complex shock interaction regions or transition. Transitional boundary layers and interacting flows induced by shock bound layer interaction in hypervelocity flows cannot be accurately predicted by even the most sophisticated codes available because of the lack of validated turbulence models incorporating compressibility and real gas effects. Here, the designer must judiciously employ a combination of these numerical codes and semi-empirical prediction methods to estimate the aerothermal loads.

Very few ground test facilities are available in which it is possible to generate both the real-gas effects and the Reynolds number necessary to develop fully turbulent interacting flows. This also severely limits the development and validation of codes used to predict the effectiveness of film- and transpiration-cooling under flight conditions. Again, the central issues are describing the effect of compressibility, real-gas effects, transition and turbulent mixing in hypervelocity flow. Employing hydrogen as a coolant introduces significant problems in describing the properties of turbulent mixing in the presence of combusting flows. To validate the models of turbulence and real-gas effects used in the codes to predict such flows must be supported by carefully designed and conducted experiments.

In this paper, we briefly review some of the important characteristics of transitional and shock-interaction flows together with active cooling techniques, with the emphasis on the semi-empirical predictions methods needed to quantify the aerothermal loads generated in these flows. We first review the most recent measurements in hypersonic flow of the characteristics of transitional flows in regions of adverse pressure gradient, on attachment lines and in regions of crossflow. We then review simple analytical and semi-empirical prediction techniques used to calculate the aerothermal characteristics of regions of film- and transpiration-cooling. Finally, we discuss the effectiveness of film- and transpiration-cooling techniques in controlling the peak heating loads generated in regions of shock/shock and shock boundary layer interaction.

2. TRANSITION PHENOMENA IN HYPERSONIC FLOWS

2.1 Boundary Layer Transition and Transitional Flow Predictions

2.1.1 Introduction

In the development of air-breathing vehicles for hypersonic flight, the prediction of transition and transitional flows in regions of adverse pressure gradient and shock interaction represents a key factor in the design and performance of the integrated vehicle and propulsion system configuration. While boundary layer transition is one of the most important parameters in the design of hypersonic vehicles, there remains a considerable gap between "engineering" efforts to correlate the occurrence of transition and fundamental theoretical studies. The influence of surface geometry, shock impingement and radiated noise remains largely unquantified. While the engineering studies have concentrated on correlating experimental measurements of transition obtained in flight tests, ballistic ranges, and wind tunnels against almost every conceivable parameter, the fundamental studies have been aimed principally at exploring the modes of instability of the laminar boundary. The basic problem is that boundary layer transition is controlled by the detailed aerodynamic environment as well as the Reynolds number and this linkage is difficult to describe and define. Recently a series of experiments were performed on configurations of interest to air-breathing hypersonic vehicle design to examine the semi-empirical methods together with contemporary prediction techniques (e.g., the GASP code), where it is possible to examine models of the transitional flow and the turbulent non-equilibrium in a downstream of the adverse pressure gradient and to obtain predictions to compare with measurements of the distributions of

heat transfer and pressure along inlet compression surfaces, on attachment lines and in crossflow regions of vehicles at incidents.

2.1.2 Transition and Transitional Flows Over Hypersonic Compression Surfaces

To examine the performance of typical turbulence models that are employed in contemporary Navier-Stokes codes, we review some comparisons between the experimental measurements of transitional flow over a curved compression ramp, similar to that which might be used as an inlet for vehicles traveling up to Mach 12, and predictions employing the GASP code for a series of transitional flows. In the series of experiments discussed[1] here, freestream Mach numbers of 10, 11, and 12 were selected so that the unit Reynolds number of the freestream could be varied at each Mach number to move the onset of transition from the beginning of the curved section of the model, at the largest Reynolds number, to the trailing edge of the curved section at the lowest Reynolds number. In general, three comparisons were made: (1) with transition as far forward as possible; (2) with transition at the farthest downstream station; and (3) between these cases. The computer solutions were obtained either for fully laminar flow or for turbulent flow employing either a Baldwin-Lomax or k-e model of turbulence. Predictions were also made for a hybrid case where the code was switched from laminar to turbulent at an axial station prescribed by the operator. This position was generally selected to coincide with the beginning of transition as determined from the experiment.

Comparisons between the experimental measurements and computations employing the GASP code were made for the Mach 10 condition at three unit Reynolds number conditions. In each case, the flow was assumed to be laminar or turbulent close to the leading edge. Baldwin-Lomax and k-e models were used in the computation to describe transitional and turbulent flows. An additional set of calculations was made by switching from the laminar solution to a turbulent calculation employing the Baldwin-Lomax model at a prescribed axial location. In these latter calculations, there was no attempt to employ a model of the transition region. Figure 1 shows a typical comparisons between the computations and the heat transfer and pressure measurements. The comparisons between measurements of pressure and the theoretical predictions show that the boundary layer model exhibits little influence on the pressure distribution, and that the theory is in good agreement with the experimental measurements. Also, errors in the selection of the condition of the boundary layer or

the turbulent model can result in orders-of-magnitude errors in the prediction of the heating level. Assumption of a laminar boundary layer over the complete configuration would result in underestimating the heat load to a major segment of the compression surface by a factor of eight. Assuming the flow to be turbulent from the leading edge would result in underpredicting the heating load with the k-ε model and over-predicting with the algebraic model. Clearly, the position of transition and the development of the boundary layer downstream of this point must be carefully modeled. If the solution is switched to laminar from turbulent close to the point that transition was observed experimentally, we obtain a closer agreement between theory and experiment, as shown in Figure 2. One can conjecture that the theory could be brought into closer agreement to the experiment if a model of the transition region were incorporated into the prediction method.
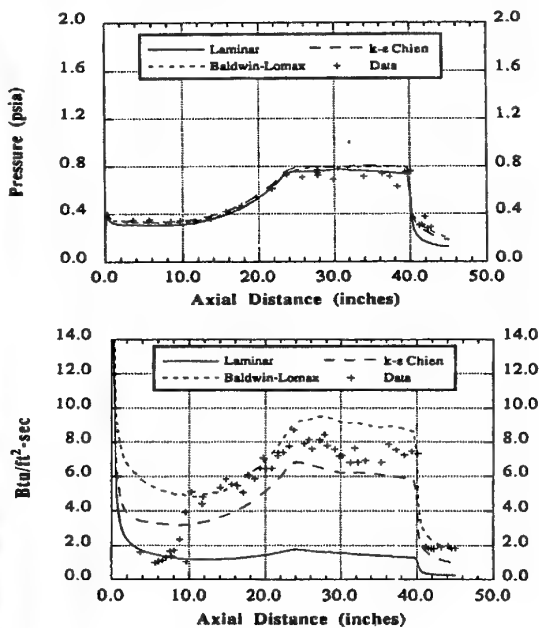
Figure 1 Surface Pressure and Heat Transfer Measurements and Predictions for Run 5 (Reference 1)
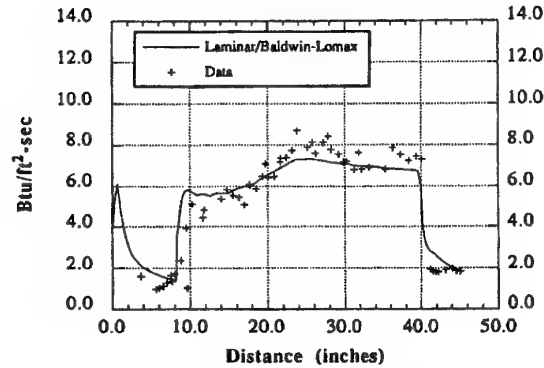
Figure 2 Heat Transfer Measurements and Predictions with Transition for Run 5 (Reference 1)

Comparisons between the GASP code predictions and the experimental measurements at Mach 12 were made for two conditions spanning the range of unit Reynolds numbers employed in the experiment. Comparisons between theory and experiment at the largest unit Reynolds number are shown in Figure 3. For these flows, where transition occurs well downstream on the curved compression surface, the theory is in good agreement in the laminar segment of the flow and is in good agreement with the Baldwin-Lomax turbulence model for heat transfer levels over the latter half of the second straight compression ramp. Again, the more complex k-ε model does not result in good agreement in the fully turbulent flow over the second straight ramp section. Switching the solution from laminar to one with the Baldwin-Lomax model close to the point where transition is experimentally observed results in a prediction (see Figure 4) that is in relatively good agreement with the experimental measurements. At the lowest Reynolds number where this segment of the study was conducted, there is an extensive laminar region over the straight initial section and curved compression ramp, and the laminar theory is in good agreement with the heat transfer measurements, as shown in Figure 5. The heat transfer along the second straight section is poorly predicted, even if the position of transition is inputted from experimental measurements, as shown in Figure 6. It is clear from this comparison that even if it were possible to predict the effects of adverse pressure gradient on boundary layer transition, the simple turbulence models employed here cannot be relied upon to provide accurate estimates of heat transfer rates downstream of the transition region.
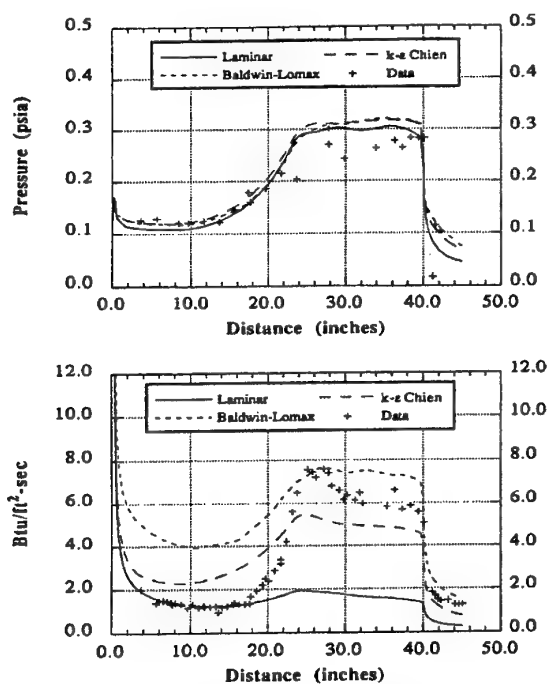
Figure 3   Surface Pressure and Heat Transfer Measurements and Predictions for Run 22 (Reference 1)
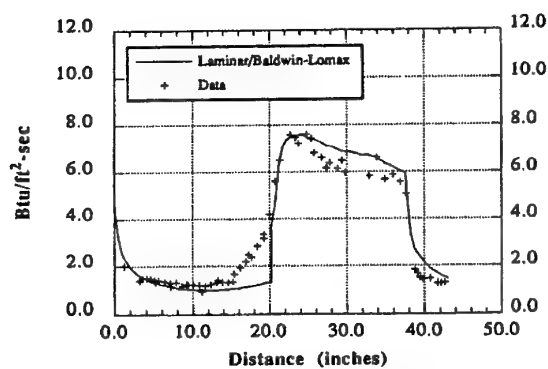
Figure 4   Heat Transfer Measurements and Predictions with Transition for Run 22 (Reference 1)
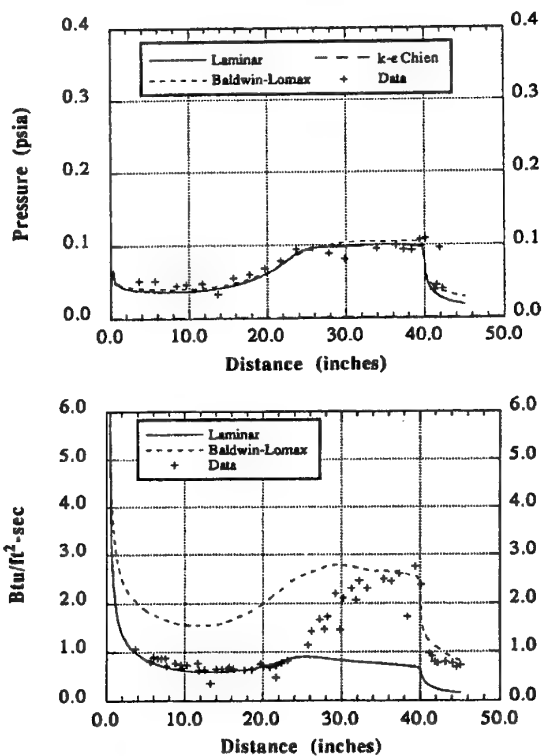
Figure 5   Surface Pressure and Heat Transfer Measurements and Predictions for Run 39 (Reference 1)
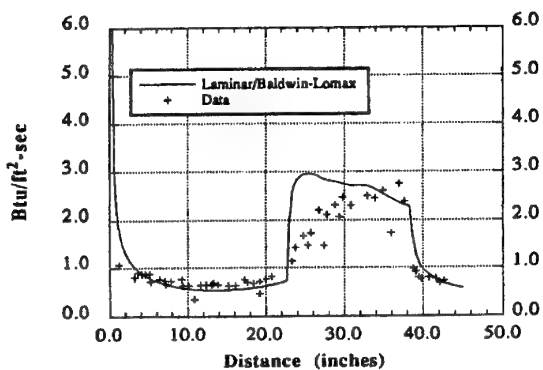
Figure 6   Heat Transfer Measurements and Predictions with Transition for Run 39 (Reference 1)

2.2   Attachment Line Transition on Swept Leading Edges

2.2.1   Introduction

The occurrence of boundary layer transition on the attachment line of highly swept leading edges is an important design consideration not only because it influences leading-edge heating, but also because

disturbances generated in this region of the flow can exert the dominant effect on transition on the three-dimensional afterbody. For example, disturbances generated on the leading edge of the Space Shuttle have been linked by Poll[2] to the occurrence of transition on the main body of the Shuttle's wing. Introducing a disturbance on the attachment line with surface discontinuities or roughness, or a wing-body junction, can result in transition Reynolds numbers that are consistently lower than those for the smooth configuration. In fact, the relatively low Reynolds numbers at which the stagnation-line heating becomes turbulent on swept wings or fins, because of disturbances introduced at the wing root, can become a major low-altitude performance limitation for finned hypersonic vehicles. Studies in supersonic flow by Bushnell and Poll[3,4] have suggested that, for highly swept fins, freestream Reynolds numbers of just over 10^5 based on leading-edge diameter are required to induce transition downstream of a wing/body junction in supersonic flows. For this configuration, Poll[4] suggests the transition criteria $\overline{Re}* = 245$, where

$$\overline{Re}_* = \left(Re_{D_\infty} \frac{\mu_\infty}{\mu_*} \frac{\rho_*}{\rho_\infty} \frac{\sin\lambda \cdot \tan\lambda}{U_1} \right) = 245 \quad (1)$$

for high Mach number flows, the boundary layer properties are evaluated at the reference temperature $T_* = T_A + 0.10 (T_W - T_A) + 0.60 (T_{aw} - T_A)$. The correlation developed earlier by Poll for supersonic flows is shown in Figure 7. For swept leading edges without disturbances introduced at the wing root or surface discontinuities on the attachment line, measurements by Creel[5] at M=3.5 suggest an $Re_D=7 \times 10^5$ for a freestream Reynolds number for transition onset for highly swept leading edges. Recently, Holden and Kolly[6] extended the range of measurements from Mach 8 to 12.
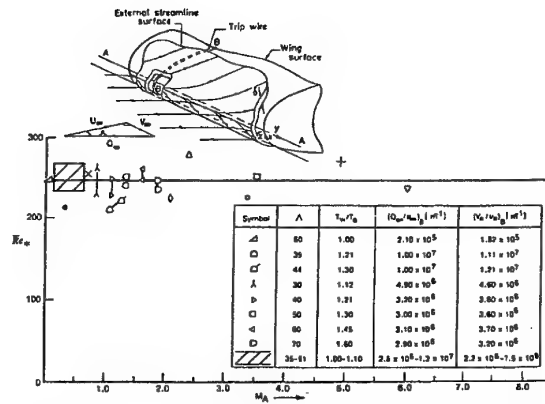
Figure 7 The Variation of $\overline{Re}*$ at the Onset of Transition with Edge Mach Number and Wall Temperature

2.2.2 Correlation of Attachment-Line Heating

There are two flow configurations of interest: (1) the smooth swept cylinder, where attachment line transition is influenced by the attachment line Reynolds number and disturbance in the freestream; and (2) the swept cylinder with attachment line contamination, where transition onset is controlled principally by the attachment line Reynolds number and the magnitude of the surface roughness or disturbance introduced at the tip. Studies in subsonic and supersonic flows have established that the major parameter controlling laminar and turbulent heating along the attachment line, as well as transition onset, is the attachment line Reynolds number ($\overline{Re}$), which is defined as

$$\overline{Re} = \frac{V_A \cdot \eta}{\nu_A}$$ evaluated on attachment line (See

Figure 8) where η is a characteristic dimension of this viscous flow.
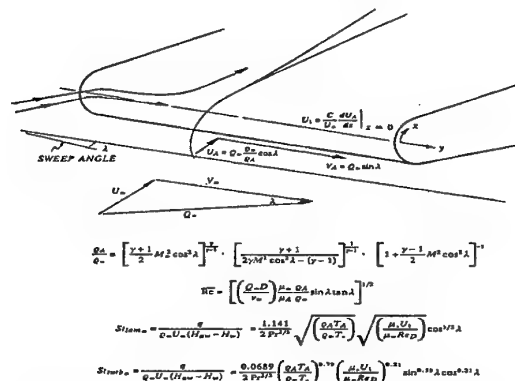
Figure 8 Flowfield and Attachment Line Equations

The expressions for laminar and turbulent attachment line heating in compressible flow, employing the above expression together with the relationships from Figure 8, then become

$$St_A = \frac{q}{\rho_\infty U_\infty (H_{aw} - H_w)} =$$

$$\frac{1.141}{2 Pr^{2/3}} \sqrt{\left(\frac{\rho_A T_A}{\rho_\infty T_*}\right)} \sqrt{\left(\frac{\mu_* U_1}{\mu_\infty Re_D}\right)} \cos^{1/2}\lambda \tag{2}$$

for laminar flows and

$$St_A = \frac{q}{\rho_\infty U_\infty (H_{aw} - H_w)} =$$

$$\frac{0.0689}{2 Pr^{2/3}}\left(\frac{\rho_A T_A}{\rho_\infty T_*}\right)^{0.79}\left(\frac{\mu_* U_1}{\mu_\infty Re_D}\right)^{0.21} \sin^{0.58}\lambda \cos^{0.21}\lambda \tag{3}$$

for turbulent flows where

$$Re_D = Q_\infty D / \nu_\infty \tag{4}$$

On the basis of analysis of the measurements made in a recent hypersonic flow study, Holden suggests a new reference condition defined by

$$T_* = 0.3 T_w + 0.5 T_{aw} + 0.28 T_A \tag{5}$$

Correlations of the attachment line heating measurements in terms of this parameter are shown in Figure 9.
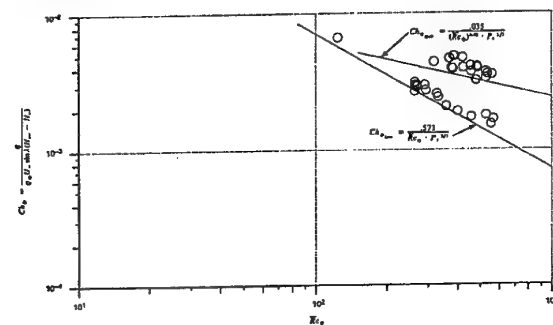
Figure 9   Correlation of Attachment Line Heating (T* in Eq. 5)

The measurements of laminar heating rates along the attachment line of smooth cylinder configurations are in good agreement with the prediction and indicate that flow can remain laminar for attachment line Reynolds numbers of up to 600 before transition is observed on the attachment line, and a Reynolds number of 800 before the flow in the attachment line boundary layer is fully turbulent. The measurements of turbulent heating rates are greater than the predicted levels, as might be expected for low Reynolds number flows close to the transition boundary.

2.2.3   Correlation of Attachment Line Transition Onset

Studies by Cumpsty and Head, and subsequently by Poll, suggested that transition onset on long swept leading edges can be evaluated in four flow regimes in terms of the parameters $\overline{Re}$ and k/η, where η is a characteristic dimension of this viscous flow and is defined by the expression

$$\eta = \left[\nu_A \left/ \left(\frac{dU_A}{dx}\right)_{x=0}\right.\right]^{1/2} \tag{6}$$

then

$$\overline{Re} = \left[V_A^2 \cdot C \cdot / (\nu_A U_\infty U_1)\right]^{1/2} \tag{7}$$

where

$$U_1 = \left[\frac{C}{U_\infty}\left(\frac{dU_A}{dx}\right)\right]_{x=0} \tag{8}$$

Poll suggests that compressibility effects might be incorporated into the roughness-effects correlation by replacing $\overline{Re}$ by $\overline{Re}_*$ and η by η_*.

In recent hypersonic flow studies[6], $\overline{Re}_*$ was varied from 200 to 600 and k/η_* from 0.8 to 2.4, which covers the range from smooth to fully rough in Poll's correlation. Here, it should be noted that the $\overline{R}$ based on inviscid flow conditions over the attachment line varies from 500 to 1200, and that employing reference conditions for η and $\overline{Re}$ has yet to be validated. For the smooth configuration, turbulent bursts were observed at $\overline{Re}_*$ of 550, and laminar boundary layers were observed at larger values. This value corresponds to a freestream Reynolds number based on cylinder diameter of 8 x 10^5. The effects of the alignment of the nosetip may be critical in controlling transition on the attachment line of the smooth cylinder. For the fully tripped configuration employing the 0.030-inch trips, we found that the minimum attachment line Reynolds number to induce transition was 330, rather than the 245 found in earlier studies by Poll. For roughness ratios between 2 and 0.8, we observed a trend similar

to that observed in incompressible flows, although, clearly, the data interpretation for this plot is difficult. Plotting the transition Reynolds number for the fully rough limit on Poll's transition correlation in Figure 10 shows that at local Mach number of 8, the onset of transition occurs at 330, rather than at Poll's value of 245, obtained at the lower Mach numbers.
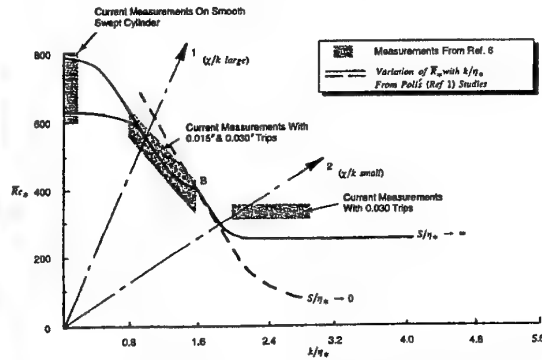
Figure 10   Correlation of Attachment Line Transition with Surface Roughness Height (Reference 6)

2.3   Crossflow Transition

2.3.1   Introduction

Recently, concerted efforts have been made to extend this understanding of boundary layer transition to the three-dimensional boundary layer, where crossflow effects can become a dominant influence on transition. Three-dimensional flowfields exist along high-speed vehicles at incidence and around swept leading edges, as well as any flows having curved streamlines/transverse pressure gradients[7-10]. Because transition is first observed on vehicles at incidence, an understanding of transition in a three-dimensional boundary layer is vital in the design of a high-speed vehicle, since 3-D transition may be the dominant transition process over most of the vehicle.

In three-dimensional flow, the combination of pressure gradient and sweep deflects the inviscid streamlines and since the fluid near the wall has a lower momentum, this deflection is larger in the boundary layer and causes a crossflow, as depicted in Figure 11. To match the boundary conditions at the wall and in the freestream, the crossflow velocity profile is zero at these points and attains a maximum at some point in the boundary layer. This crossflow acts to transfer momentum results in a decrease of momentum thickness on the windward side and in an increase of it on the leeward side. The crossflow instability produces crossflow vortices, approximately aligned in the local inviscid-flow direction. It is this crossflow instability that

dominates the transition process at angle of attack. Reed and Saric[11] provide an excellent review of this subject. This instability is fundamentally different than the two-dimensional, axisymmetric second-mode and oblique Tollmein-Schlicting[12] (TS) instabilities that lead to transition in the hypersonic zero-angle-of-attack case. As angle of attack increases, the dominant instability changes from the second-D mode and/or TS instabilities to a combination of second-mode, TS, and crossflow instabilities; eventually, the crossflow instability is dominant.
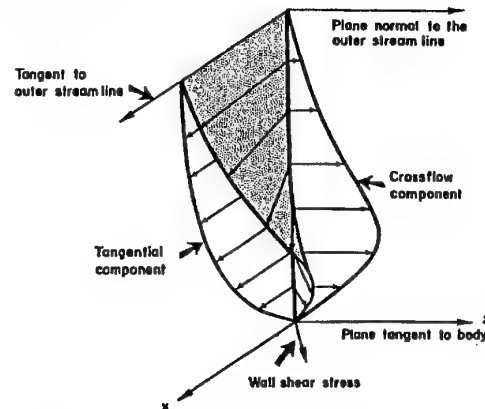
Figure 11   Three-Dimensional Profiles in a Crossflow Boundary Layer

There have been numerous experiments to investigate the movement of the point of transition as a function of angle of attack. Many experiments[13-18] have all consistently found the expected rearward movement of the transition region on the windward side, and forward movement on the leeward side. However, of particular importance is that part of the transition zone where crossflow is at a maximum (i.e., on the sides, 90° and 270° rays relative to windward, of slender cones at angle of attack). Transition data in this region has been obtained by relatively few researchers (e.g., Stetson[14], Holden[15]).

2.3.2   Influence of Angle of Attack and Bluntness on Hypersonic Boundary Layer Transition

The results of several investigations have consistently found a rearward movement of transition location on the windward side, and forward movement on the leeward side of sharp or slightly blunted cones. Crossflow that transfers momentum from the windward side to the leeward side thickens the boundary layer on the leeward side which affects the local Mach number and Reynolds numbers. Experimental studies[13,16,17] have all shown transition delayed on the windward side, and the corresponding movement forward of transition location on the

leeward side. Stability studies[18-21] have demonstrated the increase of growth rate of the dominant instabilities on the windward rays, and opposite behavior on the leeward rays. Transition is located in the region of highest crossflow, which occurs on the sides of the cone relative to the freestream direction.

Measurements by Holden[15] of heat transfer and corresponding circumferential transition locus were made for various hypersonic freestream flow conditions. Figure 12 shows the distributions of transition fronts on the sharp 6-degree cone at various angles of attack, together with previous measurements on similar cones, but at lower Mach number. All these studies show the transition point moving forward with increasing angle of attack on the leeward side, and the transition point moving towards the base of the cone on the windward side. A unique feature of the shape of the transition front determined in Reference 15 is that the positions of the most aft transition points occurred on the 90° and 270° rays, rather than on the windward rays as observed in the studies at lower Mach numbers. This feature of further reduction in transition Reynolds number on the sides of the cone is evident at all angles of attack in this study, and has an increasing effect not only with azimuthal angle, but also with angle of attack, as shown in Figure 12. As shown in this plot, the stabilizing influence of crossflow becomes more apparent as the angle of attack increases.

Source	Sym.	Technique	Facility	Θ_c	α/Θ_c	M_∞	T_w/T_{aw}	Re/ft
Reda (Ref. 17)	◊	Spark Shadowgraph	Range	5.°	.35- .45	4.5	.22 -.48	12.5 -31.9 X 10⁶
Krogmann (Ref. 16)	▲	Single Line Oil Flow	Tunnel	7.5°	.40	5.0	~1.0	7.58 X 10⁶
Stetson (Ref. 14)	□ ○	Heat Transfer	Tunnel	8.°	.25 .50	5.9	.52- .58	9.70 X 10⁶
Holden (Ref. 46)	● + ■	Heat Transfer & Schlieren Photographs	Shock Tunnel	6.°	.1667 .333 .5	13.3	.143	3.00 X 10⁶
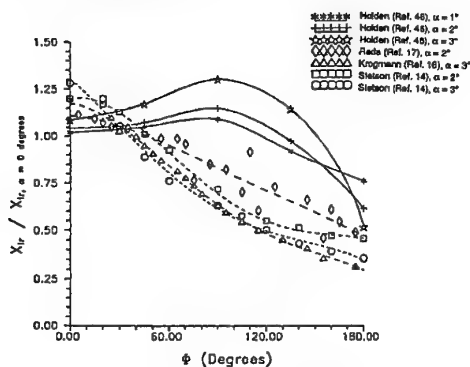
Figure 12   Transition-Front Asymmetry, Sharp Cone

This stabilizing effect is clearly not evident in the results[16,17,22] at lower Mach numbers, which implies that the interaction of the crossflow

instability in these cases exhibits a destabilizing influence. This effect is further evidenced by the reduction in transition location with increase in angle of attack in the curves reported by Potter, based on wind tunnel results[18,23,24] destabilizing effect of crossflow is also demonstrated in the calculations of Balakumar and Reed[10], who found a strong destabilizing effect of crossflow on the oblique first-mode and 2-D second-mode disturbances, which diminished as Mach number increased.

In the simple analysis of transition measurements obtained on sharp flat plates and cones, it was found that the Reynolds number based on the local momentum thickness (Re_θ) provided the best correlation of both wind tunnel and flight measurements in hypersonic flow over highly cooled walls. Thus, following Finson[25], we have plotted the measurements made in the present studies together with those from earlier work in terms of the Reynolds number local momentum thickness and the local Mach number for both sharp and blunt bodies (see Figure 13). It can be seen that for both sharp and blunt configurations, that $(Re_x/Re_{x_0})\dfrac{M_0}{M}$ is relatively independent of angle of attack. Thus, for sharp cones, it may be observed that transition moves forward on the leeside ray, principally because of the large increase in the momentum thickness; on the windward ray, the effects of crossflow and higher unit Reynolds number combine to cause a decrease in the momentum thickness. In the situation with relatively large bluntness, the entropy layer is swallowed more rapidly on the windward ray than on the leeward, which acts to increase the momentum thickness on the windward ray. This counteracts the action of crossflow to bleed some momentum from the windward ray to the leeside, and acts to further destabilize the windward side relative to the zero-angle-of-attack case. More recently, Reed and Haynes[15a] have suggested a more sophisticated correlation technique based on crossflow Reynolds number which requires detailed predictions of the crossflow velocity which are now available from Navier-Stokes solutions.
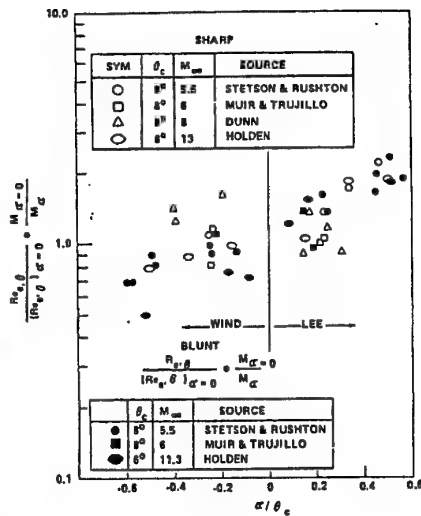
Figure 13 Correlation of Transition Front Locations on Sharp and Blunt Slender Cones at Angle of Attack

2.3.3 Correlation of Transition-Front Location Using Compressible Crossflow Transition Reynolds Number

A low-speed crossflow Reynolds number transition criterion was introduced by Owen and Randall[26], given by $\dfrac{W_{max}\delta}{v_e}$, that correlates well with low-speed data. However, extending this correlation to the high-speed range has met with limited success. Chapman[9] extended this approach into the supersonic and low-hypersonic range; however, these results have been criticized by Poll[8], claiming that contamination of the attachment line affected the boundary layer in the crossflow region. King's[28] results also found no correlation with the traditional crossflow Reynolds number.

Since the traditional crossflow Reynolds number is used successfully at subsonic speeds, Reed and Haynes[15a] developed additional factors in the definition of crossflow Reynolds number to compensate for the effects of compressibility and heat transfer to the surface. Their definition is

$$R_{CF(new)} = HL\frac{W_{max}\delta_{10}}{v_e}$$

where

$$\delta_{10} = \text{point in boundary layer above}$$
$$W_{max} \text{ where } \frac{W}{W_{max}} = 10\%$$

In their study, Reed and Haynes[15a] calculated $R_{CF(new)}$ for the experimental data of Stetson[27] at $M_\infty=6$, and King[28] at $M_\infty=3.5$ in both noisy and quiet freestream environments. The authors suggested a correlation between the crossflow Reynolds number and the maximum crossflow velocity. However, separate correlations were developed for the noisy and quiet data. Results for the sharp cone at $M_\infty=13$ from the Holden[46] study are shown in Figure 14, with the noisy and quiet correlations of Reed and Haynes. Most notable is that the present results follow the quiet correlation, especially as the level of crossflow (W_{max}/U_e) increases. The reduction in scatter as crossflow increases is expected, since, as Reed and Haynes point out, the lower end of the curve and data are somewhat suspect. At low levels of crossflow ($W_{max}/U_e <2\%$), the crossflow instabilities interact with the other more dominant instabilities (T-S, 2nd mode, helical, etc.) generated in the windward and leeside regions. The additional problem arises in the low-crossflow situation in that defining a precise δ_{10} point in the boundary layer for R_{CF} calculation becomes increasingly difficult. Nonetheless, the trend shown in Figure 15 further demonstrates the contentions that crossflow instabilities are not greatly influenced by any freestream acoustic disturbances, and that the dominant transition mechanisms in hypersonic flows are dominated by crossflow instabilities.
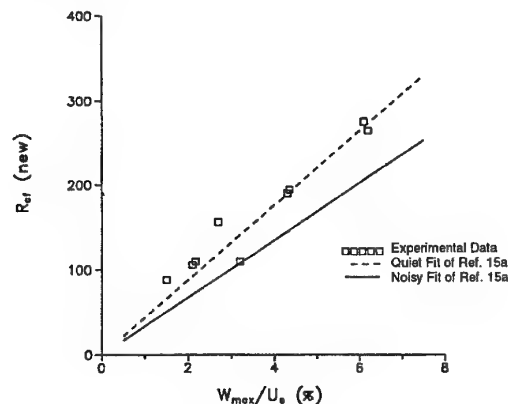
Figure 14 Correlation of Transition Front Location in Regions of Crossflow with "New" Crossflow Reynolds Number, $M_\infty=13$, $Re_\infty/Ft=3.0 \times 10^6$
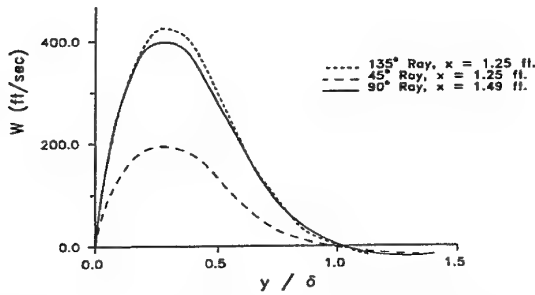
Figure 15 Crossflow Velocity Component at Transition Onset, $M_\infty=13$, $\alpha=3°$, $Re_\infty/Ft=3.0 \times 10^6$

3. FILM AND TRANSPIRATION COOLING FOR FLOWS WITH SHOCK INTERACTION

3.1 Introduction

A key aspect of the design of hypersonic vehicles is the development of active wall-cooling systems for regions of high heating loads on the airframe and engine. Apart from backface cooling methods, transpiration cooling and film cooling are two techniques that have been proposed to reduce the large heating loads which also reduce skin friction. The relative merits of film and transpiration cooling must be evaluated against complications associated with the fluid mechanical design of these systems, the sensitivity of each technique to shock impingement and combustion phenomena. Film-cooling techniques have also been used successfully to reduce the aerothermal loads on the optical windows of hypersonic seeker heads, and to alleviate the heating levels in the combusting flows downstream of the injectors in scramjet engines. For the specific application to scramjet combustors, employing film cooling is attractive, because the injectant momentum contributes directly to thrust, and the mechanical construction is intrinsically simple. However, recent studies[29-31] have demonstrated that relatively large levels of mass addition are required to maintain a cooling film over the length of the combustor. Also, if shocks generated in the inlet section and the injector region of an engine impinge on the film-cooled surface, they may destroy the integrity of the film, returning the heating levels to their uncooled values. Transpiration-cooling techniques have been used successfully to reduce the heating and skin friction levels on the nosetips and frusta of conical hypersonic reentry vehicles[32-34]. Transpiration cooling is also advantageous in that it can significantly reduce the wall skin friction (which is a major component of the engine drag). However, the

resulting low-momentum region adjacent to the wall can potentially be easily separated by a shock system impinging on the wall. The sensitivity to flow separation on a transpiration-cooled surface was demonstrated in studies[35] of transpiration-cooled maneuvering reentry vehicles (MRVs), where flap effectiveness was significantly reduced by the introduction of a low-momentum layer adjacent to the surface upstream of the flaps. However, recent studies[36] have indicated that transpiration-cooled surfaces are not as sensitive to shock interaction as one might have deduced from the results of wedge-induced separated regions.

3.2 Film and Transpiration Cooling in the Absence of Shock Interaction

3.2.1 Film-Cooling Studies

To illustrate the major features of these flows, we first discuss typical measurements from film-cooling studies[29] of interest to combustor design without incident shocks. Measurements of heat transfer and pressure were made downstream of 0.120-inch cooling slot for non-dimensional blowing rates λ_c from 0.0 to 0.28. Figure 16 shows a typical set of heat transfer measurements in hypersonic flow downstream of a 0.120-inch slot. For the cases without helium film cooling where a strong recompression shock was generated downstream of the step, a local peak in the heating rate was observed, followed by a gradual return to the flat-plate heating level. For the matched-pressure coolant condition, there was a very weak wave at the top of the nozzles and the initial turbulent boundary layer moved smoothly from the step. In contrast, for the highest blowing rates where the flow was underexpanded, strong shocks were generated above and behind the nozzle exit, which leads to enhanced mixing. It is clear from Figure 16 that the greatest rate of heating reduction occurred for the largest cooling rates. However, beyond a certain coolant mass-flow rate, there was relatively little change in the heat transfer to the plate with increased coolant flow rate. Close to the matched-blowing condition the measurements from the two slot heights scale relatively well in terms of non-dimensional slot height. This can be seen by plotting the measurements in terms of cooling effectiveness (as shown in Figures 17 and 18). Cooling effectiveness (η) is defined as

$$\eta = \frac{T_{aw} - T_{T\infty}}{T_{TC} - T_{T\infty}}$$

taking the reference value from the no-cooling run, we have

$$h_r = q_{nc}/(T_{aw}-T_w);$$

for coolant flow $\quad T_{aw} = \dfrac{q}{h_r} + T_w$

thus, $\eta = (q/h_r + T_w - T_{T\infty})/(T_{TC} - T_{T\infty})$

$$\therefore \eta = \left[1 - \frac{q(T_{aw} - T_w)}{q_{nc}} \frac{}{T_{o\infty} - T_{TC}}\right] \qquad (10)$$
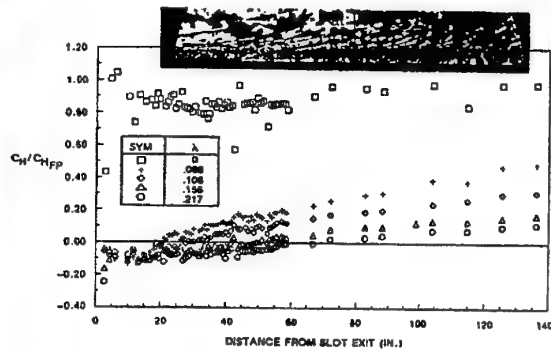
Figure 16 Heat Transfer Variation with Mass Addition for 0.120-Inch Slot
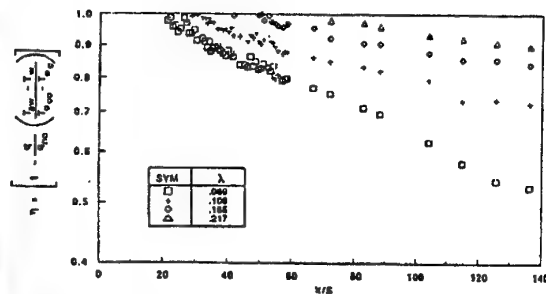
Figure 17 "Effective Efficiency" of Film Cooling for 0.120-Inch Slot
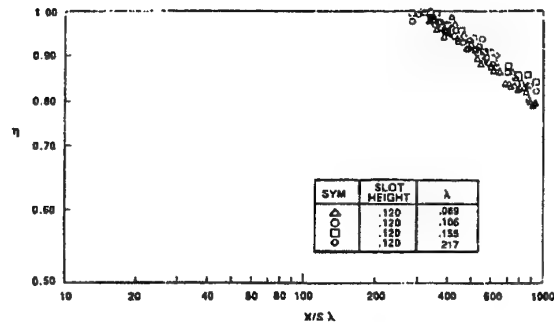
Figure 18 Correlation of Film-Cooling Effective Efficiency with Simple Scaling Parameters

These measurements made in the film-cooling studies correlated well when plotting η in terms of the scaled slot-height parameter $(X/S)/\lambda^{0.8}$ as shown in Figure 19. Also shown in Figure 19 are high Mach number measurements[29] for a nitrogen coolant, demonstrating the superior cooling properties of helium. The measurements made in these studies for a specific slot height, in fact, scale better in terms of λ^{-1}, as shown in Figure 18. To account for the effects of the molecular weight and specific heat of the coolant and the specific injection Mach number of the coolant, we have employed a modified cooling-length parameter

$$\frac{x}{s\lambda}\left(Re_c\frac{\mu_c}{\mu_e}\right)^{-0.25}\left(\frac{\rho_c}{\rho_e}\right)^{0.4}\left(\frac{\mu_e}{\mu_c}\right)^{0.75}\left[1+\frac{\gamma-1}{2}M_c^2\right]^{-0.5}\left(\frac{C_{pe}}{C_{pc}}\right)^{0.8} \quad (9)$$

in the correlation shown in Figure 20. Employing this parameter appears to correlate the existing measurements for the two slot heights, and those compiled earlier by Majeski and Weatherford[31] suggest a break point of close to two.
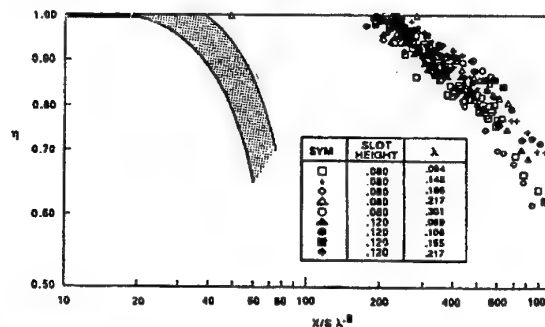
Figure 19 Correlation of Film-Cooling Effective Efficiency with Simple Scaling Parameters
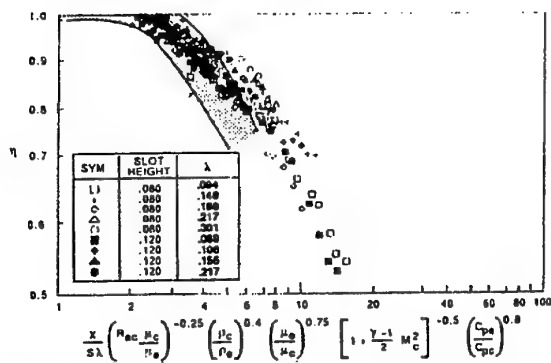
Figure 20 Correlations of Effective Efficiency of Film Cooling

$$\frac{x}{s\lambda}\left(R_{ec}\frac{\mu_c}{\mu_e}\right)^{-0.25}\left(\frac{\mu_c}{\rho_e}\right)^{0.4}\left(\frac{\mu_e}{\mu_e}\right)^{0.75}\left[1,\frac{\gamma-1}{2}M_c^2\right]^{-0.5}\left(\frac{c_{pe}}{c_{pc}}\right)^{0.8}$$

Figure 21 Summary of Blockage Heating from Studies on Flat Plates and Cones in Turbulent Flow (Reference 34)

Figure 22 Comparison Between the Measurement Made in the Nosetip Studies with Nitrogen Injectant and the Earlier Blockage Data (Reference 34)

3.2.2 Transpiration-Cooling Studies on Blunt, Intrinsically Rough Nosetips

The lack of techniques to predict the effectiveness of transpiration/ablative cooling techniques reflects the lack of a fundamental understanding of turbulent mixing in compressible shear layers in the presence of mass injection and intrinsic surface roughness. Earlier studies of transpiration cooling techniques were designed principally to evaluate how the blockage heat transfer C_H/C_{Ho} varied with the Mach number, Reynolds number and properties of the freestream and injectant. There is a dearth of fully turbulent data at hypersonic speeds where transpiration cooling is of considerable interest because it is difficult to generate the high Reynolds number, high velocity test conditions necessary for the correct simulation. Experimental studies have been conducted in supersonic flow with flat plates[37-40] and cones[41-43] and there has been some work on the transpiration cooling of blunt nosetips[32,44]. Based on a survey of the existing experimental data[32], the correlation shown in Figure 21 was developed. This correlation indicates that for large blowing rates (B'>10), increased blowing does not significantly improve thermal protection. This may well result from a decrease in the stability of the mixing layer and an increase in the scale of turbulence with increasing blowing. However, Holden's measurements on a spherical nosetip, shown in Figure 22 suggest that heating levels significantly lower than those found on flat plates and cones were obtained for the higher blowing rates. These latter measurements could be correlated in the form $(C_{Ho}-C_H)/C_{Ho} = 1/3\, B'^{1/3}$, where

$$B' = \frac{\dot{m}}{\rho_e U_e C_{Ho}} .$$

The measurements made in earlier studies of transpiration cooling conducted with spherical nose tips suggest that the initial effect of mass addition from a rough nosetip is to modify the flow around the rough surface by eliminating the cavity flows in such a way that the roughness-induced momentum defect is small. If indeed the initial effects of mass addition is to remove surface roughness as an important mechanism for surface drag, this introduces serious questions on the validity of correlations of flight measurements on ablating nosetips based on an effective surface roughness. The computational procedures where the ablation rate is determined from heating levels enhanced by surface-roughness effects are highly questionable.

3.2.3 Transpiration-Cooling Studies of Flat CombustorSurfaces

Typical measurements of the effects of blowing rate on the heat transfer and pressure in the transpiration-cooled flat surface are shown for the

Mach 6 condition with nitrogen and helium coolants in Figures 23 and 24, respectively. For the nitrogen coolant, a mass-addition level of 1.5% resulted in a 50% reduction in the heating rate; employing a helium coolant accomplished this reduction with one-third of the mass-flow rate. The measurements made with nitrogen coolants suggest that beyond a certain level for blowing rate (for blowing rates to achieve a 70% reduction in heating) significantly more coolant is required to further reduce the heating level. For helium, this "knee" occurred at approximately a 90% heating reduction. The effectiveness of transpiration cooling was not strongly influenced by Mach number. Correlations of the heating reduction for the nitrogen and helium coolants are shown in Figures 25 and 26, respectively. To account for the effects of the molecular weight and specific heat of the coolant gases, we have correlated the measurements in terms of a modified blowing parameter

$$B' = \dot{m} / \left(\rho_s U_s C_{H_s}\right) \left(\widetilde{M}_{fs} / \widetilde{M}_{inj}\right)$$

or

$$B' = \dot{m} / \left(\rho_s U_s C_{H_s}\right)\left(C_{p inf}/C_{p fs}\right)^{0.7}\left(\widetilde{M}_{fs} / \widetilde{M}_{inj}\right)^{0.5} \qquad (11)$$

which was deduced in earlier studies[33]. As shown in Figure 27, the measurements for both the helium and nitrogen coolants as well as the Mach 6 and 8 data can be correlated well with these parameters. Also shown is the empirical relationship

$$\frac{C_{H_0} - C_{H_s}}{C_{H_0}} = 0.92 \, (1 - e^{-B'/4}) \qquad (12)$$

which provides a simple analytical expression for first order design estimates of heating reductions in transpiration-cooled flows.
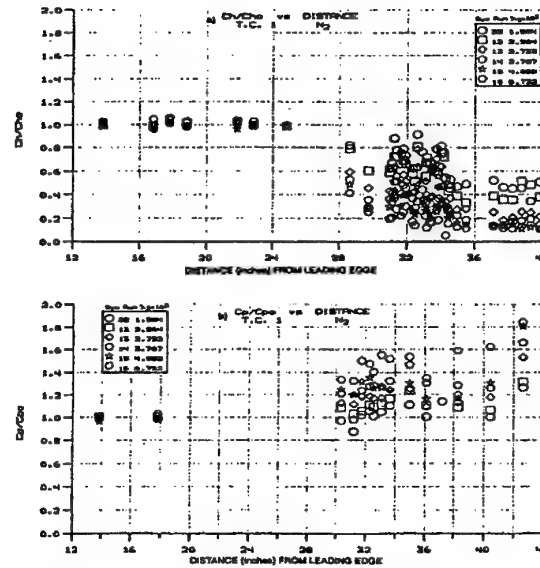
Figure 23   Heat Transfer and Pressure Distributions Along Flat Plate-Transpiration Surface for Nitrogen Coolant at Mach 6 (Reference 45)
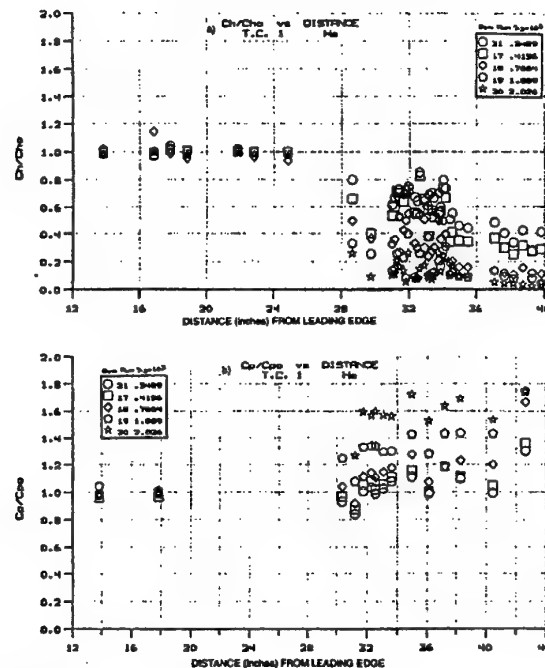
Figure 24   Heat Transfer and Pressure Distributions Along Flat Plate-Transpiration Surface for Helium Coolant at Mach 6 (Reference 45)
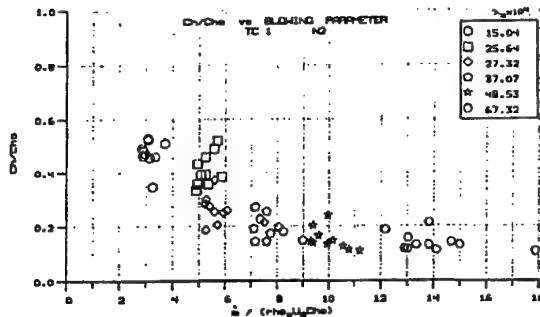
Figure 25 Correlation of Heat Transfer Measurements with Transpiration Cooling in Terms of Simple Blowing Parameter for Nitrogen Coolant at Mach 6 (Reference 45)
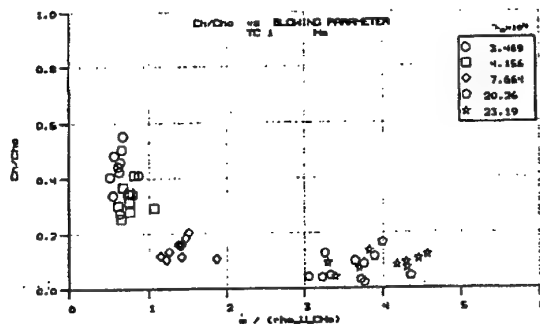
Figure 26 Correlation of Heat Transfer Measurements with Transpiration Cooling in Terms of Simple Blowing Parameter for Helium Coolant at Mach 6 (Reference 45)
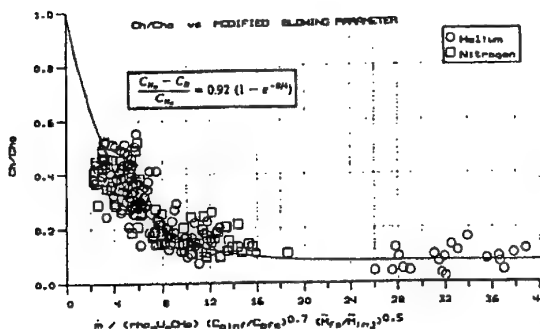
Figure 27 Correlation of Nitrogen and Helium Transpiration-Cooling Heat Transfer Measurements with Modified Blowing Parameter (Reference 45)

3.3 Shock Interaction With Film-Cooled and Transpiration Cooled Surfaces

3.3.1 Shock Interaction with Film-Cooled Surfaces

Figures 28a and 28b illustrate the major features of the viscous/inviscid interaction regions in regions of shock-wave/film-cooling interactions. In Figure 28a, we have shown a case where the flow remains attached and the coolant layer was not dispersed by the interaction region. In Figure 28b, we show a flow where the coolant layer was separated in the interaction region. Again, the flow was for a large cooling rate; however, the shock from a 10.5° shock generator created a large separation region as it impinged on the boundary layer. The two nozzles shocks are, again, clearly evident; however, just upstream of the point that the incident shock struck the boundary layer, a third shock, the separation shock, was induced upstream of the point of shock impingement as the boundary layer separated. A separation (plateau) region was formed in which the heat transfer and pressure were relatively constant. As the flow turned parallel to the surface, the separated shear layer reattached, and a recompression shock was formed. In these turbulent flows, the separated region extended from the beginning of the heat transfer rise to the end of the plateau region. For the separated region shown in Figure 28b, the coolant layer was rapidly dispersed in the separation and the reattachment regions, resulting in heating levels downstream of the incident shock that were not reduced by film cooling as shown below.
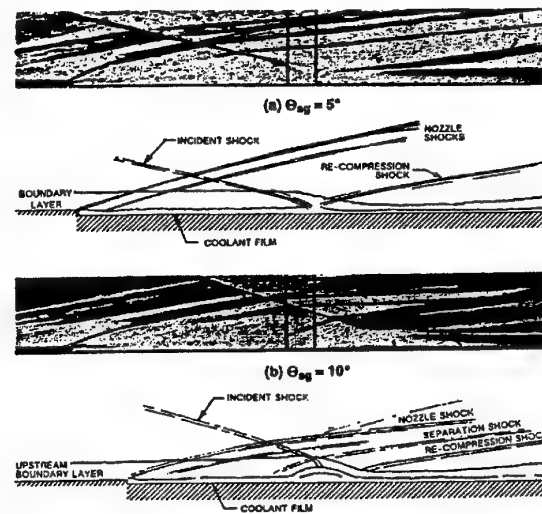
Figure 28 Separated Shock-Wave/Cooling-Film Interaction

Typical measurements showing the heat transfer and pressure characteristics of a shock-coolant-layer

interaction are shown in Figures 29 and 30 for a slot height of 0.120 inch and a shock-generator angle of 8°. The Schlieren photographs shown in Figure 31 indicate that the flow, which was attached without blowing, was fully separated for the two blowing conditions. As can be seen in Figure 29, the heating rate at the end of the recompression process was not reduced by film cooling. Also, a twofold increase in the blowing rate from the matched-flow conditions did not significantly increase the cooling capability downstream of the incident shock. A similar set of heat transfer and pressure measurements for the 5.5° shock generator is shown in Figure 32 and 33. Figure 34 shows the Schlieren photographs for this case. For the 8° shock generator, a large separated region was formed ($l_{sep}/\delta_{FP=5}$) that decreased only slightly as the blowing rate was doubled. For the 5.5° shock generator, the small separated region that was formed in the matched-blowing case was swept away when the blowing rate was doubled. As illustrated in Figure 32, the coolant film remained intact and caused a reduction in the peak heating of 90% to 50%, depending on the position downstream of the cooling slot. However, in general, a film cooled layer can easily be dispersed by a plain incident shock.

Figure 30   Pressure Distribution in Regions of Incident Shock/Wall-Jet Interaction (Θsg=8.0 Degrees, Slot Height=0.120 Inch)

(a) $\lambda = 0$

(b) $\lambda = 0.102$

(c) $\lambda = 0.237$
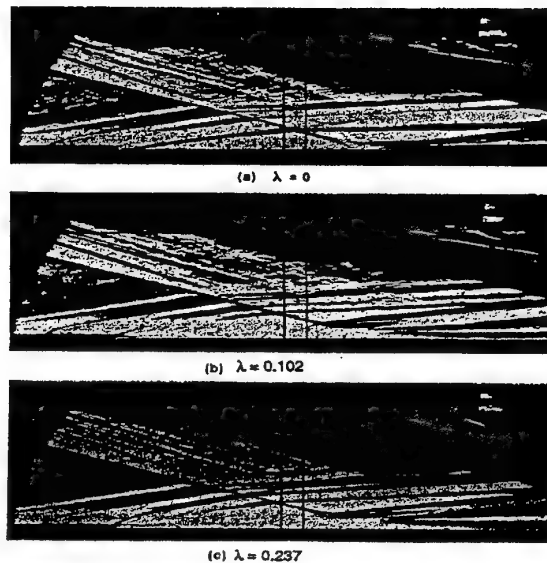
Figure 31   Schlieren Photographs for Incident-Shock/Wall-Jet Interactions (Θsg=8.0 Degrees, Slot Height=0.120 Inch)

Figure 29   Heat Transfer Distribution in Regions of Incident Shock/Wall-Jet Interaction (Θsg =8.0 Degrees, Slot Height=0.120 Inch)
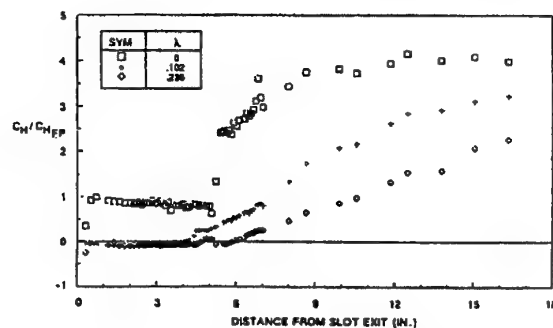
Figure 32   Heat Transfer Distribution in Regions of Incident-Shock/Wall-Jet Interaction (Θsg=5.5 Degrees, Slot Height=0.120 Inch)

Figure 33 Pressure Distribution in Regions of Incident-Shock/Wall-Jet Interaction (Θsg=5.5 Degrees, Slot Height=0.120 Inch)

(a) $\lambda = 0$

(b) $\lambda = 0.102$

(c) $\lambda = 0.256$
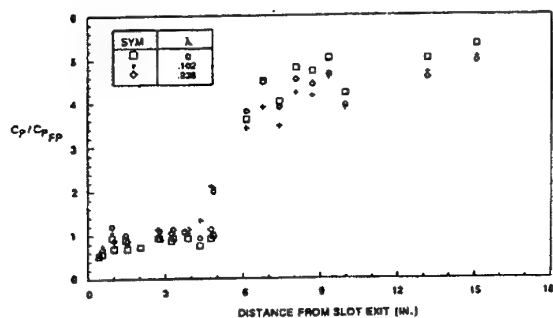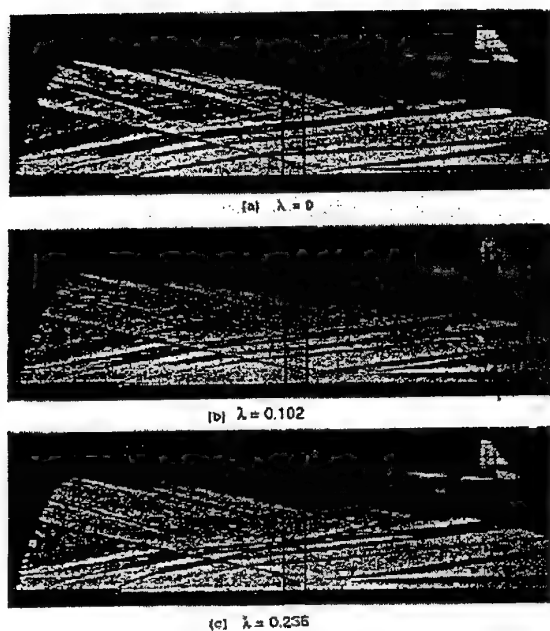
Figure 34 Schlieren Photographs for Incident-Shock/Wall-Jet Interactions (Θsg=5.5 Degrees, Slot Height=0.120 Inch)

3.3.2 Shock Interaction with Transpiration-Cooling Surfaces

Figures 35 and 36 show the distribution of heat transfer and pressure in regions of shock/coolant-layer interaction for a 5.3° shock generator and nitrogen and helium coolants. For the non-blowing case, the shock interaction caused a pressure increase that was fed upstream of shock impingement through the transpiration-cooled surface, introducing air into the sublayer upstream of shock impingement. The heat transfer rate in this region was dramatically reduced, even in the absence of coolant addition.

However, it can be seen from the pressure distribution in Figure 35b that the pressure upstream of shock impingement was not significantly modified by this influx of gas into the base of the boundary layer. It is observed that introducing a nitrogen coolant rate of less than 5% or a helium coolant rate of one-third this value is required to reduce the heating level downstream of shock impingement to less than that upstream of the shock on the smooth plate. It can be seen from Figure 36b that the pressures upstream of shock impingement were not significantly modified by introduction of gas through the transpiration-cooled surface. The heat transfer and pressure distributions for the interaction strength generated by the 7.5° shock generator are shown in Figures 37 and 38. Even with this increase in shock strength, there was, little upstream influence of the shock, both in the presence and in the absence of transpiration cooling. Again, we observed a decrease in heat transfer upstream of the incident shock resulting from flow under the porous surface for the non-blowing case.
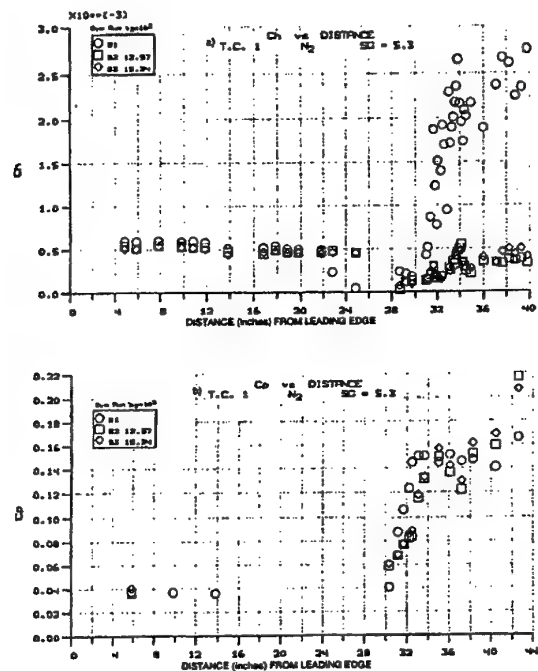
Figure 35 Heat Transfer and Pressure Measurements at Mach 6 on Nitrogen-Cooled Transpiration Surface with Shock Interaction from 5.3° Shock Generator
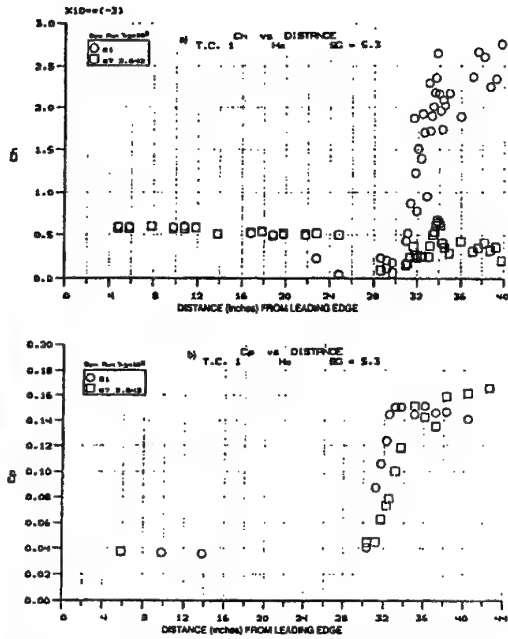
Figure 36 Heat Transfer and Pressure Measurements at Mach 6 on Helium-Cooled Transpiration Surface with Shock Interaction from 5.3° Shock Generator

Figure 37 Heat Transfer and Pressure Measurements at Mach 6 on Nitrogen-Cooled Transpiration Surface with Shock Interaction from 7.35° Shock Generator

Figure 38 Heat Transfer and Pressure Measurements at Mach 6 on Helium-Cooled Transpiration Surface with Shock Interaction from 7.35° Shock Generator

Introducing coolant upstream of the shock induced a small upstream influence as a result of flow separation, which is clearly evident from what appears in the plateau in the pressure distribution (see Figures 37 and 38). However, as observed earlier, there was a significant decrease in heat transfer in this region. Schlieren photographs of these flows indicate that transpiration cooling does not induce strong distortions in the inviscid flow, and that the pressure levels and distribution downstream of shock impingement were basically uninfluenced by the introduction of coolant. The heat transfer downstream of the incident shock can be reduced to the initial flat-plate levels by the introduction of 2% of the freestream mass-flow rate of helium downstream of the incident shock. Measurements with heat transfer and pressure with the 10.5° shock generator are similar in nature to those obtained with the weaker shock strength. However, at the highest blowing rates, we began to observe flow distortions in the freestream downstream of the incident shock. In general, however, it was observed that transpiration cooling is an effective way of controlling peak heating in regions of shock-wave/boundary layer interaction. From these studies, a simple relationship for predicting the cooling requirements in regions of shock-wave/transpiration-

cooling interaction was developed. By employing correlations based on the heat transfer coefficients and blowing parameters determined from the local inviscid conditions downstream of the reflected shock, it was possible to collapse the data sets from the different interaction strengths and test conditions into a single correlation shown in Figure 39. The form of this correlation

$$\frac{C_{H_{LO}} - C_{H_S}}{C_{H_{LO}}} = 0.92\,(1 - e^{-B_L'/4}) \tag{13}$$

is similar to that for the constant-pressure flat-plate data. By employing this correlation together with simple calculations to determine the local inviscid flow conditions, it is possible to provide good estimates for the levels of mass addition required to control the peak heating levels downstream of shock impingement.
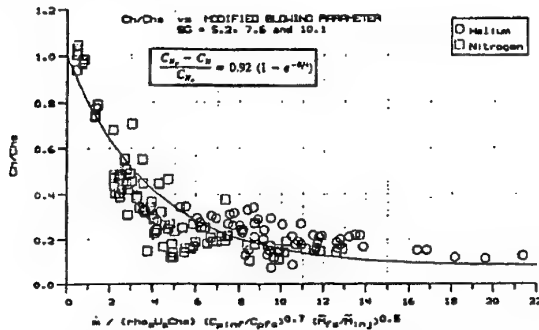
Figure 39　Correlation of Heating Reduction Ratio with Modified Blowing Parameter m(rho$_s$U$_s$Ch$_s$) (C$_{pint}$/C$_{pfs}$)$^{0.7}$ (M$_{sf}$/M$_{inj}$)$^{0.5}$ for Shock-Generator Angles of 5°, 7.5°, and 10° and Both Nitrogen and Helium Coolants

3.3.3　Comparison Between Film and Transpiration-Cooling Techniques with Shock Interaction

To make a comparison of film cooling versus transpiration cooling, for a given cooling surface area, the cooling effectiveness is compared for the two techniques based on mass flow rates of the cooling injectant; in this case, the cooling injectant. Figures 40 and 41 show the results for the 5.5° incident shock generator cases for transpiration cooling as compared to the 0.08 inch and 0.120 inch slot cases. Figures 42 and 43 depict similar results for the 8° shock generator results. There is a dramatic difference in the cooling effectiveness of the two techniques downstream of the shock interaction region. For the 5.5° case (Figures 39 and 40), increasing the mass flow rate does reduce the

heating levels downstream of the interaction region. For the two cases shown, by nearly doubling the injectant mass flow, the heating load is approximately reduced by a factor of two. However, the effectiveness of the film cooling is continuously degrading in the downstream direction. In each of the two figures (Figures 40 and 41) downstream of the interaction regions are lines which represent approximate heating values for the equivalent mass addition rate as the depicted transpiration cooling case. These were obtained by simply interpolating between the two sets of measured data. There is a significant improvement in the cooling levels of the transpiration case over that of the interpolated film cooling result. In fact, the heating level is reduced by over a factor of two for both comparisons shown. Moreover, the transpiration cooling is more effective than the film cooling case with 50% more mass addition as shown in Figure 40 and is as effective as the case with twice the mass addition as shown in Figure 41.

3.3.4　Transpiration Cooling for Shock/Shock Heating

While transpiration cooling has been shown to be effective in protecting flat surfaces in regions of shock/shock interaction, employing a similar technique for protecting leading edge surfaces from heating generated by shock/shock interaction has been far less successful as demonstrated by Holden[33] in experiments with transpiration-cooled spherical nosetips. Two sets of measurements were made to provide an evaluation of the effectiveness of transpiration cooling in the presence of shock/shock interaction heating. Measurements were made first on a smooth and transpiration cooled model without coding. Figure 44 shows the heat transfer and pressure distribution for a Type IV interaction over the smooth model indicating enhancements factors close to 20 for the Type IV interaction region. A similar set of measurements were made on the transpiration-cooled nosetip without blowing as shown in Figure 45, and then with the same transpiration-cooled nosetip for a high blowing rate ($\lambda = 0.2$) as shown in Figure 46. It is clear from comparing these sets of measurements that transpiration cooling had little or no effect on the peak heating or the distribution of heat transfer in the shock interaction regions. Measurements of this type were made for a series of shock locations and are plotted together in Figure 47. These measurements of the variation of peak heating with position of the interaction demonstrate the neither the magnitude or the shape of the peak heating region were significantly altered by transpiration cooling.

Heat Transfer Comparison, Transpiration Cooling
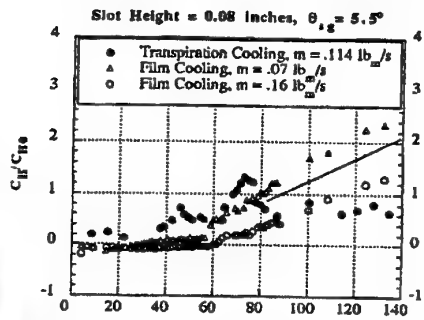and Film Cooling with Shock Interaction

Slot Height = 0.08 inches, θ_{sg} = 5.5°

Transpiration Cooling, m = .114 lb$_m$/s
Film Cooling, m = .07 lb$_m$/s
Film Cooling, m = .16 lb$_m$/s

Figure 40   Distance (Slot Heights) From Slot
Exit/Transpiration Leading Edge

Heat Transfer Comparison, Transpiration Cooling
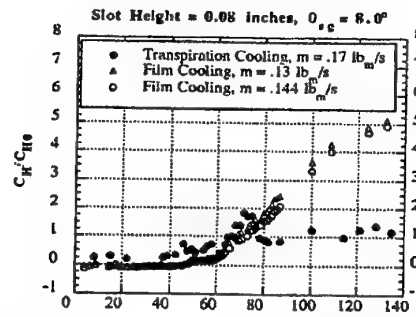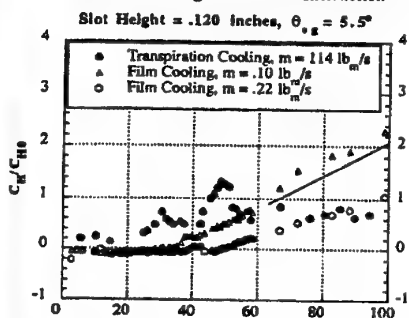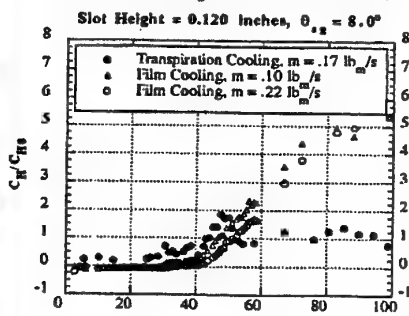and Film Cooling with Shock Interaction

Slot Height = .120 inches, θ_{sg} = 5.5°

Transpiration Cooling, m = 114 lb$_m$/s
Film Cooling, m = .10 lb$_m$/s
Film Cooling, m = .22 lb$_m$/s

Figure 41   Distance (Slot Heights) From Slot
Exit/Transpiration Leading Edge

Heat Transfer Comparison, Transpiration Cooling
and Film Cooling with Shock Interaction

Slot Height = 0.120 inches, θ_{sg} = 8.0°

Transpiration Cooling, m = .17 lb$_m$/s
Film Cooling, m = .10 lb$_m$/s
Film Cooling, m = .22 lb$_m$/s

Figure 42   Distance (Slot Heights) From Slot
Exit/Transpiration Leading Edge

Heat Transfer Comparison, Transpiration Cooling
and Film Cooling with Shock Interaction

Slot Height = 0.08 inches, θ_{sg} = 8.0°

Transpiration Cooling, m = .17 lb$_m$/s
Film Cooling, m = .13 lb$_m$/s
Film Cooling, m = .144 lb$_m$/s

Figure 43   Distance (Slot Heights) From Slot
Exit/Transpiration Leading Edge

Run 8
Mach = 12.15
Re/Ft = 3.692 x 10^5

X — C$_P$
□ — Q/Q$_{FR}$
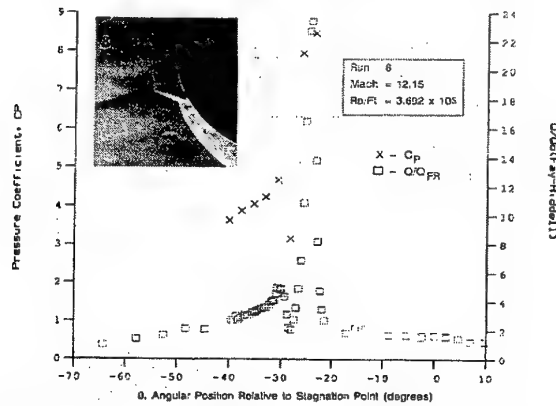
Figure 44   Heat and Pressure Distributions in
Shock/Shock-Interaction Regions
Induced by a 10° Shock Generator
Over a Smooth 12-Inch Diameter
Hemisphere at Mach 12.15 for
Run 8

REGION 8

MORRIS and KEYES
TYPE IV

REGION 7

Run 37
Mach = 12.160
Re/Ft = 3.507 x 10^5
λ = 0.00
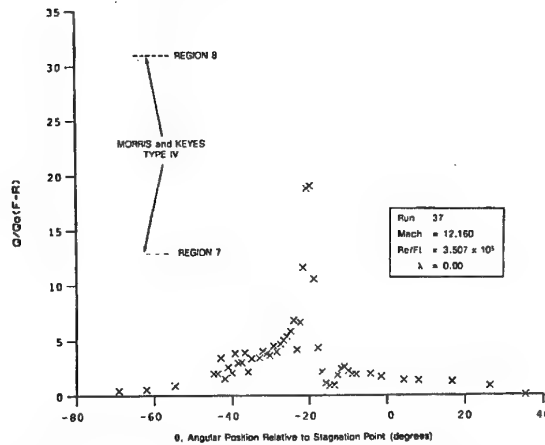
Figure 45   Heat Transfer Distribution in
Shock/Shock-Interaction Regions
Induced by a 10° Shock Generator
Over a Transpiration-Cooled
Hemisphere Without Blowing at
Mach 12 for Run 37
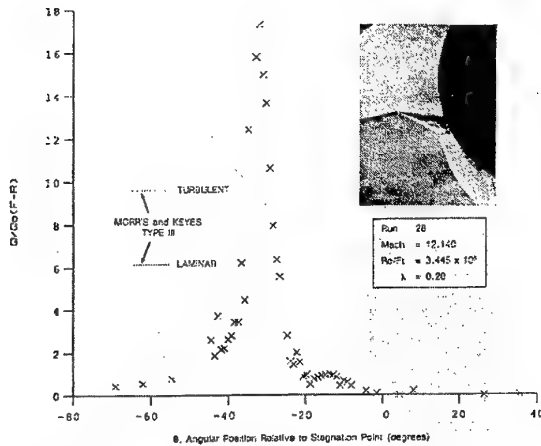
Figure 46 Heat Transfer Distribution in Shock/Shock-Interaction Regions Induced by a 10° Shock Generator Over a Transpiration-Cooled Hemisphere With $\lambda = 0.20$ at Mach 12 for Run 28
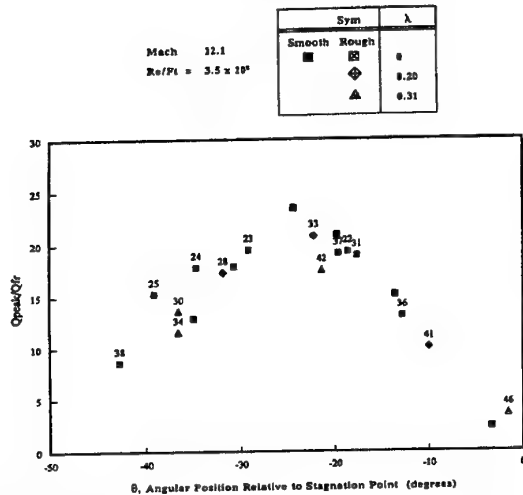
Figure 47 Variations of Peak Heating With Angular Position of the Interaction Region for Various Blowing Parameters, λ, at Mach 12

4. CONCLUSIONS

The aerothermal loads generated in regions of attachment line transition and crossflow transition can be predicted with reasonable accuracy if the disturbance levels in the freestream or on the vehicle surface can be described. Turbulent models to describe the transitional and nonequilibrium development of hypersonic turbulent boundary layers in regions of adverse pressure gradient, while lacking a phenomenological basis can be employed to bracket the levels of heating developed on forebody

and compression ramps of air breathing hypersonic vehicles in the absence of active cooling techniques. Both film and transpiration cooling can be used effectively in hypersonic flow to control regions of peak heating, however, film cooling techniques have been found to be particularly susceptible to dispersion by shock impingement. While it has been found that transpiration cooling is effective on flat surfaces in the presence of shock impingement, this technique has been found to be totally ineffective in cooling leading edge surfaces subjected to shock/shock interaction.

5. REFERENCES

1. Holden, M.S. and Chadwick, K.M., "Studies of Laminar, Transitional and Turbulent Hypersonic Flows Over Curved Compression Surfaces," AIAA 95-0093, paper presented at the 33rd Aerospace Sciences Meeting and Exhibit in Reno, NV, January 9-12, 1995.

2. Poll, D.I.A., "Boundary Layer Transition on the Windward Face of Space Shuttle During Re-Entry," AIAA Paper Number 85-0899, Presented at the AIAA 20th Thermophysics Conference, Williamsburg, Virginia, June 19-21, 1985.

3. Bushnell, D.M., "Interference Heating on a Swept Cylinder in Region of Intersection with a Wedge at Mach 8," NASA TN-D-3094, December 1965.

4. Poll, D.I.A., "The Development of Intermittent Turbulence on a Swept Attachment-Line Including the Effects of Compressibility," *The Aeronautical Quarterly*, Vol. XXXIV, February 1983, pp. 1-23.

5. Creel, T.R., "Transition on Swept Cylinders in the Langley Supersonic Low Disturbance Tunnel," 4th NASP Transition Workshop, NASA-LaRC, December 4, 1990.

6. Holden, M.S. and Kolly J., "Attachment Line Transition Studies on Swept Cylindrical Leading Edges at Mach Numbers from 10 to 12, AIAA 95-2279, 26th AIAA Fluid Dynamics Conference, San Diego, CA, June 19-22, 1995.

7. Cumpsty, N.A., and Head, M.R., "The Calculation of Three-Dimensional Boundary Layers, Part II-Attachment Line Flow on an Infinite Swept Wing," The Aeronautical Quarterly, Vol. XVIII, pp. 150-164, May 1967.

8. Poll, D.I.A., "Transition Description and Prediction in Three-Dimensional Flows," Special Course: Stability and Transition of Laminar Flows, *AGARD-R-709*, March 1984.

9. Chapman, G.T., "Some Effects of Leading Edge Sweep on Boundary Layer Transition at Supersonic Speeds," NASA TN D-1075,1961.

10. Balakumar, P. and Reed, H.L., "Stability of Three-Dimensional Supersonic Boundary Layers," *Physics of Fluids A*, Vol. 3, No. 4, 1991, pp. 617-632.

11. Reed, H.L. and Saric, W.S., "Stability of Three-Dimensional Boundary Layers," <u>Annual Review of Fluid Mechanics</u>, Vol. 21, Jan. 1989, pp. 235-284.

12. Schlicting, H., <u>Boundary-Layer Theory</u>, 4th Edition, McGraw-Hill Book Co., New York, NY 1960.

13. Stetson, K.F. and Rushton, G.H., "Shock Tunnel Investigation of Boundary Layer Transition at M=5.5," *AIAA Journal*, Vol. 5, No. 5, May 1967, pp. 899-906.

14. Stetson, K.F., "Hypersonic Laminar Boundary Layer Transition, Part II: Mach 6 Experiments of Transition on a Cone at Angle of Attack," AFWAL-TR-3089, December 1986.

15. Holden, M.S., "Experimental Studies of the Effects of Asymmetric Transition on the Aerothermal Characteristics of Hypersonic Blunted Slender Cones,", AIAA Paper 85-0325, January, 1985.

15a. Reed, H.L. and Haynes, T.S., "Transition Correlations in 3-D Boundary Layers," AIAA Paper 93-3054, Presented at the AIAA 24th Fluid Dynamics Conference, Orlando, FL, July 6-9, 1993.

16. Krogmann, P., "An Experimental Study of Boundary Layer Transition on a Slender Cone at Mach 5," AGARD-CPP 224, AGARD Symposium on Laminar-Turbulent Transition, Copenhagen, Denmark, 1977.

17. Reda, D.C., "Boundary Layer Transition Experiments on Sharp, Slender Cones in Supersonic Free Flight," AIAA Paper No 78-1129, July 1978.

18. Di Cristina, V., "Three-Dimensional Laminar Boundary Layer Transition on a Sharp 8-Degree Cone at Mach 10," *AIAA Journal*, Vol. 8, No. 5, May 1970, pp. 852-856.

19. Stetson, K.F., Thompson, E.R., Donaldson, J.C., and Siler, L.G., "Laminar Boundary Layer Stability Experiments on a Cone at Mach 8, Part 3: Sharp Cone at Angle of Attack," AIAA Paper No. 85-0492, January 1985.

20. Simon, M. and Dallman, U., "On the Instability of Hypersonic Flow Past a Pointed Cone - Comparison of Theoretical and Experimental Results at Mach 8," Deutscher Luft - und Raumfahrtkongreb/DGLR - Jahrestagung, 1992.

21. Hanifi, A. and Dahlkild, A.A., "Some Stability Characteristics of the Boundary Layer on a Yawed Cone," AIAA Paper No. 93-3048, July 1993.

22. Potter, J.L., "Boundary Layer Transition on Supersonic Cones in an Aeroballistic Range," *AIAA Journal*, Vol. 13, No. 3, March 1975, pp. 270-277.

23. Ward, L.K., "Influence of Boundary Layer Transition on Dynamic Stability at Hypersonic Speeds," Transactions of the Second Technical Workshop on Dynamic Stability Testing, Vol. II, AEDC, Tullahoma, TN, April 1965.

24. Mateer, G.C., "Effects of Wall Cooling and Angle of Attack on Boundary Layer Transition on Sharp Cones at $M = 7.4$," NASA TN D-6908, August 1972.

25. Finson, M. "Frustum Transition Modeling," Proceedings of the <u>ABRES</u> Accuracy Review, Vol. 8, No. 9, November 1977.

26. Owen, R.R., and Randall, D.J., " Boundary Layer Transition on the Swept Wing," *RAE TM Aero* 277, 1952.

27. Stetson, K.F., "Mach 6 Experiments of Transition on a Cone at Angle of Attack," *Journal of Spacecraft*, Vol. 19,No. 5, 1982, p. 397.

28. King, R. A., "Mach 3.5 Boundary Layer Transition on a Cone at Angle of Attack," AIAA Paper 91-1804, June 1991.

29. Holden, M.S., and Rodriquez, K., "Experimental Studies of Shock-Wave/Wall-Jet Interaction in Hypersonic Flow," NASA Final Report Part A, Grant No. NAG1-790, May 1994.

30. Baker, N.R., Kamath, P.S., McClinton, C.R., and Olsen, G.C., "A Film Cooling Parametric Study for NASP Engine Applications Using the 'SHIP' Code," Paper No. 40, Presented at the Fifth National AeroSpace Plane Technology Symposium, October 1988.

31. Majeski, J.A. and Weatherford, R.H., "Development of an Empirical Correlation for Film-Cooling Effectivenss," AIAA Paper 88-2624, June 1988.

32. Holden, M.S., "An Experimental Simulation of Massive Blowing from a Nosetip During Jovian

Entry," in *Thermophysics of Atmospheric Entry*, Vol. 82, *Progress in Astronautics and Aeronautics*, Edited by T.E. Horton, Dept. Mech. Eng., The University of Mississippi, Published by AIAA, 1982.

33. Holden, M.S., Rodriguez, K.M., and Nowak, R.J., "Studies of Shock/Shock Interaction on Smooth and Transpiration-Cooled Hemispherical Nosetips in Hypersonic Flow," AIAA Paper 91-1765, presented at the AIAA 22nd Fluid Dynamics, Plasma Dynamics and Lasers Conference, Honolulu, Hawaii, 24-26 June 1991.

34. Holden, M.S., "Studies of Surface Roughness and Blowing Effects on Hypersonic Turbulent Boundary Layers Over Slender Cones," AIAA Paper 89-0458, presented at the AIAA 27th Aerospace Sciences Meeting, Reno, Nevada, 9-12 January 1989.

35. Holden, M.S., Neumann, R.D., Burke, J., and Rodriguez, K.M., "An Experimental Study of the Effects of Injectant Properties on the Aerothermal Characteristics of Transpiration-Cooled Cones in Hypersonic Flow," AIAA Paper 90-1487, presented at the AIAA 21st Fluid Dynamics, Plasma Dynamics and Lasers Conference, Seattle, Washington, 18-20 June 1990.

36. Holden, M.S., "Experimental Studies of Transpiration Cooling with Shock Interaction in Hypersonic Flow," NASA Final Report Part B, Grant No. NAGI-790, May 1994.

37. Bartle, E.R. and Leadon, B.M., "The Effectiveness as a Universal Measure of Mass-Transfer Cooling for a Turbulent Boundary-Layer," *Proceedings of 1962 Heat Transfer and Fluid Mechanics Institute*, Stanford University Press, Stanford, CA 1962.

38. Danberg, J.E., "Characteristics of the Turbulent Boundary-Layer with Heat and Mass Transfer at Mach Number 6.7," *Proceedings 5th U.S. Navy Symposium on Aeroballistics*, White Oak, MD 1961.

39. Spalding, D.B. and Chi, S.W., "The Drag of a Compressible Turbulent Boundary Layer on a Smooth Flat Plate with and without Heat Transfer," *Journal of Fluid Mechanics*, Vol. 18, 1964, pp. 117-143.

40. Kays, W.M. and Moffatt, R.J., "The Behavior of Transpired Turbulent Boundary Layers," Stanford University, Report No. H MT-20, April 1975.

41. Brunner, M.J., "Transpiration Cooling Tests at a Sharp Sphere-Cone in a Rocket Exhaust Using N_2, H_e and H_2O Coolants," Paper 64-WA/Ht-50 presented at ASME Winter Annual Meeting, New York, 1964.

42. Pappas, C.C. and Okuno, A.F., "Measurements of Heat Transfer and Recovery Factor of a Compressible Turbulent Boundary-Layer on a Sharp Cone with Foreign Gas Injection," NASA TN D-2230, 1964.

43. Fogaroli, R.P., "Measurements of Turbulent Heat Transfer and Skin Friction Reduction on a Porous Cone with Air Injection at High Mach Numbers," General Electric Rep. 64SD5291, 1964.

44. Holden, M.S., "Studies of Transpiration Cooling, Surface Roughness and Entropy Swallowing in Transitional and Turbulen Boundary Layers over Nose Tips," paper presented at IAF-79-F-42, XXX Congress International Astronautical Federation, Sept. 17-22, 1979.

45. Holden, M.S. and Sweet, S.J., "Studies of Transpiration Cooling With Shock Interaction in Hypersonic Flow," AIAA-94-2475, Paper presented at the 18th AIAA Aerospace Ground Testing Conference, Colorado Springs, CO, June 20-23, 1994.

46. Holden, M.S., Bower, D. and Chadwick, K., "Measurements of Boundary Layer Transition on Cones at Angle of Attack for Mach Numbers from 11 to 13," AIAA-95-2294, Paper presented at the 26th AIAA Fluid Dynamics Conference, San Diego, CA, June 1995.

Design of High L/D Vehicles Based on Hypersonic Waveriders

Th. Eggers
D. Strohmeyer
DLR, Institute of Design Aerodynamics, Lilienthalplatz 7
D-38108 Braunschweig, Germany

1. SUMMARY

The aerodynamic behavior of a waverider representing the hypersonic lower stage of a TSTO system is discussed. The investigation covers the complete speed range from subsonic high lift up to hypersonic flight close to the design point of the waverider geometries. Several interesting flow phenomena are described which govern the aerodynamic behavior. It is found that the favourable off-design behavior of hypersonic waveriders allows the practical use of waverider vehicles far away from their particular design flow conditions. Studies concerning the planform show, that the modification of a gothic planform towards combined forebody - delta wing planforms allows a significant improvement of the aerodynamic efficiency L/D in sub- and transonic flow. In addition the longitudinal stability is increased without compromising the favourable high speed qualities. These benefits are partly compensated by an increasing neutral point shift along the trajectory.

2. INTRODUCTION

The payload transport into the lower earth orbit during the last 3 decades shows a rapid increase [1]. In order to reduce the specific launch costs, to obtain a higher mission flexibility and mission safety, as well as for environmental protection, work on the next generation of space transportation systems is necessary. The investigated projects include single stage to orbit (SSTO) as well as two stage to orbit transportation systems (TSTO). Compared to SSTO vehicles the most important advantage of a TSTO system is a higher payload ratio (percent payload of total launch mass) leading to a lower sensitivity concerning design and mission parameters. Since integrated predesign studies of airbreathing TSTO systems show a high sensitivity with respect to the aerodynamic efficiency L/D of the first stage, waverider configurations with a high L/D in the design point as well as under off-design conditions seem to be a realistic alternative to conventional blended body and wing body configurations respectively [2].

Based on integrated predesign studies the DLR-F8 wa-

verider configuration was designed as a promising waverider shape. For the aerodynamic investigation of this configuration detailed numerical simulations along a complete TSTO trajectory [3] as well as wind tunnel experiments were performed [4]. During more detailed predesign studies it was found that the aerodynamic potential of DLR-F8 is not put to full use. For this reason two new waverider configurations with modified planforms and reduced planform area have been designed and aerodynamically investigated.

3. CONFIGURATIONS

The generation of waverider geometries at DLR Braunschweig is based on the Osculating Cones Concept [5], using the program WIPAR [6]. In order to fulfill the requirements coming from the integrated predesign - such as integration of tanks, engine and other systems - as well as to reduce the base area and the resulting base drag especially in sub- and transonic flow, the WIPAR geometries have to be modified. This is illustrated in Fig. 1a by means of WR-12-G-FR (WR ... waverider; 12 ... design Mach number, $M_{Des.}$; G ... gothic planform; FR ... upper surface = freestream surface) which was realized with a CAD system and led to the configuration WR-12-G-EXP (EXP ... upper surface = expansion surface). This waverider is also called DLR-F8 since it is built as a wind tunnel model. The mean features of the modification are:

- Introduction of an expansion surface in the wing region, leading to a sharp trailing edge and to the reduction of the base area. Starting from the trailing edge, the upper surface is inclined with an average ratio of 1:7 towards the free stream, which coincidents with an estimation of the viscous lift to drag ratio (L/D) in hypersonic flow.

- Introduction of straight hinge lines for the integration of aileron and elevator.

- Shaping the body in spanwise direction to allow the integration of tanks and systems as well as to guarantee a low base drag.

A side effect of the introduced expansion surface is a rigging angle of incidence between wing and body ridge line of approximately $\alpha_{inc.} \approx 5°$, leading to a zero-lift angle of about $\alpha_0 \approx -5°$. As the geometry was also used for a wind tunnel model, the wing tip was cut. Furthermore, inlet, propulsion box and nozzle are not modeled and the propulsive jet is represented by a solid sting with constant cross-section in the aerodynamic analyses. In order to get data for global design work the effect of the propulsion system (inlet, propulsion box and nozzle) on the aerodynamic behavior should be taken into account by a propulsion bookkeeping method.

The detailed integrated predesign studies of DLR-F8 showed that the configuration as the lower stage of a TSTO system fulfills the mission with flight C_L below the C_L for optimum L/D. To improve the mission L/D two waveriders with about 20% reduced planform area, $S_{Ref.}$, and different aspect ratio, A, were designed and modified to WR-12-GD-EXP-A and WR-25-GD-EXP-A in order to fulfill the boundary conditions coming from the integrated predesign, Fig. 1b.

The area reduction was obtained by changing the gothic planform of DLR-F8 into a combined planform, coupling a gothic forebody with a delta wing (-GD- ... combined planform: gothic forebody - delta wing), which resembles the planform of typical wing body configurations. For the geometric modification of both waveriders a numerical program was used instead of the CAD system. This procedure is significantly less costly but leads also to less even surfaces.

In Fig. 2a the three planforms are illustrated. A comparison of WR-12-GD-EXP-A and DLR-F8 shows the reduced planform area, whereas the centre of gravity of the planform area remained the same. Due to the smaller span WR-12-GD-EXP-A has almost the same aspect ratio as DLR-F8, see Fig. 1b. WR-25-GD-EXP-A is characterized by the largest span and an aspect ratio which is almost 50% larger than those of DLR-F8 and WR-12-GD-EXP-A. In addition the center of gravity of its planform area is shifted 2% of the body length closer to the trailing edge. This leads to a greater longitudinal stability in hypersonic flow since under high speed conditions the neutral point coincides approximately with the center of gravity of the planform area.

For an additional increase of the longitudinal stability the usable body volume of WR-12-GD-EXP-A and WR-25-GD-EXP-A was also redistributed, as Fig. 2b illustrates. The thickness of the former body with upper freestream surface was smoothly increased in the nose region and reduced in the tail region, leaving the usable body volume unchanged (-A ... variation with modified distribution of the body volume). This procedure allows a shift of the center of gravity to the nose, increasing the longitudinal stability.

4. NUMERICAL SIMULATIONS

The numerical simulation of the waverider aerodynamics is based on the solution of the Euler equations using the DLR Euler-/Navier-Stokes code CEVCATS [7], [8]. In sub- and transonic flow a code version with central differencing and artificial dissipative terms was used. In the super- and hypersonic speed regime upwind discretization was applied. For the spatial discretization of the flowfield in sub- and transonic flow a grid with about 660000 grid points was generated, covering a domain of about 5 body lengths, l, around the configuration. A second grid was designed for the simulation of the super- and hypersonic flows in order to follow the bow shock more closely. It consists of about 330000 points. The influence of viscous effects on the aerodynamic efficiency was estimated by adding the skin friction of a flat plate in turbulent flow. The Reynolds numbers, Re, were chosen according to typical trajectories of airbreathing TSTO systems.

5. OFF-DESIGN BEHAVIOR IN SUPER- AND HYPERSONIC FLOW

5.1 Influence of upper surface and Mach number

With view to the off-design behavior of waveriders in Fig. 3 the L/D of the configuration WR-12-G-FR and DLR-F8 is plotted versus the Mach number for the case of $\alpha=0°$. The base drag of the configurations is not included in these results. Two main results are illustrated in this figure. At first, the consideration of the hypersonic range for $M_\infty>6$ obviously shows that the additional lift and drag of the expansion surface, which has the ratio of about 7:1, does not degrade the overall L/D of configuration DLR-F8. Hence, it is demonstrated that the design of integrated waverider configurations with sharp trailing edges is possible without compromising the L/D at hypersonic flow conditions, if skin friction is taken into account. The second effect which can be taken from Fig. 3 is the increase of the L/D with decreasing Mach number. The reason for this effect is that the shock wave detaches from the leading edge, if the sweep angle is sufficiently large. In regions with a detached shock wave and a supersonic leading edge an expansion around the sharp nose appears. At lower supersonic Mach numbers the leading edge is mostly subsonic and flow separation from the leading edge occurs already for $\alpha=0°$. The resulting suction forces from the leading edge vortex and the supersonic expansion around the leading edge respectively induce an additional lift but due to the fact that a free stream upper surface is considered no additional wave drag appears. Therefore, the L/D is improved. A description of these

phenomena may be taken from Figs. 4 and 5. Here, the surface streamlines and the pressure distributions in selected x=const. planes are plotted. For M_∞=6, α=0° (Fig. 4) the leading edges are always supersonic and therefore, the streamlines are aligned with the freestream. The pressure distributions in the rear part of the body show the influence of the expansion introduced along the upper surface. In Fig. 5 similar plots are given for M_∞=2, α=0°. Along the nose the influence of the leading edge vortex is obvious due to the occurence of detachment and attachment lines. Considering the pressure distributions we find the induced suction region along the upper surface. Additionally, these distributions show the expansion flow region which appears due to the redesigned upper surface. It is also visible that the influence of the upper surface on the aerodynamic forces increases with decreasing Mach number.

5.2 Influence of Nose Bluntness

With view to the design of realistic waverider shapes the effect of a blunt leading edge onto the aerodynamic performance is considered too. In the design point waverider shapes are always sharp nosed, but leading edges of realistic designs have to be properly blunted in order to reduce the heat loads. On the other hand the chosen nose radius should be as small as possible for low wave drag. Here, a conservative bluntness of R/l=0.0008 was fitted into configuration WR-12-G-FR (see Fig. 6). The planform remained unchanged during this modification. The effects of the nose bluntness is discussed refering to Fig. 7. Obviously, the shock detaches from the leading edge as shown for the outflow plane. Considering the lines of constant pressure and the surface pressure distributions in different x=const. planes we see that the blunt leading edge yields increased pressure values in the leading edge region which decreases the obtainable inviscid L/D about 13%. The shock strength and its position in the other body regions remain unchanged. Evidently, the sensitivity of waverider drag with respect to the nose radius is quite large. However, according to ref. [9] a nose radius of about R/l=0.0001 seems feasible for l=70m. In ref. [9] the coupling of a Navier-Stokes code for the flow analysis with a thermal code for the structural analysis was developed and applied to investigate the thermal behavior of the leading edge structure. For aerodynamically sharp leading edges (R/l≈0.0001) under hypersonic conditions the resulting wall temperatures at the stagnation point are significantly below (about 200 - 300 K) the wall temperatures calculated according to a local balance of radiation and aerodynamic heat flow on the wall. This wall temperature reduction is based on the heat conduction of the structure. It is reached without any additional active cooling. Therefore, the use of conventional materials with operational

temperatures below 2000 K for the leading edge structure is sufficient for the technical realization. Since the influence of the nose bluntness behaves linear with the leading edge radius the L/D will only decrease approximately 1.6% for the conditions considered here. Hence, the effect of leading edge bluntness on the aerodynamic coefficients can be neglected.

6. PLANFORM EFFECTS ON THE WAVERIDER AERODYNAMICS

Key parameters for the investigation of planform effects on the waverider aerodynamics with respect to the integrated predesign of a TSTO system are the aerodynamic efficiency L/D and the neutral point position. In the discussion of both parameters for the three waverider configurations special emphasis is laid on the subsonic and lower supersonic flight regime up to M_∞=1.5 for two reasons: On the one hand the changes of the aerodynamic characteristics of a flight vehicle in higher super- and hypersonic flow are very small since the aerodynamic forces are determined by the pressure side with an almost constant pressure distribution. The reason for this behavior is the limited force maximum on the suction side (vacuum) in contrast to the unlimited maximum force on the pressure side. On the other hand the speed range up to M_∞=1.5 has a great influence on the mission performance: Mission simulations show that almost 25% of the fuel are consumed in this segment of the mission [10].

The aerodynamic efficiency as a function of the lift coefficient for different Mach numbers is given in Fig. 8a for the three waverider configurations. The corresponding drag polars shows Fig. 8b. As a result of the asymmetry of the configurations with respect to the horizontal plane, the apex of the drag polars is shifted in positive C_L- and C_D-direction. Neglecting the C_L-shift of the curves, which is permissible up to M_∞=1.5 since the offset is small and changes only little with increasing Mach number, the drag polars can be approximated as:

$$C_D(C_L) = C_{D,\,min.} + \frac{(C_L - C_{L,\,C_{D,\,min.}})^2}{e\ \pi\ A}$$

or

$$C_D(C_L) \approx C_{D,\,min.} + \frac{C_L^{\,2}}{e\pi A}\ , \tag{1}$$

with $C_{D,min.}$ as the minimum drag coefficient and e as the Oswald factor, describing the deviation of the lift distribution in spanwise direction from the elliptical lift distribution (e=1 for elliptical lift distribution, e<1 for deviation from the elliptical one). Since π and A in Eq. (1) are constants the shape of the parabolic polar is con-

troled by the Oswald factor. The L/D maximum of the L/D-C_L curves in Fig. 8a is located at:

$$C_L\left(\left(\frac{C_L}{C_D}\right)_{max.}\right) = \sqrt{C_{D,min.}e\pi A} \ ,$$

with

$$\left(\frac{C_L}{C_D}\right)_{max.} = \frac{1}{2}\sqrt{\frac{e\pi A}{C_{D,min.}}} \ . \tag{2}$$

A comparison of the L/D-C_L curves at M_∞=0.3 shows that WR-25-GD-EXP-A obtains the greatest $(L/D)_{max.}$ at the highest C_L due to its large aspect ratio, Fig. 8a. Although WR-12-GD-EXP-A and DLR-F8 have almost the same aspect ratio the $(L/D)_{max.}$ of WR-12-GD-EXP-A is smaller and obtained at a slightly lower C_L. The reason for this effect is the less elliptical lift distribution and hence the smaller e of WR-12-GD-EXP-A.

In order to illustrate this phenomenon the lift distribution of the configurations in spanwise direction is shown in Fig. 9a for constant C_L, with $C_{l,y}=C_l(y/l) \cdot l(y/l) \cdot 1/S_{Ref.}$. Here $C_l(y/l)$ is the local lift coefficient of the section y/l and l(y/l) describes the local chord length at y/l. Additionally the best fitting ellipse for each lift distribution as well as the total difference between best fitting ellipse and real lift distribution ΔC_L is given.

All lift distributions show a lift decrease close to the symmetry plane (y/l $\approx$ 0.0 ... 0.1) which results from the lower angle of attack of the body compared with the wing, see Fig. 1. This effect is strongest for WR-25-GD-EXP-A on account of its large body part, leading to the largest deviation from the elliptical lift distribution of ΔC_L=12.2 %. In comparison with DLR-F8, WR-12-GD-EXP-A shows an additional deviation from the best fitting ellipse in the region y/l $\approx$ 0.1 ... 0.2. The reason for this additional lift is illustrated by means of the pressure distribution on the upper surface of all configurations for C_L=0.175, see Fig. 9b, and the corresponding C_p distribution in the cross-section x/l=0.9 in Fig. 9c. Compared with DLR-F8, where the pressure distribution indicates a single leading edge vortex, the flowfield of WR-12-GD-EXP-A at this angle of attack is characterized by two separated leading edge vortices: A forebody vortex and the delta wing vortex. Both can be clearly identified in the cross-section pressure distribution. A second pressure minimum occurs also in the cross-section of DLR-F8 (y/l $\approx$ 0.25) but this results from the swelling of the upper surface in this region where the modified expansion surface transitions into the original waverider shape close to the leading edge. The additional suction force below the forebody vortex of WR-12-GD-EXP-A leads to the observed lift increase in the region y/l=0.1 ... 0.2 (see also Fig. 2a) and hence to the less elliptical lift distribution with ΔC_L=12.0%.

Proceeding from M_∞=0.3 to M_∞= 0.9 in Fig. 8a the $(L/D)_{max.}$ of WR-25-GD-EXP-A moves to higher C_L due to a more elliptical lift distribution (increasing gradient of the drag polar compared to M_∞=0.3 in Fig. 8b). However, the value of $(L/D)_{max.}$ remains almost constant since $C_{D,min.}$ increases, an effect which results from the additional wave drag based on a local supersonic region and the shock on the upper surface. Compared with WR-25-GD-EXP-A the $(L/D)_{max.}$ of WR-12-GD-EXP-A and DLR-F8 increases a little and moves to a slightly higher C_L, based on the increasing e. For both configurations the influence of the supersonic flow and the terminating shock is small compared with WR-25-GD-EXP-A.

Going up to M_∞=1.5 the $(L/D)_{max.}$ of WR-25-GD-EXP-A decreases drastically and moves to an even higher C_L, as shown in Fig. 8a. The reason is the increased $C_{D,min.}$ on account of the additional wave drag, Fig. 8b. At this Mach number the delta wing leading edge is supersonic. WR-12-GD-EXP-A and DLR-F8 show the same behavior. Since in the supersonic regime the influence of the vortex flow on the pressure distribution is reduced with increasing Mach number, the difference between DLR-F8 and WR-12-GD-EXP-A decreases. Two effects are responsible for this decreasing influence of the vortex. On the one hand the supersonic part of the leading edge grows and avoids the feeding of the downstream vortex with circulation, on the other hand with the existing bow shock new boundary conditions - the oblique shock relations - have to be fulfilled closer to the vortex in comparison with the subsonic case.

For hypersonic flight conditions, M_∞=6.0, only the drag polars and L/D-C_L curves of DLR-F8 and WR-12-GD-EXP-A were determined. Both L/D-C_L curves are nearly identical, Fig. 8a, the influence of the upper surface of WR-12-GD-EXP-A is almost negligible. This was expected since both configurations have the same body angle and the influence of the suction side on the aerodynamic behavior in hypersonic flow plays a minor role as discussed before.

Compared with M_∞=1.5 the polar is now symmetric to the abscissa. Every deviation from α=0° leads to an additional wave drag and decreasing L/D: The numerical simulation shows that increasing the angle of attack leads to a worse L/D of the dominating pressure side, decreasing the angle of attack improves the lower side L/D which is overcompensated by the additional pressure force on the upper side. The resulting location of the drag polar leads to a further reduction of $(L/D)_{max.}$ and the shift to a significantly smaller C_L.

The analysis of the aerodynamic efficiency shows that both configurations WR-12-GD-EXP-A as well as WR-25-GD-EXP-A promise a mission with higher L/D com-

pared to DLR-F8. In super- and hypersonic flow where all configurations show the same L/D characteristic the reduced reference area of WR-12-GD-EXP-A and WR-25-GD-EXP-A leads to a mission C_L closer to $(L/D)_{max}$. In sub- and transonic flow WR-25-GD-EXP-A is the most promising configuration due to the highest $(L/D)_{max}$, an advantage which is slightly moderated by the shift of $(L/D)_{max}$ to higher C_L. Even though the $(L/D)_{max}$ of WR-12-GD-EXP-A is below that of DLR-F8, the C_L location is almost the same and the smaller reference area overcompensates the $(L/D)_{max}$ disadvantage.

The second aspect concerning the planform effects on the waverider aerodynamics is the influence on the neutral point position. The neutral point is defined as the point where, in any case of change of the steady state of a flight vehicle, the additional aerodynamic force attacks. In Fig. 10a the behavior of the neutral point as a function of the Mach number is illustrated for the three waverider configurations at $\alpha=1.25°$ and compared with the neutral point regime of typical blended body and wing body configurations. All waveriders show the similar characteristic which is discussed comprehensively in [3]:

- Slight rearward movement in subsonic flow

- Rearward movement in subcritical transonic flow of approximately 6% of the body length with a distinct noseward drop close to $M_\infty=1.0$ due to the shock influence on the upper surface pressure distribution

- Almost constant position in the high speed regime according to the increasing influence of the lower surface pressure distribution on the lift of the vehicle

But the more the planform is changed from the gothic shape (DLR-F8) to the combined type (WR-12-GD-EXP-A, WR-25-GD-EXP-A) the more rearward is the neutral point located. This effect is based on the different aspect ratios and hence different lift curve slopes of the slender forebody and the delta wing. The larger this difference is, the larger the lift curve slope of the delta wing is compared to that of the forebody, shifting the neutral point rearwards.

This behavior is illustrated in Fig. 10b for $M_\infty=0.3$ showing the lift distribution for the two angles of attack $\alpha= 0°$ and $\alpha=2.5°$ in x/l-direction, with $C_{l,x}=C_l(x/l) \cdot s(x/l) \cdot l / S_{Ref}$. Here $C_l(x/l)$ is the local lift coefficient of the cross-section x/l and s(x/l) stands for the local half span at x/l. The corresponding difference lift distribution in Fig. 10c shows clearly the influence of the different aspect ratios of forebody and delta wing of WR-12-GD-EXP-A and WR-25-GD-EXP-A on the lift distribution, shifting the neutral point, which can be interpreted as the x/l-position of the center of gravity of the

area below the ΔC_L curve, to the tail.

Having in mind that at hypersonic speeds the neutral point coincidences approximately with the center of gravity of the planform of a flight vehicle, the resulting movement of the neutral point from transonic to hypersonic flow increases the more the gothic planform is modified towards the combined one which may lead to higher trim losses. In this context it should be mentioned that for all three configurations the neutral point at hypersonic speeds is located slightly upstream the center of gravity of the planform area, see also Fig. 1b. This effect is primarily due to the introduced expansion surface: In contrast to a freestream upper surface, the expansion surface, which is introduced up from $x/l \approx 0.3$, provides for small angles of attack no additional contribution to the aerodynamic forces in the case of a disturbance of the angle of attack. The vacuum remains unchanged, leading to the neutral point shift in upstream direction compared with a configuration with freestream upper surface. For WR-12-GD-EXP-A and WR-25-GD-EXP-A this effect is increased by a change of the compression flow in the nose region based on the upper surface modification in this region as illustrated in Fig. 2b.

7. SUMMARY

In the present paper selected aerodynamic investigations concerning the design of high L/D vehicles based on the waverider concept where analysed in a condensed form. It was shown, that the introduction of an expansion along the upper surface does not degrade the overall L/D of a waverider configuration near its design point, if skin friction is taken into account. Furthermore, due to additional suction forces which are induced by supersonic expansions and leading edge vortices the hypersonic L/D increases with decreasing Mach number.

Investigations concerning the effect of the leading edge bluntness show that the obtained losses are negligible, if realistic nose radii of $R/l\approx0.0001$ are considered.

Investigations concerning the planform effects on the waverider aerodynamics show that the modification of a gothic waverider planform towards a combined planform with gothic forebody and delta wing can be used for planform area reduction and neutral point shift almost without an influence on the aerodynamic performance in super- and hypersonic flow. Limiting factor of the modification is the overall stability characteristic from sub- up to hypersonic flow: The more the gothic planform is changed towards a wing body design, the larger is the neutral point movement along the trajectory, increasing from 6.5% up to 10% of the body length.

8. REFERENCES

1. Koelle, D.E.; "Entwicklungstendenzen bei Raumtransportsystemen", Zeitschrift für Flugwissenschaften und Weltraumforschung, Vol. 16, 1992, pp. 67-76.

2. Bardenhagen, A.; Kossira, H.; Heinze, W.; "Interdisciplinary Design of Modern Hypersonic Waveriders Using the Integrated Program PrADO-Hy", ICAS Paper 94-1.4.1, 19th International Council of the Aeronautical Sciences, 1994.

3. Eggers, Th.; Strohmeyer, D.; Nickel, H.; Radespiel, R.; "Aerodynamic Off-Design Behavior of Integrated Waveriders from Take-Off up to Hypersonic Flight", AIAA Paper 95-6091, 1995.

4. Seltsam, M.; Strohmeyer, D.; "Windkanalmessungen am DLR-F8 Wellenreiter-Windkanalmodell im Transsonischen Windkanal Göttingen (TWG)", DLR-IB 29112-96A05, 1996.

5. Sobieczky, H.; Doughtery, F.C.; Jones, K.D.; "Hypersonic Waverider Design for Given Shock Waves", 1st International Hypersonic Waverider Symposium, Oct. 17-19, 1990, University of Maryland.

6. Center, K.B.; "Interactive Waverider Design and Optimization", PhD Thesis, University of Colorado, Boulder, 1993.

7. Rossow, C.-C.; "Berechnung von Strömungsfeldern durch Lösung der Euler-Gleichungen mit einer erweiterten Finite-Volumen Diskretisierungsmethode", Dissertation TU Braunschweig, 1988, DLR-FB 89-38, 1989.

8. Kroll, N.; Radespiel, R.; "An Improved Flux Vector Split Discretization Scheme for Viscous Flows", DLR-FB 93-53, 1993.

9. Haupt, M.; Kossira, H.; Radespiel, R.;"Analyse von aerothermodynamisch belasteten Flügelvorderkanten mit einer Methode der Fluid-Struktur-Kopplung", Annual Book No. 3, DGLR-Paper DGLR-JT95-115, DGLR-Jahrestagung, Bonn, 1995.

10. Kossira, H.; Bardenhagen, A.; Heinze, W.; "Investigation on the Potential of Hypersonic Waveriders with the Integrated Aircraft Design Program PrADO-Hy", AIAA Paper 93-5098, 1993.

a)

CAD
(ICEM)

Program
(WR-TRAFO)

WR-12-G-FR

WR-12-G-EXP $\equiv$ DLR-F8

b)

DLR-F8

$M_{Des.}$ = 12
$S_{Ref.}/l^2$ = 0.37
A = 1.15

WR-12-GD-EXP-A

$M_{Des.}$ = 12
$S_{Ref.}/l^2$ = 0.31
A = 1.11

WR-25-GD-EXP-A

$M_{Des.}$ = 25
$S_{Ref.}/l^2$ = 0.31
A = 1.64
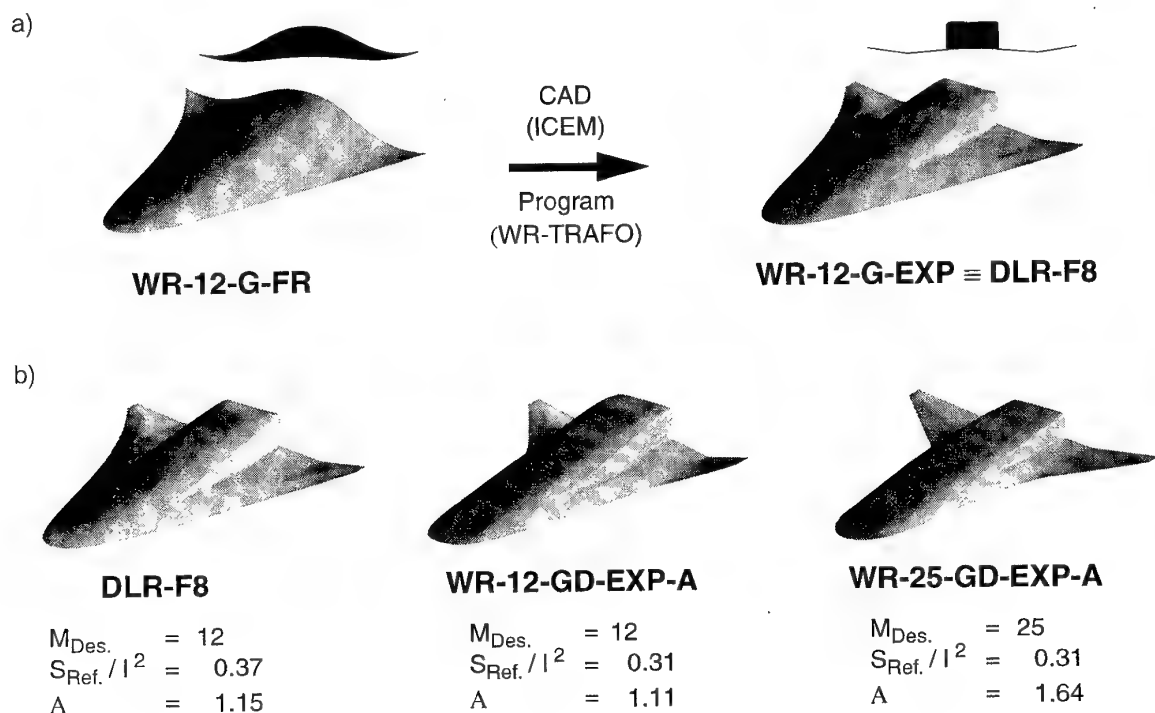
Fig. 1: Waverider modification (a) and aerodynamically investigated configurations

a)
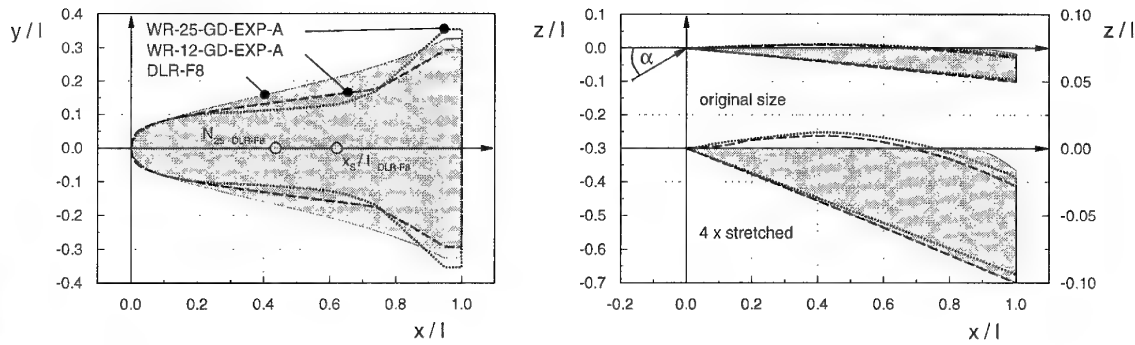
Fig. 2: Comparison of planform (a) and symmetry plane (b) of the investigated configurations
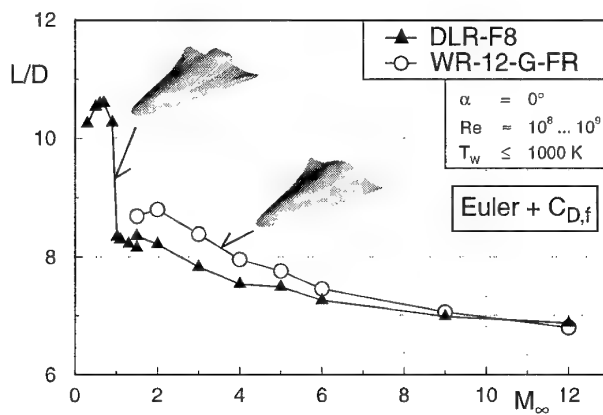
Fig. 3: Influence of Mach number on L/D
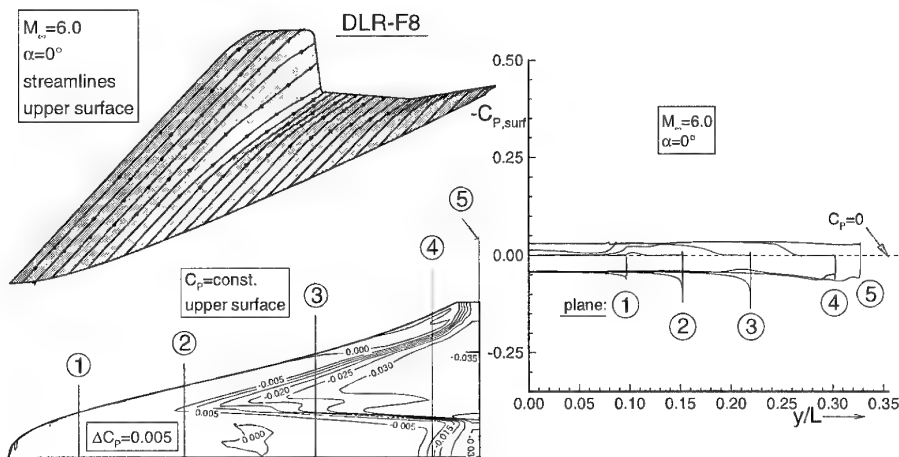
Fig. 4: Surface flow on configuration DLR-F8, M_∞=6
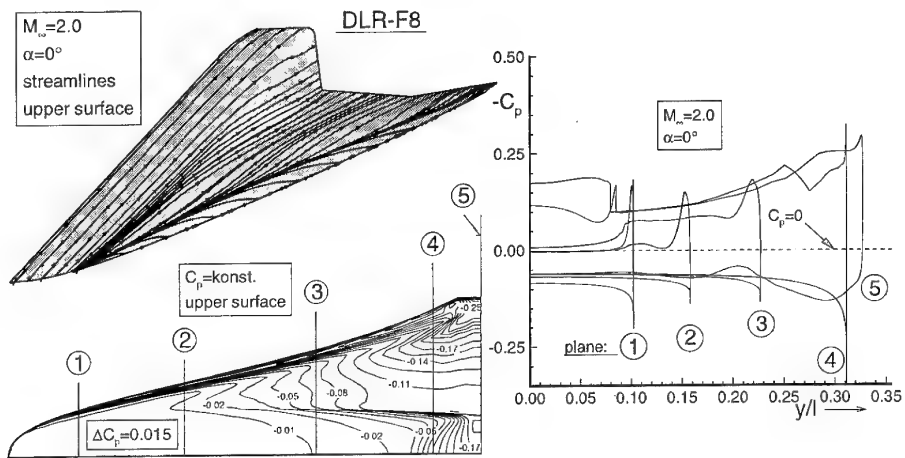
Fig. 5: Surface flow on configuration DLR-F8, $M_\infty=2$

Fig. 6: Introduction of a leading edge bluntness
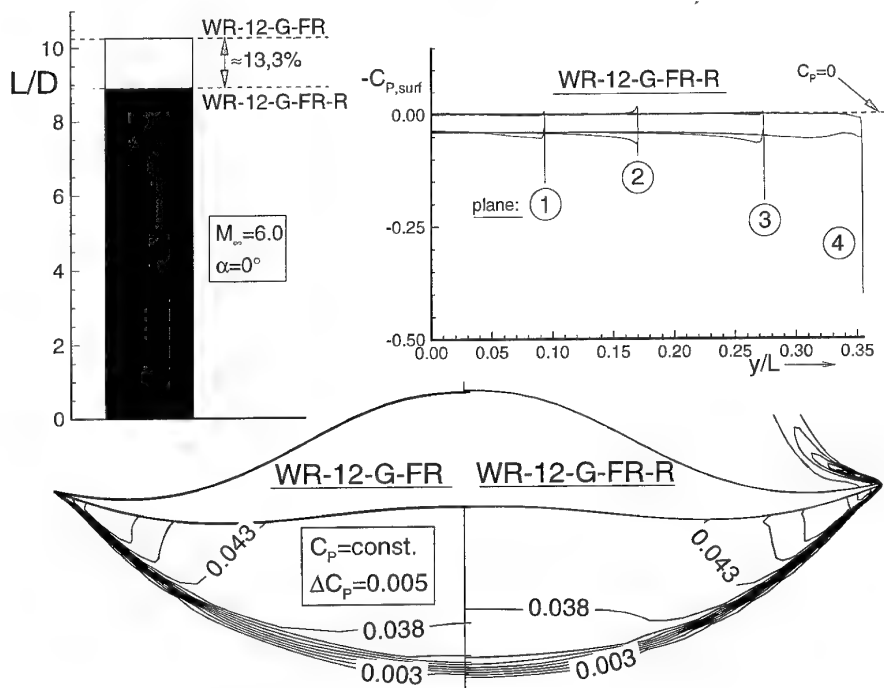
Fig. 7: Effect of nose bluntness
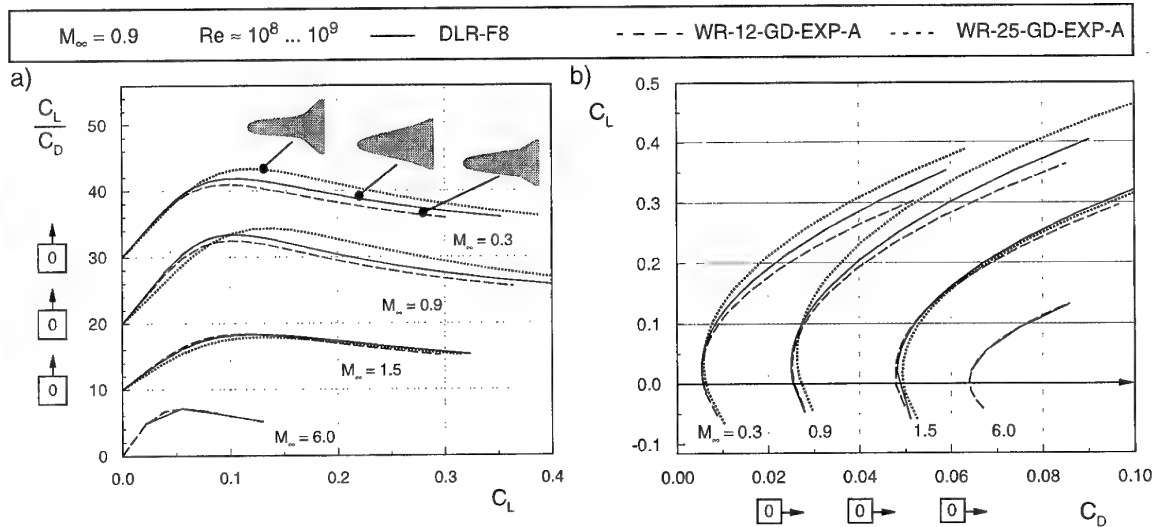
Fig. 8: Influence of the planform on the aerodynamic efficiency (a) and the drag polars (b)
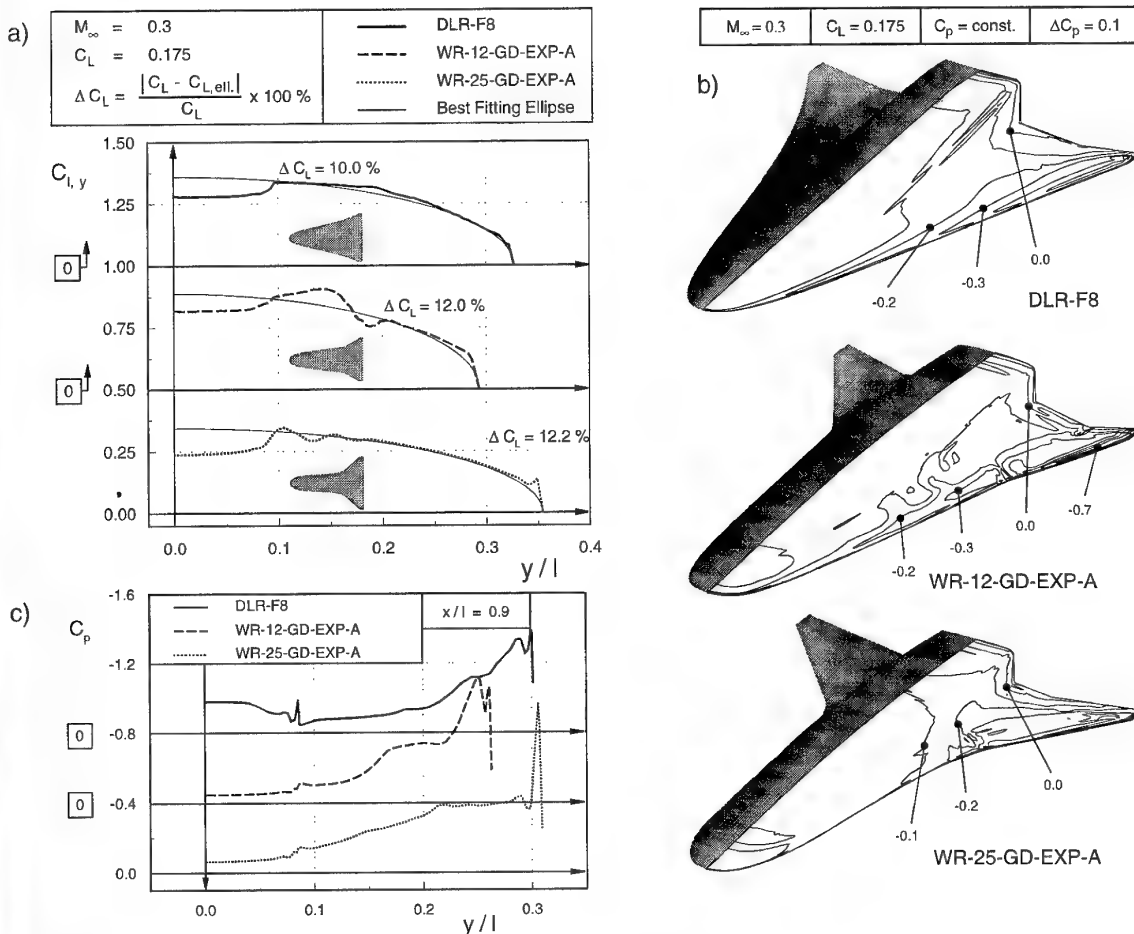
Fig. 9: Influence of the planform on the lift distribution (a) and pressure distribution on the upper surface (b) and in the cross-section x/l = 0.9 (c)
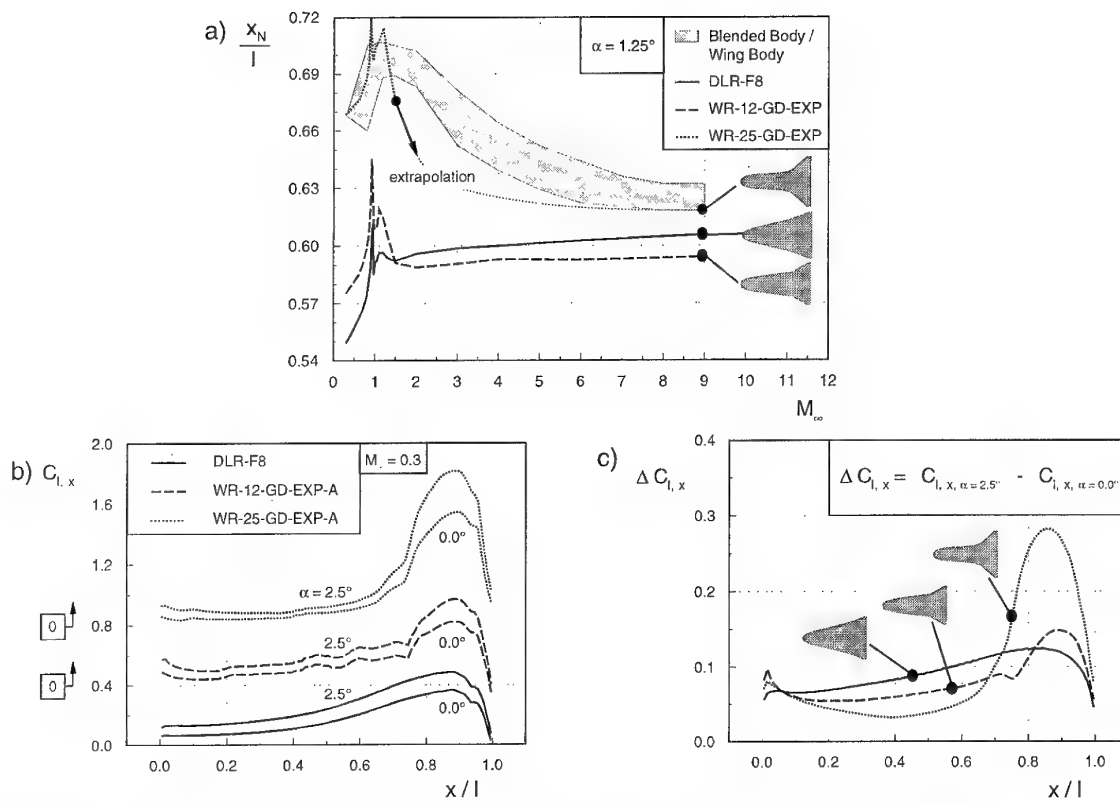
Fig. 10: Influence of the waverider planform on the neutral point position (a), lift- (b) and difference lift distribution (c) of the investigated waverider configurations

INSTALLATIONS D'ESSAIS POUR LES RECHERCHES FONDAMENTALES EN PROPULSION

G. Collin, O. Dessornes, P. Magre
ONERA
B.P. 72, 92322 Châtillon Cedex, FRANCE

1. RESUME

Deux installations d'essai de la combustion d'hydrogène dans des écoulements supersoniques d'air ont été développées dans le cadre des études de superstatoréacteurs. L'une est dédiée aux études de base de couches de mélange supersoniques réactives, l'autre à l'évaluation des concepts d'injection et de chambre de combustion. Ces installations et l'instrumentation associée sont décrites. Les premiers résultats démontrent leur capacité à réaliser des écoulements en combustion supersonique et à fournir des informations sur les délais d'inflammation et sur des injecteurs élémentaires.

2. INTRODUCTION

L'étude du statoréacteur à combustion supersonique pose de nombreux problèmes liés aux mécanismes d'injection, de mélange et de combustion de l'hydrogène dans des écoulements supersoniques à température élevée. Ce problème est abordé, dans le cadre du programme français PREPHA (Programme de Recherche sur la Propulsion Hypersonique Avancée [1]), dans deux domaines expérimentaux complémentaires, intéressant les chambres de combustion des superstatoréacteurs. A cet effet l'ONERA a conçu et réalisé deux installations d'essai, au centre de Palaiseau, dédiées respectivement :

- à l'étude des phénomènes d'aérothermochimie, caractéristiques du mélange réactif turbulent entre des écoulements supersoniques d'hydrogène et d'air. C'est l'étude de base du LAERTE (LAboratoire des Ecoulements Réactifs et de leurs Techniques d'Essai), portant sur une configuration d'écoulement volontairement simplifiée.

- à l'évaluation des concepts de chambres de combustion pour superstatoréacteurs et de leurs systèmes d'injection.

Après la présentation des objectifs des études conduites dans ces deux laboratoires, les deux installations de combustion supersoniques sont décrites (géométrie, capacités, techniques de mesure associées). Les premiers résultats de mesure obtenus sur des écoulements supersoniques réactifs présentés montrent que ces installations sont opérationnelles et contribuent aux objectifs initialement prévus (par exemple, la mise au point d'injecteurs, la mesure des délais d'inflammation de l'hydrogène).

3. CARACTERISTIQUES DES BANCS D'ESSAI

3.1 Objectifs des études du LAERTE

L'ensemble des études du LAERTE doit permettre, à la fois, une validation des techniques numériques employées dans les codes de calcul et une évaluation des modèles physiques, aptes à prédire l'évolution d'une couche de mélange supersonique réactive. Les conditions régnant dans cet écoulement doivent être représentatives des conditions de vol d'un superstatoréacteur à Mach 6. La configuration expérimentale retenue est donc la suivante.

Une zone de mélange réactive est créée entre un écoulement supersonique d'air, à Mach 2 et à 1100 K et un jet parallèle d'hydrogène également supersonique (Mach 2). Le cas du mélange non réactif doit pouvoir aussi être étudié, en remplaçant l'hydrogène par de l'hélium, ainsi que celui d'une injection perpendiculaire d'hydrogène. Ces conditions dans les deux écoulements conduisent à une valeur nominale du nombre de Mach convectif de 0.62 [2]. Cette valeur est suffisante pour engendrer des effets de compressibilité significatifs sur le développement des couches supersoniques de mélange [3].

La conception et le dimensionnement du montage d'essai ont tenu compte également des mécanismes de base attendus, tels que les délais d'inflammation de l'hydrogène [4] et les risques de blocage thermique. Ainsi, un profil modulable de la veine d'essai est retenu : section constante (sur une longueur variable) puis divergente (possibilité d'ajuster l'angle), pour éviter le blocage thermique. Plusieurs tuyères d'injection d'hydrogène, au Mach nominal de 2, de tailles différentes permettent de fonctionner à différentes richesses pour éviter la situation de blocage thermique. La géométrie finalement retenue est présentée figure 1.

Enfin, l'accessibilité optique de la veine d'essai, doit être assurée puisque la plupart des investigations dans la zone de mélange sont basées sur des diagnostics laser, tels que: diffusion Rayleigh, Fluorescence induite par laser du radical OH, DRASC pour la mesure des températures, vélocimétrie laser..

3.2 Objectifs des études ATD

La cellule 5 des Laboratoires d'Aérothermodynamique de Palaiseau est aménagée pour permettre l'évaluation de concepts de chambre et de systèmes d'injection pour superstatoréacteur. A cet effet, elle permet de générer des écoulements supersoniques à haute enthalpie représentatifs de Mach de vol de 6 et 7.5. Sa modularité lui permet d'étudier de nombreuses configurations, depuis une simple injection pariétale jusqu'à une géométrie avec un mât d'injection, plus représentative d'une chambre de combustion de superstatoréacteur.

Pour répondre à ces différents besoins, des Mach d'écoulement d'air de 2.5 et 3 sont d'ores et déjà réalisables. Cela permet par exemple l'évaluation d'une chambre de superstatoréacteur à Mach 5 et 6 ou, en faisant varier le Mach de l'air et son enthalpie, autorise l'étude d'injecteurs élémentaires dans des conditions de vol à M=7.5.

Enfin, l'accessibilité optique de la veine d'essai permet l'utilisation de diagnostics optiques relativement simples tels que la strioscopie, la pyrométrie ou l'émission spontanée du radical OH pour aider à l'interprétation des résultats obtenus.

3.3 Capacités des installations

Les capacités des deux installations de Palaiseau sont présentées dans le tableau I en annexe.

4 DESCRIPTION DETAILLEE DU BANC LAERTE

4.1 Installation d'essai

Le schéma de l'installation est donné figure 2. L'air alimentant la veine d'essai est d'abord réchauffé, jusqu'à 850 K, par deux échangeurs de chaleur dont les flux chauds sont fournis par des foyers classiques au kérosène (température de sortie de 1200 K). La suroxygénation de l'écoulement est assurée par une injection d'oxygène spécifique. Des foyers de préchauffage à l'hydrogène élèvent la température de cet air suroxygéné de 800 K environ jusqu'à une température maximum de 2000 K.

La tuyère bidimensionnelle Mach 2, calculée avec correction de couche limite, est refroidie par eau. Elle comporte un mât central d'injection, également refroidi par eau, muni de la tuyère Mach 2 de diamètre de sortie 6 mm. La conception de la chambre de combustion supersonique (§ 3.1) doit tenir compte d'un certaine modularité de la géométrie tout en permettant les accès optiques les plus larges possibles. Celle-ci n'est pas refroidie : l'ensemble fonctionne en puits thermique pendant des rafales de quelques dizaines de secondes.

La veine d'essai est constituée d'un premier tronçon, à section constante (45 x 45 mm²), de longueur 370 mm. La deuxième partie de la veine est constituée d'une manchette divergente, de 500 mm : l'angle de divergence est de 1,3°.

Les faces latérales des trois manchettes sont munies de hublots affleurants, en silice fondue, permettant la visualisation de toute la hauteur de la veine d'essai. Les planchers supérieur et inférieur disposent d'accès optiques pour l'introduction de nappes laser destinées aux diverses techniques de visualisation par tomographie.

4.2 Mesures spécifiques associées

Une instrumentation classique est mise en oeuvre sur le banc d'essai : 150 voies de mesures (pression, température, débitmètres) ou de commande (vannes, dômes régulateurs de pression) sont scrutées à 10 Hz. La mise en régime thermique de l'installation (la température génératrice passant de 800 à 1800 K) et la rafale de combustion supersonique sont régies par une séquence minutée. La stabilité et la reproductibilité des rafales de combustion supersonique sont contrôlées par l'affichage en temps réel des paramètres principaux sur le pupitre de commande. Un commutateur de pression pour 80 voies permet de suivre l'évolution, au cours des rafales, des pressions pariétales réparties sur les parois supérieure et inférieure du foyer supersonique.

Une des originalités de cette installation d'essai réside dans la présence de deux laboratoires optiques contigus, abritant une chaîne de mesure des températures par DRASC et une chaîne d'imagerie laser. Afin de faciliter la mise en oeuvre de ces méthodes, un système de transport et de focalisation de faisceaux laser est implanté à demeure sur le banc de combustion. Il est conçu pour supporter l'environnement hostile du banc (bruit, vibrations mécaniques, rayonnement thermique).

4.3 Qualification

La mise en régime de l'installation, au moyen de la séquence de tir automatisée, en vue de l'obtention des conditions génératrices a fait l'objet des premiers essais. Cette séquence réalise successivement les injections d'oxygène, d'hydrogène du brûleur de préchauffage, l'injection supersonique d'hydrogène puis la phase d'arrêt. La séquence d'essai permet d'ajuster le débit d'oxygène de sorte que la fraction molaire d'oxygène dans l'air alimentant la veine d'essai soit toujours vérifiée à ±0,5 %. Après obtention de conditions génératrices stables, la durée de l'injection d'hydrogène dans l'écoulement supersonique est limitée à 15 s. Une séance d'essai courante permet la réalisation d'une dizaine de rafales de combustion supersonique au maximum.

La qualification du nombre de Mach à l'entrée de la veine d'essai est réalisée à l'aide des mesures des pressions génératrice, statique et Pitot. On constate un très bon accord entre toutes ces mesures qui indiquent que le Mach réel moyen, au voisinage du point d'injection de l'hydrogène est de l'ordre de 2,1. L'évolution du nombre de Mach obtenu, sur un profil transversal (figure 3), à une distance de 1,3 diamètre de l'injecteur, reste comprise entre 2 et 2,2.

5 DESCRIPTION DETAILLEE DE LA CELLULE ATD 5

5.1 Installation d'essai

Le schéma de l'installation est donné figure 4. La température du flux d'air alimentant la veine d'essais est obtenue à l'aide d'une combustion air/ hydrogène accompagnée d'une réoxygénation au taux molaire nominal de l'air. Dans le but de diminuer, pour certains essais, la viciation de l'air injecté dans la maquette, une partie du chauffage, jusqu'à 1000 K, est obtenu grâce à un échangeur situé en cellule 7 ATD de Palaiseau (fig 5). Le raccordement à l'amont de la veine d'essais de la cellule 5 est assuré par une tuyauterie calorifugée d'environ 15 mètres de long.

Deux types de configurations d'essais peuvent se produire pour l'établissement des conditions génératrices de l'écoulement supersonique en cellule 5 selon que l'on réchauffe l'air d'alimentation de la veine d'essais ou non avec l'échangeur :

- utilisation de l'échangeur :

L'échangeur situé en cellule 7 alimente en air chaud (~ 1000 K) la cellule 5 et le complément nécessaire en température est fourni par un foyer air/H_2.
La viciation de l'air par la vapeur d'eau due à la combustion de l'hydrogène est alors minimisée. Pendant le temps de mise en régime de l'échangeur, d'environ 40 minutes, l'air chaud alimentant la cellule 5 est by-passé pour éviter de chauffer la maquette qui fonctionne en puits de chaleur. Lorsque les conditions sont établies, le by-pass est fermé et la vanne haute pression/haute température isolant le montage du flux chaud est ouverte.
Dans cette configuration d'essai, une seule rafale peut être effectuée, en raison de l'échauffement du montage.

- non-utilisation de l'échangeur :

L'utilisation de l'échangeur ne permettant pas de réaliser plusieurs rafales pendant un essai, cette configuration n'est retenue que pour des études spécifiques sur les effets de la viciation. Pour un certain nombre d'essais, en particulier ceux ne nécessitant que la simulation d'un flux thermique représentatif (essais de matériaux, essais de tenue thermique de mâts d'injection,...), il est apparu intéressant de disposer d'une configuration où il n'y ait pas fonctionnement de l'échangeur mais utilisation de foyers de préchauffage à l'hydrogène. Dans cette configuration, l'air circulant dans la tuyauterie calorifugée est froid (T = 250 K) et provient d'un stockage d'air haute pression.

On peut rappeler les différents éléments constitutifs de la veine d'essais, de l'amont vers l'aval. L'air est tout d'abord acheminé en cellule 5 par une tuyauterie calorifugée. Il est alors réchauffé au travers de foyers air/hydrogène montés en série pour atteindre 2400 K au maximum, avec réoxygénation au taux normal molaire de l'air.

Une tuyère bidimensionnelle refroidie par eau accélère ensuite l'écoulement à Mach 2.5 ou 3 pour alimenter la chambre de combustion supersonique de section d'entrée 100x100 mm^2. Après une section constante, comprise entre 250 mm et 1400 mm selon les essais, le foyer diverge afin d'éviter le blocage thermique de la veine d'essais. Enfin, un tube de reprise dans lequel se désamorce le jet amène les gaz brûlés vers le carneau d'évacuation, après un passage au travers d'un brûleur de sécurité chargé de brûler l'hydrogène qui n'aurait pas été consommé dans la chambre.
Selon la température génératrice, des rafales de quelques secondes à quelques dizaines de secondes sont réalisables.

5.2 Mesures spécifiques associées

L'installation est dotée de 176 voies de mesures " classiques " de type pression ou température, scrutées à 10 Hz, à l'exception de 10 mesures de pression à 100 Hz. La mise en régime de l'installation et la rafale d'essai sont pilotées informatiquement par minuterie séquentielle.
Une interface de puissance permet de commander les actionneurs des différents organes du banc (vannes, électrovannes, pilotage des dômes, détendeurs, etc...).
Soixante-quatre voies de conversion numérique/analogique sont disponibles pour restituer sur les voltmètres du pupitre de commande et du synoptique les valeurs des différents paramètres à afficher.
Dix paramètres peuvent être suivis simultanément sur écran pendant une rafale.

Cette veine d'essai est équipée de hublots affleurants en silice fondue qui permettent de visualiser l'écoulement sur toute la hauteur de la veine d'essai. Des diagnostics optiques " simples ", tels que l'émission spontanée sur le radical OH, la pyrométrie ou la strioscopie sont ainsi réalisables ([5] et [6]).

Une sonde spécifique d'analyse de gaz a été conçue pour cette veine d'essai. Il s'agit d'une sonde en cuivre refroidie par eau. Elle permet 6 prélèvements simultanés en fin de foyer. Sa tenue à l'ambiance du jet a déjà été démontrée et des prélèvements devraient être réalisés au cours du second semestre 1997.

La veine d'essai a été qualifiée au cours de l'année 1995 et quatre campagnes d'essais se sont déjà déroulées en cellule 5 ATD.

6. PREMIERS TRAVAUX REALISES

6.1 LAERTE

6.1.1 Mesures des pressions pariétales

L'obtention du régime de combustion supersonique est vérifiée par l'évolution longitudinale des pressions pariétales, premières mesures mises en oeuvre sur l'installation d'essai (figures 6 et 7). Les profils de pression, obtenus sans injection d'hydrogène (figure 6a), sont caractéristiques d'un écoulement supersonique avec frottement dans la partie à section constante jusqu'à une distance de $x = 370$ mm (le système de coordonnés x,y,z étant représenté figure 1). Dans la partie divergente de la veine (de $x = 370$ mm à $x = 870$ mm), l'écoulement subit une nouvelle détente jusqu'à un Mach de sortie d'environ 2,4. Les profils de pression laissent apparaître de légères perturbations liées aux réflexions des ondes de détente et de compression provoquées par les discontinuités de paroi (manchettes de raccordement, passages des hublots). Les profils de pressions statiques aux parois supérieure et inférieure de la veine d'essai traduisent une bonne symétrie de l'écoulement (figure 6a).

L'essai de démonstration de la combustion supersonique dans la veine d'essai est réalisé dans les conditions nominales (Pi = 7,2 bar, Ti = 1750 K). Les pressions et températures génératrices de l'hydrogène sont respectivement 6,5 bar et 300 K, de sorte que les conditions de sortie du jet d'hydrogène soient adaptées à celles de l'écoulement externe d'air. Dans ce cas, la valeur du Mach convectif initial dans la couche de mélange est de 0,38 et la richesse globale de la flamme est 0,3.

La comparaison des profils longitudinaux des profils des pressions pariétales pour les cas non réactif et avec injection d'hydrogène (Figure 7a), met bien en évidence l'inflammation de l'écoulement, à une distance d'environ 240 mm en sortie de la tuyère principale, soit une distance de 34 diamètres d'injecteur depuis son plan de sortie. La remontée de pression observée, caractéristique d'un apport de chaleur dans un écoulement supersonique en canal à section constante, est de l'ordre de 0,3 bar. On constate également que la veine d'essai reste amorcée sur toute sa longueur. La rafale demeure stable pendant les 15 s que dure l'injection d'hydrogène. Il a été également contrôlé que la symétrie de l'écoulement était conservée en combustion (figure 6b).

L'effet de la viciation par la vapeur d'eau de l'écoulement supersonique d'air sur cette distance d'inflammation est également déterminé. La même température génératrice d'environ 1800 K est obtenue avec les échangeurs de chaleur et un foyer de préchauffage à l'hydrogène, puis sans les échangeurs (foyers de préchauffage à l'hydrogène tous deux en service). Dans ces différentes conditions, la fraction molaire de vapeur d'eau passe de 15 à 21 %, celle de l'oxygène étant toujours maintenue à 21 %. Il n'est pas possible de déceler d'influence de la viciation, sur les relevés de pression (figure 7b) et donc sur la distance d'inflammation.

6.1.2 Emission spontanée de OH

L'image de l'émission créée par le radical OH présent dans la flamme est obtenu par un objectif U.V. Nikkor de 105 mm et une caméra CCD EGG obturable, à intensificateur de lumière. Un filtre interférentiel centré à 309 nm est utilisé pour rejeter l'émission de la flamme dans le visible. Le champ visualisé sur toute la hauteur de la veine est long d'environ 90 mm. Il est choisi à l'abscisse $180 < x < 270$ mm, région de début de la combustion supersonique selon les mesures de pression.

La figure 8 présente la visualisation de la flamme obtenue dans les conditions nominales précédemment indiquées. Le niveau d'émission varie d'un facteur 3 entre le fond et le maximum observé. Le radical OH émet d'une manière significative à partir d'une abscisse de 200 mm. Cette valeur est à comparer à la distance d'inflammation de 240 mm déduite des relevés des pressions pariétales (figures 7a et b) : les distances relevées par ce moyen semblent légèrement supérieures puisqu'elles dépendent du dégagement de chaleur de la réaction, moins précoce que la formation du radical OH.

L'imagerie spontanée offre des images intégrées dans l'espace et leur interprétation reste délicate. Cependant, on peut confirmer la bonne symétrie de la flamme déjà constatée sur les relevés de pression. Les zones d'émissivité maximale sont localisées au niveau de l'interface combustible-air comme attendu dans une telle flamme de diffusion. Le taux d'ouverture de la flamme estimé à 5% sur cette visualisation semble proche de la valeur déduite des corrélations de [2], pour une couche non réactive de même nombre de Mach convectif.

6.2 Cellule 5 ATD

6.2.1 Refroidissement de matériaux composite

Le refroidissement d'une chambre de superstatoréacteur, sur un engin en vol, pose de nombreux problèmes, en raison des flux de chaleur pouvant atteindre plusieurs MW/m^2. Plusieurs solutions peuvent être envisagées pour refroidir de telles chambres. Par exemple, on peut utiliser l'hydrogène embarqué ou utiliser des matériaux résistants aux températures élevées.

Deux campagnes d'essais, qui combinent ces deux solutions, ont été réalisées sur le thème du refroidissement de matériaux composites par hydrogène. Ces études de type technologique permettent d'étudier des concepts qui pourraient être directement utilisés dans une chambre de superstatoréacteur.

La première campagne a porté sur l'étude du refroidissement par effusion d'hydrogène d'un matériau composite multiperforé. Dans ce cas les ΔP d'injection sont faibles (<1 bar).

La seconde campagne a permis d'étudier le refroidissement de matériaux composites " poreux " par transpiration d'hydrogène. Dans ce cas, la porosité naturelle du matériau permet le passage de l'hydrogène. Les ΔP d'injection sont dans ce cas beaucoup plus élevés et atteignent quelques bar à quelques dizaines de bar.

L'efficacité de ces deux concepts, dans des conditions représentatives de vol à Mach 6 et 7, a pu être étudiée au cours de ces campagnes.

6.2.2 Etudes d'injecteurs élémentaires

La cellule 5 ATD permet aussi bien de réaliser des études technologiques que des études à caractère un peu plus fondamental. Ainsi, une campagne d'essai sur des injecteurs élémentaires a débuté.

Pour l'instant, l'étude d'une injection d'hydrogène dans une cavité est en cours (fig 9). Dans le plan de sortie de l'injecteur, l'hydrogène est injecté à Mach 2.5 dans l'écoulement principal également à Mach 2.5 (fig 10). L'influence de paramètres tels que la température d'arrêt ou la quantité de mouvement du jet sur le délai d'inflammation est étudiée.

La figure 11 montre une visualisation obtenue par émission spontanée du radical OH, pour un jet à $Pi = 24,2$ bar et une Température d'arrêt de l'air de 2400 K qui correspond à un Mach de vol de l'ordre de 7.5. La combustion s'initie en fin de cavité, grâce au choc créé par l'écoulement principal. L'image est obtenue par un objectif U.V. Nikkor de 105 mm et une caméra intensifiée Hamamatsu fonctionnant à une cadence vidéo de 25 images/s. Un filtre interférentiel centré à 309 nm permet de rejeter l'émission de la flamme dans le visible.

L'image obtenue est une image intégrée dans l'espace et est d'interprétation délicate. Toutefois, des fluxmètres ou des thermocouples de paroi, situés dans l'axe du jet, derrière la cavité, confirment l'inflammation de l'hydrogène par augmentation du flux mesuré ou augmentation de la pente de montée en température (fig 12).

Suite à l'étude de l'injection dans une cavité, deux autres injecteurs seront étudiés :

- un injecteur de paroi incliné à 45° et précédé d'un nombre variable de petits injecteurs perpendiculaires à la paroi. L'étude de l'influence de ces petits injecteurs sur l'initiation de la combustion de l'injecteur principal sera étudiée.

- un injecteur de culot sera également étudié pour mieux comprendre l'influence des paramètres d'injection sur l'inflammation des jets de culot.

7. CONCLUSION

Les deux installations complémentaires, développées au centre ONERA de Palaiseau, dans le cadre du PREPHA, sont opérationnelles. La possibilité d'y réaliser des rafales stables et reproductibles de combustion supersonique y a été démontrée. De par sa taille et son accessibilité optique, la chambre de combustion supersonique du LAERTE est particulièrement bien adaptée aux études fondamentales en combustion supersonique. Par ses capacités, en pression, débit, température d'arrêt, la cellule ATD 5 est tout à fait propre aux études appliquées de composants de superstatoréacteur ou de petites chambres complètes.

Les premières mesures de pressions pariétales, au cours des rafales de combustion supersonique obtenues au LAERTE ont permis de relever la distance d'inflammation d'un jet supersonique d'hydrogène à Mach 2 dans un écoulement supersonique d'air à Mach 2, pour deux niveaux de viciation de l'air par la vapeur d'eau. Les possibilités de visualiser l'écoulement ont également été démontrées par la technique d'imagerie de l'émission spontanée du radical OH par la flamme. Ces visualisations constituent une première étape avant la mise en œuvre des techniques d'imagerie de fluorescence induite par laser et Rayleigh. Elles seront complétées par des relevés des températures locales et instantanées par DRASC.

La cellule 5 ATD a déjà permis d'étudier des concepts de refroidissement de matériaux composite par l'hydrogène. Des études sur des injecteurs élémentaires sont en cours et vont se poursuivre. Au courant du second semestre 1997, une chambre mono-mât complète devrait être essayée en cellule 5 ATD, jusqu'à Mach 7.5. La pesée des mâts devrait notamment être réalisée.

8. REFERENCES

[1] Falempin F.H., "Overview of French Research Center ONERA Activities on High-Speed Airbreathing Propulsion", 12th ISABE, Melbourne, Australie, September 10-15, 1995

[2] Messersmith N.L., Goebel S.G., Frantz W.H., Krammer E.A., Renie J.P., Dutton J.C., Krier H., "Experimental and Analytical Investigations of Supersonic Mixing Layers" AIAA paper 88-702, AIAA 26th Aerospace Sciences Meeting, Reno, 11-14 Jan 1988.

[3] Papamoschou D., Roshko A., "The compressible free shear layer : an experimental study", J. Fluid Mech., Vol 197, 453-477, 1988

[4] Cathonnet M., Dagaut P., Boettner J.C.,"Cinétique de combustion des mélanges H2-Air dans les conditions d'un superstatoréacteur", Actes du 1er Colloque du PRCCS, 21-22 Octobre 1991.

[5] Scherrer D., Dessornes O., Montmayeur N., Ferrandon O., « Injection studies in the french hypersonic technology program », AIAA sixth International Aerospace Planes and Hypersonics Technologies Conference, Chattanooga, TN (USA) April 3-7, 1995.

[6] Scherrer D., Dessornes O., Jourdren C., Leboucher C., Bouchez M., Saucereau D., « Injection and combustion challenges in scramjets », AAAF : 5ème Symposium International sur la Propulsion dans les Transports Spatiaux, Paris, 22-24 Mai 1996.

Tableau I : Caractéristiques principales des installations d'essais

	LAERTE	ATD5
dimension veine	45 x 45 mm²	100 x 100 mm²
débit air	1.3 kg/s	4 kg/s
débit Oxygène	0,15 kg/s	1,3 kg/s
débit H2	0,025 kg/s	0,3 kg/s
débit hélium	0,010 kg/s	non
type d'injection	parallèle axisymétrique pariétale	pariétale mât
Mach air	2	2,5 et 3
Mach H2	2	1 et 2,5
Pression génératrice Air (bar)	7	27
Température génératrice air non vicié	850 K	950 K
taux de viciation par la vapeur d'eau	15 à 21 %	27 à 33%
Température génératrice air vicié	1800 K	2400 K
Pi H2 (bar)	25	40
Température génératrice H2	500 K	290 K

Section ....45 x 45 mm^2
Longueur ....870 mm

Mach Air = 2
Mach Hé ou H$_2$ = 2
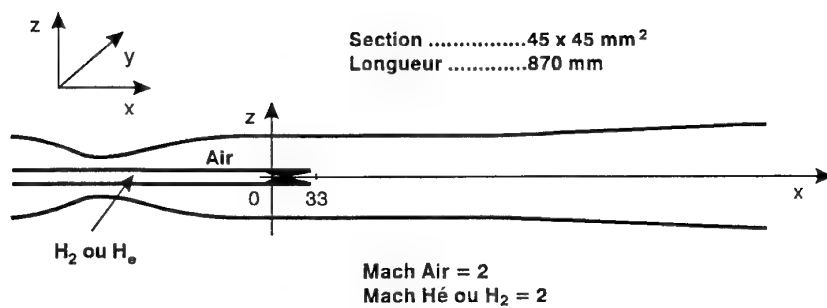
Fig. 1 - Principe de l'expérience
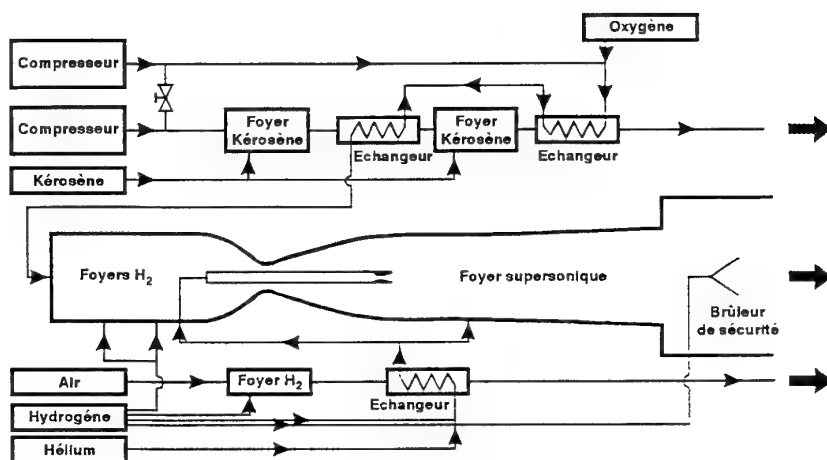
Fig. 2 - Schéma d'ensemble du banc
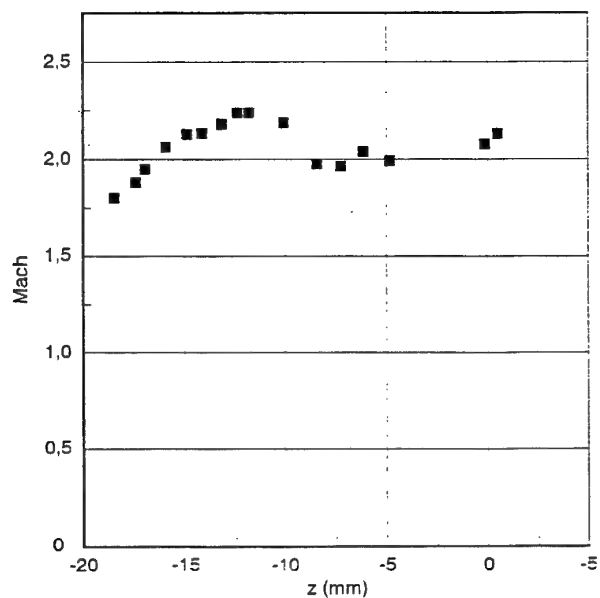
**Fig. 3 - Distribution du nombre de Mach
en entrée de la veine d'essai**

Alimentation air chaud
Température : 900 K
Débit air : 4 kg/s
Pression : 40 Bar

Bride de refroidissement
Col
Diaphragme
Générateur d'hétérogénéité
Oxygénation
Isolateurs
Chambre divergente
Porte-mât
Diffuseur

Vannes pilotées - hautes pressions, hautes températures

Brûleur de sécurité
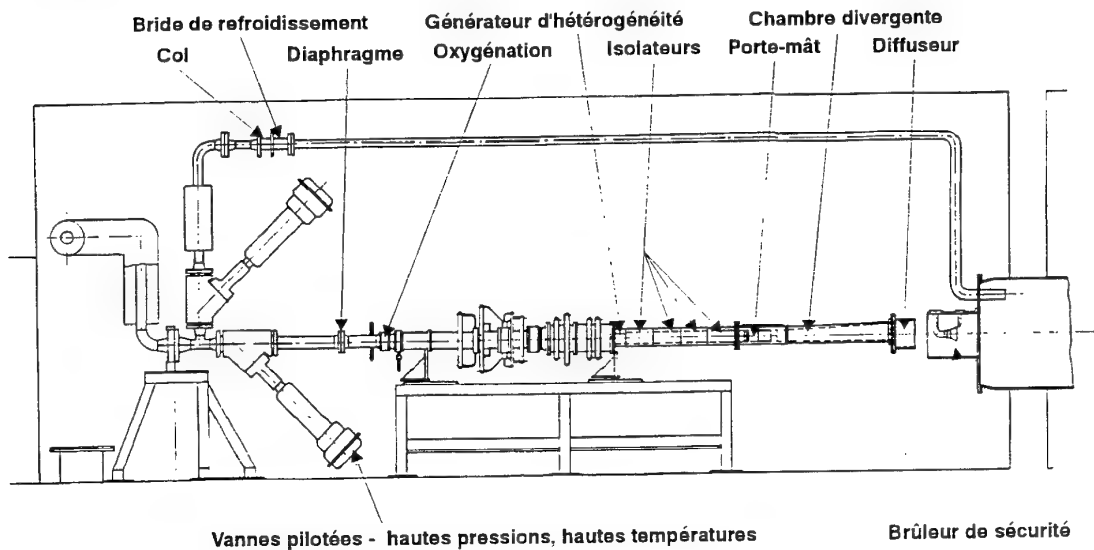
Fig. 4 - Schéma de l'installation de la cellule ATD 5

Echangeur
Cellule 7
Tuyauterie chaude
Cellule 6
Cellule 5
Cellule de conduite
Axe de la veine d'essais

① ② ③ ④ ⑤ ⑥
⑦ ⑧ ⑨
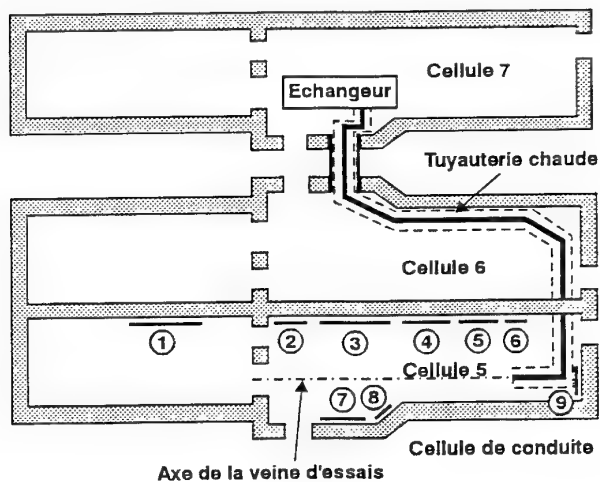
1 - Détente O2
2 - Brûleur de sécurité
3 - Détente H2
4 - Injection O2 - Balayage N2
5 - Injection O2
6 - Torches O2 et H2
7 - Détente H2
8 - Kérosène
9 - Air HP

Fig. 5 - Alimentation en air chaud de la cellule 5

.... Paroi supérieure
———— Paroi inférieure

P_s/P_i
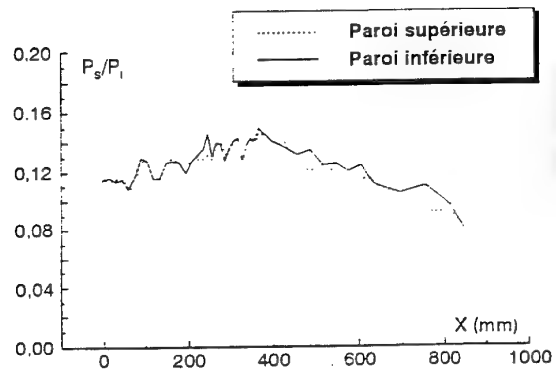
6a) Sans combustion

P_s/P_i
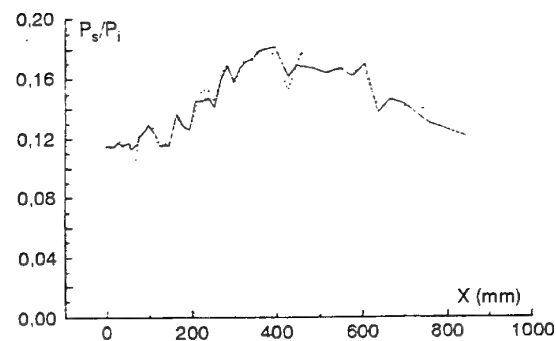
6b) Avec combustion

Fig. 6 - Distribution des pressions pariétales
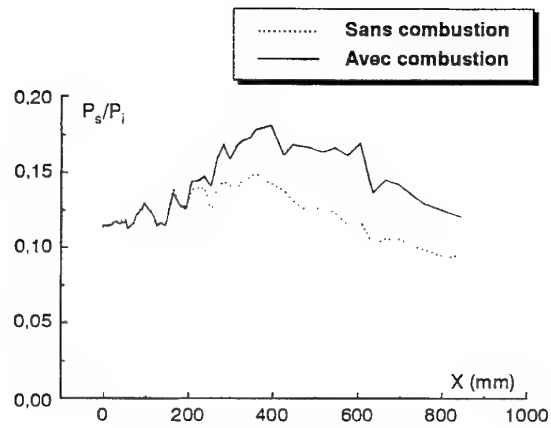
7a) Partiellement vicié
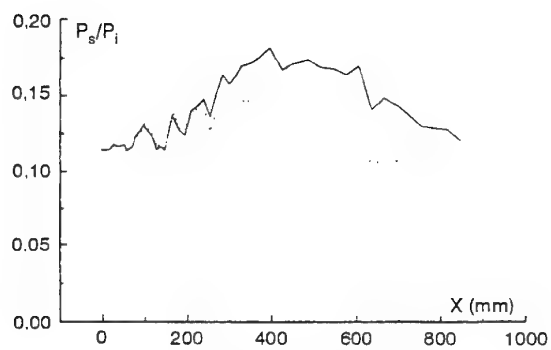
7b) Totalement vicié

Fig. 7 - Effet de la viciation sur le développement
de la combustion supersonique
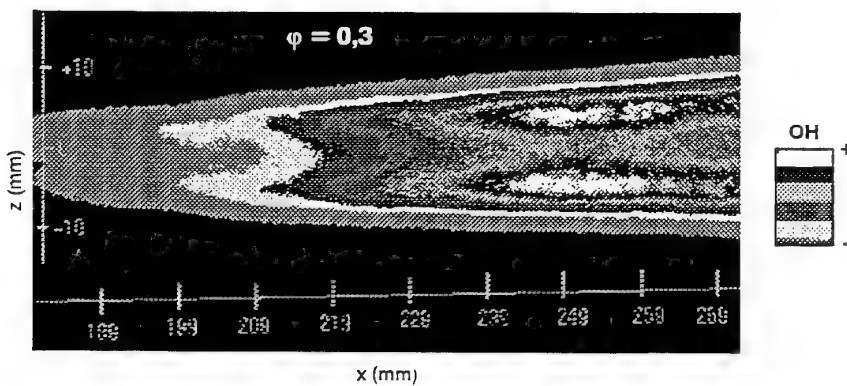
Fig. 8 - Emission spontanée du radical OH
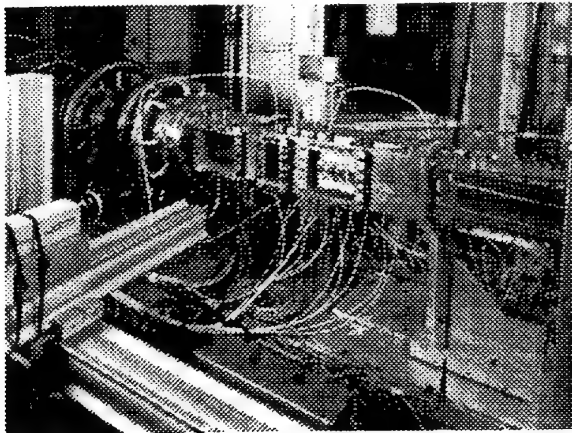
Fig 9 - Montage d'essai pour l'étude de l'injection d'hydrogène dans une cavité

Fig. 10 - Schéma de principe de l'injection dans une cavité

Air chaud
Mach 2,5

H₂ (froid)

Sens écoulement

Fin cavité
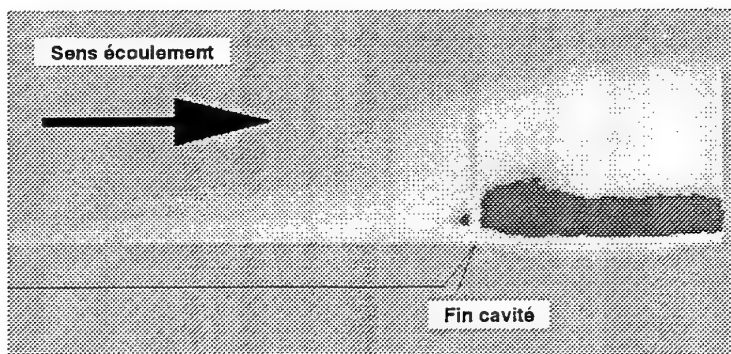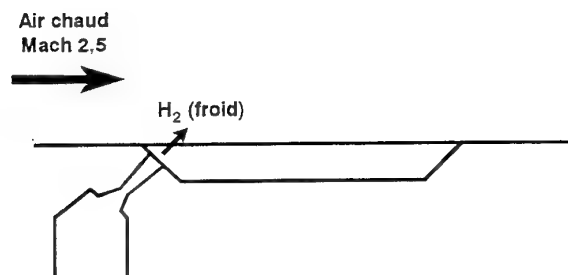
Fig. 11 - Visualisation par émission spontanée du radical OH
(Ti = 2400 K, injection dans une cavité)

Fig. 12 - Température de paroi dans l'axe du jet, en aval de la cavité

Injection H2
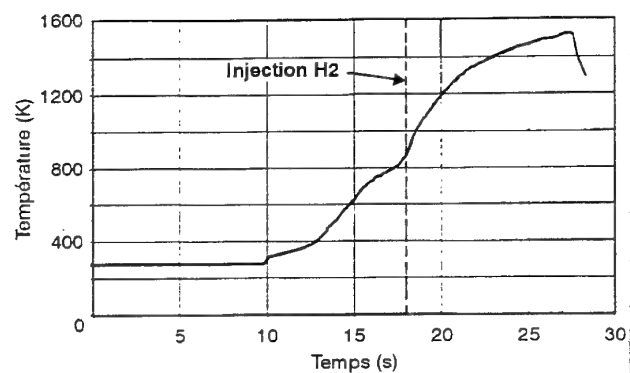
Test Facilities for Large Ramjets

W.W. Koschel

DLR Lampoldshausen

D-74239 Hardthausen, Germany

F. Heitmeier

Daimler Benz Aerospace MTU

D-80976 München

1. SUMMARY

Within the German Hypersonics Technology Program (GHTP) a subscale ramjet was to be ground tested in a free jet configuration. The propulsion system selection process for a hypersonic experimental flight vehicle will be briefly reviewed. A ramjet type propulsion system with subsonic combustion was chosen as the baseline configuration. The rationale of technology and component development will be presented. The final goal of the program was a ramjet test in the simulated flight Mach number range from Ma = 3.5 up to Ma = 6.8 in order to demonstrate the engine's steady state operation and thrust capability. A general concept for the ramjet ground testing was developed specifying as well the operational requirements for the engine characteristics as the test and measurement plan. A ramjet propulsion system with a ram combustor diameter of 500 mm was designed as the demonstrator engine. Based on the predefined specifications an evaluation of existing large scale test facilities was made including a total of 11 existing facilities in the United States, in Russia and in France. Engine installation and necessary adaptation of existing hardware were studied and discussed with the operators in detail. Major results of this facility evaluation study and lessons learned will be presented in the paper. The APTU wind tunnel of the AEDC at Tullahoma was finally selected for the planned tests of the full engine. Due to funding restrictions only the ram combustor with the variable geometry nozzle could be demonstrated in operation in the connected-pipe test facility at Ottobbrunn in Germany.

2. INTRODUCTION

The German Hypersonics Technology Program was set up in 1988 by the Federal German Ministery of Research and Technology (the former BMFT).

As a result of preliminary studies a reference concept for a reusable space transportation system with the main features [1]:

> TSTO, HTOHL with an airbreathing first stage and a rocket powered second stage

was selected for all the development and technology work to be performed within the program. The TSTO reference concept was named after the German space pioneer *Eugen Sänger*. Fig. 1 shows an artist's view of the TSTO Sänger winged vehicle.

The focal point was the definition of a reusable space transportation system with a cruising capability of the lower stage at hypersonic speed in order to allow take-off and landing capability in central Europe for launch and autonomy reasons. Thus the requirements for the airbreathing propulsion system had to meet the needs of a sustained hypersonic flight.

The schedule of the German Hypersonics Technology Program is shown in Fig. 2. The program started in 1988 and ended in December 1995. It was split into three phases. Phase 1a was dedicated mainly to the definition of the lead concept for the system definition and to propulsion systems studies where work was focused on the identification of key technologies to be explored, especially concerning the selection of the airbreathing propulsion concept for the lower stage.

During the second phase called Phase 1b from end 1990 through 1992 work was spent on the predevelopment in the main areas of hypersonic technologies:

- airbreathing propulsion,

- aerothermodynamics and propulsion integration,

- materials and structures,

- GNC & subsystems and

- development of test facilities.

The final Phase 1c which lasted from 1993 until December 1995 covered the following topics:

- detailed definition of the technology development and verification concept
- the flight test vehicle study
- propulsion component development
- propulsion system ground testing.

A more detailed overview on the technology work performed within the GHTP is given in [2].

3. SELECTION OF THE REFERENCE PROPULSION CONCEPT

The Sänger TSTO vehicle configuration was defined to stage at a flight Mach number of Ma = 6.8 due to reasons for technology risk limitations Therefore 6 different candidates for the airbreathing hypersonic propulsion system of the lower stage were taken into a closer consideration at the beginning of the program (see Fig 3):

Concept 1: Turbojet engine with a ramjet engine in a coaxial arrangement

Concept 2: Turbojet and a ramjet engine in a parallel arrangement

Concept 3: Turbofan with a ramjet engine in a tandem arrangement - the so-called HYPER-CRISP

Concept 4: Turbojet engine with precooling

Concept 5: Turborocket

Concept 6: Expander cycle engine

In an interim assessment the number of concepts were reduced to the first 3 of the listed concepts, since the last three showed a lot of drawbacks in performance and higher technology risks for the component technology development.

After a more detailed system analysis of the first three engine configurations Concept 1 - the turbojet with a ramjet in a coaxial arrangement - was chosen as the baseline propulsion system due its lowest risk of development, its lowest complexity, and due to its adequate performance over the whole flight range from subsonic to hypersonic speed including the cruising range in comparison with the competitive concepts.

In Fig. 4 the general arrangement of the Sänger airbreathing propulsion system in the lower stage is depicted. The engine is operated in the turbo engine mode with a ram burner serving as an afterburner up to the flight Mach number of Ma = 3.5 Then the engine is switched to the ramjet mode. The cruise was planned with ramjet operation at a constant flight Mach number of about Ma = 4.5. The staging Mach number of Ma = 6.8 was considered as the limit of the ramjet operation.

4. RATIONALE OF AIRBREATHING PROPULSION SYSTEM DEVELOPMENT AND DEMONSTRATION

The majority of funds of the GHTP were spent on the technology development for airbreathing propulsion since it was regarded as the most critical system component. The technology for the turbojet engine though demanding for a flight regime up to Ma = 3.5 was considered to be deducible from existing military engine technology. Therefore all efforts were focused on the ramjet engine development and demonstration.

The rationale of the ramjet development can be seen in Fig. 5. The development of component technology for the intake, the ram combustor and the variable nozzle were the key issues for the work in Phase 1b. The feasibility of the ramjet engine was to be demonstrated in a stepwise approach starting from component testing of subscale intakes, ramjet burners and nozzles and followed by a connnected-pipe test of the ram combustor together with a variable SERN-type nozzle [3],[4],[5]. The airbreathing technology work was accompanied in a parallel activity throughout the Phase 1b by a system study for a subscale hypersonic flight vehicle. The first concept was a manned winged vehicle called HYTEX with a maximum flight speed up to M = 5.6. Since it turned out very soon that the development of such a test vehicle would be to risky and costly a down-sized unmanned vehicle called HYTEX R-A3 became the lead configuration for the ramjet engine flight demonstration in the Mach number range between Ma = 3.5 up to Ma = 6.8 [5]. The geometry of the flight demonstrator ramjet engine was fixed to an inner diameter of the combustor of 500 mm defining the baseline engine size also for the ground testing.

The rationale of the ground testing of the demon-

strator baseline engine is shown in Fig. 6. The stepwise approach was split up into the follwing parts:

- intake test in a free-jet test. facility

- combustor-nozzle test in a connected-pipe test

- full engine test in free-jet test facility.

5. DEMONSTRATION GOALS AND TEST PROGRAM

The program planning for the ramjet demonstration test which had to be performed within a 31 months´ period and should cover the design, the manufacturing, test facility adaptation, engine control lay-out, the design of the measuring equipment and finally the test execution and evaluation. An integrated team was formed by engine and component specialists of Dasa and Dasa MTU to cope with that tough time schedule.

The general goal was defined to be the demonstration of the function, the performance and the control of the ramjet engine in a simulated flight Mach number range from Ma = 3.5 up to 6.8. Taking into account the forebody compression the maximum simulated inlet Mach number was fixed at Ma = 5.8 to be achieved in a ground test facility. The ground testing was set up in a stepwise approach with detailed component testing of the intake, the combustor and the nozzle together with the combustor. The full engine test should finally give answers to the following identified problem areas:

- the starting behaviour and the stabilized operation,

- the performance achievements in comparison to predictions based on component testing,

- the upstream effect of ignition and combustion concerning intake aerodynamics,

- the operational behaviour of the combustor and the nozzle under inlet conditions supplied by the mixed compression intake in comparison to results obtained from the connected-pipe testing,

- the engine behaviour under transient conditions and finally

- the prove of the engine control concept.

Subsequently a test program was defined in order to determine the engine performance within the envisaged flight Mach number envelloppe. The following parameters to be varied during the free-jet testing were chosen:

- Mach numbers at the intake Ma = 3.5, 4.3 and 5.8 corresponding to flight Mach numbers Ma = 3.6, 4.5 and 6.8 taking forebody compression of the flight test vehicle into consideration,

- 3 typical throttling conditions at the throat area and

- variation of the fuel/air ratio between ER = 0.5 to 1.0.

The tests at the inlet Mach numbers at Ma = 3.5 and 4.5 should be performed at real flight stagnation temperature conditions whereas at the maximum Mach number Ma = 5.8 the test conditions concerning pressure and temperature levels were reduced due to structural limitations of the test specimen and due to heat load limitations of the ground test facility.

Refering to the predefined test conditions a performance analysis of the ramjet engine was done resulting in requirements for engine air flow data to be supplied by the free jet ground test facility. (Table 1). Furtheron requirements of supply quantities were set-up for fuel (GH2), for the hydraulic actuators of the intake and nozzle control, for the pressurization of the intake and nozzle cavities and for cooling purposes of the combustor and the nozzle walls. The required supply quantities are listed in Table 2..

The necessary aerodynamic contours of the ramjet engine with the combustor diameter of 500 mm can be taken from Fig. 7. The test specimen geometry resulted in a total engine length of 8 m with a maximum cross area of 900x800 mm at the intake throat position.

6. EVALUATION OF EXISTING GROUND TEST FACILITIES

Within the German Hypersonics Technology Program a connected pipe test facility was built-up to run tests for ramjet combustors at Ottobrunn, Germany. In a first step this test facility was designed to run tests of combustors with an inner diameter of 300 mm up to simulated inlet conditions of a flight Mach number of Ma = 7.0. Within Phase 1c the test facility was extended to accomodate combustors with a diameter of 500 mm. This facility was used for the component tests of the combustor and the nozzle of the demonstration ramjet engine. A laughing gas reactor

was used in connection with the preburner in order to minimize the vitiation effects in the heated air supply. The built-up of the connected-pipe installation for the ram burner with the reactor and variable geometry nozzle is shown in Fig. 8.

Since in Germany no free-jet hypersonic test facility was available to meet the aforementioned requirements for a full engine ground test, an evaluation of existing free-jet and semi-free jet test facilities in the United States, in Russia and in France was made.

A total of 11 test facilities were included in the evaluation process, most of them were visited by a specialist´s group in order to discuss details of the ramjet testing feasibility and necessary modifications of the test installations with the operators. The list of potential candidates for the ramjet test facilities are listed in Table 3..

In the United States the test facility CELL 2 of the Marquardt Company, in Los Angeles, and the wind tunnel 8 HTTT at NASA Langley turned out to be unavailable for access due to different reasons and were therefore not examined in more detail in regard to the fullfillments of specifications for the ramjet engine testing.

The test facility HYTEST of Aerojet in Sacramento was excluded from further analysis since its test cabin was too small to accomodate the full GHTP ramjet engine. Furtheron the size of the free jet nozzles with an exit area of 925x925mm did not meet the requirement for an undisturbed inlet flow to the intake.

The most suitable test facility in regard to the specified test requirements is the hypersonic wind tunnel APTU (Aerodynamic and Propulsion Development Test Unit) at the Arnold Eginneering Development Center (AEDC) in Tullahoma, Tenessee, USA. This test facility could meet most of the specifications concerning as well the operational inlet conditions and the needed size of the test cell as the supply quantities of air, GH2, N2 and hydraulics. The APTU operating envelope is shown in Fig. 9 [6]. The 22,000-cu ft high pressure air reservoir, pressurized to 3,800 psi, allows running times of the blow-down-type wind tunnel between 3 and 12 minutes according to the chosen inlet conditions and enables high test frequencies. Furtheron this facility is equipped with a comfortable data acquisition and evaluation system with a sufficient high number of low speed and high speed channels for the data acquisition. Only minor modifications concerning three new free jet nozzles for the predefined inlet Mach numbers and the exit diffusor would have been

necessary.

In Russia 4 different high speed wind tunnel installations had been visited and examined in detail. All these facilities were located in the area of Moscow. The largest facility is the hypersonic blow-down wind tunnel U306-3 at TSNIIMASH in Kaliningrad which would have been allowed to run the full operating range of the ramjet and which with slight modifications would have been suitable to accomodate the ramjet engine in full size. The manufacturing of new cooled free-jet nozzles were regarded by the operators as time-critical items. Furtheron the supply for the demanded quantities of hydrogen to be installed was questionable.

The test facility TS-9N at NIITP, Lytkarino, offered also the potential to accomodate the ramjet engine in full size. Though this installation had the advantage of a continous air supply, missing free-jet nozzles, thrust measuring system, computer-aided data acquisition and hydrogen supply dropped this facility out of the further analysis.

The large test installations 131 A at TsAGI, Zhukovsky, and U-16 at CIAM, Lytkarino, which had been formerly used for ramjet/scramjet testing turned out to be too small in size. Their use for the GHTP ramjet testing would have lead to major modifications, which could not be taken into a nearer consideration due to the limitations of the fixed time schedule and the cost frame.

In France 3 potential test facilties were studied together with the operators if they could be modified for housing and testing the ramjet engine. The blow-down test facility S4M4 at ONERA in Modane was built in the late fifties for scramjet testing. Though the performance of the test rig concerning the specified air supply conditions at the inlet was sufficient its use would have needed some major modifications and aditional investments concerning a new exhaust diffusor system. It should be pointed out that the S4M4 is the only test rig which delivers a heated air supply with no vitiation by preburners due to its unique pebble bed heater supplying stagnation temperatures up to 1850 K. A sectional view of the test rig with a preliminary arrangement of the German ramjet engine is presented in Fig. 10.

The CEPr in Saclay studied modifications of the existing test cells R5 and K11 in order to accomodate the ramjet engine. The time schedule and the costs needed to realize the extension of the test rigs finally did not meet the program frame.

The third French test facility suitable for ramjet/scramjet operation is located at Aerospatiale in

Le Subdray/Bourges. This test facility which is actually used for scramjet testing within the French PREPHA program offers a high degree of flexibility and meets all the specifications of air, GH2 and N2 supply. Several options of the GHTP ramjet engine installation were studied by the French operators A preliminary sketch of the GHTP ramjet engine arrangement option with two exhaust diffusors in the Le Subdray facility is shown in Fig. 11. But several necessary major modifications and additional installations like a second preburner and a new test cell were needed..

It should be noted that all three French facilities would have met the operational requirements by introducing some modifications. But budget constraints and the limitations of the program schedule were finally the reasons not to choose a French test facility.

In conclusion the APTU at AEDC was selected as the test facility of preference. A detailed test planning was started and the control and supply interfaces were defined (Fig. 12). But due to the budget cut-backs only the connected pipe testing of the combustor together with the variable geometry nozzle could be successfully finalized using the Ottobrunn facilities.

7. Conclusions

The selection of a test facility for the ground testing of a specified ramjet engine, which had been developed within the German Hypersonics Program was a very valuable experience. It showed that the worldwide capabilties to test large scale ramjet engines at simulated high flight Mach numbers are limited. in size and inlet conditions concerning especially the higher temperature levels to be realized. For future needs of large scale ramjet engine testing it seems to be reasonable to establish common requirements for high speed engine ground testing and to coordinate test installation extensions in an international collaborative approach.

Literature

[1] Kuczera, H., Hauck, H. and P. Sacher and P. Krammer: The German Hypersonics Technology Programme – Status 1993 and Perspectives. Fifth International Aerospace Planes and Hypersonics Technology Conference 1993, Munich, AIAA-93-5159

[2] Koschel, W. and F. Heitmeir: Overview on Airbreathing Propulsion Achievements within the German Hypersonics Technology Program. 5th International AAAF Symposium on Propulsion of Space Transportation, 22-24 May 1996, Paris

[3] Voss, N.H.: Ram Combustor Development within the German Hypersonics Technology Program. Sixth International Aerospace Planes and Hypersonics Technology Conference 1995, Chattanooga, AIAA-95-6030

[4] Kretschmer, J.: Injection and Combustion Chamber Technologies for Hypersonic Propulsion. 5th International AAAF Symposium on Propulsion of Space Transportation, 22-24 May 1996, Paris

[5] Heitmeier, F. and N. Bissinger: Development and Test of an Airbreathing Propulsion System for Hypersonic Speeds. Sixth International Aerospace Planes and Hypersonics Technology Conference 1995, Chattanooga, AIAA-95-6014

[6] AEDC Information Brochure DSN340-5586, May 1994, cleared for public release by the Office of Public Affairs, Arnold Engineering Development Center, Arnold AFB, Tenn.

[7] Sacher, P. and B. Zellner: Flight Test Objectives for Small Hypersonic Test Vehicles Featuring a Ramjet Engine. Sixth International Aerospace Planes and Hypersonics Technology Conference 1995, Chattanooga, AIAA-95-6014

Flight Machnumber Ma,∞	-	3.6	4.5	5.8 reduced pressure	
Test Machnumber Inlet, Ma,∞	-	3.5	4.3	5.8	
Total Pressure Inlet, P∞	kPa	670	1 210	2 070	for vitiated air
Static Pressure Inlet, P∞,min	kPa	8.5	4.6	1.4	"
Total Temperature Inlet, T∞	K	870	1 135	1 100	"
Total Temperature Nozzle Exit, T₉	K	2550	2 660	2 630	"
Static Pressure Nozzle Exit P₉₉,min	kPa	16.0	8.5	5.0	minimum requirement
Test Machnumber Nozzle Exit, Ma₉	-	The nozzle exit Machnumber depends on the achievable nozzle exit ambient pressure P∞			
Total Pressure Nozzle, P₁₇	kPa	In the worst case for ejector/diffusor design the following estimated figures can be assumed: $P_{17} \geq 200\,kPa$ $\dot{m} \leq 15\,kg/s$			
Air Mass Flow, ṁ	kg/s				

Table 1: GHTP ramjet engine air flow data

Supply	Component	Quantity	Pressure	Specification
Free Jet Air	Intake	15 kg/s	2070 kPa	Air (vitiated)
Fuel	Burner	0.53 kg/s	12 bar	GH_2
Hydraulic	Intake Nozzle	10 l/s 20 l/min	210 bar 300 bar	Oil Oil
Pressurization	Intake Nozzle	0.75 kg/s 0.80 kg/s	6 bar 4 bar	Air or N_2 optional N_2 mandatory
Cooling	Burner Nozzle	10 kg/s 0.20 kg/s	40 bar 30 bar	Air or N_2 optional GH2
Electricity				tbd

Table 2: Hypersonic test facilities

Operator	Location	Test Facility
AEDC	Tullahoma, Tenn., USA	APTU
Aerojet	Sacramento, Ca., USA	HYTEST
Marquardt Company	Los Angeles, Ca,. USA	CELL 2
NASA	Langley, USA	8˝HTT
TNIIMASH	Kaliningrad, Moscow Region, Russia	U306-3
TsAGI	Zhukovsky, Moscow Region, Russia	131A
CIAM	Lytkarino,Moscow Region, Russia	U-16
NIITP	Lytkarino,Moscow Region, Russia	TS-9N
ONERA	Modane, France	S4M4
CEPr	Saclay, France	R5, K11
Aerospatiale	Le Subdray, France	SCRAMJET

Table 3: Required supply quantities
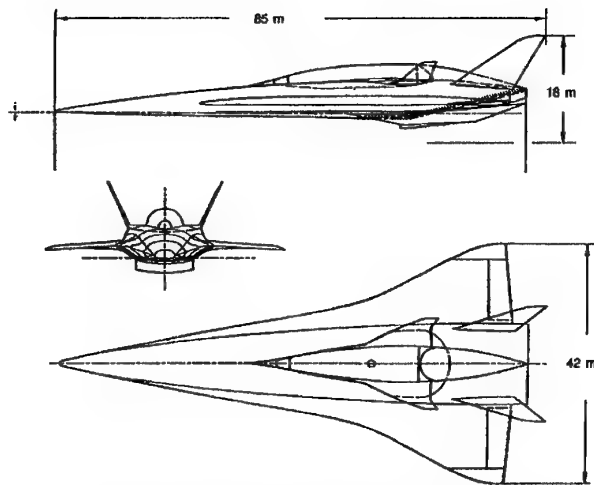
Fig. 1: The Sänger TSTO lead configuration
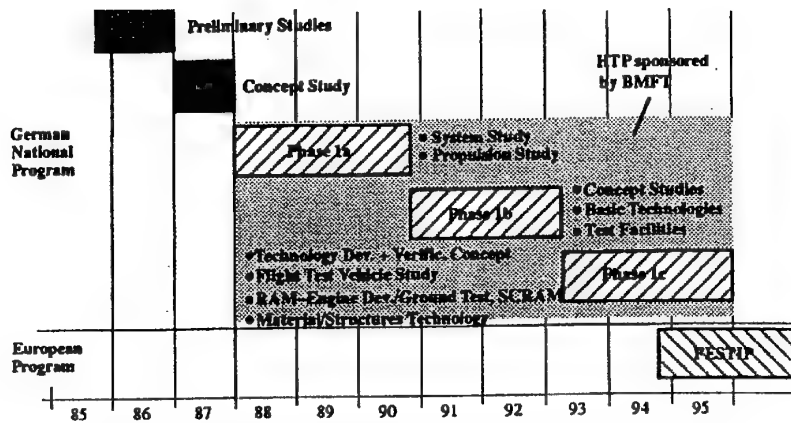
Fig. 2: Program schedule of German hypersonics activities
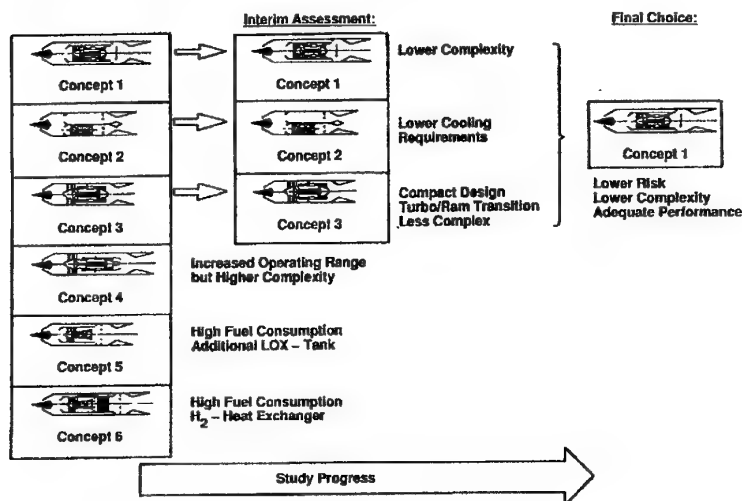
Fig. 3: Selection process of the Sänger reference propulsion concept
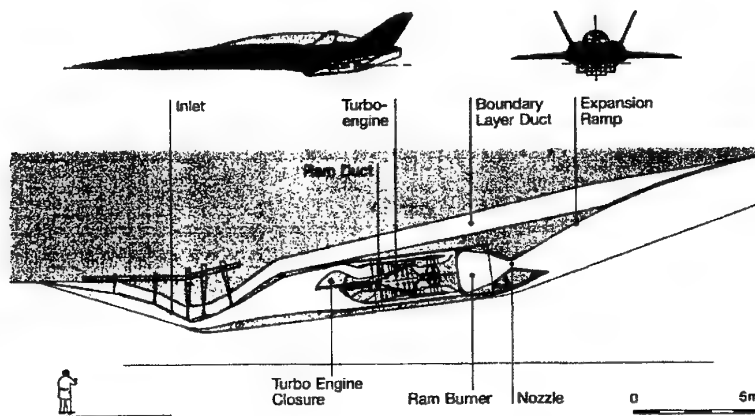
Fig. 4: Sänger propulsion reference concept
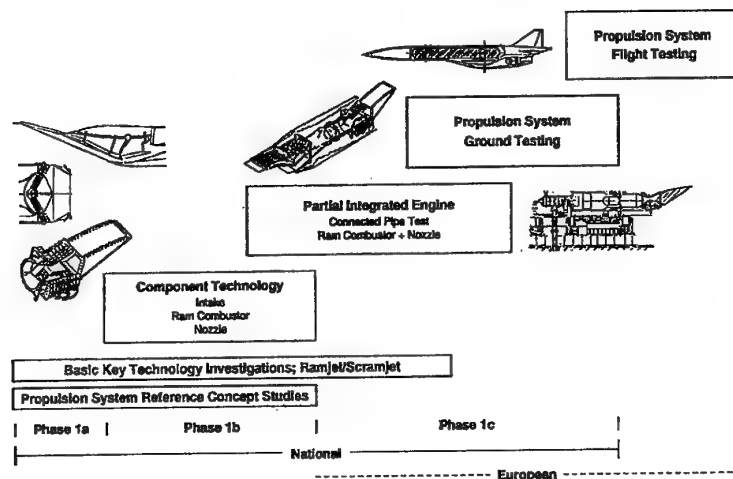
Fig. 5: Airbreathing propulsion technology and system development
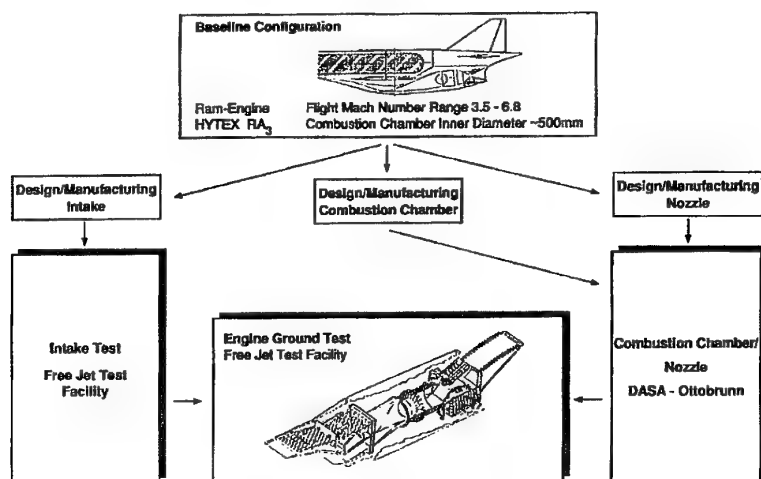
Fig. 6: Rationale of ground testing of the GHTP ramjet ground testing
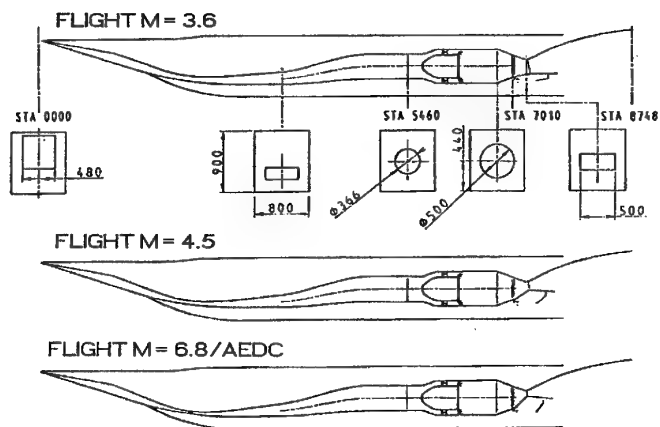
Fig. 7: Aerodynamic engine contours
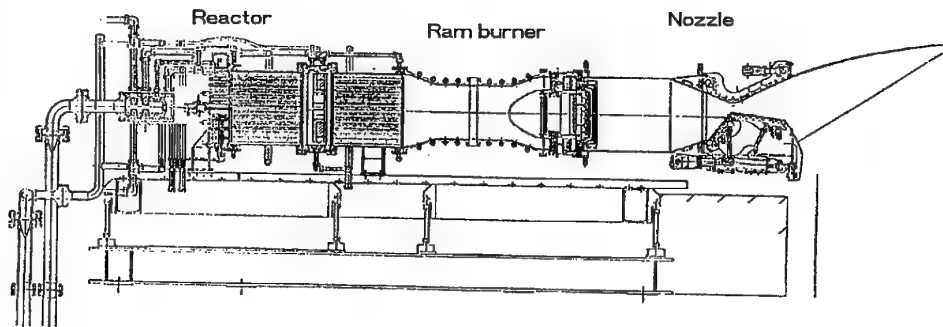
Fig. 8: Ottobrunn connected-pipe test facility
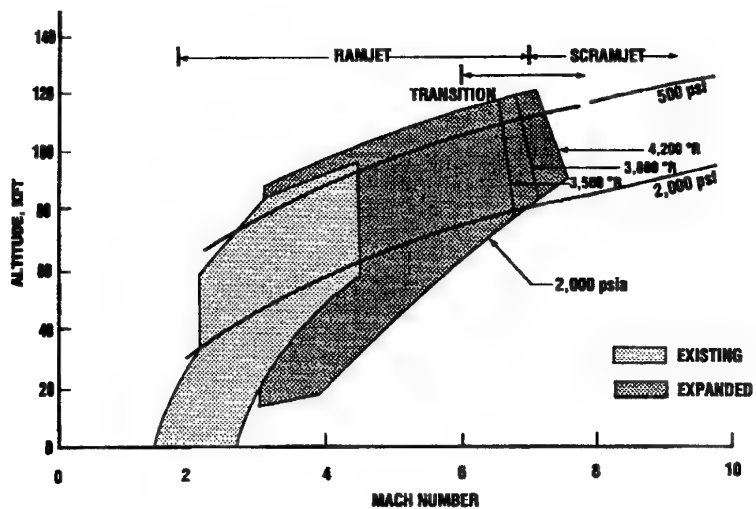
Fig. 9: Operational envelope of the APTU wind tunnel
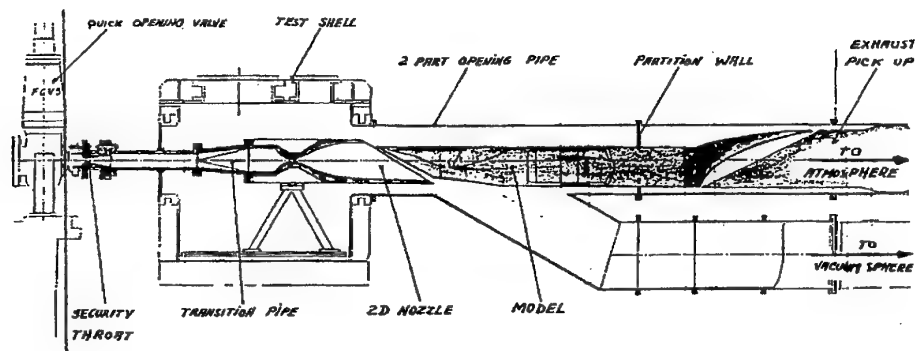
Fig. 10: Preliminary GHTP ramjet arrangement in S4M4
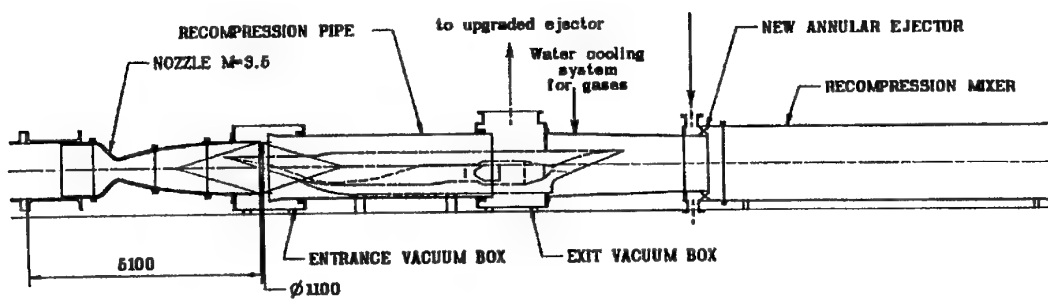
Fig.11: Optional arrangement of the GHTP engine in the Le Subdray test facitlity of Aerospatiale
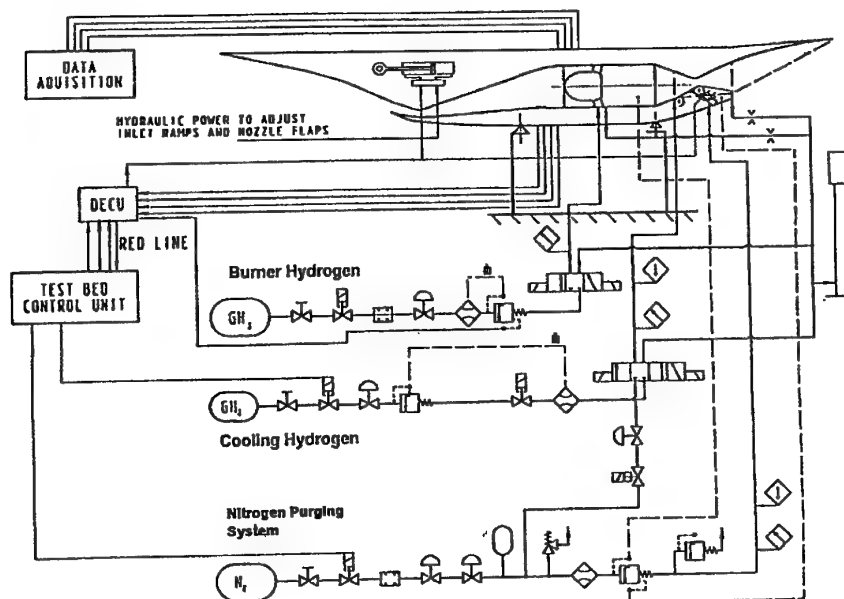
Fig. 12: Schematical lay-out of control and supply interfaces
of the GHTP engine for the APTU installation

HYPERSONIC FLIGHT EXPERIMENTATION--
STATUS AND SHORTFALLS

Dennis M. Bushnell
National Aeronautics and Space Administration
Langley Research Center
Hampton, Virginia 23681-0001

SUMMARY

For some 50 years, man has flown, very successfully, in and through the hypersonic flow regime up to Mach Number 35 and beyond with very few "surprises." In general, hypersonic vehicles have performed successfully with good-to-excellent comparisons between flight, ground facility extrapolations and computations being the norm. A consistent and glaring shortfall to date is in the boundary layer transition arena, due primarily to the dominance for flight vehicles of roughness induced transition where the roughness characteristics are extremely vehicle specific and dictated by either vehicle operational exigencies such as antennas, handling plugs, and field joints, etc. or characteristics of the thermal protection system. Emerging shortfalls for future systems which require research flight tests include transition and air-breathing propulsion-related technology for both cruise and space access. Specific flight test recommendations include "systems demonstrations" for various air-breathing propulsion options and efforts to correct a pervasive lack of adequate analysis of the existing, and very expensive to replicate, hypersonic flight data base.

1 INTRODUCTION

The applications of hypersonic technology are multitudinous and of increasing importance; e.g., space access, planetary exploration, missiles of various types (ballistic/maneuvering, interceptor, cruise, penetrator, anti-armor, boost-glide) "space planes" and, as a future possibility, in-atmosphere hypersonic air-breathing cruise and space access. Over the past 50 years, mankind has produced vehicles which have flown very successfully in and through the hypersonic regime beyond Mach 35 (lunar return) to planetary entry speeds for blunt and (to Mach 25) slender vehicles. As will be discussed herein, the vast preponderance of the experience base indicates that suitably scaled ground facility data, increasingly combined with modern computational codes can yield often surprisingly accurate predictions for flight. There have been occasional substantive disagreements between ground-based expectations and flight, but many of these are based upon fundamental limitations of ground facilities and/or computational capability or, in a few cases, lack of oversight and "homework."

The rationale for hypersonic flight experimentation devolves from essentially three requirements: (a) to obtain data not available from either ground facilities or "believable" computations; (b) "all-up" systems/functional testing (multidisciplinary); and/or (c) flight demonstration/validation,

e.g., "fly before buy"--essentially technology, systems and "product test" rationales. The downsides of hypersonic flight testing are obvious and serious--expensive (very) for essentially one (or a limited number) of "shots," with limited instrumentation suites and extensive development time, which necessarily also involves the booster and "mating" therewith as well as the experiment package.

The purpose of the current paper is to summarize the presently available hypersonic flight information vis-a-vis current and projected requirements and provide guidance and suggestions regarding further hypersonic flight experimentation. It should be noted that this paper is based, both in terms of breadth and depth, upon what countries and organizations are willing to discuss in "the open." The initial impetus and most of the developmental support for hypersonic vehicles has been based upon military requirements and much of the extant flight data, particularly that associated with RV development, is simply not yet available for detailed study and discussion in an "open forum." Further limitations on flight information are emerging from the reality of an increasingly (commercially) competitive launch vehicle market. The cost and time required to obtain hypersonic flight data [e.g., ref. 1] literally defines their uniqueness and hence the rationale for their "protection," for either military or commercial purposes. Therefore it should be understood that this paper cannot be as complete as might be desired, but the author has made an effort to include most of the serious issues which have arisen or are expected to arise in regard to hypersonic flight experimentation. The current paper is nominally limited to consideration of Mach numbers of 6 and above and to atmospheric flight tests, i.e., the numerous Ramjet flight experiments [e.g., refs. 2 and 3] and ballistic range data are specifically excluded. References 4 and 5 are suggested entrees into the subject.

2 (BRIEF) SYNOPSIS OF HYPERSONIC FACILITY/ COMPUTATIONAL SHORTFALLS

Facility and computational shortfalls constitute a major impetus for flight experimentation and therefore a brief review of these shortfalls provides a useful background for an understanding of where flight data "fits in."

Computational shortfalls exist at both the technological and system levels. Technology-wise, shortfalls in transition "prediction" and "modelling" of transitional and turbulent flows, particularly for high energy/chemically reacting flows are major critical issue(s). At the systems level, the computational capability in terms of raw computing power is

simply not available to work the complete interacting multidisciplinary systems issues to the depth required (combined aero/thermal/elasticity, propulsion, seals, controls, structures/materials, etc., etc.) In fact, many of the most serious hypersonic flight problems, which in some instances resulted in loss of all or part of the vehicle, were the result of very localized interference heating levels which were not "captured" by the present systems-level analyses and were often the result of "component interaction" [e.g., ref. 4, 6].

On the facility side the hypersonic shortfalls are quite well known [e.g., ref. 7]. The general shortfall involves the requisite combination of size, run time and dynamic pressure at enthalpy levels above Mach 8 for the "test and evaluation" (as opposed to research) function. Current and enhanced (e.g., with detonation drivers) impulse facilities [ref. 8] provide interesting high Mach number capability for research tasks but engineering-level/developmental combined load/combined discipline/"all-up" testing above Mach 8 is currently, of necessity, conducted via flight experiments.

Additional hypersonic facility shortfalls vis-a-vis flight include lack of "real" (reacting) gas quiet tunnels for transition research [see ref. 9 for a "possibility"] and the presence, in the Mach less than eight propulsion facilities, of heater-induced contaminants [e.g., ref. 10] and dynamic "disturbance fields" the influence of which can be to enhance air-breathing engine performance vis-a-vis flight.

3   EXISTING FLIGHT DATA BASE

Due to its relative availability and "completeness," the U.S. hypersonic flight data base will both serve as an example of what is available and provide the bulk of the specific examples discussed herein. In general, data from other countries are limited as to availability, due either to limitations on the information distribution or simple absence of such data/similar flight experiments and experience.

The existing flight data can be conveniently categorized into the following: (a) ballistic RV's ("reentry vehicles" -military reentry "delivery" vehicles); (b) maneuvering RV's [e.g., SWERVE--ref. 6] and other missiles; (c) lifting/winged bodies; (D) "research bodies" and aircraft (e.g., the X-15, refs. 6 and 11) and (e) blunt capsules. Data sets from such flight experiments normally consist of forces, moments, attitude, trajectory and surface pressure and heat transfer information. The latter are sometimes augmented by alternative transition detection approaches such as surface pressure fluctuations, electron density, wake observables or antenna admittance. Unusual flight measurements include surface skin friction and flow field pitot rakes (e.g., X-15), Langmuir probes and microwave reflectometer electron concentration data (e.g., RAM-C, refs. 12-14) and control effectiveness. The U.S. Lifting/Winged Body Hypersonic flight data base dates from 1964 (ASSET) [ref. 4] and includes PRIME (1967) [ref. 4] and the Shuttle (1980+) [e.g., ref. 15, 16] and its precursors (HL-10, M2-F2, X-24A) in the 1968 time frame. Corresponding non-U.S. lifting body flight programs include the Russian BOR (1980-84) [e.g., ref.

17] and Buran (1988) [e.g., ref. 18] and Japanese Hyflex (1996) [e.g., ref. 19] efforts.

The U.S. has flown several "research body" experiments including the aforementioned RAM B, C series to study radio blackout and alleviation approaches in the 60's to early 70's, Reentry F in '68 [e.g., refs. 6 and 20] for high Mach number transition research and the eminately successful X-15 airplane [e.g., refs. 6 and 11] in the 60's timeframe.

Blunt capsules have been the approach-of-choice for economical reentry bodies due to their minimization of total body heat load. Blunt capsule vehicles flown by the U.S. include the Mercury/Gemini/Apollo series (1960's to early 70's) along with project FIRE (a super-orbital speed Apollo radiative-heating load precursor--1965, e.g. refs. 21-24) and numerous planetary probes including Viking-Mars [refs. 25, 26], Pioneer-Venus [e.g., refs. 25, 27 and 28], and Galileo-Jupiter [refs. 29 and 30], etc. Non-U.S. blunt body tests/utilization include the Russian Soyuz (late 50's to present) and planetary entry bodies and the Japanese OREX [e.g., refs. 31-33] vehicle.

The RV (and intercepter) data base, both ballistic and maneuvering for U.S. and non-U.S. is essentially "unavailable" due to military classification. Bits and pieces of this data base have appeared in various open publications, but with insufficient detail to enable an independent analysis of the results. This "military" data base, most of which is sub-orbital in the M<20 range (IRBM and ICBM speeds) involves some variant of sphere-cone and is tremendous in quantity but generally somewhat sketchy in terms of research results, most of the flights being "developmental" in nature. Specific goals of these projects include/included feasibility/demonstration(s) and data acquisition for maneuverability/controls, sensors, detectability and counter detection, accuracy and reliability, including materials evaluations and boundary layer transition information--with, for example, some parametric variations in nose radius and cone angle/overall geometry.

In addition to the hypersonic flight data base cited thus far for the various categories, there is an additional/emerging category with a singular extant entry--Scramjet air-breathing propulsion as represented (at $M \approx 5.8$) by the Russian (axisymetric) hypersonic flying laboratory mounted on the SA-5 missile [refs. 34, 35].

4   THE TRANSITION PROBLEM

Historically, man has been singularly unsuccessfully in "predicting" transition on essentially everything ever flown hypersonically (or even supersonically). As an example case, wind tunnel data indicated that the flow over the X-15 aircraft at hypersonic conditions should be essentially laminar and flight experience indicated it to be almost wholly turbulent [e.g., 4, 6]. Analysis of these and other flight results strongly suggests that hypersonic flight transition location and behavior is dictated by "real vehicle" roughness and waviness and other surface "imperfections" (steps, joints, gaps, bleed/leakage,

fasteners, antenna rings, handling plugs, field joints, material fibers) etc. whose presence is the result of either service exigencies or thermal protection system design.

To further complicate the issue, such roughness dominated transition can be significantly altered, flight-to-flight on what is nominally the same vehicle, by alterations in atmospheric disturbances (especially particulates) and vehicle self/operationally induced morphological alterations such as occur on the U.S. Shuttle heat shield due to ice particle impingement from the tank dump line during liftoff or, for RV's, ablation. Examination of the Shuttle flight transition data base, for example, indicates flight-to-flight variations in entry transition Reynolds Number of a factor of 3 [e.g., ref. 36].

Unfortunately, boundary layer roughness-induced transition sensitivity embodies complex relationships parameterized by the fundamental linear disturbance mode[s] (T-S (1st or "2nd" mode), Gortler, crossflow) which can be overlain by other "bypasses" such as shock or longitudinal vortex interactions and contamination from adjacent turbulent regions and embedded (curved-shock induced) stream vorticity fields. There are a very few existing "smooth body" hypersonic flight transition data sets, notably Reentry F and a limited subset of the RV data base having Beryllium Frustra. These "smooth" data are "axisymetric," as opposed to 3-D, and indicate extraordinarily large transition Reynolds numbers in nominal agreement with the expectations of the appropriate eN and PSE computations [e.g., ref. 37]. Particular care should be taken in evaluating flight transition data as the type of sensor used tends to detect different portions of the transition process. Heat transfer distribution is the approach/measurement-of-choice for correlation with modern transition "prediction" methodologies.

5   EVALUATION OF THE EXISTING FLIGHT DATA BASE-- SHORTFALLS AND RECOMMENDATIONS

The limited (prescribed) length of the present paper precludes extensive remarks and detailed analysis of the wealth of information generated by some 40+ years of hypersonic flight experimentation. Instead a summary of such a study, conducted over several years, will be attempted.

The first, and most remarkable, conclusion from an examination of the flight literature is exceedingly favorable and reassuring-- we APPEAR to be in relatively "good shape." Such an evaluation might have been anticipated by an extremely important decision made many years ago (in the 70's)--the first U.S. Shuttle orbital flight was manned, i.e., there was sufficient confidence in the working knowledge of all of the various aspects of hypersonic flight (controls, aero, heating, etc., etc.) to commit to manned flight of an "unproven" vehicle. This with a technology base which is now some 20 years old. More recently confidence in the computational tools has progressed to where the Pegasus launch vehicle was designed and flown on the basis of computation alone, sans wind tunnel data [e.g., refs. 38, 39].

In fact over the years and in spite of continued technology advances the published experience has been virtually the same-- good agreement between flight experience and (scaled) ground facility data and computation. The few substantive disagreements have become "cause celebre" due partially to their singular nature and have been in many cases "studied in extremis" and "solved" and "resolved" many times. This discussion obviously does not apply to in-atmospheric hypersonic (M>6) air-breathing for which we have an almost complete dearth of flight data at this point. The one set of existing scramjet data went to Mach 5.8 only with a very limited amount of supersonic combustion [refs. 34, 35]. For many reasons, primarily connected with facility shortfalls, the extreme heating environment, and the sensitivity of net thrust level at high Mach number the air-breathing flight experience vis-a-vis computation and ground facility data may not be as favorable as experienced thus far on previous hypersonic flight systems.

Herewith are some typical comments gleaned from the hypersonic flight experiment literature:

* "Good agreement with theory and flight data" (base pressure, blunted 9° sphere cones, laminar flow, M∞ to 20) [ref. 40]

* "The CFD code performed remarkably well in predicting the general flow field around the Pegasus vehicle" [ref. 39]

* "The computed aerodynamics for the complete vehicles are in good agreement with the flight data considering the uncertainities in both data sets" [Space Shuttle, ref. 49]

* "Prediction of Shuttle heating rates were quite accurate"

* "The preflight test technique gives quite satisfactory results" (Russian Buran, longitudinal aero moment coefficient) [ref. 48]

* "Extensive flight testing of a nose cone (to M ≈ 15) showed that prediction of aerodynamic coefficients based on theory and data from ground facilities was correct" [ref. 46]

* "Flight-derived drag coefficients agreed within 2 percent of ground test estimates obtained from ballistic range tests and wind tunnel tests for Reynolds Number greater than 10^5 (Viking,Martian atmosphere) [ref. 26]

* "Excellent correlation between flight and wind tunnel results for the X-15"

* "Numerical results favorably predict the behavior of temperature increase of each TPS material during OREX reentry" [ref. 45]

* "The collection of codes demonstrated good existing capabilities and future potential for predicting the aerothermal environment about flight vehicles" [ref. 44]

* "At the angles-of-attack so far tested in the Orbiter program, the lift-to-drag ratio for supersonic/hypersonic flight

conditions is well predicted" [Space Shuttle, ref. 47]

• "Angular motion histories, synthesized by the use of conventional wind tunnel aerodynamics data, showed good agreement with the large amplitude nearly planar motions observed in free flight" (Apollo) [ref. 41]

• "The aerodynamic characteristic of the command module as defined by the Apollo wind tunnel program correlate well with flight up to Mach 10" (Apollo) [ref. 42]

• "Excellent trim agreement Mach 2 to 10 despite high angles of attack" (Shuttle) [ref. 43]

There are several, almost "infamous," extant discrepancies between ground-based expectations and flight. Among these is the U.S. Space Shuttle entry trim discrepancy above Mach Number order of 10 where gas chemistry effects upon effectively blunt (high angle of attack lifting/winged) body flow fields become increasingly important. The effect was large and it has since been concluded, by several groups, that the problem was in fact due to gas chemistry effects and is computable, i.e., "perfect gas" wind tunnel data should not be used where it does not apply (where reacting gas effects are strong). [e.g., refs. 18, 48, 49] Other reasons for observed flight-to-ground discrepancies include inadequate ground facility capability in terms of either test time, enthalpy level, size or dynamic pressure on the one hand (for the continuum case) and lack of adequate rarefied gas testing capability for high altitudes. An additional major rationale has already been noted--lack of careful attention to details and levels associated with very localized heating rates--the infamous cases here include the X-15 HRE dummy pylon "burnthrough" [ref. 6] and several other localized heating problems on the X-15 and Shuttle lee surface (also, by extension, the Challenger Shuttle disaster). The following constitutes some "top level" conclusions from the order of 40 plus years of hypersonic flight experimentation:

1. Overall, except for Scramjet air-breathing propulsion, which has not yet been proven in flight and therefore the associated shortfalls are, at this point, unknown, existing ground simulation and computational capability has, for quite a long time, been "satisfactory." Man has flown vehicles in and through the hypersonic regime to Mach 35+ in both Earth and planetary atmospheres with few surprises or shortfalls.

2. The few relatively major shortfalls were usually related to very detailed, but critical, design issues associated with localized interference heat transfer and/or related transition.

3. A relatively large data base is available, much of it dating from the 60's. This data base has, to far too major an extent, never been analyzed/scrutinized with "modern" computational capability. Admittedly the flight data are "incomplete" in the sense of constituting a computational technique "validation data set," but flight data uniquely constitute the "real thing" and the only method of truly evaluating the efficacy and accuracy of current predictive technology [ref. 50].

NASA is currently involved in such a partial re-evaluation, centered upon what appears to be the "best documented" hypersonic flight experiment--the X-15 (290 papers etc.).

6 SYNOPSIS OF ONGOING/PROJECTED FLIGHT EXPERIMENTS

The major known/projected hypersonic flight experiments very appropriately concern the area of current essentially absolute flight ignorance--Scramjet air-breathing propulsion [e.g., refs. 51-55]. At least three such experiments appear, at this juncture, to be "real" in the sense of being ongoing projects. The first of these in terms of flight schedule is a combined Russian-U.S. effort to fly, at Mach 6.5, a slightly modified version of the axisymetric "flying laboratory" developed by TSIAM in Russia and previously flown up to the order of Mach 5.8 [ref. 56, 57]. The specific purposes of this test are twofold--to obtain flight data with extensive supersonic combustion and "calibrate"/investigate the influences of various propulsion facility "contaminants" via comparison with "real air" flight data. A "full scale" version of the flight configuration will be tested in the U.S. 8-Foot HTT Tunnel at Langley. The other air-breathing flight tests are 2 years or more in the future and involve higher Mach Number and airframe integrated Scramjet experiments--the NASA "Hyper-X" effort (a "Mach 8+ class" airframe integrated experiment) and a somewhat larger scale combined Russian French Mach 10 class effort termed "IGLA," which is also airframe integrated [refs. 58, 59]. The prime fuel in all of these experiments is hydrogen with the prime application being space access. There is also considerable interest in (storable) endothermic hydrocarbon fuels, with obvious military applications.

Another quite near term flight experiment is termed the PHYSX project and is a combined NASA-Dryden/Langley/Ames effort to obtain crossflow dominated boundary layer transition in the Mach 6 to 8 range on a "glove" installed on the wing of the "Pegasus" first stage [ref. 60]. The purpose of this experiment is to obtain transition data applicable to the assurance of transition delay on airframe-integrated air-breather forebodies for performance enhancement (enhanced net thrust/installed Isp). These flight transition data will also be used to calibrate/validate a Mach 8 "quiet tunnel" recently constructed at NASA-Langley.

7 REFERENCES

1. Eide, D. G., Wurster, K. E., Helms, V. T., and Ashby, G. C., "Anatomy of an Entry Vehicle Experiment," AIAA/SETP/SFTE/SAE/ITEA/IEEE 1st Flight Testing Conference, Las Vegas, Nevada, November 11-13, 1981.

2. AGARD Conference Proceedings No. 307, Ramjets and Ramrockets for Military Applications, papers presented at the Propulsion and Energetics 58th Symposium, held at Church House, London, UK, October 26-29, 1981.

3. Waltrup, P. J., "Hypersonic Airbreathing Propulsion: Evolution and Opportunities," AGARD Conference Proceedings No. 428, Aerodynamics of Hypersonic Lifting Vehicles, papers presented and discussions held at the Fluid Dynamics Panel Symposium in Bristol, United Kingdom, April 6-8, 1987.

4. Hallion, Richard P., ed., The Hypersonic Revolution: Eight Case Studies in the History of Hypersoni Technology, Volume 1, "From Max Valier to Project Prime, 1924-1967;" Volume 2, "From Scramjet to the National Aero-Space Plane, 1964-1986," 1987.

5. Smith, V. K., Matthews, R. K., and Maus, J. R., "Hypersonic Flight Testing," Final Report for Period July 1992-July 1993, AEDC TR-94-7, August 1994.

6. Lliff, Kenneth W., and Shafer, Mary F., "A Comparison of Hypersonic Flight and Prediction Results," AIAA-93-0311, 31st Aerospace Sciences Meeting and Exhibit, Reno, Nevada, January 11-14, 1993.

7. Laster, Marion L., and Bushnell, Dennis M., "A National Study for Hypersonic Facility Development," AIAA-94-2473, 18th AIAA Aerospace Ground Testing Conference, Colorado Springs, CO, June 20-23, 1994.

8. Bakos, R. J., and Erdos, J. I., "Options for Enhancement of the Performance of Shock-Expansion Tubes and Tunnels," AIAA-95-0799, 33rd Aerospace Sciences Meeting and Exhibt, Reno, NV, January 9-12, 1995.

9. Erdos, J. I., and Bakos, R., "Prospects for a Quiet Hypervelocity Shock-Expansion Tunnel," AIAA-94-2500, 18th AIAA Aerospace Ground Testing Conference, Colorado Springs, CO, June 20-23, 1994.

10. Srinivasan, Shivakumar, "Influence of Test-Gas Vitiation on Mixing and Combustion at Mach 7 Flight Conditions," AIAA-94-2816,30th AIAA/ASME/SAE/ASEE Joint Propulsion Conference, Indianapolis, IN, June 27-29, 1994.

11. Dana, W., "The X-15 Airplane--Lessons Learned," AIAA-93-0309,31st Aerospace Sciences Meeting and Exhibit, Reno, NV, January 11-14, 1993.

12. Akey, N. D., and Cross, A. E., "Radio Blackout Alleviation and Plasma Diagnostic Results from a 25,000 Foot Per Second Blunt-Body Reentry," NASA TN D-5615, February 1970.

13. Grantham, W. L., "Flight Results of 25,000 Foot Per Second Reentry Experiment Using Microwave Reflectometers to Measure Plasma Electron Density and Standoff Distance," NASA TN D-6062, December 1970.

14. Jones, W. L., Jr., and Cross, A. E., "Electrostatic Probe Measurements of Plasma Parameters for Two Reentry Flight Experiments at 25,000 Feet Per Second," NASA TN D-6617, April 1972.

15. Lliff, Kenneth, and Shafer, Mary F., "Space Shuttle Hypersonic Flight Research and the Comparison to Ground Test Results (Invited)," AIAA-92-3988, 17th Aerospace Ground Testing Conference, Nashville, TN, July 6-8, 1992.

16. Holloway, Paul F., and Throckmorton, David A., "Shuttle Orbiter Experiments--Use of an Operational Vehicle for Advancement and Validation of Space Systems Design Technologies," AGARD Conference Proceedings 561, Space Systems Design and Development Testing, paper presented at the AGARD Flight Vehicle Integration Panel Symposium, held in Cannes, France, October 3-6, 1994.

17. Gorelov, V. A., Gladyshev, M. K., Kireev, A. Yu, Korolev, A. S., Nikol'sky, V. S., Byzov, V. N., Fedosov, B. M., "Ionization Near Hypersonic Vehicles: The Experience of Numerical, Laboratory, and Flight Investigations," 26th AIAA Plasmadynamics and Lasers Conference, San Diego, CA, June 19-22, 1995.

18. Neiland, V. Ya., "The Convergence of the Orbiter 'Buran' Flight Test and Preflight Study Results, and the Choice of a Strategy to Develop a Second Generation Orbiter," AIAA First National Aero-Space Plane Conference, Dayton, Ohio, July 20-21, 1989.

19. Shirouzu, M., and Watanabe, S., "On the Hypersonic Flight Experiment (HYFLEX) for the Development of HOPE," AIAA-93-5080 AIAA/DGLR Fifth International Aerospace Planes and Hypersonics Technologies Conference, Munich, Germany, November 30-December 3, 1993.

20. Wright, Robert L. and Zoby, Ernest W., "Flight Boundary Layer Transition Measurements on a Slender Cone at Mach 20," AIAA-77-719, June 1977.

21. Lewis, J. H., Jr., and Scallion, W. I., "Body Motion and Angles of Attack during Project Fire Flight II Reentry," NASA TN-D-4183, October 1967.

22. Lewis, J. H., Jr., and Scallion, W. I., "Flight Parameters and Vehicle Performance for Fire Flight 1, Launched April 14, 1964," NASA TN-D-2996, September 1965.

23. Lewis, J. H., Jr., and Scallion, W. I., "Flight Parameters and Vehicle Performance for Project Fire Flight II, Launched May 22, 1965," NASA TN-D-3569, August 1966.

24. Dingeldein, R. C., "Flight Measurements of Reentry Heating at Hyperbolic Velocity/Project Fire," NASA TM-X-1053, October 1964.

25. Seiff, Alvin and San Jose State University Foundation, "Entry-Probe Studies of the Atmospheres of Earth, Mars, and Venus: A Review," AIAA-90-0765, 28th Aerospace Sciences Meeting, Reno, Nevada, January 8-11, 1990.

26. Blanchard, Robert C., and Walberg, Gerald D., "Determination of the Hypersonic-Continuum/Rarefield-Flow Drag Coefficient of the Viking Lander Capsule 1 Aeroshell from Flight Data," NASA Technical Paper 1793, 1980.

27. Pitts, W. C., and Wakefield, R. M., "Performance of Entry Heat Shields on Pioneer Venus Probes," Journal of Geophysical Research, Vol. 85, No. A13, pages 8333-8337, December 30, 1980.

28. Wakefield, R. M., and Pitts, W. C., "Analysis of the Heat-Shield Experiment on the Pioneer-Venus Entry Probes," AIAA-80-1494, AIAA 15th Thermophysics Conference, Snowmass, Colorado, July 14-16, 1980.

29. Vojvodich, N. S., Drean, R. J., Schaupp, R. W., and Farless, D. L., "Galileo Atmospheric Entry Probe Mission Description," AIAA-83-0100, AIAA 21st Aerospace Sciences Meeting, Reno, Nevada, January 10-13, 1983.

30. Milos, Frank S., "Galileo Probe Heat Shield Ablation Experiment," AIAA 96-1823, 31st AIAA Thermophysics Conference, New Orleans, LA, June 17-20, 1996.

31. Akimoto, Toshio, Ito, Tetsuichi, Yamamoto, Masataka, Bando, Toshio, and Yasutoshi, Inoue, "Orbital Reentry Experiment (OREX)-First Step of Space Return Flight Demonstrations in Japan," 45th Congress of the International Astronautical Federation, Jerusalem, Israel, Octover 9-14, 1994.

32. Gupta, R. N., Moss, J. N., and Price, J. M., "Assessment of Thermochemical Nonequilibrium and Slip Effects for Orbital Reentry Experiment (OREX)," AIAA-96-1859, 31st AIAA Thermophysics Conference, New Orleans, LA, June 17-20, 1996.

33. Inouye, Yasutoshi, "OREX Flight--Quick Report and Lessons Learned," esa sp-367, Second European Symposium on Aerothermodynamics for Space Vehicles Proceedings, ESTEC, Noordwijk, the Netherlands, November 21-25, 1994.

34. AGARD-LS-194, Research and Development of Ram/Scramjets and Turbojets in Russia, December 1993.

35. Roudakov, A. S., Schickhman, Y., Semenov, V., Novelli, Ph., Fourt, O., "Flight Testing an Axisymmetric Scramjet-- Russian Recent Advances," IAF-93-S.4.485, 44th Congress of the International Astronautical Federation, Graz, Austria, October 16-22, 1993.

36. Bouslog, S. A., An, M. Y., Hartmann, L. N., and Derry, S. M., "Review of Boundary Layer Transition Flight Data on the Space Shuttle Orbiter," AIAA-91-0741, 29th Aerospace Sciences Meeting, Reno, Nevada, January 7-10, 1991.

37. Malik, M., Zang, T., and Bushnell, D., "Boundary Layer Transition in Hypersonic Flows," AIAA-90-5232, AIAA Second International Aerospace Planes Conference, Orlando, FL, October 29-31, 1990.

38. Curry, Robert E., Mendenhall, Michael R., and Moulton, Bryan, "In-Flight Evaluation of Aerodynamic Predictions of an Air-Launched Space Booster," NASA TM-104246, 1992.

39. Fricker, Darren, Mendoza, John, and Catton, Ivan, "A Summary of the Computational Fluid Dynamics Analysis of the Hypersonic Flights of Pegasus," AIAA 92-4059, 1992 National Heat Transfer Conference, San Diego, CA, August 9-12, 1992.

40. Bulmer, Bruce M., "Correlation of Reentry Base Pressure in Laminar Hypersonic Flow," SLA-74-0169, August 1974.

41. Malcom, Gerald N., and Kirk, Donn B., "Comparison of Free-Flight and Conventional Wind Tunnel Stability Tests for Apollo Command Module and Abort Configurations," NASA TM X-1137, September 1965.

42. Crowder, R. S., and Moote, J. D., "Apollo Entry Aerodynamics," AIAA 5th Annual Meeting and Technical Display, Philadelphia, Pennsylvania, October 21-24, 1968, AIAA Paper No. 68-1008.

43. Young, James C., "Aerodynamic Comparisons of STS-1 Space Shuttle Entry Vehicle," Miniworkshop on Wind-Tunnel/Flight Correlation, 1981, NASA Conference Publication 2225.

44. Sutton, Kenneth, Zoby, Ernest V., and Hamilton, H. Harris, "Overview of CFD Methods and Comparisons with Flight Aerothermal Data," AGARD Conference Proceedings No. 437,Validation of Computational Fluid Dynamics.

45. Yamamoto, Yukimitsu, and Yoshioka, Minako, "CFD and FEM Coupling Analysis of OREX Aerothermodynamic Flight Data," AIAA 95-2087, 29th AIAA Thermophysics Conference, San Diego, CA, June 19-22, 1995.

46. Ledu, J., Pollak, C., "Flight Testing Results on a Hypersonic Reentry Nose Cone," J. Spacecraft, Vol. 6, No. 9, September 1969.

47. Williams, John, "Technical Evaluation Report on the Flight Mechanics Panel Symposium on Ground/Flight Test Techniques and Correlation," AGARD Advisory Report No. 191.

48. Neyland, V. Ya., "Air Dissociation Effects on Aerodynamic Characteristics of an Aerospace Plane," Journal of Aircraft, Vol. 30, No. 4, July-August 1993.

49. Weilmuenster, K. James, Gnoffo, Peter A., and Greene, Francis A., "Navier-Stokes Simulations of Orbiter Aerodynamic Characteristics Including Pitch Trim and Bodyflap," Journal of Spacecraft and Rockets, Vol. 31, No. 3, May-June 1994.

50. Muylaert, J., "Extrapolation to Flight," AGARD Advisory Report 319, Hypersonic Experimental and Computational Capability, Improvement and Validation, May 1995.

51. Hicks, John W., "Flight Testing of Airbreathing Hypersonic Vehicles," NASA Technical Memorandum 4524, October 1993.

52. Falempin, F., Forrat, M., Baldeck, J., Hermant, E., "Flight Test Vehicles: A Mandatory Step in Scramjet Development," AIAA-92-5052, AIAA Fourth International Aerospace Planes Conference, Orlando, FL, December 1-4, 1992.

53. Sacher, Peter W., "Flight Testing Vehicles for Verification and Validation of Hypersonics Technology," AGARD Conference Proceedings 561, Space Systems Design and Development Testing, March 1995.

54. Heitmeir, F. J., and Sacher, P. W., "Ground- and Flight-Testing of an Airbreathing Propulsion System for Hypersonic Speed," 45th Congress of the International Astronautical Federation, Jerusalem, Israel, October 9-14, 1994.

55. Davis, J. A., "System Study of the Role of Flight Testing in Hypersonic Scramjet Development," AIAA 95-2716, 31st AIAA/ASME/SAE/ASEE Joint Propulsion Conference and Exhibit, San Diego, CA, July 10-12, 1995.

56. McClinton, C., Roudakov, A., Semenov, V., and Kopehenov, V.,"Comparative Flow Path Analysis and Design Assessment of an Axisymmetric Hydrogen Fueled Scramjet Flight Test Engine at a Mach Number of 6.5," AIAA 96-4571, 7th International Space Planes and Hypersonics Systems and Technology Conference, Norfolk, VA, November 18-22, 1996.

57. Roudakov, Alexander S., Semenov, Vyacheslav L., Kopchenov, Valeriy I., Hicks, John W.: "Future Flight Test Plans of an Axisymmetric Hydrogen-Fueled Scramjet Engine on the Hypersonic Flying Laboratory," 7th International Space Planes and Hypersonics Systems and Technology Conference, Norfolk VA, November 18-22, 1996.

58. Anfimov, N., "The Principle Directions of Russian Activities in Research for Conception of Future Reusable

Space Transportation System [The Program "Oryol" (Eagle)]," AIAA-95-6003, AIAA Sixth International Aerospace Planes and Hypersonics Technologies Conference, Chattanooga, TN, April 3-7, 1995.

59. Lanshin, A., and Sosounov, V., "Russian Space Agency Research and Development Program for Aerospace Plane Combined Propulsion Systems ("OREL-2-1" R&D)," AIAA-95-6149, AIAA Sixth International Aerospace Planes and Hypersonics Technologies Conference, Chattanooga, TN, April 3-7, 1995.

60. Bertelrud, A., Graves, S., Young, R., and Anderson, B., "Documentation of Crossflow Transition in Flight at Hypersonic Mach Numbers," AIAA-95-6060, AIAA Sixth InternationalAerospace Planes and Hypersonics Technologies Conference,Chattanooga, TN, April 3-7, 1995.

NASA AND ESA GROUND FACILITY SIMULATIONS OF SHUTTLE ORBITER AEROTHERMODYNAMICS

J.Muylaert - ESA-ESTEC, Postbus 299, 2200 AG Noordwijk, The Netherlands

P.Rostand, M.Rapuc - Dassault Aviation, 92552 St. Cloud Cedex 300, France

J.Paulson, G.Brauckmann, D.Trockmorton - NASA Langley, USA

R.Steijl - TU Delft, The Netherlands

ABSTRACT

The paper reviews a combined numerical and experimental activity on the Shuttle Orbiter, first performed at NASA Langley within the OEX workshop and subsequently at ESA, as part of the AGARD FDP WG 18 activities. The study at Langley was undertaken to resolve the pitch up anomaly observed during the entry of the first flight of the Shuttle Orbiter. The facilities used at NASA Langley were the 15-in. Mach 6, the 20-in, Mach 6, the 31-in. Mach 10 and the 20-in. Mach 6 CF4 facility. The paper focuses on the high Mach, high altitude portion of the first entry of the Shuttle where the vehicle exhibited a nose-up pitching moment relative to pre-flight prediction of $(\Delta C_m) = 0.03$. In order to study the relative contribution of compressibility, viscous interaction and real gas effects on basic body pitching moment and flap efficiency, an experimental study was undertaken to examine the effects of Mach, Reynolds and ratio of specific heats at NASA. At high Mach, a decrease of gamma occurs in the shock layer due to high temperature effects. The primary effect of this lower specific heat ratio is a decrease of the pressure on the aft windward expansion surface of the Orbiter causing the nose-up pitching moment. Testing in the heavy gas, Mach 6 CF4 tunnel, gave a good simulation of high temperature effects.

The facilities used at ESA were the 1m Mach 10 at ONERA Modane, the 0.7 m hot shot F4 at ONERA Le Fauga and the 0.88 m piston driven shock tube HEG at DLR Goettingen. Encouraging good force measurements were obtained in the F4 facility on the Orbiter configuration. Testing of the same model in the perfect gas Mach 10 S4 Modane facility was performed so as to have "reference" conditions. Comparing F4 with S4 one finds the "pitch up" on the Orbiter due to real gas effects. In addition, pressure measurements, performed on the aft portion of the windward side of the Halis configuration in HEG and F4, confirm that the pitch up is mainly attributed to a reduction of pressure due to a local decrease in gamma.

1 Introduction

During the high Mach number, high altitude segment of the first entry of the Space Shuttle Orbiter, with laminar, continuum flow over the windward surface, the vehicle exhibited a nose-up pitching-moment increment (ΔC_m) relative to pre-flight prediction of approximately 0.03. This caused the body-flap to deflect twice the amount thought necessary to achieve trimmed flight. This so-called "pitch-up anomaly" has been investigated over the years with explanations ranging from compressibility, to viscous, to real-gas (high temperature) effects on basic-body pitching moment and/or body-flap effectiveness. Compressibility and viscous effects, while affecting basic aerodynamics, also govern the behavior of flow separation ahead of deflected control surfaces. Low values of Reynolds number, such as occur in flight at high altitudes, may cause the flap to lose effectiveness by submerging it in a thick boundary layer such that the flap does not encounter the inviscid flow. In addition, high viscous shear of the cross flow in the nose region has been postulated as the mechanism to induce nose-up pitching moments. High-temperature effects occur when air heats as it crosses the strong bow shock of the vehicle in hypersonic flight. The main consequences as far as aerodynamics are concerned are an increase in the shock density ratio, hence decrease in shock detachment distance and altering of the inviscid flowfield, and a lowering of the flowfield specific heat ratio.

In order to clarify and substantiate the causes of the flight-to-preflight discrepancies, a systematic study was undertaken to examine the effects of Mach number, Reynolds number, and real gas effects on basic-body pitching moment and body-flap effectiveness.

At NASA, two approaches were used by Brauckmann et all (ref 1). First, conventional hypersonic wind tunnels, all with instrumentation upgrades and most with new nozzles that provide better flow uniformity, were used to examine the effects of Mach number and Reynolds number on configuration aerodynamics and control effectiveness. Effects due to

specific-heat ratio were examined in the 20-Inch Mach 6 CF_4 tunnel, where testing in a heavy gas simulates the higher flight density ratio and lower specific heat ratio characteristic of a real gas. Second, a full Navier-Stokes computer code utilizing finite-rate chemistry was used to predict the flow field over the entire orbiter windward geometry, including the deflected body-flap, for both wind tunnel and flight conditions. Comparisons are made between the present experimental results, computational predictions, the preflight aerodynamic data book released in 1980 and aerodynamic coefficients derived from the flight of STS-1. The results of this study are expected to help define the optimum approach for the design of the next generation space transportation system.

At ESA, the orbiter model was used for a study by Perrier et all (ref 2) on hypersonic windtunnel to flight extrapolation. The objective of the study presented here is to investigate the extent to which the use of high enthalpy facilities can contribute to the validation of such a ground to flight extrapolation, and more specifically to the validation of "real gas effects". Such high enthalpy facilities, where both forces and heat fluxes can be measured, have been developed recently in Europe, and preliminary encouraging results have been obtained on simple shapes such as Electre, which is a blunt cone and hyperboloid flare (Ref 3). A methodology to validate the ground to flight extrapolation of re-entry aircraft aerodynamics is proposed and implemented in the case of the Orbiter, based on the utilisation of European high enthalpy facilities, and theoretical rebuilding of the flow fields in these facilities and in flight . It is shown that uncertainties on the real gas effect on aerodynamic forces, and in particular on pitching moment, could be reduced through this procedure.

2   Experimental methods

2.1   NASA Facilities

Three models were used for this study. Two were scale models of the full Shuttle Orbiter configuration, with scales of .004 and .0075. Body-flap deflections tested were 0.0, 12.5, and 16.3 deg for the smaller model and 0.0, 16.0, and 20.0 deg for the larger model. The third model was a .0075 scale modified Orbiter geometry, refered to as Halis, which accurately represented the windward surface, including the body-flap, but used elliptical cross-sections to create the upper surface. All models were numerically machined from stainless steel. A verification check of the aerolines was performed prior to testing, and both larger models represented the shuttle windward surface aerolines within +/− .003 in.

Five blow-down hypersonic wind tunnels were used in this study . They were the 15-Inch Mach 6 Hi-Temperature Air Tunnel, 20-Inch Mach 6 Tunnel, 31-Inch Mach 10 Tunnel, 22-Inch Mach 20 Helium Tunnel, and the 20-Inch Mach 6 CF_4 Tunnel. (See table 2)

All data are presented about a moment reference center of 65 % of reference body length.

2.2   European Facilities

In Europe, 2 Orbiter models and 3 hypersonic facilities were used for the present study as seen from table 2. The 3 facilities are the ONERA S4 , The ONERA F4 and the DLR HEG.

The Onera S4 facility is a Mach=10 perfect gas blow down tunnel. It is considered as the European reference perfect gas mach 10 facility. It was decided to run it at its lowest Re number corresponding to a reservoir pressure of 25 Bar so as to avoid boundary layer transition in separated shear layers in front of deflected flaps.

The Onera F4 hot shot , is a high enthalpy facility which enables force and moment measurements. The F4 facility covers enthalpy levels corresponding to the dissociation of oxygen. Typical reservoir conditions are 500 bar with 250 reduced enthalpy (Hi/RTo, R= 288.2 J/Kg/K for air, To = 273.15 K). The lowest total conditions are about 200 Bar and Hi/RTo = 30. High pressure and low enthalpy levels can also be obtained such as Pi = 750 Bar and Hi/RTo = 30. The test gas used is synthetic air or N2.

The DLR HEG free piston driven shock tunnel allows both oxygen and nitrogen dissociation and presents higher enthalpy levels and Reynolds numbers than F4. Typical reservoir pressure conditions are 1000 Bar combined with a reservoir enthalpy which can vary between 10 MJ/Kg up to 25 MJ/Kg.

3   Computational Methods

At NASA , the LAURA (Langley Aerothermodynamic Upwind Relaxation Algorithm) code was used in this study to solve the thin-layer Navier-Stokes equations. The inviscid first-order flux is constructed using Roe's flux-difference-splitting and Harten's entropy fix with second-order corrections based on Yee's symmetric total variation diminishing scheme. A seven species (N, O, N_2, O_2, NO, NO^+, and e^-) chemical reaction model is used for the non-equilibrium computations. The usual no-slip boundary conditions for viscous flow is applied at the wall while freestream conditions are set at points on the outer boundary of the computational domain. The

exit plane is set such that the inviscid outer flow is supersonic. The computations presented account for a variable wall temperature. These values are based on the radiation equilibrium temperature at the wall, and were determined from computed heating rates. A catalytic wall boundary condition was used based on Scott's recombination rates for nitrogen and Zoby's rates for oxygen. A multi-block solution strategy is applied in two stages. The first stage may be regarded as a space marching solution, like the Parabolized Navier-Stokes (PNS) methods, except three-dimensional data blocks are employed rather than two-dimensional data planes. The second stage is a conventional, global relaxation which uses the first stage solution as an initial condition. The computational results presented herein are discussed further, and with more detail about the code and solution procedure in papers by Weilmuenster (ref 4).

In Europe, Dassault Aviation used an Euler and boundary layer approach rather than a Navier Stokes approach, in order to be able to perform a large number of simulations at a reasonable cost.

The Euler code used is the EUGENI code of Dassault Aviation, which solves the compressible fluid equations discretized on an unstructured mesh, for a perfect gas or a reacting mixture, either in equilibrium or in chemical or thermochemical non-equilibrium. Implicit time integration to the steady state is used; the implicitation is done by linearising the steady operator; convergence requires 100 to 500 iterations, depending on cases and accuracy requirements. The solver is based on a Galerkin finite volume method, in which inviscid fluxes are upwinded using a generalized version of Osher's Riemann solver. Second order accuracy is achieved using the MUSCL method, extended to unstructured meshes.

The finite rate dissociation of air is modeled with 5 species (O2, O, N2, N and NO) and 34 reactions. The rates are taken from Park's model. The finite rate thermal relaxation is modeled with two vibrational temperatures and one translational and rotational temperature.

The boundary layer code used is the COUL code of Dassault Aviation, which is a package containing different boundary layer solvers, ranging in complexity from integral method based codes to finite difference defect correction based ones, and able to take into account finite rate chemistry. The solver used here is the finite difference defect correction one, with finite rate chemistry and second order matching with the inviscid flow field (for velocity, temperature and concentrations).

4 NASA Results and Discussion

4.1 Ideal Gas Results at Mach 6 and 10 in Air

For the low-to-mid hypersonic Mach numbers the flight-to-preflight discrepancy is small. Post-flight analyses of heating data indicate that the orbiter windward surface boundary layer is everywhere turbulent. Results at Mach 6 are presented showing the effect of Reynolds number on C_N and C_m for the baseline (zero control surface deflections) in Figures 1 and 2, respectively. The data show only a slight effect of Reynolds number. C_N is decreased, and C_m is slightly nose-down with increasing Reynolds number; however, it should be noted that most of this is within the accuracy of the data, especially for the lower Reynolds numbers (and hence dynamic pressure). Results for a body-flap deflection of 16.0 deg are shown in Figures 3 and 4. C_N is approximately the same for all Reynolds numbers, indicating an increase relative to the baseline configuration. Pitching moment shows a marked nose-down increment with increasing Reynolds number, indicating a more effective body-flap as Reynolds number increases. The cause of these effects can be traced to changes in the location of boundary layer separation and re-attachment in front of and on the body flap. Surface-streamline patterns (oil flows) on the windward surface in the vicinity of the body-flap are shown in Figures 5 to 8. The model is at an angle of attack of 40 deg with a body-flap deflection of 16.0 deg. As Reynolds number increases, the separation region decreases. While the forward separation line moves rearward a small amount, the main effect is the forward motion of the re-attachment line on the flap itself. The separation is not as well defined at a length Reynolds number of $1.6x10^6$; the oil appearing somewhat smeared or "runny". Several repeat runs were made which verified this pattern. It is postulated that the flow is, or is near, transitional; at the next Reynolds number tested, $Re_\infty = 3.2x10^6$, the flow overcomes the pressure gradient due to the deflected flap and remains attached on the whole lower surface, and the oil flow appears clear and sharp again. Similar aerodynamic and oil-flow results were observed at Mach 10. The data and oil flow photographs can be found in papers by Brauckmann and Paulson. (Ref 5). At $M_\infty = 10$, no limiting case of flap effectiveness was obtained, as at $M_\infty = 6$, presumably due to insufficient Reynolds number variation to achieve transitional flow. Comparisons of the current $M_\infty = 6$ and $M_\infty = 10$ results to the preflight prediction (ADDB) and to STS-1 mission flight-derived data points are made in Figures 9 and 10. The highest Reynolds number experimental data are used, but are still below flight values. All data are interpolated at flight values of

α, referenced to a center-of-gravity location of 0.65L, and the flight derived data points have been adjusted to zero-control surface deflection using the ADDB effectiveness values. The agreement of the current values of C_N with the data book is very good. Both the current data and the preflight prediction over-estimate the the flight C_N by a slight amount. The agreement in pitching moment is not as good, especially at Mach 10. Values from the ADDB are in-between the current data and flight. The discrepancy between the current data and flight represents an movement in Cp location of 7.7 inches, or .6 % of the body length. It is probable that non-ideal gas effects are present. Also, recall that the flight data were corrected using ADDB control surface effectiveness values. Body-flap effectiveness, ΔC_m, at $M_\infty = 6$ and 10 is compared to the preflight prediction in Figure 11. Reynolds number plays a small role on basic-body pitching moment at these Mach numbers, primarily affecting body-flap effectiveness. As just shown, predicted body-flap effectiveness is bounded by the current tests. While not duplicating the preflight data book, the current tests are in line with the results. Conventional hypersonic wind tunnels (non-impulse) are therefore able to accurately describe the aerodynamics of this class of entry vehicles at these low to mid hypersonic Mach numbers. Proper determination of flight control surface effectiveness requires proper simulation of the state of the boundary layer (i.e. laminar, transitional, or turbulent).

5 Computational Predictions

Computational fluid dynamics (CFD) were used to examine differences between ideal gas and real-gas flowfields. Ideal gas flowfields can be duplicated in the wind tunnel, whereas in this study real-gas effects were only simulated. Solutions for the modified orbiter geometry corresponding to wind tunnel and flight conditions were obtained at angles of attack of 35, 40, 45 deg for body-flap deflections of 0, 5, 10, 15, and 20 deg. The data were interpolated for body-flap deflections of 16.0 and 16.3 deg, to compare with data presented from the wind tunnel tests. A more complete discussion of these results can be found in a paper by Weilmuenster (ref 4). The predictions were in good qualitative agreement, although the code over-predicted C_N by about 2.5 %. Differences in C_m amounted to 1 % error in Cp location. In order to examine the differences in the flowfield that occur in flight, computations were carried out using finite-rate chemistry on the modified orbiter geometry at flight conditions. As shown in Figure 12, the occurrence of high temperatures associated with this flight condition dissociates the flow within the shock layer such that the ratio of specific heats, γ, defined

here as h/e, is reduced from 1.4 in the freestream, to 1.3 immediately behind the shock to about 1.14 near the body. In the nose region, γ is reduced to about 1.12. The major effect of this change in γ is a lowering of the surface pressure on the last 20 % of the vehicle. A plot of computed center-line surface pressure for wind-tunnel and flight conditions is given in Figure 13. Included are results from a solution at a Mach number of 24 using an ideal gas value for γ of 1.4. There is a small difference due to Mach number alone, but the largest difference is due to the lower γ. The lower γ results in the expansion on the aft end occurring to a greater degree, lowering the pressure over a large area of the vehicle. It should be noted that the Orbiter geometry has a large influence on the magnitude of the real-gas effects. The Orbiter has an expansion that starts at approximately 0.8L, which coincides with the largest planform area, and thus the greater expansion of the flow, relative to ideal gas flow, lowers the pressure over a large area. The impact of this reduced pressure on the aerodynamic coefficients is shown in Figures 14 and 17. The lower pressure on the aft end causes a reduction in normal force and a nose up pitching-moment increment. The computed increment in C_N between tunnel and flight conditions is .062 and .048 for $\delta_{BF} = 0.0$ deg and 16.3 deg, respectively. This agrees well with the delta found in flight, $\Delta C_N = .059$ (preflight ADDB-to-flight, STS-1). The increment in C_m for $\delta_{BF} = 0.0$ deg is 0.040, which is larger than the increment found between flight and pre-flight prediction. For the 16.3 deg flap case however, the delta is 0.028, which is very close to that found between the preflight ADDB and flight. The difference in the two increments can be traced to greater flap effectiveness at flight conditions. There are two reasons for the greater calculated flap effectiveness. The predicted separation region in front of and on the flap is smaller in flight than in the wind tunnel, for the same length Reynolds number. Calculated streamline patterns in the region of the body-flap at both tunnel and flight conditions for two flap deflections are shown in Figures 15 and 16. The much smaller separation region for flight conditions is evident. In addition, as discussed by Weilmuenster the pressure rise on the flap was higher in flight than in the wind tunnel, but this was due to a combination of Mach and γ effects. In fact, the lower γ tends to reduce the pressure rise, but the higher Mach number in the shock layer in flight overcomes this. A solution at $M_\infty = 24$ (flight) but with $\gamma = 1.4$ (ideal gas) was not obtained on the deflected flap configuration, thus a separation of these effects cannot be made. An analysis of control-surface effectiveness was performed after the first few flights of the Shuttle Orbiter. Both an elevon and a body-flap pulse maneuver were analyzed in terms of center-of-pressure location for predicted and flight

performance. While the results were biased from the
perfect correlation line, the conclusion was reached
that flap effectiveness, as presented in the preflight
ADDB, was predicted correctly. More analysis of
this discrepancy is needed.

6 High Mach Number Simulation

Two facilities at Langley were used to examine the
high Mach number flight regime, the 22-Inch Mach
20 Helium Tunnel and the 20-Inch Mach 6 CF_4 Tun-
nel. The 22-Inch Helium Tunnel uses purified helium
which behaves as an ideal gas with a γ of 1.667.
There are a number of advantages to testing with
helium, the primary one being that very high val-
ues of Re_L may be generated at high Mach numbers
without having to heat the gas to prevent liquefac-
tion. For this study, the facility provided a close
match of flight Mach and Reynolds numbers. How-
ever, the flowfield γ remained at $\gamma = 1.667$. The
results from the helium tunnel tests showed a signifi-
cant nose-down pitching moment compared to flight,
which can be explained by γ being higher rather
than lower than ideal air. In addition, body flap
effectiveness was reduced. Thus, testing in helium is
inappropriate for the simulation of real-gas effects.
The CF_4 tunnel uses a heavy gas which has a γ lower
than ideal air to simulate this aspect of real-gas flows
such as occurs in flight. The value of γ in the CF_4
tunnel, around 1.15 in the shock layer, is close to
that determined to occur in flight. A comparison of
aerodynamic coefficients obtained in air and CF_4 at
identical values of Reynolds number and Mach num-
ber is given in Figures 18 and 19. As can be seen,
testing in a heavy gas decreases the normal force co-
fficient and causes a nose-up pitch increment, when
compared with results in air. The decrease in C_N is
.046 for $\delta_{BF} = 0.0$ deg and .077 for $\delta_{BF} = 16.3$ deg.
This decrement is approximately the same as the
flight decrement and that determined by the CFD
analysis . The change in C_m is .029 for $\delta_{BF} = 0.0$
deg and .027 for $\delta_{BF} = 16.3$ deg.

This increment is the same as the flight-to-preflight
increment, but unlike the CFD solutions, the incre-
ment is the same for both the undeflected and de-
ected body-flap configurations. For this configura-
on then, with an expansion region on the windward
urface, the real-gas effects are closely approximated
y testing in a heavy gas such as CF_4

ESA results and discussion

1 Methodology

he process of ground to flight extrapolation is the
llowing :

1. Definition of reference conditions in perfect gas
   hypersonic facilites.

2. Reduction of aerodynamic uncertainties for
   these reference conditions through comparisons
   with results from different sources, both exper-
   imental and computational and analysis of all
   possible sources of errors (shape inaccuracies
   in wind tunnel or CFD model, inadequate flow
   modeling, biased instrumentaion..).

3. Transposition to flight : utilization of the same
   prediction method for the reference and flight
   conditions.

4. Analysis of the differences in terms of flow
   physics between windtunnel and flight and
   derivation of the uncertainties in the process of
   transposition.

5. Establishment of the preflight uncertainties in
   the predictions for flight conditions, as the sum
   of the uncertainties for the reference conditions
   and those due to the transposition process.

The purpose here is to investigate to which extend
the use of high enthalpy facilities can contribute to
the validation of the real gas effects in this process
of ground to flight extrapolation. The F4 and HEG
facilities represent two intermediate steps between
the S4 perfect gas conditions and the flight condi-
tions, on which CFD results can be cross-checked in
the process of extrapolation to flight.

The real gas effects which can be expected in each
of these conditions are presented in figures 21 and
22, in the form of dissociation level, equivalent γ
and Damkholernumber versus enthalpy, for flight
and wind tunnel conditions, behind a normal shock
wave (representing the stagnation point) and be-
hind a 40 degree shock wave (representing the aft
part of forebody) , assuming thermochemical equi-
librium. The conditions are those following a typ-
ical Orbiter trajectory. It can be seen from figure
20 that the γ effect appears for relatively moderate
enthalpies, corresponding to flight Mach numbers of
about 10. Indeed the analysis of flight results shows
that, when the Mach numbers increases, the pitch-
up appears at Mach=10 and stabilizes at Mach=16
. The two high enthalpy facilities are in the range
of enthalpies representative of this *gamma* effect,
and so should be quite representative of the pitch-
up effect expected. This *gamma* effect, since it is
a function of the derivative of the equation of state
$(C^2 = \partial P/\partial \rho)$, appears as soon as deviation from
perfect gas occurs, i.e. as soon as vibrational energy
appears, which for oxygen is around 2000 K.

Equilibrium dissociation levels are also significant in
the ground facilities for oxygen; however for nitrogen
only HEG can give a limited dissociation, and only

in the stagnation area. It must be recalled however that actual dissociation levels in the ground facilities could be much smaller due to the very low Damkholer numbers. This means that finite rate effects can be expected to be significantly different between ground and flight conditions.

The base line flight point chosen is the following:

STS-2, time: 75620s

Mach number: 24.3

Altitude: 72.3 km

Angle of attack: 39.40 degrees

Elevon deflection: 1.70 degrees

Body flap deflection: 14.90 degrees

Computations and wind tunnel tests are performed for the following configuration:

Angle of attack: 40 degrees

Elevon deflection: 0 degrees

Body flap deflection: 0 and 15 degrees

Corrections for the slightly different angle of attack and deflections are introduced in the comparisons.

For the purpose of analysis, the real gas effect is subdivided in three elements:

- the equilibrium chemistry effect, defined as the difference between results with equilibrium chemistry assumption and those with perfect gas, $\gamma=1.4$ assumption.

- the effect of finite rate chemistry, defined as the difference between results with finite rate chemistry and those with equilibrium chemistry.

- the effect of finite rate thermal relaxation defined as the difference between results with finite rate chemistry and thermal relaxation and those with finite rate chemistry only.

For comparison between flight and ground facility results, the effect of Mach number must be defined also, as the difference between results obtained at flight and ground facility Mach numbers, using the perfect gas, $\gamma=1.4$ assumption.

Computations have been performed with the corresponding modelling for the four conditions investigated here (S4 "blow down", F4 "hot shot", HEG "shock tube" and flight). The conditions are summarized in the table 2.

7.2 High Enthalpy Simulation

This chapter will cover both results from the numerical computations carried out on the Orbiter as well results from high enthalpy testing. The shape of both the Orbiter and Halis are described by CAD files provided by NASA. The geometry of the Orbiter includes accurate representations of all items except windshield and elevon gaps. The aircraft surface is represented with an unstructured triangular mesh made of 7000 nodes in the case of the Orbiter and 6000 in the case of Halis. The volumic mesh is built by an advancing front method from the skin mesh, and is made of tetrahedras. Its unstructured nature facilitates the clustering of the mesh points in the shock layer. The volume mesh of the Orbiter contains 130000 nodes and that of Halis 113 000 nodes. In order to compute the flow field around models in high enthalpy facilities, it is necessary to first rebuild the flow in the facilities' nozzle, since complex phenomena are awaited in these nozzles, and significant uncertainties exist in their prediction. The flow field is rebuilt using CFD, in which unknown parameters, such as transition point of the boundary layer, are tuned in order to match measurements made at the nozzle wall and exit. The computed nozzle exit plane is then used as inflow conditions for the computations of the flow around the model.

The computed pitching moment of the US Orbiter is represented in figures 23 to 26, and compared to experimental data. It is given for the flight center of gravity, angle of attack and elevon deflection, as defined in previous paragraph, and for 0 degrees and 15 body-flap deflection. Ground facility and flight conditions are referenced in these figures by total enthalpy, which is the primary parameter controlling the chemistry effects; however other parameters, such as pressure or Mach number also play a role, so that the data presented should not be interpreted as a direct pitch(enthalpy) function, but rather as a pitch(real gas effect) one, the scale for the real gas effect being qualitative. In figure 23 the pitch for the Orbiter with no flap deflection is presented for S4, F4 and flight conditions, from computations with four different modelling (perfect gas, equilibrium chemistry, finite rate chemistry, finite rate chemistry and thermal relaxation), and from experiment. In figure 24 the same data is presented collapsed to its S4 value, which is the reference point. Consequently figure 24 illustrates best the transposition to flight of the pitch for the Orbiter with no flap deflection. It is seen that for flight conditions the major part of the real gas effect can be accounted for using equilibrium chemistry, finite rate chemistry effect being much smaller, and finite rate thermal relaxation playing no role. For F4 conditions the situation is different; because of the much smaller Damkholer number the finite rate effect roughly divides by two the equilibrium chemistry real gas effect. It is seen also that the computational and experimental results agree best on the S4 to F4 transposition if the flow is assumed to be in equilibrium.

In figures 24 to 26 the comparison of results for different conditions, and transposition to flight, are presented for the case with 15 degrees body flap deflection and for the body-flap efficiency, using the same method as for the 0 degree case. In figure 26, again, the same data as from figure 24 are shown but collapsed to its S4 value.

It must be recalled however that the computations have been performed with an Euler code, and that although a viscous correction, derived from previous studies (ref 2), has been introduced, the objective here is not to predict the control surface efficiency itself but the effect of air dissociation on this efficiency.

It is seen on figures 25 and 26 that the pitching moment for HEG conditions is lower than for F4 conditions, i.e. that the "real gas effect" on pitch in HEG is lower than in F4; this is somewhat surprising but could be explained by the evolution of the "equivalent γ" with enthalpy, figure 22, which is not monotonic. Figure 26 shows the body flap efficiency defined as the ratio of the pitching moment difference between bodyflap 15 degree and 0 degrees with the corresponding difference as obtained in the reference S4 conditions. It can be seen that the flap efficiency is much higher in flight than in F4, suggesting that not just Reynolds but also γ and local Mach number play a role.

Pressure coefficient distribution along the windward centerline are presented in figure 28 for S4, F4 and HEG conditions and for the non deflected body-flap configuration. These distributions confirm the pitch up described in the previous chapter since one can notice between S4 and F4 a small pressure coefficient increase at the nose and larger decrease at the rear. Less difference are visible between S4 and HEG, indicating that the pitch up would be smaller.

The pressure distributions obtained for the four conditions investigated are presented in figures 29 to 32, and compared to experimental data in figures 33 to 35. The real gas effect is very local, and occurs mainly in the expansion and secondary compression areas, i.e. in front of the body flap and at the leading edges / corners of the fuselage and wing, so that only the pitching moment is significantly affected by the real gas effect (lift and drag changes are small).

7.3 Ground to flight transposition

7.3.1 Reference "cold" uncertainties

The rebuilding of the cold reference point is an important part of the ground to flight extrapolation process, as presented in the introduction. In order to reduce the uncertainties to a minimum, it is necessary, in the framework of a design study, to per-

form mesh refinement studies, and to compare the results coming from a large number of sources. Also all differences and inaccuracies in the shape must be tracked and accounted for.

Such a study, which is quite lengthy, has been performed for Hermes (ref 2); here our main effort is on the transposition process, and the uncertainties on the predictions for the reference point, although reasonable, could be further reduced: the discrepancy between CFD and experimental results in terms of pitching moment is equivalent to a 3 degree deflection of the body-flap; on the body-flap efficiency it is 6 %; on the heat fluxes it is very small except on the nose part of the aircraft where it reaches 20%. The wind tunnel results are in good agreement with the computations, in terms of pitching moment, so that the remaining discrepancies between CFD and experiment are due to insufficient griding or more probably to small inaccuracies in the CFD shape.

7.3.2 Influence of real gas effects

For the flight point chosen the real gas effects can be decomposed in the following way (0 body flap deflection):

- Effect of mach number :+ 0.0045
- Effect of equilibrium chemistry : + 0.038
- Effect of finite rate chemistry : - 0.0055
- Effect of finite rate thermal relaxation :+ 0.0007
- Total real gas effect : 0.0332

On the control surface efficiency, the real gas effect can be decomposed similarly (excluding coupling between chemistry and viscous interactions):

- Effect of Mach number : - 1%
- Effect of equilibrium chemistry : + 26%
- Effect of finite rate chemistry : - 4%
- Total : + 22%

7.3.3 Assessment of uncertainties

The effect of equilibrium chemistry on pitching moment is of the same order of magnitude in F4 and flight conditions; also better agreement is obtained between CFD and experiment in F4 if equilibrium flow is assumed. The effect of finite rate chemistry and thermal relaxation is not validated at this stage. However in flight these elements only contribute to 15 % of the real gas effects; consequently the uncertainties they induce are quite small. In the present

Nature	Contribution to real gas effect,%	Intrinsic uncertainty,%	Contribution to global uncertainty
Equilibrium chemistry	115%	8%	9.2%
Finite rate	−15%	50%	7.5%
Total	100%		16.7%

Table 1: Total uncertainty on the real gas effect

exampe , the dispersion on real gas effect on pitching moment between experimental results and CFD results obtained with equilibriun chemistry is 8 % for the case with no body flap deflection and 13 % for the case with 15 degree body flap delection. (This latter number includes dispersion due to approximate representaion of viscous interactions) If the uncertainty of the effect of finate rate is taken arbitrarily to be 50 % , then the total uncertainty on the real gas effect can be estimated as follows in table 1. The total uncertainty is the sum of an 8 % (13 % for the case with 15 degree deflection) dispersion for equilibrium chemistry applied on the 115 % of the total real gas effect and an 50 % dispersion applied on 15 % of the total real gas effect, and so is globally 17 % (22 % for the 15 degree body flap case).

The figures above for dispersion can be reduced through the use of Navier Stokes equations due to improved representation of viscous interaction effects.

The mentioned 17 % uncertainty on the orbiter pitch is equivalent to a 1.9 degree body flap deflection, which is coherent with a discrepancy between flight data and prediction equivalent to a 1.3 degree deflection.

8 SYNTHESIS AND CONCLUSION.

A study was undertaken at the Langley Research Center to resolve the cause of the "pitch-up anomaly" observed during entry of the first flight of the Shuttle Orbiter. At high Mach flight conditions a reduction in specific heat ratio occurs due to high temperature effects. The primary effect of this lower specific heat ratio within the flowfield of the Orbiter is lower pressures on the aft windward expansion surface of the Orbiter, relative to those deduced from hypersonic wind tunnel tests with ideal or near ideal gas test flows, and thus a corresponding nose-up pitching moment. Computationally, good agreement with the flight aerodynamic coefficients was obtained with the flap deflected to approximately 16 deg. Testing in a heavy gas in the 20-Inch Mach 6 CF_4 Tunnel gave a good simulation of high temperature effects as the aerodynamic increments and flap effectiveness were in good agreement with flight results. The overall agreement between flight, computational solutions at flight conditions (laminar boundary layer, continuum flow regime), and measurements made in the CF4 tunnel was quite good. This study has demonstrated a preferred approach to test high fidelity models in conventional facilities to provide base-line data for design; combined with the use of the heavy gas facility for the simulation of the high temperature effects. Complementary CFD to be used for substantiating these results as well as to provide information at flight conditions.

AT ESA, through Dassault Aviation, a procedure to validate ground to flight extrapolation of re-entry aircraft aerodynamics has been proposed and implemented in the case of the Orbiter, using European high enthalpy facilities. Encouraging results have been obtained for force coefficients, leading to a possible method to significantly reduce the uncertainties in the transposition to flight and in particular the uncertainties associated with real gas effects.

REFERENCES

Brauckmann, G.J. ,Paulson, J.W. and Weilmuenster, K.J. 1995 Experimental and computational analysis of Shuttle Orbiter hypersonic trim anomaly. *Journal of Spacecraft and Rockets Vol.32, No.5*

Perrier, P. ,Rapuc, M. ,Rostand, P. ,Sagnier, P. ,Verant, J. ,Eitelberg, G. ,Bogstad, M. and Muylaert, J. 1996 Ground to flight extrapolation of reentry aircraft aerodynamics: an experimental and computational approach. *AIAA Paper 96-2434*

Muylaert, J. ,Walpot, L. and Durand, G. 1993 Computational analysis on generic forms in European facilities: standard model Electre and Hyperboloid flare. *ISSW 19, Marseille*

Weilmuenster, K.J. ,Gnoffo, P. and Greene, F. 1993 Navier-Stokes simulations of Orbiter aerodynamic characteristics including pitch trim and body flap. *Journal of Spacecraft and Rockets Vol.31, No. 3*

Brauckmann, G.J. ,Paulson, J.W. and Weilmuenster, K.J. 1994 Experimental and computational analysis of the Space Shuttle Orbiter hypersonic "pitch-up anomaly". *AIAA Paper 94-0632*

TUNNEL	Mach no.	Scale	$Re_\infty, 10^6$	γ_∞	Pt (Psia)	Tt(^0F)
15-in. Mach 6	6.0	0.004	0.2	1.4	45	780
			1.7		240	470
20-in. Mach 6	6.0	0.0075	0.4	1.4	30	400
			0.8		60	425
			1.6		125	450
			6.1		475	475
31-in. Mach 10	10.0	0.0075	0.4	1.4	350	1350
			0.9		720	1350
			1.8		1450	1350
20-in. Mach 6 CF_4	6.0	0.004	0.2	1.22	1600	800

Table 2: NASA LARC facilities for Orbiter testing

FACILITIES	ONERA S4 MA	ONERA F4	DLR HEG	FLIGHT
TYPE	BLOW DOWN	HOT SHOT	SHOCK TUBE	
MODEL SCALE	1/90	1/90	1/90	1/1
MACH NUMBER	10	8	10	24
Hi/RT	14	160	280	330
Res.PRESSURE(bar)	25	280	450	
ALTITUDE(km)				72
REYNOLDS(10^{-5})	6.	0.3	1.2	10
PL/V 10^6	3.6	0.044	0.12	0.28
MEASUREMENTS	FORCES	FORCES		
	PRESSURE	PRESSURE	PRESSURE	
	HEAT FLUX	HEAT FLUX	HEAT FLUX	

Table 3: ESA facilities for Orbiter testing
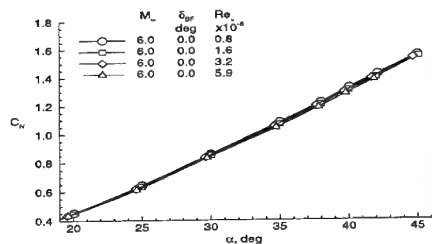
Figure 1: Effect of Re-number on Shuttle Orbiter on C_N for body flap 0 degrees
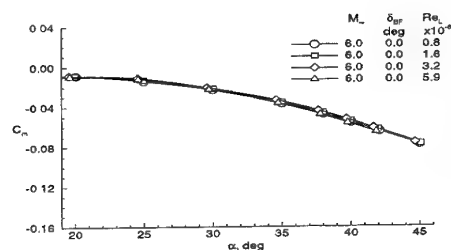
Figure 2: Effect of Re-number on Shuttle Orbiter on C_m for body flap 0 degrees
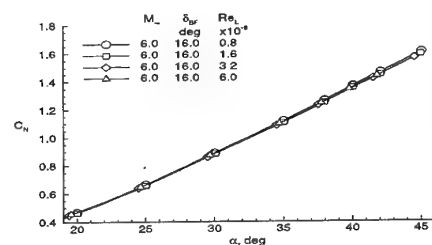
Figure 3: Effect of Re-number on Shuttle Orbiter on C_N for body flap 16 degrees
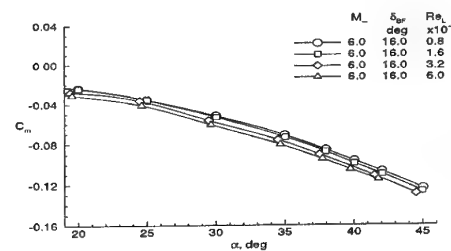
Figure 4: Effect of Re-number on Shuttle Orbiter on C_m for body flap 16 degrees

Figure 5: Oil flow for $Re_L = 0.4x10^6$

Figure 6: Oil flow for $Re_L = 0.8x10^6$
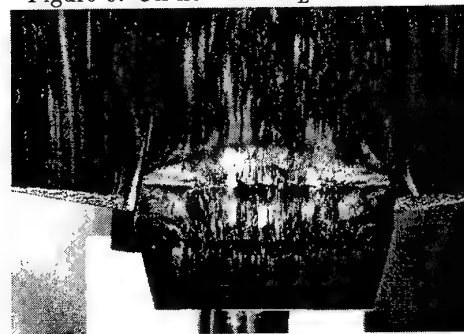
Figure 7: Oil flow for $Re_L = 1.6x10^6$
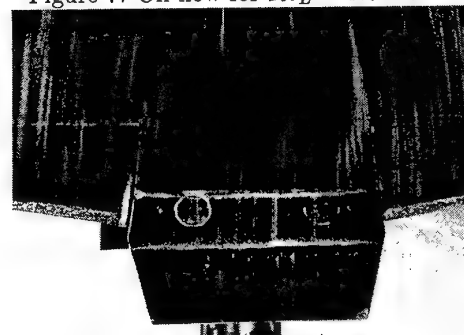
Figure 8: Oil flow for $Re_L = 3.2x10^6$
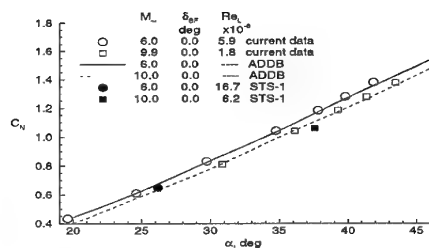
Figure 9: Comparison of C_N for present calculations with ADDB and flight
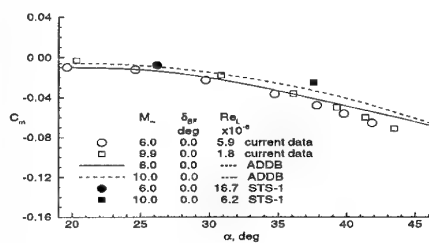
Figure 10: Comparison of C_m for present calculations with ADDB and flight
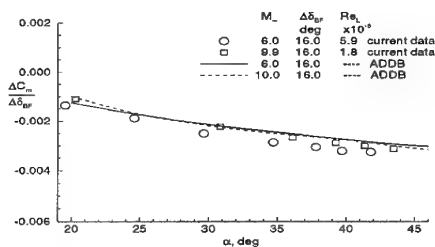
Figure 11: Comparison of flap efficiency for present calculations with ADDB and flight
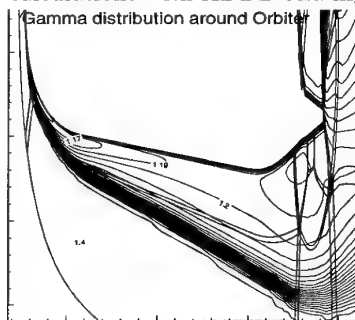
Figure 12: Computed variation of γ in windward flowfield of modified Orbiter
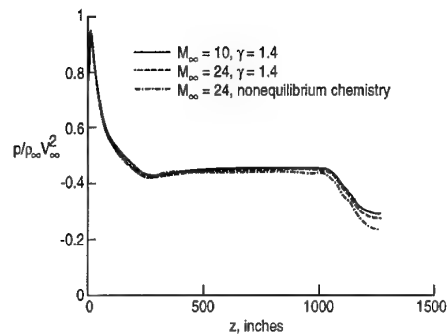
Figure 13: Computed centerline surface pressure for modified Orbiter
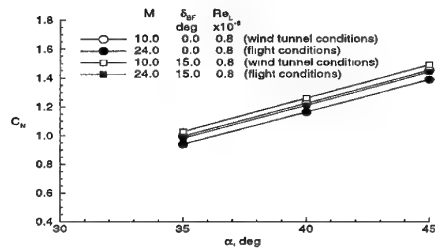
Figure 14: Comparison of modified Orbiter C_N at wind tunnel and flight conditions
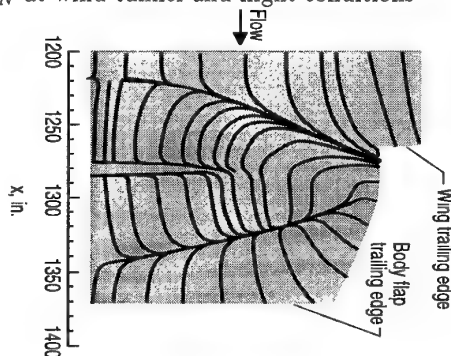
Figure 15: Calculated surface streamline patterns in vicinity of body flap at wind tunnel conditions
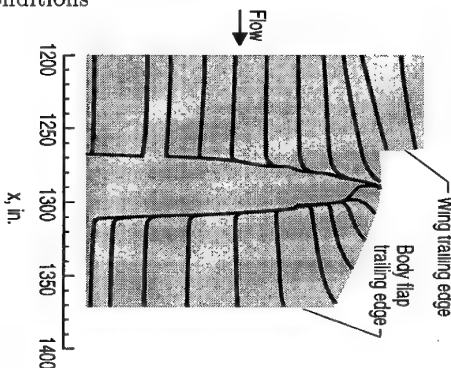
Figure 16: Calculated surface streamline patterns in vicinity of body flap at flight conditions
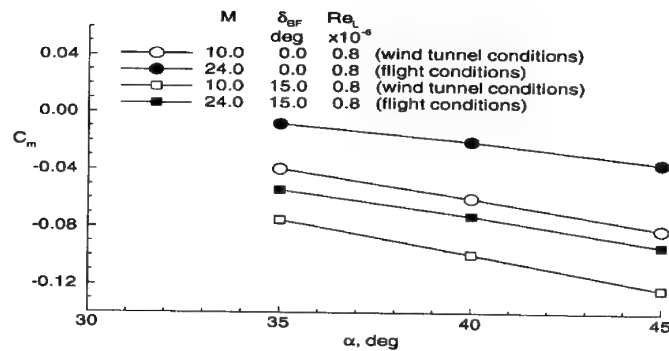
Figure 17: Comparison of modified Orbiter C_m at wind tunnel and flight conditions
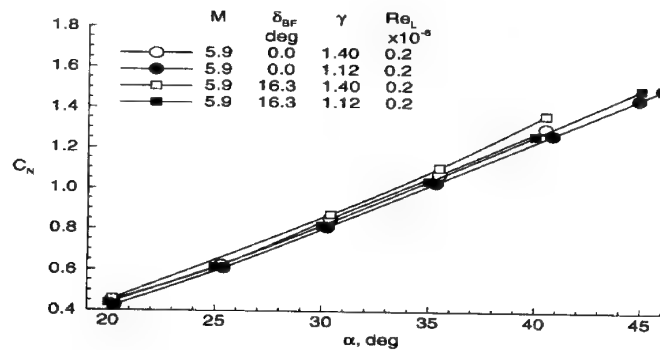
Figure 18: Comparison of Shuttle Orbiter aerodynamics in air and CF_4
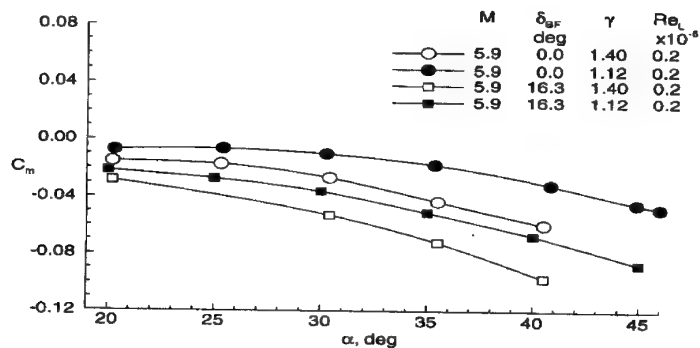
Figure 19: Comparison of Shuttle Orbiter aerodynamics in air and CF_4
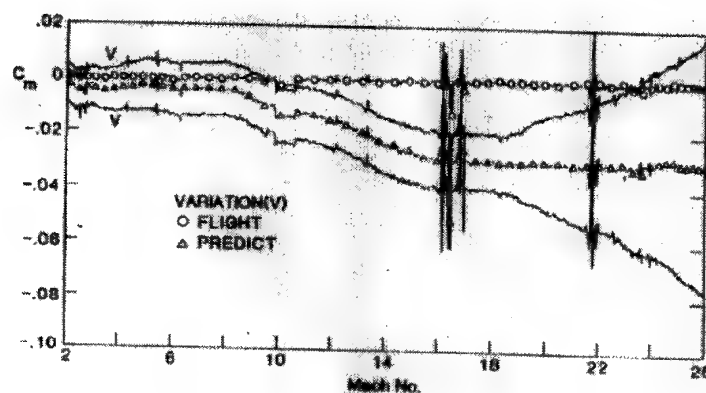
Figure 20: Pre-flight to flight discrepancy for STS-5
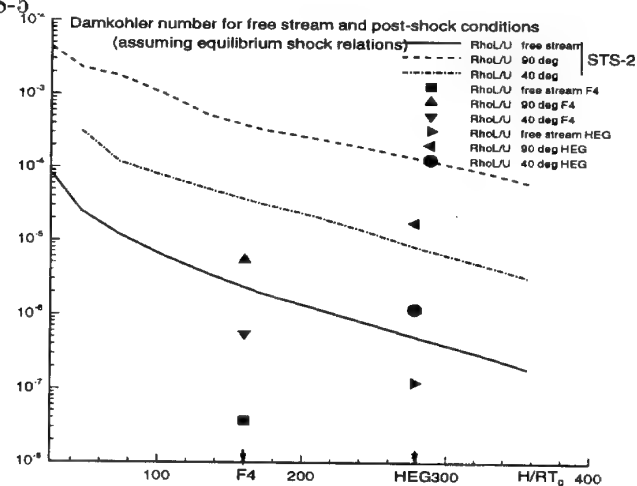
Figure 21: Damkohler number for free stream and post-shock conditions assuming assuming equilibrium flow

Figure 22: Equivalent γ's for free stream and post-shock conditions assuming equilibrium flow
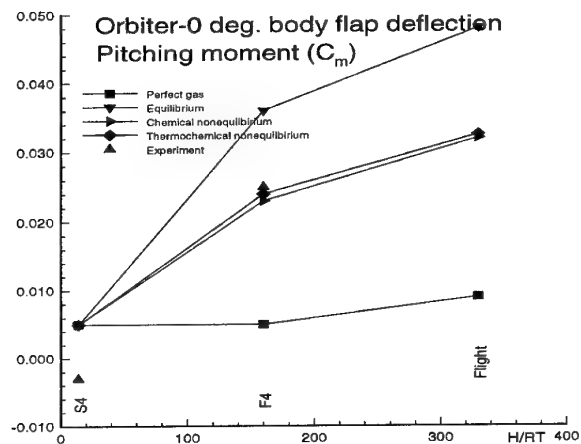
Figure 23: Pitching moment of the Shuttle Orbiter with 0 degrees body flap deflection
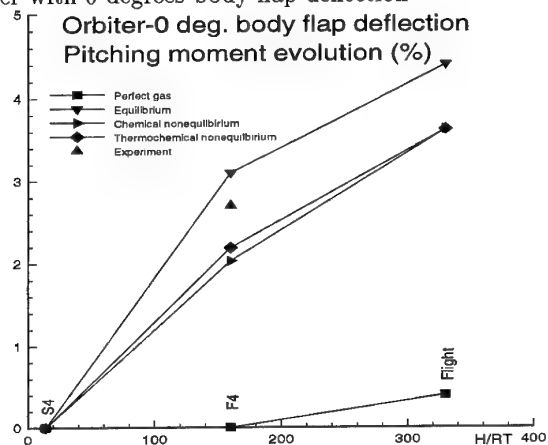
Figure 24: Pitching moment evolution of the Shuttle Orbiter with 0 degrees body flap deflection
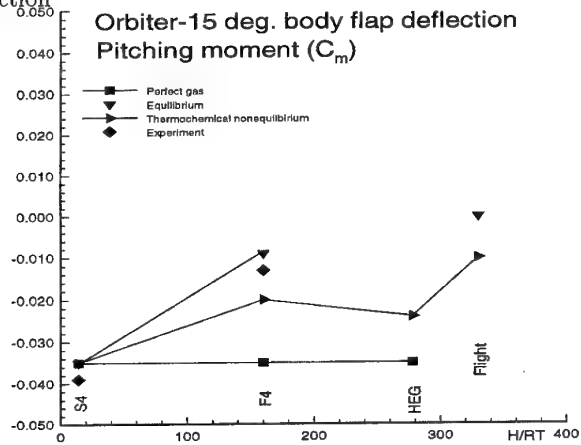
Figure 25: Pitching moment of the Shuttle Orbiter with 15 degrees body flap deflection
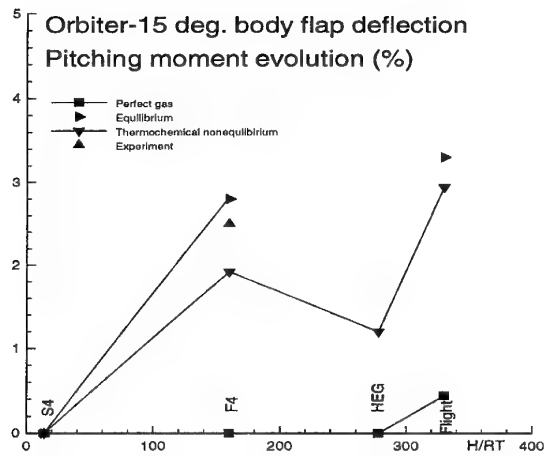
Figure 26: Pitching moment evolution of the Shuttle Orbiter with 15 degrees body flap deflection
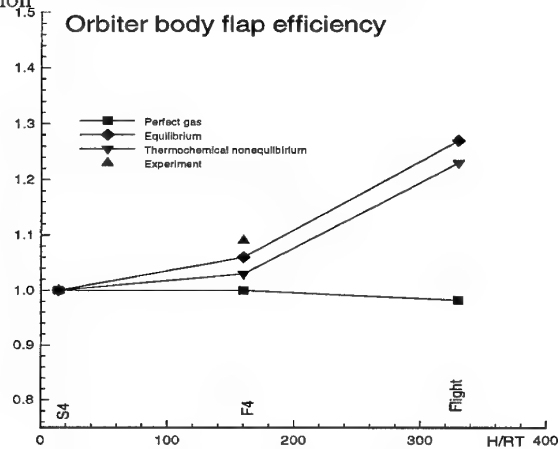
Figure 27: Flap efficiency of the Shuttle Orbiter
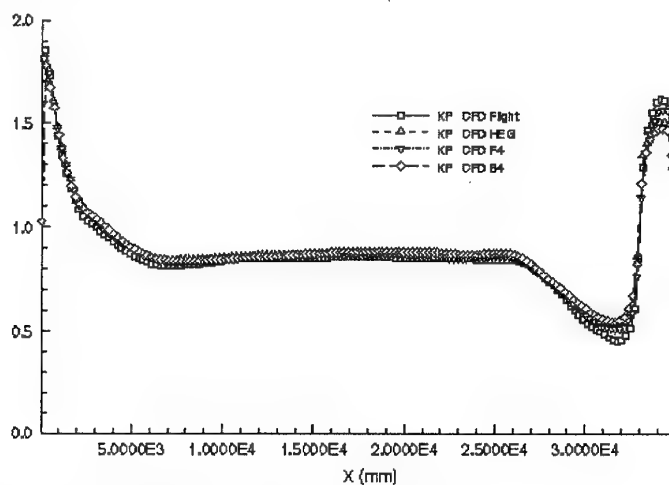
Figure 28: Centerline pressure coefficient distribution on HALIS
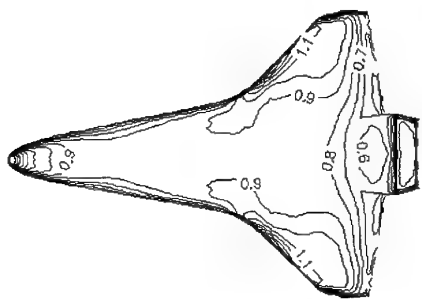
Figure 29: Pressure coefficient distribution for S4 conditions
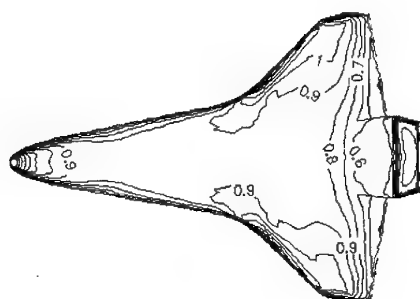
Figure 30: Pressure coefficient distribution for F4 conditions
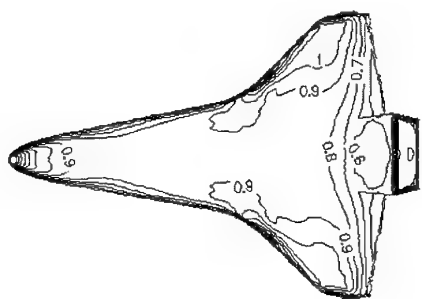
Figure 31: Pressure coefficient distribution for HEG conditions
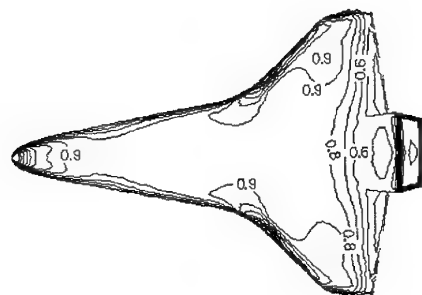
Figure 32: Pressure coefficient distribution for flight conditions
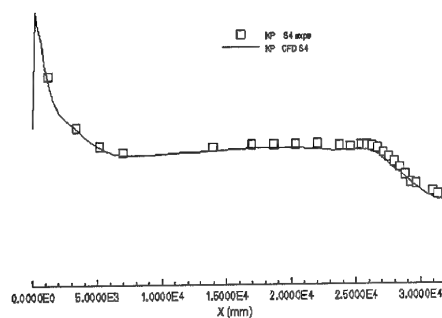
Figure 33: Pressure distribution on the symmetry line of HALIS, compared to experimental data, at S4 conditions
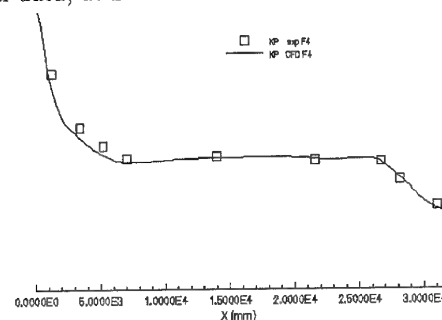
Figure 34: Pressure distribution on the symmetry line of HALIS, compared to experimental data, at F4 conditions
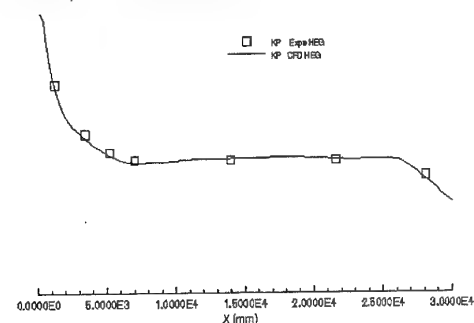
Figure 35: Pressure distribution on the symmetry line of HALIS, compared to experimental data, at HEG conditions

FLIGHT TESTING FOR HYPERSONIC SPEEDS:
AN EUROPEAN VIEW

Gérard LARUELLE and Thierry BONNEFOND
AEROSPATIALE, Espace & Défense Branch, Route de Verneuil BP 96
78133 Les Mureaux Cedex, France

Peter SACHER
DAIMLER-BENZ-AEROSPACE, DASA Military Aircraft, Postfach 801160
D-80663 München, Germany

1. INTRODUCTION

The development of future vehicles with sustained hypersonic flight, using air-breathing and/or rocket propulsion, will require new knowledge and technologies which are not yet available and therefore not validated. One of the mandatory next steps before entering prototype work will be to perform flight tests in order to investigate the topics which can not be studied on ground.

The present scenario in US (HyTech, X 33, X 34,...), Japan (Orex, Hyflex, Alflex,...) and Europe including Russia shows worldwide effort in exploring the need for flight testing advanced technologies flying at hypersonic speed. This need will be even more evident for future space launchers if reusability is required. In that case, this will mandatorily lead to a « step-by-step » approach by flight testing technologies using appropriate flying test beds. Air-breathing propulsion is still, of course, most challenging due to the problems of engine / airframe integration and to the lack of flight data during engine operations at hypersonic speed. Even for fully reusable rocket propulsion, a lot of uncertainties must be still necessarily decreased before starting development of a future advanced transportation system.

The NASA Hypersonics X-Vehicle Program, started in 1996, shows the logics and the programmatics for the development of a scramjet propulsion engine (Fig 1). First small scale testing like the inlet and the combustion chamber leads to the development of a full scale engine which will be tested integrated on the full scale flying test bed in a large wind tunnel, before flying finally as a « passenger » on already existing vehicles providing the required acceleration to reach hypersonic speeds.

Also for vehicles without air-breathing engines, a most impressive flight testing approach is undertaken by Japan (Fig 2). OREX, ALFLEX and HYFLEX have already flown sucessively and the first flight of HOPE-X, rocket boosted, is foreseen in 2000. For the future spaceplanes, a new R&D program based on other flying test beds is being established by Science and Technology Agency.
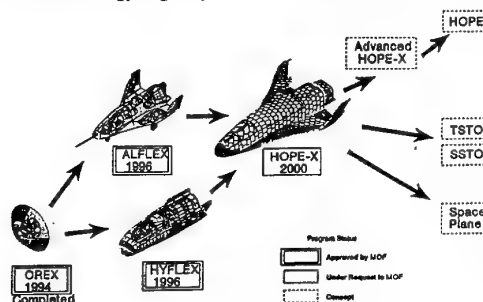
Figure 2
Japanese Flight Testing Approach

2. VEHICLES FLYING HYPERSONIC SPEED

In order to assess the needs for flight testing, all presently foreseeable potential applications of future hypersonic vehicles have to be identified and compiled as exhaustively as possible. Among the potential applications, the following ones are shown in the next figures.

The first one (Fig 3) presents an AEROSPATIALE's project of hypersonic reconnaissance vehicle: the range is approximatively 2 000 km for a flight in the Mach 6 - 8 range.
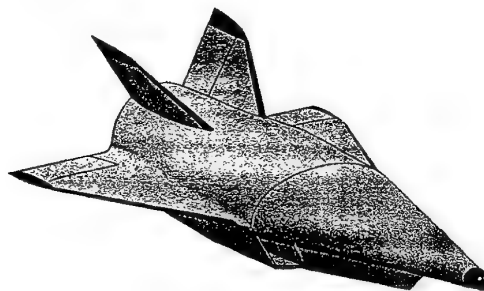
Figure 3
AEROSPTIALE's Hypersonic Reconnaissance Vehicle

Figure 1
US Hypersonic X-Vehicle Program

Some civil applications are presented on Figure 4. It shows some selected examples for reusable space launchers which are currently proposed and investigated in different programs around the World. Hypersonic atmospheric flight is also for fully rocket propelled space transport systems very important during re-entry and return flight to the landing site. In these projects, SSTO and TSTO vehicles are equally considered and, also, all the possibilities of vertical or horizontal take-offs and landings.
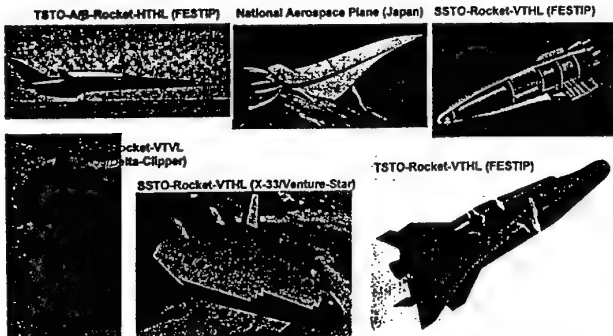
Figure 4
Reuseable Space Launch Vehicles

On Figure 5, launch systems with a first stage using an air-breathing propulsion are shown; obviously, the second stage, if it is existing, has to be propelled by rockets. According the staging Mach number (subsonic, supersonic or hypersonic), various options are highlighted and the air-breathing engines are respectively: turbojets, ramjets and scramjets. Due to their cruise capabilities, some of them have also military relevance in the near future for reconnaissance and surveillance.
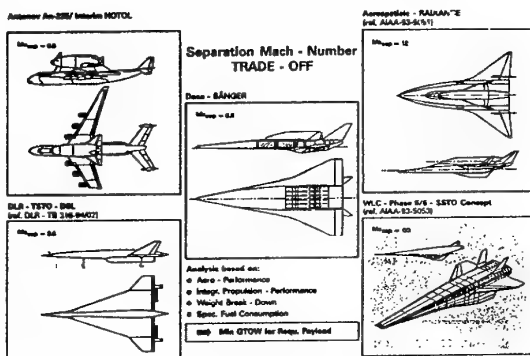
Figure 5
Air-breathing Space Launch Vehicles

3. CRITICAL « KEY-TECHNOLOGIES »

The hypersonic flight is critical for a lot of topics. The first one results of the very high temperature encountered during the flight. The second one is particularly strong for space launcher applications: the need of a very light structure for the vehicle in order to give a payload. Obviously, the reusability introduces also new constraints. Others presentations of this AGARD meeting such as « System Challenges for Hypersonic Vehicles » by JL HUNT, A WAGNER and G LARUELLE, give more details concerning the critical key-technologies, common to all future vehicles flying with hypersonic speed. Some of these key-technologies can be developped on ground but many limitations impose a complementary flight testing approach.

Without a decision on a specific future hypersonic flight vehicle and before starting the development of a full scale prototype, appropriate test vehicles must demonstrate various topics such as:

- reuseability (e.g. with respect to engines, structure, subsystems,...),
- horizontal (unpowered) landing technology,
- reliable design tools,
- heat resistant materials and structures,
- heat management technologies,
- cryogenic technologies,
- operational aspects (e.g. RAMS), ...

Figure 6 concerns an example for the reliability of prediction tools with the US Space Shuttle. The validation of prediction and design tools in real flight environment (e.g. for aerothermodynamics, structural integrity and propulsion performance) is of utmost importance for future designs. This Figure shows the surface temperature. Transition has to be predicted with high accuracy, otherwise it may occur at different location which leads to complete different levels of drag and temperature and so to over- or under-estimated thickness (therefore weight) for TPS. The first item may have a severe impact on the predicted cruise capability, and the second results in a considerable increase of gross take-off mass.
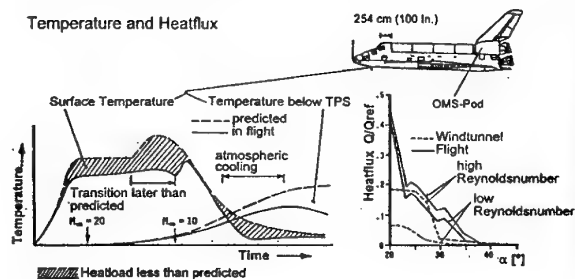
Figure 6
Temperature and Heatflux Prediction Tools

Another lesson learned from the shuttle history is shown on Figure 7. It demonstrates the under-estimated impact of effects from nonequilibrium gas on trim and control of the vehicle at very high Mach numbers. As it is well recognized, this has led nearly

to an unacceptable situation with respect to safety of the vehicle during the first flight.

Trim and Control
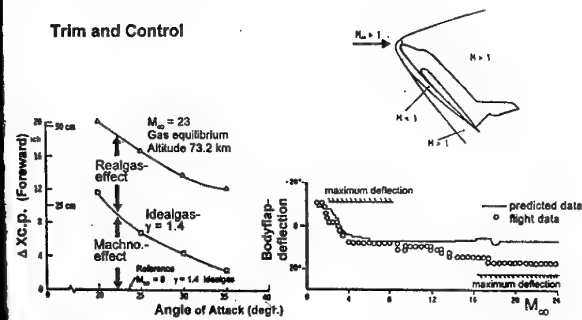
Figure 7
Trim and Control Prediction Tools

The reusability of materials and structures in hot environment has to be demonstrated by flight testing in the real atmosphere and on a representative geometry. As Figure 8 shows, temperature up to more than 1 400°C will occur along the trajectory on the windward surface of this FESTIP FSS 1 project .
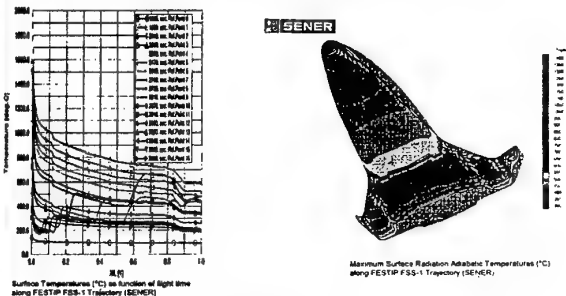

Figure 8
Heat Resistant Materials and Structures

If an air-breathing propulsion system is chosen, the integration of the engine with the airframe is the most challenging technology with respect to installed thrust (Thrust - Drag) and to longitudinal trim and control. For the first item, Figure 9 shows with an example that the installed net thrust is a small term resulting from the difference of two large ones; without a high accuracy for the prediction of the various components, the acceleration capabilities are difficult to foresee, in particular in transonic flight. Another challenge appears on this figure with the longitudinal trim and control along the trajectory, versus the flight Mach number; the nonaxisymmetric integration of the propulsive system requires a SERN nozzle which results in large Mach number dependent thrust induced pitching moments which have to be balanced by the airplane design as the left part of Figure 9 shows.
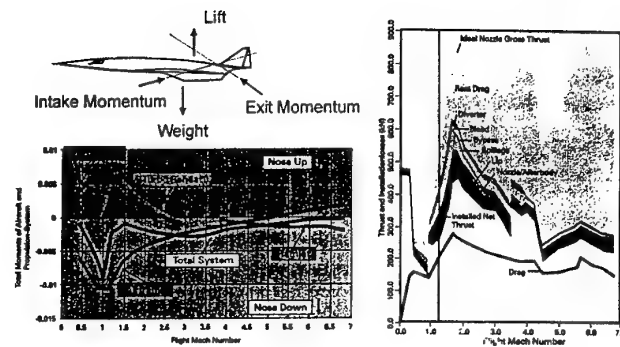
Figure 9
Engine / Airframe Integration

4. CLASSES OF FLYING TEST BEDS

A European group including Russia has worked on the possible flying test beds which must be considered in order to prepare future reusable space launchers; the partners were CIAM and TsAGI for Russia, DASA for Germany and AEROSPATIALE for France.

This first analysis has shown that three main classes of flying test beds can be identified (Fig 10):

- existing missiles or (air-launched) target drones aiming at only few carefully selected specific flight test objectives (generally with axisymmetric bodies and limited Mach number range),
- autonomous small research vehicles (typically 1 to 5 tons) launched by available rocket boosters and capable of gliding flights,
- autonomous large multi-purpose vehicles (typically 20 to 50 tons) with self acceleration capabilities, but which can be launched from an aircraft.

Figure 10 highlights the fact that, even the use of existing small vehicles is expensive in an in-flight approach and with limited results. At the opposite, large vehicle can give nearly all the neccessary data but only on one configuration and at very high cost. The intermediate class seems a good compromise at the present time, in a phase without determined configuration and limited funds.
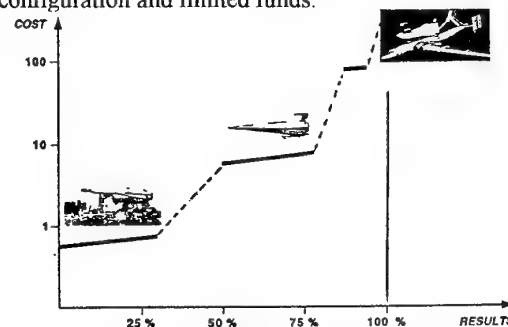
Figure 10
Classes of Flying Test Beds

RADUGA D2 (Fig 11), launched from a Russian Tupolev M22 is an example of the first class for the use of an existing flying test bed to perform « passenger »-type experiments. Even unmodified, only equipped with appropriate instrumentation, this vehicle can provide data at low cost for some of the already mentioned hypersonic test objectives, especially for providing aerothermodynamic data: heatfluxes, transition, ...

Main characteristics
* Tu22M-3 carrier aircraft
* separation Mach number Ma = 1.7
* maximum Mach number Ma = 6+
* overall lenght 11.7 m
* wing span 3.0 m
* gross mass 5.7 tons

Achieveable test objectives
* obtain in-flight acquired data base
* validation of design tools (e.g. prediction of transition and heatloads)
* heat resistant materials and structures
* familiarization with FT techniques for hypersonic speeds and FT infrastructure
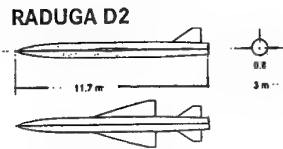
RADUGA D2

Figure 11
Russian RADUGA D2

The next figure recalls that these small flying test beds can be theoretically launched with various means in order to reach the required Mach number:

- supersonic carrier, such as American SR71,
- subsonic carrier and parachute dragging,
- vertical rocket booster,
- balloon dropping (« falke-type »).
  Advantages and drawbacks are highlighted on this figure.

Figure 12
Launch Alternatives

Figure 13 shows two projects concerning the second class of flying test beds; the first one « EDITH » is designed by AEROSPATIALE for flight up to Mach 8 approximatively and the second one « IGLA » by CIAM and NPO Mash in Russia. This last one can attempt Mach number over 15. The next figure represents the trajectories for this second class flying test beds. A rocket booster is used for a vertical lift-off; then, the flying test bed is separated. Two solutions can be proposed depending on the relative flying test bed size:

- if the vehicle is small enough versus the booster, it can be located in the booster's nose fairing (this leads to a classical launch of the existing booster without complementary studies),
- if not, the flying test bed is located just on the top of the booster (in that case, the launch phase requires a more detailed analysis as the booster is not validated for such a configuration).

According the booster capabilities, a suborbital flight is possible or not. All the measurements are possible during a gliding phase, continuously or step by step at approximatively constant Mach numbers; small engines can be used sometimes during this phase in order to keep constant flight parameters or new engines can be validated. The advantage of this concept is based on the first validation of the glider (without propulsion) then of the propulsion in the decceleration phase, without any constraints concerning the thrust - drag balance. This point is essential at the step of validation of a new engine. Parachutes are used for the recovery phase.
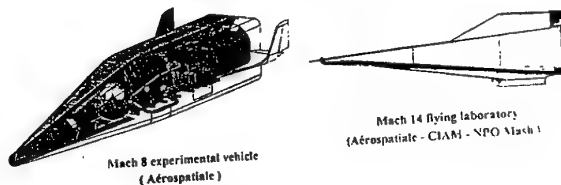

Figure 13
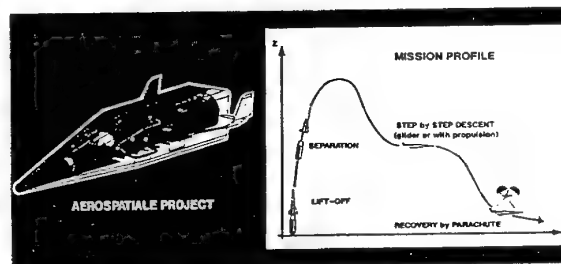**Intermediate Class Flying Test Beds**

Figure 14
Intermediate Class Flying Test Bed Trajectory

In the FESTIP Program, an overview of possible flying test beds has been given. Figure 15 shows some examples of the main vehicles studied for demonstrating reusable rocket technologies, materials, structures and operations. We find again three classes according the number of rocket engines. A progressive approach is envisaged with small vehicles at the beginning, then a large vehicle for reusability study flying at moderated Mach number (~ 4) in a first step, then above (~ 8) in a second one with adjunction of complementary boosters.

light
erimentation:

Experimental Vehicle
(Booster needed for Ma$_{max}$)

Experimental Vehicle
(Baseline Configuration)

Figure 15
FESTIP Approach

5. CONCLUDING REMARKS

For the preparation of the future, at medium and long term, research in hypersonics is mandatory and must be ambitious in front of this large challenge. Obviously, a very large part of this work must be performed on ground. Experimental and theoretical approaches must be performed in parallel, but with continuous data exchanges.

In flight tests are also mandatory because on ground tests have various limitations. Large test facilities are very expensive (buildings, test benches, energy for tests, ...) and consequently the size of models are limited. There are also some technological constraints:

- size limitations taking into account high pressure, high temperature, ...
- limitation of available power,
- limitation in test time taking into account required storage volumes.

We can add some physical limitations for hot air simulation with characteristics which are not representative of the flight (i.e: water vapor, ...), and human constraints giving limitations due to safety issues (i.e.: hydrogen in a confined space, ...).

Obviously, flight testing may also not allow to solve all problems which cannot be studied on ground, because it also has some limitations:

- depending on the experimental vehicle type,
- in function of the possible measurement techniques (external and on- booard),
- in particular, for an accurate determination of flight environment (Air Data System).

In conclusion, the need of flight testing is accepted by all the countries which are preparing the future space launchers, as shown by the current international context:

- several programs in US,
- flight testing going on in Japan,
- proposals performed in the frame of FESTIP by some European countries,
- bilateral proposals available in a French-Russian context.

Most of current proposals and programs are facing cost difficulties, so an international cooperation is necessary in order to engage flight testing, mandatory step for the preparation of future hypersonic vehicles.

6. REFERENCES

G. LARUELLE - R. THEVENOT
Future Space Transportation Systems: a Focus Point for Technological and Scientific Progress.
IAF - 94 - V.4.548
Jerusalem, Israel - October 9 -14, 1994.

G. LARUELLE
AEROSPATIALE's Implication for Reusable Launch Vehicles.
International Workshop on Spaceplane/RLV Technology Demonstrators.
Tokyo, Japan - March 10 - 12, 1997.

P.SACHER - R. THEVENOT
Key Points for Future Space Transportation Systems.
AIAA - 95 - 6007
6th International Spaceplanes and Hypersonic Systems & Technologies Conference
Chattanooga, USA - April 3 - 7, 1995.

F. FALEMPIN - P. GIRARD - P. VANCAMBERG - H. JOUBERT - R. THEVENOT
Hypersonic Air-Breathing Propulsion: Flight Test Needs.
AIAA - 95 - 6013
6th International Spaceplanes and Hypersonic Systems & Technologies Conference
Chattanooga, USA - April 3 - 7, 1995.

JL. HUNT - G. LARUELL E - A. WAGNER
Systems Challenges for Hypersonic Vehicles.
AGARD Conference C37.
Palaiseau, France - April 14 - 18, 1997.

NASA Hypersonic X-Plane Flight Development of Technologies and Capabilities for the 21st Century Access to Space

John W. Hicks and Gary Trippensee
NASA Dryden Flight Research Center
Code P/M.S. D-2102, P.O. Box 273
Edwards, CA 93523-0273, USA

ABSTRACT
A new family of NASA experimental aircraft (X-planes) is being developed to uniquely, yet synergistically tackle a wide class of technologies to advance low-cost, efficient access to space for a range of payload classes. This family includes two non-air-breathing rocket-powered concepts, the X-33 and the X-34 aircraft, and two air-breathing vehicle concepts, the scramjet-powered Hyper-X and the rocket-based combined-cycle flight vehicle. This report describes the NASA vision for reliable, reusable, fly-to-orbit spacecraft in relation to the current space shuttle capability. These hypersonic X-plane programs, their objectives, and their status are discussed. The respective technology sets and flight program approaches are compared and contrasted. Additionally, the synergy between these programs to advance the entire technology front in a uniform way is discussed. NASA's view of the value of in-flight hypersonic experimentation and technology development to act as the ultimate crucible for proving and accelerating technology readiness is provided. Finally, an opinion on end technology products and space access capabilities for the 21st century is offered.

1. NOMENCLATURE

ALT	approach and landing test
ATD	advanced technology demonstrator
CAN	Cooperative Agreement Notice
CFD	computational fluid dynamics
DoD	Department of Defense
DFRC	Dryden Flight Research Center, Edwards, California
ELV	expendable launch vehicle
FADS	flush airdata system
GPS/DGPS	differential global positioning satellite system
HTT	high-temperature tunnel
INS	inertial navigation system
JSC	Johnson Space Center, Houston, Texas
KSC	Kennedy Space Center, Cape Canaveral, Florida
LaRC	Langley Research Center, Hampton, Virginia
LOX	a propellant mixture composed of liquid hydrogen and oxygen
MSFC	Marshall Space Flight Center, Huntsville, Alabama
NASP	National Aerospace Plane
NRA	NASA Research Announcement
OSC	Orbital Sciences Corporation, Dulles, Virginia
PTO	Participating Test Organization
RBCC	rocket-based combined-cycle
RTO	Responsible Test Organization
RLV	reusable launch vehicle
SCA	Shuttle Carrier Aircraft
SSTO	single stage to orbit
STS	Space Transportation System
TPS	thermal protection system
TSTO	two stage to orbit
WSMR	White Sands Missile Range, New Mexico

2. INTRODUCTION
Through its Department of Defense (DoD) and National Aeronautics and Space Administration* (NASA) joint experimental aircraft programs, the United States has striven to develop advanced aircraft technologies and push the frontiers of flight through the use of unique, experimental aircraft. Since the X-1 beginning in 1945, these aircraft have been designated "X." These nonproduction, nonmission-oriented flight vehicles were designed to be one-of-a-kind flying laboratories that focused on solving special flight problems or developing specific technologies that might or might not find their way onto future applications. High risk and tailored to the special aeronautics problem at hand, these X-planes tackled aeronautics firsts, such as breaking the sound barrier, achieving supersonic and even hypersonic manned flight to better than Mach 6.0, and reaching altitudes in excess of 100,000 to 300,000 ft (ref 1). Technology firsts included variable-sweep wings, forward-swept wings to supersonic speeds, advanced metallic alloys for primary structure, gimbaled jet and rocket engines, and numerous other never-before-flown technologies.

3. NASA SHUTTLE AND THE QUEST
During the 1950's and 1960's, the U.S. relied heavily on expendable launch vehicles (ELV) to launch a variety of payloads and humans into Earth orbit. This expensive launch mode limited payload size and weight because of rocket payload bay sizes and, most importantly, payload weight

---

* NASA was known as the National Advisory Committee for Aeronautics (NACA) in the 1940's and 1950's.

fraction available. Required propellant fractions of up to 89 percent of the launch weight of the vehicle naturally limited what weight fraction could be made available for payload, which amounts to approximately 1.0 to 2.5 percent at liftoff. Launch operations were extensive and complex, resulting in large manpower requirements at fixed launch sites.

Starting in 1963, NASA began to develop the space shuttle as a means of providing recoverable, reusable launch capability with large payload size and lift performance (fig 1). This goal was successfully realized in 1977 when NASA carried out its approach and landing test (ALT) series of the space shuttle atop the Boeing 747 Shuttle Carrier Aircraft (SCA) (fig 2). This shuttle prototype, the *Enterprise*, was not spaceworthy. Launches were limited to subsonic speeds at altitudes of 25,000 ft to test its low-speed recovery characteristics and landing techniques. The first orbital launch of the shuttle Space Transportation System (STS-1) involved the *Columbia* in mid-April 1981.

Figure 1. NASA shuttle landing.

Figure 2. NASA shuttle on the Boeing 747 Shuttle Carrier Aircraft.

Although reusable, the aircraft-like shuttle can not takeoff and accelerate by itself to orbital escape velocity. It still requires lift to orbit by the expendable main propellant tank along with two solid rocket boosters side-mounted to the main propellant tank. These boosters are recoverable after ocean splash down and are reusable after refurbishment. Figure 3 shows the total launch
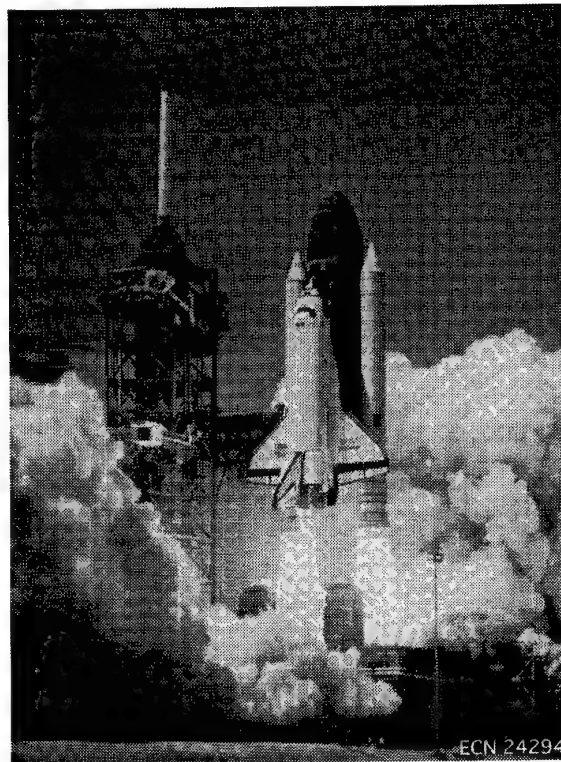
Figure 3. Shuttle launch configuration.

configuration. Free-flight recovery of the shuttle upon return from orbit is normally accomplished at either the Cape Canaveral launch site at the NASA Kennedy Space Center (KSC) in Florida or at the Dryden Flight Research Center (DFRC) at Edwards Air Force Base in California.

With mostly 1960's and early 1970's capabilities, the rapidly aging shuttle fleet is technologically out-of-date, costly, and labor intensive to operate. Thousands of people are required at KSC, Johnson Space Center (JSC) in Houston, Texas, and other facilities to conduct launch and space operations, including recovery back to Earth. Launch costs are controversial and subject to the cost-accounting methodology. Each launch has been estimated to cost at least $400 million, resulting in payload costs of $7000 to $8000 per pound. This is very comparable to the historical ELV experience as shown in table 1 (ref 2). An objective of future reusable launch

Table 1. Expendable launch vehicle payload costs in 1994 dollars (ref 2).

Launch vehicle	Payload to 160 n.m. due East, lb	Payload, $/lb
Delta	10,100	3960
Atlas Centaur	18,100	6077
Titan III	27,000	4815
Titan IV	44,400	4054
Ariane	21,000	5238
Long March	15,200	1646
Proton	38,000	1974
Zenit	28,000	2500
Saturn V	270,000	4241
INT 21	250,000	2533

vehicles (RLV), such as the X-33 Advanced Technology Demonstrator (ATD), is to reduce payload costs by a factor of 10 or better to ultimately approximately $200 to $300 per pound. Launch and flight operations for the shuttle are complex and extensive, resulting in less-than-desirable flight turnaround or launch rates with 4 vehicles of at best approximately 8 to 10 launches per year (ref 3).

The NASA desire to carry out its space mission "faster, better, cheaper," as the NASA Administrator has phrased it, has encouraged the agency to not only look for reduced cost and simplified launch systems but also to avoid heavy reliance on supplemental boost systems to carry the flight vehicle to orbit. The NASA goal for RLV's has become a class of self-boosting flight vehicles similar to aircraft which can carry a range of payload types and weight classes to orbit on their own and return to Earth to a horizontal landing. These activities are to be performed with much smaller launch crews, with more rapid turnaround times, and at greatly reduced costs. The critical operations cost reduction issues for these RLV's is to achieve high "on-demand" launch frequency, such as the shuttle's original 25 to 50 flights per year goal, and high launch reliability, better than 98 percent.

The multi-stage-to-orbit shuttle configuration has an intended operational cycle only to the turn of the century (approx-imately 2012). In recent years, studies have been conducted to replace its complex, expensive operation with either single-stage-to-orbit (SSTO) or two-stage-to-orbit (TSTO) systems that can reduce operational and thus payload costs by a minimum of one order of magnitude. Based on available or envisioned technologies expected within the next couple of decades, numerous national and international studies proved inconclusive as to whether SSTO or TSTO is the most economically viable approach for the foreseeable future over the range of required payload weights. For example, the X-33 ATD is an SSTO concept with large payload potential, and the X-34 aircraft is a TSTO concept for small payloads

with two stages within the X-34 configuration itself, air-launched from an L-1011 aircraft.

The U.S. National Aerospace Plane (NASP) X-30, begun in 1985, was an attempt to develop an SSTO concept using multiple propulsion cycles centered around the dual-mode ramjet–scramjet (fig 4). Rather than an incremental technology and flight research program, the X-30 was an attempt at a full-scale operational prototype vehicle system development. This program tried to encompass the complete development range from almost basic research to prototype flight test of the X-30 for SSTO within a single program and time frame. The goal was to achieve first flight by the early 1990's. However, it soon became apparent that the required air-breathing technology set was much too large and evolving at different stages to achieve a mission-capable vehicle even by the beginning of the 21st century without a massive national effort.

Two things were clear from the legacy of the NASP program when it was canceled in November 1994. First and foremost was the realization that a great deal of development work on scramjet propulsion systems, materials, other systems, and thermal management needed to be completed before a vehicle similar to the X-30 could be built. A large part of this development involved the complex engine-airframe integration technology. The crucial ingredient of early flight test and demonstration of incremental subsets of the needed technologies, beginning with the scramjet itself, would be required before going to a full vehicle system development program. Finally, an operational, next-generation, reusable launch system would be needed in the meantime by the beginning of the 21st century to replace the aging shuttle until the air-breathing access-to-space technology set and vehicles could be developed.

For the hypersonic speed regime, a near-term solution could only mean non-air-breathing rocketry in vehicles with improved system performance, reusability, reliability, and much lower operational costs. This need led to the idea to
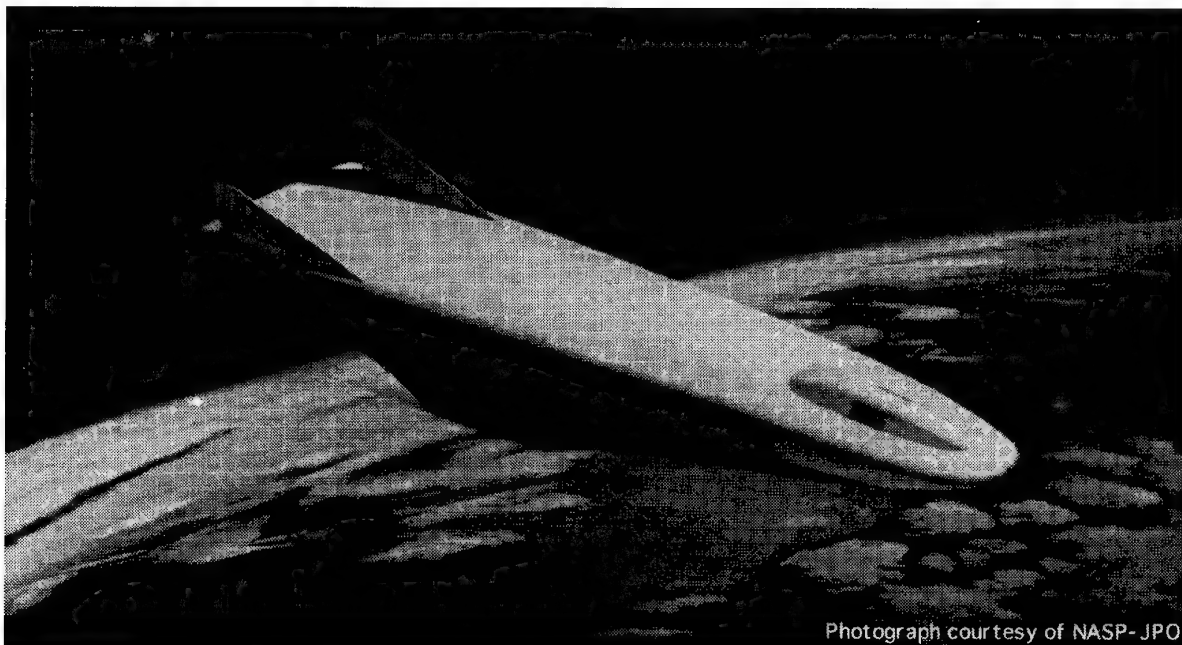
Photograph courtesy of NASP-JPO

Figure 4. National Aerospace Plane X-30.

develop the X-33 and X-34 concepts by the end of the 20th century for go-ahead decisions for operational versions early in the 21st century.

3.1 Today's Approach Behind NASA's X-Plane Access-to-Space Family

The U.S. National Space Transportation Policy (ref 3) directs NASA to lead the technology development and flight demonstration of next-generation, reusable STS's. The objective is to support government and private sector decisions for operational to-Earth-orbit space vehicles and the commercialization of reusable launch systems and near-Earth-orbit space use of a number of industrial and commercial endeavors.

The overall objective for low-cost, recoverable, and reusable access to space is to reduce payload costs to approximately $200 per pound. Another goal is to increase empty vehicle weight payload fractions toward around 35 percent, which is comparable to military cargo aircraft, such as the C-5A or C-141A. Included in this vision is rapid launch turnaround with operations similar to aircraft and small ground launch crews which do not exceed a few dozen people. Whether vertical or horizontal launch, the recovery is by horizontal landings similar to those executed by airplanes. Such recoveries could be completed at numerous sites around the world.

Realization of this agency goal requires development of new, advanced materials, including new thermal protective systems for increased atmospheric heat loads; lightweight, rugged structural fabrication techniques; and advances in vehicle propulsion systems and other vehicle subsystems, especially in guidance and control. Needed advances in propulsion systems include non-air-breathing rockets and hypersonic air-breathing systems, such as the scramjet and its close relative, the rocket-based combined-cycle (RBCC) engine. Developing new operational techniques and infrastructures to maximize use of these advanced technologies is also required.

Instead of massive developmental programs with expensive, highly system-integrated flight vehicles, future research flight vehicles need to be simpler and less costly. Guided by the NASA Administrator's vision, today's family of hypersonic X-plane concepts share common characteristics and approaches. One commonality that has perhaps the greatest challenge is the use of rapid prototyping concepts to develop and fly vehicles in 2 to 3 years from contractual go-ahead. This challenge will make the programs very aggressive, fast paced and require acceptance of increased risks to achieve program goals. The focus is on flight demonstration of a specific set of technologies and efficient, cost-effective operations rather than full-scale vehicle system development of a production, mission-sized vehicle. As a consequence, the approach emphasizes subscale, unmanned, autonomous, or remotely piloted vehicles to be flight tested at reduced cost and risk. These experimental "X" vehicles are to cost in the tens to low hundreds of millions of dollars instead of perhaps billions as was becoming apparent for building the NASP X-30 vehicle.

Experimental flight vehicles are the critical link in the ultimate validation of design methodologies for future mission applications and of an integrated vehicle system's operational capability. Flight test often reveals and hopefully solves many design issues and systems problems that were not discovered during the initial design and ground test series. In many cases, technologies and their integrated effects can only be truly

evaluated in flight. Real operating envelopes and conditions (such as real gas effects, actual atmospheric Reynolds numbers, and accurate enthalpy conditions) can only be found under actual flight conditions. Hypersonic design and analysis codes, databases, and test methodologies are immature for the development of fully operational vehicles, especially in the air-breathing class. Computational fluid dynamics (CFD) codes need further validation for aerodynamics and propulsion above hypersonic speeds, including embedded mathematical models, algorithms, and computational techniques. Ground test techniques and advanced wind-tunnel facilities are needed above Mach 8.0, and again especially for larger scale vehicles or integrated systems. The crucial test of a technology's promise is thus validation through the classical triad of correlation of flight test, ground test, and predictive analysis results.

4. X-33 REUSABLE LAUNCH VEHICLE PROGRAM DESCRIPTION, OBJECTIVES, AND STATUS

The X-33 program began with a NASA Cooperative Agreement Notice or CAN (CAN 8-3) issued by the Marshall Space Flight Center (MSFC) Huntsville, Alabama, in April 1996 (ref 4). A contract was awarded to Lockheed-Martin, Palmdale, California, in July 1996 by the MSFC after the competitive phase. The X-33 ATD (fig 5) is a one-half scale lifting body-type flight version of an envisioned operational vehicle known as *VentureStar*. The flight vehicle length is approximately 70.0 ft with a wingspan of approximately 72.0 ft and a small 6.0 ft wide × 12.0 ft high payload bay. The X-33 is launched vertically from Edwards Air Force Base, California. After an overland flight, it can be recovered in a horizontal landing at several planned landing sites at locations ranging from California to Utah to Montana. Fifteen flights are planned as the flight envelope is expanded to suborbital speeds up to Mach 15. Its newly developed J-2S linear aerospike rocket propulsion system (fig 6) has a sea-level thrust rating of 205,000 lb and uses a propellant mixture composed of liquid hydrogen and oxygen (LOX). Two engines are used to propel the X-33. No X-33 return flight to the original launch site is planned; instead, the vehicle will be returned to Edwards Air Force Base atop the SCA.

As with the X-34, the X-33 will fly as an advanced technology demonstrator to investigate and emphasize the operational

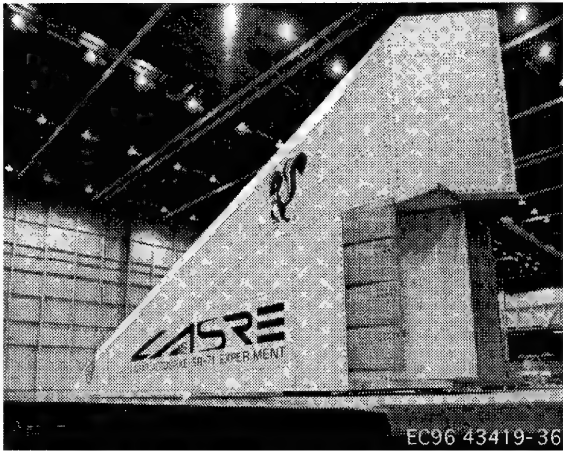

Figure 5. Lockheed-Martin X-33 flight vehicle.

Figure 6. X-33 J-2S linear aerospike rocket engine.

feasibility aspects for a full-scale version with a potential 25- to 50-percent reduction in development and production costs and empty vehicle weight payload fractions approaching 10 to 12 percent. (Maximum potential takeoff gross weight payload fraction is about 2 percent.) The X-33 is heavily focused on operational demonstration of a low-cost, reliable aircraft-like SSTO rocket system, requiring a ground crew of 50 people or less. In addition to the 15-flight demonstration under main engine rocket power up to at least Mach 15 with a minimum of two of those flights at or above Mach 15, operational

demonstration includes 7-day turnaround from landing to preflight on three consecutive flights and a 2-day turnaround from landing to reflight at least once.

Technology demonstrations include advanced reusable cryogenic propellant tank systems, such as with aluminum-lithium and graphite composite materials. Other advanced technologies to be incorporated include composite primary vehicle structure, new propulsion features of the rocket engine, advanced thermal protection system (TPS) with metallics and ceramics, and advanced vehicle system and structure health-monitoring methods.

First flight is planned for March 1999 (fig 7). A 2-week turnaround for reprocessing the vehicle between flights is to be demonstrated. The DFRC is a flight research Participating Test Organization (PTO) and, along with the contractor team, has formed a flight team at Edwards Air Force Base. DFRC is involved in the design and test support of the X-33 and in the development of the range and range communications. The Air Force Flight Test Center will conduct preflight ground tests and subsystem checkout, flight envelope expansion, X-33 vehicle recovery back to Edwards Air Force Base, and range operations. The flight envelope will be systematically expanded outbound from Edwards Air Force Base in a northeasterly direction toward Montana, up to Mach 15.

5. X-34 PROGRAM DESCRIPTION, OBJECTIVES, AND STATUS

The X-34 program began with a NASA Research Announcement or NRA (NRA-14) issued by the MSFC

Activity/task	FY96 O N D J F M A M J J A S	FY97 O N D J F M A M J J A S	FY98 O N D J F M A M J J A S	FY99 O N D J F M A M J J A S	FY00 O N D J F M A M J J A S
Aerodynamic instru. req. proposal	▼				
Computer model server setup	▼				
Provide FADS conceptual design		▼			
DFRC SIM hosted on ONYX comp.		▼			
Range requirements defined		▽⋯▽			
LASRE test complete		▽⋯⋯⋯▽			
Provide FADS preliminary design		▽			
Range design complete		▽			
Range system ready for integ. and test			▽		
Contractor award	▼				
Vehicle PDR		▼			
CDR		▽			
Launch pad construction complete			▽		
X-33 rollout			▽		
X-33 1st flight				▽⋯▽	
X-33 flight test				▬▬▬▬▬	
X-33 flight test complete					▽

970257

Figure 7. X-33 flight program schedule.

in March 1996 (ref 5). After competitive selection in the summer of 1996, a contract was signed in August with Orbital Sciences Corporation (OSC) of Dulles, Virginia, as the prime contractor to develop and flight demonstrate the X-34 vehicle (fig 8). DFRC is a PTO for this program.

The flight vehicle will be a one-half scale test bed version of an operational concept and is approximately 58.3 ft long with a wingspan of 27.7 ft and height of 11.5 ft. Two vehicles will be built and air-launched at subsonic speeds from the OSC L-1011 aircraft (fig 9). The X-34 will be rocket-boosted by a single NASA MSFC-developed Fastrac rocket (fig 10) to Mach 8.0 at or above an altitude of 250,000 ft. Rocket thrust rating will be 60,500 lb, using a LOX and kerosene propellant mixture.

Flight operations for the first two flights is planned at the White Sands Missile Range (WSMR), New Mexico, within 4 months of each other, including air-launch and landing recovery. An optional phase for operational demonstration of this aircraft-like concept with up to 25 flights in 1 year is also planned as a follow-on effort out of either WSMR or KSC.

Operational demonstration objectives include up to 25 autonomous flights per year to a recoverable landing with low-cost operation, small ground crews, and rapid flight vehicle turnaround. Safe abort capability to an alternate landing site or under emergency flight termination conditions, such as engine out, propellant dump, or subsystem failure, is also planned for demonstration. In addition to the operational flight envelope (Mach 8.0 to or above an altitude of 250,000 ft), the X-34 is to flight demonstrate such anticipated flight environments as landing in crosswinds up to 20 knots and subsonic flight through rain and fog.

Technology demonstration objectives include composite structures for the airframe; propellant tanks and cryogenic systems; and propellant system lines, ducts, and valves. Other technologies include advanced TPS, advanced low-cost avionics, rapid low-cost flight software development tools, and integrated vehicle health-monitoring systems with advanced sensors and software algorithms. Autonomous flight control and guidance and navigation will be provided by an integrated inertial navigation system (INS) and a differential global positioning satellite system (GPS/DGPS). Airdata will be furnished by a fuselage-mounted Flush Airdata System or FADS. The vehicle also will have the potential to act as a hypersonic test bed for other advanced propulsion concepts, such as the rocket-based combined-cycle engine, the pulse detonation wave rocket engines, and other advanced materials and system.

First flight is scheduled for September 1998 at WSMR with a MSFC and OSC flight team. After the second flight in January 1999, a decision will be made as to whether or not to conduct the next 25 operational demonstration flights and, if so, where. These flights will have a nominal turnaround of approximately 2 weeks, but plans include demonstrating a surge capability of two flights in 24 hr. Potential flight-test sites for that phase include the KSC and DFRC.

6. ROCKET-BASED COMBINED-CYCLE ENGINE AND FLIGHT VEHICLE DESCRIPTION, OBJECTIVES, AND STATUS

The RBCC engine is the ultimate integration of air-breathing and rocket propulsion cycles into a single configuration or flowpath. It combines the ramjet and scramjet air-breathing engine cycles in the high supersonic to mid-hypersonic speed range with an integral rocket system that can perform as a low-speed system in the subsonic to supersonic range and in the high hypersonic range above the scramjet operating regime. The MSFC RBCC program began in the summer of 1996 with the selection of four engine companies to pursue advanced ground and potentially flight development of candidate engine concepts. These companies include Aerojet, Kaiser Marquardt, Rocketdyne, and Pratt & Whitney. In addition, Pennsylvania State University provides support in CFD analysis and component laboratory tasks.

Figure 8. OSC X-34 flight vehicle.
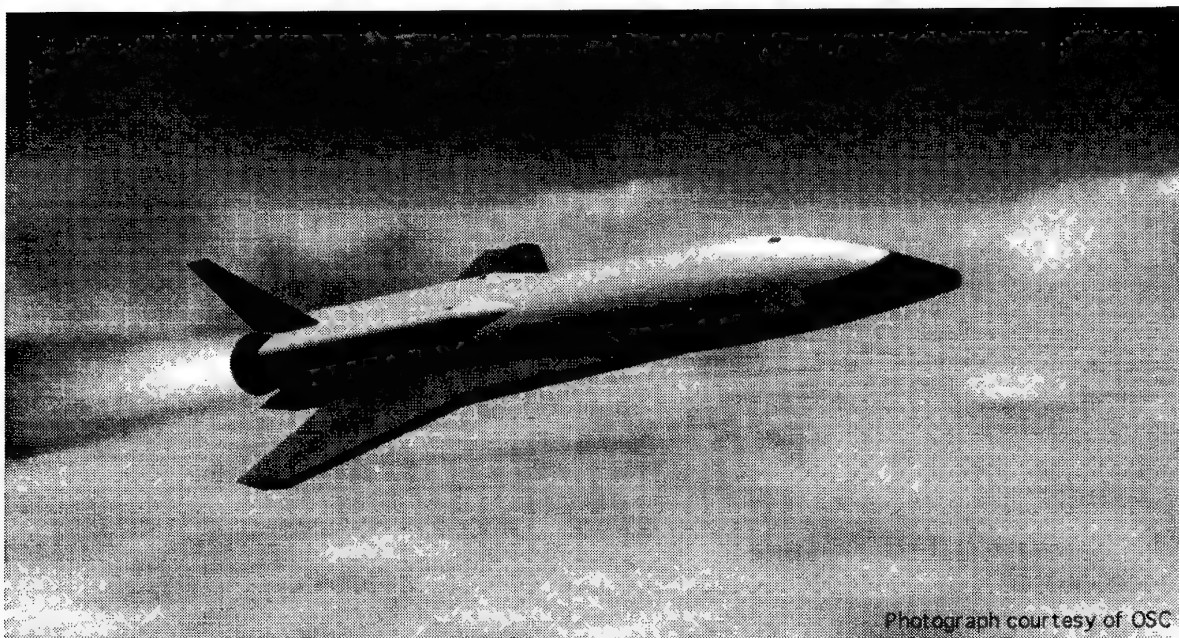
Photograph courtesy of OSC

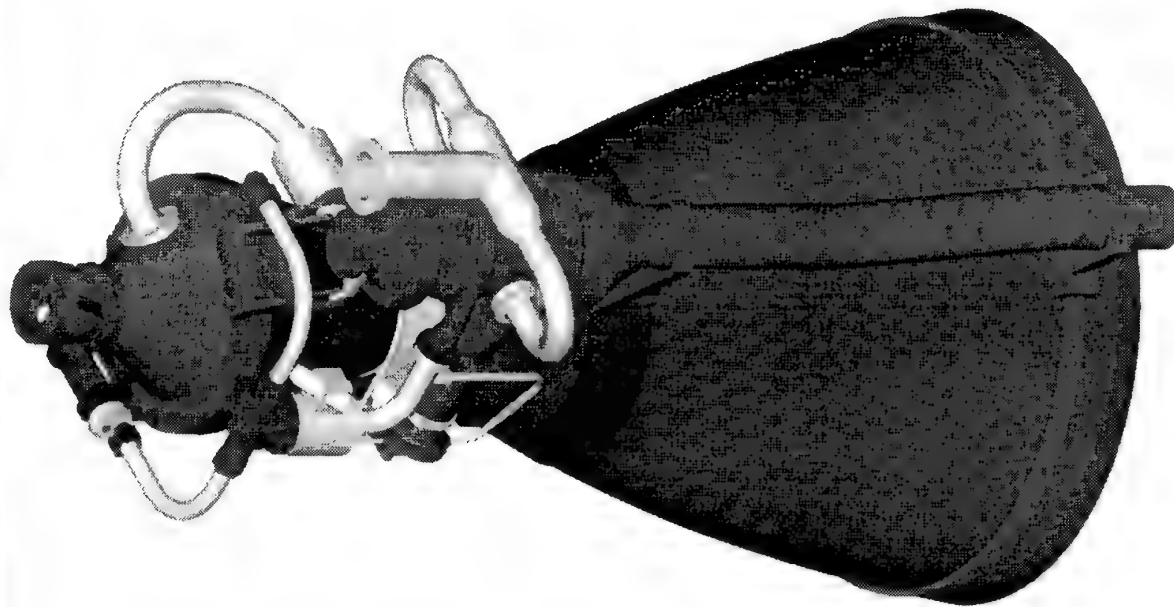Figure 9. OSC L-1011 Pegasus launch aircraft.

Figure 10. NASA MSFC Fastrac rocket engine. (Drawing courtesy of Marshall Space Flight Center, Huntsville, Alabama.)

A prototype aircraft is being studied as a possible follow-on flight research program to develop integrated designs of large-scale versions of the RBCC with an airframe. If such an integrated system were built, it would not occur until after the turn of the century, depending on NASA budgets and outcomes of preliminary studies. Current discussions include from two to four fairly large flight vehicles costing several hundred million dollars each. In the meantime, MSFC is seeking opportunities to fly smaller scale versions of the RBCC engine on existing program vehicles, such as the Hyper-X or X-34. Unlike the RBCC flight vehicle, the Hyper-X and X-34 vehicles are not optimally integrated airframes for the RBCC but would serve as simple airframe test beds to obtain measured data under true flight conditions.

The initial technology objectives center on evaluation of the integrability of multiple engine modes to smoothly transition over the largest practical speed range up to orbital speeds. An additional objective involves designing flight-weight engine structures and materials that could be carried on to airborne test platforms. Basically, the low-speed system consists of air-augmentation of a basic rocket through an inlet up to approximately Mach 3. At that point, the rocket would be throttled down to allow an air-breathing ramjet cycle to take over operation from approximately Mach 3 to Mach 6. At this point, the scramjet cycle would take over to Mach 10 or above. Beyond approximately Mach 10, the air-breathing flowpath would be closed off by the inlet and transition back to rocket

operation. The rocket cycle would then use its onboard oxidant to achieve final orbit insertion.

In addition to planned wind-tunnel ground tests over the next 4 years, studies are considering captive-carry flight tests of some concepts on such flight platforms as the SR-71 aircraft up to Mach 3.0 at dynamic pressures up to approximately 800 to 1000 lb/ft^2. Current plans center on engine-only ground tests beginning in 1997 through 1999. Possible SR-71 flight tests would begin in late 1998 or later. Prime candidates out of this test phase could be flight tested on the Hyper-X or the X-34 around the year 2000. Follow-on, large-scale testing on an integrated RBCC flight vehicle may occur after 2001.

7. HYPER-X PROGRAM DESCRIPTION, OBJECTIVES, AND STATUS

The Hypersonic Experiment or Hyper-X vehicle is being developed in a phase 1 effort to flight validate the air-breathing, dual-mode scramjet at speeds up to Mach 10.0. It is a joint project between NASA Langley Research Center (LaRC) of Hampton, Virginia, and NASA DFRC. DFRC is the Responsible Test Organization (RTO) for this program.

Using a NASA baseline vehicle design and wind-tunnel ground tests, a competitive phase for fabrication and development of the four flight vehicles was held in the fall of 1996. A contract was awarded in mid-March 1997 to begin a 9-month vehicle fabrication phase. The small, expendable vehicles (fig 11) will be approximately 12.0 ft long, have a 5.0-ft wingspan, and include a single hydrogen-fueled scramjet engine. The simple

Figure 12. OSC Pegasus launch vehicle.

Figure 11. NASA Hyper-X flight vehicle.
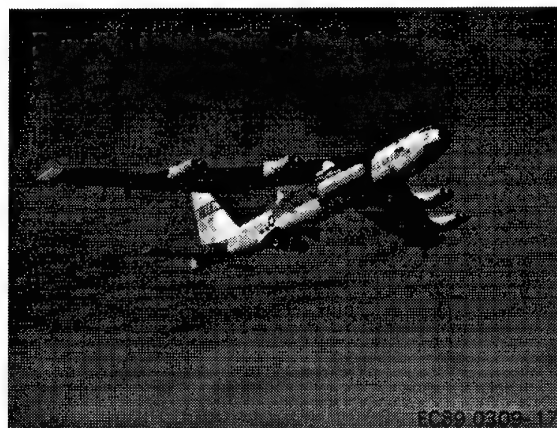
Figure 13. NASA B-52B carrier aircraft with Pegasus booster.

airframe is of cold structure design overclad with TPS. The engine is not actively cooled other than water-cooled leading edges and inlet ramp door, and the combustor is of copper heat-sink construction . It is rocket-boosted to its flight-test regime between Mach 5.0 and Mach 10.0 using the Orion 50S first stage of the OSC Pegasus launch vehicle (fig 12). The entire launch stack is air-launched from the NASA DFRC B-52 carrier aircraft (fig 13).

The variable engine geometry normally required for an air-breathing engine to cover a wide speed range, such as that for the Hyper-X, will be resolved by using incrementally fixed geometry engine designs for each discrete aim Mach number test condition. The airframes will be of a single external

aerodynamic shape. This design simplifies the vehicle system and reduces costs. An open–closed inlet ramp door will be the only variable engine geometry to allow inlet starting. This inlet door will be closed on the rocket-boost ascent and after the engine test phase for descent and flight-test termination.

In addition to the limited wind-tunnel ground tests and design analysis efforts planned as with the X-33 and X-34 for correlation with flight measurements, the Hyper-X program has the unique plan of full-scale wind-tunnel testing of the first flight vehicle at Mach 7.0 in the LaRC 8-ft High-Temperature Tunnel (HTT) facility in the early spring of 1998. The Mach 5.0 vehicle will also be tested in the 8-ft HTT before its actual flight. The vehicle test will include the complete operating systems, including operational test of the scramjet engine with hydrogen fuel.

The test stack configuration will be launched by the B-52 airplane at nominally Mach 0.8, at an altitude of 40,000 ft, and over the water off the California coast. Flight phase termination is planned on or near San Nicolas Island and the Channel Islands offshore from Los Angeles, California. At this time, there are no plans to require recovery of the flight vehicles from a potential water impact; however, such plans are not excluded.

Unlike the X-33 and X-34, the Hyper-X program focuses on technology flight validation rather than operational demonstration. No operational mission is envisioned for this purely research vehicle. The Pegasus first-stage booster is merely intended to transport the experimental vehicle to its test conditions because the scramjet cannot operate by itself below the high supersonic to hypersonic speed regime. Primary technologies consist of the scramjet and its in-flight performance and the engine-airframe integration methodology. Through flight-to-ground data correlation of ground-test and flight-test results with pretest predictive analysis, a key objective is to develop and validate hypersonic air-breathing vehicle design methods, tools, and databases to be used for future air-breathing flight vehicles.

Aim flight-test conditions for the engine evaluation phase are planned at Mach 5.0, Mach 7.0, and Mach 10.0 to afford direct correlation with ground tests. First flight will be with the Mach 7.0 vehicle followed by the Mach 5.0 vehicle and finally both Mach 10.0 vehicles. One Mach 10.0 configuration will represent an accelerator engine configuration, and the other will represent a cruise version. Nominal test dynamic pressure is 1000 lb/ft^2 which corresponds to an altitude of

approximately 100,000 ft. Small amounts of gaseous hydrogen fuel will be silane piloted for at least 5 sec of stabilized engine operation. This test sequence will be followed by engine shutdown and an unpowered descent for additional aerodynamic data down to subsonic flight conditions.

The first flight vehicle is in fabrication with completion expected by the end of 1997. Figure 14 shows the schedule. One vehicle per year thereafter will be built for subsequent flights of one per year. After the NASA LaRC 8-ft HTT wind-tunnel test in the spring of 1998, the first flight vehicle will be delivered to DFRC for preflight preparations beginning in May 1998. After additional ground tests, system checkout, and booster integration, the first flight is planned for December 1998.

8. UNIQUE YET COMMON TECHNOLOGY PATHS AND THEIR SYNERGY

These programs are tackling similar, related hypersonic technologies brought about by the common flight envelopes, similar thermal environments, and ultimate mission applications. Yet unlike the NASP X-30 program, no single program is attempting to combine the broad spectrum of technologies possible. Such an attempt would result in greatly increased costs, program complexity, and developmental lead times and in unachievable objectives. These programs are separated into two major classes: near-term operational concepts for a range of payload classes that can capitalize on more mature rocket propulsion technology and other concepts to equivalently progress air-breathing technologies that can be
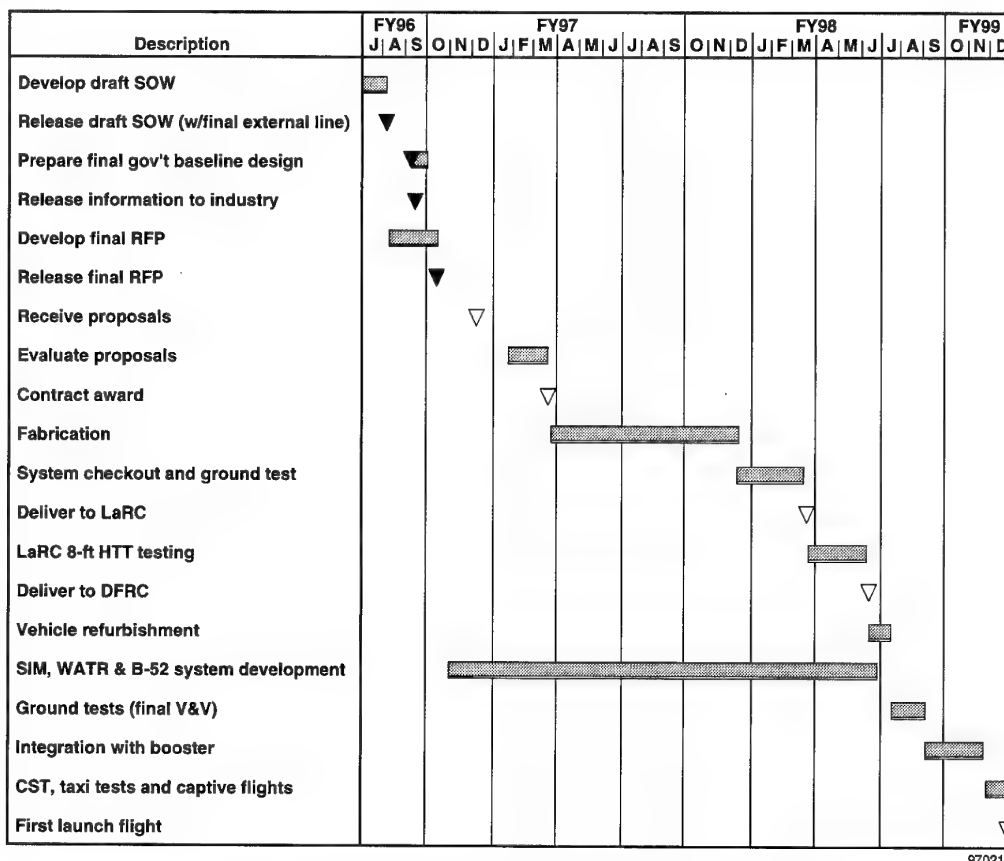
Figure 14. Hyper-X flight program schedule as of February 1997.

applied in the long term future for air-breathing space access. For example, this approach leaves the Hyper-X program to isolate and focus on the air-breathing scramjet technology question without having to dilute efforts and funds with other needed technologies, such as advanced composites, that the X-33 and X-34 can pursue.

The combined fabric of the programs produces a technology synergy which can be shared now within the planned projects or reserved for future vehicle applications. The idea is akin to a divide-and-conquer approach to solving the myriad of technological and operational problems. The immediate benefit of this approach is obtaining near-term operational low-cost, reusable, highly reliable access-to-space vehicles for the turn of the century, while continuing to pursue the ultimate goal of air-breathing access-to-space vehicles. Only air-breathing concepts offer significant promise of large reductions in required propellant fractions, increased payload fractions, and reduced-size vehicles with operations and infrastructure which are similar to aircraft.

9. CONCLUDING REMARKS

One lesson from the National Aerospace Plane program and other hypersonic research programs is that technologies and vehicle system concepts must be taken to early flight as the ultimate crucible of their viability and validation. This fact is true for all access-to-space, low-cost, reusable system candidates whether they be powered by non-air-breathing rockets or one of several air-breathing concepts. Another lesson learned is that such complex systems and highly integrated technologies are best tackled in a systematic, incremental series of steps in complimentary programs rather than in a very large, costly single operational prototype vehicle development effort. Too many technical unknowns and programmatic complexities exist to try to address the many issues, immature technologies, and design methods in a single massive program. The NASA family of experimental hypersonic X-vehicles is not only breaking down the complex technical issues into manageable pieces, resulting in reduced cost of experimental concepts, but also is achieving near-term program synergy and increased numbers of interim, at-hand solutions. Only time will bring out the best operational systems, hopefully in time to supplant the aging NASA shuttle fleet.

REFERENCES

1. Miller, Jay, *The X-Planes, X-1 to X-31*, Aerofax, Arlington, Texas, 1988.

2. McCurdy, Howard E., "The Cost of Space Flight," Space Policy, vol. 10, no. 4, Nov. 1994, pp. 2774.

3. U.S. Congress, Office of Technology Assessment, "The National Space Transportation Policy: Issues for Congress," OTA-ISS-620, Washington D.C., U.S. Government Printing Office, May 1995.

4. NASA, *X-33 Phase II: Design and Demonstration*, NASA Cooperative Agreement Notice 8-3, April 1, 1996.

5. X-34 NASA Research Announcement 8-14, March 27, 1996.

OVERVIEW OF PROPULSION PERFORMANCE

Frederick S. Billig
PYRODYNE, Incorporated
11280 Panorama Drive
New Market, Maryland 21774, USA

Introduction

Nearly forty years have passed since the concept of the supersonic combustion ramjet, *scramjet*, was first introduced. At that time, the exciting potential of airbreathing propulsion for both expendable missiles and highly efficient space launch systems were proposed. Conceptual vehicle designs, engine flowpaths, including methods for injection and flame stabilization, and estimates of cycle performance were developed. Calculations were made for typical climb and cruise trajectories which showed distinct advantages of the scramjet over all-rocket powered systems. In the intervening years, prior to the initiation of the National Aero-Space Plane (NASP), a significant technology data base had been established which had substantiated the levels of performance that had been predicted by the pioneers. Nonetheless, no system utilizing the scramjet propulsion system had been developed. On every occasion, when a selection between a scramjet and an all-rocket system had been made, the all-rocket has prevailed. Paradoxically, the NASP, which was to be a single stage access to orbit vehicle, never was required to consider an all-rocket-powered alternative. Unfortunately, NASP failed to meet its stated objectives, in part due to unforeseen limitations of the propulsion cycle, and the program was canceled. It is prudent to examine the underlying reasons for both the decision to cancel NASP and the reluctance to select scramjets for other applications.

The principal potential applications of scramjets are missiles, hypersonic cruise aircraft and access to space vehicles. Programs are currently underway in the United States and elsewhere which are intended to provide the technology that could lead to the development of vehicles for each of these applications. The HYPER X is managed jointly by the NASA Langley Research Center and Dryden which plan to flight test scramjet powered small scale vehicles that are representative of a hypersonic cruiser. Four vehicles are be boosted to "cruise" at Mach numbers between 5 and 10. The NASA Marshall Space Flight Center has initiated a program to develop technology for rocket based combined cycle engines intended for space access applications. Several concepts for combining rocket and airbreathing engines are being examined with the emphasis on rocket-ram-scramjets. Hypersonic scramjet missile technology is being supported by the United States Air Force at Wright-Patterson Air Force Base. If these or other

scramjet technology programs are to evolve to the development of operational systems, two conditions must unequivocally be met.

1) The scramjet powered vehicle must provide capabilities not achievable by all-rocket powered systems, and

2) On a life cycle cost basis, the system must be affordable.

Although many of the arguments that have been used to dissuade the development of the scramjet are political and economic, others are technical. This paper will address the technical issues with an objective of establishing a clear distinction between the inherent capabilities of rocket and airbreathing systems. Metrics will be introduced to develop the quantitative comparisons. Suggested solutions to alleviate problems and technical issues which have been raised that challenge the efficacy of the airbreather will be presented. The paper will conclude with a description of some innovative concepts for the design of highly efficient flowpaths for dual-mode ram-scramjet engines.

It is the author's opinion that basic technology programs must be complemented by aggressive efforts in vehicle conceptual design. Preliminary conceptual design of the vehicle not only provides guidance for the technology program, but helps to prevent unsubstantiated design decisions from being made. As typified by NASP, even the choice of the propulsion cycle needs to be justified. All too often, presumptive design constraints are adopted and all of the available resources are expended before a viable concept has been formulated. The access-to-orbit application is ideally suited to present some of the elements that constitute a viable strategy for vehicle conceptual design.

Background

Many of the fundamental parameters that describe the operating characteristics and performance of a broad spectrum of propulsion cycles, adequate for conceptual design, are in accessible literature. For example, a very good introduction to the use of ram-scramjet propulsion system for an access-to-orbit concept was presented at a joint ARS\IAS meeting held in Los Angeles, CA in *June 1961*[1]. This was one of the earliest comprehensive studies of the potential performance of the ram-scramjet engine cycle. It also presented considerable insight in the structural and cooling challenges that would confront the conceptual designer of a vehicle that would have to operate in the hostile environment of hypersonic flight.

Figures 1 to 5 are reproduced from this early paper. Figure 1 is a schematic drawing of a sectional view of the vehicle concept. Compression was provided by a shock from the leading edge of the inlet, the convex isentropic turning surface, the cowl reflected shock and a flame-induced shock. Properties of the inlet flowfield were obtained assuming superposition of the solutions for the inviscid and viscous portions of the flowfield. In the concept shown, a portion of the air ingested in the inlet did not participate in the combustion process and thereby provided a film barrier to mitigate the extremely high heat transfer rates in the combustor and nozzle.
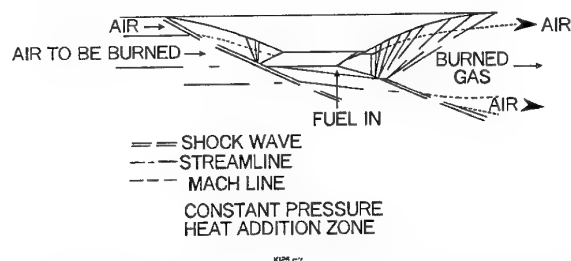
Figure 1. Schematic of Hypersonic Ram-Scramjet Engine (Ref 1)

For the cycle calculations, made at that time, the flow properties were mass averaged to obtain conditions entering the combustor. The method for calculating the kinetic energy efficiency of the diffusion in the inlet and in the flame induced shock was particularly ingenious. The boundary layer was subdivided into a finite number of stream tubes in order to calculate the losses due to the cowl reflected shock and to account for the enthalpy loss due to heat transfer to the wall. Oblique shock losses were determined by solving the two dimensional shock equations and the viscous losses were calculated by a finite difference solution of the Karman integral momentum equation. The resulting values for non-adiabatic kinetic energy efficiency of 0.970 to 0.974 in the speed range of Mach 20 to 28 are in close agreement with contemporary CFD solutions of similar flow geometries. (The writer can attest to the tedious nature of the calculations made on a mechanical desk calculator and the accompanying eyestrain from the extensive use of Mollier diagrams.) Nozzle expansions were computed for the limiting cases of frozen and equilibrium chemistry, and an assumed value of 0.33 was adopted for the non-equilibrium index. (See Ref. 2 for a discussion of nozzle loss coefficients.)
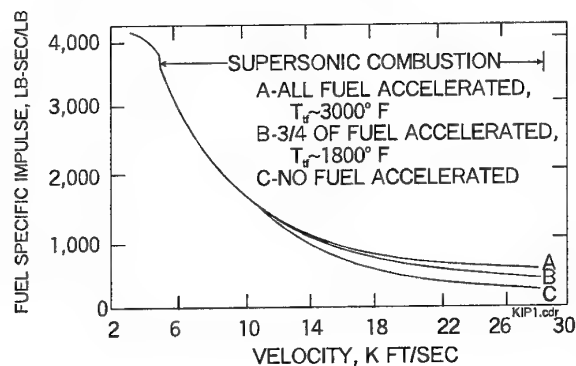
Figure 2. Hypersonic Ramjet Performance for Three Fuel Injection Schemes (Ref 1)

Engine specific impulses, I_F as a function of flight velocity are shown in Figure 2. The abrupt drop in specific impulse at 5000 ft/s (Mach 5.17) is due to the switch from ramjet operation to scramjet operation. The authors design concept implied that " a shock due to fuel injection and/ or flame initiation occurs near the point of fuel injection and is an integral part of the air diffusion system." However, at that time, they did not fully comprehend that the shock structure was indeed a shock train and that the processes was a continuous evolution from ramjet operation to that of a pure scramjet , i.e., a *dual mode* engine cycle[3,4] . The very important contribution of fuel momentum at high velocities is quite evident in the results for cases A, B, and C. In case A all of the fuel has been heated to 3000F and is injected coaxially; in Case B, the fuel is preheated to 1800F with ¾ being injected coaxially (equivalent to injection of all of the fuel at an angle of 41 deg); in Case C, the injection is normal to the air flow. At speeds of 10,000 ft/s (about Mach 10) and below, the contribution of fuel momentum is insignificant for hydrogen fueled engines. At that time, the energy balance on the entire vehicle had not yet been examined, consequently the effect of fuel momentum was a parameter of the study. Contemporary studies have concluded that the amount of energy that can be recovered from cooled sections of the airframe that would otherwise radiate heat to the atmosphere is about equivalent to that of Case B. In engine cycle calculations, heat transferred to the internal surfaces and returned to the fuel to raise its temperature does not contribute to an increase in the momentum of the exhaust gas. In contemporary parlance the precise accounting for all of the heat exchanged in a vehicle is referred to as an *energy balanced system*. This recovery of energy from cooling panels on the external surfaces is an important consideration in conceptual vehicle design. A detailed trade study is required to balance any weight penalty against the gains due to recovered energy. Note that the authors recognized that velocity rather than Mach number should be treated as the independent variable in both the analysis of engine performance at high speeds and in the study of accelerator missions. In the study, the question of the proper low speed system to use with the ram-scramjet was begged. It was suggested that a single stage to orbit system using tandem rocket or turbojet engines would be a possibility, as would the acceleration to Mach 3 by another vehicle in a two stage system. This report provided the guidance for an intensive research program in scramjet combustion technologyat the Johns Hopkins University, Applied Physics Laboratory, JHU/APL sponsored by NASA that began in 1961.

To estimate achievable accelerations, a vehicle consisting of a planar engine plus control surfaces, with sufficient engine body volume to carry the required hydrogen load plus payload and pilot compartment, was considered. Axial force coefficients for this vehicle , based on an inlet projected area of 50 ft[2], are shown in Figure 3.

The weight coefficient is based on the vehicle weight at a given velocity using thrust coefficients based on fuel momentum corresponding to case B. The net thrust coefficients, C_T, at low velocities suggest that the velocity at which the engine would obtain full capture was lower than that of contemporary engines, but a direct comparison would be difficult because the calculated values of air capture were not given. The drag coefficients also appear to be optimistic. The rise in thrust coefficient at velocities above 20,000ft/s is due to the high fuel/air equivalence ratios ER, that were used

at high velocities, viz., 2-4 at 20,280ft/s, 4 at 24,730ft/s and 6 at 28,500ft/s. High ER was shown to lead to much lower nonequilibrium flow losses in the exhaust nozzle. Without this increase in ER the values for C_T and C_D would be nearly equal, which would lead to unacceptably low values of vehicle net force specific impulse I_{EFF}.
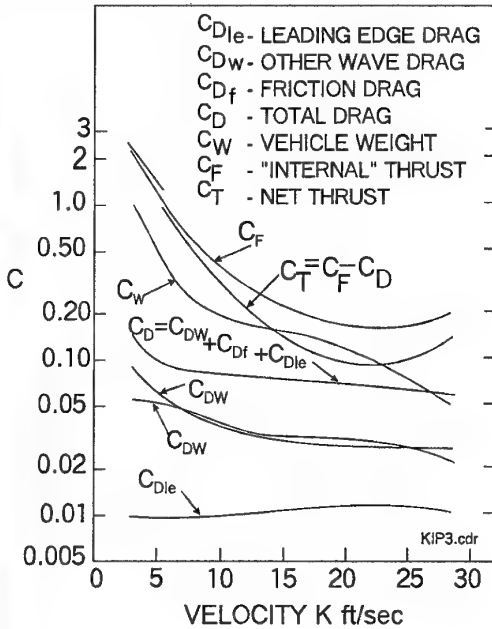

Figure 3. Axial Force Coefficients Based on Inlet Capture Area of 50 ft^2 (Ref 1)

Figure 4 shows the results of trajectory calculations based on initial conditions of 2900 ft/s at an altitude of 59,000ft. Weight as a percentage of the weight at 2900ft/s are shown for the three cases. The impact of the contribution of fuel momentum on vehicle performance is dramatically shown. The vehicle weight remaining upon arrival at a low inclination, low earth orbit of about 30%, corresponding to the Case B assumptions are in accord with those that will be subsequently discussed.
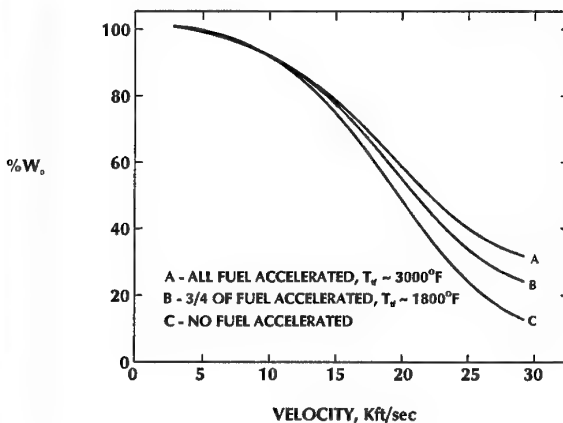
Figure 4 Vehicle Weight Referenced to 2900 ft/s (Mach 3) as Function of Velocity (Ref. 1)

Without the benefit of the contribution of fuel momentum, the airbreathing system would fail to compete with that of an all rocket system. The authors also emphasized that the flight path should be suppressed to increase engine pressure to the structural limit in order to minimize nozzle nonequilibrium losses. (Dynamic pressure levels of 2000lb$_f$/ft^2 and higher were recommended). Cognizance that the weight fractions from Mach 3 to orbit is a very convenient index is important in studies which address the selection of optional low speed propulsion systems for both single-stage-to-orbit, SSTO and two stage to orbit, TSTO, accelerators. Various alternatives to all-scramjet propulsion to orbit were cited by the authors. "…if the ramjet were integrated into an airframe with rocket motors for acceleration to Mach 3, it might prove advantageous to end the scramjet phase at 22,000 or 25,000 ft/s, coast out to some higher altitude, and use one or more rocket motors to complete the acceleration and injection into circular orbit.. Another possibility is the injection of an oxidizer into the fuel rich exhaust to raise I$_f$ and C$_T$ at the higher velocities." The former concept has now be named *lox enhacement*. Both methods have been shown to have considerable merit in contemporary studies.

The heat transfer coefficients and heat transfer rates that were computed for this study are shown in Figure 5. They showed that the liquid hydrogen fuel supply had adequate cooling capacity for the proposed flight regime. Convective cooling with hydrogen gas was adequate for the external cooling panels, but film or transpiration cooling would probably be required for the internal duct surfaces and for the small radius leading edges. By far, the highest heat transfer rates were experienced on the leading edge of the cowl of the inlet. The relatively small diameter of 0.1 or less is required to keep the drag to manageable levels.
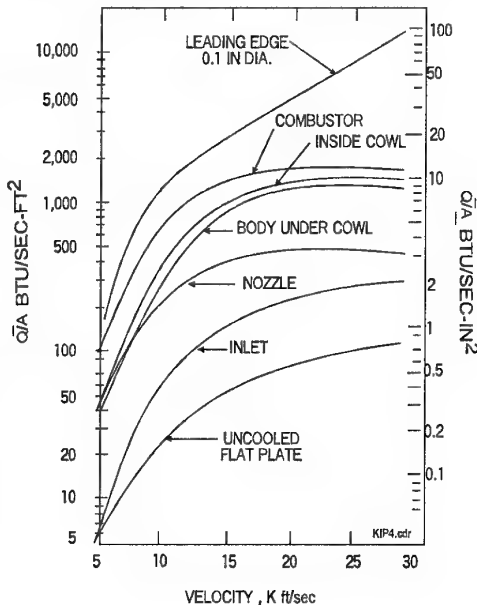
Figure 5. Heat Transfer Rates On Hypersonic Ram-Scramjet Engine (Ref. 1)

The information presented in Reference 1 should have, and does now, provide a useful point of departure for addressing the SSTO application. The I$_F$ values for case B have been added to those presented in Ref.5 from a variety of sources and are shown in Figure 6. Note that the enormous increase

in capability to conduct sophisticated analyses of these complex flowfields has had little impact on the predicted values of I_F. The underlying physics of the problem were adequately understood more that 35 years ago. To proceed with the conceptual design it is necessary to address the problem of the selection of the low speed system that is need to provide SSTO capability. The engine concept presented in Reference 6 will serve as a foundation for that process.
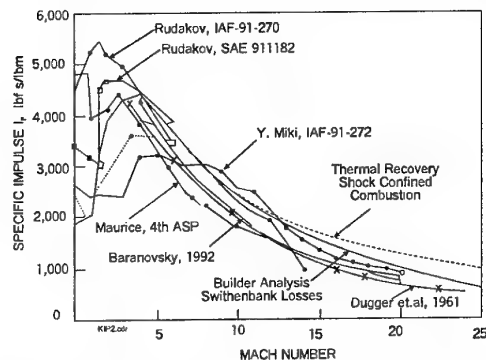

Figure 6. Comparison of I_F values for Case B (Ref 1) with Summary of Values From Ref. 5

Conceptual Design of SSTO Vehicle

A 400,000 lb class gross weight cargo carrier to space is used to exemplify the conceptual design. Emphasis is directed on the characteristics of the propulsion path, not on the specifics of the vehicle. Only the general geometric features of the vehicle, needed to quantify the performance, will be discussed. Consequently, some of the results will be presented in a parametric form which will permit their use on a variety of vehicle designs and/or climb trajectories. Figure 7 is an enlarged view of the midsection of the vehicle showing the main engine ducts. The vehicle is 160 ft in length and has a mid-body width of 32.4 ft.
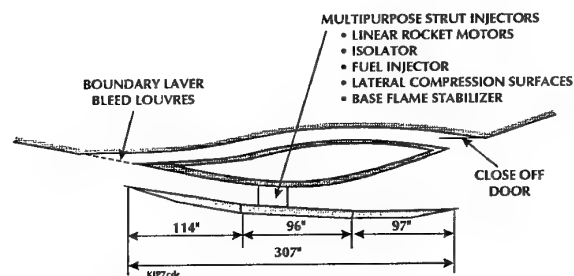
Figure 7. MidSection of Transatmospheric Accelerator

The 307-inch-long engine cowl translates vertically with maximum and minimum duct heights of 21 inches and 5 inches, respectively. The 114-inch-long cowl lip section flap rotates to provide modulation of the air capture, variable cowl wave compression and inlet closure during final access to orbit, in orbit, and on reentry. The cowl leading edge is in its maximum outboard position when the cowl lip section is at an angle of 11.5° to the compression surface. The corresponding maximum capture area of 210.3 ft^2 is used as the inlet reference area A_i. The 97 inch long cowl trailing edge rotates to prevent overexpansion of the internal flow, and a corresponding large base drag at very low flight speeds.

With the cowl in the outboard position, the projected area of the engine in the plane of the trailing edge is $A_e = 452$ ft^2 at an angle of attack of 0° and 395.7 ft^2 at a = 2°. In the inboard position the projected areas reduce to 414.4 ft^2 and 357.2 ft^2 at $\alpha = 0°$ and 2°, respectively. The corresponding vehicle reference expansion ratios A_e/A_i are 2.15 and 1.88 at $\alpha = 0°$ and 1.97 and 1.70 at $\alpha = 2°$ for the outboard and inboard cowl positions

A boundary layer bleed duct lies inboard of the main propulsion duct. The louvered close-off door seals this duct at M_0 less than about 1.05 and at high flight Mach number when the flow is no longer needed to reduce or eliminate base drag. A controllable flap at the exit of the duct is used to regulate flow into the duct.

Figure 8 shows more detail of the geometry of the internal engine. Internal compression is obtained from the cowl lip when the lip is rotated outward while the cowl translates inboard. Compression in the lateral plane is provided by the multipurpose retractable instream injectors. In addition to the compression on the 10° one-half angle wedge leading edges, the strut injectors serve as insolation ducts to prevent combustion induced disturbances from disrupting the flow in the inlet. The aft portion of the injectors are segmented linear rocket motors. At low flight Mach numbers when the engine is operating in the air-augmented mode these injectors function as rockets. At higher Mach numbers they are tangential hydrogen injectors.
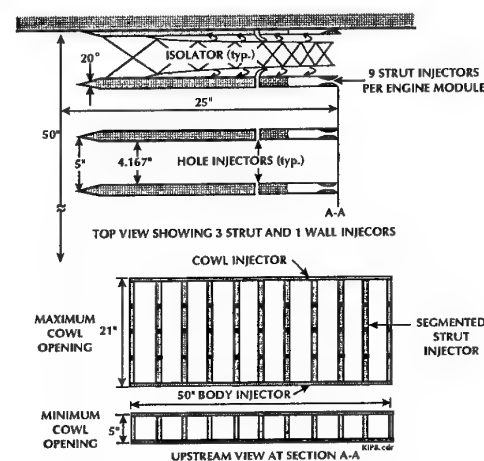

Figure 8. Detailed View of Strut Injectors

The vertical segmentation provides the dual capability to reduce rocket thrust as the engine transitions from the air-augmented mode to the ramjet mode and to turn off a portion of the injectors when the cowl translates inboard. The engine is subdivided into six, 50-inch-wide engine modules. Each module houses nine, 0.933-inch-thick, 25-inch-long injectors spaced 5.00 inches on center. The side walls of each bay also contain rocket/hydrogen injectors having a width one-half that of the instream injectors. The resulting internal contraction is 15% which permits self starting of the inlet at about Mach 2 for vehicle angles of attack typical of flight. Each isolator duct has a width of 4.17 inches and a length of 22.69 inches which results in a l/w = 5.43. Additional rocket/hydrogen injectors are located in the cowl and engine body in the plane of the exit of the instream injectors. The instream injectors are fully retracted from the stream at high Mach number to reduce internal shear, drag, and heat transfer and assure survivability.

Transverse hole hydrogen injectors are located upstream of the rocket motors in the instream struts, in the side walls, and on the internal sides of the cowl and body. Hole injectors are also located on the surface of the expansion nozzle downstream of the exhaust of the boundary layer duct. These downstream injectors supply the fuel for "base burning" of boundary layer bleed air.

Engine operability and performance are dependent on the geometry of the vehicle forebody which serves as the external compression surface of the engine inlet. The planform of the vehicle has a spatular shaped forebody which blends into a near-to-planar compression surface. The compression surface is comprised of a 351-inch-long plane having a wedge angle of 4° and a curved surface to provide near-to-isentropic compression that terminates in a 11.5°, 98.95-inch-long wedge surface

It is convenient to subdivide the description of the engine design, its performance and operability into four speed ranges; low, low-mid, high-mid, and high speed ranges. In the low speed range, $M_O = 0$ to 3, the engine evolves from an air-augmented rocket to a subsonic combustion ramjet. In the low-mid speed range, $M_0 = 3$ to 7, the engine operates as a dual-mode ramjet transitioning to a scramjet. In the high-mid speed range $M_0 = 7$ to 15, the engine is a scramjet. From $M_0 = 15$ to orbit, the high speed range, the engine transitions from a scramjet back to a ducted rocket.

Low Speed System Design, Performance and Operability

One of the complexities in the design of the engine for a transatmospheric accelerator is the interdependence of the engine and airframe, thrust and drag, weight and flight path. The approach taken in Ref. 6, is the design of an engine wherein the flow rates of the propellants can be modulated to accommodate a broad range of vehicle drags, weights and angles of attack on a variety of flight paths.

To initiate the design, calculations of engine performance were carried out to determine optional fuel/oxidizer flow rates for a broad range of input parameters. For the low speed cycle, the more important parameters are the inlet total pressure recovery $P_{t4'}/P_{to}$, the bypass ratio β = weight flow of air entering the engine, the weight flow of the propellants; the equivalence ratio of the injected propellants, ER_{ij} = (Y_{H2}/Y_{O2}) (2.016/16) = 0.126 Y_{H2}/Y_{O2} and the overall area ratio of the mixing and combustion process.

The concept of the "thermal throat" depends on setting the combustor exit Mach number, $M_5 = 1$ at the desired area during the low speed and low-mid speed modes of engine operation. Precise control of the injection, mixing and combustion, together with rotation of the aft cowl flap is needed to optimally locate the thermal throat. Less than optimal control can be tolerated, i.e. relatively slower rates of the mixing and combustion yield $M_5 > 1$ and an associated loss in performance. At $M_0 > 2$, the inlet is started and higher than optimal combustion rates would cause premature engine "choking" and an inlet unstart with a larger loss in thrust.

The engine uses the translation of the cowl and the rotation of the cowl lip to obtain the guideline performance. A relatively simple analysis was used in this study to assess the inlet performance. The analysis used began with inviscid calculations of the shock losses and turning on the forebody assuming planar flow for $M_0 = 1.125$. For $M_0 < 1.125$ the

flow on the forebody is governed by the internal engine flow which is set by the ejector pumping of the strut rockets and the rotation of the cowl lip. Maximum engine specific impulse was the criteria for selecting the Mach number in the cowl lip plane for $0 < M_0 < 1.125$. At all flight conditions the cowl lip rotation is set to minimize cowl drag. For $1.25 < M_0 < 2.00$ the flow is supersonic in the cowl lip plane, i.e. $M_2 > 1.0$, the inlet is unstarted and the cowl is rotated to maintain "critical" inlet operation. In this speed range, the Mach number downstream of the terminal normal shock is less than 0.8 and the cowl lip is rotated to provide an increasing area in the upstream portion of the internal duct. At $M_0 > 2$ the inlet is started and the forebody flow is unaffected by the internal flow.

With flow conditions defined at the cowl lip and the inlet started ($M_0 > 2$), calculations were made with the cowl lip aligned with the flow and at various incidence angles to the flow. Solutions were found for properties of the flow following the shock train using integral methods and stream-thrust averaging. Figure 9 compares results of the calculated inviscid pressure recoveries for an unstarted inlet with those for a started inlet with no cowl compression and a started inlet with cowl compression for $\alpha=0°$ and 2°. The curves marked "Engine Design" are the modeled values of pressure recovery which should adequately account for the viscous losses and non-optimal wave cancellation not included in the inviscid analysis.
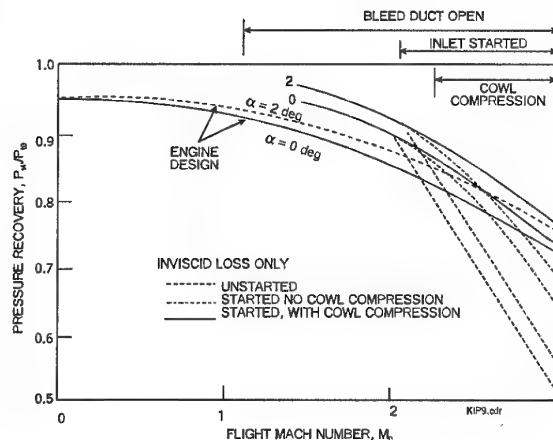

Figure 9. Inlet Pressure Recovery

The models are:

for $\alpha=0°$,

$$P_{t'4}/P_{t0} = 0.96 - 0.02586\ M_0^2 \qquad 1)$$

and for $\alpha=2°$,

$$P_{t4'}/P_{t0} = 0.96 - 0.02272\ M_0^2 \qquad 2)$$

where station 4' corresponds to mean flow conditions at the downstream end of the isolator duct.

The inlet starts at a Mach number slightly greater than two and the cowl forward flap begins to rotate slightly above Mach 2.25. Note that the boundary larger bleed duct opens at a Mach number slightly greater than one, so forebody viscous losses do not degrade the pressure recovery in the main engine flow path at $M_0 > 1$. Equations 1 and 2 were used for $P_{t4'}$ in the cycle analysis. Complimentary calculations made with lower values of pressure recovery at $M_0=3$ showed that large

losses in performance would accrue if the inlet would have had to be operated unstarted.

To limit the number of discrete points in the engine performance analysis and to provide guidance in design of a vehicle using this engine, a reference trajectory was specified. Modeling was then introduced to provide engine performance for flight on alternative trajectories. Trajectories presented in Reference 7 for velocities > 1200 ft/s were adopted. For velocities < 1200 ft/s a new trajectory was introduced to limit load factors at takeoff and to provide a continuous derivative, du/dz at 1200 ft/s. The modeling for this low speed portion of the climb out was as follows:

$$z = 1.2276 \times 10^{-4} (u-u_m)^3$$
$$+9.5939 \times 10^{-8}(u-u_m)^4 - 2.435 \times 10^{-10}(u-u_m)^5 \quad (3)$$

where z is the altitude in ft, u is velocity in ft/s and u_m is the velocity at takeoff.

For $1200 < u < 6500$ ft/s

$$u = 500 + 7.23 \times 10^{-3}z + 8.95 \times 10^{-7}z^2 \quad (4)$$

For $6500 < u < 14,000$ ft/s

$$\rho = .003046 \exp [4.748 \times 10^{-5} (77,396 - z)] \quad (5)$$

For $14,000 < u < u_2$ where u_2 is the velocity required for an unpowered climb on an elliptic transfer orbit.

Low trajectory

$$u = -39,256 + 0.6647z - 1.648 \times 10^{-6}z^2 \quad (6)$$

High trajectory

$$u = -4490 + 0.2059z - 3.465 \times 10^{-7} z^2 \quad (7)$$

This method of defining analytic formulations for climb trajectories has proved to be invaluable in conceptual design studies. The gravity loss term in the acceleration equation can now be explicitly defined and separated from the drag losses. Figure 10 shows the altitude-velocity relationships for these climb trajectories and a comparison with a typical climb trajectory for Shuttle. With the altitude defined as a function of velocity, engine cycle calculations were made at $M_0=0$, 0.5 and 1.0 and at intervals of 0.25 between $M_0=1$ and 3. At $M_0=3$, Z=47,950 ft and u=2914.1 ft/s, thus only equations 3 and 4 are pertinent for the low-speed range cycle analysis.
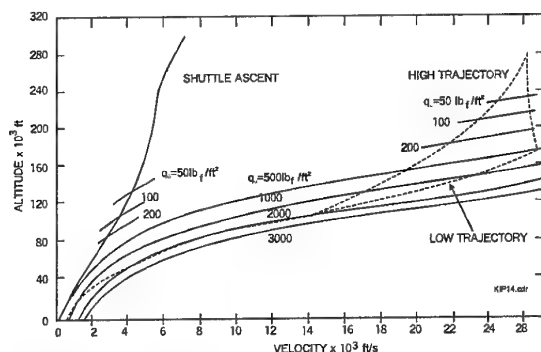
Figure 10. Referenced Trajectory for Single Stage to Orbit Vehicles and Shuttle

An extensive design study resulted in the operation of the rocket injectors at a fixed $P_{tij} =2250$ psia and $ER_{ij}=2.0$ with $A_{ij}/A^*=13.9$. This produces a $M_{ij}=3.623$ at $P_{ij}=16$ lbf /in^2. For the total strut plus wall rocket injector $A_{ij}=1195$ in^2 and the mass flow is 755.88 lb$_m$/s. In the absence of a quantitative

evaluation of vehicle heating loads and auxiliary power requirements, the temperature of the propellants entering the strut rockets was set at 500°R. The internal thrust of the rocket injectors was based on an exhaust-stream-thrust-efficiency of 0.98. The corresponding specific impulse for $P_{tij}=2250$ lbf/in^2 at $ER_{ij} =2$ is $453 \times 0.98 = 443.94$ lb$_f$s/lb$_m$. At a flow rate of 755.82 lb$_m$/s, the thrust of the rocket injectors is 335,539 lbf.

The engine cycle calculations were carried out using the JHU/APL, RJPA Ramjet Performance Analysis Program[8]. Several thousand cases were run in the course of examining the effects on engine performance and operability of ER_{ij} variation, the bypass ratio β (mass flow into main engine duct/injectant mass flow) and M_4. From this matrix of solutions, 44 cases were selected to represent the engine operation in the low-speed regime. Values of engine thrust are shown in Figure 11 and a representative curve is drawn through the data. The thrust increases from $M_0=0$, where the air augmentation is trivial, to a maximum of approximately 513,000 lbf at $M_0=2.25$ where the contribution of ram-air-augmentation is nearly equal to that of the rocket injectors. The rocket injectors are gradually shut down as the speed increases from $M_0=2$ to 3 as shown in Figure 12.
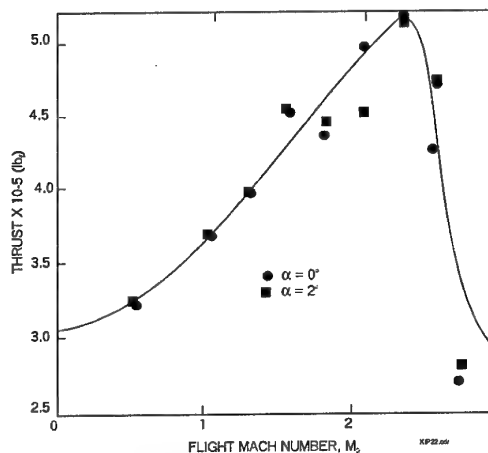
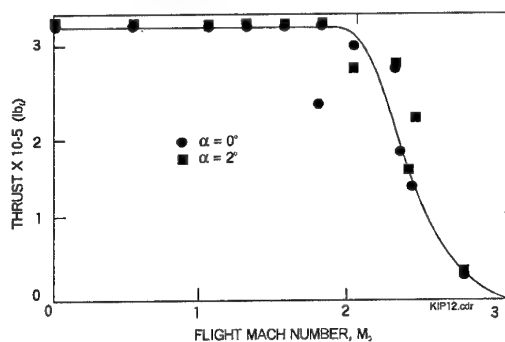**Figure 11. Engine Thrust at Maximum Ieff - Referenced Trajectory Nominal Vehicle Drag**

Figure 12. Rocket Motor Thrust at Maximum Ieff - Referenced Trajectory Nominal Vehicle Drag

The decrease in engine thrust as M_0 increases from 2.25 to 3.00 is due to the combined effect of the reduced rocket thrust and the optimization of I_f and I_{eff} at lower overall equavaline ratio, ER_0. Engine specific impulses increase gradually from about 405 lb$_f$s/lb$_m$ at $M_0=0$ to about 775 lb$_f$s/lb$_m$ at $M_0=2.25$ and then climb rapidly to greater than 3000 lb$_f$s/lb$_m$ at $M_0=3.00$ as shown in Figure 13.
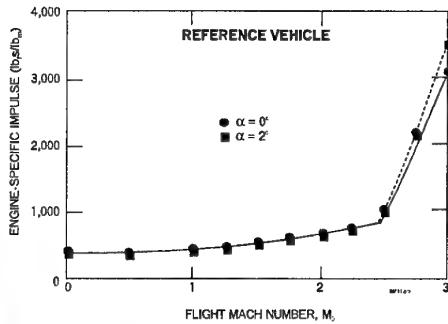
Figure 13. Engine Specific Impulse at Maximum I_{EFF} - Referenced Trajectory Nominal Vehicle Drag

Revised Models of Trajectory Aerodynamics

With this description of a rocket based combined cycle, RBCC engine, it is now possible to examine alternative low speed propulsion systems and to investigate the sensitivity of vehicle performance to changes in the formulation for the climbout trajectory. Moreover, more recent data for the aerodynamic characteristics of wing-body accelerator configurations had been provided by Professor Paul Czysz of St. Louis University[9]. The first step was to fly the engine on the reference trajectory, using the preliminary estimates for the aerodynamic coefficients. These results showed that a larger than desired change in the angle of attack occured in transitioning from the first to the second segment of the analytically defined trajectory. Consequently revised formulations were adopted The first segment was changed as follows:

For $500 < u < u_a$ $\quad Z = 7.8 \times 10^{-10}(u-500)^5$ (8)

Three different cases were examined to join segment 1 with the segment defined by eq 4. These expressions are:

Case 1: $\quad 960 < u < 1300 \quad 16,065 < Z < 26,130$

$(1300 - u) = 5.4 \times 10^{-2}(26,130 - Z)$

$\quad -1.231 \times 10^{-6}(26,130 - Z)^2 -7.731 \times 10^{-11}(26,130 - Z)^3$ (9)

Case 2: $\quad 985 < u < 1545 \quad 20,932 < Z < 30,369$

$(1545 - u) = 6.159 \times 10^{-2}(30,369 - Z)$

$\quad + 5.32 \times 10^{-6}(30,369 - Z)^2 -5.89 \times 10^{-10}(30,369 - Z)^3$ (10)

Case 3: $\quad 1010 < u < 1905 \quad 26,912 < Z < 36,894$

$(1985 - u) = 7.327 \times 10^{-2}(36,894 - Z)$

$\quad + 1.43 \times 10^{-5}(36,894 - Z)^2 -1.188 \times 10^{-9}(36,894 - Z)^3$ (11)

These new trajectories are shown in Figure 14. When the trajectory is formulated as in Eqs. 4 - 11 the numerator in the general equation for the motion of the vehicle along the flight path (Equation 12) can be evaluated in closed form (see Ref. 7 for a detailed discussion).

$$\int_0^2 \frac{dW}{W} = \int_0^2 \frac{\left(1 + \frac{gdZ}{UdU}\right)}{g\frac{T}{Wp}\left(1 - \frac{D}{T}\right)} (du)$$ (12)

The values can then be compared with those for other trajectories which can be obtained from graphical or numerical

integration. Figure 15 depicts the graphical technique. The gravity loss term is obtained by integrating the area under the curve of g/u vs Z. A representative climb trajectory for Shuttle and a typical trajectory for a horizontally launched space access vehicle used in studies by others are shown. These trajectories are typically constrained to fly level through the transonic speed range, having reached that prescribed altitude by a steep climb at nearly constant velocity. Values of the gravity loss term are listed in Table 1.
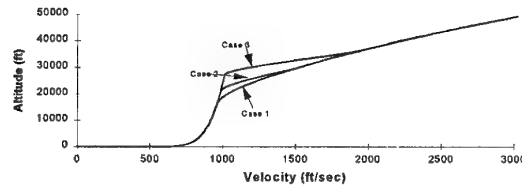
Figure 14. Low Speed Climb Out Trajectories
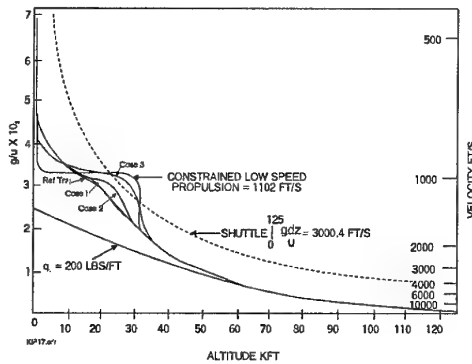
Figure 15. Gravity Loss Term in Acceleration Equation 0 to 125,000 ft.

As expected, the gravity losses for the new trajectories increase for Case 1 to Case 3, as a consequence of flying at a lower velocity for a given altitude in the region of 16,000ft to 36,000 ft. The constrained low speed trajectory, which came from a 3DOF trajectory optimizer, has the lowest gravity loss term due to flying at to a higher velocity before entering a steep climb. Subsequent revisions to the analytic trajectory formulations will be made to more closely approximate the initial climb suggested by the optimizer. Gravity losses for vertical launch are nearly double those for horizontal launch as exemplified by the Shuttle trajectory. This is an important factor that must be addressed in conceptual design studies that compare vertical with horizontal launch.

Trajectory	Gravity Loss ft/s
Reference	1617.0
Case 1	1614.4
Case 2	1631.2
Case 3	1686.2
Constrained	1592.2
Shuttle	3000.4

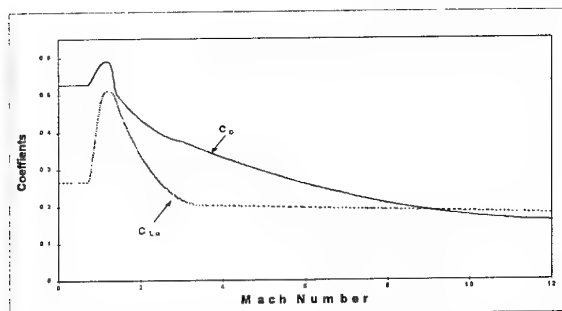**Table 1. Gravity Loss Terms in Acceleration Equation from 0 to 125,000 ft.**

Figure 16. Aerodynamic Coefficients for Transatmospheric Accelerators

The new aerodynamic coefficients used in this study are shown in Figure 16. Values from Ref. 9, which were based on planform area have been modified to use the projected reference area of the engine inlet instead of the planform area of the vehicle to define the coefficients. This vehicle has a planform area of 4,763 ft^2 and an inlet reference area of 210.3 ft^2. The lift of the vehicle is then obtained from the value of the lift slope curve give in Fig. 16 as $C_L = C_{L\alpha}\alpha$ the zero lift drag is obtained from the coefficient shown in the figure for C_{do}, and the drag due to lift is $C_{DL} = L'C_L\sin\alpha$ where $L' = 0.4$ for M < 0.72, $L' = 0.4 - .045M + 0.0625M^2$ for 0.72 < M < 4 and $L' = 1.22 + 0.165(M-4)$ for M > 4. The aerodynamic coefficients are for vehicles that are capable of eliminating base drag at low flight speeds. Without the base burning concept, the drag would be about 50% higher at Mach 1.2. The zero lift drag coefficient of 0.18 at Mach 12 is about 20% higher than those used in previous studies[7,10] which would increase the mass fraction of propellant required to reach orbit shown therein.

A compilation of data from numerous previous studies of the author was used with the current engine configuration to obtain engine specific impulse. Figure 17, which compares these values with those from the seminal paper of 1961[1]. The major difference is the significant increase in I_F for the scramjet cycle at velocities < 20,000 ft/s. With engine specific impulse and vehicle aerodynamics defined, flight along the defined trajectories can be obtained by simultaneous solution of the axial and normal force equations along the flight path.
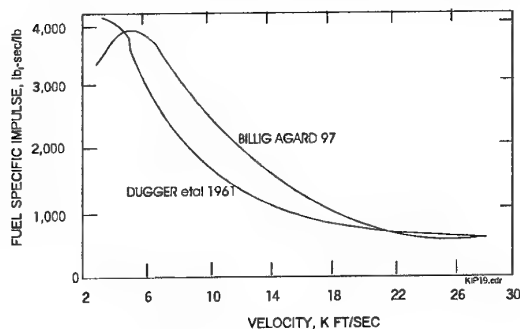
Figure 17. Comparison of Current Engine Specific Impulses with Reference 1 Values

Conceptual Design of Turbojet Installation

To examine the issue of alternative low speed propulsion systems, the conceptual design of the reference vehicle was modified to accommodate turbojet engines. Figure 18 is the concept for the installation of nine 33.3in diameter turbojets in

a tandem duct similar to, but much larger than, that used for the base bleed system. Two rotateable inlet doors have been added to permit the turbojet to capture the maximum amount of available air. When the air flow is limited, as it invariably is in this class of vehicle configurations, better overall engine performance is realized when all of the air is used in the turbojet and none in the ramjet flow path. At Mach 3 the doors return to the folded condition and all of the flow enters the ramjet flowpath. At Mach 3 the turbojet performance would still be slightly better than that of the ramjet but the weight penalties associated with operation at higher temperature would result in lower overall vehicle performance. The nozzle close off door prevents the hot gases from the ramjet flow path from backflowing into the exhaust of the turbojet. With the base burning duct removed, control and elimination of base drag would be problematic, but no penalty for increased base drag was assumed in the study. Because issue has been taken with the conclusions from previous studies[7,10] very optimistic assumptions are being adopted for the turbojet performance. Most notable is that the Mach number at the compressor inlet has been raised from 0.3 to 0.5. No penalty in inlet pressure recovery, relative to that in the RBCC flowpath, has been taken, even though it is doubtful that the flow path to the compressor could be capable of exploiting internal contraction in the inlet. Figure 9 shows that this could lead to a 8 to 20% reduction in total pressure at Mach 3. For an accelerator mission, the turbojet engines must operate with full augmentor at an equivalence ratio of 1. The nine engines produce a total thrust of 345,667 lb$_f$ at sea level static. The corresponding specific impulse is 5635 lb$_f$s/lb. Engine performance calculations resulted in a specific impulse variation with Mach number given by $I_F/I_{FSL} = 1 - 0.035M - 0.00917M^2$. Fuel flow at other than sea level static is proportional to the inlet air flow. When flying the Case 1 trajectory, the thrust reaches a maximum of 643,000lb$_f$ just before it transitions to the ramjet mode of operation at a velocity of 2910 ft/s.
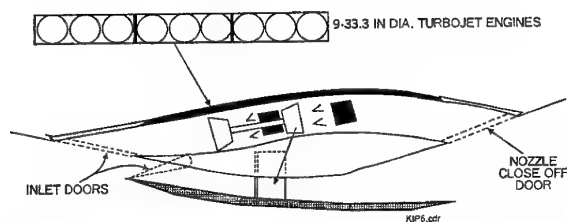

Figure 18. RBCC Engine Modified for Turbojet Installation

Comparison of RBCC with Turbojet System

When compared to the RBCC engine the turbojet uses a remarkably small amount of fuel during the acceleration to 2910 ft/s. For a gross weight at brake release of 396,000lb, the turbojet uses 13,622lb of fuel, whereas the RBCC uses 98,248lb. The corresponding mass fractions are 0.9656 and 0.7519, respectively. Based on this information, it would appear that the turbojet would be the engine of choice for a SSTO accelerator. However, this is not the whole story. The turbojet engines are quite heavy and an enormous amount of fuel is used while accelerating their mass to orbital speeds. This issue is addressed with the help of Figures 19 and 20.
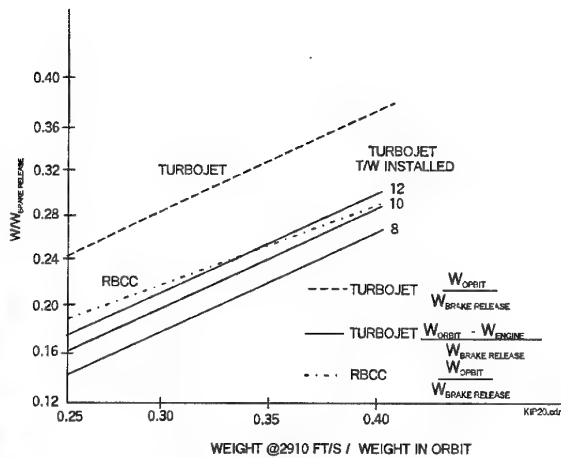
Figure 19. Orbital Weight Fractions for RBCC and Turbo-Ram Scramjet

In Figure 19, the orbital weight fraction of turbojet and RBCC powered vehicles are shown as a function of the weight fraction of propellant required to accelerate from 2910ft/s to orbital velocity. Recall that in the 1959 study (Fig. 4), a value of about 0.3 was projected. The flyout trajectories for the engines in this study using the recently available aerodynamic force coefficients is not yet completed, but preliminary calculations also show results with a weight fraction of about 0.3. The weight fraction of propellant for the turbojet is indeed smaller than that of the RBCC powered vehicle. However, when the weight of the engines is deducted from the total weight, the remaining weight fraction of the RBCC is larger, unless the climb from 2910 ft/s is remarkably efficient and the thrust to weight ratio, T/W of the turbojet engines is very high. For example, if the weight fraction from 2910ft/s to orbit is 0.30 the turbojet would consume 267,665lb of propellant and the RBCC would consume 208,426lb, a net difference of 25,387lb in this phase of the climbout. For the turbojet, the weight of propellant consumed in the entire climb is 281,287lb, leaving a weight in orbit of 114,713lb. The RBCC consumes 306,673lb of fuel, leaving a weight of 89,326lb. If the turbojet T/W = 10, the additional "engine" weight is 34,567lb. Thus, the weight "available" for structure and payload is 114,713 - 34,567 = 80,146lb or 9,180lb less than the RBCC.

When the additional weight of the inlet doors, the nozzle close off door and the larger duct are included with the spool weight, T/W values in excess of 10 would be unlikely. Propellant tank weights for the two vehicles would be comparable. Total tank volume is about the same. The additional propellant used in the RBCC is dense liquid oxygen. The assumption of equal mass fraction in the Mach 3 to orbit phase of the climbout biases the results in favor of the turbojet. Actually, the fuel fraction would have to be somewhat larger to account for the larger induced drag.

Although the differences in weight fraction are small, the effect on payload is quite significant. Figure 20 shows the weight of additional payload, or margin in the structural weight budget that corresponds to the weight fractions shown in Figure19. With a nominal value of 0.3 for the weight ratio required to accelerate from 2910 ft/s to orbit and a T/W =10 for the turbojet, the additional payload of 9180lb is about 2.3% of the gross take off weight.

There are numerous other propulsion cycles that have been promoted for as alternatives for the turbojet and the RBCC for the SSTO mission. Nearly all of those that have been given

serious attention have the characteristic that they are lighter than the turbojet, but have lower engine specific impulse. The lower weight systems also have much lower thrust capability. Generally the thrust is insufficient to provide enough accelerative capability to transgress the transonic pinch and adjunct rocket propulsion is required. This problem was encountered with NASP. The knowledge base for the propulsion system performance for most of these alternative engine cycles is sufficient to perform conceptual design studies with sufficient fidelity to expose these deficiencies. There remains the question of whether the structural designer can meet the weight budget with adequate margin to provide a useful payload.
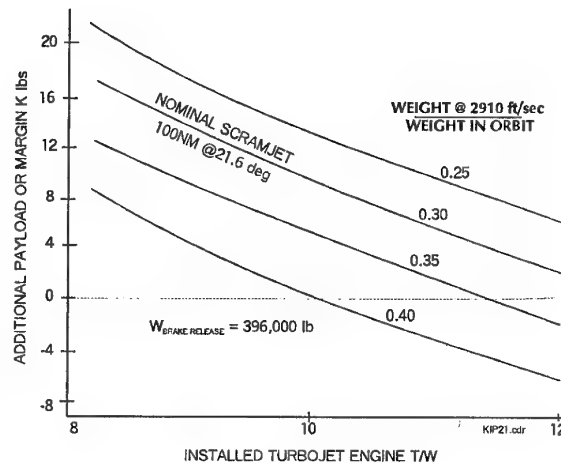

Figure 20. Additional Payload or Margin or RBCC vs Turbojet

Optimization of the engine design, wherein the design point for full air capture and the amount of lox added in the combustor are tailored to optimize I_{EFF} from Mach 3 to orbit, is hoped to raise the mass fraction above 0.30. However, the weight budget is still uncomfortably small. This pales in comparison with the challenge faced by the developers of all rocket powered SSTO vehicles. The recently funded NASA X-33 program can give some perspective of the realities of the problem. The currently stated gross take of weight GTOW, is 273,277lb and the propellant mass fraction is 0.77. The vehicle is expected to reach a maximum velocity about 15,000ft/s with no payload. To reach an easterly, low earth orbit would require a propellant mass fraction of 0.89. Venture Star, the SSTO Recoverable Launch Vehicle that is being marketed as the follow-on to the X-33, has the objective of reaching a 51.6deg, 220nm orbit with a useful payload, requires a propellant mass fraction of about 0.90. This means the structural mass fraction will have to be reduced by more than a factor of 2, from that of the X-33. The substitution of aluminum-lithium for aluminum oxygen tanks will save some weight, as will some anticipated reductions in the weight of the rocket motor components. Scaling up to the 2,186,000lb Venture Star will lead to some decrease in the structural mass fraction, but the sum of all these factors still falls way short of the factor of 2 that is needed.

New Conceptual Designs

Rather than relying on modest improvement in the currently configured RBCC, or for that matter airbreathing systems using other low speed cycles, it would be prudent to examine the possibility of a radical change in the engine flowpath and in turn the overall vehicle configuration. Ideally, not only would the vehicle have better engine performance and lower structural weight but the drag would be reduced. The concept that is currently being examined by the author and Dr. Ajay Kothari of Astrox Corporation is based on the flowpath cut from streamline traces of inward turning flowfields. The design of the highly successful SCRAM[12] engine that was tested in a freejet at Mach 5-7.3 in 1968-73 was based on a similar design technique. Figure 21 shows conceptual design of four vehicles which have inward turning inlet compression fields and the reverse process in the nozzle.

Some of the attributes of theses designs are:

1) An inlet-forebody that produces more uniform flow in combustor, thereby simplifiying the fuel control and distribution system as well as increasing the engine performance.

2) Very simplified methods for attaining changes in the contraction ratio of the inlet that eliminates the requirement for translation and rotation of large cooled panel sections in hydrogen cooled systems.

3) Very simplified methods for providing engine starting and control of the air capture characteristics of the inlet.

4) Swept leading edges to minimize heat transfer, cowl drag and inlet losses.

5) Significant reductions in wall shear losses by simultaneously decreasing the ratio of surface-to-cross-sectional area and increasing the boundary layer thickness in the high shear region of the engine flow path.

6) Large reduction in the length of the combustor-inlet isolator due to thick incoming boundary layers.

7) Significant reduction in the surface area requiring active cooling.

8) Reduction of stress concentration by the elimination of sharp corners in the highly loaded internal ducts.

9) Large reduction of the trim requirements by closely aligning the resultant thrust vector with the vehicle axis and with a small, or no offset from the vehicle c.g.

10) A family of designs appropriate for either horizontally or vertically launched vehicles for accelerators and another family suitable for expendable missiles.

More detailed descriptions of the conceptual design and performance of vehicles embodying these features will be presented in forthcoming publications.

Concluding Remarks

An approach to generate the conceptual design and performance of airbreathing single stage access to orbit vehicles has been presented. Comparison of RBCC and turbo-ram-scram jet accelerators showed that less fuel was expended by the turbojet system but the useful weight in orbit was greater for the RBCC devise. Allowable structural weights for either system are marginal but are considerably more comfortable than those for all-rocket powered vehicles. A terse introduction to a new class of flow paths that could lead to significant savings in propellant and structural mass factions concludes the discussion.
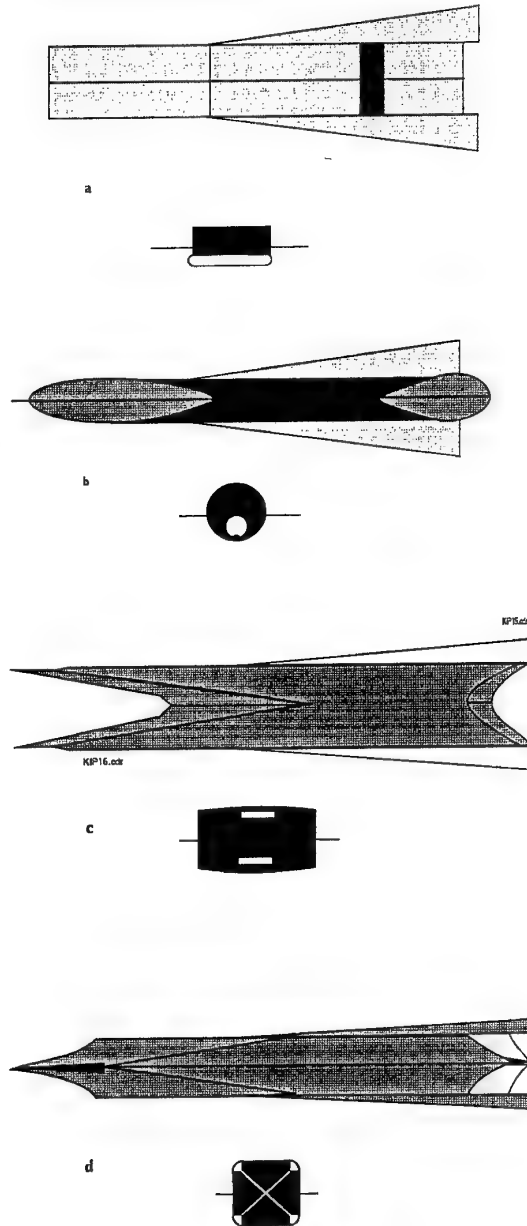
Figure 21. Conceptual Designs of SSTO Vehicles Based on Inward Turning Flow Fields, Front and Bottom Views

a) **Two Dimensional - Planar Configuration**

b) **Minimum Surface Area Configuration**

c) **Two-Module Symmetric Configuration for Vertical Launch - Carved from an Assymmetric Flow Field**

d) **Four Module Symmetric Configuration for Vertical Lanuch - Carved from an Axisymmetric Flow Field**

C-33

Question 1: Prof. E. Reshotko

What about cooling requirements (for inward turning designs?)

Author's reply:

Two features of the inward turning design lead to reduced requirements for cooling. First, the leading edges of the inlet are highly swept which reduces the heat transfer and drag. Second the radial compression in the inlet and radial expansion in the nozzle thickens the boundary layer, relative to planar designs, in the regions of highest heat transfer. Thicker boundary layers lead to lower total heat loads.

Question 2: Prof. Ir. W.B. de Wolf

Could you briefly comment on the off-design characteristics of Busemann-type inlets?

Author's reply:

CFD calculations of Busemann inlets at off-design conditions are currently underway. At present, no results are available. However, the fixed geometry inlet for the SCRAM engine (ref. 12), with a design Mach number of 7.78 was tested over the Mach number range of 4 to 10 at angles of attack up to 15 degrees. Results from these tests showed remarkably good performance at off-design conditions.

Aerothermodynamics and Propulsion Integration:
Synthesis of the AGARD-FDP-VKI Special Course, April 15-19, 1996

E.H. Hirschel
Daimler-Benz Aerospace AG
81663 München
Germany

SUMMARY

The AGARD-FDP-VKI Special Course "Aerothermodynamics and Propulsion Integration for Hypersonic Vehicles" dealt with basic topics of aerothermodynamics, with configurational aerothermodynamic of re-entry vehicles, airbreathing vehicles and missiles, and with inlet and aerothermodynamic airframe/propulsion integration of RAM and SCRAM propelled vehicles. In this paper the contributions, which were devoted to aerothermodynamic airframe/propulsion integration in the widest sense, are synthesized.

After a general discussion of the problem, the main topics forebody, inlet, nozzle/afterbody, the whole vehicle, are detailed, partly with illustrating examples. Finally the potentials and deficits of simulation means are considered.

1. INTRODUCTION

The AGARD-FDP-VKI Special Course "Aerothermodynamics and Propulsion Integration for Hypersonic Vehicles", Rhode-Saint-Genèse, Belgium, April 15-19, 1996, had the following objectives:

- Review of recent research and industrial work in aerothermodynamics and propulsion integration.
- Consolidation and dissemination of newly gained knowledge, experience and techniques.
- Identification of new development and evolution needs in the field.

The structure of the course is given in Table 1. The content is published in Ref. 1.

In the following the contributions dealing with aspects of aerothermodynamic airframe/propulsion integration in the widest sense are synthesized. The material considered is that presented on day 3 and day 4 of the course, Table 1. The respective articles are Refs. 2, 3, 4, 5, which were published in Ref. 1.

2. THE PROBLEM OF AEROTHERMODYNAMIC AIRFRAME/PROPULSION INTEGRATION

Aerothermodynamic airframe/propulsion integration is the most demanding problem in airbreathing hypersonic vehicle design because of the strong coupling of the lift and the propulsion system, which increases with increasing flight speed, Ref. 6. Actually the whole lower side of the vehicle is a combined lift and propulsion system. The outer flow path (on the airframe) and the inner flow path (through inlet, engine, nozzle) are intimately coupled together, Fig. 1.

The shaping of these flow paths in view of the large Mach number and altitude span, possibly with several propulsion modes (Turbo, RAM, SCRAM), is the main problem. A positive net thrust, Fig. 2, must be attained. At the same time performance, flyability, and controllability in design and off-design flight must be assured. Fig. 1 shows also the many flow phenomena, whose qualitative and quantitative properties determine the functions of forebody, inlet and nozzle/afterbody. Both the outer and the inner flow path are viscous-effects dominated. Heat loads and heat-loads alleviation on the outer flow path by surface-radiation cooling influence, and are influenced by the properties of the viscous flow (third lecture on the first day), Ref. 7. The whole problem is finally complicated by the strong coupling of the aerothermoelastic behaviour of the forebody into both the outer and the inner flow path (last lecture of the course), Ref. 8.

Current design strategies, simulation and optimization tools as well as ground-facility simulation must be much improved in order to permit "to get a positive net thrust in the right direction", Fig. 2, with sufficient prediction accuracy and reliability. For military applications this certainly is possible today in the low hypersonic Mach number regime. For space transportation systems with the demand of high cost-efficiency still a large technology development effort is necessary, Ref. 8.

3. THE MAIN TOPICS

In the following the three main topics "forebody", "inlet", "nozzle/afterbody" are treated and finally the fourth main topic "the whole vehicle". Considered are only those contributions, which were major parts of a lecture. For details the reader is referred to the pertinent papers (Refs. 2, 3, 4, 5).

3.1 Forebody

The forebody was a major topic of the two lectures on the third day, Refs. 2 and 3. The forebody of a hypersonic airbreathing vehicle serves a function, which is a not so accentuated function of, for instance, a fighter aircraft forebody. "Forebody pre-compression" reduces the inlet capturing area, and therefore also the vehicle length, because the bow shock should not interfere ("inlet shielding", Ref. 2), with the propulsion system, which would lead to wave drag increases, Ref. 6, but also to severe interference processes with the inlet. Of course the vehicle nose shape plays also a major role. Its form and dimensions affect the bow-shock shape and location, too. Here already very important couplings with the wave drag and the heat loads must be considered: small nose → small wave drag → large heat loads, and vice versa, Ref. 7. Finally the entropy layer thickness will be affected by the nose shape, with consequences for the boundary-layer development on the lower side

of the forebody, the transition laminar-turbulent, and the inlet-onset flow.

The baseline shape of the lower side of the forebody is an almost flat shape, Ref. 6. This should lead to an almost two-dimensional inlet-onset flow. It is, however, affected by the entropy layer, which, together with the forebody boundary-layer also governs the flow homogeneity of the inlet-onset flow. This in turn affects the mass-flow, and the total pressure efficiency of the inlet, Refs. 2 and 3. How much distortion a RAM or a SCRAM engine can tolerate has not been settled yet. Large tolerances would be ideal, because then no boundary-layer diversion would have to be considered, which, however, is mandatory for the turbo engine mode. Fig. 3 from a systematic study in Ref. 2 shows different nose and forebody configurations, of which one with a flat lower side appears to be the one suited best. The flow pattern on a similar shape is shown in Fig. 4, which is a HYTEX forebody, Ref. 3. This has been systematically studied, too, in Ref. 9, where also volume, wetted surface, and lift, drag and pitching moment increments were investigated.

3.2 Inlet

The inlet was a major topic of the second lecture on the third day, Ref. 3, and the first lecture on the fourth day, Ref. 4. The inlet for RAM propulsion ($M < 7$) has to decelerate the flow to low subsonic Mach numbers in the RAM combustor, Ref. 3, whereas for SCRAM propulsion ($3 < M < 20$) the deceleration is necessary to low supersonic Mach numbers ($M \approx 1.5$ to 3) in the SCRAM combustor, Ref. 4. Of course, with forebody pre-compression, the inlet "sees" a Mach number smaller than the flight Mach number. In principle this means, that the RAM inlet design in any respect poses larger problems than SCRAM inlet design (note that a SCRAM propelled hypersonic vehicle in general first flies in turbo and RAM mode, so that the inlet must cover all propulsion modes). However, increasing flight Mach number entails increasing severity of thermochemical effects and of heat loads, which are strongly enhanced in areas of shock/boundary-layer interactions (fourth lecture on the first day), Ref. 10. Detail topics treated were inlet efficiency (mass-flow ratio, total pressure recovery), which must be attained with little inlet drag and losses, and sufficiently good quality (low distortion and swirl) of the flow entering the engine (combustor). This is a problem especially for turbo engines. Inlet control, e.g. prevention of unstart (turbo engine, RAM inlet (SCRAM inlet: isolator blockage)), is a major issue, too.

Geometrical features, like the capture area, mixed external/internal compression, side wall compression (SCRAM inlet), Fig. 5, Ref. 11 (taken from Ref. 4), throat area (RAM inlet) and lip angle are major issues because the inlet flow path has to be minutely supported and controlled by a light-weight structure with, for hypersonic flight vehicles, rectangular (!) cross-sections and movable (sealing problem) ramps.

This must be viewed in conjunction with the enormous pressure and heat loads, for which an example is given in Fig. 6, Ref. 3. The outer ramps are radiation cooled, therefore the wall temperatures are rather low, but increase almost stepwise from ramp to ramp (an explanation was given in the third lecture on the first day, Ref. 7). The inner portion of the inlet, which cannot be radiation-cooled, becomes very hot, with the possi-

ble need of active cooling. The inlet lip poses extra large structural problems, because it must be thin (wave drag, distortion), but must bear large pressure loads and large heat-loads differentials from the inner to the outer surface.

The flow phenomena are very demanding in the design and verification processes. The boundary-layer of the inlet-onset flow on the lower side of the forebody will be turbulent in the RAM regime, but laminar-turbulent transition will happen downstream of the lip in the inner and the outer flow path. In the high SCRAM regime, transition may occur only after sufficient compression on the ramp(s). Shock/boundary-layer interactions, corner flow with glancing shocks, shock/shock interactions on the lip, et cetera, combined with thermochemical effects, which even may couple into the combustion process, are partly not well understood, which poses large prediction and verification problems, especially if transition and turbulence are involved, Ref. 10.

3.3 Nozzle/Afterbody

This was a major topic of the lectures on the third day, Refs. 3 and 2, and of the first lecture on the fourth day, Ref. 4. Since the flight Mach number and altitude span of hypersonic vehicles is very large, the nozzle throat must be controlled, which leads to a rectangular cross-section, and to an asymmetric outer nozzle (single expansion ramp nozzle (SERN)). The outer nozzle then must be considered as a constituent part of the afterbody, which becomes larger with larger flight speed (SÄNGER $M = 6.8$: approximately 40 m²). Nozzle/afterbody efficiency (thrust coefficient) and the thrust-vector angle, which couples strongly into the pitching moment and the lift of the vehicle, Figs. 1 and 2, pose major design problems especially also with regard to the overall aerothermodynamic airframe/propulsion integration. Plug nozzles in principle could overcome the thrust-vector angle problem, if they would be employed with a bell nozzle. However, vehicle integration needs make a combination with an asymmetric outer nozzle (Plug SERN) necessary, which poses other problems, unfortunately also shock/boundary-layer interaction problems, Fig. 7, Ref. 12.

Performance and operation problems are especially large at low supersonic transonic (transonic pitch problem) and subsonic Mach numbers. For this flight regimes external combustion on base surfaces (nozzle flap) is proposed, as well as heating of the diverted forebody boundary-layer flow, Ref. 3, which is then expanded through a secondary nozzle on top of the primary nozzle, Fig. 1.

The flow phenomena to be regarded are very complex, too. Thermochemical effects in the engine exhaust flow (optimum external nozzle length for the recovery of dissociation losses), radiation cooling of outer surfaces (shielding effects by water vapor of the exhaust gas?), three-dimensionality effects, and shock/boundary-layer interaction and separation pose formidable prediction and verification problems. Fig. 8 gives a schematical comparison of effects due to the presence or non-presence of SERN sidewalls.

3.4 The Whole Vehicle

The "whole vehicle", which combines the three elements sketched above, is the final design challenge of airbreathing hypersonic vehicles. It was treated especially in the first lec-

ture of the third day, Ref. 2, and for missiles in the last lecture on the fourth day, Ref. 5.

Two basic paradigms can be distinguished: the "flying engine", and the "propelled airframe", Ref. 2, depending on, obviously, whether one looks with the eyes of an aircraft designer, or that of an engine designer. In any case the external and the internal flow path have to be considered in an integrated manner in order to shape the flow paths in such a way that all functions are optimally served: forces and moments, pitch and yaw, trim and stability, control (control surfaces, thrust, thrust vectoring, reaction-control system at large altitudes (?)) on all trajectory segments, in general also with low-speed compatibility. Special problems must be handled in off-design situations, e.g. engine-flame out, in order to avoid or to counter-act the build-up of a large pitching moment.

Tip-to-tail computations are today the major means to approach the problem. The core engine can be handled as input/output model, which still entails many serious problems. The approach is highlighted in the following with regard to the pitching-moment problem. Fig. 9, Ref. 13 (discussed in Ref. 3) shows the pitching moments of the airframe, the propulsion system and the total system (SÄNGER) as function of the flight Mach number. The airframe has a pitch-down in the whole Mach number range up to $M \approx 5$. It is strongly accentuated in the transonic regime. The propulsion system has a similar accentuation in the transonic regime, however, it is the pitch-up in the turbo reheat mode, which then reduces fast to zero at $M \approx 2.6$ (at $M \approx 3.9$ the propulsion mode changes from the turbo mode to the RAM mode). The total system finally exhibits a pitch-down moment in its whole flight Mach number domain, with a strong accentuation in the transonic regime, which all must be trimmed. Trimming with aerodynamic control surfaces of course entails trim drag, which hurts especially in the transonic regime. The efficiency of control-surface trim of a pitch-down moment in the high Mach number regime is another problem, if the wing or body portion ahead of the control surface flies at angle of attack, so that the upward-deflected control surface is shielded.

Tip-to-tail studies permit to analyse in detail where the forces and moments are created and what remedies can be considered, if adverse effects are present. An example of a result of such a study is shown in Fig. 10, Ref. 2, with the integrated evolution of the lift along the vehicle (generic vehicle at $M = O$ (10)).

The forebody gives positive lift, except for $\alpha = 2°$ in the most forward portion. This lift, of course, increases with increasing angle of attack. In the inlet a strong reduction of lift happens, because the airstream on the lower side of the vehicle is forced upwards. At the (SERN) nozzle finally the lift recovers, again increasingly with increasing angle of attack. Similar results are given in Ref. 2 for the pitching moment and the drag.

At this time the state of the art permits considerations of this kind only for rigid airframes. In Ref. 8 it was discussed that the aero(thermo)elastic behaviour of especially the forebody couples via the pre-compression effect strongly into the internal (engine) flow path, with large consequences for the net thrust of the (RAM) propulsion system. The still unabated growth of computer performance will allow soon also to take

aerothermoelastic effects into account, provided the model building for such simulation problems, also on the structural side, can be achieved soon, especially in view of possible hot primary structure solutions for the airframe.

4. POTENTIALS AND DEFICITS OF SIMULATION MEANS

Potentials and deficits of simulation means were topics of all contributions. Simulation means, i.e. computational simulation tools (approximate methods for design and investigation, numerical methods for investigation, design, diagnose and verification), and ground-simulation facilities and techniques for investigation and verification, are needed in the vehicle definition and development (engineering) phases. Computational simulation (and optimization) has a very large potential due to the growth of computer power, which will reach Petaflops performance in the next ten years.

The very big deficits lie in flow-physics (transition and turbulence) and thermochemical models, and in view of the aerothermoelastic coupling problem also in structure-physics models (non-linearities and damping in joints, properties of heat-loaded materials & structures, et cetera).

While computational simulation is the natural tool in vehicle definition and development processes, the ground-facility simulation is the classical tool for investigation and verification processes. Airframe, inlet, afterbody (jet simulation?) can be sub-scale tested in "cold" and "hot" hypersonic facilities. The engine and the whole propulsion system, i.e. inlet, engine, nozzle can be tested in connected pipe, semi-free jet, and free-jet facilities with sub-scale, and depending on the vehicle size, also with full-scale hardware. However, large deficiencies exist in ground-facility simulation with regard to scale effects, viscous effects, thermochemical effects, which in general increase with increasing flight speed. Ground-facility simulation of the flow past and through the whole (elastic) vehicle, even in sub-scale, is not feasible. Therefore new simulation strategies are envisaged, which combine systematically computational simulation, ground-facility simulation and in-flight simulation in order to overcome the ground-facility simulation shortcomings on the one hand, and to tackle the design and verification problem of the "whole, free-flying, propelled, elastic vehicle" on the other hand. Examples are the "Integration Validation Object Methodology", Ref. 2, and the "Transfer-Model Approach", Ref. 8.

5. CONCLUDING REMARKS

A large part of the special course was dedicated to aerothermodynamic propulsion integration. Aerothermodynamic airframe/propulsion integration is a most challenging topic. The design and verification problems increase with increasing flight speed due to the increasing coupling of lift and propulsion. Flow physics and thermochemical phenomena pose large problems in understanding and prediction. Aerothermoelastic couplings pose additional grave problems. However, with continuous and dedicated technology development and verification efforts, which include appropriate experimental vehicles, these problems can be overcome.

6. REFERENCES

1. N.N., "Aerothermodynamics and Propulsion Integration for Hypersonic Vehicles", AGARD-R-813, 1996.

2. Perrier, P., Courty, J.C., "Configurational Aerothermo-dynamics of RAM and SCRAM Propelled Vehicles", AGARD-R-813, 1996, pp. 7-1 to 7-36.

3. Bissinger, N.C., "Inlet and Propulsion Integration of RAM Propelled Vehicles", AGRD-R-813, 1996, pp. 8-1 to 8-45.

4. Povinelli, L.A., "Inlet and Propulsion Integration of SCRAM Propelled Vehicles", AGARD-R-813, 1996, pp. 9-1 to 9-22, 9A1 to 9A-10, 9B-1 to 9B-17.

5. Pagan, D., Lacau, R.-G., "Missile Aerothermodynamics and Propulsion Integration", AGARD-R-813, 1996, pp. 10-1 to 10-44.

6. Hirschel, E.H., "Aerothermodynamic Phenomena and the Design of Atmospheric Hypersonic Airplanes", in: Advances of Hypersonics II, Vol. I, Defining the Hypersonic Environment, J.J. Bertin, J. Periaux, J. Ballmann, eds., Birkhäuser, Boston, 1993, pp. 1-39.

7. Hirschel, E.H., "Aerothermodynamics of Radiation-Cooled Surfaces", AGARD-R-813, 1996, p. 3-1 to 3-16.

8. Hirschel, E.H., "The Technology Development and Verification Concept of the German Hypersonics Technology Programme", AGARD-R-813, 1996, pp. 12-1 to 12-15.

9. Berens, T.M., Bissinger, N.C., "Study on Forebody Precompression Effects and Inlet Entry Conditions for Hypersonic Vehicles", AIAA-Paper 96-4531, 1996.

10. Holden, M.S., "Viscous/Inviscid and Real-Gas Effects Associated with Hypersonic Vehicles", AGARD-R-813, 1996, pp. 4-1 to 4-81.

11. Rose, W.C., Perkins, E.W., Benze, D.P., NASA Ames Research, Review, 1989.

12. Koschel, W., Rick, W., "Design Consideration for Nozzles of Hypersonic Airbreathing Propulsion", AIAA-Paper 91-5019, 1991.

13. Heitmeier, F., Lederer, R., Herrmann, O., "German Hypersonics Technology Programme - Airbreathing Propulsion Activities", AIAA-Paper 92-5057, 1992.

7. TABLES AND FIGURES

Table 1   *The structure of the course*

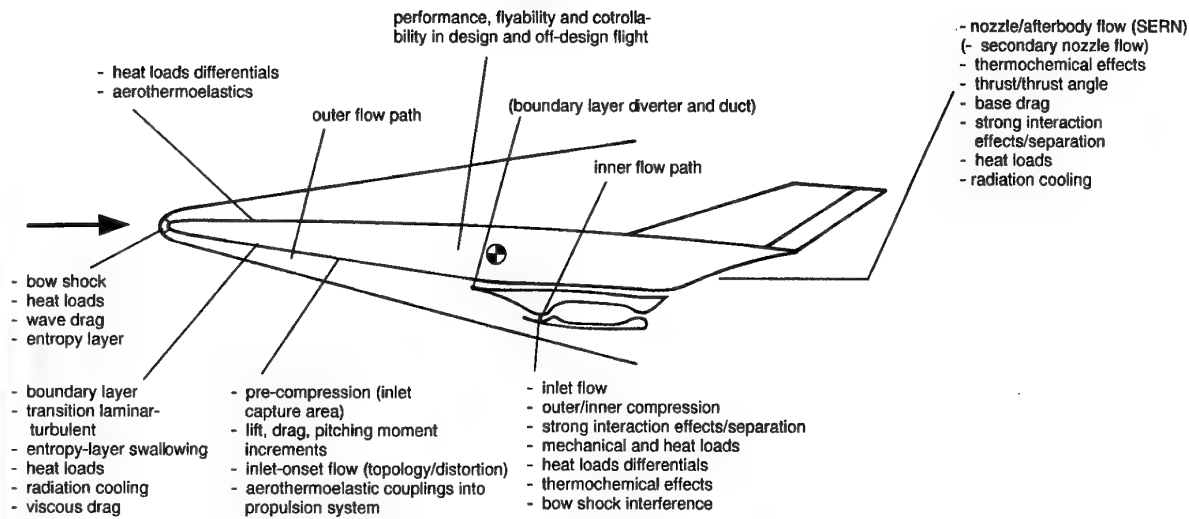| Day 1	Day 2	Day 3	Day 4	Day 5
Introduction *E.H. Hirschel, Daimler-Benz Aerospace, Germany* **Hypersonic aerothermo-dynamics at VKI** *M. Carbonaro, J.-M. Charbonnier, H. Deconinck, VKI, Belgium* **Aerothermodynamics of radiation-cooled surfaces** *E.H. Hirschel*	**Hypersonic laminar-turbulent transition and turbulence modelling** *D.I.A. Poll, University of Manchester, United Kingdom*	**Configurational aerothermodyna-mics of RAM and SCRAM propelled vehicles** *P. Perrier, J.C. Courty, Dassault DGT/DEA, France*	**Inlet and propulsion integration of SCRAM propelled vehicles** *L.A. Povinelli, NASA Lewis Research Center, U.S.A.*	**Stage integration and separation aerothermo-dynamics** *C. Weiland, Daimler-Benz Aerospace, Germany* **Technology development and verification** *E.H. Hirschel*
Real-gas and strong interaction phenomena *M.S. Holden, Calspan Advanced Technology Center, U.S.A.*	**Configurational aerothermo-dynamics of reentry vehicles** *D.A. Throckmorton, NASA, Langley, U.S.A.*	**Inlet and propulsion integration of RAM propelled vehicles** *N.C. Bissinger, Daimler-Benz Aerospace, Germany*	**Missile aero-thermodynamics** *D. Pagan, R.-G. Lacau, Aerospatiale, France*	

- heat loads differentials
- aerothermoelastics

performance, flyability and cotrolla-
bility in design and off-design flight

outer flow path

(boundary layer diverter and duct)

inner flow path

- nozzle/afterbody flow (SERN)
(- secondary nozzle flow)
- thermochemical effects
- thrust/thrust angle
- base drag
- strong interaction
  effects/separation
- heat loads
- radiation cooling

- bow shock
- heat loads
- wave drag
- entropy layer

- boundary layer
- transition laminar-
  turbulent
- entropy-layer swallowing
- heat loads
- radiation cooling
- viscous drag

- pre-compression (inlet
  capture area)
- lift, drag, pitching moment
  increments
- inlet-onset flow (topology/distortion)
- aerothermoelastic couplings into
  propulsion system

- inlet flow
- outer/inner compression
- strong interaction effects/separation
- mechanical and heat loads
- heat loads differentials
- thermochemical effects
- bow shock interference

Fig. 1   Major topics and issues of aerothermodynamic airframe/propulsion integration (schematically)

net thrust

thrust

vehicle
weight

inlet drag

aerodynamic lift

vehicle drag

g-reduction
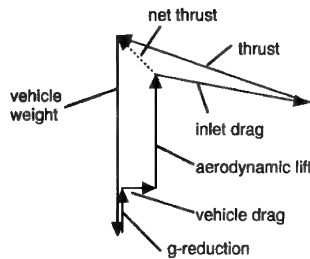
Fig. 2   Point force polygon (schematically), Ref. 6

F_1

F_2

F_3

F_4

F_5

b)

c)

d)

e)

f)
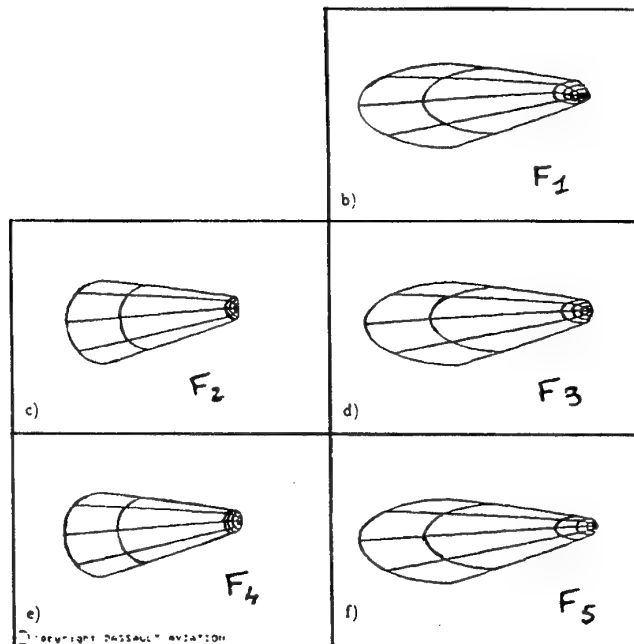
Fig. 3   Different forebody configurations (M = 8 flight), Ref. 2

View from below, left

HYTEX
Ma=5.6 α=5.0°

δ₁ [mm]

Verdrängungsdicke δ̂

COUSTEIX–Verfahren

Theory: flat plate

Theory: cone

L = 14.5 m

Front view

Lateral distance y [m]
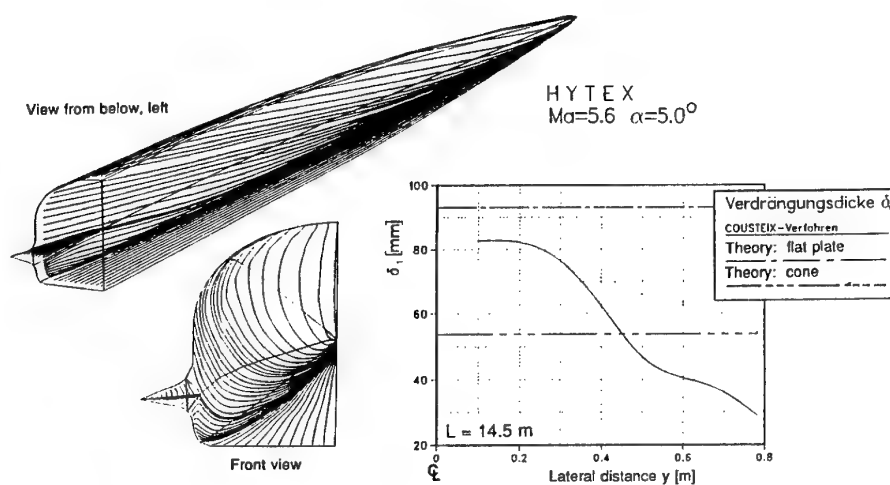
Fig. 4   *Surface stream-line pattern (left) and displacement thickness at the inlet plane (right) of a HYTEX forebody, Ref. 3*

FREESTREAM CASE

$M_\infty = 21.6$ $M_\infty = 18.1$
$P_t = 2000$ psi $P_t = 300$ psi
$T_t = 520$ °R $T_t = 520$ °R

COWL

30 deg

HORIZONTAL
CENTERPLANE

RAMP

FLOW   VERTICAL
CENTERPLANE
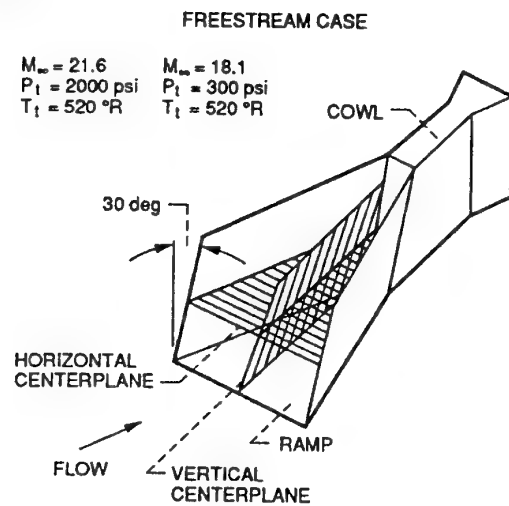
All laminar boundary layer

Fig. 5   *SCRAM sidewall compression inlet schematic, Ref. 11 (Ref. 4)*

750 °C
0.05 bar

890 °C
0.15 bar

1030–1610 °C   1610 °C
0.2 bar   0.41 bar

ca.1800 °C
3.4–3.9 bar
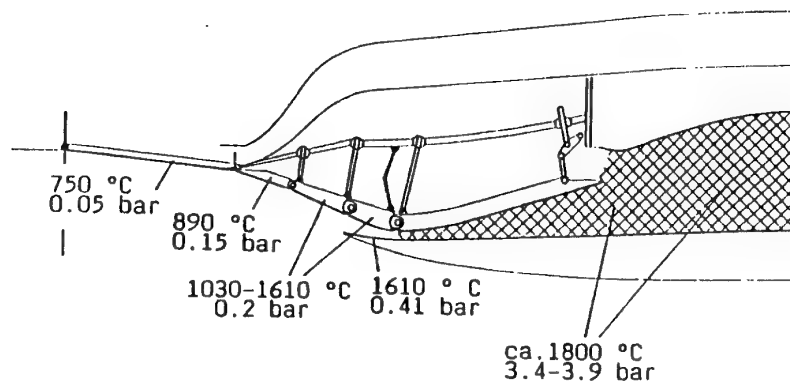
Fig. 6   *RAM inlet for flight Mach number M = 6.8, surface temperatures and pressures, Ref. 3*
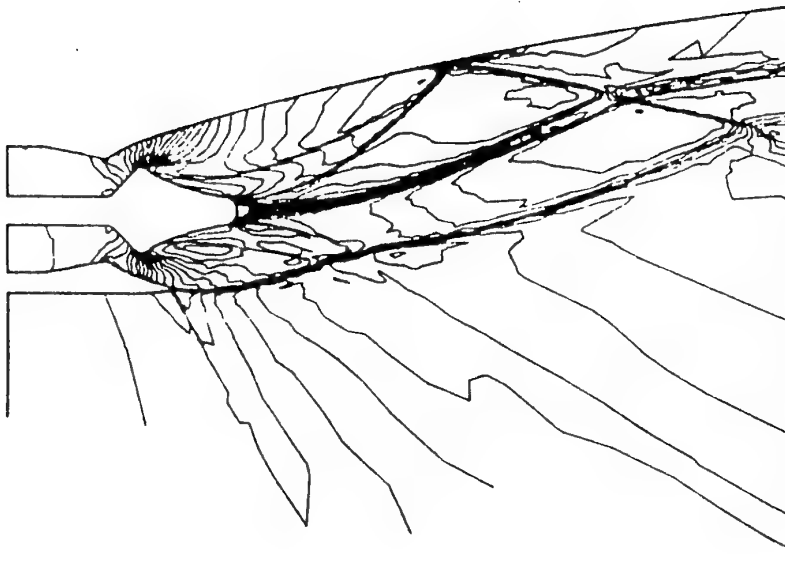
Fig. 7   Numerical study of plug SERN flow at M = 3.5 flight, Ref. 12
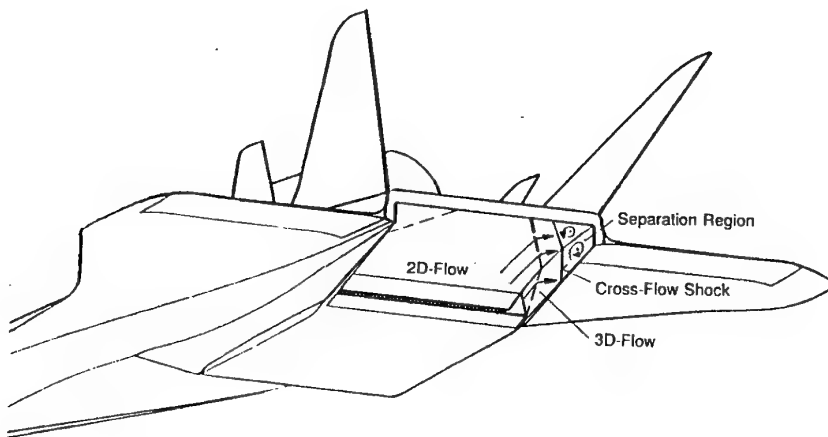
Compared with case without sidewalls:

- Sidewalls delay 3D expansion → higher pressures (thrust, nose-down moments)
- 2D flow area on ramp enlarged
- Complex flow on sidewall depending on NPR and external flow
- Cross flow shock on ramp and sidewalls possible → separation

Fig. 8   SERN nozzle, comparison of configurations with/without sidewalls (NPR: nozzle pressure ratio), Ref. 3
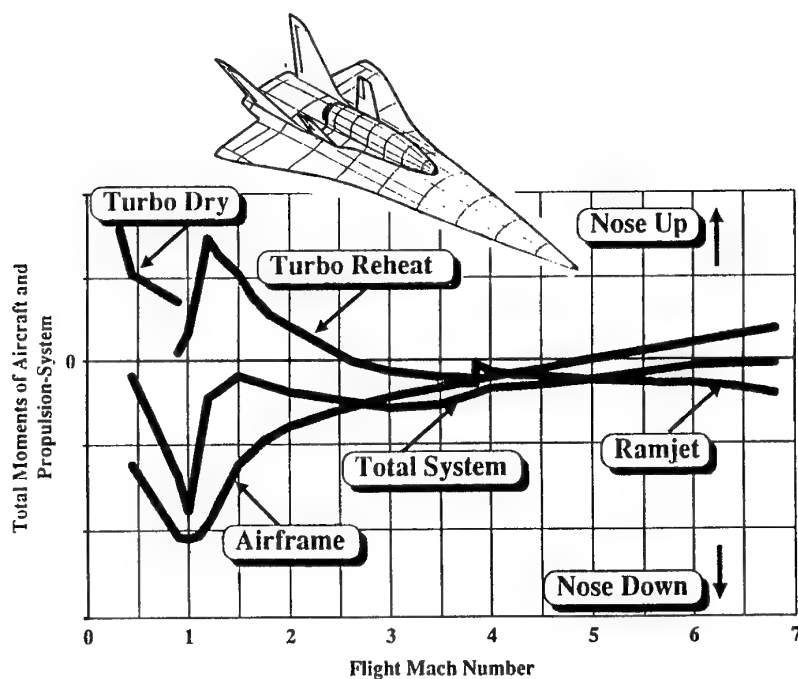
Fig. 9   *Pitching moments of airframe and propulsion system (SÄNGER), Ref. 13*
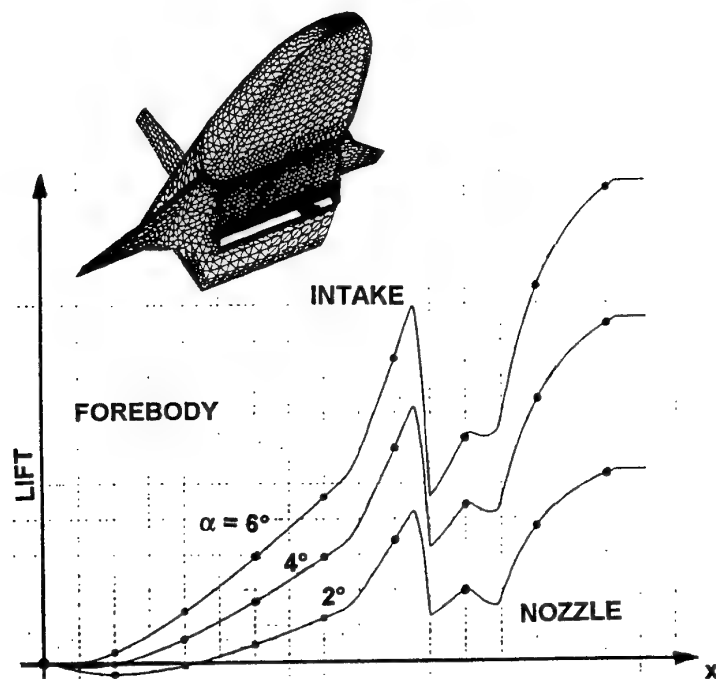
Fig. 10   *Integrated evolution of lift along the vehicle: effect of angle of attack in the scramjet mode (generic vehicle at M = O (10)), Ref. 2*

Scramjet Engine/Airframe Integration Methodology

by

James L. Hunt and Charles R. McClinton
NASA Langley Research Center, MS 353
Hampton, Virginia 23681-0001, USA

1. ABSTRACT

Scramjet engine/airframe integration methodology currently in use at the NASA Langley Research Center for design/analysis of hypersonic airbreathing vehicles is presented with illustrative example applications. The matrix encompasses engineering and higher order numerical methods that cover the major disciplines as well as a multidiscipline design/optimization approach.

2. INTRODUCTION

The Systems Analysis Office (SAO) and the Numerical Applications Office (NAO) of the Hyper-X Phase I Program Office (HXPO)/Aerospace Transportation Technology Office (ATTO) at NASA Langley Research Center provide evaluation, analysis and design of hypersonic airbreathing vehicles for both industry and government. A wide range of vehicles and missions are investigated, including single-, two-, and three-stage-to-orbit vehicles, as well as endoatmospheric cruise and accelerator vehicles (fig. 1, ref. 1). For all these vehicles, the forebody acts as an external inlet, precompressing air for delivery to the dual-mode scramjet inlet/combustor and the aftbody acts as an external nozzle for the expansion of exhaust gases. The result is a propulsion system that is totally integrated from nose to tail, and thus it is a major shaping influence on the design of the vehicle. Due to the highly integrated engine/airframe and the extensive flight envelope inherent in airbreathing hypersonic vehicle design, analyses of these vehicles involve many interdependent disciplines with high sensitivities among the large set of design variables and a highly nonlinear design space. It is therefore necessary to resolve most airbreathing hypersonic vehicles to a preliminary design level, even for those that would traditionally be considered as conceptual design. With this amount of detail required as well as the requirement for a short

design response time, analysis methods have been developed and improved to provide both rapid and accurate results. The stable of software tools span engineering and computational fluid dynamics (CFD) methods.

In order to minimize vehicle characteristics such as fuel fraction for performing a mission and resultant gross/dry weight, the airframe integrated subsonic/supersonic combustion ramjet should have at least four desirable features. First, the installed performance of the engine should be maximized over the Mach number range of operation; second, the engine integration should be such that the effective specific impulse of the vehicle is maximized over the accelerated portion of the trajectory; third, the engine should be able to be regeneratively cooled (except for missiles); and fourth, the engine should be light weight. These features should accrue in either a fixed geometry or highly variable geometry engine architecture or something in between. In addition, the subsonic/supersonic combustion ramjet/scramjet must have inlet and nozzle shapes that are conducive to airframe integration. The large nozzle area relative to freestream capture area requirements for hypersonic speeds necessitates integrating the engine with the airframe in order to use the afterbody of the vehicle as the engine nozzle and thereby minimizing the cowl drag. Vehicle design considerations in hypersonic flow show that the reliable prediction of a dual-mode scramjet performance is an absolute must in resolving hypersonic airbreathing vehicle designs. This becomes evident upon consideration of the fact that the net thrust for these vehicles is a relatively small difference between two large forces, the nozzle thrust and the forebody ram drag; thus, the potential for error and resultant sensitivity is high.

Because of the significance of the ramjet/scramjet integration on the design of hypersonic airbreathing vehicles, this paper focuses on the dual-mode ramjet engine/airframe integration methodologies currently in use in the SAO and the NAO and the enhancements in progress and those planned. Engineering and CFD methods to insure the evolution of engine/airframe integrated dual-mode ramjet designs with the desirable features mentioned above are discussed.

3. PROPULSION FLOWPATH/FORCE ACCOUNTING

For an underslung ramjet/scramjet airframe-integrated vehicle in which the vehicle lower forebody acts as a precompression surface and the vehicle lower aftbody acts as a high expansion ratio nozzle, the entire undersurface of the vehicle is a propulsion flowpath. This propulsion flowpath is defined by those surfaces that are wetted by air that flows through the engine nacelle and the forces acting thereon are charged to
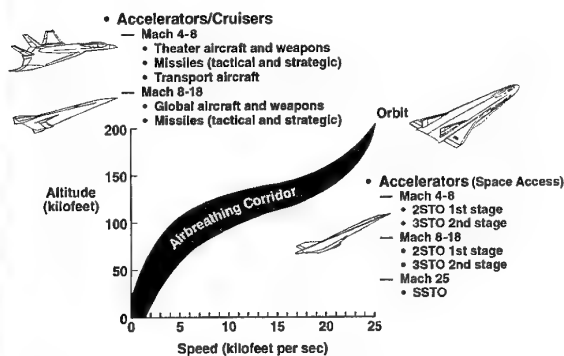

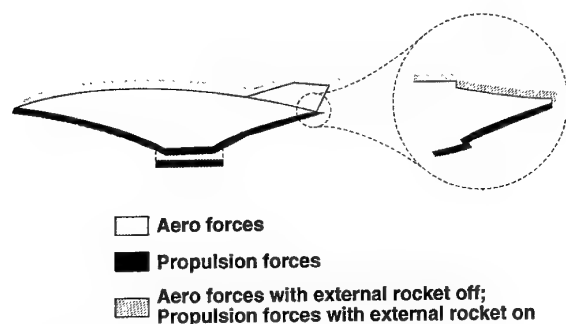Figure 1. Hypersonic airbreathing vehicle design matrix.

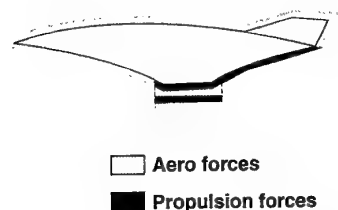*Figure 2a. Cowl-to-tail force accounting system.*

Figure 2b. Cowl-to-tail force accounting system.

propulsion (fig. 2a). This includes the lower external forebody, the interior nacelle, and the exterior nozzle aftbody. Forces on all other exterior surfaces including the exteriors of the engine cowl and sidewall are charged to aerodynamics. This classic force accounting system is referred to as freestream-to-freestream or more commonly nose-to-tail. When the engine is not operating (e.g., during reentry), exterior forebody and nozzle forces are charged to aerodynamics.

A second force accounting system, known as cowl-to-tail, is shown in figure 2b. Here, the propulsion accounting begins at the cowl lip rather than the apex of the vehicle and proceeds through the engine and out the aftbody nozzle. This approach usurps the need to trace streamlines forward from the cowl lip to the freestream in order to define the forebody control volume in the nose-to-tail accounting system and gives the aerodynamics a more conventional role that now includes the lower forebody.

If a control volume (momentum balance) cycle analysis approach is used to resolve the forces in the propulsion flowpath as depicted in figure 3a, then additional propulsion related forces should be designated which do not represent actual forces acting on the vehicle propulsion flowpath surfaces but rather are a result of the way in which control volumes are defined. These are: (1) spillage drag due to shock losses associated with uncaptured spilled air (fig. 3a); (2) plume drag which is a fictitious drag captured by the control volume at the external nozzle flow interface with the freestream flow (a virtual surface, fig. 3a) and thus must be added back into the force accounting; (3) ram drag which is the stream-thrust at the forward control volume interface with the forebody flow (subsequently captured); and (4) nozzle gross thrust which is the stream-thrust at the nozzle exit control volume interface. At the time that this approach was first implemented in hypersonic propulsion cycle analysis, only forces in the flight

direction were of interest; effective specific impulse, Isp was the primary focus. The control volume approach could not adequately predict propulsive lift and pitching moment, so an improved method was needed.

In propulsion cycle analysis methods that integrate the pressures on the propulsion surfaces in contrast to the control volume and momentum balance approach, none of the above corrections are required. This also applies to hybrid schemes (ref. 2) in which a control volume is used only for the combustor force resolution, and wall pressure plus skin friction integration's are used to resolve the forces on the remainder of the flowpath surfaces. Consequently, hybrid schemes lend themselves very well to propulsive lift and pitching moment computations. Figure 3b illustrates a hybrid scheme. This approach has become more practical in recent history due to improvements in computational technology. Thus, in general, forces resolved from control volumes confined to interior surfaces require no virtual interface corrections.

4.   CLASSES OF METHODS

Scramjet engine/airframe integration methodology can be classified into four levels (fig. 4. ref. 3). Level 1 uses analytical methods and generally include iteration on closed form solutions which are coded into fast running computer programs. Level 2 makes the transition to numerical analysis and includes finite difference/element/volume inviscid (Euler) flow field analysis and heat conduction/transfer codes. Also included in Level 2 are the integral boundary layer codes and finite element stress analysis codes. Levels 1 and 2 constitute the engineering methodology category since they are used extensively in conceptual/preliminary design and performance tasks. Level 2 also includes hybrid methods which combine and integrate methodologies across the fluid-structural-thermal disciplines.
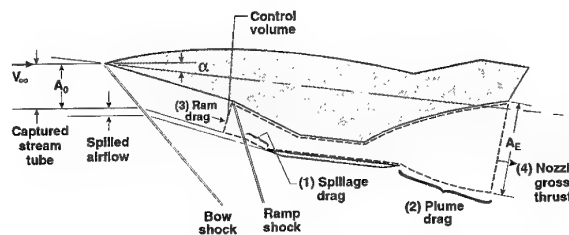

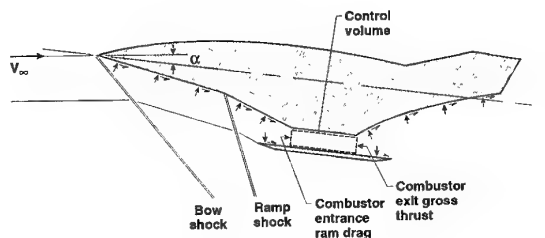*Figure 3a. Propulsion flowpath, control volume, and vectoral relationships—traditional approach.*

Figure 3b. Propulsion flowpath, control volume, and vectoral relationships—hybrid approach.
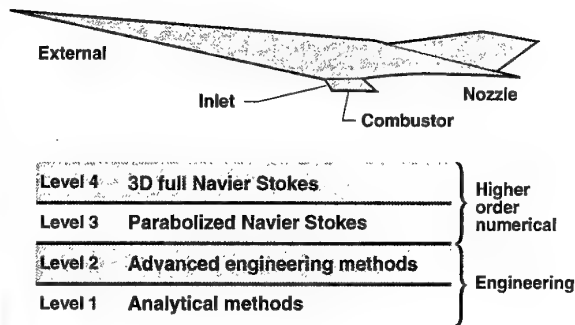
Figure 4. Methodology classification levels.

Level 3 consists of the Parabolized Navier Stokes (PNS) finite difference/volume codes which are used for parabolic problems. These flows generally consist of large supersonic regions with only embedded subsonic pockets. Level 4 is the highest level of analysis and consists of time-averaged Navier Stokes (TANS) codes. These can be Full Navier Stokes (FNS) codes or Navier Stokes solutions using the thin layer approximation (TLNS). These are used for flows which are viscous dominated and elliptic in nature, i.e. downstream pressure feed-back effects are included. The NS codes allow shear stress and heat transfer to be computed directly. Also included in Level 4 are the new coupled multi-disciplinary codes which include significant interaction among the fluid-structure-thermal effects.

Do not be confused by the levels. More is not always better. PNS is completely appropriate for some flows, those which have no separation. Engineering methods are also best for preliminary trade studies.

4.1 Engineering Methods
Engineering methods constitute the Level 1 and 2 classes of methodologies. They are used primarily in conceptual/preliminary design and performance tasks.

4.1.1 Cycle Analysis
The ramjet/scramjet cycle code used for characterizing performance as well as refining flowpath design for highly integrated engine/airframe configurations in SAO/NAO is SRGULL (fig. 5, ref. 2). SRGULL was developed at Langley
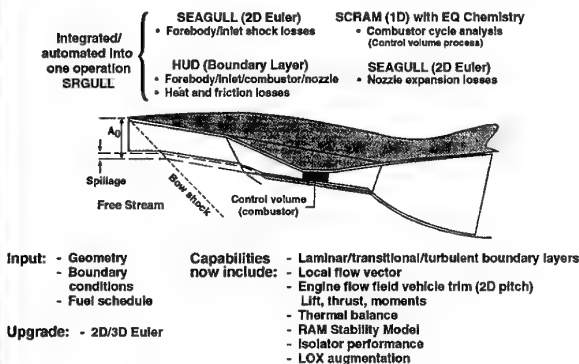
Figure 5. Tip-to-tail scramjet/ramjet cycle analysis, SRGULL.

over the last twenty five years by S. Z. Pinckney. It accurately resolves the net propulsive thrust of an airbreathing vehicle as a small difference between the combustor/nozzle thrust and the forebody/inlet drag. The forebody flowfield properties and the mass capture which SRGULL predicts are critical in resolving the net thrust.

SRGULL uses a 2-D/axisymmetric Euler (finite-difference, shock fitting) algorithm on the forebody and inlet, coupled with a boundary-layer solution, to predict the forebody/inlet drag and the flow properties entering the engine. The ramjet/scramjet solution is then completed using a 1-D cycle analysis with equilibrium chemistry and multiple steps through the combustor. A fuel mixing distribution with length is required input. Finally, the nozzle forces are resolved using the 2-D Euler and boundary-layer codes. A 3-D Euler capability is now being implemented into the code.

Capabilities in the SRGULL code include the analysis of laminar, transitional, and turbulent boundary layers; engine flowpath forces such as lift, thrust, and moments; and LOX augmentation of the scramjet which consists of small rocket motors firing parallel to the flow just downstream of the throat either at stoichiometric, fuel-rich or fuel-lean conditions. To first order, a thermal balance can also be accomplished. Given the wall temperature, heat flux to the walls (calculated by the code) and the fuel injection temperature, the amount of fuel required to actively cool the vehicle is determined. This fuel flow rate is then used to predict the net thrust for a thermally balanced system. Particularly at high hypersonic flight Mach numbers, the increased fuel flow rate, which is generally above an equivalence ratio of one, can significantly increase thrust but decreases specific impulse. The prediction of coolant fuel flow rate is further refined in the thermal management analysis as described in the corresponding section below.

SRGULL (ref. 2) also has the capability to predict engine unstart (ref. 4), which is another unique feature of this cycle code. Figure 6 (ref. 4) shows an isolator/ramjet/scramjet keel-line at the top. The arrows mark points where fuel can be injected. The four plots show the pressure distribution through the engine as a function of distance along the engine for various freestream Mach numbers where transition between pure ramjet and pure scramjet occurs. Note that in the top plot, fuel is being injected from the middle injectors at an equivalence ratio of 0.3 and from the downstream injectors at an equivalence ratio of 0.7. Also note the rise in pressure that occurs upstream of the $\phi = 0.3$ fuel injector. If more fuel were to be added at this fuel injector, the pressure rise would be pushed farther and farther upstream, until at some point an engine unstart occurs. Note that as the freestream Mach number increases, the fuel can be injected farther upstream without causing the disturbance to move upstream.

Figure 7 (ref. 4) shows an experiment run in a Langley tunnel to study the effects of geometry changes on isolator flowfield characteristics. As shown, SRGULL accurately predicts the pressure disturbance in the isolator.

The NASP Concept Demonstrator Engine (CDE) was tested in the 8-ft. diameter High Temperature Tunnel (HTT) at
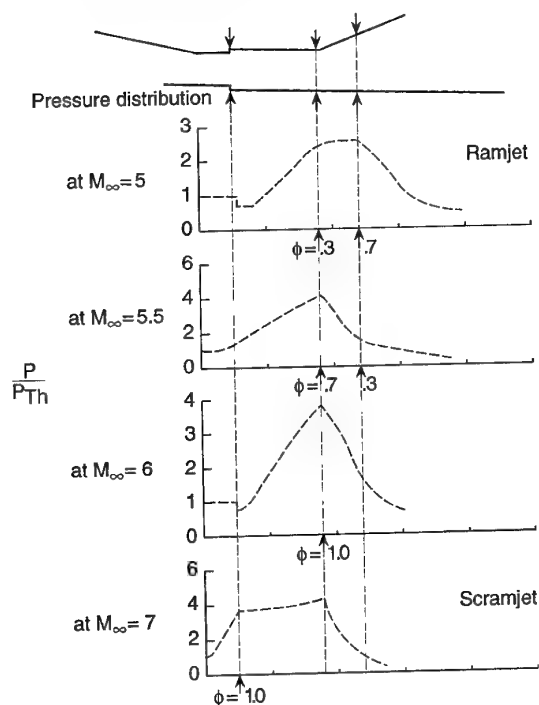
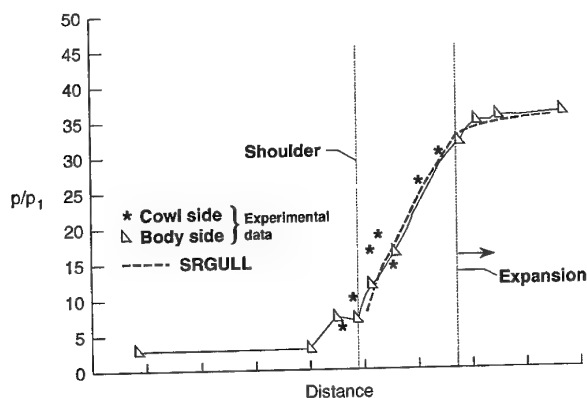Figure 6. Ramjet to scramjet mode transition with SRGULL.

Figure 7. Isolator model comparison with Mach 4 experimental data.

Langley. SRGULL accurately predicted the flowpath pressure distribution, including the pressure-rise magnitude and location, of the CDE in the 8' HTT at Mach 7 test conditions.

4.1.2 Inviscid Flow

Euler codes are used to approximate these flows in support of flowpath design/performance for underslung engine/airframe integrated configurations in which forebodies precompress the air entering the inlet and aftbodies provide combustor flow expansion surfaces.

4.1.2.1 2-D/Axisymmetric Euler

The 2-D/axisymmetric Euler code used in SAO/NAO is SEAGULL (ref. 5). It was developed by Manual Salas at

Langley in the mid 70's. It is a floating shock fitting technique in which second-order difference formulas are used for the computation of discontinuities. A procedure, based on the coalescence of characteristics is used to detect the formulation of shock waves. Mesh points that are crossed by discontinuities are recomputed. The technique provides resolution for 2-D external or internal flows with an arbitrary number of shock waves and contact surfaces. An example solution for the inviscid flow internal to a 2-D scramjet is presented in figure 8.

4.1.2.2 3-D Euler

To resolve 3-D inviscid flows, an unstructured, adaptive mesh Euler code (SAMflow, ref. 6) has been implemented in SAO/NAO by Dr. M. K. Lockwood. The unstructured, adaptive mesh methodology (ref. 7) was selected to provide resolution of shocks in a capturing technique with minimum griding effort by the analyst.

The spatial discretization is accomplished via finite element techniques on unstructured tetrahedral grids. In order to achieve high execution speeds, edge-based data structures are used. Either central or upwind flux (van Leer, Roe) formulations can be used. For the temporal discretization, both Taylor-Galerkin and Runge-Kutta time integration schemes are available. Monotonicity of the solution may be achieved through a blend of second- and fourth-order dissipation, Flux-Corrected Transport (FCT), or classic Total Variational Dimensioning (TVD) limiters. The equations of state supported by SAMflow include ideal gas, polytropic gas and real air table look-up.

A variety of boundary conditions can be prescribed to simulate engineering flows: subsonic, transonic, and supersonic in/outflow boundary conditions, total pressure inflow boundary conditions, static pressure, Mach number and normal flux outflow boundary conditions, and porous walls and periodicity boundary conditions.

An example application is shown in figure 9 in which the SAMflow code is used to resolve the 3-D nose-to-tail inviscid flow on a Mach 10, lifting-body airplane. These calculations were used to quantify the 3D inlet and nozzle flows in a dual-fuel lifting body configuration development study (ref. 8).

Also, the methodology (ref. 7) includes the capability for treating moving boundaries with prescribed motion or moving rigid bodies with motion computed from six degree of free-
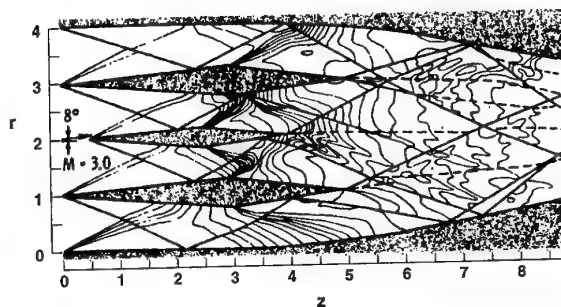

Figure 8. Flowfield for a simulated scramjet, showing shock waves, vortex sheets and isobars.
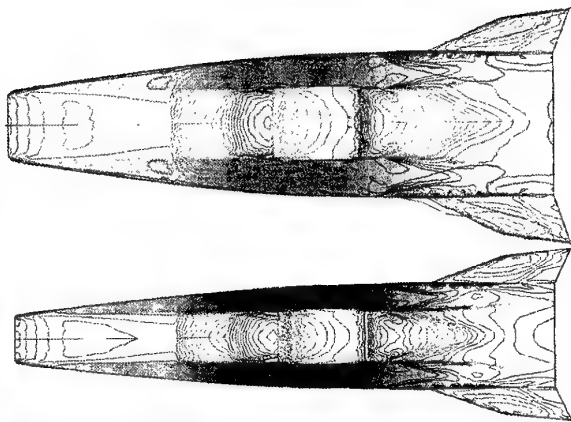
Figure 9. 3-D inviscid pressure contours on lifting-body cruise configuration at Mach 10 (design point) for two fineness ratios.

dom mechanics based on aerodynamic forces which are then linked back to the flow solver. To this end, the equations that constitute SAMflow are solved in the Arbitrary Lagrangean-Eulerian (ALE) frame. It is from this perspective, in addition to steady state solutions, that SAMflow is being used to assist in resolving the Hyper-X staging/separation flow/dynamics.

4.1.3 Boundary Layer

Boundary-layer calculations are required in the propulsion flowpath in conjunction with inviscid flow predictions to quantify heat transfer, skin friction (shear) and displacement thicknesses. For engineering calculations, SAO/NAO relies on integral methods.

In the cycle calculation, SRGULL (ref. 2), the basic integral method used (ref. 9) is applicable to the prediction of axisymmetric and two-dimensional laminar and turbulent boundary layers. It requires the simultaneous solution of the integral momentum, moment of momentum, and energy equations. In order to obtain this simultaneous solution, auxiliary relations are used for the boundary-layer velocity and enthalpy profiles, the shear distribution across the boundary layer, and the local surface friction and heat transfer, all of which are derived to be a function of the local pressure gradient and the total heat removed from the boundary-layer forward of the local station. These relations are derived using modified flat-plate log-log type velocity profiles for pressure gradients as a basis of departure from flat plate solutions (ref. 9), modified flat-plate Crocco-type enthalpy-velocity profile (ref. 10) to account for the total heat removed from the boundary layer, and flat-plate friction and heat transfer methods (Reynolds analogy). For laminar boundary layers, the flat-plate friction correlation method used is a combination of the Blasius incompressible friction coefficient correlation (ref. 11) and Eckert's reference temperature method for the compressibility correction (ref. 12). For turbulent boundary layers, the flat-plate friction correlation method used is the modified Spalding-Chi method of Neal and Bertram (ref. 13). For the heat transfer, the flat-plate method is the modified Reynolds analogy of Colburn (ref. 14).

For more general applications, boundary-layer predictions are

calculated with a Boundary-Layer Integral Matrix Procedure (BLIMP, ref. 15). This well-known/widely used code was developed through U.S. Air Force funding to compute viscous boundary-layer effects over 2D axisymmetric or planar conditions as inputs. SAO/NAO results from the Euler solver SAMflow (ref. 6) is used to provide boundary-layer edge conditions to BLIMP. The edge conditions are supplied along inviscid streamlines along which the integral BLIMP procedure parabolically marches. This provides a reasonable merging of the accuracy of SAMflow for 3D inviscid flowfield computations and the reliability of BLIMP for viscous computations. In this manner, boundary layers on 3-D configurations (propulsion flowpath or aerodynamic surfaces) can be approximated; streamline divergence is included but without boundary-layer crossflow. An example of the coupled SAMflow-BLIMP software application on a hypersonic configuration in terms of pressure contours and heat transfer/shear stress distribution at Mach 2 is given in figures 10a and 10b respectively.

4.1.4 Thermal Management

The thermal management approach used for hypersonic airbreathing vehicles in SAO was developed by D. H. Petley and associates (ref. 16) and is based on a 3-D transient thermal analyzer (SINDA-85, ref. 17). It has been deemed the "Integrated Numerical Methods for Hypersonic Aircraft Cooling Systems Analysis" and includes capability for Thermal Protection System (TPS) sizing (ref. 18). The focus here is the propulsion flowpath.

Generally it is known a priori that the engine flowpath requires active cooling. An example of a coolant routing along the keel-line of the inlet, combustor and nozzle on the body
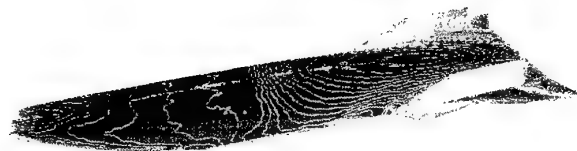

Figure 10a. SAMFLOW-generated surface pressure contours for a hypersonic cruise vehicle design.
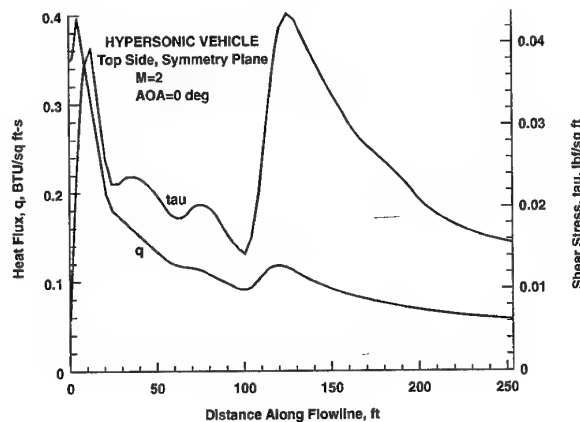

Figure 10b. BLIMP-generated heat flux and shear stress along top centerline for a hypersonic cruise vehicle design.
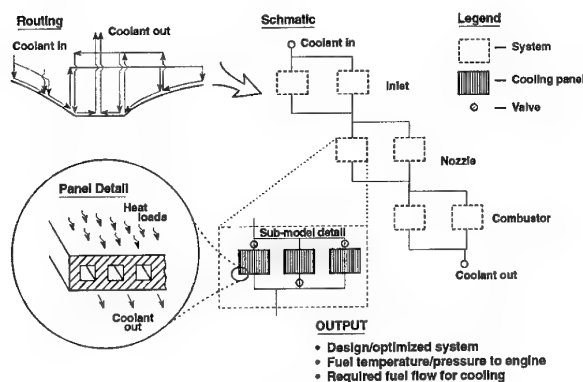
Figure 11. Cooling system design/analysis.

side of the propulsion flowpath is shown in the upper left-hand corner of Figure 11. Schematically, the active cooling network is shown in the middle of the figure. Inputs to the network analysis include the initial coolant system architecture, propulsion heat loads and flowpath geometry, coolant supply temperature, coolant and material properties, and the total pressure drop through the network, based on the pumping system and the desired fuel injection pressure. From this, the coolant mass flow, temperature and pressure distribution, along with the panel temperature distribution are determined. The panel temperatures are checked to ensure that they remain below the material temperature limits. Also, panel stresses are calculated. For example, if a hole is punctured in one of the cooling panel walls, the stress on that wall must not be high enough to cause the panel to "un-zip." The network architecture and panel designs are modified until the overall cooling system weight and coolant flow rate are minimized, while meeting the above constraints. As noted in the propulsion section, the coolant flow rate and the fuel injection properties have a significant impact on the net propulsive thrust.

As an example, consider the cooling network design for the Access to Space airbreathing/rocket SSTO vehicle (ref. 19). Slush hydrogen was stored in the tank at 20 psig and 25° R. It was pumped to 5500 psi and 60° R before circulating through the cooling panels, then through a turbine to drive the pump, back into the cooling network again, and out into the combustor. The heat exchangers were sized at Mach 15 conditions, where the heat loads were the greatest. The cooling panel network was designed to deliver hot hydrogen to the injectors. Detailed thermal and fluid analysis was conducted on the cooling panels to determine the channel dimensions, pressure drop across each panel, and material selection.

4.1.5 Structures

Hypersonic vehicle structures are characterized by thermal loads that are as high as the mechanical loads; for portions of the propulsion flowpath, the thermal loads can be even higher than the mechanical loads. Due to the design sensitivities inherent in airbreathing hypersonic vehicles, it is necessary to accurately predict structural weight, as well as the aerothermoelastic flight response of the vehicle even at the conceptual/preliminary design level. Some of the codes used in the SAO include Pro/ENGINEER (ref. 20) for computer aided design, MSC/NASTRAN (ref. 21), P3 PATRAN (ref. 22),

and Pro/MECHANICA (ref. 23) for finite element analysis to predict element loads; and an in-house developed software package, ST-SIZE (ref. 24), to perform panel failure mode analysis and panel sizing.

The automated structural design process (ref. 24), developed under the supervision of P.L. Moses, a non-personal services (NPS) contractor to SAO, is shown schematically in figure 12. This figure illustrates how a structural panel is sized in ST-SIZE (ref. 24). Starting on the left-hand side of the figure, initial element stiffnesses, thermal coefficients, thermal and mechanical loads, and the finite element geometry are input into the finite element analysis code. Forces on each of the elements are then determined. Moving to the right of the figure, the element forces, material selections and panel and beam concepts are input to the ST-SIZE code. Here up to 30 failure mode analyses in strength and 26 failure mode analyses in stability are performed, and the panel is sized to meet these failure modes. Given the new panel design, the element stiffnesses and thermal coefficients change and the FEA must recalculate the element forces. This iterative process continues until convergence is achieved. The net result is the minimum panel weight, which results from a maximally stressed panel that also meets each of the failure mode tests, all with the margin-of-safety.

In general, the structural panels of airbreathing hypersonic vehicles are unsymmetric—geometrically and/or thermally. As a result, traditional 2-D panel methods, which do not account for panel asymmetry, can predict inaccurate panel sizes. In contrast, an enhanced version of ST-SIZE, developed in SAO (ref. 25), models the panel asymmetry. This is accomplished by calculating the membrane bending coupling in the 2-D element. The methods of ST-SIZE are the basis for the HyperSizer™ code which is a commercial product of Collier Research and Development Corporation (ref. 25).

The unit weights of the engine primary structure for the Access to Space airbreathing single-stage-to-orbit (SSTO) vehicle (ref. 19) were the results of FEM analysis and automated structural design using the structural/thermal sizing code, ST-SIZE. The primary structure for supporting the propulsion flowpath operating pressure loads was a system of
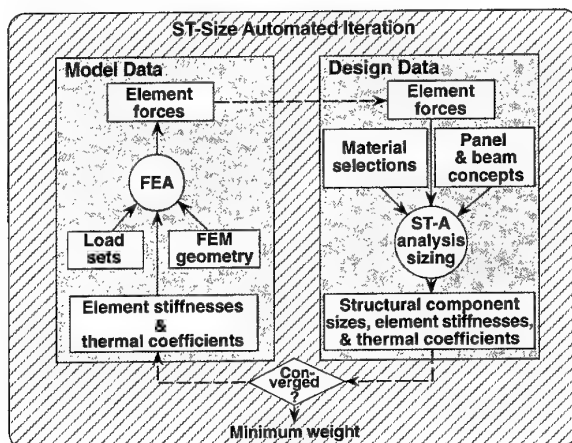

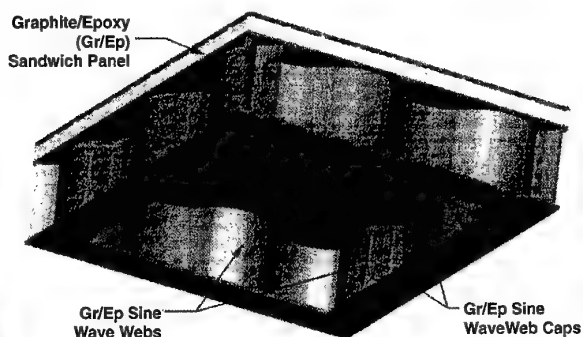*Figure 12. Structural sizing process.*

Figure 13. Primary structure concept for engine of SSTO vehicle.

honeycomb panels, backed by integrally attached stiffening beams made up of sine-wave webs and flat caps, as shown in Figure 13. This arrangement transmits the engine forces into trusses which are directly attached to the integral tank structure of the airframe. These trusses also provide stiffness to the airframe and naturally invoke some load sharing. The primary structure of the engine is isolated from the hot gas in the flowpath by non-integral heat exchangers that transmit the pressure forces through to the honeycomb panels.

4.2   Higher Order Numerical Methods

Resolution of the scramjet propulsion flowpath in preliminary to final design activities, and especially the resolution of mixing and combustion in the combustor requires the most sophisticated, more computationally intensive and less stable numerical methodologies of Level 3 and 4. These high fidelity approaches with suitable modelings of turbulence, viscous effects, and chemistry are the full Navier Stokes (elliptic) and parabolic Navier Stokes (marching) codes that capture both the inviscid and viscous flow characteristics simultaneously.

4.2.1   Full Navier Stokes

The code most relied on in NAO to resolve the most complex problems in the flowpath from 3-D shock/boundary-layer interaction in the inlet to fuel injection and mixing modeling in the combustor to 3-D expansion and possible relaminarization in a chemically reacting nozzle is the GASP code (General Aerodynamic Simulation Program, ref. 26 & 27). It was developed to provide generalized numerical predictions, encompassing flows over aerodynamic and propulsion-flowpath surfaces, that are required for the detail of hypersonic airbreathing vehicles.

GASP is a finite volume, upwind-biased code that can solve 1-dimensional, 2-dimensional, axisymmetric and fully 3-dimensional flows (ref. 28). It has various chemical and thermodynamic models for solving (single or multiple species) perfect gas flows, flow in chemical equilibrium, chemically frozen flows, and flows with finite chemical reactions. It can be run in the Space Marching (time-dependent parabolized Navier Stokes) or elliptic mode, either implicit or explicit, with Euler, Thin-Layer Navier Stokes (TLNS), and Full Navier Stokes (FNS) terms. Turbulence is modeled by either the standard algebraic Baldwin-Lomax model, a high Reynolds Number model for shear flows, or a choice of two 2-equation turbulent models that integrate completely through

the boundary layer: The Lam-Bremhorst model (ref. 29) and Chien's model (ref. 30).

The GASP code is versatile (ref. 31) because of multi-block and multi-zone features and convenient to use for solving complex flowfields. The ability to switch from solving the full Navier- Stokes equations (elliptically) to the parabolized Navier-Stokes equations (in the marching mode) at any streamwise location in the computational domain makes it very convenient and efficient to use.

GASP is routinely utilized for analysis of scramjet component and engine flowpath performance. Figure 14 illustrates one such solution, for a powered wind tunnel model tested at NASA LaRC. This type of analysis provides comparison with experimental data. Comparison with the experimental data provides confidence in predicted flight vehicle engine performance. The GASP code has also been compared with simple "unit" inlet, combustor and nozzle experimental data bases. Figure 15 represents calibration (ref. 28) of the GASP turbulence modeling for nozzle heat transfer. This study demonstrated the requirement for a two-equation turbulence modeling for nozzle "relaminarization" effects on heat transfer. Similar studies have illustrated turbulence modeling requirements for the inlet shock boundary-layer interactions (ref.
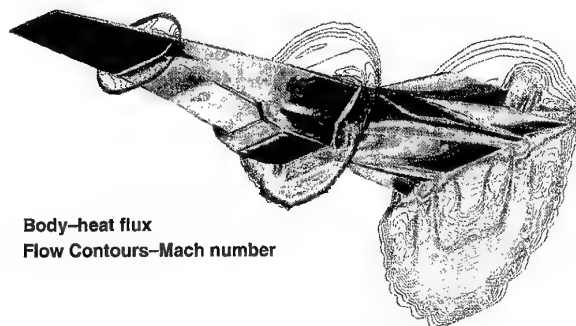

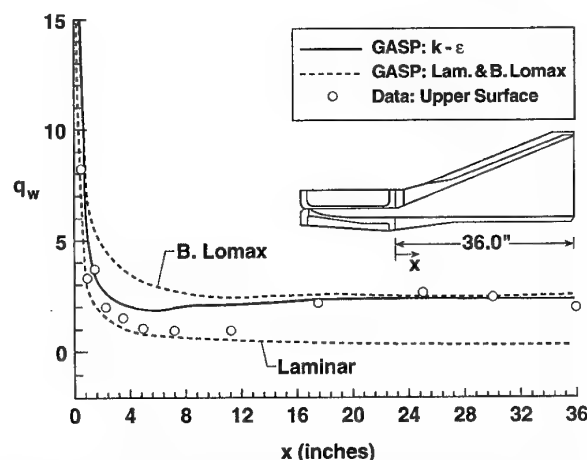*Figure 14. Powered hypersonic (Mach 7) vehicle CFD solution.*

Figure 15. Heat transfer comparisons on nozzle upper surface.

a. Comparison with experimental PLIIF

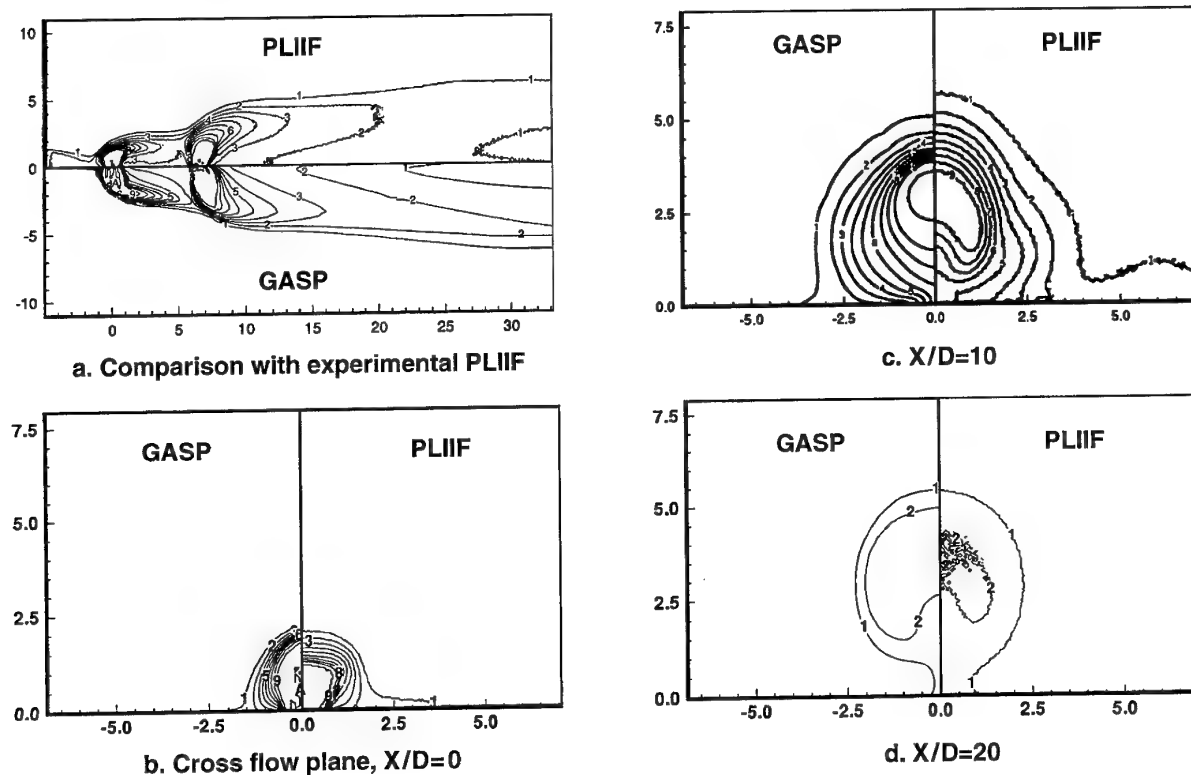

b. Cross flow plane, X/D=0

c. X/D=10

d. X/D=20

Figure 16. Comparison of injectant mole fraction contours on a flat plate from GASP solutions with experimental PLIF images.

32), including flow separation modeling, and grid resolution for shock-shock interaction cowl leading edge heat flux resolution. The GASP code has also been extensively verified for combustor analysis. An example of this is presented in figure 16 (ref. 31). This comparison with the University of Virginia (ref. 34) in-line flush wall injector, Planar Laser Induced Fluorescence (PLIF) data demonstrated that the GASP code can accurately predict the complex fuel mixing process. Similar comparisons have been made for cold and reacting flows at conditions up to flight Mach number 17 simulation (for example, ref. 35). In addition, GASP has been used to study facility effects on scramjet combustor performance (ref. 33). Figure 17 illustrates a solution for a cavity flame holder (ref. 36), which provided both fuel mixing and combustion efficiency, and evaluation of the combustor wall heating.

4.2.2 Parabolic Navier Stokes
PNS or space marching solutions are adequate for much of the scramjet flowpath, including large regions of the forebody and all of the nozzle. Design and analysis of scramjet fuel injection, mixing and combustion is one of the best uses for 3-D CFD methods. This process cannot be modeled with simpler methods, as the flow will always be three-dimensional. Effective design evaluation of scramjet combustor performance requires a rapid, approximate method for screening of concepts. The SHIP (Supersonic Hydrogen Injection Program) was developed for that purpose. The scramjet combustor, being predominantly supersonic flow, can be approximated using either space marching (GASP) of PNS (SHIP) solutions. The small subsonic regions are approximated by wakes, established by forcing

the flow downstream, as described in reference 37. The SHIP3D code solves the parabolized, Favre averaged equations for the conservation of mass, momentum, total energy, total fuel and turbulence fields in a variable area domain of rectangular cross section (ref. 38). Turbulence closure is at the two-equation level, with one of several high-Re or low-Re models, including corrections for compressibility. The governing transport equations are solved by the SIMPLEC pressure correction algorithm (ref. 39) extended to compressible flow.
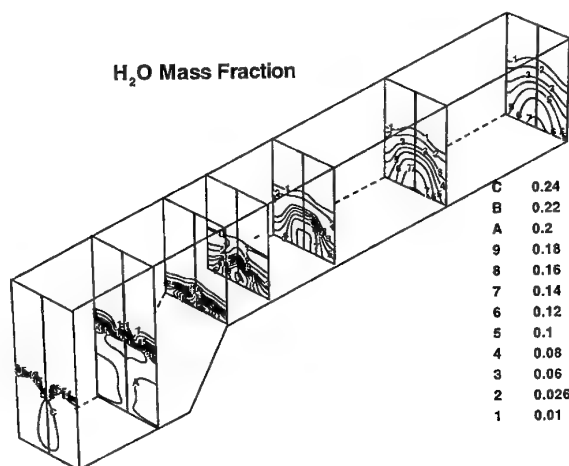

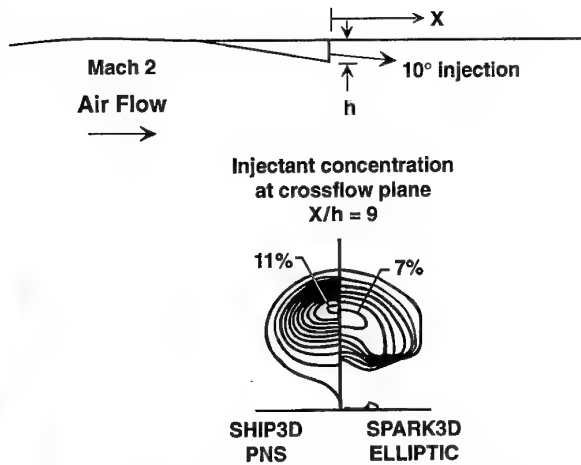*Figure 17. Water mass fraction from GASP for flame holding cavity injector.*

*Figure 18. SHIP-SPARK comparison for ramp injection.*

Figure 18 illustrates a comparison between fuel plume from a ramp-type fuel injector, predicted with a full Navier Stokes code, and with the SHIP PNS code. The SHIP code is routinely used for evaluation of scramjet combustor design options, including the effects of fuel and film/transpiration injector design, combustor expansion effects on mixing, etc. Parametric combustor design studies are possible with the SHIP code, an example of which is presented in reference 40.

5. DISCIPLINE INTERDEPENDENCE

The emphasis here is scramjet engine/airframe integration methodology, and thus the focus is on the propulsion flowpath; however, the remainder of the vehicle cannot be ignored in the design of the flowpath because of the strong couplings that reflect throughout in hypersonic airbreathing vehicle designs. Figure 19 illustrates the complex interdependence among the disciplines in airbreathing hypersonic vehicle design (ref. 41). For example, aerodynamic's input surface coordinates from geometry; interacts with propulsion in defining the entire vehicle configuration; outputs heat loads to the thermal management analysis; outputs forces and temperatures to structures; and iterates with the trajectory to yield flight conditions, forces, and moments. As noted previously, not only are there a large number of couplings, but the sensitivities are high and the system is highly nonlinear. Thus, resolution requires a high degree of accuracy with all disciplines involved.

5.1 Automation/Optimization

In order to automate the design process and to be sure to capture all the interaction, a working environment for the multidisciplinary design, analysis, and optimization of airbreathing hypersonic vehicles (HOLIST) is being developed by SAO (ref. 41) in part through a contract with McDonnell Douglas (ref. 42). D.H. Petley is coordinating the effort. The implementation of HOLIST in SAO is being performed by J.G. Martin, an NPS contractor to SAO. HOLIST will help eliminate disconnects between disciplines, enable rapid multidisci-
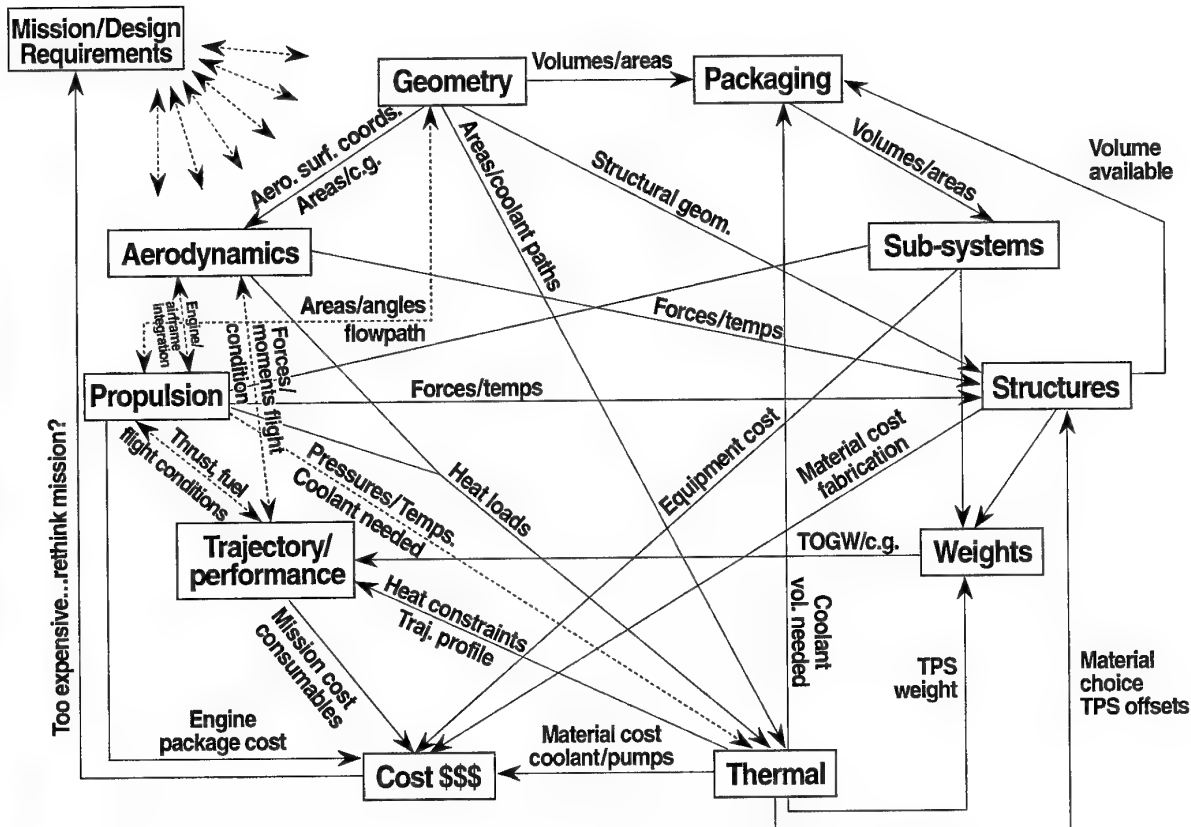
Note: Solid lines represent one-way flow of information; dashed lines represent two-way flows.

Figure 19. Discipline interdependence.

plinary parametrics, allow the evaluation of design sensitivities, and will enable the optimization of the vehicle design and trajectory. Currently a parametric geometry model, Pro/ENGINEER (ref. 20), is being incorporated into HOLIST. This will enable the entire vehicle configuration to be represented with a number of specified design variables. HOLIST is constructed modularly such that when improvements are made in any of the discipline tools, or new tools are available, these can be easily incorporated. A user-friendly optimizer, Optdes-X (ref. 43), has been integrated into the environment, and the entire system is set up on workstations, complete with graphical user interfaces.

Figure 20 is a simplified flowchart illustrating how an optimization proceeds in HOLIST. In the upper left-hand corner, the process set-up includes defining the design variables, objective function, constraints and convergence criteria for a run. The baseline vehicle geometry and packaging, together with a definition of the mass and thermo properties, follow. Analysis of the configuration proceeds with aerodynamics, propulsion, etc. (Note that for simplification of the diagram, several disciplines are not represented here, including structures and thermal management, for example.) The analysis can either be performed in real time, i.e., by running an analysis code, or a database can be accessed to obtain the discipline results. It is important to note that there is more than just one result being passed through this flowchart. In other words, since the vehicle will fly some trajectory, matrices of aerodynamic and propulsion data representing the coefficients of lift, drag, and thrust, and fuel flow rate, for example, at appropriate values of angle of attack and Mach number, must be passed through the loop. In addition, the propulsion flowpath geometry may vary along a trajectory requiring multiple geometry definitions.

Once the analyses are completed, the vehicle is flown as represented by the "Analyze Mission" box. From the mission results, the vehicle is sized. (It is also possible to define a scaling factor as a variable and use |PFR-PFA| ≤.1 as a constraint. This would eliminate the need to perform the sizing process in the extra loop.) At this point, if only a single vehicle analysis were required, the process would be complete. However, if it is desired to optimize the vehicle, the optimization process begins. Finite differences are used to calculate the derivatives of the objective function with respect to each of the design variables. Thus, for the perturbation of each design variable, one pass through the loop is made. Based on the derivative information, the vehicle design for the next iteration is defined. The objective function for the new design is evaluated, the derivatives at the new point in the design space are determined, and the process continues with the vehicle definition for the next iteration. Iterations continue until convergence criteria and all the constraints are satisfied, yielding the optimum vehicle configuration.

6. SUMMARY

The development of the scramjet engine/airframe integration methodology has progressed to a degree that allows resolution of hypersonic airbreathing vehicle designs for space access vehicles, cruise airplanes, and missiles for the dual-mode-ramjet flowpath segment of the design. The challenges ahead lie in reducing the turn-around time required with the application of this methodology in the hypersonic airbreathing vehicle design process, in refinement/implimentation of low speed aero/ propulsion integration methods, and in the development and automation of multidiscipline design processes. As these design processes mature, viable space access and hypersonic cruise airbreathing vehicle designs will evolve.
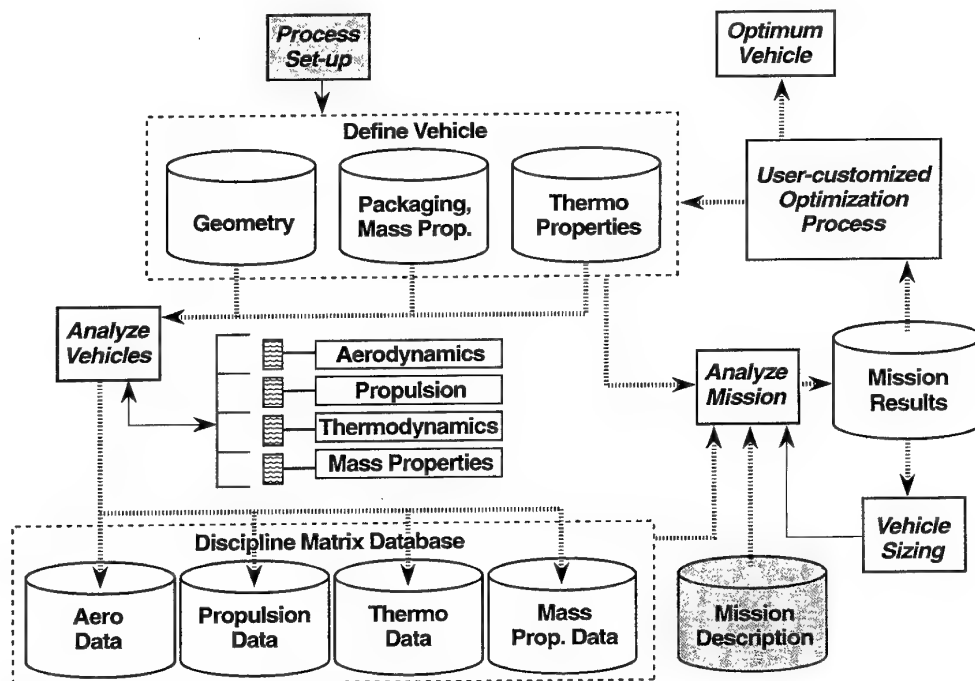

Figure 20. HOLIST design optimization.

7. REFERENCES

1.   Hunt, J. L.; Lockwood, M. K.; Petley, D. H.; and Pegg, R. J.: Hypersonic Airbreathing Vehicle Visions and Enhancing Technologies. Presented at the 1997 STAIF Conference, Albuquerque, NM, January 26-30, 1997.

2.   Pinckney, S. Z. and Walton, J. T.: Program SRGULL: An Advanced Engineering Model for the Prediction of Airframe-Integrated Subsonic/Supersonic Hydrogen Combustion Ramjet Cycle Performance. NASP TM-1120, January 1991.

3.   McClinton, C. R.; Bittner, R.; and Kamath, P.: CFD Support of NASP Design. AIAA 90-5249, presented at the AIAA Second International Aerospace Planes Conference, Orlando, Florida , October 29-31, 1990,.

4.   Pinckney, S. Z.: Isolator Modeling for Ramjet and Ramjet/Scramjet Transition. National Aero-Space Plane Technology Review, Paper Number 171, 1993.

5.   Salas, M. D.: Shock Fitting Method for Complicated Two-Dimensional Supersonic Flows. Vol. 14, No. 5 in AIAA Journal, May 1976.

6.   Spradley, L. W.; Robertson, S. J.; Mahaffey, W. A.; and Lohner, R.: The Solution Adaptive Modeling (SAM) CFD Software System. RSI 96-002, September 1996.

7.   Lohner, R., et. al.: Fluid-Structure Interaction Using a Loose Coupling Algorithm and Adaptive Unstructured Grids. AIAA 95-2259, San Diego, California, June 1995.

8.   Bogar, T. J.; Alberico, J. F.; Johnson, D. B.; Espinosa, A. M.; and Lockwood, M. K.: Dual-Fuel Lifting Body Configuration Development. AIAA 96-4592, Norfolk, Virginia, November 1996.

9.   Pinckney, S. Z.: Turbulent Heat-Transfer Prediction Method for Application to Scramjet Engines. NASA TN D-7810, November 1974.

10.   Pinckney, S. Z.: Flat-Plate Compressible Turbulent Boundary-Layer Static Temperature Distribution with Heat Transfer. Presented at AIAA Fifth Aerospace Sciences Meeting, New York, New York, January 23-25, 1967.

11.   Schlichting, H.: Boundary Layer Theory. Pargamon Press, 1955.

12.   Nestler, D. E.: Survey of Theoretical and Experimental Determinations of Skin Friction in Compressible Boundary Layers: Part I. The Laminar Boundary Layer on a Flat Plate. Thermodynamics Technical Memorandum No. 100, September 29, 1958.

13.   Neal, L., Jr. and Bertram, M. H.: Turbulent-Skin-Friction and Heat-Transfer Charts Adapted from the Spalding and Chi Method. NASA TN D-3969, 1967.

14.   Nestler, D. E.: Survey of Theoretical and Experimental Determinations of Skin Friction in Compressible Boundary Layers: Part II. The Turbulent Boundary Layer on a Flat Plate. Thermodynamics Technical Memorandum No. 109, January 29, 1959.

15.   Murry, A. L.: Further Enhancements of the BLIMP Computer Code and User's Guide. Air Force Wright Aeronautical Labs, AFWAL-TR-88-3010, June 1988.

16.   Petley, D. H.; Jones, S. C.; and Dziedzic, W. M.: Integrated Numerical Methods for Hypersonic Aircraft Cooling Systems Analysis. AIAA 92-0254, Reno, Nevada, January 6-9, 1992.

17.   Anon.: SINDA '85/FLUINT User's Manual. Denver Aerospace Division of Martin Marietta Corp., Denver, Colorado, November 1987.

18.   Petley, D. H. and Yarrington, P.: Design and Analysis of the Thermal Protection System for a Mach 10 Cruise Vehicle. Presented at the 1996 JANNAF Propulsion & Joint Subcommittee Meeting, Albuquerque, New Mexico, December 9-13, 1996.

19.   Hunt, J. L.: Airbreathing/Rocket Single-Stage-to-Orbit Design Matrix. AIAA 95-6011, Chattanooga, Tennessee, April 3-7, 1995.

20.   Parametric Technology Corporation: Pro/ENGINEER Fundamentals. Release 17.0.

21.   Reymond, M. and Miller, M. of the McNeal-Schwendler Corporation: MSC/NASTRAN—Quick Reference Guide. Version 69.

22.   PDA Engineering, PATRAN Division: P3/PATRAN User Manual. Vol. 1, Part 1: Introduction to PATRAN 3 and Part 2: Basic Fundamentals. Publication No. 903000, 1993.

23.   Parametric Technology Corporation: Pro/MECHANI-CA™ Installation Guide. Release 17.0, August 1996.

24.   Collier, C.: Thermoelastic Formulation of Stiffened, Unsymmetric Composite Panels for Finite Element Analysis of High Speed Aircraft. Paper 94-1579, 1994.

25.   Collier, C.: Structural Analysis and Sizing of Stiffened, Metal Matrix Composite Panels for Hypersonic Vehicles. AIAA 92-5015, 1992.

26.   Walters, R. W.; Cinnella, P.; Stack, D. C.; and Halt, D.: Characteristics Based Algorithms for Flows in Thermo-Chemical Nonequilibrium. AIAA 90-0393, January 1990.

27.   Walters, R. W.: GASP - A Production Level Navier-Stokes Code Including Finite-Rate Chemistry. Proceedings of the Fourth Annual Meeting of the Center for Turbomachinery and Propulsion Research, April 1990.

28.   Jentink, T. N.: An Evaluation of Nozzle Relaminarization Using Low Reynolds Number k- e Turbulence Models. AIAA 93-0610, Reno, Nevada, January 11-14, 1993.

29.   Lam, C. K. G. and Bremhorst, K.: A Modified Form of the k- ε Model for Predicting Wall Turbulence. Transactions of the ASME, Vol. 103, pp. 456-460, September 1981.

30. Chien, K.: Predictions of Channel and Boundary-Layer Flows with a Low-Reynolds Number Turbulence Model. AIAA Journal, pp. 33-38, January 1982.

31. Srinivasan, S.; Bittner, R. D.; and Bobskill, G. J.: Summary of the GASP Code Application and Evaluation Effort for Scramjet Combustor Flowfields. AIAA 93-1973, Monterey, California, June 28-30, 1993.

32. Mekkes, G. L.: Computational Analysis of Hypersonic Shock Wave/Wall Jet Interaction. AIAA 93-0604, January 11-14, 1993.

33. Srinivasan, S. and Erickson, W. D.: Influence of Test Gas Vitiation on Mixing and Combustion at Mach 7 Flight Conditions. AIAA 94-2816, June 27-29, 1994.

34. MacDaniel, J. M.; Fletcher, D.; Hartfield, R.; and Hollo, S.: Staged Transverse Injection into Mach 2 Flow Behind a Rearward Facing Step: A 3-D Compressible Test Case for Hypersonic Combustion Code Validation. AIAA 91-5071, December 1991.

35. Rogers, R. C.; et. al.: Quantification of Scramjet Mixing in the Hypervelocity Flow of a Pulse Facility. AIAA 94-2518, June 1994.

36. McClinton, C. R.: Comparative Flowpath Analysis and Design Assessment of an Axisymmetric Hydrogen Fueled Scramjet Flight Test Engine at a Mach Number of 6.5. AIAA 96-4571, November 1996.

37. Kamath, P. S.; Mao, M.; and McClinton, C. R.: Scramjet Combustor Analysis with the SHIP3D PNS Code. AIAA 91-5090, 1991.

38. Kamath, P. S. and Mao, M.: Computation of Transverse Injection Into a Supersonic Flow with the SHIP3D PNS Code, AIAA 92-5062, 1992.

39. Braaten, M. E.: Development and Evaluation of Direct and Iterative Methods for the Solution of Equations Governing Recirculating Flows. Ph.D. Thesis, University of Minnesota, 1985.

40. Kamath, P. S.; Mao, M.; and McClinton, C. R.: A Parametric Study of Scramjet Combustors for Mach 8 to Mach 20 Flight. AIAA 91-1412, June 24-26, 1991.

41. Lockwood, M. K.; Petley, D. H.; Hunt, J. L.; and Martin, J. G.: Airbreathing Hypersonic Vehicle Design and Analysis Methods. AIAA 96-0381, Reno, Nevada, January 15-18, 1996.

42. Alberico, J.: The Development of an Interactive Computer Tool for Synthesis and Optimization of Hypersonic Airbreathing Vehicles. AIAA 92-5076, Orlando, Florida, December 1-4, 1992.

43. Design Synthesis, Inc.: OptdesX—A Software System for Optimal Engineering Design Users Manual. Release 2.0.3, 1994.

Entrée d'air et intégration entrée d'air / chambre de combustion

(Air intake and air intake / combustion interaction)

Isabelle AUNEAU

AEROSPATIALE Missiles - 18000 Bourges Cedex - France

Philippe DUVEAU

ONERA - 92322 Châtillon Cedex - France

Résumé

Des études de véhicules à propulsion aérobie (missiles, lanceurs) sont entreprises à AEROSPATIALE et ONERA depuis des années.
La conception de ces véhicules nécessite l'étude de prises d'air.
Le choix des prises d'air qui seront installées sur un véhicule donné est relatif à plusieurs considérations, parmi lesquelles le type de véhicule, sa mission et les performances attendues, ainsi que d'autres contraintes telles que l'intégration du système propulsif, la furtivité, ...

L'étude des prises d'air ne peut pas être découplée de la conception du moteur ainsi que des autres éléments du véhicule.
En effet, pour les véhicules hypersoniques, l'avant-corps est utilisé comme une surface de compression à part entière et les mâts d'injection prennent part au processus de compression interne; ces deux éléments doivent être pris en compte dès le début de la définition de la prise d'air, ainsi que les besoins liés à la combustion.
Pour ce qui concerne les véhicules supersoniques propulsés par statoréacteurs, le fuselage prend une part moins importante sur la définition de la prise d'air; néanmoins, des interactions fortes existent entre l'entrée d'air et la chambre de combustion, ceci en termes de performances ainsi qu'en termes de distorsions acceptables pour la combustion.

Tous ces éléments doivent être pris en compte dès le tout début de l'étude de la prise d'air.
Une méthodologie de conception et d'optimisation a été mise en place dans ce but; elle combine expériences et calculs.

Abstract

High speed air-breathing vehicle studies (missiles, combines cycle engines single or two stage-to-orbit launchers) have been undertaken at AEROSPATIALE and ONERA for many years.
The design of these vehicles requires the study of air intakes.
The choice of the air intakes to be installed on a given vehicle is related to different considerations, among which the type of vehicle, its mission and expected performances, other constraints such as propulsive system integration, stealthiness,...

The study of inlets can not be uncoupled from the design of other vehicle elements.
Indeed, for hypersonic vehicles, the forebody usually acts as a pre-compression ramp and the scramjet injection struts take part of the internal compression process : both of these elements have to be taken into account at the very beginning of the inlet design, as well as flowfield requirements for combustion.
For the supersonic vehicles using ramjets, though the forebody flowfield has less importance on the inlet design than for the hypersonic case, strong interactions exist between the inlet and the combustion chamber; and this, not only in terms of system performances, but also in terms of acceptable flowfield distortions for the combustion.

All these elements have to be integrated since the very beginning of the inlet study.
A design and optimisation methodology has been settled down with this aim, combining wind tunnel tests and computations.

1. Introduction

Ce document présente tout d'abord des considérations générales relatives à l'utilisation de prises d'air de stato et superstato-réacteurs.
Ensuite, l'intégration de la prise d'air, avec le fuselage d'une part et la chambre de combustion d'autre part, est traitée.
Enfin, la méthodologie de conception est détaillée.

2. Prises d'air - Généralités - Critères de choix

Une prise d'air a pour objet d'alimenter le moteur d'un engin aérobie par un écoulement adapté au fonctionnement de ce dernier. Dans le cas particulier des prises d'air supersoniques, celles-ci doivent ralentir l'écoulement capté jusqu'à un certain nombre de Mach interne. Ce nombre de Mach est en règle générale subsonique (turboréacteur et statoréacteur classique), mais il peut aussi être supersonique comme c'est le cas dans un superstatoréacteur (statoréacteur à combustion supersonique).

Pour le concepteur, il s'agit le plus souvent de garantir en outre, une efficacité élevée, la "moindre" distorsion de l'écoulement interne dans le plan d'entrée du moteur et une marge de stabilité suffisante, d'intégrer au mieux les prises d'air au véhicule et de limiter la masse et les coûts. Il peut éventuellement s'ajouter une exigence de furtivité (limitation de la SER : Surface Equivalente Radar et de la SIR : Signature Infra-Rouge) pour certains missiles.

Ces contraintes sont à prendre en considération dans tout le domaine de vol de l'appareil en nombre de Mach, incidence et dérapage. Elles différeront largement selon que l'on s'intéressera à un avion civil ou militaire, à un missile à vitesse de croisière subsonique ou supersonique ou enfin à un engin aérobie évoluant dans le domaine hypersonique, du type lanceur trans-atmosphérique et détermineront dans une large mesure le choix des prises d'air.

La définition d'une prise d'air résulte donc d'un compromis prenant en compte les contraintes liées au véhicule, aux missions assignées à ce dernier et au mode de pilotage dans le cas d'un missile. Elle repose sur l'expérience acquise et fait appel dans un premier temps à des méthodes de prédiction semi-empiriques. Par la suite, les formes aérodynamiques peuvent être optimisées à l'aide de simulations numériques plus complexes [1-2].

Nous limiterons ici notre propos aux missiles et aux lanceurs aérobies.

2.1. Application aux missiles

Selon le type de missile aérobie considéré, on recherchera une vitesse de croisière ou une portée élevée en respectant des contraintes d'encombrement, d'installation de prises d'air, de discrétion radar, de limitation des coûts et de simplicité technologique.

Ce dernier point exclut en général le recours à des prises d'air à géométrie variable.

L'étendue du domaine de vol, les manoeuvres à réaliser ainsi que le mode de pilotage retenu conditionnent le choix de la motorisation (turboréacteur ou statoréacteur), du nombre de prises d'air et de leurs formes ainsi que de la configuration aérodynamique du missile.

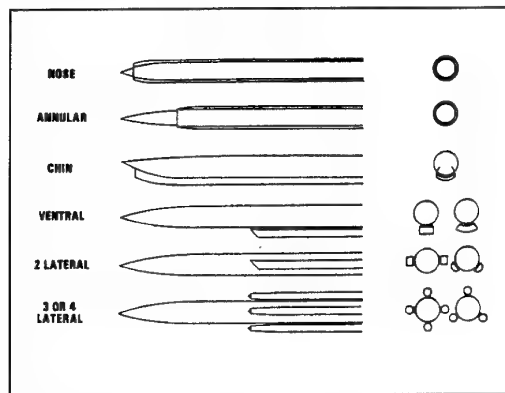Quelques configurations typiques sont schématisées ci dessous, figure 1 :

fig. 1 : différentes configurations aérodynamiques de missiles

Les avantages et inconvénients respectifs des différentes configurations ont déjà été exposés en détail par de nombreux auteurs tant du point de vue de l'aérodynamique externe [3] qu'interne [4-5]. Rappelons simplement que le type de pilotage est un facteur déterminant pour le choix de la configuration aérodynamique.

Ainsi, pour un pilotage tous azimuts, qui permet une grande manoeuvrabilité et convient particulièrement pour des croisières à basse altitude, des configurations à 3 ou 4

prises d'air latérales sont souvent employées. L'alimentation des prises d'air peut cependant poser problème en incidence.

En revanche, pour un pilotage de type avion, souvent associé à la recherche d'une portée élevée, les configurations à une prise d'air ventrale ou à deux prises d'air sont préférables. Il est en effet possible d'optimiser l'adaptation des prises d'air et leur emplacement pour tirer le meilleur parti du champ aérodynamique du fuselage, même à incidence élevée (figure 2) :
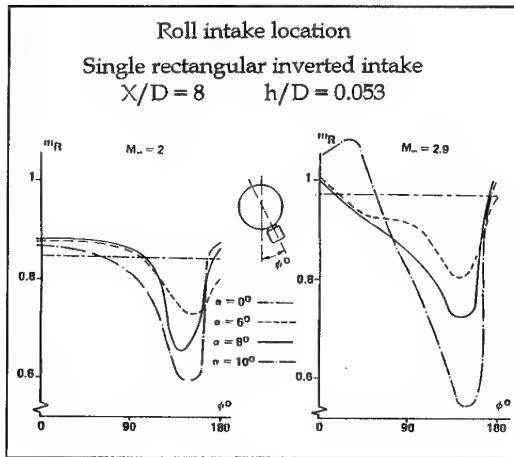

fig. 2 : débit capté fonction de la position de la prise d'air autour du fuselage

Le choix de la position longitudinale (X/D) des prises d'air, de leur adaptation en nombre de Mach (rampes de compression) et de la position de la carène relativement au fuselage (classique, latérale ou inversée) nécessite une étude approfondie de l'écoulement autour de ce dernier. Cette étude peut être réalisée expérimentalement, par sondage d'écoulement en diverses sections X/D, mais aussi par simulation numérique en fluide visqueux.

2.2 Application aux véhicules hypersoniques

Dans le cas d'un lanceur aérobie, l'objectif est de mettre en orbite à moindre coût une charge utile maximale. Il faut donc définir un système propulsif performant qui dépendra de l'architecture du véhicule (mono ou bi-étages).

Le foisonnement des modes de propulsion envisageables rend le choix et l'optimisation des prises d'air particulièrement délicats [6-7-8].

Dans tous les cas, il s'agit de disposer de prises d'air performantes à bas nombre de Mach pour assurer une bonne capacité d'accélération au lanceur.

Quand ce dernier est de type mono-étage, la prise d'air doit de plus être en mesure d'alimenter correctement un superstatoréacteur à partir de Mach 6 environ. Pour donner une idée de la complexité du dimensionnement des prises d'air, on a représenté figure 3 l'évolution du tube de courant infini amont à capter pour alimenter un système propulsif de type fusée-statomixte-fusée en veines séparées en fonction du nombre de Mach de vol :

fig. 3 : tube de courant à capter en fonction du nombre de Mach

Pour répondre aux besoins de tels moteurs, l'ONERA a mis au point et expérimenté avec succès des prises d'air à géométrie variable [9].

L'intégration du fuseau moteur au fuselage devient primordiale compte tenu de la difficulté d'assurer un bilan poussée moins traînée favorable à grand nombre de Mach. En particulier, l'intrados du fuselage devient partie intégrante du système propulsif en agissant comme rampe de précompression pour les prises d'air.

3. Intégration prise d'air - fuselage

3.1. Application aux missiles

Le champ local d'écoulement au droit des prises d'air est fortement affecté par la forme du fuselage et l'attitude du missile (α, β).

Considérons pour fixer les idées l'écoulement autour d'un corps cylindrique en incidence. La théorie des corps élancés indique en fluide parfait l'existence de survitesses transversales qui conduisent à des incidences locales élevées, défavorables au bon fonctionnement des prises d'air (figure 4) :
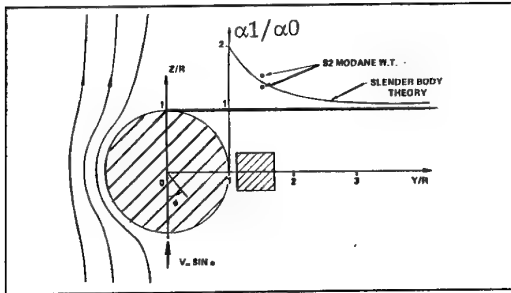

fig. 4 : influence de l'incidence de vol sur les incidences locales autour du fuselage.

En outre, dans ces conditions, la couche limite a tendance à épaissir du côté extrados et à être sensible aux gradients de pression adverses, d'où d'éventuels décollements et tourbillons associés (figure 5) :
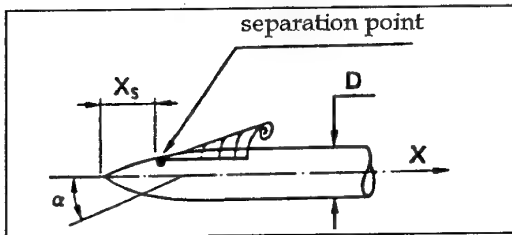
fig. 5 : tourbillons d'ogive lors de la mise en incidence.

On voit qu'on aura tout intérêt à éviter de placer les prises d'air latéralement ou à l'extrados de tels fuselages, mais plutôt à l'intrados.

De même, la position longitudinale des prises d'air doit être étudiée avec soin. Il faut en effet tenir compte le cas échéant du développement des structures tourbillonnaires et éviter particulièrement le raccord ogive-cylindre, générateur de survitesses (figure 6) :
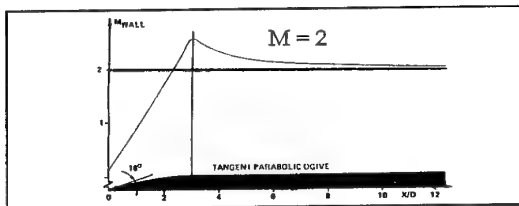
fig. 6 : survitesses au raccordement ogive-cylindre

Afin de faciliter l'intégration des prises d'air, on peut dessiner des fuselages non circulaires, de type lenticulaire, à l'intrados aplati. Dans ce cas, l'installation d'une prise d'air ventrale est préférable, l'effet du fuselage devenant particulièrement intéressant pour la prise d'air (figure 7) :
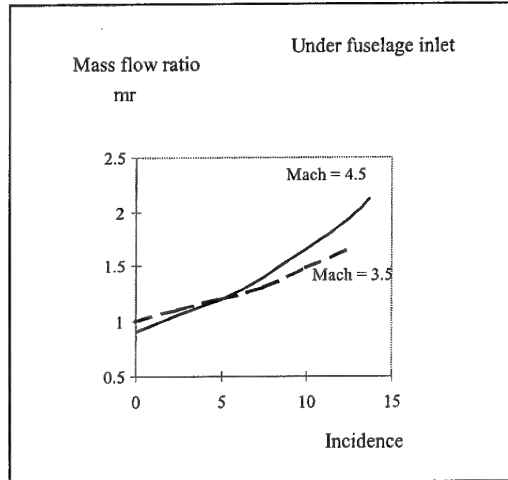
fig. 7 : débit d'air capté par la prise d'air ventrale.

L'évaluation de l'écoulement autour du fuselage nécessite alors le recours à des calculs en fluide visqueux. A titre d'exemple, la figure 8 montre le champ aérodynamique obtenu autour d'un fuselage lenticulaire, à Mach 2 et incidence 10°, par calcul 3D en laminaire à l'aide du code FLU3M [10]. On constate que les structures tourbillonnaires sont particulièrement bien captées par le calcul.

Si des prises d'air en écope, ou affleurantes sont particulièrement indiquées pour les missiles subsonique, il devient par contre important de décaler les prises d'air du fuselage en supersonique en ménageant un piège à couche limite externe. En effet, le fait de capter de la couche limite à l'entrée de la prise d'air se traduit systémati-quement par une perte d'efficacité, même en l'absence d'interaction choc-couche limite.

Il est alors usuel de séparer l'entrée d'air de la paroi du missile par une étrave qui dévie la couche limite entre la prise d'air et le fuselage. L'intérêt de ce dispositif a été clairement mis en évidence du point de vue de l'efficacité des prises d'air (figure 9) :
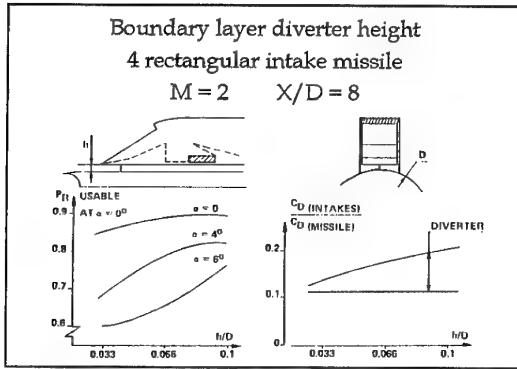
fig. 9 : influence du piège à couche limite externe

fig. 10 : méthodes semi-empiriques pour prédire les performances des prises d'air.

Le choix d'une étrave résulte évidemment d'un compromis entre le gain en rendement escompté pour les prises d'air et l'augmentation de la traînée du missile.

Une rampe de précompression semi-conique, placée en amont de la prise d'air peut dans certains cas jouer un rôle similaire à une étrave, en améliorant l'efficacité de l'écoulement capté tout en évacuant la couche limite latéralement.

Si des essais de prise d'air isolée restent intéressants pour balayer un grand nombre de configurations et permettre de compléter des modèles aérodynamiques, les essais avec prises d'air intégrées au fuselage sont indispensables pour connaître les caractéristiques de fonctionnement réelles de ces dernières.

De même, pour prédire les performances des prises d'air, l'écoulement autour du fuselage doit être pris en compte dès l'avant-projet.

A cet effet, des méthodes semi-empiriques fondées sur l'utilisation de la notion d'écoulement moyen, de calculs chocs-détentes et d'une modélisation des pertes internes dans les diffuseurs de prises d'air sont employées à l'ONERA et à AEROSPATIALE Missiles. Elles permettent d'estimer avec une précision satisfaisante les performances des prises d'air (figure 10).

Par ailleurs, des simulations numériques plus élaborées sont réalisées par AEROSPATIALE Missiles et l'ONERA en immergeant la prise d'air dans le champ aérodynamique du missile, celui-ci étant obtenu par calcul ou sondage d'écoulement en soufflerie, de façon à disposer de conditions aux limites réalistes.

3.2. Application aux véhicules hypersoniques

Comme signalé précédemment, la prise d'air d'un lanceur aérobie doit être étroitement intégrée à l'intrados du fuselage pour ne pas pénaliser le bilan de traînée à grand nombre de Mach.

Il faut en particulier que les prises d'air restent situées au dessus du choc de tête de l'avant-corps durant tout le vol aérobie pour éviter le cisaillement des rampes de compression, à l'origine de surflux pouvant endommager les structures.

Dans le cas d'un lanceur, on cherche plutôt à optimiser la forme de l'avant-corps pour faciliter l'intégration des prises d'air.

A ce stade, de nombreux paramètres interviennent comme la forme du nez (figure 11) et la forme en plan de l'avant-corps. Un nez trop émoussé tendra par exemple à créer une épaisse couche d'entropie au niveau des prises d'air par le biais du choc fort de tête.
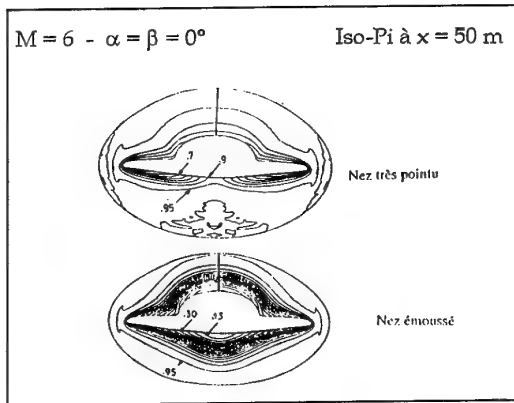
fig. 11 : influence de la forme du nez

Un avant-corps à l'intrados aplati comme celui retenu dans le cadre du programme PREPHA (figure 12) facilite l'intégration de prises d'air à géométrie variable, de type bidimensionnel. En revanche, la couche limite a alors tendance à s'accumuler au niveau du plan de symétrie vertical de l'avant-corps, faute de pouvoir se déverser latéralement. La figure 13 illustre ce phénomène en présentant la répartition de pression d'arrêt isentropique dans le plan d'entrée des prises d'air. Celle-ci est obtenue à partir d'un calcul pseudo-PNS turbulent réalisé à Mach 6,4 autour de l'avant-corps PREPHA avec le modèle de turbulence standard de Baldwin-Lomax.

Afin qu'un statoréacteur classique contribue efficacement à l'accélération du véhicule, il est préférable de ménager un piège à couche limite externe de façon à évacuer une partie de la couche limite en amont des prises d'air. Par contre, le fonctionnement d'un superstatoréacteur nécessite de capter un tube de courant important à des températures très élevées (1650 K à Mach 6 et près de 5000 K à Mach 12) (voir paragraphe 2), ce qui exclut d'évacuer tout ou partie de l'épaisse couche limite en amont des prises d'air, même si l'efficacité de ces dernières s'en trouve affectée, d'autant plus que la traînée générée par une étrave serait trop pénalisante à grande vitesse, compte tenu des incertitudes pesant sur le bilan poussée moins traînée du véhicule.

4. Intégration prise d'air - chambre de combustion

Nous venons de décrire, dans le chapitre précédent, les interactions entre la partie amont (fuselage) et la prise d'air. Nous allons maintenant aborder la prise en compte de la partie aval, à savoir la chambre de combustion.

L'ensemble propulsif composé de la prise d'air et du moteur va atteindre, pour un point de vol donné (Mach, α, β, croisière ou accélération,...) un état d'équilibre qui fournira une certaine poussée. Pour cet état d'équilibre, la prise d'air sera caractérisée par deux éléments: d'une part sa performance (η_{02} : récupération de pression totale et ε : coefficient de débit) et d'autre part sa distorsion, c'est à dire la structure de l'écoulement à l'entrée du moteur.

La performance (η_{02} , ε) se répercute directement sur la poussée du véhicule tandis que la distorsion va tout d'abord influencer le fonctionnement de la combustion.

Les contraintes liées à la présence du moteur étant relativement différentes en fonction de la vitesse associée au véhicule, nous allons détailler l'environnement de chaque mode de fonctionnement.

4.1. Cas du turboréacteur

Pour le cas des missiles subsoniques propulsés par turboréacteurs, la prise d'air doit assurer la fonction de captation du débit d'air nécessaire au fonctionnement du moteur, ainsi que sa compression.
Cette compression doit être effectuée avec le soucis de limitation des pertes de charges qui se traduisent directement par une limitation de la poussée du moteur.

Pour un nombre de Mach, une incidence et un dérapage de vol donnés, on obtient une courbe caractéristique du fonctionnement de la prise d'air :
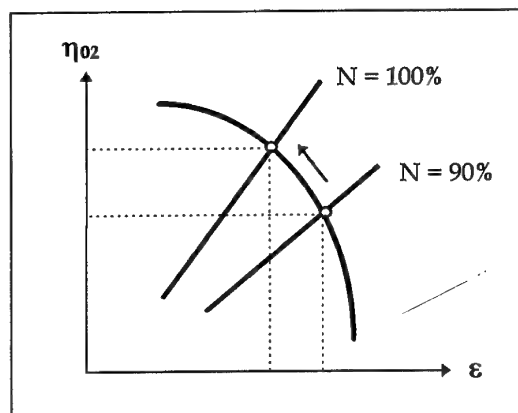

fig. 14 : performances de la prise d'air

Le point de fonctionnement de l'ensemble propulsif se situe à l'intersection de la courbe caractéristique de la prise d'air et de la droite de fonctionnement moteur (qui dépend principalement du régime moteur N (tr/min), puis de l'altitude et de l'atmosphère,...).

Au point de fonctionnement déterminé, la cartographie de l'écoulement (en iso-Mach ou iso - pression totale) va qualifier les hétérogénéités en entrée de compresseur (figure 15).

Les **cartographies** fournissent des informations qualitatives quant au faciès de l'écoulement. Notamment, elles permettent de déceler la présence éventuelle de décollements tournants, néfastes puisqu'ils peuvent conduire au désamorçage du moteur.
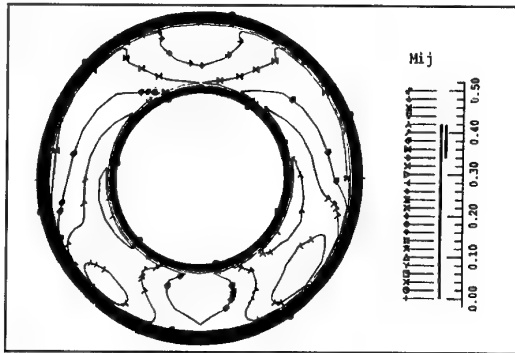
fig. 15 : cartographie iso-Mach

En plus de cette information qualitative, le motoriste juge de l'adéquation de la prise d'air au turboréacteur grâce aux **coefficients de distorsion**, qui doivent se situer en deçà de maximums admissibles, variables selon le turboréacteur.

Les coefficients les plus fréquemment utilisés sont **les coefficients sectoriels** DC45 ou DC60.

$$DC45 = \frac{Pi2moy45}{Q2}$$
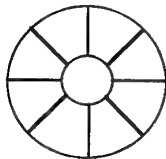
Pi$_{2moy45}$: moyenne des Pi2 sur un secteur angulaire de 45°,

Pi$_2$: moyenne des pressions d'arrêt sur tout le disque,

Q$_2$: pression cinétique moyenne dans le plan 2.

Ce coefficient traduit la répartition de pression totale autour de la pression moyenne sur le disque divisé en huit secteurs et indique le positionnement de l'hétérogénéité.

Le coefficient DC60 se calcule par le même principe, le disque étant divisé cette fois en six secteurs.

Il existe d'autres coefficients qui permettent également de quantifier l'hétérogénéité de l'écoulement : il s'agit des **coefficients circulaires** IDC et IDR qui se définissent à partir des "j" couronnes de mesures :

IDC : coefficient circonférenciel

$$IDCj = \frac{Pij - Pij\,min}{Pi2} \qquad IDCmoy = \frac{\sum IDCj}{j}$$

Pij : pression totale moyenne sur la couronne j,

IDR : coefficient radial

$$IDRj = \frac{Pi2 - Pij}{Pi2} \qquad IDRmax = max(IDRj)$$

4.2. Cas du statoréacteur

La prise d'air de statoréacteur peut être caractérisée par ses trois régimes de fonctionnement, ceux-ci dépendant de la condition aval, c'est à dire de la contre pression imposée par la combustion.

Pour une basse richesse injectée φ$_i$, la prise d'air fonctionne en régime dit **supercritique** ①, la pression en fin de diffuseur est faible; l'adaptation de la prise d'air à cette condition correspond à un positionnement du choc droit relativement en aval dans le diffuseur. Le débit capté est alors maximum tandis que l'efficacité est faible, du fait de la forte intensité du choc droit.
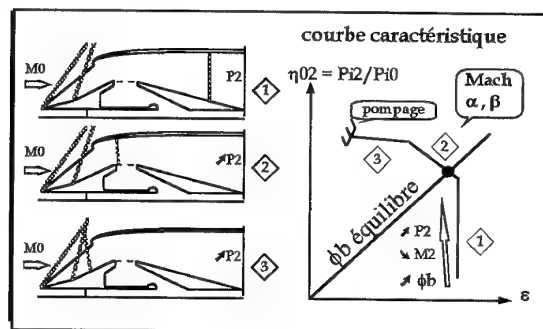

fig. 16 : régimes de fonctionnement de la prise d'air

Lorsque l'on augmente la richesse du mélange, la contre pression s'accroît et le choc droit est progressivement repoussé vers l'amont. Lorsqu'il se situe au niveau du col de la prise d'air, le régime est appelé **critique** ②, le piège interne débite, ce qui fait chuter le débit moteur et l'efficacité est maximale. Le régime **subcritique** ③ correspond au cas où le choc droit est en amont du col.

A un nombre de Mach donné et pour une configuration de prise d'air et de chambre de combustion donnée, les iso - richesse brûlée φb apparaissent sur le digramme (η_{02}, ε) comme des droites passant par l'origine.

La connaissance de la relation : $\varphi b \Leftrightarrow (\eta_{02} / \varepsilon)$ permet donc de déterminer, de la même manière que pour le turboréacteur, le point de fonctionnement de l'ensemble propulsif pour une configuration de vol donnée (accélération maximale, croisière, ...).

La prise d'air du statoréacteur sera également caractérisée par la distorsion qu'elle va générer en fin de diffuseur.
Cette distorsion est fonction de nombreux paramètres, parmi lesquels :

- la géométrie de la prise d'air, longueur de diffuseur,...
- le nombre de Mach, relatif au Mach d'adaptation,
- le régime de fonctionnement,
- les intensités des interactions internes,...

La figure 17 illustre les distorsions obtenues en fin de prise d'air pour deux nombres de Mach et pour différents régimes de fonctionnement :
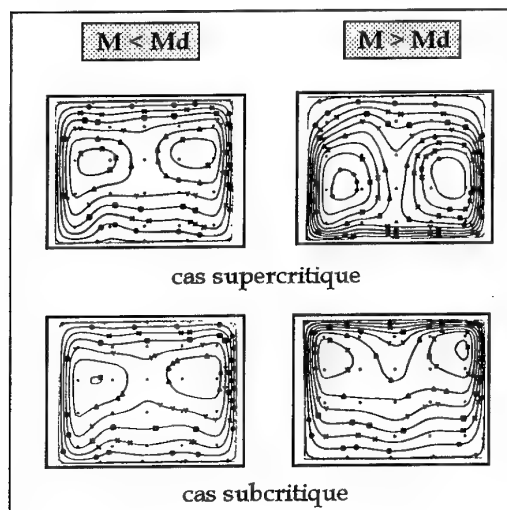

fig. 17 : iso-Mach en fin de diffuseur

On peut qualitativement dresser un état des distorsions en fin de diffuseur.

En revanche, contrairement au cas du turboréacteur pour lequel des critères quantitatifs permettent de juger de l'admissibilité des distorsions, qui doivent par ailleurs être minimales, il n'existe pas de critère simple pour la cas du statoréacteur; une certaine hétérogénéité "maîtrisée" pouvant être favorable au mélange air-combustible, en fonction de la position des injecteurs.

Cette hétérogénéité ne doit toutefois pas être trop importante, car :

- elle se répercute sur l'efficacité η_{24} du moteur. En conséquence, on doit par exemple éviter des écoulements localement transsoniques,...
- elle peut conduire à l'obtention de zones où l'écoulement présente des décollements avec recirculations aux parois; ce qui peut amener à des remontées de combustion dans la prise d'air.

4.3. Cas du superstatoréacteur

Pour des nombres de Mach de vol très élevés, le statoréacteur classique ne convient plus car il fournit des niveaux de poussée trop faibles, notamment à cause de l'efficacité très réduite de la prise d'air; on a alors recours au superstatoréacteur (statoréacteur à combustion supersonique).

La prise d'air équipant ce type de moteur fournit un débit d'air ralenti jusqu'à un Mach supersonique compatible avec le mélange et de la combustion.

Les interactions entre la prise d'air et la chambre de combustion sont en conséquence moins importantes, puisque la notion de régime de fonctionnement disparaît; pour une attitude de vol donnée (Mach, α, β), la prise d'air fournira un couple (η_{02}, ε).

D'un point de vue géométrique, la relation prise d'air - chambre est plus étroite, puisque dans certains cas les mâts d'injection participent à la compression interne, comme par exemple dans le cadre du programme PREPHA [2, 8, 11].
La conception de ces mâts doit alors prendre en compte tant les contraintes liées à l'aérodynamique interne (amorçage, efficacité) que celles liées à la combustion (mélange).

Dans d'autres cas, chambre de combustion et prise d'air sont séparées par un "isolateur"; il s'agit d'un tronçon de section constante,

relativement long qui va isoler les chocs de compression de la prise d'air du train de chocs issu de la chambre de combustion et causé par les décollements de la couche limite soumise aux gradients de pression. Cet "isolateur" évite ainsi les déversements de débit et les désamorçages de la prise d'air. De nombreux travaux ont été consacrés à ce sujet [11 - 14].

La connaissance de la cartographie de l'écoulement dans le plan d'injection est aussi primordiale que la connaissance de l'efficacité globale η02 de la prise d'air car la distorsion peut être très importante du fait que l'on obtient un écoulement supersonique issu d'interactions multiples avec des effets tridimensionnels souvent non négligeables.

L'illustration de la planche 19 montre les Mach locaux obtenus au col de la prise d'air, pour une configuration présentant deux mâts d'injection (planche 18). Ces résultats sont issus de mesures de peignage de pression d'arrêt et statique dans ce plan. L'hétérogénéité est assez grande et résulte partiellement de la présence des mâts.
. Cette illustration montre qu'il est extrêmement délicat de déterminer des grandeurs moyennes dans ce plan (Pi2, P2, M2); d'ailleurs, le choix de la méthode de calcul de moyenne n'est pas sans conséquences sur le résultat obtenu.

Comme pour le statoréacteur et de manière a priori encore plus importante, une certaine hétérogénéité peut être favorable pour le mélange.

4.4. Prise en compte de la combustion en aérodynamique interne

Pour ce qui est de la **prise d'air hypersonique** de superstatoréacteur, la prise en compte de la combustion en aérodynamique interne se traduit par la mise en place dans la maquette d'essais et dans les calculs des mâts d'injection. Dans les deux cas, les caractéristiques (performances et distorsions) de la prise d'air sont fournies au col des mâts, donc dans le plan d'injection; on évince dans ce cas la prise en compte de l'influence de l'obstruction que créé la combustion.

Pour la **prise d'air subsonique** alimentant un turboréacteur, les mesures de peignage de l'écoulement sont effectuées dans le plan d'entrée du compresseur.

Du point de vue de la méthodologie d'essais, la variation du débit capté par la prise d'air est obtenue la plupart du temps par effet trompe, ce qui permet de simuler une variation du régime de fonctionnement du moteur et de décrire la courbe caractéristique.

Pour la **prise d'air supersonique** alimentant un statoréacteur ou un turboréacteur, on utilise le théorème d'Hugoniot généralisé qui indique qu'une obstruction mécanique est équivalente à une obstruction thermique.

Ainsi, en essais, on aura un obturateur placé en aval de la prise d'air, qui, en se déplaçant, permettra la simulation des différents régimes de fonctionnement (figure 20) : on obtiendra ainsi la courbe caractéristique de la prise d'air.
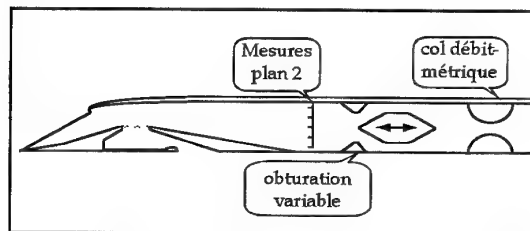

fig. 20 : simulation de la combustion statoréacteur

Pour les calculs numériques d'aérodynamique interne, la modélisation de la combustion sera effectuée en appliquant une condition aux limites en pression, condition évolutive de manière à décrire la courbe caractéristique.

4.5. Prise en compte de l'aérodynamique interne en combustion

Lors d'une phase avancée du développement du véhicule, la validation des performances du système propulsif est en général effectuée grâce à des essais dits en **"jet libre"**; c'est à dire que l'ensemble comprenant la prise d'air, le moteur et éventuellement le fuselage est installé dans une veine d'essai et est immergé dans les conditions de vol réelles de l'engin.

Dans ce cas, on est assuré d'une bonne représentativité des éléments constitutifs et de leurs interactions.

Lors de la phase de définition - mise au point de l'ensemble propulsif, les thèmes aérodynamique interne et combustion sont traités séparément, de manière à limiter le temps et le coût de développement. Les essais de combustion sont ainsi effectués dans la plupart des cas par l'intermédiaire d'une technique dite **"veine forcée"**, en l'absence de

prise d'air. Le moyen d'essai délivre donc un écoulement homogène réglé pour les conditions de vol souhaitées par l'intermédiaire d'une tuyère.

Comme on l'a vu lors des chapitres précédents, la prise d'air délivre un écoulement qui a certaines caractéristiques d'hétérogénéité qui vont influencer le fonctionnement du moteur. Il apparaît donc important de pouvoir simuler cette distorsion dès le début de la conception du moteur.

Pour cela, on intercale entre la tuyère d'alimentation et le système de peignage du plan 2 - injection un dispositif qui va simuler la distorsion naturelle de la prise d'air (figure 21). L'artifice peut être très simple (système de cornières) ou beaucoup plus complexe; ceci est fonction de la distorsion de la prise d'air.
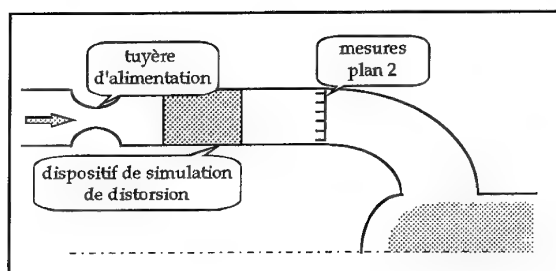
fig. 21 :   alimentation en veine forcée de la chambre de combustion

L'intérêt d'un tel dispositif est prépondérant si celui-ci est capable de simuler la distorsion réelle de la prise d'air sur tout le domaine de fonctionnement statoréacteur, y compris lors des éventuels changements de régime.

Les prises d'air hypersoniques sont le théâtre d'interactions multiples, l'écoulement résultant est par conséquent très hétérogène; de plus, les chocs issus des rampes ou de la carène peuvent venir interagir avec les mâts d'injection.

Dans le cadre du programme PREPHA, il est apparu intéressant de simuler une hétérogénéité "représentative" lors d'essais de combustion réalisés avec le superstatoréacteur expérimental CHAMOIS à Bourges-Subdray. Pour cela, un dièdre a été placé entre la tuyère d'alimentation et les mâts de manière à générer un choc incident [15, 16].

Cette technique d'essais novatrice a permis d'apporter des informations qualitatives et quantitatives sur les caractéristiques de la

combustion supersonique en présence d'un écoulement hétérogène.

La figure 22 montre un calcul réalisé dans les conditions d'essais avec une configuration à deux mâts d'injection. Il s'agit d'un calcul 2D, Navier Stokes, du mélange turbulent et réactif. Le choc issu du dièdre vient dans ce cas interagir avec un des mâts :
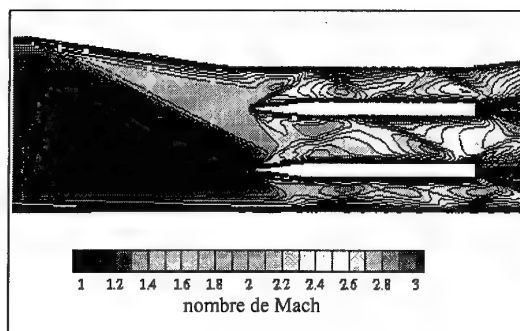

fig. 22 : simulation d'une hétérogénéité

On réalise parfois des essais dits en **"jet semi-libre"**, la prise d'air est cette fois présente devant la chambre de combustion, donc sa distorsion intrinsèque est simulée. Par contre, la prise d'air est elle-même alimentée de manière homogène, l'influence de l'attitude de vol et des effets de fuselage n'est donc pas prise en compte (figure 23).
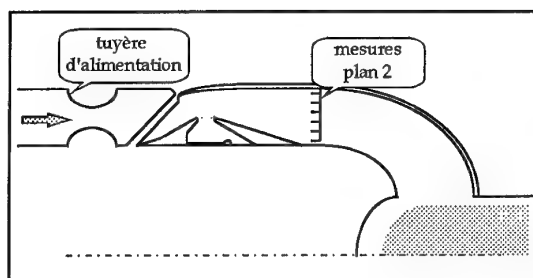

fig. 23 : alimentation en jet semi-libre

5. Méthodologie

La méthodologie utilisée à AEROSPATIALE pour la mise au point des systèmes propulsifs peut être résumée sur la figure 24.

Cette méthodologie combine calculs et essais et a pour objectif la réduction des coûts et des durées de mise au point et de développement.

Les calculs numériques sont utilisés d'une part en temps que calculs prédictifs tant en aérodynamique interne qu'en aérodynamique externe; ils permettent dans ce cas de mieux cibler les configurations qui seront testées par la suite.

Dans le cas de l'aérodynamique interne, les performances globales et les distorsions associées sont ainsi évaluées. Les calculs sont également utilisés en combustion et dans les travaux préparatoires, c'est à dire dans la définition des artifices qui seront utilisés pour simuler la distorsion lors des essais de combustion en veine forcée.

Selon les performances obtenues lors des campagnes d'essais d'aérodynamique interne et de combustion, des itérations sont nécessaires pour s'ajuster aux niveaux de poussée requis.
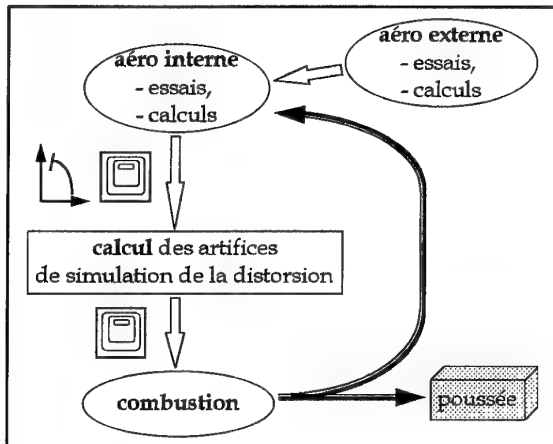
fig. 24 : méthodologie de conception de l'ensemble propulsif

6. Conclusion

La prise d'air d'un missile ou d'un lanceur ne peut pas être conçue indépendamment de son environnement; en effet, le fuselage sur lequel elle va être installée va imposer la captation d'un écoulement qui diffère de celui du vol, et ce, d'autant plus que la vitesse, l'incidence et le dérapage du véhicule augmentent.

La prise d'air peut également difficilement être découplée du moteur, quel qu'il soit; globalement, la conception du système propulsif devra prendre en compte les

exigences de performances formulées en termes de poussée.

AEROSPATIALE utilise une méthodologie de mise au point et d'optimisation de cet ensemble propulsif associant calculs numériques et essais d'aérodynamique interne . et de combustion dans le soucis de limitation des coûts et des durées de développement.

Cette méthodologie tient compte des couplages importants existants entre les différents éléments.

Remerciements

Références

[1] - Ph. DUVEAU, R. THEPOT
"Prediction Methods for Supersonic Inlets"
X[th] ISABE Nottingham (UK), September 1-6, 1991.

[2] - I. AUNEAU, P. GARNERO, P. DUVEAU
"Design and Optimization Methods for Scramjet Inlets"
6th International Aerospace Planes and Hypersonics Technologies Conference.
Chattanooga,TN (USA), April 3-7, 1995.

[3] - P. CHAMPIGNY
"Problèmes liés à l'Aérodynamique Externe des Missiles Aérobies"
Symposium AGARD sur l'Aérodynamique des Missiles
Trondheim, 20-22 Septembre 1982.

[4] - G. LARUELLE
"Air Intakes for Supersonic Missiles - Design criteria and Developement"
VIII ème Congrès International sur les Moteurs Aérobies (ISABE)
Cincinnati (USA), 15-19 Juin 1987.

[5] - G. LARUELLE
"Prises d'air de Missiles Supersoniques - Critères de Choix et mise au point"
Réunion AAAF, Paris Février 1986.

[6] - F. FALEMPIN, H. LACAZE, ...
"Reference and Generic Vehicle for the French Hypersonic Technology Program"
AIAA - 95 - 6008 - Chattanooga - 1995.

C36-12

[7] -   E. H. HIRSCHEL
"Aerothermodynamic Challenges of the Sanger Space Transportation Systems"
Proc. First European Symposium on Aerothermodynamics for Space Vehicles
Noordwijk, May 28-30, 1991 , ESA, SP - 318 , 1991.

[8] -   G. LARUELLE, I. AUNEAU, Ph. DUVEAU, O. PENANHOAT
"Air Intakes Challenge for Hypersonic Launchers"
Réunion AAAF, Paris, Mai 1996.

[9] -   F. FALEMPIN, Ph. DUVEAU
"Prises d'Air à Section de Captation Variable - Application aux Lanceurs Aérobies"
Aerodynamic Engine / Airframe Integration for High Performance Aircrafts and Missiles
AGARD - Fort-Worth (USA) , October 1991.

[10] -   C. JOUET, P. D'ESPINEY
"3D Laminar and 2D Turbulent Computations with the Navier-Stokes Solver FLU3M"
8th Int. Conf. on Numerical Methods in Laminar and turbulent Flow.
University of Swansea (UK), July 18-23, 1993.

[11] -   F.S. BILLIG, G.L. DUGGER, P.J. WALTRUP
"Inlet-Combustor interface problems in scramjet engines"
The Johns Hopkins university, A.P.L.

[12] -   G.A. SULLINS, D.A. CARPENTER, M.W. THOMPSON, F.T. KWOK, ...
"A demonstration of Mode Transition in a scramjet combustor"
27th Joint Propulsion Conference
Sacramento, CA (USA), June 24-27, 1991

[13] -   D.A. BEMENT, J.R. STEVENS, M.W. THOMSON
"Measured operating Characteristics of a Rectangular Combustor/Inlet Isolator"
26th Joint Propulsion Cionference
Orlando, FL (USA), July 16-18, 1990

[14] -   S.I. BARANOVSKY, V.M. LEVIN
"Precombustion shock wave as a means of the working process control in a supersonic combustion chamber"
Moscow Aviation Institute

[15] -   M. BOUCHEZ, F. FALEMPIN
"Scramjet and dual mode ramjets"
AGARD - Palaiseau (Fr) , April 1997.

[16] -   C. ROTHMUND, D. SCHERRER, M. BOUCHEZ
"Propulsion system for airbreathing launcher in the French PREPHA program"
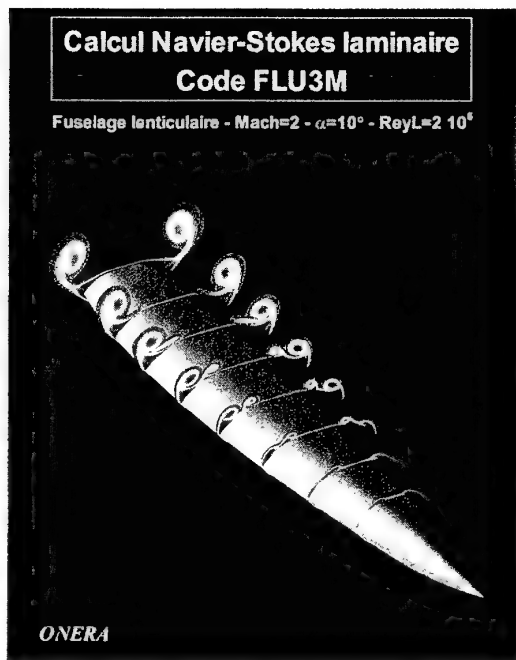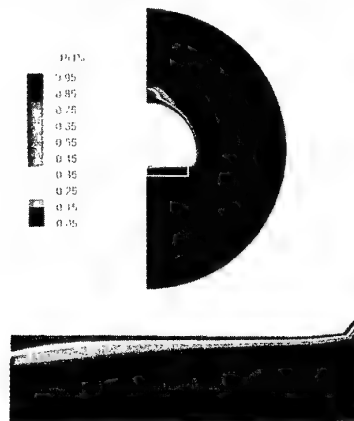AIAA-96-4498, Norfolk, Nov. 18-22, 1996

Calcul Navier-Stokes laminaire
Code FLU3M

Fuselage lenticulaire - Mach=2 - α=10° - ReyL=2 10^6

ONERA

fig. 8 : champ aérodynamique autour du fuselage

CALCUL PPNS turbulent Baldwin-Lomax (α=5 conditions d'essai)
plan de captation de la prise d'air

fig. 13 : répartition de pression d'arrêt
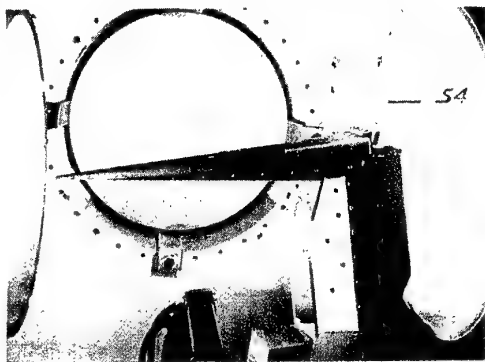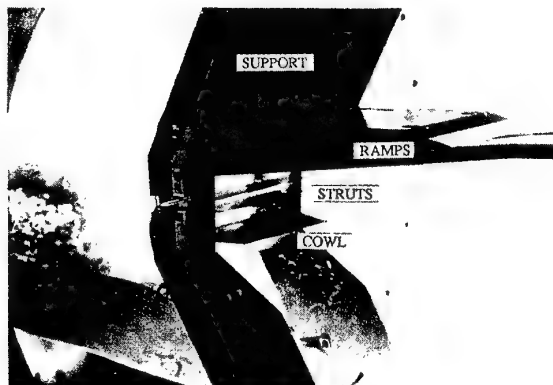autour du fuselage

FOREBODY MODEL IN S4MA WIND TUNNEL

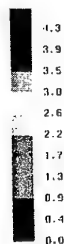fig. 12 : essai de l'avant-corps PREPHA
à S4 Modane

SUPPORT

RAMPS

STRUTS

COWL

fig. 18 : configuration d'essais à R2 CH
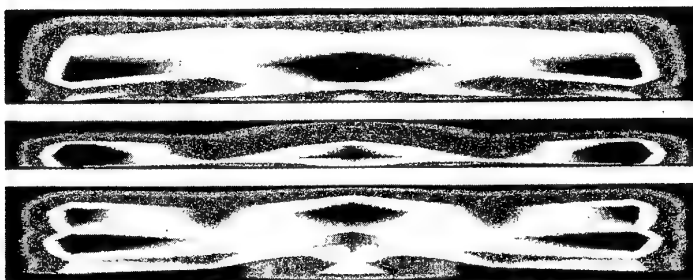
fig. 19 :

Mach locaux au col de la prise d'air
essai à Mach 7 - R2 CH

Systems Challenges for Hypersonic Vehicles

by

James L. Hunt
NASA Langley Research Center, MS 353
Hampton, VA 23681-0001, USA

Gerard Laruelle and Alain Wagner
Aerospatiale Espace & Defense
Route de Verneuil, BP 96, 78133 Les Mureaux Cedex, France

1. ABSTRACT

This paper examines the system challenges posed by fully reusable hypersonic cruise airplanes and access to space vehicles. Hydrocarbon and hydrogen fueled airplanes are considered with cruise speeds of Mach 5 and 10, respectively. The access to space matrix is examined. Airbreathing and rocket powered, single- and two-stage vehicles are considered. Reference vehicle architectures are presented. Major systems/subsystems challenges are described. Advanced, enhancing systems concepts as well as common system technologies are discussed.

2. INTRODUCTION

Vehicles for sustained hypersonic flight encompass airplanes, space access vehicles and missiles. Functional and architectural categories impose major differentiation from a systems/subsystems perspective. Important categories are: a) take-off (launch); horizontal, vertical, staged/air-dropped or launch assist, b) landing; horizontal or vertical, c) propulsion; airbreathing, rocket or combination, d) fuel (propellant); cryogenic and/or noncryogenic, solid or liquid, e) reusability; expendable or reusable, f) mission; cruise, acceleration, or combination, and g) staging; one versus two or more. In order to constrain the scope of this paper, air-dropped, launch assist, vertical landing, solid propellants systems and expendables including missiles will be omitted.

There are also commonalities in the system challenges across the hypersonic vehicle matrix. These commonalities exist primarily within the framework of features/disciplines that are unique to the vehicles for sustained hypersonic flight, i.e. structures, materials, and thermal protection systems (TPS) compatible with the very high thermal constraints of sustained hypersonic flight and the requirement for extremely low dry weight. There are also commonality requirements such as fast response of the control systems in which nonlinearities and cross-couplings are the norm.

Herein, system challenges for hypersonic vehicles will be addressed in terms of endoatmospheric operations and exoatmospheric delivery/return with major systems differentiations such as hydrocarbon and hydrogen fuel for airplanes and airbreathing and rocket propulsion for access to space vehicles.

3. CRUISE AIRPLANES

For hypersonic airplanes, range for a given payload at a given cruise Mach number is a good figure of merit (ref. 1). How is this figure of merit impacted for hydrocarbon-fueled airplanes and liquid hydrogen-fueled airplanes? Calculations indicate that Mach 8 is approximately the cruise speed limit to which a dual-mode ramjet/scramjet can be cooled with endothermic fuels (depends on contraction ratio and dynamic pressure, ref. 1). On the other hand, liquid hydrogen has much more cooling capacity and provides considerably more range than hydrocarbons for the same Mach as indicated in figure 1. The range of hydrogen fueled vehicles maximizes at about Mach 10, beyond the cooling limits of the hydrocarbons. The take-off gross weight (TOGW) of the hydrocarbon-fueled airplanes is much greater for the same cruise Mach number than that for hydrogen-fueled airplanes as shown in figure 2. Although the dry weight of hydrocarbon vs. hydrogen airplanes for the same cruise Mach number and for the same
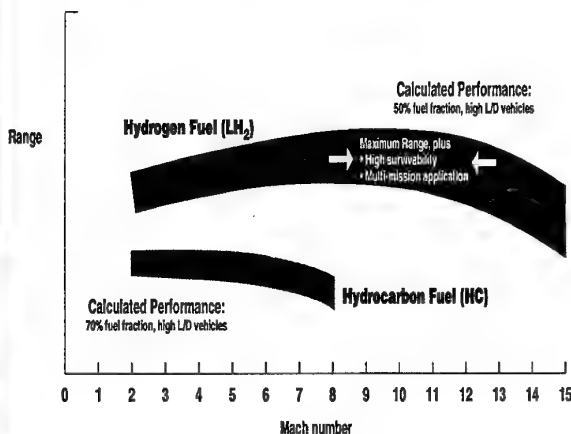

Figure 1. Range potential for hypersonic airplanes (fixed payload, ref. 1).
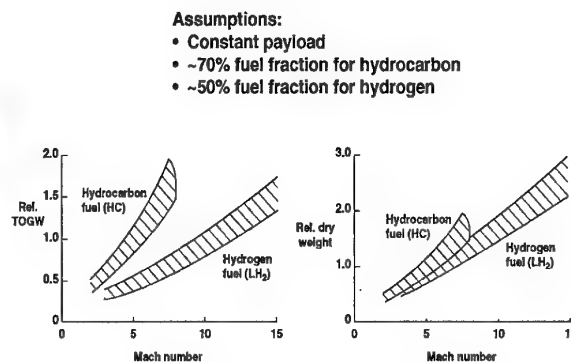

Figure 2. Weight potential for hypersonic airplanes (fixed payload, ref. 1).

payload is much closer, it still tends to break favorably for the hydrogen-fueled aircraft (figure 2).

Thus, for airplanes the fuel break appears to be about Mach 8; that is, endothermic fueled/ hydrocarbon vehicles are limited to below Mach 8 and airplanes with cruise speed above Mach 8 will require hydrogen. Since the shape of the vehicle and the systems that constitute it will be considerably different for hydrocarbon-fueled machines than for hydrogen because of the fuel density differences and resultant planform to accommodate loading, the discussion will be broken along these lines with the assumption that the speed break point is Mach 8 even though hydrogen-fuel systems could be designed for lower cruise Mach numbers. The hybrid approach, dual-fuel, will be considered as a subset of hydrogen-fueled systems.

Other than the fuel, the biggest influence on the system architectures will come from engine integration. All hypersonic airplanes considered herein are engine-airframe integrated in that the forebody serves as an external precompression surface for the engine inlet and the aftbody as a high expansion ratio nozzle. Also, for the purpose of discussion continuity, the airbreathing propulsion flowpath is considered on the lower surface of the vehicle (underslung). The differences are in whether the engine integration embodies a single duct or a two-duct approach, or something in between.

3.1 Hydrocarbon Fueled Airplanes (4 < M < 8)

The engine integration architecture for hydrocarbon-fueled hypersonic airplanes depends on the design cruise speed of the vehicle. For cruise Mach numbers between 4 and 5, underslung, single-duct, turboramjet, airframe-integrated systems can be used. For cruise Mach numbers between 5 and 8, two-duct, turboramjet/ramjet-scramjet, over/under, airframe-integrated systems are required. Single duct, ejector-ramjet, airframe-integrated systems do not appear favorable for hydrocarbon-fueled airplanes because of the low efficiency of the propulsion system and the large planform loading incurred by the airplane due to the high propellant density of hydrocarbon fuel plus liquid oxygen (LOX) used for an oxidizer in the ejector rocket motors.

For hypersonic speeds, liquid hydrocarbon (LHC) fuels must be selected primarily on cooling characteristics. Fuels with the highest energy per pound of cooling capacity are required; this class of fuels is endothermic. Thus, when heat is added to

the fuel in the presence of a catalyst, the fuel is transformed through an endothermic chemical reaction in which the original fuel molecules decompose into combustible chemical constituents with the absorption of substantial amounts of heat (figure 3). The catalyst can be applied inside the cooling panels of the engine for direct cooling or a secondary fluid can be used with the catalyst being applied to one side of a heat exchanger which is outside of the engine for indirect cooling. The most likely solution would be to use a combination of direct and indirect cooling systems as was used for the Mach 5 waverider airplane design study in reference 2.

3.1.1 Example Baseline

The Mach 5 waverider airplane (ref. 2) was selected as a reference vehicle design (example baseline), representing system architectures for hydrocarbon fueled, hypersonic airplanes. It is an underslung, over/under, turbojet/ramjet, two-duct airframe-integrated design. A 3-view drawing of the Mach 5 waverider configuration is presented in figure 4. Performance estimates (ref. 2) indicated a 6,000 nm tanker-to-tanker range with a refueled gross weight of 550K lbs.; take-off gross weight (TOGW) was 400K lbs. with an empty weight (EW) of 141K lbs., and a vehicle length of 135 ft.

3.1.1.1 Propulsion System/Integration

As designed (ref. 2), the baseline waverider airplane, fueled by an advanced paraffin endothermic would be powered by four turboramjet engines. The STRJ-1011 powerplant system design was supplied by Pratt & Whitney and is based on current technology using endothermic fuel. The turbojet would operate from take-off to turbojet/ramjet transition (approximately Mach 2-3). The ramjet engine is to be started at a low supersonic Mach number and operated in parallel with the turbojet through transition, after which the ramjet would operate alone to complete the high-Mach acceleration and cruise.

The over/under integration of the turbojet/ramjet engines is shown in the propulsion system schematic of figure 5. An effective transition from a conical flowfield to a 2-D variable geometry inlet is provided. Inlet strakes (figure 4) are incorporated to isolate each inlet in case of an unstart or engine-out condition in one module. The outboard strakes are extended forward to control side spillage. The cowl is fixed so flow con-
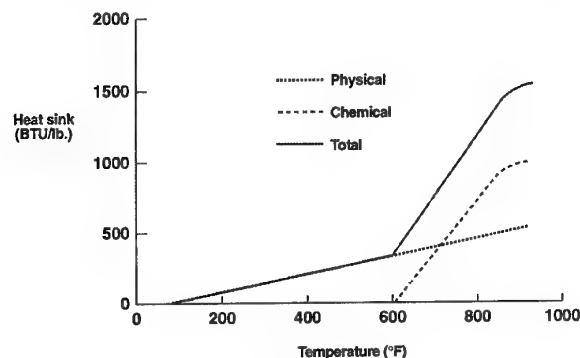

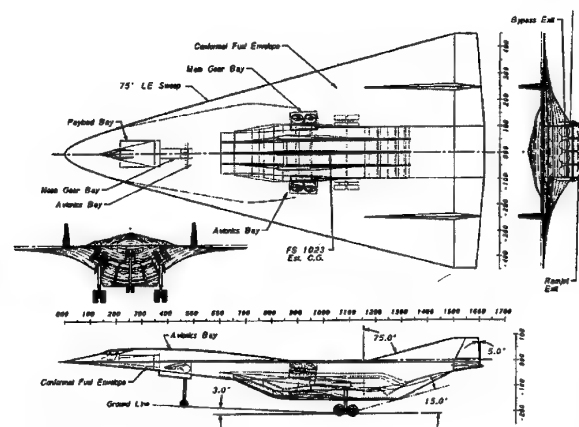Figure 3. Heat sink of methylcyclohexane (approximate).

Figure 4. Aircraft three-view (ref. 2).

trol in the inlet is to be accomplished by the variable bodyside ramp system. A splitter vane that controls the flow between the turbojet and ramjet is located behind the inlet throat.

A boundary-layer diverter duct (figure 5) was integrated just forward of the first external inlet ramp to remove the low energy boundary-layer flow during turbojet operation only. This may not preclude the need for bleed internal to the inlet, but it does minimize the volume required, and thus, simplifies the bleed system. Inlet bleed has a substantial impact on range performance; with an 8% inlet bleed, the tanker-to-tanker range was 6,000 nm… assuming inlet functionality, the range was 7,600 nm without the bleed.

The turbojet, turbojet nozzle, ramburner, ramjet nozzle, and external expansion nozzle are aligned in a 2-D arrangement. As seen in figure 5, a door opens to allow the turbojet nozzle flow to exit to the external nozzle just above the ramjet nozzle. As conceived, the ramjet will be started at approximately Mach 2. When the turbojet shuts down at Mach 2.5, the turbojet nozzle exit doors seal shut, leaving a large, unobstructed expansion surface.

3.1.1.2   Thermal Management / Power Generation
Both direct and indirect fuel cooling were used in the reference design (ref. 2). In either case, a catalyst is needed to promote the endothermic chemical reaction of the fuel. The thermal management system is shown in figure 6. Direct fuel cooling is used in the ramburner and nozzle where the heat load is highest. For these areas, the catalyst is installed on the inside of the superalloy cooling panels. Indirect cooling is used for the inlet, avionics, and turbojet engine bay, and a catalytic heat exchanger reactor (CHER) is employed to transfer heat from the low-viscosity, secondary fluid to the fuel. The inlet has integral titanium alloy cooling panels with insulation and a cobalt L-605 heat shield.
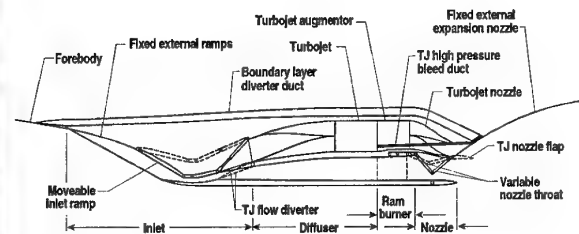

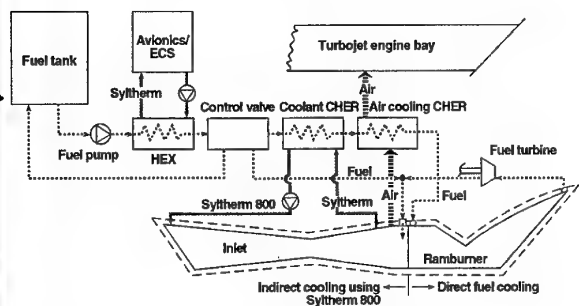*Figure 5. Propulsion system schematic (ref. 2).*

Figure 6. Thermal management system (ref. 2).

Power for the fuel pump and other aircraft systems requirements are derived from the turbine shaft while the turbojet is operating and from a fuel expansion turbine (figure 6) when the ramjet is operating. Both sources are available during transition. The power generated by the fuel turbine is much greater than the power needed to drive the fuel pump during Mach 5 cruise. Engine start and engine-out power is obtained from an auxiliary power unit (APU).

3.1.1.3   Structural/Material/Tank System
The Mach 5 cruise aircraft was designed (ref. 2) as a hot structure with integral tanks lined with insulation and containing flexible fuel cells. Honeycomb sandwich panels of a monolithic titanium alloy (Ti6242) were selected for airframe skins because they provide a lightweight structural solution (figure 7) requiring only modest ringframes between the major frame and bulkheads. Maximum structural temperatures approach 900°F. Wing and tail leading edges are more severely heated (1,300-1,500°F), so a metal matrix material is used which has silicon carbide fibers in a titanium-aluminide alloy matrix (TMC).

The fuel tank design uses flexible fuel cells within the integral tank. This allows the airframe to be completely assembled before installing the fuel cells. Rigid insulation (figure 7) was used to protect the fuel cells from the hot airframe.

3.1.1.4   Other Systems
Certain systems that are common to several classes of hypersonic aircraft such as avionics and actuation will be deferred to example baselines to come later herein (sections 3.2.1 and 4.1.1).

3.1.1.5   Challenges
Developing a turboramjet and ramjet powerplant for a hydrocarbon-fueled hypersonic airplane is the first challenge. Integrating in a viable arrangement that will accommodate an efficient inlet system and allow a smooth transition from the turbojet to the ramjet is a close second. Given the sensitivity of inlet bleed on range, designing high performance inlet systems with minimum bleed is a challenge worth undertaking.

Also, the inlet/diffuser system presented (figure 5) with its internal flow diverter (splitter) to control engine flows is very long. The engine nacelle could be shortened by using a split two-inlet system; whether or not the performance could be maintained is the question.

One of the biggest challenges for the thermal management system is cooling of the aircraft during high-speed decelera-
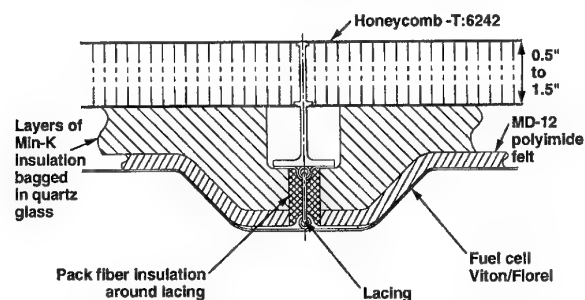

Figure 7. Structural/tank wall concept (ref. 2).

tion. Thrust must be reduced which results in less fuel needed for combustion, while the heat loads remain high. A layer of air could act as film cooling near the wall while combustion is restricted to the center core of the ramjet combustor.

3.2 Hydrogen Fueled Airplanes (M > 8)

Hydrogen-fueled airplane designs offer more options in engine integration architecture than their hydrocarbon fueled counterparts, which again centers on whether the engine integration embodies a single duct, a duct and one-half or a two-duct approach. The single duct would be an ejector ramjet/ scramjet in which the ejector rocket motors operate on liquid oxygen/liquid hydrogen (LOX/LH2) or gaseous oxygen/ gaseous hydrogen (GOX/GH2) propellant. Remove the LOX tank and add a Liquid Air Cycle Engine (LACE) system, for which the ejector operates on LAIR/LH2, and the duct and one-half approach results since the LACE system requires an auxiliary inlet. Remove the LACE system and add a turboramjet and the two duct system emerges since the turboramjet requires both an inlet and an exhaust nozzle.

3.2.1 Example Baseline

A design data base exists for an underslung turboramjet/dual mode scramjet over/under integrated Mach 10 cruise vehicle (figure 8), namely NASA's Dual-Fuel Airbreathing Hypersonic Vehicle Study (ref. 3 and 4), in which an all-hydrogen-fueled design option was examined. This all hydrogen version was selected as the reference with respect to system architectures for hydrogen-fueled cruise airplane designs providing continuity with the two-duct hydrocarbon-fueled example. Accommodating a payload of 10,000 lbs. in a 2,000 ft^3 payload bay, the range of the Mach 10 reference airplane ia approximately 10,000 nm. in a 200 ft. long vehicle with a TOGW less than 500,000 lbs.

3.2.1.1 Propulsion

The airbreathing propulsion system (ref. 5, 6, and 7) operates in three speed regimes (low, M = 0 to 4; mid, M = 4 to 4.5; and high speed, M = 4.5 to 10) with a distinct engine and/or engine combination for each as depicted in figure 9. During low and mid-speed the turboramjets (Air Core Enhanced Turboramjet (AceTR) for this study) operate at full power to provide acceleration thrust; the turboramjets were sized such that no external burning was required to augment thrust production at transonic speeds. The ramjet/scramjet engine remains shut-down/closed-off in the low-speed regime. Engine close-off is achieved by upward rotation of the inlet and nozzle cowl flaps until each flap contacts its respective

Figure 8. Mach 10 aircraft (ref. 3).

upper bodyside surfaces. From Mach 4.0 to 4.5 both the turboramjet and the ramjet/scramjet systems are functioning to provide uninterrupted maximum thrust during the transition from turbojet to ramjet/scramjet operation. During high speed operation, the turboramjets are shutdown/closed-off and the ramjet/scramjet is used to accelerate to and cruise at Mach 10.

At the completion of the Mach 10 cruise segment the scramjet is shutdown/closed-off. The vehicle then descends unpowered from Mach 10 to approximately Mach 0.8/30K feet altitude, where the low-speed inlet and nozzle are reopened and the turboramjets are airstarted. The turboramjets then operate at partial power for the remainder of the mission including subsonic cruise and landing.
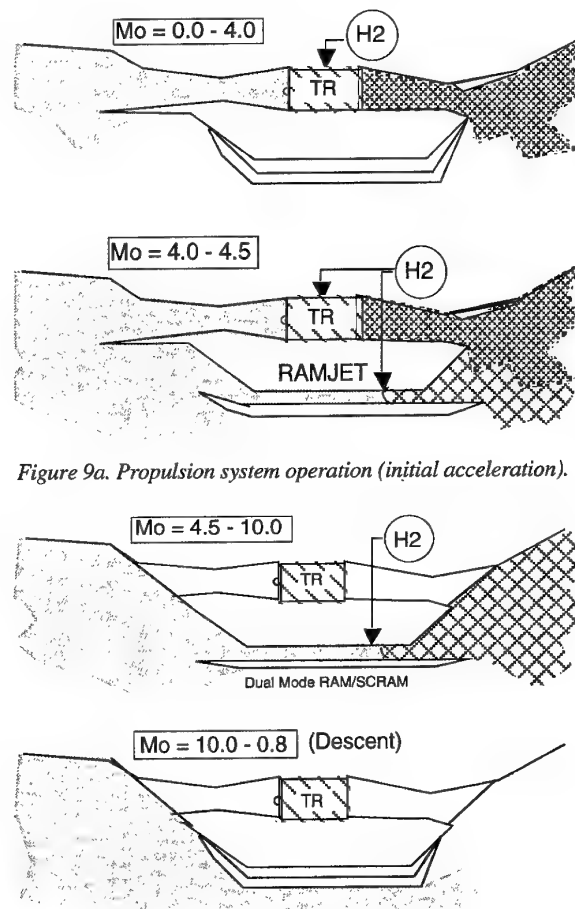

Figure 9a. Propulsion system operation (initial acceleration).

Figure 9b. Propulsion system operation (high speed acceleration, cruise, descent).
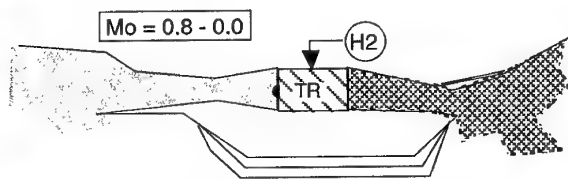

Figure 9c. Propulsion system operation (low speed cruise and landing).

3.2.1.2 Thermal Management System

An overview of the thermal management approach (ref. 6) for the Mach 10, hydrogen-fueled cruise vehicle is shown in figure 10. Fuel is routed from the aircraft's main fuel tank through heat exchangers with a secondary cooling loop, to the actively-cooled fuselage leading edge, and then to the propulsion active cooling system including the internal propulsion flowpath and the initial part of the external nozzle, and finally out into the combustor. The hydrogen boil-off handles most of the airframe aerodynamic heat loads. The propulsion system is cooled by the fuel via non-integral heat exchangers mounted to the structure on the internal heated surfaces of the engines; the system layout is shown in Figure 11 including the hydrogen flow network for providing hot hydrogen flow back from the combustor heat exchanger to the turbines for operating boost pumps, main fuel pump and auxiliary power unit. The subsystems are cooled by the fuel via coldplate heat exchangers; the layout is shown in figure 12 where Ethylene Glycol/Water is used in the second coolant loop between the hydrogen heat exchangers off the main tank and the subsystems.

3.2.1.3 Fuel Supply System

The hydrogen fuel system for the Mach 10 cruise vehicle (ref. 6) was designed for horizontal takeoff and aircraft-type operability. The forward and aft tankage were interconnected among themselves to form functionally individual tanks. Each forward and aft tank has separate fill loops to allow for tankage to be at different elevations and filled to satisfy center-of-gravity requirements. Each tank has a self-contained chill system which consists of spray bars in which hydrogen is circulated to keep the tank near equilibrium. The tanks vent to a ground disposal system when filling and allow free venting during flight or ground maneuver operations. The system includes all composite valves, all electric valves/actuators and zero-push boost pumps. The boost pump will allow continuous tank drainage. The tank bodies and actuator housings are made of graphite composite. The feedlines are composite construction with stainless steel bellows and titanium
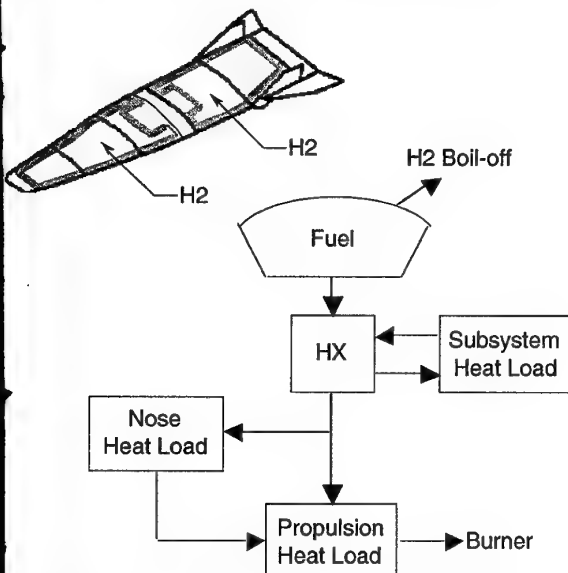
restraints bonded to the composite lines to provide flexibility (foam insulation is used on all feedlines). The fuel system is designed with fail safe redundancy.

The initial fuel system for the hydrogen vehicle in the Mach 10 global reach airplane design study was liquid hydrogen because the design was simpler for both flight system and ground support compared to a slush hydrogen-fuel system. However, slush hydrogen would allow the fuel system to operate at a much lower tank pressure as illustrated in figure 13. During design refinement, a trade study was conducted to evaluate the advantage of a slush hydrogen fuel system. The boil-off of two liquid
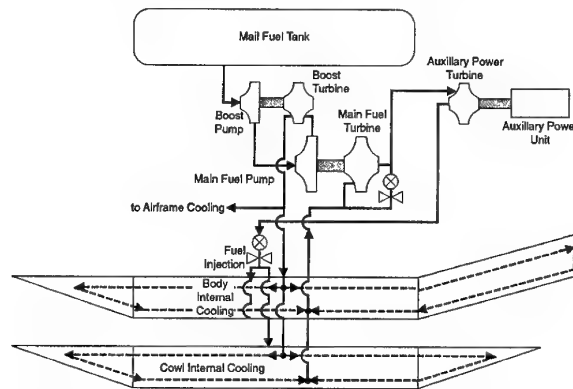

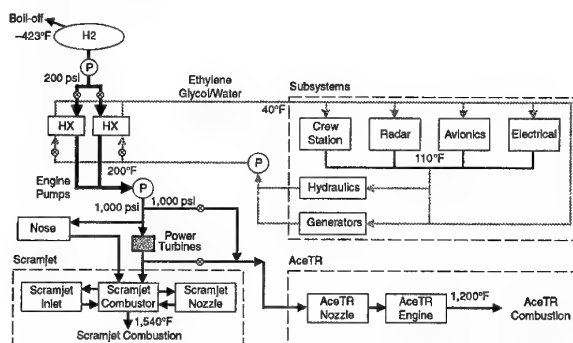Figure 11. Mach 10 cruise vehicle propulsion cooling design concept.

Figure 12. Mach 10 cruise vehicle thermal management system design concept (simplified version of dual-fuel system in ref. 6).

Figure 10. Mach 10 cruise vehicle thermal management approach (ref. 6).
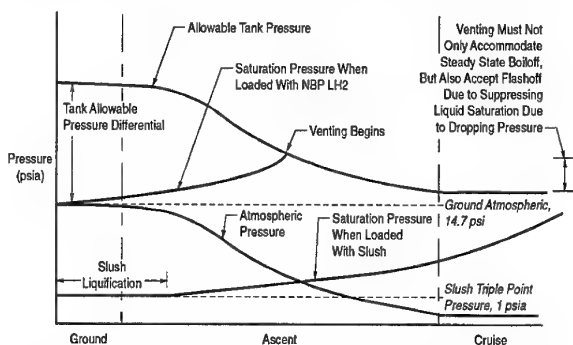

Figure 13. Difference in liquid and slush hydrogen fuel system thermodynamics. (ref. 6).

hydrogen fuel tanks at 20 or 30 psid and two slush hydrogen tanks at 5 or 20 psid were analyzed. The liquid hydrogen boil-off is small during ground hold after the ground support equipment disconnect. However, it accumulates much more rapidly during both outbound and the return flight. As a result, the slush hydrogen fuel system has much lower total boil-off as shown in figure 14. A 50% slush hydrogen fuel also provides a 15% density increase compared to normal boiling point liquid hydrogen and an added heat sink capacity of 110 Btu/lb.

For a slush hydrogen fuel system design, slush return manifold and lines must be added to melt slush in the tank to prevent clogging in inlet lines during flight. A fill return system was added to recirculate fill slush and densify propellant. The schematic of the slush hydrogen fuel system design selected as a baseline herein is presented in figure 15.

3.2.1.4 Pressurization and Purge Systems

The pressurization system (helium) provides active control of cryogenic hydrogen/slush supercritical storage. The slush hydrogen fuel system requires initial pressurization only. The liquid oxygen APU (auxiliary power unit) supply tank requires continuous pressurization. The slush hydrogen tank exterior and vehicle cavity need to be continuously purged for safety during ascent and descent below 100,000 feet altitude. The hydrogen vent also requires purge. The purge and pressurization system uses technology similar to the hydrogen-fuel system, with all composite valves and feed lines, and all-electric valve actuation. It was designed with fail safe redundancy.
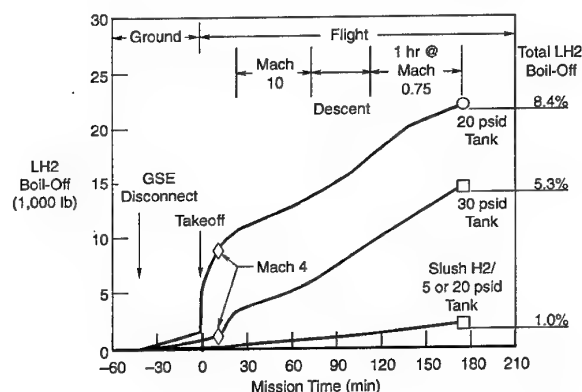
3.2.1.5 Vehicle Management System

The Vehicle Management System (VMS) design concept is based on the Versatile Flight Control System (VFCS) and is a fly-by-light (FBL) configuration. Quadruplex FBL architecture is the design approach. The major functions of the avionics are: (1) store mission information, (2) provide crew with situation awareness (engine status, terrain and star maps, GPS, etc.), and (3) provide communication capability, threat warnings, air data and radar information, aircraft subsystem status and maintenance information. The mission critical portions of the avionics are dual redundant; the remainder is single channel. All buses are fiber-optic.

3.2.1.6 Airframe Structure/TPS System

The airframe for the Mach 10 cruise airplane (ref. 7) is a cold structure with an integral slush hydrogen tank (figure 16). A cold, integral conformal graphite-epoxy (Gr/Ep) tank design is used since the maximum pressure differential for the slush hydrogen tank is only 5 psi. Graphite composite constitutes the remainder of the fuselage structure. There is tungsten in the nose area for ballast and the all-moveable wings are hot structure (titanium matrix composites, TMC). Cryogenic foam insulation is bonded to the outside of the tank using a chemical bond between the polyimide and graphite epoxy. High temperature insulation with a heat shield is then attached to stand-off posts which penetrate the foam and are secured to the GR/EP tank.

Figure 14. Boil-off comparison of liquid and slush hydrogen fuel system (ref. 6).

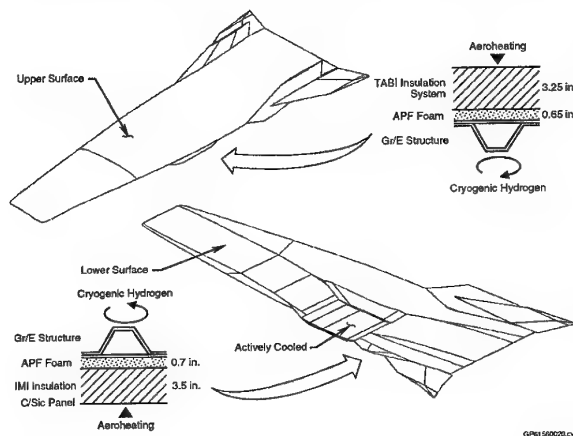Figure 16a. Fuselage TPS insulation requirements for cold structure vehicle with typical dimensions (ref. 7).

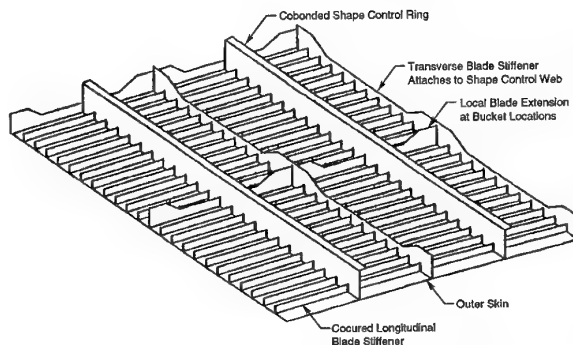Figure 15. Mach 10 cruise vehicle slush hydrogen fuel system schematic (ref. 6).

Figure 16b. Trimetric of cold skin with integral fuel tank construction (ref. 7).
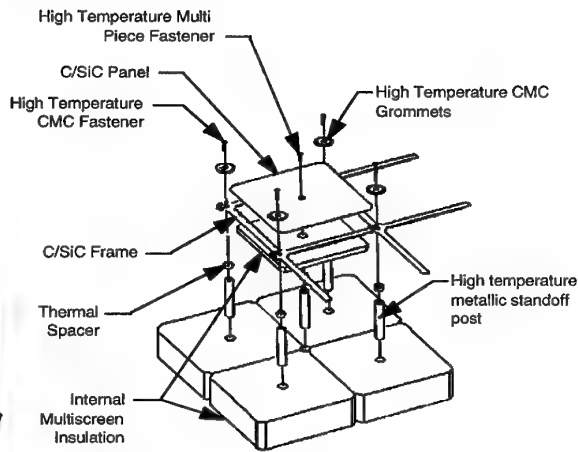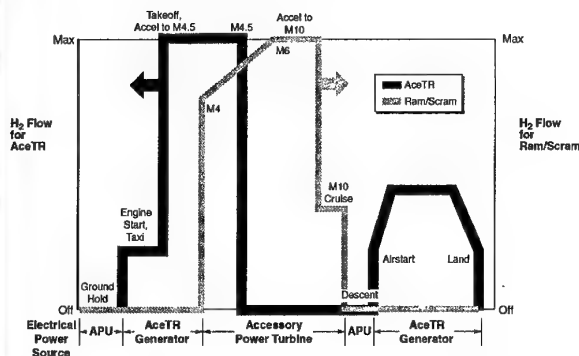
Figure 17. Advanced TPS (ref. 6).

Figure 18. Electrical power source and hydrogen flow rate as a function of use.

The flowpath (lower surface) TPS assembly (ref. 6) is shown in figure 17. It consists of a 60-mil external carbon/silicon-carbide (C/SiC) panel and frame, CMC/metallic (ceramic matrix composites) standoff attachment post, staggered Internal Multiscreen Insulation (IMI), integrated purge channel and APF insulation. The addition of purge resulted in a weight savings for the TPS while providing many operational advantages. A Tailorable Advanced Blanket Insulation (TABI) type TPS was found to be better for tank locations on the top of the vehicle. TABI consists of woven fiber mat with triangular alumina foam prisms encased inside (ref. 6).

3.2.1.7 Leading Edge Systems

Based on work done for the National Aero-Space Plane (NASP) program, the actively-cooled leading edges used on the engine are specified to be 0.1" radius (ref. 4); the vehicle and wing leading edges have a 0.2" radius. The engine cowl, sidewall and vehicle leading edges are actively cooled. The engine cowl leading edge is a particularly difficult cooling problem because it would be exposed to severe heating if the bow shock impinges on the cowl-lip. The challenge is to use materials with a combination of high conductivity and high temperature capability which can be adequately cooled to survive this heating requirement. A platelet architecture was selected for the baseline design using a copper alloy material.

The wing leading edges are made of ceramic matrix composites such as zirconium diboride or coated carbon/carbon. High temperature ceramic composite leading edges are currently being tested by the Air Force under the HyTech Program and results should be available in 1997 (ref. 8).

3.2.1.8 Power Generation

The power generation concept has two sources of power to drive one generator. Figure 18 shows which power source is driving the generator as a function of mission. When neither engine is operating, the APU (figure 11) is used to power the generator with one exception. When the vehicle is operating above Mach 4 the cooling loads generate enough gas to spin the accessory power turbine, which in turn spins the associated starter/generator.

3.2.1.9 Actuation

Actuator sizes and types were selected to meet the mission dynamics and static loads requirements. Power requirements dictate that the major portion of the actuator be hydraulic. Control surfaces, landing gear extension and nose gear steering have hydraulic actuators with electrically driven motor pumps. All other actuators are electromechanical. A typical actuator block diagram is presented in figure 19.

3.2.1.10 Challenge

The challenges for developing the hydrogen-fueled over/under type of hypersonic airbreathing propulsion system are similar to that for the lower speed, hydrocarbon-fueled example baseline. A reasonably high performance, high thrust-to-weight turboramjet is required along with a ramjet/scramjet or dual-mode ramjet. These two engine systems must be integrated together in both a viable vehicle flowpath configuration and a viable mechanical design with actuation/seal systems that allow variable geometry operations over a broad Mach range with engine mode transition.

Due to the relatively long cruises at high speed the thermal protection system (TPS) and the thermal management system (TMS) design must be analyzed as an integrated system and optimized interactively. The thermal management system must provide adequate cooling for the dual-mode combined engine structure/subsystems, the airframe leading edges, crew station, avionics, radar, hydraulics, and the electrical power. A challenge in developing the thermal management system is
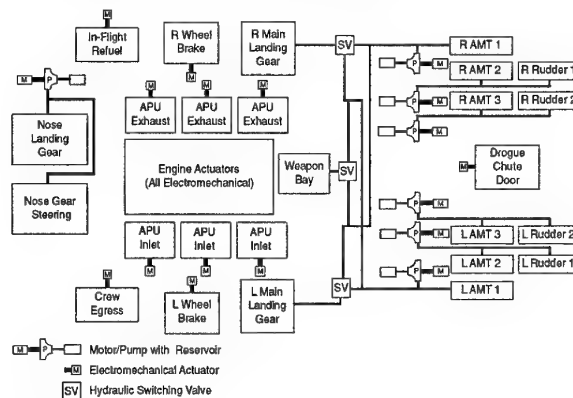

Figure 19. Actuation block diagram (generic).

the direct cooling non-integral heat exchanger for the engine; they must be reliable and allow high fuel injection temperatures without surface oxidation at a reasonable weight.

The fuel supply system presents considerable development challenges including all composite valves, feedlines and slush return manifold. Perhaps the biggest challenge is to overcome negative paradigms with respect to the use of slush hydrogen.

In structures/tankage, the challenge is to develop conformal, integral, graphite-epoxy, slush-hydrogen tankage; graphite-composite fuselage-structure and IMI TPS system with integrated purge. Also, the wing box and airframe interface for the rotating TMC wings require some development.

In avionics, the challenge is to design/develop the concept to meet the specific mission reliability requirements.
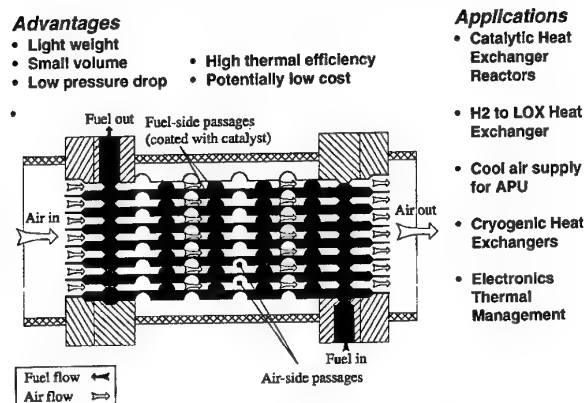
3.2.2 Ejector Ramjet/Ram-Scramjet (1.0 ducts)

This is a single propulsion duct machine and therefore offers the least engine/airframe integration challenges. Its propulsion system consists of a LOX/GH2 ejector ramjet system that operates from takeoff to Mach 2.5 or 3 where the ejector system is shut down and full ramjet mode takes over. The challenge is to design a more efficient ejector ramjet without significant engine weight increases. This hinges, to some degree, on whether or not mixing and diffusion can be allowed to occur simultaneously; the simultaneous approach would provide more performance potential, but could provide added choking risk.

The low specific impulse potential of the LOX/GH2 ejector ramjet and the added weight (high density) of the LOX may provide a rather unattractive airplane from a range vs. TOGW and loiter perspective.

3.2.3 Liquid Air Cycle Engine Ejector Ramjet Ram-Scramjet (1.5 ducts)

The Liquid Air Cycle Engine (LACE) system with its auxiliary inlet in the over position and the ram-scramjet in the under position is a duct and one-half system; the LACE requires no exhaust duct...the liquid air (LAIR) is supplied to the ejector stagnation chamber via plumbing. This system offers a much improved specific impulse potential over that of its lower derivative, the LOX/GH2 ejector ramjet. The challenge is to develop efficient, light weight heat exchangers for use in LACE architectures and to manufacture a reliable leak-proof system or one in which the leaks could be managed. The dimple foil design shown in figure 20 offers an order of magnitude reduction in weight over that of the conventional tube-bank-manifold approach for the same heat transfer capacity.

4. ACCESS TO SPACE

Access to Space is and will remain a strategic issue for leading nations. However, this does not mean that concern for cost will be disregarded. In the context of international competition, cost reductions are and will be mandatory to create new business.

Although the future prospects of expendables remain high in terms of cost reduction as reflected in simplification of the vehicles and their operations, in scalability to fit the payload/orbital-destination market and in multiplicity of launch options, their potential appears limited below that of reusable launchers in terms of cost-per-pound-to-orbit. Reusability with reliable systems that provide substantial cycle-life seems to be the only way to achieve dramatic cost reductions (ref. 9).

Will reusable launch vehicles pave the way to a dramatic cost reduction in access to space and in so doing, create a new business? Will they generate new financial and operational approaches? Will they require new infrastructures? System studies are mandatory to analyze these issues and focus on the related technology development programs. A coarse vehicle matrix for Access to Space is presented in figure 21. Only single-stage-to-orbit (SSTO) and two-stage-to-orbit (TSTO) vehicles are included in order to contain the discussion.
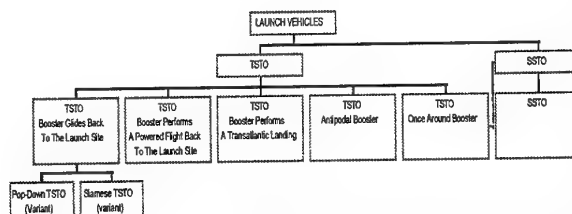
4.1 Single-Stage-To-Orbit (SSTO) Vehicles

SSTO is the aspiration of the astronautics community: only one vehicle to develop, manufacture, and operate. The feasibility, however, depends on the development of necessary technologies for required dry mass fraction with built in margins that will provide reliable systems with favorable cycle life.

The SSTO systems discussion will be segmented on the propulsion systems, i.e., airbreathing and rocket powered systems.

4.1.1 Airbreathing SSTO Vehicles

Airbreathing SSTO vehicles offer mission flexibility in terms of favorable launch window, launch offset and cross range capabilities. Discussion of SSTO airbreathing vehicles will concentrate on horizontal takeoff/landing systems since this is where most of the emphasis has been placed in recent studies

Advantages
- Light weight
- Small volume
- Low pressure drop
- High thermal efficiency
- Potentially low cost

Applications
- Catalytic Heat Exchanger Reactors
- H2 to LOX Heat Exchanger
- Cool air supply for APU
- Cryogenic Heat Exchangers
- Electronics Thermal Management

Figure 20. Dimpled foil heat exchanger technology for hypersonic vehicles (ref. 1).

Figure 21. Configuration matrix for SSTO and TSTO vehicles.

(ref. 1, 10, 11 and 12) and it provides continuity with air-planes. Also, there are compelling reasons for horizontal take-off/landing airbreathing systems such as gradual step and check engine startup and shutdown, abort during and shortly after takeoff, etc. It will be assumed that the airbreathing portion of the trajectory extends beyond Mach 8 and thus requires a scramjet since rocket-initiation/pull-up at Mach 8 or below (ramjet operations) would probably require dropping takeoff gears (trolley, etc.) at lift off and thus would not be categorized as a classic SSTO.

A definitive design study was performed on an SSTO air-breathing propelled orbital vehicle with rocket propulsion augmentation in NASA's Access to Space study activities (ref. 13 and 14; Option III Team). A credible design was established (ref. 15), but by no means an optimum. This design (figure 22) provides a reference representing system architecture for airbreathing SSTO vehicles; it was developed by the Langley Research Center's Systems Analysis Office in 1993.

4.1.1.1 Example Baseline
The airbreathing SSTO reference vehicle (figure 22) was designed to carry 25,000 lbs. of payload in a 15' x 15' x 30' rectangular payload bay to an orbit of 220 nm, 51.6° inclination, then dock with a hypothetical space station for delivery of the payload (ref. 15). It had a 15% weight growth margin, a 5-minute launch window, and an ascent delta velocity margin of 1%. The takeoff gross weight sized for the closed mission was 917,000 lbs., the dry weight was 239,000 lbs., and the length was 200 ft.

4.1.1.1.1 Architecture
The baseline design (ref. 13) as shown in figure 22 consists of:
- A wedge-shaped forebody profile, spatula-shaped fore-body planform, lifting-body configuration with all moving horizontal tails, twin vertical tails with rudders, and trailing edge body flaps.
- Underslung, 2-D airbreathing engine nacelle for which the vehicle forebody serves as a precompression surface and the aftbody as a high expansion ratio nozzle; two engine systems with 130K lbs. of thrust each at takeoff.
- Linear modular, aerospike rocket engine at the trailing edge; two engine systems with 117K lbs. of thrust each at takeoff.
- Slush hydrogen fuel (SH2) and Liquid Oxygen oxidizer (LOX) propellant (about a 50/50 split by weight).
- Actively cooled leading edges (fuselage spatula-shaped region and engine cowl); actively cooled, non-integral panels in engine.
- A 15' x 15' x 30' rectangular payload bay located in the
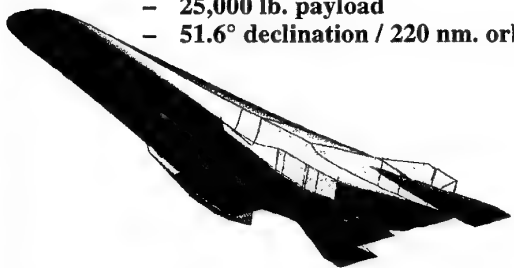
vehicle mid section with two "shuttle-like" doors that swing
- A crew station adjacent to the payload bay with access/escape from the vehicle topside and conduit to the payload bay.
- Two 6-wheel main landing gears; one nose gear (two wheels).
- Baseline vehicle airframe structure/tank/thermal protection systems (TPS).
  - Graphite/epoxy (Gr/Ep) integral, I-stiffened, conformal slush hydrogen (SH2) tank
  - Aluminum/Lithium (Al/Li) non-integral, multilobe liquid oxygen (LOX) tanks
  - Gr/Ep shell structure fore and aft of integral tank; Titanium Matrix Composites (TMC), Silicon carbide/beta 21s titanium all moving horizontal controls and twin verticals/rudder with Carbon/Silicon Carbide (C/SiC) TPS over portions exceeding 1,960°R; carbon-carbon (C/C) leading and trailing edges
  - Fibrous Refractory Composite Insulation (FRCI-12) over Rohacell insulation on windward surface and Tailorable Advanced Blanket (TABI) over Rohacell insulation on leeward surface.

4.1.1.1.2 Trajectory/Engine Modes
The airbreathing corridor to Mach 25 and the engine mode changes experienced in this acceleration process also characterize this aerospace plane. A representative ascent trajectory (ref. 13) for the SSTO vehicle is presented in figure 23 including indicators for propulsion mode events. Most of the airbreathing propelled ascent is along a high dynamic pressure isobar (2150 psf). Takeoff and transonic ascension are accomplished with the low-speed system and external rocket system performing simultaneously. The rocket is switched off at Mach 2. Transition to the scramjet mode begins at Mach 6 with the full scramjet mode in operation by Mach 7.5. Departure from the isobar above Mach 15 signals the onset of LOX augmentation through the scramjet and the activation of the external rocket system as indicated in figure 23. Scramjet main engine cutoff (MECO) is at Mach 24. Even though the external rocket system has essentially the same thrust at take-off as the airbreathing engine, the airbreathing flowpath provides 83% of the total ascent energy.

4.1.1.1.3 Thermal Management
The cooling concept of the airbreathing engine for this refer-

- **25,000 lb. payload**
- **51.6° declination / 220 nm. orbit**

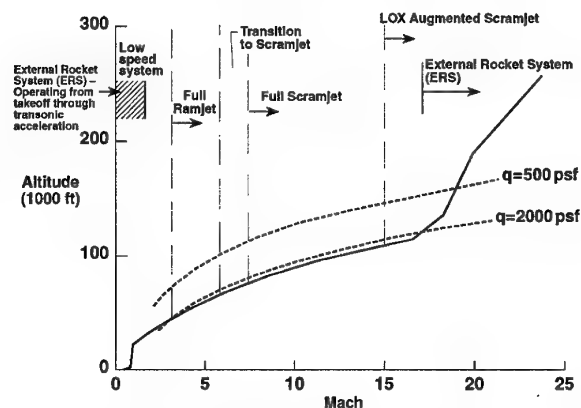*Figure 22. Reference airbreathing SSTO vehicle (ref. 13).*

Figure 23. Representative ascent trajectory (ref. 15).

ence SSTO is a cold structure (ref. 15) with mostly nonintegral, actively-cooled heat exchangers. Cryogenic hydrogen fuel is the coolant. Slush hydrogen is stored in the tank at 20 psig and 25°R. It is pumped to 5,500 psi and 60°R before circulating through the cooling panels, then through a turbine to drive the pump, back into the cooling network again, and out into the combustor. The heat exchangers were sized at Mach 15 conditions, where the heat loads are greatest. The cooling panel network was designed to deliver hot hydrogen to the injectors.

4.1.1.1.4 Subsystems

The majority of the subsystems are highly integrated with each other. The individual subsystems are (ref. 15): (1) active vehicle thermal control system (AVTCS), (2) environmental control and life support system (ECLSS), (3) electrical power generation and conversion system (EPG&C), (4) hydraulic and actuation, (5) auxiliary power unit (APU), (6) reaction control system (RCS), (7) fuel system, (8) oxidizer system, (9) vehicle pressurization, purge and drain system (VPP&D), and (10) avionics.

The AVTCS will be required to handle both cryogenic and hot hydrogen within the same fluid network. Active cooling is provided on the external nozzle, the airframe inlet ramp, engine systems, and the external rocket system. The active cooling panels will deliver hot hydrogen to the engine. Because fuel is used as the coolant, a fail-safe control system is being used. The ECLSS uses standard cryogenic hydrogen control devices, modified for low weight/volume, and provides an operation working environment for the crew. It also provides cooling for the vehicle management system, instrumentation, and hydraulic fluids.

The EPG&C consists of a number of 40 kW 270 VDC fuel cell assemblies. The fuel cells come from existing technology developed for the Space Shuttle program. They use hydrogen and oxygen and provide electrical power primarily for on-orbit duty, but are also used for avionics. APU's provide the hydraulic power for the actuators that control the aero-surfaces and the landing gear. The APU system is derived from an existing Space Shuttle system. It is driven by a dual mode, gas generator expander cycle turbine using hot gas temperature differential which is required to prevent overheating of the material, thereby making the APU power requirements virtually "free" during ascent. The hydraulic system utilizes a conventional hydraulic fluid system that operates at 8,000 psia. Hydraulic fluid cooling heat exchangers dump heat directly into a hydrogen fuel system that provides for the gasification of LH2 and LOX for use in the RCS. The RCS is a previously-developed rocket assembly.

The fuel system is a cryogenic fluid delivery system that supplies LH2 from the vehicle's tanks to the engine turbopumps and actively-cooled panels using a series of boost pumps. Because the hydrogen fuel in the tanks was sub-cooled to a slush condition, separate spray and mixing systems in the tanks are required to continually circulate the hydrogen so that it does not stratify; the ullage is kept at the same temperature as the fuel.

The oxidizer system provides LOX to the engine and external rocket system and is composed of both high and low pressure turbopumps. These pumps are used only to supply LOX to the main scramjet engine; the external rocket system has its own turbomachinery.

The VPP&D is required to provide helium for tank pressurization, vehicle cavity purge and repressurization, and pneumatic actuation. Helium is stored at 25°R within the hydrogen fuel tank.

The avionics is based on a proven quad-redundant architecture using ADA software and dual-fiber optics busses which is intended to provide for autonomous control.

4.1.1.1.5 Challenges

The system challenges extend from the actively-cooled airframe and engine cowl leading edges to the linear aerospike rocket engine at the airframe trailing edge. Some of the most critical items that are essentially the same as for the Mach 10 cruise baseline example are: the graphite/epoxy integral fuel (SH2) tank and TPS system, the ramjet/scramjet engine with mechanisms for mode transition; and the actively-cooled engine non-integral heat exchangers that allow fuel injection temperatures of 2,000°R. An 8,000 psia hydraulic system is also required, as is a health monitoring/management system for the entire vehicle. Optimization of the reference design to reduce dry weight and cost is in progress at LaRC.

4.1.2 Rocket-Powered SSTO Vehicles

Because of the enhanced propellant load due to on-board LOX as the oxidizer (LH2 as fuel). rocket-powered SSTO's must be vertical takeoff machines (launch assist is not being considered). Also, only horizontal landing is being considered to contain the scope.

The case for the SSTO rocket launch vehicle is made in reference 16 in which mass fraction, margin, minuscule payload, and sensitivity concerns are addressed and shown to be ameliorated with cumulative technology advancements.

4.1.2.1 Example Baseline

A reusable, rocket-powered, SSTO launch vehicle was designed (ref. 17 and 18) as a part of the Advanced Manned Launch System (AMLS) study in NASA Langley's Vehicle Analysis Branch and is an appropriate reference vehicle. The design reference mission for the AMLS single-stage vehicle is delivery and return of a 20,000 lb. payload and 2 crew to an international space station (51.6°, 220 nm).

4.1.2.1.2 Architecture

The vehicle design (ref. 17) is shown in figure 24. The payload bay is 15 ft. in diameter and 30 ft. long and located between an aft liquid hydrogen (LH2) tank and a forward liquid oxygen (LOX) tank. The normal-boiling-point LH2 and LOX propellants are contained in integral, reusable cryogenic tanks. On board propellants would provide an incremental velocity (ΔV) of 1100 ft./sec. following launch insertion into a 50 x 100 nm orbit. The design employs wing tip fins for directional control. The crew cabin is located on top of the vehicle. An airlock located aft of the crew cabin provides access to the cross-wise canister payload bay and to the space station through a hatch on top.

The liftoff thrust-to-weight (T/W) of the SSTO is 1.22 (ref. 17).

IOC = 2008-2010
Crew = 2 for 5 days

P/L bay = 15 × 30 ft
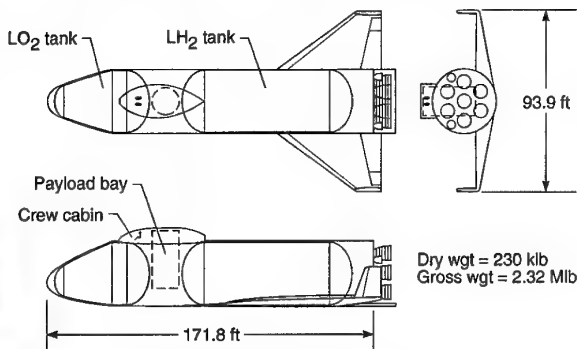P/L wgt = 20 klb to space station

93.9 ft

Dry wgt = 230 klb
Gross wgt = 2.32 Mlb

171.8 ft

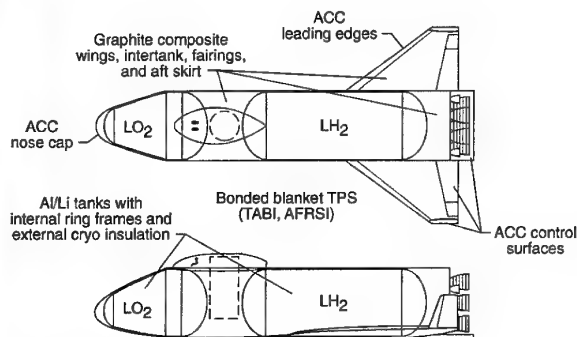*Figure 24. Reference rocket-powered SSTO configuration (ref. 17).*

Figure 25. Reference SSTO vehicle materials (ref. 17).

The vehicle dry weight is 230,000 lbs., and the gross weight is 2,320,000 lbs. (figure 24).

4.1.2.1.3 Reference Systems/Technologies

The reference AMLS SSTO has seven SSME-derivative engines that are gimballed for vehicle control during ascent and abort (ref. 18); the performance characteristics of one of these engines are summarized in Table 1. The SSME-derivative engine differs from the current SSME in a number of ways (ref. 18). Extended-life, high-pressure turbopumps are used with hydrostatic bearings. Electromechanical actuators are used for gimbals and valves. Other improvements include integrated health monitoring, a Block II controller, and a two-duct hot gas manifold.

The major materials and structural technologies assumed for the AMLS SSTO vehicle (ref. 17) are summarized in figure 25. The SSTO vehicle employs graphite composite wings, intertank, nose region, fairings and aft skirt which all act as carrier panels for a ceramic blanket TPS on most windward and leeward surfaces and for an advanced carbon-carbon (ACC) TPS on the vehicle nose and leading edges (ref. 17). All aerodynamic control surfaces are of an ACC hot structure design. The integral hydrogen and oxygen tanks are constructed of Al-Li 2095 and utilize external, closed-cell foam insulation. The thrust structure also utilizes Al-Li 2095 and graphite composite elements (ref. 18).

4.1.2.1.4 Challenges

The challenge is the maturation of technologies to enable the design of a viable, affordable SSTO rocket powered vehicle and decrease the operational complexity and empty weight of the vehicle (ref. 17 and 18). More advanced technologies would enable the design of an SSTO vehicle that is less sensitive to changes in engine performance parameters. The cumulative effect of employing a number of moderate technology advancements over STS technologies (ref. 17) is shown in figure 26. Additional technology advances over those assumed for the reference SSTO could enhance the design as shown in figure 27. These technology advancements could be traded for increased vehicle design margins and reduced sensitivities.

4.2 Two-Stage-to-Orbit (TSTO) Vehicles

For TSTO vehicles, technology requirements are reduced relative to SSTO vehicles; they require only current or near-term technologies. Also, they are less sensitive to dry weight growth. They allow the proration of the ascent energy (delta velocity) among the stages (booster and orbiter). However, TSTO systems lead to the development, manufacture, and operation of the two vehicles (in fact, three: the composite, the booster and the orbiter).

Since the design of access to space vehicles is influenced to a major extent by propulsion systems and propulsion integra-
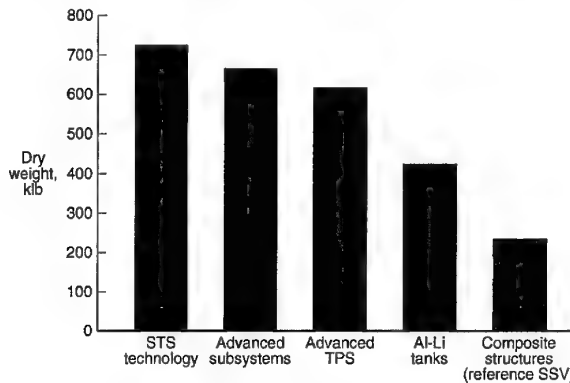

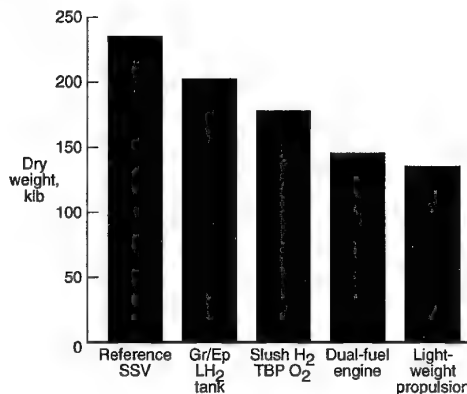*Figure 26. Cumulative effect of technology evolution from STS (ref. 17).*

Figure 27. Cumulative effect of enhancing technologies on rocket-powered vehicle (ref. 17).

tion architectures, the TSTO vehicles will be categorized according to propulsion systems. A coarse TSTO classification is given in figure 28 which has categories for airbreathing boosters and rocket powered boosters as well as combination powered orbiters and rocket powered orbiters. The airbreathing boosters are further divided with respect to ramjet (M< 6) and scramjet (M>6) propulsion systems. The remainder of the discussion centers mainly on the boosters as they constitute the greatest challenge—from a systems, operations, and cost perspective.

4.2.1 TSTO Vehicles With Airbreathing Boosters / Rocket Powered Orbiters

The focus is on a horizontal take-off and landing (HTOL) launch vehicle. The advantage is more versatile basing with airplane like operations, launch offset capability and near-term technology requirements. For launch systems that stage at Mach 6 or below, the booster could be designed with near-term technology. Boosters that stage above Mach 6 would require more advanced technology because of the need for a scramjet and more sophisticated/thicker TPS. With their ability to cruise, airbreathing boosters have the potential to return to viable landing sites, even at the higher staging Mach numbers.
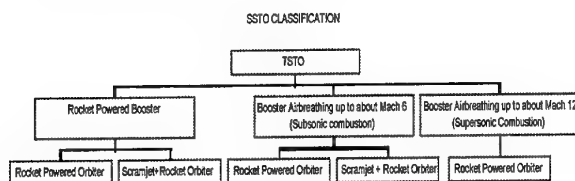

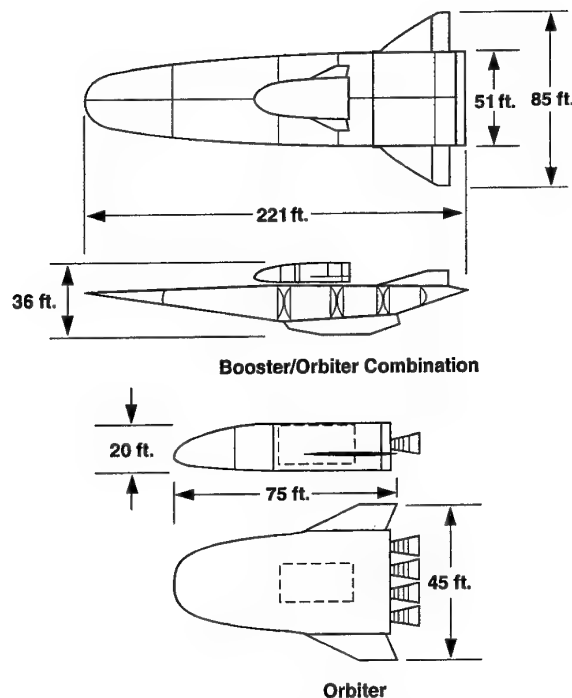*Figure 28. TSTO vehicle classification.*

Booster/Orbiter Combination

Orbiter

Figure 29. TSTO (airbreather/rocket vehicle characteristics (ref. 13).

4.2.1.1 Example Baseline
The reference vehicle is from NASA's Access to Space Study (ref. 13). The configuration is a horizontal take-off/landing system with a piggy-back orbiter on top of a two-duct, over/under airbreathing booster (figure 29). It stages at Mach 5. The booster propulsion system is a combination of LH2 fueled turbofan jet engines (to M=2.4) and ramjets (to M=5). The orbiter is rocket powered LH2 fueled. Designed to deliver 25,000 lbs. of payload in a 15' x 15' x 30' bay to a space station at 51.6°, 220nm orbit, the reference 2STO system has a combined take-off gross weight (TOGW) of 800,000 lbs. and dry weight (DW) of 300,000 lbs. The TOGW/DW of the booster and orbiter is 352,000 lbs./252,000 lbs. and 450,000 lbs./52,000 lbs., respectively.

The booster is a lifting-body with a shape very similar to the reference airbreathing SSTO of section 4.1.1.1.3. Both have a spatular airframe leading-edge and rotating wings which also serve as horizontal control surfaces. Both utilize cold integral graphite-epoxy cryogenic tanks (LH2 vs SH2); graphite composite primary structure; and passive, adhesively-bonded TPS, as well as 8,000 psi hydraulic systems.

4.2.1.1.1 Staging
As the staging Mach number is increased, total system gross weight declines (figure 30, ref. 20) because of a more optimal split of the energy content in each stage. Above Mach 6, the booster air-breathing propulsion system would require a ram/scramjet engine. Moving from a Mach 5 to a Mach 10 staging system, the combined gross weight would decrease from 800,000 lbs. to 600,000 lbs. and the combined dry weight would decrease from 300,000 lbs. to 250,000 lbs.

4.2.1.1.2 Challenges
The TSTO reference booster (for Mach 5 staging) requires
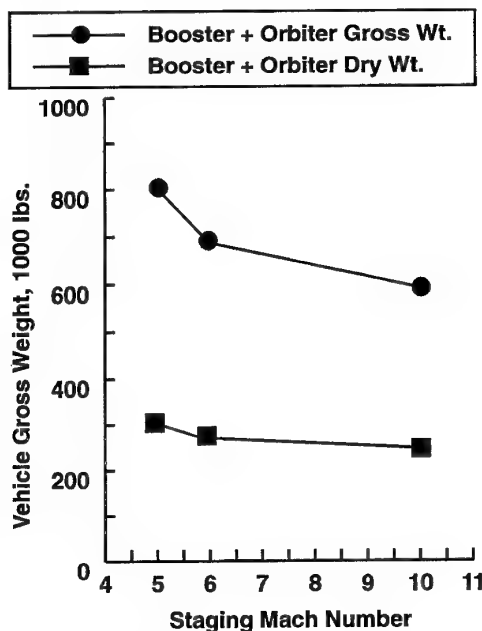

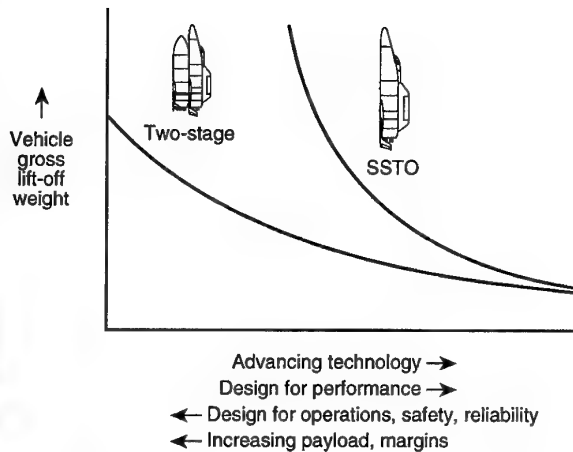*Figure 30. Staging Mach number effect on gross weight (ref. 20).*

Figure 31. Factors influencing rocket vehicle sizing (ref. 18).

development of a turbojet/ramjet airbreathing propulsion system much like the Mach 5 Waverider airplane of section 3.1.1 except the booster is fueled by LH2 rather than LHC. Also, a duct and one-half, LACE ejector ramjet could provide an interesting trade, especially for staging at higher Mach numbers (M > 7) where transition from a ram to scramjet is required. The structure/material challenges are very similar to the air-breathing SSTO—cold integral graphite-epoxy tanks and graphite composite primary structure—as is the hydraulic system.

The orbiter, as defined in reference 18, would require the development of an expander cycle LOX/LH2 rocket engine systems. Staging within the atmosphere could be quite a challenge itself. If a pull-up to low dynamic pressure for staging was desirable, then both a tail rocket system and a Reaction Control System (RCS) (for control) would be required for the booster.

4.2.2 TSTO Vehicles with Rocket Powered Boosters/ Rocket Powered Orbiters
TSTO rocket systems are considered primarily because of technology readiness. Also, they retain a gross-weight / dry weight advantage over SSTO rocket systems even at reduced technology levels (figure 31, ref. 21), but the benefits of staging are clearly reduced. For TSTO rocket systems, the recovery of the booster is a major issue since their "fly-back" capability has serious limitations. The criticalness of the recovery issue increases with staging speed, so high staging speed concepts will be considered first.

4.2.2.1 High Staging Speed Concepts (beyond 10,000 ft./sec.)
For these high staging speeds, a relatively even distribution of the ascent energy is achieved between the two stages. Since SSTO vehicles are seldom pure single-stage (for many missions, they need an intelligent upper stage to send their payloads into higher energy orbits), an approach (ref. 22 and 23) is to develop a semi-reusable TSTO, the first stage being targeted to become an SSTO vehicle. Should this SSTO vehicle appear out of reach during its development, either from a cost or technology perspective, the designers would have the following option: reduce the ΔV of the reusable first stage and increase the ΔV of the expendable upper stage. The first stage, unable to go into orbit, would have to perform a once-around flight to land at its launch site, or perhaps land at the Antipodes.

These high staging speed concepts were downselected by Aerospatiale (ref. 23) because the downrange required by the booster is very high (once around) and the ΔV reduction potential is very low, even for high lift-to-drag ratio (L/D) booster configurations. For example, to achieve a ΔV reduction of about 1600 ft./sec. in the booster would require that the hypersonic L/D exceed 5 for the booster to acquire a viable landing site.

Aerospatiale recently downselected another high speed staging concept, Taranis (ref. 24, figure 32, also dubbed "the Transatlantic"), because it raises the question of the independence of access to space activities since the booster landing strips are located outside of the launching country. However, since Taranis exhibits some major advantages such as use of near-term technologies and use of engines derived for the gas generator cycle of Ariane 5, a modified version with an extended range booster (re-boost of the main engines or cruise with turbojets) will be studied. This extended range version would allow a landing on territories belonging to the launching nation.

Having eliminated (downselected) most of the high staging speed TSTO launchers, Aerospatiale's launch system analyses have been focused on low staging speed concepts (less than 6000 ft./sec.) which allow a rather easy flight back of the booster to its launch base. The main thrust of the work was: (1) study TSTO with staging speed nearing 3,000 ft./sec., (2) assess the Pop-Down concept, (3) assess the Siamese configuration, and (4) assess the interest of using LOX/LHC rather than LOX/LH2.

4.2.2.2 Staging Speed Nearing 3,000 ft./s
This configuration is envisioned (ref. 23) as a two-stage, parallel-burn, winged, vertical take-off, horizontal landing system. When the launch system reaches a speed of about 3,000 ft./sec., the booster (first stage) is staged and glides back to the launch site runway. This system is an unbalanced configuration with respect to ascent energy having a quite "easy-to-design" first stage and a very ambitious second stage.

Despite its operational drawbacks with respect to SSTO concepts (three vehicles to operate versus only one), this TSTO configuration offers many advantages in terms of performance and technological feasibility.

* The low velocity of the first stage after the staging maneuver allows a glide back trajectory to the launch site. Therefore the operations appear greatly simplified with respect to the "transatlantic" TSTO (Taranis configuration, ref. 24).
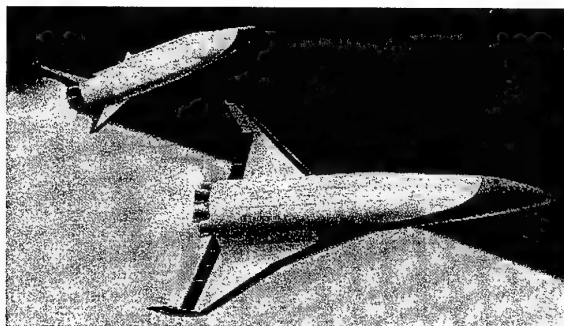

Figure 32. Taranis concept (ref. 24).

- Vertical takeoff
- LO_2/LH_2; SSME-derivative engines
- Unmanned glideback booster; Mach 3 staging
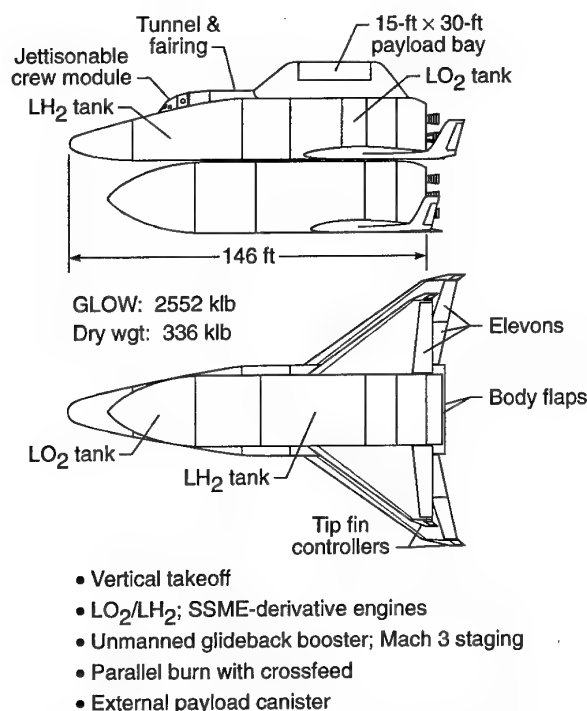- Parallel burn with crossfeed
- External payload canister

Figure 33. Near-term-technology two-stage AMLS (space-station mission), 40K payload, ref. 21).

- The design effort has to focus on the second stage which appears to be "almost an SSTO" because of the mass fraction, mechanical and thermal load requirements it has to sustain. Nevertheless, the ΔV reduction due to the booster (especially in case of crossfeeding) allows a vehicle design with lower technology level requirements, mainly in propulsion systems and structure mass fraction reduction requirements.

The numerous configurations allowed by this launch system provide many interim options on the way to an affordable SSTO vehicle: (1) expendable first stage, (2) reusable first stage with LOX/hydrocarbon propellants with or without LH2 crossfeeding to the second stage (ref. 25), and (3) reusable first stage with an increased staging speed (the first stage flies back to the launch site using an airbreathing propulsion system). This approach, after the downselection of the "Once Around" and "Antipodal" systems, appears to be one of the most promising interim options to pave the way to a really affordable launch system. Such a concept was studied at NASA Langley as part of the Advanced Manned Launch Systems (AMLS) activities (figure 33, ref.21) and provides an appropriate reference vehicle for this class.

4.2.2.2.1 LOX/LHC Siamese Pop-Down Concept
The Pop-Down procedure (ref. 25) is a method of launching a TSTO vehicle which allows recovery of both stages at the launch site. The booster flies along a strictly vertical flight path so that it always remains above the launch site. This procedure solves the downrange site recovery problem at the expense of a payload mass loss, since the TSTO ascent trajectory is no longer fully optimized.

The first staging analyses of such a Pop-Down launcher have

shown that the propellant masses of both stages were very close to one another. Moreover, since the orbiter needs a high acceleration to minimize the velocity losses, both stages needed the same number of engines. This has led Aerospatiale to select a Siamese concept for further study: both stages contain the same propellant mass and are powered by the same number of engines. Thus, this Siamese TSTO is somewhat characteristic of SSTO vehicles in that there is only one configuration to develop, manufacture, and operate.

4.2.2.3 Challenges
The challenges of the rocket powered TSTO vehicles are very similar to the SSTO systems but generally less severe. However, TSTO systems pose specific problems: aerodynamic interactions between the stages, staging (especially in case of abort) and crossfeeding.

5. ADVANCED, ENHANCING SYSTEMS CONCEPTS
There are many advanced systems concepts of current interest which may have significant benefits for hypersonic vehicles (ref. 1) that will present system challenges. Advanced concepts are currently under study for configuration, drag reduction, low speed propulsion, LAIR collection/oxygen enrichment, controls and launch assist.

In enhancing the air-breathing SSTO and TSTO designs, the configuration is extremely important. The lifting body that served as a reference may be better if it was designed upside down—inverted lifting-body—as shown in figure 34 (ref. 1). In this arrangement the profile of the vehicle would be a much more favorable airfoil and provide much greater lift at a lower angle-of-attack and thus less drag, especially throughout the subsonic and transonic region. Above the transonic region the vehicle may be more optimum in a conventional engine underslung attitude and thus require rolling 180°.

As air-breathing engine weight increased with design/technology maturation in prior programs, it became apparent that there may be an advantage to switch configurations from a lifting-body to a high-fineness ratio wing-body (figure 34) where engine weight can be traded for wing weight. High-fineness ratio configurations would have lower drag per unit volume and thus require less engine size.
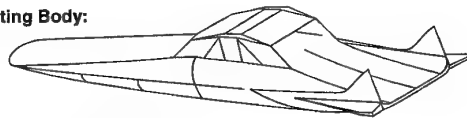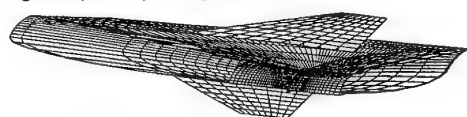

Figure 34. Extended/advanced configuration matrix (ref. 1).

The ultimate hypersonic air-breathing configuration in terms of propulsion flowpath for a point design is the inward turning inlet configuration (ref. 26) as shown in figure 34. Ideally, the funnel inlet configuration offers more air capture and more efficient compression to the inlet throat for less wetted area with an accompanying, more efficient expansion through the radial nozzle than does its two-dimensional or conical counterparts, resulting in potentially higher net thrust and specific impulse. Of course there are concerns such as "on-design/off-design" inlet spillage, volumetric efficiency, etc.

The technology area of magnetogasdynamics (ref. 27) in which a nonequilibrium cold plasma is created ahead/adjacent to the vehicle to reduce shock strength, drag and heat transfer is largely unexplored, although test results point to these favorable phenomena. Steam reforming of hydrocarbon fuel through chemical regeneration and magnetogasdynamic generation of electrical power through deceleration of inlet flows is also profiled in reference 27. As these phenomena become better understood, flight systems must be designed to accommodate them.

Pulse detonation engines (PDE), which use detonation waves propagating through a premixed fuel-air mixture to produce large chamber pressures and thereby thrust, are potentially promising for low speed (M = 0 to 5) propulsion (ref. 28). The PDE has the potential for very high specific impulse, and it may be possible to have a single system which can be converted from a low speed airbreather to an efficient pulse rocket for boost to orbit. The PDE consists of a cylinder or series of cylinders which are repeatedly filled with a combustible mixture and detonated. The oxidizer can be air provided by an inlet (airbreather) or gaseous oxygen retrieved from a tank (rocket).

The ejector ramjet allows the ramjet to operate from takeoff to ramjet takeover speed (M = 3), and thus a single duct engine that operates over a broad Mach number range is possible (ref. 29). As might be expected, the ejector ramjet requires a large amount of oxidizer which may mean that, to be practical, a vehicle using this system must also extract air and/or oxygen from the atmosphere. The system which extracts air, condenses it, and uses it in an ejector ramjet is called a liquid air cycle engine (LACE). LACE has been studied for many years (ref. 30) as well as other condensing systems such as air collection and enrichment system (ACES) where liquid oxygen is subsequently separated out and stored for later use. The original ACES used an approach where the distillation column process was accelerated through application to a rotating disk which produced centrifugal force analogous to an increase in gravity. Many other methods for extracting oxygen from air are currently being studied (ref. 1).

In the controls area, neural networks (ref. 31) appear to offer a significant advancement for both the airframe and engines controls and the coupling between the two. Accurate Automation Corporation is currently in the process of demonstrating a neural network for the rudder control of a hypersonic waverider configuration at subsonic speeds in their LoFLYTE™ flight test vehicle (figure 35).

For takeoff assist, Mag Lifter technology (magnetic field used to accelerate vehicle, ref. 32) is being examined for rail launch

in NASA's Advanced Space Transportation Program. Takeoff assist is more beneficial to vehicles that have higher LOX fractions in which a higher percentage of propellant would have been burned had not the assist delta velocity been provided.

6. COMMON SYSTEM CHALLENGES

All the hypersonic vehicles described heretofore pose formidable system problems: (1) vehicles are high speed and long range, (2) vehicles are subjected to severe environment, but must be lightweight, (3) vehicles' propulsion systems and airframes have to be intricately integrated, (4) vehicles' major characteristics have considerable uncertainties since the realm of hypersonics remains widely unexplored, and they are sensitivity intensive, and (5) vehicles must accommodate a wide flight envelope.

Most of these challenges will be resolved with tangible means (efficient propulsion, lightweight structures...). These are identified herein and addressed in other AGARD papers. However, more impalpable means can contribute.

6.1 Guidance, Navigation and Control (GN&C)

GN&C is considered an enabling technology for hypersonic vehicles because beyond the aforementioned problems: (1) they have to be autonomous for they are long range vehicles and/or military vehicles and/or subjected to the blackout phenomena, (2) they may have very short response times, flexible structures, propellant sloshing, and (3) they have to use sophisticated sensors (high speed Air Data Systems, seekers behind high temperature windows, etc.).

Hypersonic vehicles need high performance explicit/adaptive guidance and control. Explicit guidance allows on-board, real-time trajectory computations. For instance, a lifting re-entry missile whose target would be out of range may re-optimize its trajectory, make an atmospheric skip and hit the bull's eye. Adaptive control allows accounting for vehicle uncertainties in real time and to adapt, in real time, the guidance and control algorithms. Using more recent control methods, like H_{∞} or neural networks, explicit and adaptive GN&C will ease the hypersonic vehicles design and operation.
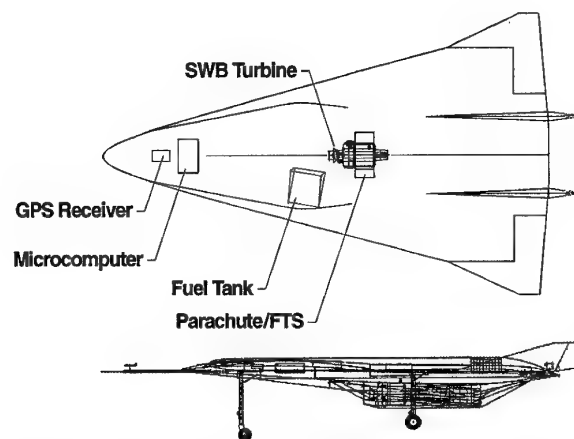

Figure 35. LoFLYTE Subsonic Neural Net Demonstrator (ref. 1).

6.2 Telecommunications

Telecommunications with hypersonic vehicles pose specific problems: (1) antennas are to be protected against high heat loads, (2) the radio communication blackout phenomena, and (3) the long range of hypersonic flight may dictate the development of a network of ground stations and/or satellites.

During its hypersonic flight, the vehicle is subjected to high heat loads which may cause air ionization (plasma). The radio communication blackout phenomena is caused by the plasma sheath which surrounds the vehicle. Possible solutions to this phenomena are: (1) use frequencies higher than the plasma cut-off frequency, (2) select a proper antenna location, and (3) use other communication means (laser...).

6.3 Reliability, Availability, Maintainability and Safety

The vehicle's reliability by itself is often not sufficient to justify the development of a hypersonic vehicle. For example, consider a reusable launcher whose reliability is only 0.99. Statistically, this translates to the loss of one vehicle every 100 flights. This is why reliability enhancement for reusable launch vehicles is so important and why built-in abort strategies have to be included to increase the probability of recovering the vehicle and its payload (crew survivability should be greater than 0.999, ref. 13).

A low availability could negate the speed advantage of most hypersonic vehicles. Responsiveness is a major operational issue, especially for military vehicles.

Maintainability is one of the key issues for hypersonic vehicles in terms of what is required and what it will cost. For instance, should the maintenance cost per mission represent 1% of the vehicle cost, the total maintenance cost over 100 missions would amount to the cost of one vehicle (2%, two vehicles, etc). Technology maturation and demonstrators are therefore mandatory to reduce the maintenance uncertainties. Proper design and operation methodology (e.g. aircraft like) and health monitoring systems are also mandatory.

Also hypersonic vehicles pose specific problems of safety, both from the range safety viewpoint and from the crew safety viewpoint. For major malfunction at hypersonic speed crew rescue is a challenge. Either vehicle integrity must be maintained before ejection seats can be used or the crew cabin has to be ejected.

6.4 Operations

Reusable vehicles must be designed for operations and maintenance (ref. 9) to minimize the life cycle costs and to maximize responsiveness. The enhancement of systems/subsystems reliability in conjunction with an extension of their cycle life is a must in reducing operational cost. Present-day operations consist of expensive tasks to prepare and operate vehicles. This is no longer affordable; vehicles and operations have to be designed concurrently. Vehicles can no longer be designed from just a performance/weight-minimization perspective.

Operations must be automated (no "standing army") to reduce costs and streamlined to increase responsiveness. The vehicle designed for operations provides more robust-

ness to the system; autonomous and fault tolerant architectures are to be favored.

Among the ideas to increase vehicle operability are: (1) to some extent use aircraft lessons learned, (2) develop and use an inflight health monitoring system, (3) use robust, fast-response, fault-tolerant software and avionics, (4) avoid hypergolic propellant, and (5) reduce the reliance on hydraulic systems; use electromechanical actuators where possible.

7. CONCLUDING REMARKS

Systems/subsystems architecture for fully reusable hypersonic airplanes and space access vehicles were examined. Screening categories were takeoff, landing, propulsion systems, fuels/propellants, mission and staging. System/subsystem challenges were identified.

For hypersonic airplanes, emphasis was focused on Mach 5 and 10 cruise with hydrocarbon and hydrogen fuel, respectively. Developing the powerplants (turboramjets or LACE ejector-ramjets and dual-mode ramjets/scramjets) and performing an efficient airframe propulsion integration as well as thermal management are the main issues. For the endothermic-hydrocarbon fueled systems (Mach < 8), hot, integral titanium tank structure appears viable. For the hydrogen-fueled systems (Mach > 8), cold, integral graphite/epoxy tank structure with graphite composite interfaces and external insulation/TPS is the architecture of choice.

For access to space vehicles, emphasis was focused on single- and two-stage, airbreathing and rocket propelled systems with horizontal takeoff for airbreathers and vertical takeoff for rockets. For the airbreather, propulsion and propulsion integration along with thermal management are still the biggest challenges; this is essentially the same as with cruise vehicles except for the additional rocket integration for orbital access in SSTO vehicles and pullup (if required) for staging in the TSTO boosters. The airbreathing propulsion systems have the potential for long cycle life which could have a positive effect on reducing operational cost (lower frequency of changing engines and pumps). For structures, the emphasis is on cold, integral graphite/epoxy hydrogen tanks and graphite composite interfaces. The airbreathing vehicles, being lifting configurations, are designed for normal loads and thus are conducive to abort situations. For SSTO vehicles, one of the biggest challenges may be to overcome negative paradigms with respect to the use of slush hydrogen.

For rocket powered systems, the main challenges are to mature the enabling technologies to ensure operation feasibility. This feasibility depends on the development of necessary technologies for required dry mass fraction with built-in margins that will provide reliable systems with favorable cycle life. Some of these technologies such as cryogenic, integral tankage, etc. are common to airbreathers as well. These technologies are being pursued in the U.S. X-33, X-34 and Advanced Space Technology Program (ASTP) programs.

Even though less demanding than SSTO vehicles, TSTO systems pose specific problems: aerodynamic interactions, cross-feeding, and staging, among others.

Vacuum thrust, lb.	463,900
Sea-level thrust, lb.	402,600
Chamber pressure, psia	3,000
Area ratio	50
Vacuum specific impulse, sec.	447.3
Sea-level specific impulse, sec.	387.9
Oxidizer/fuel	6.0
Weight, lb.	6,780

Table 1. SSME-derivative engine performance characteristics (ref. 16).

8. REFERENCES

1. Hunt, J.L.; Lockwood, M.K.; Petley, D.H.; and Pegg, R.J.: Hypersonic Airbreathing Vehicle Visions and Enhancing Technologies. Space Technology and Applications International Forum. AIP Conference Proceedings 387, Albuquerque, New Mexico, 1997.

2. Pegg, R. J.; Hunt, J. L.; Petley, D. H.; Burkardt, L.; Stevens, D. R.; Moses, P. L.; Pinckney, S. Z.; Kabis, H. Z.; Spoth, K. A.; Dziedzic, W. M.; Kreis, R. I.; and Barnhart, P. J.: Design of a Hypersonic Waverider-Derived Airplane. AIAA 93-0401, Reno, Nevada, January 11-14, 1993.

3. Hunt, J. L.; and Eiswirth, E. A.: NASA's Dual-Fuel Airbreathing Hypersonic Vehicle Study. AIAA 96-4591, Norfolk, Virginia, November 18-22, 1996.

4. Bogar, T.J.; Eiswirth, E.A.; Couch, L.M.; Hunt, J.L.; and McClinton, C.R.: Conceptual Design of a Mach 10, Global Reach Reconnaissance Aircraft. AIAA 96-2894, Lake Buena Vista, Florida, July 1-3, 1996.

5. Bogar, T.J.; Alberico, J.F.; Johnson, D.B.; Espinosa, A.M.; and Lockwood, M.K.: Dual-Fuel Lifting Body Configuration Development. AIAA 96-4592, Norfolk, Virginia, November 18-22, 1996.

6. Lau, K. Y.; Scuderi, L. F.; Petley, D. H.; and Yarrington, P. W.: Dual Fuel Vehicle Thermal Management. AIAA, Norfolk, Virginia, November 18-22, 1996.

7. Weirich, T. L.; Fogarty, W.; Dry, K.; Iqbal, A.; and Moses, P.: Dual-Fuel Vehicle Airframe and Engine Structural Integration. AIAA 96-4594, Norfolk, Virginia, November 18-22, 1996.

8. Mercier, R.A.; and Ronald, T.M.F.: U.S. Air Force Hypersonic Technology Program (HyTech). Preliminary Sections Paper, AIAA 7th International Space Planes and Hypersonics Systems and Technologies Conference, Norfolk, VA, November 1996.

9. Space Propulsion Synergy Team: A Guide for the Design of Highly Reusable Space Transportation. NASA Headquarters, November 1996.

10. Fazi, D.; Wagner, A.; and Johnson, C.: STS 2000: An Outline. IAF 90-192, 41st Congress of the International Astronautical Federation, Dresden, Germany, October 6-22, 1990.

11. Wagner, A.; and Bombled, J. P.: Oriflamme: A Reference Airbreathing Launcher to Highlight Areas that are Technological Drivers for Hypersonic Vehicles. IAF 91-207, 42nd Congress of the International Astronautical Federation, Montreal, Canada, October 5-11, 1991.

12. Falempin, F.; Lacaze, H.; Wagner, A.; and Viala, P.: Reference and Generic Vehicle for the French Hypersonic Technology Program. AIAA 95-6008, Chattanooga, Tennessee, April 3-7, 1995.

13. Access to Space Study: Summary Report; Office of Space Systems Development, NASA Headquarters, January 1994.

14. Bekey, I.; Powell, R.; and Austin, R.: NASA Studies Access to Space. Aerospace America, May 1994.

15. Hunt, J. L.: Airbreathing/Rocket Single-Stage-to-Orbit Design Matrix. AIAA 95-6011, Chattanooga, Tennessee, April 3-7, 1995.

16. Bekey, I.: Why SSTO Rocket Launch Vehicles are Now Feasible and Practical. IAF 94-V.1.524, 45th Congress of the International Astronautical Federation, Jerusalem, Israel, October 9-14, 1994.

17. Stanley, D. O.; and Piland, W. M.: Technology Requirements for Affordable Single-Stage Rocket Launch Vehicles. Space Technology, Volume 14, No.5, pp. 319-330, 1994.

18. Stanley, D. O.; Engleund, W. C.; Lepsch, R. A.; McMillin, M.; Wurster, K. E.; Powell, R. W.; Guinta, T.; and Unal, R.: Rocket-Powered Singe-Stage Vehicle Configuration Selection and Design. Journal of Spacecraft and Rockets, Volume 31, No. 5, pp. 792-798, 1994.

19. Wagner, A.: A Generic Fast Airbreathing First Stage TSTO Vehicle Radiance. AIAA 95-5084, Orlando, Florida, December 1-4, 1992.

20. Gregory, T.; Bowles, J.; and Ardema, M.: Two Stage to Orbit Airbreathing and Rocket System for Low Risk, Affordable Access to Space. SAE 941168, SAE 1994 Aerospace Atlantic Conference and Exposition, Dayton, Ohio, April 19, 1994.

21. Freeman, D. C.; Talay, T. A.; Stanley, D. O.; Lepsch, R. A.; and Wilhite, A. W.: Design Options for Advanced Manned Launch Systems. Journal of Spacecraft and Rockets, Volume 32, Number 2, pp. 241-249.

22. Wagner, A.; Deneu, F.; Grazziani, S.; and Lancelot, J.: TSTO: The Next Step. 48th IAF Congress, Torno, Italy, 1997.

23. Wagner, A.; and Deneu, F.: Future Launchers at Aerospatiale: A Status Report. 1997 AIAA Defense and Space Programs Conference and Exhibit.

24. Abriat, E.; and Bombled, J. P.: Advanced TSTO
VTOHL Reusable Rocket—A Study Report. IAF 89-866.

25. Terrenoire, P. H.; Masse, B.: An Overview of the
Reusable Rocket Launchers Based on Near Term
Technologies. IAF 94-539.

26. Kothari, A. P.; Tarpley, C. et al.: Hypersonic Vehicle
Design Using Inward Turning Flowfields. AIAA 96-2552,
1996.

27. Gurijanov, E. P.; and Harsha, P. T.: AJAX: New
Directions in Hypersonic Technology. AIAA 96-4609,
Norfolk, Virginia, November 18-22, 1996.

28. Bussing, R. R. A.; and Pappus, G.: An Introduction to
Pulse Detonation Engines. AIAA 94-0263, 1994.

29. Bulman, M.; and Siebenhaur, A.: A Strutjet Engine:
Exploding the Myths Surrounding High Speed Airbreathing
Propulsion. AIAA 95-2475, 1995.

30. Balepin, V.; Cozzog, P.; Marta, M.; and
Vanderkerckhove: Assessment of SSTO Performance with
In-Flight LOX Collection. AIAA 95-6047, 1995.

31. Sacks, R.; Cox, C.J.; and Pap, R.M.: LoFLYTE™: A
Neurocontrols Testbed. AIAA 97-0085, 35th Aerospace
Sciences Meeting & Exhibit, Reno, Nevada, January 1997.

32. Mankins, J. C.: The MagLifter: An Advanced Concept
Using Electromagnetic Propulsion in Reducing the Cost of
Space Launch. AIAA 94-2726, 30th Joint Propulsion
Conference and Exhibit, Indianapolis, Indiana, June 1994.

"SCIENTIFIC BARRIERS TO HYPERSONIC VEHICLE DESIGN"

Dr. LEONIDAS SAKELL
Air Force Office of Scientific Research
Aerospace & Materials Sciences Directorate
110 Duncan Avenue, Suite B-115
Bolling Air Force Base
Washington DC 20332-8080
USA

1. SUMMARY

This paper will discuss some of the scientific barriers to operational hypersonic vehicle design. These barriers arise from three primary sources. The first is a lack of fundamental understanding and knowledge of the aerothermodynamic flows, environments and, flow processes which arise over complex, 3D weapon system flight configurations during flight. The second source is the limitations inherent in the numerical simulations of these flows. The third is the lack of hypersonic test facilities which can operate with test times of at least seconds while also duplicating flight enthalpies and Reynolds numbers. My interest centers about the scientific issues arising with actual hypersonic configurations that are of current, planned or, potential mission relevance to the United States Air Force. I will discuss the major barriers in these categories below from the perspective of their impact on hypersonic flight vehicle design and performance.

2. INTRODUCTION

Hypersonic flight vehicles are complex, multidisciplinary, integrated flight systems. The design of these systems is an extremely challenging process which is still much more of an art than a science. The design process typically employs combinations of simulation, flight testing, ground testing and, experience based intuition. The reservoir of individuals possessing experience based intuition is rapidly declining. There are a multitude of challenges which face hypersonic vehicle system designers, as the U.S. National Aero-Space Plane program, the French Hermes program, the Japanese Hope

program and, the German Sanger program have clearly demonstrated. It was also clearly demonstrated that "flooding the market" with massive amounts of funding only ensured the rapid consumption of massive funds. Sustained, long term, focused support is the only way to successfully meet scientific challenges in general and, in particular, the hypersonic vehicle design challenges to be discussed in this paper.

On-going hypersonics basic research programs must be coordinated with hypersonics technology base needs and requirements. Broad technology base requirements must be defined and regularly reviewed and updated to establish specific goals and clear focus for on-going hypersonics basic research programs. Usually, hypersonics technology only gets supported whenever a funded hypersonics vehicle development program comes along. Typically, under these programs, there is a lot of money spent to implement "crash programs" of applied research with an insufficient technology base to meet the requirements of the vehicle development program. One of my biggest challenges is to ensure that the hypersonics research base is active to provide a sufficiently broad and mature technology base to provide direct, on-demand support for vehicle designers, as required, to develop candidate hypersonic flight vehicle systems and evaluate their potential mission performance. The research base includes numerical, experimental and, analytical research.

From the perspective of integrated vehicle system design, configuration design challenges

can be grouped into several areas namely; (1) mission requirements, i.e. performance based requirements, (2) technology base requirements, (3) advanced configuration concepts such as configurations which might employ plasma based control concepts, (4) aerothermodynamics (computational, analytical and experimental), i.e. fundamental science knowledge based and, (5) system life cycle costs including maintainability, supportability and, operability. I will briefly comment on the subject of technology base requirements and discuss at length the topic of aerothermodynamics from my perspective as program manager of the External Aerodynamics & Hypersonics fluid mechanics basic research program at the Air Force Office of Scientific Research in Washington D.C.

3. TECHNOLOGY BASE REQUIREMENTS

Technology base requirements pertain to the on-demand exploitation of <u>existing scientific knowledge</u>, including flow simulation and modeling capabilities, for the design of hypersonic vehicles to meet specific pre-defined system requirements and mission capabilities. The key phrase is "existing scientific knowledge". With long lead times associated with conducting basic research, compressed duration flight vehicle development programs can only exploit existing knowledge. This existing knowledge is what I refer to as the technology base. As discussed above, there must be ongoing coordination between the hypersonics research community and the hypersonics vehicle design community. It is one of my primary goals to stimulate and facilitate this coordination.

4. AEROTHERMODYNAMICS CHALLENGES

There are many fundamental scientific challenges to hypersonic vehicle configuration design. Very little is known or understood about hypersonic aerothermodynamics pertaining to operational flight vehicle systems. The full characterization of the flow fields and flow processes which arise over full flight vehicle system configurations during dynamic, 6 degree-of-freedom, hypersonic flight is not possible at present. Further, the fundamental aerothermodynamics processes of flows within functioning scramjet engine systems (forebody/inlet/isolator/combustor/nozzle) are not well understood or predictable. Current analyses treat hypersonic vehicles as rigid bodies. Materials which can survive hostile aerothermodynamic environments for long flight times need to be developed. Aerodynamically tailored smart materials, which deform in prescribed ways during flight to enhance vehicle performance, must be developed. Materials science is limited as to the characterization of aerothermo-structural interactions such as fatigue, aerothermo-structural response and, dynamic structural failure thresholds. Very little is known regarding hypersonic, 6-DOF flight dynamics and, more importantly, vortex dynamics. These and other aerothermodynamics scientific challenges will be discussed separately in more detail below.

4.1 Simulation & Modeling:

One of the major scientific challenges to vehicle design is the characterization of the inter-related multidisciplinary, aerothermodynamic flows and flow processes which arise over maneuvering hypersonic flight vehicle systems. Experimental facilities which duplicate flight conditions (enthalpy, mach number, Reynolds number, total pressure, plasmas etc.) continue to be prohibitively expensive so, future vehicle configuration design will be increasingly based on numerical simulation and decreasingly based on shock tunnel experimentation. Expensive flight testing will, at best, play an ever diminishing role. The development of a validated, multi-disciplinary, hypersonic weapon system aerothermodynamic simulation & modeling capability is essential. This capability must be such that a pilot can sit down at a computer display console and conduct "virtual flight testing" whereby the pilot "flies" the aircraft and weapon system.

This requires a broad based fundamental understanding of hypersonic aerothermodynamics and its effects upon integrated vehicle system components operation

and performance. Examples are, the propulsion system, external configuration, flight controls for non-rigid body motion and, internal bay stores release.

There are four broad areas where fundamental knowledge is needed and numerical simulation is currently lacking in fundamental scientific capability. They are (1) Single/Multiple body 6-DOF maneuver dynamic motion hypersonic aerothermodynamic flows, (2) the spatial and temporal evolution of both boundary layer disturbances and turbulence structure in complex 3-D aerothermodynamic flows, (3) Vortex dynamics in the presence of ionized plasmas and finite rate chemical reactions and (4) Multidisciplinary simulation. I am actively sponsoring research within each of these critical areas at AFOSR. I will discuss the scientific barriers in each of these areas below.

4.1.1 Dynamic Motion
The simulation of hypersonic flight vehicle flows has historically been limited to steady state, cruise condition flows. Today, this is for the most part still the case. Flight vehicle system mission performance is evaluated from multiple, steady state cruise, trajectory point simulations. This is an inadequate representation. Actual trajectories include full six degree-of-freedom vehicle maneuver, both planned and unplanned. Trajectory history plays a critical role for hypersonic vehicles. The aerothermodynamic loads to the vehicle structure and heat sink loads to the sub-structure are dependent upon the dynamic trajectory history. The boundary layer transition history and the associated drag history are dependent upon the surface temperature history. The time constants of the motion also play an important role, interacting with the time constants of viscous and inviscid flow processes as well as rate chemistry effects. The effects of six degree of freedom vehicle acceleration on these flow properties must be determined.

Dynamic motion effects also play a critical role during weapons release, where multiple bodies are undergoing simultaneous, dynamic, high speed motion. All in very close proximity to

each other. Complex shock wave systems, shock boundary layer interactions, wake interactions and, flow separation interactions are evolving spatially as well as temporally. These play a critical role in the flight dynamics of each vehicle. The effects of ionized and finite rate chemically reacting flows on the flows inside weapons bay cavities are unknown. Of particular importance is the control vane effectiveness of weapons passing through separated flow regions and wake zones of the launch platform as well as other weapons' flow fields. The sensitivity of finite rate chemically reacting flows and ionized flows to flap induced boundary layer separation need to be determined.

4.1.2 Computational Grids
Viscous unstructured grids, which can dynamically auto-adapt to these flows are essential if the flows about maneuvering hypersonic flight vehicles are to be computed. Geometry conservation laws must be developed for the numerics. The adaption process will by highly complex for there are multiple, fully three dimensional, spatially and temporally varying flow processes which must be accounted for. Total pressure, enthalpy, entropy, chemical heat release, pressure, plasma density etc. Each, individually or in combination, can be the most important variable to adapt to at any given point in a trajectory. Developing adaption strategies to adapt to simultaneous, multiple time scale, evolving processes is indeed a major challenge.

4.1.5 Computer Architectures
An attendant, but critical issue is computers. Parallel processor architecture machines with advanced "smart" compilers and dynamic load balancing capabilities must be developed. The architectures must be designed specifically for aerodynamic applications. Present day parallel processors require users to "brute force" codes onto the computer. Full flight trajectory simulation will require machines much faster than current gigaflop and projected terraflop systems. In-core memory will have to be increased by many orders of magnitude. Smart compilers will have to constantly be repositioning data within memory in anticipation

of the next sequence of calculations that will be performed during code execution. These compilers must also track the repositioning of unstructured grid cells as automatic adaption strategies are implemented during code execution. Advanced graphical interrogation and display systems must be developed to allow real time visualization of the simulations.

4.2 Boundary Layer Transition

The second broad area of fundamental understanding and numerical simulation encompasses the aspects of viscous flows relating to boundary layer transition and turbulence structure evolution (spatial and temporal) and interaction with plasmas and finite rate chemical reactions. This is important from the perspective of vehicle drag and heat transfer as well as scramjet fuel-air mixing. Reynolds averaged Navier-Stokes (RANS) codes form the full basis of simulation tools presently being used for design. These codes are fundamentally unable to predict detailed effects of boundary layer disturbance growth or turbulence structure evolution (spatial and temporal). Considerable effort continues to be devoted to developing RANS based turbulence models which have absolutely no hope of capturing the combined effects of all the complex aerothermodynamic flow processes (inviscid, viscous, entropy swallowing, rate chemistry, plasma, etc.) which arise over maneuvering 3-D flight configuration geometries.

The process of boundary layer transition is complex and involves the simultaneous interaction of a wide frequency spectrum of disturbances. Single eigenmode (the least stable mode) simulations simply do not model the real processes. Single eigenmode simulations in the presence of ionized plasmas and/or finite rate chemical reactions are non-existent.

Parabolized stability equation (PSE), Large eddy simulation (LES) and, Direct numerical simulation (DNS) methodologies have been available for a long time. However, until very recently they were only used to generate solutions to simple flows such as flat plate boundary layers and channel flows. And the solutions were only used as databases for turbulence model development and evaluation. This is no longer the case as, through my sponsorship, PSE, LES and, DNS methods are now being used to predict aerodynamic component flows. Coupled PSE-DNS procedures are being developed to model the full processes of boundary layer transition. These technologies must be further developed to simulate the complex aerothermodynamic flows which arise over maneuvering flight vehicles. They must also be fully validated. (PSE, LES and DNS methodologies will be discussed further in the boundary layer transition section below.)

Now, some readers (hopefully its "some" rather than "most" or "all") are probably thinking along the following lines. LES and DNS for full configuration flows will never happen. It's "well known" that the required grid points for such simulations scale with Reynolds number and, for flight Reynolds numbers, the machines will "never" exist because it will take infinite memory and time to conduct such simulations. Under my research sponsorship, the state of the art of LES and DNS has dramatically improved. A 2-D NACA 4412 airfoil LES simulation at mach number of 0.2, 12 degree angle of attack, and chord Reynolds number of 1.64 million took just 250 CPU hours on a CM-5. A full 3-D turbulence DNS solution of the flow over a Joukowsky airfoil at zero angle of attack and a chord Reynolds number of 240,000 took only 12 CPU hours using one processor of a 16 processor Cray C-90. This would scale to 45 minutes using all sixteen processors. These statistics are very exciting and continued research will further reduce machine resource requirements well below these levels. At that point, these techniques will indeed be useful design tools.

Boundary layer transition is a critical aspect of hypersonic flight vehicle configuration design. The boundary layer state directly affects vehicle aerothermal heating, drag and, control. During flight, the vehicle flowfield is quite complicated. Complex shock wave systems, entropy

swallowing effects, multiple free stream disturbances, axial & crossflow pressure gradients, exo- and endo-thermic finite rate chemical reactions, high enthalpy conditions and, plasmas coexist. The mechanisms by which the boundary layer responds (amplification or suppression) to disturbances generated under these complex conditions are not understood. The response of the boundary layer to multiple disturbance modes under these conditions cannot be predicted. The unsteady transition mechanisms present while the vehicle dynamically maneuvers are even more complex and less understood. The challenge is to develop an understanding of the unsteady transition processes and mechanisms under these combined conditions and develop numerical simulation procedures to accurately model them..

Typical transition simulations are based on the selection and evaluation of the amplification/suppression properties of the single, least stable Orr-Sommerfeld eigenvalue. Actual flows involve the simultaneous interaction of all eigenmodes and their combined effect on the transition process. Complex multiple wave mode interactions are generated from these multiple forcing functions. Experiments must be conducted to reveal the fundamental character of the transition processes. Simulation methods to model transition from multiple eigenmode interactions, including the full effects of rate chemistry, must be developed.

Under maneuvering flight conditions the boundary layer free stream conditions are varying in time. These temporal effects must be included in the evaluation of the Orr-Sommerfeld eigenvalues. For, temporally varying free stream conditions generate temporally varying boundary layer profiles which, in turn, result in temporally varying eigenvalues.

Current state-of-the-art RANS based simulations are fundamentally unable to predict the above mentioned effects on transition as these methods cannot predict turbulence structure effects. Only

Parabolized Stability Equations (PSE) coupled with Direct Numerical Simulation (DNS) simulations of these flows can, in principal, accomplish this. I use the term "in principal" because though these methods can predict turbulence structure effects and evolution, no such code has yet been fully developed and validated. Coupled PSE/DNS methods must be developed and exploited.

4.3 Hypersonic Vortex Dynamics
Very little attention has been paid to hypersonic vehicle maneuverability or agility. It has been assumed that hypersonic flight vehicles will be restricted to global transport missions in which the vehicle will fly fast and in a straight line. Nothing could be farther from reality. Operational missions will require hypersonic platforms to be both maneuverable and, particularly for missile applications, highly agile.

During maneuver, hypersonic vehicles will generate vortices from the vehicle forebody as well as wing leading edges and tail surfaces. These vortices will develop under high enthalpy, variable entropy, non-equilibrium chemically reacting, transitional boundary layer state viscous conditions. The mechanisms by which vorticity is created within boundary layers under these conditions is not understood. Further, the processes by which vorticity is convected to the outer edge of the boundary layer and disgorged into the free stream are unknown. Additionally, dense plasmas are likely to be present. The mechanisms of vorticity generation, convection and, impingement under these conditions are not understood.

Maneuvering missiles experience asymmetric vortex shedding. This asymmetric shedding induces side forces which affect the trajectory. The effects of high enthalpy and rate chemistry conditions on the asymmetric vortex shedding processes are unknown. They must be understood to design autopilots which can provide stable control of these systems.

At present vortex dynamics characteristics (vorticity generation, separation, convection,

coalescence and, impingement) cannot be evaluated by numerical simulation as current algorithms are far too dissipative in fundamental nature. New non-dissipative algorithms must be developed and utilized to predict the unsteady aerodynamics characteristics of maneuvering hypersonic flight vehicles. The processes of laminar to turbulent transition inside convecting vortices and their interaction with ionized flows in the presence of both exothermic and endothermic finite rate chemistry reactions must be determined.

4.4 Multidisciplinary Simulation

The third broad area of numerical analysis is multidisciplinary simulation. A flight vehicle is comprised of many, inter-related sub-systems. Changes in one affect all the others. For example, sudden changes in vehicle attitude or in propulsion system performance can induce inlet unstarts which alter the vehicle flow field and controllability. Dynamic vehicle maneuver causes aerothermo-structural deformation. This, in turn, changes the boundary layer transition and separation locations, control surface deflection effectiveness, vortex dynamics patterns and, propulsion system flow and performance. Additional examples include propulsion-airframe interaction effects (vortex ingestion, inlet bow shock wave ingestion, etc.) and the effects of control surface deflection and interaction with variable transition state boundary layers.

The present state-of-the-art of numerical simulation of configuration flows is not able to predict these multi-disciplinary system flows or their effects on vehicle performance. Most simulations are single discipline, being done primarily to obtain the pressure and heat transfer distributions over rigid body aerodynamic configurations without active propulsion or control. Scramjet propulsion systems are analyzed as independent, stand-alone, components. Simulations must include active sub-systems and their response i.e. propulsion, control surfaces, aerothermo-structural response, fatigue, navigation, etc.

4.4.1 Aerothermo-Structure Effects

Hypersonic flight vehicles experience sustained levels of very high thermal and pressure loading during flight. These effects can lead to structural failure during flight in many ways. High localized heating via inlet cowl shock - vehicle bow shock interactions for example, can cause the surface material to melt exposing the internal structure. Further internal material melting can lead to catastrophic failure. Sustained aerothermal loading affects the strength properties of monolithic materials as well as composite materials.

During maneuver the vehicle structure will deform under the induced flight loads. Repetitive, sustained deformation can lead to fatigue failure of structural components during flight. There are two aspects of material response namely, structural failure and, structural fatigue. The first is a macroscopic event initiated at the atomic level while the second is a microscopic event initiated at the atomic level. The fundamental processes associated with these phenomena are not known or predictable.

Structural failure cannot at present be predicted under dynamic flight conditions. This is true for monolithic materials as well as composites. The structure can respond in many ways under flight loading. Examples are, atomic structure alteration, molecular bond weakening, crack initiation, crack growth, laminate de-bonding through melting or laminate failure and, composite fiber failure. Cracks can initiate at the microscopic or macroscopic level in both monolithic material as well as composite materials. The mechanisms by which cracks initiate are not known. Further, the fundamental processes governing crack growth velocity and propagation direction are not known. These structural response mechanisms are fully unpredictable at present.

The second type of structural response is fatigue. A material may be in a state of structural fatigue well before it actually fails. How can structural fatigue be quantified? It is dependent on the

loading history as well as the loading. Repetitive or sustained loading can cause material fatigue. Materials can experience loads beyond their predicted yield strength and survive. If they do they will be structurally weakened or fatigued. The material may fail at a point well below its predicted yield point under further loading. The actual point at which this failure occurs cannot be predicted. Macroscopic loads affect the material at atomic levels, permanently weakening the material. These microscopic effects cannot be predicted.

4.4.2 Scramjet Systems

Historically, scramjet system flows have been treated as independent component flows, i.e. inlet, combustors and, nozzles. No attention was paid to these components as a single, integrated system. Scramjets are coupled inlet-shock isolator-combustor-nozzle systems which are interdependent and interrelated. Combustor instabilities and transients generate disturbances which affect the inlet shock wave system. The interaction and propagation mechanisms of complex combustion instabilities and transients with inlet-shock isolator flows are unknown. These transients can also cause the inlet to unstart. Variations in nozzle back pressure affects the inlet flow. Disturbances from the forebody flow will alter the inlet shock system and total pressure losses, and the entire engine flow field including the thrust. Forebody shock wave or vortex ingestion can unstart the inlet, shutting down the engine. Add to this the unsteady effects which are generated during dynamic, three axis vehicle maneuver, and engine throttling and the flowfield complexity increases dramatically. The most important scientific challenge is to understand the coupled aerothermodynamics of the entire propulsion system under these conditions.

For multiple bank inlet systems the unstart of any one cell can lead to the auto-induced unstart of all the neighbors. The interactions of unstarted flows being ingested by neighboring cells must be understood.

For a missile configuration with separate, multiple inlets an unstart can cause an unrecoverable, violent yaw/pitch motion.

Under certain conditions during maneuver, inlet systems can ingest forebody shock waves and/or vortices. This can generate complex sidewall shock boundary layer interactions as well as bow shock-compression surface shock system interactions. Shock wave induced boundary layer separation characteristics under non-equilibrium chemistry and/or plasma conditions are not known. Indeed, the characteristics of shock waves in ionized plasmas are unknown. Ingested vortex systems generated from the vehicle forebody further increase both the inlet flow complexity and total pressure losses.

Propulsion systems for piloted vehicles are likely to be combined cycle systems. These offer the flexibility of taking off from a runway as a normal aircraft while changing to scramjet operation during flight. The complex, unsteady viscous flows generated internally during mode transition are not understood.

It has been clearly demonstrated for a long time that traditional strut based fuel injection concepts do not provide adequate fuel-air mixing. Convective mach number effects only make things worse. Radically new fuel injection and mixing enhancement concepts are required and must be developed. Forebody fuel injection or inlet surface injection offer potential possibilities. Radically new scramjet propulsion system concepts must be developed. Current systems are only capable of providing marginal net thrust. The implementation of magneto-hydrodynamic (MHD) based systems may lead to an operational system.

4.4.3 Flight Dynamics Control Systems

The linear and non-linear flight dynamics of full, 6-degree of freedom hypersonic maneuver must be understood. Vehicles operating at hypersonic flight conditions are flying far too fast for human based flight control to be effective or practical. Artificial intelligence based flight control systems must be developed. These systems must

be able to control single flight vehicle motion as well as multiple vehicle motion during weapons/payload release.

5.EXPERIMENTAL FACILITIES:

I have deliberately delayed discussing the topic of experimental facilities until this point. While I believe that experimental facilities are very important, I also believe that in the current climate of decreased budgets a long duration run time high enthalpy, hypersonic facility is simply not viable.

We can however develop quiet tunnels to investigate the full processes of boundary layer transition over three dimensional geometries. Major investments must be made into developing non-intrusive diagnostics, such as Rayleigh scattering, which can operate in high enthalpy as well as plasma conditions.

Non-intrusive diagnostics is a critical area of research. The non-intrusive interrogation of high enthalpy and high Reynolds number flows which arise in shock tunnels is critical for the acquisition of fundamental scientific knowledge pertaining to aerothermodynamic flows. Further, experimental data must be used to validate numerical simulations.

6.CONCLUSIONS

I have discussed many challenges which pertain to hypersonic flight vehicle system design. The scientific issues are exciting and plentiful. As new scientific based aerothermodynamics knowledge is obtained it is quite likely that many more questions will be raised as new scientific issues are discovered. That is the nature of science for, the more that is learned, the more that needs to be understood.

My personal goal is to develop multidisciplinary simulation technologies which can be used to fly hypersonic flight vehicles on computers. The pilot would sit at a console station and literally fly the vehicle on the computer. Today this probably sounds too far fetched to be taken seriously. However, skeptics please take note.

Today's technology was though to be unattainable only twenty years ago.

LIGHTWEIGHT MATERIALS FOR ENGINES AND STRUCTURES

B.CAPDEPUY & P.PERES
AEROSPATIALE ESPACE ET DEFENSE BRANCH
33160 ST MEDARD EN JALLES FRANCE

Abstract

Hypersonic flight constitutes for materials developpers a big challenge considering the requirements they have to be compliant with . The mastering of this key technology is necessary to design hypersonic vehicle as they are needed to realize the thermal protection system as well as some parts of engines .The requirements can be identified ranking in three categories which are technical, industrial feasibility and producing costs . These three topics will be discussed in this paper .
For the thermal protection system of reentry vehicles, carbon/carbon composites protected against oxydation as well as carbon/silicon carbide composites have already demonstrate they are good candidates to sustain high thermomechanical loads . But in order to be compliant with development costs of future system an effort has to be performed in simplified designs .
For future engines as scramjet requirements are much more severe but a first demonstration of applicability of such materials has been performed on an injection strut . Nevertheless the demonstration of behaviour of the coatings to combustion ambiances has yet to be demonstrated for long term and reusable applications.

1- Introduction .

For future hypersonic vehicles, the need of high temperature materials is a fundamental requirement . Furthermore these materials have to be as lighter as possible, because the use of refractory metals is not possible as they would give to high mass budget . So the high temperature composites, thanks to their good specific mechanical properties, appear to be adapted to fullfill specifications .

2-General technical requirements .

From a technical point of view the main concern is related to material behaviour in an oxydative/corrosive environment at high temperature . Mission analysis conducts to following typical requirements :
Structures and engines parts will be heated during launch and reentry phases after beeing submitted to launch pad environment (humidity, thunder,...) and to orbital environment (thermal cycling from -100°C to +100°C in vacuum, micrometeorites and debris, atomic

oxygen,....) . In this paper we will consider only the high temperature phases .
For current zones of spaceplane the material will be heated to maximum temperature of 1250°K during ascent phase and of 1600°K for reentry and for both in reduced pressure air . The maximum calculated temperature is for the nose cap zone : around 2000°K . The foreseen number of flights is 100 . These typical specifications are close to those wich have been identified for reusable spaceplanes .
In case of engines, ramjet type, the specifications have established for the different parts and they are resumed in the following table 1 .

part	P (bar)	T°K	atmosphere
air intake	0.1 to 0.3	1600	air
injection strut	1 to 6	1600	air
combustion chamber wall	6	2800	H2O, N2, H2
exit cone	6	2800	H2O, N2, H2

Table 1 : engine specifications

A first analysis conducts to two types of requirements :
- behaviour at high temperature in combustion gases environment
- necessity to cool some parts

This gives for materials following specifications resumed table 2 .

part	material specification
air intake	high mechanical properties, high thermal conductivity, high emissivity
injection strut	high conductivity, thin skin
combustion chamber wall	resistance to combustion products, cooled stucture
exit cone	resistance to combustion products, cooled stucture

Table 2 : engine material specifications

3- High temperature composites state of the art

Among the composites able to meet main requirements, it can be assumed that carbon/carbon composites

protected against oxydation as well as carbon/SiC composites are able to sustain thermomechanical loads induced by thermal fluxes in oxydative environment . These materials which have been developped in order to sustain reentry type missions have demonstrated that their have good mechanical behaviour up 2000°K and more for carbon/carbon composites .

Examples of typical data of carbon/carbon composites are summerized in following tables for two types of fiber architecture : so called 3Devo which is a tridirectionnal fiber preform able to be realized in complex shapes and 2.5D which is an interlock fabric) well suited to be used for manufacturing of relatively simple parts taking advantage of its high shaping capability (see figure 1.
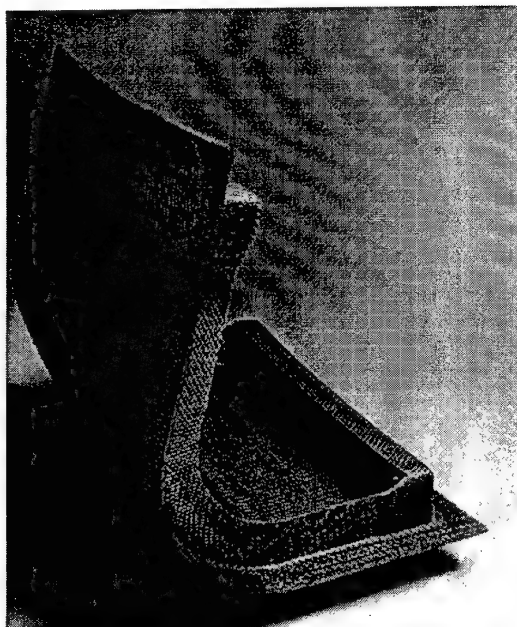
Figure 1 - 2.5D wing leading edge

property	value	
density	1.55	
tensile stress MPa	RT	110
	1500°C	130
tensile modulus GPa	RT	67
	1500°C	67
compression stress MPa	RT	180
	1500°C	290
compression modulus GPa	RT	60
	1500°C	67
interlaminar shear stress MPa	RT	10
	1500°C	22
coefficient of thermal expansion $10^{-6}°K^{-1}$	RT	1.6
	1500°C	1.6
thermal conductivity $wm^{-1}°K^{-1}$	RT	17
	1500°C	34

Table 1 : 3 D C/C Properties

property	value	
density	1.55	
tensile stress MPa	110	
tensile modulus GPa	120	
compression stress MPa	120	
compression modulus GPa	120	
interlaminar shear stress MPa	10	
coefficient of thermal expansion $10^{-6}°K^{-1}$	1.6	
thermal conductivity $wm^{-1}°K^{-1}$	RT	17
	1200°C	24

Table 2 : 2.5 D C/C properties

These materials show excellent mechanical properties up 2000°K, low density and low coefficient of thermal expansion, that last point being very interesting because it minimizes thermomechanical stresses . They have demonstrate too good resistance to thermal shock and thermomechanical fatigue .

The major problem generally encountered is their limited resitance in oxidative and corrosive environment ; currently the coatings have been developped for reentry missions as Hermes spaceplane where the maximum temperatures were 1850°K and the constraints of reusability are 40 missions .

These antioxydation coatings are mainly based on silicon carbide which have a good behaviour at such temperature range but as thermal mismatch between SiC and C/C induces microcracks in this layer, a sealing is performed thanks to glass impregnation with a sol-gel process . The silicon carbide is composed of two layers, the first is a compliant one obtained by pack cementation with the objective to avoid spallation and the second one is obtained by CVD in order to provide reliable protection for long term periods and for temperature up to 2000°K . depending on operating pressures .

These coatings give a good antioxydation efficiency which has been tested :

- in a radiant test facility able to simulate thermal conditions and atmosphere composition (atomic oxygen) : ONERA BLOX
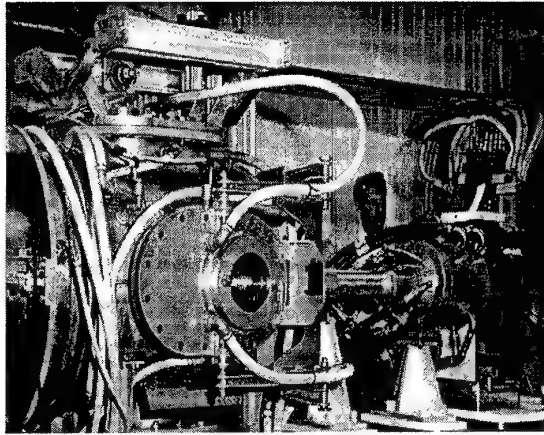- and in a convective plasma jet : AEROSPATIALE SIMOUN . (see figure 2)

Figure 2 - SIMOUN facility

Some results are given in following tables 3 and 4 which demonstrate these good performances . These mass loss rates have been measured until 40 cycles and are constant , each one lasts 20 mn at temperature plateau .

T°C	Pressure (mbar)	weight loss (%/cycle)
800	10	0.015
1000	10	0.015
1450	10	0.015
1600	10	0.025

Table 3 : BLOX oxydation results

T°C	Pressure (mbar)	weight loss (%/cycle)
1300	75	0.015
1500	75	0.020

Table 4 : SIMOUN oxidation results

Nevertheless the behaviour in real engine environment and particularly corrosive ambiances as water vapour, oxidation products of combustion,..... is not well known and has to be performed .

An other important point is to design parts taking into account mission specifications but also feasibility and costs because it has to be underlined that technical choice have to be made having in mind to use the most simplest and cheapest manufacturing processes .

For these materials a lot of processes have been developped for fiber preform manufacturing as well as for densification operations : their advantages and drawbacks are well known, so the choice can be performed taking into account all the aspects as performances, parts design and parts dimensions .

Concerning the fiber architecture the use of multidirectionnal preforms will be preferred as they allows to take advantage of their undelaminable behaviour during manufacturing phases as well operationnal ones . This increases reliability of the parts and so decreases the overall costs .

For densification processes the main used are CVI, liquid route or a mixture of both, their advantages and drawbacks can be summerized in the following table .

Process	advantages	drawbacks
liquid route	- simple process - simple toolings - no thickness limitations - easy to process furnaces	- long process : 5 times for C/C [impregnation, polymerisation, pyrolysis] - high number of handlings
CVI route	- very good properties	- thickness limitations - need of costly toolings - need of specific furnaces
mixed route	- good properties - simple toolings - short process cycle	- thickness limitations - need of specific furnaces

Table 3 - Comparison of densification processes

So it cannot be asserted which process is the best choice, it will depend of numerous factors as shape of parts, thickness, overall dimensions and number and rate of production ; however it can be stated that even if liquid route appears to be the more easy process, the mixed way could be very well appropriate for thin and numerous parts as could be a thermal protection system of a future reusable launcher or an hypersonic plane .

4- Examples of application

The two application domaines are thermal protection system and engine parts . Concerning the first one, a lot of work has been done and in-flight data are available but some thoughts about design can be given ; related to engine parts this subject is quite new, nevertheless first application results are very promising .

• **Nose cone**

Concerning the thermal protection system and in particular one of the hotest part which is the nose cone, if the research of a very optimised design with thin skin and numerous stiffeners is not a stringent requirement due to reduced mass objective (see Hermes example figure 2), a simple shape with constant thickness and flanges for attachment can be proposed (see figure 3) .

Material choice will be performed between carbon/carbon and carbon/SiC taking into account precise environment and interface requirements .

Then the manufacturing process could use multidirectionnal type fiber preform wich has already demonstrated for other applications that it is the most reliable one for manufacturing phases as well as operationnal ones (no delamination risks) : this allows to use interlock 2.5D fabric with stitched ribs .
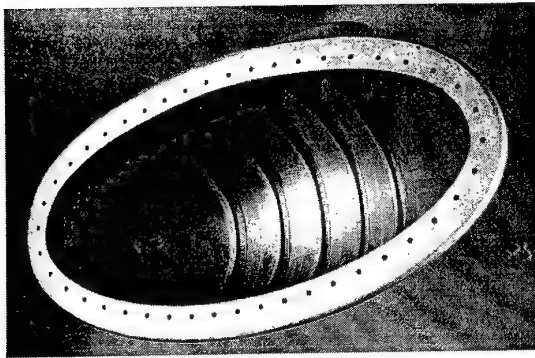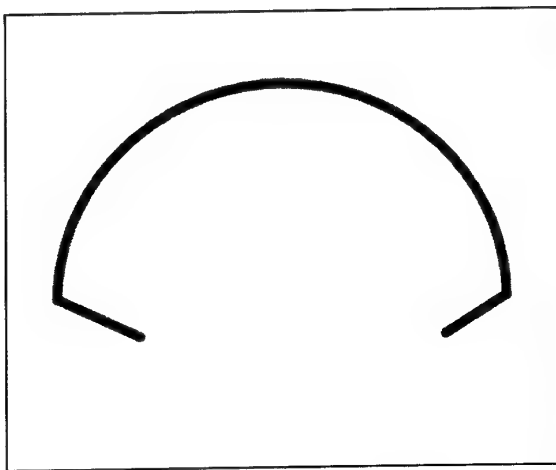
Figure 2 - Optimised design of Hermes nose cone.

Figure 3 - Simplified design for nose cone

- aerodynamuic loads due to the heterogeneity of the flowfield, (pressure difference between the two faces of the strut).

Carbon/carbon composites taking advantages of good mechanical properties and high thermal conductivity are a good candidate for such a part . In order to sustain oxidative environment carbon/carbon composites are protected against oxydation with a SiC based coating .

First design and model manufacturing have been realized . This original design consists in assembling two parts of carbon/carbon composite materials, as shown in figure 4 a structural 3D reinforced C/C composite is covered by a thin and stiff skin of C/C materials .

Figure 4 : body and skin of the St Elme strut

The shape dimensions of the first protype are sum up in table 5 .

total lenght (mm)	central thickness (mm)	central depth (mm)	leading edge radius (mm)	half diedral angle (degre)	skin thickness (mm)
330	21	100	1.7	6	1.4

Table 5 : St Elme strut dimensions

For the body the choice of a very fine weave 3D fibrous architecture allows to withstand the high hydrogen pressure and the aerodynamic one ; it is also well suited to realize the machining of integrated cooling channels . The densification process choice, pitch carbon matrix, has been performed in order to achieve a high conductivity which is required to obtain an efficient cooling .

As the drag induced by the strut has to be hold as low as possible, the design induces a slim wing with a small leading edge radius . This obtained through the

• **scramjet injection strut**

In scramjet engines application the injection strut has to feed all the combustor duct with hydrogen . These struts complete the air intake compression, help the ignition if necessary, stabilize the combustion and enhance the mixing . More precisely their main functions are :
- to fulfill the whole duct with fuel,
- to enhance the mixing
- to stabilize the combustion if necessary
- to complete the compression of the air intake .
- to provide an isolation between air intake and combustor in case of thermal blockage low Mach operation,
- to participate to the structural integrity of the engine

In the frame of internal R&D at AEROSPATIALE a project "SAINT ELME" has been performed and consists in design, manufacturing and qualification of a high performance scramjet injection strut .

The struts have to operate at least during all the airbreathing trajectory (from Mach 6 up to Mach 12) and must withstand both :
- thermal conditions of Mach 12 flight conditions

manufacturing of the skin with a 2.5D fibrous architecture which is compliant with the above requirements . The densification process is the same that for the body . Therefore thermal expansion and thermal conductivity are compatible with the body .

The efficiency of the protestion against oxydation has been checked on a test model (see figure 5), the results have been positive .
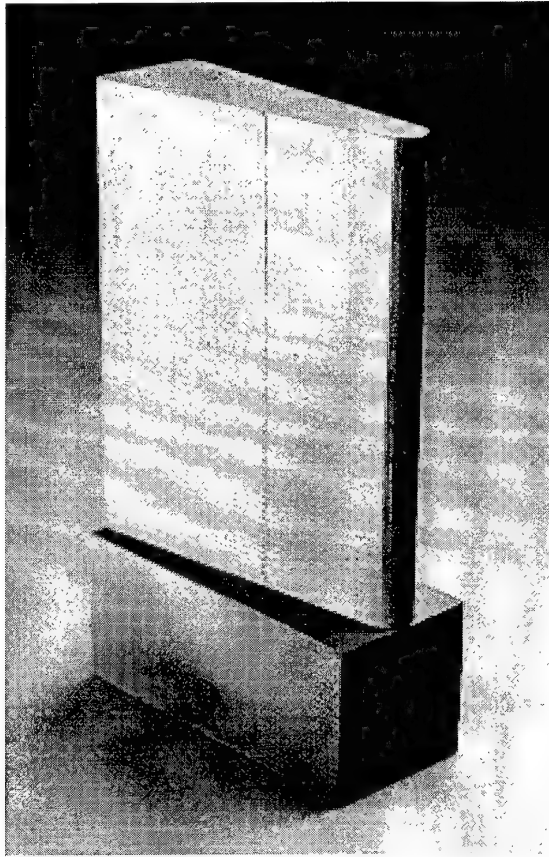

Figure 5 - test model use for validation .

Furthermore the body and the skin are assembled through an adhesive bonding which is a carbon based joint .

This design allows to have a strut half lighter than the metallic one .

Mechanical and thermal models have beeen realized with Mach 12 conditions and they demonstrate that :

- the maximum surface temperature does'not exceed the SiC allowable surface if impingement heat transfert with high presurized hydrogen flow is used .

- the maximum stresses due to the internal pressure which are preponderant especially nearby the joint do not exceed the experimental values . The assessed margin of safety is equal to 2 .

The first experiment which has been conducted successfully in CHAMOIS scramjet hypersonic test bench to demonstrate the ability of this concept to support the aerodynamic loads which are generated by the combustion process during the transient phases before reaching Mach 6 conditions . A second test is foreseen in more representative operating conditions .

5- Conclusions .

As a conclusion it can be stated that for hypersonic applications, high temperature composite materials and associated processes have a good level of development which make them very adapted to fulfill main requirements thermal protection systems. Nevertheless the design has to be performed taking into account the need of simplification manufacturing process in order to lower the costs .

Related to engines the problems are more difficult to solve and the behaviour of high temperature composites in combustion ambiance has to be assessed and solutions to manufacture cooled structure can be designed either by machining either by in process solutions .

References :

(1) O.Franc, J.L.Macret
Oxidation resistant carbon/carbon materials ESA SP303 june 1990

(2) P.Peres
C/C composite materials for Hermes'sTPS . A review of the thermomechanical characteristics of 3 Devo C/C . ESA june 21/24 1994 Paris.

(3) Marc Bouchez, Emmanuel Saunier, Patrick Peres, J.Lansalot
Advanced carbon/carbon injection strut for actual scramjet . AIAA-96-4567-CP Norfolk USA november 16/22 1996

MULTIDISCIPLINARY OPTIMIZATION METHODS
FOR PRELIMINARY DESIGN

J. J. Korte, R. P. Weston, and T. A. Zang
Multidisciplinary Optimization Branch, MS 159
NASA Langley Research Center
Hampton, VA 23681-0001 USA

SUMMARY

An overview of multidisciplinary optimization (MDO) methodology and two applications of this methodology to the preliminary design phase are presented. These applications are being undertaken to improve, develop, validate and demonstrate MDO methods. Each is presented to illustrate different aspects of this methodology. The first application is an MDO preliminary design problem for defining the geometry and structure of an aerospike nozzle of a linear aerospike rocket engine. The second application demonstrates the use of the Framework for Interdisciplinary Design Optimization (FIDO), which is a computational environment system, by solving a preliminary design problem for a High-Speed Civil Transport (HSCT). The two sample problems illustrate the advantages to performing preliminary design with an MDO process.

1.0 INTRODUCTION

Multidisciplinary optimization (MDO) methods and preliminary design are terms for processes that can have different interpretations for both engineers and designers, depending on the background and area of expertise of the individual. This paper addresses preliminary design from an aerospace point of view. The paper is organized as follows. First, definitions are given for the different levels of aerospace design that are discussed in this paper. A discussion of MDO and its conceptual elements follows, and then MDO requirements for preliminary design are presented. Finally, two applications of MDO methodology are illustrated for use in the preliminary design stage.

In this report, the aerospace design process is broken down into three major levels: conceptual design, preliminary design, and detailed design. The detailed design level involves designing for manufacturing and assembly and is beyond the scope of this paper. A short description of the conceptual and preliminary design level follows.

Conceptual design involves the exploration of alternate concepts for satisfying vehicle design requirements. Trade studies between vehicle designs are made with system synthesis tools, which encompass a broad range of disciplines (Fig. 1). Typical system synthesis tools contain extremely simple vehicle geometry descriptions and have shallow and uneven levels of analyses within the disciplines. Typical figures of merit for evaluating the relative importance of design parameters on the conceptual vehicle design are system performance and system cost.
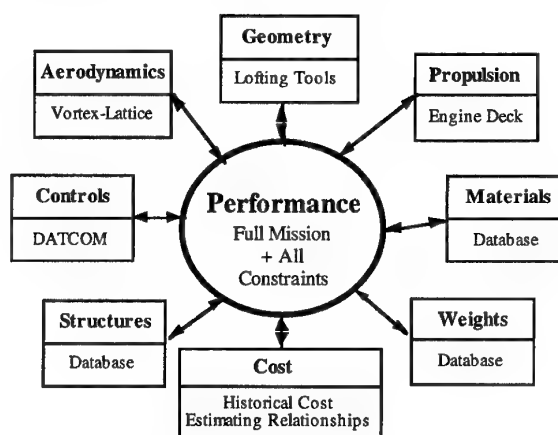
Fig. 1. Sample conceptual design disciplines and tools.

Numerous examples of conceptual design systems or methods can be found that have been used by companies and government organizations. Many companies have their own conceptual design system and processes, which contain proprietary data for the predicted cost and performance of a product. An example of a conceptual design method for aerospace vehicles is the Flight Optimization System (FLOPS).[1] For the conceptual design of hypersonic vehicles with airbreathing engines, two examples of methods under development are Holist[2,3] and PrADO-Hy.[4]

After a vehicle design concept is selected, the design and analysis process evolves from the vehicle concept toward the actual components and subsystems of the vehicle. Specialists become involved in the design and analysis of the different subsystems. Each specialist uses increased detail in their discipline, which results in a more limited interaction with other disciplines. The geometry is described in enough detail to define the subsystem but not enough to specify each assembly. Sophisticated discipline analyses, along with design by analysis or limited optimization, are often used. Typical figures of merit for preliminary design are subsystem performance, size, weight, and cost (Fig. 2).
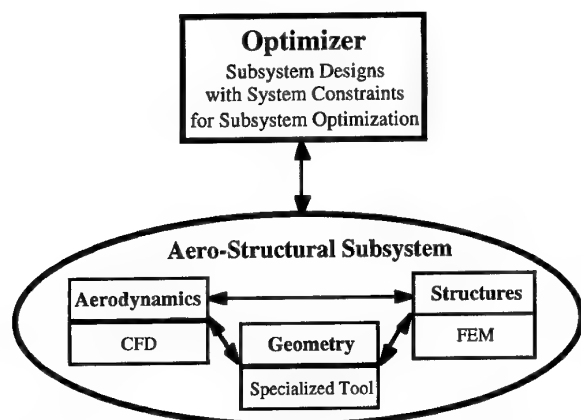
Fig. 2. Preliminary design using an optimization process.

2.0 MDO CONCEPTUAL ELEMENTS

The MDO methodology coherently exploits the synergism of mutually interacting phenomena to improve the designs of complex engineering systems. This process can be used at any stage of a design (i.e., conceptual, preliminary, or detailed design). Typical objectives consist of one or more of the following: improving performance, lowering cost, or shortening the development time for products. The current state of the art in MDO was reviewed in an AIAA white paper[5] in 1991, 1995 ICASE and NASA Langley Workshop,[6] and by Sobieszczanski-Sobieski and Haftka.[7] Additional information containing recent developments can be found in the 6th symposium on Multidisciplinary Analysis and Optimization sponsored by AIAA, NASA and ISSMO.[8]

The MDO methodology is much broader than multidisciplinary analysis and involves various design-improvement strategies, including formal optimization. Notionally,

$$\Delta_{Design} = (\sum_i \Delta_{Discipline\ i}) + \Delta_{MDO} \qquad (1)$$

where the sum on the right-hand side refers to contribution from individual disciplines and the "Δ_{MDO}" includes the contributions from the integration of the disciplines. Table 1, which is based on the discussion by Sobieszczanski-Sobieski,[9] is a "taxonomy" of the MDO discipline. A brief description of each element in the table is given, column by column.

Table 1. MDO Conceptual Elements

Information science and technology	Design-oriented multidisciplinary analysis	MDO
• Product data models • Data and software standards • Data management storage and visualization • Software engineering practices • Human interface	• Mathematical modeling • Cost versus accuracy trade-off • Smart reanalysis • Approximations • Sensitivity analysis	• Discipline optimization • Decomposition • Design space search • Optimization procedures

2.1 Information Science and Technology

The general category of information science and technology refers to the information infrastructure that enables MDO; many of the new developments have originated in computer science technology advancements. A prerequisite for even multidisciplinary analysis is the availability of common **Product Data Models**, which are the basis for the geometry and discretization models that are consistent across disciplines. Application of optimization requires that the basic model description be parametric. An elementary example of a parametric surface geometry model that is implemented in a commercial computer-aided design (CAD) system is shown in Fig. 3.[10] This particular model is for a High-Speed Civil Transport (HSCT) and is representative of a capability that is being developed to integrate a parametric CAD system into the preliminary design example covered later in section 4.2.
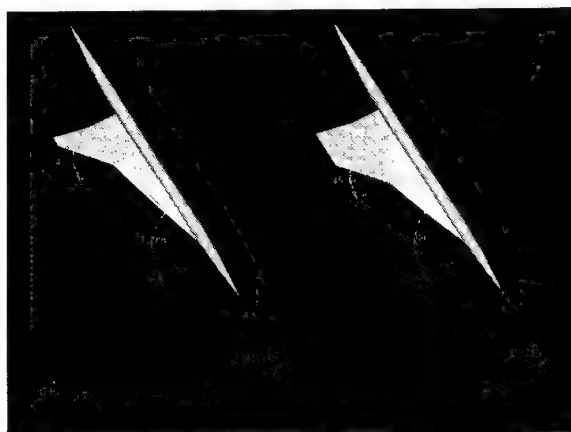

Fig. 3. Sample of CAD parametric geometry model.

Data and Software Standards are necessary for software creation, validation, and documentation, as well as for the definition and archival of data in order to facilitate the use, reuse, and efficient integration of the product software in multidisciplinary systems. **Data Management Storage and Visualization** refers to tools for collecting, storing, managing, visualizing,

and documenting data generated in a multidisciplinary analysis or design process. **Software Engineering Practices** are methods for producing, operating, maintaining, and documenting robust software for multidisciplinary applications. The **Human Interface** element is perhaps the most challenging element. Tools are needed to facilitate integration of disciplinary software in multidisciplinary processes; to direct, redirect, and monitor process execution; and, in general, to maximize the potential for human direction of the process.

2.2 Design-Oriented Multidisciplinary Analysis

The adjective *design-oriented* refers to those additional features that must be present in analysis tools if they are to be truly useful in supporting the design process and not merely in producing isolated analyses. The salient issues involve both capability and efficiency, and the MDO developments comprise basic mathematical and algorithmic advances in analysis capability. **Mathematical Modeling** may be required to enable the incorporation of new disciplines into the MDO setting; these models must be able to predict system disciplinary response and measure the impact of changes in other disciplines on disciplinary response. **Cost Versus Accuracy Trade-Off** methods enable trade-offs to be made between computational cost and computational accuracy as necessary. **Smart Reanalysis** refers to efficient reanalysis techniques that minimize the computations required in simulating a system with perturbed input parameters. **Approximations** are generic tools for reliably approximating system disciplinary or multidisciplinary response by using zero- and, potentially, higher order system information.[11] **Sensitivity Analysis** must be supplied via efficient numerical tools that predict the effect that changes in input parameters have on disciplinary and system responses.[12] Recent work on the application of automatic differentiation technology to Navier-Stokes codes to extract efficient gradients (sensitivities) with respect to design variables is compared to the conventional finite difference approach in Fig. 4.[13]

High Speed Civil Transport
Mach Number = 2.4, α = 1°

Wing Planform
Design Variables
(DV)

Aerodynamic Coefficients

CL	Lift
CD	Drag
CY	Side Force
CMY	Pitching Moment

Sensitivity Derivatives - Derivatives of Aerodynamic Coefficients
With Respect to Wing Planform Variables

$$\frac{\partial CL}{\partial DV} \quad \frac{\partial CD}{\partial DV} \quad \frac{\partial CY}{\partial DV} \quad \frac{\partial CMy}{\partial DV}$$

Time to Compute Sensitivity Derivatives (for 4 digits of Accuracy)
Automatic Differentiation (Residual reduced 4 orders) = 10.75 units
Finite Difference Method (Residual reduced 11 orders) = 15.00 units

Fig. 4. Sensitivity analysis with automatic differentiation of Navier-Stokes flow code.

2.3 MDO

The distinguishing characteristic of the MDO tools in Table 1 is the use of formal optimization methods to achieve design improvement. **Discipline Optimization** is related to MDO insofar as it uses pathfinding developments of optimization in selected disciplines that eventually target the multidisciplinary application. **Decomposition** methods examine the decomposition of complex processes to identify the best sequence of subprocesses for numerical and computational efficiency and to track the effect that changes in the input to one subprocess have on the output of other subprocesses. One multilevel optimization method that exploits disciplinary optimization techniques in a multidisciplinary setting is illustrated in Fig. 5. Braun[14] has demonstrated collaborative optimization for launch vehicle design.

Collaborative Optimization (Coordinates Subproblems)

Information Flow

Aerodynamics Optimization Subproblem · · · **Structures Optimization Subproblem** **Other Discipline Optimization Subproblem**
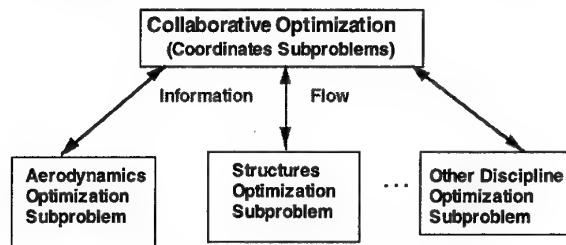
Fig. 5. Decomposition with the collaborative optimization approach.

Design Space Search algorithms facilitate exploration of large design spaces, including those that may be characterized by discrete variables, discontinuous functions, or disjoint subspaces. **Optimization Procedures** in this context refer to optimization algorithms in multidisciplinary procedures that efficiently generate improved designs for multidisciplinary systems. Typical procedures may combine search algorithms, decomposition methods, and approximations. For example, the direct method approach to optimization combines expensive analyses and sensitivity analyses for every step of the optimization algorithm. This contrasts with the indirect method, in which the optimization method is instead coupled with a local approximation which can be based on zero- and first-order information (Fig. 6). The latter approach is far more common in current MDO applications. The indirect method typically requires more optimization cycles to converge than the direct method but is often more efficient because each optimization cycle is less expensive.
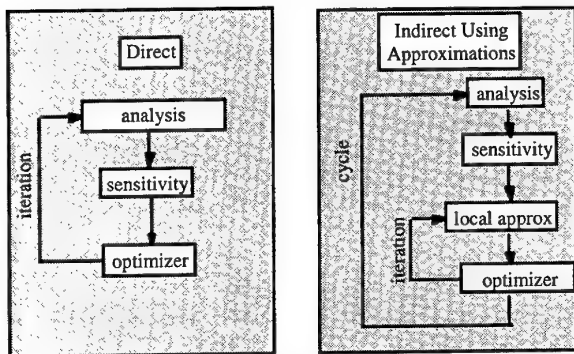
Fig. 6. Comparison of direct and indirect optimization procedures.

3.0 MDO REQUIREMENTS FOR PRELIMINARY DESIGN

The introduction of MDO at the preliminary design stage requires an appropriate information infrastructure, design-oriented multidisciplinary analysis tools, and efficient, robust MDO strategies.

The information infrastructure should provide adequate computer horsepower for the increased computational demands; a common geometry model; a collaborative work environment; an effective means of integrating analysis tools into the overall framework; management of distributed computing; the ability to handle proprietary codes and legacy codes; effective tools for presenting the results; and configuration control.

At the preliminary design level, physics-based methods have generally replaced historical databases in discipline analyses. Typically, a physics-based discipline analysis requires a suite of tools, including pre-processors (e.g., geometry modeller, grid generator, translators for input data needed from other disciplines), an analysis code, and postprocessors (e.g., visualization, translators for output data needed by other disciplines). In an MDO environment, the typical discipline output needs to be supplemented with sensitivity information, and this process needs to be automated. Well-posed interfaces are required between disciplines. This requirement may necessitate more than straightforward interpolation between, for example, aerodynamic surface pressures and structural loads and, in the reverse direction, between structural displacements and surface geometry. The transformations must respect physical principles, and the entire cycle must be consistent.

The basis for any MDO strategy is the problem definition. You need a strategy because the multidisciplinary analysis is usually expensive and difficult to develop. A clear statement of the design variables (and their allowable ranges), the objective function(s), and the constraints is necessary. The appropriate MDO strategy depends on such factors as the mix of continuous and discrete variables; the strength of the interdisciplinary interactions; the separability of the constraints with respect to the design variables; the susceptibility of the analysis tools to algorithmic noise; computational requirements of the analysis; and last, but certainly not least, the compatibility of the MDO strategy with the existing organizational structure and culture.

4.0 PRELIMINARY DESIGN EXAMPLES USING MDO

Two different applications have been selected to illustrate preliminary design with MDO. The first example uses a direct optimization procedure for the multidisciplinary design of an aerospike rocket nozzle.[15] The second example is an HSCT design that utilizes an indirect optimization approach.[16]

4.1 MDO Applied to Aerospike Rocket Nozzle

A multidisciplinary analysis of an aerospike nozzle has been developed to evaluate MDO strategies and new preliminary design processes. This effort was part of a formal collaboration between NASA Langley Research Center and the Rocketdyne Division of Boeing North American, Inc. The linear aerospike rocket engine is the propulsion system proposed for the X33 and the VentureStar[17] (Fig. 7) reusable launch vehicles (RLV).
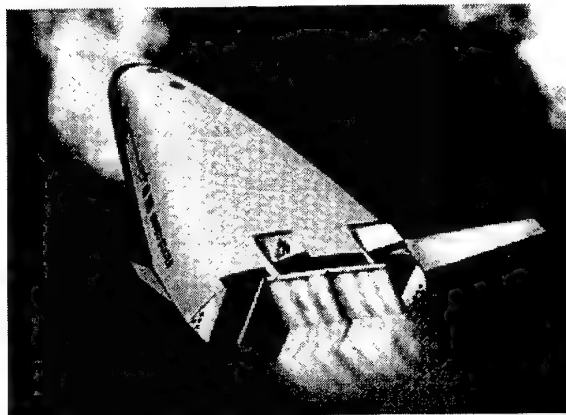
Fig. 7. VentureStar RLV with linear aerospike propulsion system.

The aerospike rocket engine consists of a rocket thruster, cowl, aerospike nozzle, and plug base region (Fig. 8). The aerospike nozzle is a truncated spike or plug nozzle that adjusts to the ambient pressure[18] and integrates well with launch vehicles. The flow-field structure changes dramatically from low to high altitude on the spike surface and in the base-flow region.[19-20] Additional flow is injected in the base region to create an aerodynamic spike[21] (thus, the name "aerospike"), which increases the base pressure and the contribution of the base region to the aerospike thrust.
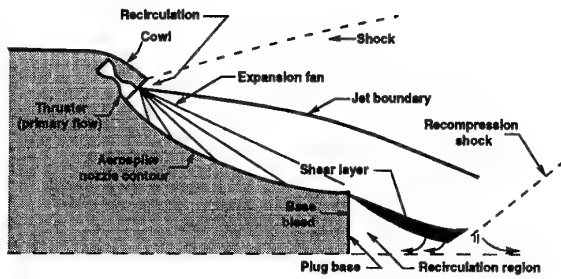
Fig. 8. Aerospike components and flow-field characteristics.

Thrust and nozzle wall pressure calculations were made by using computational fluid dynamics (CFD) and were linked to a structural finite-element analysis to determine nozzle weight and structural integrity (Fig. 9). A mission-averaged specific impulse (ISP) and engine thrust-to-weight ratio were calculated and used to determine vehicle gross-liftoff-weight (GLOW) from data that were defined in the conceptual design stage. The computational time for computing the thrust using CFD techniques was approximately 20 sec, and the computational time for computing the weight using finite element method (FEM) was approximately 35 sec on a Sun UltraSPARC. Approximately 4 months were required to develop and integrate the discipline codes to obtain a multidisciplinary analysis. A significant part of this development was devoted to developing suitable procedures for automating the use of the commercial FE code.
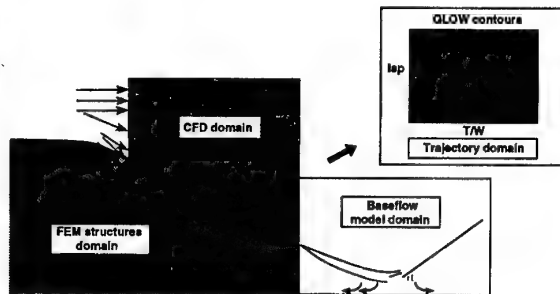
Fig. 9. Multidisciplinary domain decomposition.

The multidisciplinary analysis was integrated with an optimization code that allowed investigation of the multidisciplinary feasible[22] (MDF) strategy. Two different methods of design were investigated. The first method involved the development of a preliminary design by optimizing the disciplines separately. The optimal thrust and nozzle weight were then used to calculate the GLOW. This first method is a model of a typical design approach. The second method utilized the MDF formulation and minimized the GLOW directly, subject to satisfying the structural constraints. The MDF method was applied to a case in which the nozzle length was held constant and one in which this length was varied. The gradient-based optimization method, CONMIN,[23] was used in all cases. A typical optimization problem was solved in 1 to 3 days on a

typical workstation and required approximately 300 to 600 multidisciplinary analyses.

The design parameters included 5 geometry variables (Fig. 10) and 14 structural variables (Fig. 11). The initial geometry design variables were selected from previous design studies on aerospike nozzles that used conventional design methods and were expected to be close to an optimized aerodynamic shape.
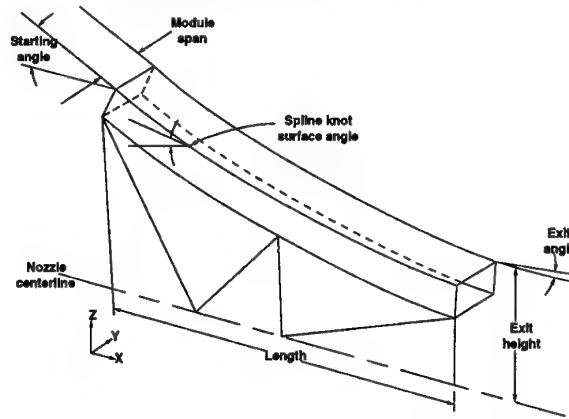
Fig. 10. Aerospike nozzle geometry design parameters.

The number of structural design variables was reduced by mapping some of the design variables with common attributes into a single design variable. In particular, the thickness of the I-beams was made to be the same in each structural box, and the six structural supports were required to have the same radius and wall thickness. The initial values selected for the structural design parameters resulted in a structural design that was infeasible (some constraints were violated). The structural design concept for the aerospike nozzle was generated explicitly for this study and does not relate to a structural configuration that has previously been designed or studied.
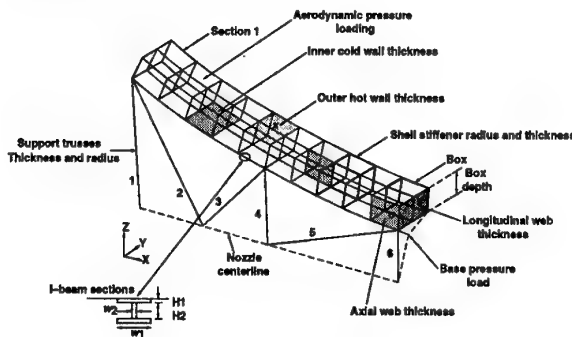
Fig. 11. Aerospike nozzle structural design parameters.

A multidisciplinary design was obtained each discipline separately for a fixed nozzle length (Fig. 12). The MDO design resulted in an improvement of approximately 5 percent in the GLOW over that of the single-discipline optimized solution. The improvement was obtained by reducing the nozzle thrust, which resulted in a lower pressure loading on the nozzle structure and a lower nozzle weight.
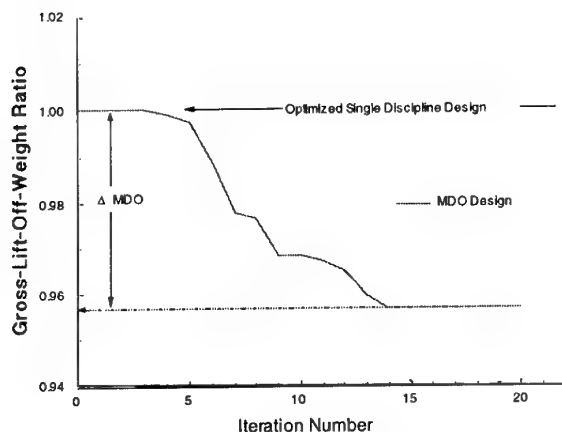
Fig. 12. Improvement of GLOW Using MDO.

The advantages of the MDO approach were evident both in the improvement that was realized in the design objective and the ease with which the multidisciplinary design variables, such as nozzle length, were included in the design process.

4.2 HSCT Preliminary Design with FIDO

The Framework for Interdisciplinary Optimization (FIDO) is being developed to demonstrate multidisciplinary computations on a networked, heterogeneous cluster of workstations, vector computers, and massively parallel computers. This project is one of NASA's contributions to the national High Performance Computation and Communication Program (HPCCP).[24] The FIDO system has been applied to a simplified case of an HSCT design (Fig. 13).

Mach 2.4 at 55,000 ft
6000-mile range
250 passengers
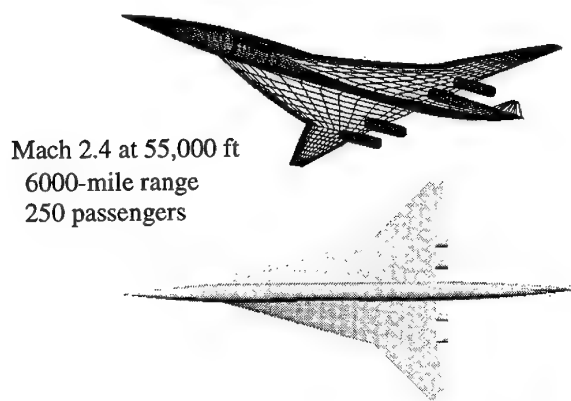
Fig. 13. Preliminary design geometry for HSCT.

The concept that is being used for FIDO is coarse-grained parallelism, with instances in which disciplinary codes are run on separate processors (including, loosely fine-grained parallel computers) under the control of an executive on another processor and with automatic data

exchange through a centralized data manager (Fig. 14).
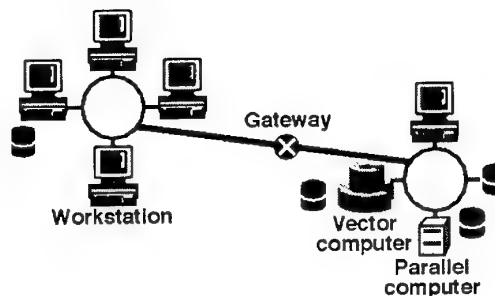
Fig. 14. Heterogeneous distributed computing environment.

The conceptual environment in which the distributed discipline and system-service codes are run is illustrated in Fig. 15. Each of these codes may be run on a separate workstation or on a high-performance computer; the communications and synchronization is handled through the FIDO communication library, which is based on a PVM (parallel virtual machine) utilities. The triangular, rectangular, and hexagonal modules at the top of Fig. 15 are system-service modules that do not change as the design problem changes; the rounded rectangular modules at the bottom of the figure represent the problem-specific computational disciplines and the application-specific, user developed Master module that controls the sequencing for a particular problem. The user interacts with the system through the graphic user interface (GUI), which displays the state of the FIDO system at all times from start-up to completion of a run. The GUI also provides access to multiple system capabilities: the setup module is used to select the design problem,
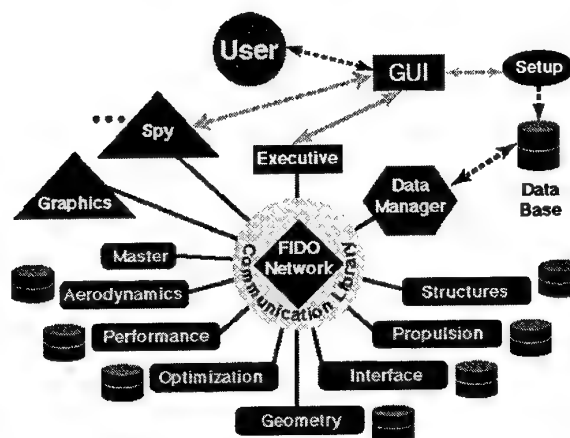
Fig. 15. Executive system of FIDO.

initial configuration, and design conditions and controls; the executive module starts a communication server on each of the distributed computers, distributes initial data and executables, and starts execution of a problem; and the spy module allows the designer, as well as multiple

remote users, to query the centralized database and invoke external graphics programs in order to plot selected output data. The data manager provides a centralized access service for the storage and retrieval of global data during a run of the FIDO system.

To update the grids for the aerodynamic and structural FEM analysis, the baseline geometry and the design variables updated in the design process are used to modify the baseline geometry descriptions (Fig. 16). The initial aero analysis provides the drag polars, and the initial structural analysis provides the structural weights. Based on the wing shape specified at the start of cruise condition, the unloaded shape (also called the jig shape) is determined through a structural analysis with the aerodynamic and inertial loads removed. An

iterative aeroelastic analysis is used to determine the shape of the configuration at the end of cruise, based on the fuel weight determined through a performance analysis. This performance analysis uses the drag polars and engine fuel-consumption characteristics at the start and end of cruise. The structural deflections, stresses, and weights are provided as input to the optimizer, along with design sensitivity derivatives that are determined during the analyses. The optimizer determines updated values for the design variables, with the objective of minimizing take-off-gross weight subject to a set of design constraints. After the designer reviews and accepts or modifies the design variables, the process begins again if convergence to a minimum weight has not been achieved.
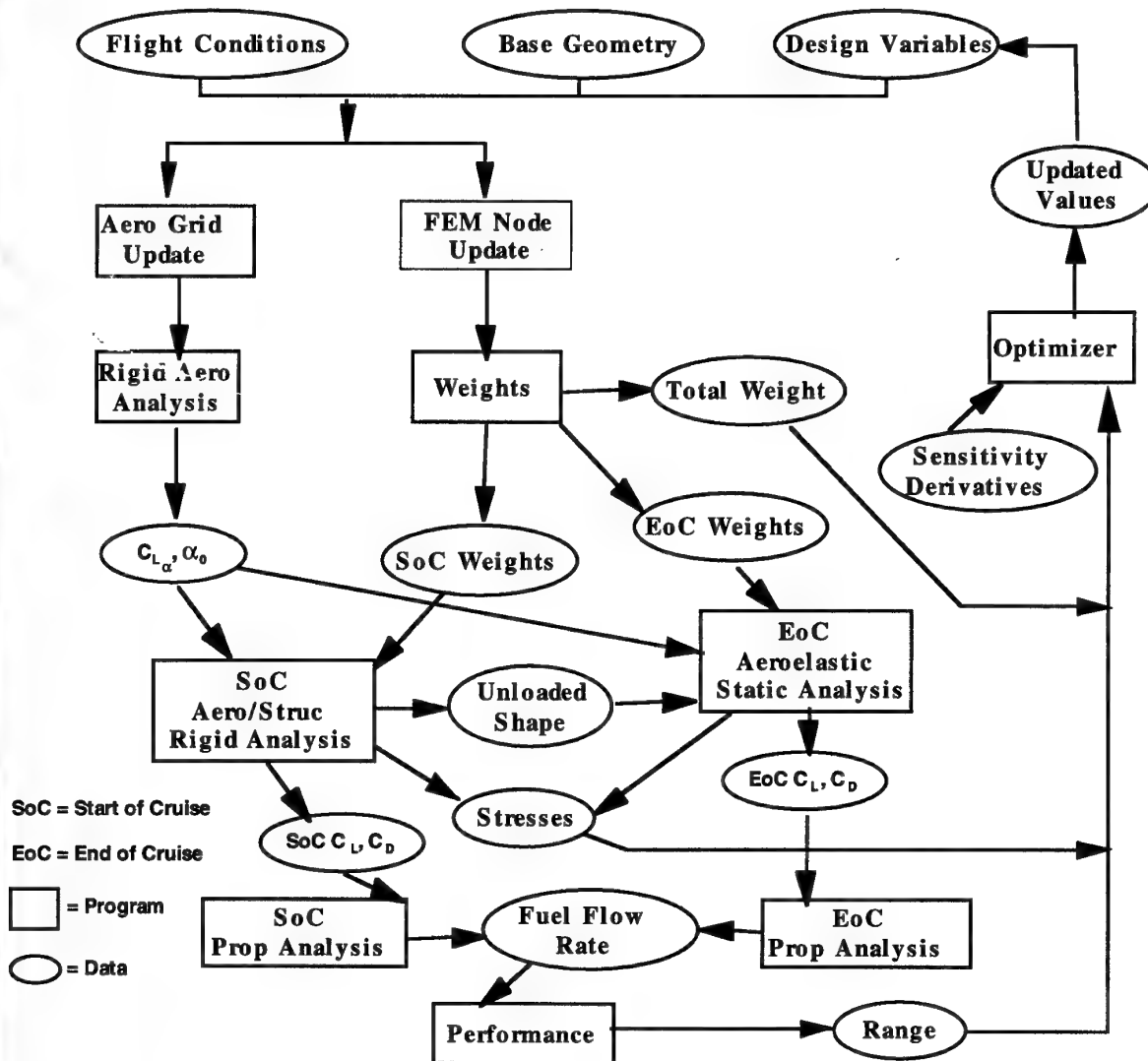
Fig. 16. Problem diagram for HSCT.

Initial Shape from Design Variables
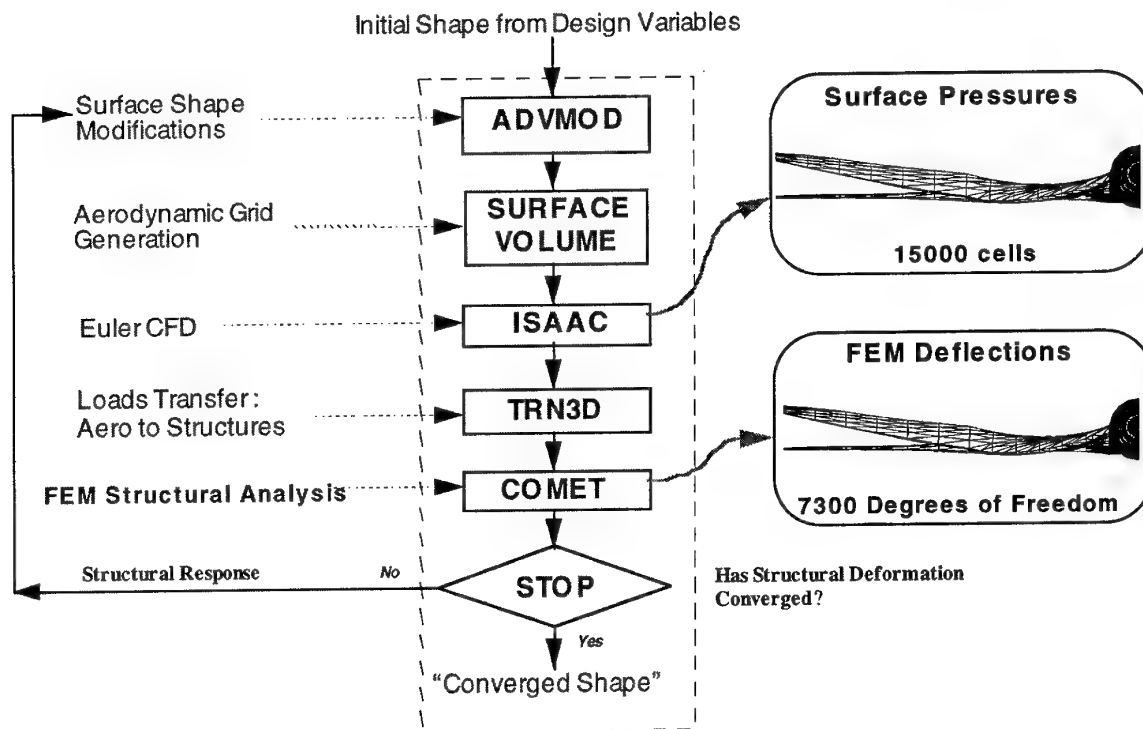
Fig. 17. Key steps in FIDO aeroelastic loop.

An aeroelastic loop implements the tight coupling between the computationally intensive aerodynamic and structural analysis programs (Fig. 17). At the beginning of the loop, the program ADVMOD uses the recently updated design variables to modify the "rubberized" aircraft surface grid and the structural FEM grid in a consistent manner. (The topologies and connectivities of the grids are maintained.) A special-purpose program is then invoked to generate a CFD volume grid that is suitable for the marching Euler program ISAAC[25]. After the aerodynamic calculations are computed, the program TRN3D is used to accurately transfer the surface pressures into FEM node forces for use in the structural analysis code COMET[26]. After COMET determines the nodal deflections that correspond to the aerodynamic and inertial forces, the movement of selected nodes is used to update the deformation of the aircraft surface grid, and the loop is ready to begin again if the shape has not converged.

The weight history from a run of the FIDO system in which the aircraft skin-thickness distribution is represented by two polynomial equations (one each for the wing both inboard and outboard of the break in the leading-edge sweep) is shown in Fig. 18. The coefficients in the polynomials are the design variables for this run. The objective is the minimization of total weight subject to constraints on the material stresses and structural deflections. The plot shows the smooth and converging reduction of the total weight as the design progresses.
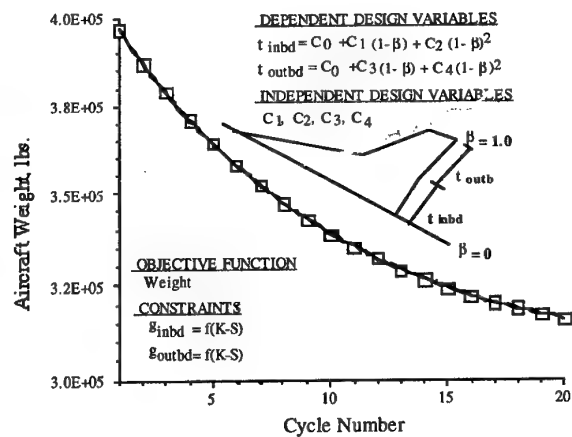
Fig. 18. Weight history for HSCT design optimization.

The spanwise distribution of the skin thickness for the baseline configuration (top curve) and the reduction in the thickness distributions are shown in Fig. 19 after five cycles of the design process.
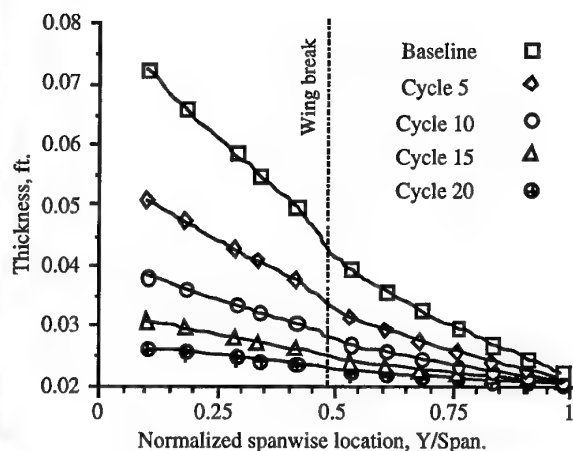
Fig. 19. Thickness history for HSCT design optimization.

The FIDO system has been designed to be adaptable to any distributed computing problem. The above problem demonstrates how a distributed computing system can be utilized in an MDO problem.

CONCLUDING REMARKS

An overview of multidisciplinary optimization (MDO) conceptual elements was presented with two examples of MDO methodology applied to preliminary design problems. The two examples demonstrate areas in which the MDO methodology can make an impact in preliminary design. The continual improvement in computers, communication networks, and the worldwide web will improve the tools available for multidisciplinary computations. However, the computational times required for most preliminary analysis methods still prohibit the use of MDO in a practical design environment. More advanced approximation methods are needed that can temporarily replace expensive analyses and automatically decide when an approximation should be updated to maintain its accuracy.

REFERENCES

[1]McCullers, L. A., "Aircraft Configurations Optimization Including Optimized Flight Profiles," Langley Research Center Recent Experiences in Multidisciplinary Analysis and Optimization, Part 1, Jan. 1984.

[2]Lockwood, M. K., Petley, D. H., Hunt, J. L., Martin, J. G., "Airbreathing Hypersonic Vehicle Design and Analysis Methods," AIAA Paper 96-0381, Jan. 1996.

[3]Alberico, J. F., "The Development of An Interactive Computer Tool for Synthesis and Optimization of Hypersonic Airbreathing Vehicles," AIAA Paper 92-5076, Dec. 1992.

[4]Kossira, H., Bardenhagen, A., and Heinze, W., "Investigations on the Potential of Hypersonic Waveriders with the Integrated Aircraft Design Program PrADO-Hy," AIAA Paper 93-5098, 1993.

[5]"Current State of the Art on Multidisciplinary Design Optimization (MDO)," Prepared by the AIAA Technical Committe on Multidisciplinary Design Optimization, AIAA White Paper, Sept. 1991. Available online at (http://endo.sandia.gov/AIAA_MDOTC/main.html).

[6]Multidisciplinary Design Optimization: State of the Art—Proceedings of the ICASE/NASA Langley Workshop on Multidisciplinary Design Optimization, (Alexandrov, N. M. and Hussaini, M. Y., eds.), SIAM, Philadelphia, 1995.

[7]Sobieszczanski-Sobieski, J. and Haftka, R. T., "Multidisciplinary Aerospace Design Optimization: . Survey of Recent Developments," AIAA Paper 96-0711, Jan. 1996.

[8]Proceedings of the 6th AIAA/NASA/ISSMO Symposium on Multidisciplinary Analysis and Optimization, AIAA CP9611, Sept. 1996.

[9]Sobieszczanski-Sobieski, J., "Multidisciplinary Design Optimization: An Emerging New Engineering Discipline," NASA TM 107761, May 1993.

[10]Townsend, J. C., Samareh, J., Weston, R. P., and Zorumski, W.E., "Integration of a CAD System into an MDO Framework," NASA TM 110333, 1997.

[11]Barthelemy, J.-F. M., and Haftka, R. T., "Approximation Concepts for Optimum Structural Design," *Structural Optimization*, Vol. 5, pp. 129-144, 1993.

[12]Carle, A., Green, L., Bischof, C., and Newman, P., "Applications of Automatic Differentiation in CFD," AIAA Paper No. 94-2197, June 1994.

[13]Tayor, A. C., III, Green, L. L., and Newman, P. A., "Automatic Differentiation of the CFL3D Flow Code in Incremental Iterative Form Using ADIFOR 2.0," 2nd International Workshop on Computational Differentiation, Feb. 12-15, 1996.

[14]Braun, R. D., Powell, R. W., Lepsch, R. A., Stanley, D. O., and Kroo, I. M., "Multidisciplinary Optimization Strategies for Launch Vehicle Design," AIAA Paper 94-4341, Sept. 1994.

[15]Korte, J. J., Salas, A. O., Dunn, H. J., Alexandrov, N. M., Follett, W. W., Orient, G. E., and Hadid, A. H., "Multidisciplinary Approach to Aerospike Nozzle Design," NASA TM 110326, Feb. 1997.

[16]Weston, R. P., Townsend, J. C., Eidson, T. M., and Gates, R. L., "A Distributed Computing Environment for Multidisciplinary Design", AIAA Paper 94-4372, Sept. 1994.

[17]Sweetman, B., "VentureStar: 21st Century Space Shuttle," *Popular Science*, Oct. 1996, pp. 42-47.

[18]Rao, G. V. R., "Recent Developments in Rocket Nozzle Configurations," *ARS Journal*, Sept. 1961, pp. 1488-1494.

[19]Mueller, T. J., and Sule, W. P., "Basic Flow Characteristics of a Linear Aerospike Nozzle Segment," ASME Paper 72-WA/Aero-2, Nov. 1972.

[20]Hagemann, G., Schley, C.-A., Odintsov, E., and Sobatchkine, A., "Nozzle Flowfield Analysis with Particular Regard to 3D-Plug-Cluster Configurations," AIAA Paper 96-2954, July 1996.

[21]Iacobellis, S. F., Larson. V. R., and Burry, R. V., "Liquid-Propellant Rocket Engines: Their Status and Future," *J. of Spacecraft and Rockets*, Vol. 4, Dec. 1967, pp. 1569-1580.

[22]Cramer, E. J., Dennis, J.E. Jr., Frank, P. D., Lewis R. M., and Shubin, G. R., "Problem Formulation for Multidisciplinary Optimization," *SIAM J. Optimization*, Vol. 4, No. 4, Nov. 1994, pp. 754-77

[23]Vanderplaats, G. N., "CONMIN-A Fortran Program for Constrained Function Minimization User's Manual," NASA TM X-62282, August 1973.

[24]Holst, T. L., Salas, M. D., and Claus, R. W., "The NASA Computational Aerosciences Program--Toward TeraFLOPs Computing," AIAA Paper 92-0558, Jan. 1992.

[25]Krishnan, R. R., and Eidson, T. M., "An Efficient Parallel Space-Marching Euler Solver for HSCT Research," AIAA 95-1749-CP, June 1995.

[26]Introduction to the Computational Structural Mechanics Testbed, NASA TM 89096, 1987.

Integrated Hydrogen Fuel Management as Heat Sink for Active Cooling in Advanced Hypersonic Aircraft

A. DENARO
G. AUDRITO
Alenia Aerospazio - Un'Azienda Finmeccanica
Divisione Spazio, Marche 41
10146 Torino, Italy

Summary

Cooling potentialities of hydrogen fuel to manage the heat dissipations of internal equipment are explored and integrated with the complete Thermal Control System of a reference hypersonic vehicle.

Nominal performances are investigated during all a mission phase and drivers are provided for the optimization of the Regenerative Cooling.

List of Acronyms

ATCS   Active Thermal Control System
C-SiC   Carbon-Silicon Carbide
FC   Fuel Cells
FEI   Flexible External Insulation
GH_2 Gaseous Hydrogen
GSE   Ground Support Equipment
HX   Heat Exchanger
IFI   Internal Flexible Insulation
LH_2 Liquid Hydrogen
LOX   Liquid Oxygen
P/L   Payload
SSTO   Single Stage To Orbit
STV   Space Transportation Vehicle
TCS   Thermal Control System
TPS   Thermal Protection System
T_w Wall Temperature

1 Introduction

A reusable SSTO hypersonic vehicle is taken into consideration to present an illustrative example of application of the Regenerative Cooling concept as a promising approach in Heat Management strategies.

The exploitation of the hydrogen fuel cooling capabilities during both the ascent powered phase (in liquid form) and the on-orbit and re-entry phases (in gaseous form) offers a very attractive thermal sink for the management of the heat dissipation generated by internal equipment. This regenerative approach that uses the hydrogen as a heat sink other than as a propulsion fuel allows to avoid mass penalties derived by the additional cooling fluids and relative tanks.

The best cooling performances of the hydrogen sink can be achieved with an efficient combination of different thermal control systems that all together affect the thermo-hydraulic history of the cryogenic cooling fluid.

The mutual interactions of the external Thermal Protection System (TPS), of the cryogenic foam that insulates the fuel tank and of the purge flow conditions are explored to define their optimization offering the most effective hydrogen cooling capabilities.

This paper provides an illustrative example of the Regenerative Cooling based on a reference vehicle; considering its shape and trajectory, first the on-ground purging flow and the Thermal Control Architecture (TPS and cryogenic foam) required to limit the aerothermal fluxes inside the tank are presented.

A description of the Active Cooling loop is presented with the relative performances and finally the links between all the Thermal Control System devices are shown.

A general overview highlighting the most effective parameters for the optimization of the hydrogen cooling capabilities will be provided.

Concluding recommendations, guidelines and limitations are provided for the best application of the Regenerative Cooling.

2 TCS and Regenerative Cooling Philosophy

An outstanding requirement for the design of the TCS in advanced hypersonic aircraft is the capability to arrange as lightweight an architecture as possible able to maintain an adequate thermal barrier against all the heat sources which the vehicle encounters during its flight by using both passive and active devices.

Such a control is realized to manage mainly three different thermal sources.

1- Environmental heating occurring on-ground after having disconnected the umbilicals of the GSE. It is responsible for liquid hydrogen fuel boiloff.

2- Convective heat fluxes produced by the air friction of the vehicle's external surface

with the surrounding boundary layer during the ascent and especially the re-entry phase at high Mach numbers and affecting the temperature peaks achieved by the fuselage structure materials.

3- Internal heat dissipation derived from the on-board subsystems (avionics, payload, fuel cell, hydraulic systems commanding landing gears and control surfaces...).

As far as the first point is concerned, a combined design of a suitable purging flow by means of the GSE (nitrogen or dry air) and of a closed cell foam installed all around the fuel tanks is able to ensure the appropriate atmosphere, minimizing the fuel boiloff and preventing ice formation until an altitude of 65000 feet.

However, in order to limit the aerothermal heat fluxes, the TPS distribution draws up several material types (ceramics, metallics, fibrous...) whose function is the limitation of the primary structure temperature below maximum allowable operating values and of the heat flux penetrating inside the vehicle, according to the requirement imposed by the internal control system.

For the internal heat dissipation control, a dedicated actively cooled loop is finally envisaged to arrange in a sound sequence all the subsystems located inside the hypersonic vehicle.

The design solution of cooling this equipment by means of a loop flowed by water, freon, ammonia or any other classical fluid is replaced by a cooling loop exploiting the availability of the hydrogen that, other than an excellent combustion energy, a rapid mixing capability and fast reaction rates, also presents a great heat sink capacity (e.g. 10 times greater than Kerosene) influenced by purging conditions, TPS and cryoinsulation designs.

The intrinsic properties of cryogenic hydrogen offer therefore a great opportunity to couple its propulsive and cooling functions simultaneously.

The application of the Regenerative Cooling principle exploits the thermal characteristics of the cryogenic hydrogen (liquid and vapor) to reject all the heat load collected in the various phases of the mission avoiding additional tanks dedicated to cooling purposes only.

3 ATCS Architecture and cryogenic hydrogen as heat sink

A schematic layout of the active cooling network devised to manage the heat dissipation of the internal subsystems is illustrated in Fig 1.
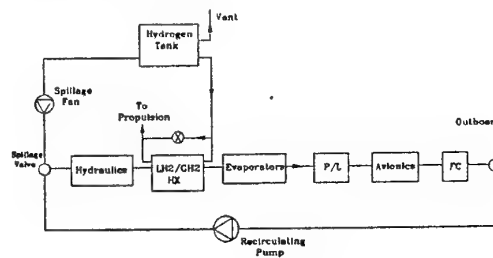
Fig. 1: ATCS schematic diagram.

All the subsystems are arranged in a flowing sequence which takes into consideration their cooling and temperature requirements.

They are interconnected by an on-ground pre-charged insulated cooling loop flowed with gaseous hydrogen by means of a dedicated pump that balances the pressure loss through the loop.

This loop interfaces with cryogenic sinks whose thermodynamic status directly depends on the mission phase.

During the ascent phase, the spillage tubing connecting the cryogenic tank to the ATCS loop is closed and all the heat load collected by the vapor hydrogen loop (primary loop) is transferred by means of a dedicated heat exchanger to the liquid hydrogen fuel which is fed by the main propulsion tank and pumped towards the combustion chamber.

During this phase, the primary vapor hydrogen loop acts as a closed circuit (ON/OFF venting valve closed) and the ultimate heat sink is the liquid hydrogen flowing in the propulsion system.

According to the Regenerative Cooling philosophy, no additional heat sink is introduced and the enthalpy of the liquid fuel hydrogen flowing through the LH_2/GH_2 is slightly increased as a consequence of the transferred heat load derived by the vehicle's dissipating equipment.

The liquid hydrogen mass flowrate required in the secondary side of the LH_2/GH_2 a few percent of the one provided by the hydrogen turbopump and sized for propulsion system performance; a bypass line with a modulating valve is therefore installed in parallel to the cryogenic HX

The actively cooling configuration described and managing the heat dissipating by the subsystems needs great flexibility according to the thermal sink available.

In fact, when the ascent powered phase is completed and the main engines are shutoff, an alternative sink replacing the no longer available LH_2 must to reject the subsystem's dissipation during the on-orbit and re-entry phases.

In these conditions, the LH_2/GH_2 HX is bypassed, the spillage valve of the mixing point located upstream of the hydraulic systems opens and the heat sink is provided by the vapor hydrogen contained inside the tank.

The gaseous hydrogen mass flowrate coming out of the tank is a function of the pressure and temperature histories that the gaseous hydrogen experiences during on-orbit and re-entry phases. The exposition of the vehicle mainly to the solar flux and to the aerothermal heating produces a temperature increase of the cryogenic residual vapors of hydrogen proportional to the incoming heat flux through the TPS and the cryoinsulation foam. In order not to exceed the designed maximum differential pressure between the interior of the tank and the external environment, the heating and consequent pressure increase of the hydrogen mass is compensated with a hydrogen flow (spillage and relief).

In order to satisfy the cooling demand, the needed gaseous hydrogen mass flowrate is spilled from the tank by a fan (spillage flow), so compensating the pressure loss of the dowstream series-connected subsystems and is finally expelled overboard by opening the ON/OFF venting valve and controlling a setpoint temperature of 30°C at the outlet of the series-flowed equipment.

The pump installed in the hot branch in parallel to the dissipating Subsystems branch recirculates gaseous hydrogen to control the temperature of the mixing point located upstream of the hydraulic systems. The tank gaseous hydrogen mass flowrate that exceeds the cooling demand is recycled outside the tank (relief flow).

So, during all the transient phase, a continuous balance between the cooling capability and the cooling demand is carried out; proceeding the re-entry phase, the increase of the external environment atmosphere reduces the hydrogen cooling potentialities for its higher temperature (aerodynamic heat load passing through the TPS) and lower differential pressure with the external environment.

The macroscopic effect is a continuous deterioration of the heat sink capabilities; the spillage flow required by the fan for cooling

regulation results higher than the mass flow available for maintaining a constant differential pressure inside the tank.

4 Reference Concept

The SSTO vehicle considered as reference configuration is represented in Fig. 2.
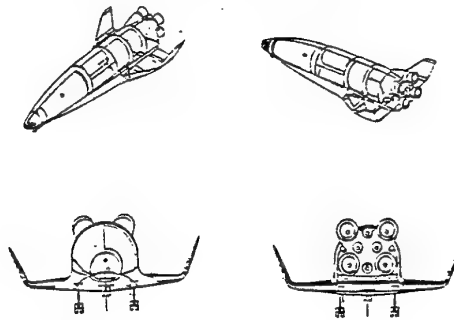
Fig. 2: Vehicle reference configuration.

In the frame of an ESA study, it is one of the concepts presently under investigation to demonstrate the technology feasibility of a low cost access to space transportation vehicle.

The winged delta shaped Space Transportation Vehicle (STV) is characterized by a vertical take-off and horizontal landing mode and is powered by 8 main rocket engines with fixed bell nozzles fed by sub-cooled LH_2 as fuel and by LOX as oxydizer. The P/L bay is integrated in parallel to the longitudinal vehicle axis and the primary goal of the vehicle is the deployment of 2 tons P/L into 250 km/98° Orbit or 15 tons P/L into 250 km/5° Orbit.

The main geometrical data are given in Tab. 1.

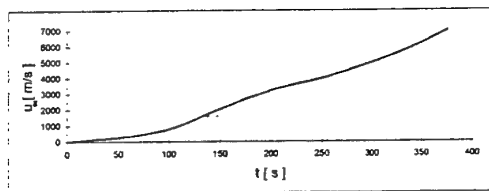| Total vehicle length (incl. Nozzles)	62.20 m
Fuselage length	59.00 m
Max. fuselage width	10.35 m
Max. fuselage height	10.33 m
Wing span b (incl. Winglets)	29.36 m
Exposed wing area (total)	270.0 m²
Winglet area (total)	84.0 m²
Aerod. Ref. Area	820.0 m²
P/L bay length	10.0 m
P/L bay width	4.72 m
P/L bay Volume	175.0 m³

Tab. 1: Vehicle Geometrical Data.

During the pre-launch phase, the internal gap between the insulated tanks and the primary structure protected with TPS is purged with a
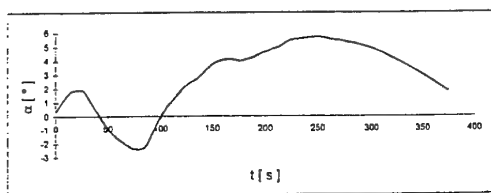
dry air flow to provide the adequate protection against the formation of vapor condensation and consequent frost formation until the GSE umbilicals are disconnected 30' before lift-off. The nominal ascent and re-entry/descent trajectories from/to Kourou for the polar orbit (most demanding cross range requirement) shown in Figs. 3 and 4 have been explored for aerothermodynamic calculations.
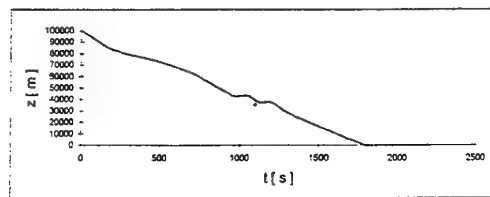The mission duration is 24 hours.
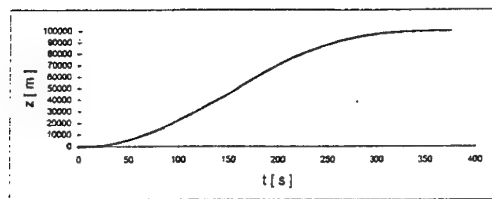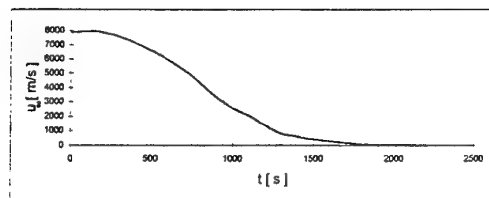
a) Altitude vs. Time

a) Altitude vs. Time

b) Relative velocity vs. Time

b) Relative velocity vs. Time
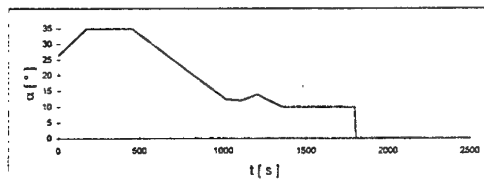
c) Angle of attack vs. Time

Fig. 4: Vehicle Re-entry Trajectory.

c) Angle of attack vs. Time

Fig. 3: Vehicle Ascent Trajectory.

The resulting convective heat fluxes encountered during the critical atmosphere re-entry are reported in Fig. 5 for both the windward $(x/l>0)$ and leeward $(x/l<0)$ centerlines of the vehicle.

t = 600 s
z = 67308 m
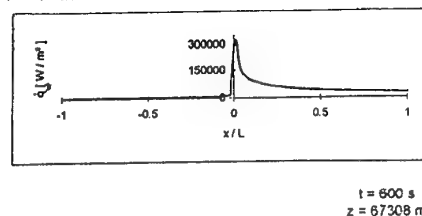
Fig. 5: Re-entry Convective Heat Flux.

It is interesting to highlight the heating of the stagnation point at values higher than 300

kw/m2; in addition, a transition from laminar to turbulent flow can be observed in the aft leeward side at about 700 sec from the de-orbiting with a consequent increase of the convective heat load.

The migration of the laminar-turbulent transition proceeds in the nose direction but the peak of the turbulent heat load always results much lower than the stagnation point.

The same effect can be observed also in the windward side; the transition zone migrates in the same nose direction but the consequent abrupt heating is comparable to the stagnation point heat load.

Re-entering deep inside the atmosphere at reduced velocity, a general reduction of the aerothermal heating throughout the surface occurs.

The re-entry adiabatic wall temperatures are shown in Fig. 6 for the vehicle's centerline.

t = 600 s
z = 67308 m
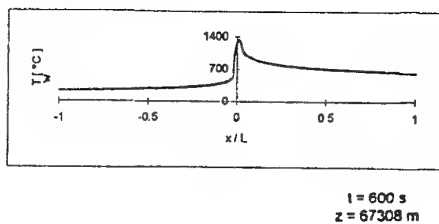
Fig. 6: Re-entry Adiabatic Wall Temperatures (Centerline).

The surface temperatures for a longitudinal station x/l=0.16 and at different angular positions (Phi=0 for windward, Phi=45, Phi=135, Phi=180 for leeward side) are reported in Fig. 7.
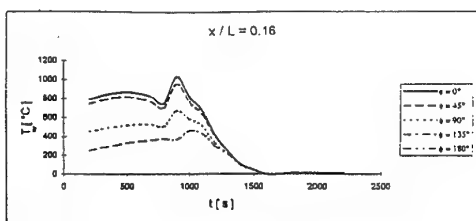
Fig. 7: Re-entry Adiabatic Surface Temperatures Distribution.

As can be seen, the major part of the exposed aerodynamic surface experiences temperatures that greatly exceed the allowable limit imposed by the structural materials (about 170 °C).

The design of both the high temperature TPS and the cryogenic insulation is carried out in close union with aerothermodynamics results a part of which is shown in Figs. 5 and 6. The logic flowchart is reported in Fig. 8.
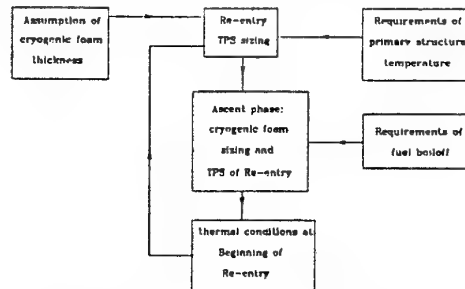
Fig. 8: Logic Flowchart for TPS and Cryoinsulation Design.

A worthwile interest is here dedicated to the TPS and cryoinsulation designed in correspondence to the hydrogen cryogenic tank section, whose schematic configuration is represented in Fig. 9.
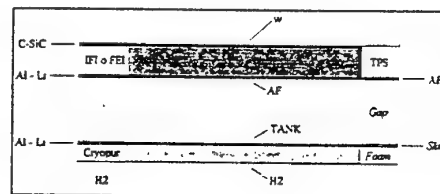

Fig. 9: Cryogenic Section Schematic.

Final dimensioning derived from the logic of Fig. 8 provides a TPS distribution relative to the cryogenic tank section as summarized in Tab. 2.

$\phi = 0°$	x/L = 0.16	$(T_w)_{max} = 1036$ °C	IFI + C-SiC ($T_{max}=1300$°C)	49.5 mm
$\phi = 90°$	x/L =0.16	$(T_w)_{max} = 681$ °C	FEI 1000 ($T_{max}=1000$°C)	30.4 mm
$\phi = 180°$	x/L = 0.16	$(T_w)_{max} = 461$ °C	FEI 650 ($T_{max}=650$°C)	14.7 mm

Tab. 2: TPS Distribution for Cryogenic Section.

Three different surface sections 90 degrees wide have been covered with different TPS materials according to the temperature levels of Fig. 7.

The TPS thickness is relative to the station x/l=0.16 correspondent to the hottest forward tank station and is maintained constant all along the tank.

A 25 mm constant thickness cryogenic foam is installed on the internal side of the hydrogen tank to avoid the isolation performance penalties derived by the numerous penetrations that would occur through the foam if located on the external side.

The above TPS distribution relative to the cryogenic section is able to withstand the external heat fluxes of Fig. 5 maintaining the operative temperature of the primary structure and of the tank below the allowable one.

The temperature profile of the cryogenic section of Fig. 9 during the re-entry phase is shown in Fig. 10.
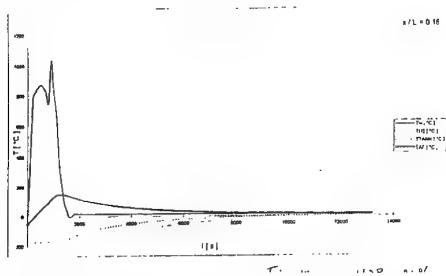
Fig. 10: Cryogenic Section Temperatures Profile.

5 ATCS Results

The reference SSTO vehicle considered foresees a TPS that is able to withstand the external aerothermal loads, and a TCS which manages the heat load dissipated by the avionics equipment located in the forward cargo-bay, by the actuators of the hydraulic systems, by the payload located inside the main central cargo-bay and by the fuel cells.

Tab. 3 reports the heat loads and the operating temperature ranges of the various subsystems during the ascent phase.

Tab. 4 and Fig. 11 provide information about the internal heat dissipations to be managed during the on-orbit and re-entry phases.

Equipment	Q [kw]
Hydraulics	72
Payloads	1
Avionics	5
Fuel Cells	7

Equipment	T [°C]
Hydraulics	10-100
Payloads	0-50
Avionics	0-50
Fuel Cells	5-90

Tab. 3: Subsystem Heat Dissipations And Operative Temperatures Range (Ascent).

	On-orbit	Re-entry
Equipment	Q [kw]	Q [kw]
Hydraulics	-	Fig. 11
Payloads	1	1
Avionics	5	5
Fuel Cells	7	7

	On-orbit	Re-entry
Equipment	T [°C]	T [°C]
Hydraulics	-	10-100
Payloads	0-50	0-50
Avionics	0-50	0-50
Fuel Cells	5-90	5-90

Tab. 4: Subsystem Heat Dissipations And Operative Temperatures Range (Re-entry).
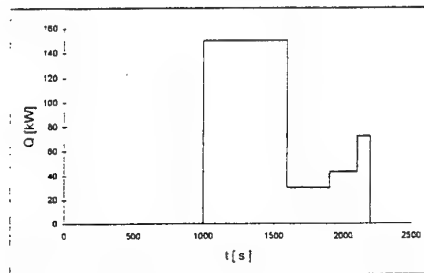

Fig. 11: Hydraulic System Heat Dissipations.

During the ascent phase the pre-charged vapor hydrogen loop collects, transports and rejects the heat dissipations of Tab. 2 to the cryogenic LH_2/GH_2 HX.

The secondary coldest loop of this HX is represented by the liquid hydrogen pumped from the cryogenic tank to the propulsion turbopump; its high specific heat and its high mass flowrate represent a high cooling

potential, so causing only a slight increase of its enthalpic content.

With reference to the ATCS of Fig. 1, the mass flowrate controls the set point temperatures at the outlet of the hydraulic systems (T=100°C) and at the inlet of the payload (T=5°C).

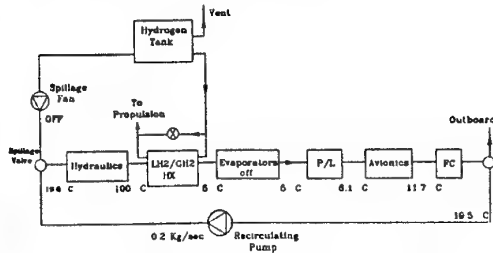The resulting steady-state temperature distribution is shown in Fig. 12.

Fig. 12: Ascent Steady-state ATCS Temperature Distribution.

During the on-orbit and re-entry phases, the reliefed GH_2 mass flowrate shown in Fig. 13 (time from the end of the powered phase) and its temperature (Fig. 14) is the sink used to cool the subsystems. The gaseous hydrogen in spillage branch is mixed with a hot recirculating flow variable with the equipments dissipations to control a temperature set-point of 5°C at the inlet of the hydraulic subsystems. During this phase, the LH_2/GH_2 HX is not active and the evaporators ensures a suitable temperature at the inlet of the P/L by vaporizing expandable fluids.
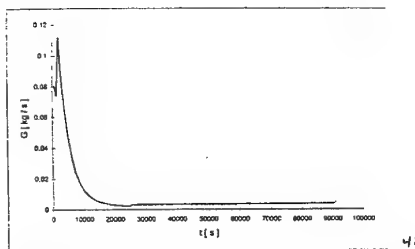
Fig. 13: Relief GH_2 Mass Flowrate (On-orbit and Re-entry).
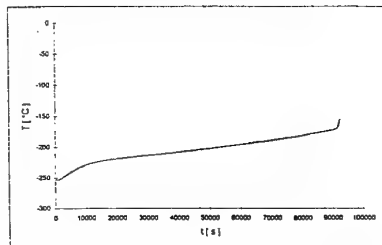
Fig. 14: Relief GH2 Temperature (On-orbit and Re-entry).

The cryogenic tank relief valve is set at 1.013 bar.

The aerothermal heating of the gaseous hydrogen produces a flow (Fig. 13) able to maintain a constant differential pressure across the tank (Fig. 15), while the external environment pressure increases.
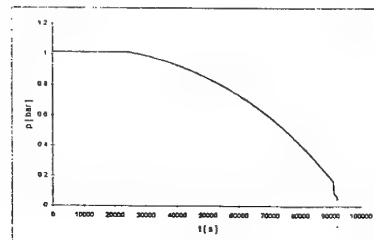

Fig.15: GH_2 Pressure Inside the Tank.

At the beginning of the re-entry phase, the great difference between the pressure inside the tank (1.033 bar) and in the external environment (nearly zero) gave rise to a mass flowrate higher than the one spilled from the fan to satisfy cooling purposes; the exceeded vapor hydrogen is reliefed outside the tank and is completely wasted.

When the vehicle penetrates more deeply inside the atmosphere, the differential pressure across the tank reduces and the fan maintains the setpoint temperature of 30°C downstream of the flowed equipment by spilling a cooling mass flowrate which results higher than the one provided by the tank for maintaining a constant differential pressure.

The consequence of this imbalance between the mass flowrate available according to the sink cooling capability and the one required by the cooling demand is a pressure drop inside the tank.

The deterioration of the sink cooling capability proved to be no longer sufficient to withstand the subsystems' dissipation after about 7 hours from the end of the powered phase.

The exposed performance of the ATCS during the on-orbit and re-entry phases is therefore directly dependent on the following design choices:

■ thermal conditions of on-ground purging affecting the thermal history of the tank skin in the beginning of the mission and consequently the heat load transferred to the vapor hydrogen in subsequent phases

■ thickness of cryogenic insulation installed internally to the hydrogen tank; a lower heat load entering the tank corresponds to

higher foam thicknesses with a related limited heating of the gaseous hydrogen which therefore better exploits its cooling potentialities.

6 Regenerative Cooling optimization

In the following, some optimization criteria regarding the best exploitation of the hydrogen cooling capabilities are provided.

With reference to Fig. 9, the driving design criterion is to maintain the cryogenic tank and the contained hydrogen as cold as possible without risk of water condensing or icing in the air gap. This approach is realized by purging the gap with dry air (low dewpoint temperature) and by isolating the tank by means of a suitable closed cell foam.

At the same time, the achievement of these requirements (cold tank and no icing/condensing) must be performed with a total mass minimization.

Fig. 16 shows the variation of the cryogenic insulation mass and of the related hydrogen boiloff (caused by the heat flux entering inside the tank through the TPS and the foam) as a function of the foam thickness; the foam has the greatest weight in the total mass budget and therefore a minimization of its thickness has great advantages.
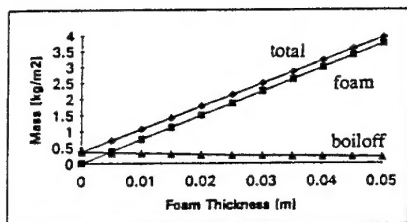
Fig. 16: Total mass vs. cryogenic insulation's thickness.

In Fig. 17, the minimum foam thickness required to avoid the risk of icing and condensing in the gap is shown (gap temperature must never drop below -173°C to prevent air condensation).
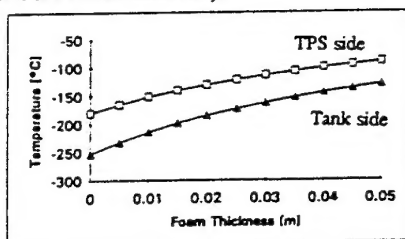

Fig. 17: Air Gap Extreme Temperatures vs. Cryogenic Insulation's Thickness.

The selection of the minimum foam thickness is therefore extremely important for a total mass minimization and, first of all, for the better thermal conditions of the hydrogen used as a cooling fluid.

7 Conclusions

The exploitation of hydrogen's cooling properties in hypersonic vehicles offers the availability of an effective thermal sink whose regenerative application allows the management of internal heat dissipations without additional fluids and relative tanks.

The optimum performance of this cooling philosophy is however limited by the following elements:

- short missions are preferred because the solar heat flux experienced during the orbital phase greatly influences the temperature of the hydrogen cooling fluid contained inside the tank and therefore its sink potentialities
- the management of the heat load derived by internal dissipating equipment is based on a cooling capability with limited resources (hydrogen in the tank and expandable fluid in the evaporators); the cooling demand is therefore related to the history of the thermodynamic properties of hydrogen during all the mission phase
- a more detailed design at component level is required to define the Active Thermal Control Architecture completely
- the maintaining of a constant differential pressure across the cryogenic tank during the Re-entry phase must be compatible with the structural requirements; increase of the maximum positive differential pressures affordable by the tank avoids that the pressure inside the tank itself will be lower than the external atmospheric pressure but at the same time it can be penalizing for the thickest tank required.

Feasibility of Regenerative Cooling also in the final phases of Re-entry must take into account a system level mass optimization such that the possible structure mass penalty never exceeds the advantages correlated to the absence of additional cooling fluids and relative tanks.

REPORT DOCUMENTATION PAGE

1. Recipient's Reference	2. Originator's Reference	3. Further Reference	4. Security Classification of Document
	AGARD-CP-600 Volume 3	ISBN 92-836-0049-5	UNCLASSIFIED/ UNLIMITED

5. Originator	Advisory Group for Aerospace Research and Development North Atlantic Treaty Organization 7 rue Ancelle, 92200 Neuilly-sur-Seine, France

6. Title	Future Aerospace Technology in the Service of the Alliance: Sustained Hypersonic Flight

7. Presented at/sponsored by	The AGARD Symposium on "Future Aerospace Technology in the Service of the Alliance" held at the Ecole Polytechnique, Palaiseau, France, 14-17 April 1997.

8. Author(s)/Editor(s)	9. Date
Multiple	December 1997

10. Author's/Editor's Address	11. Pages
Multiple	432

12. Distribution Statement	There are no restrictions on the distribution of this document. Information about the availability of this and other AGARD unclassified publications is given on the back cover.

13. Keywords/Descriptors

Hypersonic flight	Hypersonic nozzles	Military research
Hypersonic vehicles	Hypersonic characteristics	Test facilities
Scenarios	Hypersonic flow	Flight tests
Aerothermodynamics	Shock waves	Airframes
Missile propulsion	Heat transfer	Air intakes
Supersonic combustion ramjet engines	Military aircraft	Interactions
Ramjet engines	Ramjet test vehicles	Combustion
Design	Thermal insulation	Rocket fuels
Rocket propulsion	Film cooling	Reviews
Combustion chambers	Ducted rocket engines	

14. Abstract

One of three volumes containing the unclassified papers presented at a conference on "Future Aerospace Technology in the Service of the Alliance" organised by AGARD (NATO's Advisory Group for Aerospace Research and Development) at Palaiseau, near Paris, France, 14-17 April 1997. The conference took the form of three parallel symposia and three plenary sessions.

This volume contains the papers from the symposium on "Sustained Hypersonic Flight", which had introductory overview papers on "Mission Needs and Operational Scenarios for Hypersonic Vehicles", and on "Vehicle Configurations and Aerothermodynamic Challenges", and sessions on:

- Propulsion for Hypersonic Flight
- External Hypersonic Aerodynamics and Design Challenges
- Military ramjet Applications
- Test Facilities for Ramjets
- Configurational Design and Flight Validation
- Engine/Airframe Integration
- System Challenges

Volume 1 contains the papers from the three plenary sessions: "Future Directions in Aerospace Systems", "Future NATO Trends and Mission Scenarios", and "Human Machine Interaction in the Future"; and the papers on "Affordable Combat Aircraft".

Volume 2 contains the papers on "Mission Systems Technologies".

AGARD détient un stock limité de certaines de ses publications récentes. Celles-ci pourront éventuellement être obtenus sous forme de ie papier. Pour de plus amples renseignements concernant l'achat de ces ouvrages, adressez-vous à l'AGARD par lettre ou par télécopie adresse indiquée ci-dessus. *Veuillez ne pas téléphoner.*

exemplaires supplémentaires peuvent parfois être obtenus auprès des centres de diffusion nationaux indiqués ci-dessous. Si vous aitez recevoir toutes les publications de l'AGARD, ou simplement celles qui concernent certains Panels, vous pouvez demander d'être us sur la liste d'envoi de l'un de ces centres.

ublications de l'AGARD sont en vente auprès des agences de vente indiquées ci-dessous, sous forme de photocopie ou de microfiche. ains originaux peuvent également être obtenus auprès de CASI.

CENTRES DE DIFFUSION NATIONAUX

LEMAGNE
achinformationszentrum Karlsruhe
-76344 Eggenstein-Leopoldshafen 2

LGIQUE
Coordonnateur AGARD-VSL
Etat-major de la Force aérienne
Quartier Reine Elisabeth
Rue d'Evere, 1140 Bruxelles

NADA
Directeur - Gestion de l'information
(Recherche et développement) - DRDGI 3
Ministère de la Défense nationale
Ottawa, Ontario K1A 0K2

NEMARK
Danish Defence Research Establishment
Ryvangs Allé 1
P.O. Box 2715
DK-2100 Copenhagen Ø

PAGNE
INTA (AGARD Publications)
Carretera de Torrejón a Ajalvir, Pk.4
28850 Torrejón de Ardoz - Madrid

TATS-UNIS
NASA Center for AeroSpace Information (CASI)
800 Elkridge Landing Road
Linthicum Heights, MD 21090-2934

RANCE
O.N.E.R.A. (Direction)
29, Avenue de la Division Leclerc
92322 Châtillon Cedex

RECE
Hellenic Air Force
Air War College
Scientific and Technical Library
Dekelia Air Force Base
Dekelia, Athens TGA 1010

ISLANDE
Director of Aviation
c/o Flugrad
Reykjavik

ITALIE
Aeronautica Militare
Ufficio del Delegato Nazionale all'AGARD
Aeroporto Pratica di Mare
00040 Pomezia (Roma)

LUXEMBOURG
Voir Belgique

NORVEGE
Norwegian Defence Research Establishment
Attn: Biblioteket
P.O. Box 25
N-2007 Kjeller

PAYS-BAS
Netherlands Delegation to AGARD
National Aerospace Laboratory NLR
P.O. Box 90502
1006 BM Amsterdam

PORTUGAL
Estado Maior da Força Aérea
SDFA - Centro de Documentação
Alfragide
2700 Amadora

ROYAUME-UNI
Defence Research Information Centre
Kentigern House
65 Brown Street
Glasgow G2 8EX

TURQUIE
Millî Savunma Başkanliği (MSB)
ARGE Dairesi Başkanliği (MSB)
06650 Bakanliklar-Ankara

AGENCES DE VENTE

NASA Center for AeroSpace Information (CASI)
800 Elkridge Landing Road
Linthicum Heights, MD 21090-2934
Etats-Unis

The British Library Document Supply Division
Boston Spa, Wetherby
West Yorkshire LS23 7BQ
Royaume-Uni

demandes de microfiches ou de photocopies de documents AGARD (y compris les demandes faites auprès du CASI) doivent nporter la dénomination AGARD, ainsi que le numéro de série d'AGARD (par exemple AGARD-AG-315). Des informations logues, telles que le titre et la date de publication sont souhaitables. Veuiller noter qu'il y a lieu de spécifier AGARD-R-nnn et ARD-AR-nnn lors de la commande des rapports AGARD et des rapports consultatifs AGARD respectivement. Des références iographiques complètes ainsi que des résumés des publications AGARD figurent dans les journaux suivants:

cientific and Technical Aerospace Reports (STAR)
TAR peut être consulté en ligne au localisateur de
essources uniformes (URL) suivant:
  http://www.sti.nasa.gov/Pubs/star/Star.html
TAR est édité par CASI dans le cadre du programme
NASA d'information scientifique et technique (STI)
TI Program Office, MS 157A
NASA Langley Research Center
Hampton, Virginia 23681-0001
Etats-Unis

Government Reports Announcements & Index (GRA&I)
publié par le National Technical Information Service
Springfield
Virginia 2216
Etats-Unis
(accessible également en mode interactif dans la base de
données bibliographiques en ligne du NTIS, et sur CD-ROM)

AGARD

NATO -⊕- OTAN

7 RUE ANCELLE • 92200 NEUILLY-SUR-SEINE

FRANCE

Telefax 0(1)55.61.22.99 • Telex 610 176

DISTRIBUTION OF UNCLASSIFIED

AGARD PUBLICATIONS

AGARD holds limited quantities of some of its recent publications, and these may be available for purchase in hard copy form. For information, write or send a telefax to the address given above. *Please do not telephone.*

Further copies are sometimes available from the National Distribution Centres listed below. If you wish to receive all AGARD publicat or just those relating to one or more specific AGARD Panels, they may be willing to include you (or your organisation) in their distribu

AGARD publications may be purchased from the Sales Agencies listed below, in photocopy or microfiche form. Original copies of publications may be available from CASI.

NATIONAL DISTRIBUTION CENTRES

BELGIUM
Coordonnateur AGARD — VSL
Etat-major de la Force aérienne
Quartier Reine Elisabeth
Rue d'Evere, 1140 Bruxelles

CANADA
Director Research & Development
Information Management - DRDIM 3
Dept of National Defence
Ottawa, Ontario K1A 0K2

DENMARK
Danish Defence Research Establishment
Ryvangs Allé 1
P.O. Box 2715
DK-2100 Copenhagen Ø

FRANCE
O.N.E.R.A. (Direction)
29 Avenue de la Division Leclerc
92322 Châtillon Cedex

GERMANY
Fachinformationszentrum Karlsruhe
D-76344 Eggenstein-Leopoldshafen 2

GREECE
Hellenic Air Force
Air War College
Scientific and Technical Library
Dekelia Air Force Base
Dekelia, Athens TGA 1010

ICELAND
Director of Aviation
c/o Flugrad
Reykjavik

ITALY
Aeronautica Militare
Ufficio del Delegato Nazionale all'AGARD
Aeroporto Pratica di Mare
00040 Pomezia (Roma)

LUXEMBOURG
See Belgium

NETHERLANDS
Netherlands Delegation to AGARD
National Aerospace Laboratory, NLR
P.O. Box 90502
1006 BM Amsterdam

NORWAY
Norwegian Defence Research Establishment
Attn: Biblioteket
P.O. Box 25
N-2007 Kjeller

PORTUGAL
Estado Maior da Força Aérea
SDFA - Centro de Documentação
Alfragide
2700 Amadora

SPAIN
INTA (AGARD Publications)
Carretera de Torrejón a Ajalvir, Pk.4
28850 Torrejón de Ardoz - Madrid

TURKEY
Millî Savunma Başkanliği (MSB)
ARGE Dairesi Başkanliği (MSB)
06650 Bakanliklar-Ankara

UNITED KINGDOM
Defence Research Information Centre
Kentigern House
65 Brown Street
Glasgow G2 8EX

UNITED STATES
NASA Center for AeroSpace Information (CASI)
800 Elkridge Landing Road
Linthicum Heights, MD 21090-2934

SALES AGENCIES

NASA Center for AeroSpace Information (CASI)
800 Elkridge Landing Road
Linthicum Heights, MD 21090-2934
United States

The British Library Document Supply Centre
Boston Spa, Wetherby
West Yorkshire LS23 7BQ
United Kingdom

Requests for microfiches or photocopies of AGARD documents (including requests to CASI) should include the word 'AGA and the AGARD serial number (for example AGARD-AG-315). Collateral information such as title and publication dat desirable. Note that AGARD Reports and Advisory Reports should be specified as AGARD-R-nnn and AGARD-AR- respectively. Full bibliographical references and abstracts of AGARD publications are given in the following journals:

Scientific and Technical Aerospace Reports (STAR)
STAR is available on-line at the following uniform
resource locator:
    http://www.sti.nasa.gov/Pubs/star/Star.html
STAR is published by CASI for the NASA Scientific
and Technical Information (STI) Program
STI Program Office, MS 157A
NASA Langley Research Center
Hampton, Virginia 23681-0001
United States

Government Reports Announcements & Index (GRA
published by the National Technical Information Servic
Springfield
Virginia 22161
United States
(also available online in the NTIS Bibliographic
Database or on CD-ROM)

Printed by Canada Communication Group Inc.
(A St. Joseph Corporation Company)
45 Sacré-Cœur Blvd., Hull (Québec), Canada K1A 0S7

ISBN 92-836-0049-5